COMPUTATIONAL GEOMECHANICS
COMGEO II

INTERNATIONAL CENTRE FOR COMPUTATIONAL ENGINEERING (IC ^{2}E) – Proceedings, State-of-the-Art-Books and Monographs in Engineering Sciences

PROCEEDINGS OF THE 2nd INTERNATIONAL SYMPOSIUM ON COMPUTATIONAL GEOMECHANICS (COMGEO II), Cavtat-Dubrovnik, 27-29 April, 2011

Computational Geomechanics
COMGEO II

Editors

S. Pietruszczak
McMaster University, Hamilton, Canada
G.N. Pande
Swansea University, Swansea, UK

IC²E Rhodes, Greece

IC^2E International Centre for Computational Engineering (IC^2E) is a 'not for profit' organisation registered as an educational institution in the Aegean island of Rhodes, Greece.

Cover designed and CD duplicated in England by Information Press Ltd., Oxford, U.K.
Published by: ***IC^2E*** International Centre for Computational Engineering
Ethnarhou Makariou Str.
Rhodes 85100, Greece

ISBN: 978-960-98750-1-1 (CD ROM)

Table of Contents

1.2 Modelling of instabilities and localized deformation

Multiscale approach for granular materials including an intermediate scale
F. Nicot & F. Darve

Modelling the onset of rainfall-induced landslides
G. Buscarnera & C. di Prisco

A discrete element analysis of collapse mechanisms in granular materials
F. Nicot, N. Hadda, F. Bourrier, L. Sibille & F. Darve

Discrete simulations of shear zone pattern in earth pressure problems
L. Widulinski & J. Tejchman

Dynamic strain localization analysis of elasto-viscoplastic soil using updated Lagrangian finite element formulation
M. Mirjalili, B. Shahbodagh Khan, F. Oka & S. Kimoto

Comparison of distribution functions for the non-local strain approach
H. P. Jostad & G. Grimstad

Microstructural evolution in diffuse granular failure: force chains and contact cycles
A. Tordesillas, L. Sibille, S. Pucilowski, F. Nicot & F. Darve

1.3 Numerical modeling of laboratory tests; identification of material parameters

Simulating particle breakage and relative humidity effects in rockfill behaviour
E.E. Alonso, M. Tapias & J. Gili

Estimating the three-dimensional strengths of sands and clays from a single test
P. V. Lade

Delayed increase in cone penetration resistance of sand after dynamic compaction
R.L. Michalowski & S.S. Nadukuru

Discrete element modeling of stress conditions in unstable soil
M.F. Ahlinhan & M. Achmus

A study of the effects of suction and roughness on the mechanical behaviour of rock joins
M.T. Zandarin, E. Alonso & S. Olivella

Response of virtual granular specimens to undrained compression following different preconsolidation histories
S.A. Galindo-Torres, S. Fortuna & D.J. Williams

Conditional simulation for characterising the spatial variability of sand state
A. P. van den Eijnden & M. A. Hicks

DEM modelling of the shear behaviour of rock joints
C. Lambert & C. Coll

Analysis of soil-structure interaction problems involving a large number of loading cycles
J.P. Cao, H. Mroueh & S. Burlon

A model of confined comminution for granular materials
C. Ovalle & C. Dano

2 Numerical algorithms: formulation and performance

3 Modelling of transient thermo-hydro-chemo-mechanical problems

4 Application of numerical techniques

4.1 Foundations; piles, anchors

4.2 Slopes and embankments

4.3 Other applications

Preface

Over the last few decades a rapid progress has been made in many areas of computational geomechanics and a broad spectrum of software is now available to the engineer. As a result, the number of applications of numerical methods for the solution of complex geotechnical engineering problems has increased enormously and now forms a part of accepted engineering practice.

Following the success of the first Symposium on "Computational Geomechanics" (ComGeo I) held in Nice, France, the second Symposium was held at Cavtat-Dubrovnik, 27 – 29 April, 2011. ComGeo series of Symposia is a sequel to NUMOG series of symposia "Numerical Models in Geomechanics" which was launched in 1982 and included 10 international meetings that were organized over a period of 25 years. These meetings were held in various European countries (Switzerland, Belgium, UK, Austria, Italy, Greece) as well as in North America (Niagara Falls, Montreal and Ottawa, Canada). Each meeting had a limited number of participants and the focus was on preserving a high technical standard as well as an informal style. The ComGeo series is aimed to maintain the same format, however, the scope of this series is supposed to be much broader to include new areas, such as petroleum and mining engineering, geophysiscs, geo-environmental engineering, etc. The main objective of ComGeo is to provide a forum for engineers, researchers and students to exchange views and present their most recent contributions in the area of computational geomechanics.

The proceedings of ComGeo II on this CD-ROM contain approx. 100 papers, which were selected for presentation at the Symposium. The choice of papers was made on the basis of more than 160 abstracts offered. Unfortunately, we had to decline some fully completed papers due to technical deficiencies. Accepted papers are organized in four major sections:

1. *Constitutive relations for geomaterials*
2. *Numerical algorithms: formulation and performance*
3. *Modelling of transient thermo-hydro-chemo-mechanical problems*
4. *Application of numerical techniques to practical problems*

The proceedings include many papers written by internationally recognized experts in their respective fields and all papers are of a high international standard. All papers included here will be archived in a downloadable form in the e-Library of the International Centre for Computational Engineering (IC^2E) in Rhodes, Greece (http://www.ic2e.org), for wider dissemination.

We are grateful to the members of the Technical Advisory Committee, for their co-operation and helpful suggestions.

S. Pietruszczak
G N Pande
C Tamagnini
R Wan

March 2011

TOWARDS MODELLING OF STATIC LIQUEFACTION OF SATURATED LOOSE SAND

R.R. de Jager
Royal Boskalis Westminster nv, Papendrecht, The Netherlands; Faculty of Civil Engineering and Geosciences, Delft University of Technology, Delft, The Netherlands

L.C.H. Braakenburg, M.A. Hicks, F. Molenkamp
Faculty of Civil Engineering and Geosciences, Delft University of Technology, Delft, The Netherlands

ABSTRACT: *This paper describes results of on-going research on the initiation of static liquefaction of saturated loose sand and the subsequent post-stability flow. The presented results concern the modelling of the change of void ratio during monotonically increasing deviatoric deformation towards the critical state. A frictional elasto-plastic model is developed with both the mean effective stress and the void ratio as state parameters. One main classical modelling characteristic concerns the application of the stress-dilatancy theory. Another novel characteristic involves the description of the "remoulding" towards the critical state. The combined formulation results in hardening due to contractant remoulding of initially loose sands and post-peak softening due to dilatant remoulding for initially dense sands. Consequently for any monotonically increasing deviatoric deformation and any initial void ratio a critical state is always reached. With this formulation not only static liquefaction, but also post-stability flow should be modelled appropriately.*

1 INTRODUCTION

The presented research aims at the modelling of the initiation of static liquefaction and subsequent post-stability flow of submerged slopes composed of saturated loose sands, e.g. as triggered by steepening by erosion. For the computational modelling of such natural phenomena an appropriate constitutive model is needed for the sand behaviour, describing not only the occurrence of (undrained) instability, but also the post-stability liquefied flow, both as observed in laboratory specimens and physical model testing.

In engineering practice the concept of "State Parameter" (Been, Jefferies, 1985; Jefferies, Been, 2006) has been shown to be versatile for quantifying the possible occurrence of undrained instability of static liquefaction of saturated sands, not least due to the apparent correlation with the in-situ density as estimated based on measured cone penetration resistance. This "State Parameter" is expressed by the scalar variable quantifying the difference between the current void ratio e_v and the critical void ratio e_v^{cs} at the current mean effective stress, namely

$$\psi = e_v - e_v^{cs} \tag{1}$$

This paper describes the modelling of the change of the void ratio of sands during monotonically increasing deviatoric deformation towards the critical state in a way compatible with this "State Parameter" concept.

In this study a frictional elasto-plastic model is developed with two state parameters, namely the void ratio and the mean effective stress. One classical main characteristic of this constitutive model concerns a relation between the rates of volume change and deviatoric deformation according to the stress-dilatancy theory (Rowe, 1962, 1971; De Josselin de Jong, 1976). The second more novel characteristic concerns a description of the remoulding resistance towards the critical state, involving a relation between the mean effective stress, the deviatoric stress and the void ratio. In particular the latter has been missing in similarly aiming developments in the literature (Muir Wood et al., 1994, Wan & Guo, 1998, Li, 2002, Yao et al., 2004). For monotonically increasing deviatoric deformation of initially loose sands the combined formulation results in hardening due to contractant remoulding towards the critical state. Furthermore, for initially dense sands the post-peak softening towards the critical state is considered to occur due to dilatant remoulding.

However for dilatant material states localization of deformation usually occurs as shear bands tend to develop and subsequent plastic deformation remains mainly limited to the shear bands (Desrues et al., 1996). In such cases the globally observed post-peak softening of the whole specimen seems more brittle than of the actual uniformly deforming material in the shear bands (e.g. Hall et al., 2010), depending a.o. on the ratio of the applied specimen size and the mean grain size. Unfortunately this phenomenon of shear band formation in dense sands also implies that, for proper experimental validation of the softening aspect of the constitutive model, micro-mechanical testing and observations may be indispensable.

Nevertheless, combining the concepts of stress-dilatancy and remoulding resistance in the frictional elasto-plastic model guarantees that, for any monotonically increasing type of uniform deviatoric deformation, a critical state is always reached. This formulation is expected not only to enable the appropriate simulation of static liquefaction, but also the subsequent post-stability liquefied flow.

2 SURFACE OF REMOULDING RESISTANCE

For the considered constitutive model, first the existence of a surface of remoulding resistance is postulated. This surface of remoulding resistance is considered to be approached gradually for any drained proportional deviatoric deformation with fixed principal strain directions and at any constant mean effective stress, producing correspondingly fixed principal directions of effective stress. However, for simultaneously rotating principal strain directions different surfaces of remoulding resistance may be expected (Lade et al., 2008).

For fixed principal strain directions the surface of remoulding resistance is a function of the principal effective stresses $\boldsymbol{\sigma}^{(k)}$ $\left(k=1,2,3\right)$, the void ratio e_v and the plastic deviatoric strain e^p for a sufficiently large magnitude, e.g. $e^p >> 1$. Consequently this surface is

formally described by a function of the form $f\left(\sigma^{(k)}, e_v\right) = 0$. Such a surface of remoulding resistance is illustrated in figure 1 for drained purely deviatoric triaxial compression at constant mean effective stress. For this frictional material model the maximum remoulding resistance is expressed in terms of the deviatoric stress level $\left(T/S\right)\Big|^p$, involving both the principal deviatoric stress vector in principal stress space, directed in the π-plane with scalar magnitude T, and the principal isotropic effective stress vector along the space diagonal in principal stress space with scalar magnitude S. These magnitudes are expressed in terms of the axial and radial effective stresses σ_a and σ_r respectively by

$$T = \left(\sigma_a - \sigma_r\right)\sqrt{\frac{2}{3}}; \qquad S = \left(\sigma_a + 2\sigma_r\right)\sqrt{\frac{1}{3}} \tag{2}$$

Similar types of deviatoric and isotropic quantities in principal strain space can be expressed for triaxial strain rates based on the axial and radial plastic strain rates $\dot{\varepsilon}_a^p$ and $\dot{\varepsilon}_r^p$ respectively. Then the magnitudes of the deviatoric and isotropic strain rates are respectively

$$\dot{e}^p = \left(\dot{\varepsilon}_a^p - \dot{\varepsilon}_r^p\right)\sqrt{\frac{2}{3}}; \qquad \dot{v}^p = \left(\dot{\varepsilon}_a^p + 2\dot{\varepsilon}_r^p\right)\sqrt{\frac{1}{3}} \tag{3}$$

Then the scalar plastic deviatoric strain e^p is obtained by integration in time. Figure 1 illustrates a decreasing remoulding resistance with increasing void ratio e_v.

3 SURFACE OF ZERO-DILATANCY

In figure 1 a zero-dilatancy surface (Rowe, 1962, 1971) for triaxial compression is also illustrated, considering the mobilised friction level at zero-dilatancy to increase from zero at zero void ratio e_v to reach its maximum value at a void ratio around $e_v \approx 1$. It may be noted that, for the experimental determination of the zero-dilatancy surface, standard macroscopic laboratory tests on sand specimens may suffice because shear band generation will usually occur at effective stress states above this surface. However for the determination of the surface of remoulding resistance, due to the occurrence of shear bands microscopic specimens and measurement methods (e.g. Hall et al., 2010) may be necessary.

The intersection point of the surfaces of remoulding resistance and zero-dilatancy concerns the critical state. This is understood by considering that on the left side of this intersection point the remoulding resistance occurs above the zero-dilatancy surface; thus it involves dilation during continuing distortion, inducing loosening due to dilation and thus an increasing void ratio. On the other hand, on the right hand side of the intersection point the surface of remoulding resistance occurs below the zero-dilatancy surface, thus inducing contraction during continuing distortion until a state of constant volume is reached at the intersection point, which is completely consistent with the definition of the critical state.

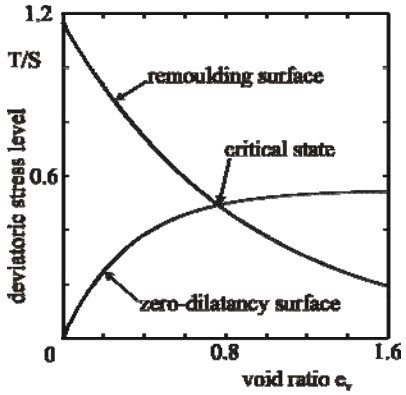

Figure 1. Illustration of remoulding and zero-dilatancy surfaces with their "critical state" intersection point.

4 CRITICAL STATE CURVE

The critical state curve shows the dependence of the critical void ratio e_v^{cs} on the isotropic stress level S/p_a as illustrated in figure 2. This relation is approximated by the following expression, namely

$$e_v^{cs} = f\left(\frac{S}{p_a}\right) = \left(1+e_{v0}^{cs}\right)\exp\left\{-C^*\left(\frac{S}{p_a}\right)^{C^p}\right\} - 1 \tag{4}$$

Table 1. Mathematical and physical material parameters.

Parameter	Equation number	Mathematical	Physical ($S/p_a = \sqrt{3}$)
e_{v0}^{cs}	(4)	0.82	
C^*	(4)	0.026	
C^p	(4)	0.3	
e_v^{cs} for $S/p_a = \sqrt{3}$	(4)		0.765
$(T/S)\big\vert^{cs}$	(10)		0.492
E^e	(21)	0.0025	
E^p	(21)	4.2	
m	(25)	3.0	
M^p	(5), (11)	1.168	
β	(5), (12)	1.13	
Slope	(12)		-1.13
C^μ	(7), (11)	0.547	
ς^μ	(7)	3.00	
Slope	(13)		0.336

For the illustration in figure 2 the following parameter values have been applied, namely $e_{v0}^{cs} \approx 0.82$, $C^* \approx 0.026$ and $C^p \approx 0.3$. All soil parameters are collected in table 1.

To demonstrate the effects of the combined concepts of stress-dilatancy and remoulding resistance, a series of numerical simulations of drained purely deviatoric triaxial compression with monotonically increasing deviatoric plastic strain will be considered later in this paper. These simulations will be done for a range of initial void ratios, namely $0.4 \le e_{vi} \le 1.1$, and a constant isotropic effective stress level $S/p_a = \sqrt{3}$, where p_a is the mean atmospheric pressure and $p_a \approx 100$ kPa. These initial states are also indicated in figure 2.

It is noted that for the above-mentioned parameter values and the isotropic effective stress level $S/p_a = \sqrt{3}$ the corresponding critical void ratio e_v^{cs} according to (4) reads $e_v^{cs} \approx 0.765$, which is represented by the intersection point of both curves in figure 2.

5 FORMULATION OF SURFACES

For the considered cases of triaxial compression in figure 1, the deviatoric stress level $(T/S)\big|^p$ of the surface of remoulding resistance at $S/p_a = \sqrt{3}$ is related to the void ratio e_v by

$$\left(\frac{T}{S}\right)\Big|^p = M^p \exp\left(-\beta^p e_v\right) \tag{5}$$

with model parameters M^p and β^p. Then for the slope of the remoulding surface in the direction of void ratio it follows that

$$\frac{d\left((T/S)\big|^p\right)}{de_v} = -\beta^p M^p \exp\left(-\beta^p e_v\right) = -\beta^p \frac{T}{S}\Big|^p \tag{6}$$

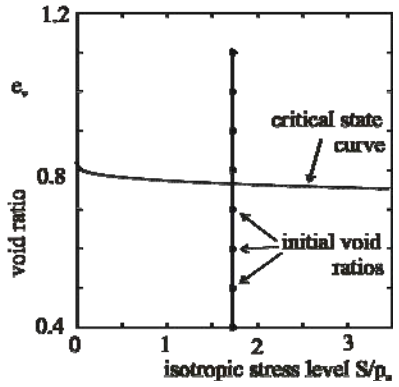

Figure 2. Illustration of critical state curve and the considered range of initial void ratios e_v at isotropic stress level $S/p_a = \sqrt{3}$.

The corresponding relation between the deviatoric stress level $\left(T/S\right)\Big|^{\mu}$ for zero-dilatancy and the void ratio e_v, illustrated in figure 1, reads

$$\frac{T}{S}\Big|^{\mu} = C^{\mu}\left(1-\exp\left(-\varsigma^{\mu}\, e_v\right)\right) \tag{7}$$

with model parameters C^{μ} and ς^{μ}. Then for the slope of the zero-dilatancy surface in the direction of void ratio it follows that

$$\frac{d\left((T/S)\Big|^{\mu}\right)}{de_v} = \varsigma^{\mu} C^{\mu} \exp\left(-\varsigma^{\mu}\, e_v\right) \tag{8}$$

6 PARAMETER DETERMINATION BASED ON CRITICAL STATE

Equations The critical state is reached at the intersection of the surfaces of remoulding resistance and zero-dilatancy, at the critical state void ratio $e_v = e_v^{cs}$ and deviatoric stress level

$$\frac{T}{S}\Big|^{cs} = \frac{T}{S}\Big|^{p} = \frac{T}{S}\Big|^{\mu} \tag{9}$$

Then at the intersection point from (5) and (7) the following relation follows, namely

$$\frac{T}{S}\Big|^{cs} = M^{p} \exp\left(-\beta^{p} e_v^{cs}\right) = C^{\mu}\left(1-\exp\left(-\varsigma^{\mu}\, e_v^{cs}\right)\right) \tag{10}$$

from which it follows for the parameters M^{p} and C^{μ} that

$$M^{p} = \frac{(T/S)\Big|^{cs}}{\exp\left(-\beta^{p} e_v^{cs}\right)}; \qquad C^{\mu} = \frac{(T/S)\Big|^{cs}}{1-\exp\left(-\varsigma^{\mu}\, e_v^{cs}\right)} \tag{11}$$

The expressions (11) show that parameters M^{p} and C^{μ} can be derived based on the observed deviatoric stress level of the critical state $\left(T/S\right)\Big|^{cs}$ if the parameters β^{p} and ς^{μ} are known. Furthermore from (6) the parameter β^{p} can be expressed in terms of the ratio of the slope $\left(d\left(T/S\right)\Big|^{p} / de_v\right)\Big|^{cs}$ of the remoulding surface at the critical state and the deviatoric stress level $\left(T/S\right)\Big|^{cs}$ at the critical state, namely

$$\frac{d\left((T/S)\big|^{p}\right)\Big|^{cs}}{de_v} = -\beta^{p}\left.\frac{T}{S}\right|^{cs} \quad \Rightarrow \quad \beta^{p} = -\frac{\dfrac{d\left((T/S)\big|^{p}\right)\Big|^{cs}}{de_v}}{(T/S)\big|^{cs}} \tag{12}$$

Similarly, based on (8) and (11) for the ratio of the slope $\left(d\left(T/S\right)\big|^{\mu}/de_v\right)\Big|^{cs}$ of the zero-dilatancy surface at the critical state and the deviatoric stress level $\left(T/S\right)\big|^{cs}$ at the critical state, it follows that

$$\frac{\dfrac{d\left((T/S)\big|^{\mu}\right)\Big|^{cs}}{de_v}}{(T/S)\big|^{cs}} = \frac{\varsigma^{\mu}\exp\left(-\varsigma^{\mu}\,e_v^{cs}\right)}{1-\exp\left(-\varsigma^{\mu}\,e_v^{cs}\right)} \tag{13}$$

In principle from (12) and (13) parameters β^{p} and ς^{μ} can also be derived if the left slope terms are known, based on experimental data.

When applying (7) and the last expression of (10) the deviatoric stress level at zero-dilatancy $\left(T/S\right)\big|^{\mu}$ can also be expressed with respect to the critical state resistance $\left(T/S\right)\big|^{cs}$ and critical void ratio e_v^{cs} at the same isotropic stress level S/p_a by

$$\left.\frac{T}{S}\right|^{\mu} = \left.\frac{T}{S}\right|^{cs} - C^{\mu}\left\{\exp\left(-\varsigma^{\mu}\,e_v\right) - \exp\left(-\varsigma^{\mu}\,e_v^{cs}\right)\right\} \tag{14}$$

This relative form has similarities to the formulation using "State Parameter" ψ (1) (Been, Jefferies, 1985; Jefferies, Been, 2006). Applying this relative form also for the remoulding resistance $\left(T/S\right)\big|^{p}$ gives

$$\left.\frac{T}{S}\right|^{p} = \left.\frac{T}{S}\right|^{cs} + M^{p}\left\{\exp\left(-\beta^{p}e_v\right) - \exp\left(-\beta^{p}e_v^{cs}\right)\right\} \tag{15}$$

7 STRESS-DILATANCY FOR TRIAXIAL COMPRESSION

The relation between the increments of the void ratio de_v and the plastic volumetric strain $d\varepsilon_{vol}^{p}$ reads, when applying the sign conventions of continuum mechanics with stretching, tension and thus dilation positive

$$de_v = \left(1+e_v\right)d\varepsilon_{vol}^{p} \tag{16}$$

The increment of the plastic volumetric strain $d\varepsilon_{vol}^{p}$ is related to the scalar norm de^{p} of the incremental plastic deviatoric strain by

$$d\varepsilon_{vol}^{p} = \sqrt{3}\, dv^{p} = 3\alpha\, de^{p} \quad \Rightarrow \quad \alpha = \frac{1}{\sqrt{3}} \frac{dv^{p}}{de^{p}} \tag{17}$$

in which the principal incremental isotropic plastic strain vector along the space diagonal in principal strain space has scalar magnitude dv^{p} and the scalar α is quantified by the application of the stress-dilatancy theory (Rowe, 1962, 1971), which expresses the dilatancy ratio dv^{p}/de^{p}. When applying the sign-convention of continuum mechanics the dilatancy ratio dv^{p}/de^{p} for triaxial compression (Molenkamp, 1983) is expressed by

$$\frac{dv^{p}}{de^{p}} = -\left[\frac{2\sqrt{2}\sin\phi_{\mu} - (3 - \sin\phi_{\mu})(T/S)}{(3 + \sin\phi_{\mu}) - 2\sqrt{2}\sin\phi_{\mu}(T/S)} \right] \tag{18}$$

In the concept of the zero-dilatancy surface the friction angle ϕ_{μ} at zero-dilatancy is considered to be a function of both the void ratio e_{v} and the isotropic stress level S/p_{a}. This friction angle ϕ_{μ} is related to the deviatoric stress level $(T/S)\big|^{\mu}$ at zero-dilatancy by

$$\frac{T}{S}\bigg|^{\mu} = \frac{2\sqrt{2}\sin\phi_{\mu}}{(3 - \sin\phi_{\mu})} \quad \Leftrightarrow \quad \sin\phi_{\mu} = \frac{3(T/S)\big|^{\mu}}{2\sqrt{2} + (T/S)\big|^{\mu}} \tag{19}$$

Then substitution of (17) in (16) leads to the relation between the incremental plastic deviatoric strain de^{p} and the increment of the void ratio de_{v} as expressed by

$$de_{v} = (1 + e_{v})\, d\varepsilon_{vol}^{p} = (1 + e_{v})\sqrt{3}\, dv^{p} = (1 + e_{v})3\alpha\, de^{p} \tag{20}$$

8 DEVIATORIC STRESS-PLASTIC STRAIN RELATION

For the initial plastic hardening phase of triaxial compression the following deviatoric stress-deviatoric plastic strain relation is applied (Molenkamp, 1983), namely

$$e^{p} = E^{e}\left(\frac{T}{S}\bigg|^{0} \right)^{E^{p}} \quad \Leftrightarrow \quad \frac{T}{S}\bigg|^{0} = \left(\frac{e^{p}}{E^{e}} \right)^{\frac{1}{E^{p}}} \tag{21}$$

for which the applied values of parameters E^{e} and E^{p} are indicated in table 1. From (17) follows for the incremental relation between the deviatoric stress level $(T/S)\big|^{0}$ of the initial hardening phase and the plastic deviatoric strain e^{p}

$$\frac{d\left((T/S)\big|^{0}\right)}{de^{p}} = \frac{T}{S}\Big|^{0}\,\frac{1}{E^{p}\,e^{p}} = \frac{1}{E^{p}\,E^{e}}\left(\frac{T}{S}\Big|^{0}\right)^{1-E^{p}} \tag{22}$$

After large deviatoric distortion in triaxial compression the remoulding resistance $(T/S)\big|^{p}$ (15) is approached. Differentiation of (15) with respect to the void ratio e_v for constant isotropic stress level S/p_a gives

$$\frac{d\left((T/S)\big|^{p}\right)}{de_v} = -\beta^{p}\,M^{p}\exp\left(-\beta^{p}e_v\right) \tag{23}$$

Combining (20) and (23) gives an incremental relation between the deviatoric stress level $(T/S)\big|^{p}$ and the plastic deviatoric strain e^{p}, namely

$$\frac{d\left((T/S)\big|^{p}\right)}{de^{p}} = \frac{d\left((T/S)\big|^{p}\right)}{de_v}\frac{de_v}{de^{p}} = 3\left(1+e_v\right)\alpha\,\beta^{p}\,M^{p}\exp\left(-\beta^{p}e_v\right) \tag{24}$$

At this stage the incremental relations between on one hand the deviatoric stress levels for both the initial plastic hardening phase $(T/S)\big|^{0}$ (22) and the remoulding resistance after large deviatoric deformation $(T/S)\big|^{p}$ (23) and on the other the plastic deviatoric strain e^{p} for purely deviatoric loading in triaxial compression at constant isotropic stress level S/p_a have been formulated. Next the combined incremental plastic deviatoric stress-strain relation is composed. To this end first for any deviatoric plastic strain e^{p} the combined deviatoric stress level T/S can be expressed by

$$\frac{T}{S} = \frac{(T/S)\big|^{0}\;(T/S)\big|^{p}}{\left(\left((T/S)\big|^{0}\right)^{m} + \left((T/S)\big|^{p}\right)^{m}\right)^{\frac{1}{m}}} \tag{25}$$

in which the weighting power m is larger than unity. Based on some experimental data this weighting power m is estimated at roughly $m \approx 3.0$. Furthermore, it may be noted that in (25) T/S describes the yield surface as function of the stresses for purely deviatoric loading in triaxial compression, while its right-hand side quantities concern functions of the corresponding plastic deviatoric deformation.

Based on (25) the following relation between the increments of the deviatoric stress level $d(T/S)$ and plastic deviatoric strain de^{p} for purely deviatoric loading in triaxial compression at constant isotropic stress level S/p_a is derived, namely

$$\frac{d\left((T/S)\right)}{de^p}=\frac{d\left[\dfrac{(T/S)\big|^0\ (T/S)\big|^p}{\left(\left((T/S)\big|^0\right)^m+\left((T/S)^p\right)^m\right)^{\frac{1}{m}}}\right]}{d\left((T/S)^0\right)}\ \frac{d\left((T/S)\big|^0\right)}{de^p}+\frac{d\left[\dfrac{(T/S)\big|^0\ (T/S)\big|^p}{\left(\left((T/S)^0\right)^m+\left((T/S)\big|^p\right)^m\right)^{\frac{1}{m}}}\right]}{d\left((T/S)\big|^p\right)}\ \frac{d\left((T/S)\big|^p\right)}{de^p} \tag{26}$$

in which $d\left(T/S\right)\big|^0/de^p$ and $d\left(T/S\right)\big|^p/de^p$ are described by (22) and (24) respectively and the other terms can be elaborated by differentiation. Finally substituting (15) and (24) in (26) gives the required expression relating the increment of the deviatoric stress level $d\left(T/S\right)$ to the increment of the plastic deviatoric strain de^p, namely

$$\begin{aligned}\frac{d(T/S)}{de^p}=&\frac{\left((T/S)\big|^p\right)^{m+1}}{\left(\left((T/S)\big|^0\right)^m+\left((T/S)\big|^p\right)^m\right)^{\frac{1}{m}+1}}\ \frac{1}{E^p\,E^e}\left(\frac{T}{S}\Big|^0\right)^{1-E^p}+..\\ ..+&\frac{\left((T/S)\big|^0\right)^{m+1}}{\left(\left((T/S)\big|^0\right)^m+\left((T/S)\big|^p\right)^m\right)^{\frac{1}{m}+1}}\ 3\left(1+e_v\right)\alpha\,\beta^p\,M^p\exp\left(-\beta^p e_v\right)\end{aligned} \tag{27}$$

9 DEMONSTRATION OF MODEL CAPABILITIES

The frictional elasto-plastic material model (27), combining the concepts of remoulding resistance (15) and zero-dilatancy (18), has been elaborated for purely deviatoric triaxial compression at constant isotropic stress level S/p_a. For any initial void ratio e_{vi} and any isotropic stress level S/p_a this model (27) describes an increment of the deviatoric stress level $d\left(T/S\right)$ as a function of an increment of plastic deviatoric strain de^p.

In this section the capabilities of this constitutive model are demonstrated by means of various calculated results for drained purely deviatoric triaxial compression, to reach the critical state for monotonically increasing purely deviatoric large plastic deformation at the ultimate state of monotonic deviatoric plastic flow.

Figure 3 illustrates the paths of deviatoric stress level T/S versus void ratio e_v, starting from the same isotropic effective stress state with $S/p_a=\sqrt{3}$ and for a range of initial void ratios e_{vi}, namely $0.4\le e_{vi}\le 1.1$. In the initial phase of deviatoric deformation the plastic deviatoric strain e^p is expressed by (21). The corresponding change of the void ratio e_v is calculated using the stress-dilatancy theory as expressed by (17), (18) and (20). Figure 3 illustrates that, for the applied scale of the void ratio, the change of void ratio is hardly observable as the paths are practically vertical.

When the paths approach the surface of remoulding resistance, rather than intersecting this surface the paths start to bend gradually towards this surface. This characteristic of gradual approach is achieved by the application of (25) in combination with (27), but becomes less gradual with increasing weighting parameter $m >> 1$. For figure 3 $m = 3$ has been used.

When approaching the surface of remoulding resistance even further, the increasing plastic deviatoric deformation causes decreasing changes of the deviatoric stress level T/S as governed by the local slope of the surface. However the effect of the corresponding change of the void ratio as expressed by the dilatancy theory (18) remains as active, causing the paths to proceed towards the critical state, where the plastic dilation rate becomes zero, while the monotonically increasing purely plastic deviatoric deformation can continue.

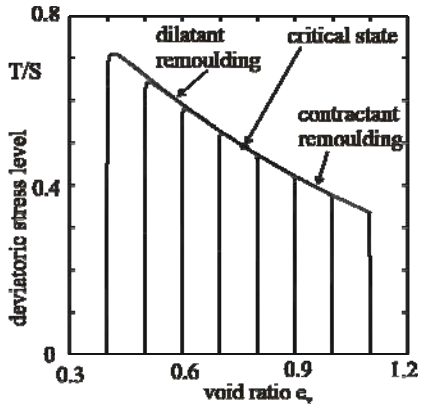

Figure 3. Calculated paths of deviatoric stress level T/S and void ratio e_v towards the critical state for drained purely deviatoric triaxial compression with monotonically increasing deviatoric deformation at constant isotropic stress level $S/p_a = \sqrt{3}$ for a series of initial void ratios $0.4 \le e_{vi} \le 1.1$.

The corresponding relation between the deviatoric stress level T/S and the plastic deviatoric strain e^p is shown in figure 4. All stress-strain paths are shown to approach the same critical state, reaching it at very large plastic flow. For the considered initial states looser than critical, the critical state is approached by plastic contraction along the contractant part of the surface of remoulding resistance. This plastic contraction induces the monotonic plastic hardening as illustrated in figure 4 for the considered large initial void ratios: $e_{vi} \ge 0.8$. On the other hand, for the initial small void ratios $e_{vi} \le 0.7$ peaks are shown to occur in the deviatoric stress-plastic strain paths, like also observed experimentally. Subsequently gradual softening is simulated, which may be much more elongated than observed experimentally when considering element testing. This difference has been explained before to be due to the actual occurrence of shear band generation, in which case the plastic deformation becomes mainly limited to within the shear bands (e.g. Hall et al., 2010).

Figure 5 depicts the calculated paths of the plastic dilatancy ratio dv^p/de^p and the deviatoric stress level T/S. It is noted that the left part concerns contraction and the right dilation. The inclined lines from contraction towards dilation are based on the stress-dilatancy

(18). These inclined stress-dilatancy lines reach their upper limits on a curve fully related to the surface of remoulding resistance.

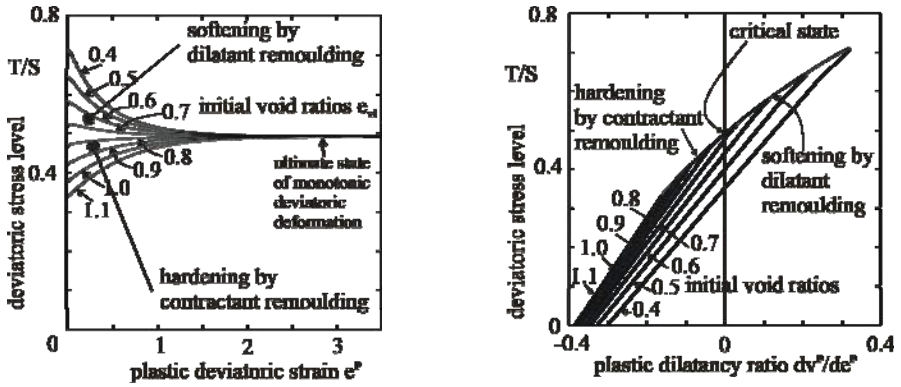

Figures 4 and 5. Calculated relations between deviatoric stress level T/S and plastic deviatoric strain e^p (figure 4) and plastic dilatancy ratio dv^p/de^p (figure 5) respectively, towards the critical state for drained purely deviatoric triaxial compression with monotonically increasing deviatoric deformation at constant isotropic stress level $S/p_a = \sqrt{3}$ for a series of initial void ratios $0.4 \le e_{vi} \le 1.1$.

For the initially dense void ratios $e_{vi} \le 0.7$ this upper limit concerns softening by dilatant remoulding, while for the initially loose void ratios $e_{vi} \ge 0.8$ along the upper limit hardening by contractant remoulding occurs. Both parts of the upper limit curve carry the paths to the critical state.

All material parameters have been collected in table 1. Apart from the respective equation numbers for their definition, two types of material parameters are indicated; namely the parameters as occurring in the mathematical expressions of the model and the more physical parameters, which in the background are affecting the magnitudes of most other mathematical parameters. The determination of the links between both types of parameters and the physical parameters for observed undrained behaviour is the subject of future research.

10 CONCLUSIONS

This paper describes results of on-going research on the initiation of static liquefaction of saturated loose sand and subsequent post-stability flow. A frictional elasto-plastic model has been developed for sands with both the void ratio and the mean effective stress as state parameters. In the model formulation the "critical state" plays a central role. One main classical modelling characteristic concerns the application of the stress-dilatancy theory. Another more novel characteristic involves the description of the "remoulding" towards the critical state. This constitutive model has been demonstrated to enable the simulation of both the initial phase of elasto-plastic contractant and/or dilative behaviour, the monotonic hardening behaviour for initially loose sands, the pre-peak behaviour of initially dense sands

and its subsequent post-peak softening and finally the gradual approach of the critical state for large plastic flow. Consequently for any monotonically increasing deviatoric deformation and any initial void ratio a critical state is always reached. This formulation is expected not only to enable the appropriate simulation of static liquefaction, but also the subsequent post-stability liquefied flow.

To facilitate parameter determination several physical parameters characterizing the critical state have been recognised. The determination of the relations between such physical types of parameters for both drained and undrained behaviour and the model parameters of the mathematical formulation is the subject of future research.

ACKNOWLEDGEMENT

This research is supported by the Dutch Technology Foundation STW, applied science division of NWO, and the Technology Program of the Ministry of Economic Affairs.

REFERENCES

Been, K. & Jefferies, M.G. (1985), "A state parameter of sands", Géotechnique, Vol. 35(2), 99-112.

De Josselin de Jong, G., (1976), "Rowe's stress-dilatancy relation based on friction", Géotechnique, Vol. 26(3), 527-534.

Desrues, J., Chambon, R., Mokni, M., Mazerolle, F., (1996), "Void ratio evolution inside shear bands in triaxial sand specimen studied by computed tomography", Géotechnique, Vol. 46(3), 529-546.

Hall, S.A., Bornert, M., Desrues, J., Pannier, Y., Lenoir, N., Viggiani, G., Bésuelle, P., (2010), "Discrete and continuum analysis of localised deformation in sand using X-ray μCT and volumetric digital image correlation", Géotechnique, Vol. 60(5), 315-322.

Jefferies, M.G. & Been, K. (2006), Soil liquefaction: A critical state approach, Taylor & Francis.

Lade, P.V., Nam, J., Hong, W.P., (2008), "Shear banding and cross-anisotropic behaviour observed in laboratory sand with stress rotation", Can. Geotech. J., Vol. 45, 74-84.

Li, X.S., (2002), "A sand model with state-dependent dilatancy", Géotechnique, Vol. 52(3), 173-186.

Molenkamp, F., (1983), "Elasto-plastic double hardening model MONOT", Delft Soil Mechanics Laboratory, CO-218595, Second revision.

Muir Wood, D., Belkheir, K., Liu, D.F., (1994), "Strain softening and state parameter for sand modeling", Géotechnique, Vol. 44(2), 335-339.

Rowe, P.W. (1962), "The stress-dilatancy relation for static equilibrium of an assembly of particles in contact", Proceedings of the Royal Society A: Mathematical, Physical and Engineering Sciences, Vol. 269, 500-527.

Rowe, P.W. (1971), "Theoretical meaning and observed values of deformation parameters for soil", Proceedings of the Roscoe Memorial Symposium, Cambridge, 143-194.

Wan, R.G., Guo, P.J., (1998), "A simple constitutive model for granular soils: Modified stress-dilatancy approach", Computers and Geotechnics, Vol. 22(2), 109-133.

Yao, Y.P., Sun, D.A., Luo, T., (2004), "A critical state model for sands dependent on stress and density", Int. J. Num. Anal. Methods Geomech., Vol. 28, 323-337.

DISPERSIVE WAVES IN LAYERED ROCK MASSES WITH PERIODIC JOINTED STRUCTURE

A. Bacigalupo, L. Gambarotta
Department of Civil, Environmental and Architectural Engineering, University of Genova, Italy

ABSTRACT: *A procedure for second-order computational homogenization of layered rock masses is derived in order to describe the effect of the material heterogeneities and to include scale effects on the shear wave propagation. The homogenization procedure is based on an appropriate representation of the micro-displacement field in the unit cell which is assumed as the superposition of a local macroscopic displacement field and an unknown micro-fluctuation field accounting for the effects of the heterogeneities. This second contribution is represented as the superposition of two unknown functions that guarantee the continuity of the micro-displacement field. Shear dispersive waves are obtained in a layered rock mass and in a damaged layered rock mass with periodic discontinuity planes in the stiffer layer. The obtained results differ from the corresponding ones resulting from standard Cauchy homogenization.*

1 INTRODUCTION

It is well known that the behaviour of a rock mass depends not only on the properties of the intact rock but also on the joints behaviour and distribution, i.e. their spacing, length, condition, orientation, continuity and the number of joint sets (Sayers and Kachanov, 1995). Moreover, the number of joints in a rock mass is so large that dealing with each joint individually turns out to be computationally very expensive and equivalent continuum models obtained through homogenization techniques are in most cases preferred. Nevertheless, when the spacing of the joints is of the same order of magnitude as the excavation dimensions, i.e. in condition of blocky rock (Hoeck *et al*, 1989), the influence of block size cannot be ignored and internal lengths have to be included in the continuum model to consider scale effects through the implementation of non-local homogenization procedures. In dynamic problems scale effects are more significant when the wavelength of a travelling signal decreases and become comparable with the characteristic size of the heterogeneities (Stefanou *et al*, 2008).

The paper is focused on this problem with specific reference to blocky rock masses having periodic jointed structure. The second-order computational homogenization procedure for materials with periodic microstructure developed in (Bacigalupo and Gambarotta, 2010) is here derived by considering several joint arrangements and the corresponding representative volume element. The approach is based on a two-scale kinematics, in which a proper representation of the micro-displacement field is assumed as the superposition of a local macroscopic displacement field, expressed in a polynomial form related to the macro-displacement field, and an unknown micro-fluctuation field accounting for the effects of the

heterogeneities. This second contribution is represented as the superposition of two unknown functions each of which related to the first-order and to the second-order strain, respectively. This kinematical micro-macro framework guarantees the compatibility of the micro-displacement field and implies a computationally efficient procedure that applies in two steps. The first step corresponds to the standard homogenization, while the second step is based on the results of the first step and completes the second-order homogenization.

The procedure is applied to the analysis of elastic waves propagation in a periodic blocky mass. A layered rock mass is first analysed where scale effects are more important. Is then analysed the same layered system with vertical discontinuity planes periodically located in the stiffer layer to model the damage of the rock mass. By the solution of the cell problems with properly prescribed boundary conditions, the overall elastic moduli and the characteristic lengths of the second-order equivalent continuum model are obtained on the basis of an enhanced Hill–Mandel condition. Finally, dispersive waves in both the models are analysed in the simple but important case of shear waves and the influence of the wavelength on the wave motion is discussed.

2 MULTI-SCALE IN-PLANE MODELLING OF A PERIODIC BLOCKY ROCK MASS

Let us consider the dynamics of a blocky rock mass having periodic structure as shown in Figure 1.a. If only in-plane loads are envisaged and body forces are neglected, the rock mass may be represented as a plane domain under the simplifying assumption of plane strain condition. The obtained inhomogeneous model is analysed as a Cauchy continuum undergoing small strains and the phases are assumed to behave elastically. The position vector **x** of a material point is denoted by its components (x_1,x_2) with respect to the reference $(0,\mathbf{e}_1,\mathbf{e}_2)$. The periodic continuum is fully characterized by the unit cell, the smallest plane portion that contains all the essential information about the rock mass. In the case of stratified blocky rock masses shown in figure 1.a, the rectangular unit cell $\mathscr{A}=[0,d_1]\times[0,d_2]$ shown in figure 1.b may be assumed, having width d_1 and height d_2. This unit cell is spanned by the two independent orthogonal vectors $\mathbf{v}_1=d_1\mathbf{e}_1$, $\mathbf{v}_2=d_2\mathbf{e}_2$, so that the boundary C of the unit cell is made up of two pairs of opposite sides corresponding to each other by means of a translation along $\mathbf{v}_1$ or $\mathbf{v}_2$. According to this representation, a variable is periodic in the unit cell $\mathscr{A}$, or $\mathscr{A}$-periodic, if it takes identical values at two points on the boundary of the unit cell whose difference is a vector of periodicity. Accordingly, the elasticity tensor $\mathbb{C}^m(\mathbf{x})$ is $\mathscr{A}$-periodic, i.e. $\mathbb{C}^m(\mathbf{x}+\mathbf{v}_i)=\mathbb{C}^m(\mathbf{x})$, i=1,2.

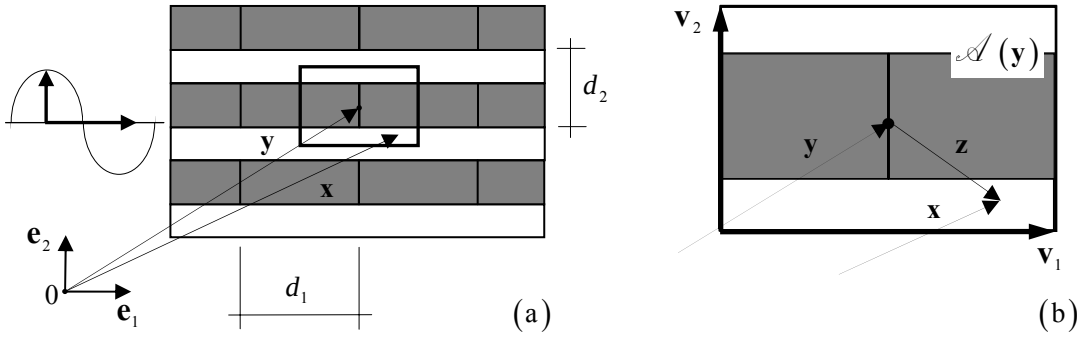

Fig. 1. (a) Blocky rock mass with periodic structure; (b) Unit cell and periodicity vectors.

At the material point $\mathbf{x}$ of the heterogeneous elastic medium the micro-displacement $\mathbf{u}(\mathbf{x},t)$ is considered together with the corresponding micro-strain tensor $\boldsymbol{\varepsilon}(\mathbf{x},t)=sym\nabla_{\mathbf{x}}\mathbf{u}(\mathbf{x},t)$ and the micro-stress tensor $\boldsymbol{\sigma}(\mathbf{x},t)=\mathbb{C}^m(\mathbf{x})\boldsymbol{\varepsilon}(\mathbf{x},t)$ which has to satisfy the local equation of motion $div_{\mathbf{x}}\boldsymbol{\sigma}(\mathbf{x},t)=\rho\ddot{\mathbf{u}}(\mathbf{x},t)$. The resulting set of partial differential equations

$$div_{\mathbf{x}}\left(\mathbb{C}^m(\mathbf{x})\nabla_{\mathbf{x}}\mathbf{u}(\mathbf{x},t)\right)=\rho\ddot{\mathbf{u}}(\mathbf{x},t) \tag{1}$$

has to be solved in terms of the micro-displacement components on the whole rock mass domain with a huge computational burden.

Being the solution of this fine-scale computational approach out of reach, it is convenient to replace the inhomogeneous model of rocky mass by an equivalent homogeneous one so obtaining equations whose coefficients are not rapidly oscillating while their solutions are close to those of the original equations. In general, an equivalent standard (Cauchy) continuum is considered, but in cases for which the unit cell size is non vanishing if compared to the rock mass size or to the wavelength it is convenient to introduce an equivalent second-order continuum model (Mindlin, 1964). This continuum model is defined at the macroscale where the slow varying macroscopic position vector $\mathbf{y}$ is considered and the displacement field $\mathbf{U}(\mathbf{y},t)$ is defined (with component U_i in the assumed reference). The displacement gradient is denoted by $\mathbf{H}(\mathbf{y},t)=\nabla_{\mathbf{y}}\mathbf{U}(\mathbf{y},t)$ and, according to Germain (1973), the strain field in the second gradient continuum is represented by the symmetric first-order strain tensor and by the second-order strain tensor, respectively,

$$\mathbf{E}(\mathbf{y},t)=sym\nabla_{\mathbf{y}}\mathbf{U}(\mathbf{y},t),\qquad \boldsymbol{\kappa}(\mathbf{y},t)=\nabla_{\mathbf{y}}\otimes\nabla_{\mathbf{y}}\mathbf{U}(\mathbf{y},t), \tag{2}$$

the latter being a third-order tensor having components $\kappa_{ijk}=\kappa_{ikj}$ symmetric with respect to j and k.

The stress field is described by the symmetric first-order stress tensor $\boldsymbol{\Sigma}(\mathbf{y},t)$ ($\Sigma_{ij}=\Sigma_{ji}$) and the second-order stress tensor $\boldsymbol{\mu}(\mathbf{y},t)$ (third-order tensor having components $\mu_{ijk}=\mu_{ikj}$ symmetric with respect to j and k). From these stress tensors the real stress is defined as $\mathbf{T}(\mathbf{y},t)=\boldsymbol{\Sigma}(\mathbf{y},t)-Div_{\mathbf{y}}\boldsymbol{\mu}(\mathbf{y},t)$ so that, in general, $\mathbf{T}(\mathbf{y},t)$ is not symmetric. In case of vanishing body forces, the equation of motion is expressed according to Mindlin (1964) in the form

$$Div_{\mathbf{y}}\left(\boldsymbol{\Sigma}(\mathbf{y},t)-Div_{\mathbf{y}}\boldsymbol{\mu}(\mathbf{y},t)\right)=\rho_M\left[\ddot{\mathbf{U}}(\mathbf{y},t)-\left(\nabla_{\mathbf{y}}\otimes\nabla_{\mathbf{y}}\ddot{\mathbf{U}}(\mathbf{y},t)\right)\mathbf{J}\right], \tag{3}$$

being the inertia properties defined by the mass density at the macro-scale ρ_M and the inertia tensor $\mathbf{J}=\int_{\mathcal{A}}\rho\mathbf{y}\otimes\mathbf{y}da\Big/\int_{\mathcal{A}}\rho da$, where ρ is the mass density at the micro-scale. The first-order and second-order stress tensors are energetically conjugate to the corresponding strain tensors by the virtual power theorem; therefore, the constitutive equations in case of linear elasticity take the form

$$\boldsymbol{\Sigma}=\mathbb{C}\mathbf{E}+\mathbb{Y}\boldsymbol{\kappa},\qquad \boldsymbol{\mu}=\mathbb{Y}\mathbf{E}+\mathbb{S}\boldsymbol{\kappa}, \tag{4}$$

$\mathbb{C}$ being the (standard) fourth-order elasticity tensor, $\mathbb{S}$ the sixth order tensor related to second-order stress and strain tensors and $\mathbb{Y}$ a fifth order tensor taking into account the coupling between the first and second-order stress and strain tensors. From the field equations

(2), (3) and (4), the equation of motion of a second order continuum is obtained, for vanishing tensor $\mathbb{Y}$ (centro-symmetric unit cell $\mathcal{A}$), in the form

$$Div_{\mathrm{y}}\left(\mathbb{C}\nabla_{\mathrm{y}}\mathbf{U}\left(\mathbf{y},t\right)-Div_{\mathrm{y}}\mathbb{S}\nabla_{\mathrm{y}}\otimes\nabla_{\mathrm{y}}\mathbf{U}\left(\mathbf{y},t\right)\right)=\rho_{M}\left[\ddot{\mathbf{U}}\left(\mathbf{y},t\right)-\left(\nabla_{\mathrm{y}}\otimes\nabla_{\mathrm{y}}\ddot{\mathbf{U}}\left(\mathbf{y},t\right)\right)\mathbf{J}\right], \tag{5}$$

or in components

$$C_{ijhk}U_{h,kj}-S_{ijkrpq}U_{r,pqjk}=\rho_{M}\left(\ddot{U}_{i}-J_{kk}\ddot{U}_{i,kk}\right),\qquad i=1,2,3. \tag{6}$$

In order to replace the first-order heterogeneous model, where the micro-fields are defined, with the second-order homogeneous equivalent medium, the variables defined at the corresponding scales have to be properly coupled by means of transition strategies for the strains and strains gradients from the macroscale to the discribed microstructure. In the following, a kinematic multi-scale model proposed by the Authors (Bacigalupo and Gambarotta, 2010a) is considered.

3 SECOND ORDER HOMOGENIZATION OF PERIODIC MATERIALS

In order to couple the kinematics of the classical continuum at the micro-scale to the kinematics of the second-order continuum at the macro-scale, the micro-displacement field in the unit cell is represented in the form $\mathbf{u}\left(\mathbf{x},t\right)=\mathbf{u}\left(\mathbf{y},\mathbf{z},t\right)$. Here, $\mathbf{y}$ denotes the position vector of the unit cell in which $\mathbf{x}$ is located and vector $\mathbf{z}=\mathbf{x}-\mathbf{y}$ its relative position, that highlights the dependence of the displacement field on both the unit cell position $\mathbf{y}$, called the macro-position, and the local position $\mathbf{z}$ at a point of interest. The effective micro-displacement field $\mathbf{u}\left(\mathbf{y},\mathbf{z},t\right)$ is approximated by the vector field

$$\mathbf{u}\left(\mathbf{y},\mathbf{z},t\right)\approx\mathbf{u}^{\alpha}\left(\mathbf{y},\mathbf{z},t\right)=\mathbf{U}\left(\mathbf{y},t\right)+\mathbf{H}\left(\mathbf{y},t\right)\mathbf{z}+\frac{1}{2}\boldsymbol{\kappa}\left(\mathbf{y},t\right):\left(\mathbf{z}\otimes\mathbf{z}\right)+\tilde{\mathbf{u}}\left(\mathbf{y},\mathbf{z},t\right), \tag{7}$$

superposition of a polynomial function depending on the macro-displacement and the macro-strain fields and a complementary displacement field $\tilde{\mathbf{u}}\left(\mathbf{y},\mathbf{z},t\right)$ that represents the microstructural displacement fluctuation field at the microscale due to the inhomogeneities. To obtain continuous micro-displacement fields across the unit cell interfaces, the complementary displacement field is assumed according to Bacigalupo and Gambarotta, 2010, in the form

$$\tilde{\mathbf{u}}\left(\mathbf{y},\mathbf{z},t\right)=\mathbf{r}^{1}\left(\mathbf{y},\mathbf{z},t\right)+\mathbf{r}^{2}\left(\mathbf{y},\mathbf{z},t\right), \tag{8}$$

each of them having the following representation in components

$$r_{i}^{1}\left(\mathbf{y},\mathbf{z},t\right)=\theta_{ikl}^{1}\left(\mathbf{z}\right)\left[H_{kl}\left(\mathbf{y},t\right)+\kappa_{klp}\left(\mathbf{y},t\right)z_{p}\right],\quad r_{i}^{2}\left(\mathbf{y},\mathbf{z},t\right)=\theta_{iklp}^{2}\left(\mathbf{z}\right)\kappa_{klp}\left(\mathbf{y},t\right), \tag{9}$$

where the functions $\theta_{ikl}^{1}\left(\mathbf{z}\right)$ and $\theta_{iklp}^{2}\left(\mathbf{z}\right)$ have to satisfy the condition of $\mathcal{A}$-periodicity, namely $\theta_{ikl}^{1}\left(\mathbf{z}_{0}^{i}+\mathbf{v}_{i}\right)=\theta_{ikl}^{1}\left(\mathbf{z}_{0}^{i}\right)$ and $\theta_{iklp}^{2}\left(\mathbf{z}_{0}^{i}+\mathbf{v}_{i}\right)=\theta_{iklp}^{2}\left(\mathbf{z}_{0}^{i}\right)$ $\mathbf{z}_{0}^{i}\in C_{i}$, i=1,2.

The representation of the micro-displacement fluctuation field (9) is the key point on which the following two-step computational homogenization is based. The first step is the standard first-order homogenization in which the unknown functions $\theta_{ikl}^{1}\left(\mathbf{z}\right)$ have to be evaluated. Here the function $\theta_{ikl}^{1}\left(\mathbf{z}\right)$ represents the fluctuation displacement along direction $\mathbf{e}_{i}$ associated to the homogeneous component $H_{kl}=1$ of the macro-displacement gradient; it

is obtained by the computational analysis of the unit cell $\mathscr{A}(\mathbf{y})$ with prescribed classic periodic boundary conditions on the micro-displacement field

$$\mathbf{u}^I\left(\mathbf{z}_b+\mathbf{v}_i\right)-\mathbf{u}^I\left(\mathbf{z}_b\right)=\mathbf{H}\mathbf{v}_i,\qquad \forall \mathbf{z}_b\in C_i,\ i=1,2, \tag{10}$$

where $\mathbf{z}_b$ is the local position vector at a point on the boundary C_i, $i=1,2$ (see figure 2.b). Once the micro-displacement $\mathbf{u}^I\left(\mathbf{z}\right)$ in the unit cell $\mathscr{A}(\mathbf{y})$ is obtained for $H_{kl}=1$ prescribed, the 2^3 unknown functions $\theta^1_{ikl}\left(\mathbf{z}\right)$ are evaluated $\theta^1_{ijk}\left(\mathbf{z}\right)=u^I_{ijk}\left(\mathbf{z}\right)-\delta_{ij}z_k$. Following this procedure for all the components of tensor $\mathbf{H}$ the overall (Cauchy) elasticity tensor $\mathbb{C}$ is evaluated through an application of the Hill-Mandel condition.

The second step is carried out by considering a homogeneous second-order strain field and vanishing macro-strain $\mathbf{E}=\mathbf{0}$. The 2^4 unknown functions $\theta^2_{ijkl}\left(\mathbf{z}\right)$ are obtained by analysing the unit cell $\mathscr{A}(\mathbf{y})$ with prescribed boundary conditions on the micro-displacement field derived from the $\mathscr{A}$-periodicity condition (9.2). For an arbitrary prescribed second-order strain tensor $\boldsymbol{\kappa}$, the micro-displacement $\mathbf{u}^{II}\left(\mathbf{z}\right)$ is written at corresponding points on the boundary $\mathbf{z}_b$ and $\mathbf{z}_b+\mathbf{v}_i$ (see figure 2) according to representation (7), (8), (9) and including the condition of $\mathscr{A}$-periodicity on the functions $\theta^2_{ijkl}\left(\mathbf{z}\right)$

$$\mathbf{u}^{II}\left(\mathbf{z}_b+\mathbf{v}_i\right)-\mathbf{u}^{II}\left(\mathbf{z}_b\right)=\mathbf{u}^{*}\left(\mathbf{z}_b+\mathbf{v}_i\right)-\mathbf{u}^{*}\left(\mathbf{z}_b\right)+\boldsymbol{\Theta}^1\left(\mathbf{z}_b\right)\!:\!\boldsymbol{\kappa}\mathbf{v}_i,\qquad \mathbf{z}_b\in C_i,\quad i=1,2, \tag{11}$$

where the third order tensor function $\boldsymbol{\Theta}^1\left(\bullet\right)$ collects the functions $\theta^1_{ikl}\left(\mathbf{z}\right)$.

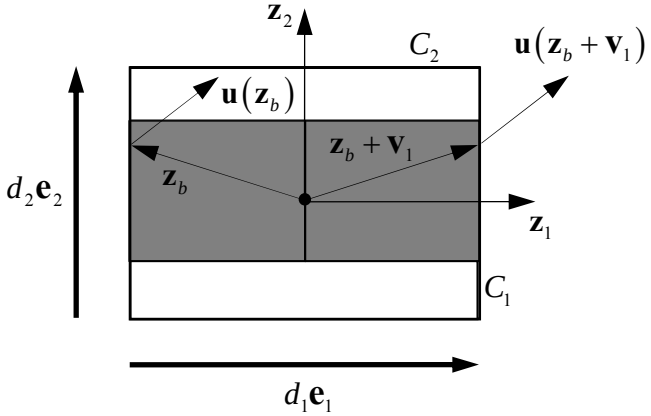

Fig. 2. Displacement vectors of points at the boundary of the unit cell.

The boundary conditions referred to the vertical side C_1 and horizontal side C_2 are written in components in the following form, respectively:

$$\begin{aligned}
&u_i^{II}\left(z_1^+\right)-u_i^{II}\left(z_1^-\right)=u_i^{*}\left(z_1^+\right)-u_i^{*}\left(z_1^-\right)+\theta^{1+}_{i11}d_1\kappa_{111}+\theta^{1+}_{i12}d_1\kappa_{112}+\theta^{1+}_{i21}d_1\kappa_{211}+\theta^{1+}_{i22}d_1\kappa_{221},\\
&u_i^{II}\left(z_2^+\right)-u_i^{II}\left(z_2^-\right)=u_i^{*}\left(z_2^+\right)-u_i^{*}\left(z_2^-\right)+\theta^{1+}_{i11}d_2\kappa_{112}+\theta^{1+}_{i12}d_2\kappa_{122}+\theta^{1+}_{i21}d_2\kappa_{212}+\theta^{1+}_{i22}d_2\kappa_{222},
\end{aligned} \tag{12}$$

where the notation $z_i^{\pm}=\pm d_i/2$, $i=1,2$ and $\theta^{1+}_{hkl}=\theta^1_{hkl}\left(z_i^+\right)$ is assumed.

The corresponding micro-displacement field $\mathbf{u}^{II}\left(\mathbf{z}\right)$ is obtained by a FE analysis of the unitcell under the assumption $\mathbf{E}=\mathbf{0}$ and $\boldsymbol{\kappa}$ homogeneous in the unit cell. Each displacement

functions $\theta^2_{iklp}(\mathbf{z})$ is obtained from the displacement field $u^{II}_{iklp}(\mathbf{z})$ resulting by the FE analysis of the unit cell with prescribed non-zero component $\kappa_{klp}=1$, as follows

$$\theta^2_{iklp}(\mathbf{z}) = u^{II}_{iklp}(\mathbf{z}) - \frac{1}{2}\left(\delta_{ik} z_l z_p + \theta^1_{ikl}(\mathbf{z}) z_p + \theta^1_{ikp}(\mathbf{z}) z_l\right), \tag{13}$$

being the fluctuation $\theta^1_{ijk}(\mathbf{z})$ known from the first-order homogenization.

The elastic moduli of the second-order continuum are evaluated in the unit cell with reference to the macro-strain vectors $\underline{E} = \{H_{11} \quad H_{22} \quad H_{12}+H_{21}\}^{\mathrm{T}}$ and $\underline{\kappa} = \{\kappa_{111} \quad \kappa_{222} \quad \kappa_{122} \quad \kappa_{211} \quad \kappa_{121} \quad \kappa_{212} \quad \kappa_{112} \quad \kappa_{221}\}^{\mathrm{T}}$. The Hill-Mandel macro-homogeneity condition is applied $\mathscr{E}^{\circ}_M = \mathscr{E}^{\circ}_m$, where $\mathscr{E}^{\circ}_M$ is the macro-strain energy at a point **y** of the homogenized continuum written in the following quadratic form

$$\mathscr{E}^{\circ}_M(\underline{E},\underline{\kappa}) = \frac{1}{2}\left\{\underline{E}^{\mathrm{T}} \quad \underline{\kappa}^{\mathrm{T}}\right\}\begin{bmatrix} \underline{\underline{C}} & \underline{\underline{Y}} \\ \underline{\underline{Y}}^{\mathrm{T}} & \underline{\underline{S}} \end{bmatrix}\begin{Bmatrix} \underline{E} \\ \underline{\kappa} \end{Bmatrix}, \tag{14}$$

$\underline{\underline{C}}$, $\underline{\underline{Y}}$ and $\underline{\underline{S}}$ being the sub-matrices of the second-order elastic stiffness matrix according to the constitutive equations (4) and $\mathscr{E}^{\circ}_m = \frac{1}{2A}\int_A \underline{\varepsilon}^{\mathrm{T}} \underline{\underline{C}}^m \underline{\varepsilon}\,\mathrm{d}a$ is the mean value of the micro-strain energy over the unit cell. According to the multi-scale kinematics here considered the micro-strain field $\underline{\varepsilon} = \{\varepsilon_{11} \quad \varepsilon_{22} \quad 2\varepsilon_{12}\}^{\mathrm{T}}$ in the heterogeneous cell may be written in the following linear form $\underline{\varepsilon} = \underline{\underline{B}}^E(\mathbf{z})\underline{E} + \underline{\underline{B}}^{\kappa}(\mathbf{z})\underline{\kappa}$, $\underline{\underline{B}}^E(\mathbf{z})$ and $\underline{\underline{B}}^{\kappa}(\mathbf{z})$ being matrices depending on the functions $\theta^1_{ikl}(\mathbf{z})$ and $\theta^2_{iklp}(\mathbf{z})$, i.e. on the microstructure of the unit cell. As a consequence the mean value of the micro-strain energy turns out to be a quadratic form in the variables $\underline{E}$, $\underline{\kappa}$ and may be compared with the macro-strain energy (14) in order to obtain the sub-matrices

$$\underline{\underline{C}} = \frac{1}{A}\int_A \underline{\underline{B}}^{E\mathrm{T}} \underline{\underline{C}}^m \underline{\underline{B}}^E \mathrm{d}a, \quad \underline{\underline{Y}} = \frac{1}{A}\int_A \underline{\underline{B}}^{E\mathrm{T}} \underline{\underline{C}}^m \underline{\underline{B}}^{\kappa} \mathrm{d}a, \quad \underline{\underline{S}} = \frac{1}{A}\int_A \underline{\underline{B}}^{\kappa\mathrm{T}} \underline{\underline{C}}^m \underline{\underline{B}}^{\kappa} \mathrm{d}a\,. \tag{15}$$

The matrices $\underline{\underline{C}}$ and $\underline{\underline{S}}$ are symmetric and because of the symmetry of the second-gradient strain $\kappa_{ijk} = \kappa_{ikj}$ the additional symmetries are obtained: $S_{i5} = S_{i7}$, $S_{i6} = S_{i8}$, $Y_{i5} = Y_{i7}$ and $Y_{i6} = Y_{i8}$, $i = 1,...,8$. In general, the stiffness matrix of the second-order elastic plane model is characterised by 45 elasticities (matrix $\underline{\underline{C}}$ - 6 elasticities, matrix $\underline{\underline{S}}$ - 21 elasticities, matrix $\underline{\underline{Y}}$ - 18 elasticities). In the case of centro-symmetric unit cell one obtains $\underline{\underline{Y}} = \underline{\underline{0}}$ and the first order-strain and the second-order strain are uncoupled.

Finally, the constitutive equations are written in the matrix form $\underline{\Sigma} = \partial\mathscr{E}^{\circ}_M / \partial\underline{E} = \underline{\underline{C}}\underline{E} + \underline{\underline{Y}}\underline{\kappa}$, $\underline{\mu} = \partial\mathscr{E}^{\circ}_M / \partial\underline{\kappa} = \underline{\underline{Y}}^{\mathrm{T}}\underline{E} + \underline{\underline{S}}\underline{\kappa}$, being the stress vectors written in the form $\underline{\Sigma} = \{\Sigma_{11} \quad \Sigma_{22} \quad \Sigma_{12}\}^{\mathrm{T}}$ and $\underline{\mu} = \{\mu_{111} \quad \mu_{222} \quad \mu_{122} \quad \mu_{211} \quad \mu_{121} \quad \mu_{212} \quad \mu_{112} \quad \mu_{221}\}^{\mathrm{T}}$, respectively.

4 DISPERSIVE SHEAR WAVES IN ROCK MASSES

The homogenization technique presented in the previous Section allows to analyse the shear wave propagation in a jointed and layered rock mass with periodic rock structure, as shown in figure 1. The propagation of shear waves along direction z_1 is represented at the macro-scale by the component of the displacement vector $U_2\left(y_1,t\right)$ with $U_1 \equiv 0$. The equation of motion of a second-order continuum is specialized to the case of an orthotropic material that is equivalent to a heterogeneous periodic material characterized by centro-symmetric unit cells and from equation (6) is written in the form

$$C_{1212}U_{2,11} - S_{211211}U_{2,1111} = \rho_M\left(\ddot{U}_2 - I_{11}\ddot{U}_{2,11}\right). \tag{16}$$

By noting that $\tilde{c}_1 = \sqrt{C_{1212}/\rho_M}$ is velocity of the transverse waves along direction z_1 in a corresponding Cauchy continuum ($S_{211211} = I_{11} = 0$ in equation (16)), $\lambda_{sh-1} = \sqrt{S_{211211}/C_{1212}}$ is the shearing characteristic length of the rock structure (see Bacigalupo and Gambarotta, 2010) and $I_{11} = \alpha d^2$, being d the cell size and α a parameter that depends on the geometrical and mechanical proprieties of the cell, the displacement equation of motion may be written in the form

$$\left(\lambda_{sh-a}\tilde{c}_1\right)^2 U_{2,1111} - \tilde{c}_1^2 U_{2,11} = \ddot{U}_2 - \alpha d^2 \ddot{U}_{2,11}. \tag{17}$$

To evaluate the dispersion functions, the solution of equation (17) is considered having the form $U_2\left(y_1,t\right) = A\exp\left[i\left(ky_1 - \omega t\right)\right]$, where $i^2 = -1$, k is the wave number and ω is the angular frequency. The wavelength and the phase velocity of the transverse waves along direction z_1 are respectively $\lambda = 2\pi/k$ and $c = \omega/k$. The dispersion curve corresponding to the transverse oscillatory motion of the derived equivalent continuum takes the following form

$$\omega = k\tilde{c}_1\sqrt{\frac{1+\lambda_{sh-1}^2 k^2}{1+\alpha d^2 k^2}} = k\tilde{c}_1\sqrt{\frac{1+4\pi^2\left(\lambda_{sh-1}/\lambda\right)^2}{1+4\pi^2\alpha\left(d/\lambda\right)^2}}, \tag{18}$$

that depends on the wave number k. From equation (18) it results that for large wavelengths $\left(\lambda \to \infty\right)$ the angular frequency tends to attain the value related to the standard continuum, i.e $\omega \to k\tilde{c}_1$.

5 LAYERED ROCK MASS: THE INFLUENCE OF DISCONTINUITY PLANES

Let us consider a layered rock mass (model *A*) with equal layer thickness $d/2 = 0.5$ m. The layered rock mass is assumed in plane strain condition and Young's modulus, Poisson ratio and the mass density of the layers are denoted by $E_1 = 80000$ MPa, $\nu_1 = 0.2$, $\rho_1 = 2500$ kg/m^3, $E_2 = 80$ MPa, $\nu_2 = 0.2$, $\rho_2 = 1800$ kg/m^3, respectively. The unit cell assumed in the homogenization procedure is represented in figure 3a. The mass density at the macro-scale ρ_M and the inertia tensor I_{11} take the following values: $\rho_M = 2150$ kg/m^3, $\mathrm{I}_{11} = 8.33\mathrm{E}-02$ m^2. Moreover, periodic jointed rocks or crack arrays located in the stiffer layer of the rock mass are considered in order to evaluate their influence on the elastic moduli

and on the phase velocities of the transverse waves $\tilde{c}_1$ and c in the equivalent first-order and second-order continua. To this end a layered rock mass is considered (model *B*) having periodic discontinuity planes located at distance d and the same geometry and elastic moduli of the two phases of model *A*; the unit-cell to represent this structure is shown in figure 3b.

The non-vanishing effective elastic moduli C_{ijhk} and S_{ijhkpq} obtained from the second-order homogenization procedure here proposed are shown in Table 1 for both the models. The characteristic lengths associated to the shear and to the extensional strain along directions z_1 and z_2 are given in Table 2.

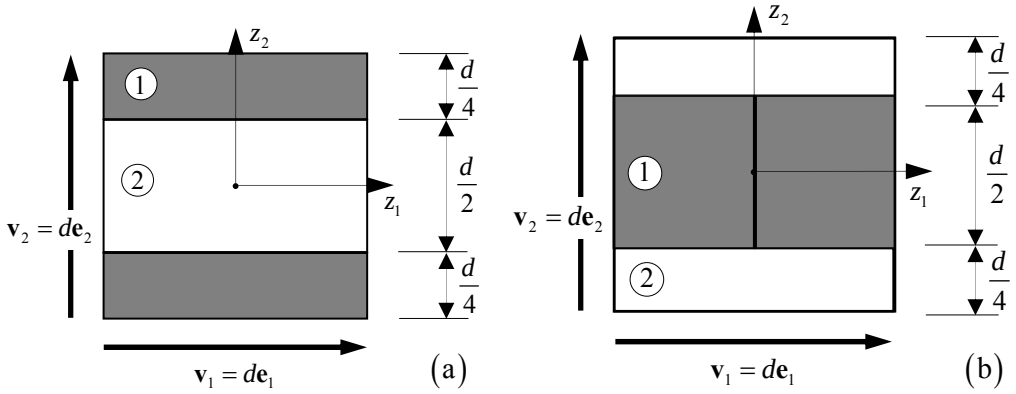

Fig. 3. Unit cell for the layered rock mass (a); periodically jointed rock mass.

The non-dimensional diagrams representing the dispersion $\omega d/\tilde{c}_1$ as a function of the wavenumber kd and the phase velocity $c/\tilde{c}_1$ as a function of the wavelength λ/d are shown in figure 4 and 5 for model *A* and *B*, respectively (the diagrams in black line and red line are referred to the first-order homogenization and second-order homogenization). Unlike the first order continuum (Cauchy), where the frequency is proportional to the wave number, dispersive waves propagate in the second-order equivalent continuum with phase velocity c and group velocity $c_g = \dfrac{\mathrm{d}\omega}{\mathrm{d}k}$ which differ at different wave numbers.

Tab.1 Non vanishing elastic moduli C_{ijhk} (MPa), S_{ijhkpq} (N) for models *A* and *B*.

	C_{1111}	C_{2222}	C_{1122}	C_{1212}
A	3.923E+04	1.611E+02	2.684E+01	2.684E+02
B	1.687E+02	1.609E+02	1.428E+01	2.319E+02

	S_{111111}	S_{222222}	S_{122122}	S_{211211}	S_{121121}	S_{212212}
A	2.609E+07	0	0	8.168E+08	2.448E+09	3.315E+06
B	1.587E+04	7.675E+0	2.594E+05	9.273E+06	1.452E+06	4.004E+06

	S_{111122}	S_{111212}	S_{222211}	S_{222121}	S_{122212}	S_{211121}
A	0	2.797E+04	0	0	0	1.223E+09
B	-5.761E+03	-7.565E+02	2.400E+03	9.645E+02	7.539E+05	9.868E+04

The inclusion of vertical discontinuity planes periodically located in the stiffer layer at a distance d as shown in figure 3b has several consequences. On the one hand, it slows down the velocity of the waves in both the first-order and the second-order equivalent continuum; on the other hand, it qualitatively modifies the wave propagation in the second order continuum with respect of the dispersion properties of the wave. While the model A is characterized by a dispersive wave velocity in the second-order continuum which is faster than the non-dispersive wave that propagates in the corresponding Cauchy continuum, in model B the opposite behavior is observed. This difference is explained by the different internal lengths in the two models considered; the internal length λ_{Sh-1} in model A is greater than the characteristic size d of the unit cell, while model B occurs in the opposite circumstance.

In the undamaged layered rock mass represented by model A a great difference between the results provided by equivalent second-order continuum and the corresponding ones from the standard Cauchy continuum are observed from the diagrams of figure 4. For wavelength $\lambda = 10d$ from the diagram in figure 4 one obtains $c \approx 1.5\tilde{c}_1$. On the other hand, in the highly damaged rock mass represented by model B the characteristic length λ_{Sh-1} is smaller than the cell size d so that the difference between the results provided by the standard first-order model and the second-order continuum is reduced: for wavelength $\lambda = 10d$ from the diagram of figure 5 one obtains $c \approx 0.98\tilde{c}_1$.

Tab.2 Characteristic lengths (mm).

	λ_{Sh-1}	λ_{Sh-2}	λ_{Ext-1}	λ_{Ext-2}
A	1744	0	26	0
B	200	33	10	0.2

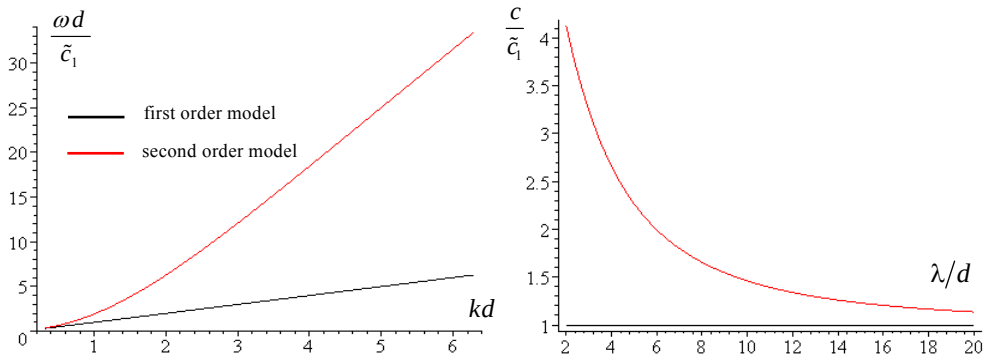

Fig. 4. Model A: dispersion function and phase velocity

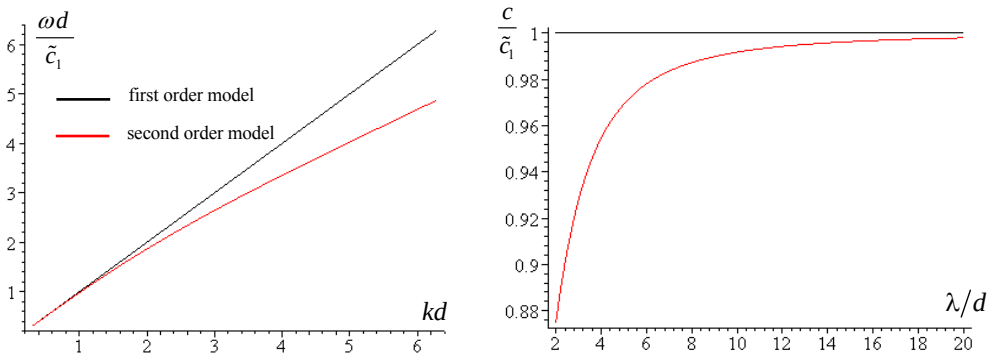

Fig. 5. Model B: dispersion function and phase velocity

6 CONCLUSIONS

A procedure for second-order computational homogenization is applied to layered rock masses with periodic structure in order to describe the effect of the material inhomogeneities and to consider scale effects in the shear wave propagation. A two step homogenization procedure proposed by the Authors to obtain an equivalent homogeneous medium is applied in order to obtain non-local equation of motion and to analyse dispersive waves.

Two examples are considered. The first one concerns a layered rock mass with equal thickness layers, but with great mismatch in the elastic moduli. In this case the scale effect results to be remarkable with characteristic length along the layers that is several times the layer thickness. The dispersion function and the phase velocity related to shear waves along the layer direction are greatly depending on the wavelength. The second example concerns the same layered system but with periodic joints located in the stiffer layer. The displacement discontinuities in the rock joints modify the elastic moduli of the second-order continuum and smaller characteristic lengths are obtained with respect to the undamaged layered system. In this case the differences in the dispersion function and phase velocity of shear waves between the second-order model and the first-order Cauchy model diminishes with increasing the rock joints density in the stiffer rock layer.

ACKNOWLEDGEMENT

The authors acknowledge financial support of the (MURST) Italian Department for University and Scientific and Technological Research in the framework of the research MIUR Prin07 project 2007YZ3B24, *Multi-scale problems with complex interactions in Structural Engineering*, coordinated by prof. A. Corigliano.

REFERENCES

Bacigalupo A., Gambarotta L. (2010) "Second-order computational homogenization of heterogeneous materials with periodic microstructure", ZAMM - Z. Angew. Math. Mech., Vol. 90, (10–11), 796 – 811.

Germain P. (1973), "The method of virtual power in continuum mechanics. Part 2: microstructure", SIAM J. Appl. Math. Vol. 25 (3), 556–575.

Hoeck E., Kaiser P. K., Bawden W. F. (1995) Support of underground excavations in hardrock*, A.A.* Balkema, Rotterdam.

Mindlin R.D. (1965), "Micro-structure in linear elasticity", Arch. Ration. Mech. Anal., Vol. 16, 51–78.

Sayers C.M., Kachanov M. (1995) "Microcrack-induced elastic wave anisotropy of brittle rocks", J. of Geophysical Research, Vol. 100, (83), 4149-4156.

Stefanou I., Sulem J., Vardoulakis I., (2008) "Three-dimensional Cosserat homogenization of masonry structures: elasticity", Acta Geotecnica, Vol. 3, (1), 71-83.

THERMAL VARIABILITY OF THE INTERNAL FRICTION IN CLAY IN A CYLINDRICAL THERMO-MECHANICAL PROBLEM

T. Hueckel
Department of Civil and Environmental Engineering, Duke University, Durham, NC, USA

B. François
Building, Architecture & Town Planning Department (BATir), Université Libre de Bruxelles, Belgium

L. Laloui
Laboratory of Soil Mechanics (LMS), Ecole Polytechnique Fédérale de Lausanne (EPFL), Switzerland

ABSTRACT: *Variability of the internal friction angle with temperature is studied in a boundary value problem numerically simulating the impact of a cylindrical heat source on the stress and strain in soil mass in which it is emplaced. Even if the thermal increase of the internal friction in that temperature range is quite modest (less than 20% in terms of the critical state parameter, M), it affects quite significantly the effective stress path near the heat source. The effective stress path approaches the yield locus and the critical state at a significantly higher principal stress difference values for the variable internal friction than for the M = cons. case. The "mean effective stress distance from the critical state" is substantially reduced during heating, in the closest vicinity of the heat source. In the case of small perturbations of any parameter this proximity may lead to a potentially unstable or statically inadmissible behaviour. The solutions obtained allow one to identify zones of influence around the heat source of several variables of interest. The presented results may be of relevance to the design of prototype in situ installations and their monitoring, and eventually of actual facilities of the nuclear waste disposal.*

1 INTRODUCTION

Temperature effect on internal friction angle is not numerically significant, but as demonstrated in a recent paper (Hueckel et al., 2009a), a 10% temperature induced increase in critical state coefficient $M(\Delta T)$ over 90°C leads to a complete pattern change in the triaxial compressive strength producing an increase in its value to up to 25%, compared to the case of temperature-independent friction angle. Experimental studies of triaxial strength of clays show that remoulded kaolin clay and natural Boom Clay exhibit temperature dependence of their internal friction, whereas this is not the case of largely smectitic or illitic clays (Hueckel and Baldi, 1990; Hueckel and Pellegrini, 1991; Cekerevac and Laloui, 2004).

Emerging technologies concerning thermally affected soil masses involve often prototype installations, the long-term performance of which requires an intense monitoring. Such technologies include nuclear waste disposal, energy storage in subsoil using geostructures, oil recovery from high pressure, high temperature reservoirs, underground pipes and cables. The monitoring systems need to be placed in the ground early during the construction phase for such installations. The sensor design is to be largely based on the numerical prediction.

This paper presents numerical investigations of the effect of temperature on the thermomechanical response of saturated soil mass at the scale of a boundary value problem of a cylindrical heat source embedded in soil. Time dependent heat conduction and water permeability affect the response of the soil mass. The presented solution demonstrates the

predictive capabilities of a numerical simulator and points out to various consequences of temperature dependent friction angle affecting the field of stress and displacement components, pore water pressure in functionally selected locations and possible points of special interests.

2 CENTRAL ASSUMPTIONS AND THE MODEL

The developments presented are an ulterior expansion of the combinantion of Prager's thermoplasticity and Cam-Clay model (Hueckel and Borsetto, 1990). The main new assumption of the model adopted here is that the critical state parameter M representing the internal friction angle, ϕ', is a function of temperature difference with respect the reference temperature T_0, $\Delta T = T - T_0$ (Laloui, 1993, Hueckel and Pellegrini, 1992, Hueckel et al., 2009a,b). Quantities marked with an "$_0$" are at the reference state.

$$M = M_0 + g\Delta T \quad ; \quad M = \frac{6\sin\phi'}{3-\sin\phi'} \quad ; \quad M_0 = \frac{6\sin\phi'_0}{3-\sin\phi'_0} \tag{1}$$

Coefficient g is constant. The variation of M affects the evolution of the yield locus, chosen here as the classical Cam-Clay form changing mainly its aspect ratio, q_{max}/p'_{max}

$$f = \frac{q}{Mp'} + \ln\left(\frac{2.718p'}{p'_c}\right) - 1 = 0 \tag{2}$$

where p' and q are the mean and deviatoric effective stress invariants. Stresses are considered positive when compressive.

The other parameter controlling the locus evolution is the apparent preconsolidation pressure p'_c, which depends on the accumulated irreversible volumetric plastic strain and temperature, represented here by a specific function originated by Laloui and Cekerevac (2003)

$$p'_c = p'_{c0}\exp\left(\beta\varepsilon_v^p\right)\left(1-\gamma\log\left[1+\frac{\Delta T}{T_0}\right]\right) > 0 \tag{3}$$

where p'_{c0} is an initial preconsolidation pressure, usually referred to the *in-situ* state, γ and β are constitutive coefficients of thermal softening and of isothermal isotropic irreversible compression.

The hypo-elastic (incrementally reversible) part of the strain increment is expressed as follows:

$$d\varepsilon_v^e = \frac{1}{K}dp' - \beta'_s dT \quad ; \quad \mathrm{d}\varepsilon_d^e = \frac{1}{3G}dq \tag{4}$$

where ε_v^e and ε_d^e are the volumetric and deviatoric elastic strain invariants. K and G are the incremental bulk and shear hypo-elasticity moduli, respectively. To reflect their well-known and pronounced variability with the depth *in situ*, they are both postulated as functions of p', $K = K_{ref}\left(p'/p'_{ref}\right)^{n'}$, $G = G_{ref}\left(p'/p'_{ref}\right)^{m'}$, where p'_{ref} is the reference pressure at which

the K_{ref} and G_{ref} are measured (Laloui and François, 2009). β'_s is the volumetric thermal (reversible) expansion coefficient of the solid skeleton.

From the analyses presented in Hueckel et al. (2009a) it transpires that in a process of continuous (thermo-plastic) yielding during heating an interesting balance of plastic straining, temperature change and effective stress change arises, driven by the balance between various components of hardening contributions and expressed through the consistency equation for thermo-plasticity (Hueckel and Borsetto, 1990)

$$df = \frac{\partial f}{\partial \underset{\sim}{\sigma}'} : d\underset{\sim}{\sigma}' + \frac{\partial f}{\partial p'_c}\left(\frac{\partial p'_c}{\partial \varepsilon_v^p} d\varepsilon_v^p + \frac{\partial p'_c}{\partial T} dT \right) + \frac{\partial f}{\partial M}\frac{\partial M}{\partial T} dT = 0 \qquad (6)$$

When temperature is controlled, like in a homogenously heated specimen, under constant stress, a one to one relationship can be established between temperature history and resulting thermo-plastic strain. In the present study, which focuses on analogous phenomena, but on a larger scale of a boundary value problem, the process is additionally affected by non-uniform and time dependent effects of heat conduction, resulting in a non-uniform distribution of temperature, thermal expansion of water and ensuing pore water pressure change, triggering in turn a flux of pore water and time-dependent dissipation of pore pressure. The pore pressure is clearly coupled, via the effective stress principle, with the evolution of the effective stress.

3 THERMO-PLASTIC BOUNDARY VALUE PROBLEM

An isolated cylindrical heat source is considered and the thermo-hydro-mechanical response of the surrounding clay mass is studied. The soil material of choice is Boom Clay, a possible host formation for nuclear waste disposal in Belgium, well-characterized from both mechanical and thermo-mechanical point of view (Baldi et al., 1991; Hueckel and Pellegrini, 1992).

Through finite element method, the field equations considered represent the medium as a deformable two-phase material, in which heat and mass transfers occur. The Thermal Cam-Clay model (Hueckel and Borsetto, 1990; Laloui and François, 2009) has been implemented in the FE code LAGAMINE (Charlier et al., 2001; Collin et al. 2002). Eight-node, 2-D, large strain finite elements are used. Four degrees of freedom at a node are considered: two solid displacements, liquid water pressure and temperature.

A horizontal unit height slice of Boom Clay is considered, placed in the mid-plane of the heating source. The slice is meshed assuming radial (horizontal) propagation of thermal and hydraulic fluxes as well as the plane strain configuration (no vertical deformation). The computation domain is axisymmetric around the vertical axis of the heat source (Fig. 1).

While the boundary value problem chosen is very simple (axial symmetry, plane strain), it epitomizes many of characteristics of the fully developed "realistic" field problems.

The initial conditions for the boundary value problem are chosen to replicate those for the planned repository in Boom Clay (François et al., 2009). The initial state is defined as follows. The initial *in-situ* Boom Clay stress-state is reproduced as slightly anisotropic, with $K_0 = 0.8$ an under an assumption that $\sigma_r = \sigma_t$=4.3 MPa. An initial pore water pressure of 2.02 MPa is considered. The initial overconsolidation ratio of the clay is about 2.4.

The heating phase consists in a gradual increase of temperature from 16.5°C (i.e. *in-situ* temperature of Boom Clay at the level of the HADES underground laboratory) to 96.5°C within 30 days. Then a constant temperature of 96.5°C is maintained during 2 years. The boundary conditions are summarized in Fig. 1.

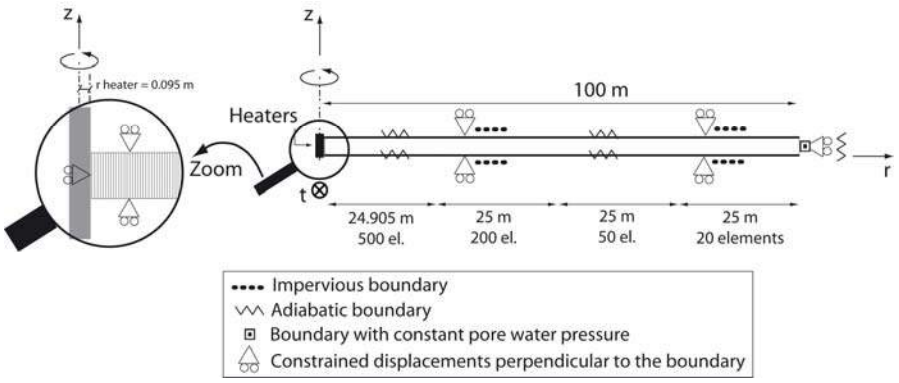

Fig. 1. Modelled domain and boundary condition in the r (radial), t (circumferential) and z (axial) axis system. Details on the finite element size.

Tables 1 and 2 report the mechanical and diffusive material parameters, respectively. Notably, permeability of water, k is assumed as dependent on water viscosity μ_w, $k = k_w / \mu_w$, which in turn is a function of temperature $\mu_w = \mu_{w0}\left(1-\alpha_T\left(T-T_0\right)\right)$. Boom Clay exhibits an increase of M with temperature (from 0.8 at 16.5°C to 1.16 at 96.5°C) resulting in a positive parameter g.

Table 1. Mechanical parameters of Boom Clay used in computations.

Elastic parameters		
K_{ref}, G_{ref}, n', m', β_s'	[MPa], [MPa], [-],[-], [°C^{-1}]	130, 130, 0.4, 0.4, 5 10^{-5}
Isotropic plastic parameters		
β, γ	[-], [-]	16, 0.55
Deviatoric plasticity parameters		
ϕ_0', g	[°], [-]	20.6, 4.5 10^{-3}

Table 2. Thermal and hydraulic diffusion parameters of Boom Clay (François et al., 2009).

Parameters	ρ_{w0}	ρ_s	n	k_w	χ_w	β_w'	μ_{w0}	α_T	$c_{p,w}$	$c_{p,s}$	λ_w	λ_s
Units	[kg/m^3]	[kg/m^3]	[-]	[m^2]	[Pa]	[°C^{-1}]	[Pa.s]	[°C^{-1}]	[J.kg.°C^{-1}]	[J.kg.°C^{-1}]	[W.m^{-1}.°C^{-1}]	[W.m^{-1}.°C^{-1}]
	1000	2670	0.39	2 10^{-19}	2.2 10^9	3.5 10^{-4}	0.001	0.011	4186	732	0.57	2.42

4 RESULTS AND DISCUSSIONS

4.1 Pore water pressure

Given the very low permeability of Boom Clay, the short-term response of the field around the heat source develops in conditions very close to the undrained ones. Hence, the pore water pressure evolution is mainly controlled by the difference between the thermal expansion of water and a much smaller of the solid skeleton. This produces a pore water pressure increase, initially following a familiar, highly localized temperature distribution around the heat source until about 50 days of heating (Fig. 2a,b). In this initial period temperature and pore pressure affect a limited volume of soil not exceeding 1.5 m in radius. However, in a later period, the pore pressure increase covers a much wider zone than temperature (Fig. 2b). Notably, near the source the pore pressure value starts decreasing, after reaching a maximum value at about 50 days (Figs 2c). In contrast, in a more remote range of

more than about r = 1.75m, the trend is opposite: pore pressure grows monotonically. The transition point between these two types of evolution corresponds approximately to a zero curvature point (as in 1-D consolidation equation), which also is approximately the location of the maximum water flux point.

The influence of mechanics on the thermal field is known to be very limited as it is induced via changes in porosity. As those changes are small, temperature distribution seems to be independent of deformation and of whether *M* is constant or variable (Fig. 2a). This is not exactly the case of pore pressure (Figs. 2b, and c).

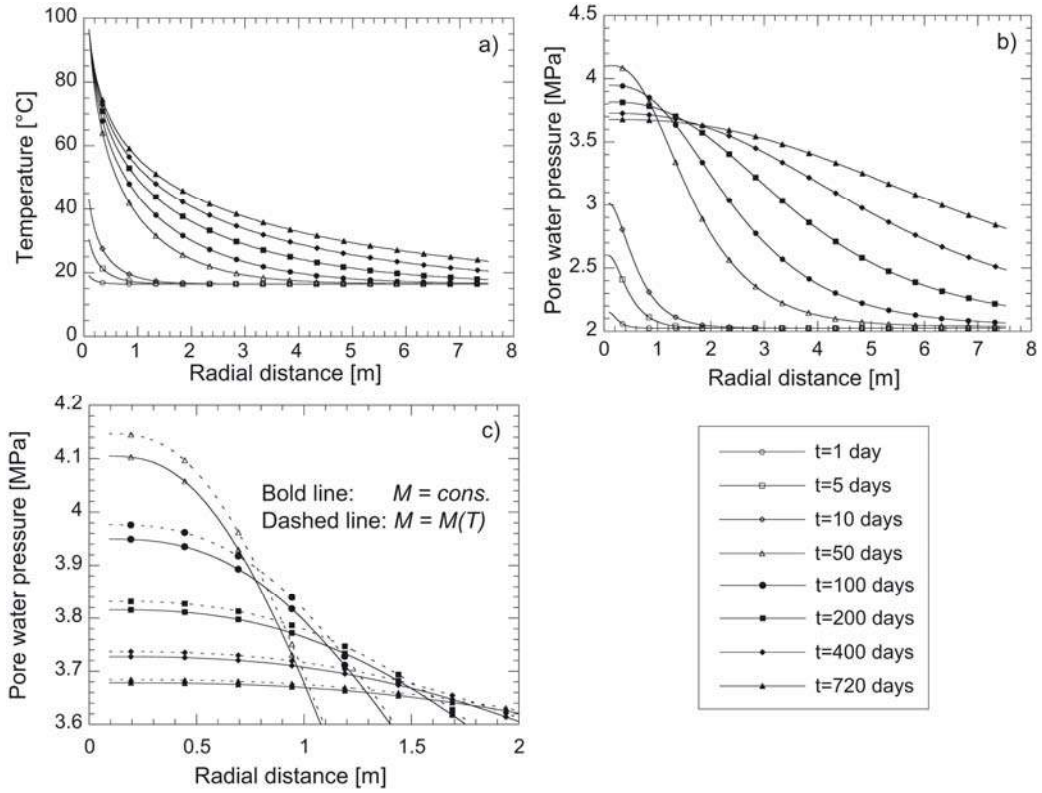

Fig. 2. Evolution of (a) temperature (identical for both *M = cons.*, and *M(ΔT)*), (b) pore water pressure distribution around the heat source (negligible dependence on *M(ΔT)* over most of the field) and (c) pore water pressure in the closest vicinity of the heat source showing a limited dependence on *M.*

4.2. Effective stress and total stress trajectories

The relatively weak dependence of pore pressure on the variations of the internal friction (or *M*) can be best explained considering its coupling to the effective stress evolution. Understanding the effective stress trajectory, in particular near the heat source, is crucial from the point of view of the stress analysis and structural safety of the soil mass supporting the heat source thermally and structurally.

It should be noted that all the material behaviour characteristics are assumed as independent of the third effective stress invariant (or Lode angle θ_L), but the plane strain states are not. Therefore, a proper representation of stress trajectories is provided in what follows in q, p', θ_L space, while the yield locus and critical state locus, are independent of θ_L.

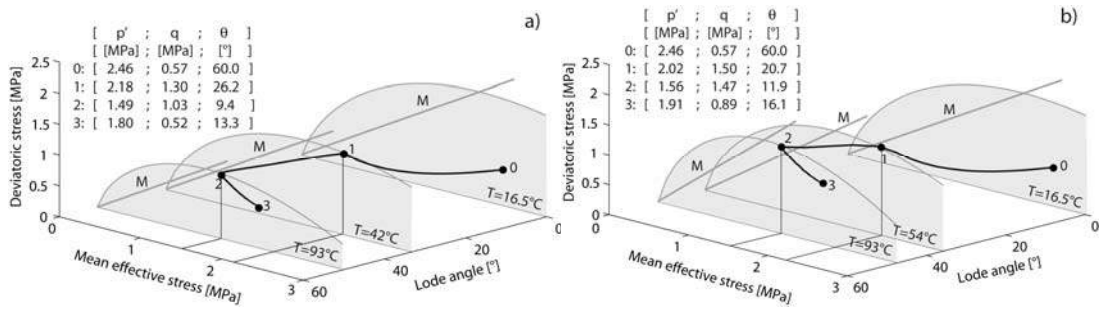

Fig. 3. Evolution of the stress path in the q, p', θ_L space in parallel with the evolution of the yield locus and the critical state line for a location r=10.6 cm (1.1cm away from the wall of the heat sorce wall), (a) for M constant and (b) for M variable.

The effective stress field arises mainly in response to the thermal generation of pore pressure, subjected to the constraints of equilibrium and boundary conditions, imposed on the total stress field. Therefore, in the first stage of the process the effective stress field evolution is mainly controlled by the heat diffusion or temperature field evolution. In a later, much slower and longer phase, due to a decreasing pore pressure gradient, the controlling factor becomes the (very slow) outflow of the pore water.

Let us focus on a point closest to the heat source wall at r = 10.6 cm (1.1 cm away from the wall) at *M=cons.* (Fig. 3). In response to the initial pore pressure growth, the effective mean stress decreases and an additional mechanical volumetric strain rate ensues, initially elastic and expansive, then with a thermo-plastic and compactive component. Such a scenario resembles a classical undrained triaxial thermal failure experiment, called Scenario II by Hueckel et al. (1987), and Hueckel et al. (2009a). However, in the axisymmetric plane strain boundary value problem considered here, the displacements near the heater are constrained vertically and circumferentially, but are not constrained in radial direction. Hence, a marked principal stress difference (i.e. deviatoric stress) develops in response to heating, not present in the above mentioned experiment, conducted at $q = cons$. The rising of this deviatoric stress critically affects the effective stress path, and is crucial in bringing the effective stress in the close vicinity of the critical state. This would not be the case of a plane stress solution.

The above-described stress trajectory responds largely to the mentioned displacement constraints. The elastic segment, (0)-(1) (Fig. 3), driven by the thermal pore pressure build up, complies with the vertical strain boundary condition imposing that $d\varepsilon_z^e = 0$. As in the undrained thermal failure case (Hueckel et al., 2009a) that determines uniquely the elastic segment of the stress trajectory via equality expressed in what follows in terms of the effective stress invariant increments, parametrized with respect to temperature T.

$$d\varepsilon_z^e = d\varepsilon_{11}^e = -\frac{1}{3}\beta_s dT + \frac{1}{3K}dp' + \frac{1}{3G}\cos\theta_L dq - \frac{q}{3G}\sin\theta_L d\theta_L = 0 \qquad (7)$$

The strains generated in the elastic regime are by definition M-independent, except for the fact that the extent of the elastic regime itself is altered by the M-variation. As may be noted in Fig. 3, the effective stress path in the case of the variable M (Fig 3b) reaches visibly higher values of q and slightly lower values of p', than those at a constant M (Fig 3a). This is clearly a result of the influence of the variable M on the evolution of the yield locus, which develops a higher aspect ratio at high ΔT, in the former case. As an outcome, the response to the unloading due to the pore water pressurisation is elastic over a longer part of the process, than in the case of *M=cons*. Consequently, yielding, point (1), starts at quite different temperatures at T = 42°C for $M = cons.$, and at 54°C for $M = M(\Delta T)$.

Yielding opens the stage to an interaction of three possible hardening mechanisms: (i) apparent preconsolidation temperature softening, active already in the elastic range, and characterized by the inequality $\left(\partial f/\partial p'_c\right)\left(\partial p'_c/\partial T\right)>0$; (ii) plastic strain hardening, and (iii) a possible effect of the variation of the critical stress state (or friction angle) also active already in the elastic range. The subsequent stress increment is a resultant of that interaction, and in this case is most likely directed inward the yield locus of the moment. This produces an abrupt turnaround in the stress trajectory. When a plastic strain rate arises, the plane strain constraint changes into a rate condition: $d\varepsilon_z^p=-d\varepsilon_z^e$, what alters the course of the effective stress trajectory. Indeed, the above stated constraint, together with the consistency equation, determines the following stress increments. This can be best seen for the case of *M=cons.*

$$df=\frac{\partial f}{\partial p'}dp'+\frac{\partial f}{\partial q}dq+d\Lambda\frac{\partial f}{\partial \varepsilon_v^p}\frac{\partial f}{\partial p'}+\frac{\partial f}{\partial p'_c}\frac{\partial p'_c}{\partial T}dT=0 \tag{8}$$

$$d\Lambda\left(\frac{\partial f}{\partial p}\frac{1}{3}+\frac{\partial f}{\partial q}\sin\left(\theta_L\right)\right)=\frac{1}{3}\beta_s dT-\frac{1}{3K}dp'-\frac{1}{3G}\cos\theta_L dq+\frac{q}{3G}\sin\theta_L d\theta_L \tag{9}$$

Eliminating the multiplier dΛ, an incremental expression for the effective stress trajectory during the plasticity phase is easily arrived at expressed in terms of the invariants dq, dp' and $d\theta_L$, for a given temperature increment.

As the stress range, in which the effective stress path reaches yielding (see Figs. 3a,b) corresponds to the top parts of the yield loci, with a miniscule plastic volumetric strain rate component (i.e. the horizontal component of the local yield locus normal), the expected contribution from the plastic strain-hardening is indeed very small. While the stress point moves through plastic states near the critical locus, the volumetric component of the plastic strain rate progressively decreases even further. Notably, the case of variable *M* is characterized by the compensatory role mainly carried by *M(ΔT)* hardening, hence the overall softening is less evident. The *M = cons.* case, in addition to a more evident softening, is characterized by reaching a very close vicinity of the Critical State Line.

At 95°C, the source temperature stops increasing (and hence, so does the pore pressure) by the imposed heating program and soon after that the pore pressure starts decreasing due to water outflow. At the same time, the yield locus is arrested at the location corresponding to the maximum imposed temperature, point (2). Water outflow is in a limited quantity, given that the pore pressure gradient is quite small. The pore pressure hence starts decreasing at a low rate, while the effective stress re-enters into elastic domain, producing a next effective stress trajectory segment (2) – (3), nearly parallel to the elastic loading segment (0)–(1).

Figs. 4a,b show projections of the effective stress paths on the plane of $\theta_L=0°$, which is the plane of the initial stress state. As discussed earlier, the constitutive properties of the material are all independent of θ_L. The figures show the differences between the effective stress trajectories at three locations within the plastic strain range, at a relatively small distance from the heat source (40 cm away from the interface at most). Most prominently, the figures demonstrate the difference in the evolution of the yield locus between the *M = cons.* case and the variable *M* case. It is clear that when *M* grows, and hence the aspect ratio of the yield locus, $q_{\max}/p_{\max}$ increases, the value of the maximum deviatoric stress reached is higher, and the subsequent drop in the deviatoric stress component during the thermo-plastic yielding process is consistently much more limited, than in *M = cons.* case. Hence, the ensuing softening at a given location for a given stress history, is much less pronounced.

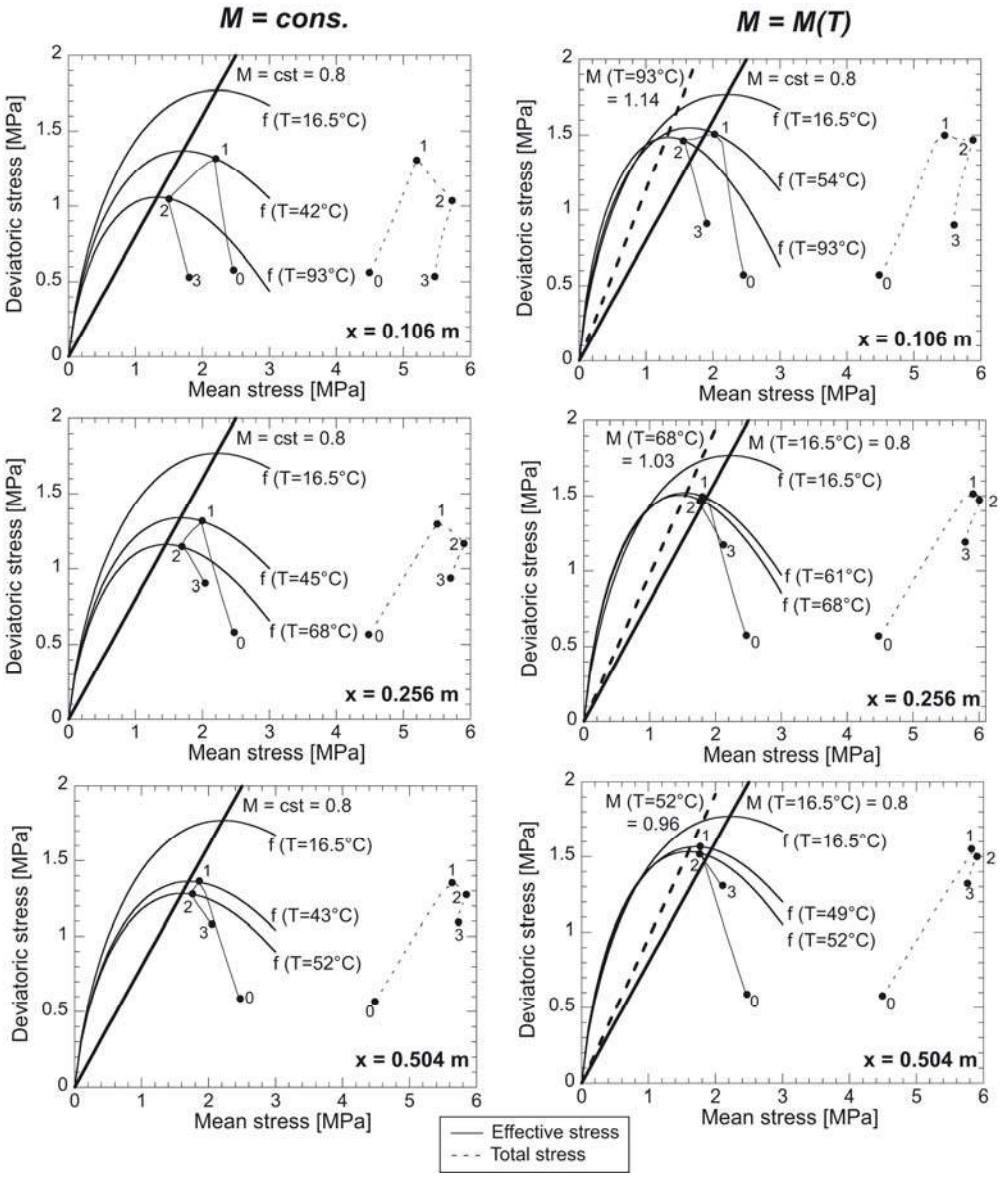

Fig. 4. Evolution of the stress path in the *q, p'* space in parallel with the evolution of the yield locus and the critical state line for different locations within the zone of thermo-plasticity (r=10.6 cm, r=25.6 cm and r=50.4 cm). Left column: for *M* constant; Right column: for *M* variable.

It is also instructive to note that only a portion of the pore pressure increase of about 1.2 MPa (1.24 MPa for constant M and 1.13 MPa for variable M) between the moment of yielding onset at point (1) and yielding demise (point (2)) is accommodated by the effective mean stress change, which is about 0.6 MPa (0.61 MPa for the constant M and 0.59 MPa for the variable M). The rest of the difference affects the total stress development, also shown in Fig. 4. Indeed starting at the point of yielding (1), the total mean stress exhibits an abrupt increase in both cases of *M,* causing the total stress trajectory to make a turn, which is opposite to the one exhibited by the effective stress path. For more remote locations, at r = 25.6 and 50.4 cm the effective and total stress paths shown in Fig. 4 show somewhat different picture. For the variable *M* case, the plasticity episode (1)-(2) is much less significant, with less plastic deviatoric strain. For the *M = cons.* case there is more plasticity at both locations and more deviatoric plastic strain.

Most remarkably, for both cases and for all three locations the effective stress path comes very close to the critical state line, at the end of their plastic process and the maximum attained temperature. In terms of mean effective stress, the distance from the critical states amount to as little as 0.1 MPa. While there is no established quantitative criterion for the margin of safety in such situation, it certainly is not a healthy situation. In other words, the margin of safety, in whatever terms it is expressed, for those more remote locations is alarmingly low. Any adverse local material inhomogeneity or random load fluctuation may bring the effective stress trajectory to the other side of the critical state locus, where the material behavior may become either unstable, non-unique, or statically inadmissible (Bigoni and Hueckel, 1991; Hueckel et al., 2009b). Counter-intuitively, these locations are not locations where the highest (spatially) temperature or highest pore pressure is attained.

4.3. Stress and strain state distribution evolution

Deviatoric stress invariant distribution along the radius is shown in Fig. 5. During the elastic phase the distribution follows that of temperature, with a maximum value near the contact with the heat source (until 10 days). Soon after the yielding starts, the value at the contact drops almost by half, and the maximum is at the interface of the elastic and plastic zones.

As far as the individual effective stress components are concerned, the evolution of axial stress (Fig. 6) is strongly related to the kinematic constraint of plane strain ($\varepsilon_z = 0$) and the generation of thermo-elastic expansion first, and later accompanied by thermo-plastic axial compression, which reduces the reacting compressive stress. Notably, with the entering in the plastic range the plane strain constraint, $\varepsilon_z = 0$ converts into a rate condition: $d\varepsilon_z^p = -d\varepsilon_z^e$.

Both elastic and plastic axial strains have components proportional to temperature rate and the rate of change of the effective stress. The latter is largely influenced by the development of pore water pressure due to a substantial thermal expansion of water. Note that, as mentioned in Sect. 4.1, the pore pressure in the vicinity of the heat source (r< 0.5m) stops growing at 50 days and after that starts dissipating. This induces a transfer of a portion of the load onto the solid phase (in terms of compressive effective stress). Interestingly, in contrast to the nearest vicinity of the heater for radii larger than about 1.75 m the pore pressure increases monotonically all the time, see Fig. 2b. As a result, the effective compressive stress also decreases there, even if less, because of the lower temperatures.

In consequence, directly near the heat source wall, the axial effective stress initially increases in response to thermal expansion and then after about 15 days drops over 0.90 MPa with respect to the *in situ* value to 1.95 MPa, for the *M = cons.* case. In the case of the variable *M,* the drop is somewhat less (0.60 MPa) after about 20 days. Indeed, yielding occurs significantly later (as the yield locus changes significantly its aspect ratio).

The drop is confined to about 0.5 m initially and after about 50 days another development takes place in an outer ring of the plastic range, between radii of 0.8-0.2m. The drop is clearly related to the appearance of plastic strains, which counteract the thermal expansion effect. Notably, the onset of yielding, occurring after 30 days of heating leads to an abrupt and quite substantial change in axial effective stress distribution. Between day 10 and day 50, there is "rapid" change of about 0.8 MPa in axial stress.

For the case of the variable *M,* the stress increases over 0.2 MPa at the interface between plastic and elastic zone, whereas in the *M = cons.* case it generally drops or increases imperceptibly at the very end of the process. Consequently, the resulting range of axial stress affected by the thermo-plastic developments is larger for the variable *M* case (Fig 6b), even if the plastic strain zone itself is smaller in the case of variable *M*, as seen in Figs 5a,b (the elasto-plastic interface position).

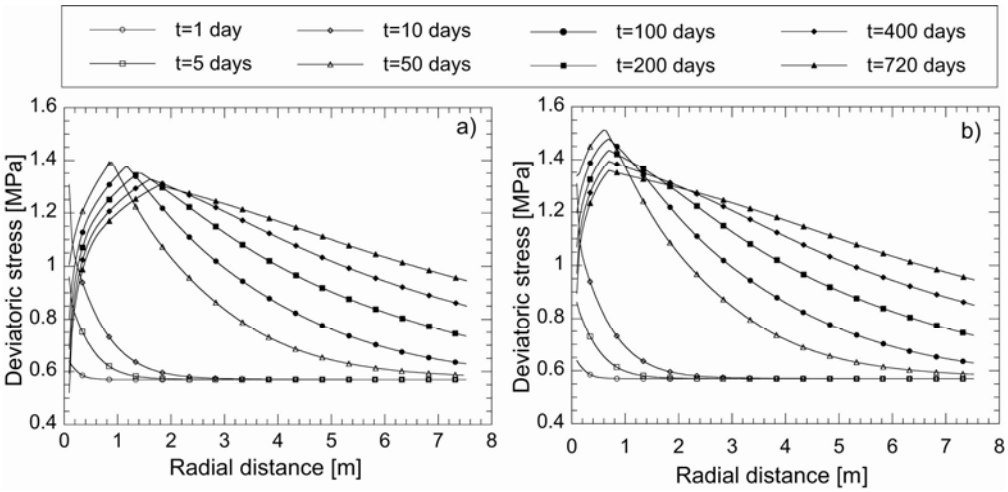

Fig. 5. Distribution of the deviatoric stress invariant for (a) $M = cons.$ and (b) for variable M case.

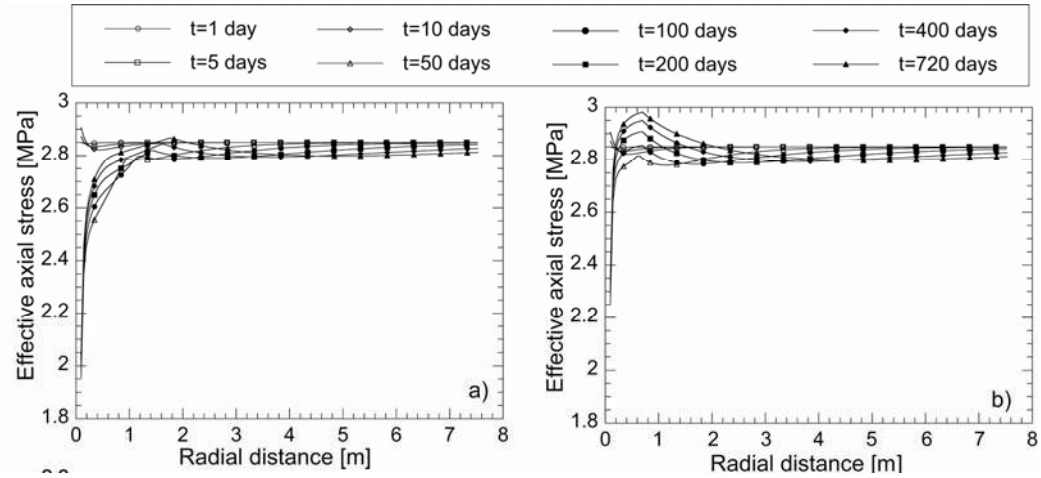

Fig. 6. Distribution of the effective axial stress for (a) $M = cons.$ and (b) for variable M case.

4.4. Implications for monitoring system design and spacing of the heating devices

The conducted simulations allow one to study the extent of zones of influence of the triggered phenomena around a heat source. Proper assessment of such zones is crucial for a rational design of monitoring systems. It is vital for a meaningful monitoring to measure variables where they reach extreme values. A good monitoring system is also the one that measures the variables with sensors with an adequate sensitivity.

It needs to be emphasized that the presented numerical study, while based on a set of actual data concerning material properties of specific clay, is not to be construed as a simulation of a specific technical project. Rather, it is to be treated as an academic study, not necessarily technically realistic. Notably, this simulation ignores the effects of the weight of the heat source, which may be crucial in a situation that involves thermo-plastic yielding. However, the concept of the zone of influence, as depicted in Fig. 7, remains critical for good monitoring system design.

The size of the zone of influence of thermo-plastic yielding (about 1.6m in diameter) is most worrying from the point of view of the structural safety of the soil mass. Equally troublesome is the extent of the zone (about 1.0m) in which the effective stress state is less

than 0.1 MPa away in terms of the mean effective stress from the critical state. While a rigorous criterion of the safety margin is still to be established for a soil mass, this is probably the most critical finding from this simulation. A largest zone of influence (6.6 m in diameter) is that of the thermally elevated pore pressure of up to 1.5 MPa and a significant change in the effective stress components.

Especially the former finding is of relevance for the design of heat emanating facilities, where multiple heat sources may overlap in terms of the influence zones, giving rise to higher values in the overlap areas, and affecting other parameters of the performance. It is customary to design such multi-source facilities based on a non-interaction criterion of the heat fields only. It is clear that heat influence zone is the smallest of all both hydraulic and mechanical fields, hence rendering the heat non-interaction criterion a least safe criterion.

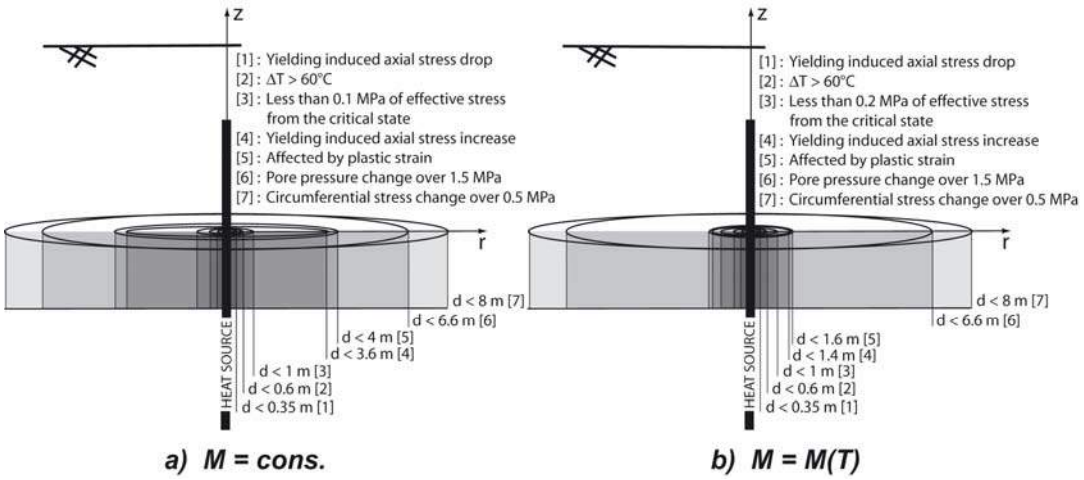

Fig. 7. The extent of zones of interest in the considered case study for (a) $M = cons.$ and (b) variable M.

4.5. Further considerations on thermal failure at the field scale

Simulations show that independently of the temperature variation of coefficient M during heating up to 96.5°C, the thermal pressurization of the pore water brings the effective stress path very closely to the critical state. While the amount of associated irreversible deviatoric strain is not posing any threat to the imbedded structure, small heterogeneities in material properties as well as small perturbations in the load parameters, may easily cause a variation of the effective stress path, such that the stress state may migrate to the "wet" side of the yield locus. This may lead to a possible instability, strain localization and/or non-uniqueness of response, or alternatively a statically inadmissible response (Hueckel et al., 2009b). First, such an occurrence is more likely to take place, when $M=cons.$, rather than when the material internal friction is thermally strengthen by temperature. Second, the likelihood of such occurrence is plausible in the entire zone of yielding. Indeed in the considered case, it is highest at the distance of 40.9 cm from the wall of the heat source, which is the most remote of the considered points in the yielding zone. Finally, in the studied case the effective stress state is closest to the critical state at the end of the plastic process, which is to be reminded is arrested by an arbitrarily imposed end of heating. The notion of a thermal global failure is still awaiting a rigorous treatment. In this paper (see also Hueckel et al., 2011), we have adopted an intuitive criterion of a "mean effective stress distance from the critical state" as a measure of local instability.

As for the influence of the temperature dependence of the internal friction (and coefficient of the critical state M) with temperature, the main findings are as follows. The biggest impact

of the evolution of the internal friction is on the effective stress trajectory. In general, as might be expected, the growth of the internal friction lowers a chance that the effective stress may reach the critical state. That happens mainly because a higher internal friction allows a larger portion of the response to be elastic, by increasing the aspect ratio of the yield locus. Second, the increasing friction angle decreases almost by half the zone of influence of axial stress alteration around the heat source. Finally, the rising internal friction reduces, again almost by half, the amount of the deviatoric plastic strain at the most heated locations.

5 CONCLUSIONS

The performed simulations, which are using the actual parameters identified for a numerical model of an actual clay, allow us to reveal: (i) general features of the mechanical fields generated by a heat source in the clay mass surrounding it and in particular the proximity of the stress state to failure condition; (ii) the effect of dependence of one of the key soil mechanical parameters, the internal friction, on temperature; (iii) a quantitative extent of influence zones of various variables of relevance. A more detailed analysis of the performed simulation is reported by Hueckel et al. (2011).

The first of the above findings is of paramount importance in such applications as geological nuclear waste disposal or underground heat storage and emphasizes a need for more attention toward margin of safety of the heat source embedded in the soil. The second one suggests that even a relatively modest thermal sensitivity of a key parameter may play a large role in a boundary value problem (that is at the field scale). Previous laboratory studies have shown that this temperature dependence is not very strong. Indeed, in many experimental studies on different soils it was considered as marginally significant. However, several known clays materials consistently exhibit a response, which without considering a thermal dependence of internal friction would be at least confusing.

The determination of zones of influence offers a foundation for a rational design of the respective monitoring system in a heated soil mass. It is also crucial for the design of spacing of heat emitters ensuring a limited superposition of a series of effects of neighbouring devices. Designing the heat source spacing based on the temperature field alone is by far inadequate.

It is sometimes argued in the nuclear waste disposal community that thermal pressurization pulse of pore water around the heat source is irrelevant, because of its short duration. There is a merit in this statement from the hydraulics (or a potential radionuclide transport) point of view. However, the analysis of the resulting effective stress trajectory shows that despite its short duration the pore pressure increase causes the effective stress path to approach the critical state, hence substantially reducing the structure margin of safety.

REFERENCES

Baldi, G., Hueckel, T., Peano A. & Pellegrini, R. (1991). Developments in modelling of thermo-hydro-mechanical behaviour of Boom clay and clay-based buffer materials (Vol 1 and 2). EUR 13365/1 and 13365/2. Luxembourg, Commission of the Eur. Communities.

Bigoni, D. & Hueckel, T. (1991). Uniqueness and localization - I. Associative and non-associative elastoplasticity. Int. Journal of Solids and Structures, 28, No. 2, 197-213.

Cekerevac, C. & Laloui, L. (2004). Experimental study of thermal effects on the mechanical behaviour of a clay. Int. J. for Num. and Anal. Methods in Geomechanics, 28, 3: 209-228.

Charlier, R., Radu, J.P. & Collin, F. (2001). Numerical modelling of coupled transient phenomena. Revue Française de Génie Civil 2001, 5, No. 6, 719–741.

Collin, F., Li, X., Radu, J.P. & Charlier, R. (2002). Thermo-hydro-mechanical coupling in clay barriers. Engineering Geology, 64, 179–193.

François, B., Laloui, L. & Laurent, C. (2009). Thermo-hydro-mechanical simulation of ATLAS in-situ large scale test in Boom Clay. Computer and Geotechnics, 36, 626-640.
Hueckel, T. & Baldi, G. (1990). Thermoplasticity of saturated clays: Experimental constitutive study. Journal of Geotechnical Engineering, 116, No. 2: 1778-1796.
Hueckel, T. & Borsetto, M. (1990). Thermo-plasticity of saturated soils and shales: Constitutive equations. Journal of Geotechnical Engineering, 116, No. 12, 1778-1796.
Hueckel, T. & Pellegrini, R. (1992). Effective stress and water pressure in saturated clays during heating-cooling cycles. Canadian Geotechnical Journal, 29, 1095-1102.
Hueckel, T., Borsetto, M. & Peano, A. (1987). Modelling of coupled thermo-elasto-plastic-hydraulic response of clays subjected to nuclear waste heat. Chapter 11, in Numerical Methods in Transient and Coupled Problems, edited by R. W. Lewis et al., 213-235, J. Wiley, Chichester.
Hueckel, T., François, B. & Laloui, L. (2009a). Explaining thermal failure in saturated clays. Geotechnique, 59, No. 3, 197–212.
Hueckel, T., Laloui L. & François B. (2009b). Implications of thermal sensitivity of the static internal friction angle. 1st International Symposium on Computational Geomechanics (ComGeo I), 104-115.
Hueckel, T., Laloui L. & François B. (2011). Temperature dependent internal friction of clay in a heat source problem, Geotechnique, 61 [doi: 10.1680/geot.2011.61.00.1]
Laloui, L. & Cekerevac, C. (2003). Thermo-plasticity of clays: an isotropic yield mechanism. Computers and Geotechnics, 30, No. 8, 649-660.
Laloui, L. & François, B. (2009) ACMEG-T: Soil thermo-plasticity model. Journal of Engineering Mechanics, 135, No. 9, 932-944.
Laloui, L. (1993). Modélisation du comportement thermo-hydro-mécanique des milieux poreux anélastique. PhD Thesis, Ecole Centrale de Paris.

ON THE MECHANICAL BEHAVIOUR OF CRUSHED LIMESTONE

S. Pietruszczak & P. Guo
Department of Civil Engineering, McMaster University, Hamilton, Ont., Canada

ABSTRACT: *The main focus in this work is on modeling of mechanical response of granular materials that display inherent anisotropy. Both the experimental and numerical investigations are described. First, the results of direct shear as well as drained/undrained triaxial tests are reviewed that involve crushed limestone with elongated angular-shaped particles. Later, a mathematical framework is presented for modeling of inelastic deformation that incorporates the multi-laminate approach. The deformation is monitored on a set of randomly oriented planes and the formulation incorporates the thickness of the shear band that is associated with sliding/separation process. A systematic procedure for identification of material functions/ parameters is outlined that is based on the results of direct shear tests and the framework is later applied to simulate the behaviour under triaxial conditions. The results of numerical simulations are compared with the experimental data.*

1 INTRODUCTION

Granular materials often display anisotropy in the mechanical behaviour, which is strongly linked with the microstructural arrangement. Such anisotropy may occur in sands that comprise flat, elongated grains, but may also be induced by densification process in sands that have nearly spherical particles. In either case, mechanical characteristics at the macroscale display a pronounced directional dependence. The existing evidence indicates that a parallel alignment of particles is often observed in river, beach and dune sand (e.g. Oda & Koishikawa, 1977; Oda et al., 1978), as well as in artificially deposited sand. The presence of oriented structure affects both the deformation response and the conditions at failure (Lam & Tatsuoka, 1988; Yamada & Ishihara, 1979). Consequently, it has a significant impact on the behavior of geotechnical structures (such as tunnels and foundations, slopes, retaining walls, etc.) and should be adequately accounted for in the context of design and/or stability analysis.

The work presented here is focused on anisotropic response of crushed limestone. Both experimental and numerical aspects are addressed. In Section 2, the experimental data is presented that involves the results of direct shear and triaxial tests conducted on samples at different orientation relative to direction of deposition. In Section 3, a mathematical framework is outlined for modeling of inelastic deformation. It incorporates the critical plane approach, whereby the mechanical response is described in terms of evolution of displacement discontinuities along a set of discrete planes. Later, a general procedure for identification of material functions is outlined and the performance of the framework is verified against the results of both drained and undrained triaxial tests.

2 EXPERIMENTAL DATA

The material used in this investigation was crushed limestone with elongated angular particles of size between 0.15mm and 2mm. The results of a series of experimental tests on this material have recently been reported by Azami, Pietruszczak & Guo (2010). They included a number of direct shear as well as triaxial tests on samples prepared at different orientation relative to the direction of deposition. Here, the key results of direct shear tests are reviewed first, followed by discussion of the results of drained and recently conducted undrained tests.

The samples were prepared by the sand rain method using a constant falling height of 80cm. This procedure provided fairly uniform specimens with the void ratio of approx. 0.6. The direct shear tests were carried out at normal stress of 1kPa, 25kPa, 50kPa and 75kPa, respectively, for different values of the deposition angle, α. Typical results are presented in Figs.1-2, which show the mechanical response at normal stress of 25kPa and 50kPa. Clearly, the material exhibits a significant degree of anisotropy, as both the strength and deformation characteristics are affected by the angle of angle of deposition. For all tests, the material response becomes unstable (strain softening) after reaching the peak. In terms of evolution of volume change, a progressive transition from compaction to dilatancy takes place as the shear stress increases (Figs.1b and 2b).

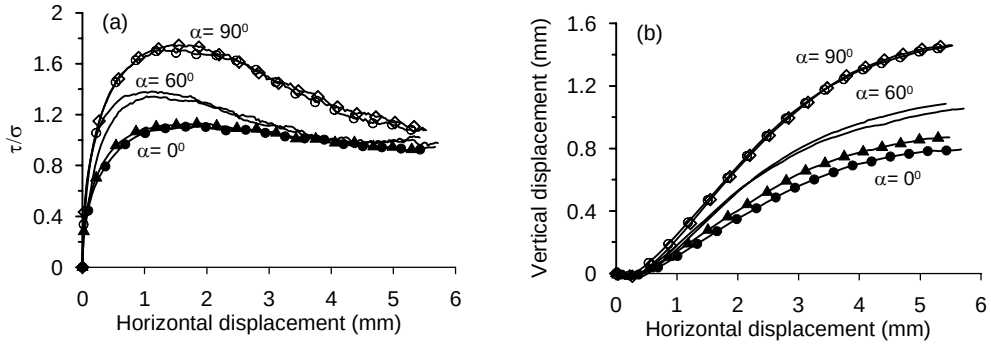

Fig.1. Results of direct shear tests at normal stress σ = 25 kPa; (a) τ/σ vs. horizontal displacement, (b) vertical vs. horizontal displacement

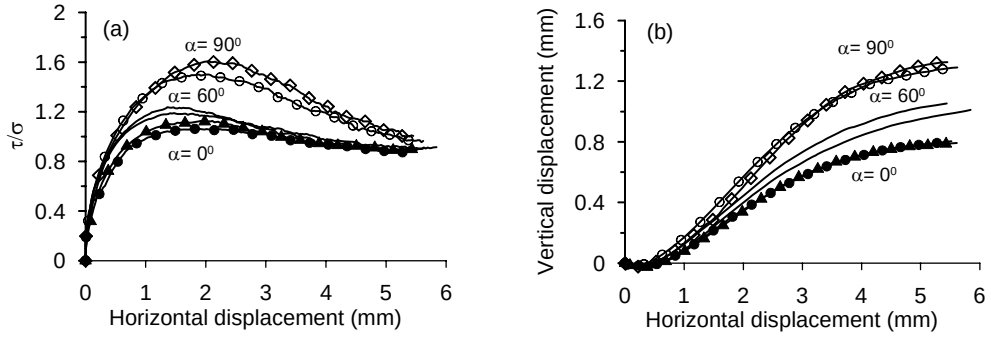

Fig.2. Results of direct shear tests at normal stress σ = 50 kPa; (a) τ/σ vs. horizontal displacement, (b) vertical vs. horizontal displacement

The triaxial tests were conducted on vertical and horizontal samples only. Note that for intermediate values of α, the sample has a tendency to distort under the increasing axial load. In a triaxial cell such distortion is constrained by the presence of loading platens.

Consequently, the stress field is no longer uniform and the results do not reflect the behaviour of the material *per se*. The details of the sample preparation procedure are provided in Azami et al. (2010). The tests were conducted under different initial confining pressures ranging from 10kPa to 150kPa. Typical results, corresponding to confinements of 50kPa and 100kPa are shown in Figs.3 and 4, respectively. Again, it is evident that the behaviour is orientation-dependent. The anisotropy effects, in terms of both strength and deformation response, are quite pronounced. The trends are similar to those depicted in direct shear tests. The strength is the highest for samples tested in the direction of deposition ($\alpha = 0^0$). The volume change characteristics exhibit a transition from compaction to dilatancy; their orientation-dependency, however, is not very significant.

In addition to drained tests, a series of undrained tests was also conducted. Typical results, corresponding to initial confinements of 20kPa and 50kPa, are presented in Fig.5. It is evident that the sample orientation affects both the effective stress trajectories (Fig.5a) as well as the deformation characteristics (Fig.5b). The behaviour is typical of dense sand, i.e. a negative excess of pore pressure develops as the deformation progresses. The most significant impact of anisotropy is on the stress-deformation response, as evidenced in Fig.5b.

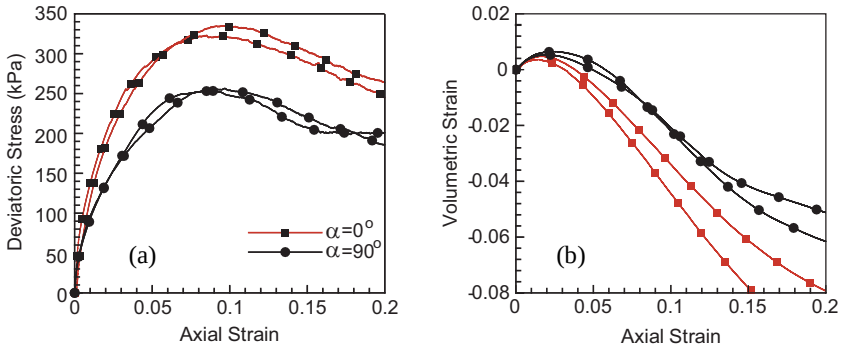

Fig.3. Results of triaxial tests at confining pressure $p_0 = 50$ kPa ; variation of (a) deviatoric stress, $\sigma_1 - \sigma_3$, and (b) volumetric strain with axial deformation

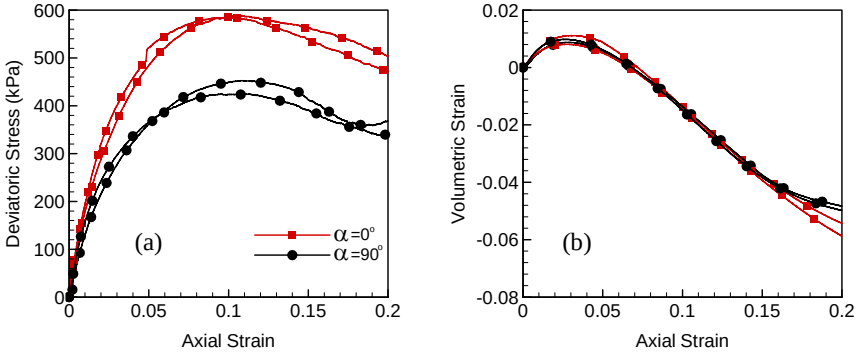

Fig.4. Results of triaxial tests at confining pressure $p_0 = 100$ kPa ; variation of (a) deviatoric stress, $\sigma_1 - \sigma_3$, and (b) volumetric strain with axial deformation

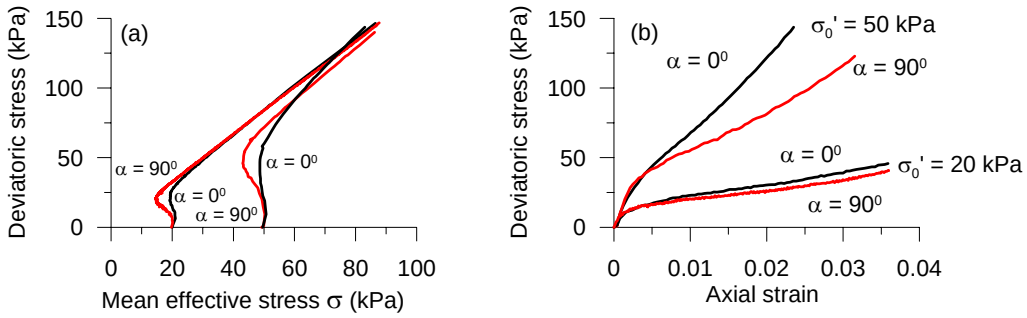

Fig.5: (a) effective stress trajectories and (b) deviatoric characteristics for undrained tests at initial confining pressures of 20 kPa and 50 kPa

3 MODELLING OF INELASTIC DEFORMATION; CRITICAL PLANE APPROACH

In this approach, the failure criterion is defined in terms of traction components acting on the critical/localization plane. The approach employs a spatial distribution of strength parameters and the direction of the localization plane is obtained by solving a constrained optimization problem that involves searching for an orientation that maximizes the value of the failure function.

The conditions at failure are specified in terms of shear and normal components of the traction vector t_i acting on a plane with unit normal n_i, i.e.

$$\tau = \left|\sigma_{ij} n_i s_j\right|; \quad \sigma = \sigma_{ij} n_i n_j; \quad s_i = t_i^s \Big/ \left\| t_i^s \right\|; \quad t_i^s = \left(\delta_{ij} - n_i n_j\right)\sigma_{jk} n_k \tag{1}$$

where $n_i n_i = 1$, $s_i s_i = 1$, $n_i s_i = 0$. The particular form employed here incorporates Coulomb's criterion

$$F = \tau - \eta_f \sigma - c; \quad \eta_f = \eta_f(n_i), \; c = c(n_i) \tag{2}$$

where

$$\begin{aligned} \eta_f &= \hat{\eta}\left(1 + \Omega_{ij} n_i n_j + a_1 (\Omega_{ij} n_i n_j)^2 + a_2 (\Omega_{ij} n_i n_j)^3 + ...\right); \\ c &= \hat{c}\left(1 + \Omega^c_{ij} n_i n_j + b_1 (\Omega^c_{ij} n_i n_j)^2 + b_2 (\Omega^c_{ij} n_i n_j)^3 + ...\right) \end{aligned} \tag{3}$$

and Ω's is traceless symmetric tensors describing the bias in the spatial distribution of the strength parameters η_f and c. The orientation of the critical plane is defined in terms of maximization of F's with respect to n_i, s_i and the failure is said to take place if

$$\underset{n_i, s_i}{\max}(F) = 0 \;\Rightarrow\; \underset{n_i, s_i}{\max}\left(\tau - \eta_f(n_i)\sigma - c(n_i)\right) = 0 \tag{4}$$

The problem can be solved by Lagrange multipliers or any other known optimization technique (e.g. interior point method).

The description of the deformation process can be accomplished by attributing the inelastic behaviour to sliding/separation along an infinite set of randomly oriented planes. For each plane, the conditions at failure are represented by the local criterion (2), which incorporates the distribution functions (3). The inelastic deformation can then be accounted for by invoking an appropriate plasticity formulation. This approach is conceptually similar

to the so-called multi-laminate framework (Pande & Sharma, 1983; Pietruszczak & Pande, 1987).

Assume that the yield and plastic potential functions for the *i*-th plane, with unit normal n_i, have a general form

$$f(n_i) = f(\sigma, \tau, \kappa) = 0; \qquad \psi(n_i) = \psi(\sigma, \tau) = const. \tag{5}$$

where κ is a hardening parameter, which is a function of the plastic deformation history. The latter is typically recorded by measuring the evolution of displacement discontinuities for a given stress history (via a direct shear test). Thus, referring the problem to a local frame $\bar{x}_i$ associated with the base vectors n_i and s_i, the flow rule may be written as

$$\dot{\bar{g}}_i^p = \dot{\lambda} \frac{\partial \psi}{\partial \bar{t}_i} \tag{6}$$

where $\dot{\bar{g}}_i^p$ is the velocity discontinuity vector, whereas the corresponding traction $\bar{t}_i$ has the components $\bar{t}_i = \{\sigma, \tau, 0\}$. The strain rates contributed by this plane are expressed as a symmetric part of a dyadic product

$$\dot{\varepsilon}_{ij}^p = \frac{1}{2t}(\dot{g}_i^p n_j + \dot{g}_j^p n_i); \qquad \dot{g}_i^p = T_{ij}\, \dot{\bar{g}}_j^p \tag{7}$$

where t is the thickness of the shear band that is associated with sliding/separation along a specific plane and T_{ij} is the standard transformation matrix.

The global macroscopic deformation is now obtained by averaging the contributions from all active planes. Thus,

$$\dot{\underset{\sim}{\varepsilon}}_{ij}^p = \frac{1}{(8\pi)t} \int_S \dot{\lambda} (T_{ip}\, n_j + T_{jp}\, n_i) \frac{\partial \psi}{\partial \bar{t}_p} dS \tag{8}$$

where the integration is carried out over a surface area (S) of a unit sphere. In practical implementations, the integration process is performed numerically by adopting a set of 'sampling planes'. Details concerning the orientation of these planes and the distribution of weight coefficients are provided by Pande & Sharma (1983). Given the representation (8), the macroscopic constitutive relation can be obtained by invoking the additivity postulate

$$\dot{\varepsilon}_{ij} = C_{ijkl}^e\, \dot{\sigma}_{kl} + \dot{\varepsilon}_{ij}^p = C_{ijkl}^e\, \dot{\sigma}_{kl} + \frac{1}{(8\pi)t} \int_S \dot{\lambda} (T_{ip}\, n_j + T_{jp}\, n_i) \frac{\partial \psi}{\partial \bar{t}_p} dS \tag{9}$$

where C_{ijkl}^e is the elastic compliance operator, whose functional form may be affected by the presence of anisotropy. It should be noted that the elastic properties associated with each sampling plane can be defined by invoking, once again, the dyadic decomposition in eq.(7). Thus,

$$\dot{\varepsilon}_{ij}^e = \frac{1}{2t}(\dot{g}_i^e n_j + \dot{g}_j^e n_i); \qquad \dot{g}_i^e = T_{ij}\, \dot{\bar{g}}_j^e; \quad \dot{\bar{g}}_i^e = k_{ij}\, \dot{\bar{t}}_j \tag{10}$$

where the components of k_{ij} are the tangential (k_T) and normal (k_N) elastic moduli of the interface. By rearranging the set of equations (10), the elastic strain rates can be defined as

$$\dot{\varepsilon}_{ij}^e = \frac{1}{2t}(T_{ip}\, n_j + T_{jp}\, n_i) k_{pq}\, T_{kq} n_l \dot{\sigma}_{kl} \tag{11}$$

so that the macroscopic deformation is governed by

$$\dot{\varepsilon}_{ij}^{p} = C_{ijkl}^{e}\dot{\sigma}_{kl}\,; \qquad C_{ijkl}^{e} = \frac{1}{8\pi t}\int_{S}(T_{ip}\,n_j + T_{jp}\,n_i)k_{pq}\,T_{kq}n_l\,dS \tag{12}$$

Note that the integration in eq.(12) can be carried out analytically thereby establishing the relation between the classical engineering constants and the respective interface moduli.

The plasticity formulation employed here attributes the hardening effects to irreversible shear deformation. In particular, the yield function is taken as

$$f(n_i) = \tau - \eta\,\sigma - c = 0; \qquad \eta = \eta(\kappa) = \eta_f\,\frac{\kappa}{A+\kappa}; \qquad \kappa = \int\left|dg^{p}\right| \tag{13}$$

Here, $\eta_f = \eta_f(n_i)$, $c = c(n_i)$ have the functional form consistent with representation (3), $dg^{p} = \left((d\bar{g}_2^{p})^2 + (d\bar{g}_3^{p})^2\right)^{1/2}$ and A is a material constant. It should be noted that for $\kappa \to \infty$ there is $\eta \to \eta_f$ which implies that $f(n_i) \to F(n_i)$. Thus, the conditions at failure are consistent with those stipulated by equation (4).

Finally, the plastic potential is defined as

$$\psi(n_i) = \tau - \eta_c\,(\sigma + \sigma_0)\ln\frac{\sigma_0 + \sigma}{\bar{\sigma}} = 0; \qquad \sigma_0 = c/\eta_f \tag{14}$$

where $\bar{\sigma}$ is evaluated from the condition of $\psi(n_i) = 0$, whereas $\eta_c \sim \eta_f$ is a parameter which represents the value of $\eta = (\tau - c)/\sigma$ at which a transition from compaction to dilatancy takes place.

4 NUMERICAL SIMULATIONS

In this section, the numerical simulations of experimental tests on crushed limestone, as presented in Section 2, are provided. First, the procedure for identification of material parameters/functions, based on the results of direct shear tests, is outlined followed by the simulation of a series of triaxial tests.

(i) Identification of material parameters

The specification of material parameters requires examining of both the conditions at failure as well as the deformation characteristics. Consider first the variation of strength parameters, as defined viz. eq. (3). Fig.6a shows the best-fit approximations of Coulomb failure envelopes for samples prepared at $\alpha = 0^{o}$ and $\alpha = 90^{o}$. It is interesting to note that the material develops a residual cohesion due to interlocking of particles. A complete set of experimental data, in terms of variation of η_f and c with the deposition angle α, is provided in Figs.6b and 6c. The same figures show the best-fit approximations employing representation (3). The results presented in Fig.6b incorporate the terms up to degree 4. It is evident that the linear approximation ($a_1 = a_2 = ... = 0$) is not very accurate so that the higher order terms are required. The representation including 4^{th} order terms corresponds to the set of coefficients

$$\Omega_1 = 0.1419679,\ \hat{\eta} = 1.06463,\ \ a_1 = 5.1768,\ \ a_2 = 31.2851,\ \ a_3 = 87.8614$$

A similar methodology has been employed in the context of defining the bias in the spatial variation of cohesion, c, Fig.6c. In this case, the second-order approximation is accurate enough and corresponds to the following coefficients of the best-fit approximation

$$\Omega_1^{c} = 0.2229053,\ \hat{c} = 3.509254,\ \ b_1 = 0.8161$$

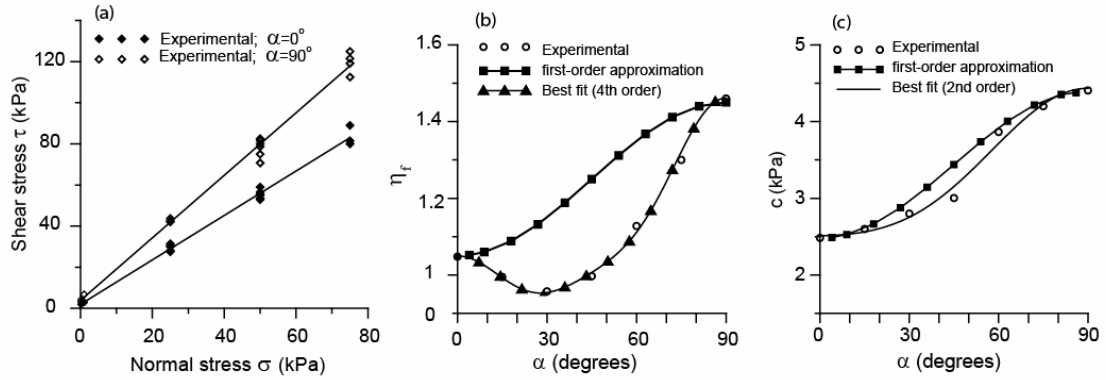

Fig.6. (a) Best-fit approximations of failure envelopes; (b,c) approximations to spatial variation of the friction coefficient η_f and cohesion *c*

The plasticity formulation requires information on the material parameters A, η_c that are incorporated in eqs.(13)-(14). The specification of hardening function, eq.(13), involves the identification of material constant A. In order to accomplish this, the mechanical characteristics given in Figs.1-2 are now re-plotted in $\{ g^p, \eta = (\tau - c)/\sigma \}$ space. Note that constructing such characteristics requires the identification of the elastic tangential modulus k_T, so that the irreversible part of the horizontal displacement discontinuity can be determined via the additivity postulate. The value of k_T should normally be assessed from the initial slope of the *unloading* branch, i.e. $k_T = d\tau / dg^e$. Here, the experimental information is limited to active loading histories only. Given this restriction, the value of k_T was estimated from the initial slope of the *loading* branch. Fig.7 shows the variation of k_T as a function of the deposition angle, α, for different normal stress σ ranging from 25kPa to 75kPa. It is evident that the value of k_T increases with an increase in normal stress magnitude; however, the orientation dependency is rather insignificant and can, in fact, be neglected. The orientation average of k_T, estimated as k_T=550kPa/mm, was selected as representative over the range of $\sigma \in (25-75)$ kPa that was employed later in the numerical simulations.

Fig.8 presents the hardening characteristics at normal stress of 25kPa and 50kPa, for deposition angles of $\alpha = 0^0, 90^0$, respectively. At the same time, Fig. 9 shows the best fit approximation employing the hyperbolic representation (13). It is noted that the experimental characteristics become unstable (strain softening) after reaching the peak. This will, in general, lead to localization of deformation into a shear band, when samples are tested under more general conditions (e.g., in triaxial or biaxial tests). The modelling of localized deformation mode should be conducted at the level of a *boundary-value problem* using one of the approaches that explicitly incorporate a characteristic dimension. Given this, the identification procedure outlined here is restricted to hardening regime, including the specification of the onset of unstable response. Note that, since the hardening function is of the type $g^p \to \infty \Rightarrow \eta \to \eta_f$, the incorporation of a criterion for the onset of softening requires a revision in the functional form (13). Perhaps, the simplest approach is to define the asymptotic condition as $g^p \to \infty \Rightarrow \eta \to \zeta \eta_f$ where ζ is a constant within the range, say $1 < \zeta < 1.05$. In such case, the onset of unstable behaviour can be associated with $\eta = \eta_f$.

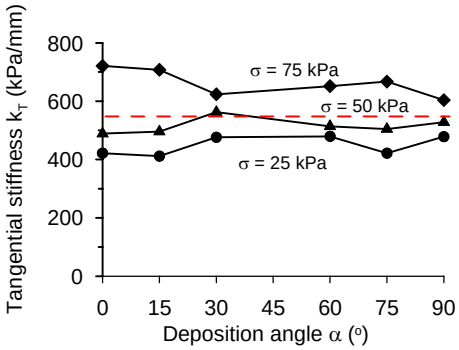

Fig.7. Variation of k_T with deposition angle, α, for different normal stress σ ranging from 25kPa to 75kPa

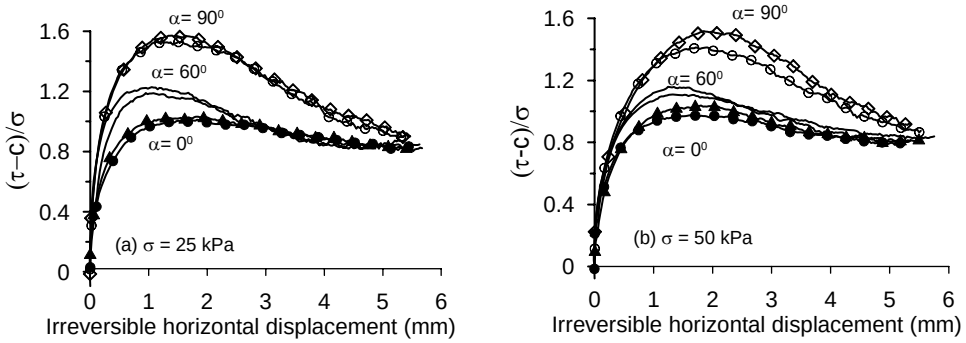

Fig.8. Experimental hardening characteristics at different deposition angles, α, for (a) σ = 25 kPa, and (b) σ = 50 kPa

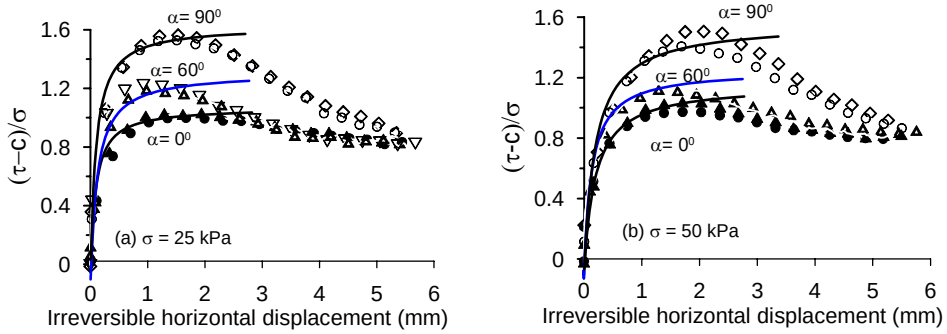

Fig.9. Best-fit approximations to hardening characteristics at different deposition angles, α, for (a) σ = 25 kPa, and (b) σ = 50 kPa

The spatial variation of parameter A, for normal stress within the interval 25-75kPa, is shown in Fig.10. In general, the orientation dependence of A is not very pronounced, as all values are within a relatively narrow range of 0.1-0.2mm. Thus, a constant value of A=0.12mm, which is the average for all tests considered, was selected as representative and was employed later in the numerical simulations.

The next step of the identification procedure involves the specification of the parameter η_c, viz. eq.(14), that defines the transition from plastic compaction to dilatancy. The value of this parameter can be assessed by examining the volume change characteristics, as depicted

in Figs.1-2. Again, these characteristics need to be re-plotted in the affine space $\{\eta, g_1^p\}$. The irreversible part of the vertical displacement discontinuity, g_1^p, has been estimated here by assuming that $k_N = 5k_T$ and invoking the additivity postulate. Note that, in general, a sufficient degree of accuracy may be maintained by associating the transition points with the evolution of total vertical displacement. Fig.11 shows the variation of η_c with the deposition angle. It is evident that the evolution of η_c is qualitatively similar to that of the strength parameter η_f. Therefore, the estimated value of η_c was taken as $\eta_c = 0.6\eta_f$.

Finally, the thickness associated with sliding/separation along each specific plane was assumed to be a multiple of the average particle size, viz. *t*=8mm. Furthermore, given the evidence provided in Fig.7, the elastic properties were taken as isotropic (k_T =550kPa/mm, $k_N = 5k_T \Rightarrow$ G = 4 MPa, $\nu = 0.33$).

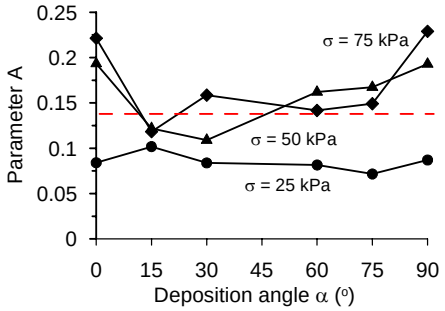

Fig.10. Variation of hardening parameter A with deposition angle α for different normal stress σ

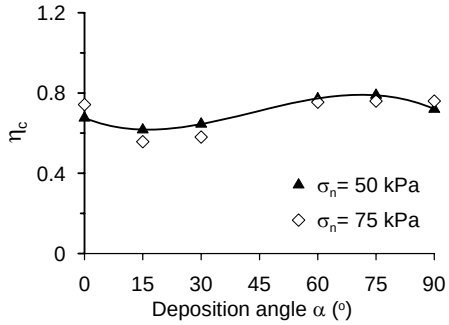

Fig.11. Variation of η_c with the deposition angle α for σ within the range 50kPa - 75kPa

(i) Numerical simulations of triaxial tests

Based on the considerations above, a unique set of material parameters can now be assigned and the performance of the framework verified for various triaxial loading histories, as discussed in Section 2.

Fig.12 shows the simulations of drained traixial tests conducted at the initial confining pressure of 50kPa. Fig.12a shows the deviatoric stress-strain characteristics for the deposition angles of $\alpha = 0^0, 90^0$. It should be mentioned that the deformation mode is axisymmetric only for the sample tested at $\alpha = 0^0$. For $\alpha = 90^0$, the lateral deformation is different in the respective in-plane directions, while for samples at other orientations, the generation of shear strains will be predicted. The results are fairly consistent with the experimental evidence. The simulations do not involve the unstable strain softening response, as the latter is associated with the onset of localized deformation and, as mentioned earlier, should be analyzed at the

level of a boundary-volume problem. Note that the muli-laminate framework employed here can be easily extended to strain-softening range by adopting the averaging scheme similar to that in Pietruszczak (1999) or Azami et al. (2010). The latter is, in fact, conceptually similar and requires setting the weighting coefficient (w) on the localization plane to w=1 and averaging the response over the volume associated with the corresponding integration point.

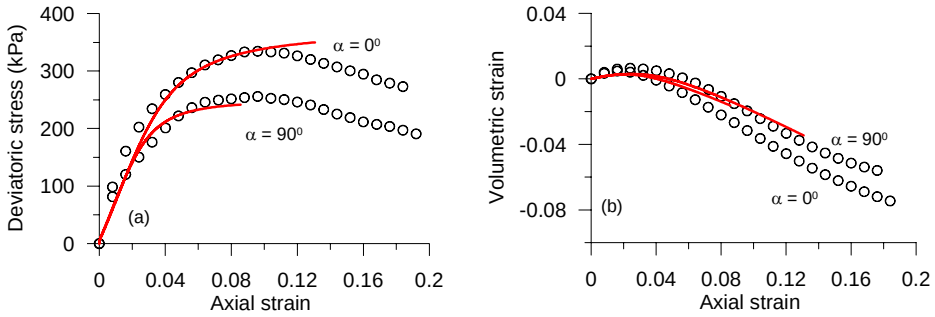

Fig.12. Results of triaxial compression tests at σ_3 = 50kPa; (a) stress-strain characteristics and (b) evolution of volume change (model parameters: t =8 mm G = 4 GPa, A = 0.12mm)

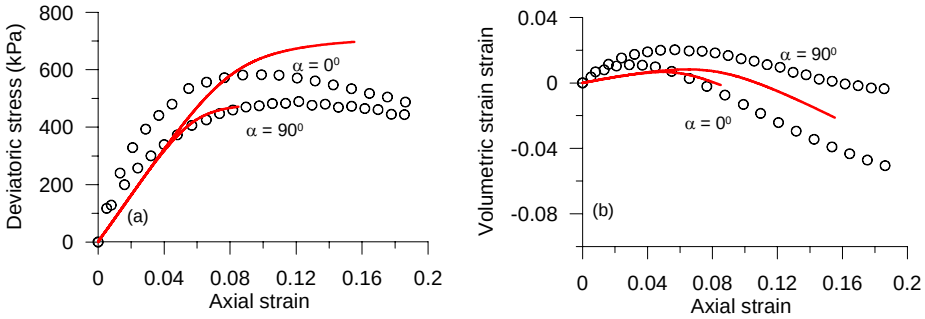

Fig.13. Results of triaxial compression tests at σ_3 = 100 kPa (a) stress-strain characteristics and (b) evolution of volume change (model parameters: t =8 mm G = 4 GPa, A = 0.12mm)

Fig.12b shows the corresponding volume change characteristics. Here, a progressive transition from compaction, at the early stages of the deformation process, to dilatancy takes place. The predicted quantitative response is not very sensitive to the orientation of the sample, which is consistent with the experimental data.

Fig.13 shows a similar set of simulations for samples tested at the initial confining pressure of 100kPa. The predictions, for both the deviatoric characteristics as well as the evolution of volume change, again appear to be reasonable. It is noted though that the strength at $\alpha = 0^0$ is overpredicted by about 15%.

Finally, the results of undrained analysis are presented in Figs. 14-15. Fig. 14 shows the effective stress trajectories and the corresponding deviatoric characteristics for samples tested at the initial confining pressure of 50kPa. The numerical predictions are again compared with the experimental data and show that the trends are fairly similar. It is noted that at early stages of the deformation process, the predicted effective stress paths show little sensitivity to the orientation of the sample. This is primarily due to the fact that the simulations were completed assuming that both the elastic stiffness and the hardening parameter A are orientation-independent. While for the drained analysis this simplification has virtually no effect on the response, under undrained conditions the impact is more pronounced. This is illustrated in Fig. 15, which shows a parametric study on the influence of the hardening

parameter A. Evidently, a decrease in the value of A affects the shape of effective stress trajectories and results in reduction in the generated excess of pore water pressure.

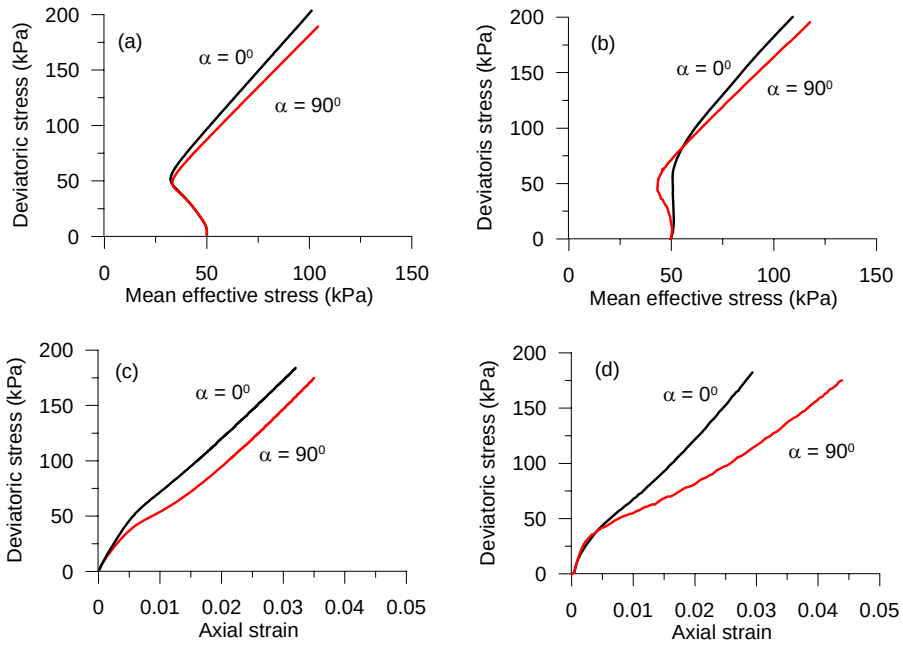

Fig.14. Effective stress characteristics in undrained triaxial compression: (a, c) numerical modelling and (b,d) triaxial test results

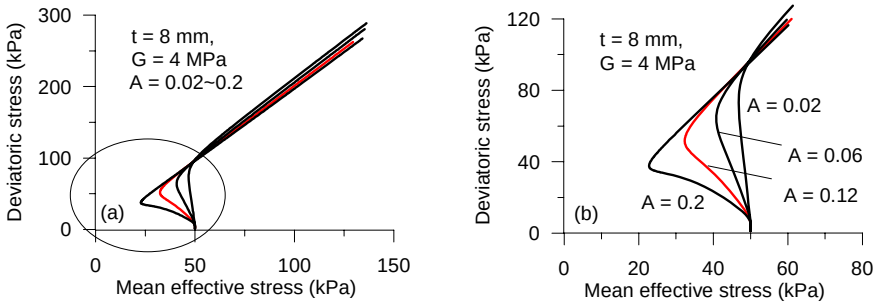

Fig. 15. Influence of hardening parameter A on effective stress trajectories in undrained triaxial compression

5 FINAL REMARKS

The methodology presented here makes use of the results of direct shear tests to formulate the problem and to identify the material parameters/functions involved. In order to predict the response under general loading conditions, the formulation incorporates the thickness of the shear band that is associated with the sliding/separation process.

It is evident that the proposed approach is adequate in terms of predicting the basic trends in the mechanical response of granular materials exhibiting an inherent anisotropy. The

results capture the sensitivity of the strength, as well as the deformation characteristics, to the orientation of the sample. The predicted trends are, in general, fairly consistent with the experimental evidence.

REFERENCES

Azami, A., Pietruszczak, S. and Guo, P. (2010), "Bearing capacity of shallow foundations in transversely isotropic granular media". Int. J. Num. Anal. Meth. Geomech., 34(8), 771-880.

Lam, W.K. and Tatsuoka, F., (1988), "Effect of initial anisotropic fabric and σ_2 on strength and deformation characteristics of sand". Soils and Foundations 28(1), 89–106.

Oda, M. and Koishikawa, I. (1977), "Anisotropic fabric of sand". Proc. 9th Int. Conf. Soil Mech. Found. Eng., Vol. 1, 235-238.

Oda M., Koishikawa I. and Higuchi T. (1978), "Experimental study of anisotropic shear strength of sand by plane strain test". Soils and Foundations, 18(1), 25-38.

Pande, G.N. and Sharma, K.G., (1983), "Multi-laminate model of clays – a numerical evaluation of the influence of rotation of the principal stress axes". Int. J. Num. Anal. Meth. Geomech. 7, 397-418.

Pietruszczak S. (1999), "On homogeneous and localized deformation in water-infiltrated soils", Journal of Damage Mechanics, 8(3), 233-253.

Pietruszczak, S. and Pande, G. N, (1987), "Multilaminate framework of soil models – Plasticity formulation". Int. J. Num. Anal. Meth. Geomech. 11, 651-658.

Yamada, Y., Ishihara, K. (1979), "Anisotropic deformation characteristics of sand under three dimensional stress conditions". Soils and Foundations, 19(2), 79–94

NEW APPROACH FOR MODELING TIME-DEPENDENT BEHAVIOR OF GEOMATERIALS

T. Nakai, H.M. Shahin, M. Kikumoto, H. Kyokawa & F. Zhang
Department of Civil Engineering, Nagoya Institute of Technology, Nagoya, Japan

M.M. Farias
Department of Civil and Environmental Engineering, University of Brasilia, Brasilia, Brazil

ABSTRACT: *A simple method to describe time-dependent behavior for various kinds of soils is presented. The model is formulated not using usual viscoplastic theories but utilizing the subloading surface concept by Hashiguchi (1980) and paying attention to the experimental results, which show that the normal consolidation line (NCL) and the critical state line (CSL) on the e – lnσ plane shift depending on the strain rate. The formulation is first explained in one-dimensional conditions in order to understand the method easily. After that, using the t_{ij} concept proposed by Nakai and Mihara (1984), the one-dimensional model is extended to a three-dimensional one. The validity of the present model is verified using various kinds of simulations of time-dependent behavior in both conditions – e.g., one-dimensional compression tests under different strain rate, oedometer tests including secondary consolidation, creep and stress relaxation tests, constant strain rate triaxial tests and others.*

1 INTRODUCTION

Several time-dependent constitutive models for soils are found in the literature. Sekiguchi (1977) proposed a viscoplastic model with a non-stationary flow surface. In his model, the non-stationary flow surface is obtained from the ordinary differential equation having a unique relation among stress, plastic volumetric strain and plastic strain rate. The viscoplastic strain rate is calculated assuming an associated flow rule. Nova (1982) also developed a viscoplastic model by extending an inviscid model using non-stationary flow surface theory. Another type of viscoplastic model based on the over-stress viscoplastic theory by Perzyna (1963) (e.g., Adachi and Oka, 1982; Dafalias, 1982; Katona, 1984) is available in literature, in which the strain rate effects can be described by assuming a Bingham like material and utilizing the difference of sizes of the static yield surface related to the current plastic strains and the dynamic yield surface related to the current real stresses. Hashiguchi and Okayasu (2000) developed a time-dependent subloading surface model introducing a creep potential function. Zhang et al. (2005) developed a time-dependent model for heavily over consolidated clays and soft rocks, modifying the subloading t_{ij} model developed by Nakai and Hinokio (2004). A comprehensive report on time dependent behavior of soils and its modeling has been written by Sekiguchi (1985).

In this paper, a simple method to model time-dependent characteristics in normally consolidated soils, over consolidated soils and structured soils (such as naturally deposited clays) is presented. The method is not based on the usual viscoplastic theories rather it is based on the subloading surface concept which is derived from the basis of the experimental results that indicate a shift between the normal consolidation line (NCL) and the critical state line (CSL), in the e – lnσ plane, depending on the strain rate.

2 ONE-DIMENSIONAL MODELING OF STRUCTURED CLAY

2.1 Formulation of 1D Time-Independent Model

Fig. 1 shows a typical e – $\ln\sigma$ relation of natural clay schematically. Asaoka et al. (2002) developed a model to describe such structured soils, introducing subloading surface concept (Hashiguchi, 1980) and superloading surface concept to the Cam-clay model. In their modeling, a factor related to the over consolidation ratio (corresponding to imaginary density) has been introduced to increase the stiffness, and a factor related to the soil skeleton structure has been introduced to decrease the stiffness. By controlling the evolution rules of these factors, they described various features of consolidations and shear behavior of structured soils.

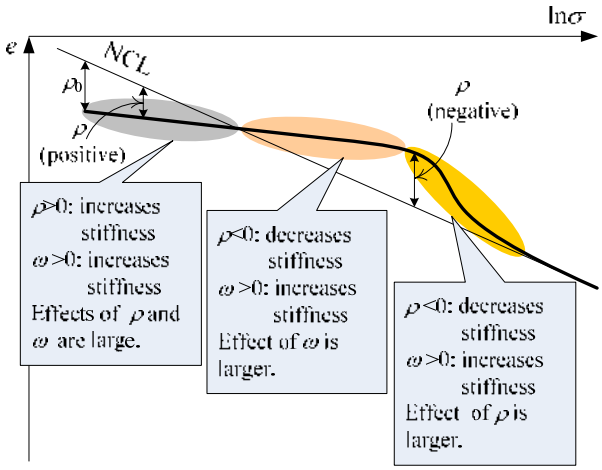

Fig. 1 Void ratio (e): $\ln\sigma$ relation in structured clay

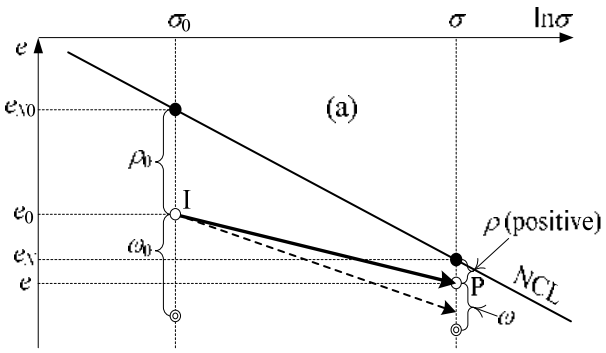

Fig. 2 Change of void ratio in structured clay

In the present paper, attention is focused on the real density and the bonding as the main factors that affect the behavior of structured soil, because it can be considered that the soil skeleton structure in a looser state than that of a normally consolidated soil is formed by bonding effects. Fig. 2 shows the change of void ratio when the stress condition moves from the initial state I ($\sigma=\sigma_0$) to the current state P ($\sigma=\sigma$). Here, e_0 and e are the initial and current void ratios of structured soil, and e_{N0} and e_N are the corresponding void ratios on the normal consolidation line. It can be understood that the structured soil is stiffer than non-structured over consolidated soil, when the initial void ratios e_0 are the same. Then, the change in void ratio for structured soil indicated by the solid line is smaller than that for non-structured over consolidated soil (broken line). Now, the state variable ρ ($=e_N - e$) which represents the effect of the density is defined by the difference between the void ratio on NCL and the current void ratio of the soil at the same stress. The initial value of the state variable is expressed as $\rho_0 = e_{N0} - e_0$. To describe such increase in stiffness of structured soil, we introduce an imaginary increase of density ω which represents the effect of the bonding, in addition to the real density ρ. Here, ω_0 is the initial value of ω.

When stress condition moves from σ_0 to σ, the plastic change of void ratio $(-\Delta e)^p$ for the clay is obtained. Referring to Fig. 2.

$$\begin{aligned}(-\Delta e)^p &= (-\Delta e) - (-\Delta e)^e \\ &= \{(e_{N0} - e_N) - (\rho_0 - \rho)\} - (-\Delta e)^e \\ &= \lambda \ln\frac{\sigma}{\sigma_0} - (\rho_0 - \rho) - \kappa \ln\frac{\sigma}{\sigma_0}\end{aligned} \tag{1}$$

Here, $(-\Delta e)^e$ is the elastic change of void ratio, and λ and κ denote compression and swelling indices, respectively. From this equation, yield function for the soil is expressed as follows:

$$F + \rho = H + \rho_0 \quad \text{or} \quad f = F - \{H + (\rho_0 - \rho)\} = 0 \tag{2}$$

where, F and H denote the terms of stress and the plastic change in void ratio.

$$F = (\lambda - \kappa)\ln\frac{\sigma}{\sigma_0}, \qquad H = (-\Delta e)^p \tag{3}$$

From the consistency condition (df=0) at the occurrence of plastic deformation with satisfying Eq. (2), the following equation is obtained:

$$\begin{aligned} df &= dF - \{dH - d\rho\} \\ &= (\lambda - \kappa)\frac{d\sigma}{\sigma} - \{d(-\Delta e)^p - d\rho\} = 0 \end{aligned} \tag{4}$$

Now, it can be considered that the evolution rule of ρ with the development of plastic deformation for structured soil is determined not only by the state variable ρ related to real density but also by the state variable ω related to the imaginary increase of density (bonding effect). Larger values of the state variables ρ and ω can be assumed to have more effects for the degradation of ρ and ω. Then, the evolution rules of ρ and ω can be given in the following form, using increasing functions $G(\rho)$ and $Q(\omega)$ which satisfy $G(0)=0$ and $Q(0)=0$, respectively:

$$d\rho = -\{G(\rho) + Q(\omega)\} \cdot d(-e)^p \tag{5}$$

Simply, the evolution rule of ω is also given as follows using the same function $Q(\omega)$:

$$d\omega = -Q(\omega) \cdot d(-e)^p \tag{6}$$

Equations (4) and (5) give the increment of the plastic change in void ratio as

$$d(-e)^p = \frac{\lambda - \kappa}{1 + G(\rho) + Q(\omega)} \cdot \frac{d\sigma}{\sigma} \tag{7}$$

The increment of total change in void ratio is expressed as the summation of the plastic components $(-\Delta e)^p$ and the elastic component $(-\Delta e)^e$.

$$\begin{aligned} d(-e) &= d(-e)^p + d(-e)^e \\ &= \left\{\frac{\lambda - \kappa}{1 + G(\rho) + Q(\omega)} + \kappa\right\}\frac{d\sigma}{\sigma} \end{aligned} \tag{8}$$

As shown in Eq. (8), positive ρ and ω have effects to increase stiffness of soil, because $G(\rho)$ and $Q(\omega)$ are positive when both ρ and ω are positive. Assume an initial state with positive ρ_0 and positive ω_0. At the first stage (ρ>0 and ω>0), the stiffness of the soil is much larger than that of remolded NC soil because of the positive values of $G(\rho)$ and $Q(\omega)$. When the current void ratio becomes the same as that on NCL (ρ=0), the stiffness of the structured soil is still greater than that of remolded NC soil (because of ω>0). So, it is possible for the structured soil to have the state which is looser than that on NCL. In this stage (ρ<0 and ω>0), the effect to increase the stiffness by positive value of ω is larger than the effect to decrease the stiffness by negative value of ρ. After this stage the effect of ω becomes small with the development of plastic deformation. On the other hand, the effect of ρ to reduce the stiffness becomes prominent because of the negative value of ρ. Finally the void ratio approaches to

that on NCL from the looser state than NCL, because ρ and ω converge to zero. Such feature of structured soil can be described by extending the defined domain of the increasing function $G(\rho)$ to the negative value of ρ - e.g., $G(\rho)$ and $Q(\omega)$ are given by increasing functions such as $G(\rho)=a\rho$ and $Q(\omega)=b\omega$. That is to say, though $Q(\omega)$ is monotonically approaching to zero with the development of plastic deformation, $G(\rho)$ has an effect to the current void ratio to approach to that on NCL, regardless the sign of ρ.

2.2 Simulations

In order to check the validity of the present model, numerical simulations of one-dimensional compression tests are carried out. Assuming Fujinomori clay which was used in the previous experimental verification of constitutive models (e.g., Nakai and Hinokio, 2004; Nakai, 2007), following material parameters are employed in the numerical simulations – compression index λ=0.104, swelling index κ=0.010 and void ratio on NCL at σ=Pa=98kPa (atmospheric pressure) N=0.83. Fig. 3(a) shows the calculated e-lnσ relation of the one-dimensional compression using the same bonding effect (ω_0=0.2) and the different initial void ratios. Fig. 3(b) shows the calculated results using the same initial void ratio e_0=0.73 (ρ_0=0.1) and the different bonding effects. Since the state variable related to density ρ (=e_N - e), which is represented by the vertical distance between current void ratio and void ratio at NCL, of the clay without bonding (ω_0=0) decreases monotonically, the void ratio converges to NCL from the downside of NCL. The void ratio of the clay with bonding (ω_0>0) decreases less compare to the condition without bonding (ω_0=0) and enters the upside of NCL (ρ<0). After then, it converges to NCL from the negative side of ρ with a sharp reduction of the bulk stiffness. In these figures, the parameters (a and b) which represent the degradation rate of ρ and ω are fixed. It can be seen from these figures that it is possible to describe the deformation of structured clay only considering the effect of density and bonding and their evolution rules. Furthermore, Fig. 3(c) shows the results in which the initial void ratio and the initial bonding are the same but the parameter b is different. We can see that the result with a large value of b (=100) describes void ratio-stress relation with strain softening.

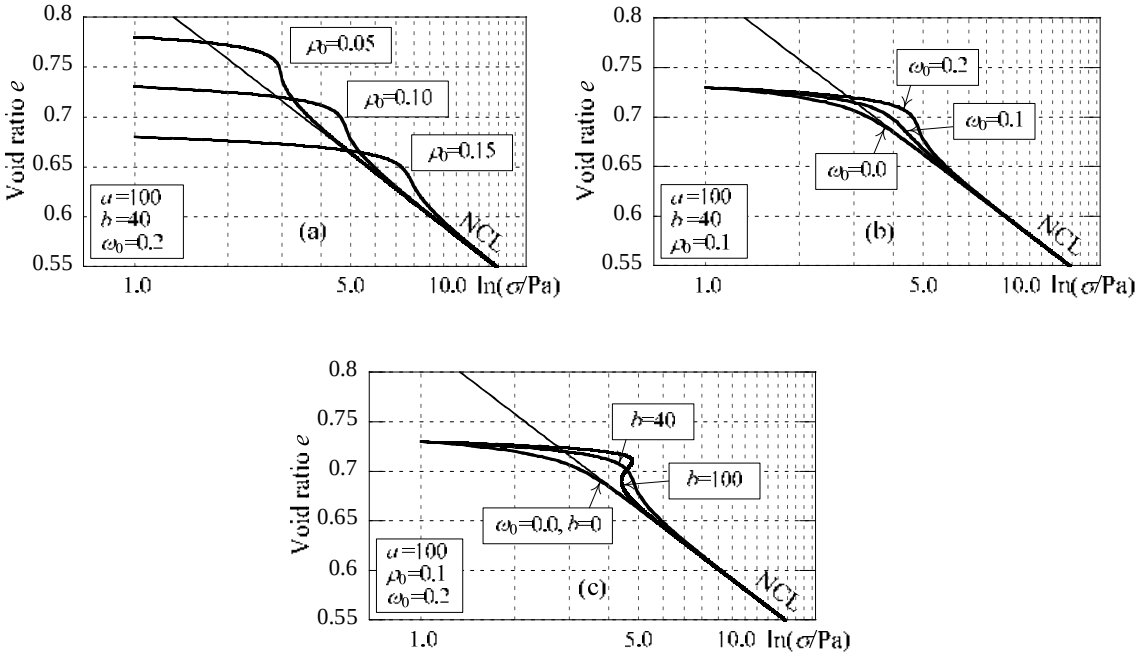

Fig. 3 Calculated results of clay with different ρ_0, ω_0 and b

3 ONE-DIMENSIONAL MODELING OF TIME-DEPENDENT BEHAVIOR

3.1 Formulation of 1D Time-Dependent Model

We will formulate the time-dependent behavior of soils not using the past elasto/viscoplastic theories but by an extension of the above-mentioned formulation for the structured soils. Fig. 4 shows a time-dependent behavior of normally consolidated clay in one-dimensional condition schematically. It is well known that the normally consolidation line (NCL) shifts due to strain rate (rate of plastic change in void ratio $(-\dot{e})^p$), and the void ratio (e) changes linearly against time on a log scale (ln$t$) under creep condition. In order to model these features, introducing a state valuable ψ which is given by a function of strain rate, we shift the position of NCL due to the strain rate (the rate of the change of void ratio, as shown in Fig. 5. Here, ψ_0 is the initial value of ψ, and point I and point P indicate the initial state ($\sigma=\sigma_0$, $e=e_0$ and $\psi=\psi_0$) and the current state($\sigma=\sigma$, $e=e$ and $\psi=\psi$), respectively.

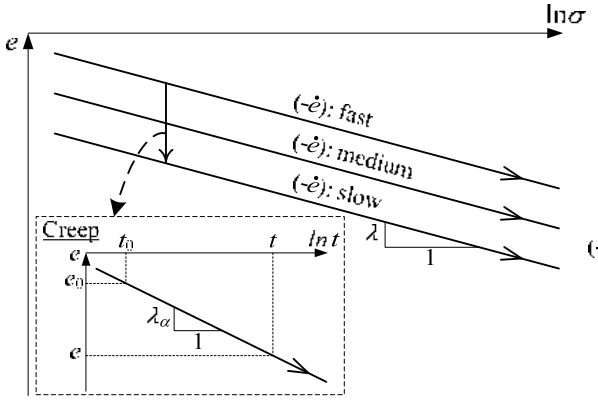

Fig. 4 Time dependent behavior of normally consolidated clay

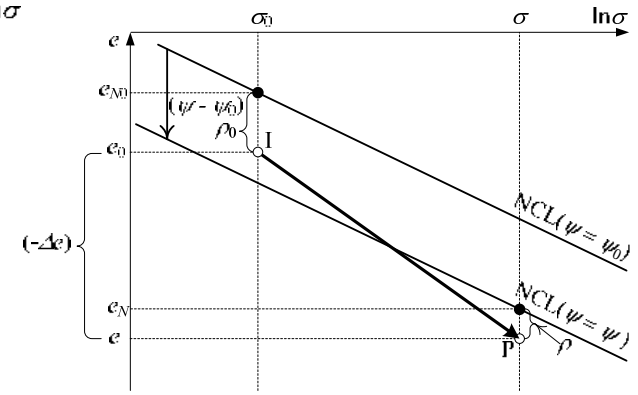

Fig. 5 Change of void ratio in structured clay with time dependent behavior

By referring to this figure, the plastic change of void ratio $(-\Delta e)^p$ for soil in which the above features should be considered is expressed as.

$$\begin{aligned}(-\Delta e)^p &= (-\Delta e) - (-\Delta e)^e \\ &= \{(e_{N0} - e_N) - (\rho_0 - \rho)\} - (-\Delta e)^e \\ &= \left\{\lambda \ln\frac{\sigma}{\sigma_0} + (\psi - \psi_0) - (\rho_0 - \rho)\right\} - \kappa \ln\frac{\sigma}{\sigma_0} \\ &= \lambda \ln\frac{\sigma}{\sigma_0} - (\rho_0 - \rho) - (\psi_0 - \psi) - \kappa \ln\frac{\sigma}{\sigma_0}\end{aligned} \tag{9}$$

Therefore, the following equation holds between F and H:

$$\begin{aligned}&F + \rho + \psi = H + \rho_0 + \psi_0 \\ &\text{or} \quad f = F - \{H + (\rho_0 - \rho) + (\psi_0 - \psi)\} = 0\end{aligned} \tag{10}$$

Consistency condition (df=0) gives

$$\begin{aligned}df &= dF - \{dH - d\rho - d\psi\} \\ &= (\lambda - \kappa)\frac{d\sigma}{\sigma} - \{d(-e)^p - d\rho - d\psi\} = 0\end{aligned} \tag{11}$$

Now, referring to Fig. 4, we can get the distance (ψ-ψ_0) in Fig. 5 as a function of the elapsed time t or the rate of plastic change in void ratio $(-\dot{e})^p$:

$$\psi - \psi_0 = \lambda_\alpha \ln \frac{t}{t_0} = \lambda_\alpha \ln t - \lambda_\alpha \ln t_0$$
$$= \lambda_\alpha \ln \frac{(-\dot{e})_0^p}{(-\dot{e})^p} = \left\{-\lambda_\alpha \ln(-\dot{e})^p\right\} - \left\{-\lambda_\alpha \ln(-\dot{e})_0^p\right\} \tag{12}$$

Here, λ_k is the coefficient of secondary consolidation. To obtain the above equation, the following relation during creep deformation in normally consolidated soil was used:

$$(-\dot{e})^p = \frac{d(-\Delta e)^p}{dt} = \frac{d\left(\lambda_\alpha \ln \frac{t}{t_0}\right)}{dt} = \lambda_\alpha \frac{1}{t} \tag{13}$$

Then, ψ and ψ_0 which represent the positions of initial and current NCL and the increment $d\psi$ are expressed as

$$\begin{cases} \psi = -\lambda_\alpha \ln(-\dot{e})^p \\ \psi_0 = -\lambda_\alpha \ln(-\dot{e})_0^p \end{cases} \tag{14}$$

$$d\psi = \frac{\partial \psi}{\partial t} dt = \lambda_\alpha \frac{1}{t} dt = (-\dot{e})^p dt \tag{15}$$

Now, it is assumed that Eqs. (14) and (15) hold not only for normally consolidated soils but also for over consolidated soils and naturally deposited soils. Substituting Eqs. (5) and (15) into Eq. (11), the increment of the plastic void ratio can be obtained as

$$d(-e)^p = \frac{(\lambda-\kappa)\frac{1}{\sigma} d\sigma + (-\dot{e})^p \cdot dt}{1+G(\rho)+Q(\omega)} \cong \frac{(\lambda-\kappa)\frac{1}{\sigma} d\sigma + (-\dot{e})^{p*} \cdot dt}{1+G(\rho)+Q(\omega)} \tag{16}$$

Here, $(-\dot{e})^{p*}$ denotes the rate of the plastic void ratio change at the step immediately before the current calculation step. Finally, the total increment of void ratio is given in the following equation:

$$d\left(-e\right) = d\left(-e\right)^p + d\left(-e\right)^e = \left(\frac{\lambda-\kappa}{1+G\left(\rho\right)+Q\left(\omega\right)} + \kappa\right)\frac{d\sigma}{\sigma} + \frac{\left(-\dot{e}\right)^{p*}}{1+G\left(\rho\right)+Q\left(\omega\right)} dt \tag{17}$$

In order to simplify the numerical calculations, the known rate $(-\dot{e})^{p*}$ in the previous calculation step can be used, instead of the current rate, as described in Eqs. (16) and (17). The error caused by using the previous known rate is negligible in the calculations, because an incremental method with small steps is used in non-linear analysis. As can be seen from Eq. (5), the void ratio approaches the condition satisfying $G(\rho)+Q(\omega)=0$, regardless of the sign of ρ. Here, ρ represents the difference between the current real void ratio and the void ratio on the NCL, which shifts depending on the current rate $(-\dot{e})^p$ as mentioned above. Therefore, even if there occurs some small error by using $(-\dot{e})^{p*}$ in the numerical calculation, updating the rate with the calculated plastic change in void ratio at each time increment and reflecting it on the state variable ψ at the next step, the error caused in the present calculation step is automatically corrected in the next one. The model requires only one additional parameter, which is the coefficient of secondary consolidation λ_α, to account for time effects. An important point of the present model is that the present model does not include time variable t and is formulated using the rate of void ratio change $(-\dot{e})^p$ alone. If time t is used in a model, the results will depend on the way of determining the origin of time. Another characteristic of the proposed approach is that by only eliminating the term of the

rate effect $(-\dot{e})^{p^*}$ in Eq. (17), or by setting λ_α=0, this model easily results in the elastoplastic model without time effect.

The loading condition of the present model is presented as follows by assuming the plastic volume expansion does not occur:

$$\begin{cases} d(-e)^p \neq 0 \ : & \text{if } d(-e)^p > 0 \\ d(-e)^p = 0 \ : & \text{otherwise} \end{cases} \tag{18}$$

3.2 Simulations

The validity of the proposed time-dependent model is checked by some simulations of one-dimensional compression tests under constant strain rate and conventional oedometer tests with instantaneous loading of constant stress. The adopted parameters are the same as those of Fujinomori clay used in the previous section – i.e., compression index λ =0.104, swelling index κ=0.010, void ratio on the NCL at σ=98kPa N=0.83. The evolution rule for ρ is considered as a linear function, $G(\rho)=a\rho$, and the evolution rule for ω is also considered as a linear function, $Q(\omega)=b\omega$. The parameter for density and confining pressure a =100 and the degradation parameter of bonding b=40. The rate of the plastic void ratio change at reference state is $(-\dot{e})^p_{ref}$ =1.0x10^{-7}/min. Here, the coefficient of secondary consolidation λ_α is 0.003, unless otherwise stated.

Fig. 6(a) shows the simulated results of one-dimensional compression behavior of normally consolidated clay for different strain rates, arranged in terms of the e-logσ relation. The initial rate of plastic void ratio change is the same as that at reference state ($(-\dot{e})^p_0 = (-\dot{e})^p_{ref}$ =1.0x10^{-7}/min). In the figure, the solid straight line (no creep) shows the simulated relation without time effect. It is seen from this figure that with the increase in strain rate the resistance to compression increases and the lines of constant strain rate are parallel to each other which is a good agreement with published experimental results (e,g., Bjerrum, 1967). It is also seen that when the strain rate is changed at a certain point, the curve follows exactly the same path which is supposed to follow for the new strain rate. This is valid for both increasing and decreasing of the strain rates, and in the case where the strain rate is increased the simulation gradually reaches the target curve following the phenomenon of 'isotache'. Therefore, it can be said that the present model can describe properly the strain rate effects of non-structured normally consolidated clay (ω_0=0 and ρ_0=0) under constant strain rate consolidation tests.

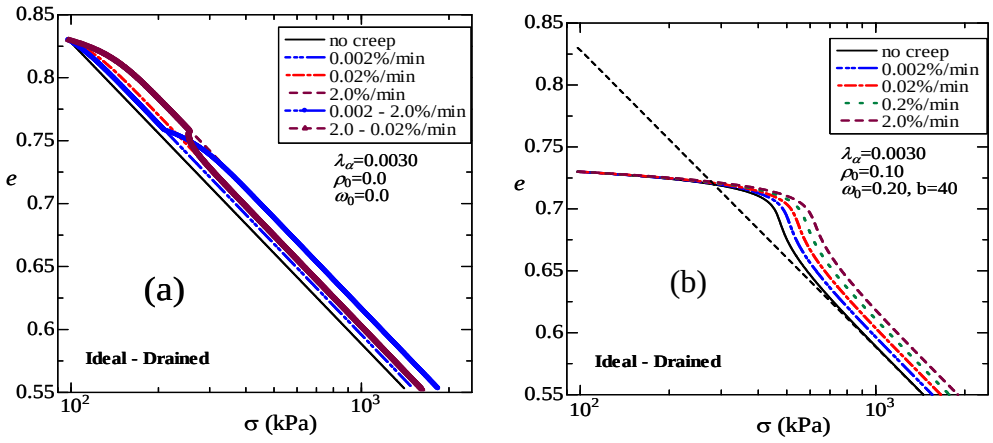

Fig. 6 Strain rate effects of normally consolidated clay and natural clay in one-dimensional conditions

Fig. 6(b) illustrates the results for over consolidated-structured soil. Here, the initial void ratio and the initial rate of strain are the same as those of diagram (a). The initial value of the state variable reflecting the bonding effect is ω_0=0.20, and the bonding degradation parameter is b=40. In the figures, the dotted straight line denotes the normal consolidation line (NCL) for $(-\dot{e})^p = (-\dot{e})^p_{ref}$ =1.0x10^{-7}/min. It can be observed that for over consolidated states the strain rate dependency of the soil is less significant compared to normally consolidated states. However, each e-logσ relation for over consolidated soils and structured soils finally approaches the line simulated for normally consolidated soil under corresponding strain rate. The phenomenon of 'isotache' is simulated for over consolidated and structured soils, in the same way as observed for the normally consolidated soil. In diagrams (b) in Fig. 6, each solid curve designated as 'no creep' corresponds to the curve without time effect in Fig. 3(c). It is also seen that the "preconsolidation" stress (effective consolidation yield stress) p_c increases with increasing strain rates, particularly in structured clays. These simulations in Fig. 6 describe well the strain rate effects in one-dimensional compression for over consolidated clay and structured clay reported in the literature (e.g., Leroueil et al., 1985; Tanaka et al, 2006; Watabe et al., 2008).

4 EXTENSION OF ONE-DIMENSIONAL TIME-DEPENDENT MODEL TO THREE-DIMENSIONAL ONE

4.1 t_{ij} Concept

For considering the influence of intermediate principal stress automatically, the concept of modified stress t_{ij} is proposed (Nakai and Mihara, 1984). The modified stress t_{ij} is defined by the product of a_{ik} and σ_{kj}, using a symmetric non-dimensional tensor a_{ik}

$$t_{ij} = a_{ik}\sigma_{kj} \tag{19}$$

And its principal values are given as follows using the principal values of t_{ij} and a_{ij}:

$$t_1 = a_1\sigma_1,\ t_2 = a_2\sigma_2,\ t_3 = a_3\sigma_3 \tag{20}$$

Here, a_{ij} is the symmetric tensor whose principal values (a_1, a_2 and a_3) are given by the direction cosines of the normal to the spatially mobilized plane (abbrev., SMP; Matsuoka and Nakai, 1974)

$$a_1 = \sqrt{\frac{I_3}{I_2\sigma_1}}\ ,\ a_2 = \sqrt{\frac{I_3}{I_2\sigma_2}}\ ,a_3 = \sqrt{\frac{I_3}{I_2\sigma_3}} \tag{21}$$

(I_2, I_3 : 2nd and 3rd stress invariants of σ_{ij})

The invariants of modified stress (t_N and t_S) used in t_{ij} concept are defined as the normal and parallel components of t_{ij} to the SMP as shown in Fig. 7.

$$t_N = \overline{\mathrm{ON}} = t_1a_1 + t_2a_2 + t_3a_3 = t_{ij}a_{ij} \tag{22}$$

$$t_S = \overline{\mathrm{NT}} = \sqrt{t_1^2 + t_2^2 + t_3^2 - (t_1a_1 + t_2a_2 + t_3a_3)^2} = \sqrt{t_{ij}t_{ij} - (t_{ij}a_{ij})^2} \tag{23}$$

Fig. 8 shows the yield surfaces of an elastoplastic model based on the t_{ij} concept, represented on the $t_N - t_S$ plane. The broken curve and solid curve indicate the initial and current yield surfaces when the stress condition moves from the initial state I (t_N=t_{N0}) to the current state P

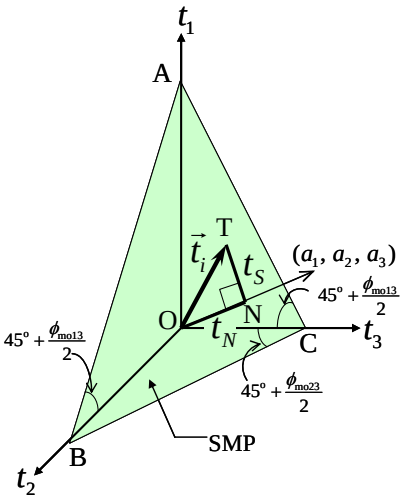

Fig. 7. Definitions of t_N and t_S

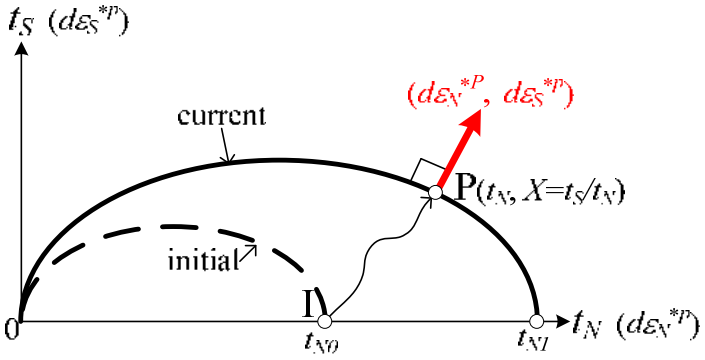

Fig. 8 Initial and current yield surfaces in the t_N– t_S plane and direction of plastic flow for the model based on the t_{ij} concept

(t_N=t_N, X=t_S/t_N) with elastoplastic deformation. Now, as described before, in one-dimensional modeling, the term F in the yield function f=0 (Eqs. (2) and (10)) is given by Eq. (3) as the function of stress σ and its initial value σ_0. In the three-dimensional modeling based on t_{ij} concept, the function F is expressed as follows by replacing σ_0 and σ in one-dimensional model with t_{N0} and t_{N1}:

$$F = (\lambda - \kappa)\ln\frac{t_{N1}}{t_{N0}} = (\lambda - \kappa)\left\{\ln\frac{t_N}{t_{N0}} + \varsigma(X)\right\} \qquad (\text{where } X = t_S/t_N) \tag{24}$$

Here, t_{N0} and t_{N1} are the values of t_N on t_N-axis representing the sizes of the initial and current yield surfaces, and $\zeta(X)$ is an increasing function of stress ratio X(=t_S/t_N) which satisfies the condition $\zeta(0)$=0. In the present modeling, the following function of $\zeta(X)$ is given:

$$\varsigma(X) = \frac{1}{\beta}\left(\frac{X}{\mathrm{M}^*}\right)^{\beta} \qquad (\beta: \text{ material parameter}) \tag{25}$$

Then, the plastic strain increment is calculated using an associated flow rule in t_{ij} space (see Fig. 8), as follows:

$$d\varepsilon_{ij}^{p} = \Lambda\frac{\partial F}{\partial t_{ij}} = \Lambda\left(\frac{\partial F}{\partial t_N}\frac{\partial t_N}{\partial t_{ij}} + \frac{\partial F}{\partial X}\frac{\partial X}{\partial t_{ij}}\right) \tag{26}$$

The derivation process of the positive proportionality constant Λ, which is obtained from the consistency condition (df=0) in the same way as in the ordinary models, will be described in the subsequent section.

4.2 Formulation of 3D Time-Dependent Model

It is assumed that the yield function in Eq. (10) holds in thee-dimensional condition in the same way as in one-dimensional condition, and the term H is also correspond to the plastic change of void ratio.

$$H = \left(-\Delta e\right)^{p} = (1 + e_0)\cdot\varepsilon_v^{p} \tag{27}$$

From the consistency condition (df=0) and the flow rule in Eq. (26), the following expression can be obtained:

$$
\begin{aligned}
df &= dF - \{dH - d\rho - d\psi\} \\
&= dF - \{d(-e)^p - d\rho - d\psi\} \\
&= dF - \left\{(1+e_0)\Lambda\frac{\partial F}{\partial t_{ii}} - d\rho - d\psi\right\} = 0
\end{aligned} \tag{28}
$$

Here, the evolution rule of ρ is given using increasing functions $G(\rho)$ and $Q(\omega)$ which satisfy $G(0)=0$ and $Q(0)=0$ in the same manner as those in one-dimensional model.

$$
d\rho = -(1+e_0)\left\{\frac{G(\rho)}{t_N} + \frac{Q(\omega)}{t_N}\right\}\Lambda \tag{29}
$$

Therefore, from Eqs (28) and (29), Λ is expressed as

$$
\Lambda = \frac{dF + d\psi}{(1+e_0)\left\{\dfrac{\partial F}{\partial t_{kk}} + \dfrac{G(\rho)}{t_N} + \dfrac{Q(\omega)}{t_N}\right\}} = \frac{dF + d\psi}{h^p} \tag{30}
$$

In the three-dimensional model, the evolution rule for ω is given by a linear function, $Q(\omega)=b\omega$ in the same way as one-dimensional model, but the evolution rule for ρ is considered as $G(\rho)=a\rho^2$.

Now, in the one-dimensional time-dependent model, the state variable ψ is related with the rate of plastic void ratio change. However, multi-dimensional stress condition, $(-\dot{e})^p$ (or the plastic volumetric strain rate $\dot{\varepsilon}_v^p$) is not necessarily be positive during plastic deformation because of soil dilatancy, and then the rate of plastic void ratio change (or plastic volumetric strain rate) is not suitable for the measure of time-dependent behavior. Since the norm of plastic strain rate $\left\|\dot{\varepsilon}_{ij}^p\right\|$ is always positive during plastic deformation even in multi-dimensional conditions and gives the magnitude of the plastic strain rate, it seems logical to relate ψ with some quantity using the norm of the plastic strain rate. Leroueil and Marques (1996) shows, from experimental results of oedometer tests and undrained and drained shear tests on clay, that time-dependent behavior of clays under consolidation and shear can be arranged uniquely using the norm of the strain rate as the strain rate measure. Besides, it is known that the void ratio change for normally consolidated soils subjected to pure creep conditions under isotropic compression satisfies a linear *e*-ln*t* relation with the slope of λ_α (coefficient of secondary consolidation) in the same way as that in one-dimensional model. Under isotropic compression, the norm of plastic strain rate $\left\|\dot{\varepsilon}_{ij}^p\right\|$ is expressed as follows using the rate of plastic void ratio change $(-\dot{e})^p$:

$$
\left\|\dot{\varepsilon}_{ij}^p\right\| = \sqrt{\dot{\varepsilon}_{ij}^p\dot{\varepsilon}_{ij}^p} = \sqrt{\dot{\varepsilon}_1^{p2} + \dot{\varepsilon}_2^{p2} + \dot{\varepsilon}_3^{p2}} = \sqrt{3}\,\dot{\varepsilon}_1^p = \frac{\dot{\varepsilon}_v^p}{\sqrt{3}} = \frac{(-\dot{e})^p}{\sqrt{3}(1+e_0)} \tag{31}
$$

It is assumed that $(-\dot{e})_{(equ)}^p$ is an equivalent rate of plastic void ratio change, which is defined by Eq. (31) not only under isotropic compression but also under any other of stress condition.

$$
(-\dot{e})_{(equ)}^p = \sqrt{3}(1+e_0)\left\|\dot{\varepsilon}_{ij}^p\right\| \tag{32}
$$

The increment of ψ is expressed as follows in the same way as Eq. (15) in one-dimensional model:

$$
d\psi = \frac{\partial\psi}{\partial t}dt = \lambda_\alpha\frac{1}{t}dt = (-\dot{e})_{(equ)}^p dt \tag{33}
$$

Substituting Eq. (33) into Eq.(30), the proportionality constant Λ for the three-dimensional model considering time-dependent behavior can be obtained:

$$\Lambda = \frac{dF + (-\dot{e})^{p}_{(equ)}\,dt}{(1+e_0)\left\{\dfrac{\partial F}{\partial t_{kk}} + \dfrac{G(\rho)}{t_N} + \dfrac{Q(\omega)}{t_N}\right\}} = \frac{dF + (-\dot{e})^{p}_{(equ)}\,dt}{h^{p}} \cong \frac{dF + (-\dot{e})^{p^*}_{(equ)}\,dt}{h^{p}} \tag{34}$$

Here, $(-\dot{e})^{p^*}_{(equ)}$ denotes the equivalent rate of plastic void ratio change at the calculation step immediately before the current one, in the same way as in the one-dimensional model. Also, the position of the NCL (ψ) for the next calculation step can be determined by using the updated value of $(-\dot{e})^{p}_{(equ)}$.

4.3 Simulations

The validity of the proposed time-dependent model is checked by performing some simulations of constant strain rate tests, creep tests and others on normally consolidated clay, over consolidated clay and structured clay. The material parameters used are shown in Table 1. The parameter *b* for the bonding effect and the added material parameters for describing time-dependent behavior are also listed in the table, i.e., the coefficient of secondary consolidation λ_α and the equivalent rate of plastic void ratio change at the reference state $(-\dot{e})^{p}_{(equ)ref}$. In the following simulations, the initial equivalent rate of plastic void ratio change is assumed to be the same as that at the reference state $(-\dot{e})^{p}_{(equ)0} = (-\dot{e})^{p}_{(equ)ref}$.

Table 1. Material parameters for simulations of 3D time-dependent model

λ	0.104	Same parameters as Cam clay model
κ	0.010	
N (e_N at p = 98kPa)	0.83	
$R_{CS}=(\sigma_1/\sigma_3)_{CS\,(comp.)}$	3.5	
ν_e	0.2	
β	1.5	Shape of yield surface (same as original Cam clay if β = 1)
$a/(\lambda-\kappa)$	500	Influence of density
$b/(\lambda-\kappa)$	40	Influence of bonding
λ_α	0.003	Coefficient of secondary consolidation
$(-\dot{e})^{p}_{(equ)ref}$	1 x 10^{-7}/min.	Rate of plastic void ratio change at reference state

Fig. 9 shows the calculated results ((a) effective stress paths, (b) stress-strain curves) of undrained triaxial compression and extension tests with different axial strain rates $\dot{\varepsilon}_a$ on a normally consolidated clay (ρ_0=0.0, ω_0=0.0). Here, the curves named ‘no creep’ represent the results without time-effect, and the thick curves indicate the results of the tests in which the strain rate changes from 2.0%/min to 0.002%/min and then 2.0%/min during shear. The model can describe well-known rate effects on the strength and the development of pore water pressure – higher undrained shear strength and less pore pressure development with increasing strain rates. It is also seen that the calculated stress-strain state shifts between the corresponding stress-strain curves and effective stress paths when the strain rate changes during shear, a phenomenon known as ‘isotache’.

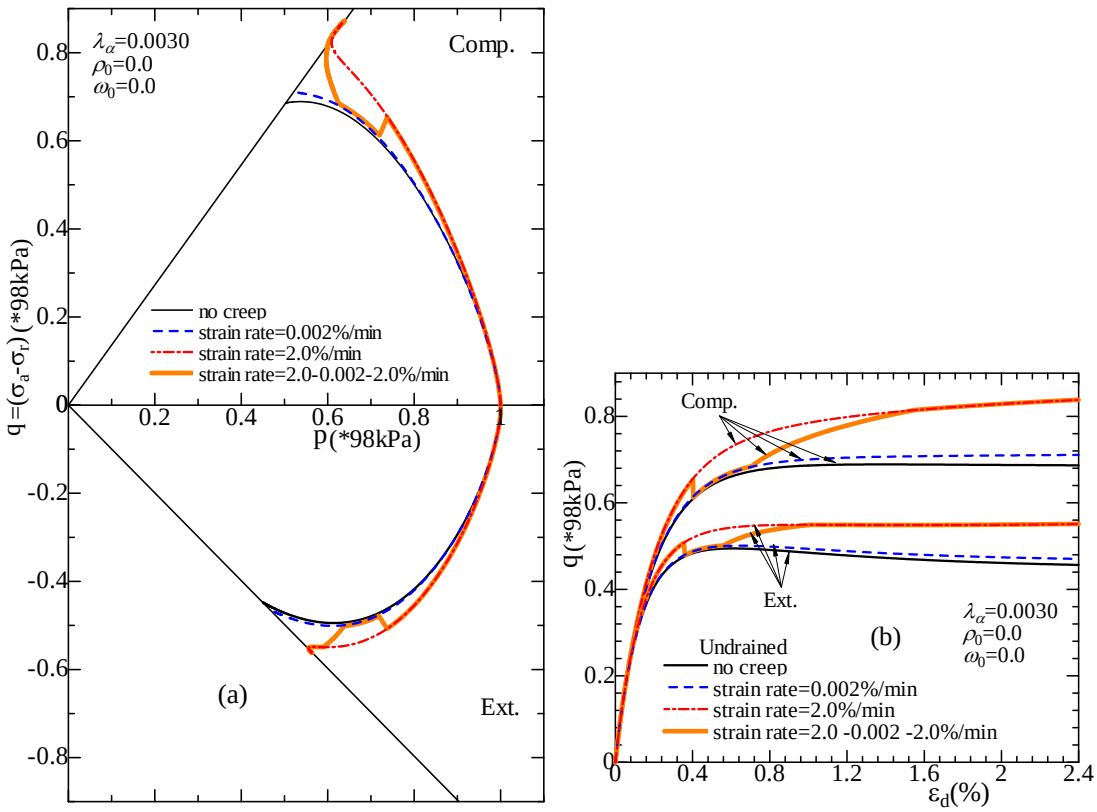

Fig. 9 Simulation of undrained triaxial compression and extension tests on a normally consolidated clay with different strain rates

Fig. 10 shows the calculated results of undrained creep on normally consolidated clay under triaxial compression condition. The clay is sheared up to a certain deviatoric stress condition with the strain rate of $\dot{\varepsilon}_a$ =2.0%/min, and then the deviatoric stress is kept constant. Diagram (a) shows the stress paths during shear and creep condition, and diagram (b) shows the creep curves during creep. It can be seen that the model represents the typical undrained creep behavior including transient creep, stationary creep and accelerating creep (e.g., Sekiguchi, 1984).

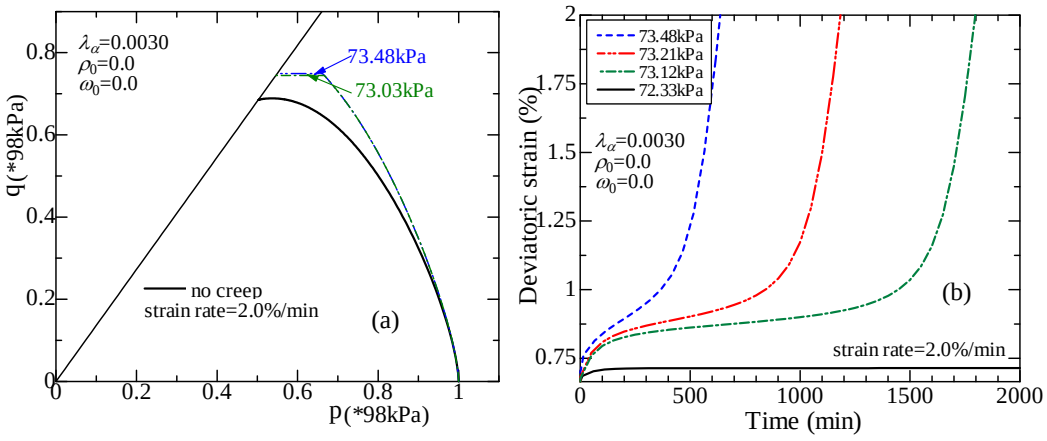

Fig. 10 Simulation of undrained creep tests after constant strain rate ($\dot{\varepsilon}_a$ = 2.0% / min) triaxial compression tests on a normally consolidated clay

Simulations of undrained triaxial compression tests on structured clay with different strain rates are shown in Fig. 11. Here, the structured clay is sheared under undrained condition with different strain rates from the initial conditions (A) and (B) in diagram (a). Diagram (b) shows the effective stress paths and diagram (c) shows the stress-strain curves. The curves represented by 'no creep' are the results without time-effect, and the thick curves indicate the results of the tests in which the strain rate changes from 2.0%/min to 0.002%/min and then 2.0%/min during shear. The phenomenon of 'isotache' has been seen experimentally in structured soils as well as in non-structured soils (e.g., Graham et al., 1983). It can be seen that the present model describes such time-dependent behavior of structured soils as well.

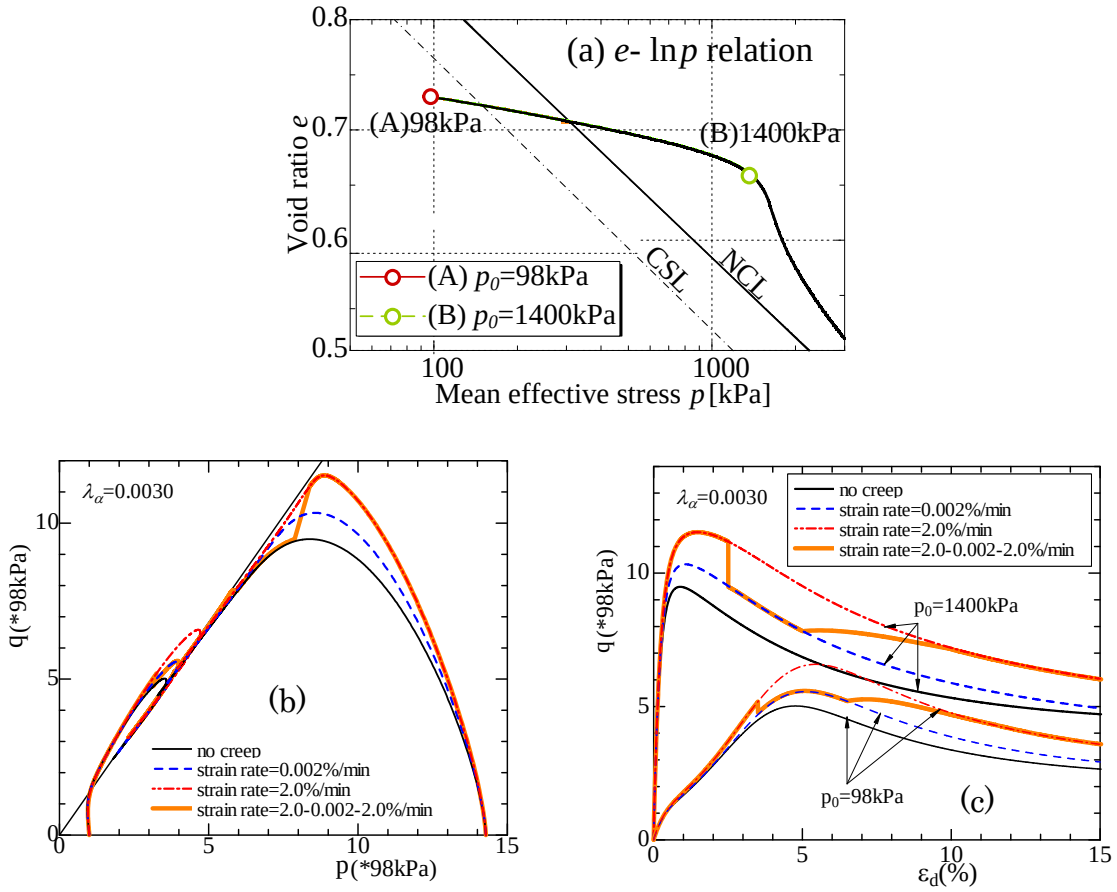

Fig. 11 Simulation of undrained triaxial compression tests on a structured clay with different initial conditions and different strain rates

5 CONCLUSIONS

As one-dimensional model a simple method to describe the behavior of over consolidated soil and structured soil is presented by using the state variables of density (ρ) and bonding (ω), and their monotonous evolution rules. Next, introducing the state variable (ψ) which fixes the position of NCL depending on the strain rate, the model is extended to one considering time-dependent behavior for not only normally consolidated soil but also for over consolidated soil and structured soil. The validities of these models have been checked by the simulations of one-dimensional compression tests on clays with different initial densities, bonding effects and strain rate. The one-dimensional time dependent model is extended to three-dimensional one only by introducing the t_{ij} concept. The validities of the three-dimensional model are also confirmed by the simulation of constant strain rate triaxial tests

and undrained creep tests on normally consolidated clay, over consolidated clay and structured clay. The simulated results correspond to the observed results reported before by many researchers.

REFERENCES

Adachi. T & Oka. F. (1982), "Constitutive equation for normally consolidated clays based on elasto/viscoplasticity". Soils and Foundations, Vol. 22(4), 57-70.

Asaoka, A., Nakano, M. & Noda, T. (2000), "Superloading yield surface concept for highly structured soil behaviour". Soils and Foundations, Vol. 40(2), 99-110.

Dafalias, Y. (1982), "Bounding surface elastoplasticity-viscoplasticity for particulate cohesive media". Proc. of UTAM Conference on Deformation and Failure of Granular Materials, Delft, 97-107.

Graham, J., Crooks, J.H.A. & Bell, A.L. (1983), "Time-effects on the stress-strain behavior of natural soft clays". Geotechnique, Vol. 33(3), 327-340.

Hashiguchi, K. (1980), "Constitutive equation of elastoplastic materials with elasto-plastic transition". Jour. of Appli. Mech,. ASME, Vol. 102(2), 266-272.

Hashiguchi, K. & Okayasu, T. (2000), "Time-dependent elastoplastic constitutive equation based on the subloading surface model and its application to soils". Soils and Foundations, Vol. 40(4), 19-36.

Katona, M.G. (1984), "Evaluation of viscoplastic cap model". J. Getech. Eng., Proc. of ASCE, Vol. 110(8), 1106-1125.

Leroueil, S. & Marques, M. (1996): Importance of strain rate and temperature effects in geotechnical engineering, *Measuring and Modeling Time dependent Soil Behavior*, Geotechnical Special Publication No. 61, ASCE, 1-60.

Matsuoka, H. & Nakai, T. (1974), "Stress-deformation and strength characteristics of soil under three different principal stresses". Proc. of JSCE, No.232, 59-70.

Nakai, T. & Hinokio, T. (2004), "A simple elastoplastic model for normally and over consolidated soils with unified material parameters". Soils and Foundations, Vol. 44(2), 3-70.

Nakai, T. & Mihara, Y. (1984), "A new mechanical quantity for soils and its application to elastoplastic constitutive models". Soils and Foundations, Vol. 24(2), 82-94.

Nova, R. (1982), "A viscoplastic constitutive model for normally consolidated clay". IUTAM Conference on Deformation and Failure of Granular materials, Delft, 287-295.

Perzyna, P. (1963), "The constitutive equations for rate sensitive plastic materials". Quart. Appli. Math., Vol. 20(4), 321-332.

Sekiguchi. H. (1977), "Rheological characteristics of clays". Proc. of 9th International Conf. on Soil Mech. and Foundation Eng., Tokyo, Vol. 1, 289-292.

Sekiguchi, H. (1984), "Theory of undrained creep rupture of normally consolidated clay based on elasto-viscoplasticity". Soils and Foundations, Vol. 24(1), 53-66.

Sekiguchi, H. (1985), "Macrometric approaches – static – intrinsically time-dependent". Proc. of Discussion Session on Constitutive laws of Soils, 11th International Conf. on Soil Mech. and Foundation Eng.,San Francisco, 66-98.

Tanaka, H., Udaka, K. & Nosaka, T. (2006), "Strain rate dependency of cohesive soils in consolidation settlement". Soils and Foundations, Vol. 46(3), 315-322.

Watabe, Y., Udaka, K. & Morikawa, Y. (2008): "Strain rate effect on long-term consolidation of Osaka bay clay". Soils and Foundations, Vol. 48(4), 495-509.

Zhang, F., Yashima, A., Nakai, T., Ye, G.L. & Aung, H. (2005), "An elasto-viscoplastic model for soft sedimentary rock based on t_{ij} concept and subloading surface". Soils and Foundations, Vol. 45(1), 65-73.

RVE SIZE DETERMINATION FROM A DIGITAL IMAGE OF MICROSTRUCTURE

A. Rozanski, D. Lydzba
Institute of Geotechnics and Hydrotechnics,Wroclaw University of Technology, Poland

ABSTRACT: *The notion of the representative volume element (RVE) plays a central role in the field of micromechanics. The definitions of RVE that can be found in the literature are mathematically strict but do not quantify its size. Furthermore, all available methods of RVE size determination are usually based on the investigation of the convergence of apparent properties as the size of RVE is increasing. Therefore these methods require a large number of numerical calculations. In this work it is shown that the size of RVE can be evaluated based only on the morphology of microstructure that is contained in the 2-point correlation function. A methodology is applied to the digital image of the reconstructed 2D realization of the Fontainebleau sandstone. The condition for the minimum size of RVE which is used in the numerical procedure is the one due to Rozanski (2010). The size of RVE is determined for different values of estimation error and the contrast in properties of phases. The method is verified by performing numerical calculations of effective thermal conductivity coefficient.*

1 INTRODUCTION

In the case of random composites the overall response (effective properties) of composite is defined as the relation between expectations of appropriate local fields (of local flux and of local intensity). These expectations, for statistically homogeneous and ergodic medium, can be replaced by volume averages in the limit that the volume tends to infinity. From the engineering point of view, volume averaging over infinite volume means averaging over statistically representative finite sized sample of the material which is referred to as the representative volume element (RVE).

In the existing literature a large number of RVE definitions can be found (Kanit et al., 2003; Stroeven et al., 2004; Gitman et al., 2006). These definitions are usually mathematically strict, however, none of them provides precise information on its size - in other words, the definitions do not quantify the size of RVE. A lot of attempts have been made to quantify the RVE on the basis of statistical and numerical analysis. Within all the methods proposed in the literature (e.g. Povirk, 1995; Gusev, 1997; Kanit et al., 2003), the RVE size is usually determined by investigating the convergence of apparent property with increasing size of RVE. As a result, the process of RVE size evaluation requires a very large number of numerical calculations, e.g. finite element analysis.

In the previous paper of authors (Rozanski et al., 2009) an innovative procedure of RVE size determination, for the particular type of random microstructure (two-phase random checkerboard) has been proposed. The condition for the minimum size of RVE has been

formulated based on the properties of the 2-point correlation function. This condition has been then generalized for the case of any two-phase microstructure in the PhD thesis of the author (Rozanski, 2010). What is remarkable is that the proposed method utilizes only the microstructure morphology that is contained within the 2-point correlation function, and therefore, it gives the possibility of RVE size determination with no large number of numerical calculations; the numerical analysis like those based on FEM or other methods are not necessary.

In this paper, based on the condition proposed by Rozanski (2010), a numerical procedure of RVE size determination from a digital image of microstructure is proposed. It has to be emphasized that the procedure of RVE size evaluation is restricted here to the case of thermal conductivity. The methodology is applied to the digital image of the reconstructed 2D realization of the Fontainebleau sandstone. The digital image is obtained by the 2-point correlation function reconstruction procedure (see Yeong & Torquato, 1998a; Yeong & Torquato, 1998b) which is briefly outlined in next Section. It is shown in the paper that the size of RVE depends on the value of estimation error, volume fraction of phases as well as the contrast in phase properties (conductivities). The proposed methodology is verified by performing numerical calculations of effective thermal conductivities for different values of both estimation error and the contrast in phase properties.

The paper is organized as follows. In Section 2 a digital image of the Fontainebleau sandstone as well as a brief description of reconstruction procedure are provided. Next, the condition for the minimum size of RVE with respect to overall thermal conductivity is presented. Section 4 describes a procedure of the 2-point correlation function evaluation. A Monte Carlo (MC) approach of the 2-point correlation function integration is outlined in Section 5. The general scheme of RVE size determination, together with the RVE sizes for the digital image of the Fontainebleau sandstone, is provided in Section 6. In the last Section the validation of proposed algorithm is performed.

2 THE FONTAINEBLEAU SANDSTONE MICROSTRUCTURE

As mentioned in previous Section the methodology of RVE size determination is applied to the digital image of the reconstructed 2D realization of the Fontainebleau sandstone. This microstructure has been obtained via 2-point correlation function reconstruction procedure. Roughly speaking, the reconstruction process consists in finding such realization for which the calculated 2-point correlation function, $\widetilde{S_2^{(i)}}$, best matches the "target" 2-point correlation function $S_2^{(i)}$ (note that $S_2^{(i)}$ is the phase *i* 2-point correlation function). The target function can be established e.g. in the way of laboratory experiments or theoretical models.

Starting from some initial realization, preserving volume fractions of phases, the microstructure is evolved towards $S_2^{(i)}$ by minimizing the energy *E*, which at any time step, is defined as:

$$E = \sum_r \left[\widetilde{S_2^{(i)}}(r) - S_2^{(i)}(r) \right]^2 \tag{1}$$

The minimization of *E* (at any time step) is performed by simulated annealing algorithm (Kirkpatrick et al., 1983). Namely, the states of two randomly chosen pixels of different phases are interchanged - white pixel is changed into black one, while black pixel is

filled with white color. Interchanging the states of two pixels causes the change in energy, such that $E \to \overline{E}$. Therefore the difference between two states can be calculated, i.e.

$$\Delta E = \overline{E} - E \tag{2}$$

The phase interchange is accepted with the following probability

$$P_{\Delta E} = \begin{cases} 1, & \Delta E \le 0 \\ \exp\left(-\Delta E / T\right), & \Delta E > 0 \end{cases} \tag{3}$$

where T is the fictitious temperature and its actual value is defined by the cooling schedule procedure applied. The solution is obtained as $T \to 0$.

It has been shown by Jiao et al. (2008) that in the case of the Fontainebleau sandstone the target 2-point correlation function for void phase can be approximated by the following relation:

$$\widetilde{S_2^{(1)}(r)} = \left(0.77\exp\left(-r/3\right) + 0.23\exp\left(-r/6.5\right)\cos\left(0.2r\right)\right)\phi_1\phi_2 + \phi_1^2 \tag{4}$$

where $\phi_1 = 0.175$ and $\phi_2 = 0.825$ are the volume fractions of void and solid phases, respectively.

Utilizing the methodology presented above the microstructure of the Fontainebleau sandstone has been reconstructed. In Fig. 1 the digital image of 2D reconstructed realization of the Fontainebleau sandstone is provided. The resolution of the digital image is 500×500 pixels. The void phase is shown in white, whereas black pixels are associated with solid phase.

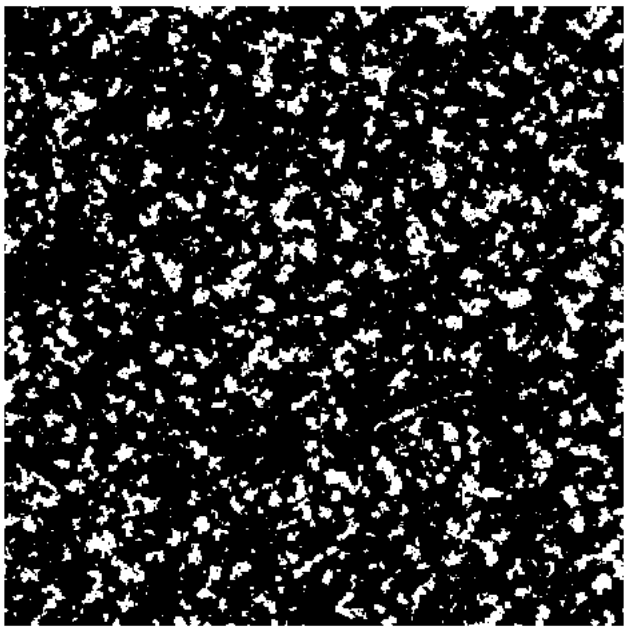

Fig. 1. Digital image (500×500 pixels) of the reconstructed 2D realization of the Fontainebleau sandstone

3 THE CONDITION FOR THE MINIMUM SIZE OF RVE

The condition for the minimum size of RVE $\left(\|\Omega\|_{\mathrm{RVE}}\right)$, proposed by Rozanski (2010) with respect to effective thermal conductivity, reads:

$$\|\Omega\|_{\mathrm{RVE}} \geq \max\left[\|\Omega\|_1;\|\Omega\|_2;\|\Omega\|_3\right] \tag{5}$$

where

$$\|\Omega\|_1 = \frac{2|1-\Theta|}{\left(\phi_1+\phi_2\Theta\right)}\sqrt{\frac{\int_0^a\int_0^b\left(S_2^{(1)}(r)-\phi_1^2\right)(a-x)(b-y)\,dxdy}{\varepsilon}} \tag{6a}$$

$$\|\Omega\|_2 = \frac{2|1-\Theta|}{\left(\phi_2+\phi_1\Theta\right)}\sqrt{\frac{\int_0^a\int_0^b\left(S_2^{(1)}(r)-\phi_1^2\right)(a-x)(b-y)\,dxdy}{\varepsilon}} \tag{6b}$$

$$\|\Omega\|_3 = 4l_p^2(\Theta,\varepsilon) \tag{6c}$$

In the relations above Θ stands for the contrast in phase properties, ε is the value of assumed error tolerance and l_p is so-called correlation length which is defined as:

$$\forall r \geq l_p(\Theta,\varepsilon) \Rightarrow \frac{\left(1-\eta(\Theta)\right)^2\phi_1^2}{\left(\phi_1+\eta(\Theta)\phi_2\right)^2}\left|\frac{S_2^{(1)}(r)-\phi_1^2}{\phi_1^2}\right| \leq \varepsilon \tag{7}$$

where

$$\eta(\Theta) = \min\left\{\Theta,\frac{1}{\Theta}\right\} \tag{8}$$

Note that the size of RVE is associated with $\|\Omega\|_{\mathrm{RVE}} = ab$. Therefore, utilizing the properties of Eq. (8) the relations (6a) and (6b) can be rewritten and interpreted as:

$$\text{find } a \text{ and } b \text{ such that: } \quad ab = \frac{2\left(1-\eta(\Theta)\right)}{\left(\phi_1+\eta(\Theta)\phi_2\right)}\sqrt{\frac{\int_0^a\int_0^b\left(S_2^{(1)}(r)-\phi_1^2\right)(a-x)(b-y)\,dxdy}{\varepsilon}} \tag{9}$$

It can be seen that in order to determine the size of RVE, first, the void phase 2-point correlation function has to be evaluated. The methodology of $S_2^{(1)}(r)$ determination is presented in next Section.

4 EVALUATION OF THE 2-POINT CORRELATION FUNCTION

In general, evaluation of the 2-point correlation function can be successfully performed by simple MC simulations (Torquato, 2002). Nevertheless, if one works, with the digital image

of microstructure, this procedure can lead to a large computational cost. Yeong & Torquato (1998a) proposed - for isotropic digitized systems - more accurate procedure, which appears to be more efficient, and furthermore, it produces a smoother $S_2^{(i)}$ profile comparing to the MC sampling. The methodology is briefly outlined in a following.

Consider a binary - $M \times M$ pixels – an image of random microstructure. We attribute to each pixel only one of two possible values: 0 or 1. Therefore, the digital image can be expressed by a square matrix $\mathbf{A}_{[M \times M]}$, in such a way, that each element of matrix **A** is equal to 0 or 1, i.e.: $A[i,j]=1$ if pixel "contains" the phase for which the 2-point correlation function is going to be evaluated. Indices *i* and *j* correspond to the localization of the pixel within the image and denote the number of a row and a column, respectively.

Then, the 2-point correlation function for phase 1 can be expressed as:

$$S_2^{(1)}(r)=\frac{1}{M^2}\sum_{j=1}^{M}\sum_{i=1}^{M}\frac{A[i,j]\left(A[i,j+r]+A[i+r,j]\right)}{2}, \qquad r=1,2,... \tag{10}$$

Geometrical interpretation of this procedure is as follows. The 2-point correlation function is evaluated by translating a line segment of length *r* (in pixels) at a distance of one pixel at a time and spanning the whole image. Each time the end points of *r* are located at the pixel centers. The number of successful events, such that two end points of line segment of length *r* are found in phase 1, are counted and divided by the total number of trials. Note that by the assumption of system isotropy sampling is performed only along two orthogonal directions: rows and columns.

5 INTEGRATION OF THE 2-POINT CORRELATION FUNCTION: MONTE CARLO APPROACH

In order to evaluate the integral of the 2-point correlation function the MC integration approach is proposed. Hereafter, we assume that RVE is a square consisted of N^2 pixels (*N* in a row and *N* in a column).

Consider the function *g* which is given in the following form:

$$g(N)=\frac{4}{\|\Omega\|^2}\int_0^N\int_0^N\left(S_2^{(1)}\left(\sqrt{x^2+y^2}\right)-\phi_1^2\right)(N-x)(N-y)\,dxdy \tag{11}$$

One can simply notice that:

$$\frac{4}{\|\Omega\|^2}\int_0^N\int_0^N(N-x)(N-y)\,dxdy=\left[\frac{2}{N^2}\int_0^N(N-x)\,dx\right]\left[\frac{2}{N^2}\int_0^N(N-y)\,dy\right]=1 \tag{12}$$

and therefore the function

$$p(x,y)=p(x)\,p(y) \tag{13}$$

where

$$p(x) = \frac{2}{N^2}(N - x) \tag{14a}$$

$$p(y) = \frac{2}{N^2}(N - y) \tag{14b}$$

can be treated as the probability density functions in Ω.
Introduce now the function $h(x, y)$ defined as:

$$h(x, y) = \left(S_2^{(1)}\left(\sqrt{x^2 + y^2}\right) - \phi_1^2 \right) \tag{15}$$

Substituting (14a) and (14b) in the relation (11) we can express g as an expectation of function h, i.e.:

$$g = \int_0^N \int_0^N h(x, y)\, p(x)\, p(y)\, dxdy = \langle h(X, Y) \rangle \tag{16}$$

where $\langle * \rangle$ stands for the expected value operator.

Thus, the estimation of considered integral consists in generating random numbers X_i and Y_i from the density functions $p(x)$ and $p(y)$ and then computing the mean of $h(x, y)$, i.e.:

$$g \approx \frac{1}{n} \sum_{i=1}^{n} h(X_i, Y_i) \tag{17}$$

In order to evaluate the MC estimator (17), pseudo random numbers from a non-uniform distribution have to be drawn. Following Janke (2002) this problem is divided into two parts. First, a simple generator is used to generate uniformly distributed random numbers, which in a second step are transformed to follow the required distribution. This generation process is referred to as the inverse method.

The non-decreasing cumulative distribution function (CDF) of $p(x, y)$ is as follows:

$$Q(X, Y) = Q(X)Q(Y) = \int_0^X \frac{2}{N^2}(N - x)\, dx \int_0^Y \frac{2}{N^2}(N - y)\, dy \tag{18}$$

Calculating the integrals in relation (18) one gets:

$$Q(X) = 1 - \frac{(N - X)^2}{N^2} \tag{19a}$$

$$Q(Y) = 1 - \frac{(N - Y)^2}{N^2} \tag{19b}$$

Note that the CDF always grows monotonically from 0 to 1, such that Q values are uniformly distributed. Therefore, the problem of generating the numbers of any distribution

consists in drawing a uniformly distributed random number, say *RN*, such that $RN = Q(X)$ and, if the inverse function exists, setting $X = Q^{-1}(RN)$.

It is evident that in the case of relations (19a) and (19b) the inverse functions exist and have the following form:

$$X(Q) = N\left(1 - \sqrt{1 - Q(X)}\right) \tag{20a}$$

$$Y(Q) = N\left(1 - \sqrt{1 - Q(Y)}\right) \tag{20b}$$

The estimator of the integral (16) can therefore be rewritten as:

$$g \cong \frac{1}{n_r}\sum_{i=1}^{n_r}\left(S_2^{(1)}\left(\sqrt{X(Q_i)^2 + Y(Q_i)^2}\right) - \phi_1^2\right) \tag{21}$$

where the values of Q_i are obtained from the uniform distribution on the interval [0,1], while $X(Q_i)$ as well as $Y(Q_i)$ are the non-uniformly distributed random numbers determined via relations (20a) and (20b).

6 A NUMERICAL PROCEDURE OF RVE SIZE DETERMINATION

6.1. General scheme

The process of the minimum size of RVE determination, from the digital image of microstructure, can be summarized in the following steps:

- having a digital image of microstructure, evaluate the 2-point correlation function of one of the phases, say phase 1, using relation (10),
- assume the value of error tolerance ε and determine the correlation length l_p given by expression (7),
- calculate the value of $\|\Omega\|_3$ - use relation (6c),
- using MC integrating procedure (Eq. 21) find *N* such that:

$$\frac{\left(1 - \eta(\Theta)\right)^2}{\left(\phi_1 + \eta(\Theta)\phi_2\right)^2} g(N) \le \varepsilon \tag{22}$$

- evaluate the value of $\|\Omega\| = N^2$ and determine the size of RVE as:

$$\|\Omega\|_{\mathrm{RVE}} \ge \max\left[\|\Omega\|; \|\Omega\|_3\right] \tag{23}$$

6.2. The size of RVE for the Fontainebleau Sandstone

Utilizing the method outlined in Section 4 (Eq. 10) the void phase 2-point correlation function for the digital image of the Fontainebleau sandstone has been evaluated. This function is graphically presented in Fig. 2.

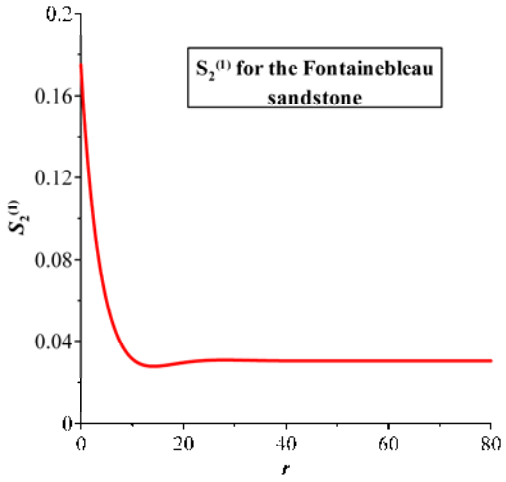

Fig. 2. The void phase 2-point correlation function for the Fontainebleau sandstone (the distance r in pixels)

Using relations (7) and (8) the correlation length has been determined for different values of the error tolerance ε as well as for various values of the contrast in phase properties Θ. The results are summarized in Table 1. Note that the size of RVE corresponding to the correlation length is expressed in terms of the number of pixels in a row and in a column, i.e. $N_3 = \sqrt{\|\Omega\|_3} = 2l_p$. It can be seen that the larger the value of contrast Θ the greater the value of the correlation length and, as a consequence, the value of the size N_3. Furthermore, for a fixed value of Θ, as the error ε is decreasing the size N_3 is increasing.

Table 1. The correlation length l_p and the size N_3 for different values of both ε and Θ

Θ	ε	l_p	N_3
5	3%	6	12
10		12	24
50		25	50
100		27	54
1000		30	60
5	1%	7	14
10		14	28
50		29	58
100		33	66
1000		36	72

Utilizing the MC approach - Eq. (21) - the integral of the 2-point correlation function, given by Eq. (11) has been determined. The function g, is graphically presented in Fig. 3. Note that this function is plotted against the size N. It can be seen that with increasing N the function g is decreasing.

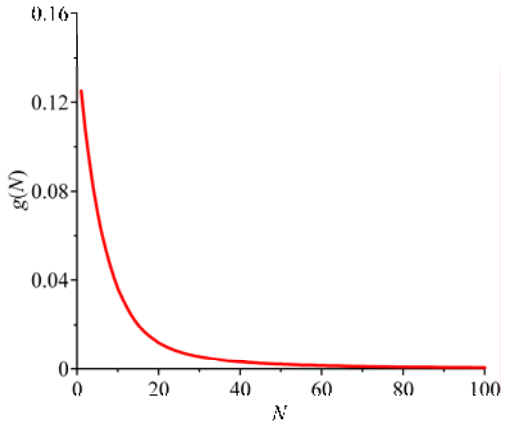

Fig. 3. The function g plotted against the size N

Following the procedure presented in Section 6.1 the value of N has been determined by making use of the relation (22). The results are summarized in the Table 2. Once again, the sizes have been evaluated for different values of both error tolerance ε and the contrast in phase properties Θ. It can be seen that the same dependence as in the case of N_3 can be observed for the size N, i.e. as the value of Θ is increasing the size N is also increasing. The lower value of error ε corresponds to the larger size N.

Table 2. The sizes N determined via relation (22)

Θ	ε	N
5	3%	31
10		46
50		68
100		72
1000		77
5	1%	54
10		81
50		119
100		128
1000		133

As mentioned in Section 6.1 the final size of RVE is the maximum value of two quantities - see relation (23). Nevertheless, comparing the results summarized in Tables 1 and 2 we see that, for all values of Θ and ε, $\max\left[N; N_3\right] = N$ and therefore, in the case of considered microstructure, the size of RVE is $N_{\mathrm{RVE}} = N$.

7 NUMERICAL VALIDATION OF PROPOSED METHODOLOGY

It has been strongly emphasized in the previous work (Rozanski et al., 2009) that the size of RVE is directly associated with the number of random microstructure realizations. In other words, for the evaluation of the effective thermal conductivity coefficient a set of n independent microstructure realizations has to be considered. Therefore in what follows we introduce the notion of a sample.

The sample is a set of finite number n of RVE elements, each having the same finite size N_{RVE} (Fig. 4). Then, the effective thermal conductivity coefficient K^{eff} can be estimated as the mean value averaged over the sample, i.e.:

$$K^{\text{eff}} \approx \overline{K} = n^{-1} \sum_{j=1}^{n} K_j \tag{24}$$

where K_j is the property determined from the solution of the boundary value problem stated for the RVE_j whereas n is the sufficient number of realizations (the size of the sample). The sample size n can be estimated based on the Central Limit Theorem (CLT) – for more details concerning CLT, see e.g. (Feller, 1961).

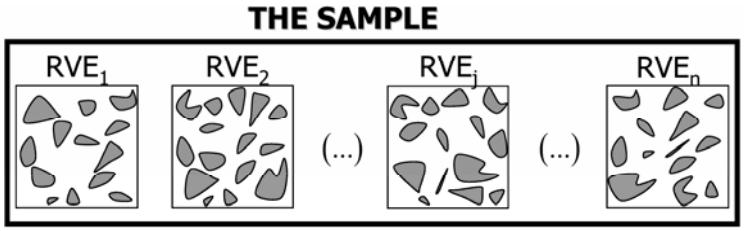

Fig. 4. The graphical illustration of the notion of the sample

Finally, the number of realizations n is governed by the following inequality (Rozanski, 2010):

$$n \geq \frac{\left(1-\eta(\Theta)\right)^2}{\left(\phi_1+\eta(\Theta)\phi_2\right)^2}\left(\frac{\Phi^{-1}\left(1-\alpha/2\right)}{\varepsilon}\right)^2 g\left(N_{\text{RVE}}\right) \tag{25}$$

where Φ is the CDF of the standard normal random variable, α denotes the significance level and ε is the relative error of estimation.

The verification of proposed methodology has been done by performing numerical calculations for different values of estimation error and contrast in properties Θ. For previously estimated RVE sizes (Table 2) the mean values have been evaluated and compared with the effective property (thermal conductivity coefficient corresponding to RVE size for which only one realization is sufficient). The results are summarized in Table 3.

Table 3. Mean values of thermal conductivity coefficients corresponding to various values of both estimation error ε and the contrast in properties Θ

Θ	ε	N_{RVE}	n	$\overline{K}[W/mK]$	$K^{\text{eff}}[W/mK]$
5	3%	31	132	3.851	3.779
10		46	128	6.976	6.814
50		68	122	30.135	29.516
5	1%	54	398	3.826	3.779
10		81	378	6.865	6.814
50		119	367	30.108	29.516

It should be noted that the values of n have been determined with assumption that the significance level is α=5%. Furthermore the numerical calculations of the effective properties have been performed for the case of periodic boundary conditions prescribed at the peripheries of each RVE_j.

It can be seen that for all values of contrast in properties Θ there is a good agreement between the mean value $\overline{K}$ and the effective property K^{eff}. In Fig. 5 the mean value of thermal conductivity coefficient is plotted against the size of RVE. The results correspond to

the case of Θ=10 and estimation error ε=3%. Moreover, the effective property K^{eff} and the bounds of Voigt/Reuss as well as Hashin – Shtrikman are also provided. It can be seen that as the RVE size is increasing the difference between $\overline{K}$ and K^{eff} is decreasing.

Note that the value of $\overline{K}$ corresponding to the case of N_{RVE}=46 is between assumed error bounds (see Fig. 5). In other words the following inequality is fulfilled:

$$K^{\text{eff}}(1-\varepsilon) < \overline{K}(N_{RVE}) < K^{\text{eff}}(1+\varepsilon) \tag{26}$$

This is also observed for all remaining values of ε and Θ.

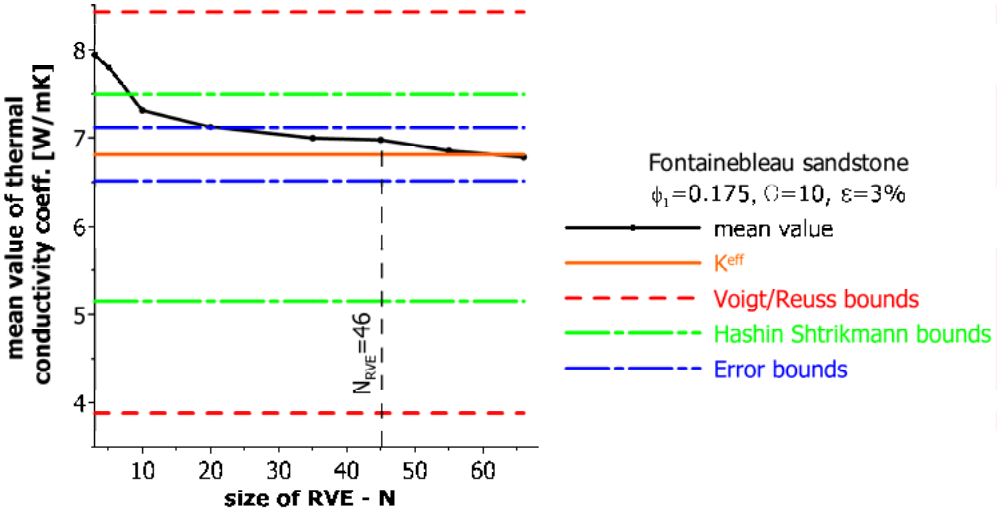

Fig. 5. The mean value of the thermal conductivity coefficient [W/mK] plotted against the size of RVE; Voigt/Reuss and Hashin-Shtrikman bounds

8 CONCLUSIONS

In the paper the numerical algorithm of RVE size determination from the digital image of microstructure has been formulated. The methodology utilizes the minimum RVE size condition proposed by Rozanski (2010). This condition is based on the statistical microstructure descriptor, namely the 2-point correlation function and is devoted to the case of effective thermal conductivity.

In general, the RVE size determination procedure consists in evaluation, for the digital image, the 2-point correlation function $S_2^{(1)}$ and than by calculating the specific integral of this function. It is proposed to calculate $S_2^{(1)}$ by simple procedure based on translating a line segment of length r at a distance of one pixel at a time and spanning the whole image. Then $S_2^{(1)}$ can be determined by making use of Eq. 10. The integration of the 2-point correlation function is performed by making use of the MC approach – Eq. 21.

The methodology has been applied to the digital image of the reconstructed 2D realization of the Fontainebleau sandstone. Using the algorithm provided in Section 6.1 the RVE sizes have been evaluated for different values of estimation error ε and the contrast in properties Θ. Validation of proposed method has been performed by calculating the mean values of effective thermal conductivity coefficients. Relation (26) confirms that the

numerical procedure presented in the paper is proper and can be successfully applied to the case of digital images. What is remarkable, a procedure formulated in the paper gives the possibility of determining the size of RVE (for the case of thermal conductivity) with no large number of numerical calculations - the numerical analysis like those of FE are not necessary.

REFERENCES

Feller, W. (1961), An Introduction to Probability Theory And Its Applications, Vol. I, 2nd Edition, John Wiley and Sons, NY.

Gitman, I.M. & Askes, H. & Sluys, L.J. (2007), "Representative volume: Existence and size determination". Engineering Fracture Mechanics, Vol. 74, 2518-2534.

Gusev, A. (1997), "Representative volume element size for elastic composites: a numerical study". J. Mech. Phys. Solids, Vol. 45, 1449–1459.

Jiao, Y. & Stillinger, F. H. & Torquato, S. (2008), "Modeling heterogeneous material via two-point correlation functions. II. Algorithmic details and applications". Phys. Rev. E, Vol. 77(3).

Janke, W. (2002), "Pseudo random number: generation and quality checks". Lecture Notes John von Neumann Institute for Computing, Vol. 10, 447.

Kanit, T. & Forest, S. & Galliet, I. & Mounoury, V. & Jeulin, D. (2003), "Determination of the size of the representative volume element for random composites: statistical and numerical approach". Int J Solids Struct, Vol. 40, 3647.

Kirkpatrick, S. & Gelatt, C.D. & Vecchi M.P. (1983), "Optimization by simulated annealing". Science, Vol. 220, 671-680.

Povirk, G.L. (1995), "Incorporation of microstructural information into model of two-phase materials". Acta Metall. Mater., Vol. 43 (8), 3199-3206.

Rozanski, A. & Lydzba, D. & Shao, J. F. (2009), "Numerical determination of minimum size of RVE for random composite materials: two-point probability approach", Proceedings of the First International Symposium on Computational Geomechanics, COMGEO I, Juan les Pins.

Rozanski A. (2010), Random composites: representativity, minimum RVE size, effective transport properties, PhD dissertation, Universite Lille 1, LML (UMR CNRS 8107), No.: 40444.

Stroeven, M. & Askes, H. & Sluys L. J. (2004), "Numerical determination of representative volumes for granular materials". Comput. Methods Appl. Mech. Engrg., Vol. 193, 3221-3238.

Torquato, S. (2002), Random Heterogeneous Materials. Microstructure and Macroscopic Properties, Springer-Verlag, New York.

Yeong, C.L.Y. & Torquato, S. (1998a), "Reconstructing random media". Phys. Rev. E, Vol. 57, 495.

Yeong, C.L.Y. & Torquato, S. (1998b), "Reconstructing random media II. Three dimensional media from two-dimensional cuts". Phys. Rev. E, Vol. 58, 224.

COMPUTATION OF ELASTIC STIFFNESS OF ROCK JOINTS – A MICROMECHANICAL APPROACH

G. N. Pande
Centre for Civil & Computational Engineering, Swansea University, UK

A. Orlando
Instituto de Estructuras, Facultad de Ciencias Exactas y Tecnología, Universidad Nacional de Tucumán, Argentina

ABSTRACT: *For analysis and safe design of rock structures such as tunnels, shafts and other underground openings, the engineer needs information on deformation and strength characteristics of rock masses which generally include multiple sets of joints and discontinuities. These, however, can neither be determined reliably from physical tests in the laboratory nor from in-situ tests. Results from computer models, either based on the finite element method or any other computational technique are dependable only if rational material properties for the rock mass are used in the analysis. A systematic procedure for computing the elasticity matrix of jointed rock masses from elastic properties of intact rock, rock joints and their orientation and spacing has been available for many years now (Pande, Beer & Williams, 1992). However, a reliable determination of elastic normal and tangential stiffnesses (k_n, k_s) for a rock joint has been problematic. Physical experiments on joints are extremely time consuming, expensive and beyond the budget of most projects. Moreover, very few data from such tests are available in the literature. In this paper, an procedure for estimating the nonlinear stiffness matrix of rock joints, including off-diagonal terms from the idealised shape and inclination of asperities is presented. Results of a parametric study in which the average density and orientation is varied are presented. This research is an attempt to fill a gap in the process of computation of complete anisotropic elasticity matrix of jointed rock masses from data contained in an engineering geologists' report and laboratory tests on intact rock and rock joints.*

1 INTRODUCTION

Construction of rock structures such as tunnels, shafts and other underground openings for power, transport infrastructure and mineral exploration is continuing at a rapid pace in developing countries like China, India and Brazil. For their analysis, design and safe operation a deeper understanding of deformation and strength characteristics of jointed rock masses at an appropriate scale is required. Many more complex rock structures are being planned for construction throughout the world and their safety poses an enormous challenge for the engineers. Computer models, either based on the finite element method or any other computational technique are dependable only if rational material properties for the rock mass are used in the analysis. Rock masses generally include multiple sets of joints and discontinuities which are a source of weakness and give rise to elastic and strength anisotropy. The mechanical properties of jointed rock masses can neither be determined reliably from the

physical tests in a laboratory nor from in-situ tests. In-situ tests, if at all possible, are not only expensive but also very time consuming.

In many practical situations, little attention is focussed on determination of anisotropic elastic moduli of jointed rock masses whilst some investigations are undertaken to identify strength anisotropy. However, the two are inter-linked and it is important to obtain a good estimate of anisotropic elasticity matrix for the analysis of rock structures, since it influences the stress state on rock joint planes on which the failure is likely to take place. It may be noted that for the description of a general anisotropic material, 21 parameters are required. Moreover, these parameters are not constant but stress dependent.

In this paper, a procedure for determining the nonlinear stiffness matrix of rock joints, including off-diagonal terms from the information on size, shape and inclination of asperities is presented. The required data on geometrical characteristics of asperities can be obtained from recently developed optical or laser profiling techniques (Hardygóra et al., 2004). In the past, the influence of asperities has been taken in account in plasticity formulations of fracture surfaces in concrete (Xu & Pietruszczak, 1977) but the authors have not noted any previous investigation in the equally important elastic range. The computational procedure adopted here was originally proposed by Pande (1987) and is an extension of work of Scharinger, Schweiger & Pande (2008) who determine 'small strain' stiffness for granular soils through the application of Hertz-Mindlin theory of contact of two elastic spheres. Here, asperities on rock joint, orientation of which is generally subnormal to the joint plane, contribute to normal and tangential deformations attributed to rock joint. Contribution of all asperities is summed up to obtain stiffness of rock joint. Once stiffness matrix of individual joints is established, a procedure to compute elasticity matrix of the jointed rock mass, as described in Pande, Beer & Williams (1992) can be adopted. Section 2 describes computation of nonlinear values of the normal and tangential stiffness (k_n, k_s and k_t) of a rock joint based on the hemispherical shape, density, orientation and mechanical characteristics of asperities on the joint planes. Section 3 deals with the general case of subnormal orientation of asperities and their influence on the off-diagonal terms in the joint stiffness matrix K_J. Results of parametric studies showing the influence of the joint asperities' inclination on the ratio of the horizontal to the vertical displacement of an horizontal joint subject to a normal stress is presented in Section 4. Conclusion and recommendations for further research are given in Section 5.

2 STIFFNESS OF A ROCK JOINT WITH ASPERITIES NORMAL TO THE JOINT PLANE

From the geological point of view rock masses have numerous types of joints, discontinuities, planes of weakness, shear bands etc. How to deal with them in numerical analysis has been discussed in Pande, Beer & Williams, 1992. Here we restrict ourselves to the rock joints having no infilling gouge material. These types of joints are formed due to tensile cracking at the time of cooling in geological past in metamorphic rocks. It can be conceived that cracking takes place along the grain boundaries giving rise to asperities of the rock joint which degrade due to environmental forces. Asperities of rock joints are generally subnormal to the plane of the joint and may not even coincide with the orientation of the 'dip' of joint planes. In laboratory experiments on rock joints obtained from field, a displacement in the out-of-the-plane direction is usually observed on application of a shear force on the joint, proving this point.

2.1 Assumptions

In the first instance it is assumed that all asperities are hemispherical in shape and oriented normal to the joint plane. The size of the asperities also determines their density, i.e. number of asperities per unit area of the joint. It is also assumed that asperities on both faces of a joint mate perfectly. This assumption will be relaxed in the later sections of the paper when asperities are subnormal to the joint plane. In all cases, however, it is assumed that asperities transmit normal and tangential forces on the joint.

2.2 Normal and tangential stiffness of a contact (asperity)

The required data on geometrical characteristics of asperities of rock joints can be obtained from recently developed optical or laser profiling techniques (Hardygóra et al., 2004). The computational technique presented here is based on basic concepts presented by Pande (1987) and is an extension of the recent work by Scharinger, Schweiger & Pande (2008) who determine 'small strain' stiffness for granular soils through the application of Hertz-Mindlin theory (Mindlin et al., 1953).

We start with the closed form solution of normal and tangential contact stiffness (k_n and k_s) respectively of two elastic spheres (rock joint asperities) which are:

$$k_n = \left[\frac{3rG^2}{(1-\nu)^2} F_n \right]^{1/3} \tag{1}$$

$$k_s = \frac{2(1-\nu)}{(2-\nu)} \left(1 - \frac{F_s}{F_n \tan\phi} \right)^{1/3} k_n \tag{2}$$

In the above equations, r is the average radius of asperities, G and ν are the elastic shear modulus and Poisson's ratio respectively of rock material forming the asperities. F_n and F_s are the normal and tangential contact forces on the asperities and ϕ is the inter-asperity friction angle (Bowden & Tabor 1964, Johnson 1985).

It is noted that though the asperities are made of a linear elastic material, k_n and k_s are both nonlinear, dependent on F_n, F_s and ϕ. The elastic parameters of asperities can be assumed to be the same as those for intact rock in the case of fresh un-weathered rock joints whilst a reduced G can be applied for weathered joints. It is also noted that the ratio k_s/k_n can vary from 1 (F_s=0; ν=0) to 0 ($F_s=F_n\tan\phi$). Obviously, the situation $F_s>F_n\tan\phi$ cannot arise as inter-asperity slip would have already taken place limiting the F_s value equal to $F_n\tan\phi$.

2.3 Joint stiffness matrix

To study the characteristics of a rock joint, it is convenient to set up a global Cartesian reference system of axes (n',s',t') with (s',t') defining the joint plane and n' being the orthogonal direction. Let us then denote with (n,s,t) the reference system associated with the asperity, with n being the normal direction to the contact area. The contact stiffness matrix is still assumed of the diagonal form with the three components k_n, k_s and k_t; the values of which will depend on the forces F_n, F_s and F_t in respective directions. In the first instance, we consider the case where we have a joint with N equal hemispherical asperities with their axes *(n,s,t)* coinciding with the global axes *(n',s',t')* of the joint. Since the asperities act as springs in parallel, then

$$K_j = \sum_N k_a \tag{3}$$

where

$$k_a = \begin{bmatrix} k_n & 0 & 0 \\ 0 & k_s & 0 \\ 0 & 0 & k_t \end{bmatrix} \tag{4}$$

By resolving the contact forces F_n, F_s, F_t, applied to the asperity in terms of the contact stresses σ_n , τ_s and τ_t, it can be easily seen that $F_n=\pi r^2\sigma_n$, $F_s=\pi r^2\tau_s$ and $F_t=\pi r^2\tau_t$, which replaced in Eqns. (1) and (2) will give

$$k_n = \alpha r\left(\frac{\sigma_{n'}}{N}\right)^{1/3} \tag{5}$$

$$k_s = \frac{2(1-\nu)}{2-\nu}\left(1-\frac{\tau_{s'}}{\sigma_{n'}\tan\phi}\right)^{1/3}\alpha r\left(\frac{\sigma_{n'}}{N}\right)^{1/3} \tag{6}$$

$$k_t = \frac{2(1-\nu)}{2-\nu}\left(1-\frac{\tau_{t'}}{\sigma_{n'}\tan\phi}\right)^{1/3}\alpha r\left(\frac{\sigma_{n'}}{N}\right)^{1/3} \tag{7}$$

where we have set

$$\alpha = \left(\frac{3\pi G^2}{(1-\nu)^2}\right)^{\frac{1}{3}} \tag{8}$$

and we have used the fact that from the equilibrium, $\sigma_n=\sigma_{n'}/N$, $\tau_s=\tau_{s'}/N$ and $\tau_t=\tau_{t'}/N$ with $\sigma_{n'}$, $\tau_{s'}$ and $\tau_{t'}$ the normal and tangential stresses, respectively, applied on the joint, and σ_n, τ_s and τ_t are the normal and tangential stresses acting along the axis *(n,s,t)* of the asperity. The assumption of hemispherical shape of asperities normal to the joint leads to there being $N = 1/\pi r^2$ asperities per unit area. In contrast to what is generally assumed in most engineering analyses, the stiffness of a joint is nonlinear being dependent on normal and shear stress on joints.

The joint compliance matrix (C_j) will be then simply the inverse of the joint stiffness matrix K_j. Thus, it follows

$$C_j = K_j^{-1} = \frac{1}{N}\begin{bmatrix} \frac{1}{k_n} & 0 & 0 \\ 0 & \frac{1}{k_s} & 0 \\ 0 & 0 & \frac{1}{k_t} \end{bmatrix} = \frac{1}{N}\begin{bmatrix} \frac{1}{\alpha r}\left(\frac{N}{\sigma_{n'}}\right)^{1/3} & 0 & 0 \\ 0 & \frac{2-\nu}{2(1-\nu)}\left(\frac{\sigma_{n'}\tan\phi-\tau_{s'}}{\sigma_{n'}\tan\phi}\right)^{1/3}\frac{1}{\alpha r}\left(\frac{N}{\sigma_{n'}}\right)^{1/3} & 0 \\ 0 & 0 & \frac{2-\nu}{2(1-\nu)}\left(\frac{\sigma_{n'}\tan\phi-\tau_{t'}}{\sigma_{n'}\tan\phi}\right)^{1/3}\frac{1}{\alpha r}\left(\frac{N}{\sigma_{n'}}\right)^{1/3} \end{bmatrix} \tag{9}$$

3 JOINT STIFFNESS MATRIX – ASPERITIES SUBNORMAL TO JOINT PLANE

Let us consider now the case where the asperities are subnormal to the joint plane, that is, the asperity axes are rotated through an angle θ about the axis t and an angle Ω with respect to the axis n; θ and Ω being taken positive if anticlockwise. That is, the asperities are assumed

with a preferred orientation which is described by the rotation matrix T given by the product of the two above rotations and which is equal to

$$T = \begin{bmatrix} \cos\theta & -\sin\theta\sin\Omega & \sin\theta\cos\Omega \\ 0 & \cos\Omega & \sin\Omega \\ -\sin\theta & -\cos\theta\sin\Omega & \cos\theta\cos\Omega \end{bmatrix}. \tag{10}$$

The transformation matrix T characterizes the change of reference from the asperity local base *(n,s,t)* to the joint global base *(n',s',t')*. In this case, the joint compliance matrix C_J in the coordinate system *(n',s',t')* of the rock joint, will be given by

$$C_J = \frac{1}{N}\left(T^T k_a T\right)^{-1} = \frac{1}{N} T^T k_a{}^{-1} T\,. \tag{11}$$

Note also that since k_a has been assumed symmetric and T is a rotation matrix, then C_J is also symmetric. It is also noted that the joint compliance is no longer diagonal as is often assumed in practical applications. The off-diagonal terms are a function of the shape, size and average orientation of the asperities. The assumption of hemispherical asperities pre-determines the density (number per unit area) of asperities, N. In the case of non-hemispherical asperities, we can still use Eqn (11) for the joint compliance but N will be assumed as an independent variable together with the radius r of an asperity contact.

The joint compliance C_J given by Eqn. (11) relates the global forces applied to the joint to the relative movement, i.e.

$$\begin{bmatrix} \delta_{n'} \\ \delta_{s'} \\ \delta_{t'} \end{bmatrix} = C_J \begin{bmatrix} F_{n'} \\ F_{s'} \\ F_{t'} \end{bmatrix}, \tag{12}$$

where $F_{n'}=A\sigma_{n'}$, $F_s=A\tau_{s'}$ and $F_t=A\tau_{t'}$, with A being the joint area. In the simplified case of 2D plane strain, with (n',s') the plane of deformation, from Eqn (12) one obtains that the ratio of displacement in shear direction to that in the normal direction ($\delta_{s'}/\delta_{n'}$) is given by

$$\frac{\delta_{s'}}{\delta_{n'}} = \frac{\left(1-\frac{k_s}{k_n}\right)\tan\theta + \left(\frac{k_s}{k_n}\tan^2\theta + 1\right)\frac{\tau_{s'}}{\sigma_{n'}}}{\frac{k_s}{k_n} + \tan^2\theta + \left(1-\frac{k_s}{k_n}\right)\tan\theta\,\frac{\tau_{s'}}{\sigma_{n'}}} \tag{13}$$

The components of the average strain ε_J in a unit block contributed by a set of joints having frequency f (number of joints/unit length) are given by

$$\begin{bmatrix} \varepsilon_{n',J} \\ \gamma_{n's',J} \\ \gamma_{n't',J} \end{bmatrix} = fC_J \begin{bmatrix} \sigma_{n'} \\ \tau_{s'} \\ \tau_{t'} \end{bmatrix}, \tag{14}$$

To obtain the total strains, the strains in the intact rock must also be added, which gives

$$\begin{bmatrix} \varepsilon_{n'} \\ \gamma_{n's'} \\ \gamma_{n't'} \end{bmatrix} = (fC_J + C_I) \begin{bmatrix} \sigma_{n'} \\ \tau_{s'} \\ \tau_{t'} \end{bmatrix}, \tag{14}$$

where C_I is the compliance of the intact rock given in general by

$$C_I = \begin{bmatrix} \frac{1}{E} & 0 & 0 \\ 0 & \frac{1}{G} & 0 \\ 0 & 0 & \frac{1}{G} \end{bmatrix}, \tag{14}$$

with E and G being the Young modulus and shear modulus of intact rock respectively.
In the simplified setting of 2D plane strain, with (n',s') in the plane of deformation, using Eqn. (14) one then obtains

$$\varepsilon_{n'} = \frac{\sigma_{n'}}{k_s}\left[\frac{f}{N}\left(\frac{k_s}{k_n}\cos^2\theta + \sin^2\theta\right) + \frac{k_s}{E}\right] + \frac{f\tau_{s'}}{Nk_s}\left(1 - \frac{k_s}{k_n}\right)\cos\theta\sin\theta \tag{15}$$

$$\gamma_{n's'} = \frac{f\sigma_{n'}}{Nk_s}\left(1 - \frac{k_s}{k_n}\right)\cos\theta\sin\theta + \frac{\tau_{s'}}{k_s}\left[\frac{f}{N}\left(\frac{k_s}{k_n}\sin^2\theta + \cos^2\theta\right) + \frac{k_s}{E}\right] \tag{16}$$

4 NUMERICAL EXAMPLES

In this section we present two numerical examples to emphasise the importance of the characteristics of asperities of rock joints in the analysis of a jointed rock masses. For the sake of simplicity and illustration, we will consider the asperities in the simplified 2D coordinate framework but it is obvious that the formulation applies for a general three-dimensional case as well.

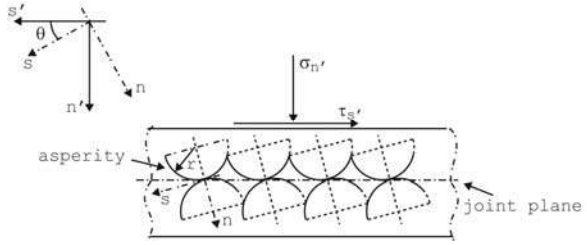

Figure 1: Joint and Asperity Geometry

Example 1

Let us consider an isolated rock joint as shown in Figure 1. It is recalled that samples of isolated joints are obtained and tested in the laboratories for large projects throughout the world. Studies of artificial rock joints with different geometries and characteristics are also conducted to develop a deeper understanding of the hydro-mechanical behaviour of rock joints. In this example, asperities are assumed to be normal to the joint plane (Fig. 1 corresponds to a general case).

Figure 2 displays variation of the normal and tangential stiffness with normal (σ_n) and shear stress (τ_s) applied on the joint for ratio $\tau_s/\sigma_n = 0$ and $\tau_s/\sigma_n = \tan\phi/2$. The diagrams shows curves for different values of ϕ and asperity sizes r. It is seen that as the size of asperities increases, the normal and tangential stiffnesses of the joint also increase. It is also noted that a reduction in the value of ϕ leads to a reduction in the values of stiffnesses for a rock joint.

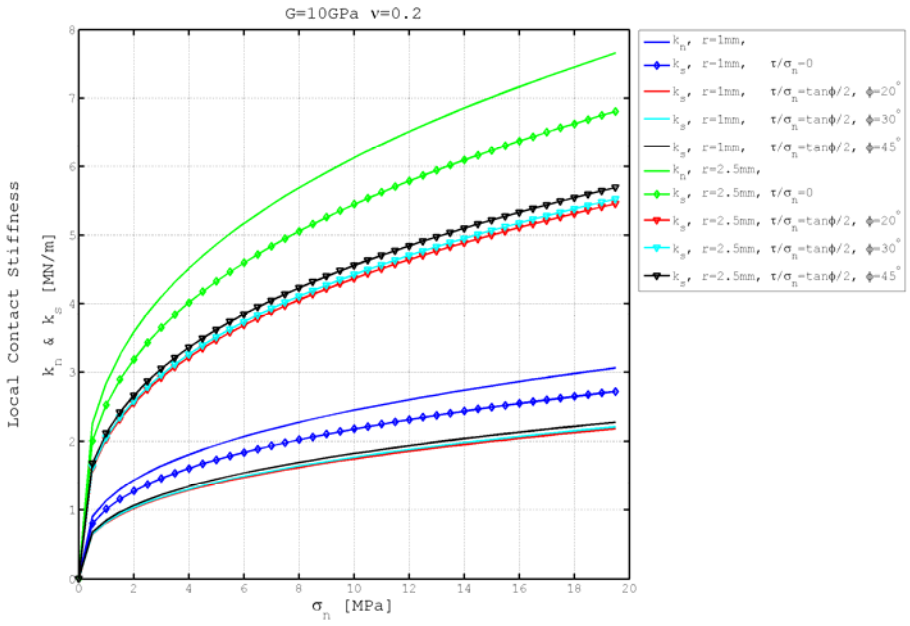

Figure 2: Variation of normal and tangential stiffness of a joint with normal stress

Figure 3 displays variation of the stiffness ratio k_s/k_n of a rock joint with respect to the ratio τ_s/σ_n of the applied stresses and inter-asperity friction angle, ϕ. It is noted that the admissible values of τ_s/σ_n are bounded by the condition $\tau_s/\sigma_n \leq \tan\phi$, which guarantees that the inter-asperity friction is not exceeded.

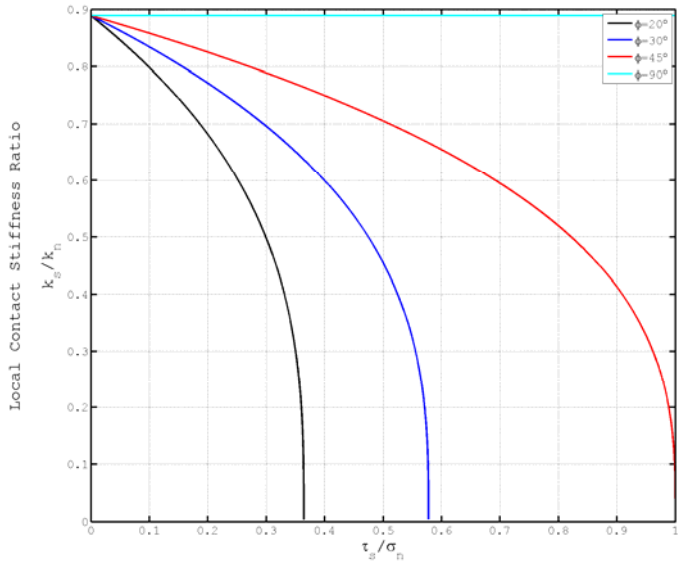

Figure 3: Variation of the stiffness ratio k_s/k_n of a rock joint with the ratio τ_s/σ_n of the applied stresses and the inter-asperity friction angle ϕ

Figure 4(a) and Figure 4(b) display variation of the normal and tangential stiffnesses of a rock joint having different density of asperities, inter-asperity friction angle ϕ and τ_s/σ_n .It is seen that for given applied normal stress σ_n on the joint the stiffness decreases by increasing the number N of asperities. In this example the radii of contacts are assumed constant at *r=1mm* and *r=2.5mm*, respectively

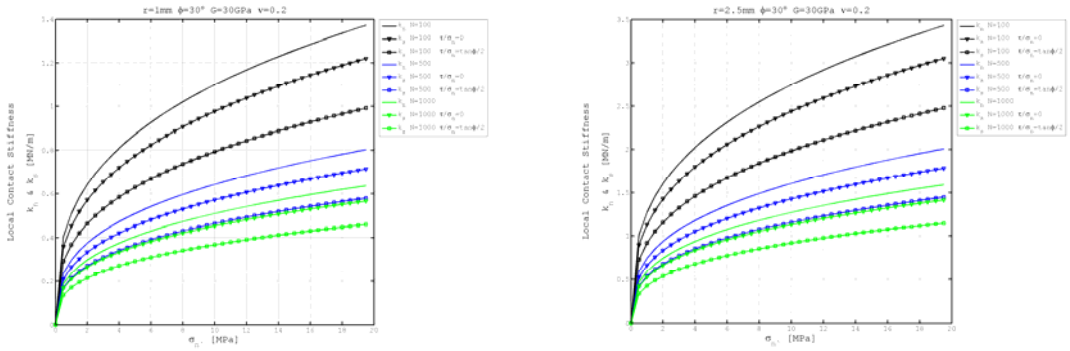

(a) (b)

Figure 4: Variation of the normal k_n and tangential stiffness k_s for different values of the number of asperities N, applied stress ratio τ_s/σ_n and different values of the radius r with (a) *r=1mm* and (b) *r=2.5mm*.

Example 2

In this example we study the influence of the inclination of asperities on the stiffness of rock joints. Figure 5 displays the variation of the joint displacement ratio $\delta_{s'}/\delta_{n'}$ with respect to the ratio ($\tan\theta/\tan\phi$). The figure refers to the case when a purely normal stress and no tangential stress $\tau_{s'}$ is applied on the joint, i.e. $\tau_{s'}=0$. It is observed that in presence of a normal stress $\sigma_{n'}$ on the joint, if the asperities are subnormal, the joint will move along the shear direction. This figure shows that these displacements can be substantial. It is clear that subnormal asperities introduce anisotropy in the elastic behaviour of the joint.

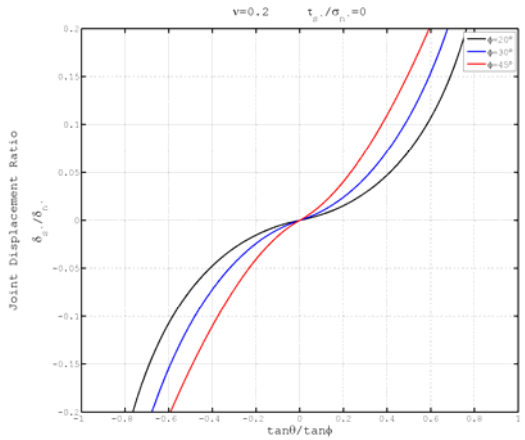

Figure 5: Variation of the joint displacement ratio $\delta_{s'}/\delta_{n'}$ with the ratio $\tan\theta/\tan\phi$.

Figure 6 depicts the geometry of a long vertical mine pillar (wall) 1 m wide and 2 m high. It has horizontal joints at an interval of 100 mm. The density of asperities is $1000/m^2$ and their orientation is considered as a variable.

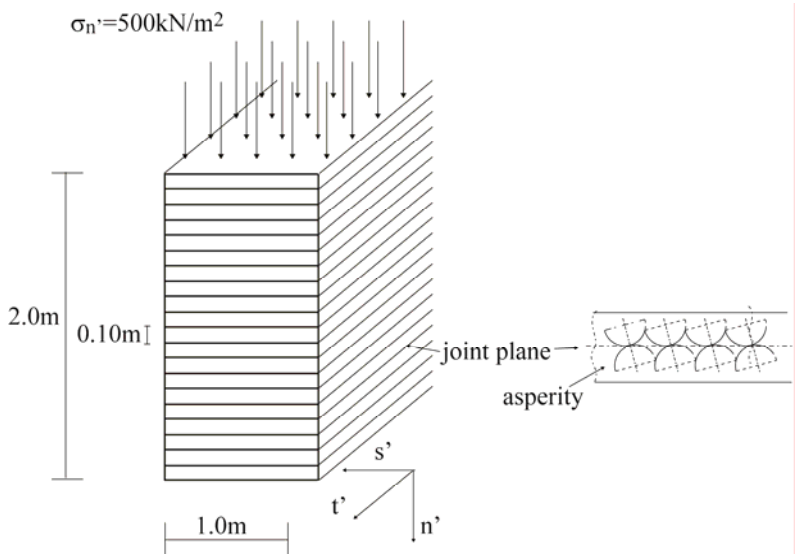

Figure 6: Wall mine pillar geometry subject to a uniaxial stress $\sigma_{n'} = 500$ kPa.

Figure 7 shows the deformed shapes of the wall clamped at the base and subject to a uniaxial normal stress $\sigma_{n'} = 500$ kPa, for different asperity inclination ($\theta=20^0$ and $\theta=30^0$) and different values of the rock friction angle ϕ. The tangential displacement $\delta_{s'}$ is obtained as $H\gamma_{n's'}$ where H=2m is the height of the wall and $\gamma_{n's'}$ is obtained from Eqn. (14). It is noted that by increasing the rock friction, the effect of the asperity inclination on the tangential displacement is reduced. This effect is, on the contrary, amplified for the asperity inclination close to the asperity friction angle.

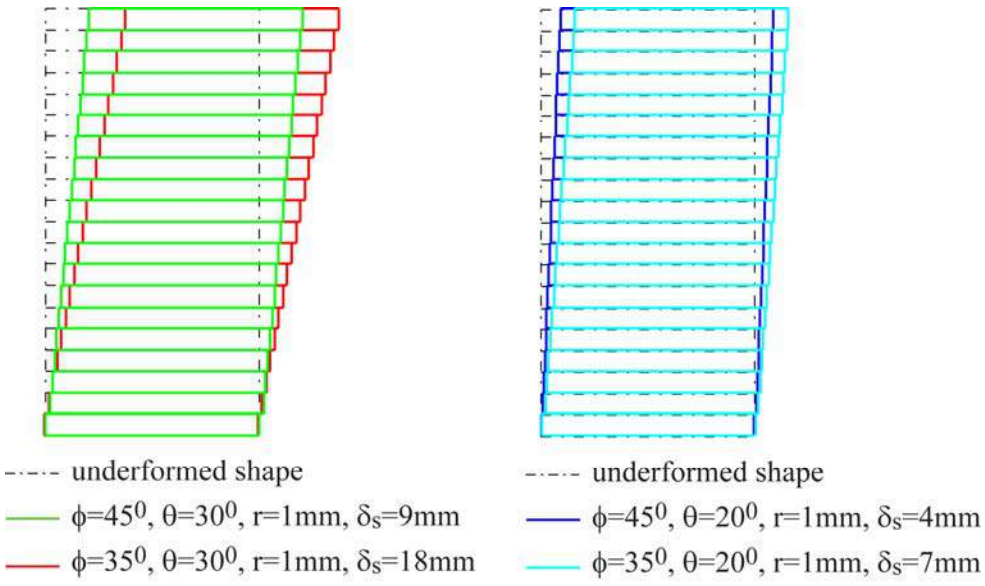

Figure 7: Deformed shape of the wall mine pillar shown in Figure 6. Joint frequency, *f=10*, and average number of asperities *N* for all joints = 1000.

5 CONCLUSIONS AND IMPLICATIONS FOR OTHER RESEARCH AREAS

A model for the computation of normal and tangential elastic stiffness of rock joints has been proposed. It is shown that the stiffnesses are nonlinearly stress dependent and are a function of the radius and density of asperities. The off-diagonal terms of the stiffness matrix are zero only when asperities are oriented normal to the joint plane. The model enables computation of off-diagonal terms which are generally ignored due to lack of availability of data or understanding. The model is likely to be useful in the analysis of jointed rock masses for which no physical testing is possible.

The research has wider implications in engineering analysis. Estimated contact stiffness coefficients are used in a variety of contact problems and are widely used in discrete element analyses of continua. It is clear that such analyses are qualitative and cannot be relied upon in real engineering situations. Data from laser scanning and data for joint profiles need to be studied in greater depth to extend the model for practical cases.

REFERENCES

Hardygóra M, Paszkowska G., Sikora M. (Eds)., Mine Planning and Equipment Selection. Proceedings of the 13th International Symposium on Mine Planning and Equipment Selection, Taylor & Francis, 2004

Mindlin RD, Deresiewicz H., Elastic spheres in contact under varying oblique forces. Journal of Applied Mechanics, 20 (1953) 327–344

Pande GN., Influence of grain shape and size on the behaviour of granular materials. In Proceedings of the 2nd International Conference on Numerical Methods in Engineering, Theory and Applications, Swansea, U.K., Pande GN, Middleton J (eds). Martinus Nijhoff Publishers: Dordrecht, 1987

Pande GN, Beer G, Williams JR., Numerical Methods in Geomechanics, John Wiley & Sons, 1992

Scharinger F, Schweiger HF, Pande GN., On a multilaminate model for soil incorporating small strain stiffness. Int. J. Numer. Anal. Meth. Geomech. 33 (2009) 215–243

G. Xu, S. Pietruszczak, Numerical analysis of concrete fracture based on a homogenization technique. Computers & Structures, Vol.63, No.3, pp.497-509, 1977

FAILURE MECHANISM OF SEDIMENTARY ROCKS: MICROMECHANICS APPROACH

D. Lydzba, M. Kawa
Institute of Geotechnics and Hydrotechnics, Wroclaw University of Technology, Wroclaw, Poland

ABSTRACT: *The paper deals with formulation of anisotropic strength criterion for sedimentary rocks. Using micromechanics approach the 3-D anisotropic failure surface for periodically layered rocks with constituents obeying Drucker-Prager or Mohr-Coulomb criterion is determined numerically. The macroscopic response is found to be associated with two different types of microscopic failure mechanisms, i.e. a localized shearing in a weaker constituent or a simultaneous failure of both constituents. Using numerical results based on the micromechanical considerations, a general form of macroscopic failure criterion for sedimentary rocks is deduced. Later, a particular form of this criterion is proposed and identified based on fitting of numerical results obtained from the microstructural analysis. A very good agreement is obtained that clearly shows the potential of the proposed methodology.*

1 INTRODUCTION

Observing sedimentary rocks one can easily recognize their typical structure: two or more constituents are found in a form of thin, periodically repeating layers. This specific pattern is an effect of decomposition and sedimentation in different, but periodically repeating conditions during diagenesis. Sandstone, claystone and schist are some of the most typical examples. All these materials are widely known as strongly anisotropic in both an elastic and inelastic range. From an engineering point of view identification of an adequate anisotropic strength criterion for sedimentary rocks is an especially important problem.

Over the last few decades a rapid development of so-called homogenization techniques took place. These techniques are based, in general, on analysis of stress and strain fields at the level of a microstructure. Suqet (1987) showed that using this technique, an identification of a macroscopic failure surface of a medium with periodic microstructure consists in solving a problem formulated at the level of a single periodic cell. This approach has also been successfully used for sedimentary rocks, mainly in a case of in-plane loadings (e.g., Pietruszczak et. al. (2002), Lydzba et.al. (2003)).

Independently of a development of the homogenization theory a number of researchers focused on a formulating a macroscopic anisotropic strength criterion for sedimentary rocks based, mainly, on a phenomenological approach. Brief review of some of these criteria is presented in a work of Duveau et al. (1997). Two of these criteria are especially worth noting, i.e. Pariseau criterion (Pariseau 1972) which is an extension of Drucker-Prager isotropic criterion for the case of anisotropy, and Jaeger criterion (Jaeger 1960) which can be interpreted as a foundation of a so-called critical plane approach.

In the work of Jaeger (Jaeger 1960) two main mechanisms of failure of laminated rock have been introduced, viz. a localized shearing on a "weakness plane" or a destruction of entire structure by failure of all constituents. Similar results, namely failure as an effect of reaching the strength by a "weak" constituent only or simultaneous failure of all constituents, can also be obtained using the micromechanics approach (e.g., Lydzba *et al* (2003)).

The main focus of this work is to investigate the particular forms of a macroscopic failure response associated with these different failure mechanisms taking place at microstructure level. Two-constituent periodic structures with constituents governed by Drucker-Prager or Mohr-Coulomb criterion are analyzed. As a result of this analysis, a clear mathematical form of macroscopic strength criteria for sedimentary rocks is deduced.

2 LIMIT SURFACE

Macroscopic strength criterion, in terms of micromechanics, is defined as set of admissible macro stress states (Suqet 1987). Macro stress state is admissible if associated micro stress field is self-equilibrated and does not violate the respective failure criterion for all constituents involved. In addition the micro stress field has to be locally periodic for periodic structures. Above formulation can be written as:

$$f(\sigma_{ij}) \le 0 \Leftrightarrow \{\sigma_{ij}\} \in A = \{ < \tau_{ij} > | \exists \tau_{ij}(y) : \frac{\partial \tau_{ij}(y)}{\partial y} = 0, f(\tau_{ij}(y), y) \le 0, \tau_{ij}(y) \text{ - periodic} \} \qquad (1)$$

where σ_{ij}, $\tau_{ij}(y)$ represents macro stress tensor and associated micro stress field respectively, $f(\tau_{ij}(y),y)$ is a local strength criterion in point with coordinates $y \in V_{RVE}$ and V_{RVE} is a volume of periodic cell. Symbol <.> denotes operation of volume averaging over a periodic cell.

For all constituents of considered sedimentary rock local criterion of failure has been assumed to be either Druker-Prager:

$$f(\tau_{ij}^{(i)}) = a_i I_1(\tau_{ij}^{(i)}) + \sqrt{J_2(\tau_{ij}^{(i)})} - k_i \le 0 \qquad (2)$$

or Mohr-Coulomb one:

$$\begin{aligned} f^{(i)}(\tau_{ij}^{(k)}) &= I_1(\tau_{ij}^{(i)}) \sin\phi_i \\ &+ \frac{1}{2}\Big[\; 3\left(1 - \sin\phi^{(i)}\right)\sin\theta(\tau_{ij}^{(i)}) + \sqrt{3}\left(3 + \sin\phi_i\right) \; \cos\theta(\tau_{ij}^{(i)})\Big]\sqrt{J_2(\tau_{ij}^{(i)})} - 3c_i\cos\phi_i . \end{aligned} \qquad (3)$$

In the expressions above $\theta(\tau_{ij}^{(i)})$ denotes Lode's angle, $I_1(\tau_{ij}^{(i)})$ and $J_2(\tau_{ij}^{(i)})$ are the first invariant of the micro stress tensor and the second invariant of the micro stress deviator for constituent i, respectively.. The constants a_i, k_i and ϕ_i, c_i are constituents' strength parameters of Drucker-Prager or Mohr-Columb criterion, respectively.

The closure of the set defined by (1), in space of principal macro stresses, is typically represented by a so-called macroscopic failure surface. This surface can be specified in a discrete manner by solving a set of optimization problems. Numerical procedure used in a present paper is described in detail in the work of Lydzba and Kawa (2011). Here the final results of the anisotropic limit surfaces are presented.

Two-constituents structures with equal volume fractions of constituents t_1=t_2=0.5 are considered. Strength parameters of criteria are assumed to be: k_1=100kPa, k_2=20kPa, a_1=0.2, a_2=0.05 for Drucker-Prager constituents and c_1=100kPa, c_2=20kPa, ϕ_1=5º, ϕ_2=25º for Mohr-Coulomb constituents. In order to show failure surface of material in 3D stress state, results are plotted in forms of cross-sections of this surface by octahedral planes. Anisotropy of the

surface is improved by presenting cross-sections of the surface corresponding to different values of α and β being the angles between principal load direction and material directions.

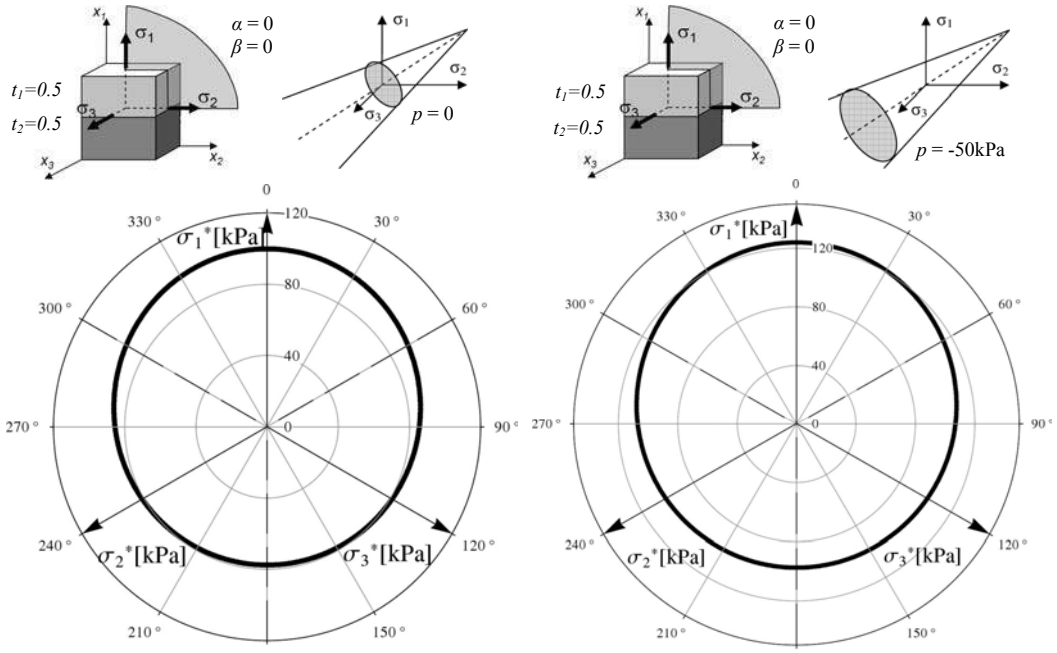

Fig. 1 Macroscopic strength surface on octahedral plane for two-constituent sedimentary rock with constituents governed by Drucker-Parger criterion.

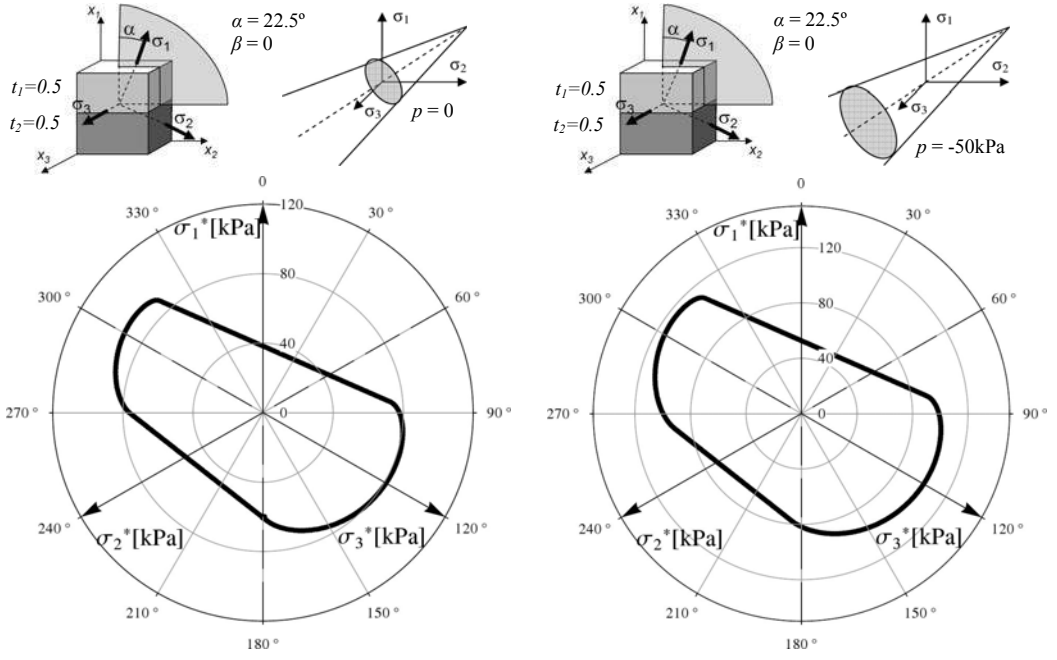

Fig. 2 Macroscopic strength surface on octahedral plane for two-constituent sedimentary rock with constituents governed by Drucker-Parger criterion.

Effect of a confining pressure on a shape of a cross-section is also investigated. Results obtained for a microstructure with Drucker-Prager constituents are plotted in figures 1-3 whereas for Mohr-Coulomb constituents in figures 4-6. Values of orientation angles: α, β and a confining pressure p are specified above each the graph.

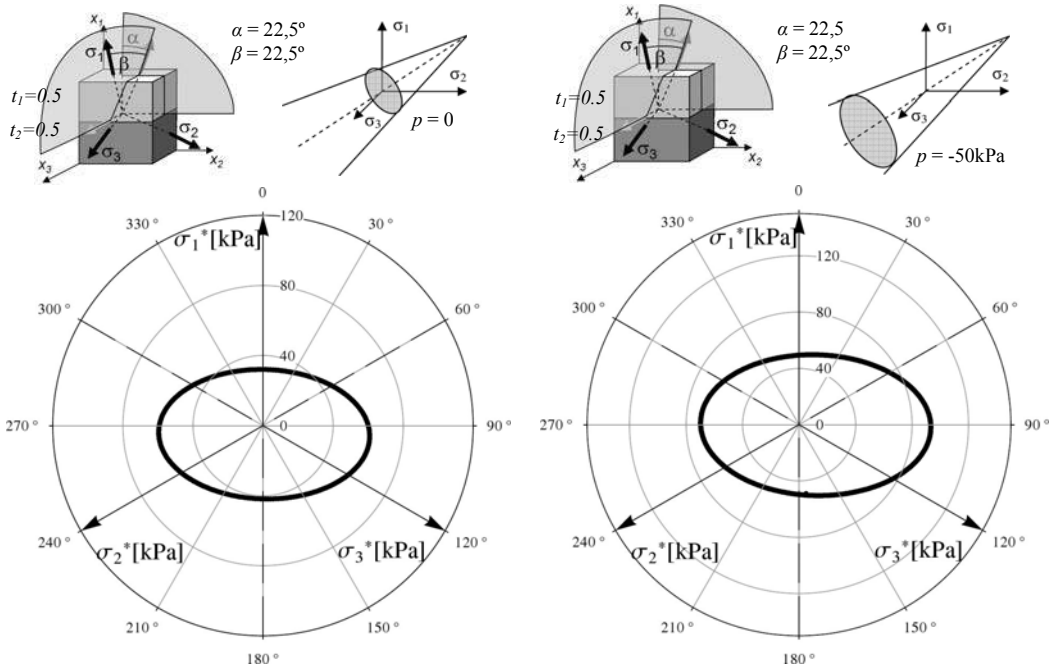

Fig. 3 Macroscopic strength surface on octahedral plane for two-constituent sedimentary rock with constituents governed by Drucker-Parger criterion..

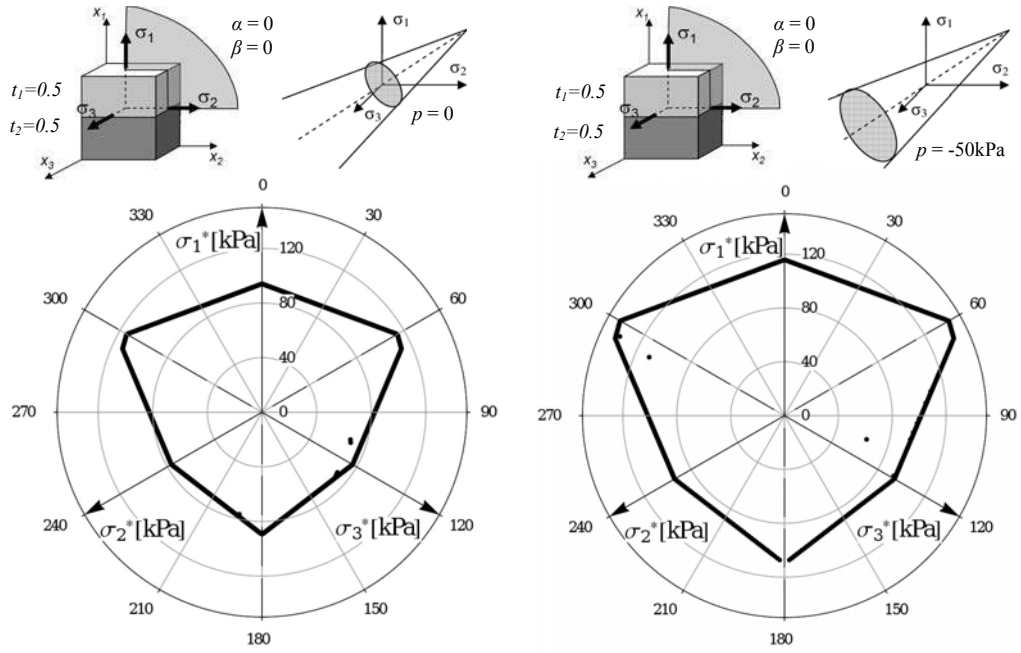

Fig. 4 Macroscopic strength surface on octahedral plane for two-constituent sedimentary rock with constituents governed by Mohr-Coulomb criterion.

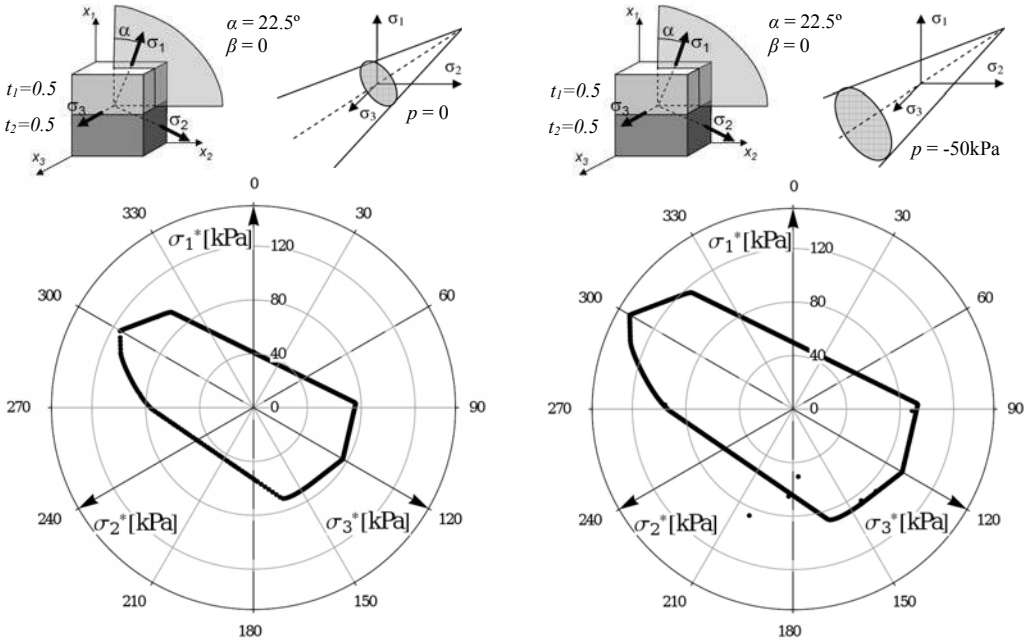

Fig. 5 Macroscopic strength surface on octahedral plane for two-constituent sedimentary rock with constituents governed by Mohr-Coulomb criterion.

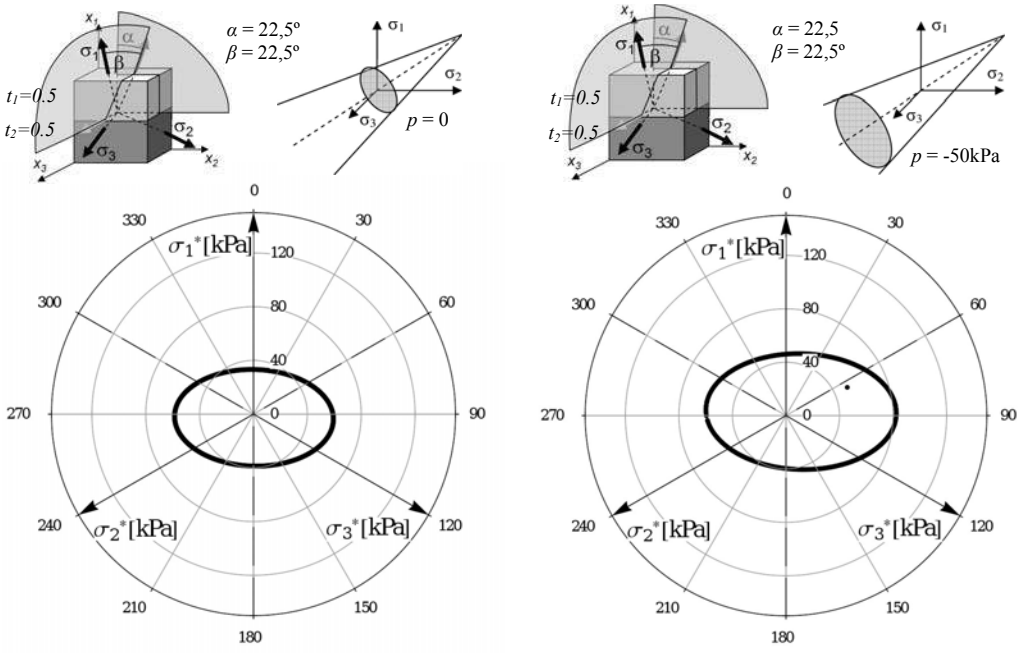

Fig. 6 Macroscopic strength surface on octahedral plane for two-constituent sedimentary rock with constituents governed by Mohr-Coulomb criterion

An influence of microstructure composition, i.e. an effect of volume fraction t_1 of "stronger" constituent on the macroscopic failure response of the sedimentary rock is

investigated in figure 7 and figure 8. A few cross-sections of the failure surface corresponding to different values of volume fraction t_1 are presented on these graphs.

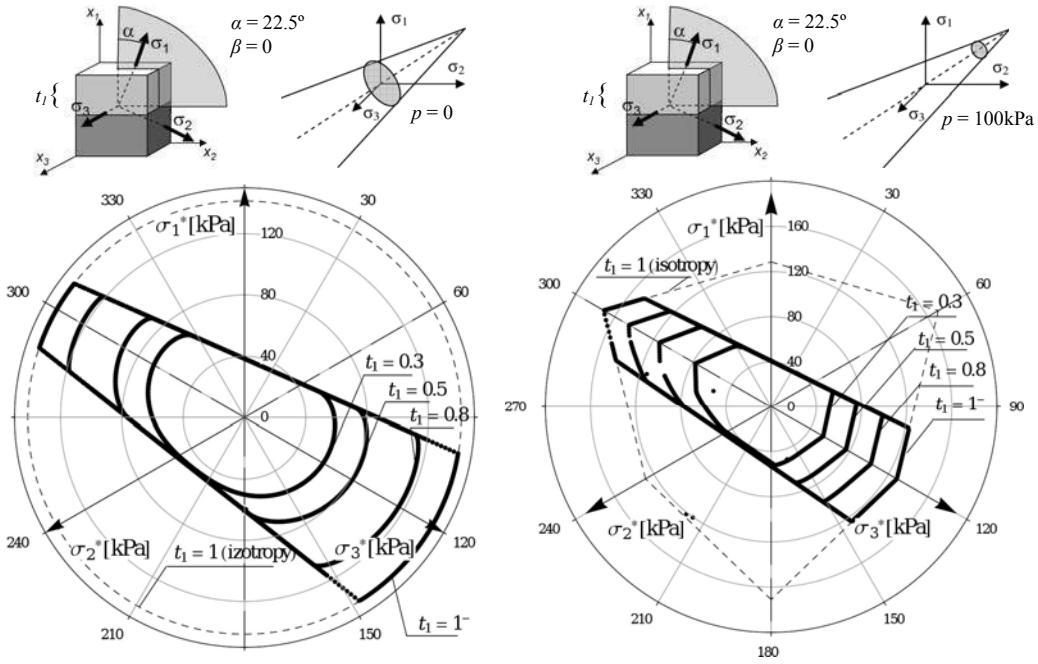

Fig. 7. Influence of volume fraction t_1 on shape of limit surface for two-constituents sedimentary rocks with constituents ruled by Drucker-Prager (on left) and Mohr-Coulomb criterion (on right) under in-plane loading (3rd principal direction of load parallel to stratification plane);

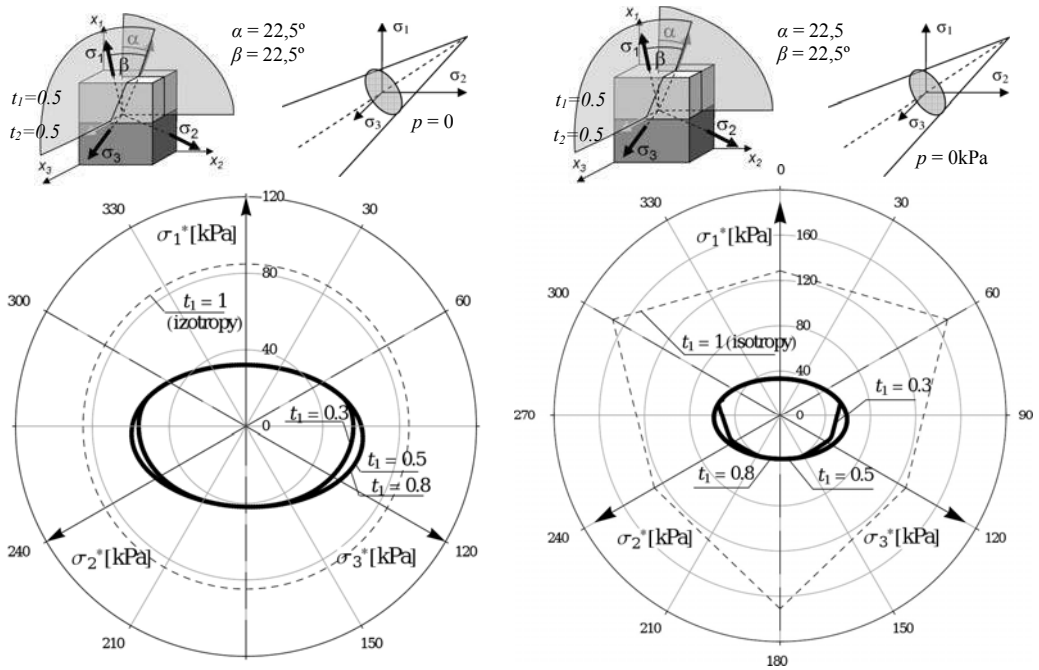

Fig. 8. Influence of volume fraction t_1 on shape of limit surface for two-constituents sedimentary rocks with constituents ruled by Drucker-Prager (on left) and Mohr-Coulomb criterion (on right) under out-of-plane loading (all principal directions of load rotated form material directions).

Examining the results shown in figure 7 one can easily conclude that the linear part of the cross-sections is common characteristic for all the microstructure considered. The actual "length" of this part is ruled by a value of the volume fraction of the stronger constituent. Furthermore, a micromechanical analysis allows in addition to associate with this linear part of the surface the failure mechanism taking place in the microstructure, i.e. reaching a strength by the weaker constituent only.

It is worth noting that states associated with failure of only weaker constituent are not always represented by a straight line. In figure 8 an effect of the volume fraction t_1 on shape of limit surface under conditions of out-of plane loading is presented. As can be observed the common part of a graph becomes oval when all the three principal directions of load are rotated from material directions.

3 FAILURE MECHANISM AND FAILURE FORMAT

In a failure of sedimentary rocks two main mechanisms can be distinguished. One of them can be described as localized shearing parallel to a stratification plane with the macroscopic response as being brought about by a sliding on a surface of a thickness measure zero. In this mechanism shearing localizes in the weakest constituent and it is parallel to the lamination plane. Second mechanism involves the failure of both constituents. In this mechanism "direction of shearing" can vary but it is not associated with stratification direction in any visible manner.

Model of material which distinguishes these two basic mechanisms has been proposed by Jaeger (1960). In Jaeger work laminated material is modeled as an isotropic matrix with inclusions in form of identically oriented, dimensionless weakness planes. Failure of material occurs either when matrix reaches its strength or when vector of load on weakness plane causes localized shearing. Strength criterion for the model is then a conjunction of an isotropic criterion for the matrix and a criterion for weakness plane expressed in term of the stress vector.

As it was stated in the previous paragraph, micromechanics approach shows that for a number of loading programs failure of layered microstructure occurs when only the weakest constituent of structure reaches its strength. As can be seen in figure 7. this situation, represented on graph by straight line, appears with even minimal volume fraction of weaker constituent (t_1=1$^-$). It is obvious that when t_1 tends to 1 layered microstructure becomes identical with Jaeger model: dimensionless weakness planes made of second, weaker constituent are only inclusions in the first constituent forming the matrix. Since part of the graphs associated with the failure of weaker constituent is common for cases with different volume fraction t_1 it can be concluded that this part of limit surface is only associated with the mechanism of localized shearing along stratification plane and that the strength of the weakness plane made of second constituent should be a good model for it.

Criterion for the weakness plane has to be expressed in components of the stress vector. Assuming that direction 1 is perpendicular to the stratification plane the appropriate criteria for weakness plane can be presented as:

for Drucker-Parger constituent:

$$\sqrt{{\sigma_{12}}^2+{\sigma_{13}}^2}+\frac{3a_2\sigma_{11}-k_2}{\sqrt{1-12(a_2)^2}}\le 0 \qquad (4)$$

for Mohr-Coulomb constituent:

$$\sqrt{\sigma_{12}^2+\sigma_{13}^2}+\sigma_{11}\mathrm{tg}\phi_2-c_2\le 0\ . \tag{5}$$

Formulas (4) and (5) transformed on an octahedral plane are in a perfect agreement with points associated with failure of weaker constituent.

The cases, which are not associated with shearing along stratification plane, failure occurs in both constituents. In Jaeger model strength in these cases is represented by an isotropic criterion of a matrix. It can be seen in figure 1 and figure 4 that the strength part of layered structure which is not influenced by the weakness plane is not the isotropic. This fact is confirmed by laboratory tests: for many sedimentary rocks strength results obtained for mechanism which involves failure of all constituents strongly depends on a test direction.

Natural extension of Jaeger model is to replace an isotropic criterion for a matrix by the properly defined anisotropic one. The appropriate failure format of criterion for sedimentary rocks should be a conjunction of a critical plane concept and an adequately identified anisotropic criterion for description of secondary anisotropic effects.

In the work of Lydzba and Kawa (2011) a strength criterion following proposed format is identified. Criterion has been proposed as a macroscopic strength description of a two-constituent Drucker-Prager laminated material. Its critical plane equation is Drucker-Prager condition for weaker constituent expressed in term of the stress vector on a plane. For a strength condition of the matrix the anisotropic criterion formulated by Pariseau has been adopted. Pariseau criterion is an extension, for a case of anisotropy, of Drucker-Prager isotropic condition and can be presented as:

$$A_{ij}\sigma_{ij}+(A_{ijkl}\sigma_{ij}\sigma_{kl})^{\frac{1}{2}}-1\le 0 \tag{6}$$

where A_{ij} and A_{ijkl} are anisotropic material tensors of the criterion. These tensors, in the material directions, can be expressed as:

$$A_{ij}=\begin{bmatrix} U & 0 & 0 \\ & V & 0 \\ sym. & & V \end{bmatrix},\quad A_{ijkl}=\begin{bmatrix} 2G & -G & -G & 0 & 0 & 0 \\ & F+G & -F & 0 & 0 & 0 \\ & & F+G & 0 & 0 & 0 \\ & & & 2M & 0 & 0 \\ & sym. & & & 2M & 0 \\ & & & & & 4F+2G \end{bmatrix} \tag{7}$$

In authors work (Lydzba and Kawa (2011)) the parameters of Pariseau criterion are identified as functions of the microstructure parameters.

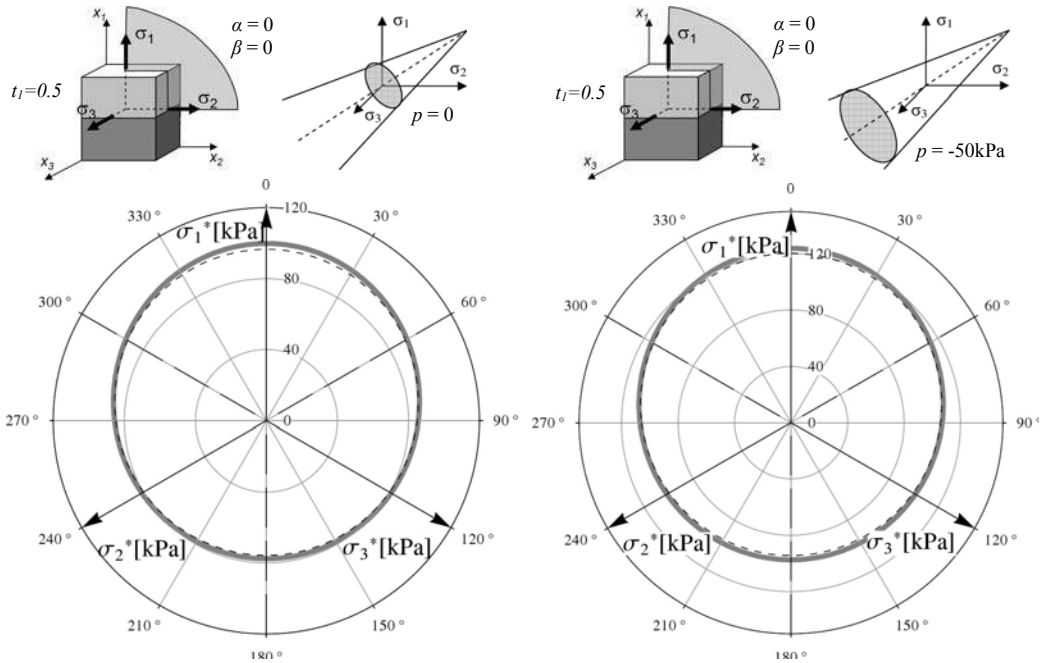

Fig. 9 Comparison of identified criterion satisfying failure format (thin dashed line) with strength of sedimentary rock presented in figure 1.(gray bold line

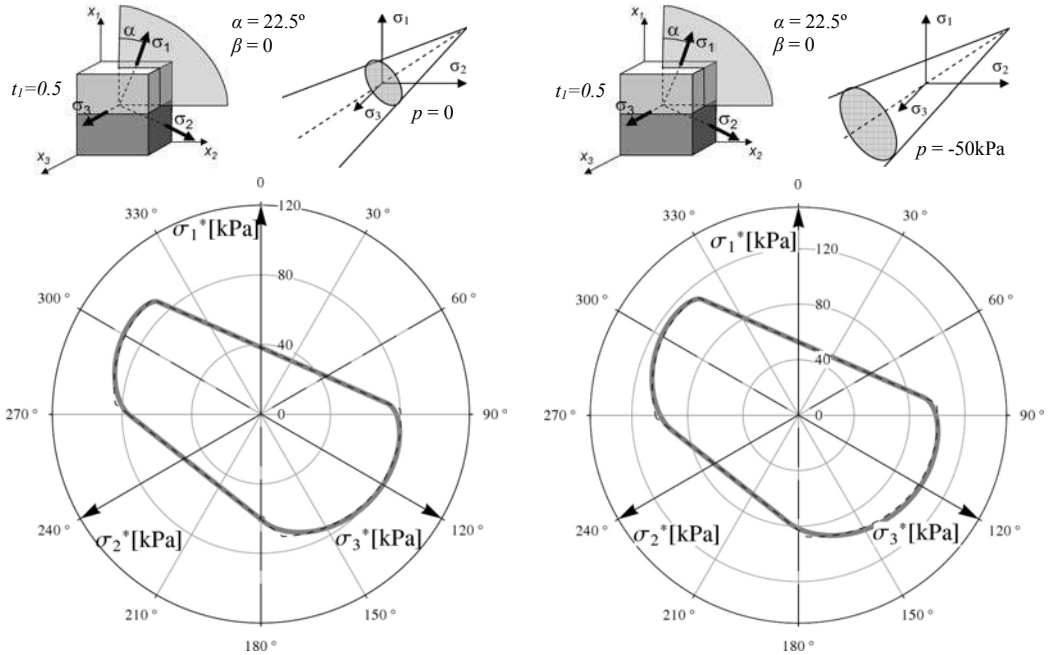

Fig. 10 Comparison of identified criterion satisfying failure format (thin dashed line) with strength of sedimentary rock presented in figure 2.(gray bold line);.

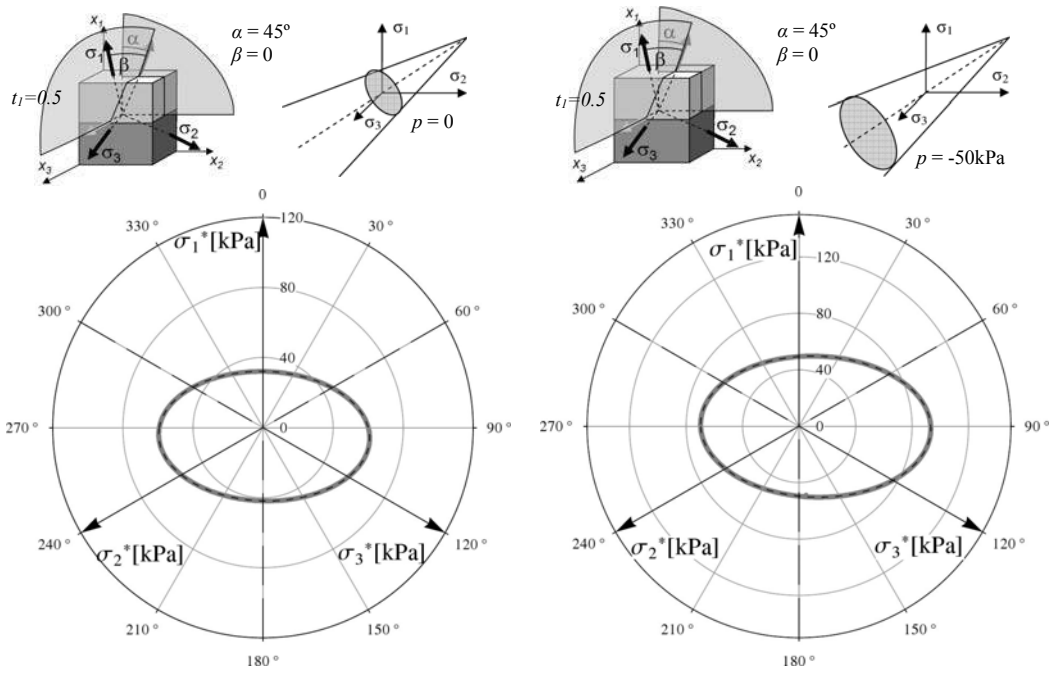

Fig. 11 Comparison of identified criterion satisfying failure format (thin dashed line) with strength of sedimentary rock presented in figure 2.(gray bold line);

In figures 9-11 verification of the proposed criterion against numerical results of the micromechanics is shown. Results of the micromechanics, presented in figures 1-3 before, are drown with gray bold line and identified criterion is drown by dashed line. As it can be seen criterion almost ideally agrees with the micromechanics prediction. This shows potential of the failure format proposed by the authors.

4 FINAL REMARKS

In this work mechanisms of failure of sedimentary rocks have been considered. Two main mechanisms have been distinguished, i.e. first brought about only by a localized shearing in the weakest component and the second corresponding to a failure of both microstructure components. Basing on this two mechanisms a failure format for sedimentary rocks has been proposed. Verification of the criterion proposed shows a very good agreement between identified criterion and micromechanics results.

Macroscopic criterion proposed is straightforward for a numerical implementation. In work of Lydzba and Kawa (2011) it used for 3D analysis of bearing capacity of layered soil under square footing.

REFERENCES

Duveau G, Shao J.F. , Henry J.P (1997), "Assesment of some failure criteria for strongly anisotropic rocks". Int. J. Numer. Anal. Meth. Geomech., Vol. 1, 1-26.

Jaeger J. C. (1960), "Shear failure of anisotropic rocks". Geol. Mag., Vol. 27, 65-72.

Lydzba D, Kawa M., (2011), "3D failure surface for geomaterials with layered microstructure". (submitted).

Lydzba D., Pietruszak S., Shao J.F. (2003), “On anisotropy of stratified rocks: homogenization and fabric tensor approach”. Comput. Geotech., Vol. 30, 289-302.

Pietruszak S., Lydzba D., Shao J.F. (2002), “Modelling of inherent anisotropy in sedimentary rocks”. Int. J. Solids Struct.., Vol. 39, 637-648.

Pariseau W. G. (1972), “Plasticity theory for anisotropic rocks and soils”. Proceedings of 10th Symposium on Rock Mechanics.

Suquet P. (1987), Elements of homogenisation for inelastic solid mechanics, Homogenization Techniques for Composite Media, Springer-Verlag, Berlin

XFEM MODELING OF CRACK PROPAGATION IN GEOMATERIALS UNDER HYDROMECHANICAL LOADING

H.B. Bian
LEM3, UMR CNRS 7239, Université Paul Verlaine-Metz, Ile du Saulcy,57045 Metz, France

J.F. Shao
LML, UMR CNRS 8107, Université Lille I, Cité scientifique,59655 Villeneuve d'Ascq, France

Y. Jia
LML, UMR CNRS 8107, Université Lille I, Cité scientifique,59655 Villeneuve d'Ascq, France

ABSTRACT: *This paper contributes to study of the initiation and propagation of crack in geomaterials subjected to hydromechanical loading . The transition from diffuse microcracks to localized macrocracks is taken into account in the framework of eXtended Finite Element Method (XFEM). In order to describe the material failure process, an elastic damage model is proposed. The diffuse damage is represented by a scalar internal variable and the macroscopic fractures are formed as a consequence of the coalescence of microcracks. A specific criterion based on a critical damage state is proposed as the initiation and propagation condition of macrocracks. Finally, the proposed model is applied to the numerical modeling. The numerical results show that the proposed XFEM approach is capable to reproduce the full failure process of the structure due to hydromechanical loading.*

1 INTRODUCTION

In many engineering applications, such as infrastructures in civil engineering, gravity dams in hydroelectric engineering and underground storages for radioactive wastes, the geomaterials are subjected to complex hydromechanical processes. In order to evaluate the stability and durability of such structures, it is necessary to achieve a good understanding of the coupled hydro-mechanical behavior of geomaterials. In general, the failure process of geomaterials is characterized by two stages: a diffuse failure phase followed by a localized failure phase. The first stage concerns an important degradation of the material's mechanical properties and irreversible deformations, which correspond to the onset and propagation of microcracks. Generally, elastic damage or elasto-plastic damage models are used to describe the behavior of geomaterials in the framework of the continuum mechanics. Afterwards, the microcracks localize and coalesce to macrocracks (fractures) and the failure process goes into the second stage. The discontinuity of displacement is observed along the surfaces of fractures.
During the first stage of failure the mechanical behavior of material can be described by an appropriate damage model and solved by the traditional numerical methods, such as FEM. However, in the second stage the appearance of macrocracks with moving surfaces causes much problems for the traditional numerical method. In view of this, the eXtended Finite Element Method (XFEM) was proposed to deal with these difficulties. The XFEM method funded by Belytschko et al. (Belytschko et al., 1999; Möes et al., 1999) has been widely used in the last decades for fracture analysis in many fields of discontinuous problems. In this paper, the XFEM method is adopted to study and analyze the fracture process in geomaterials subjected to hydromechanical loading.

In the first part, the XFEM method is briefly reviewed. Then, a new coupled elastic damage model is formulated to describe the mechanical behavior of studied material. The condition for the crack initiation and propagation is proposed in the framework of XFEM. Finally, the proposed model is used to analyze the mechanical behavior of concrete structure subjected to desiccation. The numerical results help us get a good understanding of the impact of drying on the failure process in concrete structures.

2 XFEM

In this section, a synthesis of XFEM method will briefly presented. A representative volume element (RVE) of geomaterial which has been crossed by the crack Γ_d (Figure 1) is firstly given in the Fig.1. The crack has a direction from the end to its head (crack tip). The crack splits the volume into two parts: locates at the left side of crack V^+ and at the right side V^-.

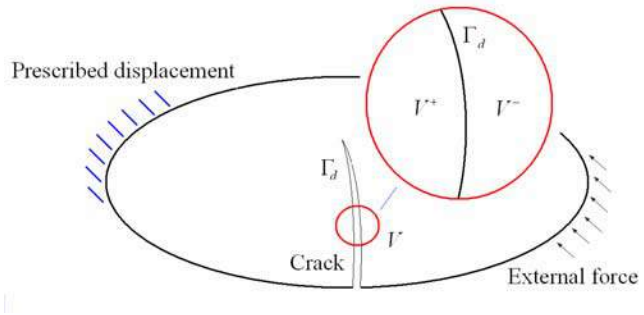

Fig. 1. Representative volume element of geomaterial crossed by a crack

The displacement field can be decomposed into two parts: a continuous part for the classical finite element method u_n and a discontinuous part for the enriched nodes u_r, as:

$$u(x,t) = u_n(x,t) + H(x)u_r(x,t) \tag{1}$$

$H(x)$ is the Heaviside step function as:

$$H(x) = \begin{cases} +1 & \text{if } x \in V^+ \\ -1 & \text{if } x \in V^- \end{cases} \tag{2}$$

The strain field then can be given directly by taking the gradient of the displacement field. The governing equations for XFEM are: the equilibrium equation together with the boundary equations. In fact, the cracking surface should be considered as the external boundary too. After applying the virtual work principle and adopting suitable geometrical discretization, the local governing equations are transformed to a discrete system of equations to be solved for the global equilibrium condition. The general form of global equilibrium equations is similar to that of classical FEM. The main differences between the traditional FEM and XFEM lie on the elementary stiffness matrix and elementary nodal force vector for elements containing enriched degrees of freedom. With the assumption of smooth cracks, the elementary stiffness matrix can be written as follows:

$$K^e = \begin{bmatrix} K^{uu} & K^{ur} \\ K^{ru} & K^{rr} \end{bmatrix} \tag{3}$$

The four components are directly given by the integration over the elementary volume:

$$K^{\alpha\beta} = \int_{\Omega e} (B^{\alpha})^{T} C B^{\beta} d\Omega \quad (\alpha, \beta = u, r) \tag{4}$$

The component of matrix B^i contains the derivatives of the interpolation functions N, which are the same as those used in classical FEM. In case of 2D problems, they can be expressed as follows:

$$B_I^u = \begin{bmatrix} N_{I,x} & 0 \\ 0 & N_{I,y} \\ N_{I,y} & N_{I,x} \end{bmatrix}; B_I^r = \begin{bmatrix} (N_I H)_{,x} & 0 \\ 0 & (N_I H)_{,y} \\ (N_I H)_{,y} & (N_I H)_{,x} \end{bmatrix} \tag{5}$$

3 DAMAGE MODEL

Based on experimental investigations, the damage due to microcracks is the main mechanism of inelastic deformation in geomaterial. However, the kinetics of damage evolution differs under tensile and compressive stresses. Under compressive loading, the damage is mainly induced by the frictional sliding along closed microcracks. On the other hand, opened microcracks are developed in tensile stress conditions. In practice and in order to describe loading path dependency of damage evolution, two scalar damage variables are generally used, ω_c for compressive damage and ω_t for tensile one. The macroscopic effects of induced damage on mechanical properties are also different between compressive and tensile damage. For instance, with open microcracks, the bulk and shear moduli are both affected by damage while only the shear modulus is affected by damage with closed microcracks. In order to account for such unilateral effects, the global damage effects are represented by the following global damage coefficient:

$$\omega = (1 - \alpha_t)\omega_c + \alpha_t \omega_t \tag{6}$$

The coefficient $\alpha_t \in [0,1]$ describes the contribution of compressive and tensile damage to the global effects of microcracks on mechanical behavior. It is defined by:

$$\alpha_t = \left\| \bar{\bar{\sigma}}^{+} \right\| / \left\| \bar{\bar{\sigma}} \right\| \tag{7}$$

$\bar{\bar{\sigma}}^{+}$ is the positive cone of the stress tensor. $\| \ \|$ represents the norm of a second order tensor.

Based on the assumption of small microcrack density and no interaction between microcracks, the following linear functions can be proposed for the description of degradation of the two elastic moduli:

$$K(\omega) = K_0(1 - \omega); \ G(\omega) = G_0(1 - \omega) \tag{8}$$

K_0 and G_0 are respectively the initial drained bulk and shear moduli of undamaged material. This form is equivalent to classical Mazars models (Mazars, 1984). Inspired by the damage model proposed by Mazars and based on the theoretical analysis, the following exponential form is used to describe the damage evolution:

$$\omega_c = 1 - \frac{1}{\exp\left[B_c (Y_\omega - Y_{c,0}^{\omega}) \right]}; \quad \omega_t = 1 - \frac{1}{\exp\left[B_t (Y_\omega - Y_{t,0}^{\omega}) \right]} \tag{9}$$

The parameters B_c and B_t control the evolution kinetics of the compressive and tensile damage. $Y_{c,0}^{\omega}$ and $Y_{t,0}^{\omega}$ define the initial threshold of damage driving force respectively under compressive and tensile conditions. While Y_{ω} represents the damage driving force, which is defined as the maximum value reached of the equivalent tensile strain ε_{eq}. Under the hydromechanical loading, the equivalent tensile strain can be given directly as:

$$\varepsilon_{eq} = \sqrt{\sum_{i=1}^{3} \langle \varepsilon_i \rangle^2} + \sqrt{\sum_{i=1}^{3} \left\langle \varepsilon_i - \frac{b}{3K_0} \pi \right\rangle^2} \tag{10}$$

ε_i denotes the principal strains. The bracket $\langle . \rangle$ means that only the positive value will be taken into consideration. The parameter b is the Biot coefficient. π represents the equivalent pore pressure, it is defined as follows:

$$\pi = \int d\pi; \; d\pi = dp_{gm} - S_{lq}(p_{cp}) dp_{cp} \tag{11}$$

p_{gm} is the pore air pressure and p_{cp} is the capillary pressure. The saturation S_{lq} in geomaterial is generally in function of capillary pressure.

In the proposed model, there are six parameters to be determined: two elastic parameters and four damage parameters. The general methodology for the determination of these parameters is outlined here. The initial elastic constants, namely the initial drained bulk modulus and shear modulus of undamaged material are related to the Young's modulus and Poisson's ratio. And they can be determined by using the linear part of stress-strain curves before the initiation of damage and plastic deformation. Further, the parameters related to the tensile damage can be identified from a direct tension test. On the other hand, the compressive damage parameters should be also determined from the stress-strain curve obtained in a uniaxial compressive test. In the present work, the typical values of parameters used for a concrete used in the numerical simulation followed are given in Table 1.

Table 1. Parameters of the constitutive model for concrete

Elastic parameters	Damage parameters
$E_0 = 40GPa$	$B_c = 1700$
$\nu_0 = 0.26$	$B_t = 6000$
	$Y_{c0} = 6E-5$
	$Y_{t0} = 1E-5$

4 CRACK INITIATION AND CRACK GROWTH ORIENTATION

For modeling crack onset and crack propagation, two important features should first be considered. The first one concerns the determination of fracture onset condition, i.e. the condition for the transition from diffuse damage state to localized fracture. The second feature is related to the orientation along which the fracture will propagate.

4.1 Crack initiation and extension criteria

Physically, the macrocracks are the result of the coalescence of microcracks. We adopt the damage as the macrocrack onset criterion. In fact; in the diffuse failure stage, the evolution of the microcracks is controlled by the damage criterion. When the damage reaches a critical

value, the coalescence occurs and the macrocracks are initiated. This critical damage value is identified from a uniaxial tension test. In Figure 2, the variation of the axial stress and that of induced damage are plotted versus the axial strain. The axial stress is normalized by it is peak value. From this result, we assume that the onset of macrocrack occurs when the damage value reaches the characteristic value corresponding to the peak stress state in the uniaxial tension test, say 0.4. In the following, this critical damage value will be used as the onset condition of macrocrack.

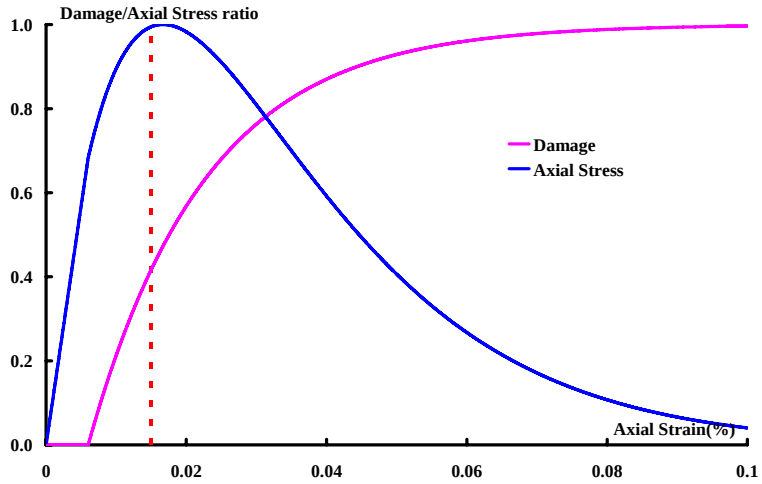

Fig. 2. Crack initiation criteria in function of damage

4.2 Crack growth direction

The most difficult question in modeling the propagation of macrocracks is to determine the direction of macrocracks. In the present work, the average stress criterion proposed by Wells et al. (Wells et al., 2002) is adopted. The macrocracks extend from its tip in the direction perpendicular to the maximum tensile stress which is determined from the average stress tensor. The later can be determined by using the following integration of local stress field:

$$\sigma_m = \int_\Omega w\sigma d\Omega \quad \text{with} \quad w = \frac{1}{(2\pi)^{3/2} l^3} \exp(-\frac{r^2}{2l^2}) \tag{12}$$

In the equation above, r is the distance from the crack tip and l is the material length parameter which determines how fast the weight function decays from the crack tip. The value of parameter l depends on the element size.

5 HYDROMECHANICAL PROCESS

In many engineering applications, the geomaterial is generally partially saturated. Typically, the pore space is saturated by a liquid water phase (lq) and a gas mixture phase (gz). The gas phase is considered as a perfect mixture of dry air (da) and water vapor (vp). The basic governing equations for the hydraulic process include: Darcy's law for the water flow,

$$\frac{\vec{w}_i}{\rho_i} = \frac{k}{\mu_i} k_i^r \left(-\nabla p_i + \rho_i \vec{g}\right) \quad (i = lq, mg) \tag{13}$$

Fick's law controlling the vapor (vp) diffusion in dry air (da),

$$\frac{\vec{w}_{vp}}{\rho_{vp}} - \frac{\vec{w}_{da}}{\rho_{da}} = -F_{ik}\nabla C_{vp}, C_{vp} = \frac{p_{vp}}{p_{mg}} \tag{14}$$

Mass conservation of water ($lq + vp$) and dry air (da),

$$\dot{m}_{lq} + \dot{m}_{vp} = div\left(\vec{w}_{lq} + \vec{w}_{vp}\right); \quad \dot{m}_{da} = div\left(\vec{w}_{da}\right) \tag{15}$$

k is the intrinsic permeability, k_i^r defines the relative permeability related to the fluid phase i, which is a function of saturation degree S_i. $\vec{w}_i$ and m_i are respectively the flow rate vector and mass of fluid i. ρ_i and μ_i are respectively the volumetric mass and the dynamic viscosity of fluid i. The parameter F_{ik} is the Fick's coefficient, which may be a function of porosity, gas pressure, temperature, water saturation and vapor concentration. C_{vp} denotes the vapor concentration in the gas mixture, it can be simply given by the ratio of vapor pressure to the pressure of mixture. For the reason of simplicity, the isothermal condition is adopted in this work and the influence of the transition between liquid water and water vapor is neglected. The relation between the capillary pressure and the relative humidity is calculated using the Kelvin's relation. The capillary pressure is related to the water saturation by the water retention curve. In some applications, the variation of gas pressure is generally very small with respect to that of liquid pressure. Therefore, it is possible to make a simplification. The gas pressure is assumed to be constant and equal to the atmospheric pressure p_{atm}. In addition, the intrinsic permeability may be affected by the damage due to the opening of microcracks and macrocracks. This should be taken into account in the hydromechanical modeling, especially after the macrocracks appearance. However because of no available relevant experimental data, at this stage of work, the variation of permeability is not taken into consideration.

6 NUMERICAL EXAMPLES

In this section, we present two numerical examples of cracks initiation and crack propagation under the hydromechanical loading, with the assumptions of plane strain.

6.1 Concrete beam under desiccation loading

We consider now one concrete beam with the length as 1.5 meters and 0.5metre for hauteur. The beam is supposed as initially full saturated. And then the bottom of bean is exposed in an environment with a relative humidity as 87%. So there begins the desiccation process. Due to the structure effect; the damage has increased rapidly in the lower centre of the beam.

In Fig. 3 the distribution of damage along the bottom of this concrete beam was given at different time (corresponds to the appearance of four macrocracks). At the beginning, the damage is generated at the lower centre of the beam, and the distribution is quasi homogeneity between 0.4 and 1.1 meter. The maximum value however is in the centre of beam and then the first macrocrack appears. With the process of desiccation loading, the damage in the centre of beam is almost constant, however at two sides the damage increase slightly, and then two cracks (as marked as crack 2 in Fig. 3) appear. Then this tendency continues, the damage in two sides increase rapidly, while the damage at beam centre rests as constant until the appearance of two other cracks (as marked as crack 3 in Fig. 3). Then the damage in centre of the beam just at two sides of crack 1 has a little increase, which results to two small cracks (crack 4 as marked in Fig. 3).

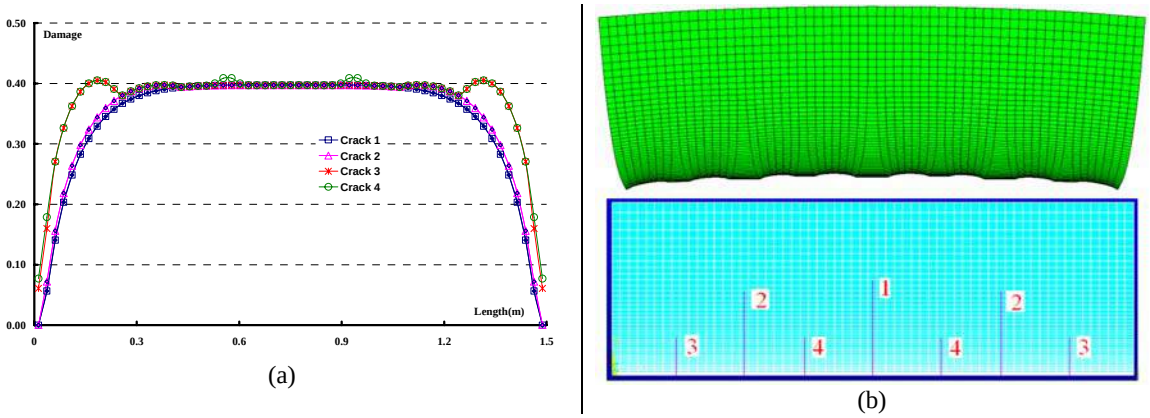

(a) (b)

Fig. 3. (a) The distribution of damage at the bottom of the beam corresponds to the appearance of 4 cracks; (b) The distribution of cracks and deformed mesh (right)

6.2 Desiccation of concrete liner of underground gallery

The underground gallery is excavated in one layer of argillites in the context of geological storage of nuclear wastes. The gallery is firstly excavated and its radius is 3.7m. The concrete liner is then put on the interior wall of the gallery and the thickness of the liner is 0.55m. In order to better account for the stresses applied by the argillite formation on the concrete liner, the argillite layer with a radius of 25m is taken into consideration in the numerical simulation. Fore the reason of symmetry, one quarter of the structure is considered. The geometry and the boundary conditions are presented in Fig. 4. The mesh is composed of 4500 quadratic elements: 2500 elements for the concrete liner and 2000 elements for the argillite formation.

The loading path is divided into three steps: excavation, construction of the concrete liner and ventilation. During the excavation, the radial stress and liquid pressure are unloaded from the initial values to the atmospheric pressure. After that, the concrete liner is installed instantaneously and the ventilation is then activated. According to the ventilation phase, the boundary conditions are summarized as follows: the horizontal displacement and the vertical displacement are respectively blocked on the left side (AD) and on the lower side (BC). The initial conditions are applied on the outer radius of rock (CD). The equivalent negative pore pressure is prescribed, corresponding to a relative humidity of 60% inside the gallery (AB). In order to taken into account the spatial heterogeneity distribution of geomaterial properties, it is assumed that the elastic modulus of concrete verifies the classical Weibull distribution (Weibull, 1951), as illustrated in Fig. 5.

Due to the structural effects of shrinkage deformation during desiccation process, the first crack is initiated in the element where the smaller Young's modulus is observed. After the first crack, the desiccation process continues, and the damage along the inner liner wall increases, excepted for those elements just located at the two sides of the first crack. This can be explained by the fact that with the appearance of the macrocrack, the local material around the crack becomes more deformable, especially on the two sides of the macrocrack. Local tensile stresses are then relaxed and there is no additional damage evolution with the increase of equivalent pore pressure. However, the damage in the elements located far away from the first crack continues to increase. It can be observed that, for the cracks generated during the first stages, the crack length is more important than those created later. The macrocrack generation pattern predicted by the proposed numerical model is quite representative of some real cases.

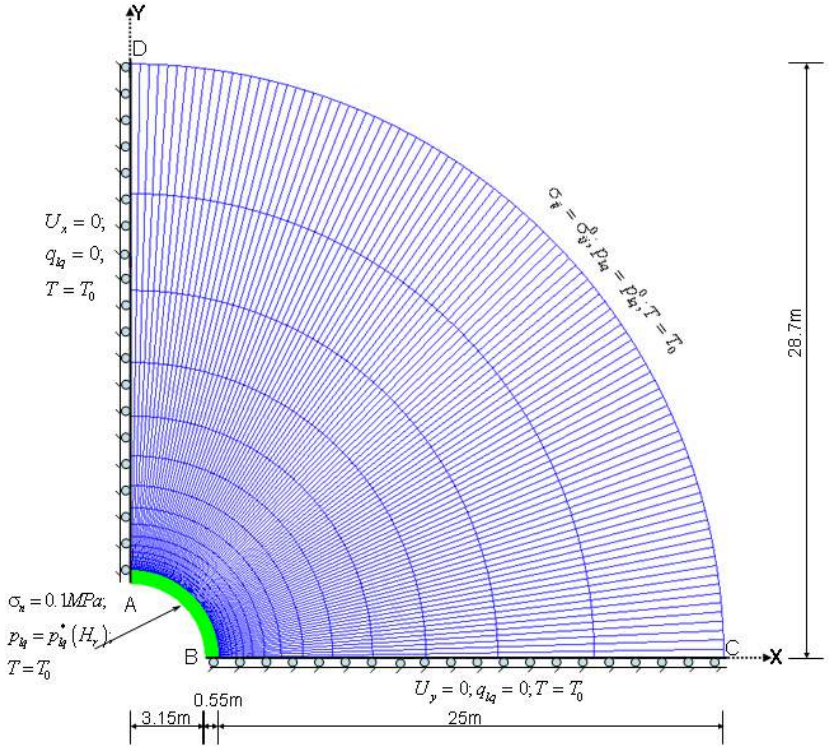

Fig. 4. Geometry, mesh and boundary conditions for the concrete lining in underground gallery

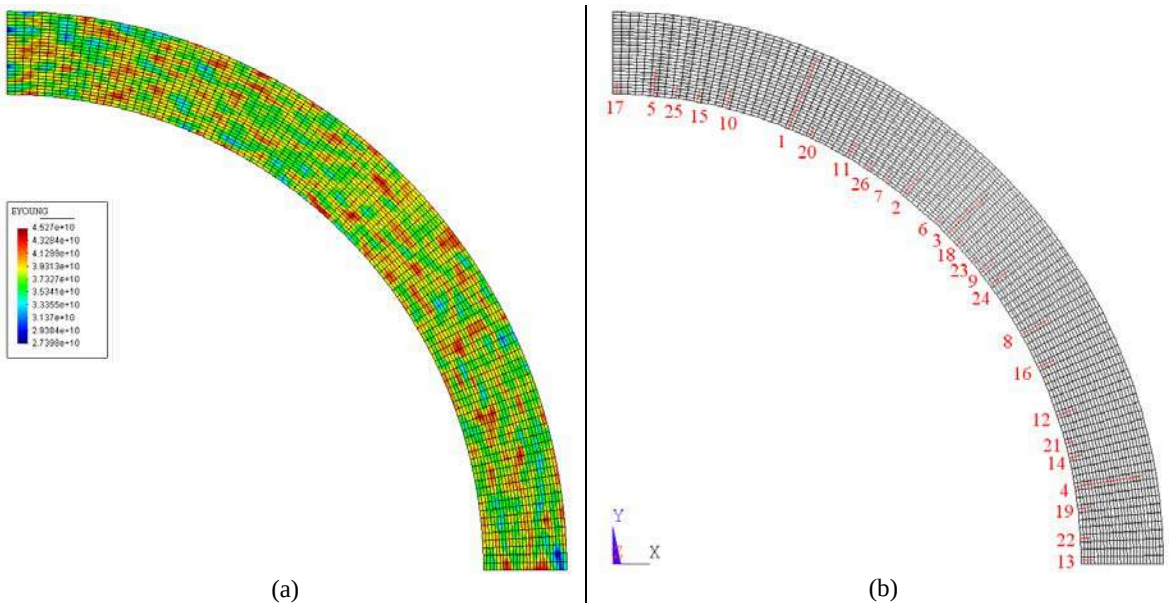

Fig. 5. (a) Random distribution of Young's modulus in concrete lining; (b) The macrocracks distribution in concrete lining after ventilation

7 CONCLUSIONS

The full failure process of geomaterial under hydromechanical loading is studied based on XFEM in this work. The failure is seemed as the transition from the diffuse damage state to

localized fracture onset. The mechanical behavior of geomaterial has been represented by an isotropic continuum elastic damage model. And the difference between tensile and compressive damage is taken into account. The onset and propagation of macrocracks are described in the framework of XFEM. The critical damage–based criterion is proposed as the onset condition of macrocrack. Then, the orientation of macrocracks propagation is determined according to the direction perpendicular to the maximum tension stress. The damage model, as well as the XFEM method, is implemented in computer codes for coupled hydromechanical problems. In the last part of the paper, the proposed approach is applied to the analysis of fracture process in two typical concrete structures: concrete beam and concrete liner of underground gallery. The failure process in the concrete structure due to drying is well reproduced by the numerical method.

ACKNOWLEDGEMENT

This work was partially supported by the ANDRA (French Agence Nationale de Gestion des Déchets Radioactifs), which is gratefully acknowledged.

REFERENCES

Belystshko, T. & Black, T. (1999), “Elastic crack growth in finite elements with minimal remeshing”. Int. J. Num. Meth. Eng., Vol. 45(5), 601-620.

Mazars, J. (1984), Application de la mécanique de l’endommagement non linéaire et à la rupture du béton de structure. Doctoral thesis (in French), University of Paris.

Möes, N., Dolbow, J. & Belytschko T. (1999), “Finite element method for crack growth without remeshing”. Int. J. Num. Meth. Eng., Vol.46(1), 131-150.

Weibull W. (1951), “A statistical distribution function of wide applicability”. J. Appl. Mech. Vol. 18, 293–297.

Wells, G.N., Sluys, L.J. & de Borst, R. (2002), “Simulating the propagation of displacement discontinuities in a regularized strain-softening medium”, Int. J. Num. Meth. Eng., Vol. 53, 1235–1256.

HOMOGENIZATION OF A DUCTILE POROUS SANDSTONE WITH ACCOUNT OF MATRIX PRESSURE SENSITIVITY

Jian Lin
Département de Génie Civil, Université de Strasbourg, France

Wanqing Shen, Jian-Fu Shao
Laboratoire de Mécanique de Lille, UMR 8107 CNRS, Université de Lille, France

Djimédo Kondo
Institut d'Alembert, Université Pierre et Marie Curie (UPMC), Paris, France

ABSTRACT: *The present study aims at formulating and assessing a micromechanical model of ductle porous rocks. The model takes advantage of a recent homogenization-based macroscopic yield function which couples Drucker-Prager type plasticity of the solid matrix and evolving porosity. We first describe the model formulation and its implementation. Through applications to a Vosges sandstone, it is shown that, except for very low confining pressures for which the mechanical behavior is quasi-brittle, the model predicts well the ductile behavior at moderate or high confining pressures (in these cases the pore collapse mechanism is expected to play a dominant role).*

1 INTRODUCTION

Evolving porosity strongly affects the macroscopic mechanical behavior of cohesive geomaterials undergoing plastic deformation (Li, Aubertin, Simon, & Boussière 2009), (Menéndez, Zhu, & Wong 1996), (Zimmermann 1991). A relevant way to incorporate the effects of voids in ductile materials behavior consists in deriving the macroscopic yield function from an homogenization procedure. For instance, the Gurson yield function (see (Gurson 1977)) predicts effects of spherical voids on plastic behavior of metallic porous materials whose matrix obeys to a von Mises criterion. Despite its interest which has been widely demonstrated by means of various applications in mechanics of porous metals, the Gurson model fails to be applicable to non metallic materials such as polymers or geomaterials for which their appear a dissymetric response between tension and compression. For this class of materials, the solid matrix may generally exhibit a pressure-sensitivity. The later has been taken into account for ductile porous materials by Jeong (Jeong 2002), and more recently Guo et al. (Guo, Faleskog, & Shih 2008) who extended the Gurson limit analysis approach by considering ductile porous media having a Drucker-Prager type matrix.

The main objectives of the present study are: i) to formulate a micromechanical constitutive model of ductile porous materials having a Drucker-Prager (pressure-sensitive) matrix; ii) to implement this model and assess its capabilities by comparing its predictions to experimental data on a porous sandstone.

2 ON MACROSCOPIC BEHAVIOR OF POROUS MEDIA WITH PLASTICALLY COMPRESSIBLE MATRIX

In order to describe the mechanical behavior of rocks, it is desirable to develop a constitutive model of ductile porous materials taking into account the plastic compressibility of the matrix. Although cavity expansion in a plastically incompressible matrix[1] induces a pressure sensitivity of the porous material response, the consideration of matrix plastic compressibility is needed in order to account for the dissymmetry between tension and compression. To this end, we present here a new Gurson-type model based on a recent macroscopic criterion, derived by (Guo, Faleskog, & Shih 2008) by applying limit analysis theory to a hollow sphere whose solid matrix obeys to a Drucker-Prager criterion. As it will be pointed out later, this macroscropic criterion exhibits a clear dissymmetry between positive and negative hydrostatic pressures.

2.1 Methodology of derivation of Gurson-type model

Let us consider a representative elementary volume (*r.e.v.*) Ω of a porous material with porosity f. The derivation of the Gurson-type model presented below is based on Limit Analysis theory whose main elements can be found in (de Buhan 1986) or (Suquet 1985). The textbooks (Leblond 2003) and (Dormieux, Kondo, & Ulm 2006) also introduced the main concepts of this theory for the derivation of the macroscopic strength of ductile porous media (see also (Dormieux & Kondo 2010)). Let $\mathbf{\Sigma}$ and $\mathbf{D}$ respectively denote the macroscopic stress and strain rate tensors. $\mathcal{V}(\mathbf{D})$ is the set of microscopic velocity fields, $\underline{v}(\underline{z})$, kinematically admissible with $\mathbf{D}$. These velocity fields comply then with uniform strain rate boundary conditions:

$$\mathcal{V}(\mathbf{D}) = \{\underline{v},\ \underline{v}(\underline{z}) = \mathbf{D}\cdot\underline{z}\,(\forall \underline{z} \in \partial\Omega)\} \tag{1}$$

We denote by $\boldsymbol{\sigma}(\underline{z})$ the microscopic stress field, in equilibrium and related to the macroscopic stress tensor $\boldsymbol{\Sigma}$ by the average rule $\boldsymbol{\Sigma} = \dfrac{1}{|\Omega|}\displaystyle\int_\Omega \boldsymbol{\sigma}\, dV$. As classically, Hill lemma states that:

$$\boldsymbol{\Sigma} : \mathbf{D} = \frac{1}{|\Omega|}\int_\Omega \boldsymbol{\sigma} : \mathbf{d}\, dV \tag{2}$$

with $\mathbf{d} = \frac{1}{2}(\mathrm{grad}\,\underline{v} + {}^t\mathrm{grad}\,\underline{v})$, the microscopic strain rate tensor.

The strength of the solid phase is characterized by the convex set G^s of admissible stress states whose support function $\pi^s(\mathbf{d})$ is defined on the set of symmetric second order tensors $\mathbf{d}$ as:

$$\pi^s(\mathbf{d}) = \sup(\boldsymbol{\sigma} : \mathbf{d}, \boldsymbol{\sigma} \in G^s) \tag{3}$$

$\pi^s(\mathbf{d})$ represents the microscopic maximum "plastic" dissipation. Its macroscopic counterpart is defined as:

$$\Pi^{hom}(\mathbf{D}) = (1-f)\inf_{\underline{v}\in\mathcal{V}(\mathbf{D})}\left[\frac{1}{|\Omega^s|}\int_{\Omega^s}\pi^s(\mathbf{d})\, dV\right] \tag{4}$$

Using equation (2) together with (4) allows to show that Π^{hom} is the support function of the domain G^{hom} of macroscopic admissible stresses:

$$\Pi^{hom}(\mathbf{D}) = \sup(\boldsymbol{\Sigma} : \mathbf{D}, \boldsymbol{\Sigma} \in G^{hom}) \tag{5}$$

[1] As in the Gurson model dedicated to porous metals.

It follows that the limit stress states at the macroscopic scale are shown to be given by:

$$\boldsymbol{\Sigma} = \partial \Pi^{hom} / \partial \mathbf{D} \tag{6}$$

Let us recall that the above approach has been implemented by Gurson (Gurson 1977), assuming a Von Mises criterion for the solid matrix and considering the following simplifications.

- The first simplification consists in representing the microstructure of the porous material by a hollow sphere instead of considering an *r.e.v.* If we denote R_e (resp. R_i) the external (resp. cavity) radius, the pore volume fraction (the porosity) readily reads as $f = (R_i/R_e)^3$.
- $\Pi^{hom}(\mathbf{D})$ is estimated by considering a particular microscopic velocity field $\underline{v}(\underline{z})$, composed of an homogeneous deviatoric part and a radial heterogeneous one (corresponding to the solution of the hollow sphere obeying to a Von Mises criterion and subjected to an external hydrostatic pressure).

2.2 A brief summary of the considered criterion for a porous material having Drucker-Prager matrix

The aim of this subsection is to briefly summarize the methodology leading to the macroscopic yield function (of the porous medium) established by Guo et al. (Guo, Faleskog, & Shih 2008) who follow the Gurson approach, applying it to the case where the solid phase is plastically compressible and obeys to a Drucker-Prager criterion. The later is defined as:

$$\phi^s(\boldsymbol{\sigma}) = \sigma_{eq} + 3\alpha\sigma_m - \sigma_0 \tag{7}$$

where σ_m is the hydrostatic part of the local stress tensor $\boldsymbol{\sigma}$, $\sigma_{eq} = \sqrt{\frac{3}{2}\boldsymbol{\sigma}' : \boldsymbol{\sigma}'}$ (with $\boldsymbol{\sigma}'$ the deviatoric part of $\boldsymbol{\sigma}$) is the local von Mises equivalent stress. σ_0 is linked to the yield stress of the matrix under pure shear ($\sigma_m = 0$). As classicaly, α is related to the friction angle of the matrix ψ_α by $\tan\psi_\alpha = 3\alpha$. ψ_α represents the slope of the criterion in $\sigma_{eq} - \sigma_m$ stress space.

The corresponding support function $\pi^s(\mathbf{d})$ (local plastic dissipation) then reads:

$$\pi^s(\mathbf{d}) = \sigma_0 d_{eq} \tag{8}$$

in which, due to the plastic compressibility of the solid matrix, d_{eq} is related to the volumetric strain $\mathrm{tr}\mathbf{d}$ by:

$$\mathrm{tr}\mathbf{d} = 3\alpha d_{eq} \quad \text{with } d_{eq} = \sqrt{\frac{2}{3}\mathbf{d}' : \mathbf{d}'} \tag{9}$$

where $\mathbf{d}'$ represents the deviatoric part of $\mathbf{d}$.

For the determination of the macroscopic yield function, Guo et al. (Guo, Faleskog, & Shih 2008) considered the following velocity field, consisting, as in the Gurson work, in a radial heterogeneous part (associated here to a Drucker-Prager matrix) and an homogeneous one expressed in the cylindrical frame (coordinates r, θ, z) as:

$$\underline{v}(\underline{z}) = C_0 \left(\frac{b}{r}\right)^{3/s} (\rho \underline{e}_\rho + z \underline{e}_z) + C_1 \rho \underline{e}_\rho + C_2 z \underline{e}_z \tag{10}$$

where C_0, C_1 and C_2 are three constants to be determined, $s = 1 \pm 2\alpha$ when $C_0 \gtrless 0$ and ρ is such that $r = \sqrt{\rho^2 + z^2}$. It follows that $\Pi^{hom}(\mathbf{D})$ (equation (4)), computed with (8) in which d_{eq} is derived from (10), reads (Guo, Faleskog, & Shih 2008):

$$\Pi^{hom}(\mathbf{D}) = \frac{|C_1 - C_2|}{3} \int_f^1 \int_0^\pi \sqrt{\left[1 + \frac{1}{2}\left(3\cos^2\theta - 1\right)\zeta\right]\left(1 + \omega^2 x^{-2/s}\right)} \sin\theta \mathrm{d}\theta \mathrm{d}x \tag{11}$$

where $\zeta = \dfrac{2\omega x^{-1/s}}{1+\omega^2 x^{-2/s}}\text{sign}(C_1 - C_2)$ and $\omega = \dfrac{3C_0}{s|C_1 - C_2|}$.

Introducing (11) in (6) allows to obtain an implicit parametric form of the macroscopic yield function. Moreover, Guo et al. (Guo, Faleskog, & Shih 2008) proposed an approximate closed-form expression Φ_A of this yield function:

$$\Phi_A = \left[\frac{\Sigma_{eq}/\sigma_0}{\Theta(\Sigma_m,\alpha,f)}\right]^2 + 2f\cosh[\frac{1}{\gamma}\ln(1-3\alpha\frac{\Sigma_m}{\sigma_0})] - (1+f^2) = 0 \tag{12}$$

with:

$$\gamma = \frac{2\alpha}{2\alpha + \text{sign}(\Sigma_m)} \tag{13}$$

Two forms of the function $\Theta(\Sigma_m,\alpha,f)$ have been proposed by the authors. In the present study devoted to rocks-like porous materials such as Vosges sandstone, the following form which appears to be appropriate in compression ($\Sigma_m < 0$) will be adopted:

$$\Theta(\Sigma_m,\alpha,f) = 1 - \frac{3\alpha\Sigma_m}{\sigma_0[1+\gamma\ln(1+sf)]} \tag{14}$$

with:

$$s = 1 + 2\alpha\ \text{sign}(\Sigma_m) \tag{15}$$

3 FORMULATION OF THE MODEL AND NUMERICAL IMPLEMENTATION

We aim now at formulating and implementing a constitutive plastic-damage model by considering the approximate criterion (12) together with (13), (14) and (15). Even though the model will be used here just for homogeneous experimental tests, the implementation has been performed in ABAQUS finite element software via the user-routine UMAT. This has the advantage to prepare the next step of the present research which will concern structural analysis. After presenting the constitutive equations of the new model, we will describe the corresponding solution procedure.

3.1 Evolution equations

An usual approach in the context of ductile porous materials consists in introducing in the above macroscopic yield function a hardening variable $\bar{\sigma}$ at the place of σ_0. According to normality rule which can be shown to be upscaled at macroscale, the macroscopic plastic flow rule reads:

$$\mathbf{D}^p = \dot{\lambda}\frac{\partial\Phi}{\partial\mathbf{\Sigma}}(\mathbf{\Sigma},\bar{\sigma},f) \tag{16}$$

in which $\mathbf{D}^p$ represents the macroscopic plastic strain rate tensor; $\dot{\lambda}$ denotes the plastic multiplier. The porosity evolution is derived from the microscopic relation $\dot{J} = J\ \text{tr}\mathbf{d}^p$, where J is the ratio of current cell volume to initial one. It follows that:

$$\dot{f} = (1-f)\text{tr}\mathbf{D}^p - \frac{1}{|\Omega|}\int_{\Omega^s}\text{tr}\mathbf{d}^p dV \tag{17}$$

where Ω^s represents the solid matrix domain and $|\Omega|$ the total cell volume. $\mathbf{d}^p$ is the microscopic plastic strain rate tensor. With the definition $\bar{d}^p_{eq} = \frac{1}{|\Omega|}\int_{\Omega^s} d^p_{eq}dV$, and using (9) in the second term of this expression, one has:

$$\frac{1}{|\Omega|}\int_{\Omega^s}\text{tr}\mathbf{d}^p dV = \frac{1}{|\Omega|}\int_{\Omega^s} 3\alpha d^p_{eq}dV = 3(1-f)\alpha\bar{d}^p_{eq} \tag{18}$$

Applying this expression to (17) gives:

$$\dot{f} = (1-f)(\mathrm{tr}\mathbf{D}^p - 3\alpha\bar{d}^p_{eq}) \tag{19}$$

To determine the porosity evolution, this equation must be combined with the following evolution law of the yield stress in the matrix (see for instance (Gurson 1977)):

$$(1-f)\,\bar{\sigma}\bar{d}^p_{eq} = \boldsymbol{\Sigma} : \mathbf{D}^p \tag{20}$$

For simplicity, an isotropic hardening of the matrix has been considered in the form:

$$\bar{\sigma} = \sigma_0 + H(\bar{\varepsilon}^p)^a \tag{21}$$

in which the hardening parameters H and a are calibrated from triaxial compression tests.

3.2 Solution procedure for the constitutive equations

The algorithm for the numerical implementation of the developed model in ABAQUS software is an implicit scheme which mainly includes two steps. For the non viscous solution procedure, the strain rate $\mathbf{D}$ and its plastic part $\mathbf{D}^p$ have to be replaced by the increment of strain $\Delta\mathbf{E}$ and its plastic part $\Delta\mathbf{E}^p$, respectively. These two steps are:

- Elastic prediction:

$$\boldsymbol{\Sigma}_{n+1} = \mathbb{C}^{hom} : \left(\mathbf{E}_{n+1} - \mathbf{E}^p_{n+1}\right) = \boldsymbol{\Sigma}^{pred} - \mathbb{C}^{hom} : \Delta\mathbf{E}^p \tag{22}$$

  where $\mathbb{C}^{hom}$ is the homogenized elastic modulus tensor of the porous medium; the index n and $n+1$ are related to the beginning and the end of the increment respectively; the quantity $\boldsymbol{\Sigma}^{pred} = \mathbb{C}^{hom} : (\mathbf{E}^e_n + \Delta\mathbf{E})$ is the elastic predictor.
- Plastic correction:
  Taking into account the yield function and computing $\partial\Phi/\partial\boldsymbol{\Sigma}^{pred}$, we get for the deviatoric part, $(\Delta\mathbf{E}^p)'$, and for the hydrostatic part ΔE^p_m of the macroscopic plastic strain:

$$\left\{\begin{array}{l} (\Delta\mathbf{E}^p)' = 3\Delta\lambda/\left(\bar{\sigma}^2\Theta^2\right)\left(\boldsymbol{\Sigma}^{pred}\right)' \\ \Delta E^p_m = \Delta\lambda\left\{\dfrac{2\alpha\Sigma^2_{eq}}{\Theta^3\bar{\sigma}^3\left[1+\gamma\ln(1+sf)\right]} + \right. \\ \qquad \left.\dfrac{\frac{2f}{\gamma}\sinh\left[\frac{1}{\gamma}\ln(1-3\alpha\Sigma_m/\bar{\sigma})\right]}{3\Sigma_m - \bar{\sigma}/\alpha}\right\} \end{array}\right. \tag{23}$$

  From equation (23) and the definition of $\Delta E^p_{eq} \equiv (2/3\Delta\mathbf{E}^{p\prime} : \Delta\mathbf{E}^{p\prime})^{1/2}$, the following expression of $\Delta\lambda$ depending on ΔE^p_{eq} is obtained:

$$\Delta\lambda = \bar{\sigma}^2\Theta^2\Delta E^p_{eq}/\left(2\Sigma^{pred}_{eq}\right) \tag{24}$$

  The consistency condition, $\dot{\Phi} = 0$, allows to compute ΔE^p_{eq}. One can then compute $\Delta\lambda$ with ΔE^p_{eq}; the plastic correction can then be obtained:

$$\Delta\mathbf{E}^p = \Delta\lambda\frac{\partial\Phi}{\partial\boldsymbol{\Sigma}^{pred}} \tag{25}$$

4 CALIBRATION AND VALIDATION OF THE PROPOSED MODEL ON A VOSGES SANDSTONE

The purpose of this section is to evaluate the performance of the proposed model to describe the mechanical behavior of a porous geomaterial, the so-called "Vosges sandstone" (coming from the Vosges mountains, France), which has been studied in a series of experimental investigations (see (Khazrarei 1996), (Shao & Khazraei 1996) or (Bésuelle, Desrues, & Raynaud 2000)). This material is considered as a typical quasi-brittle rock, whose mechanical behavior exhibits a brittle-ductile transition from low to high confining pressures (Bésuelle, Desrues, & Raynaud 2000) (Menéndez, Zhu, & Wong 1996). The deformation of this sandstone results from a combination of pore compaction and a shearing mechanism under macroscopic triaxial loading.

The Vosges Sandstone is mainly composed of quartz grains (93%), with a few percent of feldspar and white mica. This sandstone is cemented and cohesive with a porosity about 20%. Existing data considered in the present study correspond to triaxial compression tests which have been performed by (Shao & Khazraei 1996) for various confining pressures. In these tests, the cylinder samples are first subjected to a hydrostatic stress, the so-called confining pressure. Then the axial stress (Σ_1) is increased while the lateral stress (confining pressure, $\Sigma_2 = \Sigma_3$) is kept constant.

We first proceed to a calibration of the model parameters and then to its validation (particularly for high confining pressures) by comparison of the predictions with triaxial tests data.

4.1 Identification of the model parameters

The two parameters of the matrix Drucker-Prager criterion, α and σ_0, are identified from macroscopic yield stresses data in the triaxial compression tests with different confining pressures. This calibration procedure has led to $\alpha = 0.25$ and $\sigma_0 = 2MPa$.

Concerning the elastic characteristics of the solid matrix of Vosges sandstone, they are determined from consideration of triaxial compression tests. Assuming spherical pores, an Hashin-Shtrikhman upper bound has been used for this determination. Let us recall that for a porous material with an isotropic elastic matrix having a compression modulus k^s and a shear modulus μ^s, Hashin-Shtrikhman upper bound delivers the following well-known homogenized elastic moduli :

$$k^{hom} = \frac{4(1-f)k^s\mu^s}{4\mu^s + 3fk^s}; \quad \mu^{hom} = \frac{(1-f)\mu^s}{1 + 6f\dfrac{k^s + 2\mu^s}{9k^s + 8\mu^s}} \tag{26}$$

which explicitly incorporates the effects of voids via the porosity f.

By inversion, this allows to determine k^s and μ^s as function of porosity f, k^{hom} and μ^{hom} which are all known from the macroscopic behavior of the porous sandstone in elastic regime. The measured value of porosity f being equal to 0.2, this procedure has led to $k^s = 22700MPa$ and $\mu^s = 11700MPa$ which corresponds to $E^s = 30000MPa$ and $\nu^s = 0,28$. The values of parameters H and a in the hardening rule are obtained from a calibration procedure:
$H = 500MPa$ and $a = 0.3$.

4.2 Comparison of the model results to experimental data

As the triaxial compression tests are partly used for the calibration of the model parameters, the simulation of the complete set of material responses can be considered as a first step of assessment of the capability of the model.

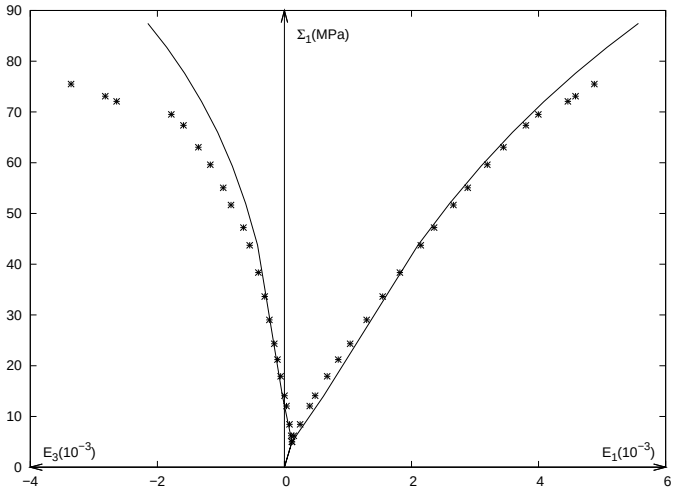

Fig. 1. Simulation of a triaxial compression test on Vosges sandstone with $5MPa$ confining pressure (points: experimental data; line: model prediction)

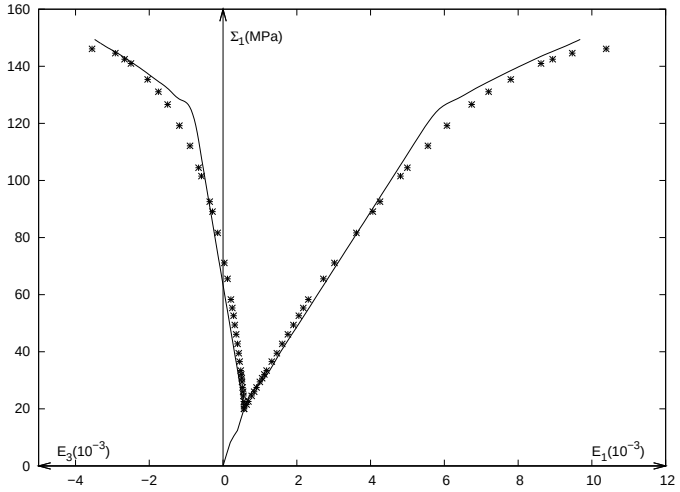

Fig. 2. Simulation of a triaxial compression test on Vosges sandstone with $20MPa$ confining pressure (points: experimental data; line: model prediction)

Figures 1 - 3 compare the predictions of macroscopic axial stress Σ_1 - macroscopic strains (axial strain E_1 and lateral strain E_3) curves to experimental data obtained from triaxial compression tests with different confining pressures ($5MPa$, $20MPa$ and $40MPa$). The obtained results are in good agreement with the experimental data for the tests performed with high confining pressures ($20MPa$ and $40MPa$). However, the predictions appear to be less accurate for tests with low confining pressure ($5MPa$). This confirms that the model may be appropriate for the description of the ductile behavior of the porous Vosges sandstone which is mainly governed by the pore compaction mechanism (Bésuelle, Desrues, & Raynaud 2000) (Menéndez, Zhu, & Wong 1996) combined with matrix shearing. In contrast, damage mechanism due to microcracking phenomena should be introduced in the micromechanical model in order to predict more accurately the macroscopic behavior of the considered sandstone in the quasi brittle regime associated to low confining pressure tests.

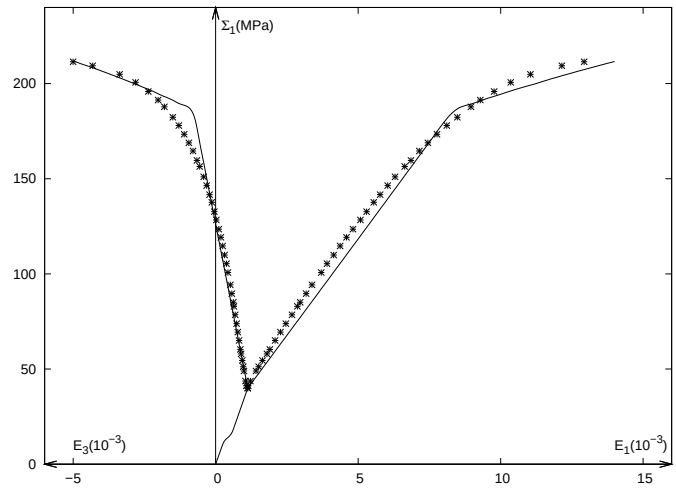

Fig. 3. Simulation of a triaxial compression test on Vosges sandstone with $40MPa$ confining pressure (points: experimental data; line: model prediction)

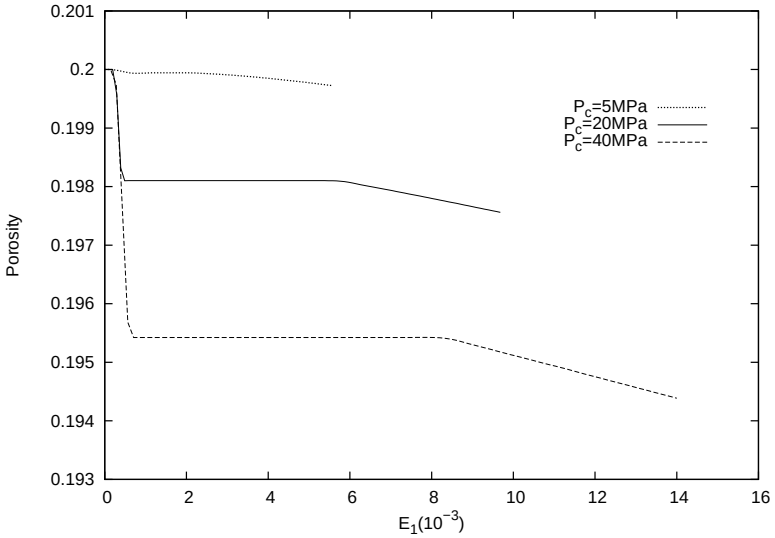

Fig. 4. Predicted evolution of porosity

Figure 4 shows the evolution of porosity as function of macroscopic axial strain E_1 predicted by the proposed model in the three tests. For the low confining pressure test the decrease of porosity is quite negligible. In contrast, in the two other tests, during the application of the confining pressure, we note relative important decreases of porosity. This confirms the role of the pore compaction in the plastic deformation of the sandstone under high confining pressures. Note that the kink-like behavior observed during the application of confining pressures (see figures 2 and 3) can be interpreted as a consequence of the plastic response related to the pore compaction phenomenon.

5 CONCLUSIONS

In the present work, we have proposed a new micromechanical constitutive model based on a macroscopic yield function recently formulated by Guo et al. (Guo, Faleskog, & Shih 2008) for ductile porous materials with plastically compressible matrix (assumed to obey to a Drucker-Prager criterion). This constitutive model has been fully described and then implemented. Furthermore, it has been applied for the modeling of the mechanical behavior of a porous Vosges sandstone under triaxial compression loadings. It has been shown that the model is appropriate for the description of the ductile behavior (observed for tests with high confining pressures) of this sandstone which is mainly governed by the pore compaction mechanism and a matrix shearing. This is illustrated by the significant decrease of porosity predicted by the model during the first stage of these tests. In contrast, the predictive capabilities of the model seem to be limited for the description of the material quasi brittle behavior observed for tests with low confining pressures. To this end, the micromechanical model should be extended by incorporation of damage mechanisms due to microcracking phenomena.

REFERENCES

Bésuelle, P., Desrues, J., & Raynaud, S. (2000). Experemental characterisation of the localisation phenomenon inside a vosges sandstone in a triaxial cell. *International Journal of Rock Mechanics and Minging Sciences 37*, 1223–1237.

de Buhan, P. (1986). *A fundamental approach to the yield design of reinforced soil structures - Chap. 2: yield design homogenization theory for periodic media*. Ph. D. thesis, Univ. Paris VI.

Dormieux, L. & Kondo, D. (2010). An extension of gurson model incorporating interface stresses effects. *Int. Journ. of Engineering Science 48*, 575–581.

Dormieux, L., Kondo, D., & Ulm, F. (2006). *Microporomechanics*. Wiley.

Guo, T., Faleskog, J., & Shih, C. (2008). Continiuum modeling of a porous solid with pressure-sensitive dilatant matrix. *J. Mech. Phys. Solids 56*, 2188–2212.

Gurson, A. (1977). Continuum theory of ductile rupture by void nucleation and growth: Part i-yield criterion and flow rules for porous ductile media. *J. Engrg. Mat. Technol. 99*, 2–15.

Jeong, H.-Y. (2002). A new yield function and a hydrostatic stress-controlled void nucleation model for porous solids with pressure-sensitive matrices. *International Journal of Solids and Structures 39*, 1385–1403.

Khazrarei, R. (1996). Experimental study and constitutive modeling of damage in brittle rocks. *PhD thesis, Université de Lille I, France*.

Leblond, J.-B. (2003). *Mécanique de la rupture fragile et ductile*. Hermes.

Li, L., Aubertin, M., Simon, R., & Boussière, B. (2009). Formulation and application of a general inelastic locus for geomaterials with variable porosity. *Can. Geotech. J. 42*, 601–623.

Menéndez, B., Zhu, W., & Wong, T.-F. (1996). Micromechanics of brittle faulting and cataclastic flow in berea sandstone. *Journal of Structural Geology 18*, 1–16.

Shao, J. & Khazraei, R. (1996). A continuum damage mechanics approach for time independent and dependent behavior of brittle rock. *Mechanics Research Communications 23*, 257–276.

Suquet, P. (1985). *Homogenization techniques for composite media*, Chapter Elements of homogenization for inelastic solid mechanics, pp. 193–278. Sanchez-Palencia E. ed., Springer Verlag.

Zimmermann, R. (1991). *Compressibility of sandstones*. Elsevier.

MICROMECHANICAL ANALYSIS OF STRESS IN AN UNSATURATED GRANULAR MEDIUM

R. Wan & S. Khosravani
Department of Civil Engineering, University of Calgary, Calgary, AB, Canada
F. Nicot
Cemagref, Grenoble, France

ABSTRACT: *The paper is concerned with a micromechanical formulation of force transmission within an unsaturated soil as a three-phase system composed of idealized spherical particles connected by a pore water menisci network. A tensorial effective stress equation is being proposed as a generalized Bishop's equation whereby the effective stress parameter χ is elucidated. The latter can be expressed as an explicit function of the number of water menisci, particle packing and degree of water saturation. Also, interparticle forces are found to be dependent on the distribution of pore fluid pressure and the contractile skin arising from the interaction of interfaces. Two major findings of this work are: (1) the determination of the analytical relationship between χ and degree of saturation, and (2) the identification of a suction based internal shear effect even under isotropic external loading. The understanding of suction stress and its dependency on the degree of saturation is a longstanding problem both theoretically and experimentally.*

1. INTRODUCTION

Unsaturated soils represent an important three-phase system in which internal forces arise from the interaction of solid, liquid and gas phases. As such, in determining the behaviour and strength of unsaturated soils, it becomes difficult to choose the controlling stress variable that would substitute for the role of effective stress in the saturated case. Bishop (1959) extended Terzaghi's effective stress principle to account for the presence of an air phase by intuitively introducing an average pore fluid pressure weighted over the pore air (u_a) and water (u_w) pressures, i.e.

$$\sigma' = \sigma - \left[\chi u_w + (1-\chi)u_a\right] = (\sigma - u_a) + \chi(u_a - u_w) \tag{1}$$

where σ and σ' are the total and effective stresses respectively, and χ is the weighted parameter that is arbitrarily confounded with the degree of saturation, S_r. Here, soil mechanics sign convention is used, i.e. positive stresses mean compression. Understanding the suction stress as a function of the difference between air and water pressures, as well as its dependency on the degree of saturation is a longstanding problem both theoretically and experimentally.

The present paper examines the notion of stress and its definition for a three-phase system composed of idealized soil particles and pore water menisci through a micromechanical

analysis. By considering air and water pressures, surface tension, as well as interparticle forces within an assembly of spherical particles, the (Cauchy) stress tensor can be readily calculated as a volume average of the various constituents (phases) just like in the case of a solid body consisting of interacting point masses in a representative elementary volume (Love, 1944). The proposed derivation ultimately leads to a tensorial effective stress equation which can be viewed as a generalized Bishop's equation explicitly written as a function of the spatial distribution of water menisci and an anisotropic tensor describing the distribution of pore fluid around particle surfaces, including the effect of the contractile skin. It is noteworthy that similar formulation could be reached based on virtual work as shown in Li (2003) where internal capillary surfaces were not explicitly accounted for.

One of the implications of this generalized formulation is that the stress tensor formulation engenders a suction based shear effect even under isotropic loading, which is fundamental to the understanding of the strength behaviour of unsaturated soils. Furthermore, as a by-product of this micromechanical derivation, an analytical expression is obtained for the weighting parameter χ. By considering regular spherical particle assemblies such as in two-particle or multi-particle configurations with tetrahedral and cubical packings, together with changing the geometry of the pore water meniscus to mimic filling, the relationship between χ and degree of saturation can be computed explicitly. The variation of χ as a material parameter with the degree of saturation on both water meniscus and particle packing is discussed in the light of experimental data already available for different types of soils. The work constitutes a rational approach within which the role of capillary forces and their distributions can be accounted for through the microscale physics that governs the state of stress in an unsaturated soil and its macroscopic engineering properties.

2. STRESS DERIVATION IN A THREE-PHASE SYSTEM

The stress tensor in a representative elementary volume (REV) consisting of an ensemble of interacting solid particles in the presence of a water and air phase can be generally written as a volume average of each individual phase stress over the total volume *V*, i.e.

$$< \sigma_{ij} >= \frac{1}{V}\int_V \sigma_{ij} dV = \frac{1}{V}\sum^{N}\int_{V^p} \sigma_{ij} dV + \frac{V^w}{V} u_w \delta_{ij} + \frac{V^a}{V} u_a \delta_{ij} \tag{2}$$

where V^α, $\alpha = p, a, w$ represent solid particle, water and air phase volume respectively, N the number of particles, and δ_{ij} the Kronecker delta. In Eq. (2), the stress in the water and air phases have been considered to be hydrostatic and equal to u_w and u_a respectively. As a result, the last two terms on the right in Eq. (2) simply refer to the partial pressures due to air and water phases with their respective volume fractions applied to each individual pressure.

Next, suppose the above system is idealized as an ensemble of mono-disperse spherical particles of radius R joined by independent concave liquid bridges with negligible interparticle contact area. Since we are primarily interested in the transport of forces in the REV, we will then focus on the first term on the right in Eq. (2) related to particle interactions. Applying Gauss' divergence theorem to the latter term for the case of static and weightless media, the following so-called granular stress tensor is obtained:

$$< \sigma_{ij} >_g = \frac{1}{V}\sum^{N}\int_{V^p} \sigma_{ij} dV = \frac{1}{V}\sum^{N}\int_{\Gamma^p} x_i t_j d\Gamma \tag{3}$$

where Γ^p is the surface of a particle, x_i the spatial position of points on Γ^p at which various surface tractions t_j act. Among the various surface tractions exerted on an individual particle, we will find contributions from pair-wise particle contact forces due to external loading, actions of air and water pressures on dry (Γ_d^p) and wetted (Γ_w^p) surfaces respectively, and surface tension arising from air/water/solid interfaces formed by water menisci along contour Γ_m as illustrated in Fig. 1.

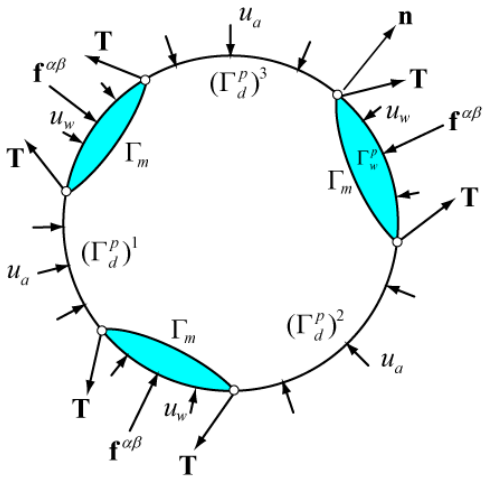

$$\Gamma_d^p = (\Gamma_d^p)^1 \cup (\Gamma_d^p)^2 \cup (\Gamma_d^p)^3$$

Figure 1 Free body diagram for analysis of interparticle forces with 3 water menisci

Furthermore, noting that $x_i = x_i^c + Rn_i$, where x_i^c is the position vector of the particle centroid, and considering equilibrium of forces on the closed surface of each particle, we finally get:

$$< \sigma_{ij} >_g = \frac{1}{V} \sum_{\alpha\beta}^{N} f_j^{\alpha\beta} l_i^{\alpha\beta} + \frac{u_a . R}{V} \sum^{N} \int_{\Gamma_d^p} n_j n_i d\Gamma + \frac{u_w R}{V} \sum^{N} \sum^{L} \int_{\Gamma_w^p} n_j n_i d\Gamma - \frac{R}{V} \sum^{N} \sum^{L} \int_{\Gamma_m} T_j n_i d\Gamma \quad (4)$$

where n_j is the normal to the particle surface, $f_j^{\alpha\beta}$ is the mutual contact force between particle pair α and β, $l_i^{\alpha\beta}$ the so-called branch vector defining to the separation distance between the same two particles, T_j the surface tension forces per unit length related to water meniscus action on Γ_m formed by the intersection of the water meniscus with the particle's surface, L the number of liquid bridges, Γ_w^p is the part of the particle wetted by the liquid bridge, whereas Γ_d^p is the union of all dry parts of the particle's surface (see Fig. 1). Interestingly, the air/water interface at the particle's surface, seen as a contractile skin, allows the REV to withstand tensile stresses.

It should be noted that the decomposition of surface tractions as laid out in Fig. 1 and which is reflected in Eq. (4) leads to the well-known result that capillary forces arising from a concave liquid bridge between two spherical particles have two sources. The first source comes from the pressure difference between air and water described by the Young-Laplace equation, whereas the second source originates from the surface tension force acting on the boundary of the wetted area on the particle surfaces where solid, air and water coexist (e.g. see Megias-Alguacil and Gauckler, 2009).

The tensor moment of force, defined by the first term to the right of Eq. (4) as a dyadic product between $\mathbf{f}^{\alpha\beta}$ and $\mathbf{l}^{\alpha\beta}$, is easily identified as the effective stress tensor σ'_{ij} used in the fully saturated case. Therefore, further rearrangement of Eq. (4) and substitution into Eq. (2) finally leads to the form of a generalized Terzaghi's effective stress relation:

$$\sigma'_{ij} = (\sigma_{ij} - u_a\delta_{ij}) + (u_a - u_w)\phi S_r\delta_{ij} + (u_a - u_w)\frac{R}{V}\sum^{N}\sum^{L}\int_{\Gamma_w^p} n_j n_i d\Gamma + \frac{R}{V}\sum^{N}\sum^{L}\int_{\Gamma_m} T_j n_i d\Gamma \quad (5)$$

in which ϕ is the porosity, S_r is the degree of saturation, whereas the last two terms relate to distributional descriptions of liquid bridges (menisci) and contractile skin effects respectively as surface integrals of dyadic products of contact normals and surface tension forces as illustrated in Fig. 2.

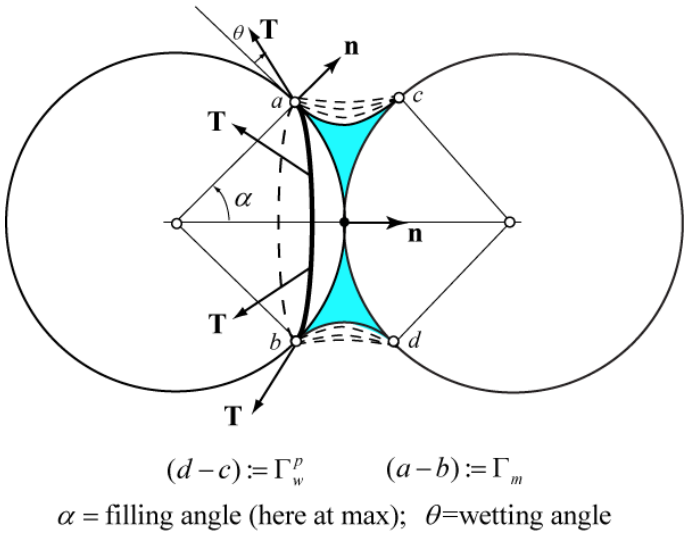

Figure 2. Geometry of meniscus and surface tension forces for a pair of spherical particles

These integrals over each pair of particles can be readily calculated and as their contributions are assembled over the entire REV, we get the following general relationships distinguishing isotropic from deviatoric components:

$$\sum^{N}\sum^{L}\int_{\Gamma_w^p} n_j n_i d\Gamma = \frac{\pi R^2}{3}(\omega\delta_{ij} + A_{ij}) \quad \text{and} \quad \sum^{N}\sum^{L}\int_{\Gamma_m} T_j n_i d\Gamma = \pi\gamma R\sin\alpha(\varpi\delta_{ij} + B_{ij}) \quad (6)$$

in which γ is the surface tension, A_{ij} and B_{ij} are deviatoric fabric tensors with respect to liquid bridge arrangements, whereas ω and ϖ are parameters corresponding to their isotropic part respectively.

Finally, substituting Eq. (6) into (5) and after rearranging leads to some form of equation that is recognizable as a generalized Bishop's equation, i.e.

$$\sigma'_{ij} = (\sigma_{ij} - u_a\delta_{ij}) + \chi(u_a - u_w)\delta_{ij} + \kappa\delta_{ij} + G_{ij} \quad (7)$$

where

$$\chi = \phi S_r + \frac{V^p}{4V}\omega;\ \kappa = \frac{\pi R^2}{V}\gamma\varpi\sin\alpha;\ G_{ij} = (u_a - u_w)\frac{V^p}{4V}A_{ij} + \frac{\pi R^2}{V}B_{ij}\gamma\sin\alpha \tag{8}$$

in which α is the filling angle attached to a water meniscus.

As discussed earlier, the current derivation inherently accounts for capillary forces that arise from the pressure difference between air and water, and surface tension force acting on the wetted surface on the surface of grains, i.e. the contractile skin. Therefore, referring to Eq. (8), the term κ refers to the isotropic part of the distribution of surface tension forces with its anisotropic (deviatoric) part represented by the second term of the tensor $\mathbf{G}$. It turns out that the latter term is of second order (since $\gamma R^2 / V$ is small) relative to the first term of $\mathbf{G}$ which describes the anisotropic distribution of capillary forces due to pressure difference between air and water. In other words, the effect of capillary forces in unsaturated soils is mostly controlled by the contribution due to air-water pressure difference. Accordingly, Eq. (7) can be simply written as

$$\sigma'_{ij} = (\sigma_{ij} - u_a\delta_{ij}) + \chi(u_a - u_w)\delta_{ij} + \bar{G}_{ij},\ \text{with}\ \bar{G}_{ij} = (u_a - u_w)\frac{V^p}{4V}A_{ij} \tag{9}$$

The micromechanically derived Eq. (7 or 9) shows that the effective stress in unsaturated soil is governed by not only two independent state variables: net normal stress $(\sigma_{ij} - u_a\delta_{ij})$ and matric suction $(u_a - u_w)$ including a material variable χ as in Bishop (1959 & 1961), but also by distributions of contractile skin surface tension and matric suction. Since the latter distribution can be anisotropic depending on liquid bridge spatial distribution and particle packing, effective stresses can also be affected by deviatoric loading. Turning to Eqs. (8 & 9), the derived effective stress parameter χ emerges as a function of degree of saturation as well as distributional quantities such as particle packing and number of meniscus per unit volume of REV. This will be investigated in the next section as to the capturing of the dependency of χ on the degree of saturation and other parameters.

3. EFFECTIVE STRESS COEFFICIENT FOR SIMPLE PACKINGS

The effective stress parameter χ, as a function of degree of water saturation S_r, is theoretically evaluated for two limiting cases, namely simple cubic (SC) simple packing (loosest state) and tetrahedral (TH) packing (densest state) in idealized soil comprised of mono-sized spherical particles. Figures 3a,b show simple cubic and tetrahedral packing geometries respectively with liquid bridges between each pair of particles. The water meniscus is assumed to be a surface of revolution with constant curvature and circular in section so as to form a toroid. In all subsequent calculations, a small wetting angle $(\theta = 0.5°)$ is chosen to maximize the filled volume of menisci and hence achieve high degrees of saturation in the pendular regime. The effect of contact angle could be explored, but this is not the focus of the paper.

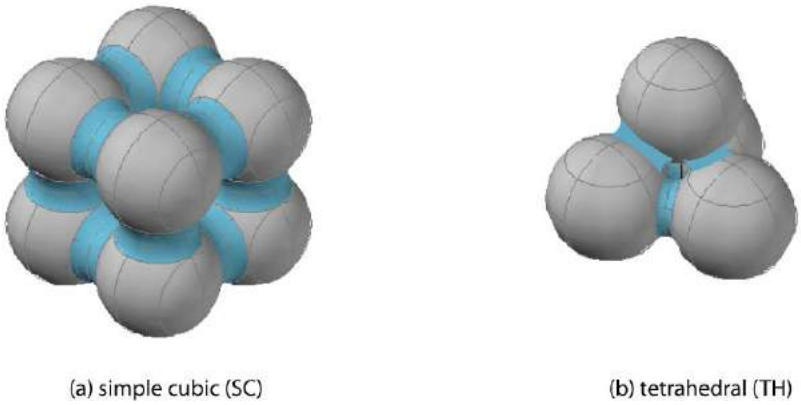

Figure 3. Loosest and densest packings with interconnecting water menisci

3.1 Calculation of χ

Referring back to Eqs. (5) & (6), the effective stress parameter χ emerges as the isotropic part of the integral giving the distribution of liquid bridges. For each meniscus connecting a pair of particles, we readily compute the fabric tensor as

$$F_{ij} = \int_{\Gamma_w^p} n_j n_i d\Gamma = \frac{\pi R^2}{3}\begin{bmatrix} \lambda_1 & 0 & 0 \\ 0 & \lambda_2 & 0 \\ 0 & 0 & \lambda_2 \end{bmatrix};\ \lambda_1 = 2(1-\cos^3\alpha) \text{ and } \lambda_2 = (1-\cos\alpha)^2(2+\cos\alpha) \quad (10)$$

According to Eq.(10), F_{ij} is a symmetric tensor with its first invariant, *trace*(**F**), being independent of the rotation of the coordinate system. Thus, referring to Eq. (6) and summing contributions of the fabric tensors over all liquid bridges on all particles, and then taking into account the isotropic part of the resultant tensor we finally find $\omega = 2L(\lambda_1 + 2\lambda_2)/3$ for different packings. Furthermore, noting Eq. (8), the explicit expression of the effective stress parameter for different packings of spherical particles can thus be derived, i.e.

$$\chi = \phi S_r + \frac{2\pi R^3}{9V} L(\lambda_1 + 2\lambda_2) = \phi S_r + (1-\phi)\frac{L}{6N}(\lambda_1 + 2\lambda_2) \quad (11)$$

which depends on the filling angle α, among others.

Using a toroidal meniscus geometry, the volume of the liquid bridge between two contacting spherical particles can be readily calculated based on α at equilibrium conditions during saturation, see Megias-Alguacil and Gauckler (2009). Therefore, χ as given in Eq. (11) can be readily calculated as a function of S_r. The maximum degree of saturation is reached whenever the filling angle reaches its maximum and the curvature of the meniscus decreases to a minimum so that the toroid degenerates into a cylinder. For example, considering a packing of two particles, this would give a value of $S_r = 28\%$.

Furthermore, the maximum degree of saturation that can be reached (in both SC and TH cases) without any of the liquid bridges overlapping can be readily calculated based on the maximum filling angle. Table 1. summarizes the results for the these packings.

Table 1. Expressions of χ for various packings

Packing	Porosity ϕ	$\mu = L / N$	χ	Maximum α	Maximum S_r
A pair of particles	0.4764	1/2=0.5	$\phi S_r + \frac{2\pi R^3}{9V}(\lambda_1 + 2\lambda_2)$	90°	28%
Tetrahedral (TH)	0.1285	6/4=1.5	$\phi S_r + 6\left(\frac{2\pi R^3}{9V}\right)(\lambda_1 + 2\lambda_2)$	30°	25%
Simple Cubic (SC)	0.4764	12/8=1.5	$\phi S_r + 12\left(\frac{2\pi R^3}{9V}\right)(\lambda_1 + 2\lambda_2)$	45°	17%

4. DISCUSSIONS AND CONCLUSIONS

Figure 4 shows the computed effective stress values as a function of degree of saturation with the line $\chi = S_r$ also plotted here as a reference. All simulations produce a curve that plots above the $\chi = S_r$ line showing a perceptible bend with a break in slope at some characteristic degree of saturation when the water meniscus reaches its maximum filling angle $\alpha_{\max}$. Subsequent filling would then proceed at fixed wetting points on the particle while the curvature of the meniscus (dotted lines in Fig. 2) continues to decrease towards reaching a larger water volume.

The simulations reveal that both packing and the number of liquid bridges influence the shape of the χ vs. S_r curve. For instance, the tetrahedral packing gives much lower χ values than those associated with the simple cubic packing for the same degree of saturation. Also, as one would expect for the same packing with decreasing number of liquid bridges, lower values of χ are predicted for the same degree of saturation because of a decrease in overall suction. We recall that overall suction depends on χ as is evident in Eq. (9) or in Bishop's original equation.

Experimental data for various types of soils are shown in Fig. 5 for comparisons with the numerical results of Fig. 4. It should be noted that the range of degree of saturation, examined in the numerical computations based on idealized mono-sized spheres, is well below 30% since the menisci are not allowed to merge to give full water saturation. The restriction of the packing to rather simple configurations with mono-sized spherical particles could plausibly account for the difference between experimental and computed data. This matter will require a more detailed investigation. At any rate, it is also not evident that the experimental data in the range of such small degree of saturation investigated (less than 30%) is accurate and reliable, given known difficulties in measuring low suction in soils.

The theory developed in this paper is being extended to poly-disperse and non-spherical particles, which should give more realistic χ vs. S_r curves. Given the limited experimental data for low to extremely low suctions on soils, discrete element simulations is an alternative means for exploring, among other things, the validity of the proposed theory. Another interesting outcome of this work arising from Eq. (9) is that the contribution of the matric suction to the effective stress is by no means isotropic, but is generally anisotropic as dictated by the spatial distribution of liquid bridges and fabric of the solid skeleton evolving during deformation history. It is thought that this issue becomes particularly relevant in the pendular regime where material instabilities in the form of skeleton collapse are common; see Scholtès et al. (2009). Indeed, discrete element numerical simulations may be of great value for

elucidating volume changes in unsaturated soils as a result of increase or decrease in water saturation and also for formulating constitutive models for unsaturated soils.

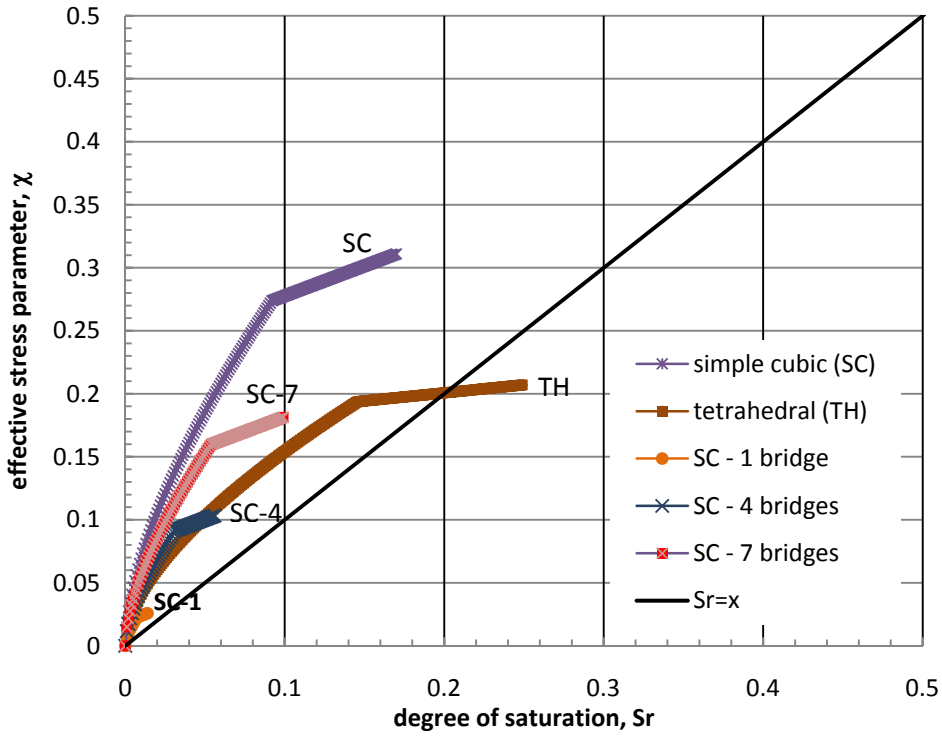

Figure 4. Computed relationships between degree of saturation *Sr* and effective stress parameter χ for various packings

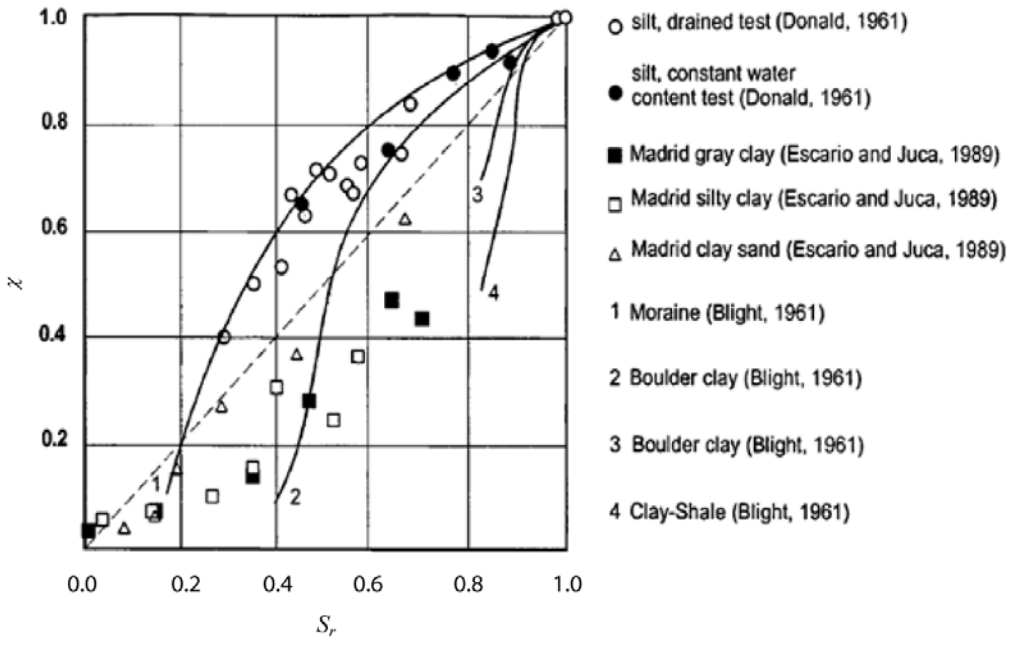

Figure 5. Relationship between degree of saturation *Sr* and effective stress parameter χ for various soils (from Ning & Griffiths, 2004)

ACKNOWLEDGEMENTS

The first two authors acknowledge the Natural Science and Engineering Research Council of Canada and the Computer Modelling Foundation for their financial support through a NSERC-CRD project. The third author is grateful for funding provided by the CEMAGREF in the form of a research visit fellowship to Calgary in the summer 2010.

REFERENCES

Bishop, A.W. (1959), “The principle of effective stress”. Teknisk Ukeblad, 106(39): 859-863.

Bishop, A.W. (1961), “Some aspects of effective stress in saturated and partially saturated soils”. Géotechnique, 13(3): 177-197.

Li, X.S. (2003). “Effective stress in unsaturated soil: a microstructural analysis”. Géotechnique, 53(2): 273–277.

Love, A. E. H. (1944). Theory of Elasticity, 4th. Ed. Dover, New York.

Megias-Alguacil, D. & Gauckler, L.J. (2009), “Capillary forces between two solid spheres linked by a concave liquid bridge: regions of existence and forces mapping”. J. AIChE, 55(5): 1103-1109.

Ning, L. & Griffiths, D.V. (2004), “Profiles of steady-state suction stress in unsaturated soils”. J. Geotech. Geoenviron, 130(10): 1063-1076.

Scholtès, L., Hicher, P.-Y., Nicot, F., Chareyre, B. and Darve, F. (2009), “On the capillary stress tensor in wet granular materials”. International Journal for Numerical and Analytical Methods in Geomechanics, 33: 1289–1313. doi: 10.1002/nag.767.

A KINEMATIC-HARDENING MODEL FOR LOCALIZED FAILURE WITH ANISOTROPIC FABRIC EFFECTS

J.G. Qian, M.S. Huang
Department of Geotechnical Engineering, Tongji University, Shanghai,200092,China

T.M. Su
Research Institute of Highway Ministry of Communications, Beijing, China

ABSTRACT: *Based on two-dimensional micromechanical analysis, the total stress is decomposed into two components, respectively related to the contact force anisotropy and the fabric anisotropy. In accordance with the standard kinematic hardening theory and microscopic investigations, the back stress tends to be interpreted as the contribution of the partial fabric anisotropy, reproduced only under non-proportional loading. The back stress can be determined with reference to the principal direction deviation between the rate of the fabric tensor and the reduced stress tensor. On the basis of the micro-macroscopic combined analysis, a mixed (isotropic-kinematic) hardening model is proposed. The model is attempted to reproduce non-coaxiality between stress and inelastic strain rate when non-proportional loading is involved. In the particular case of proportional loading, the fixed hardening law can be reduced into the classical isotropic hardening law. Finally, the proposed model is validated by examining the localized failure of granular materials. It has been found that the fabric anisotropy plays a significant role on the formation of shear band. A higher degree of fabric anisotropy can delay the initiation of the strain localization. The constitutive theory incorporating the fabric anisotropy may also give a reasonable prediction for the dependence of shear band inclination angle on initial confining pressure.*

1 INTRODUCTION

The localized failure accompanied by the appearance of shear band is commonly observed in the laboratory soil samples or natural soils when subjected to shear forces. Over the past decades, extensive experimental investigations have been conducted to understand the mechanism of localized failure of granular soils (e.g., Arthur et al. 1977; Desrues et al. 1985; Tatsuoka et al., 1990; Han & Drescher 1993; Oda, 1998). Although these experiments have showed that the localized failure may be affected by a number of factors, the most fundamental aspect should be inherent or induced material anisotropy. Theoretically, the formation of localized failure was seen as a kind of instability that can be attributed to the bifurcation behavior from a homogeneous deformation (Rudnicki&Rice, 1975). As a result, the theoretical prediction for localized failure is strongly dependent upon the pre-failure constitutive relationship. However, so far it still remains unclear how to rationally introduce anisotropic response into the well-established constitutive framework. This problem is arising due to extreme difficulty with experimental explorations on anisotropic yield mechanism, particularly under complex non-proportional loadings. Therefore, an element of speculation should be used to build up an anisotropic plasticity model within the framework of continuum mechanics.

As a step towards accounting for the microscopic behaviour of geomaterials, it has been recognized that in order to gain an insight into anisotropy of geomaterials, more attention should be paid to the properties of their microstructure. Numerous microscopic studies (Mehrabadi et al 1982; Oda et al, 1982; Rothenburg&Bathurst,1989) showed that the overall material response observed in the laboratory is a result of various micromechanical processes such as particle rolling and sliding in granular soils. Therefore, an ideal pre-localization model should capture all of these processes at the microscopic level. However, it is also extremely difficult to seek for a mathematical modeling technique to fulfill the microscopic description of the constitutive behavior. In addition, most of microscopic techniques are not well accepted yet since they are not as straightforward as conventional phenomenological approaches.

Departing from the two approaches mentioned above, some researchers attempt to resort to the third approach, namely macro-micromechanical couple theory, in which the anisotropic parameters was explicitly derived with respect to the evolution of anisotropic microstructure. For instance, Rothenburg & Bathurst(1989) presented an analytical relation between microscopic parameters and macroscopic deformation behaviors. In a similar manner, Nemat-Nasser (2000) proposed a kinematic plastic model for granular material with full considerations of the fabric anisotropy and its evolution.

The above considerations provide motivations for this work. Within the context of macro-micromechanical approach, this study proposes a mixed (isotropic-kinematic) hardening model to simulate the induced anisotropy. The present model is validated by capturing the localized failure behavior of geomaterials. The present work is limited to two dimensional cases, but can be generalized to three-dimensional cases with some additional efforts.

2 MICROMECHANICAL-BASED FORMULATION FOR STRESS

At the microscopic level, the stress tensor in a unit volume is associated with the boundary forces as follows (Landau & Lifshitz,1959)

$$\sigma_{ij} = \frac{1}{V}\sum_{S} f_i^b x_j^b \tag{1}$$

where f_i^b represents the loading applied to the point location, x_j^b, on the boundary S of sample.

For the overall particles within sample of a representative volume (V), the static equilibrium relationship between boundary and internal forces is satisfied:

$$\sum_{S} f_i^b x_j^b = \sum_{V} f_i \, l_j \tag{2}$$

where f_i is the internal contact force between two particles, and l_j is the contact vector that connects the centroids of two particles.

Eqs.(1) and (2) lead to the relationship among the stress, fabric and contact force as follows:

$$\sigma_{ij} = \frac{1}{V}\sum_{V} f_i \, l_j \tag{3}$$

Consider further that m_i is the unit vector of l_i , i.e.,

$$l_i = l m_i \tag{4}$$

where l denotes the length of l_i . Substitution Eqs.(3) and (4) into Eq.(5) yields:

$$\sigma_{ij} = \frac{1}{V} \sum_V l \left(f_i m_j \right) \tag{5}$$

Without loss of generality, two-dimensional problem is considered below. The contact force, f_i , can be decomposed into the normal and tangent components:

$$f_i = f^n n_i + f^t t_i \tag{6}$$

where f^n and f^t are the normal (n_i) and tangent (t_i) contact force components, respectively. Both of them are positive.

In general, m_i does not necessarily coincide with n_i for non-spherical particles. However, n_i and m_i may be considered to be the same and interchanged with each other on the average level (Rothenburg&Bathurst,1992; Nemat-Nasser,2000). Under this condition, Eq.(5) becomes

$$\sigma_{ij} = \frac{1}{V} \sum_V l \left(f^n m_i m_j + f^t t_i m_j \right) \tag{7}$$

The orientation distribution of the unit branch vector(m_i) is approximately described by the following density function:

$$E(\theta) = \frac{1}{2\pi} \left[1 + \omega \cos \left(2\theta - 2\theta_0 \right) \right] \tag{8}$$

where ω is the parameter that defines the magnitude of anisotropy and θ_0 represents the orientation with the maximum distribution density of branch vector, i.e., principal direction of the fabric.

Following Eq.(8), one may find

$$2 \int_0^{\pi} E(\theta) \mathrm{d}\theta = 1 \tag{9}$$

Using the assumption that the distribution of branch length is not correlated with the distribution of branch orientation, Eq.(7) can be rewritten in the continuous form:

$$\sigma_{ij} = 2N\bar{l} \int_0^{\pi} E(\theta) \left(f^n m_i m_j + f^t t_i m_j \right) \mathrm{d}\theta \tag{10}$$

where N is the number of contacts over a unit volume. $\bar{l}$ is the average spacing of the centroids of two contact particles.

Similar to the anisotropic distribution of m_i given by Eq.(8), the spatial distributions of f^n and f^t may be also approximated as the following direction-dependent functions (Rothenburg&Bathurst, 1992):

$$f^n = f_0\left[1+a_n\cos 2\left(\theta-\theta_f\right)\right] \tag{11a}$$

$$f^t = -f_0\, a_t \sin 2\left(\theta-\theta_f\right) \tag{11b}$$

where a_n and a_t are used to describe anisotropic degrees of f^n and f^t, respectively. θ_f is the principal direction of contact force anisotropy. f_0 is the average value of $f^n\left(\theta\right)$.

Eqs.(10)~(11) may lead to the hydrostatic pressure

$$p = \sigma_{ii}/2 = N\overline{l}\int_0^{\pi} E\left(\theta\right) f^n \mathrm{d}\theta \simeq N\overline{l}f_0 \tag{12}$$

Analogously, the deviatoric stress components can be evaluated as follows:

$$\sigma_{11}-\sigma_{22} = 2p\left[\left(a_n+a_t\right)\cos 2\theta_f + \omega\cos 2\theta_0\right] \tag{13a}$$

$$\sigma_{12} = p\left[\left(a_n+a_t\right)\sin 2\theta_f + \omega\sin 2\theta_0\right] \tag{13b}$$

Combining Eqs.(12) and (13), the stress can be decomposed into three parts:

$$\sigma_{ij} = p\delta_{ij} + s_{ij} = p\delta_{ij} + s_{ij}^f + s_{ij}^a \tag{14}$$

where s_{ij} is the devietoric part of σ_{ij}; s_{ij}^a is referred to the stress induced by the fabric anisotropy, and s_{ij}^f is referred to the difference between s_{ij} and s_{ij}^a, related to the contact force anisotropy.

As seen from Eq.(13), s_{ij}^a can be expressed as

$$\left[s_{ij}^a\right] = p\left[F_{ij}\right] \tag{15a}$$

with

$$\left[F_{ij}\right] = \omega\begin{bmatrix}\cos 2\theta_0 & \sin 2\theta_0\\ \sin 2\theta_0 & -\cos 2\theta_0\end{bmatrix} \tag{15b}$$

where F_{ij} is introduced to represent the fabric tensor, which is symmetric and traceless. Clearly, s_{ij}^a will vanish when ω=0.

Now let us recall the standard kinematic hardening plasticity, where the stress consists of three components, i.e.,

$$\sigma_{ij} = p\delta_{ij} + s_{ij} = p\delta_{ij} + \tau_{ij} + \alpha_{ij} \tag{16}$$

where τ_{ij} and α_{ij} represent the reduced (deviatoric) stress and the back stress, respectively.

Comparing (14) with (16), one may make the following assumption:

$$\alpha_{ij} = -pF_{ij} \tag{17}$$

where the minus sign implies that the major principal direction of back stress corresponds to the minor principal direction of fabric. It is due to the fact that a less density of contact normal may induce a larger dilatancy, and result in a positive shear resistance.

Eq.(17) implies that the back stress may be ascribed to the fabric anisotropy on microscopic level. It should be emphasized that the s_{ij}^a given by Eq.(15a) may be derived with respect to other different underlying microscopic mechanisms (e.g., Nemat-Nasser,2000; Guo&Stolle,2005). However, s_{ij}^a defined by Eq.(15a) can not be simply equivalent with the classical back stress, although its formulation sounds mathematically. This issue will be addressed below.

3 MICROMECHANICALLY-BASED MIXED HARDENING MODEL

Based on the above analysis, a simple two-dimensional model with a mixed (isotropic-kinematic) hardening law is proposed in this study. For this purpose, we attempt to revise the classical isotropic-hardening law into the mixed-hardening law by replacing the deviatoric stress with the deviatoric reduced stress. As an example, one of isotropic hardening models proposed by Pietruszczak(1995) will be reformulated here. The revised yield and plastic potential functions are given as follows:

$$F = \tau - \eta p = 0 \tag{18a}$$

$$Q = \tau + \eta_c p \ln\left(p / p_0\right) = \text{const} \tag{18b}$$

where $\tau = \sqrt{\tau_{ij}\tau_{ij}}/2$ with $\tau_{ij} = s_{ij} - \alpha_{ij}$, $p = \sigma_{ii}/2$, $i, j = 1,2$, p_0 is initial confining pressure. $\eta = \eta_f \dfrac{\varepsilon_s^{cp}}{A + \varepsilon_s^{cp}}$ with η_f =the failure stress ratio at an ideal state and A= material constant . η_c represents the value of η in the critical state, corresponding to the vanishing rate of plastic volumetric strain.

In order to complete the constitutive relations in terms of Eq.(18), it is necessary to quantify α_{ij} with respect to a general loading process. To this end, we restrict our attentions to Eq.(13) and consider the two loading cases: (1) In the case of proportional loading, the condition of θ_0=θ_{f} holds and consequently results in an isotropic hardening law (Rothenburg & Bathurst, 1989; Bardet, 1994). (2) In the case of non-proportional loading, plastic non-coaxiality can be observed and a kinematic hardening mechanism tends to be involved (Nemat-Nasser,2000; Jiang et al, 2007). With these considerations, the evolution of the back stress is here defined as

$$\dot{\alpha}_{ij} = -\left(\dot{s}_{ij}^a - \frac{\tau_{ij}\tau_{kl}}{\tau_{ab}\tau_{ab}}\dot{s}_{kl}^a\right) = -p\left(\dot{F}_{ij} - \frac{\tau_{ij}\tau_{kl}}{\tau_{ab}\tau_{ab}}\dot{F}_{kl}\right) \tag{19a}$$

where the fabric tends to change with the stress according to microscopic experimental observations, which also showed that $\dot{F}_{ij}$ appears to become proportional to $\dot{\eta}_{ij}$ (η_{ij}=s_{ij}/p) under proportional loading(Oda, 1972;1993). On the other hand, for a non-proportional loading case, it may be more reasonable to assume that the fabric changes with τ_{ij}. With these considerations, we attempt to define the change of the fabric by:

$$\dot{F}_{ij} = \omega_c \dot{\eta}_{ij}^{\tau} \tag{19b}$$

where $\eta_{ij}^{\tau} = \tau_{ij} / p$, and ω_c can be seen as a macroscopic material function that equally governs the degree of fabric anisotropy (ω).

By introducing (19b) into (19a), the back stress is quantified as

$$\dot{\alpha}_{ij} = -\omega_c \left(\dot{\tau}_{ij} - \frac{\tau_{ij}\tau_{kl}}{\tau_{ab}\tau_{ab}} \dot{\tau}_{kl} \right) \tag{19c}$$

Based on Eqs.(18) and (19), the elasto-plastic tangent stiffness tensor can be explicitly given as

$$\dot{\sigma}_{ij} = \dot{\tau}_{ij} + \dot{\alpha}_{ij} = \left(D^e_{ijkl} - \frac{D^e_{ijab} \frac{\partial Q}{\partial \tau_{ab}} \frac{\partial F}{\partial \tau_{cd}} D^e_{cdkl}}{H_p + \frac{\partial F}{\partial \tau_{ab}} D^e_{abcd} \frac{\partial Q}{\partial \tau_{cd}}} - \frac{\omega_c}{1-\omega_c} D^e_{ijmn} A_{mnkl} \right) \dot{\varepsilon}_{kl} \tag{20a}$$

with

$$A_{ijkl} = \frac{1}{2} \left(\delta_{ik}\delta_{jl} + \delta_{il}\delta_{jk} - \delta_{ij}\delta_{kl} - \frac{2\tau_{ij}\tau_{kl}}{\tau_{ab}\tau_{ab}} \right) \tag{20b}$$

where D^e_{ijkl} is the elastic tangent stiffness tensor; and H_p is the plastic hardening modulus.

The formulation of (19c) implies that the rate of back stress tensor ($\dot{\alpha}_{ij}$) is normal to the deviatoric reduced stress tensor (τ_{ij}). Consequently, the rate of back stress vanishes under proportional loading. In this particular case, the proposed isotropic-kinematic hardening law will be reduced into an isotropic hardening law. Figure 1 shows the yield mechanism in the deviatoric stress space when the proposed isotropic-kinematic hardening law is included. It implies that the tensor of plastic strain rate($\dot{e}^p_{ij}$) is not necessarily coaxial with s_{ij} under non-proportional loading . It is of great interest to note that the present description of back stress rate is less or more in line with the macroscopic tangent plasticity (Papamichos&Vardoulakis, 1995;Yu,2008).

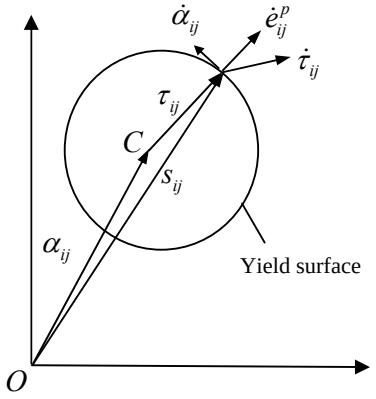

Fig 1. Yield mechanism with the proposed isotropic-kinematic hardening

APPLICATION FOR LOCALIZATION ANALYSIS

A series of biaxial tests for the localized failure of dry sands were carried out by Han & Drescher (1993). The present isotropic-kinematic model will used to predict the experimental observations. The degree of fabric anisotropy (ω_c), for simplicity, is selected to be a material constant in this analysis. The criterion for the localized failure may be referred to Qian et al (2008). All other model parameters are given as: Elasticity modulus =175MPa and Poisson's ratio=0.1667, and plastic parameters η_f=0.66, η_c =0.36 and A=0.0001.

Figure 2 has showed a profound effect of fabric anisotropy on the bifurcation state. It is evident that the localized failure behaviors strongly depend on the degree of anisotropy. In general, an isotropic model may severely underestimate the strength. For the fixed hardening model, as the degree of anisotropy is increasing, the discrepancy between theoretical predictions and experimental observations become negligible.

Figure 3 further presents the inclination angle of shear band (θ_s) as affected by the fabric anisotropy. The experiments show that the inclination angle of shear band decreases as increasing initial confining pressure. Clearly, the isotropic-hardening model fails to simulate this trend. The theoretical predictions can be improved with fabric anisotropy incorporated. As the increasing degree of anisotropy, the theoretical trend tends to change and becomes close to the experimental observations.

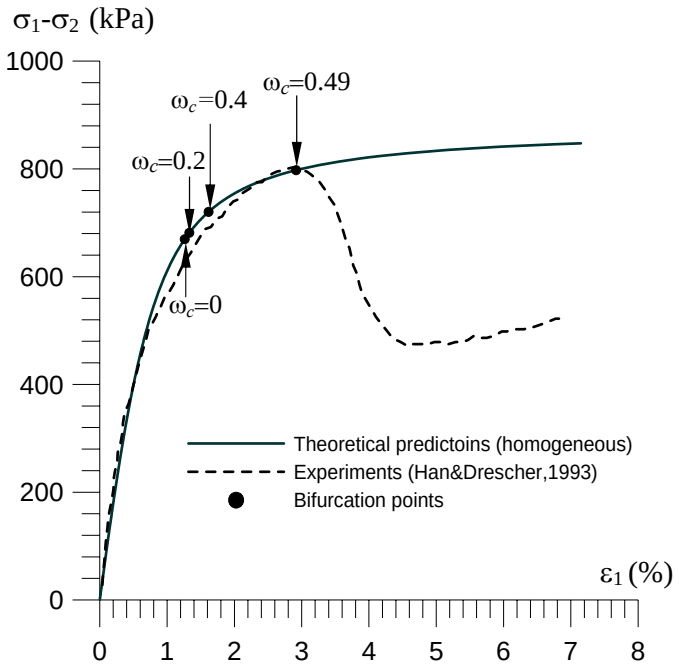

Fig. 2. Effect of fabric anisotropy on localized failure

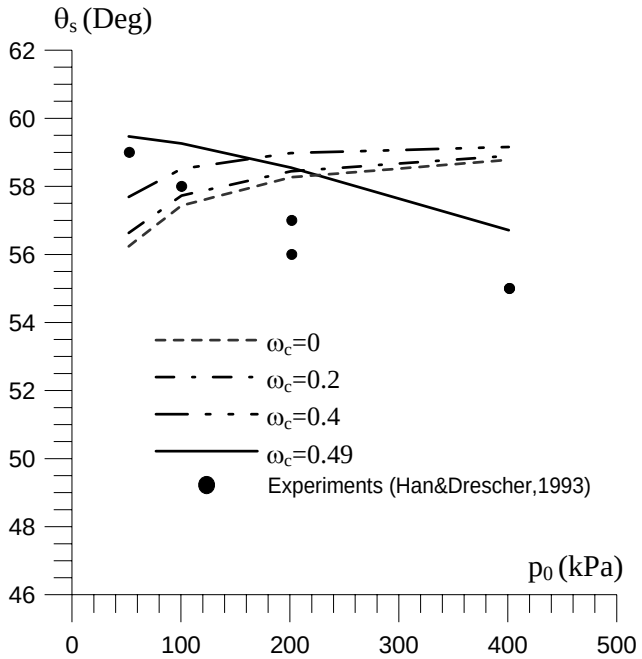

Fig. 3. Effect of fabric anisotropy on the inclination angle of shear band

4 SUMMARY AND CONCLUSIONS

Departing from classical continuum theory as well as discrete element method (DEM), this study has proposed a simple micromechanically-based constitutive framework for the description of induced anisotropy of granular materials. With considerations of micromechanics, the deviatoric stress tends to be contributed by the contact force anisotropy as well as the fabric anisotropy. The stress component related to fabric anisotropy may result in both isotropic-hardening and kinematic-hardening during a generalized loading process. Its component associated with the tangential loading effect appears to coincide with the back stress in the context of the standard kinematic hardening theory. The back stress vanishes under a simple proportional loading and corresponds to the classical isotropic hardening.

In order to validate the framework of the proposed model, the model is used to capture the localized failure behaviors. The proposed mixed-hardening model is capable to simulate the features of bifurcation as experimental observations. It is found that the onset of localized failure strongly depends on the degree of fabric anisotropy. A higher degree of fabric anisotropy may delay the bifurcation state. The fabric anisotropy also has a significant affect on the inclination angle of shear band.

In closing, it should be pointed out that this work aims to propose a simple micro-macroscopic coupling approach for the description of the induced anisotropy. The validation of the proposed model is also limited to the analysis of localized failure. With respect to other anisotropic behaviors of geomaterials, much work should be done in the future.

ACKNOWLEDGEMENT

The work reported in this paper was supported by National Natural Science Foundation of China (Grants No. 10972159 and 50825803) and Natural Science Foundation of Shanghai, China (Grant No. 08ZR1420100).

REFERENCES

Arthur, J.R.F., Chua, K. S.&Dunstan, T.(1977), "Induced anisotropy in a sand". Geotechnique, Vol.27(1),613–622.

Bardet J. P.(1994), "Numerical simulations of the incremental responses of idealized granular materials". Int. J. Plasticity, Vol.10,879–908

Desrues, J., Lanier, J.& Stutz, P.(1985), "Localization of the deformation in tests on sand samples". Engineering Fracture Mechanics, Vol.21,909–921.

Guo, P. & Stolle, D.F.E. (2005), "On the failure of granular materials with fabric effects". Soils and Foundations, Vol.45(4), 1-12.

Han, C., &Drescher, A.(1993), "Shear bands in biaxial tests on dry coarse sand". Soils and Foundations, Vol.33(1),118–132.

Jiang, M.J., Harris, D.&Yu, H S (2005), "Kinematic models for non-coaxial granular materials: Part II, evaluation". International Journal for Numerical Analytical Methods in Geomechanics, Vol.29(7),663-689.

Landau, L.D., Lifshitz, E.M.(1959), Statistical physics: course of theoretical physics 5, Pergamon Press, Oxford.

Mehrabadi, M.M., Nemat-Nasser, S. &Oda M (1982), "On Statistical description of stress and fabric in granular materials". Int. J. Num. Anal. Methods in Geomechanics, Vol.6, 95-108.

Nemat-Nasser, S. (2000), "A micromechanically-based constitutive model for frictional deformation of granular materials". J. Mech.Phys. Solids, Vol. 48,1541-1563

Oda, M. (1972), "The mechanism of fabric changes during compressional deformation of sand". Soils and Foundations, Vol. 12(2), 1-18.

Oda, M., Konishi, J., Nemat-Nasser, S.(1982), "Experimental micromechanical evaluation of strength of granular materials: effects of particle rolling". Mech. Mat., Vol.1 (4), 269-283.

Oda, M.(1993), "Inherent and induced anisotropy in plasticity theory of granular soils". Mech. Mat., Vol.16, 35-45.

Oda, M., Kazama,H &Konishi, J.(1998). "Effects of induced anisotropy on the development of shear bands in granular materials". Mechanics of Materials, Vol.28,103–111.

Papamichos, E.,&Vardoulakis, I.(1995), "Shear band formation in sand according to noncoaxial plasticity model". Geotechnique, Vol.45(4),649-661.

Pietruszczak, S.(1995), "On the undrained response of granular soil involving localized deformation". Journal of Engineering Mechanics , ASCE , Vol.114:1292-1298.

Qian, J. G.,Yang, J. & Huang, M. S.(2008) . "Three-dimensional non-coaxial plasticity modeling of shear band formation in geomaterials". Journal of Engineering Mechanics,ASCE, Vol.34(4), 322-329

Rothenburg, L.& Bathurst, R.J.(1989), "Analytical study of induced anisotropy in idealized granular materials". Geotechnique, Vol.39(4),601-614.

Rudnicki, J. W. & Rice, J. R. (1975). "Conditions for the localization of the deformation in pressure sensitive dilatant materials". J. Mech.Phys. Solids, Vol. 23, 371–394.

Tatsuoka, F., Nakamura, S., Huang, C. C. & Tani, K.(1990), "Strength anisotropy and shear band direction in plane strain tests on sand". Soils and Foundations, Vol. 30(1),35–54.

Yu, H.S.(2008),"Non-Coaxial Theories of Plasticity for Granular Materials", The 12th International Conference of International Association for Computer Methods and Advances in Geomechanics (IACMAG),Goa, India.

A CRITICAL PLANE APPROACH TO ANISOTROPIC STRENGTH OF ROCKS

R. Wan & M. Pouragha
Department of Civil Engineering, University of Calgary, Calgary, AB, Canada

F. Nicot
Cemagref, Grenoble, France

ABSTRACT: *The paper is concerned with the derivation of failure criteria for anisotropic materials through a simple extension of the Mohr Coulomb failure criterion and embracing the critical plane concept. We revisit the classic problem of determining the macroscopic strength of a rock specimen with an initial structural anisotropy in relation to directions of externally applied principal stresses. Macroscopic friction angle and cohesion, as two main elements of material strength, are essentially made to be direction dependent following a distribution that depends on only 3 additional parameters describing: (1) the ratio of the maximum to minimum strength, (2) a shape parameter for the transition rate from maximum to minimum values, and (3) the non-coaxiality between principal stress and strength directions. The search for the critical plane is interpreted graphically showing the existence of multiple solutions and the switching of resulting modes for the same externally applied stress. One of the essential benefits of the proposed model is the capture of material characteristics such as failure plane orientation and macroscopic strength over a large range of stress conditions using only a few parameters that have physical meaning and which can be easily determined experimentally. This is demonstrated through various examples involving experimental results. Finally, a micromechanical model and the developed critical plane model are juxtaposed to show the same trend in results.*

1 INTRODUCTION

Geomaterials such as soils and rocks exhibit anisotropic behaviour (strength) as a result of their microstructure such as particle arrangement, micro cracks, and bedding (weakness) planes, among others. During the past several years, a plethora of approaches to derive yield or failure criteria have been proposed in order to address material strength anisotropy. For instance, Hill (1950) presented a failure criterion for metals based on a quadratic function of stresses expressed in axes of anisotropy, which was later extended to rocks by Pariseau (1972). Other treatments are based on the critical plane concept whereby a potential failure plane is searched such that certain failure conditions based on anisotropy are met; see e.g. Jaeger (1960) and McLamore & Gray (1967). Unlike the latter, there are also other criteria that are purely empirical in nature such as in Ramamurthy et al. (1988) and Garagon & Can (2010) with fitting parameters that often do not have any physical meaning.

In more modern incarnations of the critical plane approach, Pietruszczak and Mróz (2001) apply directional strength variation with the relative orientation of stress and anisotropy axes to work out an anisotropic failure criterion involving a fabric tensor. In this paper, we follow the same above-mentioned approach except that we limit our study to a small number of

model parameters through a simple extension of Mohr-Coulomb failure criterion with direction dependent strength. Attention is focused on the physical interpretation of failure modes in the anisotropic case as to whether failure occurs near a plane of weakness (anisotropy) or elsewhere. Two sets of available experimental data have been used to verify the proposed model. The latter can be easily implemented into constitutive models to provide more accurate predictions on the behaviour of sedimentary rocks in stability problems.

Finally, the validity of strength distribution concept has been examined through a micro-scale model in which the strength in a particular orientation has been related to the density of contacts between particles along the same direction. It has been shown that if the density of contacts is made to vary with the same proposed macro-scale distribution function, the results will exhibit acceptable consistency.

2 BASICS OF THE MODEL

The present work considers the simple 2-D case where failure is governed by Mohr-Coulomb theory with both friction (φ) and cohesion (c) as material strengths defined through a failure function (criterion), i.e.

$$F_f = \tau - \sigma_n \tan\varphi - c = 0 \tag{1}$$

in which τ and σ_n are the shear stress and the normal stress acting on a given plane as a result of applied external principal stresses (σ_1 and σ_3) such as in a biaxial test. Positive stresses here mean compression. In the anisotropic case, for every plane oriented at an angle θ with the direction σ_3 and corresponding strength parameters k_θ and c_θ, the failure function is

$$\begin{aligned} F_f &= \tau - \sigma_n k_\theta - c_\theta = 0 \\ \sigma_n &= \tfrac{1}{2}(\sigma_1 + \sigma_3) + \tfrac{1}{2}(\sigma_1 - \sigma_3)\cos 2\theta \\ \tau &= \tfrac{1}{2}(\sigma_1 - \sigma_3)\sin 2\theta \end{aligned} \tag{2}$$

Against the above backdrop, k_θ and c_θ are deemed to follow a certain distribution in space according to the following trigonometric functions:

$$k_\theta = \tan\varphi_\theta = k_0\left[1 + \omega\cos 2(\theta-\beta) + \frac{\omega\lambda\sin^2 2(\theta-\beta)}{1+\lambda\cos 2(\theta-\beta)}\right] \tag{3a}$$

$$c_\theta = c_0\left[1 + \omega_c\cos 2(\theta-\beta) + \frac{\omega_c\lambda_c\sin^2 2(\theta-\beta)}{1+\lambda_c\cos 2(\theta-\beta)}\right] \tag{3b}$$

in which β represents the angle between the major strength orientation and the direction of the minor principal stress, σ_3; ω and ω_c are related to anisotropy ratios of maximum to minimum friction and cohesion respectively; λ and λ_c are shape factors controlling the transition rate from maximum to minimum friction and cohesion respectively; and k_0 and c_0 refer to the mean friction and cohesion respectively.

Figure 1 illustrates the 'peanut' shape of the proposed strength distribution such that the maximum and minimum values of strength occur at $\theta = \beta$ and $\theta = \beta + \pi/2$ respectively.

Such strength distribution could be experimentally determined in a direct shear box test in which the imposed failure plane is varied and the corresponding strength subsequently measured.

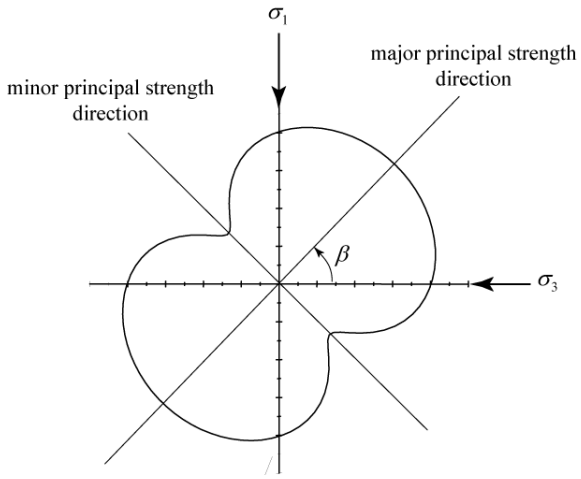

Figure 1. Schematic representation of strength distribution with respect to applied principal stresses

Figure 2 further illustrates the effect of parameter λ on the shape of the strength distribution for $\beta = 30^{\circ}$. For λ equal to 0.999 approaching 1, the distribution here shows a sharp drop in strength for a particular orientation (here $\theta = 120°$), whereas for other directions the strength is essentially the same. Such a distribution mimics a plane of weakness which was first addressed by Jaeger (1960), but in a more primitive manner. By contrast, for smaller values of λ, the spatial strength distribution becomes smoother and resembles the failure criterion proposed by McLamore & Gray (1967) where failure parameters were empirically related to the angle β, the principal strength direction, using experimental data from a biaxial test. It is worth mentioning that results of such tests require careful interpretation in order to construct the spatial strength distribution.

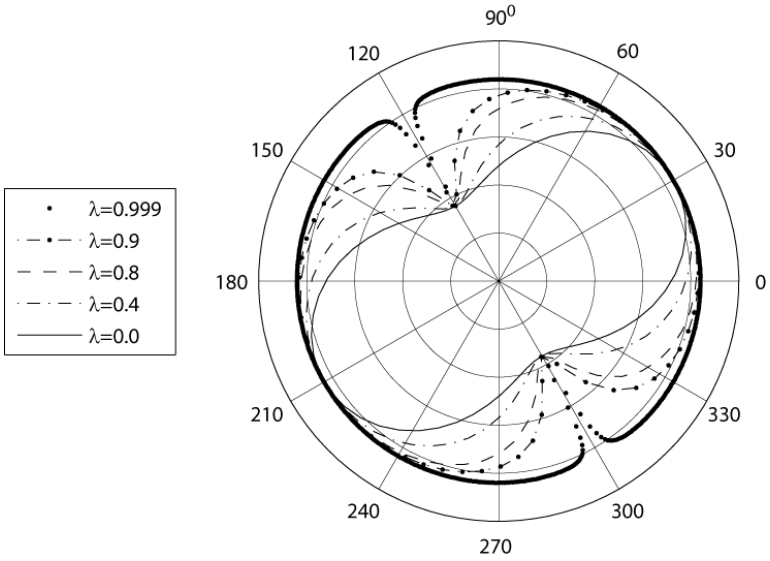

Figure 2. Effect of λ on strength distribution shape

3 SOLUTION PROCEDURE

The failure analysis of the prototype problem referring to a sample subjected to principal stresses σ_1 and σ_3 entails finding the orientation, θ_f, of the critical (failure) plane for which the failure criterion F_f (Eqs. 2&3) is satisfied with the smallest external stress ratio (σ_1/σ_3). Since the failure criterion and local stresses (τ, σ_n) are both direction dependent as described by $F_f(\theta)$ and $S(\theta)$ respectively, the above-mentioned failure condition is met whenever $d(F_f - S)/d\theta = 0$. In other words, we find the plane θ for which the failure criterion is optimized under externally applied biaxial stresses, i.e. the conditional derivative $d(F_f \mid S)/d\theta = 0$. As such, failure is not necessarily interpreted as a tangency condition between the Mohr circle and the failure criterion in the traditional (τ vs. σ_n) plot where the spatial direction θ does appear explicitly. Therefore, we propose a new graphical representation of the search for failure in the anisotropic case.

3.1 Polar representation of failure

Let us consider a non-cohesive material $(c = 0)$ for simplicity to illustrate a polar representation of failure. Rearranging Eq. (2), we get

$$\left(\frac{\tau}{\sigma_n}\right)_\theta = \frac{\sin 2\theta}{\left(\frac{R+1}{R-1}\right) + \cos 2\theta} = k_\theta;\ R = \sigma_1/\sigma_3 \tag{4}$$

such that the search for the critical failure plane simply reduces to finding when the stress ratio (τ/σ_n) coincides with the strength k_θ in a polar plot.

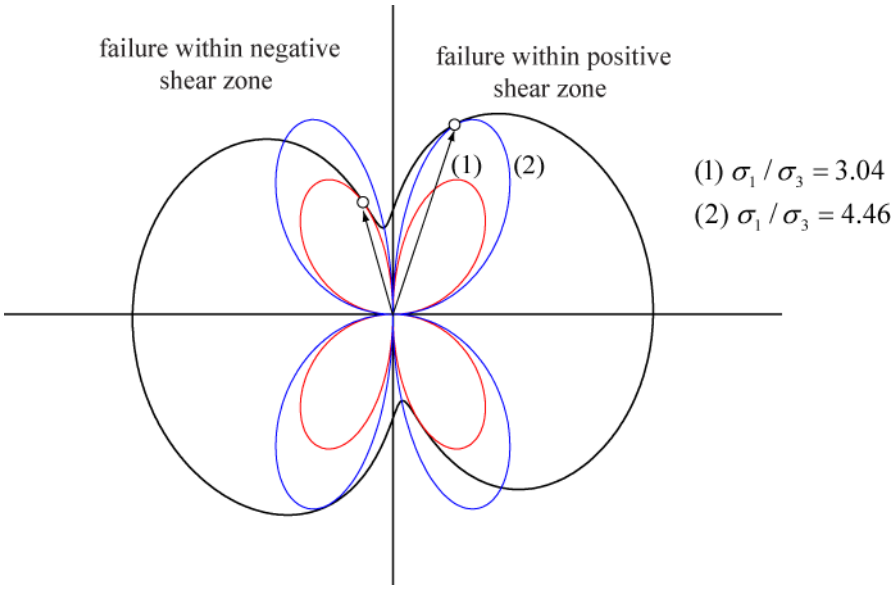

Figure 3. Polar representation of failure conditions for an anisotropic case (φ_{max}=π/4, c=0, ω=0.5, λ=0.8, and β=6°)

Figure 3 illustrates an example of the search for failure conditions for a given strength distribution (with $0 < \beta < \pi/2$) where two mathematically possible solutions occur as plausible failure plane orientations. These are not conjugate solutions as in the isotropic case, given that they occur at distinct externally applied stress (ratio) levels. Here, the solution with

the smaller stress ratio is chosen, this being first encountered during loading history. It turns out that the chosen solution refers to a failure plane whose orientation θ_f gives a negative shear stress whereby $\pi/2 < \theta_f < \pi$.

Figures 4 and 5 show the evolution of the two numerical solutions expressed in terms of normalized deviatoric stress and failure plane orientation respectively for various directions β of major strength. As mentioned earlier, the solution with the lower stress ratio (segments A & C) is retained, which necessarily leads to symmetry in the overall result over the range $0 \le \beta \le \pi$. To effectively interpret general trends of failure as a function of β, the numerical results in Figs. 4 & 5 are next cross-referenced with those in Fig. 6 which shows graphical representations of the failure conditions at selected values of β.

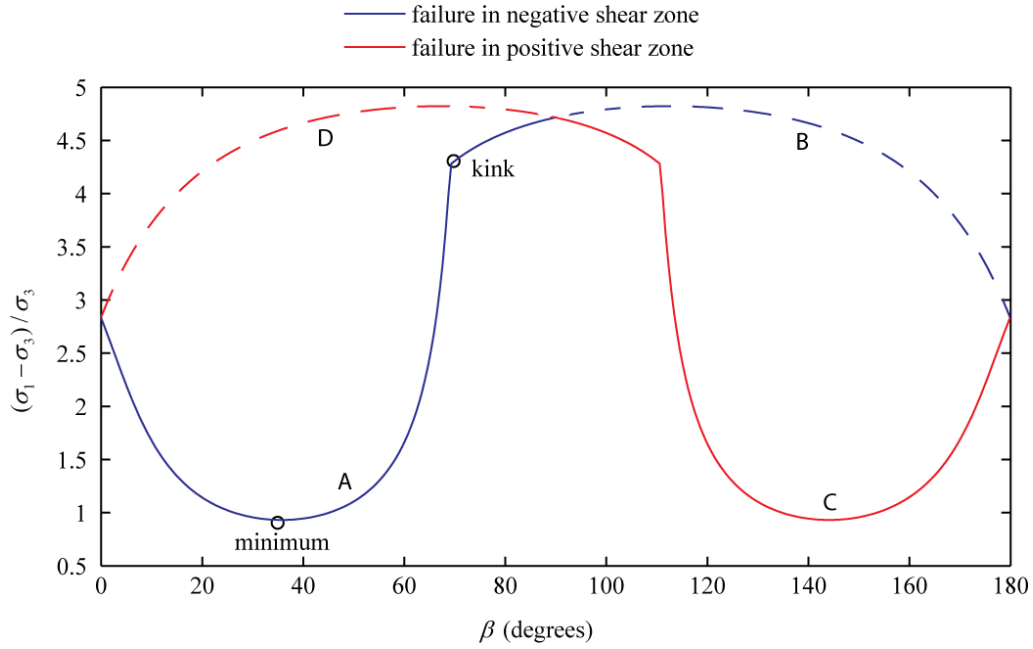

Figure 4. Deviatoric stress ratio at failure in negative and positive shear zone versus β for an anisotropic example (φ_{max}=π/4, c=0, ω=0.5, λ=0.8, and β=6°)

Contrary to expectations, the macroscopic strength variation with major anisotropy axes as deduced from Fig. 4 is not smooth, but presents a perceptible kink at a characteristic value of $\beta = 65.1^\circ$. This kink corresponds to a sharp discontinuity in computed failure plane orientation, indicating a switching of failure mode from failure occurring near a plane of weakness to failure within the intact material. This is also immediately seen in Fig. 6d where two equally possible failure plane orientations occur as the stress ratio rosette tangents the strength envelope at two locations: one near the direction of minimum strength (weakness plane) and the other in a direction of much higher strength (intact material).

In general, as β increases from zero, the direction of minimum strength tends toward the location of maximum stress ratio on the rosette (Figs. 6a,b), which accordingly causes the failure stress ratio to decrease until it reaches a minimum value at which both the failure plane and the direction of minimum strength are coaxial. This occurs at $\beta = 34.4^\circ$ in Fig. 6b, in fact, the only time when the failure plane orientation can be defined as $\theta_f = \pi/4 + \varphi_{\min}/2 = \beta + \pi/2$. At higher values of β there is a switch from failure near a plane of weakness to one in the intact material as marked by the sharp drop in failure plane orientation (Figs. 5 & 6d) and at the kink in Fig. 4.

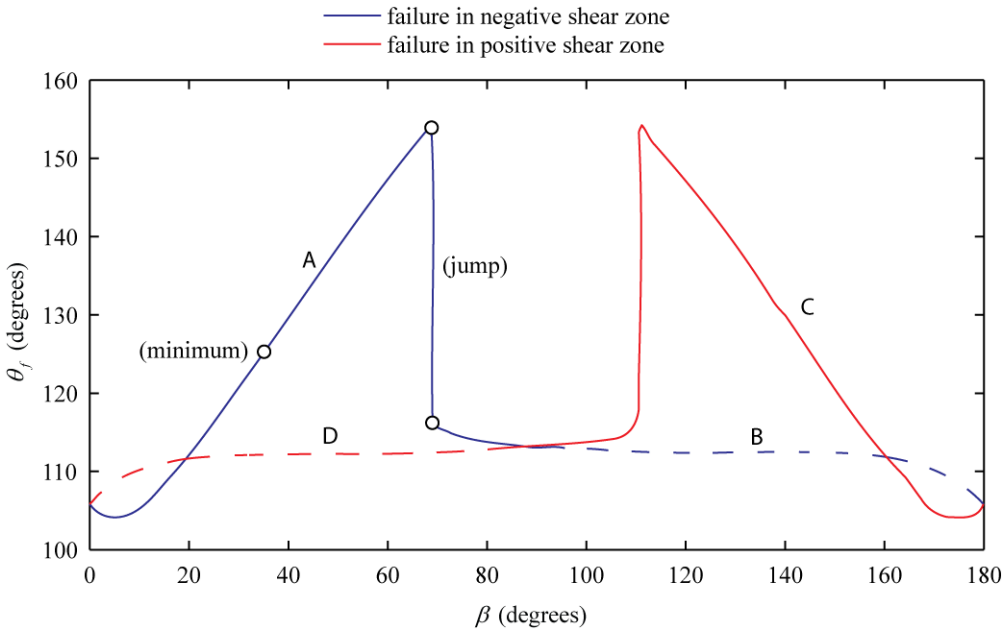

Figure 5. Variation of failure plane angle at failure in negative and positive shear zones versus β for an anisotropic example (φ_{max}=π/4, c=0, ω=0.5, λ=0.8, and β=6°)

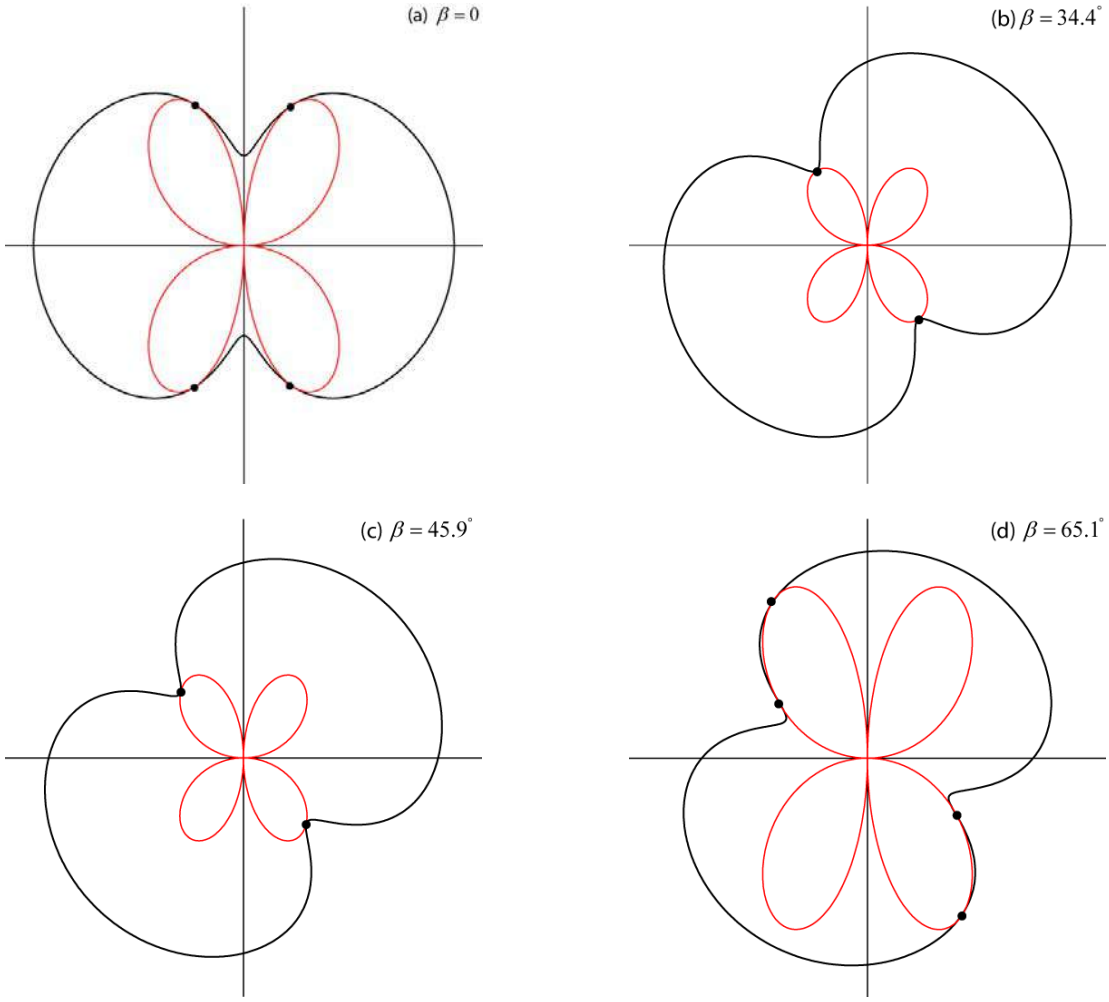

Figure 6. Failure conditions illustrated using 2D visualization for an anisotropic case: φ_{max}=π/4, c=0, ω=0.5, λ=0.8, and; a) β=0, b) β=34.4°, c) β=45.9°, d) β=65.1°

Further exploration of the model indicates that the transition rate with respect to β from failure near the weakness plane to one in the intact material is controlled by λ which describes both the curvature and shape of the strength distribution. Indeed, experimental data (e.g. Liao & Hsieh, 1999) show that there may not always be a switching of failure modes as captured remarkably by the model for small values of λ, see Fig. 7. Also, note that as λ approaches 1, the switching of modes becomes evident as characterized by a 'shoulder' where the strength reverts to its intact value.

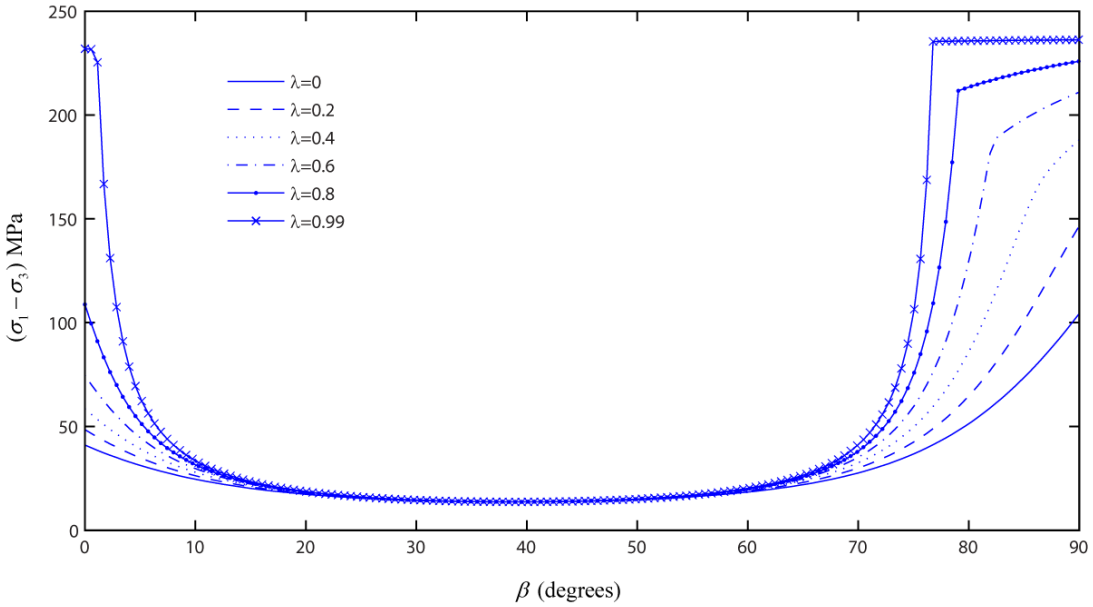

Figure 7. Effect of λ on deviatoric stress at failure

4 NUMERICAL RESULTS

The proposed model has been calibrated for two sets of experimental results available for two different sedimentary rocks, i.e. Martinsburg slate (Donath, 1961) and argillite (Liao & Hsieh, 1999).

The model parameters have been determined following a systematic procedure in which salient points in the experimental curves are examined. As previously discussed, the minimum macroscopic (sample) strength occurs at a characteristic β whereby failure occurs along the direction of lowest strength; hence the minimum friction angle can be deduced. The evolution of the above-mentioned minimum strength with confining stress in turn allows us to calculate the minimum cohesion.

Furthermore, if there is a 'shoulder' which refers to strength in the intact material, both the maximum friction angle and cohesion can be easily determined. If there is no apparent 'shoulder', then the maximum friction and cohesion are found following an iterative process whereby deviations between experimental data and numerical simulations are minimized at $\beta = 90^{\circ}$. Finally, λ is found by calibrating experimental data with simulations at $\beta = 0$ where the effect of λ on the macroscopic strength is quite pronounced as shown in Fig. 7. This value of λ then enters into a recursive calculation to reach a better estimation of maximum friction and cohesion in the case there is no 'shoulder'. Model parameters for chosen sets of data are presented in Table 1.

Table 1. Calibrated model parameters for experimental data sets

	k_0	ω	c_0	ω_c	$\lambda = \lambda_c$
Donath (1961)	0.61	0.316	24.26	0.796	0.90
Liao & Hsieh (1999)	0.39	0.095	7.43	0.472	0.65

The overall predictions as seen in Figure 8 for the two data sets are indeed very good considering that the calibration of the model was performed using only few characteristics points of the experimental results. There are two aspects that need to be considered during the simulations: one refers to the capture of confining stress effect and the other is the characteristic variation of macroscopic strength as a function of β for a particular confining stress. Both aspects have been successfully fulfilled since different strength characteristics related to the type of rock have been correctly captured.

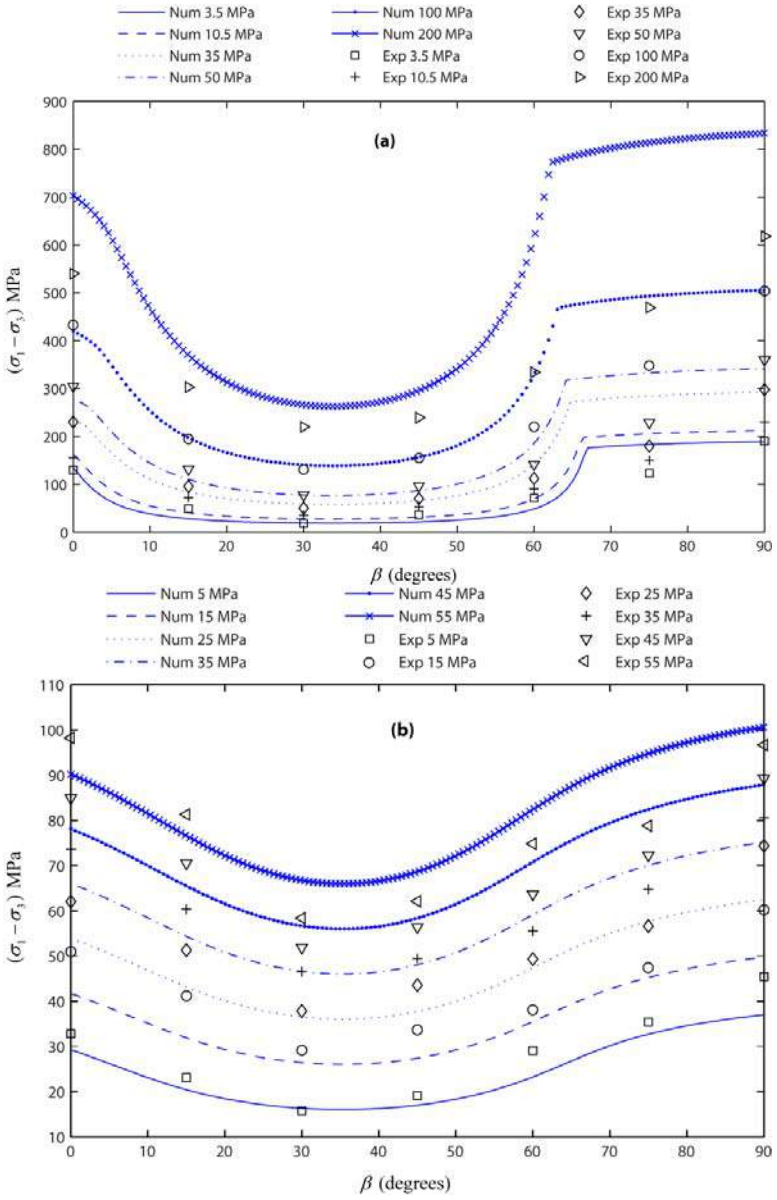

Figure 8. Comparisons between model prediction and experimental data from (a) Donath (1961) and (b) Liao & Hsieh (1999)

However, in Fig. 8a, the model over-predicts the strength for a confining pressure of 200 MPa. This is because a linear Mohr-Coulomb failure criterion was used which is not able to capture the decrease in strength (friction) at such a high confining pressure.

5 DISCUSSION AND CONCLUSION

The modelling approach followed in this work hinges on the idea of introducing directionally dependent strength parameters (friction angle and cohesion) into Mohr-Coulomb failure criterion to capture the anisotropic strength of structured materials. While this approach is at the macroscopic level, the counterpart reasoning at the microscopic level is one which introduces the notion of particle contact density varying along directions in space with yet a unique strength parameter (friction) at the particle level. This has been worked out by Nicot and Darve (2011) in their micro-directional model which considers particle contact density at the meso-level to enrich the micro level kinematics. As such, it is the multiplicity of micro/meso interactions described by simple physics that give way to complex macro properties such as anisotropy in macroscopic strength as those discussed in this paper.

The duality between the two approaches can be verified in Fig. 9 where the two models are juxtaposed for qualitative comparison only. In the micro-directional model, the same macroscopic distribution as that introduced to describe the friction angle variation (Eq. 3a) was used to describe the statistics of meso-scale particle contact density, while the inter-particle friction was kept constant. This is based on the assumption that particle contact density correlates directly with macroscopic friction angle. The trends of the two models are generally similar, except that in the micro-directional model, the strength (macroscopic friction) does not go through a minimum value as captured by the macro model and experiments. This discrepancy is due to the meso-structure (particles arranged in an open hexagonal packing) used in the micro-directional model that cannot express distortion that would give rise to failure along a plane of weakness as shown in the macro-model earlier in the paper. The micro-directional model describes the material as a directional (not a spatial) distribution of hexagonal meso-structures, and cannot therefore give way to any geometric localization. This is by no means a shortcoming for the micro-directional model as the meso-structure can be further enriched to encompass other local failure mechanisms.

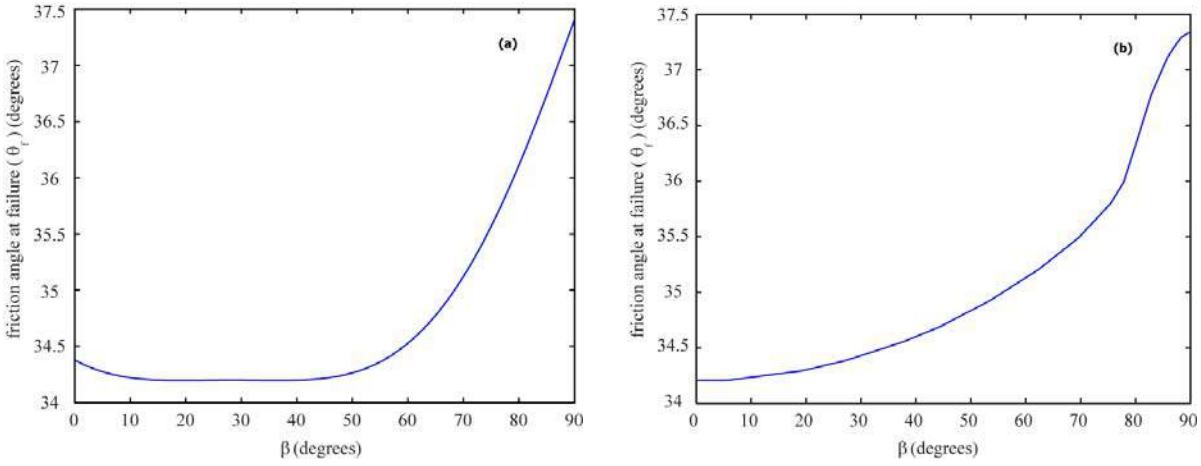

Figure 9. Comparison between (a) proposed macro model with (b) micro-directional model

In conclusion, the above discussion seems to validate (although not formally) the idea of enriching simple models like Mohr-Coulomb with directionally dependent strength

parameters to capture experimentally observed anisotropic characteristics of structured materials. Although the work presented in this paper was limited to 2D stress states, the extension to 3D stress configuration can be readily carried out and thereafter integrated into elasto-plasticity framework to arrive at a tangential constitutive tensor with embedded anisotropy. It would be then of interest to explore under what anisotropic conditions would the constitutive tensor be prone to well-known instability phenomena such as localization and diffuse failure.

6 ACKNOWLEDGEMENTS

The first two authors acknowledge the Natural Science and Engineering Research Council of Canada and the Computer Modelling Foundation for their financial support through a NSERC-CRD project. The third author is grateful for funding provided by the CEMAGREF in the form of a research visit fellowship to Calgary in the summer 2010.

REFERENCES

Donath, F. A. (1961), “Experimental study of shear failure in anisotropic rocks”. Geol. Soc. Am. Bull. , 72, 985-990.

Garagon, M., & Can, T. (2010), “Predicting the strength anisotropy in uniaxial compression of some laminated sandstones using multivariate regression analysis”. Mater. Struct. , 43, 509-517.

Hill, R. (1950), The Mathematical Theory of Plasticity, Oxford, Oxford University Press.

Jaeger, J. (1960), “Shear failure of anisotropic rocks”. Geol. Mag. , 97, 65-72.

Liao, J. J., & Hsieh, H. Y. (1999), “Triaxial residual strength of an anisotropric rock”. In Rock Mechanics for Industry, Amadei, Kranz, Scott, & Smeallie (Eds.), Totterdam: Balkema.

McLamore, R., & Gray, K. E. (1967), “The mechanical behavior of anisotropic sedimentary rocks”. J. Eng. Ind.,Trans. of the A.S.M.E. , 89, 62-67.

Nicot, F., and Darve, F. (2011), “The H-microdirectional model: accounting for a mesoscopic scale”. Mech. Mater., *submitted.*

Pariseau, W. G. (1972), “Plasticity theory for anisotropic rocks and soils”. Proceedings of 10th Symposium on Rock Mechanics, 1, 267. AIME.

Pietruszczak S, Mróz Z (2001), “Formulation of failure criteria for anisotropic frictional materials”. Int. J. Num. Anal. Meth. Geomech., 25, 509-524

Ramamurthy, T., Rao, G. V., & Singh, J. A. (1988), “A strength criterion for anisotropic rocks” Proceedings of 5th Australia, New Zealand Conference on Geomechanics, Sydney, 1, 253.

DEVELOPMENT OF AN EXTENDED DRUCKER-PRAGER HARDENING MODEL FOR CROSS-ANISOTROPY OF SOFT ROCKS

B. François
Building, Architecture & Town Planning Department (BATir), Université Libre de Bruxelles, Belgium

F. Collin, A. Dizier
FRS-FNRS – Fonds National de la Recherche Scientifique, Bruxelles, Belgium

ArGEnCo Department, Université de Liège, Belgium

R. Charlier
ArGEnCo Department, Université de Liège, Belgium

ABSTRACT: *The mechanical behaviour of natural geomaterials is often anisotropic. Sedimentary rocks usually show a limited form of anisotropy, called cross-anisotropy. The behaviour is isotropic in the plane of bedding and the unique direction of anisotropy is perpendicular to bedding. This paper presents an original constitutive model based on a Drucker-Prager elasto-plastic framework that has been adapted to consider cross-anisotropic elasticity as well as an anisotropic plastic criterion. The cohesion is a function of the angle between the direction of the major compressive stress and the normal to the bedding plane. The numerical simulations of two sets of experimental tests on Opalinus Clay and Boom Clay reveal the dependency of the direction of loading on the mechanical response of the material. The model consists of a relatively simple upgrading of a well-known elasto-plastic model, well-adapted for sedimentary hard soils or soft rocks.*

1 INTRODUCTION

Anisotropy is an important factor determining the behaviour of clay soft rocks. Clay rocks, as most of the sedimentary rocks, exhibit anisotropy mainly related to their bedding plane orientation due to their depositional nature. The properties of such materials are usually independent of rotation about an axis of symmetry normal to the bedding plane. This type of anisotropy is called transverse isotropy or cross-anisotropy. In addition to the anisotropy of the reversible mechanical behaviour of soil, as observed for low levels of loading on highly overconsolidated materials, irreversible deformations are also affected by the direction of loading.

This work presents the development and the validation of a mechanical constitutive model that extends the symmetric Drucker-Prager yield criterion (Drucker and Prager, 1952) to cross-anisotropic materials and that is coupled with the classical cross-anisotropic elasticity (Lekhnitskii, 1977; Graham and Houslby, 1982). The new criterion assumes that the strength of materials may vary according to the orientation of the principal compressive stress with respect to the bedding plane orientation. This evolution of the strength as a function of the loading direction follows from experimental observations (e.g. Niandou et al. 1997) as already used for failure criteria of sedimentary rocks (e.g. Duveau et al., 1998; Pietruszczak and Mroz, 2001). In addition, the developed model allows a progressive hardening or softening process through the evolution of the mobilized cohesion and friction angle with an equivalent plastic strain (Barnichon, 1998).

The ability of the model to reproduce the directional dependency of the elasto-plastic response of clayey rocks, as observed in triaxial tests, is proved by the means of comparison

between numerical predictions and experimental results on an homogeneous sample of Opalinus Clay. Finally, the model, introduced in the LAGAMINE finite element code (Collin, 2003), is used to predict the hydro-mechanical behavior of non-conventional hollow cylinder tests on Boom Clay (You et al., 2010). In those tests, the hollow cylinders are submitted to mechanical unloading fairly similar to the evolution that would be encountered during gallery excavation. The results are compared with experimental measurements in term of radial displacements.

2 MECHANICAL CONSTITUTIVE MODEL

The elasto-plasticity principle (concept of a loading surface, f, in the stress space which limits the region of elastic deformation) allows that the total strain rate, $\dot{\varepsilon}_{ij}$, be split into elastic, $\dot{\varepsilon}_{ij}^{e}$, and plastic, $\dot{\varepsilon}_{ij}^{p}$, components :

$$\dot{\varepsilon}_{ij} = \dot{\varepsilon}_{ij}^{e} + \dot{\varepsilon}_{ij}^{p} \tag{1}$$

Because of elastic anisotropy, the elasto-plastic stress-strain relations are more convenient to be expressed in the anisotropic axis, as indicated by the star in exponent ($\sigma_{ij}'^{*}$ and ε_{ij}^{*})

$$\dot{\sigma}_{ij}'^{*} = C_{ijkl}\dot{\varepsilon}_{kl}^{*} \tag{2}$$

where C_{ijkl} is the elasto-plastic constitutive matrix.

In the more general situation, the reference axes do not coincide with the axes of anisotropy and the expression of $\sigma_{ij}'^{*}$ and ε_{ij}^{*} can be obtained from σ_{ij}' and ε_{ij} expressed in the system of reference through the following transformation:

$$\sigma_{ij}'^{*} = R_{ki}R_{lj}\sigma_{kl}' \quad ; \quad \varepsilon_{ij}^{*} = R_{ki}R_{lj}\varepsilon_{kl} \tag{3}$$

where R_{ij} is the ij component of the rotation matrix:

$$R = \begin{bmatrix} \cos\alpha\cos\varphi & \sin\alpha\cos\varphi & \sin\varphi \\ -\sin\alpha\cos\theta - \sin\theta\sin\varphi\cos\alpha & \cos\alpha\cos\theta - \sin\theta\sin\varphi\sin\alpha & \sin\theta\cos\varphi \\ \sin\theta\sin\alpha - \cos\alpha\sin\varphi\cos\theta & -\sin\varphi\sin\alpha\cos\theta - \sin\theta\cos\alpha & \cos\varphi\cos\theta \end{bmatrix} \tag{4}$$

α is the rotation angle around the axes $\underline{E}_3$ (rotation in the $(\underline{E}_1, \underline{E}_2)$ plane), the angles φ and θ defines the rotation around the axes $\underline{e}'_2$ and $\underline{e}_1$, respectively (Figure 3). The positive direction of rotation is counter-clockwise. $(\underline{E}_1, \underline{E}_2, \underline{E}_3)$ and $(\underline{e}_1, \underline{e}_2, \underline{e}_3)$ are the reference axes and the anisotropic axes, respectively.

At the end of each step of computation, the stress and strain obtained in the anisotropic axes ($\sigma_{ij}'^{*}$ and ε_{ij}^{*}) are re-transformed to be expressed in the global axes (σ_{ij}' and ε_{ij}):

$$\sigma_{ij}' = R_{ik}R_{jl}\sigma_{kl}'^{*} \quad ; \quad \varepsilon_{ij} = R_{ik}R_{jl}\varepsilon_{kl}^{*} \tag{5}$$

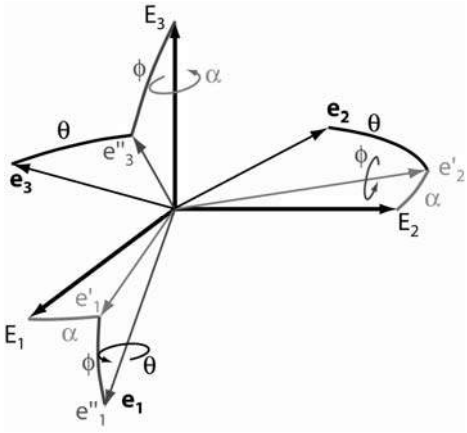

Fig. 1. Transformation of the global axis $(\underline{E}_1, \underline{E}_2, \underline{E}_3)$ into anisotropic axes $(\underline{e}_1, \underline{e}_2, \underline{e}_3)$.

2.1 Elastic anisotropy

$\dot{\varepsilon}_{ij}^{*e}$ is the ij strain rate component that does not modify the hardening state of the material. $\dot{\varepsilon}_{ij}^{*e}$ is linked to stress rate through the Hooke law :

$$\dot{\varepsilon}_{ij}^{*e} = D_{ijkl}^{e} \dot{\sigma}_{kl}'^{*} \tag{6}$$

The D_{ijkl}^{e} matrix considers anisotropic elasticity. The anisotropic elasticity needs a maximum of 21 independent parameters to be fully described. However, axes of symmetry in the structure of many materials limit the number of independent parameters. Sedimentary rocks show usually a more limited form of anisotropy. The behaviour is isotropic in the plane of bedding and the unique direction of anisotropy is perpendicular to bedding. The properties of such materials are independent of rotation about an axis of symmetry normal to the bedding plane. This type of elastic anisotropy, called transverse isotropy or cross-anisotropy, requires 5 independent parameters (Lekhnitskii, 1977). The elastic compliance matrix is:

$$D_{ijkl}^{e} = \begin{bmatrix} \frac{1}{E_{//}} & -\frac{\nu_{////}}{E_{//}} & -\frac{\nu_{\perp//}}{E_{\perp}} & & & \\ -\frac{\nu_{////}}{E_{//}} & \frac{1}{E_{//}} & -\frac{\nu_{\perp//}}{E_{\perp}} & & & \\ -\frac{\nu_{//\perp}}{E_{//}} & -\frac{\nu_{//\perp}}{E_{//}} & \frac{1}{E_{\perp}} & & & \\ & & & \frac{1+\nu_{////}}{E_{//}} & & \\ & & & & \frac{1}{2G_{//\perp}} & \\ & & & & & \frac{1}{2G_{//\perp}} \end{bmatrix} \tag{7}$$

where the subscripts // and $\perp$ indicates, respectively, the direction parallel to bedding (directions 1 and 2) and perpendicular to bedding (direction 3). The symmetry of the stiffness matrix imposes that

$$\frac{\nu_{\perp//}}{E_{\perp}} = \frac{\nu_{//\perp}}{E_{//}} \tag{8}$$

2.2 Plasticity

The limit between the elastic and the plastic domain is represented by a yield surface in the principal stress space. This surface corresponds to the Drucker-Prager yield surface f (Drucker and Prager, 1952):

$$f = II_{\hat{\sigma}} - m\left(I_{\sigma} - \frac{3c}{\tan\phi}\right) = 0 \tag{9}$$

where c is the cohesion and m is a function of the friction angle ϕ:

$$m = \frac{2\sin\phi}{\sqrt{3}(3-\sin\phi)} \tag{10}$$

I_{σ} and $II_{\hat{\sigma}}$ are the first stress tensor invariant and the second deviatoric stress tensor invariant, respectively:

$$I_{\sigma} = \sigma'^{*}_{ii} \tag{11}$$

$$II_{\hat{\sigma}} = \sqrt{\frac{1}{2}\hat{\sigma}'^{*}_{ij}\hat{\sigma}'^{*}_{ij}} \quad ; \quad \hat{\sigma}'^{*}_{ij} = \sigma'^{*}_{ij} - \frac{I_{\sigma}}{3}\delta_{ij} \tag{12}$$

In Equation (9), the linear coefficient m between the first and the second stress invariant being independent of the third invariant (or alternatively, the Lode angle), the plastic surface is a cone in the principal stress space. The trace of this plasticity surface on the Π plane (deviatoric plane) is a circle (Figure 2).

The material cohesion depends on the angle between major principal stress and the normal to the bedding plane. Three cohesion values are defined, for major principal stress parallel ($\alpha_{\sigma_1} = 0°$), perpendicular ($\alpha_{\sigma_1} = 90°$) and with an angle of 45° ($\alpha_{\sigma_1} = 45°$) with respect to the normal to bedding plane. Between those values, cohesion varies linearly with α_{σ_1}. The mathematical expression of the cohesion is as follows (Figure 3):

$$c = \max\left[\left(\frac{c_{45°} - c_{0°}}{45°}\right)\alpha_{\sigma_1} + c_{0°} \; ; \; \left(\frac{c_{45°} - c_{0°}}{45°}\right)\left(\alpha_{\sigma_1} - 45°\right) + c_{45°}\right] \tag{13}$$

with α_{σ_1} being the angle between the normal to the bedding plane $\vec{n}$ and the major principal stress $\vec{\sigma}_1$:

$$\alpha_{\sigma_1} = \arccos\left(\frac{\vec{n}.\vec{\sigma}'_1}{\|\vec{n}\|\|\vec{\sigma}'_1\|}\right) \tag{14}$$

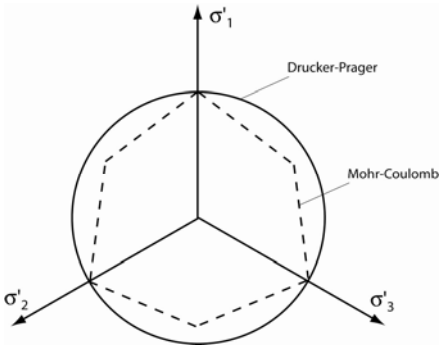

Fig. 2. Yield surface of the Drucker-Prager criterion in the deviatoric plane. Comparison with the Mohr-Coulomb yield surface.

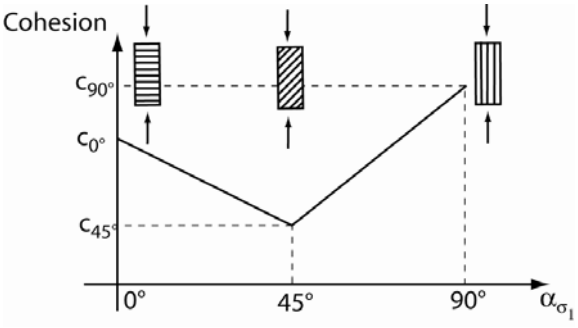

Fig. 3. Schematic view of the cohesion evolution as a function of the angle between the normal to bedding plane and the direction of major principal stress.

A general non-associated plasticity framework is considered:

$$\dot{\varepsilon}^{*p}_{ij} = \dot{\lambda}\frac{\partial g}{\partial \sigma'^{*}_{ij}} \tag{15}$$

with the plastic potential g defined as:

$$g = II_{\hat{\sigma}} + m' I_{\sigma} = 0 \tag{16}$$

with

$$m' = \frac{2\sin\psi}{\sqrt{3}(3-\sin\psi)} \tag{17}$$

where ψ is the dilatancy angle.

The plastic multiplier $\dot{\lambda}$ is obtained from the consistency condition:

$$df = \frac{\partial f}{\partial \sigma'^{*}_{ij}} \dot{\sigma}'^{*}_{ij} + \frac{\partial f}{\partial \kappa} \dot{\kappa} = 0 \tag{18}$$

with κ being the hardening variable(s). The used model is a hardening Drucker-Prager model that allows hardening/softening processes during plastic flow. This is introduced via an hyperbolic variation of the friction angle and the cohesion between initial (ϕ_0 and c_0) and final (ϕ_f and c_f) values as a function of the Von Mises equivalent plastic strain ε^p_{eq} (Barnichon, 1998):

$$\phi = \phi_0 + \frac{\left(\phi_f - \phi_0\right)\varepsilon^p_{eq}}{B_p + \varepsilon^p_{eq}} \tag{19}$$

$$c = c_0 + \frac{\left(c_f - c_0\right)\varepsilon^p_{eq}}{B_c + \varepsilon^p_{eq}} \tag{20}$$

where B_p and B_c are materials parameters and the Von Mises equivalent plastic strain ε^p_{eq} is obtained by integration of the Von Mises equivalent plastic strain rate $\dot{\varepsilon}^p_{eq}$:

$$\varepsilon^p_{eq} = \int_0^t \dot{\varepsilon}^p_{eq} dt \quad ; \quad \dot{\varepsilon}^p_{eq} = \sqrt{\frac{2}{3} \dot{\hat{\varepsilon}}^{*p}_{ij} \dot{\hat{\varepsilon}}^{*p}_{ij}} \tag{21}$$

Thus, the consistency condition (Equation 18) reads:

$$df = \frac{\partial f}{\partial \sigma'^{*}_{ij}} \dot{\sigma}'^{*}_{ij} + \left(\frac{\partial f}{\partial \phi} \frac{d\phi}{d\varepsilon^p_{eq}} + \frac{\partial f}{\partial c} \frac{dc}{d\varepsilon^p_{eq}} \right) \dot{\varepsilon}^p_{eq} = 0 \tag{22}$$

The Von Mises equivalent plastic strain can be expressed as a function of the plastic multiplier combining Equations (15) and (21), for the specific expression of the Drucker-Prager plastic potential (16):

$$\dot{\varepsilon}^p_{eq} = \sqrt{\frac{2}{3}\left(\frac{\partial g}{\partial \sigma'^{*}_{ij}} \frac{\partial g}{\partial \sigma'^{*}_{ij}} - \frac{1}{3} \frac{\partial g}{\partial \sigma'^{*}_{kk}} \frac{\partial g}{\partial \sigma'^{*}_{ll}} \right)} \dot{\lambda} = \frac{\sqrt{3}}{3} \dot{\lambda} \tag{23}$$

Combining together the elastic relation (6) and the expression of plastic strain rate (15) gives:

$$\dot{\sigma}^{*}_{ij} = C_{ijkl} \left(\dot{\varepsilon}^{*}_{kl} - \dot{\lambda} \frac{\partial g}{\partial \sigma'^{*}_{kl}} \right) \tag{24}$$

where C_{ijkl} is the stiffness matrix ($C = D^{-1}$). That allows us to determine the plastic multiplier $\dot{\lambda}$:

$$\dot{\lambda} = \frac{\dfrac{\partial f}{\partial \sigma'^{*}_{ij}} C^{e}_{ijkl} \dot{\varepsilon}^{*}_{kl}}{\dfrac{\partial f}{\partial \sigma'^{*}_{mn}} C^{e}_{mnop} - \dfrac{\sqrt{3}}{3}\left(\dfrac{\partial f}{\partial \phi} \dfrac{d\phi}{d\varepsilon^{p}_{eq}} + \dfrac{\partial f}{\partial c} \dfrac{dc}{d\varepsilon^{p}_{eq}} \right)} \tag{25}$$

3 CONSTITUTIVE BEHAVIOUR

Laloui and François (2008) compile a series of triaxial tests on Opalinus Clay at various confining pressure. They clearly underlines that the mechanical response of the clay is highly affected by the direction of loading with respect to the bedding plane. Three different directions of loading have been considered: bedding planes parallel (P-Sample), perpendicular (S-Sample) and with an inclination of 45°C (Z-Sample) with respect to the loading direction. The numerical simulation of the test at a confining pressure of 15 MPa has been performed. It can be observed that the elastic stiffness and the shear strength are clearly affected by the direction of loading with respect to the bedding plane. The elastic rigidity of the Z-sample is included between the rigidity of P- and S- samples which is characteristics of cross-anisotropic behaviour. The shear strength is the maximum for samples loaded in the direction of bedding (P-sample) while the minimum strength is observed for Z-sample (for loading direction at 45° to the bedding plane orientation). The comparison between experimental results and numerical simulations is made in Figure 4. The mechanical parameters allowing the best matching between numerical simulations and experimental results are reported in Table 1. In spite of some discrepancies in the experimental results (probably due to the heterogeneity of the Opalinus Clay), the model is able to reproduce the strong elastic and plastic anisotropy of the material.

Table 1. Geomechanical characteristics of Opalinus Clay and Boom Clay, used in the numerical simulations

Geomechanical characteristics			**Opalinus Clay**	**Boom Clay**
Young elastic modulus	[GPa]	$E_{//}$	16	400
Young elastic modulus	[GPa]	$E_{\perp}$	3	200
Poisson ratio	[-]	$\upsilon_{////}$	0.27	0.125
	[-]	$\upsilon_{//\perp}$	0.27	0.125
		$c_{0,0°}$	4200 (0°)	255 (0°)
Initial cohesion	[kPa]	$c_{0,45°}$	700 (45°)	240 (45°)
		$c_{0,90°}$	7000 (90°)	330 (90°)
		$c_{f,0°}$	6000 (0°)	85 (0°)
Final cohesion	[kPa]	$c_{f,45°}$	3000 (45°)	80 (45°)
		$c_{f,90°}$	10000 (90°)	110 (90°)
Softening parameter	[-]	B_c	0.01	0.01
Initial friction angle	[°]	ϕ_{c0}	14	5
Final friction angle	[°]	ϕ_{cf}	20	18
Hardening parameter	[-]	B_{ϕ}	0.01	0.01
Dilatation angle	[°]	Ψ	0	0

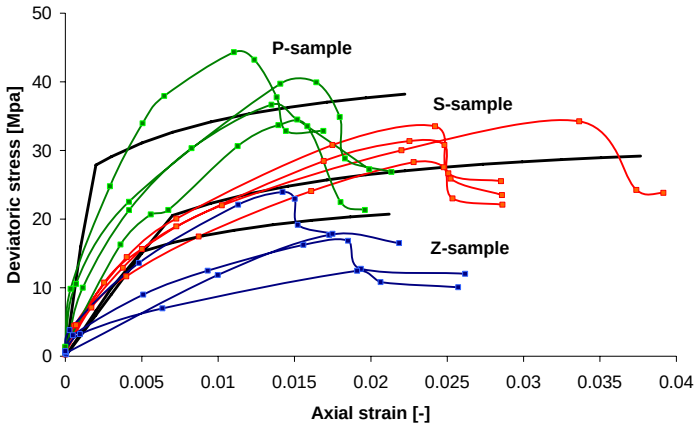

Fig. 4. Comparison between numerical simulations and experimental results of triaxial compression tests with a confining pressure of 15 MPa and three different orientation of bedding with respect to axial loading.

4 SIMULATION OF A HOLLOW CYLINDER TEST

You et al. (2010) designed non-conventional hollow cylinder tests on Boom Clay. It consists in hollow cylinder samples which are submitted to mechanical loadings fairly similar to the evolution of clays around a gallery excavation. The first results obtained by You et al. (2010) clearly reveal the significant anisotropic response of Boom Clay. The experimental measurements of the central hole displacement show a clear directional dependency. The initial circular hole is transformed into an oval hole after the mechanical unloading (Figure 4). The displacements in the direction parallel to bedding is much than twice larger than the displacement perpendicularly to bedding. Consequently, the measured radial displacements have been analysed in three particular directions: in the bedding direction ($\theta = 0°$), with an angle of 45° ($\theta = 45°$) with respect to the bedding plane and perpendicular to bedding plane ($\theta = 90°$).

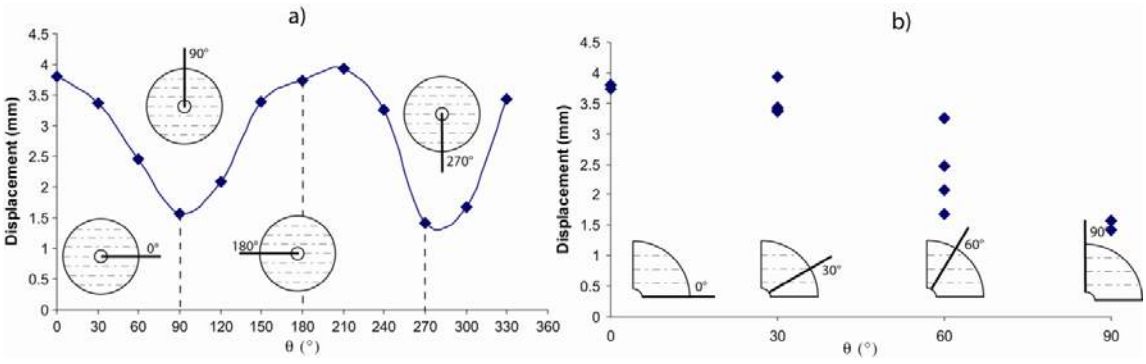

Fig. 4. Experimental measurements of the central hole displacement at the end of the mechanical unloading and pore water pressure dissipation. The measurements in the entire section (a) are reported in the quarter of the section (b) by considering the symmetry of the problem.

The objective of this simulation is to reproduce the behaviour of the material in the mid-plane section of the hollow cylinder, assuming plane strain conditions in the axial direction. The mechanical cross-anisotropy being considered, a directional dependency of the

encountered behaviour is expected. Consequently, the problem is not axisymmetric and it must be addressed through a two-dimensional plane strain mesh. The internal and external radii of the hollow cylinder are 7 mm and 43 mm, respectively. The clay sample is considered as homogeneous and to be fully saturated. The considered initial conditions consist in an isotropic total stress field of 4.5 MPa and a pore water pressure of 2.2 MPa. The unloading is performed by decreasing the internal mechanical stress down to 1.0 MPa and the pore water pressure down to 0.6 MPa in 70 minutes. The simulations have been performed until reaching a hydro-mechanical steady-state that has been obtained after 45000 s (12 hours 30 minutes). The results are presented at the end of the simulation.

The boundary value problem has been addressed through the finite element method with the LAGAMINE code (Collin et al., 2002) in which the developed constitutive model has been implemented. The use of the mechanical constitutive models requires the calibration of material parameters in agreement with the hydro-mechanical behaviour of the Boom Clay. The parameters of the anisotropic Drucker-Prager model are presented in Table 1. The water permeability has been assumed isotropic with $k = 4.\ 10^{-12}$ m/s.

The results of numerical simulations are compared with experimental results in terms of the central hole displacement as a function of the orientation with respect to bedding plane (Figure 5) and the radial profile of radial displacements in three different directions (Figure 6). The developed anisotropic model allows us to reproduce the magnitude of radial displacements as measured experimentally, including its directional dependency. The larger displacements are obtained in the direction parallel to bedding. The major principal stress being circumferential, $c(0°)$ corresponds to the cohesion in the direction for which the circumferential stress is parallel to the normal to the bedding plane, i.e. in the direction of bedding ($\theta = 0°$). This direction is weaker than the perpendicular direction ($\theta = 90°$), governed by $c(90°)$. So, the plastic strain is larger for $\theta = 0°$, inducing larger radial displacements for $\theta = 0°$ than for $\theta = 90°$. As experimentally observed, the central hole displacement is almost constant between $\theta = 0°$ and $\theta = 30°$ (at a value around 3.6 mm). Then, the predicted displacements decrease to 3 mm for $\theta = 90°$ while the experimental measurements are around 2 mm. This discrepancy between the experimental and numerical results is only concentrated in the last 3 mm of the radial profile (Figure 12, "exp 90°" and "simulation 90°"). Also, the radial displacement profiles shows a small discrepancy in the obtained displacements in the outer zone for $\theta = 0°$ (Figure 12) for which experimental displacements are larger than the modelling results.

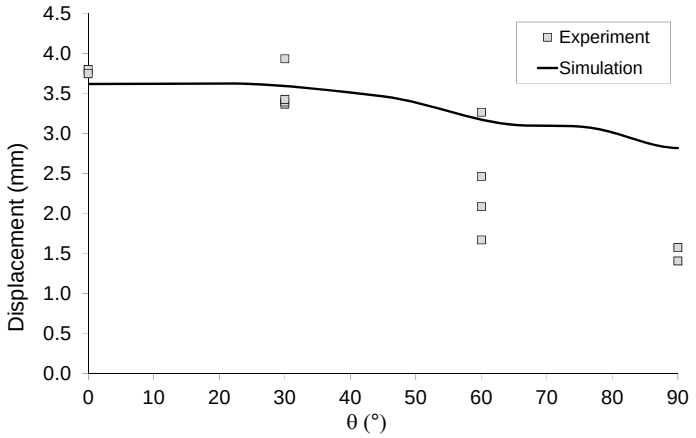

Fig. 5. Central hole displacement as a function of the orientation with respect to bedding plane. Comparison between experimental and numerical results.

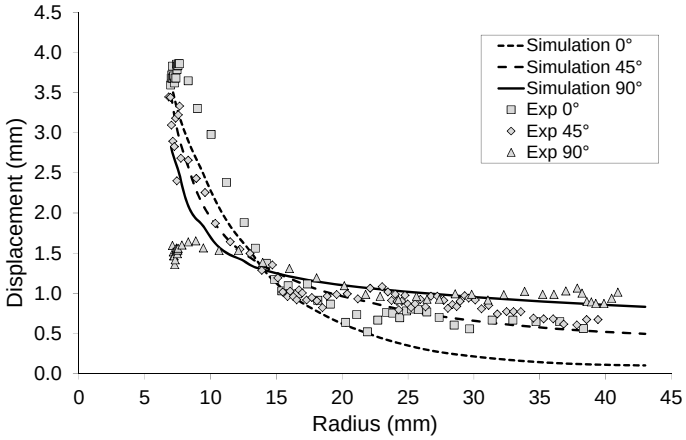

Fig. 6. Radial profile of radial displacements. Comparison between experimental measurements in three different directions and numerical results.

5 CONCLUSIONS

In many applications the anisotropic character of the natural hard soil or soft rock must be carefully considered. In particular, a gallery excavation in sedimentary rocks produces a non-axisymmetric response of the rock mass due to the cross-anisotropic behaviour of the soil. The displacements of the gallery walls are usually larger in the direction of bedding. So, the circular excavated cavity deforms into an oval shape. In such case, classical isotropic elasto-plastic models fail to reproduce properly the observed deformations of the soil and the use of an anisotropic model is required.

Consequently, in addition to cross-anisotropic elasticity the Drucker-Prager plastic criterion has been upgraded considering that the cohesion depends on the angle between the direction of the major compressive stress and the normal to the bedding plane. It is generally observed that the cohesion is the maximum when the major compression stress is in the direction of the bedding plane (i.e., perpendicular to the normal to the bedding plane, $\alpha_{\sigma_1} = 90°$) while the minimum cohesion is observed for α_{σ_1} around 45°.

This model has been used for the simulation of a non-conventional hollow cylinder test that reproduces a gallery excavation, at small scale. It has been shown that the model is able to catch the anisotropic response of the rock mass. This original model consists in a relatively simple upgrading of the Drucker-Prager elasto-plastic model, well-adapted for sedimentary hard soils or soft rocks.

ACKNOWLEDGEMENT

The authors would like to acknowledge Dr. Vincent Labiouse from the Rock Mechanics Laboratory of EPFL (Lausanne, Switzerland) for providing the experimental results of the hollow cylinder tests.

REFERENCES

Barnichon J.D. (1998). Finite element modelling in structural and petroleum geology. PhD Thesis, Université de Liège

Collin F. (2003). Couplages thermo-hydro-mécaniques dans les sols et les roches tendres partiellement saturés, PhD Thesis, Université de Liège.

Collin F., Li X.L., Radu J.P., Charlier R. (2002). Thermo-hydro-mechanical coupling in clay barriers. Engineering Geology, Vol. 64, 179-193.

Drucker D.C., Prager W. (1952). Solid mechanics and plastic analysis for limit design. Quarterly of Applied Mathematics, Vol. 10(2), 157-165.

Duveau G., Shao J.F. and Henry J.P. (1998). Assessment of some failure criteria for strongly anisotropic geomaterials. Mechanics of cohesive-frictional materials, Vol. 3, 1-26.

Graham J., Houlsby G.T. (1982) Anisotropic elasticity of a natural clay. Géotechnique, Vol. 33(2), 165-180.

Laloui L., François B. (2008). Benchmark on constitutive modelling of the mechanical behaviour of Opalinus clay – Focus on the material anisotropy. Internal report. Ecole Polytechnique Fédérale de Lausanne.

Lekhnitskii S.G. (1977). Theory of elasticity of an anisotropic elastic body. 2nd Edition, Moscow, MIR Publishers.

Niandou H., Shao J.F., Henry J.P., Fourmaintraux D. (1997). Laboratory investigations of the mechanical behaviour of Tournemire shale, Int. J. Rock Mech. Min. Sci., Vol. 34, 3-16.

Pietruszczak S. and Mroz Z. (2001). On failure criteria for anisotropic cohesive-frictional materials. Int. J. Numer. Anal. Meth. Geomech. Vol. 25, 509-524

You S., Labiouse V., Vigne L., Gastaldo L., Bernasconi M. (2010). Medium resolution X-Ray computed tomography of hollow cylindrical samples of Boom Clay. EUROCK 2010. Rock Mechanics in Civil and Environmental Engineering: 755-758.

A GENERAL FAILURE CRITERION FOR GEOMATERIALS WITH CROSS ANISOTROPY

J.D. Zhao & Z.W. Gao
Department of Civil Engineering and Environmental Engineering, Hong Kong University of Science and Technology, Clearwater Bay, Kowloon, Hong Kong

Y.P. Yao
Department of Civil Engineering, Beihang University, Beijing, China

ABSTRACT: *The strength of soils and rocks is greatly influenced by cross anisotropy which cannot be properly characterized by an isotropic failure criterion. A novel anisotropic failure criterion is proposed for geomaterials in this paper. To account for the influence of cross anisotropy, an anisotropic variable defined by the invariants and joint invariants of the stress tensor and the fabric tensor is introduced into the expression of the criterion. We formulate the new anisotropic failure criterion in both the deviatoric plane and the meridian plane, which collectively lends a general three-dimensional description for the strength anisotropy. All parameters in the criterion can be conveniently determined by conventional laboratory tests. By comparing the model predictions with experimental data, we demonstrate that the new criterion is general and robust enough to characterize the strength anisotropy for a wide range of materials, including clays, sands and rocks. Further extension of the failure criterion for constitutive modeling of geomaterials is discussed.*

1 INTRODUCTION

Cross anisotropy is commonly observed in geomaterials and has been known to have a significant influence on the strength of these geomaterials (Casagrande & Carrilo, 1944; Duncan & Seed, 1966; Arthur & Menzies, 1972; Oda et al., 1978; Abelev & Lade, 2004). Numerous experimental data have proved that the strength of geomaterials varies considerably with direction. Yong & Silvest (1979), for example, have found the unconfined compression strength of sensitive clay varies continuously with loading directions and the minimum strength observed is about 60% to 75% of the maximum. Similar observations were reported by Kirkgard & Lade (1991, 1993) from true triaxial tests on San Francisco Bay Mud, by Nishimura et al. (2007) on natural London clay and by Niandou et al. (1997) and Duveau et al. (1998) on sedimentary rocks. The degree of strength anisotropy (e.g., difference in strength at different direction) is significantly higher in rocks than in soils. Indeed, strength anisotropy of geomaterials is important to a variety of geotechnical structures, such as footings, retaining walls and slopes. Oda et al. (1978) have investigated the bearing capacity of two model strip foundations built on the same sand, and found the difference in bearing capacity for the model with load perpendicular to the bedding plane and the other one with a parallel load to the bedding plane can reach as much as 34%. Proper consideration of cross anisotropy in the evaluation of the soil/rock strength appears to be necessary.

Most well-received failure criteria in the literature have been isotropic ones (e.g., Matsuoka & Nakai, 1974; Lade & Duncan, 1975; Lade, 1977; van Eekelen, 1980). Despite their popularity, these isotropic criteria may find difficulties in interpreting the yielding and

failure for anisotropic soils/rocks. In a comparison of experimental data on isotropically consolidated San Francisco Bay Mud against predictions by Lade's (1977) isotropic failure criterion, Kirgard & Lade (1993) have found Lade's isotropic criterion can fit reasonably well for the failure stress points of specimens with Lode's angle θ in the range from 0° to 90° in the octahedral plane, but leads to An appreciable discrepancy, however, has been observed between Lade's failure surface and the failure data points for tests conducted with θ greater than 90° wherein Lade's failure criterion generally overestimates the strength of the specimen. An anisotropic failure criterion is indeed necessary to take into account the influence of cross anisotropy in cases like this.

In this paper, we propose a novel anisotropic failure criterion. As will be shown in the following section, this new criterion differs in essence from the existing anisotropic failure criteria appearing recently, such as those proposed by Duveau et al. (1998), Pietruszczak & Mroz (2000, 2001), Liu & Carter (2003), Abeleve & Lade (2004), Guo & Stolle (2005), Lade (2007, 2008), Lee & Pietruszczak (2008), Mortara (2009) and Schweiger et al. (2009). All model parameters introduced in the new criterion can be conveniently calibrated by conventional laboratory tests. It is general and robust enough to be capable of describing the failure behavior for a wide range of soils and rocks with cross-anisotropy.

2 THE GENERAL ANISOTROPIC FAILURE CRITERION

We propose the following failure criterion for geomaterials with cross anisotropy

$$\alpha\sqrt{\bar{I}_1^2-3\bar{I}_2}+(1-\alpha)\frac{2\bar{I}_1}{3\sqrt{\left(\bar{I}_1\bar{I}_2-\bar{I}_3\right)/\left(\bar{I}_1\bar{I}_2-9\bar{I}_3\right)}-1}=M_f f(A)\bar{p} \qquad (1)$$

where M_f is the frictional coefficient of the material which depends on its peak frictional angle φ. $\bar{I}_1$, $\bar{I}_2$ and $\bar{I}_3$ are the three invariants of a transformed stress tensor $\bar{\sigma}_{ij}$ defined below (see Fig.1a for the transformation based on the meridian plane)

$$\bar{\sigma}_{ij}=\sigma_{ij}+(\bar{p}-p)\delta_{ij}=\sigma_{ij}+\left[p_r\left(\frac{p+\sigma_0}{p_r}\right)^n-p\right]\delta_{ij} \qquad (2)$$

where δ_{ij} is the Kronecker delta. σ_{ij} is the commonly referred Cauchy stress tensor. As is shown in Fig. 1(a) in the meridian plane, the transformation essentially renders that $\bar{q}=q$ and $\bar{p}=\bar{q}/M_f=p_r\left[\left(p+\sigma_0\right)/p_r\right]^n$, where p and q are the commonly referred mean stress and shear stress, and $\bar{p}$ and $\bar{q}$ are their corresponding transformed values. n is a exponential constant and p_r a reference pressure. σ_0 denotes the triaxial tensile strength of the material, or equivalently the cohesion of the material. α is an interpolation constant as shown in Fig. 1(b). If $\alpha=1$, the underlying isotropic failure criterion of Eq. (1) (e.g., when $f(A)=1$) becomes identical to the extended Mises criterion. When $\alpha=0$, it coincides with the Matsuoka-Nakai (or so-called Spatial Mobilized Plane, SMP in brief) curve-sided triangle (Matsuoka and Nakai, 1974). The anisotropic failure criterion proposed in Eq. (1) has been based on an isotropic one originally developed by Yao et al. (2004). Key to the new failure criterion is the addition of the function $f(A)$ defined below to introduced the influence of anisotropy

$$f(A)=\exp\left\{d\left[(A+1)^2+\beta(A+1)\right]\right\} \tag{3}$$

where d and β are material constants. A is an anisotropic variable reflective of the influence of loading direction with respect to fabric, defined as follows

$$A=\frac{\mathrm{tr}\left(s_{ik}d_{kj}\right)}{\sqrt{s_{mn}s_{mn}}\sqrt{d_{pq}d_{pq}}} \tag{4}$$

where $s_{ij}=\sigma_{ij}-p\delta_{ij}$, $d_{ij}=F_{ij}-F_{kk}\delta_{ij}/3$. F_{ij} denotes a fabric tensor representing the inherent anisotropy in a material. For materials with cross anisotropy, it is common F_{ij} adopts the following form

$$F_{ij}=\begin{bmatrix}F_1 & 0 & 0\\ 0 & F_2 & 0\\ 0 & 0 & F_3\end{bmatrix}=\frac{1}{3+\Delta}\begin{bmatrix}1-\Delta & 0 & 0\\ 0 & 1+\Delta & 0\\ 0 & 0 & 1+\Delta\end{bmatrix} \tag{5}$$

where Δ is a scalar that characterizes the magnitude of the cross-anisotropy. Its value ranges from zero when the material is absolutely isotropic, to unity when the degree of anisotropy is the maximum. For materials with cross anisotropy, A in Eq. (4) can be rewritten specifically for different loading conditions, in terms of the intermediate principal stress ratio b and the relative angle between stress direction and axis of cross anisotropy (for detail, please refer to Gao et al., 2010). Note that when $f(A)\equiv 1$, the anisotropic failure criterion expressed in Eq. (1) becomes identical to the underlying isotropic failure criterion as in Yao et al.(2004). The primary effect of the function $f(A)$ is to change the shape of the underlying isotropic failure surface in the deviatoric plane. When $f(A)>1$, it plays a role in Eq. (1) in expanding the failure surface with respect to the isotropic one, and to shrink it when $f(A)<1$.

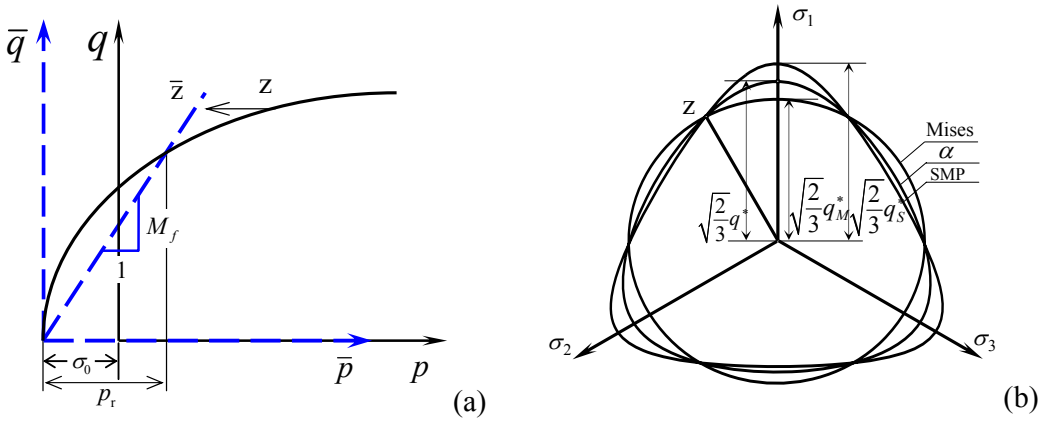

Fig. 1. Illustration of stress transformation in the meridian plane (a) and interpolation of failure surface in the deviatoric plane (b).

Model parameters introduced in the criterion can be calibrated using conventional laboratory tests, such as conventional and true triaxial compression/extension tests and

rotational shear tests. Detailed procedures on their calibration can be referred to Gao et al. (2010), wherein specific examples on determining the model parameters for a soil or rock based on data from triaxial tests and/or rotational shear tests have been provided.

3 VALIDATION WITH EXPERIMENTAL DATA

To demonstrate the generality and robustness of our failure criterion, we have chosen a total of two clays, four sands and two rocks reported in the literature to validate our model prediction. According to the procedures outlined in Gao et al. (2010), the model parameters for these materials are calibrated and summarized in Tab. 1 below.

Table 1 Summary of model parameters calibrated for soils and rocks under study in this paper

Materials (Data source)		M_f	p_r	σ_0	n	α	d	β
Clay	Isotropically consolidated San Francisco Bay Mud (Kirkgard & Lade, 1993)	1.45	67 kPa	0	0.83	0.49	0.013	-7.69
	K_0-consolidated San Francisco Bay Mud (Lade & Kirkgard, 2000)	1.38	—*	0	1	0	0.058	1.44
Sand	Cambria Sand (Ochiai & Lade, 1983)	1.62	—	0	1	0.48	0.014	-3.57
	Dense Santa Monica Beach Sand (Abelev & Lade, 2004)	1.87	—	0	1	0.33	-0.05	-1
	Toyoura Sand (Lam and Tatsuoka, 1988; Tatsuoka et al., 1990)	1.68	—	0	1	0.17	0.05	-2.6
	Dry-pluviated Santa Monica Beach Sand (Lade et al., 2008)	1.63	—	0	1	0.36	-0.04	0
Rock	Touremire Shale (Niandou et al., 1997)	1.58	50 MPa	2.5 MPa	0.54	—	0.5	-1.5
	Angers Schist (Duveau et al., 1998)	2.36	100 MPa	8 MPa	0.76	—	2.5	-1.52

* — : not specified.

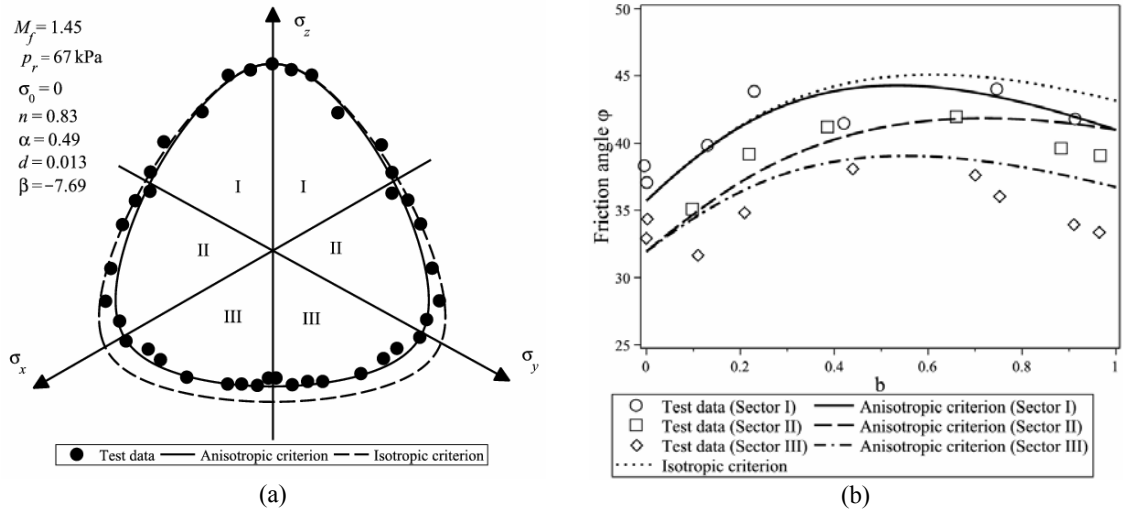

(a) (b)

Fig. 2. Comparison of the isotropic and anisotropic failure criteria with experimental data for isotropically consolidated San Francisco Bay Mud (Kirkgard & Lade, 1993), (a) in the deviatoric plane, and (b) in the φ-b diagram.

3.1 Isotropically Consolidated San Francisco Bay Mud (Kirkgard & Lade, 1993)

The anisotropic failure criterion proposed in Section 2 is first employed to predict the anisotropic strength of isotropically consolidated San Francisco Bay Mud tested by Kirkgard & Lade (1993). The test data are compared in Fig. 2 against the predictions by the anisotropic

failure criteria in Eq. (1) as well as the underlying isotropic failure criterion (by using $f(A) \equiv 1$ and the same α value in Eq. (1)) in the deviatoric plane for which $p = 167$ kPa and the plane of $\varphi \sim b$ where φ is the peak friction angle of the soil. As is shown, the anisotropic criterion captures the overall trend of the test data in the deviatoric plane reasonably well, with only a slight underestimation of the soil strength in Sector II (see Fig. 2(a) for the different sections defined in the deviatoric plane. The same zonation of sections is followed for all subsequent figures on the description of deviatoric plane). In contrast, the isotropic criterion clearly overestimates the strength at large, particularly in Sector III. The tested $\varphi \sim b$ relation and the corresponding predictions of the two failure criteria are also shown in Fig. 2(b). The isotropic criterion gives a single $\varphi \sim b$ relation for all sections which significantly overestimates the value of friction angle in Sectors II and III. In contrast, the prediction of the anisotropic failure criterion is in good accordance with the test data in Sectors I and II, only slightly overestimates the value of friction angle in Sector III with a maximum difference of 4° at $b = 1$ in sector III, about 10% of the measured friction angle.

3.2 K_0-Consolidated San Francisco Bay Mud (Lade & Kirkgard, 2000)

A series of torsion shear tests have been carried out by Lade & Kirkgard (2000) on K_0-consolidated San Francisco Bay Mud using hollow cylinder torsion shear apparatus. Various stress paths were applied to achieve the full range of stress rotation from $\zeta = 0^\circ$ to $\zeta = 90^\circ$ where ζ is the rotation angle between the direction of major principal stress and the axis of bedding plane of the soil. As there are insufficient test results available in the meridian plane, we assume here $n = 1$ and $\sigma_0 = 0$ kPa for simplicity. M_f is calculated based on the peak friction angle at $b = 0$ ($\varphi_c = 34.1^\circ$), which corresponds to the conventional triaxial compression shear mode. d and β are determined based on the results at $b = 0.5$ and $b = 1.0$ by assuming $\alpha = 0$. Presented in Fig. 3 is the comparison between the test data and the prediction of the anisotropic criterion. The anisotropic failure criterion performs better in the prediction of high b regime than the isotropic one does. It slightly overestimates the values of friction angle when $0.1 < b < 0.4$. Lade & Kirkgard (2000) have remarked that the K_0-consolidated samples of San Francisco bay mud appear to retain the original in-situ fabric which is essentially different from that in the isotropically consolidated remolded specimens tested by Kirkgard & Lade (1993).

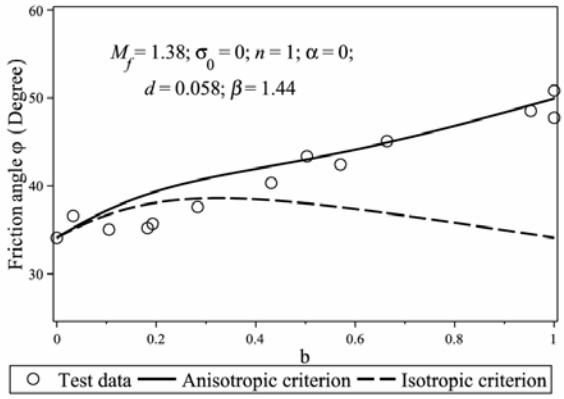

Fig. 3. Comparison between model predictions and torsion shear test results on K_0-consolidated San Francisco Bay Mud (Lade & Kirkgard, 2000) in the φ-b diagram.

3.3 Cambria Sand (Ochiai & Lade, 1983)

The anisotropic failure criterion has also been employed to predict the strength of Cambria sand with comparison against the test data obtained by Ochiai & Lade (1983). All the triaxial test results are projected onto the same deviatoric plane with a mean stress $p = 334$ kPa. As shown in Fig. 4(a), for Cambria sand, the effect of anisotropy on the failure curve in the deviatoric plane appears to be relatively small, while the two criteria produce very close predictions. In the $\varphi \sim b$ plane, however, the variation of friction angle with b demonstrates an appreciable dependence on anisotropy in all three sectors, as is shown in Fig. 4(b). The isotropic failure criterion fails to capture this property of Cambia sand. We also notice that the prediction by Lade's anisotropic failure criterion (Lade, 2008) slightly underestimates the φ value between $b = 0.7$ and $b = 1.0$ in all three sectors. Our anisotropic failure criterion captures the trend of $\varphi \sim b$ relation better in both Sector I and Sector II. It only slightly overestimates the value of φ at $b = 0.3$ to $b = 1.0$ in Sector III by about 1°.

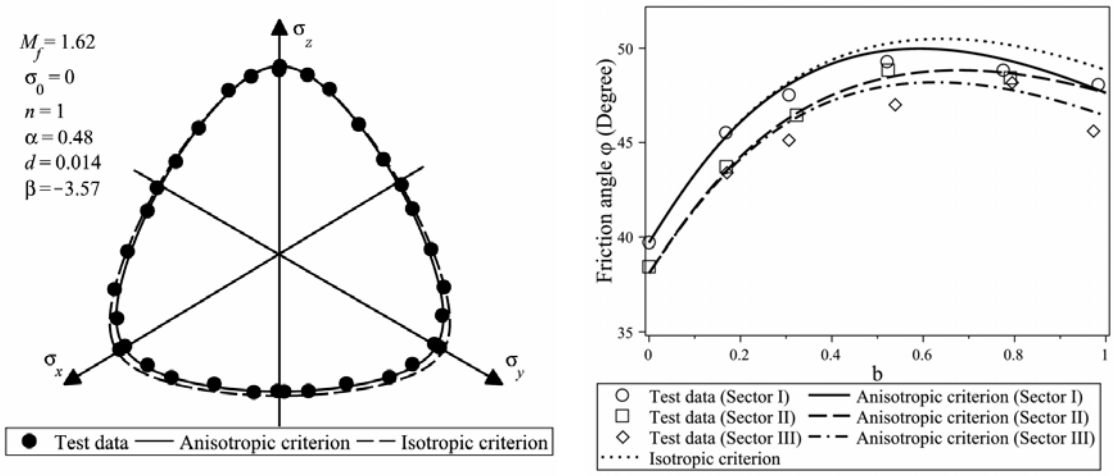

(a) (b)

Fig. 4. Comparisons of the test data on Cambria Sand (Ochiai & Lade, 1983) with predictions by the isotropic and anisotropic failure criteria in (a) the deviatoric plane and (b) the φ-b diagram. Variation of the friction angles shows more significant anisotropic effect than that of the strength in the deviatoric plane does.

3.4 Dense Santa Monica Beach Sand (Abelev & Lade, 2004)

True triaxial tests have been carried out by Abelev & Lade (2004) on dense Santa Monica Beach sand deposited with a cross-anisotropic fabric. All tests have been performed with a constant effective cell pressure of $\sigma_3 = 50$ kPa and a constant value of b. Shear banding was observed in the hardening regime in the midrange of b values in each sector of the deviatoric plane. Model predictions by our model and the isotropic criterion are compared to the test data in Fig. 5. As is shown, our anisotropic criterion demonstrates an overall better fitting to the acquired test data than the isotropic failure criterion in both the deviatoric plane and the $\varphi \sim b$ diagram. Nevertheless, we also observe in Fig. 5(b) that the peak friction angle of the sand in the midrange of b values is overestimated by the anisotropic failure criterion in all three sectors. The formation of shear banding may be the attributable to this difference. Indeed, according to Abelev & Lade (2004) and Lade (2007, 2008), occurrence of shear banding may reduce the strength measured from the boundary of the samples. The anisotropic

criterion is therefore expected to serve as a target of strength that the material could have attained if the deformation were uniform in the tested sample. We also comment that the prediction by Lade's anisotropic failure criterion (Lade, 2008) in the deviatoric plane is roughly the same as our prediction for this sand; whereas for the $\varphi \sim b$ relation, the prediction by Lade (2008) appears to be slightly better.

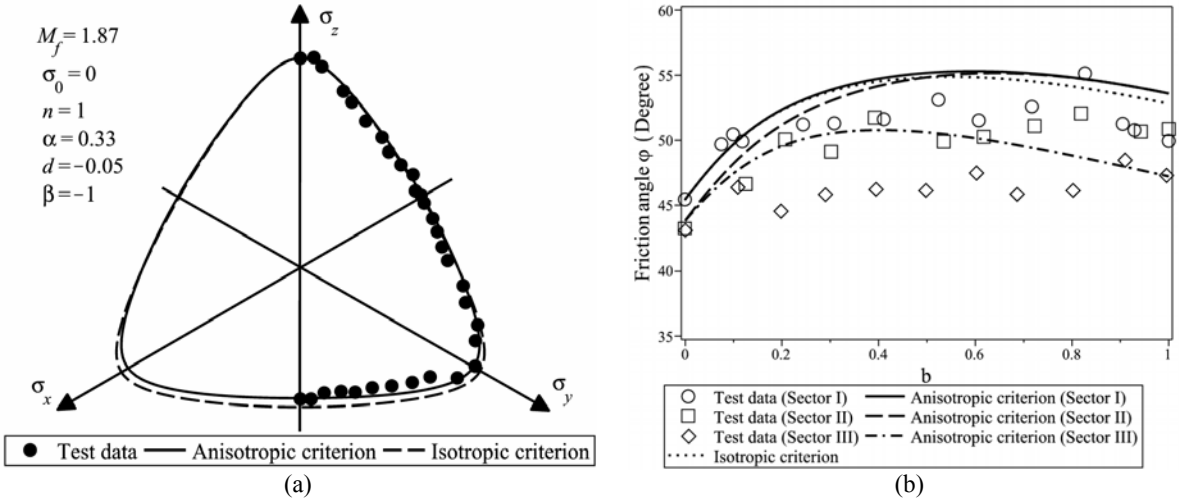

Fig. 5. Failure of dense Santa Monica Beach sand predicted by the isotropic and anisotropic failure criteria in comparison with test data (Abelev & Lade, 2004), in (a) the deviatoric plane and (b) φ-b diagram in three sectors. The anisotropic criterion overestimates the strength in the midrange of b due to shear banding.

3.5 Toyoura Sand (Lam & Tatsuoka, 1988)

Lam & Tatsuoka (1988) carried out true triaxial tests on Toyoura sand with a constant cell pressure of $\sigma_3 = 98$ kPa where the sand samples have been prepared by the air-pluviating method to introduce initial cross-anisotropic fabric. Shear banding has been observed in their testing. The predicted strength by our model is compared to the test data in Fig. 6(a). In the deviatoric plane, the anisotropic failure criterion provides a better correlation with the test data than the isotropic criterion does. It does, however, slightly overestimate the strength in the midrange of b values in Sector II and Section III, which is similar to the case of Santa Monica Beach sand.

Tatsuoka et al. (1990) have later carried out triaxial compression tests on Toyoura sand for which it is also interesting to make a comparison with our model prediction. Presented in Fig. 6(b) is the variation of the friction angle with the loading direction in term of ξ (the angle between the direction of major principal stress and the axis of bedding plane of the soil, same as the ζ in the rotoational shear case) at a constant confining pressure of 98 kPa obtained by the triaxial compression tests (Tatsuoka et al., 1990), in close comparison with the predictions by the isotropic and anisotropic failure criteria. Note that two set of data are presented in the figure which correspond to samples with different initial void ratios. Since the strength of sand is known to be affected by the initial void ratio as well as confining pressure, the data in Fig. 6(b) have been normalized by the friction angle at $\xi = 0^\circ$ (denoted as φ_0) for consistency. No shear banding has been observed in the triaxial compression tests. As is shown in Fig. 6(b), the prediction by the anisotropic failure criterion for the triaxial tests on Toyoura sand compares favorably with the test data, whilst the constant prediction by the isotropic criterion deviates from the test data by a large extent when ξ becomes greater.

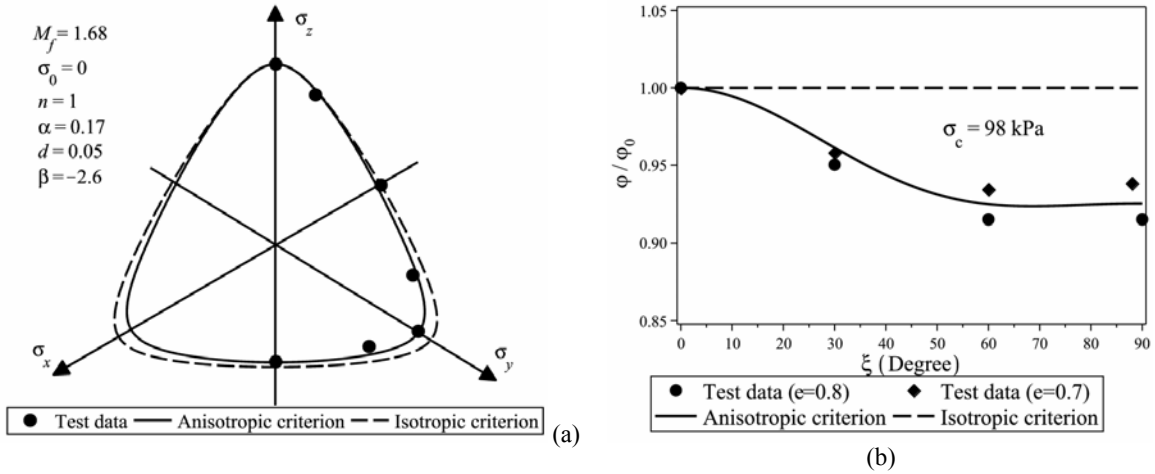

Fig. 6. Prediction of the strength of Toyoura Sand by the isotropic and anisotropic failure criteria in comparison with (a) the true triaxial test results by Lam & Tatsuoka (1988) in the deviatoric plane; and (b) the triaxial compression test results by Tatsuoka et al. (1990) in the $\varphi / \varphi_0 - \xi$ diagram.

3.6 Santa Monica Beach Sand (Lade et al., 2008)

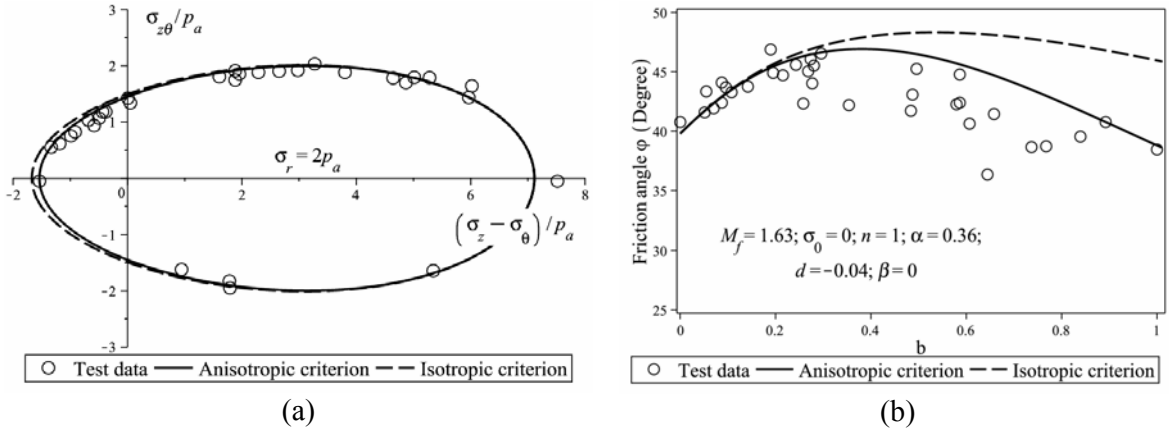

Fig. 7. Comparison between the torsion shear test results on dry-pluviated Santa Monica Beach sand (Lade et al., 2008) with the predictions by the isotropic/anisotropic failure criteria in (a) the $\sigma_{z\theta} \sim (\sigma_z - \sigma_\theta)$ diagram, and (b) the φ-b diagram.

A total of 34 torsion shear tests have been carried out by Lade et al. (2008) on dry-pluviated Santa Monica Beach sand. The tests were conducted under drained conditions at a cell pressure of 200 kPa applied to both the inner and outside cell walls. For comparison with the torsion shear tests, 11 true triaxial tests have also performed in the cubic triaxial apparatus with four different confining pressures. Since the curvature of the failure curve in the meridian plane can not be determined based on the available test data, n is set to be unity here. M_f is calculated based on the average value of the friction angles obtained in the conventional triaxial compression tests performed in the torsion shear apparatus and the cubic triaxial apparatus respectively ($\varphi_c = 34.1^\circ$). The friction angle obtained in true triaxial tests at

$b = 1$ ($\varphi_e = 46^\circ$), which corresponds to the shear modes of $\theta = 60^\circ$ and $\xi = 0^\circ$, is used to determine the parameter α. Shear banding has been observed in most of the torsion shear tests by Lade et al. (2008). To minimize the influence of shear banding, we only select the results obtained at $b = 1$, which corresponds to the shear mode of $\theta = 180^\circ$ and $\xi = 0^\circ$, for determining the parameter d by setting $\beta = 0$. The predictions are presented in Fig. 7. While both the isotropic criterion and the anisotropic criterion capture the test data reasonably well in the plane of $(\sigma_z - \sigma_\theta) \sim \sigma_{z\theta}$ in Fig. 7(a), it is in the $\varphi \sim b$ plane that the difference can be better depicted. As shown in Fig. 7(b), the isotropic failure criterion clearly overestimates the measured strength when $b > 0.3$. The anisotropic failure criterion, on the other hand, can capture the overall trend of strength variation with b better. Noticeable overestimation, though, is still observed in the range of $0.3 < b < 0.85$ where shear banding comes into effect.

3.7 Touremire Shale (Niandou et al., 1997)

A comparison has also been made between predictions by our anisotropic failure criterion with the triaxial test data on the Touremire shale in Niandou et al. (1997), which is shown in Fig. 8. The prediction by the isotropic criterion is also shown for the convenience of comparison. As is seen in Fig. 8(a), the anisotropic failure criterion satisfactorily captures the $p \sim q$ relation at different loading directions for Touremire shale. Its predictions also agree well with the test data at most confining pressure levels, only with a slight overestimation on the strength at a low confining pressure of $\sigma_c = 1$ MPa when $\xi > 0^\circ$ and a moderate underestimation for the case of $\sigma_c = 20$ MPa (Fig. 8(b)). The observed deviation may be possibly due to the fact that the anisotropic variable A introduced in this paper is assumed to be only a measure of the stress direction relative to the material fabric orientation but independent on the mean stress. According to Niandou et al. (1997), the degree of strength anisotropy is greater at lower confining pressure levels than that at higher ones. This pressure-dependent strength anisotropy has also been observed by Lade & Abelev (2005) in sand. A potential improvement of the current anisotropic failure criterion may be done by incorporating the effect of mean stress in the criterion, e.g., via the anisotropic variable A.

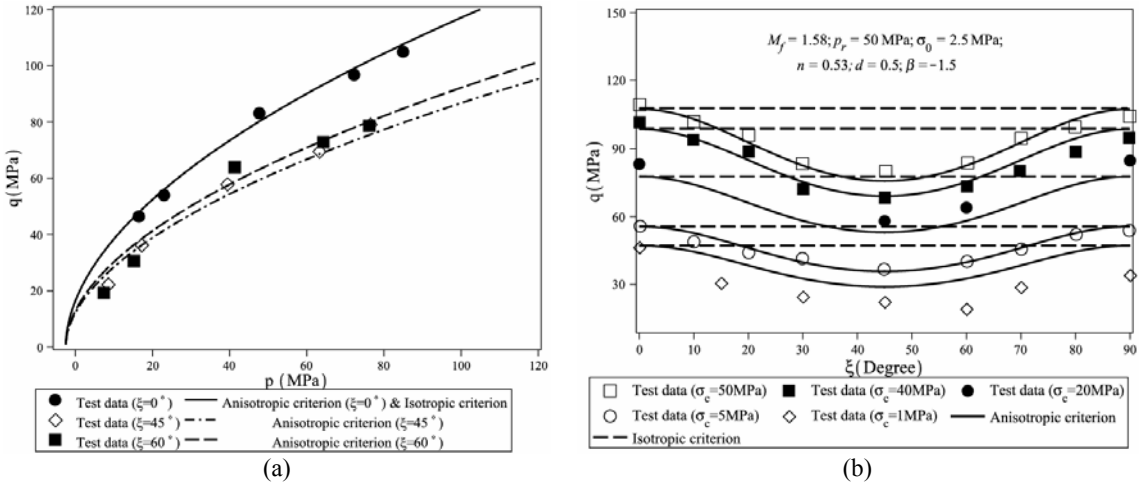

Fig. 8. Comparison between the triaxial compression test data on the Touremire shale (Niandou et al., 1997) and the prediction of the anisotropic and underlying isotropic failure criteria in (a) the *p*-*q* diagram with different loading directions and (b) the *ξ*-*q* diagram with different confining pressures.

3.8 Angers Schist (Duveau et al., 1998)

Another rock, the Angers schist reported in Duveau et al. (1998), has been used to validate our failure criterion. The test data for Angers schist are more scattered compared to those for the Touremire shale (Fig. 9). Our anisotropic failure criterion, with the chosen parameters, can reasonably capture the overall trend of the data set in both the $p \sim q$ and $\xi \sim q$ planes. In the $\xi \sim q$ plane as shown in Fig. 9(b), the criterion slightly overestimates the strength at all range of ξ except $\xi = 0^\circ$ and 90°. The isotropic failure criterion fails to capture the strength variation with loading directions for both rocks in either the $p \sim q$ plane or the $\xi \sim q$ plane.

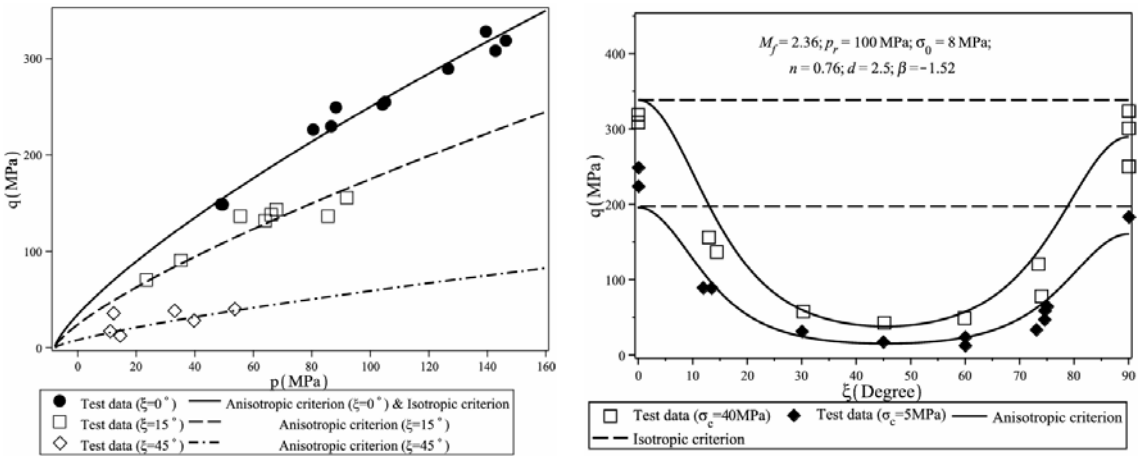

Fig. 9. Comparisons of the triaxial compression test data on the Angers schist (Duveau et al., 1998) with the prediction of the anisotropic and underlying isotropic failure criteria in (a) the *p-q* diagram with different loading directions and (b) the *ξ-q* diagram with different confining pressures.

4 CONCLUSION AND DISCUSSION

The new anisotropic failure criterion presented in this paper has been demonstrated to be general and robust enough to provide excellent predictions on the strength anisotropy for a wide range of soils and rocks. The introduction of the anisotropic variable A in terms of the invariants and joint invariants of the stress tensor and the fabric tensor appears to be effective in characterizing the effect of fabric anisotropy. Parameters introduced in the criterion can be conveniently calibrated by conventional laboratory tests. We note that the usefulness of this criterion is not limited to geomaterials only. For any materials that exhibit appreciable strength anisotropy, such as *concrete*, *ceramics*, *porous metals*, *polymers* and *solid metals*, it can be equally useful. The specific procedures in determining the required parameters may differ from those mentioned in this paper, though, depending on the availability of routine tests for these different materials. Meanwhile, we have mentioned that shear banding has been observed in the hardening regime in true triaxial tests on sand (Wang & Lade, 2001; Abelev & Lade, 2003) in the midrange of b values (from about 0.18 to approximately 0.85). The occurrence of shear banding in the hardening regime prevents the attainment of a smooth peak on the stress-strain relation for which a failure criterion tends to fit with. For the range of b where shear banding occurs, the current anisotropic failure criterion slightly overestimates the strength of the soils in the deviatoric plane. In this case, the prediction of strength by our criterion can be regarded as a targeted upper bound that a soil can achieve if the deformation is uniform in the tested sample. In addition, the anisotropic failure criterion

presented here can be easily extended for constitutive modeling of geomaterials as well, by simply considering it as the yield function with suitable hardening rules specified, as is the way done by Pietruszczak et al. (2002) and Azami et al. (2009). It is also possible to introduce a cap in the meridian plane for the proposed failure criterion for various useful purposes in constitutive soil modeling.

ACKNOWLEDGEMENT

This work was supported by RGC HK (under Grants No. 622910, 623609 and DAG08/09.EG04).

REFERENCES

Abelev, A. & Lade, P.V. (2004), "Characterization of failure in cross-anisotropic soils". J. Eng. Mech. ASCE 130(5), 599-606.

Arthur, J.R.F. & Menzies, B.K. (1972), "Inherent anisotropy in a sand". Géotechnique 22(1), 115-128.

Azami, A., Pietruszczak, S., Guo, P., 2009. Bearing capacity of shallow foundations in transversely isotropic granular media. Int. J. Numer. Anal. Meth. Geomech. DOI: 10.1002/nag.827.

Casagrande, A. & Carillo, N. (1944), "Shear failure of anisotropic materials". J. Boston Soc. Civ. Eng. 31(4), 74-87.

Duncan, J.M. & Seed, H.B. (1966). "Strength variation along failure surfaces in clay". J. Geotech. Eng. Div. ASCE 92 (SM6), 81-104.

Duveau, G., Shao, J.F. & Henry, J.P. (1998), "Assesment of some failure criteria for strongly anisotropic geomaterials". Mech. Cohes-Frict. Mater. 3, 1-26.

Gao, Z.W., Zhao, J.D. & Yao, Y.P. (2010), "A generalized anisotropic failure criterion for geomaterials". Int. J. Solids Struct. 47(22-23): 3166-3185.

Guo, P. & Stolle, D.F.E. (2005), "On the failure of granular materials with fabric effects". Soils Found. 45(4), 1-12.

Kirkgard, M.M. & Lade, P.V. (1991), "Anisotropy of normally consolidated San Francisco Bay Mud". Geotech. Test. J., ASTM 14 (3), 231-246.

Kirkgard, M.M. & Lade, P.V. (1993), "Anisotropic three-dimensional behavior of a normally consolidated Clay". Can. Geotech. J. 30(4), 848-858.

Lade, P.V. & Duncan, J.M. (1975), "Elastoplastic stress-Strain theory for cohesionless soil". J. Geotech. Eng. Div. ASCE 101 (GT10), 1037-1053.

Lade, P.V. (1977), "Elasto-plastic stress–strain theory for cohesionless soil with curved yield surfaces". Int. J. Solids Struct. 13(11), 1019-1035.

Lade, P.V. (2007), "Modeling failure in cross-anisotropic frictional materials". Int. J. Solids Struct. 44(16), 5146-5162.

Lade, P.V. (2008), "Failure criterion for cross-anisotropic soils". J. Geotech. and Geoenvir. Eng. ASCE 134 (1), 117-124.

Lade, P.V. & Kirkgard, M.M. (2000), "Effects of stress rotation and changes of b-values on cross-anisotropic behavior of natural K0-consolidated soft clay". Soils Found. 40(6), 93-105.

Lade, P.V., Nam, J. & Hong, W.P. (2008), "Shear banding and cross-anisotropic behavior observed in laboratory sand tests with stress rotation". Can. Geotech. J. 45, 74-84.

Lam, W.K. & Tatsuoka, F. (1988), "Effects of initial anisotropic fabric and σ_2 on strength and deformation characteristics of sand". Soils Found. 28(1), 89-106.

Lee, Y.K. & Pietruszczak, Z. (2008), "Application of critical plane approach to the prediction of strength anisotropy in transversely isotropic rock masses". Int. J. Rock Mech. Min. Sci. 45(4), 513-523.
Liu, M.D. & Carter, J.P. (2003), "General strength criterion for geomaterials". Int. J. Geomech. ASCE 3(2), 253-259.
Matsuoka, H. & Nakai, T. (1974), "Stress-deformation and strength characteristics of soil under different principal stresses". Proc., JSCE 232, 59-70.
Mortara, G. (2009), "A yield criterion for isotropic and cross-anisotropic cohesive-frictional materials". Int. J. Numer. Anal. Meth. Geomech. In press.
Niandou, H., Shao, J.F., Henry, J.P. & Fourmaintraux, D. (1997), "Laboratory investigation of the behaviour of Tournemire shale". Int. J. Rock Mech. Min. Sci. 34(1), 3-16.
Nishimura, S., Minh, N.A. & Jardine, R.J. (2007), "Shear strength anisotropy of natural London clay". Géotechnique 57(1), 49-62.
Ochiai, H. & Lade, P.V. (1983), "Three-dimensional behavior of sand with anisotropic fabric". J. Geotech. Eng. 109(10), 1313-1328.
Oda, M., Koishikawa, I. & Higuchi, T. (1978), "Experimental study of anisotropic shear strength of sand by plane strain test". Soils Found. 18(1), 25-38.
Pietruszczak, S. & Mroz, Z. (2000), "Formulation of anisotropic failure criteria incorporating a microstructure tensor". Comput. Geotech. 26 (2), 105-112.
Pietruszczak, S. & Mroz, Z. (2001), "On failure criteria for anisotropic cohesive-frictional materials". Int. J. Numer. Anal. Meth. Geomech. 25(5), 509-524.
Pietruszczak, S., Lydzba, D. & Shao, J.F. (2002), "Modelling of inherent anisotropy in sedimentary rocks". Int. J. Solids Struct. 39, 637-48.
Schweiger, H.F., Wiltafsky, C., Scharinger, F. & Galavi, V. (2009), "A multilaminate framework for modelling induced and inherent anisotropy of soils". Géotechnique 59(2), 87-101.
Tatsuoka, F., Nakamura, S., Huang, C.C. & Tani, K. (1990), "Strength anisotropy and shear band direction in plane strain tests of sand". Soils Found. 30(1), 35-54.
van Eekelen, H.A.M. (1980), "Isotropic yield surface in three dimensions for use in soil mechanics". Int. J. Numer. Anal. Meth. Geomech. 4(1), 89-101.
Wang, Q. & Lade, P.V. (2001), "Shear banding in true triaxial tests and its effect on failure in sand". J. Eng. Mech. ASCE 127(8), 754-761.
Yao, Y.P., Lu, D.C., Zhou A.N. & Zou, B. (2004), "Generalized non-linear strength theory and transformed stress space". Sci. China E: Tech. Sci. 47(6), 691-709.
Yong, R.N. & Silvestri, V. (1979), "Anisotropic behaviour of a sensitive clay". Can. Geotech. J. 16, 335-350.

MULTISCALE APPROACH FOR GRANULAR MATERIALS INCLUDING AN INTERMEDIATE SCALE

F. Nicot
Cemagref, ETNA, Geomechanics Group, Grenoble, France

F. Darve
Laboratory 3S-R, INPG-UJF-CNRS, Grenoble, France

ABSTRACT: *This paper proposes an advanced micromechanical model that introduces an intermediate scale (mesoscopic scale): elementary hexagonal patterns of adjoining particles. This is a breakthrough with respect to current micromechanical models that generally describe the material by a single distribution of contacts. In essence, such models can incorporate a variety of local physical mechanisms. In this paper, the occurrence of diffuse failure is investigated, and the existence of a broad bifurcation domain inside the plastic limit surface is verified.*

1 INTRODUCTION

Numerous materials can be regarded as granular – or quasi-granular – because a scale at which the granular micro-structure clearly appears can be defined. This scale is often denoted the microscopic scale. The micro-structure is composed of an assembly of elementary particles whose contact interactions can be described by simple laws. On the macroscopic scale, these materials behave as continuous media with an acceptable approximation; in a sample containing a sufficient number of particles, the granular structure may indeed no longer be visible, even if it continues to play a fundamental role on the macroscopic mechanical behavior. The local behavior on the contact scale can usually be simulated in a very straightforward manner by elastic–plastic laws to address the overall behavior of the assembly. In fact, the complexity of the constitutive behavior of granular assemblies does not stem only from the local properties, but also from the disordered packing. In the particular case of frictional granular materials that is considered throughout this paper, the influence of the packing is of paramount importance, since the local behavior can be roughly described by a simple elastic-plastic relation including Coulomb's solid friction law. As a result, there is a clear advantage to developing constitutive models that embed a refined description of the micro-structure of the material.

In the continuity of the micro-directional model, the hexagonal model recently developed is presented here. It is shown how incorporating an intermediate scale is advantageous.

2 A BRIEF REVIEW OF THE MICRO-DIRECTIONAL MODEL

The micro-directional model was initially developed to describe the mechanical behavior of snow (Nicot, 2003). Then, the model was generalized to any type of granular assembly, with a particular emphasis on frictional granular materials (Nicot and Darve, 2005).

The micro-directional model, which is formulated in a small-strain Eulerian formulation, allows the Cauchy stress tensor $d\sigma$ to be related to the small strain tensor $d\varepsilon$ by taking micro-mechanical characteristics into account. The reverse scheme can also be considered: starting from a given stress tensor $d\sigma$, the small strain tensor $d\varepsilon$ is deduced (Cambou *et al.*, 1995; Chang and Hicher, 2005). Fundamentally, this model is based on a homogenization/localization procedure (Fig. 1) within a representative volume element (RVE), which is assumed to contain a sufficient number of spherical grains (or contacts). The homogenization/localization procedure can be resolved in three stages that are very briefly reviewed here (For more details, see Nicot and Darve, 2005).

The stress averaging corresponds to the Love formula (Love, 1927; Mehrabadi *et al.*, 1982):

$$\sigma_{ij} = \frac{1}{V} \sum_{c=1}^{N_c} F_i^c \, l_j^c \tag{1}$$

where $\mathbf{l}^c$ is the branch vector joining the centers of particles in contact on contact *c*, $\overrightarrow{F^c}$ is the contact force, and the sum is extended to all the N_c contacts occurring in the RVE of volume V. The norm of the branch vector $\mathbf{l}^c$ is assumed to be a constant parameter (equal to the mean diameter of the grains) whose evolution over loading programs is ignored. This ensures that the terms $\mathbf{F}^c$ and $\mathbf{l}^c$ are uncorrelated. The discrete summation given in Eq. (2) can be replaced with a continuous integration over all the contact directions in the physical space. This scheme confers the directional character to the model:

$$\sigma_{ij} = 2 r_g \iint_D \hat{F}_i \, n_j \, \omega \, d\Omega \tag{2}$$

where ω is the density of contacts along each space direction $\mathbf{n}$, r_g denotes the mean radius of the sphere-shaped grains, $\hat{\mathbf{F}}$ is the average of all contact forces $\mathbf{F}^c$ associated with contacts oriented in the direction $\mathbf{n}$, $d\Omega$ is the elementary solid angle and the integration surface D is the half sphere.

The kinematic localization is given by:

$$d\hat{u}_i(\vec{n}) = 2 r_g \, d\varepsilon_{ij} \, n_j \tag{3}$$

where $\hat{\mathbf{u}}(\mathbf{n})$ is the kinematic variable linked to $\hat{\mathbf{F}}(\mathbf{n})$ along the contact direction $\mathbf{n}$. As $\hat{\mathbf{u}}(\mathbf{n})$ depends only on the direction $\mathbf{n}$, this term is also denoted the directional kinematic variable.

The local behavior is described properly using an elastic-plastic mechanical model relating both the local normal force F_n^c and the local tangential force F_t^c to both the local normal relative displacement u_n^c and the local tangential relative displacement u_t^c. This model includes a Mohr-Coulomb criterion and can be expressed under the following incremental formalism, which introduces a normal elastic stiffness k_n and a tangential elastic stiffness k_t, both constant, and a local friction angle φ_g

The micro-directional model takes into account the change in the fabric of the granular assembly by directly modeling the increase or the decrease in the number of contacts along each direction of the physical space. In this approach, the number of contacts along a given direction is not computed from any fabric tensor, but is related to the normal strain rate along this direction. Following pioneering work based on physical evidence (Oda, 1972), it is thought that the number of contacts increases along contractive directions, whereas it decreases along dilative directions. Therefore, the distribution of contacts is likely to evolve over a loading path, inducing anisotropy to the texture (see Nicot and Darve, 2005, for more details).

3 THE *H* MICRO-DIRECTIONAL MODEL

The main weakness of the micro-directional model is related to the kinematic description (Eq. 3), inducing a too large stiffness along the principal loading direction. The global stiffness of a granular assembly does not stem only from the contact stiffness, but also from the ability of the assembly for rearranging. Thus, limiting our investigation to two-dimensional conditions, an intermediate scale, made up of an hexagonal patterns of grains, is introduced.

Basically, the granular assembly is described by a distribution of regular hexagonal patterns of grains (Fig. 1). Each hexagon is assumed to deform symmetrically with respect to a given direction $\mathbf{n}$ (Fig. 2). Then, given a macroscopic incremental strain, the balance equations of each hexagon of volume $V(\mathbf{n})$ can be solved, yielding both the strained configuration and internal forces. In elastic regime, we have (see Fig. 2 for the definition of the symbols used):

$$\begin{bmatrix} 2\cos\alpha & 1 & -2d_1\sin\alpha \\ 2\sin\alpha & 0 & 2d_1\cos\alpha \\ \cos\alpha & -1 & \dfrac{(k_t\, d_1 + N_1)\sin\alpha - T_1\cos\alpha}{k_n} \end{bmatrix} \begin{bmatrix} \delta d_1 \\ \delta d_2 \\ \delta\alpha \end{bmatrix} = \begin{bmatrix} \delta l_1 \\ \delta l_2 \\ 0 \end{bmatrix} \tag{4}$$

and in plastic regime,

$$\begin{bmatrix} 2\cos\alpha & 1 & -2d_1\sin\alpha \\ 2\sin\alpha & 0 & 2d_1\cos\alpha \\ \cos\alpha & -1 & \dfrac{N_1\sin\alpha - T_1\cos\alpha}{k_n} \end{bmatrix} \begin{bmatrix} \delta d_1 \\ \delta d_2 \\ \delta\alpha \end{bmatrix} = \begin{bmatrix} \delta l_1 \\ \delta l_2 \\ -\dfrac{\delta T_1\sin\alpha}{k_n} \end{bmatrix} \tag{5}$$

Averaging all incremental contact forces over the overall specimen gives the macroscopic incremental stress tensor (Love formula):

$$\underline{\underline{\sigma}} = \frac{1}{V}\int \omega_e(\vec{n})\, \underline{\underline{P}}^{-1} \begin{bmatrix} V(\vec{n})\,\tilde{\sigma}_1 & 0 \\ 0 & V(\vec{n})\,\tilde{\sigma}_2 \end{bmatrix} \underline{\underline{P}}\, d\theta \tag{6}$$

with

$$V(\vec{n})\,\tilde{\sigma}_1 = 4N_1\, d_1\cos^2\alpha - 4T_1\, d_1\cos\alpha\sin\alpha + 2N_2\, d_2 \tag{7}$$

$$V(\vec{n})\,\tilde{\sigma}_2 = 4N_1\, d_1\sin^2\alpha + 4T_1\, d_1\cos\alpha\sin\alpha \tag{8}$$

$$\underline{\underline{P}} = \begin{bmatrix} \cos\theta & \sin\theta \\ -\sin\theta & \cos\theta \end{bmatrix} \tag{9}$$

A major difference with respect to the micro-directional model (Nicot and Darve, 2005), is that grains appear explicitly, giving rise to both solid and void (or, more generally, internal fluid) phases. Moreover, the compressibility of the specimen is mainly due to the relative sliding between particles, rather than to the normal stiffness at contacts. This is a great advantage, giving rise to more realistic simulations of the mechanical response of granular assemblies. A first example of simulation of the response of a dense specimen over a drained biaxial test (after an initial isotropic compression at 200 kPa) is reported in Fig. 3. For this simulation, $k_n = 1000$ kN/m, $k_t = 500$ kN/m and $\varphi_g = 20$ degree. As seen in Figs. 3 and 4, the simulated response is qualitatively satisfying. The stress peak is obtained at a small strain (2%), and then a softening regime is observed. The macroscopic friction angle is 31 degrees at the peak. This is a typical response for dense materials, as confirmed by the volumetric

strain response shown in Fig. 4: after initial contractant behavior, a dilatant regime develops. It must be noted that the softening regime obtained is constitutive, as both stress and strain are considered homogeneous. It is associated with no geometrical effect that would lead to kinematical discontinuities.

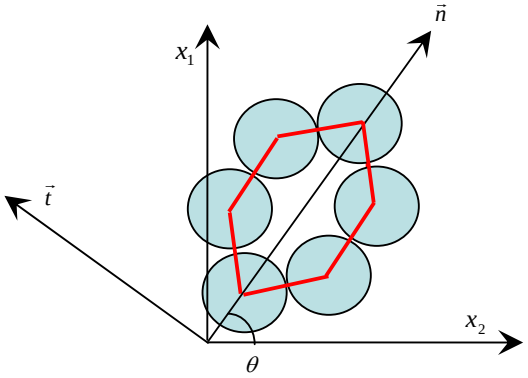

Fig. 1. Hexagonal set of contacting particles.

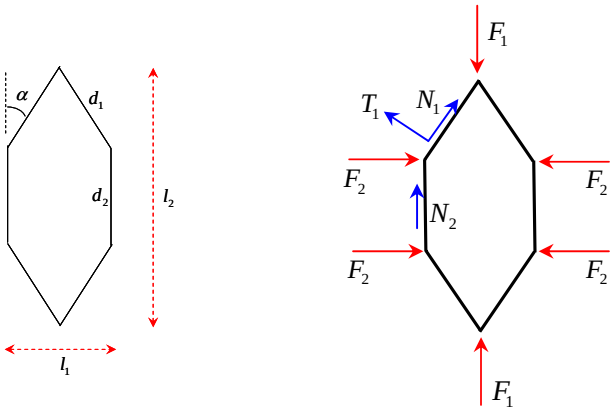

Fig. 2. Geometrical description and external forces applied to each hexagon.

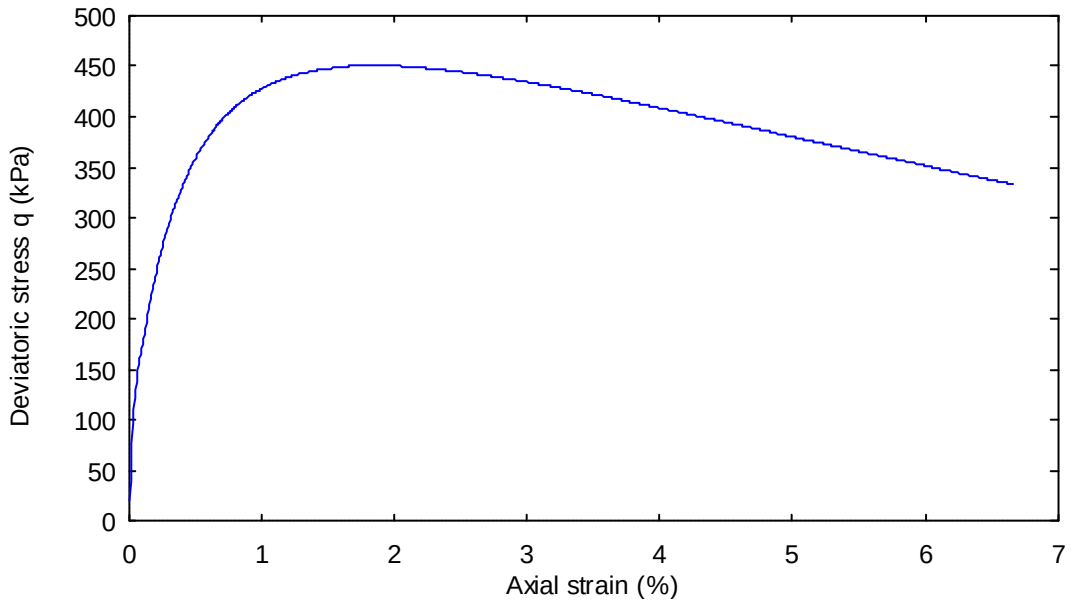

Fig. 3. Response over a drained biaxial test using the *H*-microdirectional model. Evolution of the deviatoric stress versus the axial strain.

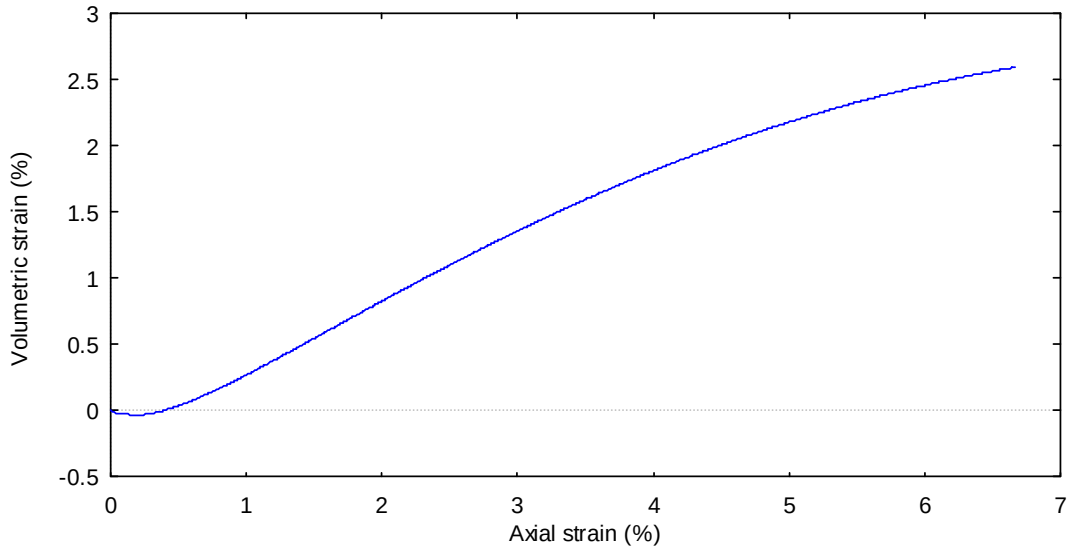

Fig. 4. Response over a drained biaxial test using the *H*-microdirectional model. Evolution of the volumetric strain versus the axial strain.

4 INSTABILITY ANALYSIS

It is of a great interest to investigate the occurrence of instability by using micromechanical models. Such enriched models can give rise to a wide set of different failure modes, such as, for example, the diffuse failure. The diffuse failure of a material is characterized by the abrupt collapse of the material, associated with a chaotic kinematic field. No localization pattern is visible. At the material point scale, such a failure mode is detected by the vanishing of determinant of the symmetric part $\mathbf{K}_s$ of the constitutive tensor $\mathbf{K}$. In two-dimensional conditions, and without rotation of the principal axes, the constitutive tensor $\mathbf{K}$ relates both the incremental stress ($\delta\sigma_1, \delta\sigma_2$) to the incremental strain ($\delta\varepsilon_1, \delta\varepsilon_2$). In fact, it can be shown that the vanishing of the determinant of $\mathbf{K}_s$ corresponds also to the existence of incremental strain directions vanishing the second-order work W_2, where $W_2 = \delta\sigma_i \, \delta\varepsilon_i$ (Darve et al., 2004). Let ($\delta\overline{\varepsilon}_1, \delta\overline{\varepsilon}_2$) be such a direction, that can be also characterized by the ratio $\overline{R} = \delta\overline{\varepsilon}_2 / \delta\overline{\varepsilon}_1$. If proportional strain paths are considered (the axial strain rate $\delta\varepsilon_1$, the proportional condition $\delta\varepsilon_2 = R\,\delta\varepsilon_1$ is prescribed where R is constant), this also means that the curve of the conjugate stress variable $\sigma_1 + R\,\sigma_2$ against the axial strain ε_1 passes through a peak for R lower than the critical value $\overline{R}$ (Nicot et al., 2009; Prunier et al., 2009).

To exemplify this, the simulation of such proportional strain loading paths was run, using the same parameters as those given in section 3. The initial confining pressure was also fixed to 200 kPa. As reported in Fig. 5, for R values lower than $R = -1.2$, the curves of $\sigma_1 + R\,\sigma_2$ against ε_1 passes through a peak. At the peak, the second order work is negative or nil, corresponding to the existence of a singular matrix $\mathbf{K}_s$. According to the theoretical background (Nova, 1994; Darve et al., 2004; Nicot and Darve, 2007), an abrupt collapse of the specimen is expected if any additional loading is applied at the peak, or along the descending branch. The ability of the micro-directional model to give rise to diffuse failure was ever discussed (Nicot and Darve, 2006). The above results show that this feature remains with the *H* micro-directional model. This result confirms the relevance of such micro mechanical approaches to investigate failure issues, in relation for instance with mechanical properties degradation.

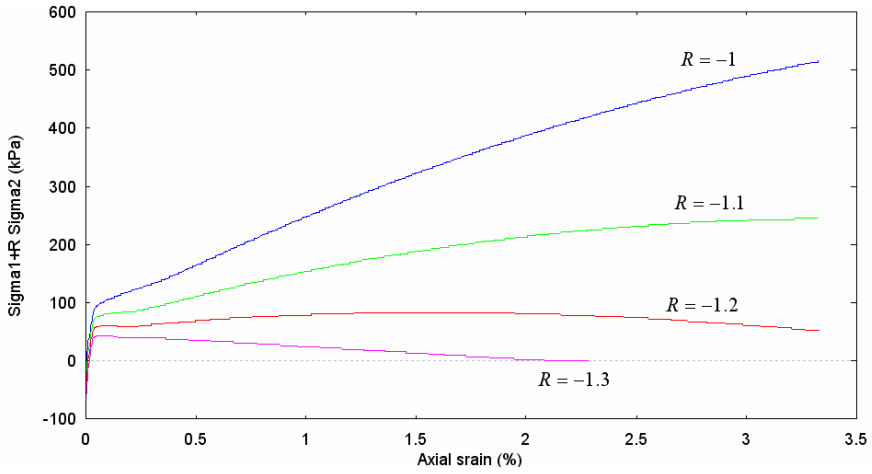

Fig. 5. Response over a proportional strain loading path using the H micro-directional model.

5 CONCLUDING REMARKS

This paper has presented the *H*-microdirectional model (Nicot and Darve, 2010), that introduces an intermediate scale between the microscopic scale and the REV scale. This multiscale model is based on a homogenization procedure that involves successively three scales: a microscopic scale, corresponding to the grain scale, a mesoscopic scale related to a hexagonal pattern of grains, and the whole assembly macroscopic scale. As such, the model allows relating the different scales, by expressing macroscopic terms from microscopic variables. The main advantage of this model, with respect to standard micromechanical approaches (Nicot and Darve, 2005) is that elementary grains patters are introduced. The deformation of such patterns results from the relative sliding between grains, rather that the deformation of grains. This leads to a more realistic kinematic description of grain assemblies, leaving aside the classical affine kinematic localization relation.

The capability of the model to exhibit a wide bifurcation domain was shown. By simulating proportional strain paths, it was shown that limit states could be obtained well before the plastic limit is reached.

This investigation draws new perspectives in the understanding of the key mechanisms leading to the failure of granular specimens. Numerical simulations based on a discrete element method are now in progress in order to examine the influence of the internal inertial mechanisms in the macroscopic destabilization of granular specimens.

REFERENCES

Cambou, B., Dubujet, P., Emeriault, F., and Sidoroff, F. (1995): Homogenization for granular materials. *European Journal of Mechanics, A/Solids*, Vol. 14, n° 2, pp. 255-276.

Chang, C.S., and Hicher, P.Y. (2005): An elasto-plastic model for granular materials with microstructural consideration. *Int. J. of Solids and Structures*, Vol. 42(14), pp. 4258-4277.

Darve, F., Servant, G., Laouafa, F., and Khoa H.D.V. (2004): Failure in geomaterials, continuous and discrete analyses. *Comp. Methods Appl. Mech. Engrg.*, Vol. 193, pp. 3057-3085.

Love, A.E.H. (1927): A treatise of mathematical theory of elasticity. Cambridge University Press, Cambridge.

Mehrabadi, M.M., Oda, M., and Nemat-Nasser, S. (1982) : On statistical description of stress and fabric in granular materials. *Int. J. Num. Anal. Meth. Geomech.*, Vol. 6, pp. 95-108.

Nicot, F. (2003): Constitutive modelling of a snowcover with a change in scale. *European Journal of Mechanics (A / Solids)*, Vol. 22-3, pp. 325-340.

Nicot, F., and Darve, F. (2005): A multiscale approach to granular materials. *Mechanics of Materials*, Vol. 37 (9), pp. 980-1006.

Nicot, F., and Darve, F. (2006): Micro-mechanical investigation of material instability in granular assemblies. *Int. J. of Solids and Structures*, Vol. 43, pp. 3569-3595.

Nicot, F., and Darve, F. (2007): A micro-mechanical investigation of bifurcation in granular materials. *Int. J. of Solids and Structures*, Vol. 44, pp. 6630-6652.

Nicot, F., Sibille, L., and Darve, F. (2009): Bifurcation in granular materials: an attempt at a unified framework. *Int. J. of Solids and Structures*, Vol. 46, pp. 3938–3947.

Nicot, F., and Darve, F. (2010): The H-microdirectional model: accounting for a mesoscopic scale. Mechanics of Materials, *submitted*.

Nova, R. (1994): Controllability of the incremental response of soil specimens subjected to arbitrary loading programs. *Journal of Mechanical behavior of Materials*, Vol. 5, n° 2, pp. 193-201.

Oda, M. (1972): The mechanism of fabric changes during compressional deformation of sand. *Soils and Foundations*, Vol. 12, pp. 1- 23.

Prunier, F, Nicot, F., Darve, F., Laouafa, F., and Lignon, S. (2009): 3D multiscale bifurcation analysis of granular media. *J. of Eng. Mechanics* (ASCE), Vol. 135(6), pp. 1-17.

MODELLING THE ONSET OF RAINFALL-INDUCED LANDSLIDES

G. Buscarnera
Department of Structural Engineering,Politecnico di Milano, Milano, Italy

C. di Prisco
Department of Structural Engineering,Politecnico di Milano, Milano, Italy

ABSTRACT: *The paper presents a simplified modelling approach for unsaturated infinite slopes. As it is well known, during severe rainstorms the progressive saturation of natural deposits is the main triggering cause of slope instability. The goal of the approach suggested here is to evaluate the magnitude of the triggering perturbations, distinguishing among different forms of hydro-mechanical instability. For this purpose, the mechanical effects of partial saturation are reproduced by means of a coupled hydro-mechanical constitutive model and stability conditions are evaluated through the theory of test controllability. This enables to study the outcome of both mechanical and hydraulic perturbations by means of simple shear test simulations. The numerical results clearly suggest that both initial conditions (e.g., the initial suction) and behavioural properties (e.g., the soil compressibility) are dominant factors in determining the magnitude of the triggering perturbations and the type of expected instability mode.*

1 INTRODUCTION

The evaluation of stability conditions for natural slopes is a complex task which requires the use of consistent geomechanical approaches. Unfortunately, very often the notion of instability is not used in a proper mechanical sense (Nova, 2001), and the analyses are often restricted to the study of localized shear failure modes. The major implication of this common engineering practice is that many instability phenomena exhibited by geomaterials can be overlooked, preventing from the possibility of analysing important classes of natural phenomena. The most striking example of slope failures departing from classical conceptual schemes is the case of flow slides. In these cases, the slide is originated by liquefaction processes, and the slope suffers a dramatic and rapid collapse which cannot be explained by standard methods of analyses. Flow slides (i) initiate at mobilized stress levels strictly within the shear failure domain and (ii) are characterized by a distributed (or diffuse) instability mode involving large portions of the soil deposits. Advanced methods are therefore required to address these phenomena and appropriate instability indices must be used to assess the susceptibility to liquefaction and the magnitude of triggering perturbations (di Prisco et al. (1995), Laouafa and Darve (2002)).

Hereafter, the principles of geomaterial instability are applied to the triggering analysis of rapid landslides provoked by rainstorms. Also these natural phenomena often evolve into flow-like mass movements, whose features resemble flow slides in subaqueous slopes and the complexity of the problem requires extension of the classical notion of material instability to include unsaturated soils.

In the following, an innovative methodology, aimed at predicting the onset of generalized hydro-mechanical instability resulting from saturation processes, is proposed. This extension is based on three main cornerstones: (i) a coupled constitutive model including hydraulic hardening/softening processes deriving from suction changes (Buscarnera and Nova, 2009-a); (ii) a theoretical approach predicting possible activation of latent instabilities in unsaturated soils (Buscarnera and Nova, 2009-b; Buscarnera and di Prisco, 2010) and (iii) the application to ideal infinite slopes by means of the simplified approach proposed by di Prisco et al. (1995).

To achieve this goal, the response of the slope is simulated through material point analyses. In particular, simple shear simulations are used to describe the effects of soil deposition, shearing processes and suction changes. Critical mechanical and hydraulic perturbations are predicted and the influence of slope inclination, thickness of the deposit and initial suction is discussed.

2 HYDRO-MECHANICAL INSTABILITY: CONSTITUTIVE MODEL AND THEORETICAL FRAMEWORK

2.1 Coupled hydro-mechanical constitutive approach for unsaturated soils

The study of material stability in unsaturated soils requires the definition of an appropriate constitutive model for this class of materials. A variety of constitutive models exist for unsaturated geomaterials, many of them relying on the theory of strain-hardening elastoplasticity. Comprehensive reviews of recent models in this area of geomechanics are given by Nuth and Laloui (2008) and Gens (2010). This paper uses a modelling approach deriving from a constitutive law originally conceived to reproduce several forms of instability in saturated geomaterials (Nova et al. 2003). This model has been adaptated to unsaturated conditions using the constitutive approach proposed by Jommi and di Prisco (1994) and the work conjugate framework suggested by Houlsby (1997). Thus, the model is based on the use of the following stress measures:

$$\sigma_{ij}^{"} = \sigma_{ij} - \left[S_r \cdot u_w + (1 - S_r) \cdot u_a \right] \delta_{ij} \text{, and } s^* = ns \tag{1}$$

where σ_{ij} is the total stress, u_w the pore water pressure, u_a the air pore pressure, $s = u_a - u_w$ the suction, n the porosity, S_r the degree of saturation and δ_{ij} is the Kronecker delta. The skeleton stress $\sigma_{ij}^{"}$ represents a mechanical stress-like variable, while s^* plays the role of a hydraulic stress-like variable. The stress measures given by (1) are work conjugate to two generalised strain variables, given by:

$$\varepsilon_{ij} \text{ and } -S_r \tag{2}$$

being respectively the mechanical and the hydraulic work conjugate strain measures.

Starting from these premises, the model has been formulated in a coupled hydro-mechanical form. The constitutive law is in fact based on an extended formulation, including modified suction and degree of saturation as additional generalised stress-strain variables, as follows:

$$\dot{\boldsymbol{\Sigma}} = \begin{Bmatrix} \dot{\sigma}_{ij}^{''} \\ \dot{s}^{*} \end{Bmatrix} = \begin{bmatrix} \mathbf{D}_{\boldsymbol{\sigma\sigma}} & \mathbf{D}_{\boldsymbol{\sigma w}} \\ \mathbf{D}_{\mathbf{w}\boldsymbol{\sigma}} & \mathbf{D}_{\mathbf{ww}} \end{bmatrix} \cdot \begin{Bmatrix} \dot{\varepsilon}_{ij} \\ -\dot{S}_r \end{Bmatrix} = \mathbf{D}_{\mathbf{ext}} \cdot \dot{\mathbf{E}} \tag{3}$$

A detailed description of both the constitutive functions and the mechanical implications resulting from hydro-mechanical coupling is in Buscarnera and Nova (2009).

2.2 Test controllability for unsaturated soils

Several approaches can be used to study stability conditions in geomaterials. Hereafter, the stability of unsaturated specimen is approached by means of material point analyses. This strategy follows the concepts expounded by Nova and co-workers (Nova, 1994; Imposimato and Nova, 1998) into the so-called theory of test controllability. This theory has been recently extended to unsaturated soils (Buscarnera and Nova, 2009-b; Buscarnera and di Prisco, 2010): appropriate scalar instability indices, derived from the definition of both a set of hydro-mechanical control parameters and an extended coupled constitutive matrix, are introduced.

In order to illustrate the basics of the theory, let us consider two sets of variables: the incremental control variables, $\dot{\phi}$, and the associated response variables, $\dot{\psi}$. These two sets of variables are related through the following expression:

$$\dot{\phi} = \mathbf{X}\dot{\psi} \tag{4}$$

where $\mathbf{X}$ is the coupled control matrix. Once the type of perturbation is defined, a potential instability is associated with the singularity of matrix $\mathbf{X}$, as follows:

$$\det(\mathbf{X}) = 0 \tag{5}$$

Particular expressions for $\mathbf{X}$ can be defined both for localised shear failure and wetting-induced volume collapse. These matrices will suffer a singularity when either the former or the latter instability mode is achieved, and their vanishing will be henceforth used for predictive purposes.

3 EVALUATING TRIGGERING PERTURBATIONS IN UNSATURATED SLOPES

3.1 Modelling methodology for infinite slopes: static and kinematic assumptions

The theory of test controllability is hereafter employed to assess stability conditions for infinite slopes. The kinematic constraints underlying such a simplified geometric assumption, in fact, are reflected by a particular set of control conditions. A brief outline of this methodology is reported here below. More comprehensive studies are provided by di Prisco et al. (1994) for the case of saturated subaqueous slopes and Buscarnera (2010) for the case of unsaturated subaerial slopes.

If the reference system of Figure 1 is considered, the mechanical behaviour of any point belonging to the slope can be modelled by means of the following set of constitutive equations:

$$\begin{Bmatrix} \dot{\sigma}''_{\xi} \\ \dot{\sigma}''_{\eta} \\ \dot{\sigma}''_{\chi} \\ \dot{\tau}_{\xi\eta} \\ \dot{\tau}_{\xi\chi} \\ \dot{\tau}_{\chi\eta} \\ \dot{s}^{*} \end{Bmatrix} = \begin{bmatrix} D_{11} & D_{12} & D_{13} & D_{14} & D_{15} & D_{16} & D_{17} \\ D_{21} & D_{22} & D_{23} & D_{24} & D_{25} & D_{26} & D_{27} \\ D_{31} & D_{32} & D_{33} & D_{34} & D_{35} & D_{36} & D_{37} \\ D_{41} & D_{42} & D_{43} & D_{44} & D_{45} & D_{46} & D_{47} \\ D_{51} & D_{52} & D_{53} & D_{54} & D_{55} & D_{56} & D_{57} \\ D_{61} & D_{62} & D_{63} & D_{64} & D_{65} & D_{66} & D_{67} \\ D_{71} & D_{72} & D_{73} & D_{74} & D_{75} & D_{76} & D_{77} \end{bmatrix} \begin{Bmatrix} \dot{\varepsilon}_{\xi} \\ \dot{\varepsilon}_{\eta} \\ \dot{\varepsilon}_{\chi} \\ \dot{\gamma}_{\xi\eta} \\ \dot{\gamma}_{\xi\chi} \\ \dot{\gamma}_{\chi\eta} \\ -\dot{S}_{r} \end{Bmatrix} \tag{6}$$

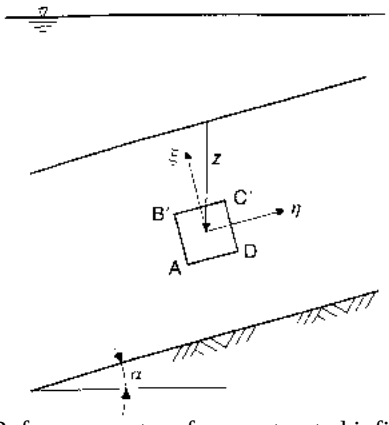

Figure 1. Reference system for unsaturated infinite slopes

Given the assumption of infinite slope, the kinematic constraints deriving from symmetry and plane strain conditions must be imposed. Therefore, four stain rate components in Equation (6) must be set equal to zero, being $\dot{\varepsilon}_{\chi} = \dot{\varepsilon}_{\eta} = \dot{\gamma}_{\xi\chi} = \dot{\gamma}_{\chi\eta} = 0$. In addition, constant total stress conditions will be assumed along the normal to the slope, imposing $\dot{\sigma}^{net}_{\xi} = \dot{\sigma}''_{\xi} - \dot{s}S_r - s\dot{S}_r = 0$.

The remaining hydro-mechanical conditions depend on the type of perturbation considered for the analysis. In the following, two situations are accounted for: suction and water content control. In the former case, suction increments will be governed, having $\dot{s} = 0$ during constant suction tests and $\dot{s} < 0$ during saturation processes. A direct control of water content will instead be used to model either rapid water undrained perturbations or water injection conditions on unsaturated slopes. Water undrained conditions imply $\dot{e}_w = \dot{e}S_r + e\dot{S}_r = 0$ (where $e_w = eS_r$ is the water ratio), while water volume injection is modelled by imposing $\dot{e}_w > 0$. The study of the latter hydro-mechanical constraint will be very important to envisage latent instability conditions.

3.2 Saturated infinite slopes: drained and undrained failure

A review of the most significant features of the mechanical response of infinite saturated slopes allows to better appreciate the engineering implications of partially saturated conditions. In particular, drained simple shear simulations enable the evaluation of the shear stresses inducing a localised shear failure (Rudnicki and Rice 1975), while undrained simple shear tests can be used to study static liquefaction and the onset of flow slides (di Prisco et al., 1995). In order to assess the effect of the slope angle on triggering perturbations, these two tests can be combined with a deposition stage prior to shearing (Figure 2).

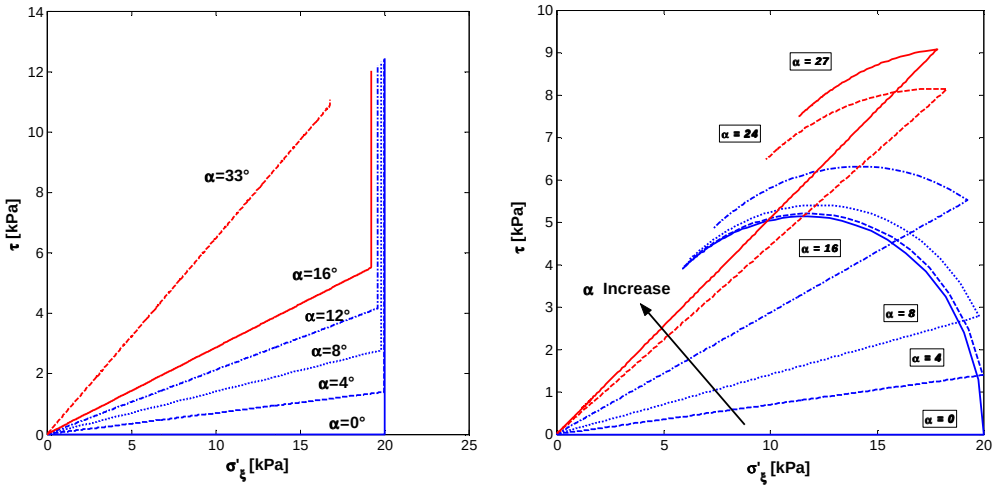

Figure 2. Examples of stress paths in the σ'_{ξ}-$\tau_{\xi\eta}$ plane: a) deposition followed by drained simple shear tests; b) deposition followed by undrained simple shear tests

As extensively outlined by di Prisco et al. (1995), if loose sandy slopes are considered, the magnitude of triggering perturbations and the range of critical slope angles associated with the two forms of instability can be quite different (Figure 3). In particular, static liquefaction becomes the most critical instability mode for gentle slopes, being spontaneous liquefaction possible even for very low inclinations. Figure 3-b shows that also the onset of seepage prior to shearing has a relevant influence on triggering perturbations ($\Delta\tau$) and critical slope angles.

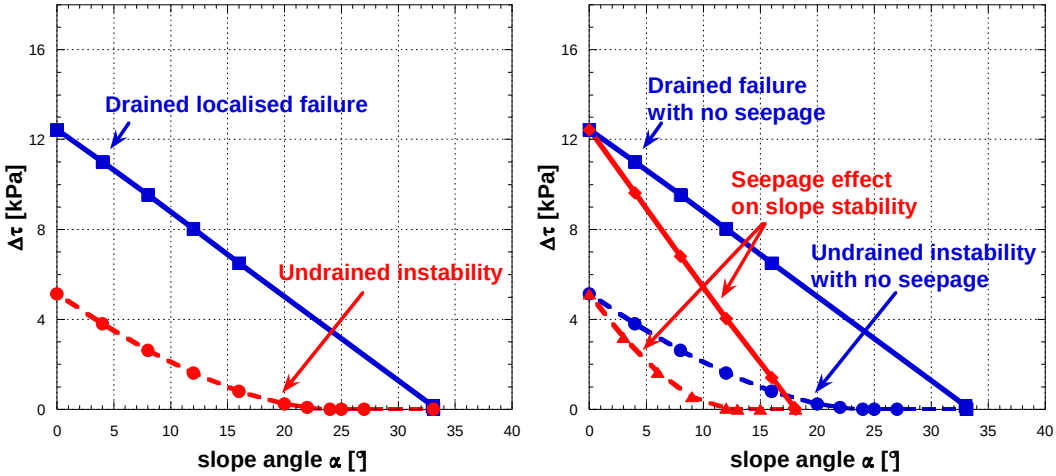

Figure 3. Comparison between drained and undrained failure modes: a) deposition followed by a shearing stage; b) deposition followed by stationary seepage (drained pre-shearing) and final shearing stage (layer 1m thick) .

3.3 Mechanical perturbations: influence of suction on stability conditions

As is well known, the effect of suction at the local level is to stabilise and strengthen the material. This stabilization results from the pre-stressing action exerted by capillary forces at the contacts among grains and provides the so-called *apparent cohesion*, i.e. the increase in shear strength associated with partially saturated conditions. As a result, unsaturated slopes can sustain inclinations much steeper than those the same slopes could sustain without such an additional strength contribution.

This concept is consistent with the well established knowledge in the field of unsaturated slope stability. Nevertheless, more comprehensive constitutive models can provide a deeper

insight into the failure mechanisms occurring in unsaturated slopes. When the slope failure is treated as a proper strain localization process, it is possible to better appreciate the role of plane strain kinematics, as well as capture changes in suction resulting from coupled loading conditions . In the following, these argumentations will be illustrated by means of *stability curves*, i.e. by means of graphical charts plotting the triggering perturbations as a function of the slope angle. In order to simplify the interpretation of the results, most of the curves are represented in a normalized form.

Figure 3 refers to localized shear failure under constant suction. The figure illustrates a summary of model predictions, plotting the value of triggering shear perturbations as a function of both slope angle and initial degree of saturation.

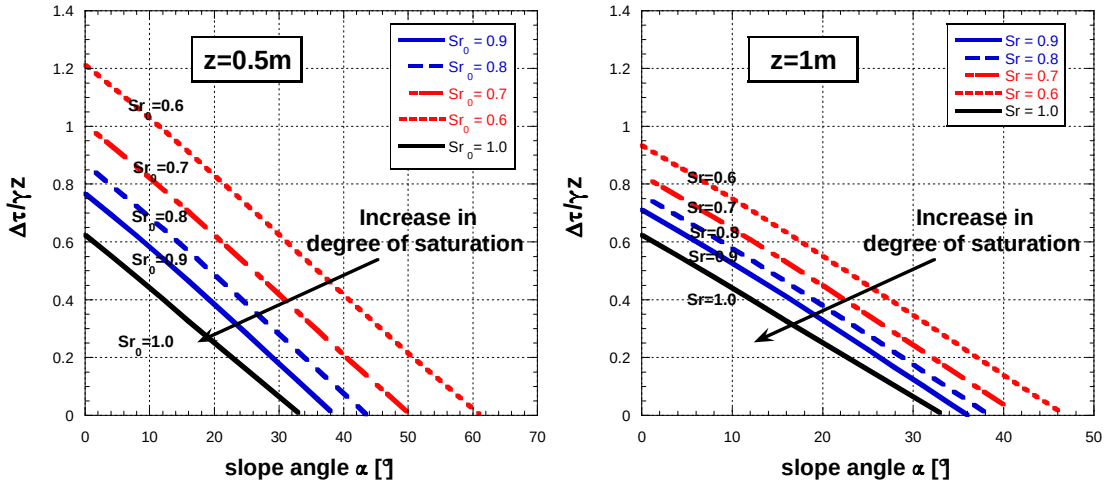

Figure 3. Normalized stability curves of triggering shear perturbations ($\Delta\tau/\gamma z$; γ=20 kN/m^3). The figure illustrates the effect of the slope inclination on the distance from incipient failure for a) z=0.5m and b) z=1m

A remarkable effect of the apparent cohesion is readily apparent. Larger initial suctions are associated with larger triggering perturbations (and, hence, with higher values for the safety factor F_S). However, the range of variation of critical perturbations, as well as the magnitude of the maximum slope angle, become progressively smaller as long as the vertical depth is increased, since the effect of apparent cohesion at larger depths reduces.

Another set of stability curves in terms of triggering perturbations can be also evaluated by imposing a water undrained constraint (Figure 4-a). The simulations show that a progressive increase in degree of saturation upon loading leads to a marked qualitative change of the curves. During loading, large plastic volumetric strains can take place, resulting into full saturation upon straining. As a result, a different type of instability can be predicted, in which soil liquefaction substitutes shear strain localization.

The transition from a typical localized failure mode to a volumetric collapse is chiefly governed by the susceptibility of the material to exhibit volumetric collapse during loading and/or saturation. Figure 4-b illustrates this effect, investigating the role of plastic volumetric compressibility (here reflected by the material constant B_p) on the stability curves of triggering perturbations.

Figure 4 shows a substantial reduction in critical water undrained shear perturbations as a result of an increase in soil compressibility. Most simulations characterised by high compressibility tend to develop a liquefaction instability, with the normalised stability curves moving towards that characterising fully saturated conditions. This change in the predicted failure mode reflects a significant change in the expected post-failure response of the slope. In other words, soils characterised by a potentially liquefiable undrained response and relevant plastic compressibility are particularly prone to give rise to catastrophic flow slides.

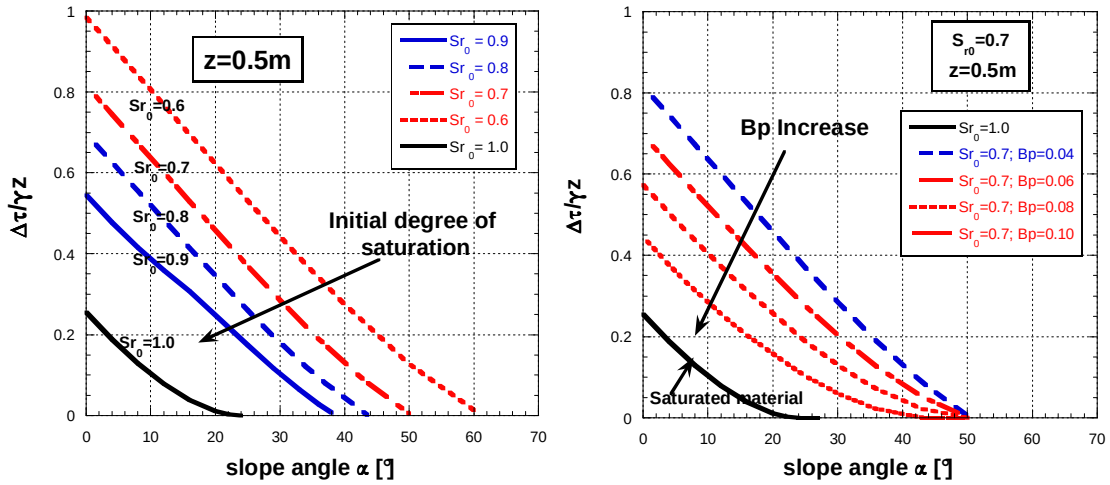

Figure 4. a) Normalized stability curves of triggering shear perturbations under constant water content ($\Delta\tau/\gamma z$; γ=20 kN/m^3); b) Role of soil compressibility on water undrained stability curves. Caratteri greci nelle ordinate

3.4 Hydraulic perturbations: potential instability induced by saturation processes

As is well known, the additional shear strength associated with capillary effects can disappear as a consequence of saturation processes and during rainfall events, suction decreases as long as water progressively infiltrates into the slope. Thus, the irreversible phenomena taking place because of saturation events can result either into remarkable volumetric deformations (wetting-collaspe) or shear failure modes. The modelling methodology outlined in the previous sections can provide a useful criterion to define the most likely type of instability that can be expected upon saturation.

The most common form of slope instability achieved during rainstorms is the localization of shear strains on a narrow band. This form of instability, often identified with the classic phenomenon of shear failure, results from the progressive vanishing of the apparent cohesion. If a slope is steeper than the angle of natural repose (α_{NR}, i.e. the maximum slope inclination under saturated/dry conditions), equilibrium conditions are guaranteed only because of the presence of the additional strength contributions provided by water menisci. Thus, whenever the reduction in suction is large enough, a slide may take place. The magnitude of hydraulic perturbation Δs (suction removal) depends on the initial degree of saturation, the slope angle and the depth of the soil veneer.

Figure 5 shows model prediction of hydraulic perturbations leading to localized shear failure. The values of critical variation of suction are normalized for the initial suction s_0. As was expected, initial suction and depth of the layer play an important role in defining the interval of slope angles susceptible to a landslide during saturation. The results show that rainfall-induced landslides with localised failure can occur only in steep slopes, i.e., when the inclination is larger than the angle of natural repose under saturated/dry conditions and the stability of the system is ensured by the presence of capillary contributions.

Even though shear strain localization is the most common form of instability mode, very often rainfall-induced slides evolve into fast flow-like movements. Such a transition implies a susceptibility of the material to liquefy. This possibility can be investigated by performing latent instability analyses. This terminology addresses a procedure through which, even though suction controlled saturation processes are numerically performed, the instability indices associated to water injection or water undrained loading are monitored: the evolution

of these indices allow to quantify the susceptibility of the system to a dramatic slope instability.

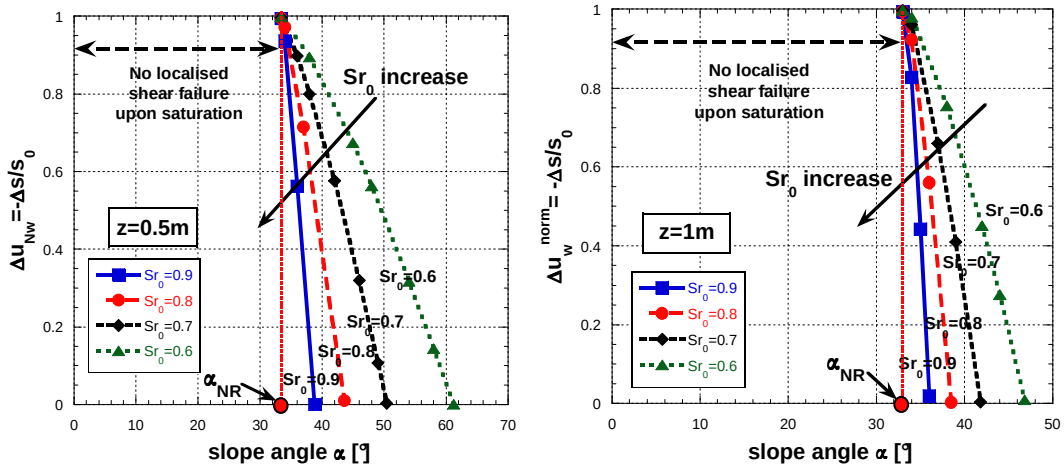

Figure 5. Normalized stability curves of hydraulic triggering perturbations (Δu_w is the normalised variation in pore water pressure; Δs is the change in suction; s_0 is the initial suction); a) z=0.5m and b) z=1m

An example of this type of analysis is illustrated in Figure 6, which refers to the simulation of a simple shear test with a final saturation stage under constant shear stress. The instability index for water injection vanishes for a degree of saturation lower than one, and hence before full saturation is achieved. The example shows that, contrary to common expectations, volumetric instabilities are possible even before shear failure or full saturation are achieved.

It can be concluded that latent instability may be in some cases the first unstable phenomenon arising during saturation. Also these simulations illustrate a significant dependence of these potential collapses on the magnitude of plastic volumetric compressibility (Figure 7). In particular, soils with higher plastic compressibility require smaller hydraulic perturbations to achieve latent instability and imply the initiation of slides even at slope angles lower than α_{NR}. Under these circumstances, latent instability can be considered to be more critical than localised shear failure, since it produces a more dramatic response respect to shear strain localization.

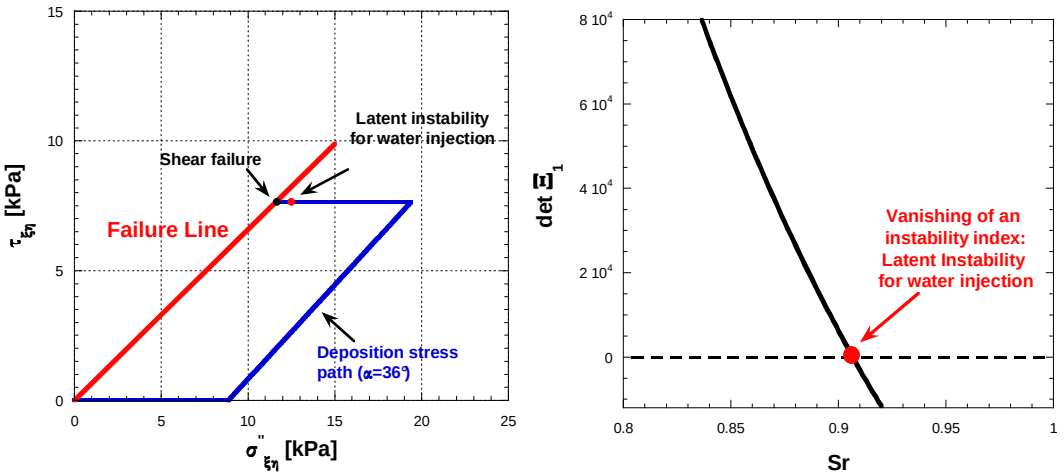

Figure 6. Simple shear saturation test under constant total stresses: a) stress path and stress state at instability; b) evolution of the instability index during saturation.

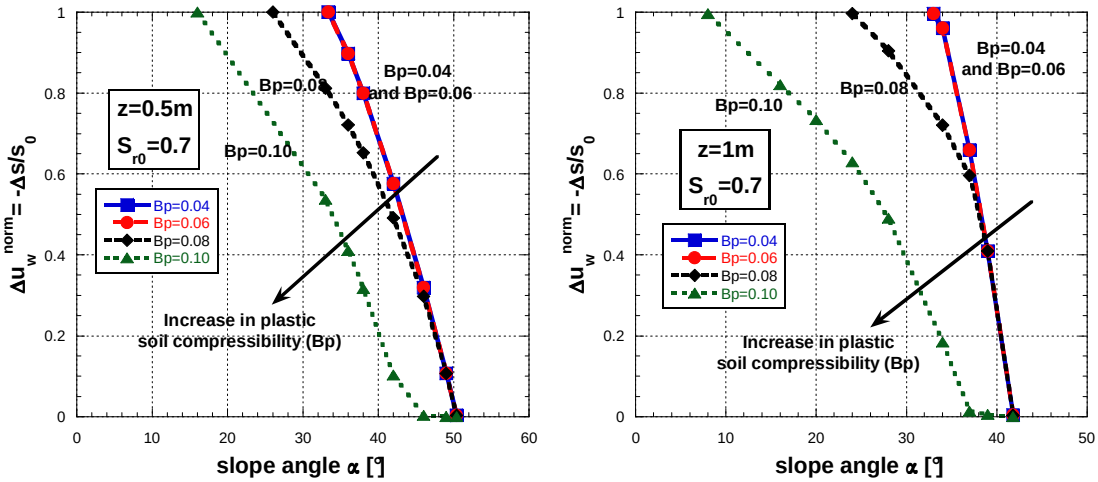

Figure 7. Stability curves of hydraulic perturbations (effect of plastic volumetric compressibility). a) z=0.5m; b= z=1m.

4 CONCLUSIONS

This paper described a simplified modelling methodology for the study of triggering mechanisms in natural slopes. Unsaturated conditions have been considered and both mechanical and hydraulic perturbations have been studied. The results of model predictions have been presented, reinterpreting them from a theoretical perspective. The main goals have been to improve the understanding of saturation-induced slope failure and establish a unified framework for studying both localised shear failure and flow-like instability.

For this purpose, the assumption of infinite slope has been used, considering both mechanical and hydraulic perturbations. The study focused on the evaluation of the environmental perturbations capable of triggering a slope failure. It has been shown that, depending on model parameters, two well distinguished types of triggering mechanisms can occur upon saturation: (i) a localised shear failure and (ii) a volumetric collapse followed by liquefaction. In particular, soil compressibility has been shown to play a crucial role in favouring either the former or the latter. While a material having low compressibility tends to suffer a localised shear failure with a shear band parallel to the slope, highly collapsible soils tend to exhibit a liquefaction instability taking place essentially because of purely hydraulic perturbations. Model simulations show that, contrary to common expectations, material saturation is not a necessary condition for this forms of slope failures to occur. Thus, a volumetric collapse followed by static liquefaction can take place when the saturation event is still proceeding, with a material which is not yet saturated at the inception of the collapse.

In other words, this paper shows that the application of the theory of test controllability to unsaturated slopes enables to study within a unified framework a number of different instability modes, like shear failure, wetting-induced collapses and static liquefaction. Thus, according to the authors, the methodology proposed in this work represents a promising starting point for a consistent evaluation of triggering perturbations for landslides and for the assessment of the most likely form of instability expected during rainfall events.

REFERENCES

Buscarnera, G. (2010) “Rainfall-induced flow slides: constitutive modelling, mechanical instability and theoretical interpretation. PhD Thesis, Politecnico di Torino.

Buscarnera, G. and Nova, R. (2009-a) “An elastoplastic strain-hardening model for soil behaviour allowing for hydraulic bonding-debonding effects”. *Int. J. Numer. Anal. Meth. Geomech*. 2009; 33:1055–1086.

Buscarnera, G., Nova, R. (2009-b). Modelling instabilities in triaxial testing on unsaturated soil specimens. Published online on the *Int. J. Numer. Anal. Meth. Geomech*. D.O.I. 10.1002/nag.832.

Buscarnera G., di Prisco C. (2010) “Discussing the definition of second-order work in unsaturated soils”. Published online on the *Int. J. Numer. Anal. Meth. Geomech*. D.O.I. 10.1002/nag.991.

di Prisco, C., Matiotti, R., Nova, R. (1995). Theoretical investigation of undrained stability of shallow submerged slopes. Géotechnique 45, pp. 479–496.

Gens, A. (2010) Soil-environment interactions in geotechnical engineering. Géotechnique; 60(1), 3-74.

Jommi, C. and di Prisco, C. (1994). “Un semplice approccio teorico per la modellazione del comportamento meccanico dei terreni granulari parzialmente saturi”. Atti Convegno sul Tema: Il Ruolo dei Fluidi nei Problemi di Ingegneria Geotecnica, Mondovı´, pp. 167–188.

Houlsby, G.T. (1997). “The work input to an unsaturated granular material”. Géotechnique, Vol. 47(1), 193–196.

Imposimato, S. and Nova, R. (1998) “An investigation on the uniqueness of the incremental response of elastoplastic models for virgin sand”. Mech. of Cohes.-Frict. Mat., Vol. 3, 65-87.

Laouafa, F., Darve, F. (2002). Modelling of slope failure by a material instability mechanism. Computers and Geotechnics, 29, 301-325.

Nova, R. (1994). Controllability of the incremental response of soil specimens subjected to arbitrary loading programmes. *J. Mech. behav. Mater.* 5 (2), pp. 193–201Nova, R. (2001). Analysis of the stability of slopes, invited lecture, XV Congrès Français de Mécanique, Nancy, 729-734.

Nova, R. (2001). Analysis of the stability of slopes, invited lecture, XV Congrès Français de Mécanique, Nancy, 729-734.

Nova, R. Castellanza, R. and Tamagnini, C. (2003) “A constitutive model for bonded geomaterials subject to mechanical and/or chemical degradation”. Int. J. Numer. Anal. Meth. Geomech. Vol. 27, 705-732.

Nuth, M., Laloui, L. (2008). Effective stress concept in unsaturated soils: Clarification and validation of a unified framework, *Int. J. Numer. and Anal. Meth. Geomech.*; 32: 771–801.

MULTISCALE APPROACH FOR GRANULAR MATERIALS INCLUDING AN INTERMEDIATE SCALE

F. Nicot
Cemagref, ETNA, Geomechanics Group, Grenoble, France

F. Darve
Laboratory 3S-R, INPG-UJF-CNRS, Grenoble, France

ABSTRACT: *This paper proposes an advanced micromechanical model that introduces an intermediate scale (mesoscopic scale): elementary hexagonal patterns of adjoining particles. This is a breakthrough with respect to current micromechanical models that generally describe the material by a single distribution of contacts. In essence, such models can incorporate a variety of local physical mechanisms. In this paper, the occurrence of diffuse failure is investigated, and the existence of a broad bifurcation domain inside the plastic limit surface is verified.*

1 INTRODUCTION

Numerous materials can be regarded as granular – or quasi-granular – because a scale at which the granular micro-structure clearly appears can be defined. This scale is often denoted the microscopic scale. The micro-structure is composed of an assembly of elementary particles whose contact interactions can be described by simple laws. On the macroscopic scale, these materials behave as continuous media with an acceptable approximation; in a sample containing a sufficient number of particles, the granular structure may indeed no longer be visible, even if it continues to play a fundamental role on the macroscopic mechanical behavior. The local behavior on the contact scale can usually be simulated in a very straightforward manner by elastic–plastic laws to address the overall behavior of the assembly. In fact, the complexity of the constitutive behavior of granular assemblies does not stem only from the local properties, but also from the disordered packing. In the particular case of frictional granular materials that is considered throughout this paper, the influence of the packing is of paramount importance, since the local behavior can be roughly described by a simple elastic-plastic relation including Coulomb's solid friction law. As a result, there is a clear advantage to developing constitutive models that embed a refined description of the micro-structure of the material.

In the continuity of the micro-directional model, the hexagonal model recently developed is presented here. It is shown how incorporating an intermediate scale is advantageous.

2 A BRIEF REVIEW OF THE MICRO-DIRECTIONAL MODEL

The micro-directional model was initially developed to describe the mechanical behavior of snow (Nicot, 2003). Then, the model was generalized to any type of granular assembly, with a particular emphasis on frictional granular materials (Nicot and Darve, 2005).

The micro-directional model, which is formulated in a small-strain Eulerian formulation, allows the Cauchy stress tensor $d\sigma$ to be related to the small strain tensor $d\varepsilon$ by taking micro-mechanical characteristics into account. The reverse scheme can also be considered: starting from a given stress tensor $d\sigma$, the small strain tensor $d\varepsilon$ is deduced (Cambou *et al.*, 1995; Chang and Hicher, 2005). Fundamentally, this model is based on a homogenization/localization procedure (Fig. 1) within a representative volume element (RVE), which is assumed to contain a sufficient number of spherical grains (or contacts). The homogenization/localization procedure can be resolved in three stages that are very briefly reviewed here (For more details, see Nicot and Darve, 2005).

The stress averaging corresponds to the Love formula (Love, 1927; Mehrabadi *et al.*, 1982):

$$\sigma_{ij} = \frac{1}{V} \sum_{c=1}^{N_c} F_i^c \, l_j^c \tag{1}$$

where $\mathbf{l}^c$ is the branch vector joining the centers of particles in contact on contact *c*, $\overrightarrow{F^c}$ is the contact force, and the sum is extended to all the N_c contacts occurring in the RVE of volume V. The norm of the branch vector $\mathbf{l}^c$ is assumed to be a constant parameter (equal to the mean diameter of the grains) whose evolution over loading programs is ignored. This ensures that the terms $\mathbf{F}^c$ and $\mathbf{l}^c$ are uncorrelated. The discrete summation given in Eq. (2) can be replaced with a continuous integration over all the contact directions in the physical space. This scheme confers the directional character to the model:

$$\sigma_{ij} = 2 r_g \iint_D \hat{F}_i \, n_j \, \omega \, d\Omega \tag{2}$$

where ω is the density of contacts along each space direction $\mathbf{n}$, r_g denotes the mean radius of the sphere-shaped grains, $\hat{\mathbf{F}}$ is the average of all contact forces $\mathbf{F}^c$ associated with contacts oriented in the direction $\mathbf{n}$, $d\Omega$ is the elementary solid angle and the integration surface D is the half sphere.

The kinematic localization is given by:

$$d\hat{u}_i(\vec{n}) = 2 r_g \, d\varepsilon_{ij} \, n_j \tag{3}$$

where $\hat{\mathbf{u}}(\mathbf{n})$ is the kinematic variable linked to $\hat{\mathbf{F}}(\mathbf{n})$ along the contact direction $\mathbf{n}$. As $\hat{\mathbf{u}}(\mathbf{n})$ depends only on the direction $\mathbf{n}$, this term is also denoted the directional kinematic variable.

The local behavior is described properly using an elastic-plastic mechanical model relating both the local normal force F_n^c and the local tangential force F_t^c to both the local normal relative displacement u_n^c and the local tangential relative displacement u_t^c. This model includes a Mohr-Coulomb criterion and can be expressed under the following incremental formalism, which introduces a normal elastic stiffness k_n and a tangential elastic stiffness k_t, both constant, and a local friction angle φ_g

The micro-directional model takes into account the change in the fabric of the granular assembly by directly modeling the increase or the decrease in the number of contacts along each direction of the physical space. In this approach, the number of contacts along a given direction is not computed from any fabric tensor, but is related to the normal strain rate along this direction. Following pioneering work based on physical evidence (Oda, 1972), it is thought that the number of contacts increases along contractive directions, whereas it decreases along dilative directions. Therefore, the distribution of contacts is likely to evolve over a loading path, inducing anisotropy to the texture (see Nicot and Darve, 2005, for more details).

3 THE *H* MICRO-DIRECTIONAL MODEL

The main weakness of the micro-directional model is related to the kinematic description (Eq. 3), inducing a too large stiffness along the principal loading direction. The global stiffness of a granular assembly does not stem only from the contact stiffness, but also from the ability of the assembly for rearranging. Thus, limiting our investigation to two-dimensional conditions, an intermediate scale, made up of an hexagonal patterns of grains, is introduced.

Basically, the granular assembly is described by a distribution of regular hexagonal patterns of grains (Fig. 1). Each hexagon is assumed to deform symmetrically with respect to a given direction $\mathbf{n}$ (Fig. 2). Then, given a macroscopic incremental strain, the balance equations of each hexagon of volume $V(\mathbf{n})$ can be solved, yielding both the strained configuration and internal forces. In elastic regime, we have (see Fig. 2 for the definition of the symbols used):

$$\begin{bmatrix} 2\cos\alpha & 1 & -2d_1\sin\alpha \\ 2\sin\alpha & 0 & 2d_1\cos\alpha \\ \cos\alpha & -1 & \dfrac{(k_t\, d_1 + N_1)\sin\alpha - T_1\cos\alpha}{k_n} \end{bmatrix} \begin{bmatrix} \delta d_1 \\ \delta d_2 \\ \delta\alpha \end{bmatrix} = \begin{bmatrix} \delta l_1 \\ \delta l_2 \\ 0 \end{bmatrix} \tag{4}$$

and in plastic regime,

$$\begin{bmatrix} 2\cos\alpha & 1 & -2d_1\sin\alpha \\ 2\sin\alpha & 0 & 2d_1\cos\alpha \\ \cos\alpha & -1 & \dfrac{N_1\sin\alpha - T_1\cos\alpha}{k_n} \end{bmatrix} \begin{bmatrix} \delta d_1 \\ \delta d_2 \\ \delta\alpha \end{bmatrix} = \begin{bmatrix} \delta l_1 \\ \delta l_2 \\ -\dfrac{\delta T_1\sin\alpha}{k_n} \end{bmatrix} \tag{5}$$

Averaging all incremental contact forces over the overall specimen gives the macroscopic incremental stress tensor (Love formula):

$$\underline{\underline{\sigma}} = \frac{1}{V}\int \omega_e(\vec{n})\, \underline{\underline{P}}^{-1} \begin{bmatrix} V(\vec{n})\,\tilde{\sigma}_1 & 0 \\ 0 & V(\vec{n})\,\tilde{\sigma}_2 \end{bmatrix} \underline{\underline{P}}\, d\theta \tag{6}$$

with

$$V(\vec{n})\,\tilde{\sigma}_1 = 4N_1\, d_1\cos^2\alpha - 4T_1\, d_1\cos\alpha\sin\alpha + 2N_2\, d_2 \tag{7}$$

$$V(\vec{n})\,\tilde{\sigma}_2 = 4N_1\, d_1\sin^2\alpha + 4T_1\, d_1\cos\alpha\sin\alpha \tag{8}$$

$$\underline{\underline{P}} = \begin{bmatrix} \cos\theta & \sin\theta \\ -\sin\theta & \cos\theta \end{bmatrix} \tag{9}$$

A major difference with respect to the micro-directional model (Nicot and Darve, 2005), is that grains appear explicitly, giving rise to both solid and void (or, more generally, internal fluid) phases. Moreover, the compressibility of the specimen is mainly due to the relative sliding between particles, rather than to the normal stiffness at contacts. This is a great advantage, giving rise to more realistic simulations of the mechanical response of granular assemblies. A first example of simulation of the response of a dense specimen over a drained biaxial test (after an initial isotropic compression at 200 kPa) is reported in Fig. 3. For this simulation, $k_n = 1000$ kN/m, $k_t = 500$ kN/m and $\varphi_g = 20$ degree. As seen in Figs. 3 and 4, the simulated response is qualitatively satisfying. The stress peak is obtained at a small strain (2%), and then a softening regime is observed. The macroscopic friction angle is 31 degrees at the peak. This is a typical response for dense materials, as confirmed by the volumetric

strain response shown in Fig. 4: after initial contractant behavior, a dilatant regime develops. It must be noted that the softening regime obtained is constitutive, as both stress and strain are considered homogeneous. It is associated with no geometrical effect that would lead to kinematical discontinuities.

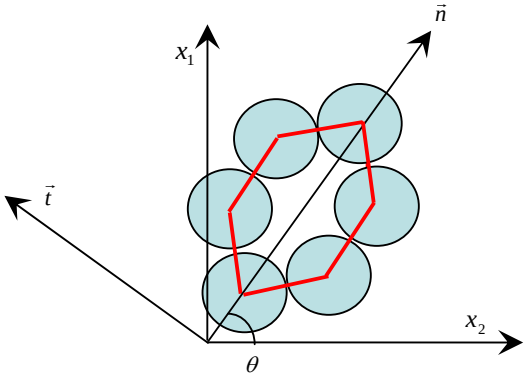

Fig. 1. Hexagonal set of contacting particles.

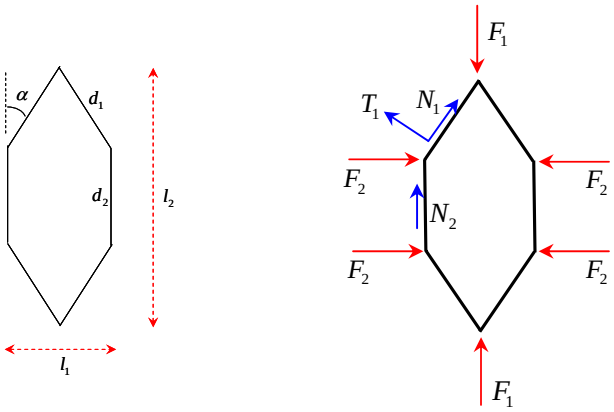

Fig. 2. Geometrical description and external forces applied to each hexagon.

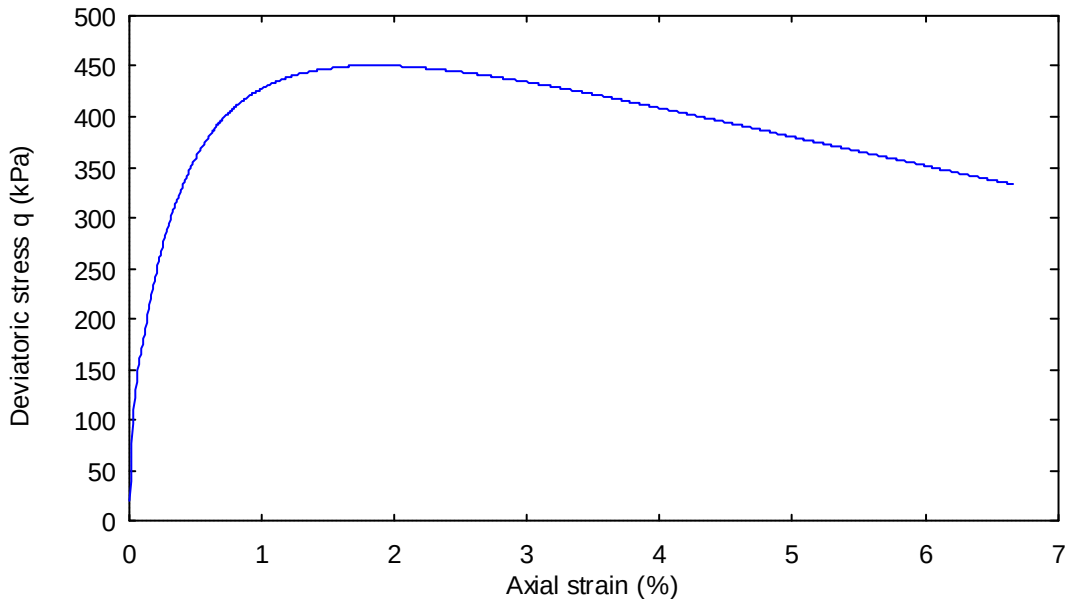

Fig. 3. Response over a drained biaxial test using the *H*-microdirectional model. Evolution of the deviatoric stress versus the axial strain.

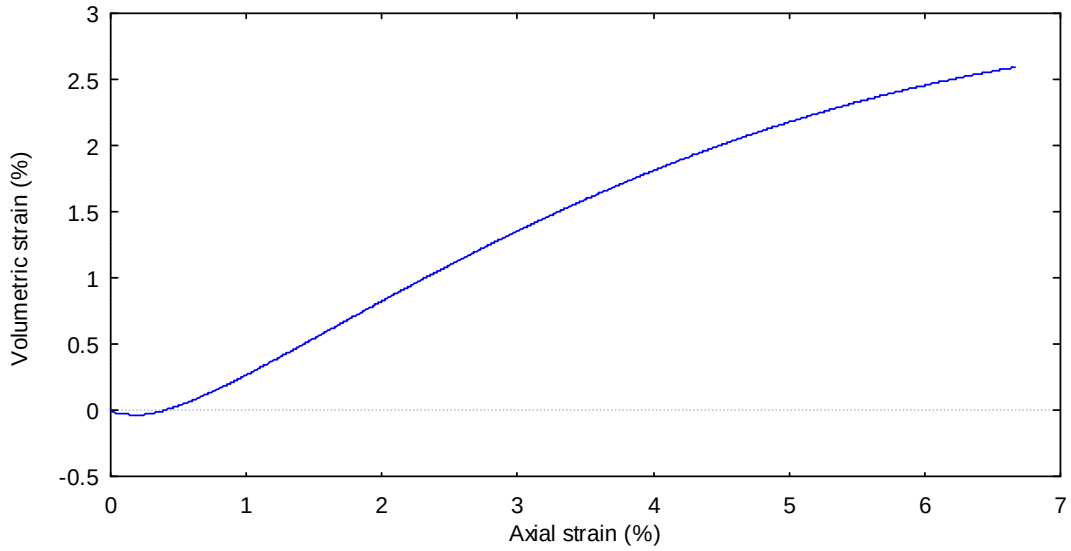

Fig. 4. Response over a drained biaxial test using the *H*-microdirectional model. Evolution of the volumetric strain versus the axial strain.

4 INSTABILITY ANALYSIS

It is of a great interest to investigate the occurrence of instability by using micromechanical models. Such enriched models can give rise to a wide set of different failure modes, such as, for example, the diffuse failure. The diffuse failure of a material is characterized by the abrupt collapse of the material, associated with a chaotic kinematic field. No localization pattern is visible. At the material point scale, such a failure mode is detected by the vanishing of determinant of the symmetric part $\mathbf{K}_s$ of the constitutive tensor $\mathbf{K}$. In two-dimensional conditions, and without rotation of the principal axes, the constitutive tensor $\mathbf{K}$ relates both the incremental stress ($\delta\sigma_1, \delta\sigma_2$) to the incremental strain ($\delta\varepsilon_1, \delta\varepsilon_2$). In fact, it can be shown that the vanishing of the determinant of $\mathbf{K}_s$ corresponds also to the existence of incremental strain directions vanishing the second-order work W_2, where $W_2 = \delta\sigma_i \, \delta\varepsilon_i$ (Darve et al., 2004). Let ($\delta\overline{\varepsilon}_1, \delta\overline{\varepsilon}_2$) be such a direction, that can be also characterized by the ratio $\overline{R} = \delta\overline{\varepsilon}_2 / \delta\overline{\varepsilon}_1$. If proportional strain paths are considered (the axial strain rate $\delta\varepsilon_1$, the proportional condition $\delta\varepsilon_2 = R\,\delta\varepsilon_1$ is prescribed where R is constant), this also means that the curve of the conjugate stress variable $\sigma_1 + R\,\sigma_2$ against the axial strain ε_1 passes through a peak for R lower than the critical value $\overline{R}$ (Nicot et al., 2009; Prunier et al., 2009).

To exemplify this, the simulation of such proportional strain loading paths was run, using the same parameters as those given in section 3. The initial confining pressure was also fixed to 200 kPa. As reported in Fig. 5, for R values lower than $R = -1.2$, the curves of $\sigma_1 + R\,\sigma_2$ against ε_1 passes through a peak. At the peak, the second order work is negative or nil, corresponding to the existence of a singular matrix $\mathbf{K}_s$. According to the theoretical background (Nova, 1994; Darve et al., 2004; Nicot and Darve, 2007), an abrupt collapse of the specimen is expected if any additional loading is applied at the peak, or along the descending branch. The ability of the micro-directional model to give rise to diffuse failure was ever discussed (Nicot and Darve, 2006). The above results show that this feature remains with the *H* micro-directional model. This result confirms the relevance of such micro mechanical approaches to investigate failure issues, in relation for instance with mechanical properties degradation.

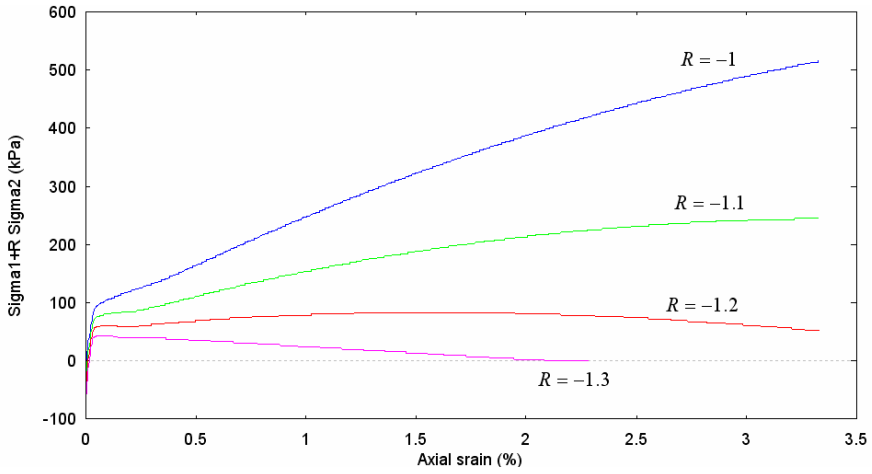

Fig. 5. Response over a proportional strain loading path using the H micro-directional model.

5 CONCLUDING REMARKS

This paper has presented the *H*-microdirectional model (Nicot and Darve, 2010), that introduces an intermediate scale between the microscopic scale and the REV scale. This multiscale model is based on a homogenization procedure that involves successively three scales: a microscopic scale, corresponding to the grain scale, a mesoscopic scale related to a hexagonal pattern of grains, and the whole assembly macroscopic scale. As such, the model allows relating the different scales, by expressing macroscopic terms from microscopic variables. The main advantage of this model, with respect to standard micromechanical approaches (Nicot and Darve, 2005) is that elementary grains patters are introduced. The deformation of such patterns results from the relative sliding between grains, rather that the deformation of grains. This leads to a more realistic kinematic description of grain assemblies, leaving aside the classical affine kinematic localization relation.

The capability of the model to exhibit a wide bifurcation domain was shown. By simulating proportional strain paths, it was shown that limit states could be obtained well before the plastic limit is reached.

This investigation draws new perspectives in the understanding of the key mechanisms leading to the failure of granular specimens. Numerical simulations based on a discrete element method are now in progress in order to examine the influence of the internal inertial mechanisms in the macroscopic destabilization of granular specimens.

REFERENCES

Cambou, B., Dubujet, P., Emeriault, F., and Sidoroff, F. (1995): Homogenization for granular materials. *European Journal of Mechanics, A/Solids*, Vol. 14, n° 2, pp. 255-276.

Chang, C.S., and Hicher, P.Y. (2005): An elasto-plastic model for granular materials with microstructural consideration. *Int. J. of Solids and Structures*, Vol. 42(14), pp. 4258-4277.

Darve, F., Servant, G., Laouafa, F., and Khoa H.D.V. (2004): Failure in geomaterials, continuous and discrete analyses. *Comp. Methods Appl. Mech. Engrg.*, Vol. 193, pp. 3057-3085.

Love, A.E.H. (1927): A treatise of mathematical theory of elasticity. Cambridge University Press, Cambridge.

Mehrabadi, M.M., Oda, M., and Nemat-Nasser, S. (1982) : On statistical description of stress and fabric in granular materials. *Int. J. Num. Anal. Meth. Geomech.*, Vol. 6, pp. 95-108.

Nicot, F. (2003): Constitutive modelling of a snowcover with a change in scale. *European Journal of Mechanics (A / Solids)*, Vol. 22-3, pp. 325-340.

Nicot, F., and Darve, F. (2005): A multiscale approach to granular materials. *Mechanics of Materials*, Vol. 37 (9), pp. 980-1006.

Nicot, F., and Darve, F. (2006): Micro-mechanical investigation of material instability in granular assemblies. *Int. J. of Solids and Structures*, Vol. 43, pp. 3569-3595.

Nicot, F., and Darve, F. (2007): A micro-mechanical investigation of bifurcation in granular materials. *Int. J. of Solids and Structures*, Vol. 44, pp. 6630-6652.

Nicot, F., Sibille, L., and Darve, F. (2009): Bifurcation in granular materials: an attempt at a unified framework. *Int. J. of Solids and Structures*, Vol. 46, pp. 3938–3947.

Nicot, F., and Darve, F. (2010): The H-microdirectional model: accounting for a mesoscopic scale. Mechanics of Materials, *submitted*.

Nova, R. (1994): Controllability of the incremental response of soil specimens subjected to arbitrary loading programs. *Journal of Mechanical behavior of Materials*, Vol. 5, n° 2, pp. 193-201.

Oda, M. (1972): The mechanism of fabric changes during compressional deformation of sand. *Soils and Foundations*, Vol. 12, pp. 1- 23.

Prunier, F, Nicot, F., Darve, F., Laouafa, F., and Lignon, S. (2009): 3D multiscale bifurcation analysis of granular media. *J. of Eng. Mechanics* (ASCE), Vol. 135(6), pp. 1-17.

DISCRETE SIMULATIONS OF SHEAR ZONE PATTERN IN EARTH PRESSURE PROBLEMS

Ł. Widuliński
Department of Civil Engineering, Gdańsk University of Technology, Gdańsk, Poland

J. Tejchman
Department of Civil Engineering, Gdańsk University of Technology, Gdańsk, Poland

ABSTRACT: *The intention of the paper is to check the capability of a discrete element method (DEM) to simulate a pattern of quasi-static shear zones in initially dense sand. Discrete calculations were carried out with a rigid and very rough retaining wall, undergoing passive and active horizontal translation, rotation about the top and rotation about the toe. To simulate the behavior of sand, the three-dimensional spherical discrete model was used allowing for grain rolling resistance.*

1 INTRODUCTION

Earth pressure on retaining walls is one of the soil mechanics classical problems. In spite of an intense theoretical and experimental research over more than 200 years, there are still large discrepancies between theoretical solutions and experimental results due to the complexity of the deformation field in granular bodies near the wall caused by localization of shear deformation (which is a fundamental phenomenon of granular material behavior) (Tejchman 2008). It was experimentally observed that localization can appear as single, multiple or pattern of shear zones, depending upon both initial and boundary conditions. It can be plane or curved. Within shear zones, pronounced grain rotations and curvatures connected to couple stresses, large strain gradients, and high void ratios together with material softening (negative second-order work) are expected. The thickness of shear zones depends on many various factors, as: the mean grain diameter, pressure level, initial void ratio, direction of deformation, grain roughness and grain size distribution (Tejchman 2008). The knowledge of both the distribution of shear zones and distribution of shear and volumetric strains within shear zones is important to explain the mechanism of granular deformation. The multiple patterns of shear zones are not usually taken into account in engineering calculations.

The intention of our paper is to check the capability of a discrete element model (DEM) to simulate a pattern of quasi-static shear zones in initially dense sand (Widuliński et al. 2010). The plane strain DEM calculations were carried out with sand placed behind a rigid and very rough retaining wall, undergoing passive and active movements: horizontal translation, rotation about the top and rotation about the toe. In a passive mode, a retaining wall moved towards the backfill and in an active mode away from it. To simulate the behavior of sand, the three-dimensional spherical discrete model YADE developed at University of Grenoble was used, allowing for introducing grain rolling resistance in order to take into account the grain roughness (Kozicki & Donze 2008). The attention was laid on the influence of the different wall movement on the characteristic evolution of shear zones. The layout of calculated shear

zones was qualitatively compared with corresponding experimental results of laboratory model tests employing X-rays and a Digital Image Correlation (DIC) technique (Niedostatkiewicz et al. 2010). The experiments with X-rays and DIC were carried out with different sands, granular specimen sizes and initial void ratios. The discrete element (DE) results were also quantitatively compared with the finite element (FE) results obtained by modeling the sand behaviour with a micro-polar hypoplastic constitutive model (Tejchman et al. 2007, Tejchman 2008) for the same sand, its initial void ratio, specimen size and boundary conditions.

The capability of DEM to simulate a single shear zone during plane strain compression, direct and simple shearing was several times confirmed in the scientific literature. However, its capability to simulate complex patterns of shear zones in the interior of granulates has not been comprehensively checked yet. This paper is focused mainly on a direct comparison between finite and discrete results at the global level, i.e. with respect to patterns of shear zones and load-displacement diagrams.

2 PATTERNS OF SHEAR ZONES OBTAINED BY FEM

The patterns of shear zones in "Karlsruhe sand" were calculated by the finite element method (FEM) using a micro-polar hypoplastic constitutive model (Tejchman et al. 2007, Tejchman 2008, Tejchman & Górski 2008) which was obtained by enhancement of a non-polar hypoplastic model (Gudehus 1996) by introducing a characteristic length of microstructure according to the assumptions of a micro-polar theory.

The plane strain FE calculations were performed with a Karlsruhe sand using a body of a height of H=200 mm and length of L=400 mm to simulate an earth pressure test with a passive translating wall by Gudehus and Schwing (1986) performed at Karlsruhe University. Totally, 3200 triangular elements were used. The size of the quadrilaterals is $\leq 20 \times d_{50}$=10 mm for d_{50}=0.5 mm. The height of the retaining wall located at the right side of the sand body was assumed to be h=170 mm (h/H=0.85). The calculations were performed out with large deformations and curvatures (updated Lagrange formulation) by changing the element configuration and the element volume. The initial stresses were generated using a K_o-state without polar quantities (K_0=0.47). Two sides and the bottom of the sand specimen were assumed to be very rough. The top of the sand specimen was traction and moment free. The retaining wall was assumed to be stiff and very rough.

The FE-results of a plane strain earth pressure problem for initially dense sand within a micro-polar continuum are shown in Figs.1-3. Figure 1 presents the evolution of the normalized horizontal earth pressure force $2E_h/(\gamma h^2)$ versus the normalized horizontal wall displacement u/h for three different wall movements (initial density γ=16.5 kN/m^3). In the case of a rotating wall, the horizontal displacement u is related to the wall displacement of the bottom point (wall rotating about the top) or top point (wall rotating around the bottom). In Figures 2 and 3, the deformed meshes with the distribution of the void ratio and Cosserat rotation in the residual state are shown. The darker region indicates the higher void ratio. The Cosserat rotation is marked by circles with a diameter corresponding to the magnitude of the rotation in the given step.

The evolution of the passive horizontal earth pressure force $2E_h/(\gamma h^2)$ is similar in three cases (Figure 1A). The horizontal force increases, reach a maximum for about u/h=1-5%, next shows softening and tends to an asymptotic value. For the wall rotation around the bottom, a decrease of the curve after the peak is smaller (in the considered range of u/h). The maximum horizontal force on the wall is the highest for the wall translation, and the lowest for the wall rotation about the top. The maximum normalized horizontal earth pressure forces are high ($2E_h/\gamma h^2$=12-31) due to the high initial void ratio of sand, large wall roughness, high

ratio between the mean grain diameter and wall height and low initial stress level. They are in the range of the usual (engineering) earth pressure coefficients determined under the assumption of one circular slip line (K_{pr}=11.3-25.8) and three straight slip lines (K_{pt}=13.4-23.7) at $\delta=\varphi^p=40^o$-45^o (δ - wall friction angle, φ^p- internal friction angle of dense sand at peak). However, the actual friction angles at peak φ^p in the shear zones are not known in advance (they depend strongly on the initial and boundary conditions of the entire system). Therefore, it is difficult to obtain realistic earth pressures with a conventional earth pressure theory. In addition (as the numerical calculations show), the different friction angles are mobilized in the various shear zones at the same time. The varying friction angles occur also along the same shear zone.

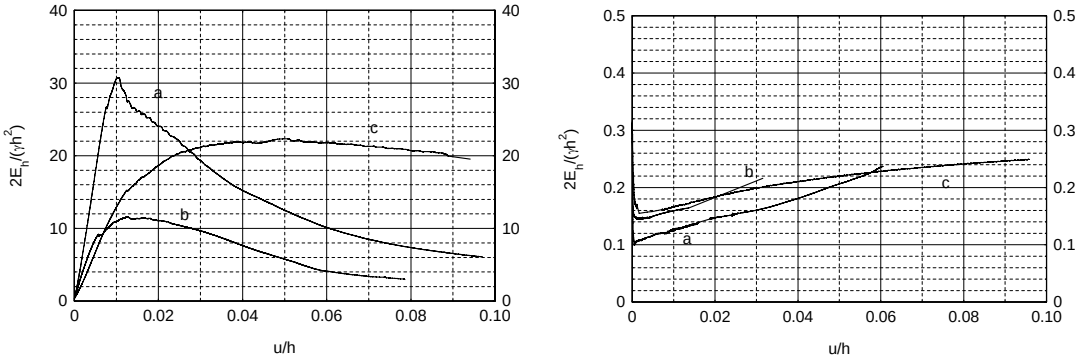

Fig. 1. Calculated resultant normalized horizontal earth pressure force $2E_h/(\gamma h^2)$ versus normalized horizontal wall displacement u/h from FEM: A) passive case, B) active case, a) translating wall, b) wall rotating around top, c) wall rotating around bottom (E_h – horizontal earth pressure force, γ – initial density, h – wall height, u – horizontal wall displacement) (Tejchman 2008)

In the case of active earth pressure, the horizontal normalized forces drop sharply at the beginning of the wall movement, reach the minimum at u/h=0.001-0.002 and next increase continuously (Figure 1B). The lowest earth pressure force occurs with the wall translation, and the largest with the wall rotation around the top. Thus, the relationship between the minimum active earth pressure and the type of the wall movement is inversed as compared to the maximum passive earth pressure and the type of the wall movement. The minimum normalized earth pressure forces ($2E_h/(\gamma h^2)$=0.10-0.16) are slightly smaller than the usual earth pressure coefficients assuming a circular slip line (K_a=0.16-0.20) or a straight slip line (K_a=0.14-0.16) with $\delta=\varphi^p$ ($\varphi^p=40^o$-45^o).

The geometry of shear zones, which are characterized in initially dense granulates by the appearance of Cosserat rotation and a strong increase of the void ratio, is very similar to those in experiments (Niedostatkiewicz et al. 2010) For the wall translation (Figure 2a), five shear zones are obtained: one vertical along the very rough retaining wall, one zone projecting horizontally from the wall base, one inclined (slightly curved) zone spreading between the wall bottom and free boundary, and two radial oriented shear zones starting to form at the wall top. The inclined shear zone becomes dominant in the course of deformation. The second radial shear zone is not fully developed at u/h=0.07. The maximum Cosserat rotation in the shear zones (at residual state) is about $|15^o|$. In the case of the wall rotation about the top (Figure 2b), only one curved shear zone occurs. When the retaining wall rotates around the bottom (Figure 2c), a pattern of curved parallel shear zones is obtained.

In the case of the active wall translation, two pronounced shear zones are obtained (Figure 3a). A vertical one occurs along the wall, and the second one propagates from the wall bottom up to the free boundary. The internal shear zone is almost straight. When the wall rotates around the top, two shear zones are obtained again: the first along the wall and the second inside of sand starting from the wall bottom (Figure 3b). The shear zone is strongly curved. In the case of a wall rotating around the bottom (Figure 3c), three shear zones are obtained: one shear zone along the wall and two parallel internal shear zones.

The computation time was about 10 hours on PC 2.0 GHz.

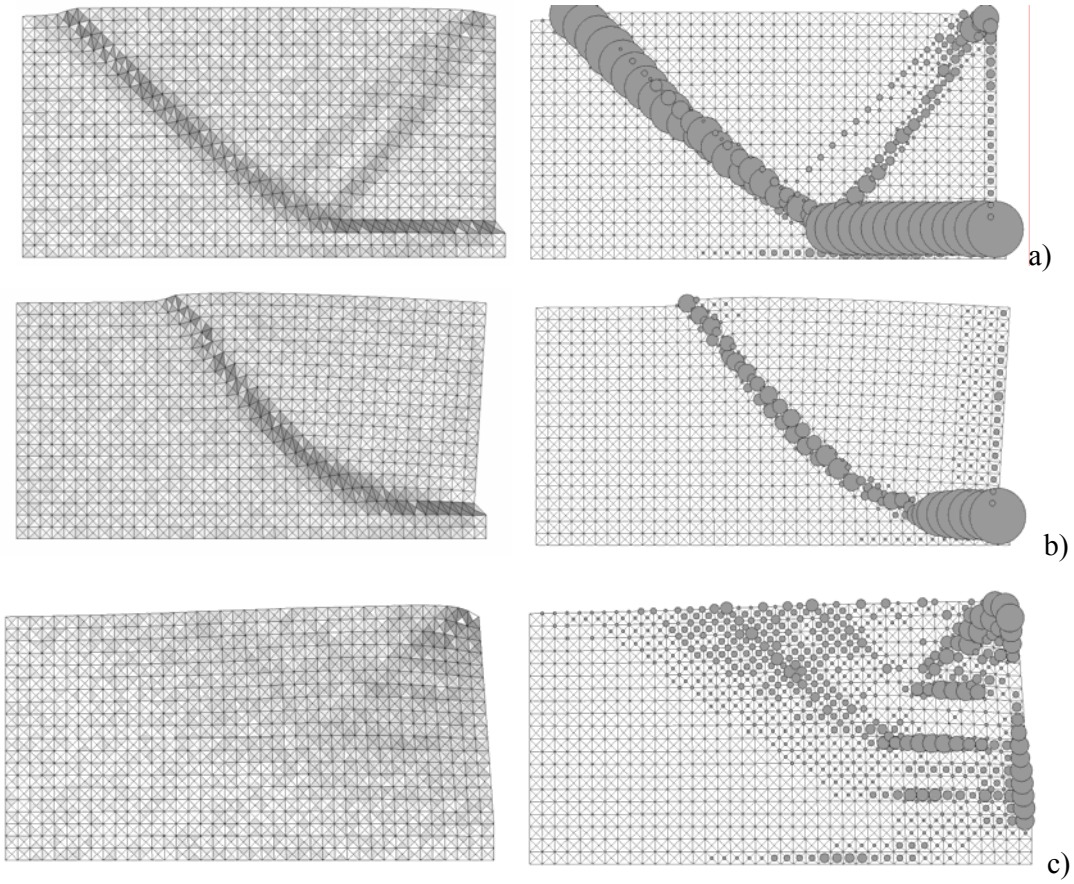

Fig. 2. Deformed FE-meshes with distribution of void ratio and Cosserat rotation at residual state for initially dense sand from FEM (passive case, u/h=0.05): a) translating wall, b) wall rotating around toe, c) wall rotating around top (Tejchman 2008)

3 DISCRETE ELEMENT METHOD

To simulate the behaviour of sand, a three-dimensional spherical discrete model YADE was developed at University of Grenoble (Kozicki and Donze 2008) by taking advantage of the so-called soft-particle approach (i.e. the model allows for particle deformation which is modeled as an overlap of particles). A dynamic behaviour of the discrete system is solved numerically using a force-displacement Lagrangian approach and tracks the positions, velocities, and accelerations of each particle individually. It uses an explicit finite difference algorithm assuming that velocities and accelerations are constant in each time step. To calculate forces acting in particle-particle or particle-wall contacts, a particle interaction model is assumed in which the forces are typically subdivided into normal and tangential

components. The total forces and moments acting on each particle are summed. Next, the problem is reduced to the integration of Newton's equations of motion for both translational and rotational degrees of freedom. As the results, the accelerations of each particle are obtained. The time step is incremented and accelerations are integrated over time to determine updated particle velocities and positions. To maintain the numerical stability of the method and to obtain a quick convergence to a quasi-static state of equilibrium of the assembly of particles, damping forces have to be introduced. Discrete elements can have different geometries, but to keep a low calculation cost, usually the simplest spherical geometry is chosen (dealing with realistic shapes would lead to a prohibitive calculation cost). However, the spherical geometry is too idealized to accurately model phenomena exhibited by real granular materials. It has been shown that spherical particles have a smaller angle of repose and reduced shear strength as compared to non-spherical particles. It is due to that the rotation is only resisted by frictional contacts with neighboring particles whereas for non-spherical particles the rotation tends to be inhibited by mechanical interlocking.

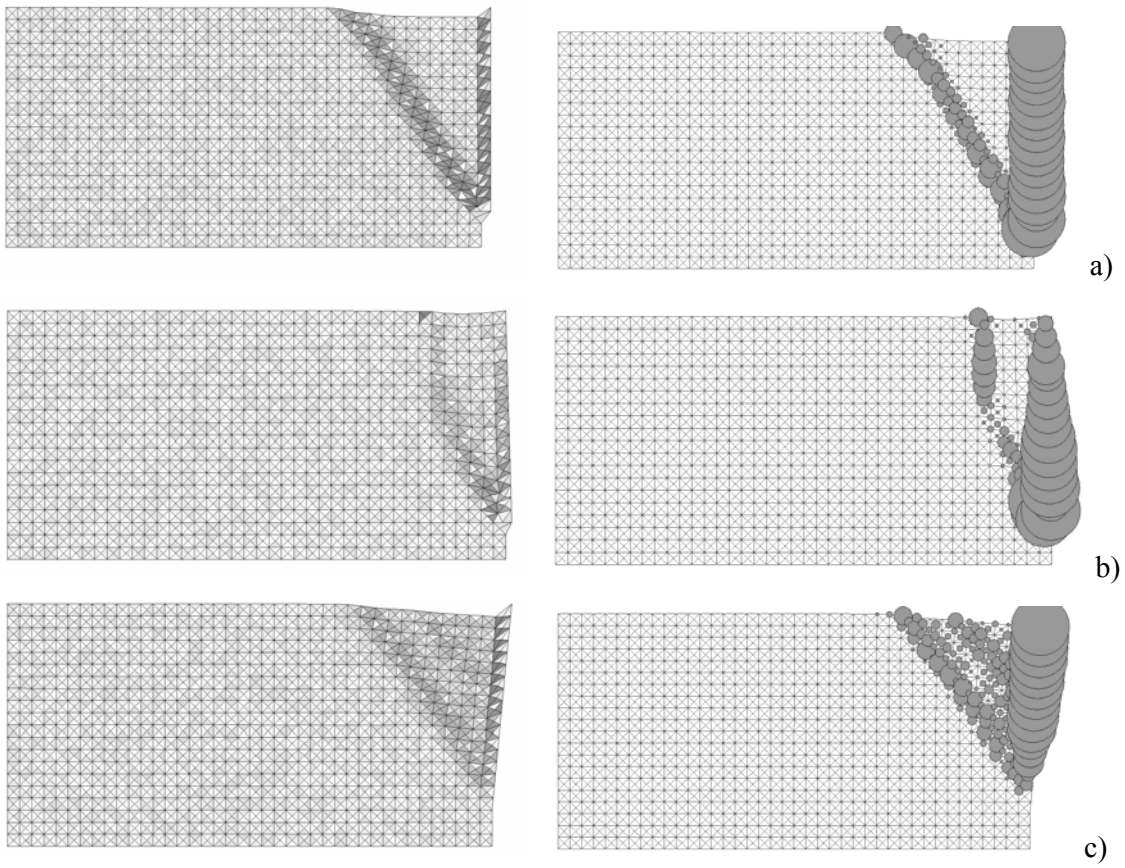

Fig. 3. Deformed FE-meshes with distribution of void ratio and Cosserat rotation at residual state for initially dense sand from FEM (active case, u/h=0.03-0.06): a) translating wall, b) wall rotating around toe, c) wall rotating around top (Tejchman 2008)

In the paper, spherical elements were used only. To simulate grain roughness, additional moments were introduced into a 3D model, which were transferred through contacts and resisted particle rotations (Kozicki and Donze 2008). In this way, grains were in contact with their neighbors through a certain contact surface. The limitation of all discrete methods is a necessity of long computational time and a difficulty to validate it experimentally.

The following five main local material parameters are needed for discrete simulations: E_c (modulus of elasticity of grain contact), υ_c (Poisson's ratio of grain contact), μ (inter-particle friction angle), β (rolling stiffness coefficient) and η (rolling limit coefficient) which were calibrated with corresponding triaxial laboratory test results (Wu 1992). In addition, the particle radius R, particle density ρ and damping parameters α are required.

The material sand parameters in our discrete model were calibrated with discrete simulations of a homogeneous triaxial test for cohesionless "Karlsruhe sand", which were directly compared with the corresponding experimental results of several triaxial tests performed by Wu (1992) at Karlsruhe University. The calculations of a triaxial test were carried out with the real mean grain diameter of sand (d_{50}=0.5 mm) using a linear size distribution curve (the radius of spheres varied between 0.2 mm and 0.8 mm). In numerical comparative simulations of a homogeneous triaxial test, a cubic granular specimen of $10\times10\times10$ cm^3 including about 10000 spheres with contact moments was used. The spheres were distributed at random. The test was modeled using confining smooth rigid wall elements (without inducing shear localization). Isotropic compression took place under gravity free conditions. The top and bottom boundaries moved vertically as loading platens under strain-controlled conditions to simulate the confining pressure p.

The experimental curves (global vertical normal stress versus global vertical normal strain and global volumetric strain versus global axial strain) are very well reproduced. The calculated maximum internal friction angle, ϕ=42.3^o, compares well with the experimental value of ϕ=43.7^o (Wu 1992). The calculated dilatancy angle ψ=27.1^o and modulus of elasticity E=101 MPa are also in a satisfactory agreement with experimental outcomes of ψ=28.5^o and E=104 MPa.

4 DEM RESULTS OF EARTH PRESSURE PROBLEM

The plane strain discrete calculations were performed with a sand body of a height of H=200 mm and length of L=400 mm to compare them directly with the FE results (Section 3). The height of the retaining wall located on the left-hand side of the granular body was assumed to be h=200 mm. The vertical retaining wall and the bottom of the granular specimen were assumed to be stiff and very rough, i.e. there were no relative displacements along a vertical and bottom surface. The granular specimen depth was equal to the grain size.

4.1 Effect of mean grain diameter

First, to investigate the effect of a mean grain diameter of sand d_{50} on shear localization, the discrete calculations were carried with three different mean grain diameters d_{50}: 0.5 mm, 1.0 mm and 5 mm during a uniform horizontal passive translation u of the wall against the backfill. 5000 spheres with different radii in the range 2-8 mm (d_{50}=5 mm), 31000 spheres with different radii of 0.7-1.3 mm (d_{50}=1.0 mm) and 110000 spheres with different radii of 0.2-0.8 mm (d_{50}=0.5 mm) were assumed for calculations. The initial void ratio was about e_o=0.63 (similar as in FE analyses). Figure 4 present the deformed granular body with the distribution of grain rotation for initially dense sand from DEM during passive earth pressure with translating wall. The values of grain rotations in the arc measure are expressed by a colour scale attached. The gray color indicates no rotations, the color between gray and white-red symbolizes rotations in the right direction (positive rotation) and the color between gray and black-blue symbolizes rotations in the left one (negative rotation). The geometry of shear zones was similar independently of d_{50} (Figure 5). In turn, the width of shear zones and the load-displacement curve strongly depended upon d_{50} (the maximum earth pressure force obviously increased with increasing d_{50}). The thickness of the main curved shear zone was 35

mm ($7\times d_{50}$) with d_{50}=5.0 mm, 22 mm ($22\times d_{50}$) with d_{50}=1.0 mm and 18 mm ($36\times d_{50}$) with d_{50}=0.5 mm.

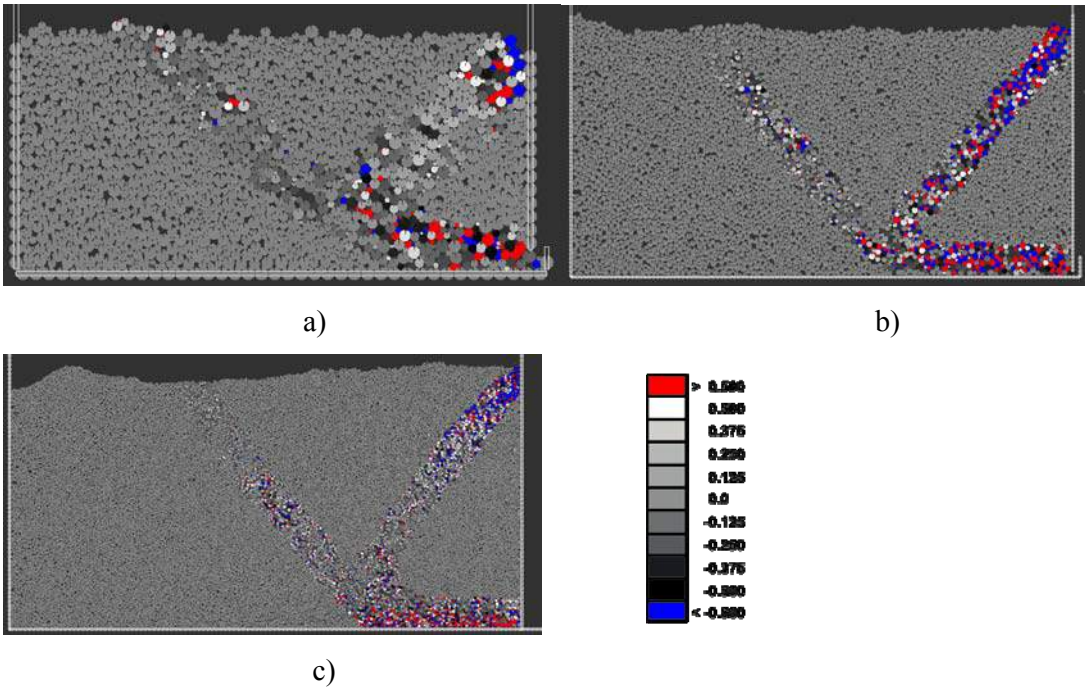

Fig. 4. Deformed granular body with distribution of rotation for initially dense sand from discrete simulations during passive earth pressure with translating wall: a) d_{50}=5 mm, b) d_{50}=1 mm, c) d_{50}=0.5 mm (u/h=0.05, e_o=0.63, E_c=30 GPa, υ_c=0.3, μ=30°, η=1.0, β=0.15) (values of grain rotation in arc measure are expressed by scale)

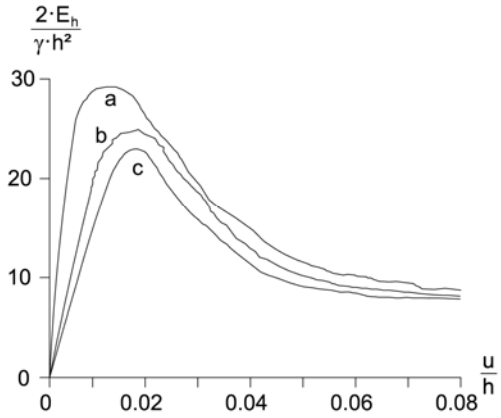

Fig. 5. Resultant normalized earth pressure force $2E_h/(\gamma h^2)$ versus normalized wall displacement u/h from discrete simulations during passive earth pressure with translating wall with different mean grain diameter d_{50} : a) d_{50}=5 mm, b) d_{50}=1.0 mm, c) d_{50}=0.5 mm (E_h – horizontal earth pressure force, γ – initial density, h – wall height, u – horizontal wall displacement) (e_o=0.63, E_c=30 GPa, υ_c=0.3, μ=30°, η=1.0, β=0.15)

The computation time was about 24 days (d_{50}=0.5 mm), 7 days (d_{50}=1.0 mm) and 1 day (d_{50}=5 mm) on PC 3.2 GHz.

4.2 Effect of wall movement type

The discrete simulations results for passive and active earth pressure problem are shown for initially dense sand *(e_o=0.63)* in Figures 6-8. To reduce the computation time, further simulations were solely carried out with d_{50}=1.0 mm. Figure 6 presents the evolution of the normalized horizontal earth pressure force $2E_h/(\gamma h^2)$ versus the normalized horizontal wall displacement u/h for three different active and passive wall movements. In the case of a rotating wall, the horizontal displacement u is related to the wall displacement of the bottom point (wall rotating about the top) or top point (wall rotating around the bottom). In turn, the deformed granular body with the distribution of grain rotations is demonstrated in Figures 7 (passive case) and 8 (active case).

The evolution of the horizontal earth pressure force $2E_h/(\gamma h^2)$ against the wall displacement is very similar as in FE calculations (Fig.1). The maximum normalized passive horizontal forces $2E_h/\gamma h^2$ are between 9 and 25 (in FEM: $2E_h/\gamma h^2$=12-31, respectively), and the minimum normalized active earth pressure forces $2E_h/\gamma h^2$ lie between 0.08 and 0.16 (in FEM: $2E_h/\gamma h^2$=0.10-0.16, respectively). In turn, the calculated minimum (residual) earth pressure coefficients are about 3-18 in a passive case (in FEM: $2E_h/\gamma h^2$=4-20, respectively).

The pattern of shear zones in DEM simulations on the basis of grain rotations is similar as in FE calculations (Figures 2 and 3) and experiments (Niedostatkiewicz et al. 2010). However, some discrepancies exist. For the passive wall translation, in contrast to FE-calculations and experiments recorded by X-rays, one radial zone (as in experiments with DIC) was obtained instead of two. In addition, secondary shear zones were not numerically obtained. The shear zones from discrete simulation are straighter than these from the FEM (during wall rotation around the toe). The differences between calculations and experiments are probably due to the fact that different sand was used in laboratory tests and in FE and DE analyses and due to a too small deformation range assumed in numerical calculations.

A horizontal shear zone and a radial shear zone develop first at the beginning of the passive wall translation. The material starts to generate grain rotations there. Next, a shear zone (starting from the wall base) curves upwards. At the same time, it is reached by a radial shear zone. The thickness of a shear zone reaching a top boundary surface is about $22\times d_{50}$ (d_{50}=1.0 mm) with the inclination of 43° to the horizontal (in FEM: $30\times d_{50}$ with d_{50}=0.5 mm and 40°, respectively) and of a radial shear zone is also about $22\times d_{50}$ with d_{50}=1.0 mm. In the case of the passive wall rotation around the top, the thickness of a curved shear zone is $25\times d_{50}$ (the thickness of a curved shear zone from FEM is $25\times d_{50}$ with d_{50}=0.5 mm). The thickness of parallel shear zones during the passive wall rotation around the bottom is about $(15\text{-}18)\times d_{50}$ with d_{50}=1.0 mm (in FEM the thickness was about $15\times d_{50}$ with d_{50}=0.5 mm). Their mean inclination against the bottom is 43°.

In the case of the active wall movement, the thickness of the interior shear zones is $25\times d_{50}$ (wall translation, wall rotation around the top) and $(15\text{-}18)\times d_{50}$ (wall rotation around the toe), respectively (with d_{50}=1.0 mm). The shear zone inclination to the horizontal is 58° (wall translation), 60° (wall rotation about the top) and 62° (wall rotation about the toe), respectively. In FEM, the thickness of the interior shear zones was $32.5\times d_{50}$ (wall translation) $27.5\times d_{50}$ (wall rotation around the top) $25\times d_{50}$ (wall rotation around the toe), respectively (with d_{50}=0.5 mm), and the shear zone inclination in to the horizontal was 50° (wall translation), 60° (wall rotation about the top) and 60° (wall rotation about the toe), respectively.

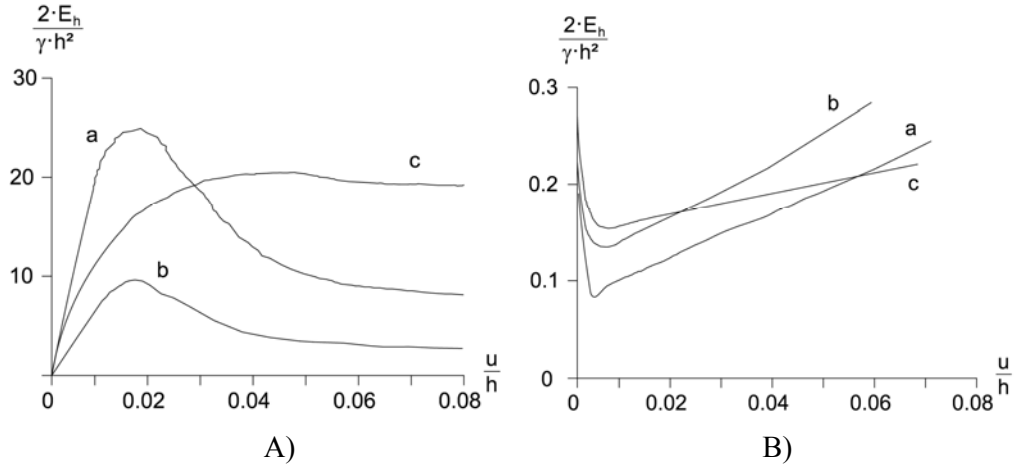

Fig. 6. Resultant normalized earth pressure force $2E_h/(\gamma h^2)$ versus normalized wall displacement u/h from DEM for: A) passive case, B) active case: a) translating wall, b) wall rotating around top, c) wall rotating around toe (E_h – horizontal earth pressure force, γ – initial density, h – wall height, u – horizontal wall displacement) (e_o=0.63, d_{50}=1 mm, E_c=30 GPa, υ_c=0.3, μ=30°, η=1.0, β=0.15)

The maximum grain rotation in the shear zones is about ±(15°-35°) at the residual state during passive wall translation. In turn, the resultant grain rotation in the middle of the radial shear zone from the area $5d_{50}\times5d_{50}$ is about 10° (and is approximately equal to the maximum Cosserat rotation in FE calculations, Tejchman et al. 2007).

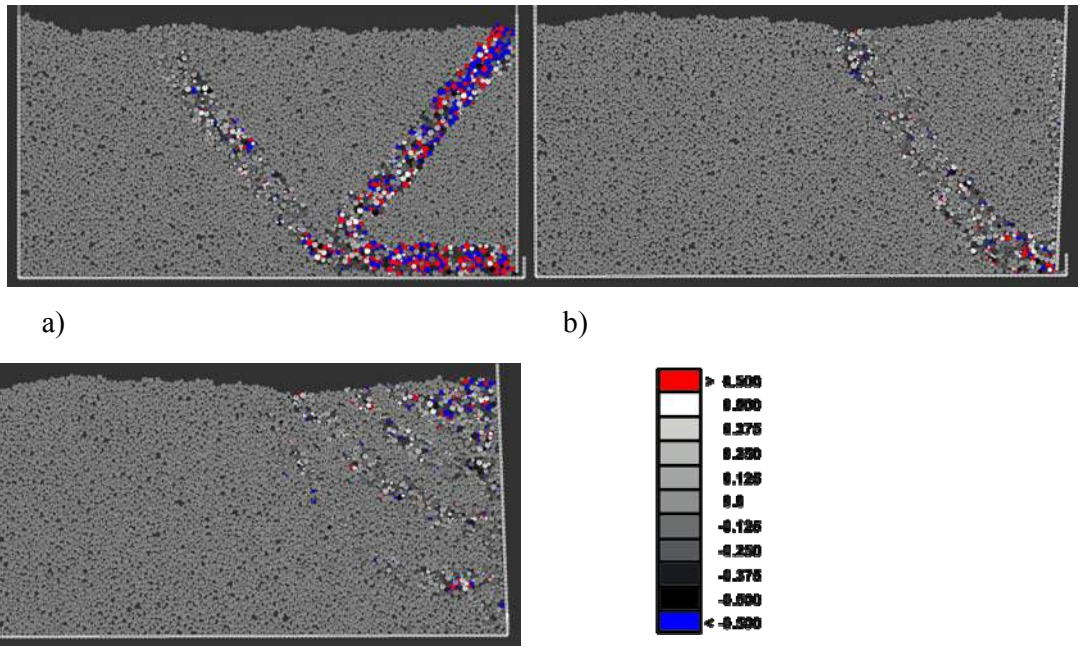

Fig. 7. Deformed granular body with distribution of rotation for initially dense sand from DEM (passive case, u/h=0.06) for: a) translating wall, b) wall rotating around top, c) wall rotating around toe (e_o=0.63, d_{50}=1 mm, E_c=30 GPa, υ_c=0.3, μ=30°, η=1.0, β=0.15) (values of grain rotation in arc measure are expressed by scale)

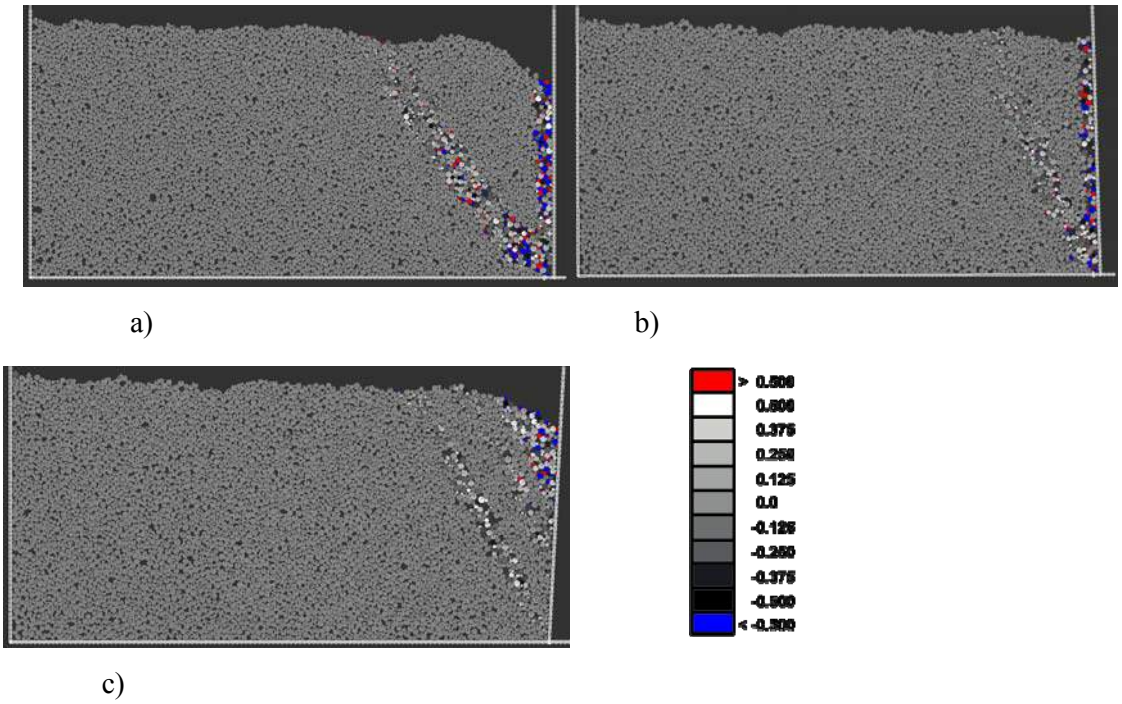

Fig. 8. Deformed granular body with distribution of rotation for initially dense sand from DEM (active case, u/h=0.06): a) translating wall, b) wall rotating around top, c) wall rotating around toe (e_o=0.63, d_{50}=1 mm, E_c=30 GPa, υ_c=0.3, μ=30°, η=1.0, β=0.15) (values of grain rotation in arc measure are expressed by scale)

4.3 Internal work, external work and dissipation

Figures 9 and 10 show the calculated internal work, external work and dissipation in initially dense sand specimen during passive wall translation (d_{50}=1.0 mm). The internal work δU was done by contact tangential forces on tangential displacements, contact normal forces on penetration depths and contact moments on angular rotations. The external work δW was done by the external horizontal force on the horizontal wall displacement. The total dissipation δD was calculated from the difference between the external work done on the assembly and internal work done by contact forces and moments.

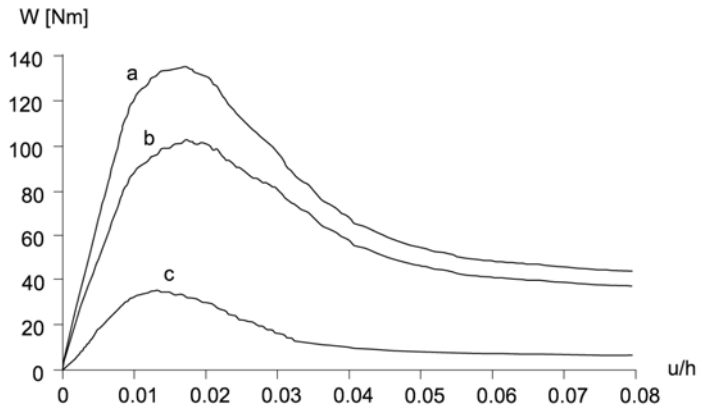

Fig. 9. Passive wall translation: a) external work, b) internal work and c) dissipation from discrete simulations (d_{50}=1.0 mm)

The evolution of three components of the internal work (Figure 10) is similar to the evolution of the horizontal wall force (Figure 6). The normal contact forces, tangential contact forces and contact moments increase up to the peak, indicate softening and reach their asymptotes. The largest internal work at peak was performed by contact normal forces (45% of the total work) and contact tangential forces (40% of the total work) and the smallest one by contact moments (15% of the total work). In the residual state, the work performed by normal and tangential contact forces was similar and the work performed by contact moments was about 3 times smaller than the remaining ones.

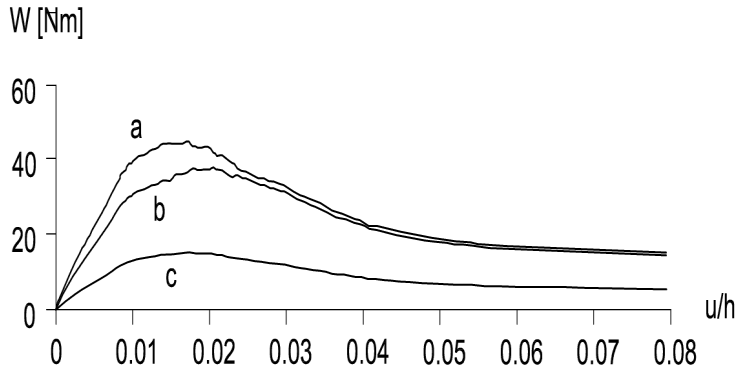

Fig. 10. Internal work done by: a) normal contact forces, b) tangential contact forces and c) contact moments and during passive wall translation from discrete simulations (d_{50}=1.0 mm)

The total dissipation in the granular specimen during deformation was about 25% at peak and 10% at the residual state, respectively (as compared to the total external work) (Figure 9).

5 CONCLUSIONS

The numerical simulations of earth pressures behind a retaining wall show that a discrete element method is capable to reproduce the most important macroscopic properties of cohesionless granular materials without being necessary to describe the granular structure perfectly. The results confirm the previous discrete element results obtained for a single shear zone in granular bodies. Comparing discrete simulations with experimental tests and continuum calculations demonstrates that a discrete model realistically predicts experimental results of a complex pattern of shear zones in the interior of initially dense sand. Thus, it can be used to comprehensively study the mechanism of the initiation, growth and formation of multiple shear zones at the micro-level.

The following detailed conclusions can be also drawn:

The geometry of shear zones depends strongly on the direction and type of the wall movement (passive or active, translation or rotation). The experimental patterns of shear zones were realistically reproduced in discrete calculations. The finite element and discrete results were very similar with respect to the geometry of shear zones and load-displacement curves.

The largest passive earth pressures occur with the horizontal translation of the wall, they are smaller with the wall rotation around the bottom and again smaller with the wall rotation around the top. The smallest active earth pressures are created during wall translation, and the largest during wall rotation around the top.

A mean grain size has a significant effect on a load-displacement diagram in DEM when shear localization is taken into account.

The granular material tends to a critical state inside shear zones. The grain rotations are noticeable only in shear zones.

The largest internal work in DEM simulations is performed by contact normal forces and the smallest one by contact moments.

The maximum horizontal passive force on the wall grows with increasing micro-mechanical parameters μ, β and η. In turn, the residual horizontal passive force depends on β only.

Conventional earth pressure mechanisms with slip surfaces are roughly reproduced. Realistic earth pressure coefficients can be obtained with actual values of internal friction angles only.

A continuum model is more advantageous due to a possibility to simulate larger granular specimens with smaller grain sizes. The discrete model is still limited by computation time. However, a discrete model has a smaller amount of parameters to be calibrated.

REFERENCES

Gudehus, G. & Schwing, E. (1986), Standsicherheit historischer Stützwände. Internal Report of the Institute of Soil and Rock Mechanics, University Karlsruhe.

Gudehus, G. (1996), "A comprehensive constitutive equation for granular materials". Soils and Foundations 36(1), 1-12.

Kozicki, J. & Donze, F.V. (2008), "A new open-source software developed for numerical simulations using discrete modelling methods". Computer Methods in Applied Mechanics and Engineering 197, 4429-4443.

Niedostatkiewicz, M., Leśniewska, D. & Tejchman, J. (2010), "Experimental analysis of shear zone patterns in sand for earth pressure problems using Particle Image Velocimetry". *Strain,* doi: 10.1111/j.1475-1305.2010.00761.x2010.

Tejchman, J., Bauer, E. & Tantono, S.F. (2007), "Influence of initial density of cohesionless soil on evolution of passive earth pressure". Acta Geotechnica 2, 1, 53-63.

Tejchman, J. (2008), FE modeling of shear localization in granular bodies with micro-polar hypoplasticity. Springer Series in Geomechanics and Geoengineering (eds. W. Wu and R. Borja), Springer Verlag, Berlin-Heidelberg.

Tejchman, J. & Górski, J. (2008), "Computations of size effects in granular bodies within micro-polar hypoplasticity during plane strain compression". Int. J. for Solids and Structures 45, 6, 1546-1569.

Widuliński, L., Tejchman, J., Kozicki, J. & Leśniewska, D. (2010), „Discrete simulations of shear zone patterning in sand in earth pressure problems of a retaining wall". IJSS (accepted).

Wu, W. (1992), Hypoplastizität als mathematisches Modell zum mechanischen Verhalten granularer Stoffe. Heft 129, Institute for Soil- and Rock-Mechanics, University of Karlsruhe.

DYNAMIC STRAIN LOCALIZATION ANALYSIS OF ELASTO-VISCOPLASTIC SOIL USING UPDATED LAGRANGIAN FINITE ELEMENT FORMULATION

M. Mirjalili, B. Shahbodagh Khan, F. Oka, and S. Kimoto
Department of Civil and Earth Resources Engineering, Kyoto University, Kyoto, Japan

ABSTRACT: *The dynamic analysis of strain localization in a water-saturated clay specimen is numerically studied as a three-dimensional problem using a cyclic elasto-viscoplastic constitutive model. The model is derived based on the nonlinear kinematic hardening rules incorporated with the structural degradation of soil particles. In order to appropriately simulate the large deformation phenomenon in strain localization analysis, the dynamic finite element formulation for a Biot's type two-phase mixture is derived in the framework of the finite deformation theory with updated Lagrangian scheme. The shear band development is shown through the distributions of viscoplastic shear strain, axial strain, and mean effective stress in the specimen. The effect of mesh-size on the shear banding is also investigated. Using the finer meshes causes the strain to localize into a slightly narrower band than the default mesh pattern; nonetheless, the results manifest convergence through the mesh refinement in terms of the overall shape of shear banding and stress-strain relations.*

1 INTRODUCTION

Strain localization is an important large deformation geotechnical problem and the onset of failure such as slope failure in which large deformation occurs in a narrow zone.
From the numerical point of view, the strain localization of geomaterials has been widely studied under quasi-static and dynamic loading conditions. Under quasi-static deformations, Oka et al. have studied the shear band development of water-saturated clay by using an elasto-viscoplastic constitutive model (Oka et al. 1995; 2000; 2002).

The aim of the present study is to extend the finite element analysis of shear banding in elasto-viscoplastic clays to the analysis under dynamic transient loading conditions. The development of shear bands is examined numerically in a three-dimensional geometry. A cyclic elasto-viscoplastic constitutive model is adopted to simulate the behavior of clay under dynamic loading conditions. The model is developed by incorporating the nonlinear kinematic hardening rules for the changes in the stress ratio, in the mean effective stress, and in the viscoplastic volumetric strain. In addition, the structural degradation of the soil skeleton is considered in the constitutive model as the strain softening with respect to the viscoplastic strain. The finite element equations based on the *u-p* formulation and the Biot's type two-phase mixture theory are derived in the framework of finite deformation theory with updated Lagrangian description. A numerical program is then developed to perform three-dimensional finite element simulations under dynamic loading conditions.

2 CYCLIC ELASTO-VISCOPLASTIC CONSTITUTIVE MODEL

The cyclic elasto-viscoplastic constitutive model is presented following the concept of structural degradation, as described in the elasto-viscoplastic model by Kimoto and Oka (2005), incorporated with the nonlinear kinematic hardening rules (Armstrong & Frederick, 1966; Chaboche & Rousselier, 1983). The model considers the structural degradation of the soil skeleton by shrinkage of both the static yield surface and the overconsolidation boundary surface with respect to the accumulation of viscoplastic strain. The model is derived based on an overstress type of viscoplasticity theory (Perzyna, 1963) and the non-associated flow rule. The nonlinear kinematic hardening rules are employed in addition to the viscoplastic strain dependency of elastic shear modulus.

The strain rate tensor consists of elastic strain rate and viscoplastic strain rate, in which the elastic strain rate is defined as:

$$\begin{aligned} \dot{\varepsilon}_{ij} &= \dot{\varepsilon}^{e}_{ij} + \dot{\varepsilon}^{vp}_{ij} \\ \dot{\varepsilon}^{e}_{ij} &= \frac{1}{2G}\dot{S}_{ij} + \frac{\kappa}{3(1+e_0)}\frac{\dot{\sigma}'_m}{\sigma'_m}\delta_{ij} \end{aligned} \tag{1}$$

in which G is the elastic shear modulus, S_{ij} is the deviatoric stress tensor ($S_{ij} = \sigma'_{ij} - \sigma'_m \delta_{ij}$), σ'_m is the mean effective stress, and the superimposed dot denotes the time differentiation. κ is the swelling index and e is the void ratio.

Viscoplastic potential function, f_p, is obtained by considering the nonlinear kinematic hardening rule for the changes in the stress ratio, in the mean effective stress, and in the viscoplastic volumetric strain as:

$$f_p = \bar{\eta}^*_{\chi} + \tilde{M}^* \left(\ln \frac{\sigma'_{mk}}{\sigma'_{mp}} + \left| \ln \frac{\sigma'_m}{\sigma'_{mk}} - y^*_{m1} \right| \right) = 0 \tag{2}$$

$$\bar{\eta}^*_{\chi} = \left\{ \left(\eta^*_{ij} - \chi^*_{ij} \right) \left(\eta^*_{ij} - \chi^*_{ij} \right) \right\}^{\frac{1}{2}} \tag{3}$$

in which σ'_{mk} is the unit value of the mean effective stress, and y^*_{m1} is the scalar kinematic hardening parameter. χ^*_{ij} is so-called back stress parameter, which has the same dimensions as stress ratio η^*_{ij}.

The dilatancy coefficient $\tilde{M}^*$ is defined separately for the normally consolidated region (NC) and the overconsolidated region (OC) as

$$\tilde{M}^* = \begin{cases} M^*_m & \text{:NC region} \\ \left(\sigma^*_m / \sigma'_{mc} \right) M^*_m & \text{:OC region} \end{cases} \tag{4}$$

where σ'_{mc} is the mean effective stress at the intersection of the overconsolidation boundary surface and σ'_m axis.

The evolution equation for the kinematic hardening parameter χ^*_{ij} is given by

$$d\chi^*_{ij} = B^* \left(A^* de^{vp}_{ij} - \chi^*_{ij} d\gamma^{vp} \right) \tag{5}$$

where A^* and B^* are material parameters, de_{ij}^{vp} is the viscoplastic deviatoric strain increment tensor, and $d\gamma^{vp}$ is the viscoplastic shear strain increment tensor.

The scalar kinematic hardening parameter y_{m1}^* is determined by

$$dy_{m1}^* = B_2^* \left(A_2^* d\varepsilon_v^{vp} - y_{m1}^* \left| d\varepsilon_v^{vp} \right| \right) \tag{6}$$

where A_2^* and B_2^* are material parameters, and $d\varepsilon_v^{vp}$ is the increment of the viscoplastic volumetric strain tensor.

The viscoplastic deviatoric strain rate and the viscoplastic volumetric strain rate can be respectively expressed as:

$$\dot{e}_{ij}^{vp} = C_1 \sigma'_m \exp\left\{ m' \left(\overline{\eta}_\chi^* + \tilde{M}^* \left(\ln \frac{\sigma'_{mk}}{\sigma'_{ma}} + \left| \ln \frac{\sigma'_m}{\sigma'_{mk}} - y_{m1}^* \right| \right) \right) \right\} \frac{\partial f_p}{\partial S_{ij}} \tag{7}$$

$$\dot{\varepsilon}_{kk}^{vp} = C_2 \sigma'_m \exp\left\{ m' \left(\overline{\eta}_\chi^* + \tilde{M}^* \left(\ln \frac{\sigma'_{mk}}{\sigma'_{ma}} + \left| \ln \frac{\sigma'_m}{\sigma'_{mk}} - y_{m1}^* \right| \right) \right) \right\} \frac{\partial f_p}{\partial \sigma'_m} \tag{8}$$

where C_1 and C_2 are the viscoplastic parameters for the deviatoric and the volumetric strain components, respectively. σ'_{ma} is assumed to decrease with an increase in viscoplastic strain with

$$\sigma'_{ma} = \sigma'_{maf} + \left(\sigma'_{mai} - \sigma'_{maf} \right) \exp(-\beta z) \tag{9}$$

in which z is the accumulation of the second invariant of the viscoplastic strain rate given by

$$z = \int_0^t \dot{z} dt \quad ; \quad \dot{z} = \sqrt{\dot{\varepsilon}_{ij}^{vp} \dot{\varepsilon}_{ij}^{vp}} \tag{10}$$

In Equation (9), σ'_{mai} and σ'_{maf} are the initial and the final values for σ'_{ma}, respectively. β is a parameter that stands for the changing rate of σ'_{ma}, while the proportion of $n = \sigma'_{maf} / \sigma'_{mai}$ provides the degree of possible collapse of the soil structure at the initial state.

3 FINITE ELEMENT FORMULATION

For the dynamic analysis of strain localization in the present study, the u-p formulation based on the updated Lagrangian method is employed with the Jaumann rate of Cauchy stress rate tensor.

An isoparametric 20-node hexahedron element with a reduced Gaussian integration is adopted for the displacement, the velocity, and the acceleration of the solid skeleton in three-dimensional analysis, while the pore pressure is defined at the eight corner nodes of the element.

The principle of Terzaghi's effective stress is used in the analysis by considering that extension is positive even for the pore pressure, as

$$T_{ij} = T_{ij}' + p\delta_{ij} \tag{11}$$

where T_{ij} is the Cauchy's stress tensor, T_{ij}' is the effective stress tensor, δ_{ij} is the Kronecker's delta, and p is the pore water pressure.

3.1 Equation of motion

Equation of motion of fluid saturated soil is given by

$$\rho\left(a_i^S - b_i\right) - S_{ji,j} = 0 \tag{12}$$

in which ρ is the mass density of the fluid saturated soil, a_i^S is the acceleration vector of soil skeleton, b_i is the body force, and S_{ij} is the nominal stress tensor.

3.2 Continuity equation

Continuity equation is derived by the mass conservation law and the equation of pore fluid as:

$$\rho^F \dot{D}_{ii} - p_{,ii} - \frac{\gamma_w}{k} D_{ii} = 0 \tag{13}$$

where ρ^F is the mass density of pore fluid, γ_w is the unit weight of pore water, and k is the permeability coefficient. D_{ij} is the Stretching tensor for solid phase.

3.3 Discretization of the governing equations

In order to discretize equations of motion for water saturated soil and the continuity equation for pore fluid, Newmark's β method and finite element method are used. In the formulation, acceleration vector $\{a_N\}$ and pore water pressure $\{p_N\}$ are taken
as independent variables.
Finally, the discretized governing equations are given in matrix form as:

$$\begin{bmatrix} \dfrac{[M]_{t+\Delta t} + \bar{\gamma}(\Delta t)\left\{\Delta t\left([K]_{t+\Delta t} + [K_L]_{t+\Delta t}\right) + [R]_{t+\Delta t}\right\}}{\gamma_w\left\{\dfrac{1}{g} - \dfrac{\bar{\gamma}\,\Delta t}{k}\right\}[K_v]^T{}_{t+\Delta t}} & \dfrac{[K_v]_{t+\Delta t}}{[K_h]_{t+\Delta t}} \end{bmatrix} \begin{Bmatrix} \{a_N\}_{t+\Delta t} \\ \{p_N\}_{t+\Delta t} \end{Bmatrix}$$

$$= \begin{Bmatrix} \{F\}_{t+\Delta t} - \{S^*\}_t - \left\{\Delta t\left([K]_{t+\Delta t} + [K_L]_{t+\Delta t}\right) + [R]_{t+\Delta t}\right\}\left\{\Delta t(1-\bar{\gamma})\{a_N\}_t + \{v_N\}_t\right\} \\ +[K_v]_{t+\Delta t}\{p_N\}_t - (\Delta t)\{T_W\}_t + (\Delta t)\{T_Q\}_t \\ \hline \{q\}_{t+\Delta t} + \left(\dfrac{\gamma_w}{k}\right)[K_v]^T{}_{t+\Delta t}\left\{\Delta t(1-\bar{\gamma})\{a_N\}_t + \{v_N\}_t\right\} \end{Bmatrix} \tag{14}$$

4 NUMERICAL SIMULATION AND RESULTS

The finite element mesh and the boundary conditions for the localization analysis of soft clay specimen are shown in Figure 1. The characteristic parameters of a normally consolidated clay sample from Torishima, Osaka City, Japan are assigned for the material parameters as listed in Table 1. The simulation is performed under plane strain conditions by constraining the deformation in a three-dimensional problem. The size of the specimen is assumed as 10 m in width by 20 m in height. As mentioned earlier in Section 3, a 20-node hexahedron element with a reduced Gaussian integration is used for the finite element analysis, by which the appearance of a spurious hourglass mode and shear locking can be eliminated. The mesh pattern of 10×20 (200 elements) is considered as the default mesh configuration in the analysis. The displacement boundary conditions are adjusted so as the symmetric condition can be provided. The constrained boundary conditions at the corners of the specimen are applied to trigger the localization at a fixed location. All the boundaries are assumed as impermeable, while the pore fluid is allowed to flow within the specimen. The vertical nodal acceleration is applied at the top nodes of the domain providing the vertical compelled displacement atop the specimen. The applied acceleration rises from zero to a maximum value of 3.5 gal within 0.1 sec, and remains constant afterward until 12.5 sec, as illustrated in Figure 1. The applied acceleration results in an overall axial strain of about 13.5% within 12.5 sec.

Table 1. Material parameters of Torishima clay

λ	0.341	σ'_{m0} (kPa)	200
κ	0.019	σ'_{maf} (kPa)	60
e_0	1.250	β	3.6
G_0	15040	B^*_0	100
k	5.87×10^{-10}	B^*_1	40
M^*_m	1.24	C_f	10
m'	24.68	ρ (ton/m^3)	1.70
C_1(1/s)	1.00×10^{-5}	A^*_2	5.9
C_2(1/s)	3.83×10^{-6}	B^*_2	1.8

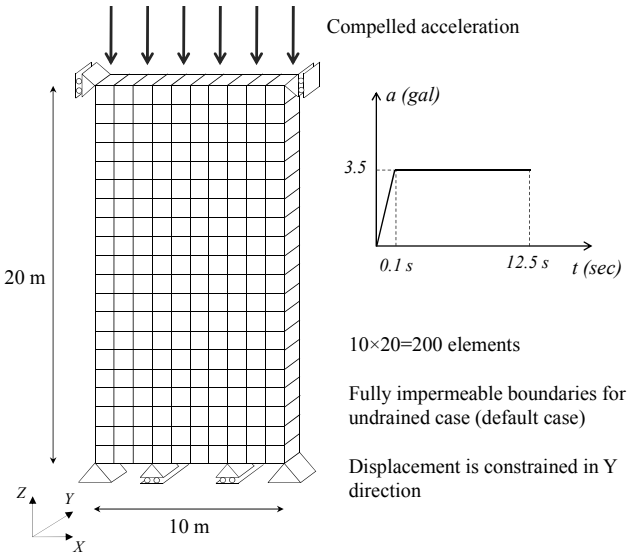

Fig. 1. Size of the specimen, boundary conditions, and applied acceleration profile

4.2 Shear banding progress

The shear band development is studied through the evaluation of the results for the accumulated viscoplastic shear strain, the axial strain, and the mean effective stress. Figure 2 demonstrates the distribution of accumulated viscoplastic shear strain in the specimen through the loading. The strain localization emerges from the trigger points at the corner of the specimen, which eventually narrows to four distinct diagonal bands by increasing the compelled displacement. The shear bands occur at an angle of about 45°.

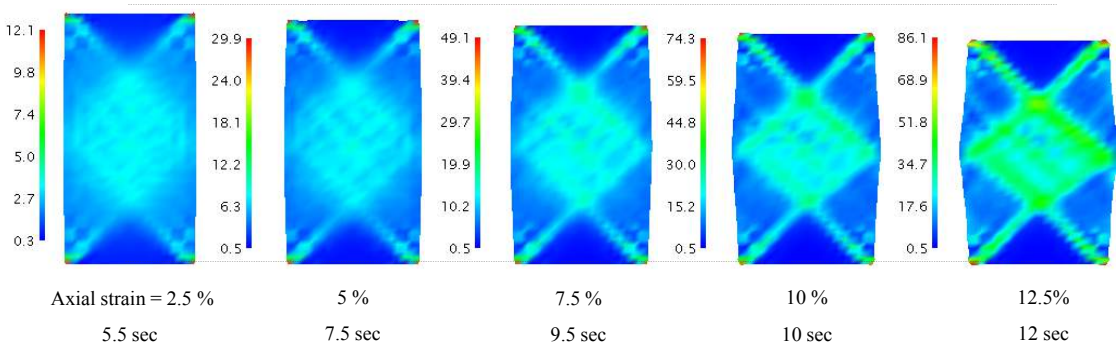

Fig 2. Distribution of accumulated viscoplastic shear strain under the compelled deformation, and progress of shear banding in time, (legend unit: %)

The distribution of the axial strain and the mean effective stress are shown in Figure 3 at various levels of the overall axial strain. The shear banding pattern, as illustrated for viscoplastic shear strain, is also observed in the distributions of axial strain and mean effective stress. For the mean effective stresses, however, the reduction along the shear bands is observed by progress of the axial displacement.

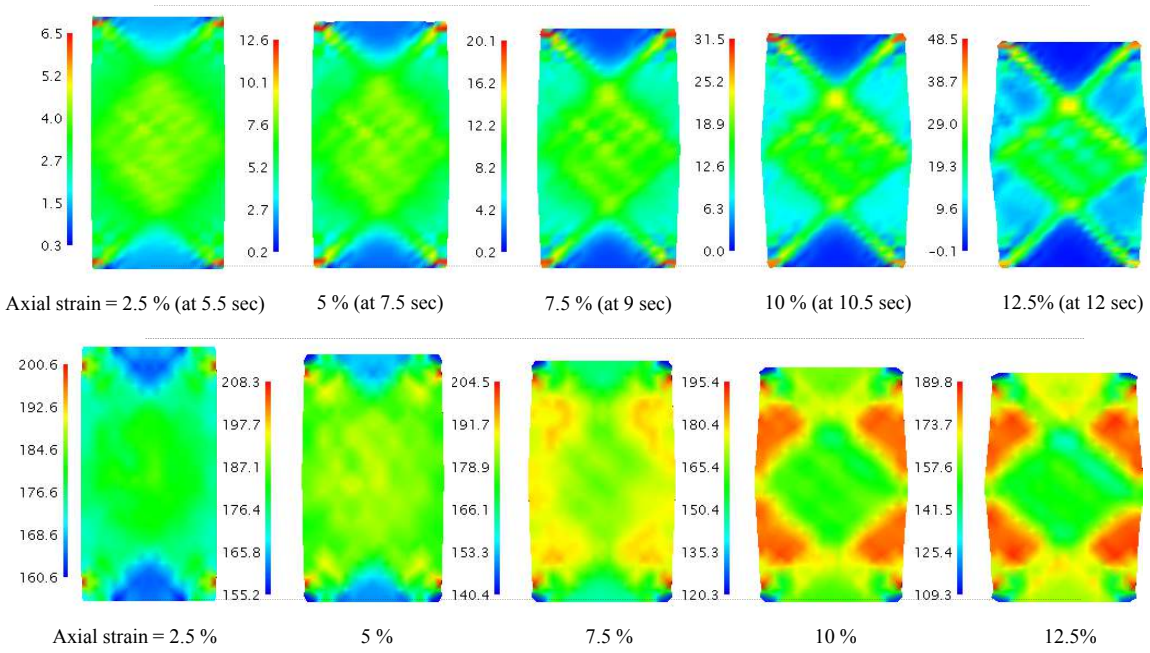

Fig 3. Distributions of the axial strain (above) and the mean effective stress (below) by progress of shear banding, (legend unit: % for strain, and kPa for stress)

4.2 Mesh-size dependency

In order to evaluate the mesh-size sensitivity of the numerical results, three extra square mesh patterns are considered besides the defaults mesh pattern for the localization analyses. The pattern of 5×10 (50 elements) is considered as the coarser mesh, and 20×40 (800 elements) and 25×50 (1250 elements) are assumed as the finer meshes. The deformed mesh and the distribution of the accumulated viscoplastic shear strain for all the cases are depicted in Figure 4 at the end of loading. Taking the finer mesh size leads to a higher level of strain localization, and narrows the width of the shear band since the shear bands span across the smaller elements. In the finer meshes, i.e., 800 elements and 1250 elements patterns, the shear banding is observed in the same shape and angle as for 200 elements pattern, emanating from the corners of the specimen and finally localizing into four diagonal bands. In the case with 50 elements, however, the strain is localized into a wider band across the specimen, of which a high level of localized strain is observed in the center of the specimen.

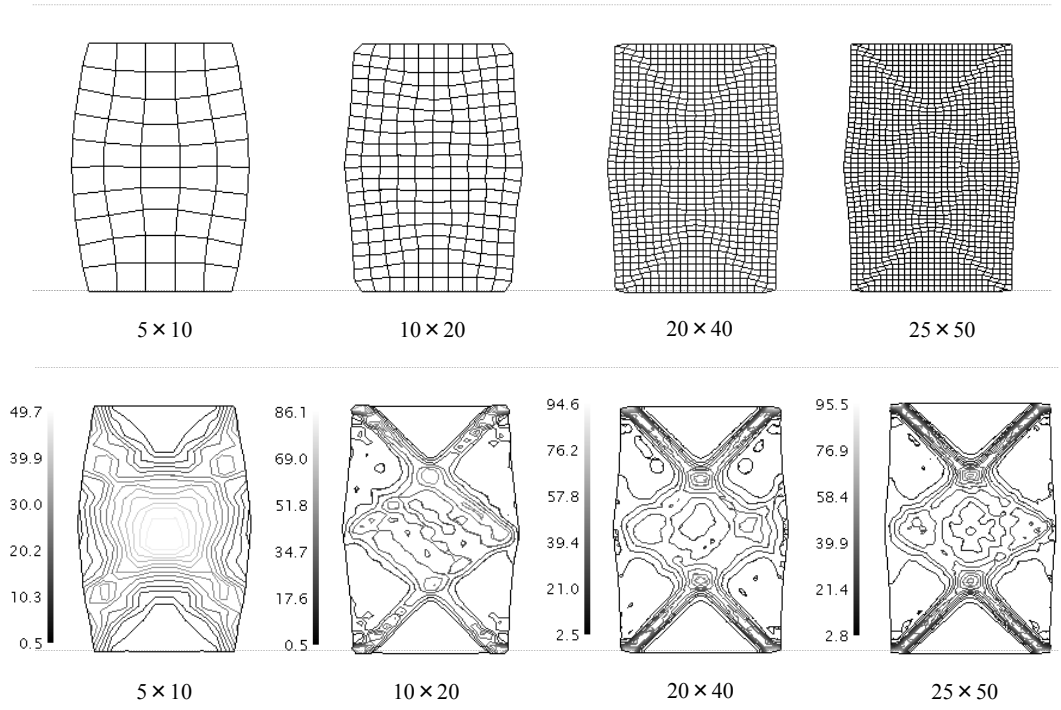

Fig. 4. Deformed meshes and localization of the viscoplastic shear strain for different mesh patterns at the end of loading (legend unit: %)

The stress-strain relations for these four cases are compared in Figure 5, where the average deviator stress is plotted versus the average axial strain. The average values are obtained by computing the average of stresses over all the elements in each case.

The initiation of shear banding in the stress-strain relations is observed as a significant change in the curve slope at strain level of 1.365% for all cases. All the cases demonstrate rather similar tendency in stress-strain relations, although slight differences are observed among the stresses during the softening after the peak stress point. In the coarser mesh pattern, the deviator stresses after the peak point tend to decrease more rapidly in comparison with those in the finer meshes. Nonetheless, the results appear to be convergent in finer meshes with 200 elements configuration, in view of the fact that the differences become

smaller between the stresses in 200 elements case and 800 elements case, and also the stresses in 800 elements case and 1250 elements case are nearly the same.

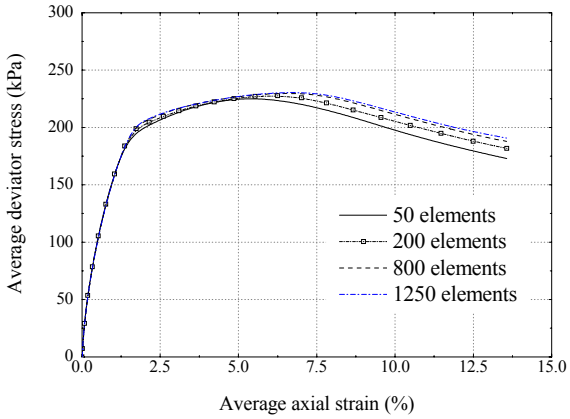

Fig. 5. Stress-strain relations for different mesh configurations

5 CONCLUSION

The dynamic analysis of strain localization was numerically studied in a water-saturated clay specimen subjected to the compelled nodal acceleration. The behavior of clay under dynamic loading conditions was represented by a cyclic elasto-viscoplastic constitutive model which incorporates the nonlinear kinematic hardening rules and the structural degradation.

The shear banding process was studied through the strain contours, as well as the distribution of mean effective stress. The shear band development was clearly observed as four dominant diagonal bands at an angle of about 45°. Considering the mesh-size dependency, the results for different mesh configurations showed good consistency in terms of the overall shape of deformation and stress-strain behavior. By taking the finer mesh sizes, shear banding occurred in a narrower width since the shear bands span across the smaller elements.

Despite the convergency of the results with finer meshes, slight hardening behavior was observed in the stress-strain relations, which requires further investigations.

REFERENCES

Armstrong PJ, Frederick CO (1966). “A mathematical representation of the multiaxial Bauschinger effect. Berkeley Nuclear Laboratories”. Technical Report RD/B/N 731.

Chaboche JL, Rousselier G. (1983) “On the plastic and viscoplastic constitutive equations; part I and Part II. J Pressure Vessel Technol”. ASME. 105: 153-64.

Kimoto S, Oka, F. (2005) “An elasto-viscoplastic model for clay considering destructuralization and consolidation analysis of unstable Behavior”. Soils Found, 45(2): 29-42.

Oka F, Adachi T, Yashima A. (1995) “A strain localization analysis of clay using a strain softening viscoplastic Model”. Int J Plasticity. 11(5): 523-45.

Oka F, Higo Y, Kimoto S. (2002) “Effect of dilatancy on the strain localization of water-saturated elasto-viscoplastic soil”. Int J Solids Struct. 39: 3625-47.

Oka F, Yashima A, Sawada K, Aifantis EC. (2000) “Instability of gradient-dependent elasto-viscoplastic model for clay and strain localization”. Comput Method Appl Mech Eng. 183: 67-86.

Perzyna P. (1963) The constitutive equations for work-hardening and rate sensitive plastic materials. In: Proc. of Vibration Problems, Warsaw. 3(4): 281-90.

COMPARISON OF DISTRIBUTION FUNCTIONS FOR THE NON-LOCAL STRAIN APPROACH

H. P. Jostad
Computational Geomechanics group, Norwegian Geotechnical Institute, Oslo, Norway

G. Grimstad
Computational Geomechanics group, Norwegian Geotechnical Institute, Oslo, Norway

ABSTRACT: *Sensitive soft clays generally display a significant post peak strain softening response under undrained deformation. A consequence of this behavior is that the continuing response beyond the peak shear stress is not unique. In finite element analyses a shear band generally develops in this phase. However, without a proper regularization technique the thickness of the shear band and generally also the orientation are governed by the finite element discretization. To overcome the problem of mesh dependency an internal length scale, that controls the shear band thickness without prescribing the orientation, must be introduced. One method to incorporate an internal length scale is to use the non-local strain approach. This approach may be implemented into any non-linear finite element programs without reformulating the governing finite element equations. This paper describes the implementation of the non-local strain approach into a user-defined material model that is used in the finite element program PLAXIS. The NGI-ADP model with a strain softening formulation is used. The effect of using different weighting functions for calculating the non-local strain is also studied in this paper.*

1 INTRODUCTION

The characteristic behavior of normally consolidated to slightly over-consolidated marine clays with moderate to high sensitivity display post-peak strain softening response in undrained loading. The reason for this behavior is the tendency of volume reduction during shear deformation (i.e. contractive response) and thus generation of pore pressure and reduction in effective stresses in undrained condition. The consequence of this characteristic behavior of sensitive clay is that failure or capacity may not be calculated using conventional limiting equilibrium methods. Instead, the peak load or capacity may be defined by an instability condition where the second order work becomes negative (see for instance the discussions in Darve (2010)). At this condition we have a deformation pattern where the effect of the reduction in shear stresses due to strain softening in part of the soil mass becomes larger than the resistance of the surrounding material. In this case we may start a progressive failure mechanism were the spreading of the failure zone may be significantly larger than captured by classical limiting equilibrium methods. This type of failure may be particularly dramatic in cases of failure in quick clay, were the fully remolded shear strength is less than 0.5 kPa.

In order to analyze this type of progressive failure in sensitive clays it is necessary to take into account the effect of strain softening behavior. This requires that these problems are analyzed by numerical methods as for instance the finite element method. However, when

analyzing strain softening problems with conventional displacement based finite element formulation, the results become mesh dependent. In order to overcome this problem an internal length scale, that controls the shear band thickness (without prescribing the orientation), must be introduced. One method to incorporate an internal length scale is to use the non-local strain approach (Eringen, 1981). This approach may be implemented into any non-linear finite element programs without reformulating the governing finite element equations. Grimstad et al. (2010) presented the implementation of a special version of the non-local strain approach proposed by Vermeer & Brinkgreve (1994) into a constitutive material model for undrained behavior of soft clay (NGI-ADP with softening). Due to some uncertainties related to the mathematical formulation of this so-called over non-local strain approach, the authors wanted to study the effect of this formulation in some more details and compare it with another formulation proposed by Galavi & Schweiger (2010). This is the main purpose of this paper.

2 NGI-ADPSOFT MODEL

To model the behavior of soft clay under perfectly undrained condition an elasto-plastic model with anisotropic strain hardening/softening response has been developed. The mathematical formulation of the model without the softening part which is called NGI-ADP, is presented in Grimstad et al. (2011). The extension in order to model the post-peak behavior of sensitive clays is obtained by including a second hardening function, κ_2, in addition to the original hardening function, κ_1, together with a non-local strain formulation. The strain softening formulation is based on previous work described for instance in Andresen & Jostad (2002), however, it is limited to plane strain conditions and without the non-local strain. A simple 1D representation of the yield function is shown in equation (1).

$$F = \tau - \kappa_1 \left(1 - \kappa_2\right) s_u - \kappa_2 \, s_{ur} = 0 \tag{1}$$

where τ is the shear stress, s_u is the peak undrained shear strength and s_{ur} is the residual undrained shear strength. The hardening functions κ_1 and κ_2 are given by equation (2) and equation (3).

$$\kappa_1 = 2\frac{\sqrt{\gamma^p / \gamma_p^p}}{1+\gamma^p / \gamma_p^p} \text{ when } \gamma^p < \gamma_p^p \text{ else } \kappa_1 = 1 \tag{2}$$

$$\kappa_2 = \begin{cases} 0 & \text{when} \quad \gamma^{p^*} \le \gamma_p^p \\ \dfrac{1}{2}\left(1 - \cos\left(\pi \dfrac{\gamma^{p^*} - \gamma_p^p}{\gamma_r^p - \gamma_p^p}\right)\right) & \text{when} \quad \gamma_p^p < \gamma^{p^*} < \gamma_r^p \\ 1 & \text{when} \quad \gamma^{p^*} \ge \gamma_r^p \end{cases} \tag{3}$$

where γ^p and γ^{p^*} are local and non-local plastic shear strains, while $\gamma_p{}^p$ and $\gamma_r{}^p$ are plastic peak and residual shear strain, respectively. The extension to a full 3D stress space with

anisotropic or stress path dependent behavior are described in more details in Grimstad et al. (2011). The full set of input parameters to the model is given below:

G_{ur} is the elastic unloading/reloading shear modulus
s_u^A, s_u^{DSS}, s_u^P are the active, direct simple shear and passive undrained shear strengths in plane strain condition
$s_u^A{}_r$, $s_u^{DSS}{}_r$, $s_u^P{}_r$ are the residual values of the active, direct simple shear and passive undrained shear strengths in plane strain condition
τ_0 is the initial cross-anisotropic shear stress
ε_{lf}^C is the maximum axial strain at the peak triaxial undrained compression strength s_u^C
γ_f^{DSS} is the maximum shear strain at the peak undrained DSS strength s_u^{DSS}
ε_{lf}^E is the maximum axial strain at the peak triaxial undrained extension strength s_u^E
ε_{lr}^C is the maximum axial strain at the residual triaxial undrained compression strength s_{ur}^C
γ_r^{DSS} is the maximum shear strain at the residual undrained DSS strength s_{ur}^{DSS}
ε_{lr}^E is the maximum axial strain at the residual triaxial undrained extension strength s_{ur}^E

These parameters may be obtained from anistropically consolidated undrained triaxial compression and extensions tests and undrained direct simple shear (DSS) tests. The ratio between plane strain and triaxial strength is based on in-house experience or obtained from additional biaxial tests. The shear strains at the residual strengths assume that the samples deform uniformly in the post-peak regime. If this is not the case, these strains must be corrected for the actual deformation pattern in the tests. These corrections can for instance be found by FE simulations as for instance described in Andresen & Jostad (1998).

3 NON-LOCAL STRAIN APPROACH

In order to regularize the strain softening behavior and control the shear band thickness the non-local strain approach has been implemented into the above constitutive model. The implementation and some applications were presented in Grimstad et al. (2010).
The classical formulation of the non-local strain proposed by Eringen (1981) is shown in equation (4)

$$\Delta\boldsymbol{\varepsilon}^{p*}(\mathbf{x}_i) = \frac{1}{V}\int\left(w(\mathbf{x})\,\Delta\boldsymbol{\varepsilon}^{p}(\mathbf{x})\right)dV \tag{4}$$

where V is the integral of $w(\mathbf{x})$ over the volume, $w(\mathbf{x})$ is the Gauss distribution function given in equation (5) and $\mathbf{x}_i$ are the integration point coordinates

$$w(\mathbf{x}) = \frac{1}{l\sqrt{\pi}}\exp\left(-\frac{\left(\mathbf{x}-\mathbf{x}_i\right)^T\left(\mathbf{x}-\mathbf{x}_i\right)}{l^2}\right) \tag{5}$$

The main purpose of this formulation is that the strain softening response in an integration point is not only governed by the local plastic strain, but instead the plastic deformation given by $\Delta\boldsymbol{\varepsilon}^{p*}$ within a specific volume governed by the internal length l. This may be a rational idealization when transforming microscopic stresses between soil grains to classical continuum based stresses. The disadvantage is at that this averaging method is governed by the internal length l and the distribution function $w(\mathbf{x})$, which are difficult to determine physically. In this study the internal length l is used to control the effective thickness of shear

bands that develop in the strain softening regime during undrained deformations of sensitive soft clays. It is assumed that the effective shear band thickness for a particular problem is known. This is therefore the motivation for another interesting research topic related to this problem at NGI and Norwegian University of Science and Technology (NTNU).

The weighting function $w(\mathbf{x})$ is so far only used to obtain an effective and robust solution during development and propagation of shear bands. To study the effect of the weighting function the different approaches proposed by Vermeer & Brinkgreve (1994) and Galavi & Schwieger (2010) are adapted into the softening formulation of the NGI-ADPSoft model.

Brinkgreve (1994) found when using the classical non local strain formulation from Eringen (1981), that the strain may still concentrate in the center points of the localized zone and not spreading to the surrounding points. Therefore he proposed a formulation which reduces the strain in the centre and increases the strain to the edge of the softening zone and consequently widens the localized zone to a thickness that can be controlled by the input parameters. This is done by introducing a parameter α that has to be larger than one for the approach to be effective. This so-called *over non-local* plastic strain increment is defined as:

$$\Delta\boldsymbol{\varepsilon}^{p^*}(\mathbf{x}_i) = \Delta\boldsymbol{\varepsilon}^{p}(\mathbf{x}_i) - \alpha\,\Delta\boldsymbol{\varepsilon}^{p}(\mathbf{x}_i) + \frac{\alpha}{V}\int\left(w(\mathbf{x})\,\Delta\boldsymbol{\varepsilon}^{p}(\mathbf{x})\right)dV \tag{6}$$

The disadvantage of this formulation is that the shear band thickness is controlled by two parameters, and it is unclear what the optimum combination of α and l is. Brinkgreve & Vermeer (1994) suggested that $\alpha = 2$ should work well. However, by considering equation (6), it is also seen that by using α larger than one the non-local plastic strain increment may even become negative and thus delaying the softening response. The effect of using different combinations of α and l will therefore be studied by numerical analyses in the next Chapter.

Due to the disadvantage of the above over non-local formulation Galavi & Schweiger (2010) proposed an alternative weighting function where a similar effect is obtained by modifying the weighting function $w(\mathbf{x})$. This function is then used in the classic non-local strain formulation ($\alpha = 1$). The weighting function proposed by Galavi & Schweiger (2010) is given in equation (7). This non-local strain formulation is for simplicity in the following called G&S.

$$w(\mathbf{x}) = \frac{\sqrt{\left(\mathbf{x}-\mathbf{x}_i\right)^T\left(\mathbf{x}-\mathbf{x}_i\right)}}{l^2}\,\exp\left(-\frac{\left(\mathbf{x}-\mathbf{x}_i\right)^T\left(\mathbf{x}-\mathbf{x}_i\right)}{l^2}\right) \tag{7}$$

3.1 Analytical solution of effective thickness of shear band as a function of l

Brinkgreve (1994) gave an analytical solution for a tension bar problem with periodical localization. This solution was found by assuming that the plastic strain is distributed in a cosine distribution. Combining the equation for the actual *non-local* strain with the cosine distribution of plastic strain results in an analytical expression for the one dimensional *non-local* strain, $\varepsilon^{p^*}(x)$. Requiring that $\varepsilon^{p^*}(x)$ is constant within the shear band, i.e. that $\mathrm{d}\varepsilon^{p^*}(x)/\mathrm{dx} = 0$ (which also gives a constant stress within the shear band), the effective thickness of the shear band can be found. For the *over non-local* approach this results in an equation for the effective shear band thickness as a function of α as given by equation (8). This means that for selection of $\alpha = 1.58$ the effective thickness of the shear band, t_{sb}, equals π times the internal length ($t_{sb} = \pi \cdot l$).

$$t_{sb} = \pi\, l_{\text{int}} \left(\ln\left(\frac{\alpha}{\alpha - 1} \right) \right)^{-\frac{1}{2}} \tag{8}$$

The same procedure is also used for the G&S approach. In such case the weighting function in the expression for $\varepsilon^{p*}(x)$ is replaced by the modified version. However, in this case the integral to be solved is more difficult that for the Gauss distribution. The solution for the effective shear band thickness using the modified weighting function is given by solving equation (9) numerically for t_{sb} as function of l, this gives $t_{sb} \approx 3.4 \cdot t$.

$$2\pi \frac{l_{\text{int}}}{t_{sb}} \exp\left(-\left(\frac{\pi l_{\text{int}}}{t_{sb}} \right)^2 \right) \int_0^{\frac{\pi l_{\text{int}}}{t_{sb}}} e^{r^2}\, dr = 1 \tag{9}$$

3.2 Implementation

The NGI-ADPSoft model is implemented into the in-house finite element code BIFURC, where the non-local strain increment (total strain increment) is calculated at the start of each iteration. The model and method is also implemented as a user-defined material model in the commercial finite element program PLAXIS. In this subroutine the non-local strain is calculated from the plastic strain increment in the previous iteration. In both cases an implicit integration scheme adopted from de Borst & Heeres (2002) is used to determine the local plastic strains. The non-local strain approach is computationally quite costly, especially if one is to compute the contribution to the non-local strain from all integration points. Therefore, in the current implementation the non-local strain is computed by the integration points inside a radius of $3 \cdot l$ for each integration point. The non-local strain contribution (i.e. the integral) is calculated numerically by summing over all integration points together with the element dependent volume of each integration point. The material model needs therefore this volume as input parameter in addition to the standard input data. Furthermore, the strain increments of all integration point must be available in the material model. These strains must therefore either be written to a file or saved in a common array.

4 SIMULATIONS

4.1 Shear test

To study the performance of the different weighting functions in more detail a 1D shear column is considered. These analyses are performed by the in-house FE program BIFURC. A 100 mm high column is modeled by 50 2-noded shear elements with the same length of 2 mm. The 2-noded element has two displacement degrees of freedom in each node (axial and lateral displacements). The bottom of the column is totally fixed. The column is deformed by applying a horizontal shear stress at the top. The material parameters used in this example are presented in Table 1. The elastic shear modulus G_{ur}, the peak undrained DSS shear strength s_u^{DSS} and the residual undrained DSS shear strength $s_u^{DSS}{}_r$ are normalized by the undrained peak active shear strength s_u^A. The blue curve in Fig. 1 shows the normalized shear stress versus the horizontal displacement at the top of the column under uniform deformation (i.e. the shear stress–shear strain curve of the material). Analyses were then performed by reducing the peak shear strength in the middle element (25 to 27 mm above the bottom) by 0.1%. The main purpose here is to study the performance of both the over non-local strain

approach and the weighting function proposed by Galavi & Schweiger (2010) (in the following called G&S for simplicity).

Table 1 Soil parameters for the NGI-ADPsoft model used in the 1D shear column

G_{ur}/s_u^A	s_u^{DSS}/s_u^A	$s_u^{DSS}{}_r/s_u^A$	γ_f^{DSS}	γ_r^{DSS}
500	0.67	0.5	5%	20%

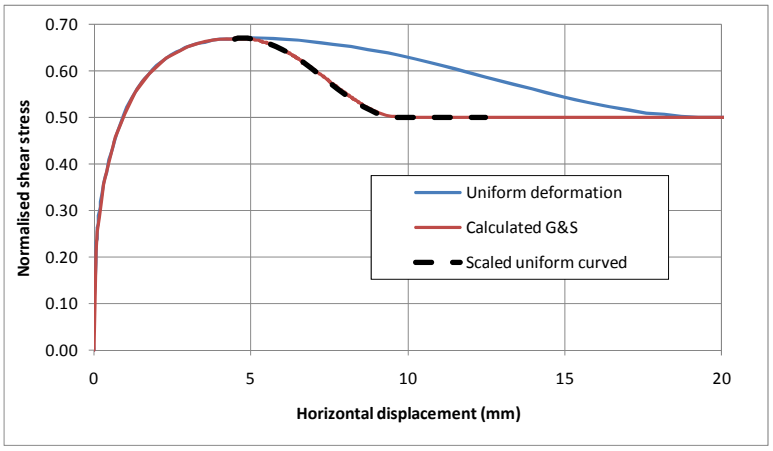

Fig. 1. Normalized shear stress versus horizontal displacement at the top of the column for uniform deformation and for a condition where the post peak plastic deformation is localized in an effective shear band of 34 mm or 34% of the total height

The red curve in Fig. 1 shows the result obtained using the G&S weighting function together with an internal length l of 10 mm. The effective shear band thickness t_{sb} is found to be 34 mm, i.e. 3.4 times the internal length l. This agrees with the idealized analytical solution presented in Section 3.1. The effective shear band thickness is here found by scaling the shear stress-displacement curve for uniform deformation by the effect of localized plastic deformation until it fits the calculated curve. It is assumed that the shear strain is constant within the effective shear band and following the post peak stress-strain softening curve. The material outside the shear band is elastically unloaded and the deformation is given by the elastic shear modulus. This effective shear band thickness which is what we want to give as input to the analyses of our strain softening sensitive clay, is very difficult to extract from the calculated results. By considering the distribution of the shear strain increment along the shear column in the strain softening regime, see Fig. 2, the shear zone is smaller than 34 mm. It is only slightly larger than two times the internal length. However, by integrating the shear strain increment over this zone, it is found the average shear strain increment over the zone is larger than the shear strain increment given by the material curve. This is the reason why the effective shear band thickness is larger than the calculated shear zone. The shear strain distribution obtained with $\alpha = 1.58$ and $l = 3.4/3.14 \cdot 10$ mm = 10.8 mm (which gives an effective shear band thickness of 34 mm) is in Fig. 2 compared with the distribution obtained with G&S and $l = 10$ mm. It is seen that the strain distribution is very smooth with the over non-local strain approach while it is significantly more irregular with G&S. These two distributions are obtained with the same equilibrium tolerance factor such it is possible that the G&S distribution becomes more regular for an even tighter tolerance factor. However, this makes the G&S method more inefficient. Even with this irregular distribution the G&S method is found to regularize the problem perfectly and with an effective shear band thickness of 3.4 l.

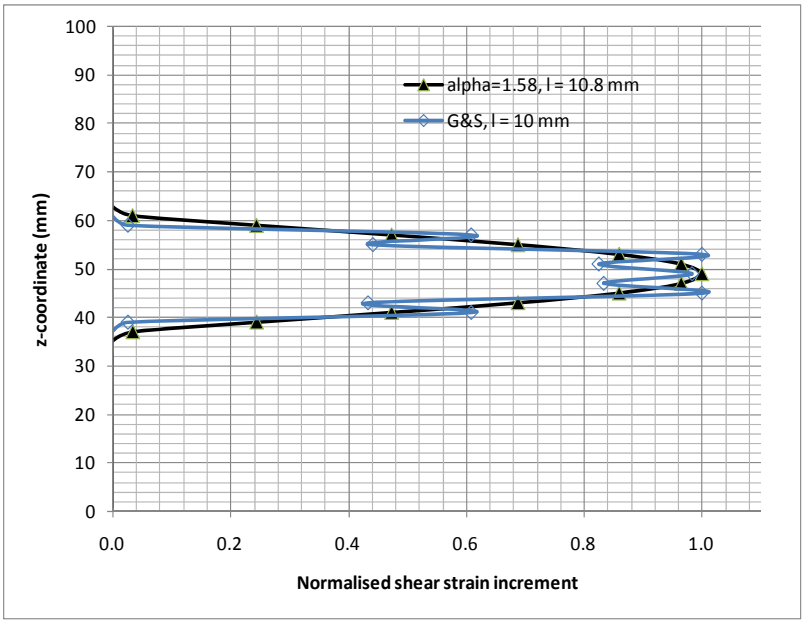

Fig. 2. Distribution of the scaled shear strain increment in the post peak softening regime obtained with the over non-local strain approach with α = 1.58 and l = 10.8 mm (black curve), and with the weighting function proposed by Galavi & Schweiger (2010) and l = 10 mm (blue curve)

The calculation time (here expressed by the accumulated number of iterations) and ratio between calculated effective shear band thickness (found by scaling the stress-strain curve) and the analytical shear band thickness (given in Section 3.1) are compared for different α-values in the over non-local strain approach together with the weighting function of G&S. The results are presented in Table 2.

Table 2. The effect of using different weighting functions

α	*1.01*	*1.1*	*1.2*	*1.58*	*2.0*	*G&S*
l (mm)	23.25	16.76	14.49	10.8	9.01	10.0
Calculated t_{sb} over analytical t_{sb}	129%	112%	106%	103%	100%	100%
No. of increments	475	647	427	361	286	739
Accumulated no. of iterations	21523	30212	18207	17142	12774	23717

Based on this study it seems that the recommendation by Brinkgreve and Vermeer (1994) of using α = 2.0 gives the most optimum solution with respect to calculation time and accuracy in calculating the effective shear band thickness. However, this result is based on a very simple problem such more complex boundary value problems need to be studied. Furthermore, the results obtained with low α-values may have been affected by the boundary conditions.

4.2 Biaxial compression test

To continue the study of the non-local strain approach and the effect of using different weighting functions a plane strain (biaxial) compression test is considered. The top and bottom boundaries are assumed to be perfectly rough in order to trigger localization without any introduction of an arbitrary perturbation. Table 3 gives the NGI-ADPSoft model parameters. This biaxial compression test simulation is also used to study the effect of

accounting for symmetry lines together with the non-local strain approach. Based on the mathematical formulation this is expected to affect the results. In all simulations 15 node triangular elements are used in Plaxis. Nine cases are presented in the following. Simulations with the G&S weighting function (called modified non-local in the figures), the original weighting function in the non-local strain approach (α = 1) and with the original weighting function in the over non-local approach (α = 1.58) are considered. Each of these sets is used together with: a "medium" mesh, a "fine" mesh and a "fine" mesh with symmetry lines. The specified internal length parameter l is 5 mm in all cases. This automatically gives somewhat different effective shear band thicknesses and is therefore one reason for the different post-peak softening responses. The analyses should therefore in the future also be repeated with varying l that theoretically gives the same effective shear band thickness. The height of the sample is 100 mm and the width is 50 mm. The initial stress condition is generated such that the initial shear stress is equal the input parameter τ_0. To obtain results that are expected to be sufficient objective, the error criteria of the norm of the unbalanced nodal force vector divided by the norm of the external nodal load vector is set to 0.01%. Such a low error criteria is found to be necessary for boundary value problems with small gradients of stresses in order to ensure localization close enough to the first critical bifurcation point. For boundary value problems that involve larger gradients in stresses a larger error criteria may be used.

Table 3 Soil parameters for the NGI-ADPsoft model

G_{ur}/s_u^A	s_u^{DSS}/s_u^A	s_u^P/s_u^A	s_{ur}^A/s_u^A	s_{ur}^{DSS}/s_u^A	s_{ur}^P/s_u^A	ε_{1f}^C	γ_f^{DSS}	ε_{1f}^E	ε_{1rf}^C	γ_r^{DSS}	ε_{1rf}^E	τ_0/s_u^A
500	0.7	0.4	0.1	0.1	0.1	1%	2%	3%	13.3%	20%	13.3%	0.7

Due to the difference in the obtained effective thickness of the shear band with the different approaches the results are presented individually in plots of normalized vertical displacement (δ_v/H) versus normalized excess stress (vertical stress in excess of the initial effective stress). The peak increase in vertical stress divided by the peak undrained active shear strength s_u^A under homogeneous deformations is then $2 \cdot (1.0 - 0.7) = 0.6$. For the simulations with different number of elements both the G&S weighting function and the over non-local approach gives mesh independent results. However, the cases where symmetry is utilized give results which are model dependent. It must be noted that the differences for this particular problem is very small. Fig. 3 shows the small difference that is obtained in the normalized load–displacement curves with the different formulations and the effect of including symmetry lines.

From the normalized load displacement curves it is seen that calculated effective shear band thickness obtained by the G&S weighting function is slightly smaller than obtained with α = 1.58, i.e. the post peak softening curve is slightly steeper. This does not agree with the analytical solutions for 1D condition, where the effective thickness with G&S weighting function should be 3.4/3.14 = 1.08 larger. An explanation for this should be found.

From the contour plots of total shear strains in Fig. 4 it is seen that the shear band orientation (where the inclination is less than 45 degrees from horizontal) is affected by the shear band thickness. This seems to be due to the assumption of rough boundaries at the top and bottom of the sample combined with the kinematics of a thin shear band. However, how the non-local strain approach affects the orientation of a propagating shear band will be studied in the future.

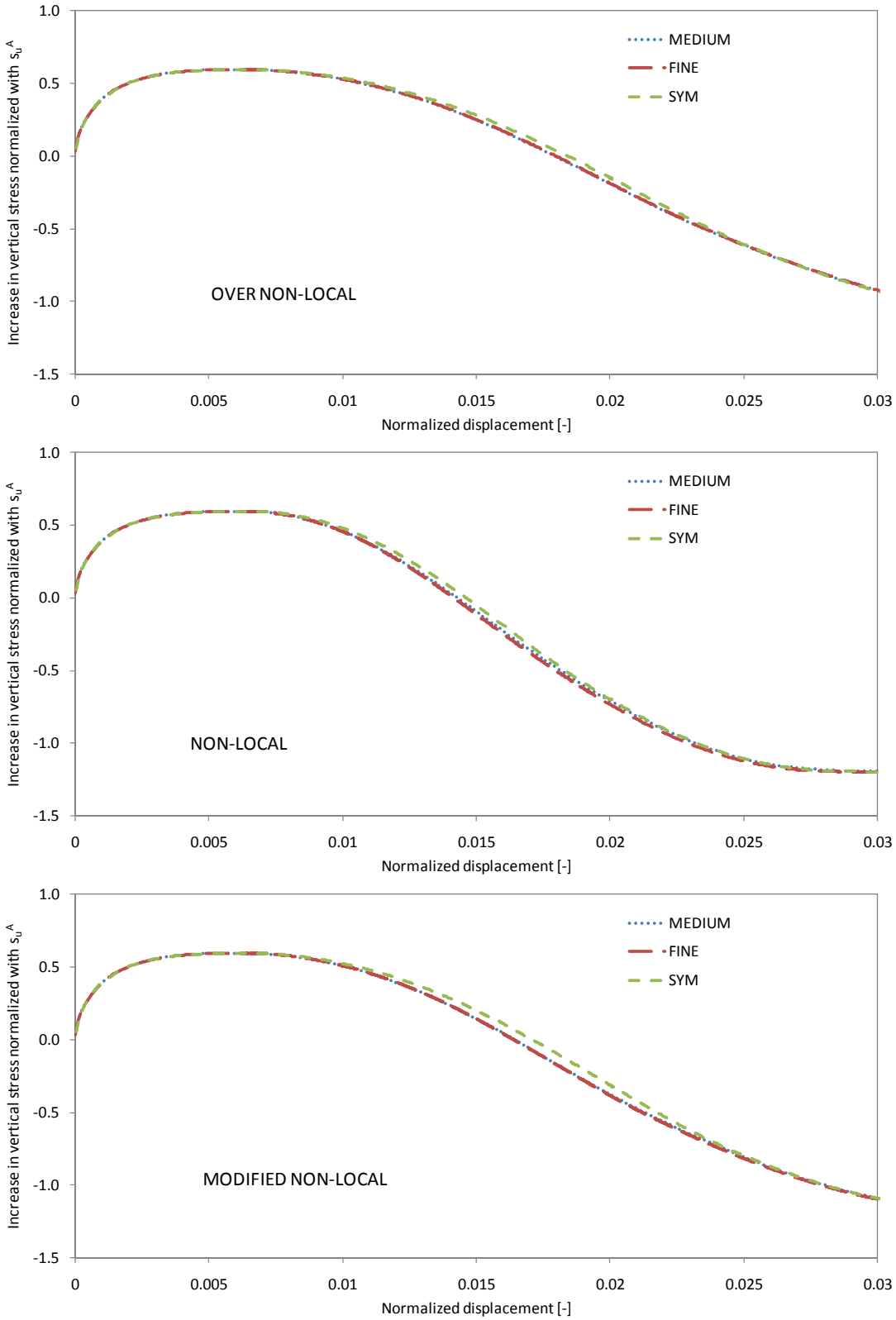

Fig. 3. Normalized load displacement curves. Over non-local with α = 1.58, non-local (α = 1.0) and Galavi & Schweiger's modified weighting function. Internal length l = 5 mm.

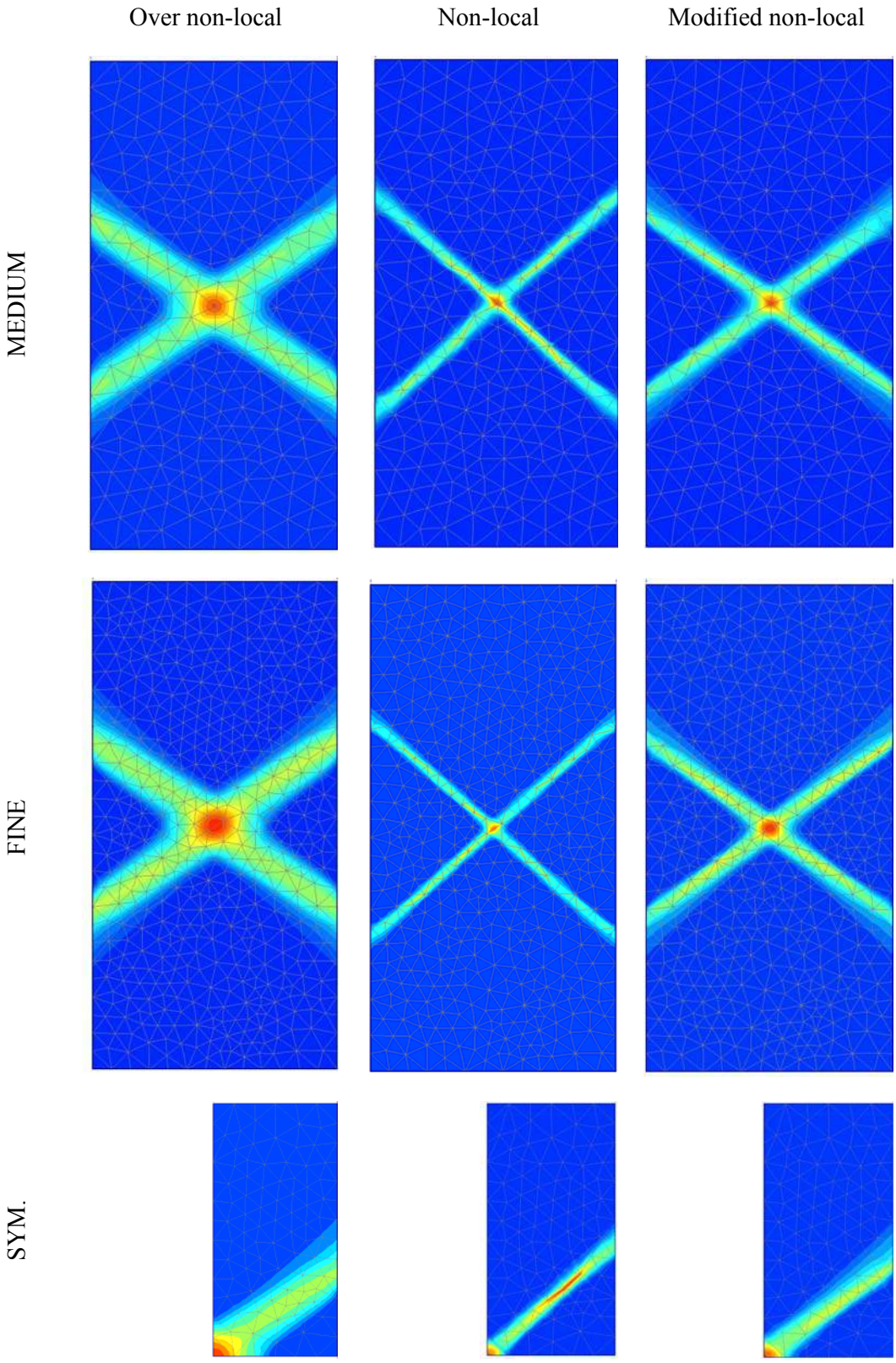

Fig. 4. Contour plots of total shear strain at the end of the analyses

5 CONCLUSIONS

This paper considers the effect of using different weighting formulations in the non-local strain approach incorporated in the strain softening elasto plastic model NGIADPSoft (Grimstad et al. 2010) for undrained behavior of sensitive soft clays. Based on this study the recommendation by Brinkgreve and Vermeer (1994) of using the over non-local strain approach with $\alpha = 2.0$ seems to be valid. However, this needs somewhat finer discretisation than using $\alpha = 1.58$ when the same effective shear band thickness should be modeled, i.e. the internal length l needs to be reduced by about 17% when α is increased from 1.58 to 2.0. The over non-local strain approach is found to be more attractive than using the weighting function proposed by Galavi & Schweiger (2010) since the G&S method gives more irregular strain distribution within the shear zone. It should also be emphasized that the effective shear band thickness assuming constant shear strain within the shear band, is larger than the calculated shear zone. This effect is important to account for when comparing different weighting functions.

The non-local strain approach as a regularization technique is attractive due to its simplicity. It may by some approximations only involve implementation at the material point level. Furthermore, it makes it possible to model shear band propagation without any criteria for when and where to develop and no need to define the orientation. The shear band formation and propagation are automatically given by the material model together with the specified effective shear band thickness as long as the element mesh is fine enough. Thin shear bands must be modeled by refining the mesh in zones where shear band develops. That the shear band thickness for this type of problem is unknown is another problem and not solved by any standard regularization techniques. Further research is therefore needed to define the actual shear band thickness to be used in this type of analyses.

ACKNOWLEDGEMENT

Part of this work has been carried out in a Joint Industry Project, financed by the Norwegian Road Authorities (SSV), The Norwegian Water Resources and Energy Directorate NVE, and The Norwegian Geotechnical Institute (NGI). The research was also partly carried out as a part of "GEO-INSTALL" (Modelling Installation Effects in Geotechnical Engineering), supported by the European Community through the program " Marie Curie Industry-Academia Partnership and Pathways" (Contract No PIAP-GA-2009-230638).

REFERENCES

Andresen, L. & Jostad, H.P. (1998), "Effect of strain-softening in interpretation of laboratory compression tests", Proceedings of 4th European Conference on Numerical Methods in Engineering - NUMGE 1998. Udine, Italia, 223-232.

Andresen, L. & Jostad, H.P. (2002), "A constitutive model for anisotropic and strain-softening clay", Proceedings of Numerical Models in Geomechanics - NUMOG VIII. Rome, Italy, 79-84.

Brinkgreve, R.B.J (1994), Geomaterial Models and Numerical Analysis of Softening, PhD thesis, TU Delft, Delft, The Netherlands.

de Borst, R. & Heeres, O. M. (2002), "A unified approach to the implicit integration of standard, non-standard and viscous plasticity models", Int. J. Numer. Anal. Meth. Geomech. 26, 1059–1070.

Darve, F., (2010), "Bifurcation in geomaterials: experiments and modelling", Proceedings of 9th HSTAM International Congress on Mechanics, Vardoulakis mini-symposia, Limassol, Cyprus

Eringen, A.C. (1981), “On non-local plasticity”, Int. J. Eng. Science, 19, 1461-1474.
Galavi, V. & Schweiger, H.F. (2010), “Nonlocal Multilaminate Model for Strain Softening Analysis” International Journal of Geomechanics, 10, 30-44.
Grimstad, G., Jostad, H.P. and Andresen, L., (2010), “Undrained capacity analyses of sensitive clays using the non-local strain approach”, Proceedings of 9th HSTAM International Congress on Mechanics, Vardoulakis mini-symposia, Limassol, Cyprus
Grimstad, G., Andresen, L. and Jostad, H.P. (2011), “NGI ADP: Anisotropic Shear Strength Model for Clay”, International Journal for Numerical and Analytical Methods in Geomechanics, DOI: 10.1002/nag
Vermeer, P. A. & Brinkgreve, R. B. J. (1994), “A new effective non-local strain-measure for softening plasticity”, Proceedings of 3rd Intern. Workshop on Localisation and Bifurcation Theory for Soils and Rocks, Grenoble, September 1993, 89-100.

MICROSTRUCTURAL EVOLUTION IN DIFFUSE GRANULAR FAILURE: FORCE CHAINS AND CONTACT CYCLES

Antoinette Tordesillas
Department of Mathematics and Statistics, University of Melbourne, Melbourne, Australia

Luc Sibille
GeM Laboratory – University of Nantes, ECN, CNRS – Nantes, France

Sebastian Pucilowski
Department of Mathematics and Statistics, University of Melbourne, Melbourne, Australia

François Nicot
CEMAGREF – Unité ETNA – Grenoble, France

Félix Darve
3S-R Laboratory – INPG, UJF, CNRS – Grenoble, France

ABSTRACT: *We focus on structural evolution inside a deforming granular material, in three-dimensions, undergoing the so-called diffuse failure, i.e. failure in the absence of strain localization. We uncover and characterize quantitatively the basic building blocks for self-organization, enabling comparisons of the material's rheology to those recently reported for dense materials undergoing localized failure. The building blocks consist of: (i) the quasi-linear, load-bearing force chains, and (ii) their supporting network of contacts, the minimal n-cycles. Our preliminary study shows that, similar to localized failure, self-organization in the system gives rise to major load-bearing, columnar force chains which are supported laterally by truss-like 3-cycles. Under continued loading, the force chains ultimately fail by buckling, precipitating a catastrophic collapse of the material. However, unlike localized failure, the buckling events uncovered here do not appear to be localized.*

1 Introduction

The recent decades have witnessed remarkable strides in uncovering the "inner workings" of granular materials – with considerable insights derived from high-resolution experiments and discrete element (DEM) simulations (e.g. Iwashita & Oda 2000; Majmudar & Behringer 2005; Rechenmacher 2006; Desrues & Viggiani 2004; Tordesillas & Muthuswamy 2009; Walker & Tordesillas 2010; Tordesillas et al. 2010a, 2010b, 2011; Arevalo et al. 2010, and references cited therein). In particular, much light has been cast on the microscale mechanisms and underpinning dynamics behind the onset of instability and failure of granular materials via strain-localization. But equally important to geomechanics are non-localized diffuse modes of failure (Darve et al. 2004, 2007; Nicot & Darve 2007; Nicot et al. 2009; Sibille et al. 2008), and yet there is a dearth of knowledge on the micromechanics of diffuse failure. Detailed consideration of both modes of failure presents a broad gamut of questions for exploration that bears the potential to advance our understanding of granular failure to a whole new level. Such questions include: How and

why does a material favour one mode over the other? What are the fundamental commonalities and differences between localized and diffuse modes in terms of force transmission? In this joint study, we examine using Complex Networks the development of diffuse failure from the standpoint of force transmission, with particular attention paid to the force chains and their supporting contact cycles – key self-organized load-bearing structures whose cooperative behaviour was first examined in Tordesillas et al. 2010a.

Data used are from discrete element simulations of proportional strain loading paths on a three-dimensional dense granular assembly (Darve et al. 2007). These loading paths are rather unique and offer an opportunity for us to explore novel rheological granular behaviour that are not otherwise possible in traditional tests. These loading paths can be seen as a generalization of the undrained compression test. Diffuse failure is triggered from stress states reached along these proportional strain paths, and located inside the Mohr-Coulomb limit condition, by adopting an appropriate mixed (stress-strain) mode of control (Darve et al. 2004, 2007; Nicot et al. 2009). Although these simulations have been reported on in the past, the concepts and methods employed here constitute a first-of-a-kind approach for studies of diffuse failure in dense granular systems. Here we employ a Complex Systems approach, and analyze the quasi-statically deforming material as an evolving complex network (Walker & Tordesillas 2010; Tordesillas et al. 2010b). Our objective is to identify the basic building block structures for self-organization, study their evolution, and establish some common features with the structural evolution recently uncovered for localized failure (Tordesillas et al. 2010a, 2010b, 2011).

The paper is arranged as follows. We first describe the Discrete Element (DEM) simulation in Section 2. Therein we highlight salient features of the loading program to provide some insight into the loading conditions to which the specimen has been subjected, and thereby render more transparent the connection between such conditions and the material's response. The studies discussed in the Section 3 characterize this connection from the standpoint of the building-blocks for self-organization. We conclude in Section 4 with a summary of our key findings and highlight future research directions.

2 Discrete numerical simulations

2.1 The discrete element model

The three-dimensional numerical model (Darve et al. 2007; Sibille et al. 2009) is based on the discrete element method (Cundall & Strack 1979). It consists of a cubical shape assembly of more than 10,000 polydisperse spherical particles. The inter-particle interaction is modelled in the normal contact direction by a linear elastic relation, and in the tangential direction by an elastic perfectly plastic relation. The macroscopic stress-strain state of the granular assembly is imposed through six frictionless walls whose positions are controlled to follow the prescribed loading programme. The strain state is determined from wall positions and the stress state from wall-particle contact forces.

2.2 Loading programme and macroscopic response

The loading programmme (Darve et al. 2007) followed during simulations can be split into two steps. First, the numerical sample is brought from an isotropic stress-strain state to a given mechanical state denoted 'initial state'. Second, from this initial state, the loading programme is changed in order to try to trigger the failure of the sample.

In the first step, the sample is fully strain controlled. It means that the three principal strain components (ε_1, ε_2 and ε_3) are controlled and imposed by the operator, whereas the three principal stress components (σ_1, σ_2 and σ_3) constitutes the response parameters resulting from simulations. However, all strain components are not controlled directly, but some of the strain components are controlled trough a linear combination of them. For instance, for an isochoric compression with respect to axis '1' and with an axisymmetric condition ($\Delta\varepsilon_2 = \Delta\varepsilon_3$), the operator controls directly the parameter ε_1 by imposing $\Delta\varepsilon_1 > 0$ (i.e. a positive strain rate). In addition, to impose the isochoric condition, the operator imposes the following linear combination: $\Delta\varepsilon_v = \Delta\varepsilon_1 + 2\Delta\varepsilon_3 = 0$. In this paper, the isochoric loading programme is generalized by imposing always directly the axial strain $\Delta\varepsilon_1 > 0$, but by generalizing the linear combination imposed between principal strain components in the following way (Darve et al. 2004):

$$\Delta\varepsilon_1 + 2\,R\,\Delta\varepsilon_3 = 0 \tag{1}$$

where R is a parameter chosen by the operator. For $R = 1$ we retrieve the isochoric condition, while for $0 < R < 1$ the path is dilatant and for $R > 1$ it is contractant. A such loading programme is named 'proportional strain loading path'. Fig 1a shows the proportional strain path followed with the discrete element model for $0.7 \leq R \leq 1$.

Besides, if each strain component are controlled directly (and separately) the associated response parameters are the stress components respectively (i.e. in axisymmetric condition, ε_1 is associated with σ_1, and ε_3 with σ_3). The sum of the products between associated control and response parameters is homogeneous to an energy density W, writing in axisymmetric condition:

$$W = \varepsilon_1\sigma_1 + 2\,\varepsilon_3\sigma_3 \tag{2}$$

Nevertheless, for the proportional strain loading programme the control parameters are ε_1 and $\varepsilon_1 + 2\,R\,\varepsilon_3$. Consequently, the corresponding response parameters are no more σ_1 and σ_3 but rather $\sigma_1 - \sigma_3/R$ and σ_3/R respectively, in order to verify:

$$W = \varepsilon_1\sigma_1 + 2\varepsilon_3\sigma_3 = \varepsilon_1\left(\sigma_1 - \frac{\sigma_3}{R}\right) + (\varepsilon_1 + 2R\varepsilon_3)\frac{\sigma_3}{R} \tag{3}$$

Therefore, the computed responses to proportional strain loading paths displayed in Fig 1a should be represented in a $\sigma_1 - \sigma_3/R$ versus ε_1 diagram, as shown in Fig 1b.

Darve et al. 2004 and Nicot & Darve 2007 shown that bifurcation points, from which diffuse failure can develop (if proper conditions with respect to the loading direction and the mode of control of the sample are verified), can be detected by the vanishing of the second-order work. For proportional strain paths, since the relation $\Delta\varepsilon_1 + 2\,R\,\Delta\varepsilon_3 = 0$ is imposed, the second-order work $W2$ simplifies in the following way:

$$W2 = \Delta\varepsilon_1\left(\Delta\sigma_1 - \frac{\Delta\sigma_3}{R}\right) + (\Delta\varepsilon_1 + 2R\Delta\varepsilon_3)\frac{\Delta\sigma_3}{R} = \Delta\varepsilon_1\left(\Delta\sigma_1 - \frac{\Delta\sigma_3}{R}\right) \tag{4}$$

In addition, the operator also imposed the condition $\Delta\varepsilon_1 > 0$, consequently the sign of the second-order work is the same as the sign of $\Delta\sigma_1 - \Delta\sigma_3/R$. For R values sufficiently small (i.e. for strain paths sufficiently dilatant), $\sigma_1 - \sigma_3/R$ *vs* ε_1 curves in Fig 1b present a peak. At the peak of $\sigma_1 - \sigma_3/R$, the second-order work vanishes and then takes negative values along the following decreasing curves.

The mechanical states corresponding to these maximum of $\sigma_1 - \sigma_3/R$ and the following decreasing curves (i.e. corresponding to nil or negative values of W2) constitute mixed limit

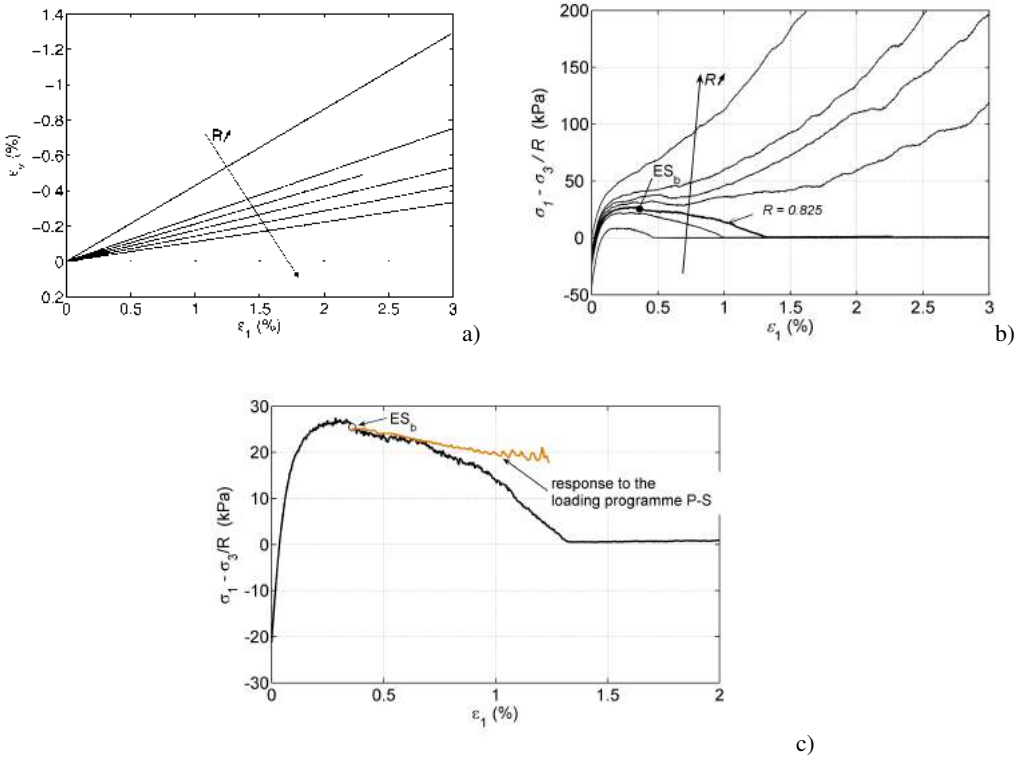

Fig. 1. a) Proportional strain loading paths applied to the sample for $R = 0.7$; 0.8; 0.825; 0.85; 0.875; 0.9; 1.0; b) computed responses; c) computed response to the proportional strain path for $R = 0.825$, and computed response to the loading programme P-S.

states (Darve et al. 2004). These mixed limit states can been seen as a generalization of classical limit stress states. Here the considered limit states are mixed because they cannot be crossed for a mixed stress-strain control mode. Therefore, the first loading programme fully strain controlled is now, in a second step, changed by a mixed loading programme (partially defined with strain components and stress components respectively) in order to try to trigger failure. We need to impose a mixed mode of control, by still imposing the strain loading direction defined by equation (1) (Darve et al. 2004), together with forcing the sample to cross the mixed limit state considered. As the response parameter $\sigma_1 - \sigma_3/R$ decreases when the sample is loaded from a mixed limit state, we simply invert the control and response parameters ε_1 and $\sigma_1 - \sigma_3/R$, in order to impose an increase of $\sigma_1 - \sigma_3/R$.

To resume, we consider now only the proportional strain loading path characterized by $R = 0.825$, the corresponding computed response path is identified in Fig 1b and c. Along this response path we consider the stress-strain state denoted ES_b in Fig 1b and c, and located slightly after the peak of $\sigma_1 - \sigma_3/R$. This state is a mixed limit state and it will constitute the initial state for the new loading programme, denoted P-S, and consisting to impose together to the sample:

$$\Delta\varepsilon_1 + 2R\Delta\varepsilon_3 = 0 \tag{5}$$

and

$$\Delta\sigma_1 - \Delta\sigma_3/R = 250 \text{ Pa} \quad \text{(representing 1 \% of } \sigma_1 - \sigma_3/R \text{ at } ES_b) \tag{6}$$

with $R = 0.825$.

Fig 2 presents the computed response to the loading programme P-S: actually the small increase in $\sigma_1 - \sigma_3/R$ that is tried to be applied cannot be reached together with the imposed condition $\Delta\varepsilon_1 + 2R\Delta\varepsilon_3 = 0$ (see also Fig 1c). In addition the stress components σ_1 and σ_3 tend

to vanish with a sharp temporal increase of strains and kinetic energy (Nicot et al. 2009) of the sample (i.e. the sum of the kinetic energy of all particles of the assembly), illustrating the sudden failure of the sample (loss of controllability in the sense of Nova 1994) characterized by a transition from a quasi-static regime to a dynamic regime (Darve et al. 2007; Nicot et al. 2009), where inertial terms are no more negligible (explaining why the axial stress σ_1 does not vanish while $\sigma_3 = 0$ at the end of the simulation). These results show that ES_b is actually a mixed limit state that cannot be passed according to the mixed loading programme P-S, resulting in the diffuse failure of the sample. From Fig 2, and more particularly from the change of kinetic

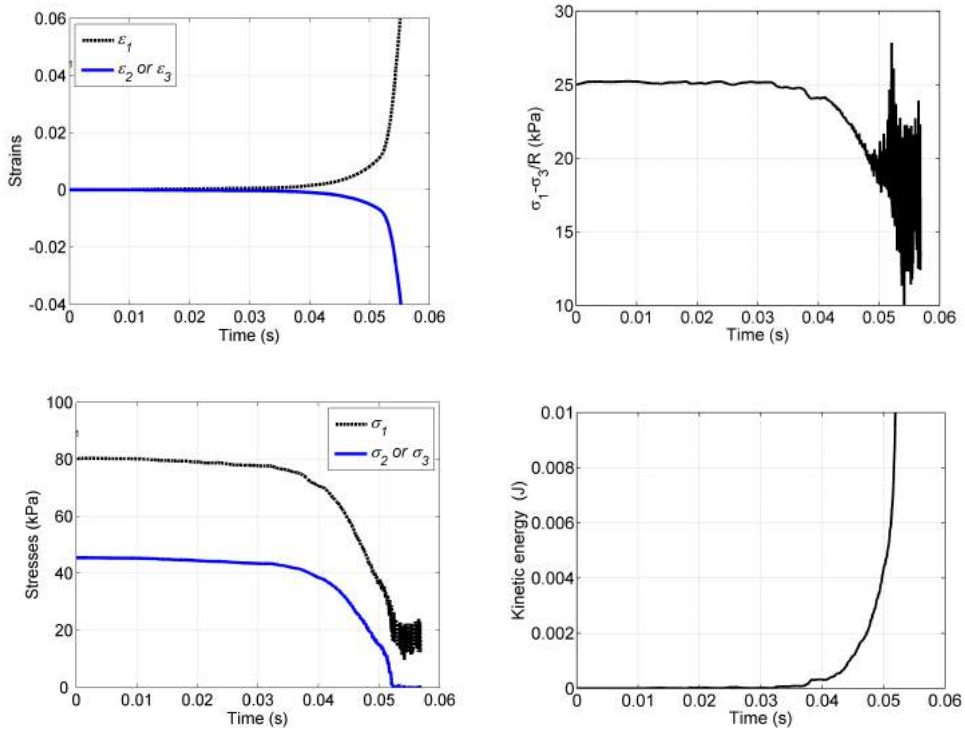

Fig. 2. Failure of the granular assembly simulated from the mixed limit state ES_b, resulting of the application of the mixed stress-strain loading programme P-S

energy, two different response regimes can be identified, firstly an almost stable and quasi-static regime followed by an unstable and dynamic regime. Table 1 give time intervals of these regimes which will be investigated in Sec 3.

Table 1. Time intervals (s) of key regimes.

Initial state	Loading programme	Stable–quasi-static	Unstable–dynamic
ES_b	P-S	$(0.0, 0.03)$	$(0.03, 0.06)$

3 Building blocks for self-organization

The process of self-organization during granular deformation presents hallmarks of complexity that are more directly tractable compared to other well-known complex systems, e.g. telecommunication, social and biological networks (Walker & Tordesillas 2010; Arevalo et al. 2010; Watts & Strogatz 1998). Complexity in granular materials emerges from the interactions of the constituent particles through their contacts: the contacts can be tracked in real time and the interactions between particles can be quantified through the forces and torques transmitted through these contacts. Other complex networks do not lend themselves so readily to this level of quantitative detail: interactions between computers or human beings or protein molecules are difficult to define, let alone measure (Watts & Strogatz 1998).

We have full information on contacts for the system described in Sec 2. Thus we can construct a complex network (or mathematical graph) comprising nodes and links, to represent the sample at every fixed simulation time or strain state of the loading history. The nodes in the network represent the particles, while the links connecting the nodes in the network represent the contacts between particles in the system. We first identify the load-bearing quasi-linear structures of m-force chains and their supporting cyclic network of contacts, the minimal n-cycles, where $m \geq 3$ and $n \geq 3$ are integers representing the number of particles that form the chain or cycle (Tordesillas et al. 2010a, 2011). We refer readers to Tordesillas et al. 2011 for details of the methods and algorithms used to identify force chains and minimal n-cycles, from the particle scale information that forms the output data of the DEM simulation described in Sec 2. At any given strain state in the simulation, a columnar force chain is confined by supporting contacts that can be succinctly summarised by the minimal cycle basis of the contact network, i.e. n-cycles, so that each force chain will have its own set of minimal cycles of various sizes n (see Fig 3). In this context, force chains are distinct from n-cycles in that force chains are physical structures made up of m particles, whereas cycles are made up of contacts and n is the number of particles that form the contact cycle. The smallest members of the n-cycles, i.e. 3-cycles, are special from the standpoint of packing and network connectivity: they are formed from three particles in mutual contact, and thus exemplify a densely packed and tightly connected structure that frustrates rotations (Tordesillas et al. 2010a). More generally, rotations are 'frustrated' in groups of particles forming an odd-cycle, whereas $even$-cycles allow free rotations (akin to the action of ball bearings) (Tordesillas et al. 2010a, 2011). Since particle rotations have long been identified as playing a crucial role in the deformation of granular materials – especially in the failure regime – the odd-cycle membership can be reasonably expected to play a key role in the mobilization of shear strength or resistance to applied loads.

Past experimental and numerical studies of dense granular materials undergoing localized failure, in both two and three dimensions, have shown that force chains and their surrounding contact cycles may be viewed as the basic building blocks for self-organization, and their collective and cooperative interactions govern global rheology (Tordesillas et al. 2010a, 2010b, 2011, 2010c). For the sample under study, we find the distributions of the populations of n-force chains in Fig 4 to be qualitatively similar to those for systems that undergo localized failure. The relative dominance of a given class of n-force chains decreases as n grows. The shortest, 3-force chains constitute the clear majority. From a structural mechanics standpoint, this makes sense: like solid columns, we can expect that, with all else equal, a short column would be more stable than a long column. Indeed in a recent study of force chains (Tordesillas et al. 2011), the 3-force chains proved to be the most stable in the system, although the inverse correlation between stability and length rapidly weakens for high values of n ($n > 4$). This is because the more particles

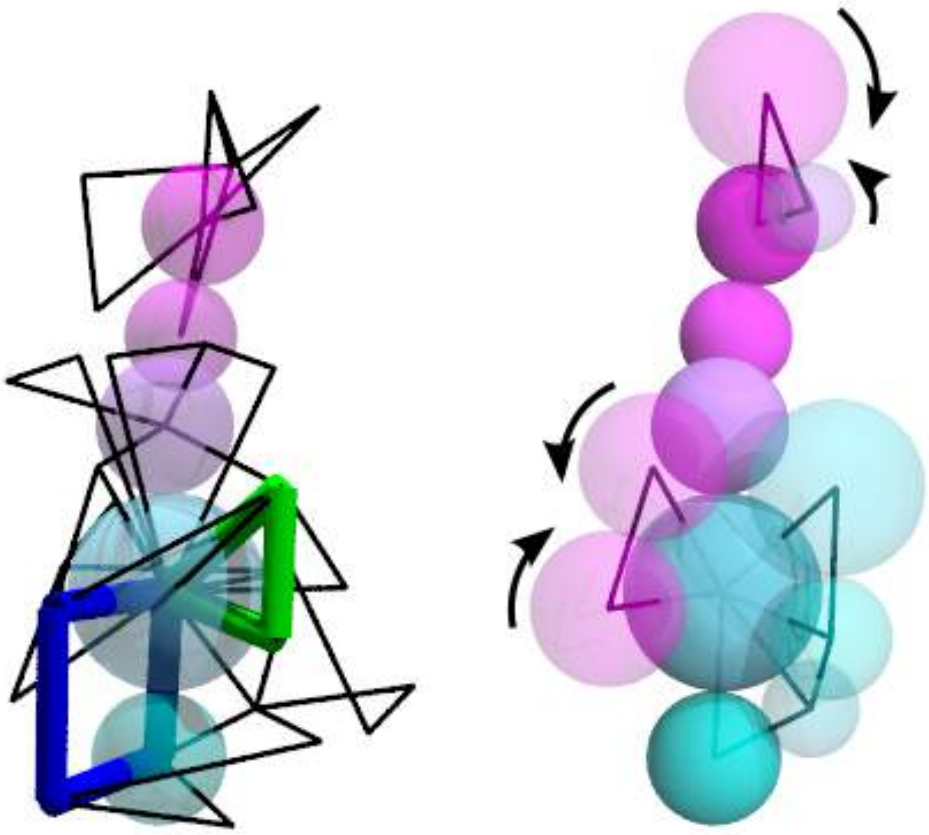

Fig. 3. *Left:* A 5-force chain in the sample and its local n-cycle membership: five 3-cycles, five 4-cycles, seven 5-cycles, two 6-cycles and one 7-cycle. A 3-cycle and 4-cycle have been highlighted to aid visualization. *Right:* The same force chain is shown with only its 3-cycles and neighbouring particles which form these cycles. An example mode of rotation in the confining neighbours of the force chain is shown in two of the 3-cycles: irrespective of the rotational direction of the force chain particle, rotation will be frustrated in one contact. This frustration prevails for all possible directional combinations in the particles' rotations.

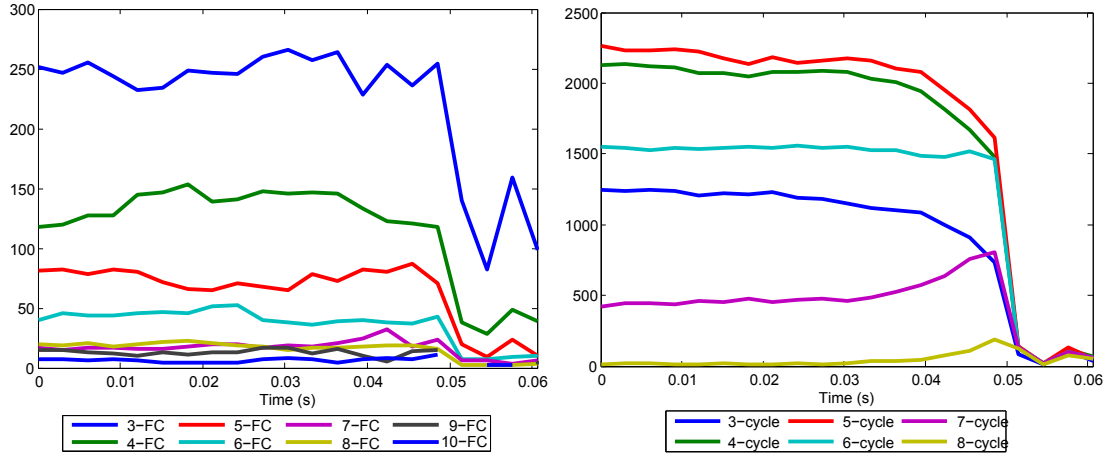

Fig. 4. Evolution of the populations of various classes of: (*left*) force chains, m-FC, and (*right*) n-cycles throughout loading.

there are in the chain, the more variations of the contributors to stability (e.g. distribution of the magnitude and topology of the lateral forces) become possible, effectively obscuring the isolated influence of length. By contrast, the distributions of the n-cycles in Fig 4 differ markedly with those for a system which fails in the presence of localization. In the latter case, the relative dominance of n-cycles decreases as their size grows, similar to the population distributions of force chains. The population in each class of n-cycle is close to being constant prior to the simulation time of 0.03. From times 0.03 to 0.04, the n-cycle populations decrease steadily but slowly for the dominant classes $n = 3, 4, 5$, while classes $n = 7, 8$ see a small increase in numbers. From times 0.04 to 0.05, we see a marked increase in the rate of population decline in the n-cycles, followed by a sudden and precipitous drop for all (except for $n = 8$) at just after the time of 0.05 – the same time that most of the force chains in the system collapse. The trends in the behaviour of the building blocks are consistent with the macroscopic stresses reported in Sec 2.

Similar to localized failure, we also observe cooperative interactions between the force chains and 3-cycles. The former resides in local neighbourhoods with not just higher concentrations of contacts per particle, but also a relatively higher number of 3-cycles per particle (Fig 5). In other words, force chains favour more contacts and prefers these contacts to be in 3-cycle formation. These truss-like 3-cycles have been shown in recent studies to provide dual support to force chains: they frustrate particle rotations (rotations being integral to buckling), and prop-up the force chain during buckling. We also considered the strongest 3-cycles, i.e. 3-force-cycles, in which *each* contact bears above the global average force (Tordesillas et al. 2010a). In earlier work (Tordesillas et al. 2010a), these strong 3-force-cycles were found to emerge at the time and locale of greatest need, i.e. during and in the region of strain localization where the buckling force chains are confined. In the sample under study, the 3-force-cycles appear to be spread throughout the sample (data not shown).

Overall, the common feature that this sample shares with systems undergoing localized failure is the reliance of load-bearing columnar force chains on the support of 3-cycles. That said, despite the material self-organizing to provide the force chains with stabilizing 3-cycles, the continued loading of the system ultimately 'wins': force chains eventually reach their load-carrying capacity and collapse by buckling as evident in times from 0.04 in Fig 6. Compare this to the preceding degradation of the supporting 3-cycles which commences at around the time of 0.02 onwards in Fig 4 and around the time of 0.03 onwards in Fig 5. The consequent collective buckling of force chains, in turn, precipitates the total collapse of the sample (Fig 6). Unlike in localized failure where the buckling is localized in distinct zones, here the buckling appears to be widespread and non-localized (Fig 6). Ongoing studies are focussed on a quantitative analysis of the spatio-temporal distributions of the buckling force chains and 3-force cycles in specimens undergoing diffuse failure, to determine whether the spread of these important mesoscopic structures throughout the material is indeed realised.

4 Conclusion

We examined self-organization in a sample undergoing diffuse failure. Quasi-linear and cyclic building blocks of force chains and their surrounding n-cycles, respectively, were identified. The evolution of these building blocks is consistent with the global measures of stress. There is evidence of cooperative evolution that elucidates *functional* behaviour among the building blocks. Truss-like 3-cycles laterally support column-like force chains, just as they do for systems that fail through strain localization. Despite the stabilizing benefits provided by the 3-cycles, columnar force chains are prone to fail by buckling. Ultimately, the collective buckling of these major

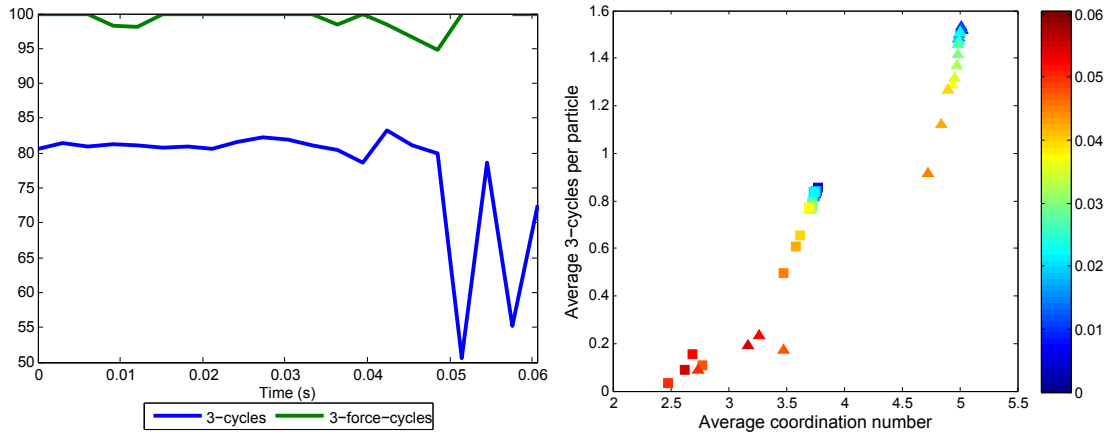

Fig. 5. (*Left*) Percentages of 3-cycles and 3-force cycles laterally supporting force chains (FCs) throughout loading. (*Right*) The evolution of the average number of contacts per particle (coordination number) and average number of 3-cycles per particle, for two subsets of the sample, i.e. those particles in force chains (△) versus the rest (□). Legend indicates simulation time.

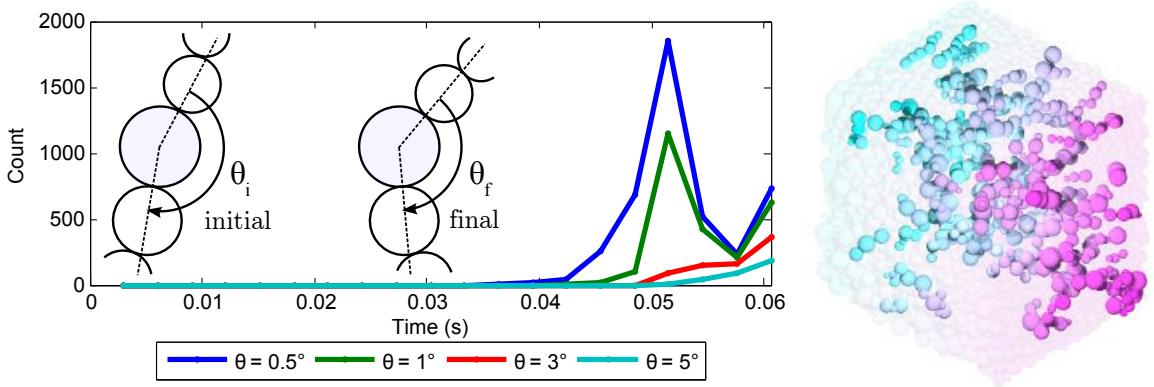

Fig. 6. (*Left*) The number of particles in buckling force chains which buckle by no less than the threshold value of θ, $\theta_b \geq \theta$, for one time step in the simulation. *Inset* illustrates the buckling angle $\theta_b = \theta_i - \theta_f$. (*Right*) Buckling force chains at simulation time of 0.0606, where $\theta_b \geq 1.0^\circ$: a total of 627 particles are in this set.

load bearing structures precipitate the collapse of the sample. Prima facie evidence suggests that the buckling of force chains are spread throughout the sample. These preliminary results provide impetus for a detailed investigation into the evolution of force chains and their minimal contact cycles, in particular, one aimed at uncovering the precise details of cooperative behaviour between them, so that we can better understand the underlying decision-making process that the material employs as it deforms under load.

REFERENCES

Arevalo, R., Zuriguel, I., & Maza, D. (2010). Topology of the force network in the jamming transition of an isotropically compressed granular packing. *Physical Review E 81*, 041302.

Cundall, P. & Strack, O. (1979). A discrete numerical model for granular assemblies. *Geotechnique 29*(1), 47–65.

Darve, F., Servant, G., Laouafa, F., & Khoa, H. (2004). Failure in geomaterials : continuous and discrete analyses. *Computer Meth. Appl. Mech. Eng. 193*(27-29), 3057–3085.

Darve, F., Sibille, L., Daouadji, A., & Nicot, F. (2007). Bifurcations in granular media : macro- and micro-mechanics approaches. *Comptes Rendus Mécanique 335*(9-10), 496–515.

Desrues, J. & Viggiani, G. (2004). Strain localization in sand: an overview of the experimental results obtained in grenoble using stereophotogrammetry. *Int. J. Num. Anal. Methods Geomech. 28*, 279–321.

Iwashita, K. & Oda, M. (2000). Micro-deformation mechanism of shear banding process based on modified distinct element method. *Powder Technology 109*, 192–205.

Majmudar, T. & Behringer, R. (2005). Contact force measurements and stress-induced anisotropy in granular materials. *Nature 433*, 1079–1082.

Nicot, F. & Darve, F. (2007). A micro-mechanical investigation of bifurcation in granular materials. *Int. J. of Solids and Structures 44*, 6630–6652.

Nicot, F., Sibille, L., & Darve, F. (2009). Bifurcation in granular materials: An attempt for a unified framework. *Int. J. of Solids and Structures 46*, 3938–3947.

Nova, R. (1994). Controllability of the incremental response of soil specimens subjected to arbitrary loading programmes. *J. Mech. behav. Mater. 5*(2), 193–201.

Rechenmacher, A. (2006). Grain-scale processes governing shear band initiation and evolution in sands. *J. Mech. Phys. Solids 54*, 22–45.

Sibille, L., Donzé, F., Nicot, F., Chareyre, B., & Darve, F. (2008). From bifurcation to failure in a granular material, a dem analysis. *Acta Geotechnica 3*(1), 15–24.

Sibille, L., Nicot, F., Donzé, F., & Darve, F. (2009). Analysis of failure occurrence from direct simulations. *European Journal of Environmental and Civil Engineering 13*, 187–201.

Tordesillas, A., Lin, Q., Zhang, J., Behringer, R., & Shi, J. (2011). Structural stability and jamming of self-organized cluster conformations in dense granular materials. *J. Mech. Phys. Solids 59*, 265–296.

Tordesillas, A. & Muthuswamy, M. (2009). On the modelling of confined buckling of force chains. *Journal of Mechanics and Physics of Solids 57*, 706–727.

Tordesillas, A., O'Sullivan, P., Walker, D., & Paramitha (2010b). Evolution of functional connectivity in contact and force chain networks: feature vectors, k-cores and minimal cycles. *Comptes rendus mecanique, CRAS (Proceedings of the French Academy of Sciences) 338*, 556–569.

Tordesillas, A., Pucilowski, S., Walker, D., Peters, J., & Hopkins, M. (2010c). A complex network analysis of granular fabric evolution in three-dimensions. *Dynamics of Continuous, Discrete and Impulsive Systems, Series B*. in press.

Tordesillas, A., Walker, D., & Lin, Q. (2010a). Force cycles and force chains. *Physical Review E 81*, 011302.

Walker, D. & Tordesillas, A. (2010). Topological evolution in dense granular materials: A complex networks perspective. *Int. J. Solids Struct. 47*, 624–639.

Watts, D. & Strogatz, S. (1998). Collective dynamics of 'small-world' networks. *Nature 393*, 440–442.

SIMULATING PARTICLE BREAKAGE AND RELATIVE HUMIDITY EFFECTS IN ROCKFILL BEHAVIOUR

E.E. Alonso, M. Tapias, J. Gili
Department of Geotechnical Engineering and Geosciences, Technical University of Catalonia – UPC, Barcelona, Spain

ABSTRACT: *The paper presents an analysis of the mechanical behaviour of rockfill using the discrete element method. A background reference is the set of results of a few large scale triaxial tests performed at the UPC geotechnical laboratory. In those tests Relative Humidity (RH) was controlled by means of a vapour equilibrium technique. RH is a fundamental aspect in the behaviour of rockfill which has received limited attention in the past. The Relative Humidity within the large pores between rock fragments controls the velocity of crack propagation within the particles. An increase in RH means faster crack propagation and eventually breakage of some particles and subsequent re-arrangement of the granular structure. The basic tool used to simulate some of the tests is the computer code PFC3D. Rockfill particles (they have the size of gravels, typically ranging from 1 cm to 4 cm) were simulated as breakable clusters of 3D balls. Particle breakage occurs in time according to fracture mechanic's laws. In a parallel study, the development of cracks in time has been examined. This information was taken into account in the numerical analysis to derive criteria for particle breakage. The paper describes the preliminary results of the work in progress. The actual shape of rock gravels has been approximated by means of clusters of spherical particles. Several arrangements, comprising a different number of particles, have been numerically tested. The results of the modelling exercise are encouraging and test results are reasonably well reproduced. The model is fairly general and it has a number of interesting capabilities*

1 INTRODUCTION

Rockfills are rock fragments of relatively large size (varying between 0.5 and 1.5 m), usually extracted from a quarry. Rockfills are used as construction materials in dams and railway projects.

Two significant aspects of rockfill behaviour are:

- Collapse deformation due to wetting.
- Time-dependent behaviour.

In the last years, a few large scale triaxial and oedometer tests have been performed at the UPC geotechnical laboratory. The size of the particles was scaled to gravel size, typically ranging from 1 cm to 4 cm. In the tests performed Relative Humidity (RH) was controlled by means of a vapour equilibrium technique. The RH existing on the large pores between rock fragments controls the velocity of crack propagation within the particles. An increase in RH

means faster crack propagation and eventually breakage of some particles and the subsequent re-arrangement of the granular structure. The results of these tests are the background reference for this study.

The paper presents the results of few numerical simulations of triaxial tests using a discrete particle method though the computer code PFC3D.

The final objective of this work is to develop a 'virtual' laboratory tool for rockfill materials.

2 A MODEL FOR COARSE GRANULAR AGREGATES

A series of testing programs on gravels, performed under Relative Humidity control have stressed the relevance of particle breakage in observed macroscopic scale (Chávez & Alonso, 2003; Oldecop & Alonso, 2001; Oldecop & Alonso, 2004; Ortega, 2010). Particle breakage is controlled by the stress level, the current RH and the time.

DEM methods are potentially useful to analyze these effects. The facility to reprogram the code PFC3D through the language FISH and the 'clump' logic (creation of group of particles to model particle shapes) has been extensively used. In the results reported the clumps are also known as 'macroparticles' to distinguish them from the basic spherical particles (microparticles).

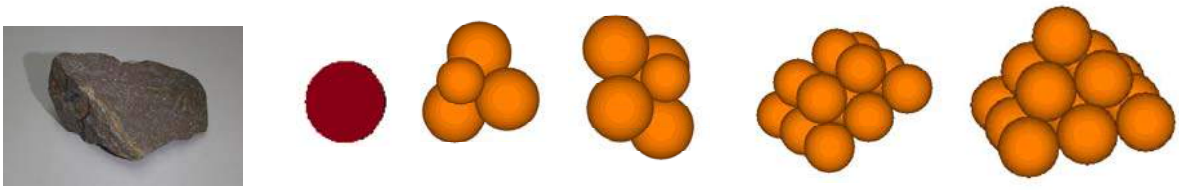

Fig. 1. Rockfill macroparticle. Real and clump models of 1, 4, 5, 13 and 14 microparticles

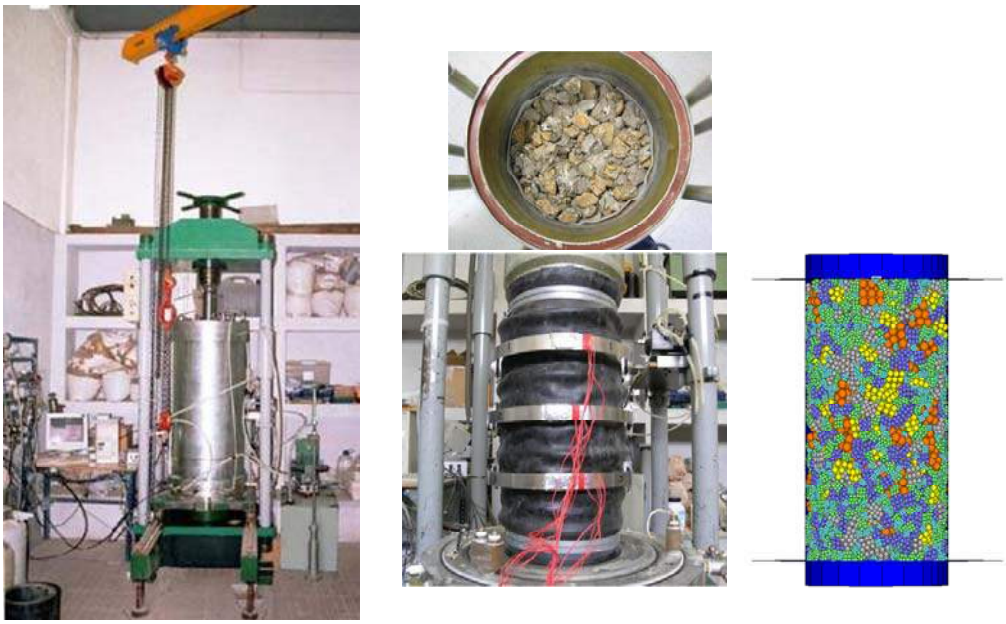

Fig. 2. Triaxial test on rockfill. At left, large diameter triaxial equipment of UPC geotechnical laboratory. Details of sample tested by Ortega (2010). At right, details of sample simulated

Actual particle shapes tested were formed by 4, 5, 13, and 14 microparticles (Fig. 1). The triaxial tests simulated reproduce the dimensions used in the triaxial experiments performed at UPC (Fig. 2):

- Sample size: ϕ:25cm; h:50cm.
- Size of macroparticles: 3 cm. The results reported here correspond to uniform initial grain size.

Tables 1 and 2 provide some fundamental properties for the simulation.
An important practical aspect is to ensure that particles do not carry any contact force before applying the real confining stress. Clumps are generated in a random manner and a desired porosity is imposed. A relaxation of internal forces is then necessary before testing.

Table 1. Rockfill properties

E (MPa)	400
n	0.4
Density (Kg/m^3)	2760

Table 2. Properties of macroparticles in DEM model

Normal stiffness, Kn	2e7 N/m
Shear stiffness, Ks	2e7 N/m
Friction coefficient, μ	0.93 – 0.5 – 0.3

3 FAILURE CRITERIA OF PARTICLES

The following issues are discussed regarding the adopted procedure to simulate particle breakage:

- Stress calculations on macroparticles
- Failure criteria for macroparticles
- Division of macroparticles

3.1 Stress in macroparticles

The concept of stress is defined for a representative elementary volume –REV- (ITASCA, 2008; Bagi, 1996, 1999). The REV in our case is the macroparticle. The following procedure was implemented in the code: a) Identify the clump; b) Identify contacts with neighbouring clumps; c) Identify forces in contacts; d) Calculate the mass centroid of the clump; e) Calculate the average stress tensor through the expression (Alonso-Marroquín & Herrman, 2005):

$$\bar{\sigma}_{ij} = \frac{1}{V}\sum_{\alpha\beta} l_i^{\alpha\beta} f_j^{\alpha\beta} \tag{1}$$

where $l^{\alpha\beta}$: Position vector between mass centroid and contact point; α : Particle; β : Contact; V: Volume of macroparticle

Principal stresses are derived from the stress invariants for each macroparticle.

3.2 Failure criteria for macroparticles

Two failure criteria were compared: a classical Mohr Coulomb criterion and a criterion based on the propagation of cracks inside particles (Oldecop & Alonso, 2007). The second criterion is based on linear elastic fracture mechanics (LEFM).

The Mohr-Coulomb criterion requires two parameters for macroparticles: cohesion, c, and internal friction coefficient, μ.

The crack propagation criterion is particularly useful because if allows the consideration of suction and time effects. The classical result for a mode of failure (say Mode I for failure in tension, σ) specifies that whenever the stress intensity factor K reaches the toughness of the rock (Kc) a fissure will propagate catastrophically and the rock particle will break. K is defined in terms of a characteristic size a:

$$K = \beta\sigma\sqrt{(\pi a)} \tag{2}$$

where β is a dimensionless coefficient which depends on particle geometry.

However, a subcritical propagation of fractures, when $K<Kc$, is also possible (Atkinson, 1984; Oldecop & Alonso 2001). Oldecop and Alonso (2007) describe a phenomenological model, based on subcritical crack growth, for the time to reach particle breakage. The model includes the effects of suction and time.

The approach followed here is to assign a random distribution of defects (cracks) to the macroparticles. Crack length follows a given statistical distribution. The factor K, which increases as the crack propagates, is calculated for the minor principal stress which corresponds to a tension state. K for each macroparticle increases also with the applied external stress to the sample tested.

For every time instant of calculation, K is compared with Kc. Whenever $K \geq Kc$ the particle is broken in two parts. This is the phenomenon included in all the simulations reported here.

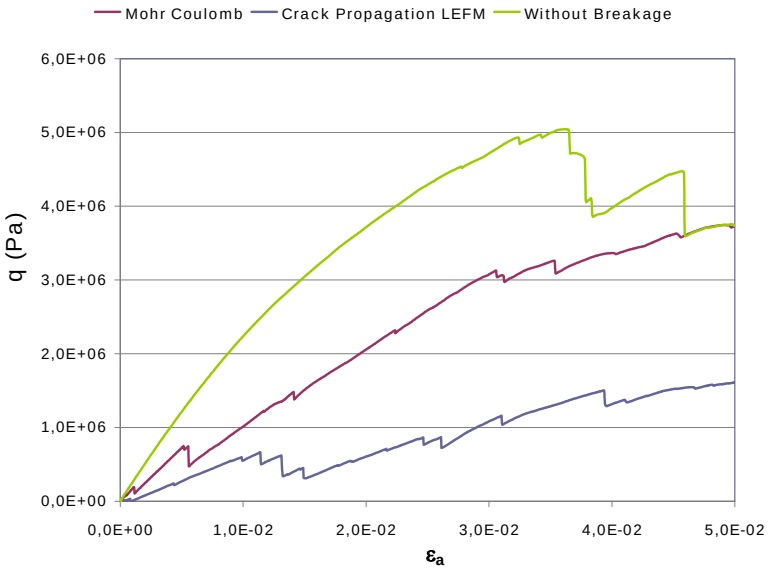

Fig. 3. Breakage criteria effect on deviatoric behaviour. Comparison among different criteria: No breakage; crack propagation based on LEFM and Mohr Coulomb. Sample of 100 macroparticles using clumps of 13 microparticles. Confining stress: 0.5MPa

3.3 Particle division

The particle division follows an arbitrary criterion which takes into account the number of particles integrating a clump and the 'pyramidal' structure of the macroparticle. Clumps are divided following the 'rule': 13→9+4; 9→5+4; 5→3+2; 4→2+2; 3→2+1; 2→1+1.

Figure 3 provides a comparison of the two criteria (Mohr Coulomb and LEFM) together with a case of no particle breakage. The simulated triaxial test exhibits the highest strength when no particles break, followed by the Mohr Coulomb rupture criterion.

4 SIMULATED TRIAXIAL TESTS

4.1 Particle Shape

Clump sizes of 1; 4(3+1); 5(4+1); 13(9+4); 14(9+4+1), which try always to simulate a pyramidal shape, were tested. Some results are given in Figure 4. The highest peak strengths are found for the highest number of particles in a clump.

4.2 Porosity

The effect of two porosities (51% and 61%) on triaxial test results is given in Figure 5. In both cases the initial macroparticle system had no initial contact forces.

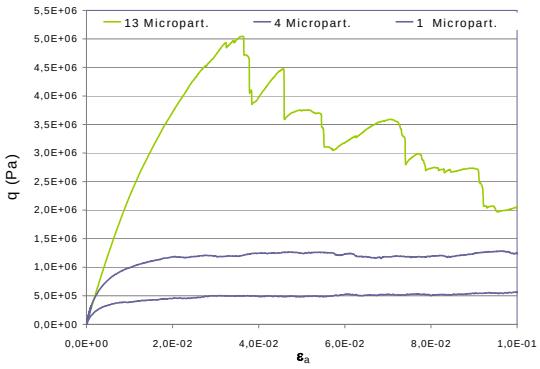

Fig. 4. Shape effects. Results of numerical simulation of triaxial test using macroparticles of 1, 4, and 13 microparticles. Confining stress 0.5 MPa

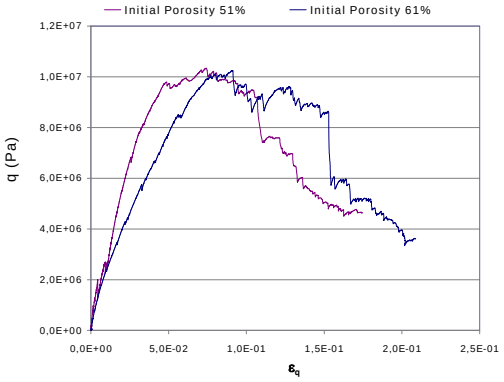

Fig. 5. Initial porosity effect. Comparison between two different initial porosities, 51 % y 61%. Confining stress 1.0 MPa. Sample of 1000 clumps of 14 microparticles

The sample exhibiting the lower porosity resulted in the higher stiffness, a consistent result with experimental observations. However, similar peak strength was calculated for the two specimens, a result which is probably explained by particle breakage.

4.3 Toughness

Particle toughness is a key property in the fracture model selected. Four values were compared: 1e6 Pa√m; 1e5 Pa√m; 1e4 Pa√m and 1e2 Pa√m. In all cases a triaxial sample having an initial porosity of 0.51 and a confining stress of 1 MPa was tested. Some results are given in Figures 6, 7 and 8.

Toughness controls the peak strength (Fig. 6) although 'residual' values seem to be less affected. Samples having a higher Kc value exhibit also a stronger dilatancy (Fig. 7). The lower the Kc value the higher the number of particles ruptured during the test. This is reflected on the calculated grain size distribution at the end of the test (Fig. 8). Crushing in

these samples result in an increase in particles having a equivalent diameter close to 2cm. It is clear that much more deformation energy will be required to achieve a stationary grain size distribution.

These are reasonable results which help to increase the confidence on the model.

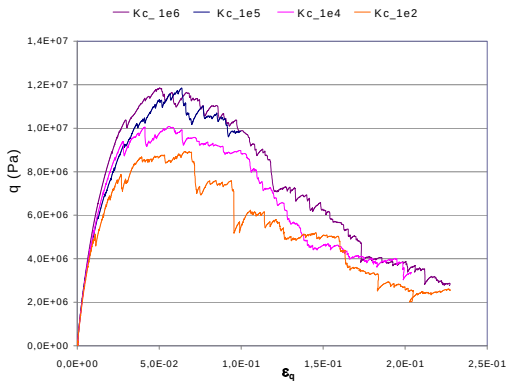

Fig. 6. Effect of macroparticle toughness on deviatoric behaviour. Comparison among four different macro-thougness (1e6, 1e5, 1e4, 1e2 Pa√m). Sample of 1000 macroparticles using clumps of 14 microparticles . Confining stress: 1.0MPa. Initial porosity: 51%

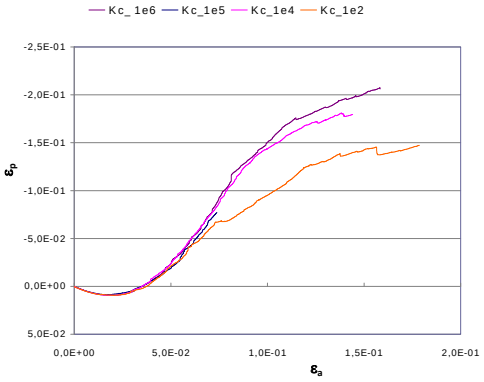

Fig. 7. Effect of macroparticle toughness on volumetric behaviour. Comparison among four different macro-toughness (1e6, 1e5, 1e4, 1e2 Pa√m). Sample of 1000 macroparticles using clumps of 14 microparticles . Confining stress: 1.0MPa. Initial porosity: 51%

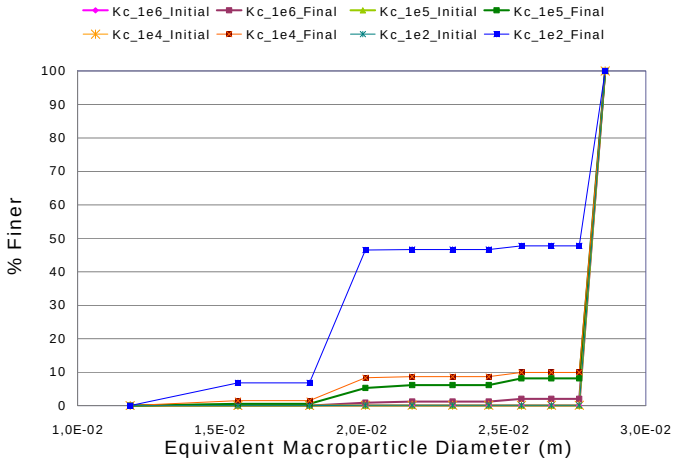

Fig. 8. Effect of macroparticle toughness on the evolution of grain size distribution. Comparison among four different macro-toughness (1e6, 1e5, 1e4, 1e2 Pa√m). Sample of 1000 macroparticles using clumps of 14 microparticles . Confining stress: 1.0MPa. Initial porosity: 51%

4.2 Friction Coefficient

Three samples having particle to particle friction coefficient (μ) equal to 0.93, 0.50 and 0.30 (φ = 43º; 27º; 17º) were tested in a triaxial experiment. Initial porosity was 51%, the initial confining stress 1 MPa and the toughness of macroparticles was 1e4 Pa√m. The specimen was defined by 970 macroparticles and the initial equivalent diameter was 2.8cm.

Figure 9 shows the deviatoric stress-strain relationship. A similar residual strength for strains in excess of 20% was found. Dilatancy is shown in Figure 10. As expected, dilatancy increases with interparticle friction. In this test most of the particles broken resulted in

equivalent particle diameters in the vicinity of 2cm. The sample having the smallest interparticle friction angle exhibited a higher number of failed clumps.

Only a small percentage of particles broke in these tests. More will be said on this aspect in the next section.

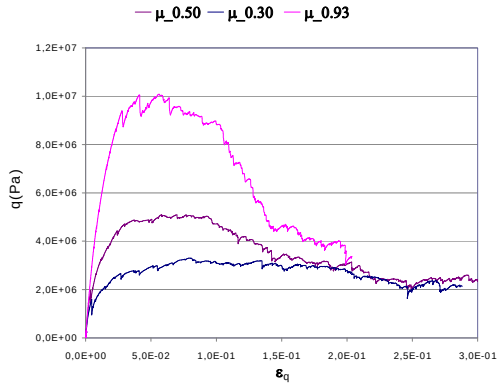

Fig. 9. Friction coefficient effect on deviatoric behaviour. Comparison among three friction coefficients (0.93, 0.50, 0.30). Sample of 1000 macroparticles using clumps of 14 microparticles. Confining stress: 1.0MPa. Initial porosity: 51%

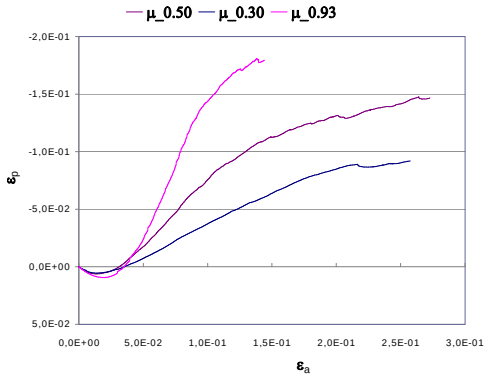

Fig. 10. Friction coefficient effect on volumetric behaviour. Comparison among three friction coefficients (0.93, 0.50, 0.30). Sample of 1000 macroparticles using clumps of 14 microparticles . Confining stress: 1.0MPa. Initial porosity: 51%

5 RELATIVE HUMIDITY EFFECTS

Investigating the effect of Relative Humidity on rockfill behaviour is one of the main objectives of the work developed. In the cases discussed below the effect of RH is imposed by reducing (suddenly) the *Kc* value of macroparticles. This technique simulates the type of triaxial tests reported by Ortega (2010). In some of his strain controlled triaxial tests (Figure 14) samples initially dry were flooded when they reached some given strain level. The vertical strain rate was maintained and the change in vertical stress was recorded. The same technique was repeated in the numerical tests performed.

The macroparticle's aggregate had the following properties: initial porosity = 51%; *Kc* = $1e^6$ Pa√m and $1e^5$ Pa√m; μ = 0.93. Uniform clump size of 14 microparticles. The confining stress was 1 MPa.

Figures 11 and 12 show the sample response for the three cases: Kc_1=1e6 Pa√m, Kc_2=1e5 Pa√m, and a 'wetting' effect when Kc_1 is reduced suddenly to Kc_2 when the vertical strain reached 5%. The sample experiences a collapse which is reflected in a sudden reduction of the deviatoric stress. Further straining, however, results in a recovery of strength. The reduction in porosity associated with this wetting is irreversible. This is shown in Figure 12, which provides the variation of porosity during the tests simulated.

Porosity increases because of dilatancy in all cases. However, wetting (*Kc* is reduced) results in a transient reduction in porosity. The wetted sample falls into the porosity plot for the specimen having initially a reduced *Kc* value.

Figure 13 provides additional information on the evolution of broken macroparticles. A value of Kc_1=1e6 Pa√m results in a limited breakage of particles. When *Kc* is decreased to Kc_2=1e5 the breakage rate increases. The sudden wetting takes the sample from the Kc_1 to Kc_2 curve.

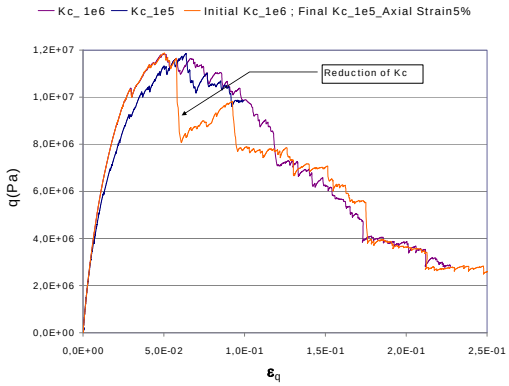

Fig. 11. Wetting effect on deviatoric stress behaviour. Sample of 1000 macroparticles using clumps of 14 microparticles. Confining stress: 1.0MPa. Initial porosity: 51%

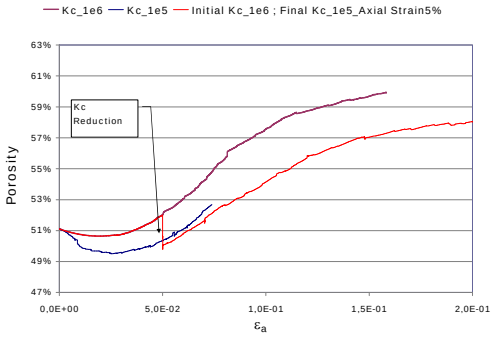

Fig. 12. Wetting effect on porosity. Sample of 1000 macroparticles using clumps of 14 microparticles. Confining stress: 1.0MPa. Initial porosity: 51%

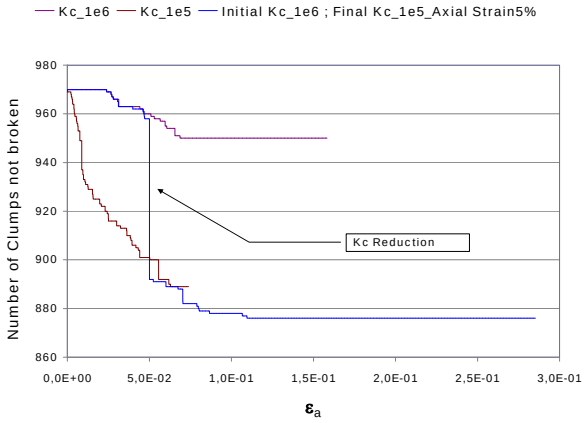

Fig. 13. Wetting effect on number of clumps not broken vs axial strain. Sample of 1000 macroparticles using clumps of 14 microparticles . Confining stress: 1.0MPa. Initial porosity: 51%

Figure 14 shows the results of triaxial tests performed by Ortega (2010) on samples of limestone fragments ranging in size from 1 to 4 cm. The plot shows stress-strain curves for samples maintained at relative humidities of RH=10%; 50% and 100%. The driest sample (RH=10%) was fully wetted, once it reached a certain deformation, by means of two processes:

- Specimen flooding by liquid water. The test was then resumed (sample HR10%-Sat-Cut)
- Deviatoric stress was reduced to zero, the sample was flooded and the test was resumed again (sample HR10%-Sat-Desc)

Samples having a smaller RH are stiffer and reach higher strength. The RH=10% sample loaded and then flooded once it was at limiting conditions experienced a sudden reduction in strength which recovered in part as deformation increased. The stress-strain curve approaches now the curve for the RH=100% case.

The discrete model results in Figure 11 and the actual experiments are qualitatively similar. Matching model and experiments require an improved geometrical definition of particles, pore geometry and particle properties.

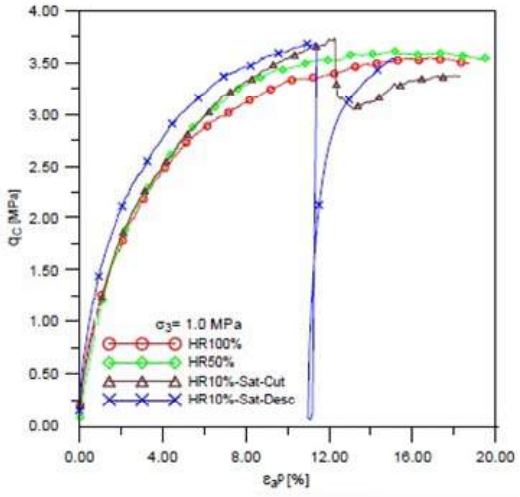

Fig. 14. Triaxial test on limestone rockfill. Stress-strain curve. Confining stress: 1.0MPa (Ortega, 2010)

6 CONCLUDING REMARKS

A key aspect of rockfill behaviour is the particle breakage during the process of deformation under stress levels of common engineering interest. This paper presents some results of an on going research aimed at developing a suitable 'particle' method to analyze rockfill behaviour.

The computer program PFC3D (Itasca, 2008) offers the possibility of grouping individual spherical particles into bigger units (macroparticles) which may simulate the actual shape of rockfill fragments. The possibility of programming internally some relevant phenomena determining the failure (breakage) of individual macroparticles was used to build a dedicated particle-based model which attempts to reproduce real behaviour as revealed by large scale triaxial tests on gravels.

A 'pyramidal' macroparticle shape, made of 14 micro-spheres, was used in the results presented. Other geometries will be explored in future analyses.

The calculated effect of particle shape (to a limited extent), porosity and angle of internal friction follows a consistent pattern.

Particle breakage was related to fracture mechanics concepts. Rock toughness enters as a natural property. Crack propagation is also controlled by the initial distribution (in the entire sample) of defects and its initial length as well as on stress intensity, current suction (or relative humidity) and time. The effect of some of these variables has been explored. It seems that the model developed has the capability of reproducing the main features of reference real triaxial tests on coarse gravels.

REFERENCES

Alonso-Marroquín, F. & Herrmann, H.J. (2005), "The incremental response of soils. An investigation using a discrete-element model". Journal of Engineering Mathematics, Vol. 52, 11–34.

Atkinson, B.K. (1984), "Subcritical crack growth in geological materials". J. Geophysical Research, Vol. 89(B6), 4077-4114.

Bagi, K. (1996), "Stress and strain in granular assemblies". Mechanics of Materials, Vol. 22, 165-177.

Bagi, K. (1999), "Microstructural stress tensor of granular assemblies with volume forces". J. of Applied Mechanics, Vol. 66(4), 934-936.

Broek, D. (1986), Elementary Engineering Fracture Mechanics, Martinus Nijhoff Publishers, Dordrecht.

Chávez, C. (2003), Estudio del comportamiento triaxial de materiales granulares de tamaño medio con énfasis en la influencia de la succión, Phd Thesis, Department of Geotechnical Engineering and Geosciences, Technical University of Catalonia. UPC, Barcelona, Spain.

Chávez, C. & Alonso, E. (2003), "A constitutive model for crushed granular aggregates which includes suction effects". Soils and Foundations, Vol. 43(4), 215-227.

Itasca, (2008), Manuals of PFC3D v.4.0: Theory and Background, Fourth Edition, Itasca Consulting Group Inc, US.

Oldecop, L. (2000), Compresibilidad de escolleras. Influencia de la humedad, PhD Thesis, Department of Geotechnical Engineering and Geosciences, Technical University of Catalonia. UPC, Barcelona, Spain.

Oldecop, L. & Alonso, E. (2001), "A model for rockfill compressibility". Géotechnique, Vol. 51(2), 127-139.

Oldecop, L. & Alonso, E. (2004), "Testing Rockfill Under Relative Humidity Control". Geotechnical Testing Journal, Vol. 27(3), 269-278.

Oldecop, L. & Alonso, E. (2003), "Suction effects on rockfill compressibility". Géotechnique Vol. 53, 289–292.

Oldecop, L. & Alonso, E. (2007), "Theoretical investigation of the time-dependent behaviour of rockfill". Géotechnique, Vol. 57(3), 289–301.

Ortega, E. (2010), Comportamiento de materiales granulares gruesos - Efecto de la succión, PhD Thesis, Department of Geotechnical Engineering and Geosciences, Technical University of Catalonia. UPC, Barcelona, Spain.

Saouma, V.E. (2007), Lecture Notes in Fracture Mechanics, Department of Geotechnical Engineering and Geosciences, Technical University of Catalonia. UPC, Barcelona, Spain.

ESTIMATING THE THREE-DIMENSIONAL STRENGTHS OF SANDS AND CLAYS FROM A SINGLE TEST

Poul V. Lade
Department of Civil Engineering, The Catholic University of America, Washington, D.C. 20064, U.S.A.

ABSTRACT: *The three-dimensional failure criterion for soils proposed by Lade (1977) requires two parameters for characterization of the strength:*

$$\left(\frac{I_1^3}{I_3}-27\right)\left(\frac{I_1}{p_a}\right)^m=\eta_1$$

in which I_1 and I_3 are the first and the third invariants of the stress tensor. One of the two parameters, η_1, is used to describe the opening angle of the failure surface, i.e. similar to the friction angle, and the other parameter, m, is employed to describe the curvature of the failure surface in the meridian planes. Typically, the results of three triaxial compression tests are required for determination of these two parameters.

Careful inspection reveals that the two parameters determined from high quality tests presented in the literature are related to each other for sands and for clays. It is therefore possible to obtain the two parameters from the results of a single triaxial compression test. The relation between η_1 and m is demonstrated for sands and for clays, and it is shown how the results from a single test may be used to determine the parameters to describe the three-dimensional failure surface for these two types of soil.

1 INTRODUCTION

Results of three-dimensional experiments have shown that failure surfaces for soils have many characteristic features in common. In the principal stress space they are shaped as pointed bullets with cross-sections in octahedral planes which are triangular, monotonically curved surfaces with smoothly rounded corners. In addition, the three-dimensional failure surfaces for soils have two characteristics: (i) the opening angle of the failure surface, which is often described by the friction angle, and (ii) the curvature of the failure surface in planes containing the hydrostatic axis, i.e. curved meridians. At least two parameters are therefore necessary for description of the two separate and distinct characteristics of the failure surface for soils.

The three-dimensional failure criterion proposed by Lade (1977) contains two material parameters as reviewed below. The two parameters have been determined for a large number of high quality tests on sand and clays presented in the literature, and close inspection reveals that they are related to each other for sands and for clays. It is therefore possible to obtain the two parameters from the results of a single triaxial compression test. The relation between η_1

and *m* is demonstrated for sands and for clays, and it is shown how the results from a single test are used to determine the parameters to describe the three-dimensional failure surface for these two types of soil.

2 THREE-DIMENSIONAL FAILURE CRITERION

A three-dimensional failure criterion was proposed for soils by Lade (1977):

$$\left(\frac{I_1^3}{I_3} - 27\right)\left(\frac{I_1}{p_a}\right)^m = \eta_1 \tag{1}$$

in which I_1 and I_3 are the first and the third invariants of the stress tensor, and p_a is atmospheric pressure in the same units as the stresses used to express the stress invariants.

Fig. 1 shows that this criterion describes a failure surface that emanates from the stress origin of the principal stress space. It is continuously curved with a smooth triangular cross-section in the octahedral plane and it has curved traces in meridian planes that contain the hydrostatic axis. One of the two parameters, η_1, is used to describe the opening angle of the failure surface, i.e. similar to the friction angle, and the other parameter, *m*, is employed to describe the curvature of the failure surface in the meridian planes. For $m = 0$ the failure surface is straight, and the shape of the cross-sections does not change with the value of I_1. For $m > 0$ the cross-sectional shape of the failure surface changes from triangular to become more circular with increasing value of I_1. Similar changes in cross-sectional shape are observed from experimental studies on soils.

This criterion has been shown to capture the isotropic three-dimensional failure conditions for sands and for clays under various conditions of void ratio and relative density as discussed in detail by Lade (2006).

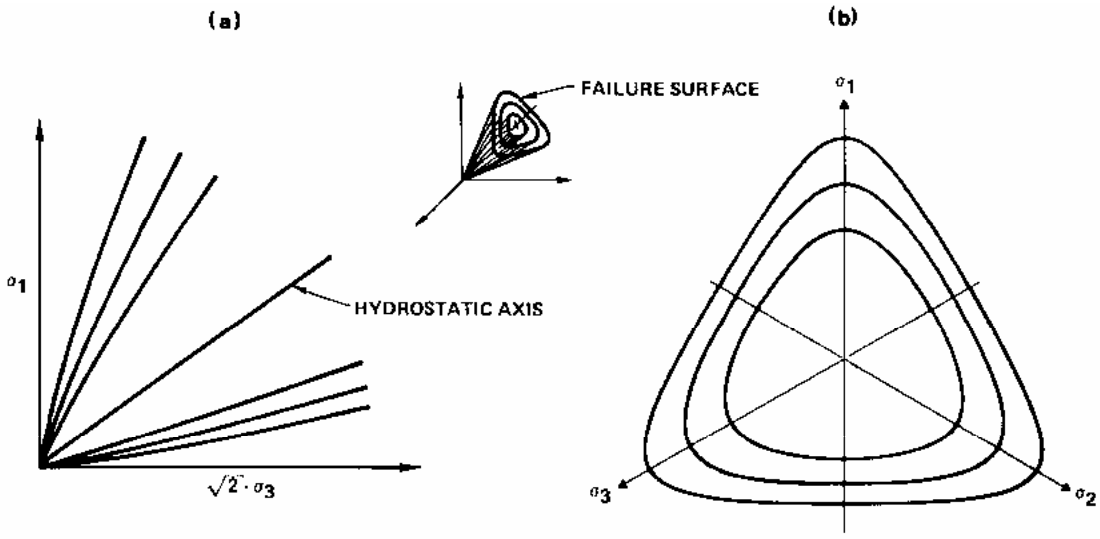

Fig. 1. Characteristics of three-dimensional failure surface shown in principal stress space. Traces of failure surface in (a) triaxial plane and in (b) octahedral plane.

3 PARAMETER DETERMINATION

Typically, the results of three triaxial compression tests are required for determination of the two parameters, η_1 and m. The expression for the failure criterion in Eq. (1) is rearranged and logs are taken on both sides of the equation:

$$\log\left(\frac{I_1^3}{I_3} - 27\right) = \log\eta_1 + m \cdot \log\left(\frac{p_a}{I_1}\right) \tag{2}$$

By plotting $(I_1^3 / I_3 - 27)$ versus (p_a / I_1) on log-log scales, as shown in Fig. 2, the value of η_1 is determined as the intercept between the best fitting straight line and the vertical line corresponding to $(p_a / I_1) = 1$. The geometric slope of the straight line is the exponent m.

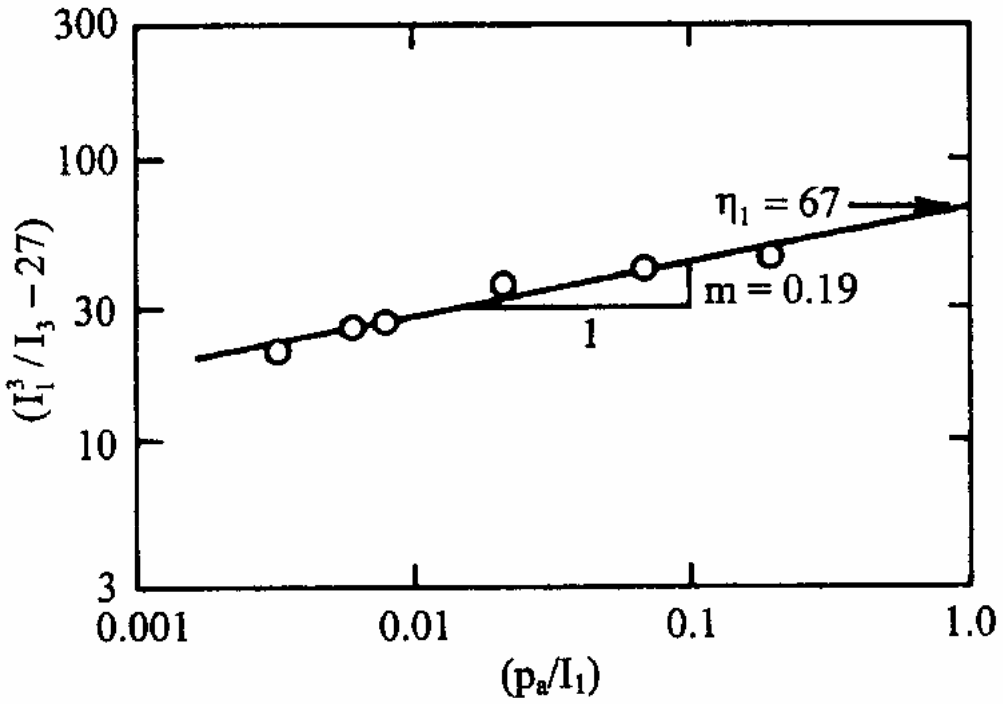

Fig. 2. Determination of η_1 and m for failure criterion for Sand N. D.

4 PARAMETER VALUES FOR SAND

The parameter values for a large number of representative granular materials have been determined from drained triaxial compression tests and presented by Lade (1978, 2005a). The data employed for this purpose included sands with a variety of (1) relative densities, (2) void ratios, (3) grain size distribution curves, and (4) maximum grain sizes up to 6 inches.

Fig. 3 shows a diagram in which m is plotted against $\log(\eta_1)$ for sands. Although there is some scatter, the data consisting of 40 sets of parameters forms a straight line which may be described by the following expression:

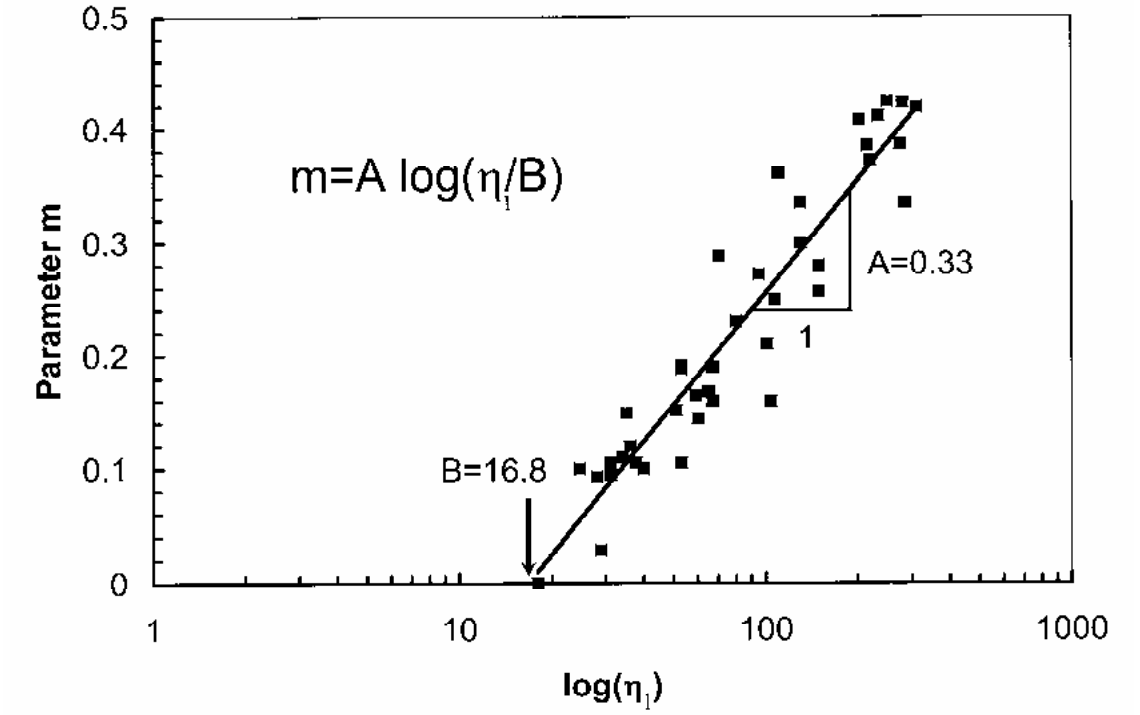

Fig. 3. Relation between m and $\log(\eta_1)$ for sands.

$$m = A \cdot \log\left(\frac{\eta_1}{B}\right) \tag{3}$$

For sands the best fitting straight line is described by values of A = 0.33 and B = 16.8 with a coefficient of determination of r^2 = 0.8914. Thus, the two parameters are related by Eq. (3).

5 PARAMETER VALUES FOR CLAYS

The parameter values for clays were presented by Lade (2005b) and they are plotted in Fig. 4. Although with greater scatter than for sands, the relation between η_1 and m may also be represented by a straight line relationship as that given in Eq. (3). For clays the best fitting straight line is described by values of A = 0.49 and B = 3.7 with a coefficient of determination r^2 = 0.4554.

6 PARAMETER DETERMINATION FROM A SINGLE TEST

Since η_1 and m may be related to each other by the simple expression in Eq. (3), it is possible to obtain both parameter values from a single test such as a triaxial compression test. It is clear that this test must be of high quality, because it is the basis for determining the three-dimensional failure stresses of the soil in question.

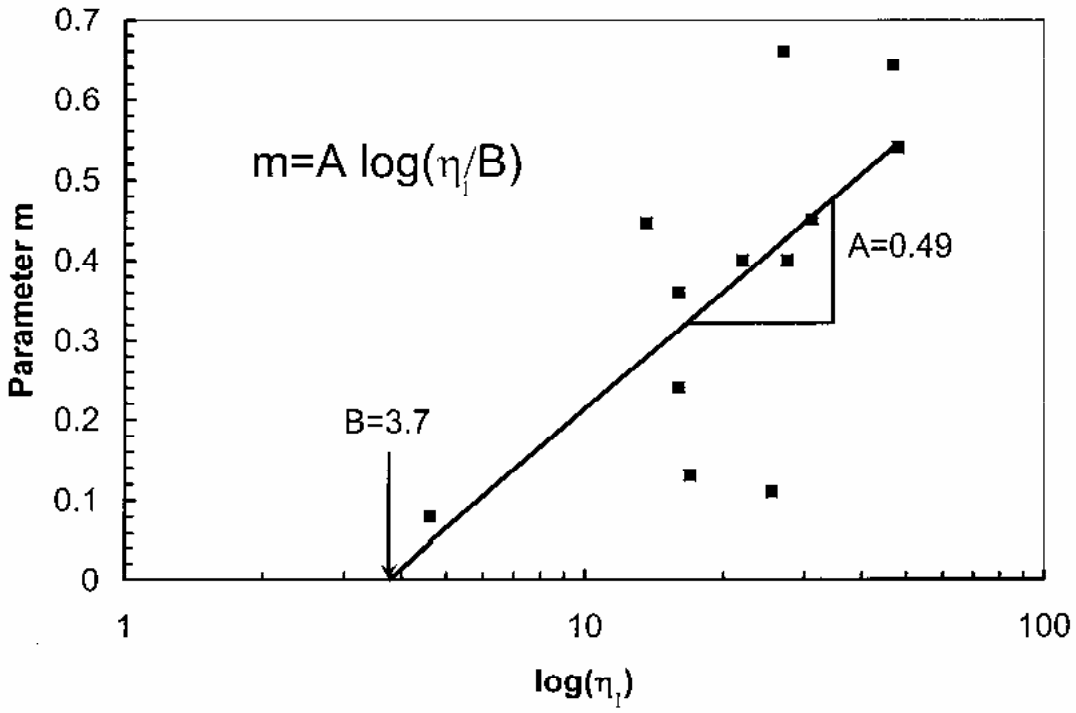

Fig. 4. Relation between m and log(η_1) for clays.

Since $m > 0$ for a concave failure surface and $m = 0$ for a straight failure surface, the lowest value of $B = \eta_1$ according to Eq. (3). This corresponds to the lowest value of η_1 possible for a given soil. The value of $B = 16.8$ for sands, and this corresponds to a friction angle in triaxial compression of 31.5°, while the lowest value of $B = 3.7$ for clays, and this produces a friction angle of 17.1°. While friction angles can be lower than these values for sands and clays, such lower friction angles are produced at higher values of (I_1/p_a), η_1 and m.

Substituting the expression for m in Eq. (3) into Eq. (2) and setting $(I_1^3 / I_3 - 27) = B$ and solving for (p_a/I_1) produces:

$$\log\left(\frac{p_a}{I_1}\right) = \frac{\log B - \log \eta_1}{A \cdot (\log \eta_1 - \log B)} = -\frac{1}{A} \tag{4}$$

from which

$$\left(\frac{p_a}{I_1}\right) = 10^{-\frac{1}{A}} \tag{5}$$

Fig. 5 shows that on a log-log diagram of $(I_1^3 / I_3 - 27)$ versus (p_a/I_1), the value of (p_a/I_1) from Eq. (5) indicates the point of interception between a horizontal line corresponding to $(I_1^3 / I_3 - 27) = \eta_1 = B = 16.8$ and all other lines describing failure surfaces in terms of η_1 and m for sands. Thus, a pattern of straight lines describing failure surfaces for all sands is established, as shown in Fig. 5. This pattern is possible because the values of η_1 and m are uniquely related for a given soil type, as indicated by Eq. (3) and shown for sands in Fig. 3 and for clays in Fig. 4. Fig. 6 shows the corresponding master diagram for clays.

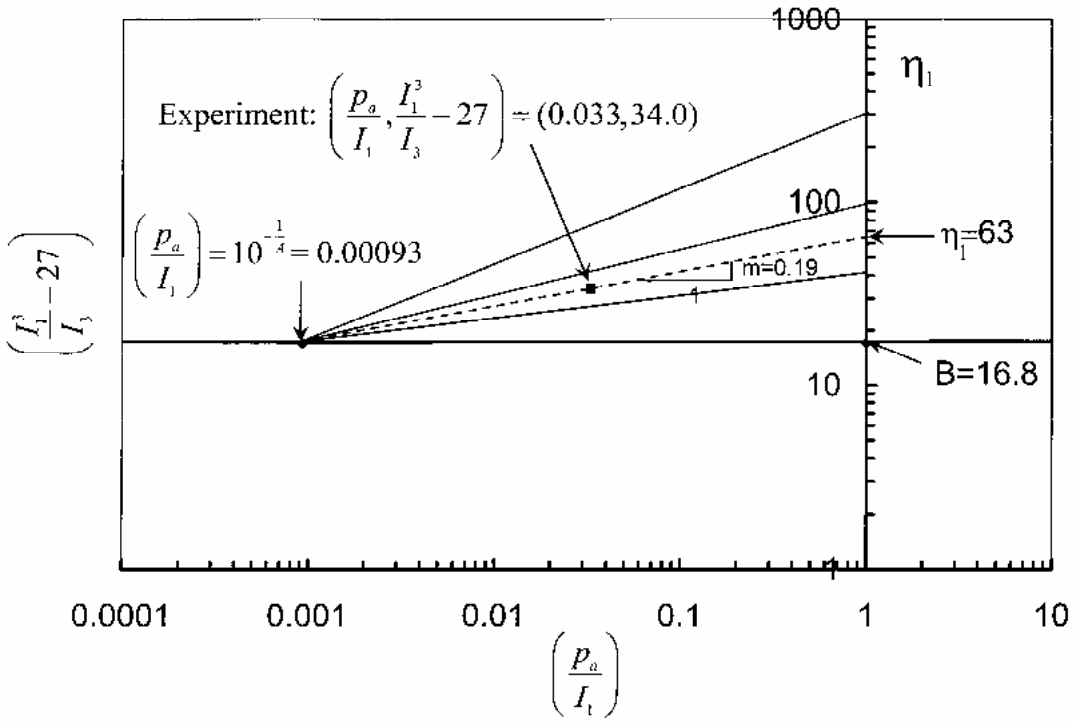

Fig. 5. Master diagram for determination of η_1 and m for sands based on one experiment.

Because such unique patterns exist for sands and for clays, it is possible to determine both η_1 and m from a single test. An example of how to use the diagram is indicated in Fig. 5. Based on the values of the effective principal stresses at failure from a triaxial compression test on a given soil, the value of $(I_1^3 / I_3 - 27) = 34.0$ is plotted versus $(p_a/I_1) = 0.033$ on the master diagram for sands. A straight line is then drawn through the corresponding experimental point and the common interception point, as indicated by the dashed line. This line crosses the η_1-axis at the value of $\eta_1 = 63$ and the geometric slope indicates the value of $m = 0.19$ for the given sand. A similar demonstration of parameter determination from a single triaxial compression test is indicated in Fig. 6 for clays.

7 CONCLUSIONS

The three-dimensional failure criterion proposed by Lade (1977) models the curvature in meridian planes and the effect of the intermediate principal stress in octahedral planes with good accuracy for both sands and clays. This criterion involves two parameters, η_1, which describes the opening angle at the stress origin (similar to the friction angle), and m, which describes the curvature of the failure surface in meridian planes. Based on numerous sets of experiments on sands and clays, it has been observed that unique relations exist between η_1 and m. These relations may be described by straight lines on a semi-log diagram, and they allow determination of both parameters from a single triaxial compression test. Master diagrams have been established for sands and for clays and determination of the values of η_1 and m from results of a single tests is demonstrated.

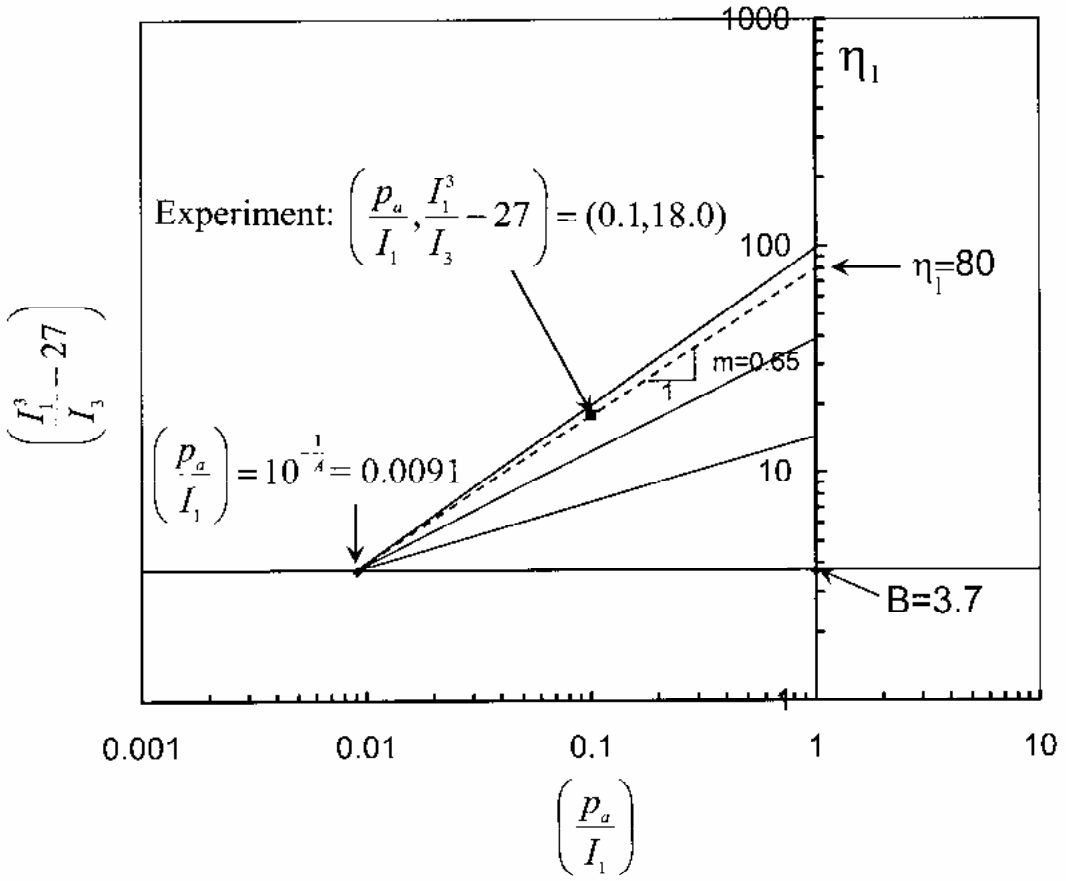

Fig. 6. Master diagram for determination of η_1 and m for clays based on one experiment.

REFERENCES

Lade, P.V. (1977), "Elasto-Plastic Stress-Strain Theory for Cohesionless Soil with Curved Yield Surfaces," Int. J. Solids Struct., Pergamon Press, Vol. 13, 1019-1035.

Lade, P.V. (1978), "Prediction of Undrained Behavior of Sand," J. Geotech. Engrg. Div., ASCE, Vol. 104(GT6), 721-735.

Lade, P.V. (2005a), "Single Hardening Model for Soils: Parameter Determination and Typical Values," ASCE GSP 128, Soil Constitutive Models: Evaluation, Selection, and Calibration, J.A. Yamamuro and V.N. Kaliakin, editors, 290-309.

Lade, P.V. (2005b), "Calibration of the Single Hardening Constitutive Model for Clays," Proc. 11th Int. Conf. Computer Meth. Geomech., Turin, Italy.

Lade, P.V. (2006), "Assessment of Test Data for Selection of 3-D Failure Criterion for Sand" Int. J. Num. Analyt. Meth. Geomech., Vol. 30, 307-333.

DELAYED INCREASE IN CONE PENETRATION RESISTANCE OF SAND AFTER DYNAMIC COMPACTION

R.L. Michalowski
Department of Civil and Environmental Engineering, University of Michigan, Ann Arbor, USA

S.S. Nadukuru
Department of Civil and Environmental Engineering, University of Michigan, Ann Arbor, USA

ABSTRACT: *Among soil improvement techniques used to increase strength of loose and medium-dense sand deposits are the dynamic means, such as vibrocompaction and blasting. Sands often exhibit a drop in cone penetration resistance immediately after the disturbance, but a gradual increase in the resistance occurs in a matter of weeks and months. An explanation of the former is sought in the analysis of the stress state immediately after the dynamic disturbance, and a justification for the latter is found in the process of stress corrosion cracking (or static fatigue) of the micro-morphologic features at the contacts between sand grains. Some experimental evidence is demonstrated for fracturing of the microscopic features on the sand contact surfaces. Discrete element method calculations are carried out to strengthen the hypothesis, and the results of finite element analysis are demonstrated to provide quantitative estimates for the time-delayed increase in the sand penetration resistance.*

1 INTRODUCTION

Sand deposits subjected to densification through dynamic means (blasting, vibrocompaction) often exhibit a drop in cone penetration resistance immediately after compaction. However, the resistance to cone penetration increases over time, far beyond the time needed for the excess pore water pressure to dissipate. An early description of this peculiar behavior was given by Mitchell & Solymar (1984), confirmed by the data from a hydroelectric project in Nigeria. Blasting was found to reduce the penetration resistance immediately afterwards, even though the densification was evident by the surface subsidence. A considerable increase in penetration resistance, however, was found after 11 weeks. A similar effect was found after vibro-compacting sand on the same project. More examples of this phenomenon can be found in Baxter (1999). Mineral dissolution and cementation at interparticle contacts developed in time after dynamic compaction was cited first as a primary reason for the time-delayed increase in cone penetration resistance. More recently, this argument was dropped as the major cause of this peculiar effect, but the behavior is still referred to as a "continuing *Enigma*" (Mitchell, 2008).

A hypothesis is suggested, indicating that the cause of the time-delayed increase in penetration resistance of sand after dynamic compaction is the change in the stress state caused in the sand by the change of its stiffness (in particular, the change in elastic properties). An increase in elastic moduli at the macroscopic scale is caused by the process of micro-fracturing of the morphological features on the surfaces of grains at their contacts. This is a time-delayed process that can be accelerated by environmental factors (such as moisture),

and often referred to as *stress corrosion cracking*. It will be argued that in confined sands this process brings the grains closer together (*grain convergence*), producing an increase in contact stiffness that manifests itself at the macro scale as an increase in elastic moduli. An evidence for delayed increase in elastic moduli of sand can be found in the results presented by Afifi & Woods (1971), who demonstrated that the velocity of the shear wave propagation increases in sands subjected to prolonged loading. As a consequence of the change in elastic moduli, the horizontal stress in a sand bed (under one-dimensional deformation conditions) will increase, leading to an increase in the cone penetration resistance. Changing stress state was mentioned earlier in the literature as a direct cause of this increase (Schmertmann, 1987); here, we suggest a hypothesis why the change in the stress state occurs.

Particle "rearrangement" and "structuration" are often cited as sources of changes in granular assemblies leading to variation in properties (Mesri et al., 1990; Bowman and Soga, 2003), and they have been used to explain the puzzling effect of delayed increase in cone penetration resistance in dynamically compacted sands. Rearrangement of particles and restructuring, however, are the results of an underlying process, and cannot be considered as causes of this mystifying behavior. A hypothesis presented in this paper places emphasis on the time-delayed micro-fracturing of the morphological features at grain surfaces. The evidence available in the literature to support this hypothesis is discussed and numerical simulations are used to complement this evidence.

2 STATIC FATIGUE AT GRAIN CONTACTS

The micro-morphology of grain surfaces is illustrated in Fig. 1. When two particles with a rich surface morphology come into contact, it is the asperities and the small crystalline fragments that are first loaded to a considerable degree as the areas of the surfaces in contact are relatively small (*microstress*).

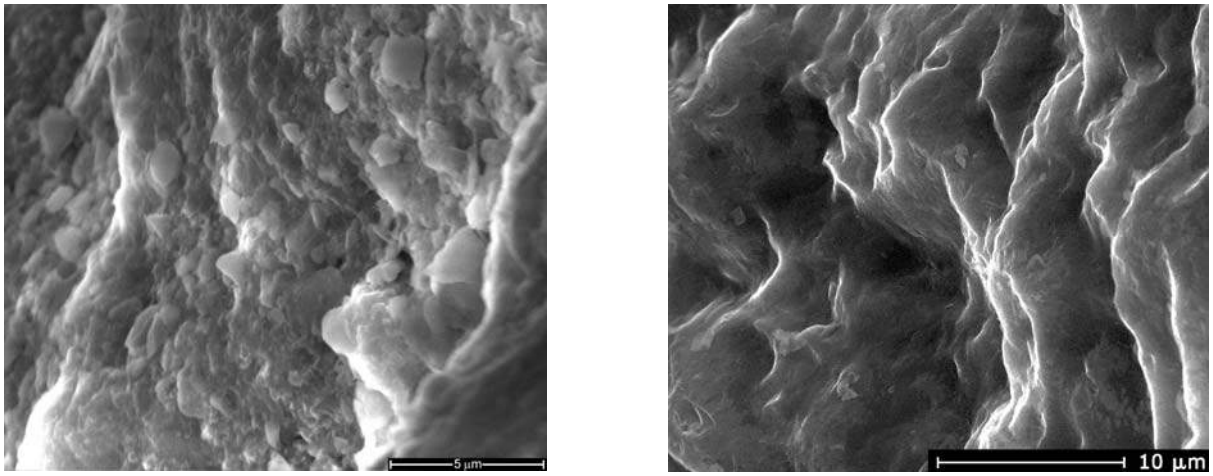

(a) (b)

Fig. 1. Micro-morphology of sand grain surfaces: (a) Michigan Lake dune sand, and (b) Ottawa 20-30 sand

Consequently, the microscopic features on the contacts are prone to develop cracks in time, the process called *stress corrosion cracking*. Because this process is time-delayed, it is often termed *static fatigue*. Micro-fracturing does not occur simultaneously at all contacts, and presumably, takes place with different intensity at different contacts, depending on the current distribution of the force chains. This hypothesis was suggested recently by Michalowski & Nadukuru (2010, 2011a, 2011b).

In an effort to gain evidence for this time-delayed fracturing, an experiment was performed where three grains placed in a triangular pattern were loaded with a total load of about 2.1 N. The load was transmitted to the grains through a glass plate. Surface morphology of the grains was inspected using scanning electron microscopy before the start of the test, 15 minutes after the load was applied, and after one week. Scanning electron imaging was used to identify regions of fracturing. A set of pictures for one grain is shown in Fig. 2.

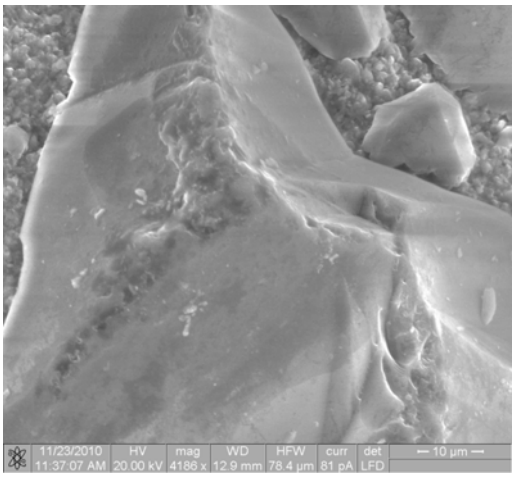

(a)

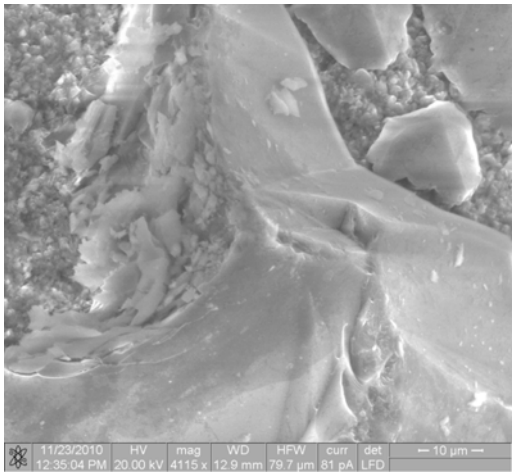

(b)

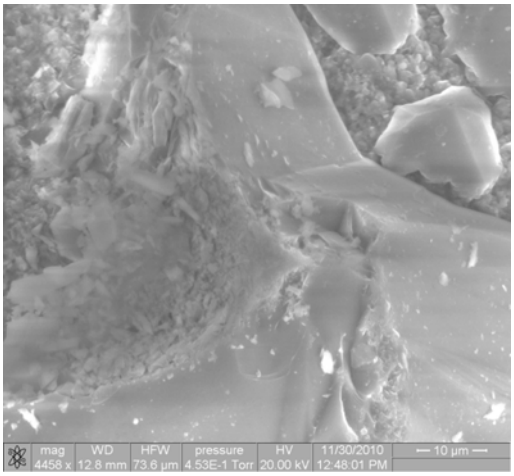

(c)

Fig. 2. Fracturing of quartz asperity: (a) before loading, (b) after 15 min. of loading, and (c) after one week

A microscopic view of a quartz asperity on the grain surface prior to testing is shown in Fig. 2(a); the width of the picture is about 70 μm. Fractured (crushed) asperity, after 15 min of loading, is shown in Fig. 2(b), with the debris deposited on the fracture surface. It is not clear whether all this fracturing occurred immediately after application of the load or was distributed in the 15-min period. The fractured zone expanded during the following week is illustrated in Fig. 2(c). Continuing fracturing is quite noticeable (the load was kept constant and equal to that in the first 15 minutes of the test).

Static fatigue is not a new concept, but only recently was it used to explain mechanical behavior of sand by Lade & Karimpour (2010a, 2010b), who considered static fatigue of grains (delayed grain fracturing). Static fatigue has been considered in material science for decades (Charles, 1958) as a time-dependent fracturing process in brittle materials. Scholz

(1968, 1972) reviewed experimental work on creep of rocks, and concluded that, at low temperatures and pressure, the primary mechanism of creep of brittle rocks is delayed micro-fracturing.

3 STRESS CHANGE IN SOIL BED AFTER DYNAMIC COMPACTION

First, the development of the stress state in freshly compacted sand is discussed, followed by discrete element simulations and energy considerations.

3.1 Dynamic disturbance and post-liquefaction stress state

Compaction of sand requires a change in its packing, so that the volume of pores can be reduced. When saturated sands are dynamically compacted, the contact forces between grains are lost (liquefaction) and reconfigured, so that a tighter packing can be achieved. The effective stresses are reduced to zero during liquefaction, but the stress state is rebuilt upon dissipation of the excess pore water pressure. The vertical macroscopic stress is governed by gravity. When the effective vertical macroscopic stress increases from zero during liquefaction to a value that balances the buoyant weight of the soil at any depth, the horizontal stress will trail with its value such, so that the stress state is just below the yield condition of the newly compacted sand. This horizontal stress is then likely to be significantly lower than the stress in the pre-liquefaction sand bed that was subjected to long-term gravity loads. To demonstrate that this conjecture is reasonable, we perform discrete element simulations.

3.2 DEM calculations

To illustrate the process of liquefaction and subsequent re-building of the stress state, discrete element simulation is carried out. An assembly of over 11 thousand grains was generated using the *PFC*^{3D} (2008) computer code, Fig. 3. These grains were predominantly spherical with radii between 2.3 and 3.7 cm. 25% of the grains were in the form of "clumps" (particles with a shape of two overlapping spheres with the centers offset by one radius, *i.e.*, peanut-shape particles, shown darker in Fig. 3).

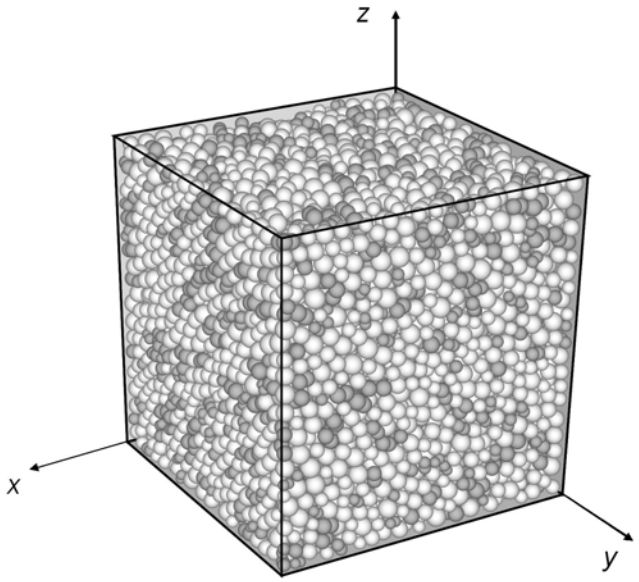

Fig. 3. An assembly of particles used in DEM simulations

The assembly was formed in a cube of 1.2 m in size, with initial porosity of 0.35. The contact normal and tangential stiffness was set to $K_n = 4.0$ and $K_t = 1.6$ MN/m, respectively, and the coefficient of grain interface friction $\mu = 0.65$ was used, or contact friction angle of 33° (mass density of the grains was 2,650 kg/m^3 and gravity acceleration was taken as 9.81 m/s^2). The ratio of horizontal-to-vertical macroscopic stress in the prepared specimen was $k = 0.473$. A numerical triaxial compression test of the specimen was then simulated with a confining pressure of 50 kPa. Interpreting the strength of the granular assembly as frictional with a linear envelope, the peak internal friction angle was found to be 33.5°.

Liquefaction simulations using DEM with two-phase medium are rarely attempted, but the phenomenon resembling liquefaction can be simulated using a granular assembly without modeling the pore fluid. The central phenomenon to liquefaction is loss of inter-granular contacts; this loss of contacts was simulated by reducing the grains' diameter by fraction 0.001. This change had no significant effect on the porosity. An alternative one-phase method of inducing liquefaction is through a constant-volume cyclic strain process of the granular assembly (Ng & Dobry, 1994). The latter was not used, because it requires zero gravity condition, whereas gravity is crucial to the simulation of stress state formation after liquefaction.

Once new contacts were formed after simulated liquefaction, the effective stress state in the granular assembly was regained. Stiffness of newly-formed contacts was taken at half of the originally used value, to reproduce the low stiffness of contacts that have not yet been subjected to *stress corrosion cracking*. The (effective) macroscopic stress state was regained with the vertical stresses governed by gravity, with the horizontal stress significantly lower than the pre-liquefaction value, leading to the horizontal-to-vertical stress ratio of $k = 0.339$ ($k = 0.473$ prior to liquefaction). This process occurred without a change in porosity, and the numerically tested internal friction angle was practically unchanged (33.6°).

Table 1. Increase in stress ratio k (1-D strain) as function of an increase in inter-granular elastic stiffness (DEM simulation)

K_n (MN/m)	K_s (MN/m)	k
2.0	0.8	0.339
2.2	0.88	0.365
2.4	0.96	0.378
2.6	1.04	0.391
2.8	1.12	0.399
3.0	1.2	0.413
3.2	1.28	0.424
3.4	1.36	0.433
3.6	1.44	0.442
3.8	1.52	0.451
4.0	1.6	0.459

In time, under one-dimensional strain conditions, static fatigue at inter-granular contacts will lead to *grain convergence* and an increase in contact stiffness. This increase was

simulated in ten equal steps. The stress ratio increased gradually, up to the value of $k = 0.459$ (Table 1), which is close to the pre-liquefaction ratio of 0.473. At this time no experimental data exists to assess the rate at which the contact stiffness increases; observations indicate that it might be the order of months (dependent on the level of loading).

3.3 Anisotropy of elastic properties and energy argument

Preliminary numerical testing using DEM indicates that the averaged elastic properties of a granular assembly consolidated under gravity conditions are cross-anisotropic. Elastic macroscopic properties are then described with five material constants: two Young's moduli and three Poisson's ratios.

A macroscopic analysis was attempted for predicting the change in the stress ratio (under one-dimensional strain conditions) with the change in the elastic stiffness caused by static fatigue. This was done using the energy balance equation applied to a soil column. Denoting the initial stress ratio by k_1, the stress ratio after the stiffness increase is described as k_2 in the following equation

$$k_2 = \sqrt{\frac{\frac{E'_h}{E_h}(1-\nu_{hh})\,k_1^2 - \frac{1}{2}\left(\frac{E'_h}{E_v} - \frac{E'_h}{E'_v}\right) + \xi(1-\chi)E'_h}{1-\nu'_{hh}}} \tag{1}$$

where E and ν are the Young moduli and Poisson's ratios, and subscripts v and h pertain to vertical and horizontal directions, respectively. The *primed* values of the elastic parameters are the altered ones by the process of static fatigue. The details of this analysis will be presented elsewhere (Michalowski & Nadukuru, 2011a).

When energy balance is used, one needs to estimate the macro-strain due to grain convergence, and the amount of energy dissipated ("used") in the process of stiffness increase. The strain due to grain convergence was assumed proportional to the depth (*i.e.*, proportional to the stress caused by gravity); this is embedded in coefficient ξ, with its value estimated at 10^{-6} - 10^{-5} (kPa^{-1}). Recent microscopic studies indicate that this value may be higher. Information about the amount of energy needed for the process of stiffness increase is contained in coefficient χ. This coefficient determines the dissipated energy as a portion of the gravity work done on grain convergence.

Calculations with eq. (1) were carried out for a sand bed with anisotropic macroscopic elastic properties obtained from numerical simulations on a grain assembly in Fig. 3. Coefficients ξ and χ were assumed to be $1.25 \cdot 10^{-5}$ and 0.2 (or 20%), respectively. Starting from the initial stress ratio of $k_1 = 0.339$, the value of 0.462 was obtained for k_2 from eq. (1), quite close to the DEM-simulated value of 0.459 (Table 1). While the energy approach contains two well-defined, but only approximately estimated parameters (ξ and χ), the preliminary result indicates that it may be a reasonable method of analysis.

4 SIMULATION OF CONE PENETRATION RESISTANCE

The hypothesis suggested here is that the initial drop in the cone penetration resistance after dynamic compaction is due to the change of the stress state caused by liquefaction. The post-liquefaction stress state is characterized by the horizontal stress lower than that in pre-liquefaction sand bed. This causes the deviatoric stress to increase, producing the stress state that is closer to the yield condition than the pre-liquefaction stress state. Subsequently, increase in the horizontal stress caused gradually by the process of stiffness increase, contributes to the time-delayed increase in the cone penetration resistance.

Finite element simulations of this process were attempted. Rather than simulating a continuous process of cone penetration, an analysis was carried out of on a block shown schematically in Fig. 4. The depth was simulated by the effective stress condition (σ_v) at the top boundary, but the soil in the block was considered weightless.

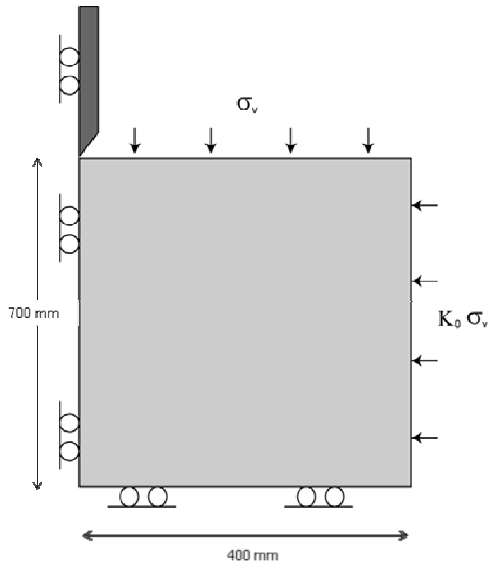

Fig. 4. Boundary conditions for FEM simulations of the cone penetration process, with depth adjusted by the stress condition on the top boundary

The analysis was carried out using Abaqus/CAE ver 6.10. The soil and cone were modeled with axisymmetric four-node elements, and the explicit solution scheme was used.

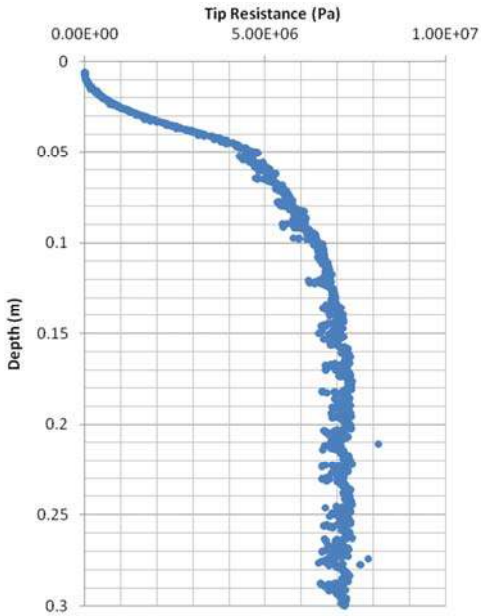

Fig. 5. Increase in cone penetration resistance with depth; steady-state resistance was taken as the value at the depth related to the stress condition at the top boundary of the simulation block

Adaptive meshing technique was utilized. The coefficient of friction between the cone and soil was assumed to be 0.3. The yielding of the soil was modeled with the Drucker-Prager criterion and the deformation was governed by the non-associative flow rule (nearly

incompressible). The details of the analysis will be presented elsewhere; here, we only use the results of the analysis as an argument for the hypothesis of variation of the stress being the primary cause of the drop and then increase in the cone penetration resistance after dynamic compaction of sands.

A typical graph of the cone resistance vs. penetration depth is illustrated in Fig. 5. The soil is characterized here by the friction angle of $\phi = 37°$ and the effective vertical stress at the top boundary is taken as $\sigma'_v = 0.25$ MPa (and $k_1 = 0.39$), which represents the stress at the depth of about 15 m. The soil in the model in Fig. 4 is weightless, and the steady-state value in Fig. 5 is taken as the cone penetration resistance at the depth set by the stress boundary condition. An example of the vertical and horizontal stress distribution in the neighborhood of the cone tip is presented in Fig 6.

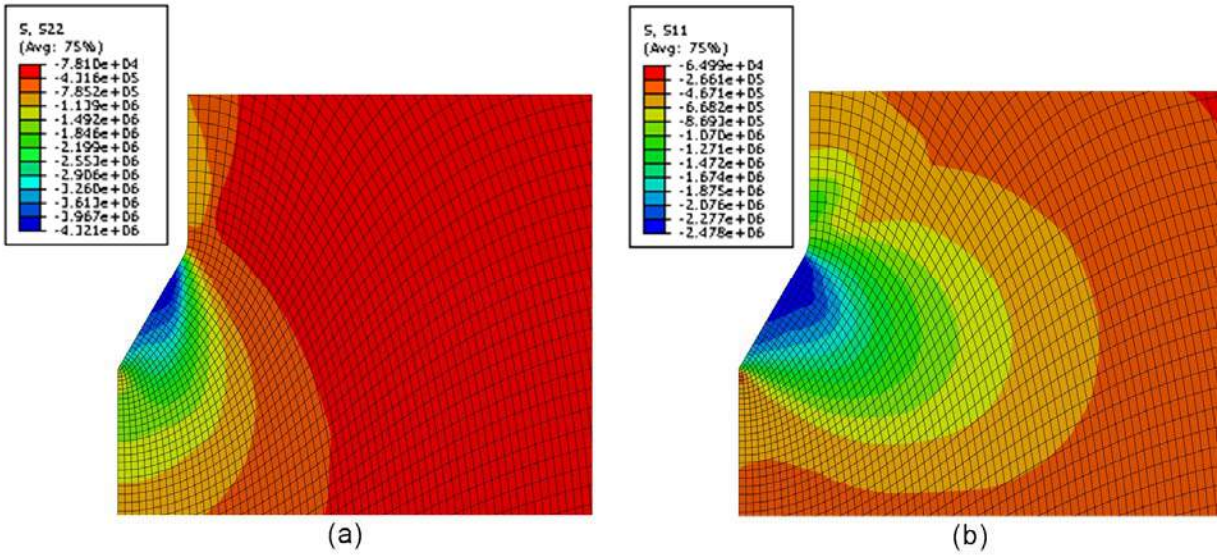

Fig. 6. Stress distribution in proximity of the cone tip: (a) vertical stress, and (b) horizontal stress

The initial horizontal-to-vertical stress ratio was taken as $k_1 = 0.33$. The consequence of an increase in soil stiffness (caused by grain convergence) is an increase in coefficient of earth pressure k. However, the relationship of the soil stiffness and k is not a material relationship; rather, it is the result of the loading history and the process of static fatigue. Triaxial tests were simulated numerically using PFC^{3D} (Fig. 3) to indicate how the stress ratio k changes with an increase in the inter-granular stiffness. These results were shown in Table 1, and the penetration resistance is simulated here for the stress ratio changing from 0.33 to 0.45.

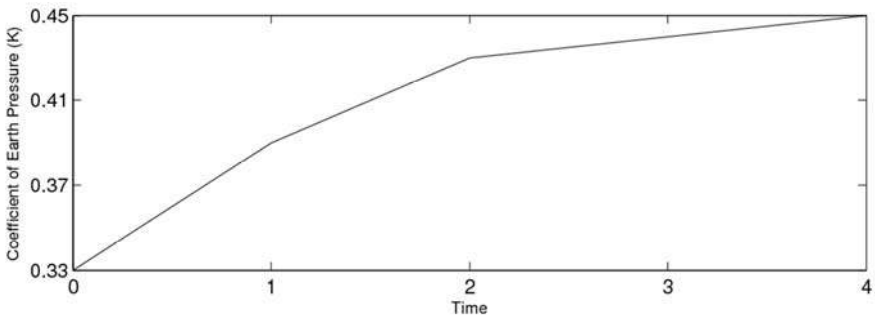

Fig. 7. Assumed increase in stress ratio k as function of time

Because the time-dependent increase in the soil stiffness (and, consequently, increase in ratio k) is still a subject of investigation, we assume the the change in k as in Fig. 7, with intervals 1 through 4 representing time. The blue line (without number designation) in Fig. 8 shows the cone penetration resistance calculated for a soil bed with internal friction angle of $\phi = 32°$ and $k = 0.45$ (the state prior to compaction).

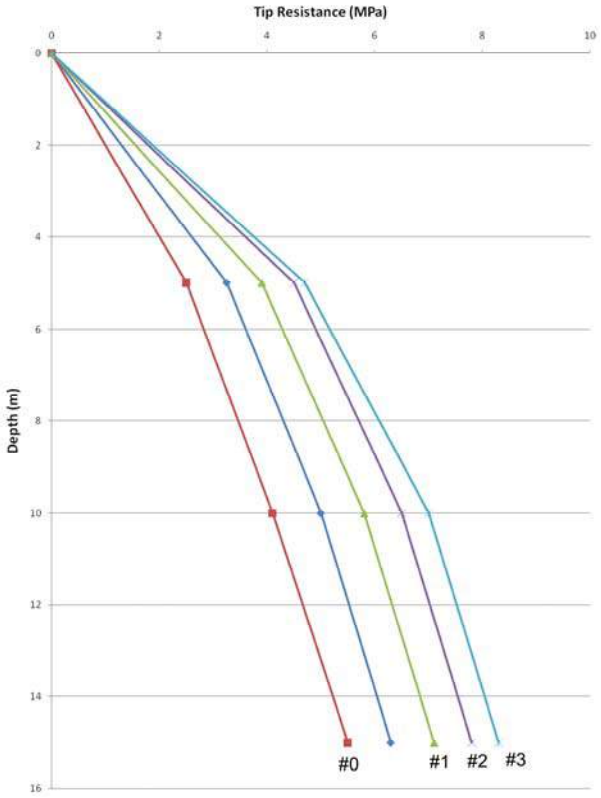

Fig. 8. FEM simulation results of cone penetration resistance

At the time of dynamic compaction the soil bed is liquefied, and the re-gained effective stress state is characterized with a low k of 0.33. Although the sand was assumed to be compacted with the internal friction angle increasing from 32° to 37°, the penetration resistance decreased (red line, #0); such is the impact of the drop in the horizontal stress. The decrease in the horizontal stress caused an increase in the deviatoric stress, moving the stress (in the stress space) closer to the failure surface. After the first time interval (0 to 1 in Fig. 7), the penetration resistance increased to reach the line marked as #1 in Fig. 8, and in the two subsequent intervals the resistance increased as indicated by lines #2 and #3. It is evident that the delayed increase in the cone penetration resistance can be caused by a gradual change in the stress state in the compacted soil and not by an increase in the soil strength. In pressure-dependent soils, of course, the shear strength is dependent on the first invariant of the stress state.

Changes in the stress state in the soil bed after dynamic compaction were considered earlier by Schmertmann (1987, 1991) as a possible cause of the delayed increase in soil penetration resistance. This cause was also alluded to by Mesri et al. (1990). The process of *static fatigue* and *grain convergence* described in this paper explains the mechanism of the delayed response of the sand bed after dynamic compaction.

5 CONCLUSIONS

While much research has been published regarding the peculiar behavior of sand deposits after dynamic compaction, no convincing explanation for the delayed increase in cone penetration resistance was presented. This paper indicates the hypothesis of *static fatigue* as the cause of that behavior. Numerical simulations seem to support this hypothesis. To gain information on the time scale of the process, further experimental research is needed, with the focus on the rate of static fatigue as a function of the stress state and environmental factors (moisture).

ACKNOWLEDGEMENT

The work presented in this paper was supported by the National Science Foundation through grant CMMI-0724022, and by the Army Research Office, grant No. W911NF-08-1-0376. This support is greatly appreciated. The authors also would like to thank Itasca Consulting Group for academic license of their *PFC*^{3D} code, and The University of Michigan Electron Microbeam Analysis Laboratory for the use of their Quanta 3D Scanning Electron Microscope supported by the National Science Foundation, grant No. DMR-0320740.

REFERENCES

Afifi, S.S. & Woods, R.D. (1971). "Long-term pressure effects on shear modulus of soils." ASCE J. Soil Mech. Found. Div., Vol. 97**(**10), 1445-1460.

Baxter, C.D.P. (1999). An Experimental Study on the Aging of Sands. Ph.D. Dissertation, Virginia Tech (Virginia Polytechnic Institute and State University), Blacksburg, VA.

Bowman, E.T. & Soga, K. (2003). "Creep, ageing and microstructural change in dense granular materials." Soils and Foundations, Vol. 43(4), 107-117.

Charles, S.J. (1958). "Static fatigue of glass. I." Journal of Applied Physics, Vol. 29(11), 1549-1553.

Lade, P.V. & Karimpour, H. (2010a). "Static Fatigue Controls Particle Crushing and Time Effects in Granular Materials." Soils and Foundations, Vol. 50(5), 573-583.

Lade, P.V. & Karimpour, H. (2010). "Static fatigue produces time effects in granular materials." ASCE Proc.: Advances in Analysis, Modeling and Design, GeoFlorida, Feb. 20-24, 2010.

Mesri, G., Feng, T.W. & Benak, J.M. (1990). "Postdensification penetration resistance of clean sand." J. Geotech. Eng., Vol. 116(7), 1095-1115.

Michalowski, R.L. & Nadukuru, S.S. (2010). "Stress corrosion cracking and relaxation of deviatoric stress after dynamic compaction of sand." 37th Solid Mechanics Conference, (SolMech 37), Keynote, Sept. 6-10, 2010, Warsaw, Poland (extended abstract).

Michalowski, R.L. & Nadukuru, S.S. (2011a). "Static fatigue and relaxation of deviatoric stress after dynamic compaction of sands." J. Geotech.Geoenv. Eng., in review.

Michalowski, R.L. & Nadukuru, S.S. (2011b). "Stress corrosion cracking and multi-scale process of delayed increase in penetration resistance after dynamic compaction of sand." Geo-Frontiers 2011, March 13-16, 2011, Dallas, TX.

Mitchell, J.K. & Solymar, Z.V. (1984). "Time-dependent strength gain in freshly deposited or densified sand." J. Geotech. Eng., Vol. 110(11), 1559-1576.

Mitchell, J.K. (2008). "Aging of sand – a continuing enigma?" Proceedings of the 6th Int. Conf. on Case Histories in Geotechnical Engineering. Arlington, VA, Aug. 11-16, 2008, 1-21.

Ng, T.T. & Dobry, R. (1994). "Numerical simulations of monotonic and cyclic loading of granular soil." Journal of Geotechnical Engineering, Vol. 120(2), 388-403.

PFC3D. (2008). *Particle Flow Code in 3 Dimensions*. Itasca Consulting Group, Inc. Minnepolis, MN.
Schmertmann, J.H. (1987). "Time-dependent strength gain in freshly deposited or densified sand." Discussion, J. Geotech. Eng. Vol. 113(2), 173-175.
Schmertmann, J.H. (1991). "The mechanical aging of soils." J. Geoecht. Eng., Vol. 117(9), 1288-1330.
Scholz, C.H. (1968). "Mechanism of creep in brittle rock." J. Geophys. Res., Vol. 73(10), 3295-3302.
Scholz, C.H. (1972). "Static fatigue of quartz." J. Geophys. Res., Vol. 77(11), 2104-2114.

DISCRETE ELEMENT MODELING OF STRESS CONDITIONS IN UNSTABLE SOIL

M.F. Ahlinhan
M. Achmus

Institute of Soil Mechanics, Foundation Engineering and Waterpower Engineering, Leibniz University of Hannover, Germany

ABSTRACT: *In unstable soils, a special erosion process termed suffusion can occur under the effect of relatively low hydraulic gradients. The critical hydraulic gradient of an unstable soil is smaller than in stable soils, which is described by a reduction factor α. According to a theory of Skempton & Brogan (1994), this reduction factor is related to the stress conditions in the soil. In an unstable soil, the average stresses acting in the fine portion are believed to be smaller than the average stresses in the coarse portion. It is assumed that the stress ratio and the reduction factor for the hydraulic gradient are almost equal. In order to prove this theory, discrete element modeling was carried out. Models of stable and unstable soils were established, and the stresses inside the sample were analysed. It was found that indeed in unstable soils the coarse grains are subject to larger stresses. The stress ratios in stable soils are almost unity, whereas in unstable soils smaller stress ratios, which are dependent on the soil composition and on the relative density of the soil, were obtained. A comparison with results of erosion tests shows that the stress ratios and the reduction factors are strongly related, as assumed by Skempton & Brogan.*

1 INTRODUCTION

For the subsoil below dams or dikes the stability against erosion with regard to seepage forces induced by under-seepage flow has to be proved. In that respect, it is of particular importance to identify and assess unstable soils, because here at relatively small hydraulic gradients a special erosion process termed "suffusion" can occur. In general, gap-graded or well-graded soils are endangered by suffusion. As result of the process, the fine fraction of the soil is washed out through the pores between the coarse-grained soil fraction. This increases the soil permeability and can lead to large dam settlements.

To assess whether suffusion is possible, in general the composition of the soil and the geometry of the pore channels have to be considered. Suffusion is only possible if the grains of the fine soil can pass through the pores of the coarse soil matrix. Since the pore channel geometry cannot be exactly measured, the assessment is based on the grain size distribution only. According to the Kenney & Lau (1986) criterion a value $(H/F)_{min}$ derived from the grain size distribution shall be less than 1.0. The authors of the paper in hand proposed to derive a parameter $(d_{c,15}/d_{f,85})_{mod}$ from the grain size distribution and to use $(d_{c,15}/d_{f,85})_{mod} < 4$ as a stability criterion (Ahlinhan & Achmus 2010).

If the "geometric" criterion yields the result that suffusion is possible, i.e. the soil is potentially unstable, the minimum hydraulic gradient necessary to cause erosion and to transport the fine soil grains has to be assessed by a "hydraulic" criterion. In stable soils, the critical hydraulic gradient for vertical upwards directed seepage flow $i_{crit,v}$ is (Terzaghi & Peck 1967)

$$i_{crit,v} = \frac{\gamma'}{\gamma_w} \tag{1}$$

with:

γ', γ_w = effective unit weight of soil and unit weight of water, respectively.

In unstable soils, the respective hydraulic gradient is generally smaller, which can be described by a reduction factor α. Skempton & Brogan (1994) supposed that the reason for the reduction of the critical vertical gradient is that the average stresses acting in the fine portion are smaller than the average stresses in the coarse portion of the soil. They further assumed that the stress ratio is the same as the reduction coefficient α:

$$i_{crit,v} = \alpha \frac{\gamma'}{\gamma_w} \tag{2}$$

and

$$\alpha = \frac{\sigma'_{m,f}}{\sigma'_{m,c}} \tag{3}$$

with:

$\sigma'_{m,f}, \sigma'_{m,c}$ = mean effective stresses acting on particles of fine and coarse fraction, respectively.

In this paper the results of experimental tests regarding critical hydraulic gradients for upwards directed flow in different soils with varying relative densities are presented. Discrete element models were established to determine the stress ratios in these soils. By comparison of the results, the validity of the Skempton & Brogan approach stated in Eqs. (2) and (3) is assessed.

2 EXPERIMENTS

Five different non-cohesive soils were tested in a specially developed test device under vertical upward seepage flow. The hydraulic gradient was increased slowly and gradually in order to identify the critical gradient at which erosion begins. The initial relative density of the soils was varied in the tests.

The grain size distributions of the five soils are shown in Fig. 1 and the relevant soil parameters are given in Table 1. The soils A1 and A2 are fine to medium and medium to coarse sands, respectively, which are poorly graded and stable with respect to all geometric criteria (Kenney & Lau parameter $(H/F)_{min}$ = 4.4 and 5.93). The soils E1, E2 and E3 are gap-graded soils, which were produced artificially. E2 and E3 are clearly unstable soils, whereas E1 has an $(H/F)_{min}$ value of 1.1 and so lies on the border between the stable and unstable region with regard to the Kenney & Lau (1986) criterion. Applying the criterion with $(d_{c,15}/d_{f,85})_{mod} < 4$ also leads to a close decision regarding internal stability.

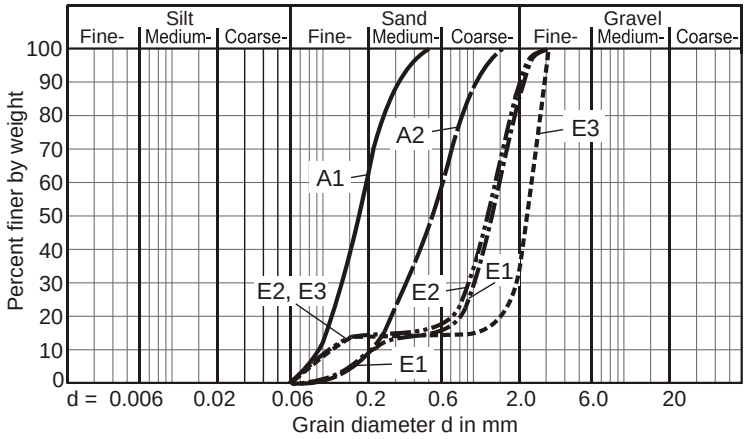

Fig. 1. Grain size distributions of the soils used in the experiments

Table 1. Properties of the soils used in the experiments

Property	Soil				
	A1	A2	E1	E2	E3
Density of grains ρ_s [t/m^3]	2.65	2.65	2.65	2.65	2.65
Minimum porosity n_{min}	0.40	0.32	0.34	0.27	0.31
Maximum porosity n_{max}	0.52	0.43	0.42	0.40	0.42
Uniformity index C_u	2.1	3.0	7.0	13.9	23.4
Index of Curvature C_c	1.0	1.0	3.3	6.7	13.8
$(H/F)_{min}$	5.93	4.44	1.10	0.20	0.03
$(d_{c,15}/d_{f,85})_{mod}$	1.31	1.50	3.30	7.20	14.40

A photographic view and a schematic drawing of the test device for vertical upward flow are shown in Fig. 2. The soil sample with a diameter of 28.5 cm and a height of 30 cm was subjected to a gradually increased vertical hydraulic gradient. During the test, the water discharge and the water pressures along the sample's height were recorded almost continuously.

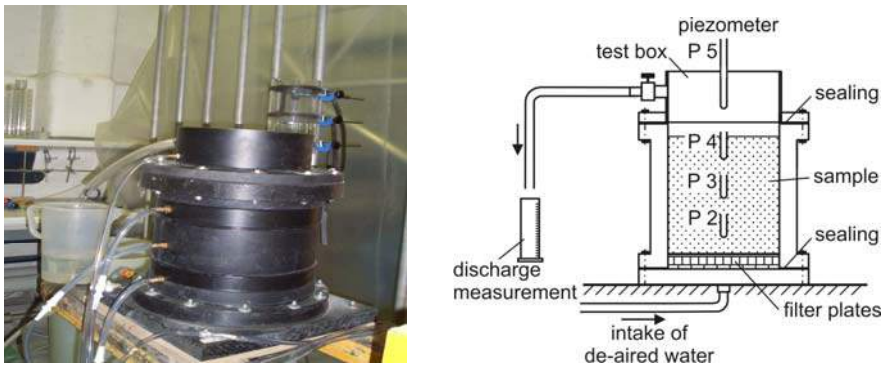

Fig. 2. Test device for vertical upward flow

Details regarding sample preparation, execution and evaluation of the tests can be found in Ahlinhan & Achmus (2010). The experimentally determined hydraulic gradients for vertical upward flow are given in Fig. 3, dependent on the initial relative density of the soil samples.

For the stable soils A1 and A2 the obtained critical gradients agree quite well with the theoretical values according to Terzaghi. In fact, slightly lower values were found with a maximum deviation of about 10%, which might be a result of unavoidable heterogeneities of the samples.

For the clearly unstable soils E2 and E3 very small critical gradients between 0.18 and 0.23 were measured. There is only a small dependence on the relative density of the sample.

On the contrary, for soil E1, which is on the border between stable and unstable, a stronger dependence of the critical hydraulic gradient on the relative densities was found. For a very dense state the critical hydraulic gradient is about double the value determined for a medium dense state. However, the value for very dense state is also significantly smaller than the theoretical critical hydraulic gradient after Terzaghi (Eq. 1). Thus, soil E1 has to be classified as potentially unstable.

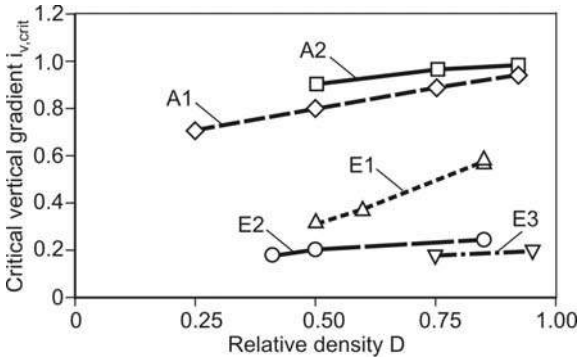

Fig. 3. Critical gradients determined for vertical upward flow

Fig. 4 shows the critical hydraulic gradients determined for the unstable soils dependent once on $(H/F)_{min}$ and once on $(d_{c,15}/d_{f,85})_{mod}$. The values obtained by Skempton & Brogan (1994) for dense sand are also depicted. The dependence on $(H/F)_{min}$ suggested by Skempton & Brogan (1994) is confirmed, with the exception of the potentially unstable soil E1, where the critical gradient is very much dependent on the initial relative density. There is also a connection of the critical hydraulic gradients with the parameter $(d_{c,15}/d_{f,85})_{mod}$, but the scatter here is slightly larger. The trend lines in Fig. 4 right are suggested curves regarding the effect of relative density. Evidently, the "more stable" a soil is, the more important is the relative density.

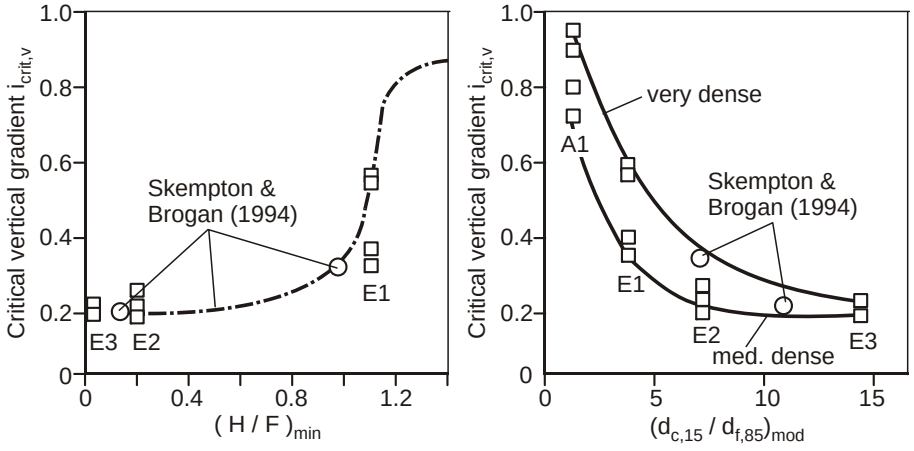

Fig. 4. Critical gradients dependent on instability parameters

3 DEM MODELING OF THE STRESS CONDITIONS IN NON-COHESIVE SOIL

The determination of stresses acting in the fine and coarse portions of the soils A1, E1, E2 and E3 given in Fig. 1 have been determined by means of the discrete element method. The Particle Flow Code programme (PFC, Itasca 2003) has been used. Here, the soil particles are idealized as perfect spheres and its behavior is idealized by a linear contact stiffness constitutive law (normal stiffness k_n, tangential stiffness k_s) and the Coulomb friction law

(friction coefficient μ_s). The values of these parameters are determined by calibration with triaxial test results.

3.1 Numerical simulation of triaxial test

For the numerical simulation of the triaxial test the particles were generated using the "fill and expand" method (Itasca 2003) inside a cylinder with diameter b and height h. The diameter has been chosen so that it was at least 10 times the maximum particle diameter of the sample and the height was chosen to be at least 2 times the diameter (cf. Fig. 5).

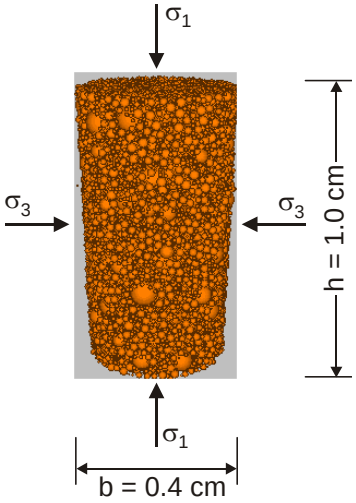

Fig. 5. Numerical triaxial test specimen for soil A1

During the calibration process first the model parameters k_n (normal stiffness) and k_s (tangential stiffness) were varied in order to match the stress-strain curve of real soil for strains lower than 1%, i.e. the deformation modulus, while the other parameters were kept constant. Then the inter-particle friction μ_s was varied to adjust the peak failure stress. The mobilized friction according to Eq. (4) and the volumetric strain development of soil A1 are shown in Fig. 6.

$$\varphi_{mob} = \arcsin\frac{\sigma_1 - \sigma_3}{\sigma_1 + \sigma_3} \tag{4}$$

As can be seen from Fig. 6, there is a fair agreement between experimental mobilized friction angle φ_{mob} and the simulated triaxial tests by using $k_n = k_s = 10^5$ *N/m*, $\mu_s = 2$ for soil A1. The volumetric strain results show that the discrete element assembly exhibits more initial compression and more subsequent dilation than the real soil. This result corresponds to those observed in similar numerical simulations by tom Woerden et al. (2004). In order to match approximately the experimental and numerical volumetric strain Belheine et al. (2008) introduced in their DEM-model other parameters such as rolling stiffness coefficient and non-dimensional plastic coefficient of the contacts. However, since here only stress conditions in the soils under vertical loading without shear shall be determined, the agreement of numerical and experimental results is considered sufficient.

In a similar way, the parameters for the soil E2 have been calibrated on triaxial tests carried out with this soil. Here, the parameters $k_n = k_s = 10^5$ *N/m*, $\mu_s = 3.2$ have been found to give optimum agreement of experimental and numerical results. The same set of parameters has been used for the other unstable soils E1 and E3.

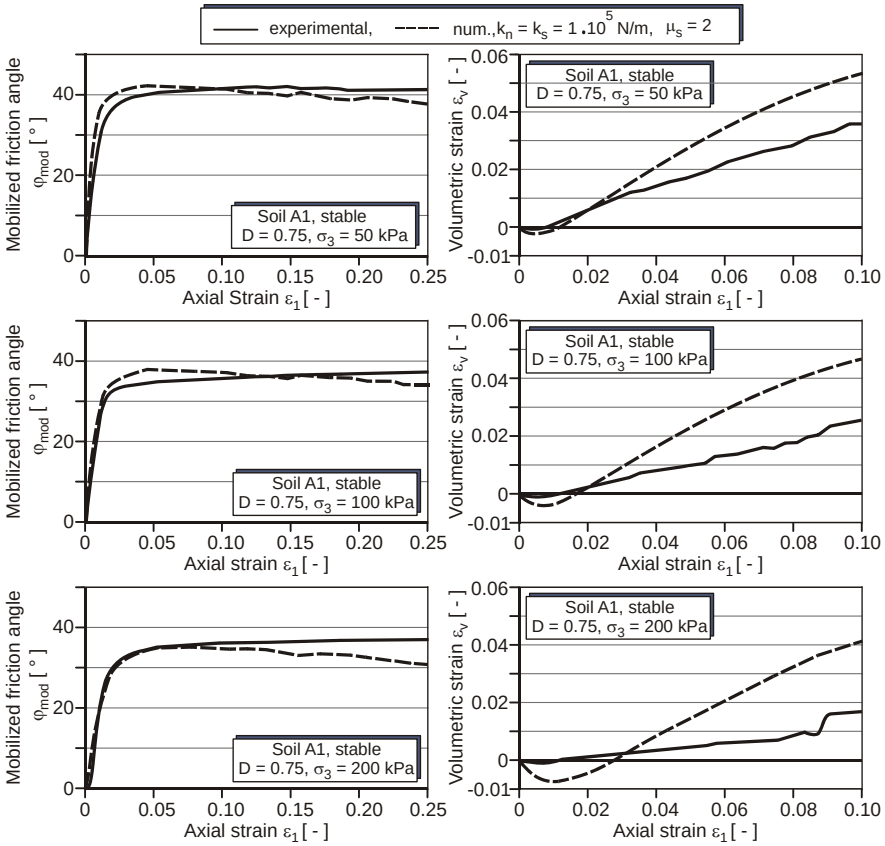

Fig. 6. Mobilized friction angle and volumetric strain versus axial strain for soil A1

3.2 Numerical model for calculation of the reduction factor α

In order to keep the calculation effort in reasonable limits, the assessment of the reduction factor α was carried out with a two-dimensional model, i.e. using the PFC^{2D} programme. A numerical model of *2.5 x 3.75 cm*^{2} was developed in PFC^{2D} (Fig. 7). First, the particles were generated randomly with respect to the grain size distribution. After activation of gravity the particle fall down into the defined container and move in mutual interaction in free positions. The calculation of the process was carried on until an equilibrium state was reached. Then the vertical and horizontal stress states in the samples were checked. To achieve a "k_0-state" ($\sigma_h = k_0\ \sigma_v$ with $k_0 = 1–sin\ \varphi'$), a small reduction of particle sizes was applied and the redistribution of particles was again calculated until equilibrium was found. In all cases, the required particle size reduction was less than 0.1%.

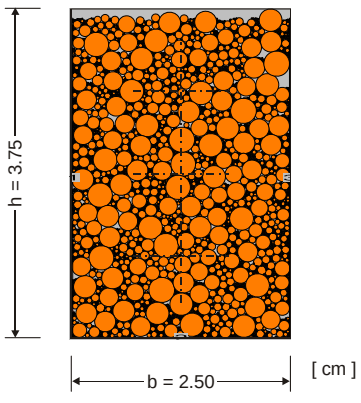

Fig. 7. PFC^{2D} model of soil E3

To realize different relative densities of the resultant sample, a method described in detail in tom Woerden et al. (2004) was used. To achieve a "densest" (D=1.0) sample, an inter-particle friction value μ_s=0 was used during sample generation, and to achieve a "loosest" (D=0.0) sample, the value was set to μ_s=15. Intermediate μ_s-values were then used to achieve relative densities of 0.25/ 0.50/ 0.75 and 0.95 (see tom Woerden et al. 2004).

The final step was the calculation of the reduction factor α. To do this, the intersected particles at a cross section through a certain depth of the sample were identified. The effective stresses in each particle were determined with a special calculation routine using the "Fish" macro language in PFC (Itasca 2003). Coarse and fine particles were distinguished by consideration of the grain diameter at which $(H/F)_{min}$ according to the Kenney & Lau criterion is obtained. With that, the mean effective stresses in the coarse and fine particle fractions could be determined separately and the reduction factor α was calculated according to Eq. (3).

It was found that the α-values are dependent on the considered depth of the cross section. This is shown by the results for the soils A1 and E2 given in Table 2. In the following evaluation, the values derived from the intermediate depth of 1.8 cm below sample surface were taken. However, it has to be noted that a certain variation with respect to the position of the considered position must be taken into account.

Table 2. Reduction factor depending on depth position of cross section

	Soil A1			Soil E2		
Depth (cm)	1.00	1.80	2.80	1.00	1.80	2.80
Reduction factor α	0.80	0.96	0.94	0.11	0.10	0.14

Regarding the random generation of particles, only minor effects on the determined α-value were found. Table 3 shows results from repeated numerical simulations with the soils A1 and E2. The maximum deviations of the results are small. Thus, the numerical model is regarded as robust as far as the random generation is concerned.

Table 3. Reduction factor depending on the random placing

	Soil A1			Soil E2		
Generation	N°1	N°2	N°3	N°1	N°2	N°3
Reduction factor α	0.96	0.98	0.97	0.10	0.09	0.09

Fig. 8 elucidates the evaluation of the results for the sample E2. In the graphs the stresses acting on particles which were identified to be intersected by the cross section line are depicted. From the mean values of the stresses in the particles of the fine and the coarse fraction, respectively, the α-values were calculated. Evidently, for the unstable soil E2 the mean values of stresses acting in the fine particle fraction are considerably smaller than the stresses acting in the coarse particles, i.e. the α-values are considerably smaller than unity.

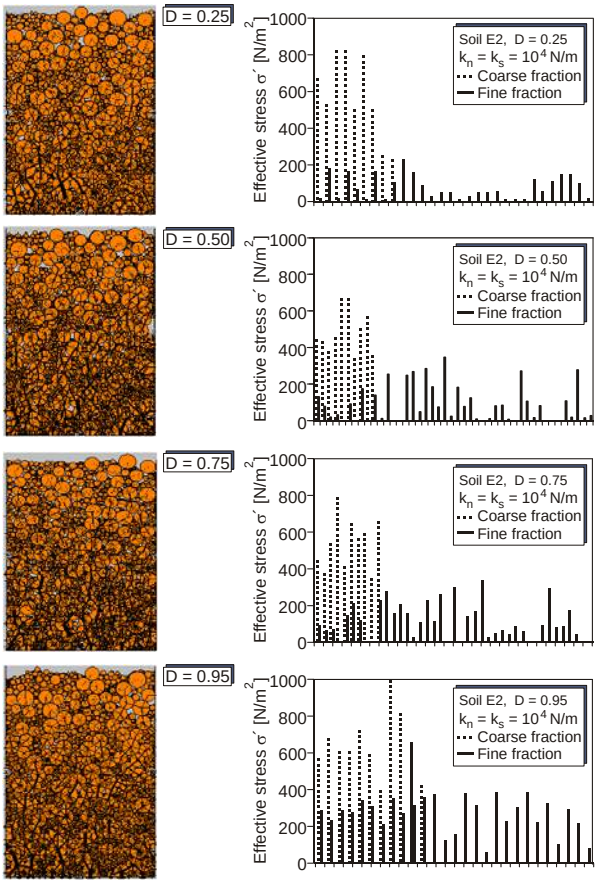

Fig. 8. Simulation results for soil E2 with different relative densities: particle positions and force chains (left); effective stress values for particles intersected by a cross section in a depth of 1.8 cm (right)

3.3. Results

In Fig. 9, the reduction factors determined in all the numerical simulations are given dependent on the considered relative densities. There is a slight influence of relative density on the reduction factor. However, the influence of the soil type, i.e. the grain size distribution, is clearly decisive. For the stable soil type A1 factors only slightly less than 1 are obtained, as was to be expected from Eq. (1). For the clearly unstable soils E2 and E5, values between 0.01 and 0.2 apply, whereas the values for the potentially unstable soil E1 lie between 0.3 and 0.38.

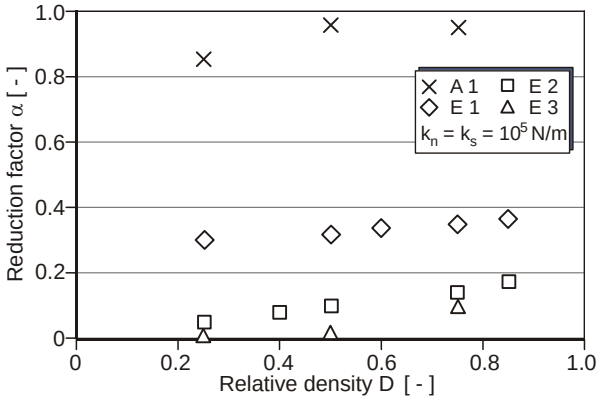

Fig. 9. Dependence of reduction factor on soil type and relative density

As mentioned in section 2, a parameter $(d_{c,15}/d_{f,85})_{mod}$ can be used to formulate an instability criterion. In Fig. 10, the numerically obtained α-values are depicted dependent on this parameter. Evidently, the stress reduction factor decreases with the index of instability in a similar manner as the critical vertical gradient does (cf. Fig. 4 right).

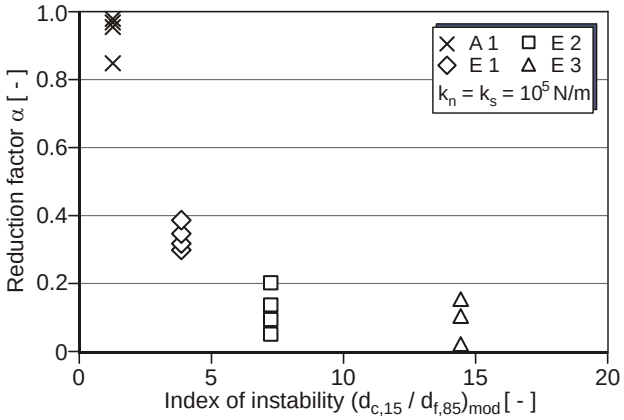

Fig. 10. Dependence of reduction factor on index of instability

4 COMPARISON OF EXPERIMENTAL AND NUMERICAL RESULTS

From the experiments, reduction factors were determined by the following Eq. (5):

$$\alpha_{\exp} = \frac{i_{v,crit,\exp}}{\gamma'/\gamma_w} \tag{5}$$

These experimental results, which are related to hydraulic gradients, are compared to the numerical simulation results related to stress ratios in Fig. 11. In general, good agreement of the values both qualitatively and to a slightly lower extent also quantitatively can be stated. Significant differences occur for the soil E1 at very dense state and for the soil E2 at medium dense states. This might partially be due to the inhomogeneous stress state in the test sample for unstable soil due to soil compaction in laboratory. However, perfect agreement of the results could not be expected due to uncertainties both in experimental and numerical modeling. The overall agreement of the experimental and numerical results can be stated as remarkably good.

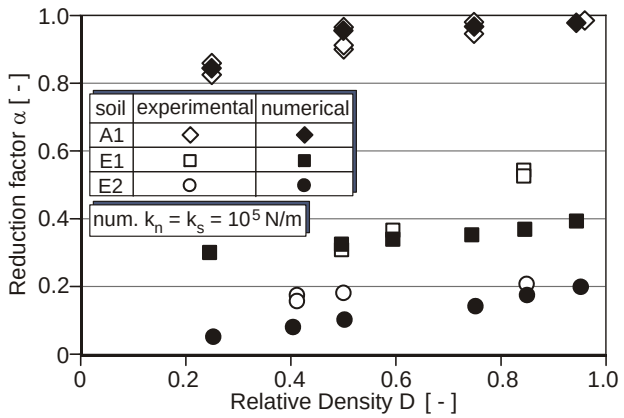

Fig. 11. Comparison of experimental and numerical results

5 CONCLUSIONS

Experimental tests presented in the paper in hand show that the critical hydraulic gradient for upward seepage flow is dependent on the instability index of a soil under consideration and to a minor extent also on its relative density. According to a hypothesis formulated by Skempton & Brogan (1994), the reduction of the critical gradients of unstable soil compared to stable soils is connected to non-homogeneous stress conditions in the fine and coarse grain portions of an unstable soils.

This hypothesis was checked by means of numerical simulations with the discrete element method. Different soils were considered, and the model parameters were calibrated by comparison with the results of triaxial tests. It was found that the non-linear behavior of cohesionless soil can be simulated fairly well. With the numerical model, stress ratios describing the non-homogeneity of stress conditions could be derived.

Good agreement was obtained between reduction factors regarding hydraulic gradients stemming from experimental tests and the stress reduction factors obtained in the numerical simulations. These results indicate that there is indeed a strong relation of these factors and thus strongly support the hypothesis of Skempton & Brogan.

ACKNOWLEDGEMENT

This research was partially supported by the Germany Ministry of Education and Research through IPSWaT (International Postgraduate Studies in Water Technologies). This support is gratefully acknowledged.

REFERENCES

Ahlinhan M. F. & Achmus, M. (2010), “Experimental Investigation of Critical Hydraulic Gradients of Unstable Soils”. Proceedings of the Fifth International Conference on Scour and Erosion, San Francisco, USA, pp. 599-608.

Belheine, N., Plassiard, J.-P. et al. (2009), „Numerical simulation of drained triaxial testing using 3D discrete element modeling“. Computers & Geotechnics Vol. 36.

Itasca (2003), Itasca Consulting Group Inc., PFC^{3D} PFC^{2D} User´s Manual, Minneapolis, USA.

Kenney, T.C. and Lau, D. (1985): “Internal stability of granular filters”, *Canadian Geotechnical Journal*, Vol. 22, pp. 215–225.

Kenney, T.C. and Lau, D. (1986): “Internal stability of granular filters: Reply”, *Canadian Geotechnical Journal*, Vol. 23, pp. 420-423.

Skempton, W. & Brogan, J.M. (1994), “Experiments on piping in sandy gravels”. Géotechnique No. 3, pp. 449–460.

Terzaghi, K. & Peck, R. B. (1967), Soil Mechanics in Engineering Practice, John Wiley & Sons, New York.

tom Woerden F., Achmus M. & Abdel-Rahman, K. (2004), “Finite element and discrete element modeling for the solution of spatial active earth pressure problems”. Proceedings of the 2nd Int. PFC-Symposium on Numerical modeling in micromechanics via particle methods, Kyoto, Japan.

A STUDY OF THE EFFECTS OF SUCTION AND ROUGHNESS ON THE MECHANICAL BEHAVIOUR OF ROCK JOINTS

M. T. Zandarin, E. Alonso & S. Olivella
Department of Geotechnical Engineering and Geosciences, Universitat Politècnica de Catalunya, Barcelona, Spain.

ABSTRACT: *The experimental investigation focused on the effects of suction on the mechanical behaviour of rock joints. Available experimental data on the effect of moisture on joint behaviour is very scarce. Laboratory tests were performed in a direct shear cell equipped with suction control. Suction was imposed using a vapour forced convection circuit connected to the cell and controlled by an air pump. Artificial joints of Lilla claystone were prepared. Joint roughness of varying intensity was created by carving the surfaces in contact in such a manner that rock ridges of different tip angles were formed. Several tests were performed for different values of suction (20, 100 and 200 MPa) and for different values of vertical stress (30, 60 and 150 kPa). A constitutive model including the effects of suction and joints roughness is proposed to simulate the unsaturated behaviour of rock joints. The new constitutive law was incorporated into the FE computer code Code-Bright and experimental results were numerically simulated.*

1 INTRODUCTION

The hydro-mechanical behaviour of joints under shear straining and joint roughness degradation has been reported by Lee & Cho,(2002), Olsson & Barton (2001), Hans (2002) and Indraratna et al., (2003). Some of these authors have also developed specific models to reproduce observed phenomena. However, the effect of suction on the degradation of joints does not seem to have been described. The effect of suction is potentially very significant in view of known suction effects on rock behaviour.

This paper describes a laboratory testing programme concentrated on the mechanical behaviour of rock joints subjected to direct shear with suction control. Suction was controlled by means of a vapour equilibrium technique (Fredlund & Rahardjo, 1993; Romero, 2001). Artificially joints of Lilla claystone were prepared by carving the surfaces in contact in such a manner that rock ridges of different tip angles were formed. These angles varied between 0º (smooth joint) to 45º (very rough joint profile). The geometric profiles of the two surfaces in contact were initially positioned in a "matching" situation. Several tests were performed for different values of suction (20, 100 and 200 MPa) and for different values of vertical stresses (30, 60 and 150 kPa).

The next section describes the mechanical properties of the claystone, the sample preparation and the procedure followed during the test. The paper ends with an analysis of test results followed by a description of the model proposed to reproduce the experiments.

2 CHARACTERISATION OF THE ROCK TESTED

The rock tested (Lilla claystone), is a sulphate-bearing argillaceous rock located in the Lower Ebro Basin, in northeast of Spain. These sulphated rocks formed during the Tertiary Period range from Early Eocene to Late Miocene in age (García-Castellanos et al., 2003). Lilla claystone has two main components: the host argillaceous matrix (composed by illite (15.85%), paligorskite (8.51%), dolomite (32.31%) and quartz), and the sulphated crystalline fraction (composed mainly by anhydrite (44.32%) and gypsum) (Berdugo, 2007; Tarragó, 2005).

The density of the rock varies from 2.56 to 2.58 g/cm^3. The clay matrix has a low plasticity. The porosity varies from 0.09 to 1.1%. The Young modulus E_0 varies from 26.5 to 28.5GPa and the shear stiffness G_0 varies from 11 to 12.5 GPa (Pineda, 2010).

3 SAMPLE PREPARATION

The samples were extracted from a core of Lilla claystone. The long core (1 m long and 110 mm in diameter) was cut into pieces with a nominal length of 500mm. Then, these pieces were drilled and cut in a machine to obtain samples 50mm in diameter and 12 mm in height. Then, the joints were carved with a diamond drill in order to create regular geometric asperities having "opening" angles of 5º, 15º, 30º, and 45º degrees respectively (Fig. 1).

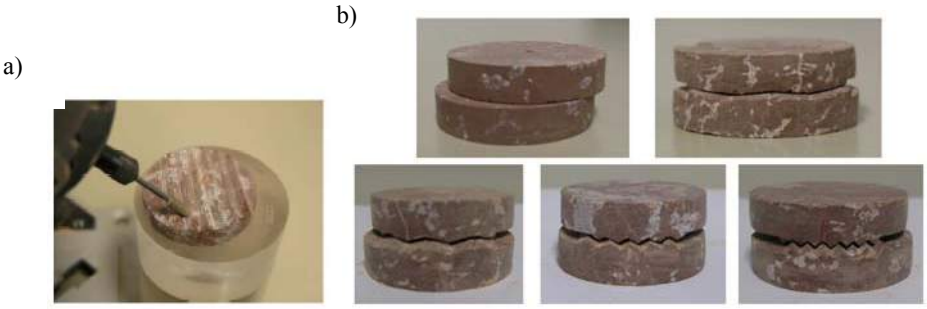

Fig. 1: Samples construction. a) Joint carving with the diamond drill. b) Rock joints having different geometric angles of 0º, 15º, 30º and 45 degrees respectively.

4 DIRECT SHEAR TESTS ON ROCK JOINTS WITH SUCTION CONTROL

Prior to shearing, each sample was equilibrated at the required suction using different techniques. The equilibrium was considered complete when there was no measurable change in the weight of samples (no changes in water content). The samples reached the equalization after a period of fifteen days.

Then samples were positioned in the shear cell, controlling that the joint was aligned with the direction of shear displacements. Once the shear cell was assembled and the sensors were positioned, a vapour equilibrium system was connected to the shear cell. Three net normal stresses were applied: 30, 60 and 150kPa respectively. When the vertical displacements induced by the vertical stress remained constant the shear displacements were applied at a rate of 0.05mm/min. The shear test ended when the shear stress reached its residual value. Some recorded shear stress versus shear displacements and normal displacements against shear displacements are plotted and analyzed in the following section.

5 TESTS RESULTS AND DISCUSSION

Test results are plotted in Figure 2 for two different joint roughness (α_a = 5º and 45º) and for three normal stresses: a) 30, b) 60 and c) 150 kPa. The left side of the figures shows the evolution of the shear stress with shear displacement. The right side shows the evolution of normal displacements with shear displacements. Each plot includes the data recorded for the three values of suction. The normal and shear stresses plotted are the averaged values acting on the middle plane of the joint. The continuous line provides the data recorded during the test and the dashed line the numerical results described below.

6.1 Shear Strength

The recorded plots of shear stress versus shear displacement show that the shear strength of joints depends on three variables namely normal stress, suction and joint roughness angle.
The effect of the normal stress is well known. The value of suction imposed also affect the peak and residual shear strength. Increasing suction results in progressively higher values of peak shear strength. However, the effect of suction on the residual strength is not seen as clearly as in the peak strength. Residual strength depends not only on suction, but also on the degradation of the asperity roughness. Degradation of asperities is controlled not only by suction but also by the irregular matching due to defects of joint construction and the heterogeneity of the rock.
Increasing the asperity roughness is associated with higher strength. Furthermore the roughness also affects the strength softening of the joint. In joints with higher roughness the residual strength is reached for smaller displacements. For example, for joints having a roughness of 45º (Fig. 2) the residual strength is reached for a displacement of approximately 2.5mm, while for a joint having roughness of 5º the residual strength occurs for a displacement of about 6mm.

6.2 Normal displacements

Dilatancy increases with roughness angle, as expected. It is also genarally observed that increasing normal stress results in lower dilatancy.
The influence of suction on dilatancy is also apparent in plots. Joints equilibrated at low suction (Ψ=20MPa, RH=86%) exhibit the lowest dilatancy. Dilatancy increases with suction. The effect is particularly intense in this rock. An explanation could be that sliding of the joint walls, one over the other, without breakage of asperities, is facilitated when suction is high.

6 A CONSTITUTIVE LAW FOR ROCK JOINTS CONSIDERING THE INFLUENCE OF SUCTION AND ASPERITY ROUGHNESS

The plastic behaviour of joint was initially based on the formulations proposed by Gens et al. (1990) and Carol et al. (1997) for rock joints. According to these elastoplastic models, it is necessary to define a yield surface, a plastic potential and a softening law.

7.1 Yield surface

A hyperbolic yield surface was adopted:

$$F \equiv \tau^2 - \left(c_0 + \sigma' \tan\phi_0\right)^2 + c_0^2 \qquad (1)$$

where τ = the shear stress; c_0' = the initial effective cohesion; σ' = the net normal stress; and $\tan\phi_0'$ = the tangent of initial effective angle of internal friction. Net stress is defined as the excess of total stress over air pressure.

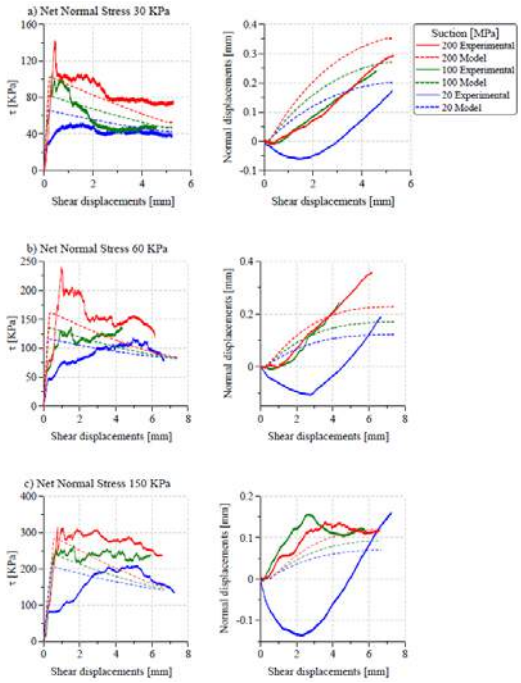

Fig. 2: Shear stress vs. shear displacements and normal displacements vs. shear displacements. Experimental tests and simulation results (α_a = 5º).

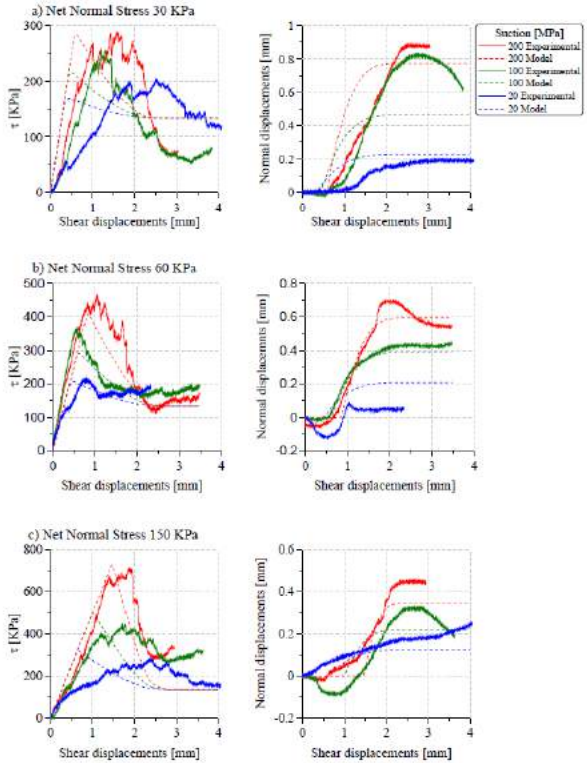

Fig. 3: Shear stress vs. shear displacements and normal displacements vs. shear displacements. Experimental tests and simulation results (α_a = 45º).

Φ_0' and c_0' are defined for the asymptote to the hyperbolic yield surface. Parameters c_0' and tan Φ_0' were obtained for each test by plotting the maximum shear stress measured against the net normal stress. One example is given in Figure 4.

Derived values of c_0' and tan Φ_0' were plotted against roughness angle (α_a) and suction (Figs. 5a,b). Figure 5a (above) shows that minimum values of cohesion are obtained for α_a=0º. Cohesion increases until α_a=15º, but remains essentially constant for higher values of α_a. Figure 5a (below) shows a linear increment of c_0'with suction.

A mathematical expression is proposed for c_0' taking into account the effect of suction and asperity roughness angle:

$$c'_{0(\psi,\alpha_a)} = (c_0 + c_1\,\psi) + (b_0 + b_1\,\psi)\left(1 - e^{-b_2 \tan\alpha_a}\right) \tag{2}$$

where c'$_{0(\Psi,\alpha a)}$ is the effective initial cohesion; Ψ is the total suction; c_0 is the cohesion for Ψ =0 and α_a = 0º; c_1 is the slope of c'$_0$ vs. suction for α_a = 0º; b_0 is the average value of c_0' for α_a = 15º-45º; b_1 is a parameter of the model which controls the increment of cohesion with Ψ for α_a = 5º-45º; and b_2 is a parameter of the model.

Figure 5b shows that tan Φ_0' increases also with α_a and suction. The increment with respect to α_a is considered dependant on tanα_a and the increment with respect to suction is made linear. The equation proposed for tan Φ_0' is:

$$\tan\phi'_{0(\psi,\alpha_a)} = (t_0 + t_1\,\psi) + (d_0 + d_1\,\psi)\tan\alpha_a \tag{3}$$

where tan Φ'$_{0(\Psi,\alpha a)}$ is the tangent of the effective initial angle of internal friction; Ψ is the total suction; t_0 is the value of tan Φ'$_0$ for Ψ = 0 and α_a = 0º; t_1 is the slope of tan Φ_0' vs. suction line for α_a = 0º; d_0 and d_1 are model parameters which control the increment of tanΦ_0' with suction for α_a = 5º-45º; and tan α_a is the geometric tangent of the asperity roughness.

Figures 5a and b show the fitting of the experimental values of c'$_{0(\Psi,\alpha a)}$ and tanΦ'$_{0(\Psi,\,\alpha a)}$ with the equations previously proposed.

7.2 Plastic potential

The flow rule is defined in terms of a plastic potential. The rule includes the parameters f_σ^{dil} and f_c^{dil} which help to define the dilatant behaviour of the joint under shear stresses (Lopez, 1999):

$$\frac{\partial G}{\partial \boldsymbol{\sigma}} = \left[\, 2\tan\phi'\left(c' - \sigma'\tan\phi'\right) f_\sigma^{dil} f_c^{dil} \quad , \quad 2\tau \,\right]^T \tag{4}$$

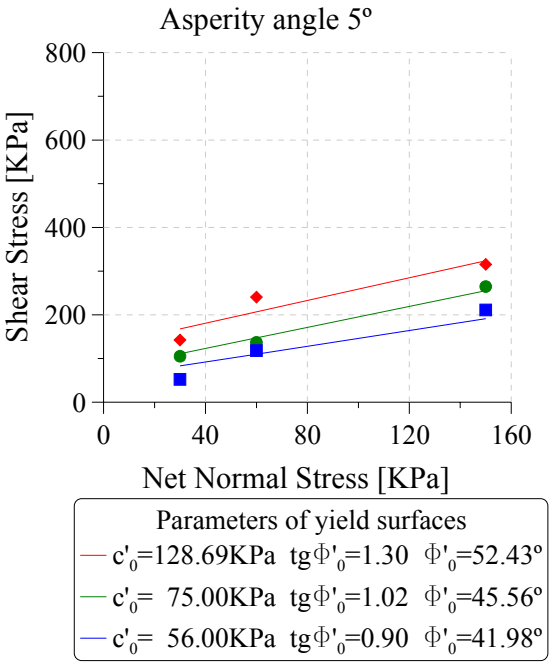

Fig. 4: Peak shear stresses vs. net normal stresses for α_a = 5º. The associated parameters of the yield surface are also given.

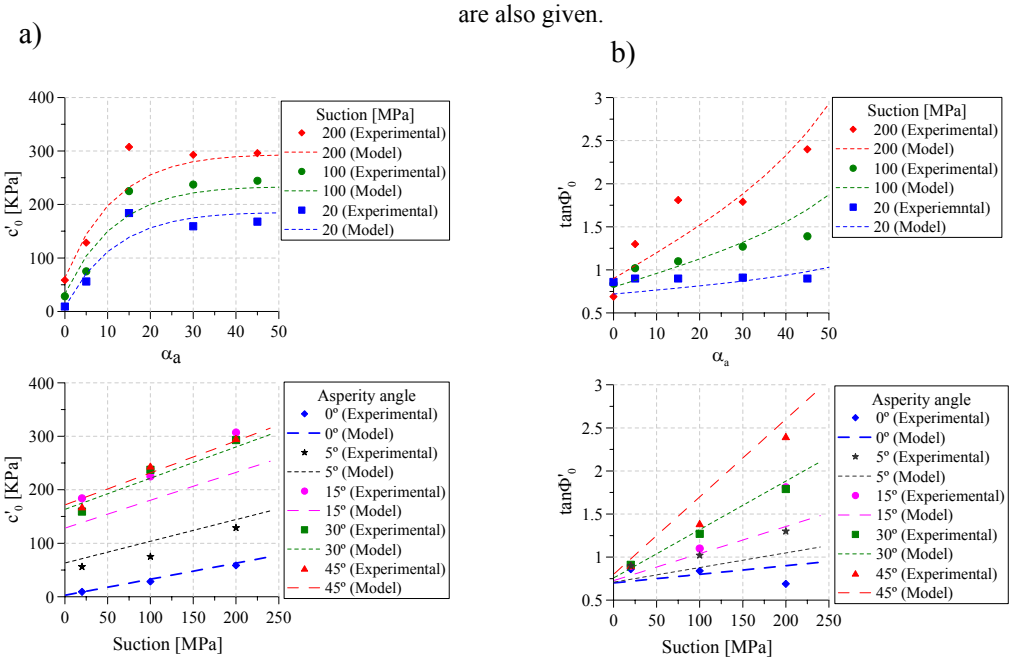

Fig. 5: a) Effective cohesion vs. α_a (above) and effective cohesion vs. suction (below). b) Effective tangent of internal friction angle vs. α_a (above) and effective tangent of internal friction angle vs. suction (below).

The original proposal for $f\sigma^{dil}$ and fc^{dil}, was modified through the following expressions:

$$f_{\sigma}^{dil} = \chi_d \sqrt{\tan \alpha_a} \left(1 - \frac{1}{q_u}\right) \exp\left(-\beta_d \frac{\sigma'}{q_u}\right) \tag{5}$$

$$f_c^{dil} = \frac{c'_{(\psi,\alpha_a)}}{c'_{0(\psi,\alpha_a)}} \tag{6}$$

where q_u is the uniaxial compression strength; χ_d and β_d are model parameters and the term $\sqrt{\tan\alpha_a}$ introduces the influence of roughness on dilatancy. Dilatancy depends on the level of normal stress, on the roughness of the joint surfaces (Eq. 5) and on the degradation of the interface surface, which varies with suction (Eq. 6).

7.3 Softening law

c'_0 and $\tan\Phi'_0$ were defined in terms of suction and asperity angle. A strain softening law was also included by means of a slip weakening model introduced by Palmer & Rice (1973). The adopted laws are:

$$c'_{(\psi,\alpha_a)} = c'_{0(\psi,\alpha_a)}\left(1 - \frac{u_s^{vp}}{u_c^*}\right) \tag{7}$$

where $c'_{(\Psi,\alpha a)}$ is the effective cohesion which corresponds to the visco-plastic shear displacement u_s^{vp}; $c'_{0(\Psi,\alpha a)}$ is the initial value of the effective cohesion; u_c^* is the critical value of shear displacement for which the value of $c'_{(\Psi,\alpha a)}$ is zero.

$$\tan\phi'_{(\psi,\alpha_a)} = \tan\phi'_{0(\psi,\alpha_a)} - \left(\tan\phi'_{0(\psi,\alpha_a)} - \tan\phi'_{res}\right)\frac{u_s^{vp}}{u_\phi^*} \tag{8}$$

where $\tan\Phi'_{(\Psi,\alpha a)}$ is the tangent of internal friction effective angle, which corresponds to visco-plastic shear displacement u_s^{vp}; $\tan\Phi'_{0(\Psi,\alpha a)}$ is the tangent of the peak friction angle; $\tan\Phi'_{res}$ is the tangent of the internal friction effective residual angle and u_ϕ^* is the critical value of shear displacement when the value of $\tan\Phi'_{(\Psi,\alpha a)}$ is equal $\tan\Phi'_{res.}$

7 NUMERICAL SIMULATION OF DIRECT SHEAR TESTS ON LILLA CLAYSTONE

The numerical simulation of the shear stress tests was carried out with the help of the FE code Code_Bright (2000) using the joint element (Zandarin, 2010) developed and the mechanical constitutive law proposed above.

The discretized model has a height of 20mm and a width of 50mm. The rock matrix was represented by an elastic material and the joint was modelled as a visco-plastic joint element. The joint is discretized using 10 joint elements.

The simulations were performed with the same constitutive parameters, except that the critical values of shear displacements u^*_c and u^*_Φ were changed according to the strength softening of shear stress and dilatancy of the joints. Main parameters are listed in Table 1.

The predictions of the numerical analysis are plotted in dashed line alongside test measurements in Figures 2 and 3. In general the mathematical results predict well the experimental results.

Table 1: Material parameters

Rock Matrix		
Mechanical Properties	Value	Unit
Young's modulus [E]	27000	MPa
Poisson's ratio [υ]	0.29	
Joint Rock		
Mechanical Properties	Value	Unit
Initial normal stiffness parameter [m]	100	MPa
Tangential stiffness [Ks]	500	MPa/m
Initial friction angle [Φ0]	35º	
Residual friction angle [Φres]	8º	
Initial opening [a0]	0.1	mm
Minimum opening [amin]	0.01	mm
Viscosity [γ]	1×10^{-2}	s^{-1}
Stress power [N]	2.0	
Uniaxial compressive strength [qu]	20	MPa
Model parameter [χd]	0.3	
Model parameter [βd]	100	

8 CONCLUDING REMARKS.

The influence of suction on joint behaviour was experimentally investigated. It is believed that this is an important issue in applications. No reference of this effect, which was found to be very significant in the rock tested, was found in the literature.

The carving process adopted to build different asperity angles allowed exploring the roughness effects on the shear strength and dilatancy of joints.

The shear test results emphasized the marked dependency of peak shear stress and dilatancy with suction and roughness. The shear strength and dilatancy decrease when suction decrease. However, the dependency of residual strength with suction was not so clear. Comparing the shear strength and dilatancy recorded for different roughness, it was noted that greater roughness implied greater shear strength as expected. It was also observed that a rougher asperity results in smaller values of displacements necessary to reach residual strength. In other words rougher joints are more brittle. This brittle behaviour induces higher damage on the joints surfaces, and this damage extends to the whole joint surfaces. A consequence of this phenomenon is that rougher surfaces exhibit a lower dilatancy.

New mathematical expressions for the strength parameters (initial effective cohesion (c_0') and initial effective tangent of internal friction angle ($\tan\Phi'_0$) of the asymptote of the hyperbolic yield surface are proposed. These expressions consider the effects of suction and asperity roughness on strength parameters. Also the dilatancy parameters were modified taking into consideration suction and geometry of joints. Both modifications were introduced in the constitutive law of the joint element implemented in Code_Bright.

The numerical simulation reproduces well the experimental features of the rock joints.

REFERENCES

Berdugo, I.R. (2007) Tunnelling in sulphate-bearing rocks expansive phenomena. PhD Thesis. Department of Geotechnical Engineering and Geosciences, UPC.

Carol I., Prat P. & Lopez C.M. (1997) A normal/shear cracking model. Application to discrete crack analysis. ASCE Journal of Engineering Mechanics, 123(8):765–773.

CODE_BRIGHT. DIT-UPC. (2000) A 3-D program for thermo-hydro-mechanical analysis in geological media. User's guide. Barcelona: Centro Internacional de Métodos Numéricos en Ingeniería (CIMNE).

Fredlund D.G. and Rahardjo H. (1993) Soil mechanics for unsaturated soils. Wiley & Sons.
Garcia-Castellanos, D., Vergés, J. Gaspar-Escribano, J. and Cloetingh, S. (2003) Interplay between tectonics, climate, and fluvial transport during the Cenozonic evolution of the Ebro Basin (NE Iberia). J. Geophys. Res., 108 (B7): ETG 8-1-8-18
Gens A., Carol I. & Alonso E.E. (1990) A constitutive model for rock joints; formulation and numerical implementation. Computers and Geotechnics, 9:3–20.
Hans J. (2002) Etude expérimental et modélisation numérique multiéchelle du comportamente hydromécanique de répliques de joints rocheux. Thése de doctorant- Université Joseph Fourier Grenoble.
Indraratna B., Ranjith P.G., Price J. R. and Gale W. (2003) Two-Phase (Air and Water) Flow through Rock Joints: Analytical and Experimental Study. Journal of Geotechnical and Geoenvironmental Engineering, Vol.129 No.10, October.
Lee H.S. & Cho T.F. (2002) Hydraulic Characteristics of Rough Fractures in Linear Flow under Normal and Shear Load. Rock Mechanics and Rock Engineering, 35(4),229-318.
López, C.M. (1999) Análisis microestructural de la fractura del hormigón utilizando elementos finitos tipo junta. Aplicación a diferentes hormigones. PhD thesis, ETSECCPB, UPC, Barcelona, España.
Olsson R. & Barton N. (2001) An improved model for hydromechanical coupling during shearing of rock joints. International Journal of Rock Mechanics and Mining Sciences, 2001, 38:317–329.
Palmer A.C., & Rice J.R. (1973) The growth of slip surfaces in the progressive failure of over-consolidated clay. Proc. Roy. Soc. Lond. A 332, 527-548.
Pineda, J.A., De Gracia, M. and Romero E., (2010) Degradation of partially saturated argillaceous rocks: influence on the stability of geotechnical structures. 4th Asia-Pacific Conference on Unsaturated Soils, Newcastle, Australia. Unsaturated soils-Buzzi, Fityus & Sheng (eds.). Taylor & Francis Group.
Romero, E.E., (2001) Controlled suction techniques. Proc 4º Simposio Brasileiro de Sols Nao Saturados. Gehling and Schnaid Edits. Porto Alegre, Brasil, 2001, pp 535-542.
Tarragó, D. (2005) Degradación mecánica de argilitas sulfatadas y su efecto sobre la expansividad. BSc dissertation. Universitat Politécnica de Catalunya, Barcelona.
Zandarin,M.T.(2010) Thermo-hydro-mecanical analysis of joint. A theoretical and experimental study. PhD Thesis. Universitat Politécnica de Catalunya, Barcelona.

RESPONSE OF VIRTUAL GRANULAR SPECIMENS TO UNDRAINED COMPRESSION FOLLOWING DIFFERENT PRECONSOLIDATION HISTORIES

S.A. Galindo-Torres, S. Fortuna, D.J. Williams
School of Civil Engineering, University of Queensland, Brisbane, Australia

ABSTRACT: *In this paper, the onset of instability of a soil-like material is investigated through the analysis of parameters derived from 3D DEM simulations of undrained triaxial compression tests, and the associated micro-mechanical behaviour of the material. Eight undrained compression tests were carried out on virtual specimens of a graded assembly of spherical particles, starting from a common isotropic state, at different initial void ratios and having overconsolidation ratios of up to 4.5. In accordance with experimental observations of real soils, the specimens with the lowest overconsolidation ratios show instability. The evolution of the total, and the (normalised) sliding and rolling numbers of contacts, describing the micro-mechanics of the assembly, is analysed as a function of the mean stress, prior to failure and under shearing at peak strength conditions. In particular, the asymptotic value of the number of sliding contacts, after a large shearing stage, appears to be a determining factor for predicting the onset of liquefaction instability under undrained shearing.*

1 METHOD

The present study was carried out using the Discrete Element Method (DEM) applied to cubic packs composed by spheres of variable diameter (with the largest diameter ten times that of the smallest), to reproduce a typical particle size distribution of natural granular soil.

At a given contact point, the particles are allowed to either roll or slide. Two generic particles interact via a spring interaction model; viscous and frictional forces are implemented, to reproduce the dissipation of energy associated with the dynamics of a granular assembly, as well as a rolling resistance at each contact to model the presence of multiple-contacts points typical of natural soil (Luding, 2008). No friction applies between the particles and the six rigid lateral walls of the cubic cell.

All specimens are randomly formed by about 1,270 spheres. To reduce the oscillation typically induced by the reduced number of particles comprising the specimens, eight tests are repeated under the same loading conditions. The data shown in the following are the averaged values from these (theoretically) identical tests. By this method, most of the statistical fluctuations are eliminated, therefore ensuring a uniform Representative Volume Element (RVE).

The DEM method used is a spherically-based model as described in (Belheine *et.al.* 2009), which includes a rolling resistance mechanism to account for the effects of the non-spherical shapes of real particles, and has been used before by one of the authors (Galindo-Torres and Pedroso, 2010). Table 1 shows the main parameters of the model.

Table 1. Model parameters

Symbol	Value	Description
K_n	5.0×10^7 (N/m)	Normal stiffness
K_t	2.5×10^7 (N/m)	Tangential stiffness
G_n	16.0×10^4 (1/s)	Normal dissipative coefficient
G_t	8×10^4 (1/s)	Tangential dissipative coefficient
μ	0.3	Microscopic friction coefficient
β	0.12	Rolling stiffness coefficient
η	1	Plastic moment coefficient, at rolling contacts

Some statistical quantities can be obtain form the proposed simulations and are important for the discussion to follow. These quantities are the coordination number CN (defined as the mean number of contacts per particle), and the normalised number of sliding and rolling contacts (CN_S and CN_R, respectively). In order to count the number of contacts that are sliding, all contacts are checked against the Coulomb friction threshold (for details on how to obtain this see (Galindo-Torres and Pedroso, 2010).

2 PROGRAM OF TESTS

Theoretically identical cubic specimens of particles were isotropically reconsolidated to a maximum preconsolidation pressure, p'_p, ranging between 100 kPa and 450 kPa, and then unloaded to a common mean stress, $p'_0 = 100$ kPa. The compression curves of tests reconsolidated up to 150 kPa, 200 kPa and 450 kPa are represented in Figure 1, plotted on the e-p' plane, to a semi-logarithmic scales. The effect of creep on unloading is visible in the tests associated with the lowest overconsolidation ratios. Prior to each stress path reversal, before restarting the loading, a standard waiting period was allowed to ensure a reasonably low residual creep.

After isotropic compression and unloading, the specimens were sheared under undrained conditions. Figure 2 shows the set of eight undrained virtual triaxial tests, starting from p'_0, plotted on the q-p' plane. All tests are carried out at a constant rate of strain, to a maximum axial strain of 5%, within which all tests have reached a phase transformation and the peak shear strength envelope. In the following, the occurrence of instability under undrained shearing is identified by softening prior to reaching the peak shear strength, in accordance with the general Hill's criterion of stability (Hill, 1958).

3 RESULTS

As shown in Figure 2, at higher $OCR = p'_p/p'_0$ values, as the initial stress state moves away from the first-yield surface, the response becomes more elastic, in that the undrained path gets closer to the vertical, and a lower positive excess pore water pressure is generated.

All tests finally reach a common peak shear strength envelope, associated with a maximum friction angle decreasing slightly as p' increases. Tests consolidated to 100 kPa, 150 kPa and 200 kPa show softening and instability, whereas the remaining tests are stable.

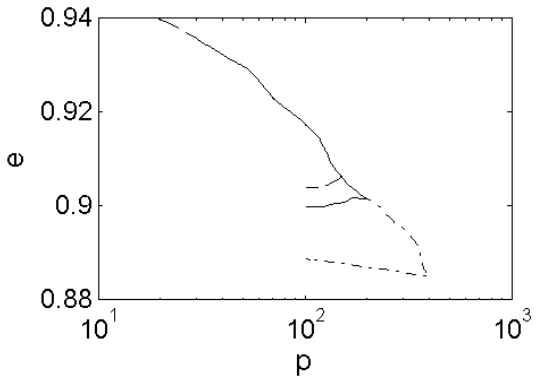

Fig. 1. Void ratio versus mean stress (in kPa) to semi-logarithmic scales, during isotropic consolidation to 150 kPa, 200 kPa and 400 kPa.

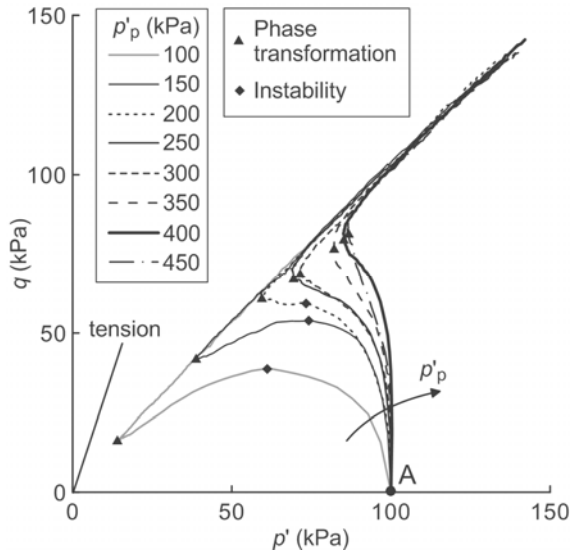

Fig. 2. Undrained stress paths on the q-p' plane.

Stress ratio $\eta = q/p'$ at instability and phase transformation, which are also denoted in Figure 2, are not unique for all tests, with the first two increasing with p'_p, and the remaining plots decreasing. No shear bands were observed during the tests.

Figure 3 shows the values of the coordination number, *CN* and the number of rolling and sliding contacts, normalised to obtain values that are comparable to those corresponding to *CN*, at end of isotropic reconsolidation. Threshold values are found for *CN* and for the

number of rolling contacts, corresponding to p'_p = 200 kPa, below which the specimens are unstable. All three quantities seem to reach a constant value with increasing pressure. It may be concluded that instability is strongly affected by the formation of a granular skeleton. For pressures below 200 kPa, the closely-packed skeleton is not yet formed, and CN is smaller than for the stable state. For larger pressures, CN reaches the limiting value when the granular ensemble is closely-packed and hence the specimen is stable.

Figure 4 shows the value of the coordination number *CN* under shearing as a function of the mean stress *p*': (a) in the stable tests, and (b) in the unstable tests. Figure 5 shows the values of the coordination number for all tests, after the tests reach (and follow) the peak shear strength envelope. The response at failure is uniquely defined by the current mean stress, and therefore the deviatoric stress q appears to be a function of the coordination number only.

The value of the coordination number at failure for *p*' = 100 kPa, $CN_{f,100}$, is about 2.25 and is intermediate between the value before probing at the normally consolidated state and the threshold value for the stable tests (compare Figs. 3 to 5). In accordance with data from the literature, all tests show a reduction in the coordination number prior to failure; however, whereas the curves corresponding to the stable tests move along the peak shear strength envelope soon after reaching it (Fig. 4a), the curves corresponding to the unstable tests form loops that move beneath the peak shear strength envelope common to all tests (Fig. 4b).

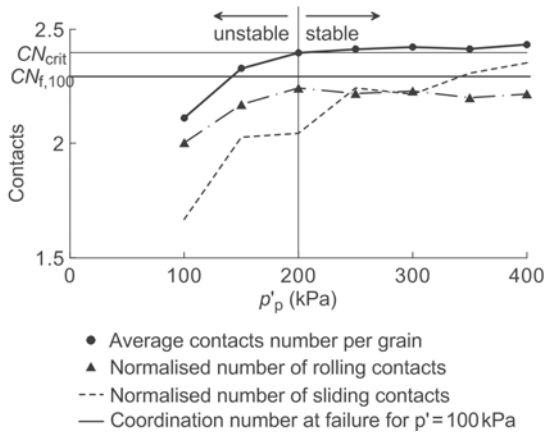

Fig. 3. Coordination number, normalised number of rolling and sliding contacts at end of reconsolidation, versus the maximum reconsolidation stress p'_p.

Figure 6 shows the value of the normalised rolling contacts NC_R under shearing as a function of the mean stress. This parameter, initially higher than that at failure for the same mean stress $NC_{R,100}$, initially decreases significantly in all tests. Once the peak shear strength envelope is reached, NC_R increases due to hardening, along a unique envelope.

Figure 7 shows the value of the normalised number of sliding contacts under shearing as a function of the mean stress. Contrary to the normalised number of rolling contacts, this parameter initially increases from the initial value at the isotropic state, decreasing once a common envelope has been reached.

Contrary to the normalised number of rolling contacts, all sliding contacts curves seem to tend to an asymptotic value, $NC_{S,\infty}$ (reached only at ideally infinite mean stress), that apparently marks the boundary between the stable and unstable tests, and could therefore be useful for defining the boundary of potentially unstable loading conditions.

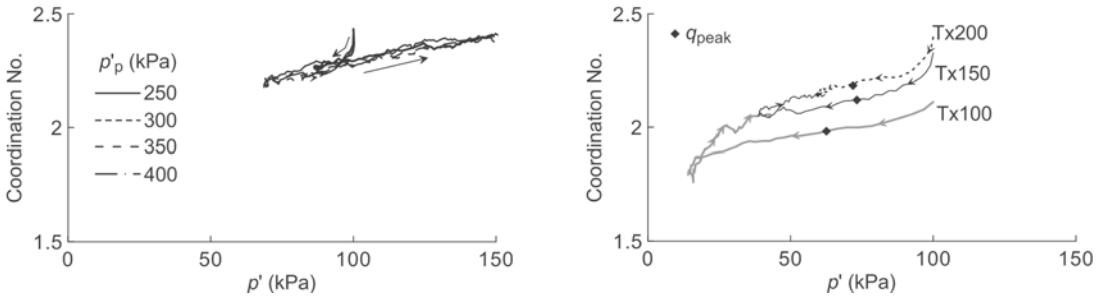

Fig. 4. Coordination number under undrained shearing in: (a) stable tests, and (b) unstable tests, versus the mean stress (same legend as Figure 2; in (b) tests are referred to as 'Tx', followed by the value of the maximum preconsolidation pressure p'_p = 100 kPa, 150 kPa, 200 kPa).

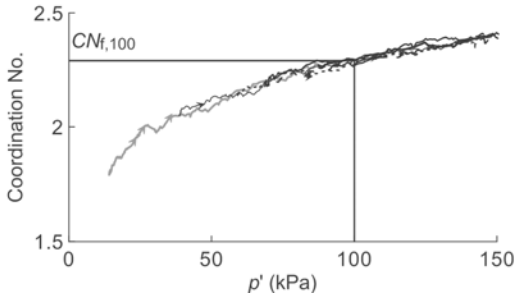

Fig. 5. Coordination number after reaching the peak shear strength in all tests, versus the mean stress (same legend as Figure 2).

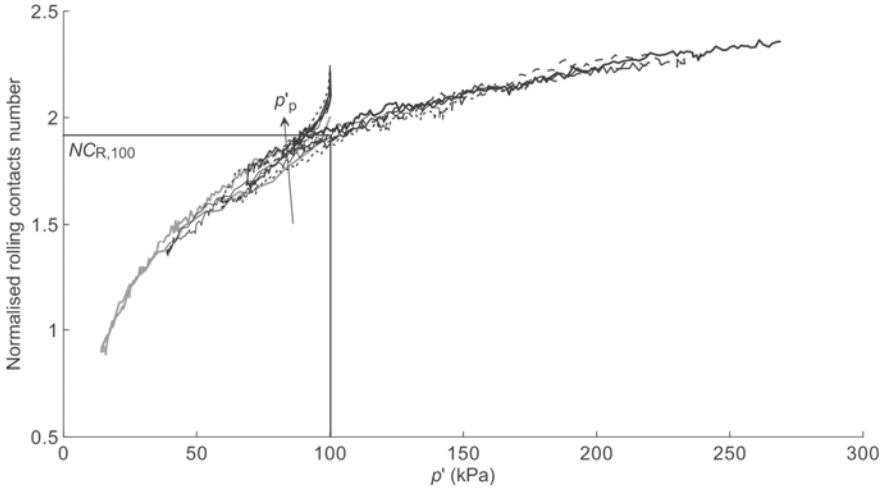

Fig. 6. Normalised number of rolling contacts throughout all tests, versus the mean stress (same legend as Figure 2).

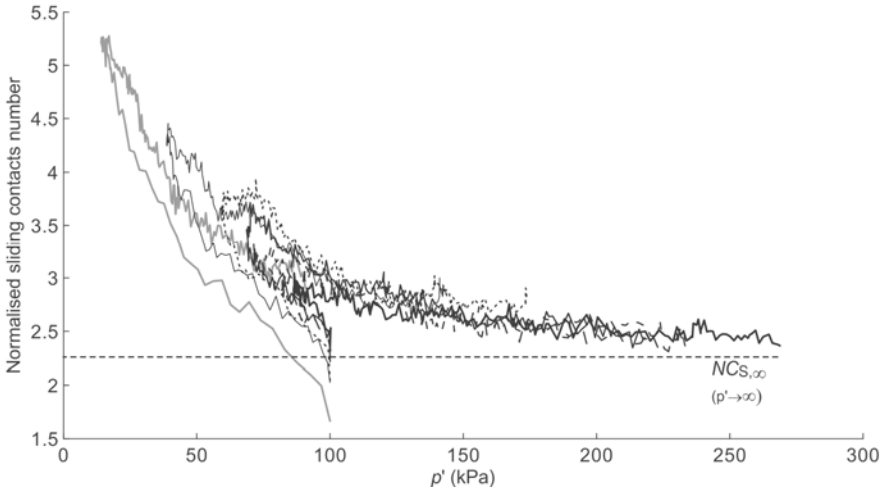

Fig. 7. Normalised number of sliding contacts throughout all tests, versus the mean stress (same legend as Figure 2).

4 CONCLUSIONS

With a spherically-based DEM model, a concise study on the microscopical origins of instabilities in granular assemblages has been carried out. It has been found that the structure is affected by the isotropic pressure applied to the specimen. This effect is characterised by the coordination number (CN) defined as the mean number of contacts per particle. It is observed that CN has a critical value corresponding to preconsolidation pressures close to 200 kPa, after which the specimen can be considered stable. This indicates that in order to have stability, a strong granular skeleton must be formed (i.e. all the particles must have the maximum number of contacts available to them). This skeleton hinders the ability of the particles to move freely by forcing them to roll or slide against their neighbours. This effect is observed by measuring CN_S and CN_R, which also present a critical value around the same preconsolidation pressure of 200 kPa, and a constant value for stable specimens. The results of this study indicate CN as a main geomechanical variable that determines the onset of instabilities in granular assemblages. It is also important to mention that CN can be modified by changing the particle size distribution or the particle shape. This fact offers a possible way to control the unstable behaviour.

SUBSCRIPTS

p	Preconsolidation
0	Initial condition (before undrained shearing)
crit	Critical (for the onset of instability)
f	Failure
100	For p' = 100 kPa

NOTATION

G	$= q/3\Delta\varepsilon_s$	Shear stiffness
σ'_a	Axial principal effective stress	
σ'_h	Horizontal principal effective stress	
p'	$= (\sigma'_a + 2\sigma'_h)/3$	Mean effective stress
p'_p	Pre-consolidation (mean) stress	
q	$= (\sigma'_a - \sigma'_h)$	Deviatoric stress
η	$= q/p'$	Stress ratio
ε_s	$= 2/3(\varepsilon_a - \varepsilon_h)$	Deviatoric strain
CN	Coordination number, or average contact number per particle	
CN_R	Normalised number of rolling contacts	
CN_S	Normalised number of sliding contacts	
OCR	$= p'_p/p'$	Overconsolidation ratio

ACKNOWLEDGEMENT

The authors wish to thank Golder Associates for financial support granted to the Golder Geomechanics Centre, at The University of Queensland during this work. The DEM code used for this study is open-source software and can be downloaded from http://mechsys.nongnu.org/ or by contacting the authors.

REFERENCES

Cundall P.A. & Strack O.D.L. (1979). A discrete numerical model for granular assemblies. Géotechnique, Vol. 29(1), 47-65.

Belheine N., Plassiardc J.P., Donzéc F.V., Darvec F. and Seridid A. (2009). Numerical simulation of drained triaxial test using 3D discrete element modeling. Computers and Geotechnics, Vol. 36(1), 320-331.

Galindo-Torres S.A. & Pedroso, D.M. (2010), Molecular dynamics simulations of complex-shaped particles using Voronoi-based spheropolyhedra. Phys. Rev. E 81, 061303.

Hill, A. (1958). A general theory of uniqueness and stability in elastic-plastic solids. J. Mech. Phys. Solids Vol. 6(3), 236-249.

Luding, S. (2008), Cohesive, frictional powders: contact models for tension. Granular matter Vol. 10(4), 235-246.

CONDITIONAL SIMULATION FOR CHARACTERISING THE SPATIAL VARIABILITY OF SAND STATE

A.P. van den Eijnden
Faculty of Civil Engineering and Geosciences, Delft University of Technology, Delft, The Netherlands

M.A. Hicks
Faculty of Civil Engineering and Geosciences, Delft University of Technology, Delft, The Netherlands

ABSTRACT: *Random fields are used to simulate heterogeneity in a sand fill, with a view to future stochastic assessments of slope stability using Monte Carlo analysis and finite elements. In order to reduce the uncertainty in the spatial variability, the random fields are conditioned to in-situ site investigation (CPT) data. This causes the range of random field solutions for the heterogeneity to decrease, which, in turn, causes a reduction in the range of possible solutions for geo-structural response and a decreased uncertainty in design. The conditional random field simulation is based on an extensive CPT database for the chosen site, supported by an extensive triaxial database for quantifying material behaviour. The conditioned random fields are shown to have the desired (geo-) statistical characteristics.*

1 INTRODUCTION

The stochastic characterisation of soil heterogeneity, for the stochastic analysis of slopes and other soil structures, has assumed increased importance in recent years (e.g. Hicks & Samy, 2002; Hicks & Onisiphorou, 2005; Hicks & Spencer, 2010). In these investigations, soil heterogeneity is often simulated by random fields, which may be used as input into finite element models of soil structure performance. For a given set of soil property statistics, there may be a large range of possible solutions for the site heterogeneity and so, because every realisation of a random field will lead to a different structure response, a range of responses will be found. This range of possible solutions, for the performance of a structure, leads to uncertainty in design and is caused by a lack of knowledge of the heterogeneity over the entire problem domain.

In numerical predictions of heterogeneity, the statistics derived from available soil investigation data are used as input for the random field generator. In previous investigations (e.g. Hicks & Onisiphorou, 2005), only the statistical characteristics of the soil investigation were used for the random field generation. That is, after determining the overall point and spatial statistics for a site, unconditioned random fields (not honouring the actual in-situ measurements) were generated. The range of values over which the unconditioned random fields can develop may be characterised by the standard deviation of the random variable, as illustrated in Figure 1. However, if the random field is conditioned to known data, such as from cone penetration test (CPT) profiles, the possibilities for the random fields to develop are constrained by the measurements and the domain in which the random fields can be expected to develop will decrease. Hence available data are used more efficiently, thereby leading to a reduction in the range of possible structure responses and to less uncertainty in design.

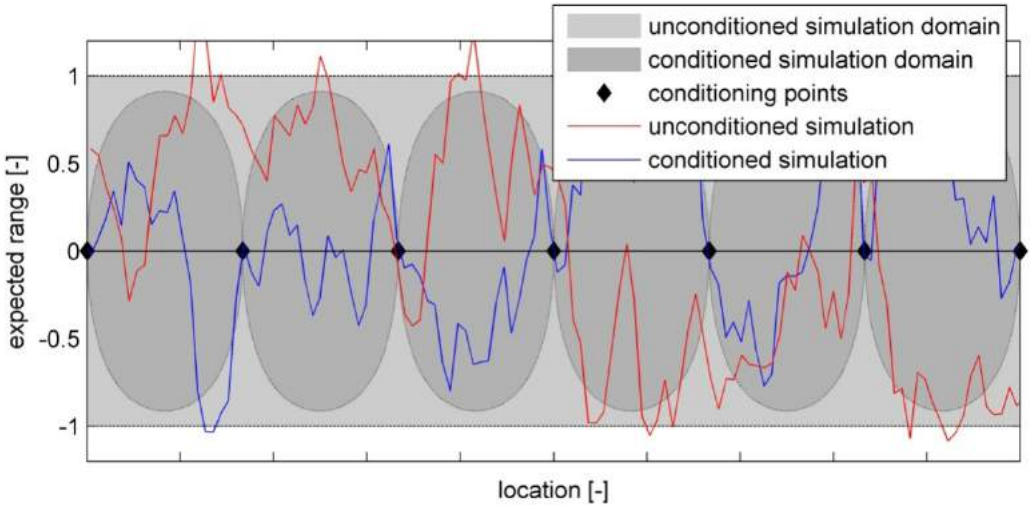

Figure 1: Schematic visualisation, based on a Gaussian distribution and an exponential correlation structure, of the reduction of the domain in which conditioned and unconditioned random fields can be expected to develop. When the random field is conditioned by the conditioning points, the domain is constrained and uncertainty in the heterogeneity is reduced.

Data from a new extension of a harbour on the North Sea coast are used for testing the developed methodology. These data are for a hydraulic sand fill, to be used in a future quay wall construction. The sand has been deposited from a depth of 11m below the water table to a height of 5m above the water table. For the fill material, data from 140 CPT profiles and 55 drained triaxial compression tests are available.

2 SOIL MODEL CALIBRATION

Sand state variability is here described using only one variable: the state parameter (Been & Jefferies, 1985), which takes account of both sand relative density and stress state. In order to determine the state parameter at the site, CPT data are transformed into state parameter profiles. Shuttle & Jefferies (1998) proposed a relationship between CPT tip resistance q_c and state parameter ψ, based on the NorSand constitutive model (Jefferies, 1993; Jefferies & Shuttle, 2005). This transformation requires calibration of the NorSand model parameters, which have here been calibrated against 55 triaxial tests performed on 16 samples taken from different locations across the test site. The calibration is summarised in Table 1.

Table 1: Results of the NorSand constitutive model calibration (van den Eijnden, 2010). The model parameters are used for transforming tip resistance q_c to state parameter ψ.

Parameter	Symbol	Value
Critical state friction ratio	M	1.28
Stress-dilatancy coupling parameter	N	0.36
Slope critical state line	λ	0.017
Critical state line at p`=1kPa	Γ	0.83
Hardening modulus	H	243
Shear rigidity	I_r	350
Poisson's ratio	ν	0.32

The NorSand parameters have been used to derive the state parameter profiles for 140 CPTs arranged in a regular grid, as illustrated for one of the profiles in Figure 2.

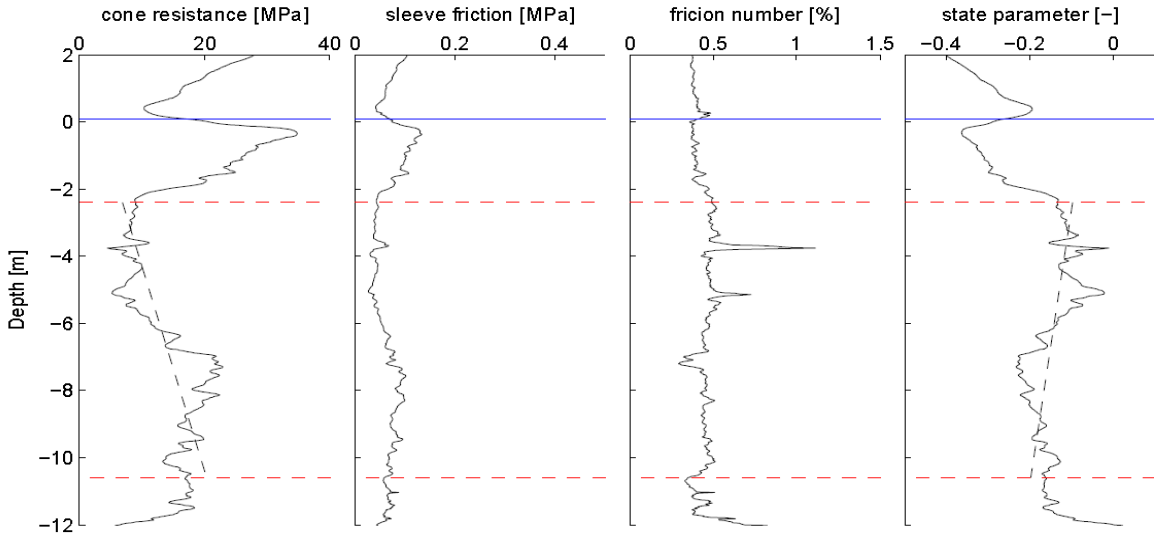

Figure 2: Typical CPT profile for (left to right): tip resistance q_c; sleeve friction fs; friction number; and state parameter ψ.

3 STATISTICAL INTERPRETATION

The CPTs are performed to determine the in-situ state of the soil. Following the transformation of tip resistance to state parameter, the spatial variability of sand state is characterised using a probability density function (pdf) and a correlation structure. In this investigation, four common pdf's have been fitted to the data: Normal (N), Lognormal (LN), Beta (β) and Gamma (Γ). Figure 3 shows that state parameter is best described by a Normal distribution, whereas tip resistance has a more skewed distribution and is best described by a Gamma distribution.

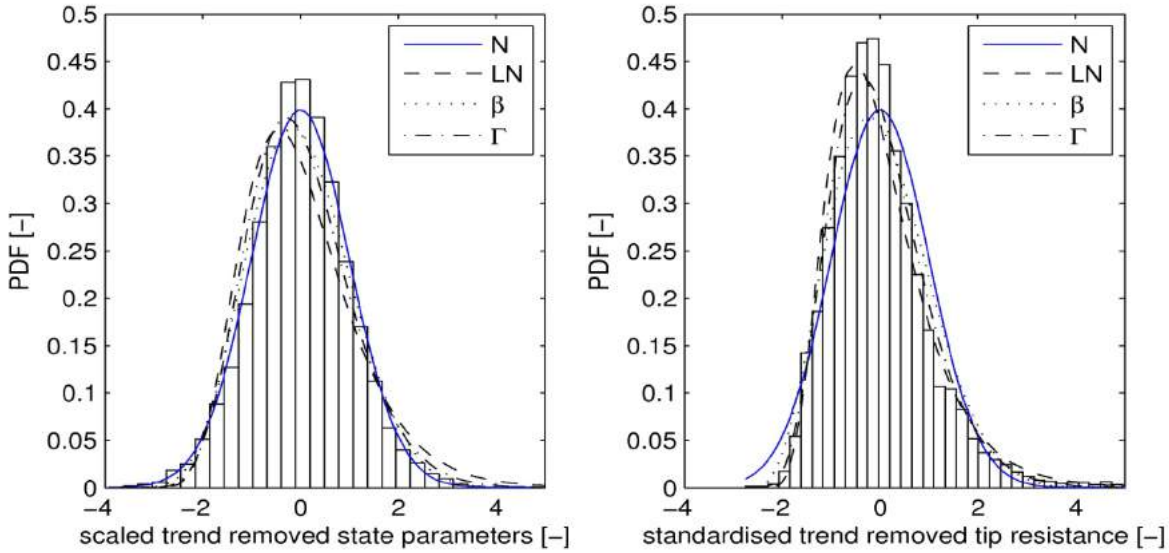

Figure 3: Statistical distributions of de-trended and normalised state parameter ψ (left) and tip resistance q_c (right).

The correlation structure describes the relationship between closely spaced points. The correlation function $\rho(\Delta \boldsymbol{x})$ and variogram $\gamma(\Delta \boldsymbol{x})$ are common functions that may be used for this purpose. A variable in the correlation structure is the scale of fluctuation θ, which describes the distance over which points are related. An estimation of the vertical scale of fluctuation (Wickremesinghe & Campanella, 1993; Vanmarcke, 1984) has been made for all CPTs (Figure 4), to characterise the spatial variability of the entire site.

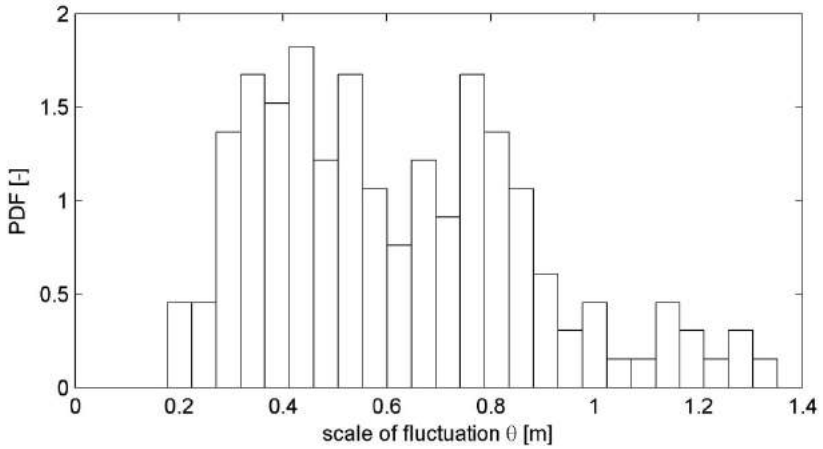

Figure 4: Distribution of vertical scales of fluctuation across the site, obtained from the state parameter profiles using the method by Wickremesinghe & Campanella (1993).

Table 2 shows the average statistics, obtained from the 140 CPTs, which are used as input for the conditional random field simulation of spatial variability (assuming an exponential correlation structure). The horizontal scale of fluctuation has not been determined, due to the lateral distance between the different CPT profiles being too large. Hence, the ratio of the horizontal to vertical scale of fluctuation, sometimes referred to as the degree of anisotropy of the heterogeneity ξ, was chosen to be between 5 and 25 (Hicks & Samy, 2002).

Table 2: Average statistics from the 140 CPT profiles.

Parameter	Symbol	ψ	q_c
Mean	μ	-0.14	14 MPa
Standard deviation from trend line	σ	0.0393	4 MPa
Variance from trend line	σ^2	0.0015	16 MPa^2
Vertical scale of fluctuation	θ_v	0.63 m	0.62 m

4 THEORY OF THE CONDITIONING ALGORITHM

The conditioning algorithm is based on kriging, an interpolation technique originally developed in mining engineering. The technique is a "Best Linear Unbiased Estimation" (BLUE) interpolator. The method gives the best estimation with respect to the variance in the expected error between the estimation and generic field. The kriged interpolation of a point, $Z^*(\boldsymbol{x}_0)$, based on the known (conditioning) points $Z(\boldsymbol{x}_\alpha)$, is given by Eq. (1) (Cressie, 1990).

$$Z^*(\mathbf{x_0}) = \sum_{\alpha=1}^{n} \lambda_\alpha Z(\mathbf{x}_\alpha), \qquad \text{with} \sum_{\alpha=1}^{n} \lambda_\alpha = 1 \tag{1}$$

In this equation, λ_α are the weights for the linear combination of the known points $Z(\boldsymbol{x}_\alpha)$ that minimise the variance in the estimation. Different types of kriging are available for

different estimation problems. In the estimation for the conditioning in this paper, Ordinary Kriging (OK) is used, which requires second order stationary data. The variance of the OK estimation is given by

$$\sigma_{OK}^2 = \begin{pmatrix} \lambda_1^{OK} \\ \vdots \\ \lambda_n^{OK} \\ \mu^{OK} \end{pmatrix}' \begin{pmatrix} \gamma(\mathbf{x_1} - \mathbf{x_0}) \\ \vdots \\ \gamma(\mathbf{x}_n - \mathbf{x_0}) \\ 1 \end{pmatrix}. \quad (2)$$

In this equation, $\gamma(\boldsymbol{x_\alpha}-\boldsymbol{x_0})$ is the variogram between location $\boldsymbol{x_0}$ and the known locations $\boldsymbol{x_\alpha}$, and μ^{OK} is the Lagrange parameter. The estimation variance is independent of the values of the known points $Z_0(\boldsymbol{x_\alpha})$. This property of kriging is used in the conditioning algorithm.

To generate random fields, the Local Average Subdivision (LAS) method (Fenton & Vanmarcke, 1990) is used. This is based on local averaging theory rather than point statistics, which makes it convenient for use with finite elements. An existing 2D LAS algorithm (Spencer, 2007) has been used to generate the random fields in this paper.

The conditioning of the random fields is a process that uses an unconditioned random field with the same characteristics as the conditioning data. This unconditioned random field is post-processed in order to condition it on the known conditioning points. The method is described by Journel & Huijbregts (1978).

To demonstrate the method of conditioning, a 1D example is given in Figure 5. In this example the correlation structure is assumed to be exponential, the scale of fluctuation θ is 1.0 m, the mean is zero and the variance σ^2 is 1. The following explanation of the conditioning method refers to this figure. Imagine an unknown stationary field Z_0 of which a limited number of points $Z_{0,\alpha}$ at $\boldsymbol{x}_\alpha$ are known. $Z_{0,\alpha}$ are the conditioning points for the field Z_0 that is to be simulated. The correlation structure of Z_0 is known (or estimated from $Z_{0,\alpha}$) and a random field is desired to give a possible realisation of this unknown field Z_0. The realisation needs to incorporate the points $Z_{0,\alpha}$. With reference to Figure 5, the process is as follows:

A. Find the best estimate of field Z_0, by kriging the field using the conditioning points (*). In this way the best estimate Z^*_0 (blue line) is generated.
B. Simulate a zero-mean random field Z_S (red) based on a correlation structure equal to that of the field Z_0. The values $Z_{S,\alpha}$ at points $\boldsymbol{x}_\alpha$ in field Z_S (•) are used to krige the simulated field to obtain Z^*_S (blue dashed). The variances of the kriged fields Z^*_0 and Z^*_S, ($\sigma^2_{0,OK}$ and $\sigma^2_{S,OK}$), are equal because they are both a function of $\boldsymbol{x}_\alpha$ and the correlation structure.
C. The expected difference between fields Z_0 and Z^*_0 is given by the kriging estimation error and is equal to $Z_S - Z^*_S$ (red).
D. Map the difference $Z_S - Z^*_S$ (C) on the best estimate of the field Z^*_0 (blue) to generate the conditioned random field $Z_{CS} = Z^*_0 + (Z_S - Z^*_S)$ (green). The produced field Z_{CS} is the conditioned simulation of field Z_0 and honours the mean and correlation structure.

The conditioning in 2D and 3D follows the same sequence; the only difference is that a 2D or 3D random field generator has to be used and that the kriging estimation is based on scales of fluctuation that can be different in the horizontal and vertical directions.

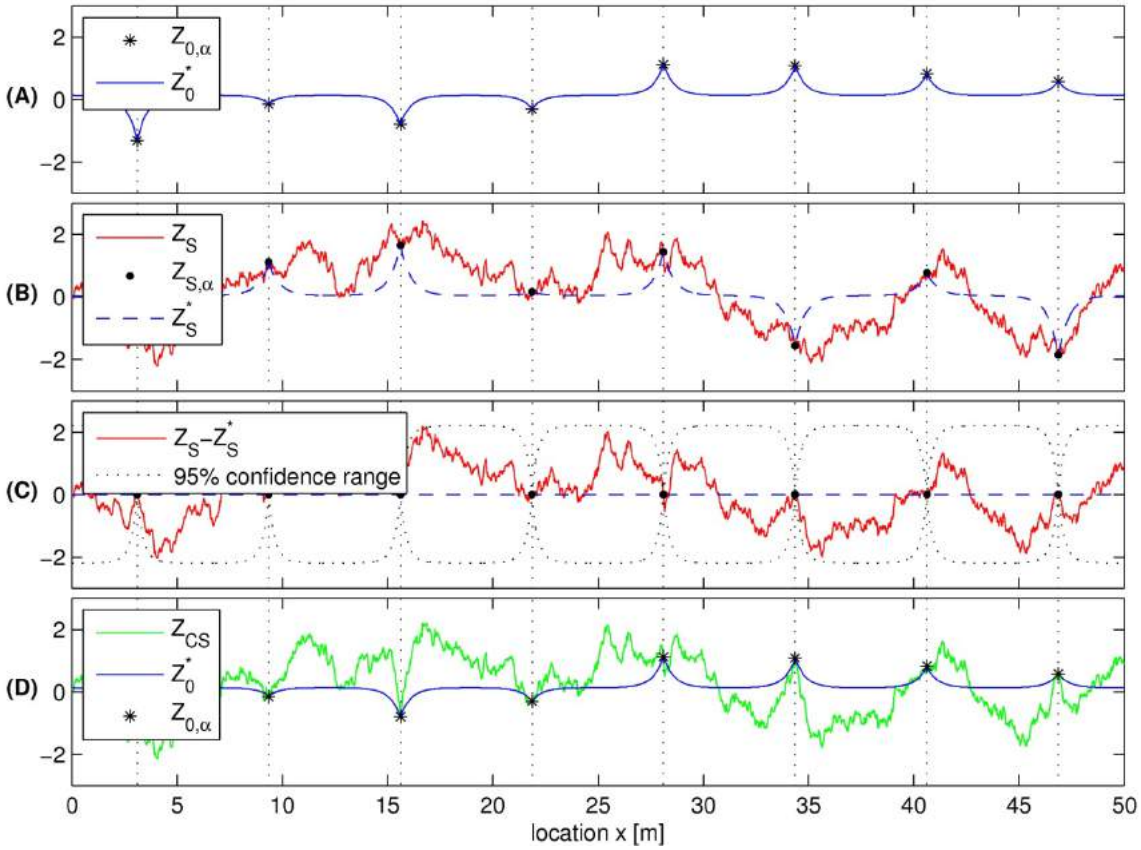

Figure 5: Example of 1D conditional random field simulation based on 8 known points.

5 APPLICATION OF CONDITIONAL SIMULATION FOR THE TEST SITE

Conditional simulation for a small part of the test site has been established. Figure 6 shows a 2D state parameter field that has been simulated and conditioned by four state parameter CPT profiles. The figure gives a possible realisation for a degree of anisotropy of $\xi = 20$.

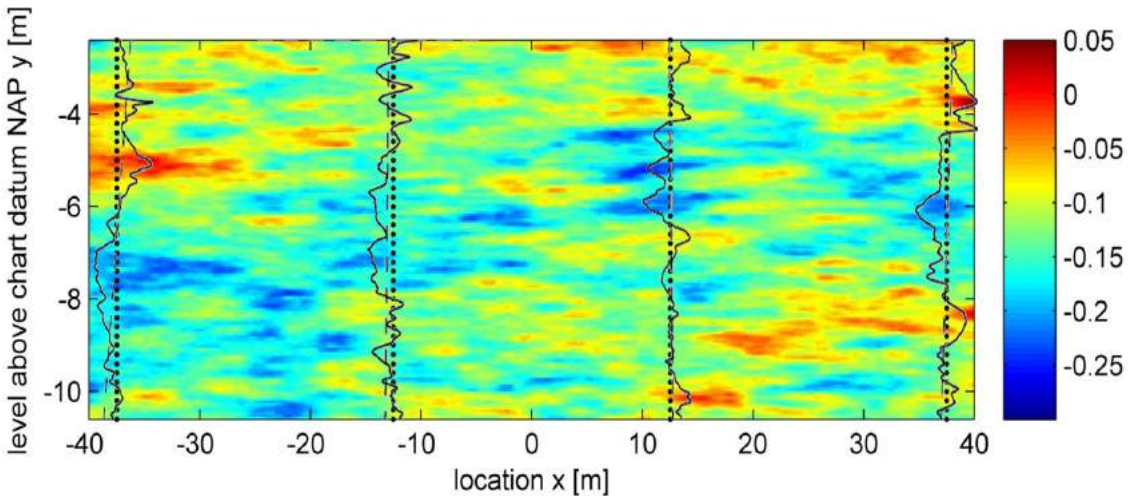

Figure 6: Conditional simulation of a small section of the test site, conditioned by 4 state parameter CPT profiles. The four state parameter profiles are included to indicate the conditioning points. LAS cell size = 0.05×0.05 m^2, $\theta_v = 0.63$m, $\xi = 20$.

6 CONSISTENCY OF STATISTICS OF THE SIMULATED FIELDS

To demonstrate that conditional simulation produces fields with the correct correlation structure, the covariance functions *C(h)* in the vertical and horizontal directions have been back figured from 100 different realisations of the example illustrated in Figure 6. The covariance functions of the simulation input and output are shown in Figure 7. Because the covariance functions of the conditioning profiles (blue) are not exactly the same as the theoretical exponential covariance function (red), the back figured covariance function (black) lies between the covariance function of the conditioning points and the theoretical covariance function. This demonstrates that conditional simulation produces fields with the correct correlation structure.

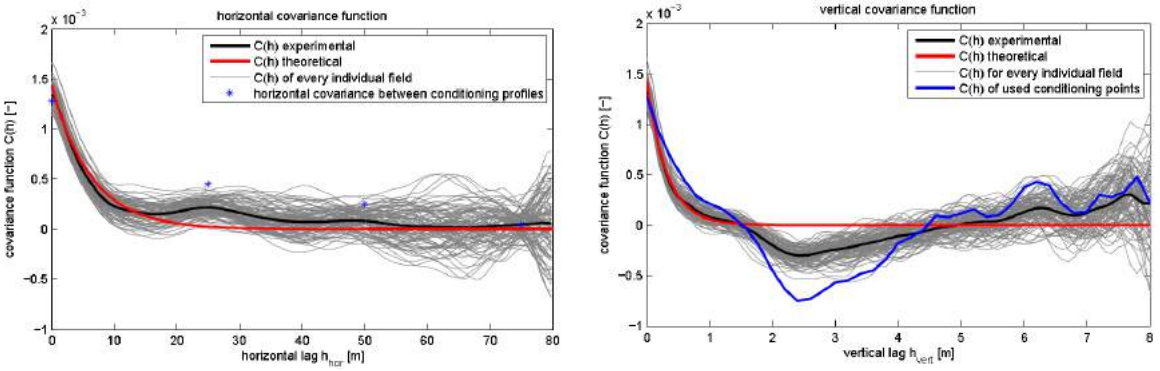

Figure 7: Results of back figuring the covariance function from 100 simulated fields. The average covariance function of the simulated fields lies between the theoretical covariance function and the covariance function of the conditioning points.

The statistical distribution of cell values from the conditioned random fields is found to be normal, as is guaranteed by the LAS method and the kriging estimation. The statistical characteristics of the input and output of the trend-removed (to obtain stationarity) simulations are given in Table 3. As seen by the correlation structure, the back figured variance is between the theoretical variance and the variance of the four conditioning profiles. The mean of all simulated fields is very close to the mean of the conditioning points.

Table 3: Mean statistical characteristics of the trend-removed conditional simulations.

Parameter	Theoretical (input LAS)	Conditioning points	Experimental (back figured)
σ	0.039	0.0359	0.0367
σ^2	0.0015	0.00129	0.00135
μ	0	$5.99\ 10^{-4}$	$6.24\ 10^{-4}$

Due to the consistency in both the distribution function and correlation structure, the method of conditional simulation used in this paper is demonstrated to produce conditioned random fields with correct characteristics.

7 REDUCTION OF UNCERTAINTY

Van den Eijnden (2010) found that the uncertainty in the simulated fields is mainly dependent on the horizontal scale of fluctuation and the lateral spacing between CPTs. The first parameter is determined by the heterogeneity of the soil itself and therefore cannot be improved. The second parameter is a direct result of the site investigation plan. Therefore the site investigation plan will play an important role in the effectiveness of the conditioning.

To quantify the effect of the conditioning on the reduction of uncertainty, the conditional simulations need to be applied in structure response analyses and the results of these analyses need to be compared with the results of unconditioned analyses. As this stage of the Authors' research has yet to be carried out, the effectiveness of the conditioning may be quantified by the relative reduction of the standard deviation of the kriging estimator σ_{OK} (Eq. (2)). The average of the kriging estimator standard deviation over the domain D, as given by Eq. (3), may be used as the uncertainty parameter u. The uncertainty parameter u represents the area of the uncertainty range, as illustrated for a 1D domain in Figure 1.

$$u = \frac{1}{\sigma D} \int_D \sigma_{OK} \partial D \tag{3}$$

When an unconditioned random field is considered to have an uncertainty $u = 1$, the reduction of uncertainty can be determined by evaluating the uncertainty u of the conditioned random fields. By analysing 2D simulations of the test site, as shown in Figure 6, it has been found that the reduction of uncertainty u for the test site can range from 5% to 45% for an anisotropy ξ ranging from 5 to 50 (van den Eijnden, 2010).

8 CONCLUSIONS

A conditional simulation method is demonstrated to be applicable for the characterisation of sand state heterogeneity based on cone penetration tests. By calibration of the NorSand constitutive model against triaxial test data for the sand, the CPT profiles have been transformed into state parameter profiles serving as conditioning data for the simulation. It has been shown that these conditioned fields successfully reproduce the initial (geo-) statistical characteristics. The reduction of the uncertainty is found to be dependent on the horizontal scale of fluctuation and the lateral distance between the CPT profiles. The reduction of uncertainty in the heterogeneity will eventually lead to a reduction of the uncertainty in design.

ACKNOWLEDGEMENT

This work is supported by the European Union FP7 Project "IRIS: Integrated European Industrial Risk Reduction System", Project Number 213968.

REFERENCES

Been, K. & Jefferies, M.G. (1985), "A state parameter for sand". Géotechnique, Vol. 35(2), 99–112.

Cressie, N. (1990), "The origins of kriging". Mathematical Geology, Vol. 22(3), 239–252.

Eijnden, A.P. van den (2010), "Conditional simulation for characterising the spatial variability of sand state". MSc thesis, Delft University of Technology, The Netherlands.

Fenton, G.A. & Vanmarcke, E.H. (1990), "Simulation of random fields via local average subdivision". Journal of Engineering Mechanics, Vol. 116(8), 1733–1749.

Hicks, M.A. & Onisiphorou, C. (2005), "Stochastic evaluation of static liquefaction in a predominantly dilative sand fill". Géotechnique, Vol. 55(2):123–133, 2005.

Hicks, M.A. & Samy, K. (2002), "Influence of anisotropic spatial variability on slope reliability". Proc. 8th Int. Symp. Num. Models Geomech., Rome, 535–539.

Hicks, M.A. & Spencer, W.A. (2010), "Influence of heterogeneity on the reliability and failure of a long 3D slope". Computers and Geotechnics, Vol. 37(7-8):948–955, 2010.

Jefferies, M.G. (1993), “Nor-sand: A simple critical state model for sand”. Géotechnique, Vol. 43(1), 91–103.
Jefferies, M.G. & Shuttle, D.A. (2005), “NorSand: Features, calibration and use”. Proc. Speciality Conf. Soil Constitutive Models: Evaluation, Selection and Calibration, ASCE Geotechnical Special Publication No. 128: 204–236.
Journel, A.G. & Huijbregts, Ch.J. (1978), “Mining Geostatistics”. Academic Press.
Shuttle, D.A. & Jefferies, M.G. (1998), “Dimensionless and unbiased CPT interpretation in sand”. Int. J. Num. Anal. Meth. Geomech. Vol. 22: 351–391.
Spencer, W.A. (2007), “Parallel stochastic and finite element modelling of clay slope stability in 3D”. PhD thesis, University of Manchester, UK.
Vanmarcke, E.H. (1984), “Random Fields: Analysis and Synthesis”. The MIT Press.
Wickremesinghe, D. & Campanella, R.G. (1993), “Scale of fluctuation as a descriptor of soil variability”. Proc. Conf. Probabilistic Methods in Geotechnical Engineering, Canberra, 233–239.

DEM MODELLING OF THE SHEAR BEHAVIOUR OF ROCK JOINTS

C. Lambert
Department of Civil & Natural Resources Engineering, University of Canterbury, Christchurch, New Zealand

C. Coll
Golder Associates Ltd, Christchurch, New Zealand

ABSTRACT: *The constitutive behaviour of rock discontinuities is highly controlled by the roughness of the surface. Its contribution is a combination of two aspects of overall roughness: the morphology of the surface (or shape) and the strength of the asperities (related to the strength of the surrounding rock). Appropriate description of rock joint behaviour entails accurate description of the morphology and provision for asperity degradation. In this study, we propose to take advantage of the latest developments in numerical techniques. The DEM code PFC3D has been used to generate a numerical replica of a joint. Microproperties have been calibrated to mimic the physical rock. The morphology has been obtained using 3D photogrammetry. The derived triangulated surface is then introduced into PFC3D to generate a synthetic rock joint. The recently developed Smooth Joint contact model is used to describe the interaction between particles lying on opposite side of the surface. The smooth joint model allows to get rid of the artificial roughness introduced by particle discretization. The generated discrete model replicates the two aspects of overall roughness: shape and strength. Direct shear tests are then performed to characterise its mechanical behaviour. Results of the simulations are presented.*

1 INTRODUCTION

The shear behaviour of discontinuities is primarily controlled by the surface roughness (Barton, 1973) which is commonly defined through an empirical parameter, the Joint Roughness Parameter or JRC. Initially estimated by visual comparison with standard roughness profiles, correlations between JRC and various statistical parameters or fractal dimension have been established (Tse & Cruden, 1979; Carr & Warriner, 1989). JRC based estimates offer simplicity of used however they are two dimensional methods and non directional. More recently the use of laser scanner and photogrammetry to define the surface topography and estimate the roughness have been described (Hans & Boulon, 2003; Haneberg, 2007). New constitutive relations have been developed based on a general description of roughness (Grasselli & Egger, 2003). Asperity shape and distribution on a discontinuity can now be measured with a great detail and potentially incorporated in any analysis. However with the complexity of the interaction between the two walls, a complete analytical formulation remains a hard task. Various constitutive models have been developed that accommodate effect of asperities (Saeb & Amadei, 1992) and their progressive degradation during shearing (Plesha, 1987; Hutson & Dowding, 1990). Despite being each time more advanced, these models still rely on empirical relations or simplified descriptions of the surface asperities. The recent development of a new contact model named “Smooth

Joint Model" (SJM) (Pierce *et al.*, 2007) in PFC3D where particles are allowed to slide past one another without overriding one another has been a major breakthrough to represent discontinuities as planar surfaces. With this new formulation, real surface morphologies can be introduced into DEM codes to generate numerical rock joint. Studies by Lambert *et al.* (2010) on the behaviour of a rock-concrete interface suggested that realistic shear behaviour, shear strength and dilation, could be obtained associating the SJM with a true morphology. Such synthetic rock joint is able to replicate the behaviour of its physical counterpart and can be used to estimate its constitutive behaviour accounting for the three dimensionality of the surface (Lambert & Coll, 2011). The behaviour of rough fractures can be explicitly simulated on the basis of measurable properties: 3D surface morphology and mechanical properties of the surrounding rock.

2 DISCRETE ELEMENT REPRESENTATION OF A ROCK JOINT

2.1 Smooth joint contact

A discontinuity is normally represented in PFC3D by debonding contacts along a surface. Previous modelling approaches used bands of particles with altered properties (Kulatilake *et al.*, 2001; Park & Song, 2010) to represent a joint. However, the particle geometry is still present and the discrete nature of the medium generates an artificial roughness that is added to the one of the introduced surface, thus creating a particle size dependent joint behaviour (see Fig. 1).

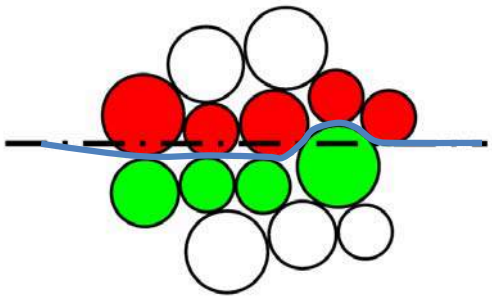

Fig. 1. 2D example of a particle size dependant surface morphology of joints (modified after Scholtes *et al.*, 2010)

In order to overcome the problem an alternate scheme, termed the "Smooth-Joint Model" or SJM, initially proposed by Pierce *et al.* (2007), has been implemented into PFC3D (Itasca, 2008). A smooth-joint model is a contact model that simulates the behaviour of an interface regardless of the local particle contact orientation along the interface. A typical smooth-joint is shown in Fig. 2. It allows particles to slide past one another without overriding one another. A joint is created by assigning this new contact model to all the contacts between particles that lie upon opposite sides of the surface. The SJM defines the tangential and normal directions according to the local orientation of the surface (by opposition to the initial normal and tangential directions of the contact, see Fig. 2). The joint normal and joint tangential force increments (ΔF_{nj} and ΔF_{tj} respectively) are derived from normal and tangential displacement increments (ΔU_{nj} and ΔU_{tj}) multiplying by the joint stiffness ($\Delta F_{nj} = k_{jn}\Delta U_{nj}$ and $\Delta F_{tj} = k_{jt}\Delta U_{tj}$). The joint force is then adjusted to satisfy the force-displacement relationship and mapped back into the global system. This new formulation accommodates the standard behaviour of a joint (sliding/opening behaviour) independently of particle

induced roughness. A complete description of the formulation can be found in the manual (Itasca, 2008).

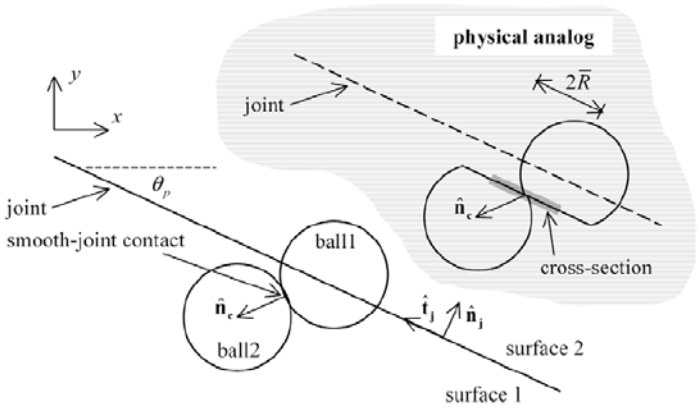

Fig. 2. Smooth Joint contact model between ball 1 and ball 2. Surface 1 and surface 2 denote either side of the joint lying at a dip angle of θ_p (after Itasca, 2008)

The model requires the definition of a set of parameters: friction coefficient, dilation angle, normal and shear bonds (responsible for cohesion), normal and shear stiffness. This new formulation has proven its ability to capture the behaviour of jointed rock mass representing joints as planar surfaces (Pierce *et al.*, 2007; Deisman *et al.* 2010; Esmaieli *et al.*, 2010; Lambert & Read, 2011) and the behaviour of rough discontinuities (Lambert *et al.*, 2010, Lambert & Coll, 2011).

2.2 3D morphology of the rock joint

The interface morphology used in this example is based on a natural discontinuity in granite studied by Grasselli (2001). The surface is 140× 140 mm^2 and the maximum amplitude of the asperities is around 9 mm. Fig. 3 shows a general view of the surface. The three dimensional surface has been triangulated using a Kriging gridding method with a horizontal spacing of 1.4 mm between the grid points (in x and y directions). 99 profiles along the x axis and y axis have been extracted for which Z_2 coefficients (root mean square of the first derivative of the profile) have been estimated:

$$Z_2 = \sqrt{\frac{1}{(N-1)\Delta x^2}\sum_{i=1}^{N-1}(z_{i+1}-z_i)^2} \qquad (1)$$

where z_i and z_{i+i} are the elevations of two consecutive grid points on a profile, N the total number of grid points on a profile and Δx the horizontal spacing.

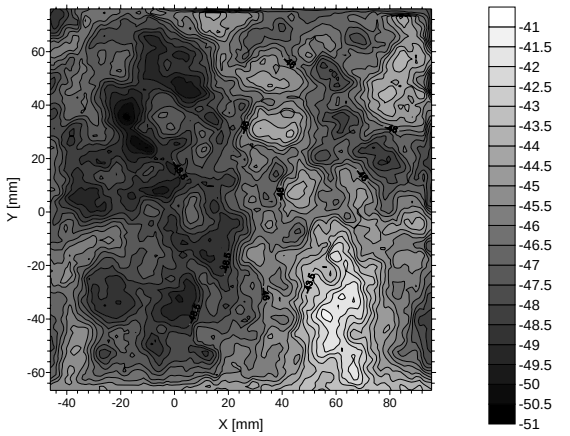

Fig. 3. Morphology of the granite surface (modified from Grasselli (2001))

For each profile a value of the Joint Roughness Coefficient (JRC) can be derived using the empirical relation proposed by Yang *et al.* (2001).

$$\mathrm{JRC} = 32.69 + 32.98 \times \log_{10}(Z_2) \tag{2}$$

The profiles of the triangulated surface exhibited in along x axis an average JRC_{prof} of 10.4, varying from 4.9 to 13.9 and along y axis an average of 10.1, varying from 5.7 to 15.3. The cumulative distribution of the JRC_{prof} is given in Fig. 4

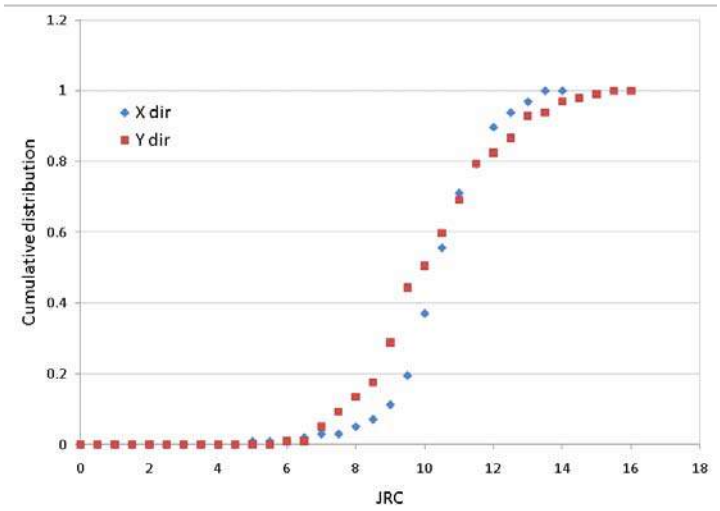

Fig. 4. Cumulative distribution of JRC values along x direction and y direction.

2.3 The synthetic rock joint

A synthetic (or numerical) rock joint is obtained first generating a particle assembly using a discrete element code and then introducing the surface morphology. Micro-properties of the particle assembly are calibrated to match the properties of the physical material (surrounding rock) following the genesis procedure described in detail in Potyondy & Cundall (2004). In

that case a granitic rock with a UCS of 143MPa has been simulated. The numerical rock joint consists of a 140 x 140 x 50mm3 (respectively X, Y, Z) parallelepiped particle assembly. The final specimen contains 98,345 particles having a radius ranging from 0.5mm (in the vicinity of the interface) to 2.4mm. The triangulated surface of the joint presented in the previous section is then imported. For each triangle a "smooth joint model" is assigned to the contacts between particles that lie on opposite side of a triangle. The orientation of the smooth joint corresponds to the orientation of the triangle. The joint surface is hence modelled as a collection of smooth-joint contacts with varying orientation. The macroscopic joint is considered to be purely frictional at the contact level (smooth joint) with a friction angle of 20°. No dilation was introduced as macroscopic dilation (i.e. at the joint level) is expected to be an emergent property of the surface topology.

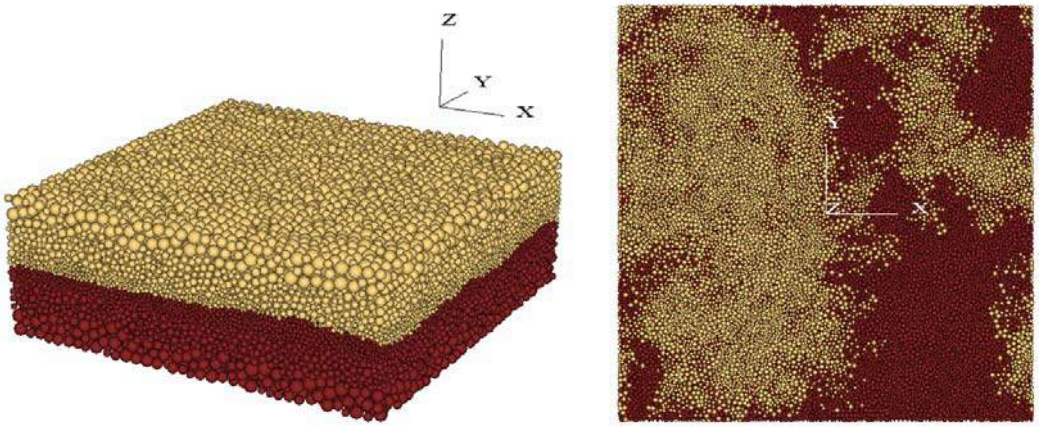

Fig. 5. Visualization of the synthetic rock joint sample. Upper wall in orange and lower wall in brown. Full 3D view on the left and lower half section on the right

3 SHEAR BEHAVIOUR OF THE SYNTHETIC ROCK JOINT

3.1 Simulations of direct shear tests

Numerical shears tests under constant normal stress have been performed on the synthetic rock joint for three values of normal confinement (0.5MPa, 1MPa, 1.5MPa). The specimen is firstly subjected to a compression along axis Z (Fig. 5) and then to a shearing along axis X at constant normal stress. Displacements along Y are restrained. The sum of contact forces on the periphery of the upper half are used to compute the average normal stress and shear stress on the interface whereas normal and tangential displacements are monitored averaging particle displacements on the periphery of the lower half (Z displacements and X displacements respectively).

Fig. 6(a) and (b) show the evolution of shear stress and normal displacement with shear displacement. It can be seen that the classical elasto-plastic response of rock joints is well captured. The mobilised shear stress increases to a peak value as roughness is mobilised and then decreases due to asperity degradation. The peak value defines the shear strength of the synthetic rock joint (the higher the normal stress, the higher the shear strength). Peak dilation angles have been measured as the slope of the normal displacement vs. shear displacement curve at the peak of the shear stress (Fig. 6). As shown in Fig. 6, dilation decreases as normal stress increases.

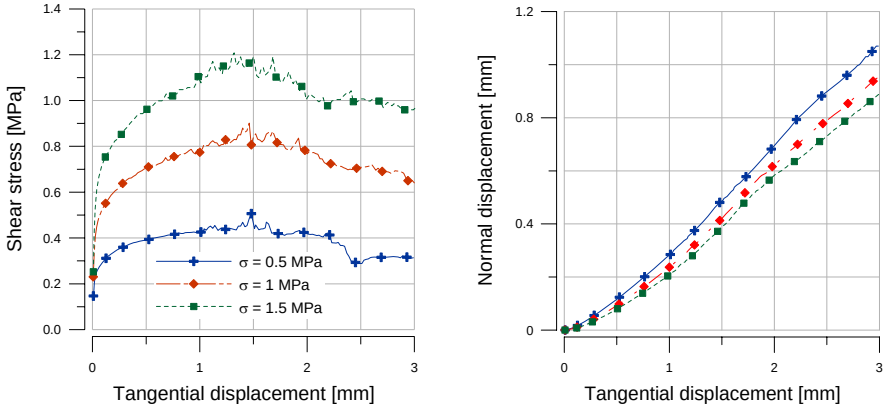

Fig. 6. Stress-displacement curves of direct shear tests under constant normal stress (ranging from 0.5 MPa to 1.5 MPa) on a 140 x 140 mm2 surface. a) Shear stress versus tangential displacement. b) Normal displacement versus tangential displacement.

The numerical shear tests performed under increasing normal stress define the strength envelope of the model from which a Barton failure criterion (Barton & Choubey, 1977) can be expressed. In Barton's formulation the shear strength is expressed as a function of the Joint Roughness Coefficient (JRC), Joint Compressive strength (JCS) and friction ϕ_b (3):

$$\tau_p = \sigma_n \cdot \tan\left(JRC \cdot \log_{10}\left(\frac{JCS}{\sigma_n} \right) + \phi_b \right) \tag{3}$$

Where τ_p is the peak shear stress and σ_n the normal stress.

A best fit of Barton's failure criterion can be seen on Fig. 7. The base friction angle ϕ_b in equation (1) corresponds to the friction angle of a perfectly planar discontinuity and corresponds to the friction angle of the in the smooth joint model (20°). *JCS* has been set to 143 MPa. The best fit returns a JRC_{back} of 9.9 with a coefficient of determination R^2 close to 1. Obtained JRC_{back} is in good agreement with the average JRC_{prof} determined on 2D profiles of the surface suggesting that the effect of roughness is well captured.

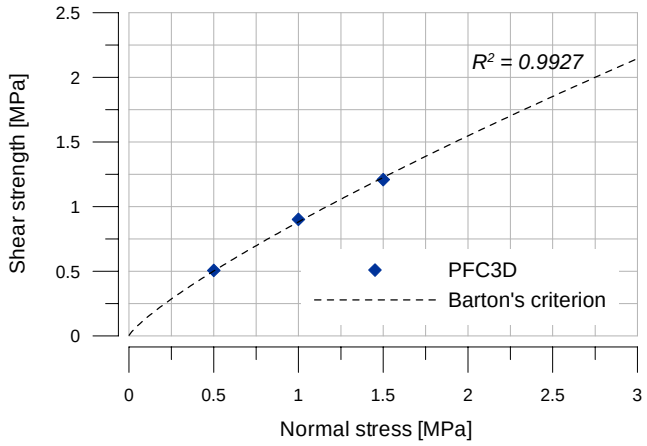

Fig. 7. Failure criterion for the synthetic rock joint with a best fitted Barton criterion (*JRC = 9.9)*

3.2 Shear strength anisotropy

Anisotropy in the shear behaviour induced by surface roughness is assessed by shearing the synthetic rock joint varying the direction of loading. Two series of direct shear tests have been performed along the x axis, towards x>0 and x<0. A series of shear tests have been performed along the y direction towards y>0. The three directions tested will be referred to as 0°, 90° and 180° for x>0, y>0 and x<0 respectively. The shear strength for the various tests are plotted in Fig. 8.

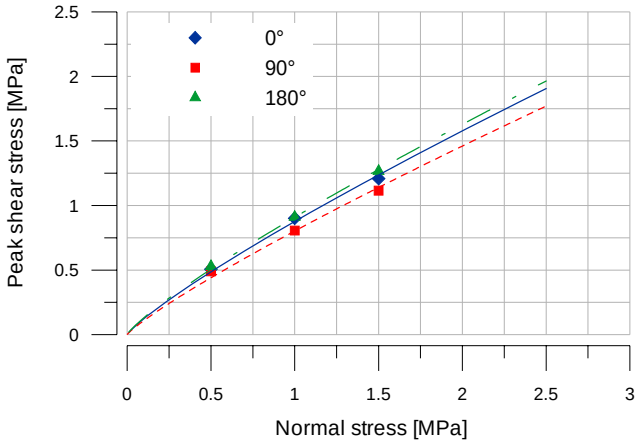

Fig. 8. Anisotropy in the peak shear strength of the synthetic rock joint

The joint strength exhibits little various between the three shearing directions. The strength is slightly lower for 90° which is consistent with a slightly lower average JRC. The relatively small difference in the strength is also apparent in the average JRC.

4 CONCLUSION

A DEM approach was developed to generate a synthetic rock joint combining a real surface morphology with a smooth joint contact model at the particle level. Unlike previous discrete approaches, such numerical model is able to mimic the mechanical behaviour of a discontinuity qualitatively and quantitatively. Direct shear tests under constant normal stress have been performed and the mechanical response of the model has been analysed. The effect of roughness was consistently captured throughout the simulations. Strength estimates can be performed with this approach accounting for the 3D aspect of surface roughness and properties such as anisotropy can be captured.

ACKNOWLEDGMENT

The authors would like to thank Dr. Giovanni Grasselli for providing the natural morphology of a discontinuity in granite.

REFERENCES

Barton, N. (1973), “Review of a new shear-strength criterion for rock joints”, Eng. Geol., Vol. 7(4), 287–332.

Barton, N. & Choubey, V.(1977), “The shear strength of rock joints in theory and practice”, Rock Mechanics, Vol. 10, 1-54.

Carr, J.R. & Warriner, J.B. (1989), "Relationship between the fractal dimension and joint roughness coefficient", Bull. Association of Engineering Geologists, XXVI(2), 253-263.
Deisman, N., Mas Ivars, D., Darcel, C., & Chalaturnyk, J. (2010), "Empirical and numerical approaches for geomechanical characterization of coal seam reservoirs", International Journal of Coal Geology, Vol. 82, 2204-212.
Esmaieli, K., Hadjigeorgiou, J. & Grenon, M. (2010), "Estimating geometrical and mechanical REV based on synthetic rock mass models at Brunswick Mine", Int. J. Rock Mech. Min. Sci., Vol. 47, 915–920.
Grasselli, G. (2001), "Shear strength of rock joints based on quantified surface description", Ph.D. thesis, Ecole Polytechnique Fédérale de Lausanne, Switzerland.
Grasselli, G. & Egger, P. (2003), "Constitutive law for the shear strength of rock joints based on three-dimensional surface parameters", Int. J. Rock Mech. Min. Sci., Vol. 40, 25–40.
Haneberg, W.C. (2007), "Directional roughness profiles from three-dimensional photogrammetric or laser scanner point clouds", In Rock Mechanics: Meeting Society's Challenges and Demands, 1st Canada–US Rock Mechanics Symposium, Vancouver, 101-106.
Hans, J. & Boulon, M. (2003), "A new device for investigating the hydromecanical properties of rock joints", Int. J. Rock Mech. Min. Sci., Vol. 27, 513-548.
Hutson, R. & Dowding, C. (1990), "Joint asperity degradation during cyclic shear", Int. J. Rock Mech. Min. Sci. Geomech. Abstr., Vol. 27, 109–119.
Itasca Consulting Group (2008), "Particle Flow Code in 3 Dimensions, version 4.0".
Kulatilake, P., Malama, B. & Wang, J. (2001), "Physical and particle flow modeling of jointed rock block behavior under uniaxial loading", Int. J. Rock Mech. Min. Sci., Vol. 38, 641–657, 2001.
Lambert, C., Buzzi, O. & Giacomini, A. (2010), "Influence of calcium leaching on the mechanical behavior of a rock mortar interface: a dem analysis", Computers and Geotechnics, Vol. 37, 258-266.
Lambert, C. & Coll, C. (2011), "A synthetic rock joint for joint strength estimates", Int. J. Rock Mech. Min. Sci., submitted.
Lambert, C. & Read, J. (2011), "Sensitivities in Sensitivities in rock mass properties: A DEM insight", European Journal of Environmental and Civil Engineering, 2011.
Park, J.-W. & Song, J.-J. (2010), "Numerical simulation of a direct shear test on a rock joint using a bonded-particle model", Int. J. Rock Mech. Min. Sci., Vol. 46, 1315-1328, 2010.
Pierce, M., Cundall, P., Potyondy, D. & Mas Ivars, D. (2007), "A Synthetic Rock Mass Model for Jointed Rock", In Rock Mechanics: Meeting Society's Challenges and Demands, 1st Canada–US Rock Mechanics Symposium, Vancouver, 341–349.
Plesha, M. (1987), "Constitutive models for rock discontinuities with dilatancy and surface degradation", International journal for numerical and analytical methods in geomechanics, Vol. 11, 345–362.
Potyondy, D.O. & Cundall, P.A. (2004), "A bonded-particle model for rock", Int. J. Rock Mech. Min. Sci., Vol. 41, 1329-1364.
Saeb, S. & Amadei, B. (1992), "Modelling rock joints under shear and normal loading", Int. J. Rock Mech. Min. Sci., Vol. 29, 267–278.
Scholtes, L., Donze, F.V. & Read, J. (2010), "3D DEM modelling of jointed rock slopes", in Rock Slope Stability Symposium RSS 2010, 2010.
Tse, R. & Cruden, C.M. (1979), "Estimating joint roughness coefficients", Int. J. Rock Mech. Min. Sci., Vol. 32, 303-307.
Yang, Z.Y., Di, C.C. & Yen, K.C. (2001), "The effect of asperity order on the roughness of rock joints", Int. J. Rock Mech. Min. Sci.,, Vol. 38, 745-752.

ANALYSIS OF SOIL-STRUCTURE INTERACTION PROBLEMS INVOLVING A LARGE NUMBER OF LOADING CYCLES

J.P. Cao
Laboratory of Civil Engineering and Geo-environment LGCgE, University of Lille 1 Science and Technology, Villeneuve d'Ascq, FRANCE
H. Mroueh
Laboratory of Civil Engineering and Geo-environment LGCgE, University of Lille 1 Science and Technology, Villeneuve d'Ascq, FRANCE
S. Burlon
Regional Laboratory of Bridges and Roads of Lille, Haubourdin, FRANCE

ABSTRACT:
This paper deals with the analysis of soil-structure interaction problems involving a large number of repeated loadings. In the first part, a constitutive model for soil-structure interface subjected to cyclic load is developed. The second part of the paper focuses on the development of a "Skipped Cycles" method to reduce computational time and to estimate efficiently the structure response after a large number of loading cycles. The performance of the "skipped cycles" method is studied through two heuristic examples and compared with results of classical 'step by step' methods. It shows that substantial economy is achieved in terms of number of iterations with the "Skipped Cycles" method.

1. INTRODUCTION

The study of cyclic loading is an essential component of the design of some geotechnical structures such as offshore platforms or viaducts. The current rules of calculation or recommendations (API and Eurocode 7) do not offer efficient methods to estimate the effect of cyclic loading, especially under high number of cycles ($>10^4$ cycles). The present work proposes a method of "Skipped Cycles" to consider the piles under a large number of repeated axially loading. This work requires firstly the development of a constitutive law for soil-structure interfaces able to reproduce the main experimental phenomena, e.g. evolution of stress and strain: relaxation, hardening, softening, adaptation and ratcheting (Lemaitre & Chaboche, 1985; Song et al, 2004). The second part of the work involves the development of a procedure to reduce the computation time with large number of loading cycles. The performance of the constitutive law and the numerical procedure of «skipped cycles» are studied through two heuristic examples: the first concerns a single interface element under large number of loading cycles and the second deals with the response of a single pile under axial loading cycles.

2. CONSTITUTIVE MODEL FOR CYCLIC LOADING

2.1 Presentation of the constitutive relation for an interface

The constitutive law presented in this paper was initially proposed by Shahrour & Rezaie (1997). This law (MDJ) is based on the principles of elastoplasticity. According to the theory of plasticity, the increment of relative displacement between soil and structure (du) is decomposed into elastic (du^e) and plastic (du^p) parts. The elastic behaviour is governed by the following two relationships:

$$d\sigma_n = K du_n^e \tag{1}$$

$$d\tau = G du_t^e \tag{2}$$

Where $d\sigma_n$ and $d\tau$ are the increments of normal and tangential stress, du_n^e and du_t^e are the increments of normal and tangential elastic displacement. K and G designate the normal and tangential elastic modulus which can possibly depend on normal stress σ_n and on the ratio of τ/τ_{max} (nonlinear elasticity).

The concept of the bounding surface is used for the description of the plastic behaviour of the interface under cyclic loading. For the reason of simplicity, the proposed model involves only two types of surfaces. The first, called the limit surface f_m which describes failure states of interface. The second one, called the cyclic yield surface f_c incorporates a mechanism of nonlinear kinematic hardening which depends on the loading history. The two surfaces are able to describe the cyclic behaviour, viz. hardening, softening, shakedown and ratcheting. These phenomena exist not only in a loading cycle but also for different cycles.

The limit surface f_m is assumed to be governed by a Mohr-Coulomb criterion. Its expression is given by:

$$f_m = |\tau| + \sigma_n R_{\max} \tag{3}$$

$$\text{where } R_{\max} = \tan(\varphi) + DR\left(1 - e^{-ADR\gamma_t^p}\right) \tag{4}$$

Equations (3) and (4) may be expressed by another way by:

$$dR_{\max} = -DR\ ADR\ e^{ADR\gamma_t^p} \left|du_t^p\right| \tag{5}$$

$$\text{with } R_{\max}(0) = \tan(\varphi) \tag{6}$$

$$\text{and } \gamma_t^p = \int \left|du_t^p\right| \tag{7}$$

where : φ is friction angle in the first loading cycle, γ_t^p presents the cumulative irreversible shear displacement. DR is a parameter equal to the ratio of shear stress between a given cycle

and the first cycle and *ADR* is a parameter of adjustment that controls the rate of evolution of the cyclic hardening.

The cyclic yield surface is defined by following relations:

$$f_c = \left|\tau - \sigma_n R_c\right| + \sigma_n R_0 \tag{8}$$

$$dR_c = \lambda H_c \tag{9}$$

$$H_c = \gamma_c \left|R_{\max} - R_c\right|^{\beta_c} \tag{10}$$

$$dR_c = \gamma_c (R_{\max} du_t^{\,p} - R_c \left|du_t^{\,p}\right|) \tag{11}$$

where : R_c is a cyclic hardening function and R_0 is additional elastic parameter at each loading reversal. H_c is a function which controls the rate of kinematic hardening. It depends on the angle between the active line of the cyclic yield surface and that of the limit surface located in the direction of the stress path. γ_c and β_c are two parameters which control the evolution of kinematic yield surface.
The main equations are summarized in the table 1. The second formulation given dR_{max} is easier to implement under a calculation code and thus will be used in the present work.

Table 1. Formulation of the constitutive law (MDJ)

Formulation using the hardening modulus	**Formulation using the evolution of the limit surface and the yield surface**
Limit surface : $f_m = \left\|\tau\right\| + \sigma_n R_{\max}$ $R_{\max} = \tan(\varphi) + DR\left(1 - e^{-ADR\gamma_t^p}\right)$	Limit surface : $f_m = \left\|\tau\right\| + \sigma_n R_{\max}$ $dR_{\max} = -DR\ ADR\, e^{ADR\gamma_t^p} \left|du_t^p\right|$ and $R_{\max}(0) = \tan(\varphi)$
Kinematic yield surface: $f_c = \left\|\tau - \sigma_n R_c\right\| + \sigma_n R_0$ $dR_c = \lambda H_c$ and $H_c = \gamma_c \left\|R_{\max} - R_c\right\|^{\beta_c}$	Kinematic yield surface : $f_c = \left\|\tau - \sigma_n R_c\right\|$ $dR_c = \gamma_c \left(R_{\max} du_t^p - R_c \left|du_t^p\right|\right)$

Cyclic tests under simple direct shear load showed that the evolution of the normal displacement presents a contraction phase followed by a dilatation one at each stress-reversal (Shahrour & Rezaie, 1997; Mortara et al, 2007). In order to describe this behaviour, a non-associated flow rule is adopted, using the following expression for the gradient of the plastic potential:

- For the initial phase of loading : $$\frac{\partial g}{\partial \sigma_n} = \left(M_g - \frac{|\tau|}{\sigma_n}\right) e^{-a_c u_{tc}^p} \tag{12}$$
- For other phases of loading : $$\frac{\partial g}{\partial \sigma_n} = \left(M_g - \frac{\left|\tau - \sigma_n R_c\right|}{\sigma_n}\right) e^{-a_c u_{tc}^p} \tag{13}$$

- And in all cases : $$\frac{\partial g}{\partial \tau} = \frac{\tau}{|\tau|} \qquad (14)$$

where M_g is expressed as a function of the dilatancy angle ψ_c: $M_g = \tan(\psi_c)$; u_{tc}^p denotes the accumulation of plastic relative shear displacement induced since the loading reversal; and a_c is a fitting parameter.

2.2 Numerical tests under direct shear cycling load

In this section we propose to check the validity of the constitutive law (MDJ) with some simulations. These simulations are carried out with the condition of the imposed displacement and stress to reproduce the experimental phenomena. One hundred numbers of cycles are performed.

The following results are observed:

- Under symmetrical imposed stress condition (figure 1), evolution of strain increases after the first cycle with a positive value of the parameter *DR*.
- Under non-symmetrical imposed stress condition (figure 2), the phenomenon of ratcheting and relaxation as defined by Lemaitre and Chaboche (1985) is clearly shown. They are controlled by the parameter R_c: if R_c remains constant and nonzero, there is always ratchet; otherwise, the adaptation is developed with cyclic loading.
- Under symmetrical imposed displacement condition (figure 3), hardening and softening are respectively represented by increasing and decreasing stress. The stabilization of the shear stress depends on the value of parameter *ADR*.
- Under non-symmetrical imposed displacement condition (figure 4), it is shown that relaxation of mean stress is associated with the phenomenon ratchet.

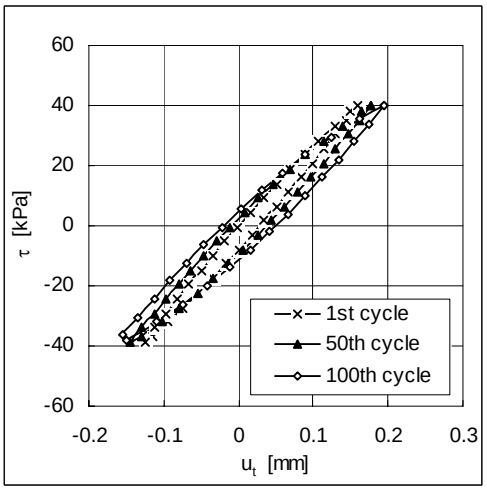

Fig. 1. Test under symmetrical imposed stress (DR=0.05)

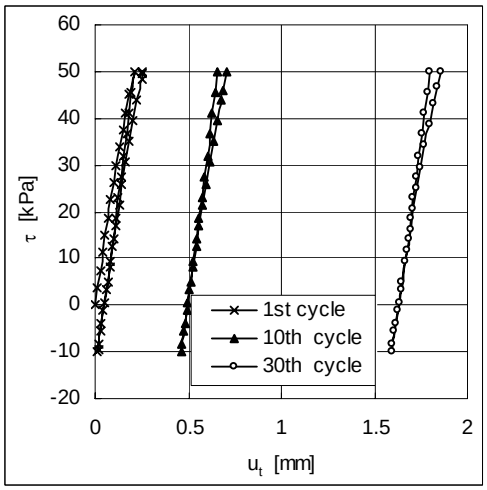

Fig. 2. Test on the non-symmetrical imposed stress — Ratcheting

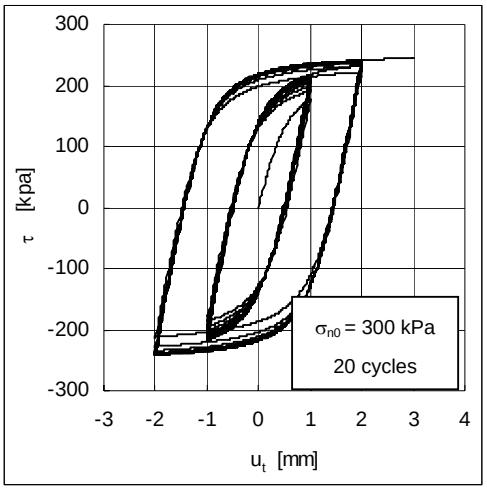

Fig. 3. Test under symmetrical imposed displacement — Cyclic hardening

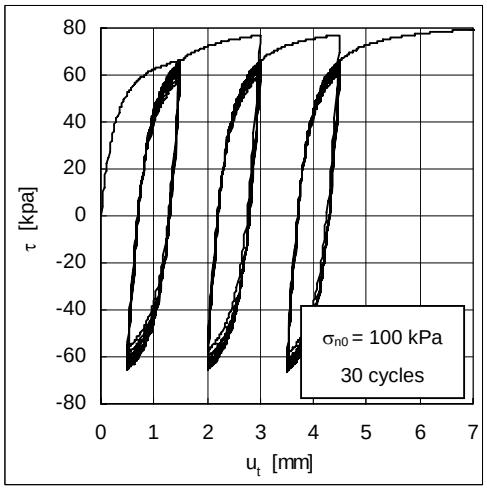

Fig. 4. Test under non-symmetrical imposed displacement — Relaxation

Some improvement of the constitutive law MDJ for interfaces are proposed by the author, in order to avoid the phenomenon of ratchet (Cao, 2010). These improvements are not presented in the present paper.

3. PRESENTATION OF THE METHOD OF "SKIPPED CYCLES"

3.1 Fundamental bases of the method "Skipped Cycles"

The method aims to estimate efficiently the structure behaviour after a certain amount of cycle Δn, from a calculated stress-strain relationship of the structure at a given cycle n. The calculation 'step by step' of the stress and strain between cycles n and n+Δn is then skipped (fig. 5). Between two considered cycles, the total loading on the structure is identical, but plastic strain is accumulated. These relations can be described by a mechanical system following as:

$$\mathrm{div}\sigma_{ij} = 0 \ \text{ on } \Omega \tag{15}$$

$$\sigma_{ij} n_j = 0 \ \text{ on } \Gamma_f \text{ and } u_i = 0 \ \text{ on } \Gamma_u \tag{16) and (17}$$

$$\boldsymbol{\varepsilon}_{ij} = \boldsymbol{\varepsilon}_{ij}^{e} + \boldsymbol{\varepsilon}_{ij}^{p} \tag{18}$$

The resolution of this mechanical system requires the nodal forces resulting from the increment of plastic strains between cycle n and n+Δn, noted $\Delta\varepsilon^p$.

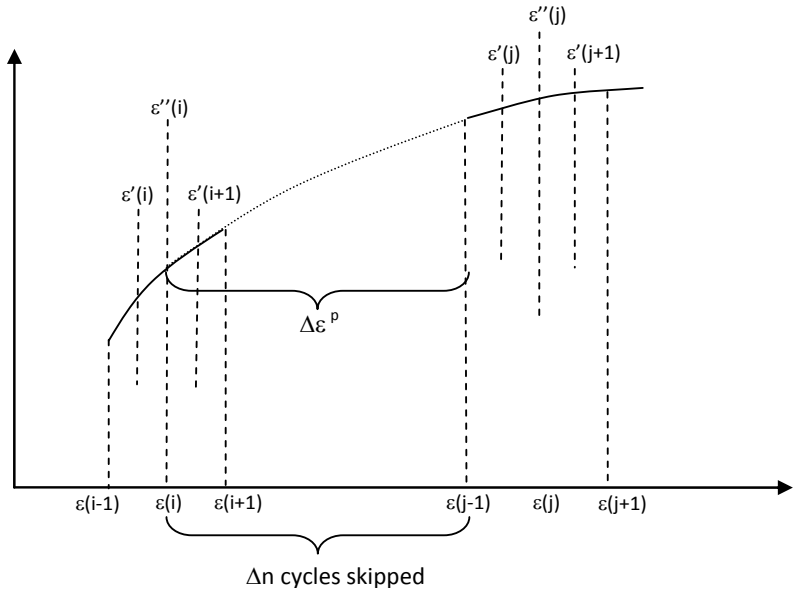

Fig. 5. Relationship between cumulative plastic strain at cycle *i* and $j = i+\Delta n$

To skip from cycle n to cycle n+Δn, it is needed to determine the accumulation of plastic strains ($\Delta\varepsilon_{kl}^{p}$) which can be achieved by extrapolation (Sai, 1993; Niemunis et al., 2005). In this paper, extrapolation of plastic strains is based on the method of least squares. Two types of function are used to describe the different evolutions of shear and normal plastic strains. In particular, the values of normal plastic strains may be negative or positive depending on the phenomenon of contraction or dilatation. Two functions have been chosen for shear and normal strains:

- For the shear plastic strains : $\varepsilon_t^p(n) = \beta n^{\alpha}$ (20)
- For the normal plastic strains : $\varepsilon_n^p(n) = \beta + \frac{\alpha}{n}$ (21)

The estimation of plastic strains at cycle n+Δn is given by the following Taylor expansion:

$$\varepsilon^p(n+\Delta n) \approx \varepsilon^p(n) + \Delta n \varepsilon^{p'}(n) + \frac{\Delta n^2}{2}\varepsilon^{p''}(n) \quad (22)$$

And the number of "skipped cycles" Δn is estimated by the following condition:

$$\Delta n \varepsilon^{p'}(n) >> \frac{\Delta n^2}{2}\varepsilon^{p''}(n) \text{ or } \Delta n = 2\rho\frac{\varepsilon^{p'}(n)}{\varepsilon^{p''}(n)} \quad (23) \text{ and } (24)$$

Where ρ is an accuracy factor. A parametric study lead to a value of ρ = 0.2 in our cases.

The number of cycles "skipped" Δn can also be determined from the Eq. (20) and (21)

- For the shear plastic strain $\Delta n = \frac{2\rho n}{|\alpha - 1|}$ (25)

- For the normal plastic strains $\Delta n = \rho n$ (26)

Two examples are proposed to study the performance of the "skipped cycles" method. The first one is a basic example based on simple shear test including one interface element. The second example deals with the response of an axially loading pile subjected to repeated loading. The constitutive law and the method of "skipped cycles" were implemented in the finite difference Flac3D code. The results are compared with those of a classical 'step by step' cyclic calculation in order to estimate the performance of the "skipped cycles" method.

3.2 Cyclic loading at one interface element

This example concerns a cyclic calculation of one interface element given by 4 points (two points at position A and two at B) (figure 6). The solid elements around the interface have an elastic behaviour (E = 200 MPa, ν = 0.3). Interface parameters used in this example are given in table 2 which are obtained from the calibration of direct shear test simulation.
Three calculations were realized (table 3): they include a monotonic loading phase until a limit loading F_u following by a cyclic loading with an amplitude ΔF (figures 8). The value of limit loading F_u is achieved until a vertical displacement at point A u_0 of 1 cm (figures 7).

Table 2. Model parameters used in the simulation

k_n [kPa/m]	k_t [kPa/m]	φ [°]	ψ_c [°]	a_c	γ_c [kPa]	β_c	DR	ADR
22.10^3	8330	41	5	-0.03	10000	1.55	-0.1	-0.05

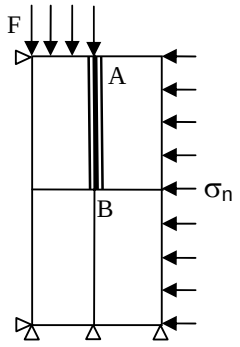

Fig. 6. One interface calculation

Table 3. Set of calculation

$\Delta F/F_u$ / $\%F_u$	0.04 %	0.08 %
90 %	C1-1	C1-2
50 %	C1-3	___

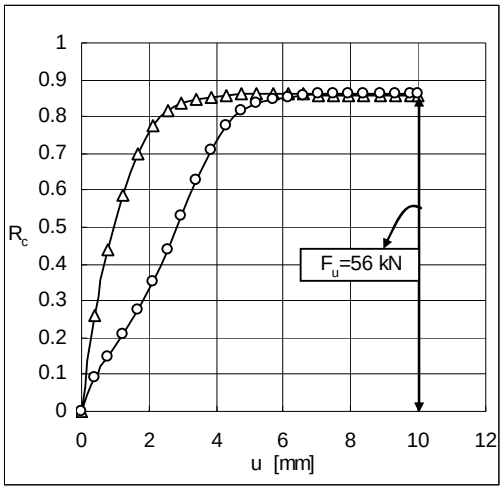

Fig. 7. Definition of the limit loading F_u

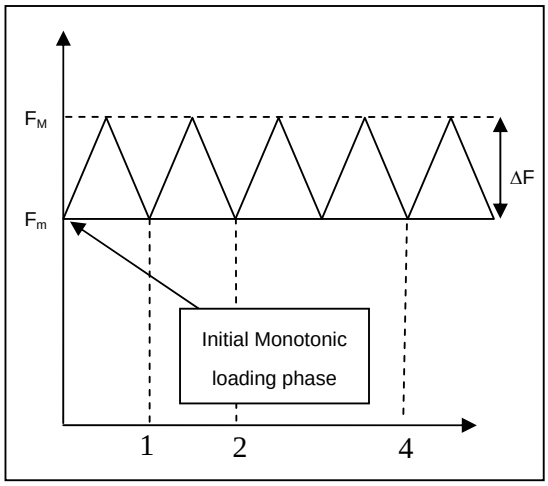

Fig. 8. Cyclic loading paths

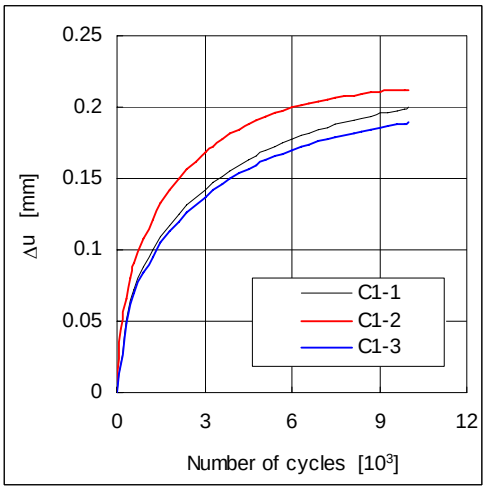

Fig. 9. Comparison of displacement between different calculations.

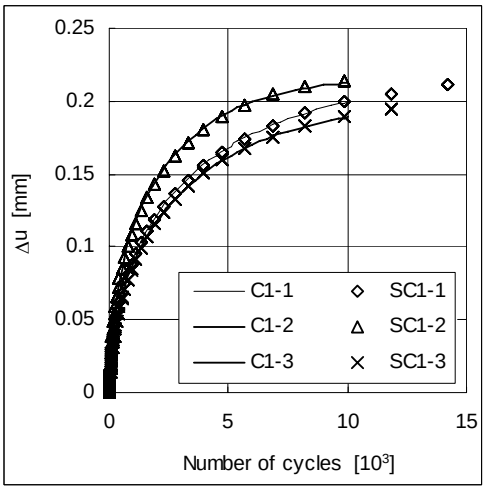

Fig. 10. Comparison of displacement between the method of cycle by cycle and the method of "skipped cycles".

Figure 9 presents the evolution of the vertical displacement at point A u_A during the cyclic loading performed with a direct 'step by step' cyclic calculation, using MDJ model for the interface. The displacement u_0 is measured at the end of monotonic loading and Δu represents the cumulative displacement induced by cyclic loading. Figure 9 shows that the increase of displacement Δu is getting more important for large amplitude of cyclic loading ΔF (comparison between C1-1 and C1-2). For two identical amplitude of cyclic loading, the increase of displacement is getting more important for greater monotonic loading (comparison between C1-1 and C1-3).

Figure 10 gives a comparison between the results of direct calculation ('step by step' calculation) and "skipped cycles" method $(SC1\text{-}i)_{i=1,3}$. It shows very close results in terms of increase of vertical displacement Δu. Furthermore, "skipped cycles" method allows reducing substantially the number of calculated steps, and thus the computation time. Figure 11

illustrates the number of calculated iterations achieved by both calculations for more than 10^5 cycles. It can be noted that "skipped cycles" methods reduces by 53 to 60 times the number of iterations (table 4).

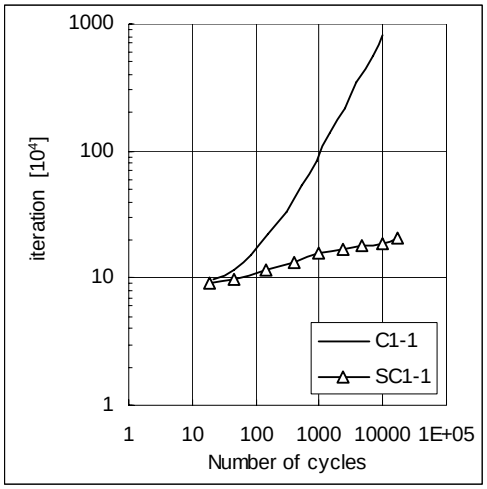

Fig. 11. Comparison of number of iterations between two methods

Table 4. Number of "skipped" cycles

	C1-1 [10^3]	SC1-1 [10^3]	C1-2 [10^3]	SC1-2 [10^3]	C1-3 [10^3]	SC1-3 [10^3]
NCT	10	14.2	10	11.8	10	11.9
NIC	8442	208	7194	195	9677	189
Gain	____	57.6	____	53.5	____	60.9

NCT : Total number of cycles of calculation
NIC: Number of calculated iteration
Gain : $NIC_{(C)} / NIC_{(SC)}$

3.3 Application of an axially loading pile with 60 interfaces

This example concerns a vertical pile with a length of 30 m and a square section of $1m^2$ (figure 12) subjected to a vertical loading F. The characteristics of the soil mass and pile are given in table 5. As it was done in the previous example, the calculation includes also two phases: a first phase of monotonic loading and a second phase of cyclic loading with amplitude ΔF (figure 13). The value of limit loading (F_u = 22MN) is fixed in order to give a vertical displacement of 10 cm (B/10, where B denotes the pile width) at the pile head. The different calculations are given in table 6.

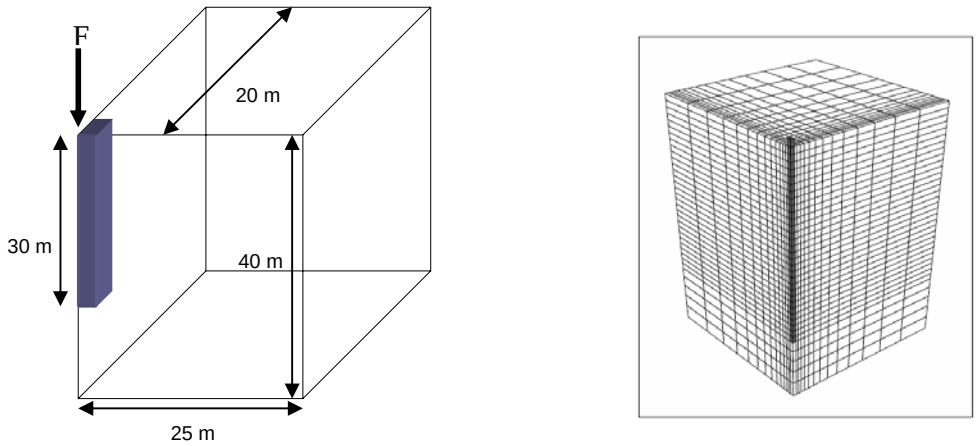

Fig. 12. Geometric and numerical model of axially loaded pile

Table 5. Properties of the pile and soil used in the simulation

	Weight-volume [kN/m^3]	E Young's modulus [kPa]	ν Poisson's ratio
Soil	20	20.10^3	1/3
Pile	25	20.10^6	1/3

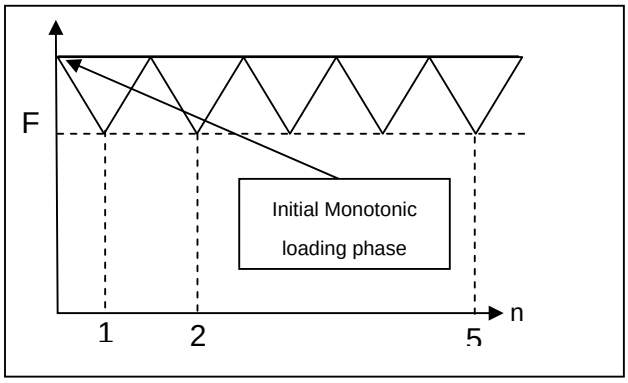

Fig. 13. Cyclic loading paths

Table 6. Set of calculation

$\Delta F/F_u$ / $\%F_u$	2.3 %	4.6 %
50 %	_____	A1-1
30 %	A1-3	A1-2

Figure 14 gives the cumulative settlement Δu at the pile head during cyclic loading. It shows that an increase of the amplitude of cyclic loading ΔF leads to an increase of cumulative displacement. For two identical amplitude of cyclic loading, the cumulative pile head settlement increases with the amount of monotonic load (A1-1). It might be noted that an increase of about 50% of the monotonic settlement is obtained after 200 cycles, which is not representative of a real case. Figure 15 shows the shear stress evolution at 5m depth. The shear stress decreases with an increase of number of cyclic loading in all cases. This phenomenon indicates a degradation of lateral friction at the soil-pile interface.

The "skipped cycles" method is then used to perform the pile response under cyclic loading, using parameters of the calculation A1-3 ($F_{monotonic} = 30\%F_u$; $\Delta F/F_u = 2.3\%$). Figure 16 gives a comparison of displacement between 'step by step' calculation and "skipped cycles" method. Figure 17 proves that "skipped cycles" method can reduce the computation time: only 1,000 cycles are achieved in the 'step by step' calculation, whereas 38,000 cycles are computed with the "skipped cycles" method. In the first thousand of cycles, results obtained with "skipped cycles" are quite close to classical calculation, which indicate a good performance of the method even for multiple interface elements. The computation time in the first thousand of cycles shows a reduction of iteration of about 10 times for "skipped cycles" method.

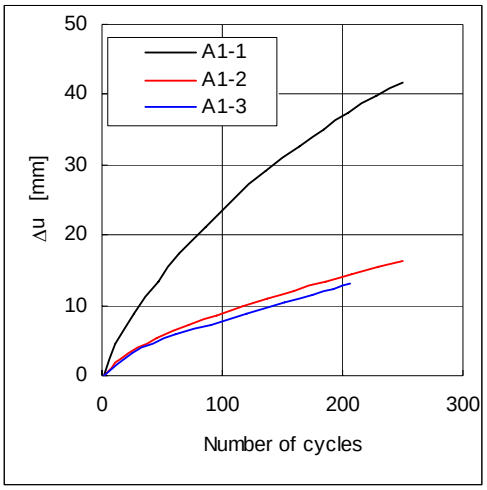

Fig. 14. Comparison of displacement on the pile head (A1-1, A1-2 and A1-3)

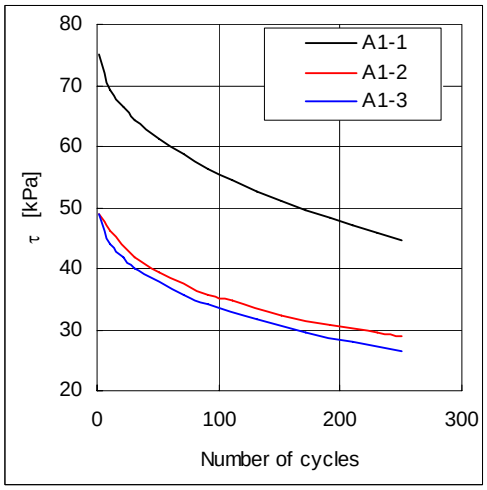

Fig. 15. Degradation of shear stress in the depth of 5m, (A1-1, A1-2 and A1-3)

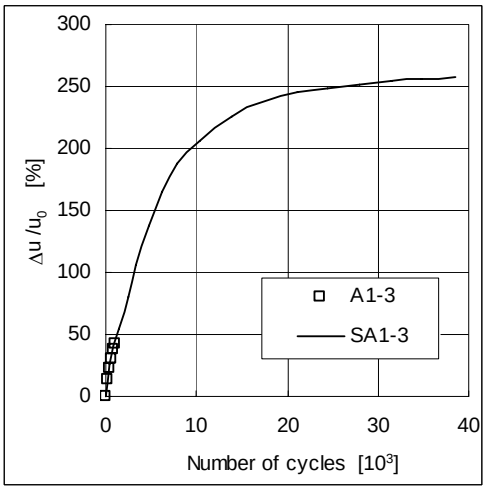

Fig. 16. Comparison of displacement between two methods

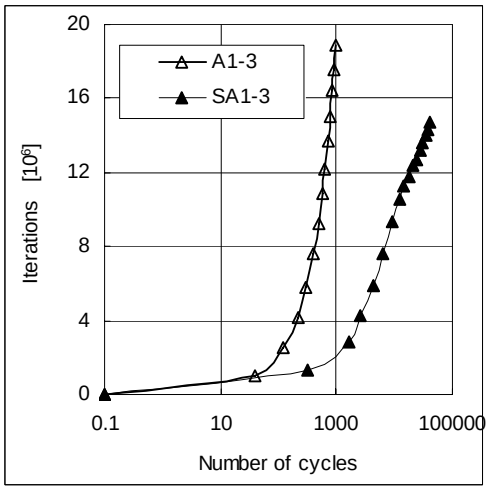

Fig. 17. Comparison of calculated iterations between two methods

4. CONCLUSIONS

This paper included a numerical analysis of soil-structure problems under large number of cyclic loading. For this purpose, a cyclic constitutive model for interface elements and a numerical procedure to reduce time computation (ie. numbers of iterations) have been proposed and implemented on the Flac3d code. Two examples have been studied, involving with respectively one and sixty interface elements. Results show that the constitutive law allows describing the experimental phenomena on cyclic tests and provides reasonable results. Some improvement of the constitutive law MDJ, to avoid the phenomenon of ratchet, has been done elsewhere (CAO 2010). The “skipped cycles” method give very close result in comparison with those obtained by classical ‘step by step’ method; and has advantage to reduce significantly the computation time.

REFERENCES

Mortara, G. Mangiola, A. & Ghionna, V.N. (2007), “Cyclic shear stress degradation and post-cyclic behaviour from sand-steel interface direct shear tests”. Canadian Geotechnical Journal., Vol.44(7), 739-752.

Niemunis, A. Wichtmann, T. & Triantafyllidis, T. (2005), “A high-cycle accumulation model for sand”. J. Computers and Geotechnics., Vol. 32(4), 245-263.

Sai, K. (1993), Modèles à grand nombre de variables internes et méthodes numériques associées. Thesis of ENSM. Paris

Shahrour, I. & Fezaie, F. (1997), “An Elastoplastic Constitutive Relation for the Soil-Structure Interface Under Cyclic Loading”. J. Computers and Geotechnics., Vol. 21(1), 21-39.

Song, B.W. Yasuhara, K. & Murakani, S. (2004) “Direct Simple Shear Testing for Post-Cyclic Degradation in steffness of Nonplastic Silt”. Geotechnical Testing Journal., Vol 27(6), 607-613.

Lemaitre, J. & Chaboche, J.L. (1985), Mécanique des matériaux solides, Dunod Paris.

Itasca Consulting Group, USER’S GUIDE of FLAC3D, (2002)

Cao J.P (2010), Modelisation Numerique des problemes d’interfaces sable-pieu pour les tres grands nombres de cycles : developpement d’une method de sauts de cycles, PhD Thesis, order number 40432, University of Lille 1, France.

A MODEL OF CONFINED COMMINUTION FOR GRANULAR MATERIALS

C. Ovalle
Research Institute in Civil and Mechanical Engineering, Ecole Centrale Nantes – University of Nantes – CNRS UM 6183, BP 92101, 44321 Nantes cedex 3, France

C. Dano
Research Institute in Civil and Mechanical Engineering, Ecole Centrale Nantes – University of Nantes – CNRS UM 6183, BP 92101, 44321 Nantes cedex 3, France

ABSTRACT: *A model to predict how grain size distribution evolves during one-dimensional consolidation is proposed, based on the probabilistic phenomenon of grain splitting in a confined granular assembly and a population balance equation. Results from micromechanical simulations allow us to describe the variability of force distribution at grain contacts from a macro-mechanical stress state. Particle strength from individual grain crushing tests can be fitted to a Weibull distribution that defines the survival probability of grains as a function of stress. Particle fragmentation process in the granular assembly is simulated by a simple fractal type equation, which integrates crushing and abrasion phenomena using only one fitting parameter. The predictions of the model properly reproduce experimental data under low and high 1D loading.*

1 INTRODUCTION

There are many situations in which soils are subjected to high stresses, such as piles tip or high dam foundations. Such stress levels can cause grain crushing, even for relatively strong materials (Vesic & Clough, 1968; Marsal, 1967). Similarly, some materials that have low strength may crush under low stress, as some limestones (McDowell & Amon, 2000; Hu, 2009), volcanic ash soils, or materials with high content of fossil or organic particles (Biarez & Hicher, 1994). In general, it can be stated that the amount of grain crushing in granular materials depends on the ratio between particle individual strength and macro-mechanical stress: if this ratio decreases, grain crushing is encouraged.

Grain crushing influences the stress-strain relationship of granular materials (Marsal, 1967; Marachi et al., 1969 and 1972; Leps, 1970; Charles & Watts, 1980; Barton & Kjaernsli, 1981; Hardin, 1985; Lade et Yamamuro, 1996; Biarez & Hicher, 1997). Except for some cases used in this paper for model validation, the intensity of particle breakage is only determined by comparison of grain size distribution (gsd) before and after a loading stage, but no information is generally available during the loading sequence. However, a more accurate measurement and modelling of grain breakage could improve constitutive models, most of them being based on strong theoretical assumptions and not representing directly the evolution of gsd (McDowell & Bolton, 1998; Daouadji et al., 2000; Muir Wood et al., 2009; Hu, 2009). In many of those models, the critical void ratio is made dependent on a breakage ratio and related to either gsd or plastic work. Einav (2007) has developed an interesting approach supported on strong thermo-mechanical bases and using a relative breakage ratio as an internal energy parameter, considering that part of that energy is dissipated from grain crushing, and not only from friction like classical critical state models. Einav's model

imposes that the material reaches an ultimate fractal gsd and is able to predict intermediate states relating the mechanical behaviour with a breakage ratio, by means of a fractional hypothesis between initial and final fractal gsd, which does not give a satisfactory fitting to experimental data in terms of uniformity; nevertheless, the model has not been enough checked with empirical data.

In this paper, we propose a model which describes the evolution of the gsd for a stressed granular assembly, with the perspective to subsequently feed an elasto-plastic model. Some interesting advances done with Discrete Element Method (DEM) models of confined comminution (Åström & Herrmann, 1998; Cheng et al., 2003; Marketos & Bolton, 2007; Ben-Nun & Einav, 2010; Ben-Nun et al., 2010), as well as experimental results on individual particle strength, are considered.

2 CONFINED COMMINUTION

Comminution is the process of grain size reduction by means of a mechanical action. This process is encountered in several fields, like chemical engineering, mining, pharmaceutics, food industry, among others. Specifically, the work presented in this paper has been developed from phenomenological approaches of the batch grinding comminution theory (GCT). Comminution has been described from a population-balance model (Bass, 1954) involving a breakage rate, or selection function *S,* and a fragment size distribution, or breakage function *b*.

Our aim is to apply GCT population balance type equation to confined granular materials, proposing a physical approach by rewriting *S* function in terms of tensile particle stress and considering micromechanical behaviour. As far as the authors know, this idea has been mentioned (Tsoungui, 1998) but never developed.

For a granular material of known initial retained mass in the i^{th} size fraction $m_i(0)$ (i = 1,…, N; N representing the coarser size fraction), gsd might evolve under some applied stress σ and new values of mass fraction can be calculated $m_i(\sigma)$. Thereafter, any additional stress increment $\Delta\sigma$ will generate further crushing and a new mass fraction $m_i(\sigma+\Delta\sigma)$. Here, we refer to stress σ as an average tensile stress within grains. The mass balance equation can be written as follows:

$$m_i(\sigma+\Delta\sigma) = \left[1 - S_i(\sigma+\Delta\sigma)\right] \cdot m_i(\sigma) + \sum_{j=i+1}^{N} \left[S_j(\sigma+\Delta\sigma) \cdot b_{i,j} \cdot m_j(\sigma)\right] \qquad (1)$$

The first term in Eq. (1) represents the mass of fraction m_i which has survived to the stress $\sigma + \Delta\sigma$ according to survival probability $[1\text{-}S_i]$. The second term is the contribution of coarser fractions j ($j=i+1$ to N), which have crushed in proportion defined by the breakage probability S_j and have been redistributed in the i^{th} fraction according to $b_{i,j}$. Hence, Eq. (1) requires to define a selection function depending on stress and adapted to gsd evolution. In doing so, we have looked to account for individual particle strength statistics as well as micromechanical behaviour into the granular assembly.

3 BREAKAGE RATE OR SELECTION FUNCTION *S*

Experimental observations from crushing tests between plates (Marsal, 1973; Lee, 1992) have shown that the force that induces failure of rock fragments or soil particles is related to their mean diameter, such as:

$$F_f = \eta\, d^{\lambda} \qquad (2)$$

Following (Jaeger, 1967), one can write the relation, known as size effect relationship, between a tensile stress σ produced by a contact force F_f:

$$\sigma = \frac{F_f}{d^2} = \eta\, d^{\lambda-2} \quad \Rightarrow \quad \sigma \propto d^{\lambda-2} \tag{3}$$

This deterministic relationship does not account for data scatter observed during crushing tests. An alternative representation of size effect can also be made by statistical analysis and the Weakest Link Concept (WLC), under some hypotheses. The WLC developed by Weibull (1939) and used by McDowell & Bolton (1998) and McDowell & Amon (2000) for representing soil particle strength of diameter d, results in the following distribution which permits, for a given survival probability and known empirical reference parameters (d_o and σ_o), to represent a size effect between strength and particle size:

$$P_s(\sigma, d) = \exp\left(-\left(\frac{d}{d_o}\right)^3 \left(\frac{\sigma}{\sigma_o}\right)^m\right) \quad \Rightarrow \quad \sigma \propto d^{-3/m} \tag{4}$$

where d_o is the characteristic particle size, σ the tensile stress, σ_o the characteristic tensile stress representing 37% of survival probability, m Weibull's modulus characterizing scatter in tensile crushing strength (a small value of m means large dispersion and m tends to infinity for perfect homogeneous materials).

Selection function S must also account for differences in contact conditions during crushing tests of single grains (spheroïdal volume and rigid plate) and in granular assemblies (assumed contact points between spheres). Curvature effect in grain-to-grain contacts increases breakage probability. Based on a 2D solution by Timoshenko & Goodier (1970), on strength correction factors used by Ben-Hun & Einav (2010) in DEM simulation and on experimental results on real grains by Nakata et al. (1999), contact conditions are taken into account in the following way:

$$f_d(d, \overline{d}) = \frac{F_f}{F_{f-pl}} = 0.5\left(\frac{d/\overline{d}}{d/\overline{d} + 1}\right) \tag{5}$$

where F_f is considered here as the breaking force for a sphere of diameter d, loaded between two spheres of diameter $\overline{d}$ (mean diameter d_{50}) (see Fig. 1) and $F_{f\text{-}pl}$ is the ultimate force for a particle of size d in a compression test between two platens. We are aware that there are many uncertainties about the geometry of the grains and the fact that f_d was initially developed for 2D problems, while our simulations are for 3D with grains that can be shaped very irregularly and angularly. However, we consider that it would be very conservative not to consider a reduction in grain strength due to contact surface. In consequence, in Eq. 4, we use a strength reduction factor f_d (≤ 1) on strength reference parameter σ_o:

$$P_s(\sigma, d_i) = \exp\left(-\left(\frac{d_i}{d_o}\right)^3 \left(\frac{\sigma}{f_{d_i}\,\sigma_o}\right)^m\right) \tag{6}$$

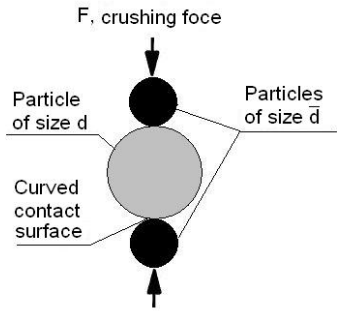

Fig. 1. Schematic contact surface between particles.

However, the grain-to-grain contact force also presents certain variability because of the very disordered nature of the granular material. We used a simplified method for calculating the mean particle contact force proposed by Nakata et al. (1999, 2001). The average grain-to-grain contact force is calculated as:

$$\overline{F} = \frac{\sigma_v^{'}}{N^{2/3}} \quad \Rightarrow \quad \overline{F} = \sigma_v^{'} \left(\sqrt[3]{\frac{(1+e)\pi}{6}} \right)^2 \cdot d_{50}^2 \tag{7}$$

where d_{50} is the mean grain size, N the number of particles per volume unit (assuming uniform spheres) and σ_v' is the macro-mechanical vertical effective stress in 1D compression.

The statistical distribution of particles contact forces in confined granular materials have been studied by several authors using 2D (Radjai et al., 1996; Radjai, 1999) or 3D DEM models (Marketos & Bolton, 2007) and also experimentally using photoelastic methods (Corwin et al., 2005; Majmudar & Behringer, 2005). Results of 2D DEM in oedometric compression have shown that, when normalized by mean values, normal contact force distributions are independent of sample size and gsd (Radjai et al., 1996). Variability is therefore considered introducing the probability $P_N(x > \xi)$ of having a mean force higher than the relative ultimate force, by integrating the following equation proposed by Radjai et al. (1996), and defining $\xi = F_f / \overline{F}$:

$$P_N(\xi) = \begin{cases} k\,\xi^{-\alpha} & \xi < 1 \\ k\,e^{\beta(1-\xi)} & \xi > 1 \end{cases} \tag{8}$$

where:

α: empirical fitting parameter

β: allows continuity: $\beta^2 = (1-\alpha)(2-\alpha)$

k: normalizing constant $\left(\frac{1}{k} = \frac{1}{1-\alpha} + \frac{1}{\beta} \right)$.

Finally, breakage probability in the confined granular material is described by S_i function, which is a combined probability of both independent events: Weibull distribution around an average tensile stress (Eq. 6) and variability of normal breakage or ultimate force by integrating (Eq. 8), so that:

$$S_i(\sigma, \xi) = \left[1 - P_S(\sigma, d_i)\right] \times P_N(x > \xi_i) \tag{9}$$

Finally, following Jaeger (1967), the tensile particle stress σ in Eq. (6) is calculated according to Eq. (3). This approach has been widely used for particle tensile stress computation (Lee, 1992; McDowell & al., 1996; McDowell & Bolton, 1998; Nakata et al. 1999, 2001b).

In a granular material, breakage probability decreases when increasing coordination number (Jaeger, 1967; Sammis et al., 1987). In general, more contact points will change internal stress distribution in a grain, decreasing maximal tensile stress and causing a confinement effect that diminishes breakage probability (Sammis et al., 1987). Thus, when crushing develops, coarse grains will be more and more surrounded by fine particles and their coordination numbers will greatly increase, while it will be generally smaller for finer grains, reversing size effect in crushing by increasing breakage probability of fine particles. Due to lack of an analytical method for computation of coordination number, in our model we avoid that and we indirectly simulate the effect of reducing breakage probability in grains with high coordination number. In other words, particles with lots of contacts are not in a strong chain force and are represented by those who have a low probability $P_N(x > \xi)$ of having a contact force higher than the average. On the other hand, particles with low coordination number are part of those which has a high probability of carrying a strong contact force.

4 BREAKAGE FUNCTION "b"

The breakage function $b_{i,j}$ gives the cumulate mass in the i^{th} size fraction, produced by crushing of larger j fractions. $b_{i,j}$ subsequently stands for the retained mass distribution of $b_{i,j}$.

Several authors have proposed gsd expressions for granular materials formed by rock fragmentation or soil crushing (Turcotte 1986; Korvin 1992; Austin et al., 1976; Perry & Green, 1997; Fukumoto, 1990, 1992). These expressions diverge in number of parameters and complexity, but they are just fitted equations and do not represent the physical sense of fragmentation. Here, we have chosen the fractal distribution because of its simple and versatile form which able us to represent different materials using only one parameter. It is worth noting that the fractal distribution for a single particle fragmentation has no relation with the ultime fractal gsd proposed for granular assemblies, normally related to a different fractal dimension (McDowell et al., 1996). Turcotte (1986) proposed the following relationship for the number of grains bigger than size d, where D is the fractal dimension:

$$N(\Delta > d) \propto d^{-D} \quad \Rightarrow \quad dN(\Delta) \propto \Delta^{-D-1}\, d\Delta \tag{10}$$

Using Eq. (10), one can obtain the mass cumulated in size fraction i (M_i) and gsd function $G(d)$ (Einav, 2007):

$$M_i(\Delta < d_i) \propto \int_{d_m}^{d_i} \Delta^3\, dN(\Delta) \quad \Rightarrow \quad G(d) = \frac{M}{M_T} = \frac{d^{3-D} - d_m^{3-D}}{d_M^{3-D} - d_m^{3-D}} \tag{11}$$

where d_m is the smallest particle size, d_M is the largest particle size and M_T the total mass. In the following developments, we neglected d_m and we use function $b_{i,j}$ describing cumulated mass fraction of size i produced by a single crushed particle from fraction j, of fractal dimension D_{sp}:

$$G(d) = \left(\frac{d}{d_M}\right)^{3-D} \quad \Rightarrow \quad b_{i,j} = \left(\frac{d_i}{d_j}\right)^{3-D_{sp}} \tag{12}$$

Fig. 2 shows that a small fractal dimension (say D=1.0-1.5) means that the size of fragments generated by a single particle breakage are of the same order of magnitude y than the original particle, and no fragments below *y/10* are created; this represents a grain splitting in two or three similar pieces, for instance. On the other hand, a D value close to 2.5-2.6 gives lots of fines particles in the zone of two to three orders of magnitude smaller than the original grain. For example, Turcotte (1986) present a summary of several fragmentation processes, from weathering to nuclear explosions, and gives fractals dimensions of 2.0 to 2.6 for geological materials like gneiss, basalt, granite and glacial till, among others. Steacy & Sammis (1991) and Sammis et al. (1986, 1987) have observed D values between 2.5 to 2.7 in fault gouges materials. Due to lack of information and experimental data for single particle fragmentation, an average value of D_{sp} = 2.3 is used. Anyway, this can still be a fitting parameter in the model, but staying in the range of 2.0 to 2.6, according to experimental data. In the confined comminution model it is assumed that this value remains constant during the process and accounts for both fragmentation and abrasion phenomena.

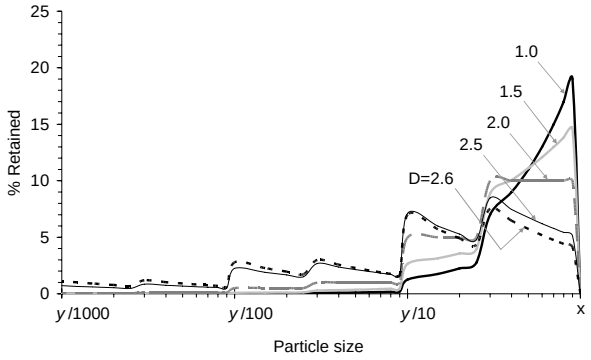

Fig. 2. Retained mass obtained from fractal gsd curves for largest size y and fractal dimension D.

5 MODEL RESULTS

In the following, we present a confined comminution simulation for published experimental results of 1D compression tests on Leighton Buzzard sand from McDowell (2002). Experimental data available are the following:

- gsd before testing and by loading stages in order to validate not only final but also intermediate stages of crushing.
- macro-mechanical 1D stress-void ratio path ;
- single particle crushing statistics (parameters d_o, σ_o and m) and fitting with Weibull theory.

Table 1 summarizes empirical parameters used in simulations.

Table 1. Empirical parameters in confined comminution simulations.

Parameter	Leighton Buzzard sand (1.8-2.0mm) McDowell (2002)	Notes
m	3.14	from particle crushing Weibull statistics
σ_o (MPa)	41.7	
d_o *(mm)*	2	
$\lambda = 2 - 3/m$	1.04	for d in (mm) and F_f in (kN)
η	0.065	

Results are expressed in terms of a breakage ratio B_r proposed by Einav (2007), which is the ratio between the area flanked by the initial gsd and any intermediate distribution, and initial over assumed ultimate fractal gsd. Note that an ultimate fractal dimension of D=2.6 is assumed.

Fig. 3 shows confined comminution simulations for 1D compression test in Leighton Buzzard sand samples up to an effective vertical stress of 100 MPa (McDowell, 2002). It can be seen in Fig. 4 and 5 that the model can approximately reproduce B_r and the order of magnitude of C_u. Differences with experimental data are assumed to be due to the non-uniformity of the initial gsd. However, simulations are quite acceptable in order to guess gsd evolution.

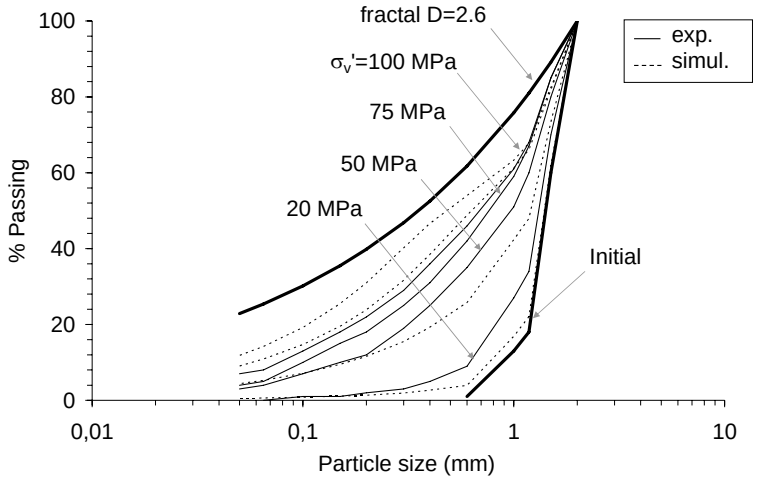

Fig. 3. Comparison between gsd simulations and experimental results from McDowell (2002) on Leighton Buzzard sand (1.8-2.0mm)

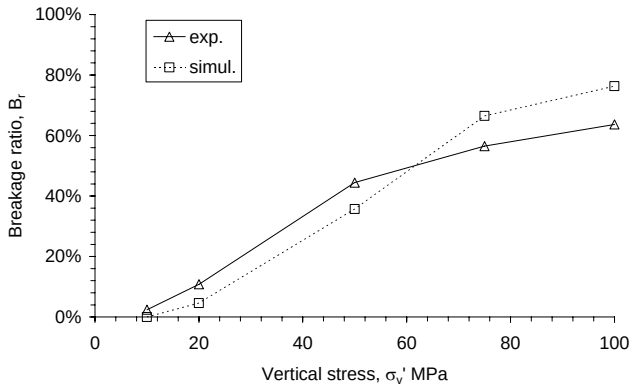

Fig. 4. Breakage ratio (Br) simulations and experimental results from McDowell (2002) on Leighton Buzzard sand (1.8-2.0mm).

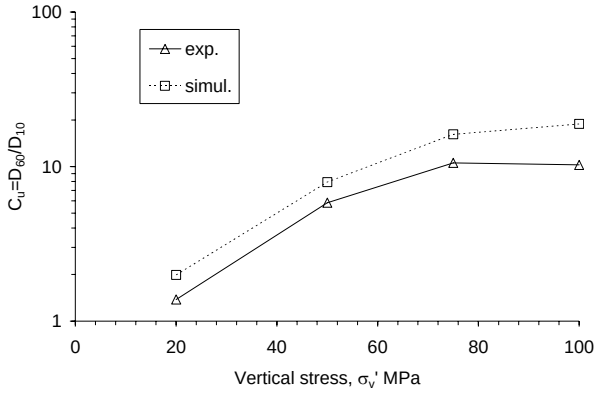

Fig. 5. Uniformity coefficient (C_u) simulations and experimental results from McDowell (2002) on Leighton Buzzard sand (1.8-2.0mm).

6 CONCLUSIONS

Confined comminution of granular materials can be modelled with a population balance equation ruled by a breakage probability function and a fragmentation function, both integrating theoretical aspects and experimental evidences. For particle crushing strength properly described by Weibull theory, one can incorporate size effects and strength dispersion due to probabilistic flaws distribution in the material. Reduction of crushing force caused by curvature effects are also introduced but this point has to be developed to take into account angularity, for instance. This model is described as a function of a unique stress variable, which it is probably not enough to represent all features of grain crushing but gives a useful prediction of practical parameters as breakage ratio and uniformity. Integration of loading paths effects in the fragmentation process or fines production (Ezaoui et al., 2010) are also likely in, for instance, in breakage function. Separately, recent developments would also be useful for future development considering particles contact force distribution evolving during confined comminution (Voivret et al., 2009; Ben Nun et al., 2010).

ACKNOWLEDGEMENTS

This work is part of the French research ECHO Project (Scale effects in fill works in Civil Engineering), sponsored by the French National Agency for Research (ANR).

REFERENCES

Åström, J.A. & Herrmann, H.J. (1998), "Fragmentation of grains in a two dimensional packing". Eur. Phys. J., B, Vol. 5, 551-554.

Austin, L.G., Shoji, K., Bhatia, V., Jindal, V. & Savage, K. (1976), "Some results on the description of size reduction as rate process in various mills". Ind. Eng. Chem. Process Des. Dev., Vol. 15, 187.

Barton N., & Kjaernsli B. (1981), "Shear strength of rockfills". J. Geotech. Eng., Vol. 107, No. 7, pp. 873-891.

Bass, Z. (1954), "On the theory of grinding". J. Appl. Math. Phys., Vol. 5(4), 283-292.

Ben-Nun, O. & Einav, I. (2010), "The role of self-organization during confined comminution of granular materials". Philos. Trans. R. Soc., A, Vol. 368, 231-247

Ben-Nun, O., Einav, I. & Tordesillas, A. (2010), "Force attractor in confined comminution of granular materials". Phys. Rev. Lett., Vol. 104, 108001.

Biarez, J. & Hicher, P.Y. (1994), Elementary mechanics of soil behaviour, Balkema, Rotterdam.
Biarez, J. & Hicher, P.Y. (1997), "Influence de la granulométrie et de son évolution par ruptures de grains sur le comportement mécanique de matériaux granulaires". Revue Française de Génie Civil, Vol. 1(4), 607-631.
Charles, J. A. & Watts, K. S. (1980), "The influence of confining pressure on the shear strength of compacted rockfill". Géotechnique, Vol. 30(4), 353-367.
Cheng, Y. P., Nakata, Y. & Bolton, M. D. (2003), "Discrete element simulation of crushable soil". Géotechnique, Vol. 53(7), 633–641.
Corwin, E., Jaeger, H. & Nagel, S. (2005), "Structural signature of jamming in granular media". Nature, Vol. 435(23), 1075-1078.
Daouadji, A., Hicher, P-Y. & Rahma, A. (2000), "An elastoplastic model for granular materials taking into account grain breakage". Eur. J. Mech. A-Solid, Vol. 20(1), 113-137.
Einav, I. (2007), "Breakage mechanics- Part I: Theory". J. Mech. Phys. Solids, Vol. 55(6), 1274-1297.
Ezaoui, A., Lecompte, T., Di Benedetto, H., & and Garcia E. (2010), "Effects of various loading stress paths on the stress-strain properties and on crushability of an industrial soft granular material". Granular Matter, Online First™, 8 November 2010
Fukumoto, T. (1990), "A grading equation for decomposed granite soil". Soils Found., Vol. 30(1), 27-34.
Fukumoto, T. (1992), "Particle breakage characteristics of granular soils". Soils Found., Vol. 32(1), 26-40.
Hardin, B.O. (1985), "Crushing of soil particles". J. Geotech. Eng., Vol. 111(10), 1177-1192.
Hu W. (2009), "Contribution à l'étude de l'effet d'échelle dans les matériaux granulaires". PhD thesis, Ecole Centrale de Nantes, France.
Jaeger, J.C. (1967), "Failure of rocks under tensile conditions". Int. J. Rock. Min. Sci., Vol. 4, 219-227.
Korvin, G. (1992), "Fractal models in the earth sciences", Elsevier, Amsterdam.
Lade P. V. & Yamamuro J. (1996), "Significance of particle crushing in granular materials". J. Geotech. Eng., Vol.122(4), 309-316.
Lee, D.M. (1992), "The angles of friction of granular fills". PhD thesis. University of Cambridge.
Leps, T.M. (1970), "Review of shearing strength of Rockfill". J. Soil Mech. Found. Div., ASCE, Vol. 96(4), 1159-1170.
Majmudar, T. & Behringer, R. (2005), "Contact Force Measurements and Stress-Induced Anisotropy in Granular Media". Nature, Vol. 435(23), 1079-1082.
Marachi, N.D., Chan, C.K., Seed, H.B. & Duncan, J.M. (1969), "Strength and deformation characteristics of rockfills materials". Report No. TE-69-5, Department of civil engineering, University Of California, Berkeley.
Marachi, N.D., Chan, C.K. & Seed, H.B. (1972), "Evaluation of properties of rockfill materials". J. Soil Mech. Found. Div., ASCE, Vol. 98(SMI), 95-114.
Marketos, G. & Bolton, M.D. (2007), "Quantifying the extent of crushing in granular materials: A probability-based predictive method". J. Mech. Phys. Solids, Vol. 55, 2142–2156.
Marsal, R.J. (1967), "Large-scale testing of rockfill materials". J. Soil Mech. Found. Div., ASCE, Vol. 93(SM2), 27-44.
Marsal, R. (1973), "Mechanical properties of rockfill dams", Ed. Hirschfeld, R. y Poulos, S., Embankment-dam engineering: Casagrande Volumen. New York, Wiley, 454 p.

McDowell, G.R. (2002), “On the Yielding and Plastic Compression of Sand”. Soils Found., Vol. 42(1), 139-145.
McDowell, G. R. & Amon, A. (2000), “The application of Weibull statistics to the fracture of soil particles”. Soils Found., Vol. 40(5), 133–141.
McDowell, G. R., Bolton M. D. & Roberston D. (1996), “The fractal crushing of granular materials”. J. Mech. Phys. Solids., Vol. 44(12), 2079-2102.
McDowell, G. R. & Bolton M. D. (1998), “On the micromechanics of crushable aggregates”. Géotechnique, Vol. 48(5), 667-679.
Muir Wood, D., Kikumoto, M. & Russell, A.R. (2009), “Particle crushing and deformation behaviour”. Prediction and simulation methods for geohazard mitigation (eds F Oka, A Murakami, S Kimoto), CRC Press/Balkema.
Nakata, Y., Y. Kato, M. Hyodo, A.F.L. Hyde, & H. Murata (2001), “One-dimensional compression behaviour of uniformly graded sand related to single particle crushing strength”. Soils Found., Vol. 41(2), 39-51.
Nakata, Y., Hyde, A.F.L., Hyodo, M. & Murata, H. (1999), “A probabilistic approach to sand particle crushing in the triaxial test”. Géotechnique Vol. 49(5), 567-583.
Perry, R.H. & Green, D. (1997), “Perry's Chemical Engineers' Handbook (7^{th} Ed;)”, McGraw-Hill, New York.
Radjai, F. (1999), “Multicontact dynamics of granular systems”. Comput. Phys. Commun., Vol. 121–122, 294–298.
Radjai, F., Jean, M., Moreau, J.J. & Roux S. (1996), “Force distributions in dense two-dimensinal granular systems”. Phys. Rev. Lett., Vol. 77(2), 274-277.
Sammis, C.G., Osborne, R.H., Anderson, J.L., Banerdt, M. & White, P. (1986), “Self-similar cataclasis in the formation of fault gouge”. PAGEOPH, Vol. 124(1/2), 53-78.
Sammis, C.G., King, G. & Biegel, R. (1987), “The kinematics of gouge deformations”. PAGEOPH, Vol. 125(5), 777–812.
Steacy, S.J. & Sammis, C.G. (1991), “An automaton for fractal patterns of fragmentation”. Nature Vol. 353, 250-252.
Timoshenko, S.P. & Goodier, J.N. (1970), “Theory of Elasticity”. McGraw-Hill, New York.
Tsoungui, O. (1998), “Modélisation numérique et expérimentale du broyage des grains par compression”. PhD thesis, Université Paris XI.
Turcotte, D. (1986), “Fractals and fragmentation”. J. Geophys. Res., Vol. 91(B2), 1921-1926.
Vesic, A.S. & Clough, G. W. (1968), “Behaviour of granular materials under high stresses”. J. Soil Mech. Found. Div., ASCE, Vol. 94(SM 3), 661-688.
Voivret, C., Radjaı, F., Delenne, J.-Y., & El Youssoufi, M. S. (2009), “Multiscale Force Networks in Highly Polydisperse Granular Media”, Phys. Rev. Lett., Vol. 102, 178001.
Weibull, W. (1939), “A statistical theory of the strength of materials”. Proc. Roy. Swedish Inst. Eng. Res. N°151 .
Weibull, W. (1951), “Statistical distribution function of wide applicability”. J. Appl. Mech., Vol. 19(2), 293-297.

ESTIMATION OF VOID RATIO OF CLAYEY SOILS USING X-RAY CT SCANNING TECHNIQUE

Hyu-Soung Shin & Kwang-Yeom Kim
Geotechnical Eng. Research Dept., Korea Institute of Const. Tech. (KICT), the Republic of Korea

ABSTRACT: *In this study, a new methodology is proposed for estimating void ratio of very fine clayey soils using the micro X-ray CT scanning technique. Since the size of particles of clays is too fine to capture the volume of voids directly by a CT scan, scanning tests with a number of clay specimens, which were artificially set to have various designated void ratios, have been carried out. From these tests, a relationship between the CT values and void ratios is developed to be used for estimating the void ratios. A linear relationship was considered adequate. It is expected that micro X-ray CT scanning can be adopted for capturing the void ratio of very fine soils with sufficient accuracy which generally is an issue in the conventional specific gravity tests.*

1 INTRODUCTION

In recent years, geotechnical engineering has benefited from the advances in various high-technology fields such as computing, sensors, electronics and information technology. However, investigation of dynamic engineering characteristics of the geotechnical materials has still many limitations. In particular, the reliable estimation of geotechnical design parameters is a matter of the utmost importance for geotechnical engineers in terms of workability, stability and economic efficiency.

In this respect, geotechnical engineers dealing with very fine soil materials from a different viewpoint have begun searching for more advanced research methods, compared with existing ones. Visualizing and quantifying micro-scale internal structures and composition without destroying and focusing on figuring out physical characteristics of materials with different natures, using 3-dimensional images by X-ray CT (Computed Tomography) is now feasible.

The advantage of X-ray CT is that it helps to obtain reliable data by saving time required for information acquisition and providing the object to be scanned with the minimum noise. Toller(1998) mentioned that X-ray CT can provide information effectively, minimizing unnecessary time consumed to prepare for a specimen in typical indoor experiment. In particular, CT can save technical effort required for the preparation of a specimen, and reduce errors occurring in the course of sample preparation. Another advantage of CT is that the same specimen can be scanned several times on a variety of conditions by conducing non-destructive test, and an interaction between a particle and voids can be investigated at any location of the specimen. The physical and chemical changes do not occur in the specimen. In addition, the CT can help to observe internal changes depending on the stress of the specimen, using appropriate experimental equipment.

This research on the measurement of void ratio, one of the important geotechnical design parameters in fine grained soil was carried out, utilizing the above mentioned micro CT X-ray scanning technique. In engineering practice an indirect method of measuring specific gravity is used. Unlike the case of sandy soil, the void ratio of cohesive soil is a crucial factor in geotechnical design since it plays a key role in deciding consolidation settlement and time (Fox and Berles, 1997). However, the void ratio measurement by specific gravity method has various error factors such as measurement error due to heterogeneous saturation state within specimen and specimen disturbance when sampling and carrying the specimen. No suitable alternatives to solve the said problem have been developed yet.

In many countries, Micro X-ray CT utilization research has been widely conduced to solve the problems of existing method for void ratio measurement and conduct more reliable and accurate void ratio measurement of soil and sand. In particular, Peyton et al. (1992) tried imaging minute void size of non-disturbed soil specimen in the early stages of void ratio measurement, and Zeng et al. (1996) measured the volume density of the specimen based on image processing analysis and precision analysis of CT data. Hereafter, the research on the changes of void structure has been conducted by Wong (2000), Alshibli et al. (2003), and Riyadh et al. (2006). However the research on mechanism and algorithm seeking for the measured data on void ratio is insufficient in spite of the abovementioned efforts. In addition, the abovementioned studies have been restricted to the scope of sandy soil.

In this study, the research on the algorithm and measurement method was carried out to calculate the void ratio of fine cohesive soil whose particle is smaller than 5 micron, a minimum pixel size of Micro X-ray CT. For this, the artificial clay specimens with various void ratios were manufactured, and the void ratios were measured through existing experimental method towards each specimen, whose result was compared with CT number analyzed in X-ray CT image for analysis. By deducing void ratio equation using CT number of X-ray CT image in fine grained soil, void ratio measurement method of fine grained soil using X-ray CT was suggested.

2 OVERVIEW OF MICRO X-RAY CT

Devised by Hounsfield and commercialized in 1971, CT (Computed Tomography) is the technology to visualize information on structure and texture of objects which cannot be obtained by existing X-ray equipment in image. This technology embodies the image obtained by seeing through objects using X-rays from various angles in 3-dimensional image, and by using this image, it can help to see image of respective sectional diagram in objects and various structures in the insides of the objects through analysis. X-ray CT is commonly used in the field of medical radiation, and used for checking out defects of semiconductor or electronic goods in industries. In addition, the utilization value of CT is being highly evaluated in the field of biotechnology and archaeology. However, the basic research to utilize CT as experiment equipment is insufficient in the application of geotechnical and civil engineering field.

X-ray equipment is composed of 3 parts such as a source to generate X-ray, a detector to detect X-ray penetrating objects and a manipulator to transfer and rotate objects. The scanned mage is obtained by making a 360-degree revolution of the object placed between X-ray source and X-ray detector as shown in Fig. 1.

The operational principle of the source is that first, electron is created, charged with electric current through a filament, and the electrons with negative electricity are accelerated in metals like tungsten with the positive pole electrically, and collided the metal surface, thereby generating X-ray. Made by Hamamatsu Corporation, the Micro X-ray source used in this study is by sealed-type source, and its permeability is up to 90kV. Its degree of definition

is 250μA, and the minimum focal spot size is 5micron, which makes it possible to identify the object of 0.005mm.

Fig. 1. Micro X-ray CT equipment of KICT

In general, the factor deciding the efficiency of X-ray equipment is the role of source, but the factor deciding the designed use of X-ray equipment is the detecting efficiency of camera. The camera used for scanning the specimen of geotechnical materials in this study protects the exterior and collects attenuation information of X-ray, attached to the equipment. The equipment before camera is a safety device to protect detector. The X-ray CT camera made by Rad-icon is 2" × 2" in its size, has a pixel pitch of 48 μm, and its limiting resolution is 10Lp/mm (line pair per millimeter).

The manipulator is used for deciding scanning location of the specimen. If the specimen is scanned, deflecting from scanning area in cone beam typed scanning, noise may occur, so it seems that the more accurate data can be obtained when the movement of object is stable in case of rotation of the object. The manipulator provides about 0.01mm noise, but it can be corrected by reconstruction software.

3 CT NUMBER STANDARDIZATION

3.1 Grayscale and CT Number

X-ray CT scan result displays grayscale image signifying the attenuation value of X-ray represented as contrast ratio opposing white to black, and its scope is $0 \sim 2^{15}$. However, the value is changed according to experimental environment and conditions. On this, the correction towards consistent value is required. In the field of medical science, the grayscale is used by being converted to CT number, which is changed depending on the unique characteristics of materials.

CT number is the method assuming air as -1,000, and water 0, and correcting the value of other materials based on the air and water. The reason for targeting water and air is that these two mediums are rarely affected by permeability or other environmental factors, and scanned essentially in case of X-ray scanning of the body since water constitutes 70% of body composition material. The information on the X-ray attenuation collected in camera is represented as the value (μ) by the density of each materials, CT Number 0 of water is the value by hydrogen and oxygen, and CT Number -1,000 of air is corresponded to nitrogen and oxygen. Thus, the CT number of specific material is the value signifying the relative location of constituent elements and material density based on air and water. However, the CT Number can't have absolute value due to the effect of permeability or other environmental

factors. For this reason, it is said that one of the major tasks for the application of CT to geotechnical field is CT Number standardization.

3.2 Change of Grayscale According to Gain and Offset

The grayscale in X-ray CT image is changed according to gain and offset set-up. In this study, X-ray CT scanning was conducted, targeting standard sand in Jumunjin to investigate the change of grayscale, or output results of image according to gain and offset change within actual geotechnical materials. To consider various conditions, a total of 6 set values was combined by changing gain into 0.1, 0.2, and 0.3, fixing offset to 0.1, and setting offset into 0.005, 0.01 and 0.2, fixing gain to 0.1 (see Table 1).

The average grayscale on each set-value condition signifies the peak value of the left side considered as air and the peak value of the right side considered as sand particles, respectively in the histogram as shown in Table 1. Upon closer examination of effect of gain value with offset fixed, the larger the gain value, the smaller the grayscale of air and the larger the grayscale of sand particles, which shows the trend hat the difference between the two grayscales becomes larger and larger. In particular, as the size of gain increases two times, the difference of average grayscale in air and sand particles increases at the same rate. In case of fixing gain vale to 0.1, the offset has 4 models of 0.005, 0.01, 0.1 and 0.2. As offset increases, the average grayscale of air and sand particles increases, showing linear relationship, but the average difference between the two is consistent, showing 146 or 147, In conclusion, the change of gain is in proportion to area scope of grayscale , and the change of offset has effect on the size regardless of the scope of grayscale.

Table 1. Gray scale variation by gain and offset

Gain/offset Setting	Histogram	Average gray scale of mediums (air/sand particle)	Minimum inflection point	The difference Between averages
0.05 / 0.1	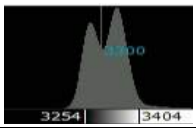	3,269 / 3,342	3,305	73
0.1 / 0.1	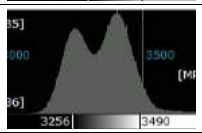	3,265 / 3,411	3,334	146
0.2 / 0.1	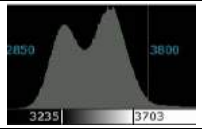	3,257 / 3,548	3,392	291
0.1 / 0.005	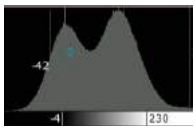	2 / 148	74	146
0.1 / 0.01	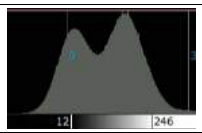	19 / 166	90	147
0.1 / 0.2		6,541 / 6,689	6,609	148

3.3 Gain and Offset Correction for CT Number Standardization

The standardization of CT number is major task for exact judgment of CT image. In this study, the jig for the gain correction was manufactured and utilized to correct the result value to be changed according to external environment and experimental conditions in the process of changing grayscale value by X-ray CT scanning into CT number. The jig for gain correction used water and air which is not affected by permeability or environmental factors, and it was made of acrylic material which is commonly used to minimize the effect in case of CT scanning. In addition, it was made as the general form so that it can be applied to various areas like stones and rocks as well (Fig. 2).

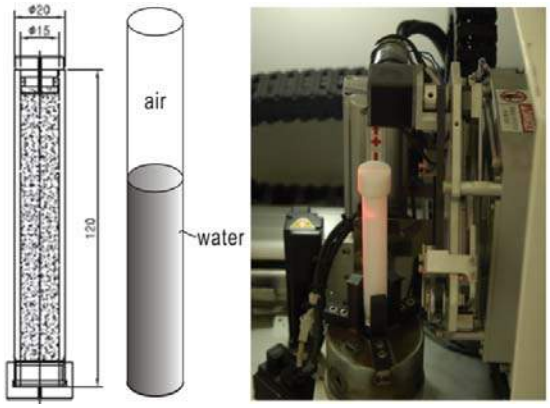

Fig. 2. The jig for gain-offset correction

For the standardization of CT Number, grayscale towards water and air in current status is measured first by conducting X-ray CT scanning, targeting the jig for gain correction. And then gain and offset is set up, correcting the average of grayscale on air sphere to -1,000 and the average of grayscale on water to 0. After completing gain and offset correction, grayscale is measured after canning the object, and the measured grayscale is converted into CT number by Eq. (1).

$$CT\ Number = \frac{(\mu_t - \mu_w)k}{\mu_w} \qquad (1)$$

Here, μ_t is grayscale value of the object, μ_w is grayscale value of water fixed to 0, and k is material constants.

4 VOID RATIO ESTIMATION OF FINE GRAINED SOIL

4.1 Basic Concept on Void Ratio Estimation of Fine Grained Soil Using X-ray CT

In general, clay has a particle less than 5 μm in Unified Soil Classification System. In case of clay, it is difficult to identify a void and a particle through existing X-ray CT equipment since the size of a particle is very small unlike coarse grained soils. For this reason, even though minimum resolution is maintained, various clay particles and void exist in one pixel as shown in Fig. 3. In general, as the specific gravity of a particle increases in a pixel, density and CT number increases at the same time (Richard et al., 2001), but as the number of clay particles decreases, the density and CT number decreases, which is easily predicted situation. However, it is very difficult to decide how much CT number increases depending on the degree of increase in the number of particles quantitatively, but it is anticipated that the clay

with specific void ratio will be distributed in the form of CT number in the specific scope, and there will be correlations between void ratio and CT number. Accordingly, this study analyzed the correlation between CT number and void ratio of various clay materials obtained by laboratory experiments, thereby inducing the correlation.

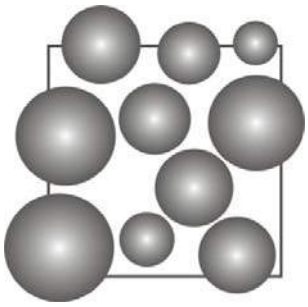

Fig. 3. Clay particles on a pixel

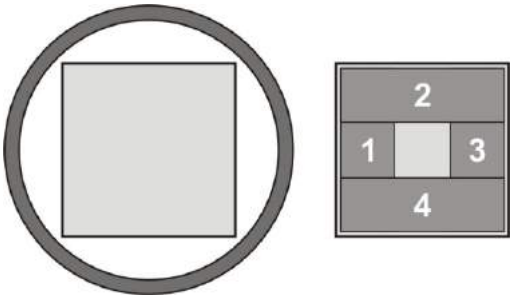

Fig. 4. Area determination for calculation of average CT Number

For estimation of void ratio, optimal scanning conditions for specimen have to be searched, and jig for gain correction has to be scanned on the same condition with scanning condition of object. After completing gain and offset set-up through gain and offset correction, the data of original material is reconstructed, applying correction value to scanning object. Among reconstructed slices, the area considered to be disturbed by friction with wall and cupping error area are excluded. in addition, the areas are divided into 4 parts as shown in Fig. 4 , considering errors occurring in the central part of the specimen, and the average CT number of each areas is obtained. The flowchart of method for void ration estimation using the abovementioned X-ray is shown in Fig. 5.

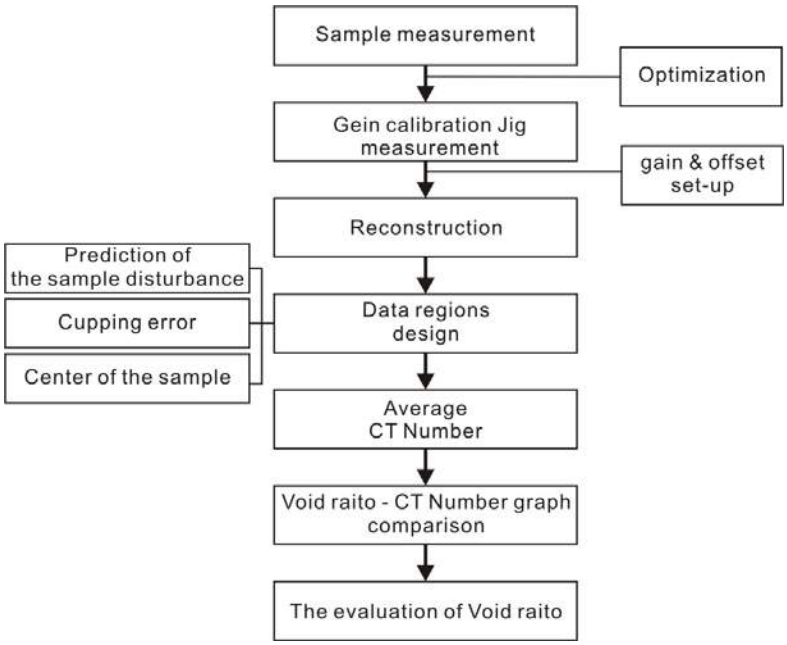

Fig. 5. A flow chart for calculation of void ratio using X-ray CT scan

4.2 Production of Artificial Clay and Void Ratio Measurement

To embody various void ratio of clay, artificial clay specimens mixed with kaolinite and bentonite were produced. Since kaolinite has low contraction, extensibility and ion exchange capacity, bentonite with high positive ion exchange capacity was mixed with kaolinite, and the ratio is divided into two kinds: kaolinite 90%, bentonite 1a% and kaolinite 100%. In this study, 2 times of liquid limit was decided as moisture content for mixing the clay specimen, and solidifying agent was added to each cases after deciding the mixture ratio. And the foreign matters were removed by shaking the mixed soils in the state of slurry with #10 sieve after stirring artificial clay and solidifying agent, using specimen stirrer. After that, preconsolidation was carried out by the end of the 1st consolidation through vertical drainage with vertical horizontal stress of 150kPa, 200kPa, 250kPa, 300kPa, 350kPa and 400kPa in specimen molding machine. The specimens are divided into 20 cases according to the mixture ratio of the specimen and the stress level of preconsolidation as shown in Table 2, and the void ratio was measured, sampling the upper part and central part of each specimens. The part marked by 'x' in Table 2 represents that the measurement is impossible due to specimen damage, and the moisture content and dry-unit weight towards the measurable specimen marked by '0' was measured, dividing the specimen into 3 parts like top, middle and bottom. And the void ratio was estimated based on the measurement value (Table 3).

4.3 Void Ratio Estimation and Analysis Using X-ray CT

The specimens for X-ray CT scanning are divided as shown in Table 2 to diversify void ratio, and 12 kinds of them in good condition, targeting the upper and central part of the specimen were used after being cut off. The specimen was sampled by inserting clay jig into the 3 locations of the clay which was cut off, and for accurate void ratio measurement, the specimen for scanning was prepared by molding the specimen to be fitted to the volume. And the prepared specimen for scanning was fixed to the jig to minimize movement. After scanning the specimen, optimal gain and offset value were set up by scanning jig for gain correction and conducting gain and offset correction.

Table 2. Artificial clay specimens for measurement of void ratio

Vertical stress (kPa)	Location	Component ratio (Kaolinite : Bentonite)	
		10 : 0	9 : 1
150	Upper part	O	×
	Middle part	×	×
200	Upper part	×	O
	Middle part	×	O
250	Upper part	O	×
	Middle part	O	×
300	Upper part	O	×
	Middle part	O	×
350	Upper part	O	O
	Middle part	O	O
400	Upper part	×	O
	Middle part	×	×

Table 3. Results of void ratio measurement and CT Number calculation of clay

Component ratio (Kaolinite : Bentonite)	Pre-consolidation	Location	Void ratio (e)	CT Number of area				Average CT-Number
				Area 1	Area 2	Area 3	Area 4	
9:1	400kPa	Upper Part	1.46	-175.2	-173.5	-172.2	-174.1	-174.1
			1.46	-163.5	-167	-166	-165.4	-165.4
			1.46	-158.4	-158.4	-162.1	-165.5	-161.1
9:1	350kPa	Upper Part	1.47	-169.2	-175.7	-162.5	-169.7	-169.3
			1.47	-165.3	-172	-166.8	-163.5	-166.9
			1.46	-164	-158.9	-161.2	-160.7	-161.2
9:1	350kPa	Middle part	1.63	-196	-194.7	-189.8	-195.1	-193.9
			1.58	-185	-179.8	-171.8	-186.6	-180.8
			Failure of specimen shaping					
10:0	350kPa	Upper Part	1.56	-181.1	-181.3	-191.1	-189.6	-185.8
			1.55	-184.9	-179.4	-177.8	-184.6	-181.7
			1.57	-172.4	-169.1	-173.5	-172.5	-172.9
10:0	350kPa	Middle part	Consolidation of inner specimen is not enough					
10:0	300kPa	Upper Part	1.69	-220.8	-209.5	-210.6	-217	-214.5
			1.64	-217.4	-213.5	-210.4	-210.9	-213.1
			1.68	-215.7	-211	-212.3	-214.4	-213.4
10:0	300kPa	Middle part	1.69	-220.3	-214.5	-214.8	-219.2	-217.2
			1.65	-210.3	-215.1	-227.7	-204.3	-214.4
			Failure of specimen shaping					
10:0	250kPa	Upper Part	1.79	-230.6	-229.8	-228	-223.2	-227.9
			1.88	-246.8	-238.9	-248.1	-251.5	-246.3
			1.82	-225.8	-239.3	-233.4	-230.5	-232.3
10:0	250kPa	Middle part	1.82	-230.9	-229.3	-224.4	-227.2	-228
			1.82	-225.8	-222.6	-217.9	-218.5	-221.2
			1.81	-212.1	-214.8	-217.7	-213.2	-214.5
9:1	200kPa	Upper Part	1.59	-188.2	-191.1	-178.3	-191.1	-187.2
			1.56	-170.6	-177.8	-173.9	-177.1	-174.9
			1.57	-179.9	-181.8	-175.3	-185	-180.5
9:1	200kPa	Middle part	1.57	-184.2	-173.3	-173.3	-169.1	-175
			1.59	-192.3	-184.2	-187.3	-183.1	-186.7
			1.48	-169.2	-172.4	-168.2	-169.6	-169.85
10:0	150kPa	Upper Part	1.61	-192.4	-189.5	-185	-200.1	-191.8
			1.61	-188.4	-190.3	-185.2	-197.6	-190.4
			1.61	-180.7	-197.3	-188.9	-199.3	-191.6

X-ray CT scanning result of the clay for void ratio estimation based on XT, YZ and XZ sectional diagram is shown in Fig. 6. It is verified that identifying a particle through image seems to be difficult, and the shape of histogram is formed as one peak type, not double peak type, which makes it difficult to distinguish a void and a particle.

The grayscale value was deduced from X-ray CT image by dividing the area into 4 parts as shown in Fig. 4, targeting 31 specimens except for 5 specimens which are not preconsolidated. The deduced grayscale formula is converted to CT number, using formula (1), and the result is as shown in Table 3.

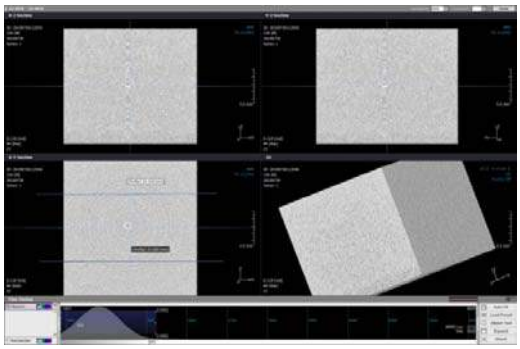

Fig. 6. X-ray CT image of clay

To check out the correlation between CT number and the void ratio, or the specific gravity of the clay particle in within a pixel, the average of CT number by areas through the analysis on Micro X-ray CT image and the void ratio measured by the experiment was illustrated as shown in Fig. 7. The void ratio and CT number shows linear relationship on the whole. In particular, it turned out that the correlation of CT number is higher in the area with small void ratio, compared with area with high void ratio. As a result of the analysis on the correlation through primary linear regression, the connection between CT number and void ratio through the analysis of X-ray CT image is shown as Eq. (2).

$$e = (-0.0566) \times (CT\ Number) + 0.6581 \tag{2}$$

Here, e is the void ratio, and CT number is the CT number in X-ray image. The coefficient of determination (r^2) and standard deviation (SD) between the void ratio and CT number is 0.91 and 0.38 respectively, which shows high correlation. Accordingly, it is concluded that the method for void ratio measurement using X-ray CT can be an effective alternative to replace experimental method which has various error factors.

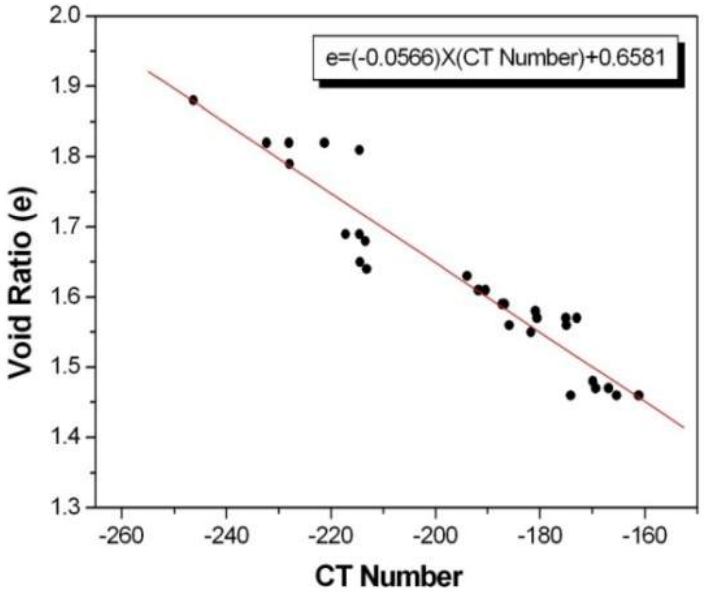

Fig. 7. Relation between void ratio and CT Number

5 CONCLUSIONS

In this study, the correlation between the void ratio of clay and CT number was figured out, using Micro X-ray CT equipment, and a more reasonable estimate of void ratio of clayey soil. The research process and results are as follows.

(1) For quantitative void ratio estimation through X-ray CT image, gain and offset correction was carried out to standardize the CT number. For this, characteristics of change in grayscale according to gain and offset were analyzed. And by manufacturing the jig for gain and offset correction and scanning X-ray CT, optical gain and offset set-up plan to secure standardized CT number was suggested.

(2) Considering the characteristics of fine grained soil containing various particles within a pixel unlike coarse-grained soil, the concept of void ratio estimation of fine grained soil was established. In general, as the specific gravity of clay particles within a pixel increases, density and CT number increases at the same time. Accordingly, the void ratio can be estimated from Micro X-ray CT image by establishing the correlation between CT number and the density of clay particle, or void ratio.

(3) To figure out the correlation between void ratio and CT number, artificial clay specimens composed of kaolinite and bentonite having differing void ratio were manufactured, by preconsolidating at different stress levels.

(4) The void ratio measurement and X-ray CT scanning of each specimen was carried out at the same time through existing experimental method. As a result of regression analysis of void ratio and CT number, it is verified that the coefficient of determination (r^2) is 0.91, which indicates linear relationship with high correlation.

(5) In conclusion, it is expected that the method for void ratio measurement of fine grained soil using Micro X-ray CT will be a reasonable alternative to the existing experimental method.

REFERENCES

Alshibli, K. A., Batiste, S. & Sture, S. (2003) "Strain Localization in Sand: Plane Strain versus Triaxial Compression" Journal of Geotechnical and Geoenvironmental Engineering, Vol. 129(6), 483-494.

Fox, P. J. & Berles, J. D. (1997) "CS2: A piecewise-linear model for large strain consolidation." International journal for numerical and analytical methods in geomechanics, Vol. 21, 453-475.

Peyton, R. L., Haeffner, B. A., Anderson, S. H. & Ganzer, C. J. (1992) "Applying X-ray CT to measure micropore diameters in undisturbed soil cores" Geoderma, Vol. 53, 329-340.

Richard A. Ketcham & William D. Carlson (2001) “Acquisition, optimization and interpretation of X-ray computed tomographic imagery: applications to the geosciences” Computers & Geosciences, Vol. 27, 381-400.

Riyadh, A. R. & Khalid A. A. (2005) "Distribution of local void ratio in porous media systems from 3D X-ray micro tomography images" Physica A, Vol. 361, 441-456.

Tollner, E. W., N. D. Melear, L. A. Rodriguez & M. E. Wright. (1998) "Soil Aggregate Size Distributions Using X-Ray Images" Transactions of the American Society of Agricultural Engineers, Vol. 41(4), 1207-1215.

Wong, R. C. K. (2000) "Shear Deformation of locked Sand in Triaxial Compression" Geotechnical Testing Journal, Vol. 23(2), 158-170.

A SIMPLE HYPOPLASTIC MODEL FOR SIMULATING THE MECHANICAL BEHAVIOUR OF MBT WASTE

I. Petrović
Faculty of Geotechnical Engineering, University of Zagreb, Varaždin, Croatia

E. Bauer
Institute of Applied Mechanics, Graz University of Technology, 8020 Graz, Austria

ABSTRACT: *This paper deals with the experimental investigation and numerical simulation of the mechanical behaviour of samples from a "Mechanical Biological Treatment" waste deposit (MBT waste deposit). Laboratory tests with samples of different moisture contents were conducted to determine the basic geotechnical characteristics as well as the stress-strain relations under loading and reloading in a large oedometer with a sample diameter of 50 cm. With respect to a moisture dependent solid hardness, the mechanical behaviour can be well predicted using a hypoplastic constitutive model. As only limited experimental results were available, a simplified hypoplastic model was used. For the calibration of this model it was sufficient to conduct oedometer tests and to use a simple procedure to estimate the angle of friction. The model proved to be satisfactory for modelling the compaction behaviour of MBT waste observed in experiments.*

Key words: *MBT waste, oedometric compaction, hypoplasticity*

1 INTRODUCTION

Waste management is actually one of the most important issues related to the protection of the environment in the Republic of Croatia (Waste Management Plan, 2007). Particular attention is paid to the separation, recycling, transfer, transport and the permanent landfilling of untreated as well as mechanically and biologically treated (MBT) municipal solid waste. This paper deals with the experimental investigation and the numerical simulation of the compaction behaviour of samples from an MBT waste deposit. In particular the results of laboratory investigations of basic geotechnical characteristics as well as stress-strain relations under loading and unloading in a large scale oedometer device with a sample diameter of 0.5 m and a height of 0.2 m are briefly summarized. They show that the values of MBT waste characteristics obtained fall well within the ranges of results published by other authors. It was verified that the material exhibits a strong inelastic behaviour and that its compressibility under oedometric boundary conditions is slightly dependent on the moisture content.

Although MBT waste materials are composed of solid particles with various material properties, for numerical modelling in this paper, the assumption is made that the material can be described like a single component material. In particular a continuum approach is used based on the concept of hypoplasticity. Originally the concept of hypoplasticity was developed to describe the behaviour of granular materials like sand (e.g. Kolymbas, 1991;

Bauer, 1996; Gudehus, 1996; Wu et al., 1996; Niemunis & Herle, 1997; Herle & Gudehus, 1999; Bauer, 2000). Hypoplastic constitutive equations can model a non-linear and inelastic stress strain behaviour taking into account the influence of pressure, density, moisture content and rate of deformation. The model has also been extended to clayey soil (e.g. Huang at al., 2006; Mašin & Herle, 2007) and to a micro-polar continuum (e.g. Tejchman & Bauer, 1996; Gudehus, 1997; Huang & Bauer, 2003; Bauer, 2005). Hypoplastic models have also been applied to solve different boundary value problems (e.g. Gudehus et al., 1997; Henke et al., 2008; Bauer et al., 2010). The constitutive relation used in this paper is a first step to model MBT waste materials using the concept of hypoplasticity. In a similar way as shown for weathered rockfill materials (Bauer, 2009), a moisture-dependent solid hardness is introduced as a key parameter to model the influence of wetting of water-sensitive MBT waste materials on the reduction of the resistance to compaction. As only limited experimental results were available, a simplified hypoplastic version for oedometric boundary conditions was developed, which models the behaviour under loading and unloading. While in the hypoplastic model by Bauer (1996) and Gudehus (1996) the solid hardness is related to the behaviour under isotropic compression, in the present version a solid hardness related to monotonic oedometric compression is considered. Herein, the solid hardness is related to the grain assembly in the sense of a continuum description and does not mean the hardness of an individual grain. Furthermore the assumption is made that for a particular initial moisture content the value of the corresponding solid hardness is kept constant because the change of suction was not recorded during the process of oedometric loading and unloading in the experiments.

Constitutive relations for waste materials have also been investigated by other researchers like for instance by Needham et al. (2007) and Bente et al. (2009). These models usually include the coupling of hydraulic, biodegradation and mechanical behaviour. Even though these models cover a wider range of special problems - unlike the simplified hypoplastic constitutive model, which covers “only” the mechanical behaviour of the solid granular material - it is demonstrated that even with a simplified model satisfactory numerical results can be obtained. Moreover an additional advantage of the simple constitutive model for practical application is the fact that only a few experimental parameters are needed for calibration.

As the hypoplastic concept does not need to distinguish between elastic and plastic deformation, the calibration of the constitutive constants is quite easy. It is demonstrated that for the calibration of the proposed simple hypoplastic model for modelling MBT waste materials it is sufficient to conduct an oedometer test and to use a simple procedure to determine the angle of friction.

2 RESULTS OF THE LABORATORY INVESTIGATION

2.1 Particle size analysis

Figure 1 shows the particle size distribution curve for the air dried MBT waste material considered in the present paper. It can bee seen that the largest particle diameter does not exceed 30 mm and therefore fulfils the requirement that the largest particle diameter should not exceed the 1/5 of the sample height which, for the oedometer used, is 40 mm. Since the fine-grained portion of the waste material is less than 10 %, a particle size analysis using the hydrometer test procedure was not conducted. According to the USCS the MBT waste can be classified as a coarse grained material, as the particle sizes lie in a range between 0.05 and 30 mm. The uniformity coefficient and coefficient of curvature is C_u = 26 and C_c = 1.5,

respectively. Thus the tested MBT waste is a well-graded material and it can be well compacted.

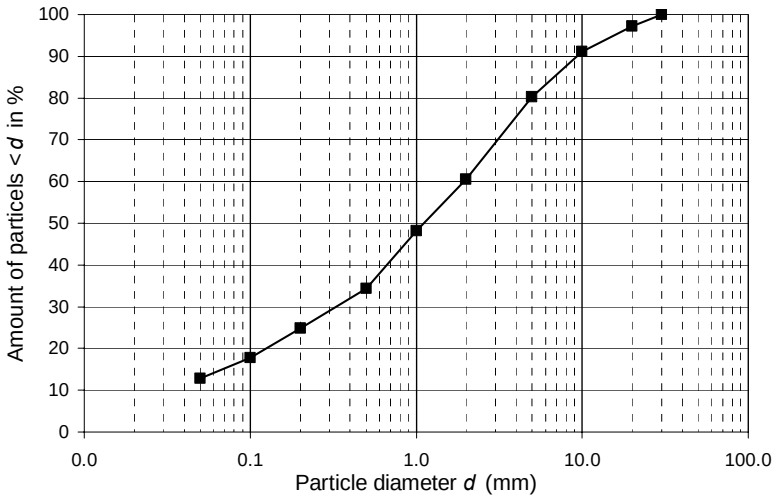

Fig. 1. Particle size distribution curve

2.2 Particle density

The average density of the solid particles, $\rho_{s,}$ was determined according to the ASTM D 854 on the air free samples with maximum particle size of 4.75 mm using a pycnometer of known volume. The particles larger than 4.75 mm were removed by sieving.

2.3 Sample preparation

In the present paper the properties of two MBT waste samples are presented, where Sample A is characterized by an initial moisture content of w = 65 % and Sample B is characterized by an initial moisture content of w = 41 %. In order to obtain a homogenous distribution of moisture content through the whole specimen after mixing with water the wetted samples were left untouched for the next 24 hours. Then the samples were installed in the oedometer cell in five layers. On average, each layer was 4 cm thick and pre-compacted to a defined initial void ratio.

2.4 Oedometric compression tests

The initial pressure obtained from the pressure plate was 4.7 kN/m^2. A sequence of loadings was applied, where the next load step was applied after the consolidation of the preceding loading step. The loading steps are 36, 82 and 180 kN/m^2, followed by unloading to 36 kN/m^2, then reloading to 365 kN/m^2 and finally unloading to 4.7 kN/m^2. Only for Sample A water was squeezed out, so that the moisture content was reduced from 65 % to 41 %. The basic geotechnical parameters for both samples at the beginning of the test and at the end of the test are presented in Table 1 and Table 2, respectively. Herein ρ denotes the density, w the moisture content, ρ_d the dry density, ρ_s the average density of solid particles, e the void ratio and S the degree of saturation. For two loading and two unloading cycles under oedometric condition the relation between the void ratio and the vertical stress is presented for Sample A and Sample B in Figure 2.

Table 1. Basic geotechnical parameters at the beginning of the test

	ρ [kg/m^3]	w [%]	ρ_d [kg/m^3]	ρ_s [kg/m^3]	e_0	S [%]
Sample A	1366	65	828	2147	1.59	88
Sample B	1093	31	834	2147	1.57	42

Table 2. Basic geotechnical parameters at the end of the test

	ρ [kg/m^3]	w [%]	ρ_d [kg/m^3]	ρ_s [kg/m^3]	e_1	S [%]
Sample A	1421	41	1008	2147	1.13	78
Sample B	1389	31	1060	2147	1.03	65

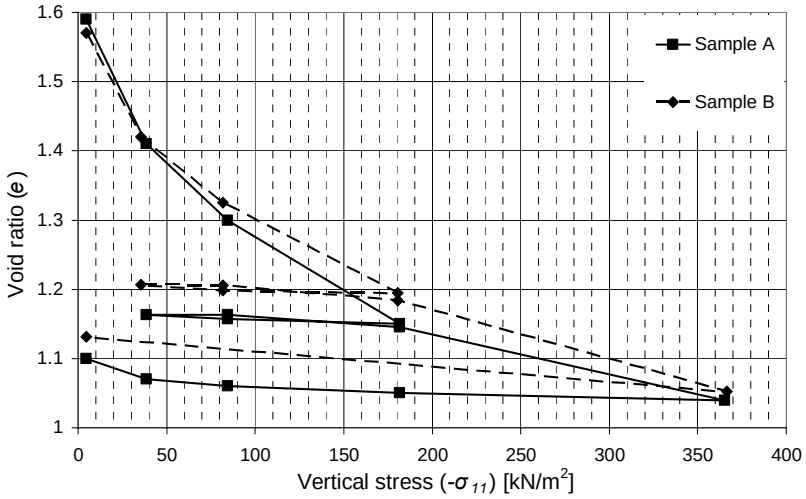

Fig. 2. Stress-strain curves under oedometric condition

It can be seen that the different initial moisture contents do not have a major influence on the stiffness behaviour of the MBT waste. However, a more thorough examination of the curves reveals that up to 200 kPa the influence of moisture content is more pronounced than at the higher pressure values. The change of the void ratio at the beginning of unloading is rather small.

2.5 Friction angle

In order to estimate the critical friction angle φ_c the angle of repose of the dry waste material is determined. The measurements are conducted on two separate samples at the bottom and at the top of the repose in twelve different points. The values measured were as follows: 37^0, 31^0, 31^0, 41^0, 38^0, 38^0, 35^0, 40^0, 41^0, 38^0, 50^0, 43^0. If the highest and lowest values are considered to be unrealistic and are disregarded, then the mean value is 39^0 with a standard deviation of ± 2.45^0. The friction angle of 39^0 is close to the values reported by other researchers, where friction angles for MBT waste materials obtained in direct shear test usually lie within a range between 35^0 and 38^0 (Kuehle-Weidemeier, 2007). A more thorough investigation conducted by Bauer et al. (2009), which was made on MBT materials that originated from three different treatment facilities and different treatment processes with maximum particle sizes of 40 mm to 60 mm, different water content and portions of fibrous

components revealed that the friction angle ranged between 28.1° and 39.8°. It was also observed that a higher water saturation could lead to a reduced shear strength. By contrast it is reported by Bidlingmaier et al. (1999) that the water content has a low influence on the shear properties of the MBT material. As no detailed investigations are available, a critical friction angle of 39^0 is assumed in the present numerical simulations.

3 CONSTITUTIVE MODEL

In order to model the behaviour under oedometric conditions first a relation between the void ratio e and the mean effective pressure p for monotonic compression is considered. In particular, the decrease of e with an increase of p is described by the following exponential function:

$$e = e_0 \exp\left[-\left(\frac{3p}{h_{oe}}\right)^n\right] \tag{1}$$

where the constant e_0 denotes the void ratio for $p \approx 0$, h_{oe} has the dimension of stress and n is a dimensionless constant. It can be noted that function (1) is similar to the approximation function for isotropic compression proposed by Bauer (1996), i.e.

$$e_i = e_{i0} \exp\left[-\left(\frac{3\bar{p}}{h_s}\right)^{\bar{n}}\right] \tag{2}$$

While in the function by Bauer the quantities e_{io}, $\bar{p}$, $\bar{n}$ and h_s are defined for the isotropic compression curve starting from the loosest possible state of the grain skeleton, the parameters e_o, p, n and h_{oe} in Eq. (1) are related to monotonic oedometric compression. Herein the mean pressure reads $p = -(\sigma_{11}+\sigma_{22}+\sigma_{33})/3 = -(1+2K_0)\,\sigma_{11}/3$, where σ_{11} is the vertical stress, $\sigma_{22} = \sigma_{33}$ the lateral stress under zero lateral strain and K_0 denotes the pressure coefficient at rest, i.e. $K_0 = \sigma_{22} / \sigma_{11} = \sigma_{33} / \sigma_{11}$. Usually K_0 is obtained in experiments by measuring the vertical and horizontal stresses simultaneously. As this was not carried out in the experiments conducted, it is necessary to make an estimation for the value of K_0. The most established semi-empirical function in engineering practice is the relation proposed by Jaky (1944), where K_0 is related to the critical friction angle φ_c according to: $K_0 = 1 - \sin\varphi_c$. A comprehensive review of experimental data obtained from different soils, however, shows that K_0 not only depends on the friction angle but also on the current density and the pressure level. Bauer (1997), for instance, reported a remarkable agreement between experiments carried out under different densities and the corresponding predictions with the hypoplastic model proposed by Bauer (1996) and Gudehus (1996). The framework of hypoplasticity is therefore suitable to get an approximation for K_0 and to model the inelastic and non-linear stress strain behaviour under axisymmetric loading and unloading. In particular for oedometric boundary conditions the constitutive equations (3-4) are proposed, which present a simplified version of the hypoplastic model by Bauer (1996) and Gudehus (1996):

$$\dot{\sigma}_{11} = f_{oe}\left\{\hat{a}^2\dot{\varepsilon}_{11} + \hat{\sigma}_{11}\hat{\sigma}_{11}\dot{\varepsilon}_{11} + f_d\hat{a}\left[2\hat{\sigma}_{11} - \frac{1}{3}\right]\sqrt{\dot{\varepsilon}_{11}^2}\right\} \tag{3}$$

$$\dot{\sigma}_{22} = \dot{\sigma}_{33} = f_{oe}\left\{\hat{\sigma}_{11}\hat{\sigma}_{22}\dot{\varepsilon}_{11} + f_d\hat{a}\left[2\hat{\sigma}_{22} - \frac{1}{3}\right]\sqrt{\dot{\varepsilon}_{11}^2}\right\} \tag{4}$$

$$\dot{e} = (1+e)\dot{\varepsilon}_{11} \tag{5}$$

Herein, $\dot{\sigma}_{11}$ is the time derivative of the Cauchy stress σ_{ij}, $\hat{\sigma}_{ij} = \sigma_{ij}/\sigma_{kk}$ are normalized quantities, $\dot{\varepsilon}_{ij}$ is the strain rate, and $\dot{e}$ is the rate of void ratio. Factor $\hat{a}$ is related to the critical friction angle φ_c and for general stress paths $\hat{a}$ also depends on the Lode angle in the deviator plane (Bauer, 2000). For axisymmetric loading paths factor $\hat{a}$ reduces to (Bauer & Herle, 2000):

$$\hat{a} = \sqrt{\frac{8}{3}}\left(\frac{\sin\varphi_c}{3-\sin\varphi_c}\right) \tag{6}$$

In Eq. (3) and Eq. (4) the density factor f_d>0 is related to the limit void ratios as outlined in more detail by Bauer (1996) and Gudehus (1996). In particular f_d<1 holds for a dense material and f_d>1 for a loose material. In the present paper f_d is assumed to be constant. The compression law (1) is embedded in the stiffness factor f_{oe} using the consistency condition for oedometric compression, which leads to the following relation:

$$f_{oe} = \frac{(1+e)}{e}\frac{h_{oe}}{n}\left(\frac{3p}{h_{oe}}\right)^{1-n}\left(\hat{a}^2 + \frac{1}{1+2K_0} - f_d\hat{a}\right)^{-1} \tag{7}$$

Under monotonic oedometric compression the following expression is obtained from Eq. (3) and Eq. (4) for the stress ratio $K_0 = \sigma_{22}/\sigma_{11} = \dot{\sigma}_{22}/\dot{\sigma}_{11}$:

$$K_0 = \frac{1}{1+3\hat{a}/f_d} \tag{8}$$

K_0 in Eq. (8) is also called the pressure coefficient at rest. It depends on the critical friction angle φ_c and the density factor f_d. From Figure 3 it can be seen that Eq. (8) allows a finer adaptation of K_0. In particular higher friction angles φ_c and lower values of the density factor f_d give significantly lower values for K_0 while Jaky's relation is independent of the current density.

The hypoplastic model proposed for MBT waste material includes five constants. Taking into account Eq. (8) for K_0, a critical friction angle of $\varphi_c = 39^0$ and $f_d = 1.1$, the values e_o, h_{oe} and n of the approximation function (1) can be calibrated. A comparison of the results obtained from Eq. (1) with the experiments is shown in Figure 4 for Sample A and Sample B. For the numerical simulations discussed in Section 4 the constants used are presented in Table 3.

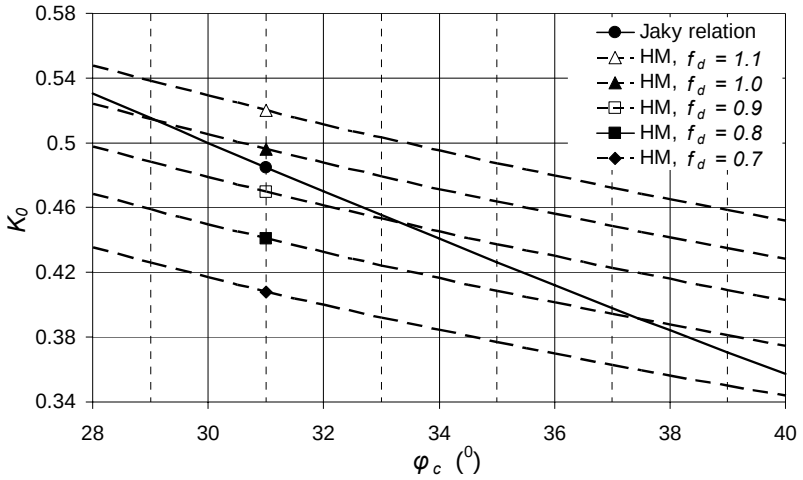

Fig. 3. Comparison of K_0 values obtained with the hypoplastic constitutive model (HM) for different density factor f_d and friction angles φ_c with the function by Jaky (1944).

Table 3. Constants used for numerical simulations

	h_s [kg/m^2]	n	e_0	f_d	φ_c [^{0}]
Sample A	3519	0.389	1.75	1.1	39
Sample B	3772	0.445	1.68	1.1	39

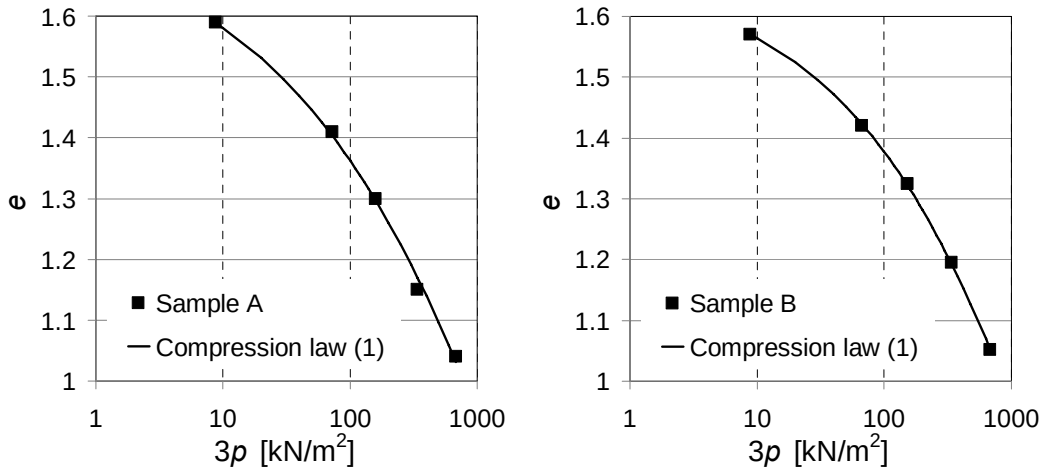

(a) (b)

Fig. 4. Comparison of the oedometric compression relation according to Eq.(1) with the experimental results for: (a) Sample A; (b) Sample B

4 COMPARISON OF NUMERICAL SIMULATIONS WITH EXPERIMENTS

In the following the results obtained from numerical simulations of oedometric compression tests are compared with the corresponding experiments by Petrovic (2010). All simulations are conducted under drained conditions. Figure 5 and Figure 6 show a good agreement between the results obtained from the numerical simulation (solid curve) and the experimental data (dots). Is should be noticed that with the presented hypoplastic model only loading and unloading can be modelled. For the simulation of loading cycles an extension of the constitutive model is needed as proposed for instance by Bauer & Wu (1992), Niemunis & Herle (1997).

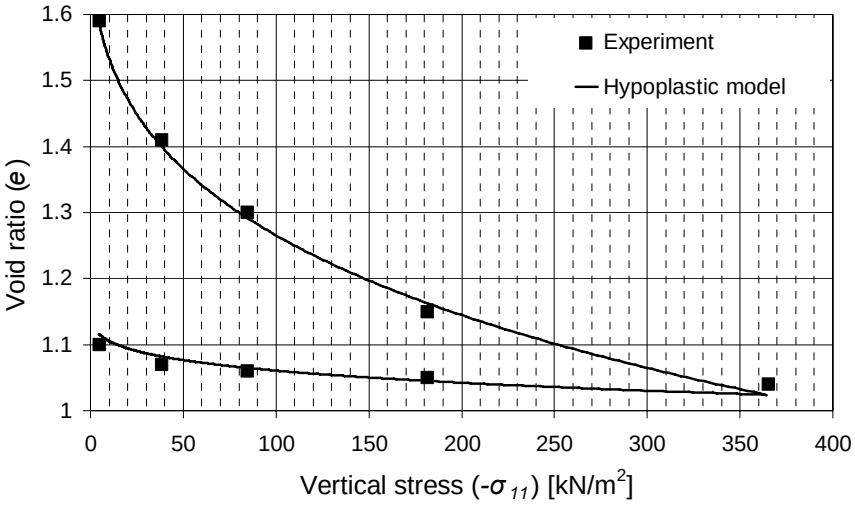

Fig. 5. Oedometric compression and extension of Sample A

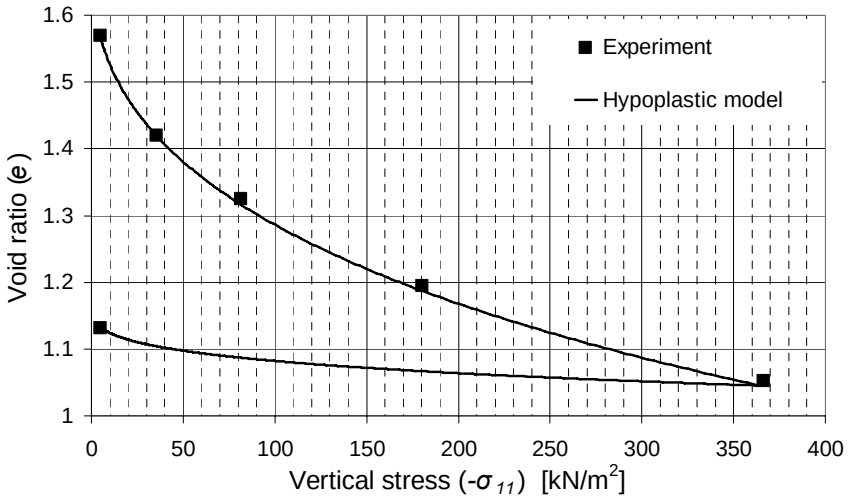

Fig. 6. Oedometric compression and extension of Sample B

ACKNOWLEDGEMENT

The first author acknowledges the financial support given by the Ministry of Science, Education and Sports of the Republic of Croatia for the scientific project "Characterization of municipal solid waste" (project number 160-0831529-3031).

REFERENCES

Bauer, E. & Wu, W. (1992), “A hypoplastic model for granular soils under cyclic loading”, Proc. of the Int. Workshop on Modern Approaches to Plasticity, ed. Kolymbas, Elsevier 1993, 225-245.

Bauer, E. (1996), “Calibration of a comprehensive hypoplastic model for granular materials”, Soils Found., Vol. 36(1), 13-26.

Bauer, E. (1997), “The critical state concept in hypoplasticity”, 9th Int. Conf. on Computer Methods and Advances in Geomechanics, IACMAG 97, Wuhan, China, Balkema press 1997, 691–696.

Bauer, E. (2000), “Conditions for embedding Casagrande’s critical states into hypoplasticity”, Mech. Cohes. Frict. Mater, 5:125-148.

Bauer, E. & Herle, I. (2000), “Stationary states in hypoplasticity”, In: Kolymbas, D. (ed), Constitutive modelling of granular materials, Springer, Berlin, 167-192.

Bauer, E. (2005), “Initial response of a micro-polar hypoplastic material under plane shearing”, J. Eng. Math., 52:35-51.

Bauer, E. (2009), “Hypoplastic modelling of moisture-sensitive weathered rockfill materials”, Acta Geotech., 4:261-272.

Bauer, E., Fu, Z., Liu, S. (2010), “Hypoplastic constitutive modelling of wetting deformation of weathered rockfill materials”, Frontiers of Architecture and Civil Engineering in China, Springer press, 4(1), 78-91.

Bauer, J., Münich, K., Fricke, K. (2009), “Response of MBT residues in large scale triaxial compression tests”, Proceedings Sardinia 2009, Twelfth International Waste Management and Landfill Symposium, S. Margherita di Pula, Cagliari, Italy

Bente, S., Kowalski, U., Dinkler, D., Krase, V. (2009), “Modelling long term settlements of MSW landfills”, Proceedings Sardinia 2009, Twelfth International Waste Management and Landfill Symposium, S. Margherita di Pula, Cagliari, Italy

Bidlingmaier, W., Scheelhaase, T., Maile, A. (1999), “Langzeitverhalten von mechanisch-biologisch vorbehandeltem Restmuell auf der Deponie”, Abschlußbericht zum Teilvorhaben 3.1 des BMBF-Verbundvorhabens „Mechanisch-biologische Behandlun von zu deponierenden Abfaellen“, Universitaet Gesamthochschule Essen, Fachbereich 10 – Bauwesen, Fachgebiet Abfallwirtschaft.

Gudehus, G. (1996), “A comprehensive constitutive equation for granular materials”, Soils Found., Vol 36(1), 1-12.

Gudehus, G. (1997), “Shear localization in simple grain skeleton with polar effect”, Proc. of the 4th Int. Workshop on Localization and Bifurcation Theory for Soils and Rocks, Adachi, T., Oka, F., Yashima, A., Eds., Balkema Publisher 1998, Gifu, Japan, 3-10.

Gudehus, G., Hügel, H.M., Niemunis, A., Pierschke, K. (1997), „Prediction and control of ground displacement due to open pit mining“, Proceedings of 14th international conference on soil mechanics and foundation engineering, Hamburg, Germany, Balkema Press, Rotterdam, 1589-1592.

Henke, S. & Grabe, J. (2008), “Numerical investigation of soil plugging inside open ended piles with respect to the installation method”, Acta Geotech., 3:215-223.

Herle, I. & Gudehus, G. (1999), "Determination of parameters of a hypoplastic constitutive model from properties of grain assemblies", Mech. Cohes. Frict. Mater., 4:461-486.
Huang, W. & Bauer, E. (2003), "Numerical investigations of shear localization in a micro-polar hypoplastic material", Int. J. for Numer. Anal. Meth. Geomech., 27:325–352.
Huang, W., Wu, W., Sun, D., Sloan, S. (2006), "A simple hypoplastic model for normally consolidated clay", Acta Geotech., 1:15-27.
Jaky, J. (1944), "The Coefficient of Earth Pressure at Rest", Journal for Society of Hungarian Architects and Engineers, 355-358.
Kolymbas, D. (1991), "An outline of hypoplasticity", Arch. Appl. Mech., 3:143-151.
Kuehle-Weidemeier, M. (2007), "Geomechanical properties of mechanically and biologically treated municipal solid waste – Review of literature in German language and own investigations", Wasteconsult International, Langenhagen, Germany
Mašin, D. & Herle, I. (2007), "Improvement of a hypoplastic model to predict clay behaviour under undrained conditions", Acta Geotech., 2:261-268.
Needham, A.D., Jones, D.R.V., McDougall, J., Dixon, N., Braithwaite, P., Rosevear, A. (2007), "Assessment of landfill settlement data for evaluation of a hydro-bio-mechanical settlement model", Proceedings Sardinia 2007, Eleventh International Waste Management and Landfill Symposium, S. Margherita di Pula, Cagliari, Italy
Niemunis, A. & Herle, I. (1997), "Hypoplastic model for cohesionless soils with elastic strain range", Mech. Cohes. Frict. Mater., Vol. 2(4), 279-299.
Petrović, I., Szavits-Nossan, V., Štuhec, D. (2010), "Preliminary laboratory testing of mechanically and biologically pretreated municipal solid waste for large odometer" Građevinar, accepted for publishing
Petrović, I., Szavits-Nossan, V., Kovačić, D. (2010), "Stiffness, consolidation and permeability properties of mechanically and biologically pretreated municipal solid waste", Građevinar, accepted for publishing
Tejchman J. & Bauer E. (1996), "Numerical simulation of shear band formation with a polar hypoplastic model", Computers and Geotechnics, Vol. 19(3), 221-244.
Waste Management Plan of the Republic of Croatia for the period 2007.-2015., Official Gazette of the Republic of Croatia, No. 85/07.
Wu, W., Bauer, E., Kolymbas, D. (1996), "Hypoplastic constitutive model with critical state for granular materials", Mechanics of Materials, Vol 23, 45-69.

ASSUMED ENHANCED STRAIN METHOD FOR MULTISCALE LOCALIZATION MODELING IN GRANULAR MEDIA

Qiushi Chen
Division of Engineering and Applied Science, California Institute of Technology, Pasadena, CA, USA

José E. Andrade
Division of Engineering and Applied Science, California Institute of Technology, Pasadena, CA, USA

ABSTRACT: *This work presents a multiscale strong discontinuity approach to tackle key challenges in modeling localization behavior in granular media: accommodation of discontinuities in the kinematic fields, and direct linkage to the underlying grain-scale information. Assumed enhanced strain (AES) concepts are borrowed to enhance elements for post-localization analysis, but are reformulated within a recently-proposed hierarchical multiscale computational framework. Unlike classical AES methods, where material properties are usually constants or assumed to evolve with some arbitrary phenomenological laws, this framework provides a bridge to extract evolutions of key material parameters, such as friction and dilatancy, based on grain scale computational or experimental data. More importantly, the phenomenological softening modulus typically used in AES methods is no longer required. Numerical examples of plane strain compression tests are presented to illustrate the applicability of this method and to analyze its numerical performance.*

1 INTRODUCTION

Failure in granular materials is often accompanied by highly localized deformations, i.e., large strains occurring over a narrow zone. Macroscopic detection of localization phenomena is relatively well understood and its modeling has been cast within the finite element method, e.g., (Borja & Andrade 2006). However, advancement of solutions beyond the localization point remains a challenge in computational mechanics due to (1) discontinuities in some kinematical fields (e.g., displacements or strains) in a deforming body; (2) the missing linkage to the underlying grain structures and particle interactions when modeling localization behavior in granular materials.

To tackle the first challenge, failure kinematics related to localization bands are approximated by means of discontinuous displacement fields embedded within the finite elements undergoing localization. In particular, the AES method, e.g., (Simo & Rifai 1990; Simo et al. 1993), will be borrowed to enhance elements for post-localization analysis. The AES method requires no additional global degrees of freedom and is insensitive to mesh refinement and alignment.

A major drawback afflicting AES method is the lack of proper material description within the band. Most implementations use simple constitutive formulations with constant material parameters, such as the friction coefficient. Moreover, some form of softening law, requiring softening moduli selected arbitrarily and *a priori*, is generally required. To overcome this drawback, we

exploit the multiscale nature of granular materials and establish the missing linkage to grain-scale information. The AES method will be reformulated within a recently proposed multiscale framework (Andrade & Tu 2009; Tu et al. 2009; Andrade et al. 2010). The evolutions of material parameters in the AES method could be provided based on the grain scale information. More importantly, phenomenological softening moduli are no longer required.

2 DISCONTINUOUS KINEMATICS AND CONSTITUTIVE EQUATIONS FOR THE AES METHOD

In the AES method, the discontinuous displacement field is decomposed into a continuous part and a discontinuous part as

$$\boldsymbol{u}(\boldsymbol{x}) = \underbrace{\bar{\boldsymbol{u}}(\boldsymbol{x})}_{\text{continuous}} + \underbrace{(H_{\mathcal{S}}(\boldsymbol{x}) - f^h(\boldsymbol{x}))[\![\boldsymbol{u}]\!](\boldsymbol{x})}_{\text{discontinuous}} \tag{1}$$

where $[\![\boldsymbol{u}]\!](\boldsymbol{x})$ is the displacement jump. $H_{\mathcal{S}}(\boldsymbol{x})$ is the heaviside function defined on the discontinuity surface $\mathcal{S}$, and $f^h(\boldsymbol{x})$ is any arbitrary smooth function that is one on the positive side, and zero on the negative side of the domain split by the discontinuity surface. Positive side refers to the side of the domain pointed by the outward normal of the discontinuity surface.

For infinitesimal deformations, the total strain rate tensor is written as,

$$\dot{\boldsymbol{\epsilon}} = \nabla^{\mathrm{s}}\dot{\boldsymbol{u}} = \nabla^{\mathrm{s}}\dot{\tilde{\boldsymbol{u}}} - ([\![\dot{\boldsymbol{u}}]\!] \otimes \nabla f^h)^{\mathrm{s}} + \delta_{\mathcal{S}}([\![\dot{\boldsymbol{u}}]\!] \otimes \boldsymbol{n})^{\mathrm{s}} \tag{2}$$

where $\delta_{\mathcal{S}}$ is the Dirac delta function.

Decomposing the displacement jump rate $[\![\dot{\boldsymbol{u}}]\!]$ into its magnitude $\dot{\xi}$ and direction vector $\boldsymbol{m}$ we obtain

$$[\![\dot{\boldsymbol{u}}]\!] = \dot{\xi}\boldsymbol{m} \tag{3}$$

If we assume that plasticity is localized to the discontinuity surface, and make use of the consistency condition on the band, we obtain the Cauchy stress rate tensor, at the post-localization stage as

$$\dot{\boldsymbol{\sigma}} = \tilde{\boldsymbol{c}}^{EP} : \nabla^s\dot{\tilde{\boldsymbol{u}}} \tag{4}$$

where $\tilde{\boldsymbol{c}}^{EP}$ is the equivalent elastoplastic tangential modulus with the presence of displacement jumps and is given as

$$\tilde{\boldsymbol{c}}^{EP} = \boldsymbol{c}^E - \frac{\boldsymbol{c}^E : (\boldsymbol{m} \otimes \nabla f^h)^s \otimes \boldsymbol{\psi} : \boldsymbol{c}^E}{\boldsymbol{\psi} : \boldsymbol{c}^E : (\boldsymbol{m} \otimes \nabla f^h)^s + \tilde{H}_\delta}, \quad \boldsymbol{\psi} = \frac{\partial F}{\partial \boldsymbol{\sigma}} \tag{5}$$

where F is the yield surface at post-localization stage and $\tilde{H}_\delta$ is the softening modulus. Currently in the AES method, constant material properties are usually assumed *a priori* and selection of values are quite arbitrary. To overcome this, we will resort to the multiscale nature of granular materials and linking the underlying grain-scale information with the continuum scale AES method.

3 AES FOR MULTISCALE FRAMEWORK

In this section, the standard AES method will be reformulated within a recently-proposed multiscale framework for granular materials, see (Andrade & Tu 2009; Tu et al. 2009) for more details. The most salient difference between the algorithm presented herein and that in the standard AES formulation is that the softening modulus H_δ is no longer required in the current framework. Moreover, the evolutions of the plastic internal variables will be extracted from the grain-scale information, instead of assuming their values *a priori*.

3.1 HIERARCHICAL MULTISCALE FRAMEWORK

At continuum description, we consider the classical two-invariant Drucker-Prager (D-P) model, where the yield function F and the plastic potential function G can be defined as

$$F(\boldsymbol{\sigma}, \mu) = q + \mu p = 0 \tag{6}$$

$$G(\boldsymbol{\sigma}, \beta) = q + \beta p \tag{7}$$

where $p = 1/3\text{tr}\boldsymbol{\sigma}$ and $q = \sqrt{3/2}||(\boldsymbol{\sigma} - p\boldsymbol{\delta})||$ are the two stress invariants. Two plastic internal variables are involved in the D-P model: the friction coefficient μ and the dilatancy parameter β. Physically, μ directly represents the mobilized friction angle of granular materials. At yielding, μ takes the form

$$\mu = -\frac{q}{p} \tag{8}$$

The dilatancy parameter β measures the change in volumetric plastic deformation for a given change in deviatoric plastic deformation. Specifically,

$$\beta = \frac{\dot{\epsilon}_v^p}{\dot{\epsilon}_s^p} \approx \frac{\dot{\epsilon}_v}{\dot{\epsilon}_s} \tag{9}$$

where, in approximation, the elastic strain increments are neglected. This is a plausible approximation once plasticity dominates the deformation, which is the case for most granular materials after yielding.

In standard AES, material properties, such as the aforementioned plastic internal variables, are usually assumed to be constant or to evolve with some arbitrary phenomenological relation. Moreover, an additional softening modulus H_δ is typically required so that the softening behavior after localization is captured. Within the multiscale framework, however, we exploit the physical significance of the plastic internal variables to extract them directly from grain-scale information available from DEM calculations or data from physical experiments.

Once evolutions of the plastic internal variables are fully defined, they will be used hierarchically as the calculations are coarsened or upscaled to the continuum scale. One of the key features of this multiscale framework is that the plastic internal variables are "frozen" within each time step, and only updated when global convergence is achieved.

3.2 STRESS INTEGRATION ALGORITHM FOR AES WITHIN THE MULTISCALE FRAMEWORK

As mentioned in the previous section, within each time step, the plastic internal variables are "frozen", and are only updated at global convergence. Therefore, the integration algorithm at each material point is analogous to that of a perfect plasticity model. Because of the delay in updating the plastic internal variables, the consistency condition is no longer enforced when integrating stresses. Instead, the yielding condition $F_{n+1} = 0$ will be enforced.

To compute the stress state at time t_{n+1}, we will start with the rate form of the Cauchy stress. In AES formulation, the Cauchy stress rate is given as

$$\dot{\boldsymbol{\sigma}} = \dot{\boldsymbol{\sigma}}^{\text{tr}} - \dot{\xi}\boldsymbol{c}^E : (\boldsymbol{m} \otimes \nabla f^h)^s, \quad \dot{\boldsymbol{\sigma}}^{\text{tr}} = \boldsymbol{c}^E : \nabla^s \dot{\boldsymbol{u}} \tag{10}$$

where $\dot{\boldsymbol{\sigma}}^{\text{tr}}$ is the trial stress rate. Integrating equation (10) from t_n to t_{n+1}, we obtain

$$\boldsymbol{\sigma}_{n+1} = \boldsymbol{\sigma}_{n+1}^{\text{tr}} - \Delta\xi\boldsymbol{c}^E : (\boldsymbol{m} \otimes \nabla f^h)^s \tag{11}$$

where $\boldsymbol{\sigma}^{\text{tr}}_{n+1}$ is the trial stress at time t_{n+1} and is written as

$$\boldsymbol{\sigma}^{\text{tr}}_{n+1} = \boldsymbol{\sigma}_n + \boldsymbol{c}^E : \left(\nabla \bar{\boldsymbol{u}}^h_{n+1} - \nabla \bar{\boldsymbol{u}}^h_n\right)^s \tag{12}$$

As mentioned before, yielding condition on the band is enforced instead of the consistency condition, such that,

$$F_{n+1} = F(\boldsymbol{\sigma}_{n+1}, \mu_n) = 0 \tag{13}$$

Note that the plastic variable μ is held at its value at the previous time step t_n, resulting in a delayed update. The integration algorithm is based on finding the stress state $\boldsymbol{\sigma}_{n+1}$ so that equations (11) and (13) are satisfied.

4 NUMERICAL EXAMPLE

In this section, we present a numerical example coupling AES with experiment to illustrate the applicability of the reformulated AES method within the hierarchical multiscale framework. Coupling of AES with DEM computation is carried out by the authors as well and will be shown in future publication. In the current example, the evolutions of plastic internal variables are extracted directly from a well-instrumented physical experiment. Different meshes are generated to demonstrate the objectivity of this framework with respect to mesh refinement and insensitivity to mesh alignment.

The experiment was performed by (Mooney et al. 1998) using a well-instrumented device. The sample dimensions are 140 x 40 x 80 mm. Plane strain is enforced by two rigid walls, in the 80 mm direction. The sample was initially consolidated anisotropically with axial stress $\sigma_a = -210$ kPa, and lateral stress $\sigma_r = -105$ kPa. After consolidation, lateral stress is kept constant while the top plate moves down under displacement control. A localization band inclined at 63^{o} from the horizontal axis was observed when the global axial strain reached about 3%. Dilation angle ψ within the band was extracted using stereophotogrammetry, shown as red circles in Figure 1. The dilation angle will be related to dilatancy parameter by $\beta = \tan\psi$. Since there is no local measurement of either forces or stresses, the friction parameter μ can not be obtained directly from the experimental measurements. Instead, the stress-dilatancy relationship $\mu = \beta + \mu_{\text{cv}}$ is used. In this study, $\mu_{\text{cv}} = 1.15$ is obtained from the experimental results.

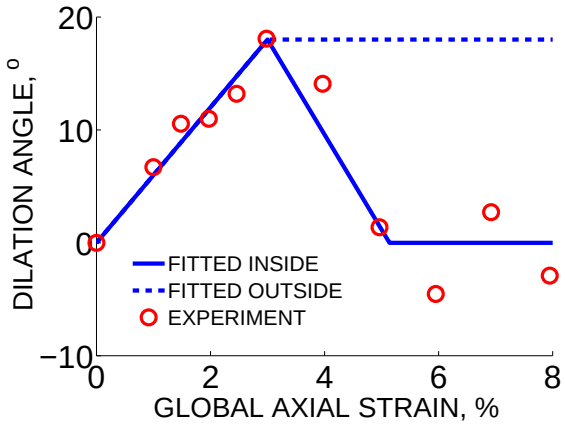

Fig. 1. Evolution of dilation angle observed in the experiment.

In the simulation, all elements are provided with the same evolution of dilation angle up to 3% global axial strain. Once localization is reached, elements crossed by the localization band

will be equipped with enrichment using the AES concept. The evolution of the dilation angle for those enhanced elements will be given by the solid line in Figure 1. The dashed line on the figure represents elements outside the localization band. Since the sample unloads elastically outside the band, the assumption of a constant dilation angle will not affect the results.

To illustrate the mesh-insensitive feature of the method, four different meshes are used. Figure 2 shows the evolution of the stress ratio $-q/p$ for both simulation and experiment, where the values from the simulation correspond to the global averaged stresses. It is clear that the multiscale simulation captures the global stress response remarkably well. Also, it should be mentioned that four different meshes produce identical results.

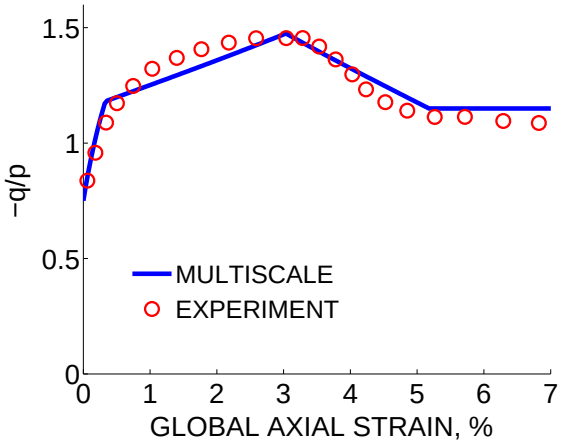

Fig. 2. Evolution of stress ratio with global axial strain.

To show that the model can capture the deformation modes observed in the experiment, we compare the computed local lateral strain with the experiment data, as shown in Figure 3. "Upper" or "lower" means that the lateral strain was computed/measured above or below the localization band. From both simulation and experiment results, it can be seen that the mechanical behavior in the "upper" and "lower" block differ significantly. Once localization occurs, the upper part of the sample will slide, inducing large amount of lateral strain, while the lower part remains almost rigid and intact. Again, four meshes give identical results.

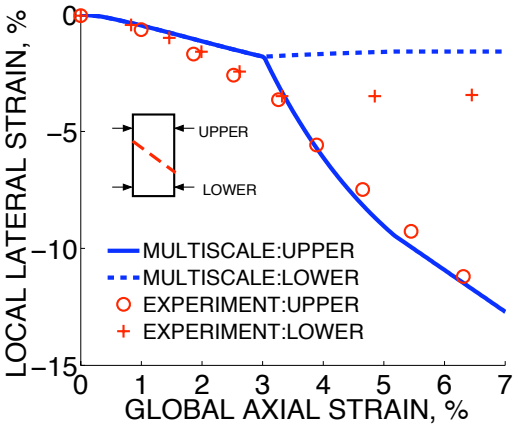

Fig. 3. Lateral strain vs. axial strain.

The deformed meshes at 7% global axial strain are plotted in Figure 4. The modes of deformation for all meshes are practically identical and all meshes propagate successfully to the end of the simulation, demonstrating the applicability of the framework to incorporate experimental data directly.

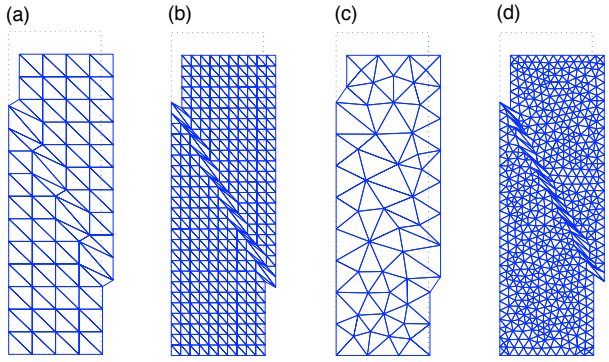

Fig. 4. Deformed samples for plane strain simulations.

5 CONCLUSIONS

We have presented a reformulated AES method within a hierarchical multiscale framework for modeling localization behavior in granular materials. A key feature of this framework is that, instead of constant or phenomenologically varied material properties typically used in standard AES methods, evolutions of material properties are extracted from grain scale computations or experimental data and used as direct input for the underlying continuum model. More importantly, the softening modulus, which appears in standard AES formulations, is bypassed. The stress-point integration algorithm is similar to the classical elastic-perfectly plastic model, resulting in a simple yet powerful method. Numerical example of plane strain compression test, coupling the AES method with experimental data, demonstrate the applicability of this method. The mesh objectivity and numerical efficiency of this method are also shown in the numerical examples.

ACKNOWLEDGEMENTS

Support for this work is provided by AFOSR grant number FA9550-08-1-1092. This support is gratefully acknowledged.

REFERENCES

Andrade, J., Avila, C., Hall, S., Lenoir, N., & Viggiani, G. (2010). Multiscale modeling and characterization of granular matter: from grain kinematics to continuum mechanics. *Journal of the Mechanics and Physics of Solids, in revision*.

Andrade, J. & Tu, X. (2009). Multiscale framework for behavior prediction in granular media. *Mechanics of Materials 41*(6), 652–669.

Borja, R. & Andrade, J. (2006). Critical state plasticity, part vi: Meso-scale finite element simulation of strain localization in discrete granular materials. *Computer Methods in Applied Mechanics and Engineering 195*, 5115–5140.

Mooney, M. A., Finno, R. J., & Viggiani, M. G. (1998). A unique critical state for sand? *Journal of Geotechnical and Geoenvironmental Engineering 124*, 1100–1108.

Simo, J., Oliver, J., & F.Armero (1993). An analysis of strong discontinuities induced by strain-softening in rate-independent inelastic solids. *Computational Mechanics 12*, 277–296.

Simo, J. & Rifai, M. (1990). A class of mixed assumed strain methods and the method of incompatible modes. *International Journal for Numerical Methods in Engineering 29*, 1595–1638.

Tu, X., Andrade, J., & Chen, Q. (2009). Return mapping for nonsmooth and multiscale elastoplasticity. *Computer Methods in Applied Mechanics and Engineering 198*, 2286–2296.

MODELING OF LANDSLIDES WITH A FINITE ELEMENT METHOD WITH LAGRANGIAN INTEGRATION POINTS

N. Prime, F. Dufour, F. Darve
Grenoble-INP, UJF-Grenoble 1, CNRS UMR 5521, 3SR Grenoble F-38041, France.

ABSTRACT: *The Finite Element Method with Lagrangian Integration Point (FEMLIP) is a particular numerical method initially developed for viscous flow study. The dissociation between the computational grid and the material points allows not only to describe the displacement of material without mesh distortion, but also to store history variables pertaining to the material point, such as plastic strains or elastic stress.*
The implementation of elasticity and plasticity in FEMLIP makes the modeling of solid like and fluid like behavior possible, and thus makes it suitable for modeling of landslides with its two main phases: the solid phase before failure and the fluid like movement after failure. The choice of the plastic constitutive relation ("plasol" model) has been made to describe both hardening and non associativity of the plastic flow. An example of an embankment simulation is presented in order to compare the results of the FEMLIP and a classical FEM for small displacements. The results show that the elasto-plastic behavior is consistent, and it underlines the ability and robustness of the method when failure state has been reached.

1 INTRODUCTION

Landslides are phenomena which can occur in different scales. In their larger form, they can be disasterous in term of human losses and structural damage (for example: landslides of Campania-Italy, 1998, Shaanxi-China, 2006, Angora Dos Reis-Brazil, 2010). They represent thus a strong societal issue in which the engineer is required to predict possible failure and consequences there of. That's why numerical models play an important role as they are helpful to anticipate the onset of instability, predict the volume of the flow, and estimate the impact loading on obstacles.

In this paper, a new numerical method well suited to model landslides will be presented. Its main characteristic is the ability to consider a continuous material evolution from its failure to flow and finally coming to a stop.

2 THE FINITE ELEMENT METHOD WITH LAGRANGIAN INTEGRATION POINTS (FEMLIP)

2.1 Requirements for the numerical method to use

To describe a landslide as a whole phenomenon, from failure in in-situ soils, to the flow along a given slope (which can be perceived as a disorganized but continuous material as in mudflows), the change in the behaviour of the soil needs to be taken into account. Thus, two forms of the material can be distinguished: an initial and stable form which can be related to a solid, and then, after an external perturbation which leads the material to lose its stability- a state that better corresponds to a viscous flow.

According to that, what are the requirements for a numerical method to model the entire phenomenon? On one hand, it must be able to solve solid mechanics problems with internal

variables necessary to model both elasticity and plasticity (elastic stress and plastic strains), and on another hand to solve fluid issues in large transformations. A third necessity would be the importance of the follow-up of interfaces, all along the landslide: to locate accurately the free surface of the ground and the possible failure localization, and to consider the interaction between the flow and structures.

2.2 Limits of the classical numerical methods

From these requirements, let's try to see if the classical numerical methods could be used in this particular context.

The Eulerian FEM works with a fixed mesh and track material properties using advection equations. This method is classically used for fluid problems based on velocity field. However, it is troublesome to accurately follow material internal variables and material interfaces. For these reasons, this method is not suitable to model neither the triggering of the instability in the solid (small perturbations) nor the flow of complex materials with a free surface. On the other hand, the Lagrangian FEM would be able to model the initial elasto-plastic behavior with the required internal variables, but not the subsequent flow because of the distortion of the mesh associated to the large deformation of the material. Finally, with the Discrete Element Method all requirements are satisfied. Nevertheless, creating a model which represents a whole natural slope as an assembly of grains would involve extremely large comutational cost.

2.3 Basis of the FEMLIP

These needs force us to look for a more versatile method. Among many methods developed to study landslides (SPH, Pastor et al., 2009, PFEM, Oñate et al. 2008) the chosen one for the present work is a method initially developed for the study of fluid convection in the Earth mantle: the Finite Element Method with Lagrangian Integration Points (FEMLIP) (Moresi et al, 2003 and Dufour, 2002).

FEMLIP is a finite element method based on the dissociation between the material points and the grid used for space discretization. The FE mesh is Eulerian and the set of material points used in the integration process is Lagrangian. Their velocity is interpolated from the nodal velocity. By this way, it benefits both from the ability of the Eulerian FEM to support any fluid like transformation, and from the possibility of the Lagrangian FEM to track internal variables during the material movement. Similarly, as the properties are carried by the moving integration points, material interfaces are accurately known at any time. The following figure illustrates this principle with a view of the integration points of two materials - in light and dark color- moving through a fixed mesh accounting for interfaces

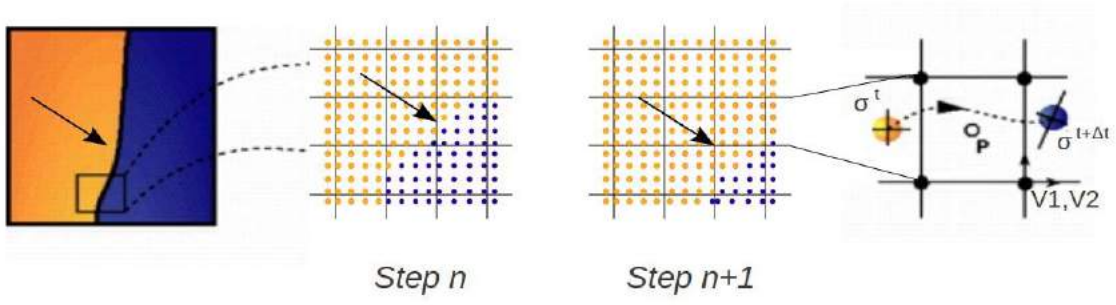

Fig.1. Illustration of the dissociation of the mesh and the integration points for a given configuration

3 THE CONSTITUTIVE RELATIONS IMPLEMENTED

3.1 Requirements for the constitutive relation

As mentioned before, the triggering of landslides occurs in in-place soils, usually considered as a solid which behavior can be represented by an elasto-plastic constitutive relation. Then the material flow induces a viscous component to be considered.

As the FEMLIP has been first used to model the mantle convection, the codes are based on viscous equations. Afterwards it has been developed to model geomaterials like fresh concrete and therefore elasticity has been added to the viscous component (Moresi et al., 2002; Moresi et al., 2003). Besides, anisotropy and Cosserat models have been added to model layered and granular materials (Mühlhaus et al., 2002). As plasticity is required in the landslides initiation phase, the constitutive relation named *Plasol* (Barnichon, 1998) has been implemented. It can describe non-associated plastic flow.

Furthermore, it has to be underlined that the plastic failure criterion is not always sufficient to detect soil instabilities, especially for diffuse failures which can appear before the Mohr-Coulomb plastic limit condition (as in the cases of landslides with a small slope angle). A more general criterion has to be used for those cases: the second order work criterion (Darve and Laouafa, 2000; Laouafa and Darve, 2002). This criterion, initially proposed by R. Hill (1958), has the following expression in its normalized form:

$$dW_2 = \frac{d\sigma_{ij} d\varepsilon_{ij}}{\left\| d\sigma_{ij} \right\| \left\| d\varepsilon_{ij} \right\|} > 0 \qquad \forall \left\| d\varepsilon \neq 0 \right\| \tag{1}$$

3.2 Implementation of the visco-elastic constitutive relation

The balance equation can be written this way (isotropic and deviatoric parts of the stress tensor, respectively p and $\underline{\underline{s}}$, are always considered separately in the code because of the possibility to have an incompressible fluid):

$$(s)_{ij,j} + (p)_{,i} + (f_{ext})_i = 0 \tag{2}$$

From (eq. 2) and a basic viscous constitutive relation, the equation to be solved can be written as follows:

$$2\eta (D_{dev})_{ij,j} + K_v (trD)_{,i} + (f_{ext})_i = 0 \tag{3}$$

(η is the viscosity, K_v is the bulk modulus in viscosity, $\underline{\underline{D}}$ is the strain rate tensor, $\underline{\underline{D_{dev}}}$ its deviatoric part, and $\underline{f_{ext}}$ the external force vector applied.)

In visco-elasticity, viscous and elastic strain rates can be summed, which leads to developed expressions of the stresses. Their integration into the balance equation (eq. 2) gives a new equation of the problem (Dufour, 2002), similar to the viscous one (eq. 3):

$$2\eta_{eff} \left(\left(D^{t+\delta te} \right)_{dev} \right)_{ij,j} + K_{v\,eff} \left[tr \left(D^{t+\delta te} \right) \right]_{,i} + (f_{ext})_i + \left(f_{élastique} \right)_i = 0 \tag{4}$$

($\eta_{eff} = \eta \dfrac{\delta t_e}{T + \delta t_e}$ and $K_{v\,eff} = K_v \dfrac{\delta t_e}{T + \delta t_e}$ are the effective viscosity and viscous bulk modulus respectively, taking into account a unique relaxation time $T = \dfrac{\eta}{\mu} = \dfrac{K_v}{K_e}$ for both the deviatoric and the isotropic behaviour. δt_e is the time interval on which the time derivatives have been linearized)

Finally the implementation of viscoelasticity did not change the form of the equations, but only changes the viscosity and bulk viscosity variables, taking into account the timestep, and adds a new force term linked to the previous stress state.

3.3 Implementation of the visco-elasto-plastic constitutive relation

The plastic component of the constitutive relation is introduced in the same manner. First, the sum of the viscoelastic strain rates gives, for the deviatoric equation (to simplify the isotropic equations will not be presented here, but the principle is the same):

$$\left(\left(D_{ve}\right)_{dev}\right)_{ij} = \left(\left(D_{tot}\right)_{dev}\right)_{ij} - \left(\left(D_{pl}\right)_{dev}\right)_{ij} = \frac{s_{ij}}{2\eta} + \frac{\hat{s}_{ij}}{2\mu} \tag{5}$$

(Index *'tot'* refers to the total tensor, whereas *'ve'* and *'pl'* refer to the the visco-elastic and the plastic ones. $\underline{\underline{\hat{s}}}$ is the Jaumann derivative of $\underline{\underline{s}}$, μ is the second elastic Lamé coefficient.)

After linearizing the time derivative of the stress on a small timestep δt_e, the stress $\underline{\underline{s}}$ can be written at $t+\delta t_e$:

$$\left(s^{t+\delta te}\right)_{ij} = 2\eta_{eff}\left(\left(D_{tot}^{t+\delta te}\right)_{dev} - \left(D_{pl}^{t+\delta te}\right)_{dev}\right)_{ij} + \eta_{eff}\frac{\left(s^{t}\right)_{ij}}{\mu\delta t_e} + \eta_{eff}\frac{\left(\left(\omega^{t}.s^{t}\right)_{ij} - \left(s^{t}.\omega^{t}\right)_{ij}\right)}{\mu} \tag{6}$$

Where $\underline{\underline{\omega}}$ is the rotation tensor.

By gathering all the terms depending on the previous timestep, and all the terms depending on the plastic strain rate, and considering them respectively as an elastic and a plastic force term, a new equation to solve can be written:

$$2\eta_{eff}\left(\left(D_{tot}^{t+\delta te}\right)_{dev}\right)_{ij,j} + K_{v\,eff}\left[tr\left(D_{tot}^{t+\delta te}\right)\right]_{,i} + \left(f_{ext}\right)_i + \left(f_{élastique}\right)_i + \left(f_{plastique}\right)_i = 0 \tag{7}$$

Comparing it to the basic viscous formulation (eq. 3), it appears that introducing plasticity in the code changes nothing in the structure of equations but the force term, which now takes into account the plastic strains.

3.4 The plastic constitutive relation 'Plasol'

The Plasol constitutive model is well suited for geomaterials: on one hand the plastic failure criterion is of Van Eekelen type, which is close to the Mohr Coulomb one with no singularity, and on another hand the plastic potential is not necessarily superposed with the yield criterion It is thus possible to describe non-associated material as soils. The plastic criterion can be written as:

$$F = J_{2\sigma} + m\left(J_{1\sigma} - \frac{3c}{\tan\varphi_c}\right) = 0 \quad \text{with} \quad m = a\left(1 + b\sin 3\theta\right)^n \quad \text{and} \quad \sin 3\theta = -\left(\frac{3\sqrt{3}}{2}\frac{J_{3\sigma}}{J_{2\sigma}^{\,3}}\right) \tag{8}$$

($J_{1\sigma}$, $J_{2\sigma}$ et $J_{3\sigma}$ are the three invariants of the Cauchy stress tensor, φ_e and φ_c are the friction angles in extension and compression, c the cohesion, n a dimensionless constant usually taken as -0.229, a and b are functions of φ_e and φ_c.)

The influence of θ in the equation induces that the trace of the criterion in the deviatoric plane is not a circle but depends on the direction considered (fig. 2).

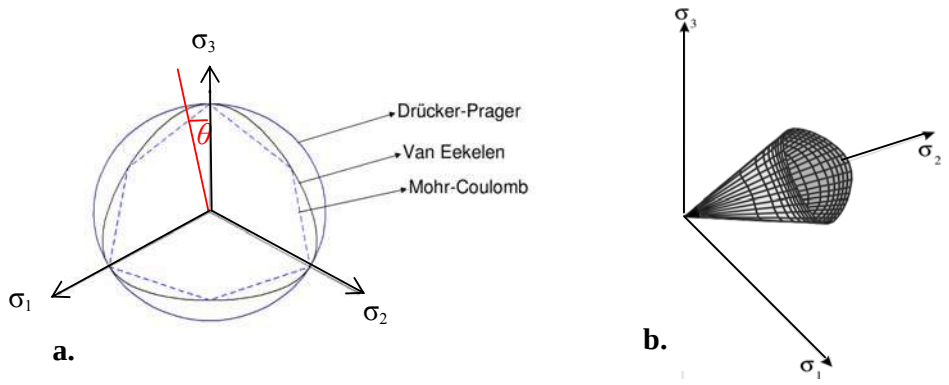

Fig.2. Van Eekelen criterion in the deviatoric plane (a), in the principal stress space (b) (Barnichon, 1998)

Along the loading path in the plastic domain, c, φ_e and φ_c vary between a minimum and a maximum according to the equivalent plastic strain stored on the integration points. The two extremes of the criterion F define the elastic (or yield) limit and the plastic limit criterion.

4 EXAMPLE OF A VERTICAL EMBANKMENT OF COHESIVE MATERIAL

The example presented here has not be chosen to be really representative of landslides in this first attempt, but to compare the calculus made with the FEMLIP with another more usual FEM. The aim is to understand the limitations of the classical FEM at a certain loading state, and to introduce the need of a transition in the constitutive relation.

4.1 Description of the model

The geometry and boundary conditions of the model are presented in the figure 3. The base nodes are fixed whereas the side ones are free slip. The mesh is made by 1x1 squares.

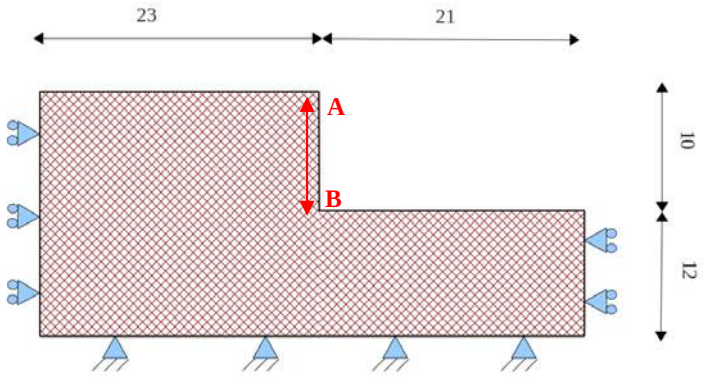

Fig.3. Geometry and BCs of the model

The gravity is increased in 10 steps up to 9.81. The soil properties are presented in table 1:

Table 1. Mechanical parameters of the soil

General parameters	Viscous parameters		Elastic parameters		Plastic parameters			
Dens. (kg/m^3) ρ	Visc. (Pa.s) η	Bulk Visc. (Pa.s) K_v	Young mod. (Pa) E	Poisson ratio ν	Cohe. (Pa) $c_o=c_f$	Fric. ang.(°) $\varphi_{co}=\varphi_{cf}$ $\varphi_{eo}=\varphi_{ef}$	Dilat. ang. (°) $\psi_{co}=\psi_{cf}$ $\psi_{eo}=\psi_{ef}$	Hard. param. B_c B_φ
1800	1.7e11	4.2e12	5,000,000	0.48	51,480	0.1 0.1	0.1 0.1	0.02 0.01

Given that the code is based on viscous equations, the viscosity input data is necessary to be given. Nevertheless, such a high value of it induces that the relaxation time is quasi infinite and the constitutive relation can be assimilated to an elasto-plastic one. The model is thus in a context of landslide initiation with no viscous flow.

With the present value of cohesion, the limit equilibrium method gives a safety factor of exactly 1.1. The embankment should thus be stable. Besides, the initial and final internal variables are the same, that is to say there is no hardening. Considering this last hypothesis, the FEMLIP results can be compared with those of a classical FEM, as Abaqus, with an elastic perfectly-plastic constitutive relation. The models are thus built identically in Abaqus and in the FEMLIP code, except that the plastic criterion is the Mohr-Coulomb one instead of the Van Eekelen one in Abaqus (but these criterion are close according to the figure 2).

4.2 Results with c=51,480 Pa: comparison of the mechanical behavior

The graphs in figure 4 represent the horizontal displacement calculated with both methods along the vertical profile AB presented in figure 3.

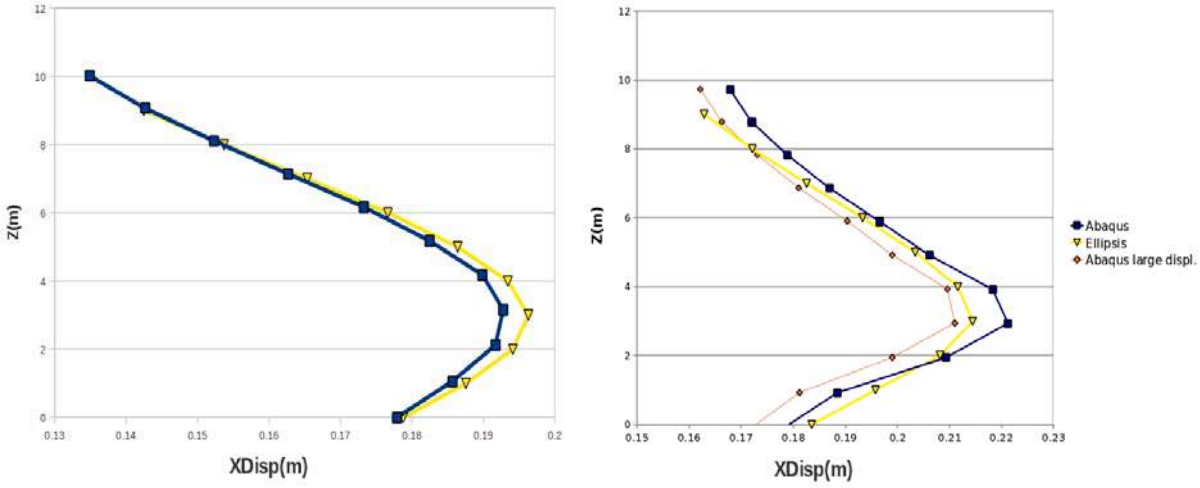

a. Elasticity **b. Elasto-plasticity**

Fig.4 Horizontal displacement along a vertical profile

Firstly one can check that, without activating the plasticity, the elastic behaviour is close in the two codes. The maximum difference is of 2.2% at z=3m. Then with plasticity, the difference is more important (it varies for large displacements between 0.6% for z=8m to 8.1 % for z=1m), but the behaviour stays rather similar.

It is important to notice that both codes converge for this case, as predicted with the limit equilibrium method. However, the simulations have produced plastic strains (fig. 5), i.e. the plastic criterion has been reached and the stress state stays on it since there is no hardening.

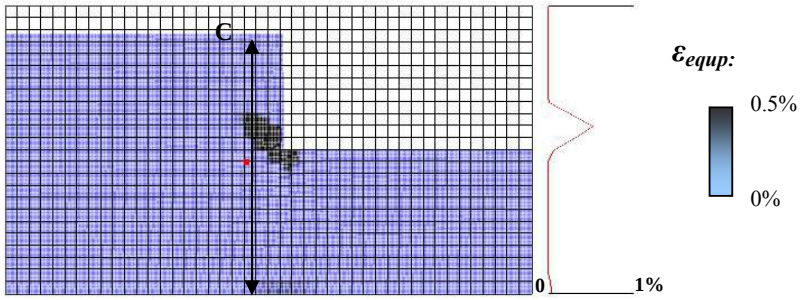

Fig.5 Equivalent plastic strain obtained with the FEMLIP. In the model, and in the cut CD

Let us examine an unstable case, more interesting for the landslides modeling .

4.3 Results with c=32,760 Pa: limitation of the classical FEM

In this case the same configuration and the same loading conditions have been considered, but the value of cohesion is changed: c=32,760 Pa. Consequently, the limit equilibrium method gives a safety factor of 0.7, which means that the failure should be reached in the soils. Indeed in the FEM Abaqus the calculus does not converge anymore which is usual in case of failure (Lignon et al., 2009). On the contrary it does with the FEMLIP; the results are presented in figures 6 and 7:

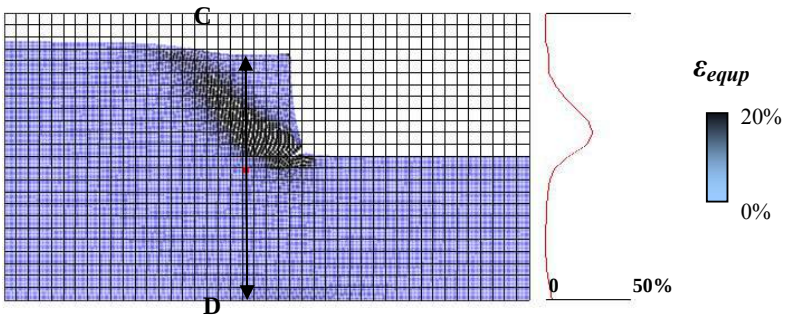

Fig.6 Equivalent plastic strain obtained with the FEMLIP. In the model, and in the vertical cut CD.

Plastic strains are localized in a zone that reaches now the top of the embankment, inducing the slip of the model top corner. Once more, as the constitutive relation is elastic perfectly plastic, the presence of plastic strain means that the plastic failure criterion is reached. Furthermore in this case, the second order work criterion field (fig. 7) shows negative values, which means that failure is reached.

Why in this case is converging the FEMLIP computation ?

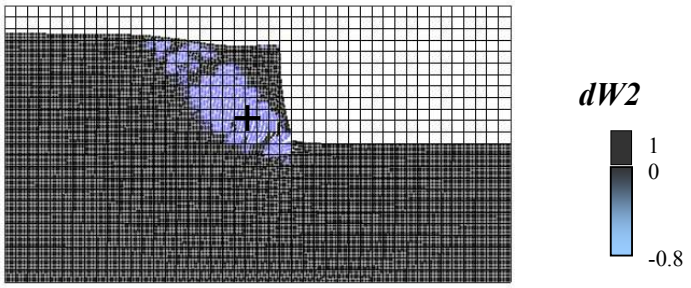

Fig.7 Normalized second order work criterion calculated with the FEMLIP (step 47)

4.4 Some remarks to explain the convergence of the FEMLIP

Before getting interest to the transitional behavior to model the mud flow itself, it is interesting to study why the computation is still converging with FEMLIP while diverging with the classical FEM in loading state for which both plastic failure limit and second order work criterion are reached.

The main difference in the FEMLIP method is the presence of the viscosity. This one, though very high, can allow equilibrium with a velocity different from zero, which could be at the origin of the convergence of the model. To study the influence of viscosity in the FEMLIP, the same numerical model is run with different values of the viscosity. Then the number of iterations needed for the convergence is compared in the different models. Value of η is decreased until reaching low but significant values of viscous strains. For that, the vertical elasto-plastic and viscous strains (respectively $(\varepsilon_{22})_{ep}$ and $(\varepsilon_{22})_v$) at a point localized in the plastic zone (cross in fig.7) is checked. For the lowest value of η (corresponding thus to the greatest influence of viscosity) $(\varepsilon_{22})_v/(\varepsilon_{22})_{ep}$=10%. The iterations needed to reach the first 10 timesteps of the simulation are gathered in the figure 8.

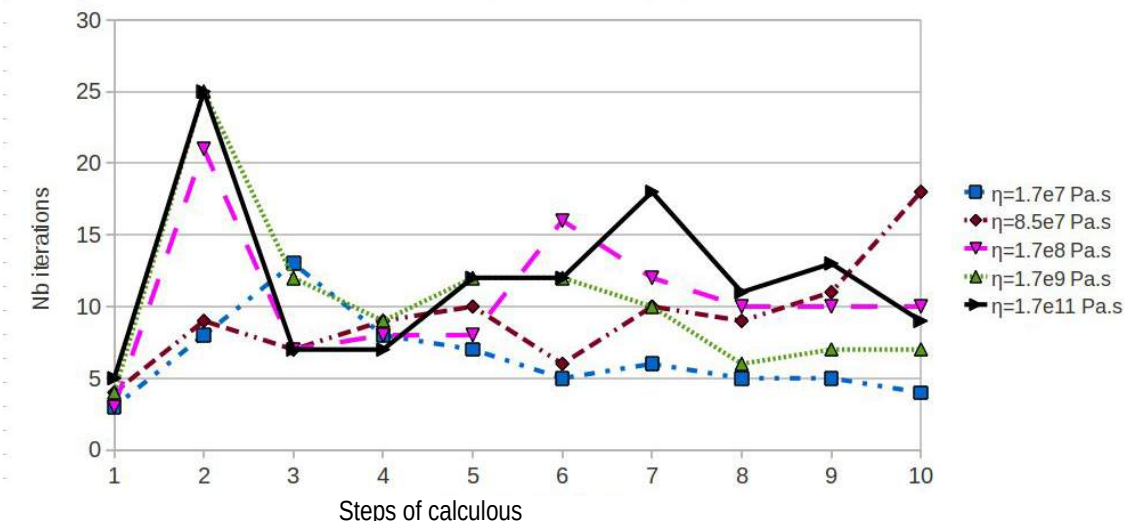

Fig.8 Iterations for the convergence at different steps of the calculus.

With these orders of magnitude of the viscosity one can see a small but notable difference between the convergence rates of the code. The increase of the number of iterations with the reduction of the viscosity effect (i.e. when η becomes infinite) is certainly linked to the non-convergence of the model with an elasto-plastic constitutive relation in Abaqus. This aspect is carefully investigated presently.

5 CONCLUSIONS

The FEMLIP is thus a numerical method well suited for landslides modeling, for the initiation of in place-soils as well as for the propagation of mud-flow and arrest or interaction with a downhill structure.

The example of the embankment shows that the implementation of the visco-elasto-plastic constitutive relation in the code gives consistent results, since the displacements calculated are very close to those obtained with a classical FEM for a stable case. Then, for a non stable case, in the sense of a safety factor smaller than 1 with the limit equilibrium method, the FEMLIP code converges whereas the FEM, Abaqus for example, does not. It might be due to the of the viscous flow (equilibrium reached with velocity different from zero) which balances the unstable state. It is a viscous regularization.

This last point has to be studied in more details, to understand how the 'artificial' viscosity introduced here (η=1.7e11) can prevent numerical instabilities.

Another aspect to be investigated is the behavior of mudflow after the failure: estimation of its viscosity, existence of a stress threshold...The transition from a constitutive law to another would thus be described and the mudflow phase would be modeled after the failure of the embankment.

In a longer term more specific triggering factors will be considered: for example the effect of a rainfall or of the water table rising in the ground.

REFERENCES

Barnichon, J.-D. (1998), "Finite Element Modeling in Structural and Petroleum Geology". PhD thesis, Université de Liège.

Darve, F., Laouafa, F. (2002), "Instabilities in granular material and application to landslides". *Mech. cohes.- frict. mat.*, Vol. 5, 627-652.

Dufour, F. (2002), "Développement de la méthode des éléments finis avec des points d'intégration lagrangiens: application à la géomécanique". PhD thesis, Ecole Centrale de Nantes.

Hill, R. (1958), "A general theory of uniqueness and stability in elasto-plastic solids*". J. Mech. Phys. Sol.*,Vol.6,236-249.

Laouafa, F., Darve, F. (2002), "Modelling of slope failure by a material instability mechanism". *Comput. Geotech.*, Vol.29, 301-325.

Lignon, S., Laouafa, F., Prunier, F., Khoa, H.D.V., Darve, F. (2009), "Hydro-mechanical modelling of landslides with a material instability criterion". *Geotechnique*, 59(6), 513-524.

Moresi, L., Dufour, F., Mülhaus H.-B. (2002), "Mantle convection with viscoelastic/brittle lithosphere: Numerical methodology and plate tectonic modeling". *Pure appl. geophys.,* Vol. 159, 10, 2335-2356.

Moresi, L., Dufour, F., Mülhaus H.-B. (2003), "A Lagrangian integration point finite element method for large deformation modelling of viscoelastic geomaterials". *J. Comput. Phys.* Vol. 184, 2, 476-497.

Mühlhaus, H.-B., Dufour, F., Moresi, L., Hobbs, B., (2002), "A director theory for viscoelastic folding instabilities in multilayered rock". *Int. J. Sol. Struct., Vol 39, 13-14, 3675-3691.*

Oñate E., Idelsohn S., Celigueta M., Rossi P. (2008), "Advances in the particle finite elements method for the analysis of fluid-multibody interaction and bed erosion in free surface flows". *Comput. Methods Appl. Mech. Engrg.*, Vol. 197, 1777-1800.

Pastor M., Haddad B., Sorbino G., Cuomo S., Drempetic V., (2009), “A depth integrated, coupled SPH model for flow-like landslides and related phenomena”, *Int. J. Num. Analyt. Meth. Geomech.*, Vol. 33, 143-172.

A COUPLED DISCRETE ELEMENT – LATTICE BOLTZMANN METHOD TO INVESTIGATE INTERNAL EROSION IN SOIL

Franck Lominé
GeM laboratory, University of Nantes ECN CNRS IUT de St-Nazaire, BP 420, 44606 Saint-Nazaire Cedex, France

Luc Sibille
GeM laboratory, University of Nantes ECN CNRS IUT de St-Nazaire, BP 420, 44606 Saint-Nazaire Cedex, France

Didier Marot
GeM laboratory, University of Nantes ECN CNRS IUT de St-Nazaire, BP 420, 44606 Saint-Nazaire Cedex, France

ABSTRACT: *In this paper, we present a coupled Discrete Element (DE) and Lattice Boltzmann (LB) method to model fluid-solid interactions. This method is applied to study and model a two-dimensional piping erosion through a set-up inspired by the Hole Erosion Test (HET). In this work, we mainly focus on grain detachments under hydraulic loading. Simulation results show that the erosion law classically used in such experiments, can be retrieved with our model. It illustrates that such coupled systems can be investigated with the LB-DE approach developed in this work. This approach is a promising tool which is well designed to perform such investigations at the grain scale.*

1 INTRODUCTION

Internal erosion in soil can be defined by the migration of solid particles due to interstitial water flow. Such migrations can result in the degradation of hydraulic and mechanical properties of soils which can induce structure breakages (Foster et al. 2000). During internal erosion process, particles can be detached, transported and filtered. The full description of internal erosion is nowadays an interesting research project but remains a great challenge due to the variety and the complexity of phenomena involved. In this paper, we focus our interest on particle detachment due to hydraulic loading through direct simulations of piping erosion. Our numerical set-up is inspired by the Hole Erosion Test (HET) (Wan & Fell 2004; Pham 2008; Regazzoni 2009), commonly used in civil engineering to characterize erodability of soils. In this paper, we develop and use a coupling between the Discrete Element (DE) and Lattice Boltzmann (LB) methods. Contact interactions between grains are described with the DE method, whereas fluid flow is computed at a very small scale (smaller than the grain scale) with the LB method. Solid-fluid interactions are described along each grain boundary by the coupling between the two methods without additional parameters.
In the first part of this paper, we present the numerical model and the set-up of our simulations used to model piping erosion. Then, preliminary results of this study will be presented in a second part.

2 NUMERICAL MODEL AND SET-UP

2.1 Discrete Element method (DE)

We use the Discrete Element (DE) method as introduced by Cundall & Strack (1979). Particles move according to Newton's law and two particles in contact can slightly overlap each other. Hence, contact interaction forces are computed, for each pair of particles in contact, with a contact law depending on the overlap between particles. In this paper, we use a cohesive frictional contact law as illustrated in Fig. 1. In the normal direction to the tangent contact plane, the interaction law is purely elastic and expressed as $F_n = k_n\,\delta_n$, where F_n is the normal contact force, k_n the normal stiffness, and δ_n the normal overlap between particles. We allow tensile normal forces for $F_n \geq C_n$, where C_n is a normal contact cohesion. If $F_n < C_n$ failure occurs and the contact is lost. In this model, we assume that compressive forces F_n are counted positively therefore C_n takes usually negative values.

Along the tangential direction (included in the contact plane), we use an elastic-plastic interaction law which follows the Coulomb's friction law. In the elastic regime, the tangential interaction force is expressed as $\Delta F_s = -k_s\,\Delta u_s$, where ΔF_s, k_s and Δu_s are respectively the shear force increment, the shear stiffness and the increment of the tangential relative displacement of particles at contact. When $|F_s| > F_n\,\tan(\Phi) + C_s$, where Φ and C_s are respectively the contact friction angle and the shear cohesion, sliding in tangential direction occurs and the contact becomes purely frictional (i.e. $C_n = C_s = 0$).

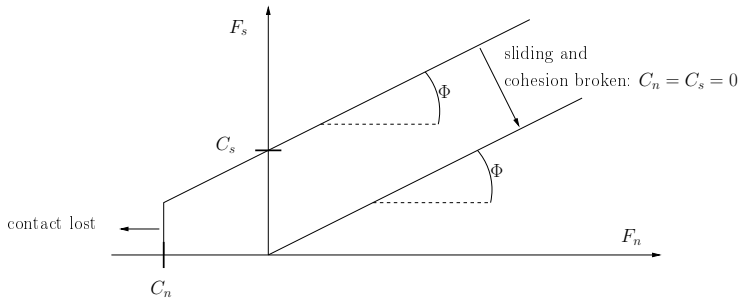

Fig. 1. Cohesive frictional contact law used in the Discrete Element method.

The Discrete Element method uses an explicit time integration of Newton's second law to update positions and velocities (in translation and in rotation) of each solid particle. Consequently, the numerical stability of the time integration scheme depends on the time-step $\mathrm{d}t_{DE}$ used for the time discretization. $\mathrm{d}t_{DE}$ should be smaller than a critical time-step determined such that the DE algorithm can describe the propagation of an elastic wave in the mass-spring system constituted by the solid granular assembly.

2.2 The Lattice Boltzmann method (LB)

To simulate fluid flow, we developed a two-dimensional Lattice Boltzmann algorithm (Lominé et al. 2010). With the LB method, the entire domain is spatially discretized using a regular square lattice of step h. In this work the D2Q9 discretization model (Qian et al. 1992) is used. With this model, for each lattice node located at position $\boldsymbol{x}$, nine directions i and nine discrete velocities

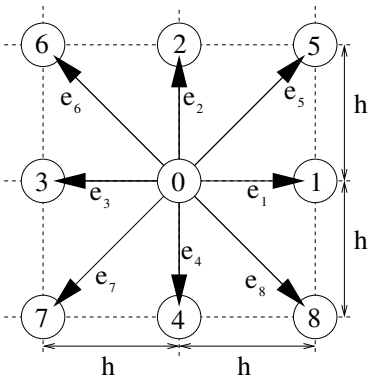

Fig. 2. D2Q9 model: discrete velocity directions from a node located at position $\boldsymbol{x}$.

$\boldsymbol{e_i}$ are defined, pointing towards the eight first neighbour nodes located at positions $\boldsymbol{x} + \boldsymbol{e_i}\mathrm{d}t$ as illustrated in Fig. 2.

Here $\mathrm{d}t$ is the time-step of the LB algorithm and discrete velocities can be expressed as follows:

$$\boldsymbol{e}_i = \begin{cases} (0,0) & \text{if } i = 0 \\ C\left(\cos\left(\frac{\pi(i-1)}{2}\right), \sin\left(\frac{\pi(i-1)}{2}\right)\right) & \text{for } i = 1,\ldots,4 \\ C\left(\cos\left(\frac{\pi(2i-9)}{4}\right), \sin\left(\frac{\pi(2i-9)}{4}\right)\right) & \text{for } i = 5,\ldots,8 \end{cases} \tag{1}$$

where $C = h/\mathrm{d}t$ is the lattice velocity. For a node located at position $\boldsymbol{x}$, a density distribution function $f_i(\boldsymbol{x}, t)$ is associated with each direction i, representing the number of fluid particles moving along the direction i with the velocity $\boldsymbol{e_i}$. The Lattice Boltzmann method can be divided into two consecutive steps: the collision and streaming steps. During the collision step, particle distribution functions relax towards equilibrium functions f_i^{eq}. This relaxation is performed here with the single-relaxation Bhatnagar-Gross-Krook (BGK) model (Bhatnagar et al. 1954):

$$f_i(\boldsymbol{x}, t^+) = f_i(\boldsymbol{x}, t) - \frac{1}{\lambda}\left[f_i(\boldsymbol{x}, t) - f_i^{eq}(\boldsymbol{x}, t)\right] \tag{2}$$

where λ is a dimensionless relaxation time linked to the kinematic viscosity of the fluid ν, the lattice velocity C, and the lattice spacing h through the relation $\nu = \frac{1}{3}\left(\lambda - \frac{1}{2}\right)Ch$. $f_i(\boldsymbol{x}, t^+)$ is called the post-collision term since it refers to particle distribution functions following the collision step.

For Newtonian fluid, the equilibrium distribution functions write (Qian et al. 1992):

$$f_i^{eq} = w_i\rho\left(1 + \frac{3}{C^2}\boldsymbol{e_i}.\boldsymbol{v} + \frac{9}{2C^4}(\boldsymbol{e_i}.\boldsymbol{v})^2 - \frac{3}{2C^2}\boldsymbol{v}.\boldsymbol{v}\right) \text{ for } i = 0,\ldots,8 \tag{3}$$

where $w_0 = 4/9$, $w_{1,2,3,4} = 1/9$ and $w_{5,6,7,8} = 1/36$. $\boldsymbol{v}$ and ρ are respectively the macroscopic fluid velocity and density at the considered node. They are determined with the following relations:

$$\rho = \sum_{i=0}^{8} f_i \text{ and } \boldsymbol{v} = \frac{1}{\rho}\sum_{i=0}^{8} f_i\boldsymbol{e_i} \tag{4}$$

The fluid pressure p is linked to fluid density using the equation of state $p = c_s^2\rho$, where $c_s = \frac{C}{\sqrt{3}}$ is the sound celerity. Macroscopic quantities converge on the solution of the incompressible Navier-Stokes equation with order M^2, where $M = v_{max}/C$ is the computational Mach

number and v_{max} the maximum fluid velocity. We used a value of $M \leq 0.1$, which leads to a compressibility error M^2 less than 1%.

During the streaming step, all distribution functions resulting from the collision process are propagated along each direction to the nearest neighbour node. With notations previously defined, this step can simply be written as:

$$f_i(\boldsymbol{x} + \boldsymbol{e_i}\mathrm{d}t, t + \mathrm{d}t) = f_i(\boldsymbol{x}, t^+) \tag{5}$$

Solid obstacles in the LB method are taken into account by placing them on the lattice. This discretization of solid obstacles leads to differentiate solid nodes (the nodes belonging to the solid obstacles), fluid nodes (nodes that do not belong to solid obstacles), solid boundary nodes (solid nodes representing an obstacle surface with at least one velocity direction pointing towards a fluid node) and fluid boundary nodes (fluid nodes with at least one velocity direction pointing towards a solid boundary node). In this paper, solid boundary nodes and fluid boundary nodes will be referred respectively as SB nodes and FB nodes. In the streaming step, fluid particles are not allowed to cross obstacle boundaries. Therefore, distribution functions coming from an FB node and propagating towards a SB node are reflected according to the following modified bounce-back rule (Ladd 1994):

$$f_{-\sigma i}(\boldsymbol{x}_{FB}, t + \mathrm{d}t) = f_{\sigma i}(\boldsymbol{x}_{FB}, t^+) - 2\alpha_i \boldsymbol{V_b}.\boldsymbol{e_i} \tag{6}$$

In equation (6), $\boldsymbol{x}_{FB}$ is the position of the FB node; σi is the direction from the FB node to the SB node constituting a boundary link; α_i is a constant defined by $\alpha_i = 3w_i\rho C^2$, and $\boldsymbol{V_b}$ is the solid boundary velocity at the middle of the boundary link σi.

Hydrodynamic force $\boldsymbol{F}_\sigma$ and torque $\boldsymbol{T}_\sigma$ contributions coming from each boundary link, are evaluated from the momentum exchange between fluid and solid particle surface (Ladd 1994; Mei et al. 2002). In two dimensions, these contributions write:

$$\boldsymbol{F}_\sigma(\boldsymbol{x}, t + \frac{1}{2}\mathrm{d}t) = 2\frac{h^2}{\mathrm{d}t}\left[f_{\sigma i}(\boldsymbol{x}, t^+) - \alpha_i \boldsymbol{V_b}.\boldsymbol{e_i}\right]\boldsymbol{e}_{\sigma i} \tag{7}$$

$$\boldsymbol{T}_\sigma(\boldsymbol{x}, t + \frac{1}{2}\mathrm{d}t) = \boldsymbol{r}_c \times \boldsymbol{F}_\sigma(\boldsymbol{x}, t + \frac{1}{2}\mathrm{d}t) \tag{8}$$

where $\boldsymbol{r}_c$ is the vector joining the centre of mass of the solid particle to the middle of the boundary link. The total hydrodynamic force and torque applied on a solid particle at time t are obtained by summing equations (7) and (8) respectively over all boundary links of the particle and by averaging the results over two consecutive LB time-steps.

2.3 Coupling between DE and LB methods.

In most situations, the time-step of the DE method is smaller than the time-step of the LB method. Therefore, the coupling is based on a subcycling scheme. During one loop of the LB method, n loops of the DE method are performed. To achieve a such subcycling, the DE time-step is set to satisfy the relation $\mathrm{d}t = n\mathrm{d}t_{DE}$ together with the condition of stability of the explicit time integration achieved during DE loop. To resume, positions and velocities of particles are computed with the DE method. Then, these particles are mapped on the LB lattice, and their positions and velocities constitute input parameters for the LB method to calculate hydrodynamic

forces and torques. These latter are added to inter-particle forces and torques determined by the DE method to compute new particle positions and velocities.
We used an open source software, named YADE (Kozicki & Donzé 2008), dedicated to the DE method. This software is designed in such a way that contact laws or functionalities are incorporated with plugins. Therefore, we developed a plugin to calculate hydrodynamic forces and torques with the Lattice Boltzmann method and integrated it into the YADE software.

2.4 Model set-up

We applied the coupled DE/LB method presented previously to the study of piping erosion. As explained previously, our numerical set-up is inspired by the Hole Erosion Test (HET), but it is here limited to the two-dimensional case. A rectangular box of length l is filled up with a packing of cohesive frictional disks of diameter d with a size dispersion of 30%. A schematic drawing is given in Fig. 3. The initial hole with inlet and outlet water chambers are created by

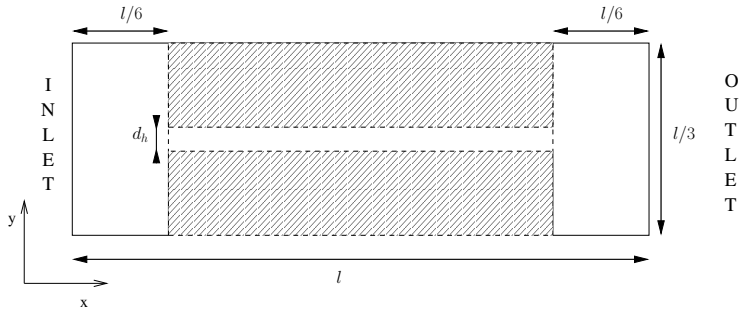

Fig. 3. Schematic representation of the numerical set-up used to simulate erosion through a pipe: $l = 0.03$ m, $d_{\text{mean}} = 5.06\ 10^{-4}$ m, $d_h = 0.2 \times l/3$. Hatched regions correspond to the locations of the cohesive material after drilling of the granular assembly.

removing grains that are not in the hatched regions as represented in Fig. 3. We also removed the left and right walls and the system is saturated with water ($\nu = 1\ 10^{-6}$ m^2 s^{-1} and $\rho_0 = 1\ 000$ kg m^{-3}). Then, a pressure gradient ΔP between the inlet and the outlet is applied, $\Delta P = p_{\text{in}} - p_{\text{out}} = c_s^2(\rho_{\text{in}} - \rho_{\text{out}})$. Nevertheless, pressure or velocity boundary conditions cannot be directly imposed on the system boundaries. These macroscopic quantities depend on the distribution functions. On system boundaries, these distribution functions have to be set to match the desired value of the fluid pressure or velocity. This is achieved on the basis of the boundary conditions defined by Zou and He (1997). For the two remaining upper and bottom walls, a zero velocity boundary condition is imposed. The DE and LB parameters used in this work are the following: $\lambda = 1.1$, $C_s/d = -C_n/d = 0.25$; 1.01 and 2.53 N m^{-1}, $k_n/d = 150\ 10^6$ N m^{-2}, $k_s/k_n = 0.4$, $\Phi = 20\,^\circ$.

3 RESULTS AND DISCUSSION

We simulated flows through the pipe described in section 2.4 for a given pressure gradient and different inter-particle cohesions. The pressure gradient applied is $\Delta P = 0.2$ Pa, corresponding to an hydraulic gradient $i = 3\Delta P/(\rho_0 g 2l) = 10\ 10^{-4}$, (where $g = 9.81$ m s^{-2} is the gravitational acceleration). Three cohesion values were considered: $C_s/d = -C_n/d = 0.25$; 1.01 and 2.53 N m^{-1}.

Fig. 4 shows snapshots from the simulation for $C_s/d = -C_n/d = 0.25$ N m^{-1}. These snapshots highlight that piping erosion can be simulated with the coupled method presented previ-

ously. Indeed, it is possible to observe the detachment and the transport of particles through the pipe due to the fluid flow.

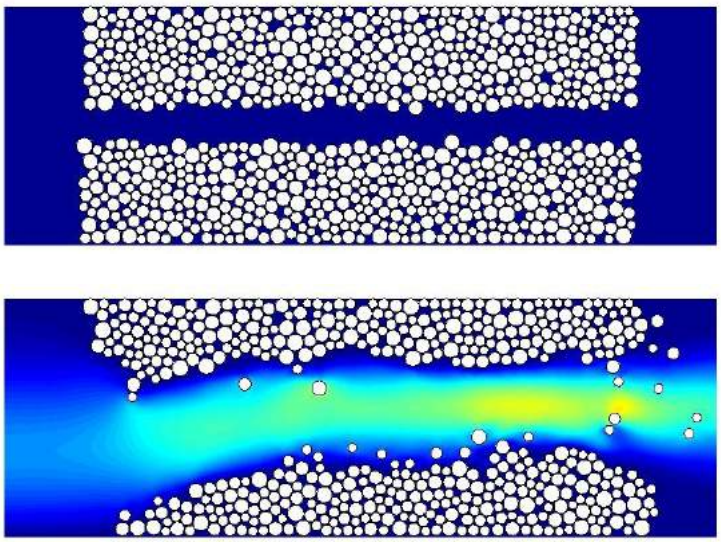

Fig. 4. Snapshots from a simulation of piping erosion obtained with the coupling between the DE and LB methods, for $i = 10\ 10^{-4}$ and $C_s/d = -C_n/d = 0.25$ N m^{-1}. The colour gradient is proportional to the fluid velocity.

Particles reaching the outlet are removed and are considered as eroded ones. During simulations, we record the eroded particle mass $M_e(t)$. Figure 5 represents the evolution of the ratio $M_e(t)/M_0$ with time, where M_0 is the total mass of the initial granular assembly.

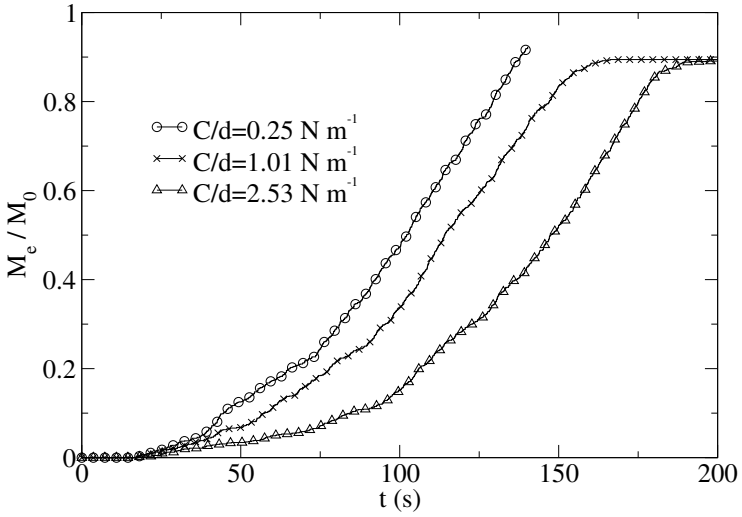

Fig. 5. Evolution of the ratio M_e/M_0 with time for different values of $C/d = C_s/d = -C_n/d$.

Figure 5 illustrates that the proportion of eroded particle mass increases with time. At the end of simulations the ratio $M_e(t)/M_0$ reaches a limit value smaller than 1 because some of the last particles, stuck to the upper and bottom walls, cannot be removed by the water flow. For the inter-particle cohesion values considered, the increase of the cohesion tends to delay the erosion

process, but not to limit it. After a given time, greater for higher cohesion values, the whole granular assembly is eroded.

A classical parameter used to evaluate the importance of the erosion process at a given time is the rate of eroded mass per unit pipe area $\dot{\epsilon}$, displayed in Fig. 6. For all cohesion values the erosion rate increases with time, highlighting the development of the kinetic of erosion as the pipe expands. At the end of simulations, erosion rate decreases due to the vanishing of granular material stock. This last tendency is not representative of the characteristics of erodability of the granular material, and only the first increasing part of erosion rate is considered later on in the paper.

Once again, the cohesion of the granular assembly has a direct influence on the erosion process by delaying the development of the kinetic of erosion.

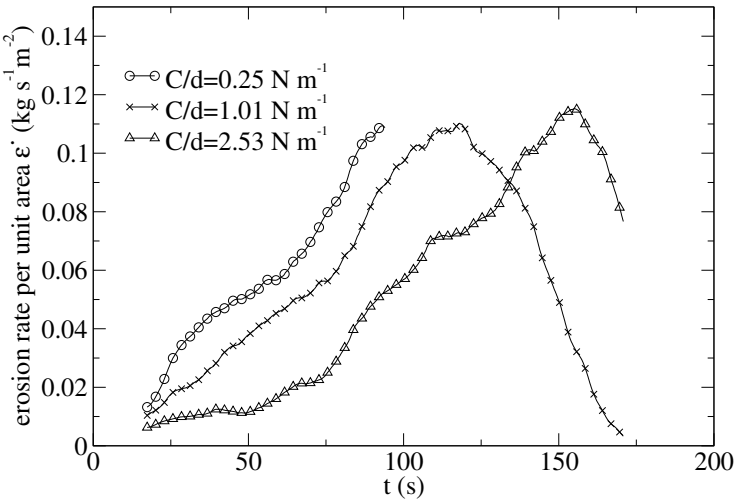

Fig. 6. Evolution of the rate of eroded mass $\dot{\epsilon}$ with time for different values of $C/d = C_s/d = -C_n/d$.

A commonly erosion law used and retrieved in HET (Wan & Fell 2004; Pham 2008) is a linear dependency of the rate of eroded mass on the hydraulic shear stress:

$$\dot{\epsilon} = k_d\,(\tau - \tau_c)\,\text{if}\;\tau > \tau_c, \tag{9}$$

where k_d is the erosion coefficient, τ is the fluid shear stress and τ_c is a critical shear stress.

Experimentally, the evaluation of the shear stress is based on the hole diameter measurement and on the pressure gradient imposed. Considering an equilibrium between pressure forces and shear forces in a two dimensional pipe of height $2R$ and length L, it comes:

$$\tau = \frac{R\Delta P}{L} \tag{10}$$

Contrary to previous experiments performed by Wan & Fell (2004), where only initial and final hole diameter where known, our simulations let us access to the hole diameter at any time during the piping erosion process. Here, we determined the mean hole diameter from an averaged cross-section density profile over the entire packing of disks. τ is calculated using equation (10) until the ratio between the hole diameter and the channel height is greater than 75%, to avoid influence of vanishing of granular material stock.

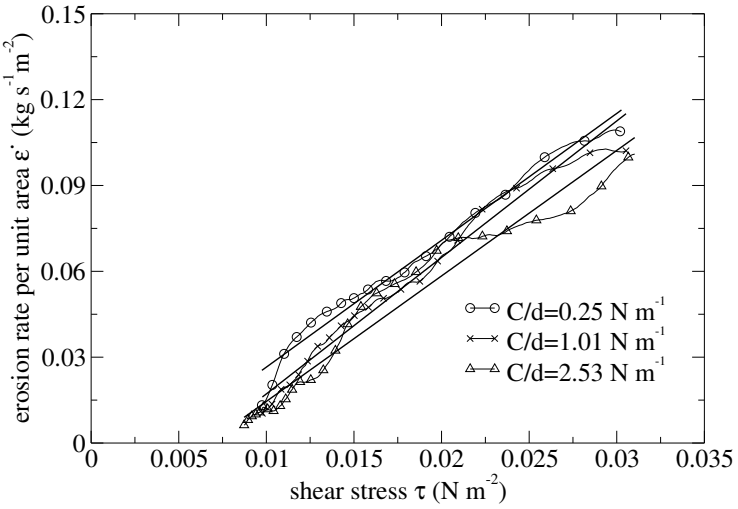

Fig. 7. Evolution of the rate of eroded mass $\dot{\epsilon}$ with the fluid shear stress τ, for different values of $C/d = C_s/d = -C_n/d$.

Figures 7 presents dependency of $\dot{\epsilon}$ on shear stress τ. Three least squares linear adjustments are also represented and illustrate that the erosion law classically used in HET can be retrieved with our simulations of piping erosion with the coupled LB-DE method.

However, the influence of the inter-particle cohesion on the development of the erosion process, shown in Figs. 5 and 6, is not clearly visible in a such representation. Approximatively the same linear relation between $\dot{\epsilon}$ and τ is found for the three cohesion values. Consequently it would mean, according to the erosion law expressed by equation (9), that the three granular assemblies with different cohesions have similar characteristics of erodability. This last point still constitutes for us an open question. Does the way used here, to estimate the fluid shear stress, allow to characterize properly the loading applied by the fluid on solid particles? Is, the fluid shear stress the only fluid parameter fixing the erosion regime, for our set-up and numerical granular material?

4 CONCLUSION

In this paper, a coupling between the Discrete Element method and the Lattice Boltzmann method was presented. In a such coupling few hypotheses are introduced in the modelling of fluid flow, solid particle interactions and fluid-solid interaction, avoiding any phenomenological description. This point constitutes a good advantage, and only six input mechanical parameters are used in this model: the fluid viscosity, the normal and tangential contact stiffnesses and cohesions between two solid particles, and finally the inter-particle friction angle.

Simulations of piping erosion through a granular assembly shown that an erosion law classically used to describe hole erosion tests can be retrieved with this numerical coupled method: the erosion rate is proportional to the fluid shear stress. It is shown, that the inter-particle cohesion influence the kinetic of erosion by delaying the erosion process. However, this influence of cohesion disappears when the erosion rate is expressed with respect to the fluid shear stress. More investigations are necessary to validate this last point or to suggest another interpretation.

ACKNOWLEDGEMENTS

We would like to gratefully acknowledge the French Region Pays de la Loire for its financial support through the EMERMOD project.

REFERENCES

Bhatnagar, P., Gross, E., & Krook, M. (1954). A model for collision processes in gases. I. Small amplitude processes in charged and neutral one-component systems. *Physical Review 94*(3), 511–525.

Cundall, P. A. & Strack, O. D. L. (1979). A discrete numerical model for granular assemblies. *Geotechnique 29*(1), 47–65.

Foster, M., Fell, R., & Spannagle, M. (2000). The statistics of embankment dam failures and accidents. *Canadian Geotechnical Journal 37*(5), 1000–1024.

Kozicki, J. & Donzé, F. V. (2008). A new open-source software developed for numerical simulations using discrete modeling methods. *Computer Methods in Applied Mechanics and Engineering 197*(49-50), 4429–4443.

Ladd, A. (1994). Numerical simulations of particulate suspensions via a discretized Boltzmann equation. Part 1. Theoretical foundation. *Journal of Fluid Mechanics 271*(1), 285–309.

Lominé, F., Scholtès, L., Poullain, P., & Sibille, L. (2010). Soil microstructure changes induced by internal fluid flow: investigations with coupled DE/LB methods. In I. Doghri, R. E. Fatmi, F. Darve, H. Hassis, & H. Zenzri (Eds.), *Third Euro-Mediterranean Symposium on Advances in Geomaterials and Structures*, Djerba, pp. 885–890.

Mei, R., Yu, D., Shyy, W., & Luo, L.-S. (2002). Force evaluation in the lattice Boltzmann method involving curved geometry. *Phys. Rev. E 65*(4), 41203.

Pham, T. (2008). *Erosion et dispersion des sols argileux par un fluide*. Ph. D. thesis, École Nationale des Ponts et Chaussées.

Qian, Y. H., D'Humieres, D., & Lallemand, P. (1992). Lattice BGK Models for Navier-Stokes Equation. *EPL (Europhysics Letters) 17*(6), 479–484.

Regazzoni, P.-L. (2009). *Confrontation et analyse d'érodimètres et caractérisation de la sensibilité à l'érosion d'interface.* Ph. D. thesis, Université de Nantes.

Wan, C. F. & Fell, R. (2004). Investigation of Rate of Erosion of Soils in Embankment Dams. *Journal of Geotechnical and Geoenvironmental Engineering 130*(4), 373–380.

Zou, Q. & He, X. (1997). On pressure and velocity boundary conditions for the lattice Boltzmann BGK model. *Physics of Fluids 9*(6), 1591–1598.

COORDINATE PERTURBATION METHOD FOR UPPER BOUND LIMIT ANALYSIS

J.P. Hambleton & S.W. Sloan
Centre for Geotechnical and Materials Modelling, University of Newcastle, Newcastle, NSW, Australia

ABSTRACT: *Conventional methods for numerical upper bound limit analysis utilize a predefined mesh of elements with nodes at fixed coordinates, and there the objective is to find the kinematically admissible velocity field associated with the mesh that minimizes the limit load. In this paper, a numerical method for optimizing the applied load with respect to both the velocity field and nodal coordinates is presented. The formulation is for the classical case of rigid elements (blocks) separated by velocity discontinuities, considering plane strain and weightless material obeying the Mohr-Coulomb yield condition. The central idea of the approach is to successively perturb velocities and nodal coordinates starting from an initial solution corresponding to a predefined mesh, where the equations governing the perturbed velocities and nodal coordinates are derived through linearization of exact expressions of the limit load and the conditions imposed on velocity jumps by the flow rule. Despite approximations made in perturbation steps, the method furnishes a final solution which satisfies the flow rule and energy balance exactly (within numerical tolerances) and therefore provides a rigorous upper bound on the true collapse load. The effectiveness of the method is demonstrated by comparing numerical results with the analytical solution for a benchmark problem in soil mechanics.*

1 INTRODUCTION

Upper bound limit analysis, otherwise known as the kinematic method of limit analysis, is a rigorous and effective means of evaluating collapse loads of structures and the soils/rocks on which they rest. As discussed in depth by Chen (1975), the technique applies to perfectly plastic materials whose flow rule obeys normality (associativity), and it hinges on constructing a kinematically admissible velocity field (collapse mechanism) for a given problem, where kinematic admissibility implies that the plastic flow rule and boundary conditions are satisfied. By balancing the rate of work dissipated within the material to the rate of work done by external forces, one may evaluate a load which is a rigorous bound on the true collapse load. This bound is an upper bound for loads inducing collapse (the case usually considered in the literature) and a lower bound for loads resisting collapse.

Limit analysis has origins as an elegant analytical or semi-analytical technique, and it continues to be used in this context to this day (e.g., Michalowski, 1997, 2004, 2007; Soubra, 1999, Maciejewski & Jarzębowski, 2004; Soon & Drescher, 2007; Hambleton & Drescher, 2011). Analytical works often employ a collapse mechanism consisting of rigid blocks separated by velocity discontinuities, where a velocity discontinuity is regarded as a material layer of vanishing thickness across which a jump in velocity occurs (Chen 1975). In this

approach, kinematic admissibility is ensured from the outset by composing a hodograph, or velocity diagram, in which velocity jumps between rigid blocks satisfy the condition imposed by the flow rule. The mechanism usually consists of free variables that can assume any value within a certain range (e.g., interior angles of the blocks), and thus an optimization procedure is employed to find values of these free variables that minimize the collapse load. For very simple mechanisms the minimum can be found analytically, but in general it is necessary to employ a numerical optimization scheme that is suitable for a general nonlinear objective function (e.g., Levenberg–Marquardt algorithm).

The concepts of limit analysis also have been utilized as the basis for efficient numerical methods (e.g., Anderheggen & Knöpfel, 1972; Bottero et al., 1980; Sloan & Kleeman 1995; Lyamin & Sloan, 2002; Chen et al. 2003; Krabbenhøft et al., 2005; Makrodimopoulos & Martin, 2007, 2008; Smith & Gilbert, 2007). With the exception of the work by Smith & Gilbert (2007), these numerical approaches rest on discretizing the problem domain using finite elements and then minimizing the load (again evaluated via energy balance) subject to constraints on the interpolated velocity field imposed by the flow rule and boundary conditions. The velocity field typically varies continuously within each element using linear or quadratic interpolation of nodal velocities, and element edges correspond to velocity discontinuities. In contrast to semi-analytical limit analysis, in which the number of free variables is quite limited, procedures for numerical limit analysis are able to take advantage of large-scale optimization schemes such as conic programming, which can efficiently operate with thousands or hundreds of thousands of free variables.

A central difference between the analytical and numerical forms of limit analysis is that the optimal location of discontinuities is usually determined as part of the solution procedure in the analytical method, whereas any discontinuities present in numerical methods have a fixed position as a consequence the mesh being predefined. Indeed, numerical methods usually allow for arbitrarily complex zones of continuous deformation but are incapable of reproducing global velocity discontinuities present in a collapse mechanism unless the location of the discontinuity is known a priori, in which case element edges can be aligned with the known discontinuity as part of the procedure for mesh generation. The formulation proposed by Smith & Gilbert (2007), which is not a finite element method, revolves around finding the optimal location of discontinuities by searching over a large set of potential locations obtained from connecting nodes of a grid laid out over the problem domain.

In this paper, a method for finding the optimal location of discontinuities using finite elements is introduced. The formulation is based on successively perturbing velocities and nodal coordinates beginning from an initial solution, where the initial solution is obtained from a predefined mesh of finite elements using well-established procedures for numerical limit analysis. The formulation presented is for triangular rigid elements (plane strain) separated by velocity discontinuities, and it is therefore identical to the classical limit analysis method employing sliding rigid blocks (cf. Chen 1975). Indeed, the terms “element” and “block” are viewed as being interchangeable, and “nodes” of the finite element mesh are none other than the vertices of the triangular blocks. It is assumed in this paper that the material is homogenous and characterized by the Mohr-Coulomb yield condition, with friction angle and cohesion denoted ϕ and c, respectively. Furthermore, the material is considered to be weightless, although it is possible to include body forces in the formulation (Hambleton & Sloan, 2011).

In Section 2, exact expressions of the conditions on velocity jumps between elements, as well are the limit load, are derived. The proposed numerical formulation based on the perturbation method is presented in Section 3, and its application to the benchmark problem of passive earth pressure behind a smooth retaining wall is considered in the penultimate

section. Detailed analysis of the proposed numerical method, as well as additional examples and verifications, will be provided in a forthcoming paper (Hambleton & Sloan, 2011).

2 GENERAL EQUATIONS FOR SLIDING RIGID ELEMENTS

As in analytical methods for limit analysis (cf. Chen 1975), the proposed formulation is based on splitting the problem domain into a number of rigid triangular elements whose edges correspond to velocity discontinuities. The initial finite element mesh is chosen somewhat arbitrarily, although it should be emphasized that it is possible to select an initial mesh for which no kinematically admissible velocity field exists. Here it is assumed that an admissible velocity field exists for the initial mesh.

Fig. 1 shows the line segment corresponding to a velocity discontinuity at the edge shared by two adjacent elements in a finite element mesh. Each discontinuity, or edge, is assigned a global number that is designated by the index k (k = 1,2,…,N_{edges}, where N_{edges} is the total number of edges). Using the convention shown in Fig. 1, the subscripts i and j denote quantities in the elements adjacent to edge k, as well as the nodes corresponding to the endpoints of the edge. Velocity vectors in the elements associated with discontinuity k are denoted as

$$\mathbf{v}_i = \begin{bmatrix} v_{x,i} & v_{y,i} \end{bmatrix}^T, \qquad \mathbf{v}_j = \begin{bmatrix} v_{x,j} & v_{y,j} \end{bmatrix}^T \tag{1}$$

In Eq. (1), $v_{x,i}$ and $v_{y,i}$ are components of velocity in the x-direction and y-direction (Fig. 1), respectively, for element i, and $v_{x,j}$ and $v_{y,j}$ are components of velocity for element j. Node i is located at coordinates (x_i,y_i), and coordinates of node j are (x_j,y_j).

In the sections that follow the condition imposed by the flow rule on velocity jumps between elements is derived, as well as an expression of the limit load based on balancing the total rate of work done by external forces with the total rate of dissipation within the material.

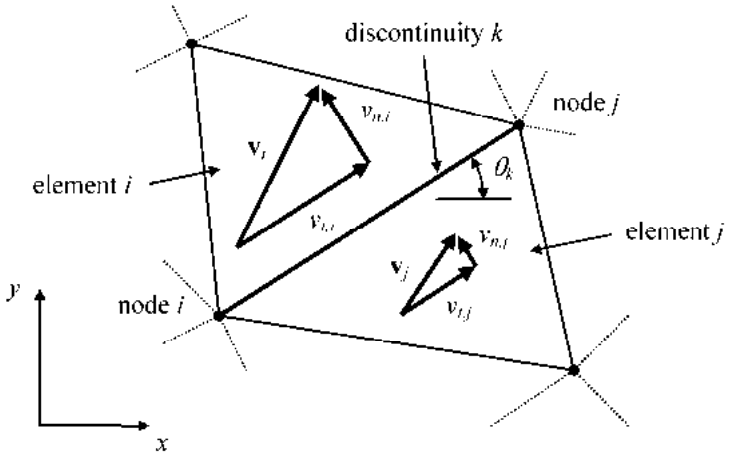

Fig. 1. Notation for a discontinuity (element edge) and velocities in adjacent elements (all quantities positive as drawn)

2.1 Jump condition

The associated flow rule for the Mohr-Coulomb yield condition requires that the jump in velocity between elements satisfies the following condition (Chen 1975)

$$\Delta v_{n,k} = \left|\Delta v_{t,k}\right| \tan\phi \tag{2}$$

where $\Delta v_{n,k}$ and $\Delta v_{t,k}$ are, respectively, jumps in the components of velocity normal and tangential to discontinuity k. The jumps are calculated as

$$\Delta v_{n,k} = v_{n,i} - v_{n,j}, \qquad \Delta v_{t,k} = v_{t,i} - v_{t,j} \tag{3}$$

where v_n and v_t denote components of velocity in directions normal and tangential to the discontinuity, with subscript i or j indicating the element (see Fig. 1). These components are related to components in the x-y system through

$$v_{n,i} = -v_{x,i}\sin\theta_k + v_{y,i}\cos\theta_k, \qquad v_{t,i} = v_{x,i}\cos\theta_k + v_{y,i}\sin\theta_k \tag{4}$$

$$v_{n,j} = -v_{x,j}\sin\theta_k + v_{y,j}\cos\theta_k, \qquad v_{t,j} = v_{x,j}\cos\theta_k + v_{y,j}\sin\theta_k \tag{5}$$

In Eqs. (4) and (5), θ_k is the angle at which the edge is inclined from the horizontal, considering the endpoint specified by subscript i as the origin (Fig. 1). The trigonometric functions in (4) and (5) are given by

$$\cos\theta_k = \frac{x_j - x_i}{l_k}, \qquad \sin\theta_k = \frac{y_j - y_i}{l_k} \tag{6}$$

where l_k is the length of the discontinuity evaluated as

$$l_k = \sqrt{\left(x_j - x_i\right)^2 + \left(y_j - y_i\right)^2} \tag{7}$$

Upon substitution of the expressions from Eqs. (3)-(6), the jump condition of Eq. (2) can be written as

$$-v_{x,i}\left(y_j - y_i\right) + v_{y,i}\left(x_j - x_i\right) + v_{x,j}\left(y_j - y_i\right) - v_{y,j}\left(x_j - x_i\right) = \alpha_k \tan\phi \tag{8}$$

where

$$\alpha_k = l_k\left|\Delta v_{t,k}\right| = \left|v_{x,i}\left(x_j - x_i\right) + v_{y,i}\left(y_j - y_i\right) - v_{x,j}\left(x_j - x_i\right) - v_{y,j}\left(y_j - y_i\right)\right| \tag{9}$$

It may be noted that the length l_k cancels in the final expressions of the jump condition given by Eqs. (8) and (9), which later on simplifies the process of linearization significantly.

2.2 Energy balance

Dissipation for the mechanism involving rigid blocks comes exclusively from velocity discontinuities, where dissipation for a single discontinuity is calculated as (Chen 1975)

$$d_k = c l_k\left|\Delta v_{t,k}\right| = c\alpha_k \tag{10}$$

In this paper, body forces are neglected, and the rate of work done by external forces involves only surface tractions. For simplicity, it is now further assumed that the rate of work done by

surface tractions comes only from the (unknown) limit load. That is, fixed tractions outside the region where the limit load is applied (i.e., surcharges) are zero. With this the total balance of energy requires simply

$$c\sum_{k=1}^{N_{edges}}\alpha_k = \int_S \left(t_x v_x + t_y v_y\right) ds \tag{11}$$

where t_x and t_y are, respectively, tractions in the x-direction and y-direction corresponding to the limit load and S is the part of the surface over which these tractions are applied.

Eq. (11) is generally applicable to a problem with no body forces or surcharge, although further information must be given in order to define the limit load explicitly. In the example considered later in Section 4, it is assumed that $v_y = 0$ and $v_x = v_0$, where v_0 is an arbitrary constant (usually taken as unity for convenience). These assumptions correspond simple translation in the x-direction, and for this case total force in the x-direction, denoted P, represents the limit load. Upon manipulating Eq. (11), the expression for P is

$$P = \int_S t_y ds = \frac{c}{v_0}\sum_{k=1}^{N_{edges}}\alpha_k \tag{12}$$

Thus, the quantity on the right-hand side of Eq. (12) is identically equal to the limit load that one wishes to minimize. Alternatives to Eq. (12) for other loading scenarios can be readily derived.

3 PERTURBATION METHOD

To determine the optimal location of velocity discontinuities, nodal coordinates defining the positions of the discontinuities must be included with the velocities as free variables (unknowns). For a single discontinuity the free variables can be combined in a single vector, $\mathbf{x}_k$, defined as

$$\mathbf{x}_k = \begin{bmatrix} x_i & y_i & x_j & y_j & v_{x,i} & v_{y,i} & v_{x,j} & v_{y,j} \end{bmatrix}^T \tag{13}$$

With a view towards implementing a standard large-scale optimization scheme (e.g., conic programming), equality constraints and an objective function that are linear with respect to the free variables are required. Since the jump condition and expression of the limit load (Eqs. (8) and (12)) are nonlinear with respect to the free variables, it is necessary to work with linear approximations rather than the exact expressions. A tacit assumption is that there is a known point $\mathbf{x}_k^0$ about which the equations can be linearized. Initially, the point $\mathbf{x}_k^0$ corresponds to the solution found using fixed coordinates, i.e., one obtained using well-established methods for numerical limit analysis (e.g., Krabbenhøft et al., 2005; Makrodimopoulos & Martin, 2008), and the concept of the proposed numerical method is to "perturb" both velocities and nodal coordinates from this initial solution using linear approximations of Eqs. (8) and (12). Upon finding a new solution with updated nodal coordinates, the velocities and nodal coordinates may again be perturbed by a small amount, and in this way the proposed scheme is incremental.

3.1 Linear approximations

In order to linearize the jump condition of Eq. (8), the equality is first written in the form $F(\mathbf{x}_k) = 0$, where the function $F(\mathbf{x}_k)$ is defined as

$$F(\mathbf{x}_k) = -v_{x,i}(y_j - y_i) + v_{y,i}(x_j - x_i) + v_{x,j}(y_j - y_i) - v_{y,j}(x_j - x_i) - \alpha_k \tan\phi \tag{14}$$

The linear approximation of the jump condition is then obtained by a first-order Taylor series expansion of $F(\mathbf{x}_k)$ about the point $\mathbf{x}_k^0$, viz.

$$F(\mathbf{x}_k) \approx F(\mathbf{x}_k^0) + (\mathbf{x}_k - \mathbf{x}_k^0)^T \left.\frac{\partial F}{\partial \mathbf{x}_k}\right|_{\mathbf{x}_k = \mathbf{x}_k^0} \tag{15}$$

Upon evaluating the derivative and performing some manipulation, Eq. (15) can be expressed as

$$\begin{aligned} F(\mathbf{x}_k) \approx\ & -v_{x,i}^0 \Delta y + v_{y,i}^0 \Delta x + v_{x,j}^0 \Delta y - v_{y,j}^0 \Delta x - v_{x,i} \Delta y^0 + v_{y,i} \Delta x^0 + v_{x,j} \Delta y^0 - v_{y,j} \Delta x^0 \\ & + v_{x,i}^0 \Delta y^0 - v_{y,i}^0 \Delta x^0 - v_{x,j}^0 \Delta y^0 + v_{y,j}^0 \Delta x^0 - D(\mathbf{x}_k) \tan\phi \end{aligned} \tag{16}$$

where

$$\Delta x = x_j - x_i, \quad \Delta y = y_j - y_i, \quad \Delta x^0 = x_j^0 - x_i^0, \quad \Delta y^0 = y_j^0 - y_i^0 \tag{17}$$

In Eqs. (16) and (17), the superscript "0" is used to indicate quantities corresponding the point $\mathbf{x}_k^0$ about which linearization is performed, and the function $D(\mathbf{x}_k)$ is the linear approximation of α_k defined as

$$\alpha_k(\mathbf{x}_k) \approx D(\mathbf{x}_k) = \alpha_k(\mathbf{x}_k^0) + (\mathbf{x}_k - \mathbf{x}_k^0)^T \left.\frac{\partial \alpha_k}{\partial \mathbf{x}_k}\right|_{\mathbf{x}_k = \mathbf{x}_k^0} \tag{18}$$

Upon manipulation, the function $D(\mathbf{x}_k)$ can be reduced to the following

$$\begin{aligned} D(\mathbf{x}_k) = \langle & v_{x,i}^0 \Delta x^0 + v_{y,i}^0 \Delta y^0 - v_{x,j}^0 \Delta x^0 - v_{y,j}^0 \Delta y^0 \rangle \big[v_{x,i}^0 \Delta x + v_{y,i}^0 \Delta y - v_{x,j}^0 \Delta x - v_{y,j}^0 \Delta y \\ & + v_{x,i} \Delta x^0 + v_{y,i} \Delta y^0 - v_{x,j} \Delta x^0 - v_{y,j} \Delta y^0 - v_{x,i}^0 \Delta x^0 - v_{y,i}^0 \Delta y^0 + v_{x,j}^0 \Delta x^0 + v_{y,j}^0 \Delta y^0 \big] \end{aligned} \tag{19}$$

where $\langle \bullet \rangle$ is the sign function defined as

$$\langle \xi \rangle = \begin{cases} 1 & \text{for } \xi > 0 \\ -1 & \text{for } \xi < 0 \\ \text{undefined} & \text{for } \xi = 0 \end{cases} \tag{20}$$

The expression for the limit load, Eq. (12), is a linear combination of α_k (k = 1,2,…,N_{edges}) and is also therefore linearized by replacing α_k with $D(\mathbf{x}_k)$.

An attempt to use Eq. (19) directly will in general lead to difficulties in the numerical scheme. The equation is undefined, for example, in the case when velocities are zero in both elements adjacent to a discontinuity. Furthermore, it is a basic requisite that dissipation is positive. Rather than use the expression for $D(\mathbf{x}_k)$ from Eq. (19), the following definition is therefore adopted

$$D(\mathbf{x}_k) = \left| v^0_{x,i}\Delta x + v^0_{y,i}\Delta y - v^0_{x,j}\Delta x - v^0_{y,j}\Delta y + v_{x,i}\Delta x^0 + v_{y,i}\Delta y^0 - v_{x,j}\Delta x^0 - v_{y,j}\Delta y^0 \right.$$
$$\left. - v^0_{x,i}\Delta x^0 - v^0_{y,i}\Delta y^0 + v^0_{x,j}\Delta x^0 + v^0_{y,j}\Delta y^0 \right| \tag{21}$$

Unlike the linear approximation, Eq. (21) leads to a robust numerical formulation even when the jump in the tangential component of velocity, $\Delta v_{t,k}$, becomes zero or changes sign. It may be noted that Eq. (21) is identical to the linear approximation of α_k provided $\Delta v_{t,k}$ does not change sign during a perturbation step.

3.2 Optimization and solution stepping

As indicated in the introduction to Section 3, the concept of the numerical formulation is to perform a number of steps in which the nodal coordinates and velocities are perturbed by a small amount, starting from an initial solution corresponding to a predefined mesh. Each perturbation step corresponds to a constrained optimization problem where the goal is to minimize the limit load (Eq. (12) with α_k replaced by $D(\mathbf{x}_k)$) subject to the equality constraints corresponding to jump conditions ($F(\mathbf{x}_k) = 0$, where $F(\mathbf{x}_k)$ is given by Eq. (16)).

The motivation for using a relatively large number of small perturbations, as opposed to a small number of large perturbations, is twofold. First, the linear approximations from Section 3.1 are valid only for small variations in the free variables. Second, the connectivity of the element mesh must remain unchanged as the nodal coordinates are adjusted, and allowing nodal coordinates to change substantially will invariably lead to mesh degeneration (e.g., elements with negative volume). By arriving at a final solution through a number of small steps, mesh degeneration is not necessarily prevented, but the method will at least furnish the best possible solution prior to the mesh becoming invalid. To ensure that the adjustment to the solution is small in each step, the following radial constraint on the nodal coordinates is introduced

$$\rho_{\max,m} \geq \sqrt{\left(x_m - x^0_m\right)^2 + \left(y_m - y^0_m\right)^2} \tag{22}$$

where m indicates the global node number ($m = 1,2,\ldots,N_{nodes}$, where N_{nodes} is the total number of nodes) and $\rho_{\max,m}$ is a specified maximum radius. The parameter $\rho_{\max,m}$ should be taken as a small fraction of the element length and may in general be different for each node.

In this paper optimization was performed using the Matlab toolbox SeDuMi. Among other functions, this software package efficiently solves large-scale constrained optimization problems using second-order cone programming (Sturm 1999), which accommodates so-called "quadratic, second-order cone constraints" of the type given in Eq. (22). As discussed by Lyamin et al. (2004), such constraints also can be introduced to handle the absolute value appearing in the equations for the jump condition and dissipation. This is accomplished by everywhere replacing $D(\mathbf{x}_k)$ with the variable μ_k ($k = 1,2,\ldots,N_{edges}$), which is constrained as follows

$$\mu_k \geq \sqrt{\lambda_k^2} \tag{23}$$

where

$$\lambda_k = v^0_{x,i}\Delta x + v^0_{y,i}\Delta y - v^0_{x,j}\Delta x - v^0_{y,j}\Delta y + v_{x,i}\Delta x^0 + v_{y,i}\Delta y^0 - v_{x,j}\Delta x^0 - v_{y,j}\Delta y^0$$
$$- v^0_{x,i}\Delta x^0 - v^0_{y,i}\Delta y^0 + v^0_{x,j}\Delta x^0 + v^0_{y,j}\Delta y^0 \tag{24}$$

The variable λ_k is simply the expression appearing in the absolute value in Eq. (21), such that $D(\mathbf{x}_k) = |\lambda_k|$. In order to force the algorithm to find a solution with $\mu_k = D(\mathbf{x}_k)$, the expression for the limit load (Eq. (12)) is replaced by

$$P = \frac{c}{v_0} \sum_{k=1}^{N_{edges}} \mu_k \tag{25}$$

By using Eq. (25) as the objective function, the global minimum for the problem corresponds to $\mu_k = D(\mathbf{x}_k)$ by construction.

To write the optimization problem for a perturbation step in the canonical form used by SeDuMi and other solvers, the following global vector of unknowns is defined

$$\mathbf{x} = \begin{bmatrix} \mathbf{x}_{crd}^T & \mathbf{x}_{vel}^T & \mathbf{x}_{\alpha\beta}^T & \mathbf{x}_{\rho}^T \end{bmatrix}^T \tag{26}$$

where

$$\mathbf{x}_{crd} = \begin{bmatrix} x_1 & y_1 & x_2 & y_2 & \dots & x_{N_{nodes}} & y_{N_{nodes}} \end{bmatrix}^T \tag{27}$$

$$\mathbf{x}_{vel} = \begin{bmatrix} v_{x,1} & v_{y,1} & v_{x,2} & v_{y,2} & \dots & v_{x,N_{elems}} & v_{y,N_{elems}} \end{bmatrix}^T \tag{28}$$

$$\mathbf{x}_{\mu\lambda} = \begin{bmatrix} \mu_1 & \lambda_1 & \mu_2 & \lambda_2 & \dots & \mu_{N_{edges}} & \lambda_{N_{edges}} \end{bmatrix}^T \tag{29}$$

$$\mathbf{x}_{\rho} = \begin{bmatrix} \rho_{\max,1} & \rho_{x,1} & \rho_{y,1} & \rho_{\max,2} & \rho_{x,2} & \rho_{y,2} & \dots & \rho_{\max,N_{nodes}} & \rho_{y,N_{nodes}} & \rho_{y,N_{nodes}} \end{bmatrix}^T \tag{30}$$

In Eq. (28), N_{elems} is the total number of elements, and in Eq. (30) the variables $\rho_{x,m}$ and $\rho_{y,m}$ ($m = 1,2,\dots,N_{nodes}$) are defined as

$$\rho_{x,m} = x_m - x_m^0 \tag{31}$$

$$\rho_{y,m} = y_m - y_m^0 \tag{32}$$

The canonical form of the optimization problem is then

$$\begin{aligned} &\text{minimize} && \mathbf{c}^T \mathbf{x} \\ &\text{such that} && \mathbf{A}\mathbf{x} = \mathbf{b} \\ & && \mu_k \geq \sqrt{\lambda_k^2} \quad \text{for } k = 1,2,\dots,N_{edges} \\ & && \rho_{\max,m} \geq \sqrt{\rho_{x,m}^2 + \rho_{y,m}^2} \quad \text{for } m = 1,2,\dots,N_{nodes} \end{aligned} \tag{33}$$

Referring to the objective function of Eq. (25), the vector of constants $\mathbf{c}$ is given by

$$\mathbf{c} = \frac{c}{v_0} [\underbrace{0 \quad 0 \quad \dots \quad 0}_{1\times(2N_{nodes}+2N_{elems})} \quad \underbrace{1 \quad 0 \quad 1 \quad 0 \quad \dots \quad 1 \quad 0}_{1\times 2N_{edges}} \quad \underbrace{0 \quad 0 \quad \dots \quad 0}_{1\times 3N_{nodes}}]^T \tag{34}$$

The matrix of constants $\mathbf{A}$ and vector of constants $\mathbf{b}$ are determined by assembling (1) jump conditions for all discontinuities, (2) definitions of auxiliary variables, and (3) constraints required to fix nodal coordinates and velocities for a particular problem. The jump conditions are simply $F(\mathbf{x}_k) = 0$ ($k = 1,2,\dots,N_{nodes}$), where $F(\mathbf{x}_k)$ is given by Eq. (16) with $D(\mathbf{x}_k)$ replaced by μ_k. The auxiliary variables are λ_k, $\rho_{x,m}$, and $\rho_{y,m}$, and they are defined by Eqs. (24), (31), and (32), respectively.

An arbitrary number of perturbation steps can be performed in the analysis of a problem. In each step, the variables with a superscript "0" are regarded as known quantities from the previous step, and the solution of (33) yields the values of unknowns at the end of the step. A natural stopping criterion in this stepping procedure is for the variation of the limit load within an increment to be below some tolerance, although other criteria can be implemented.

Finally, it is noted that by fixing all nodal coordinates as the values at the beginning of a perturbation step ($x_i = x_i^0$, $y_i = y_i^0$, etc.), exact expressions of the jump condition and energy balance (Eqs. (8) and (12)) are recovered from the linear approximations, and in this case, the only unknowns are the velocities. Fixing the nodal coordinates thus provides a means for obtaining a solution for the initial mesh, and it can also be used to obtain an exact solution (within numerical tolerances) for the limit load at any solution step.

4 EXAMPLE

In this section the proposed numerical formulation is applied to a classical problem in soil mechanics: passive earth pressure behind a smooth retaining wall. The wall has height H and translates into weightless material with friction angle $\phi = 10^\circ$. For simplicity, the maximum variation in nodal coordinates the same for all nodes and fixed at $H/100$ (i.e, $\rho_{\max,m} = H/100$ for $m = 1,2,\ldots,N_{nodes}$).

The initial finite element mesh for the problem is shown in Fig. 2 (indicated by "step number = 0"). Superimposed on the mesh are the element velocities obtained by fixing nodal coordinates at their initial values in the numerical formulation. The collapse mechanism for the initial mesh is considerably different than the one predicted analytically in the Coulomb theory of lateral earth pressure, which corresponds to the single discontinuity indicated by a dashed line in Fig. 2.

Fig. 2 also shows the finite element mesh and velocities after 20, 40, and 60 perturbation steps. The collapse mechanism becomes progressively closer to the Coulomb solution with the number of perturbation steps, and when the step number is 60, it is virtually indistinguishable from the analytical result.

Fig. 3 compares the limit load evaluated numerically with the analytical solution of $P/cH \approx 2.3835$. The limit load evaluated for the initial mesh is $P/cH \approx 13.0965$, over 5 times larger than the analytical prediction, but it rapidly approaches the analytical result as the stepping procedure proceeds. At step number 55, the numerical and analytical predictions are in agreement to all four decimal places given.

5 CONCLUDING REMARKS

The paper presents a numerical method for upper bound limit analysis in which both velocities and the location of velocity discontinuities are optimized simultaneously. The method is based on successively perturbing the velocities and nodal coordinates, starting from solution that can be obtained by conventional techniques for numerical limit analysis. The formulation presented is for collapse mechanisms consisting of sliding rigid elements (blocks) separated by velocity discontinuities, although it is expected that the approach can be generalized to finite element formulations involving continuous deformation within elements. Simulation of a benchmark problem in soil mechanics indicates that the method is robust and capable of recovering the exact (analytical) solution even when the collapse mechanism for the initial finite element mesh is significantly different from the optimal one. Additional verifications and analysis of the numerical formulation will be given in an upcoming journal paper (Hambleton & Sloan, 2011).

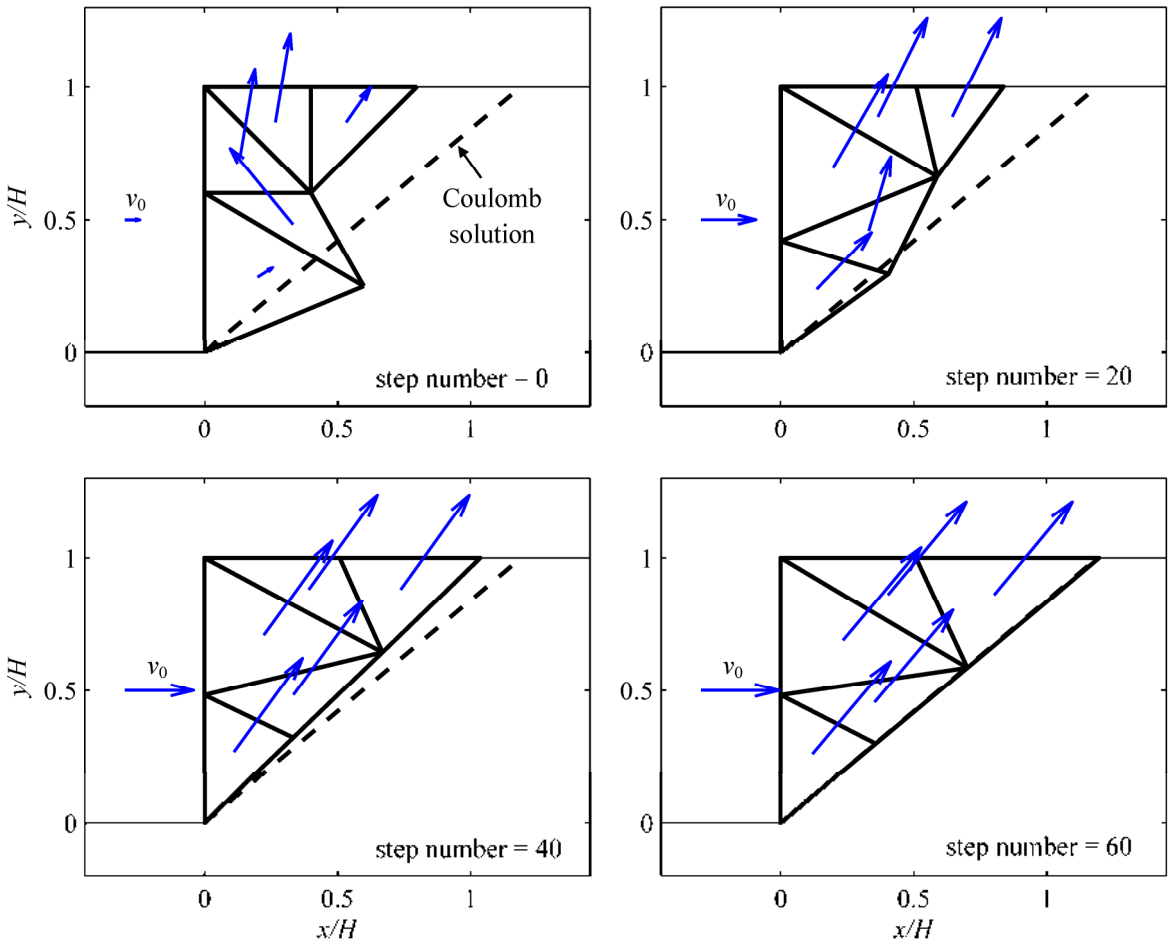

Fig. 2. Finite element mesh and velocities at various perturbation steps for passive earth pressure problem

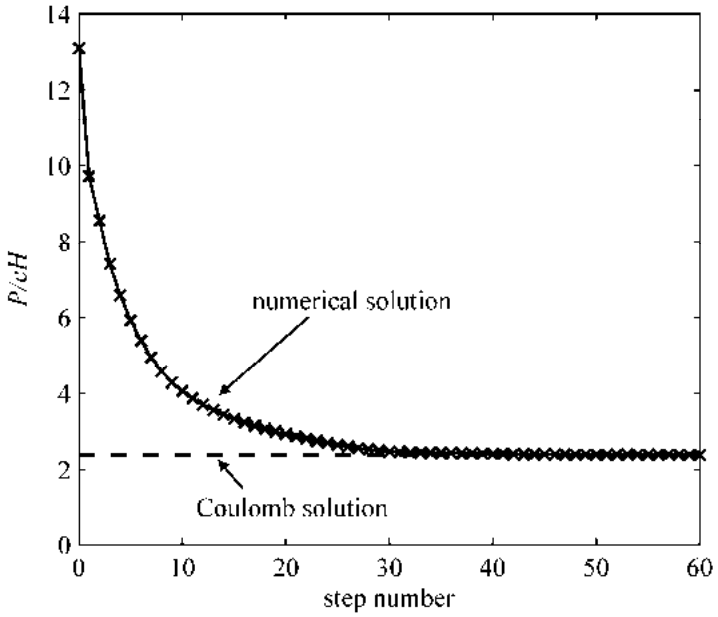

Fig. 3. Limit load as a function of the number of perturbation steps for passive earth pressure problem

The concept behind the proposed method is of potentially great benefit in contemporary numerical limit analysis techniques (cf. Lyamin & Sloan, 2002; Krabbenhøft et al., 2005; Makrodimopoulos & Martin, 2008), and the specific formulation presented provides a valuable alternative to the classical analytical approach to upper bound limit analysis. Namely, the method can be used to compute upper bounds on collapse loads without the need to geometrically construct kinematically admissible mechanisms, which can be a cumbersome process when more than a few rigid blocks are included. Even when a kinematically admissible mechanism can be ascertained analytically, a nonlinear optimization scheme is often needed to determine the optimal values of the free variables involved, and this too is usually a nontrivial endeavor. It should be evident that the formulation proposed in this paper can be applied to mechanisms involving a virtually arbitrary number of elements, and the solution to the corresponding sequence of optimization problems can be found in a matter of seconds using second-order cone programming.

ACKNOWLEDGEMENT

Financial support for this research was provided by the Australian Research Council (grant number FL0992039) in the form of an Australian Laureate Fellowship awarded to Prof. Scott Sloan.

REFERENCES

Anderheggen, E. & Knöpfel, H. (1972), "Finite element limit analysis using linear programming." Int. J. Solids Struct., Vol. 8(12), 1413-1431.

Bottero A., Negre, R., Pastor, J. & Turgeman, S. (1980), "Finite element method and limit analysis theory for soil mechanics problems". Comput. Meth. App. Mech. Eng., Vol. 22(1), 131-149.

Chen, J., Yin, J.-H. & Lee, C.F. (2003), "Upper bound limit analysis of slope stability using rigid finite elements and nonlinear programming". Can. Geotech. J., Vol. 40(4), 742-752.

Chen, W.F. (1975). Limit Analysis and Soil Plasticity, Elsevier, Amsterdam.

Hambleton, J.P. & Drescher, A. (2011), "Approximate model for blunt objects indenting cohesive-frictional material". Int. J. Numer. Anal. Methods Geomech., (in press).

Hambleton, J.P. & Sloan, S.W. (2011), "A coordinate perturbation method for optimization of collapse mechanisms in upper bound limit analysis." Int. J. Solids Struct., (to be submitted).

Krabbenhøft, K., Lyamin, A.V., Hjiaj, M. & Sloan, S.W. (2005), "A new discontinuous upper bound limit analysis formulation". Int. J. Numer. Meth. Eng., Vol. 63(7), 1069-1088.

Lyamin, A.V., Krabbenhøft, K., Hjiaj, M. & Sloan, S.W. (2004), "Discontinuous velocity field for general yield criteria". In: Numerical Models in Geomechanics–NUMOG IX, Pande, G. & Pietruszczak, S. (eds.), Taylor & Francis, London., pp. 291-296.

Lyamin, A.V. & Sloan, S.W. (2002), "Upper bound limit analysis using linear finite elements and non-linear programming". Int. J. Numer. Anal. Methods Geomech., Vol. 26(2), 181-216.

Maciejewski, J. & Jarzębowski, A. (2004), "Application of kinematically admissible solutions to passive earth pressure problems". Int. J. Geomech., Vol. 4(2), 127-136.

Makrodimopoulos, A. & Martin, C.M. (2007), "Upper bound limit analysis using simplex strain elements and second-order cone programming". Int. J. Numer. Anal. Methods Geomech., Vol. 31(6), 835-865.

Makrodimopoulos, A. & Martin, C.M. (2008), “Upper bound limit analysis using discontinuous quadratic displacement fields”. Commun. Numer. Methods Eng., Vol. 24(11), 911-927.
Michalowski, R.L. (1997), “An estimate of the influence of soil weight on bearing capacity using limit analysis”. Soils and Foundations, Vol. 37(4), 57-64.
Michalowski, R.L. (2004), “Limit loads on reinforced foundation soils”. J. Geotech. Geoenviron. Eng., Vol. 130(4), 381-390
Michalowski, R.L. (2007), “Displacements of multiblock geotechnical structures subjected to seismic excitation”. J. Geotech. Geoenviron. Eng., Vol. 133(11), 1432-1439.
Sloan, S.W. & Kleeman, P.W. (1995), “Upper bound limit analysis using discontinuous velocity fields”. Comput. Meth. App. Mech. Eng., Vol. 127(1-4), 293-314.
Smith, C.S. & Gilbert, M. (2007), “Application of discontinuity layout optimization to plane plasticity problems”. Proc. R. Soc. A, Vol. 463(2086), 2461-2484.
Soon, S.-C. & Drescher, A. (2007), “Nonlinear failure criterion and passive thrust on retaining walls”. Int. J. Geomech., Vol. 7(4), 318-322.
Soubra, A.-H. (1999), “Upper-bound solutions for bearing capacity of foundations”. J. Geotech. Geoenviron. Eng., Vol. 125(1), 59-68.
Sturm, J.F. (1999), “Using SeDuMi 1.02, A Matlab toolbox for optimization over symmetric cones”. Optim. Methods Softw., Vol. 11(1), 625-653.

A NEW CONTACT DETECTION ALGORITHM FOR NON-SPHERICAL PARTICLES IN THE DISCRETE ELEMENT METHOD

C.W. Boon
Department of Engineering Science, University of Oxford, Oxford, OX1 3PJ, United Kingdom

G.T. Houlsby
Department of Engineering Science, University of Oxford, Oxford, OX1 3PJ, United Kingdom

S. Utili
Department of Engineering Science, University of Oxford, Oxford, OX1 3PJ, United Kingdom

ABSTRACT: *Houlsby (2009) presented the concept of "potential particles", a method for modelling non-circular particles for the Discrete Element Method (DEM). Potential particles can assume a wide variety of shapes, ranging from circular to almost polygonal in 2-D and from spherical to almost polyhedral in 3-D. Here we present a new algorithm for the contact detection between potential particles in both 2-D and 3-D. The contact detection problem is formulated into a Second-Order Cone Program (SOCP) and solved using the commercial optimization software MOSEK (MOSEK, 2010). The algorithm is suitable for both rounded and angular particles, and was found to be robust in a variety of situations. Two 3-D simulations are illustrated using the new algorithm.*

1 INTRODUCTION

The Discrete Element Method (DEM) has been widely used to model discontinuous media. It was first used to model blocky rocks (Cundall, 1971), and was then used to model granular materials (Cundall & Strack, 1979) in pharmaceutical, powder and civil engineering applications. In this paper, the original DEM formulation of Cundall & Strack (1979) is used, where particles are allowed to overlap at contacts (soft contact method). In a DEM calculation, an important fraction of computation time is devoted to contact detection and calculation of the overlap distance between particles. To calculate the forces exchanged between a pair of interacting particles, the location of the contact point and the overlap distance have to be determined (see Fig. 1). The small contact area which takes place in reality is approximated in the numerical model as a single contact point.

Most available DEM codes model granular particles as circular in 2-D and spherical in 3-D, since contact detection between circular and spherical particles is straightforward. For a pair of interacting circles (see Fig. 1), the overlap distance is the sum of the radii minus the distance between the centres of the particles, i.e., $R_1+R_2 - \|\mathbf{O_1}\text{-}\mathbf{O_2}\|$ in Fig. 1. Contact detection between non-spherical particles is significantly more complicated. Various methods to model non-spherical particles have been proposed, most of which impose restrictions on the shape of the particles, i.e., either the particle has to be polyhedral (Cundall, 1988; Nezami et al., 2006; Fraige et al., 2008) or the particle shape is restricted to a particular type of function (Lin & Ng, 1997; Pournin & Liebling, 2005). The method of potential particles introduced by Houlsby (2009) can model any convex particle shape from spherical to polyhedral in 3-D. In the following, a new algorithm based on second-order cone programming (SOCP) has been implemented for both 2-D and 3-D cases. We first explain

the contact detection problem for the 2-D case. The extension to the 3-D case is conceptually straightforward.

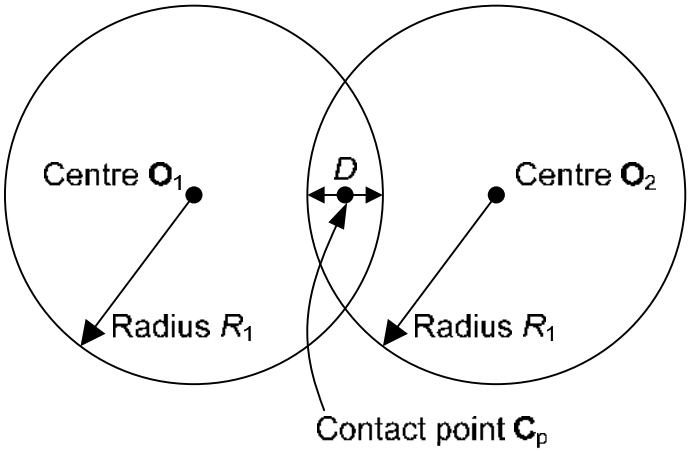

Fig. 1. Overlap distance and contact point for a pair of interacting disks in 2-D

2 POTENTIAL PARTICLES

Based on the notion that a convex particle can be constructed from an assembly of lines in 2-D or planes in 3-D, Houlsby (2009) describes an arbitrary convex particle in terms of a 2nd degree polynomial function (with respect to a local coordinate system). In 2-D, it is as follows:

$$f = (1-k)\left(\sum_{i=1}^{N}\left\langle a_i x + b_i y - d_i \right\rangle^2 - r^2\right) + k(x^2 + y^2 - R^2) \tag{1}$$

The terms $\langle a_i x + b_i y - d_i \rangle$ define the particle's constituent lines (see Fig. 2(a)), where $\langle\ \rangle$ are Macaulay brackets, i.e., $\langle x \rangle = x$, $x > 0$; $\langle x \rangle = 0$, $x \leq 0$. The lines are assembled such that their normal vectors point outward. They are summed quadratically and expanded by a distance r (see Fig. 2(b)), which is also related to the radius of the curvature at the corners (Houlsby, 2009). Further, a "shadow" circular particle is added; R is the radius of the circle, with $0 < k \leq 1$ denoting the fraction of circularity of the particle. Houlsby (2009) calls this function a "potential particle", which has the following properties:

- $f = 0$ defines the particle surface,
- $f < 0$ "inside" the particle,
- $f > 0$ "outside" the particle,
- the particle is strictly convex, and any surface f=*constant* is strictly convex.

The convexity of particles implies that only one contact point can exist between a pair of interacting particles. For computational reasons, the expression in Eq. (1) is normalized (slightly changing the meaning of k):

$$f = (1-k)\left(\sum_{i=1}^{N}\frac{\left\langle a_i x + b_i y - d_i \right\rangle^2}{r^2} - 1\right) + k\left(\frac{x^2}{R^2} + \frac{y^2}{R^2} - 1\right) \tag{2}$$

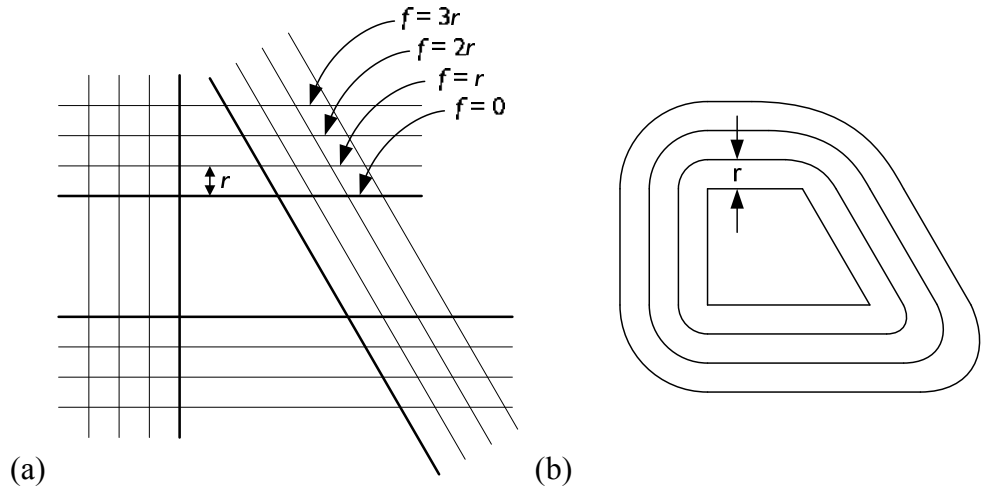

Fig. 2. Potential particles (from Houlsby (2009)) (a) A polygonal particle defined by a series of 2-D lines (b) Expanded particle with rounded corners. Lines have been quadratically summed.

3 CONTACT DETECTION ALGORITHM

To perform contact detection between a pair of potential particles f_A and f_B for the 2-D case, Houlsby (2009) proposes that one can solve one of the constrained minimization problems below:

$$\text{minimise } f_A \text{ subject to the constraint } f_B = 0 \tag{3}$$

$$\text{minimise } f_A + f_B \text{ subject to the constraint } f_A - f_B = 0 \tag{4}$$

Houlsby (2009) further shows how one can use the method of Lagrange Multipliers and implement the Newton-Raphson method to solve the equations. The method of potential particles was recently used by Harkness (2009) to simulate interlocking media. He shows how the Newton-Raphson formulation proposed by Houlsby (2009) can be extended to solve 3-D problems. He reports that the Newton-Raphson method suffers from the problem of poor convergence and suggests that the terms in the Macaulay brackets can be raised to a 3rd degree, so that the 2nd derivatives become continuous. Based on our studies, the Newton-Raphson method converges poorly when the particles are very angular (low k and r values). In the optimization literature, it is generally held that optimizers for second order cone programming (SOCP) are robust and efficient because they can use primal-dual interior-point methods (Andersen et al., 2003). The SOCP formulation for the contact detection problem is detailed in this paper. The optimization problem is then solved using the commercial software MOSEK (MOSEK, 2010).

The contact detection algorithm is first illustrated using an example in 2-D. The extension to 3-D will be explained later. Consider two potential particles, particle A $f_A(x_A, y_A) = 0$ and particle B $f_B(x_B, y_B) = 0$ defined in their local coordinates (x_A, y_A) and (x_B, y_B) respectively.

$$f_A = \frac{(1-k_A)}{r_A^2}\left(\sum_{i=1}^{N_A}\left\langle a_{iA}x_A + b_{iA}y_A - d_{iA}\right\rangle^2 - r_A^2\right) + \frac{k_A}{R_A^2}(x_A^2 + y_A^2 - R_A^2) \tag{5}$$

$$f_B = \frac{(1-k_B)}{r_B^2}\left(\sum_{i=1}^{N_B}\left\langle a_{iB}x_B + b_{iB}y_B - d_{iB}\right\rangle^2 - r_B^2\right) + \frac{k_B}{R_B^2}(x_B^2 + y_B^2 - R_B^2) \tag{6}$$

The particles f_A and f_B are translated and rotated in the global Cartesian coordinates. Define their centres in the global coordinates as (x_{0A}, y_{0A}) and (x_{0B}, y_{0B}), and their orientations as θ_A and θ_B anticlockwise. The transformation between the global Cartesian coordinates (x, y) and the local coordinates of particle A (x_A, y_A) can be expressed using the linear equations:

$$\begin{bmatrix} \cos\theta_A & -\sin\theta_A \\ \sin\theta_A & \cos\theta_A \end{bmatrix} \begin{bmatrix} x_A \\ y_A \end{bmatrix} + \begin{bmatrix} x_{0A} \\ y_{0A} \end{bmatrix} = \begin{bmatrix} x \\ y \end{bmatrix} \tag{7}$$

$$\begin{bmatrix} \cos\theta_B & -\sin\theta_B \\ \sin\theta_B & \cos\theta_B \end{bmatrix} \begin{bmatrix} x_B \\ y_B \end{bmatrix} + \begin{bmatrix} x_{0B} \\ y_{0B} \end{bmatrix} = \begin{bmatrix} x \\ y \end{bmatrix} \tag{8}$$

To find the closest point on particle B from particle A based on Eq. (3), Houlsby (2009) proposes to minimise f_A subject to $f_B = 0$. We can arrive at the same solution if we:

$$\text{minimise } f_A \text{ subject to } f_B \le 0 \tag{9}$$

where the equality constraint is replaced with an inequality constraint. Note that in Houlsby (2009), Eq. (3) and (4) are minimised using the Newton-Raphson method over the global Cartesian coordinates (x, y). However, in our SOCP formulation, we shall minimise over the local coordinates of the particles. We now have two copies of the local coordinate systems (x_A, y_A) and (x_B, y_B). They appear in the optimization problem as two linear equality constraints given by Eq. (10) and (11), based on their relationship with the global coordinates in Eq. (7) and (8).

$$x_A \cos\theta_A - y_A \sin\theta_A + x_{0A} = x_B \cos\theta_B - y_B \sin\theta_B + x_{0B} \tag{10}$$

$$x_A \sin\theta_A + y_A \cos\theta_A + y_{0A} = x_B \sin\theta_B + y_B \cos\theta_B + y_{0B} \tag{11}$$

To use the SOCP optimizer, one has to remove the Macaulay brackets in Eq. (2) by adding additional constraints and auxiliary slack variables. Taking particle A as an example:

$$f_A = \frac{(1-k_A)}{r_A^2}\left(\sum_{i=1}^{N_A} p_{iA}^2 - r_A^2\right) + \frac{k_A}{R_A^2}(x_A^2 + y_A^2 - R_A^2) \tag{12}$$

$$a_{iA}x_A + b_{iA}y_A - d_{iA} \le p_{iA}, \quad i = 1,..., N_A, \tag{13}$$

$$p_{iA} \ge 0, \quad i = 1,..., N_A. \tag{14}$$

Eq. (12) can be transformed into a second-order cone constraint:

$$\sqrt{\sum_{i=1}^{N_A} p_{iAc}^2 + x_{Ac}^2 + y_{Ac}^2} \le s_A \tag{15}$$

where

$$p_{iAc} = \frac{\sqrt{1-k_A}}{r_A} p_{iA} \tag{16}$$

$$x_{\mathrm{Ac}} = \frac{\sqrt{k_{\mathrm{A}}}}{R_{\mathrm{A}}} x_{\mathrm{A}} \tag{17}$$

$$y_{\mathrm{Ac}} = \frac{\sqrt{k_{\mathrm{A}}}}{R_{\mathrm{A}}} y_{\mathrm{A}} \tag{18}$$

Eq. (16), (17) and (18) can then be back substituted into Eq. (13) and (14). Note that the constant terms are absent in Eq. (15) because they can be dropped from the objective function for the purpose of minimisation. Similarly, particle B can be expressed as a second-order cone constraint. Since it is the constraint function, the constant terms will appear in s_{B}. To summarise, the SOCP formulation to minimise f_{A} subject to $f_{\mathrm{B}} \leq 0$ is as follows:

$$\text{minimise } s_{\mathrm{A}} \text{ subject to } s_{\mathrm{B}} \leq 1.0 \tag{19}$$

$$\sqrt{\sum_{i=1}^{N_{\mathrm{A}}} p_{i\mathrm{Ac}}^2 + x_{\mathrm{Ac}}^2 + y_{\mathrm{Ac}}^2} \leq s_{\mathrm{A}} \tag{20}$$

$$\sqrt{\sum_{i=1}^{N_{\mathrm{B}}} p_{i\mathrm{Bc}}^2 + x_{\mathrm{Bc}}^2 + y_{\mathrm{Bc}}^2} \leq s_{\mathrm{B}} \tag{21}$$

$$w_{\mathrm{As}} x_{\mathrm{Ac}} \cos\theta_{\mathrm{A}} - w_{\mathrm{As}} y_{\mathrm{Ac}} \sin\theta_{\mathrm{A}} - \left(w_{\mathrm{Bs}} x_{\mathrm{Bc}} \cos\theta_{\mathrm{B}} - w_{\mathrm{Bs}} y_{\mathrm{Bc}} \sin\theta_{\mathrm{B}}\right) = x_{0\mathrm{B}} - x_{0\mathrm{A}} \tag{22}$$

$$w_{\mathrm{As}} x_{\mathrm{Ac}} \sin\theta_{\mathrm{A}} + w_{\mathrm{As}} y_{\mathrm{Ac}} \cos\theta_{\mathrm{A}} - \left(w_{\mathrm{Bs}} x_{\mathrm{Bc}} \sin\theta_{\mathrm{B}} + w_{\mathrm{Bs}} y_{\mathrm{Bc}} \cos\theta_{\mathrm{B}}\right) = y_{0\mathrm{B}} - y_{0\mathrm{A}} \tag{23}$$

$$w_{\mathrm{As}} a_{i\mathrm{A}} x_{\mathrm{Ac}} + w_{\mathrm{As}} b_{i\mathrm{A}} y_{\mathrm{Ac}} - w_{\mathrm{Ap}} p_{i\mathrm{Ac}} \leq d_{i\mathrm{A}}, \quad i = 1,\ldots, N_{\mathrm{A}}, \tag{24}$$

$$w_{\mathrm{Bs}} a_{i\mathrm{B}} x_{\mathrm{Bc}} + w_{\mathrm{Bs}} b_{i\mathrm{B}} y_{\mathrm{Bc}} - w_{\mathrm{Bp}} p_{i\mathrm{Bc}} \leq d_{i\mathrm{B}}, \quad i = 1,\ldots, N_{\mathrm{B}}, \tag{25}$$

$$p_{i\mathrm{Ac}} \geq 0, \quad i = 1,\ldots, N_{\mathrm{A}}, \tag{26}$$

$$p_{i\mathrm{Bc}} \geq 0, \quad i = 1,\ldots, N_{\mathrm{B}}, \tag{27}$$

where

$$w_{\mathrm{Ap}} = \frac{r_{\mathrm{A}}}{\sqrt{1 - k_{\mathrm{A}}}} \tag{28}$$

$$w_{\mathrm{As}} = \frac{R_{\mathrm{A}}}{\sqrt{k_{\mathrm{A}}}} \tag{29}$$

$$w_{\mathrm{Bp}} = \frac{r_{\mathrm{B}}}{\sqrt{1 - k_{\mathrm{B}}}} \tag{30}$$

$$w_{\mathrm{As}} = \frac{R_{\mathrm{B}}}{\sqrt{k_{\mathrm{B}}}} \tag{31}$$

Eq. (19) – (27) can be input directly into the second-order cone optimizer in MOSEK. A linear inequality constraint as expressed in Eq. (24) and (25) is introduced for every "plane" i in the particles. Note that the variables w_{As}, w_{Bs}, w_{Ap}, w_{Bp} will become ill-conditioned when their denominators become zero. Specifically, this happens when the spherical term is absent, or when only the spherical term is present. This implies that some variables are redundant in these special cases, and a more concise SOCP formulation can be derived to replace Eq. (20) – (31). The minimum to Eq. (19), i.e., (x_{Ac}^*, y_{Ac}^*) has to be transformed back to the local coordinates of particle A using Eq. (17) and (18). Thereafter, one can find the global

Cartesian coordinates using Eq. (7). Once this minimum, say point P_2, at coordinates (x_{p2}, y_{p2}) is found, one can establish whether the particles overlap. There is overlap if $s_A < 1.0$ or $f_A(x_{p2}, y_{p2}) < 0.0$. The particles are just touching if $f_A(x_{p2}, y_{p2}) = 0.0$. If $f_A(x_{p2}, y_{p2}) > 0.0$, the particles are not overlapping or touching. Note that this point can be interpreted as the point on particle B which is "closest" to particle A. If there is overlap, we need to carry out a second computation by interchanging the roles of particle A and particle B, i.e., minimize s_B subject to $s_A \leq 1.0$. In other words, we need to find a new point P_1 at coordinates (x_{p1}, y_{p1}) on particle A which is "closest" to particle B. Following Houlsby (2009), the overlap distance can be taken as the Euclidean distance between (x_{p1}, y_{p1}) and (x_{p2}, y_{p2}). The contact point can be taken as the weighted mean of points (x_{p1}, y_{p1}) and (x_{p2}, y_{p2}); the weighting factors may depend on the relative stiffness of the particles (Houlsby, 2009). The contact normal can be taken as the combined first derivatives at (x_{p1}, y_{p1}) and (x_{p2}, y_{p2}) (refer to Houlsby (2009) for mathematical details).

For a 3-D problem, where particles A and particles B are defined as:

$$f_A = \frac{(1-k_A)}{r_A^2}\left(\sum_{i=1}^{N_A}\left\langle a_{iA}x_A + b_{iA}y_A + c_{iA}z_A - d_{iA}\right\rangle^2 - r_A^2\right) + \frac{k_A}{R_A^2}(x_A^2 + y_A^2 + z_A^2 - R_A^2) \quad (32)$$

$$f_B = \frac{(1-k_B)}{r_B^2}\left(\sum_{i=1}^{N_B}\left\langle a_{iB}x_B + b_{iB}y_B + c_{iB}z_B - d_{iB}\right\rangle^2 - r_B^2\right) + \frac{k_B}{R_B^2}(x_B^2 + y_B^2 + z_B^2 - R_B^2) \quad (33)$$

the SOCP formulation becomes:

$$\text{minimize } s_A \text{ subject to } s_B \leq 1.0 \quad (34)$$

$$\sqrt{\sum_{i=1}^{N_A} p_{iAc}^2 + x_{Ac}^2 + y_{Ac}^2 + z_{Ac}^2} \leq s_A \quad (35)$$

$$\sqrt{\sum_{i=1}^{N_B} p_{iBc}^2 + x_{Bc}^2 + y_{Bc}^2 + z_{Bc}^2} \leq s_B \quad (36)$$

$$w_{As}x_{Ac}Q_{A11} + w_{As}y_{Ac}Q_{A12} + w_{As}z_{Ac}Q_{A13} - \left(w_{Bs}x_{Bc}Q_{B11} + w_{Bs}y_{Bc}Q_{B12} + w_{Bs}z_{Bc}Q_{B13}\right) = x_{0B} - x_{0A} \quad (37)$$

$$w_{As}x_{Ac}Q_{A21} + w_{As}y_{Ac}Q_{A22} + w_{As}z_{Ac}Q_{A23} - \left(w_{Bs}x_{Bc}Q_{B21} + w_{Bs}y_{Bc}Q_{B22} + w_{Bs}z_{Bc}Q_{B23}\right) = y_{0B} - y_{0A} \quad (38)$$

$$w_{As}x_{Ac}Q_{A31} + w_{As}y_{Ac}Q_{A32} + w_{As}z_{Ac}Q_{A33} - \left(w_{Bs}x_{Bc}Q_{B31} + w_{Bs}y_{Bc}Q_{B32} + w_{Bs}z_{Bc}Q_{B33}\right) = z_{0B} - z_{0A} \quad (39)$$

$$w_{As}a_{iA}x_{Ac} + w_{As}b_{iA}y_{Ac} + w_{Ap}c_{iA}z_{Ac} - w_{Ap}p_{iAc} \leq d_{iA}, \quad i = 1,..., N_A, \quad (40)$$

$$w_{Bs}a_{iB}x_{Bc} + w_{Bs}b_{iB}y_{Bc} + w_{Bp}c_{iB}z_{Bc} - w_{Bp}p_{iBc} \leq d_{iB}, \quad i = 1,..., N_B, \quad (41)$$

$$p_{iAc} \geq 0, \quad i = 1,..., N_A, \quad (42)$$

$$p_{iBc} \geq 0, \quad i = 1,..., N_B, \quad (43)$$

where Q is the 3-D rotation matrix which can be conveniently be obtained from quaternion transformations (Kuipers, 2002). The variables w_{As}, w_{Bs}, w_{Ap}, w_{Bp} have been previously defined in Eq. (28) – (31).

We have detailed the SOCP formulation for the original formulation based on Eq. (3). The second formulation based on Eq. (4) is similar to Eq. (3), but we:

$$\text{minimise } s_A + s_B \text{ subject to } s_A - s_B = 0.0 \quad (44)$$

The rest of the equations for the SOCP remain the same Eq. (20) – (31). If the minimum to this problem, say point P_3 at coordinates (x_{p3}, y_{p3}), is "inside" both particles A and particles B, there is overlap. If there is overlap, P_3 is taken as the contact point. The contact normal can be taken as the combined normal vectors of the two particles evaluated at (x_{p3}, y_{p3}). The overlap distance can be found by performing a line search along the contact normal and bracketing two points, i.e., one on particle A and the other on particle B. The overlap distance can be calculated from the distance between these two points.

4 SIMULATIONS

Two simulations were run to examine the robustness of the contact detection algorithm. The open-source DEM code YADE (Kozicki & Donzé, 2008; Šmilauer, 2010) was linked to the optimization software MOSEK for the simulations.

Simulation A

In this simulation, potential particles are used to model the behaviour of granular material. The robustness of the algorithm is tested by simulating a variety of contact conditions involving faces or vertices. First a loose packing of 200 pyramidal particles is generated. Each particle is given a random orientation. Then the particles are allowed to fall under gravity to impact on a surface. Fig. 3 shows the result of the simulation at a number of time steps. Contact detection between every pair of particles potentially in contact is given as an optimization task to MOSEK. Using only one of the cores of a 3.1 GHz Core 2 Duo Processor on a PC with 4GB RAM, each optimization task was found to take a few hundred μs to a few ms on average for MOSEK to solve.

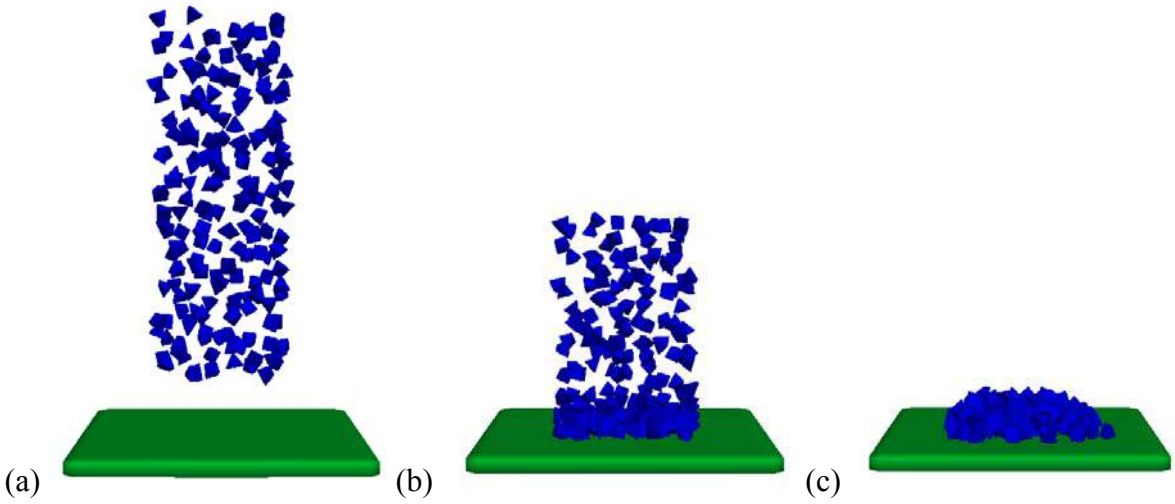

Fig. 3. Two hundred pyramidal particles falling under gravity: (a) loose packing as generated (b) after 4000 time steps (c) after 14000 time steps

Simulation B

In this simulation, the contact detection algorithm is used to simulate a sliding wedge problem in rock engineering (see Fig. 4). The model consists of four rigid blocks. Three blocks are fixed with only one wedge being allowed to move under gravity. The following discontinuities (rock joints) are present:

A: dip = 40° dip direction = 130°
B: dip = 60° dip direction = 220°

The critical friction angle at which the free wedge starts sliding is sought. The analytical solution for this problem is given in Hoek & Bray (1974). An elastic perfectly-plastic model with the Mohr-Coulomb yielding surface is assumed for the joint behaviour. This problem is statically determinate and independent of the size of the blocks. Hence, the joint stiffness and density do not affect the solution. To simulate the problem numerically, a high coefficient of friction is first assigned to the discontinuities. Once the wedge reaches static equilibrium, the friction is reduced by a small fraction. This process is repeated until static equilibrium is lost and the wedge starts sliding. The critical friction angle achieved from the simulation was 33.49°. The difference is minor compared to the analytical solution (33.36°) and the 3DEC solution (33.19°) reported by Itasca (2007). The physical behaviour was successfully captured by the contact detection algorithm, and was slightly better than that obtained by 3DEC.

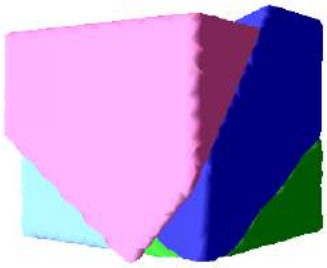

Fig. 4. Sliding wedge example (irregularities along the particle edges are an artifice of the graphical rendering package and are not present in the underlying model)

5 CONCLUSIONS

The method of potential particles introduced by Houlsby (2009) is a new way to define convex particles ranging from circular to polygonal in 2-D and from spherical to polyhedral in 3-D. This paper shows how the contact detection between potential particles can be formulated into a second-order cone program (SOCP). The commercial optimization software MOSEK is used to solve the optimization problem. No modifications have been made to tailor the optimizer specifically to solve this contact problem, and results are encouraging. The simulations show that the contact detection is robust even for particles nearly polygonal in 2-D and nearly polyhedral in 3-D. Moreover, the algorithm does not require the use of any special housekeeping algorithms even for shapes which are almost polyhedral, e.g., to identify the different types of interaction — face-face, face-edge, face-vertex, edge-edge, edge-vertex, or vertex-vertex.

6 ACKNOWLEDGEMENT

Dr. Erling Andersen from MOSEK is thanked for highlighting how the Macaulay brackets can be replaced with slack variables.

7 REFERENCES

Andersen, E. D., Roos, C., & Terlaky, T. (2003). “On implementing a primal-dual interior-point method for conic quadratic optimization”. Mathematical Programming, 95(2), 249-277.

Cundall, P. A. (1971). “A computer model for simulating progressive, large scale movement in blocky rock system”. Paper presented at the Sympo. ISRM. , Nancy, France.
Cundall, P. A. (1988). “Formulation of a three-dimensional distinct element model--Part I. A scheme to detect and represent contacts in a system composed of many polyhedral blocks”. International Journal of Rock Mechanics and Mining Sciences & Geomechanics Abstracts, 25(3), 107-116.
Cundall, P. A., & Strack, O. D. L. (1979). “Discrete numerical model for granular assemblies”. Geotechnique, 29(1), 47-65.
Fraige, F. Y., Langston, P. A., & Chen, G. Z. (2008). “Distinct element modelling of cubic particle packing and flow”. Powder Technology, 186(3), 224-240.
Harkness, J. (2009). “Potential particles for the modelling of interlocking media in three dimensions”. International Journal for Numerical Methods in Engineering, 80(12), 1573-1594.
Hoek, E., & Bray, J. (1974). Rock Slope Engineering, The Institution of Mining and Metallurgy, London.
Houlsby, G. T. (2009). “Potential particles: a method for modelling non-circular particles in DEM”. Computers and Geotechnics, 36(6), 953-959.
Itasca. (2007). 3DEC 3-dimensional distinct element code, Itasca Consulting Group Inc. Minneapolis, MN.
Kozicki, J., & Donzé, F. V. (2008). A new open-source software developed for numerical simulations using discrete modeling methods. Computer Methods in Applied Mechanics and Engineering, 197(49-50), 4429-4443.
Kuipers, J. B. (2002). Quaternions and Rotation Sequences: A Primer with Applications to Orbits, Aerospace and Virtual Reality: Princeton University Press.
Lin, X., & Ng, T. T. (1997). “A three-dimensional discrete element model using arrays of ellipsoids”. Geotechnique, 47(2), 319-329.
MOSEK. (2010). The Optimisation Tools Manual: MOSEK ApS.
Nezami, E. G., Hashash, Y. M. A., Zhao, D., & Ghaboussi, J. (2006). “Shortest link method for contact detection in discrete element method”. International Journal for Numerical and Analytical Methods in Geomechanics, 30(8), 783-801.
Pournin, L., & Liebling, T. M. (2005). A generalization of distinct element method to tridimensional particles with complex shapes. Paper presented at the Powders and Grains 2005, Stuttgart.
Šmilauer, V. (2010), “Cohesive Particle Model using the Discrete Element Method on the Yade Platform,” PhD thesis, Czech Technical University and Université Grenoble I.

PARTICLE SHAPE DESCRIPTORS AND THEIR INFLUENCE ON THE MECHANICAL BEHAVIOR

M. Chaze
LTDS, Ecole Centrale de Lyon, Université de Lyon1, 36 avenue Guy de Collongue, 69134 Ecully cedex, FRANCE
marie.chaze@ec-lyon.fr

ABSTRACT: *The present study is a part of a collaborative French national research project CEGEO/shape (Change of Scale in GEOmaterials). The purpose of benchmark collaborative numerical tests performed, using CD (Contact Dynamics) or MD (Molecular Dynamics) methods, is to quantify the non-circular shape of particles, by their degree of distortion relative to the disk, and to analyse their influence on the local and the macroscopic mechanical properties of granular materials. This contribution points out the compact collection of rigid octagonal shaped particles, built in accordance with our specific shape index. It also deals with the first investigations of realistic 3D particles. The following five biaxial compressions tests (which bring difficulties such as little deformations and multiple localizations) are numerical simulations, using NSCD (Non Smooth Contact Dynamic) method and LMGC90 software. The macroscopic behavior is studied in terms of solid fraction and internal angle of friction. We show that the internal angle is influenced by the increased anisotropy of friction forces and the contact orientations with the shape indicator. The variation of the initial assembly density (area of solids over total area) and the final density in the critical state is modelled using the number of particle edges, in order to explain the higher peak shearing resistance of assemblies with smaller initial void ratio or higher coordination number. Besides unilateral contact and Coulomb friction, other parameters relevant to the shape and contact anisotropy, which influence the anisotropy of stress transmission, as the ratio of edge-to-edge or vertex-to-edge active contacts, the stick-slip phenomenon, and the friction mobility, (ratio of tangential and normal contact forces) are quantified. Finally, different approaches have been proposed for the change of scale of kinematic variables. Analysis of local kinematics, and relation between the global strain and the local relative displacements at the contacts is studied.*

1 INTRODUCTION

Last decades, the discrete-element approach has been used as a tool to investigate the mechanical response of geomaterials at the grain level. Several averaging procedures have been proposed in order to define the stress and the strain tensor based on the contact forces and displacements of individual grains. These estimates have been used to perform a direct calculation of the incremental stress-strain response of disks and spheres assemblies. The modeling approach of DEM, especially with Coulomb friction criterion, is usually applied to clumps, by creating irregular curved composite particles. Since the spherical geometry of the particles overestimate the role of rotations, we should evaluate the incremental response by using arbitrary shaped particles. This DEM type simulation, which treat the particle as a

complex polygon was initiated by Favier et al. (1999), Alonso-Marroquin et al. (2005). Recently, some investigations appeared using three-dimensional loading paths with polyhedral particles, for example Latham J.P et al. (2008), Taylor et al. (2006).

2 BIDIMENSIONAL PARTICLE SHAPE DESCRIPTORS

The idea of our collaborative research project CEGEO, CECEO et al. (2010), is to propose a particle shape index, and to understand its role for the strength properties of the granular samples. Different 2D descriptors of shape can be extracted from the perimeter coordinates. Shape or form may be quantified from disk/sphere or from square/cube using surface area and/or volume comparison (spheres and cubes can be circumscribing into equivalent volume). It can also be quantified by axial ratios giving elongation or flatness Nouguier-Lehon (2010), Azema E. (2010). Another shape property governing both space filling and strength behavior, is the angularity or roundness. In our project we choose to vary the particle shape by their discrepancy or the degree of distortion from a circular particle (suggestion F. Radjai, LMGC). We characterized it using the scalar parameter

$$\eta = \Delta R / R \tag{1}$$

where R is the radius of the largest circle containing the particle, and ΔR is the difference between the ex- and the in-circle of the particle. The present study is performed considering inscribed octagon, see Fig. 1. All the vertices are on the same circle of radius R, consequently the form is called isometric, and circumscribed in circle of radius R-ΔR (Chaze, 2009).

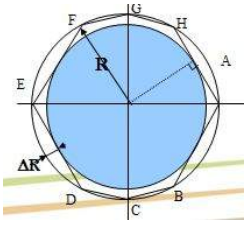

Fig. 1. Geometrical octagon design

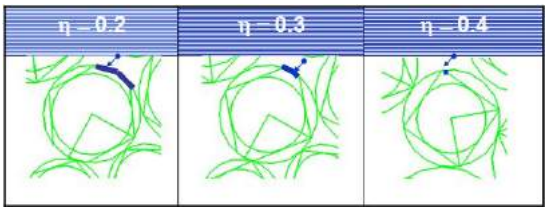

Fig. 2. Some typical octagons using the η evolution

The surface area, A, of a given particle can be obtained directly "Eq. (2)" as the sum of the area of the 12 triangles in the octagon, see Fig. 1.

$$A = 4\mathrm{R}^2\left[(1-\eta)\sqrt{\eta(2-\eta)} + |R(1-\eta)^2 - 0.5|\right] \tag{2}$$

Specific surface A_s is calculated as the ratio of surface A to surface of ex-circle of octagon. It decrease, pass by a minimum value and increase with η , Fig. 3.

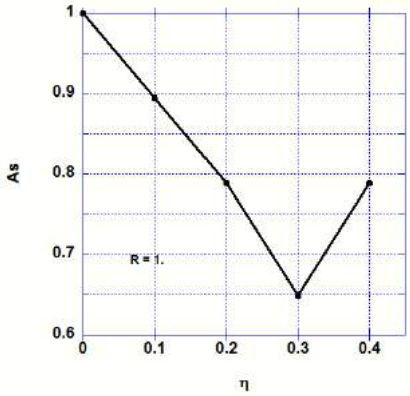

Fig. 3. Specific surface $\mathbf{A_s}$ as a function of η

η	0.	0.1	0.2	0.3	0.4
$\mathbf{A_s}$	1.	0.894	0.789	0.649	0.789
$\mathbf{A_s}°$	1.	0.81	0.64	0.49	0.36

Table 1.

These values are indeed within the intervals allowed by the construction, for example $A_s°$ specific surface of the in-circle of octagon, (see Table 1).

3 THE 2D SAMPLES

The 2D granular model assembles 5000 poly-sized frictional particles. We generated five different samples of particles, varying η from 0. to 0.4 by step of 0.1, see Figs. 2 and 4. The octagonal particles were inscribed in the disks (radius R), which are the reference.

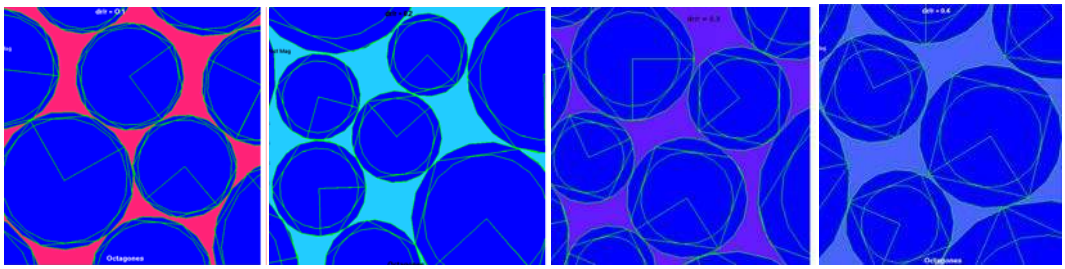

Fig. 4. Generation of different samples $\eta = 0.1, 0.2, 0.3, 0.4$

The method used for the creation of a sample is the follow: we begin with a dense packing composed of disks ($\eta = 0$), Voiret (2008), the reference, with a uniform distribution in particle volume fractions. The radius respects $R_{max} = 3R_{min}$, their ranges vary from $3.e^{-2}$ to $9.8\ e^{-2}$ m and the density is equal to 2800 $kg.m^{-3}$. The orientation of particles is given by pseudo-random generator to reduce the preferential direction. We create a square sample, by applying a constant velocity on the right wall and on the upper wall. The initial velocity is randomized. This compaction procedure provides isotropic samples, and reduces the preferential direction of contact normal, (which does not occur if instead we use deposit under gravity). The interparticle friction is $\mu=0$, for a dense confined packing and, the walls are frictionless. After that, the isotropic compression is computed by applying a constant stress**,** also called confining stress, 10 kPa, on the left, right and the upper wall. The isotropic samples were sheared by applying a displacement on the top wall and one constant confining stress on the lateral walls. To avoid dynamics effects, the velocity is chosen such as the *inertia parameter* $I \sim 10^{-4}$. The friction coefficient between grains is 0.5. The walls have masses equal approximately to the mass of the layer of grains, which has revealed to be a good choice the point of view of the dynamical response of the walls, with respect to the dynamical response of the grains.

4 THE NUMERICAL EXPERIMENTS

All simulations have been performed with the Open Source platform *LMGC90,* Dubois F. & Renouf M.(2006). http://www.lmgc.univ-montp2.fr/~dubois/LMGC90. The interaction laws use the *Contact Dynamics* approach which can treat unilateral and dry friction without smoothing approximation. We should reconsider the Signorini complementary condition, Jean M. (1999). The model used in these hereafter experiments, the IQS (Inelastic Quasi Shock) frictional contact law, is treated with NSCD method (an implicit scheme using large time steps), Cambou B. & Jean M. (2001). The computation has been performed with the same parameters, for the five benchmark tests except for the maximal number of iterations, especially during the peak in order not to deteriorate the equilibrium results.

5 MECHANICAL ANALYSIS OF THE TESTS MICROSCOPIC RESPONSE

The following figures present evolution of the samples microscopic response at the initial and critical states:

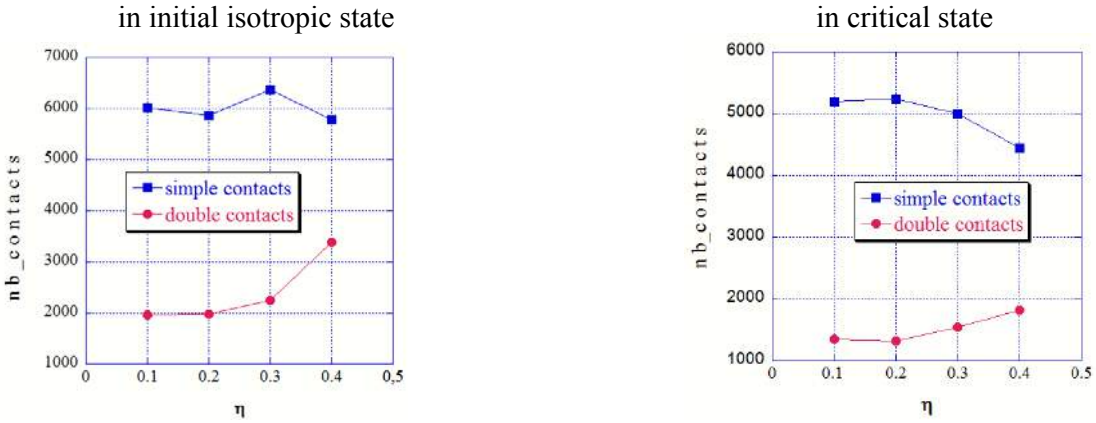

Fig. 5. Evolution of the contacts number with η at initial isotropic and critical states

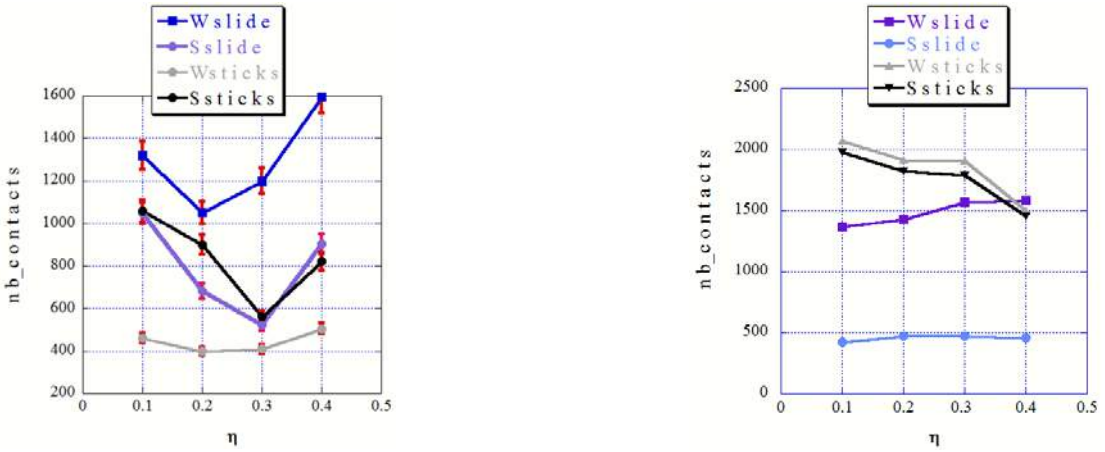

Fig. 6. Evolution of strong, weak, sticks and slide contacts number with η at initial isotropic and critical states

Fig. 5 and Fig. 6 provide evidence for large class of "weak" forces carried by vertex-to-edge slide contacts. Strong force chains are composed of edge-to-edge stick contacts. We also observe that the proportion of double contact, side-to-side contact increases with η both in initial isotropic and in critical states (especially for $\eta \geq 0.4$ when the octagons became squares result of the occurrence of facetization). Similar tendency with contact coordination number Z_{iso}, defined as the mean number of contacts per particle in initial isotropic state and, Z_{critic} in critical state. We distinguish the coordination number Z' (see Table 2) as the mean number of contacting neighbors per particles, from the Z defined as the mean number of contacts per particle, Fig. 7 Z'_{iso} may be correlated with the number of particle's degrees of freedom and, consequently, they take place in the mechanical equilibrium of particles CEGEO et al. (2010).

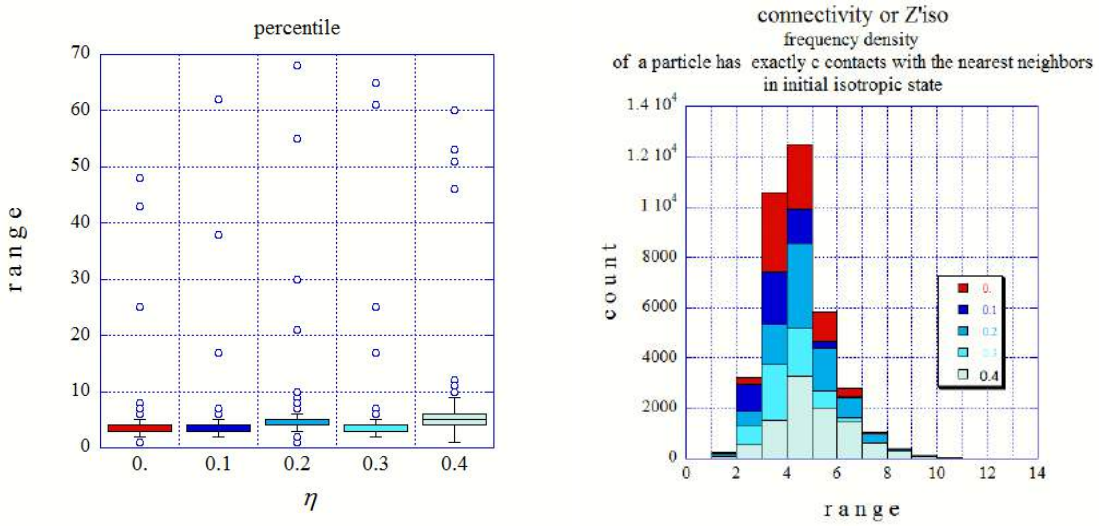

Fig. 7. Percentile rank and histogram of distribution of a dataset Z'_{iso} as a function of η

Percentiles represent the summation or integral of the area under the normal curve. Box plot: the horizontal line in the center indicates the median (50th percentile), top and bottom, 25th and 75th. For example, when $\eta = 0.$ we deduce, in Fig. 7, that the median is around four and the half of grains has a connectivity of about four. The points which are out of the box represent the number of contacts with the wall. An interesting feature of the histogram graph is that, the proportion of c contact number of a particle with its nearest neighbors, is maximum to the class [4, 5] for the non-circular particles. The sample is prepared with $\mu = 0$.

Shapes indicator	0.	0.1	0.2	0.3	0.4
Coordinence Z_{iso}' Z_{critic}'	3.81 3.116	4.25 3.890	5.90 3.868	5.20 3.945	5.01 3.850
Compacity C_{iso} C_{crit}	0.845 0.810	0.859 0.800	0.863 0.802	0.874 0.815	0.876 0.820

Table 2.

The compacity (packing fraction) is maximum in initial isotropic state C_{iso} as show in Fig. 8. This parameter should be modeled as a function of the specific surface A_s.

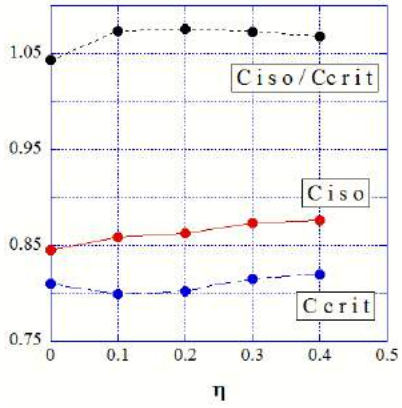

Fig. 8. Solid fraction at the isotropic state C_{iso}, at the critical state C_{crit} and C_{iso} / C_{crit} as a function of η

The texture of two packings η 0.3 and 0.4 in terms of normal contact distribution is present Fig. 9. The privileged direction rotates as a result of vertical compression and becomes vertical in the residual state.

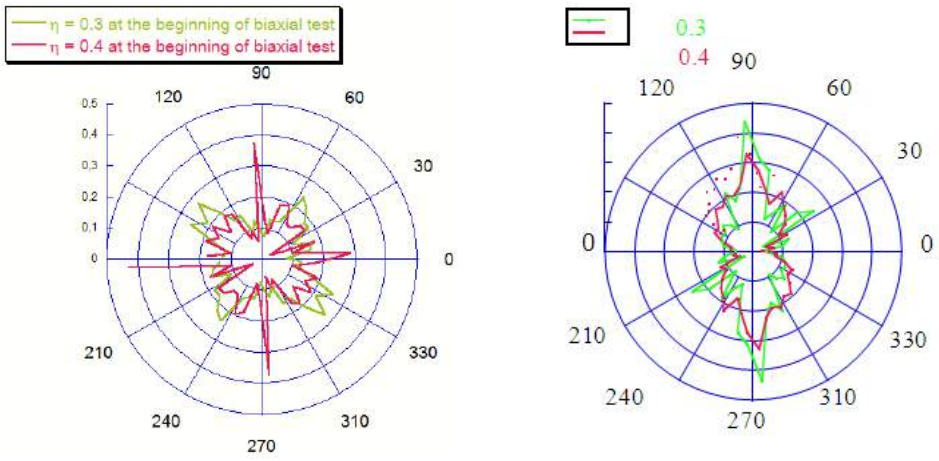

Fig. 9. Polar representation θ (π /sector) of normal conctact distribution normalized, for $\eta = 0.3$ and 0.4 at the beginning and the critical state

6 MECHANICAL ANALYSIS MACROSCOPIC RESPONSE OF THE TESTS

In Fig. 10, the dilation response of the sample containing octagons shows steeper dilatancy slope than the assembly containing disks. Squares show steeper dilatancy slope than octagons.

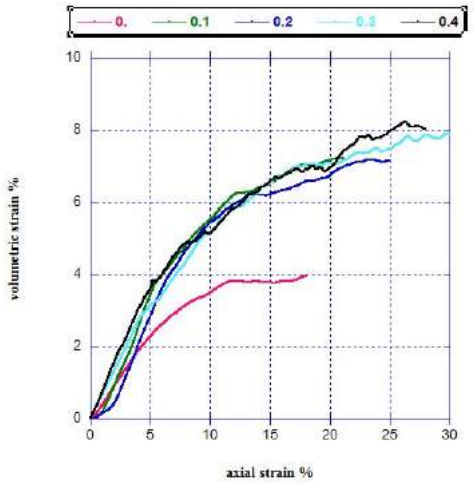

Fig. 10. Volumetric strain versus axial strain

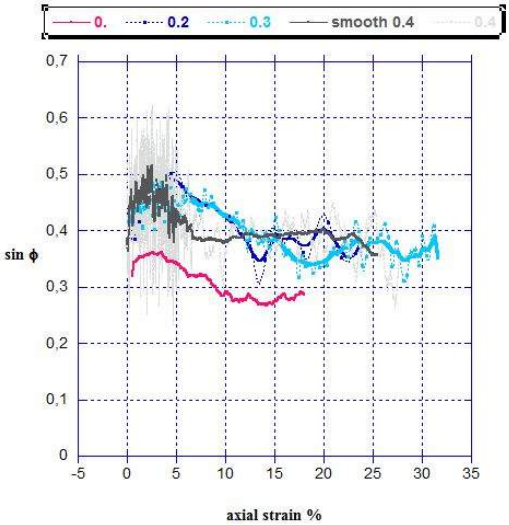

Fig. 11. Stress Strain response

The shear strength is characterized by the internal angle of friction ϕ, such the sin ϕ = q / p, where q = $(\sigma_1 - \sigma_2)/2$ and p = $(\sigma_1 + \sigma_2)/2$. The sin ϕ increases from zero to a peak value and after is relaxing to a constant material-dependents value sin ϕ^*. Fig.10 seems to indicate that sin ϕ^* increase with η. We define a static quantity, CEGEO et al. (2010),

$$M = < \frac{f_t}{(\mu f_n)} > \qquad (3)$$

where f_t is the absolute value of the friction force, f_n is the normal force. Fig. 12 shows that the rotational degrees of freedom, M, is an increasing function of η.

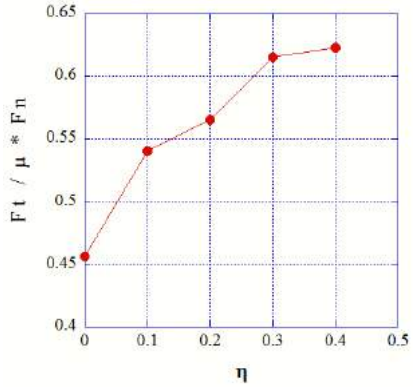

Fig. 12. Friction mobilization in the steady state as a function of η

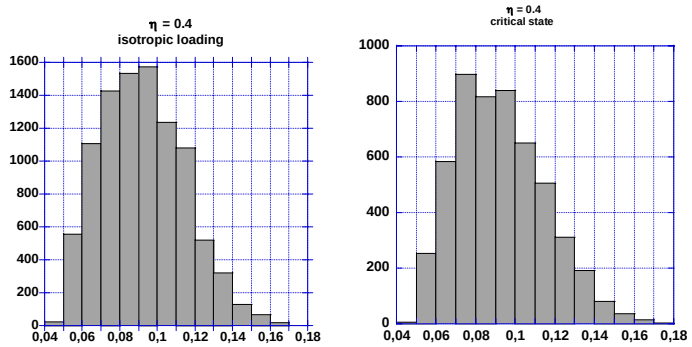

Fig. 13. Distribution of branch vector set for $\eta = 0.4$ in initial isotropic and critical states

7 ANALYSIS OF LOCAL KINEMATICS

In unconsolidated granular media an important element is the description of local arrangement of the grains and the possible correlations between their positions. The simplest way of describing neighborhood and the steric environment of a grain is to build its Voronoi cell, to study its size and shape, and to correlate them with the nearest neighbors. Here we calculate branch vector, Konishi et al. (1988), as the vector connecting two particles in contact.

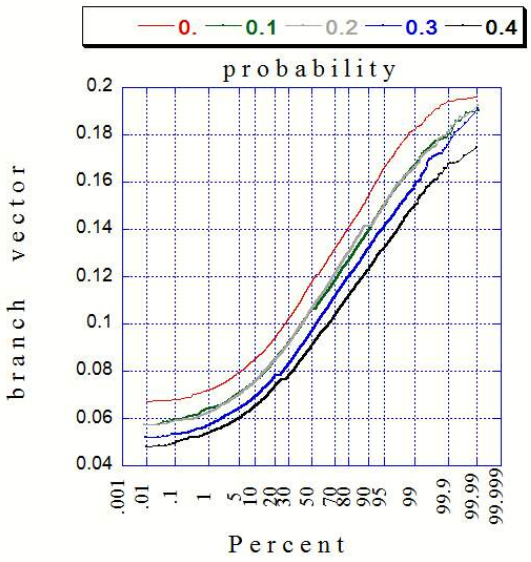

Fig. 14. Probability distribution function of branch vector set for the different value of η

The distribution of branch vector, Fig. 14, confirms the previous results of the assemblies with smaller initial void ratio or higher coordination number. To establish the link between local variables, the void ratio and the strain tensor we apply the relationship between local displacements of particles and the strain tensor, Cambou, Chaze et al. (2000). The incremental strain is defined "Eq. 4", respect to hypothesis of small strains, with the reference configuration defined at the beginning of the analyzed increment, so:

$$\delta\varepsilon_{ij}^{\alpha} = \frac{1}{2}\left(\frac{\delta u_i^{\alpha}}{\delta x_j^{\alpha 0}} + \frac{\delta u_j^{\alpha}}{\delta x_i^{\alpha 0}}\right) \tag{4}$$

where $\delta\varepsilon_{ij}^{\alpha}$ is the increment of strain defined for α increment, δu_i^{α} is the increment of displacement during α increment, $x_i^{\alpha 0}$ is the reference configuration defined at the beginning for α increment. Using the Delaunay triangulation it will be possible to derive a mean value of the global strain and it is assumed that the strain tensor defined on each triangular element is constant.

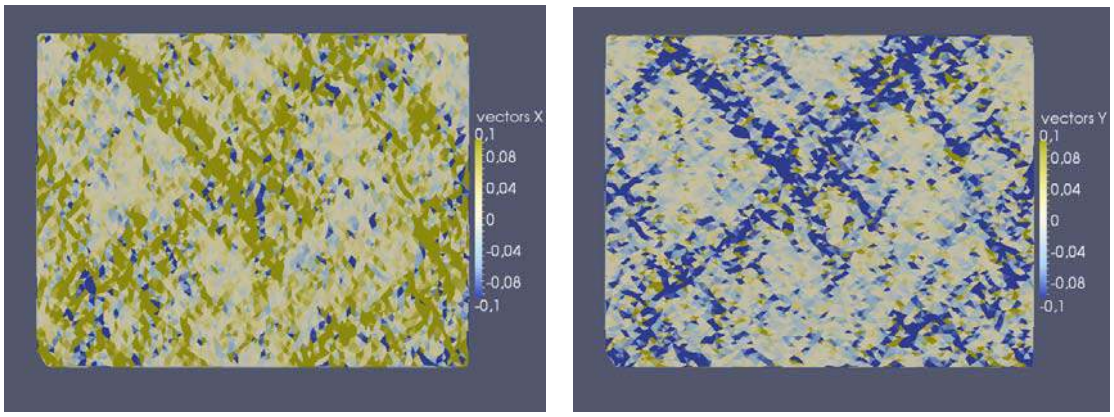

Fig. 15. View of ε_{11} for compressive displacement and ε_{22} for extension displacement for $\eta = 0.3$ near the peak value of the internal angle of friction .

Different deformation regimes may be expected: at the beginning of the compression the deformation is much more distributed Fig. 16 and, as show in Fig. 15 shear band have been developed. In the critical state the shear bands are missing, Fig. 17 For both figures the density contrasts are similar.

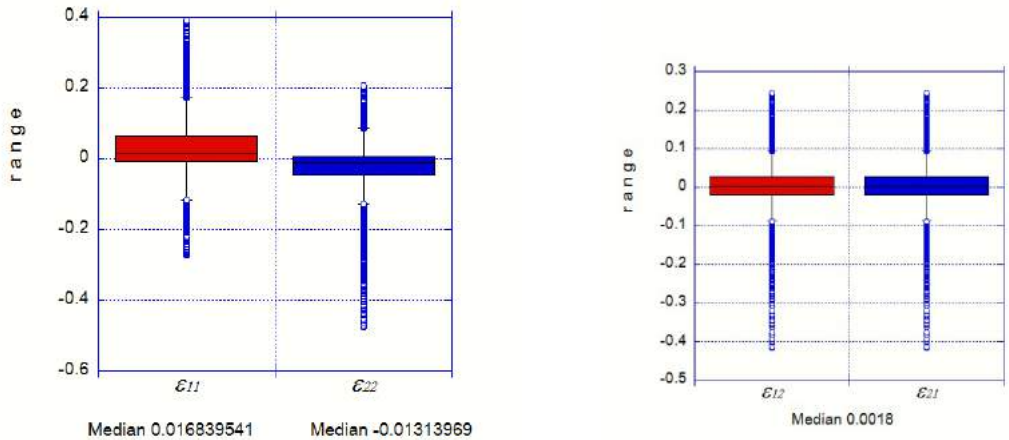

Fig. 16. Percentile of a dataset ε_{11}, ε_{22}, ε_{12}, ε_{21} according to deformation's definition

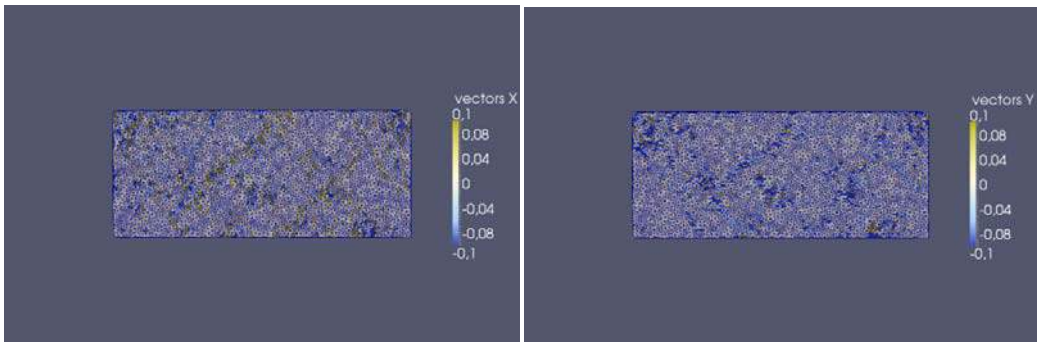

Fig. 17. Repartition of ε_{11} and ε_{22} resulting between 0.1 % increment of strain in the critical state.

To measure the localization of deformation Davy at al. (1995), use a participation ratio defined as:

$$S = \frac{1}{\Sigma} \frac{\left(\iint_{\Sigma} \varepsilon S\right)^2}{\iint_{\Sigma} \varepsilon^2 S} \tag{5}$$

ε represents a scalar measure of the deformation tensor, Σ is the surface area. The participation ratio Σ is a measure of the percentage surface that appears deformed. If ε is perfectly homogeneously distributed Σ equals to 1. As deformation becomes localized, Σ is smaller than 1; the larger the fluctuations become in local strain, smaller is Σ. If the deformation is localized in a shear band, Σ is a measurement of the surface of this shear band. These calculations provide a physical framework to understand the role of disorder and local deformation mecanisms on the deformation processes.

8 3D EXTENSION

To go further, we model 3D shape effects in granular systems. We started with the sample composed of polyhedral particles, which have the following specifications: average vertex number 10, vertex total number 9960, average face number 16, number of total faces 15936. The first results, are showing in Fig. 18 and 19, are promising and realistic.

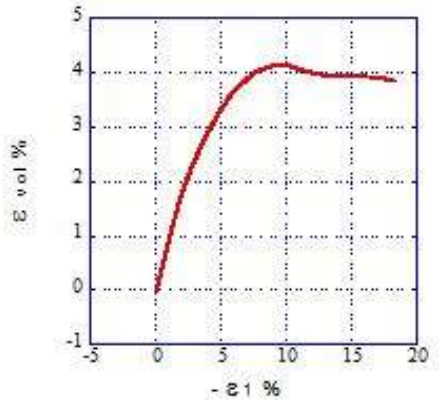

Fig. 18. Volumetric strain versus axial strain

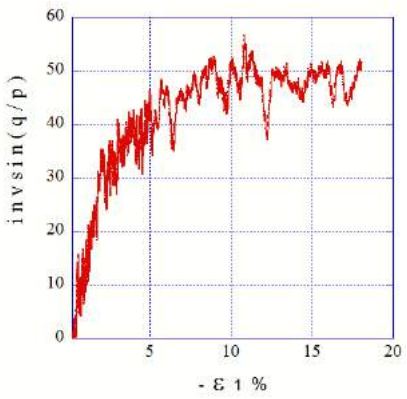

Fig. 19. Stress Strain response

9 CONCLUSIONS

The goal in these experiments is to suggest that the use of shape parameter η, describing deviation to circular shape applied to the isometric octagons, enforces and controls certain mechanically based rules of granular media. The doctrine that these samples present some

difficulties does not prevent to demonstrate that the shear strength has a monotonic dependence to η. With the variation of η, octagons become irregular, regular, and square with change of vertex number. Besides unilateral contact and Coulomb friction, the change of vertex number influences the ways of contacting, vertex against side, side against side, and also the friction mobilization. Such contacts cause severe *indetermination*, i.e. the contact forces solution of the dynamical problem, is far to be unique, due the rigid behavior of the grains, and to Coulomb friction. Also, *locking* may happen, the evolution of the grains is not possible or is possible only if the reaction forces increase dramatically, and in rough case, if at last some errors are allowed. These behaviors are favored in collections of octagons which have a tendency to organize as crystals, like clusters, while collections of poly-sized disks are easier to deform.

ACKNOWLEDGEMENT

The author is indebted Danescu A., Cambou B., Radjai F., Jean M. for theirs stimulations, Dubois F. and Renouf M., the authors of the *LMGC90* software, for many remarks.

REFERENCES

Alonzo-Marroquin, F., & Hermann, H.J., (2005) "The incremental response of soil. An investigation using a discrete-element model", Journal of Engineering Mathematics 52, 11-34.

Azéma, E., & Radjaï, F., (2010) "Stress-strain behavior and geometrical properties of packings of elongated particles", Phys. Rev. E **81**, 051304.

Cambou, B., & Chaze, M., & Dedecker. F., "Change of scale in granular materials", Eur. J. Mech. A/Solids 19(200) 999-1014.

Cambou, B., & Jean, M., (2001), Micromécanique des matériaux granulaires, Hermes Sciences, Traité MIM.

Chaze, M., (2009), "Effect of grain shape on the behaviour of granular materials in biaxial compression", Proceedings of '2009 COMGEO, France, International Center for Computational Engineering-eJournal.

CEGEO, Saint-Cyr, & Szarf, & Voiret, & Azema, & Richefeu, & Delenne, & Combe, & Nouguier-Lehon, & Villard, & Sornay, & Chaze, & Radjai, (2010), "Particle shape dependence in granular media" submitted PRL.

Davy, P., & Hansen, A., & Bonnet, E., & Shou-Zhu Zhang, (1995) "Localization and fault growth in layered bittrle-ductile systems: implications for deformations of the continental lithosphere", Journal of Geophysical Research, 100(B4), PAGES 6281-6294, APRIL 10.

Dubois, F. & Renouf, M. (2007), "Numerical strategies and software architecture dedicated to the modeling of dynamical systems in interaction. Application to multibody dynamics". MULTIBODY DYNAMICS 2007 Thematic Conference Milano, Italy.

Favier, J.P., et al. (1999), "Shape representation of axi-symetrical, non spherical particles in discrete element simulation using multi-element particles", Engineering Computation 16(4), 467-480.

Jean, M., (1999), "The non smooth contact dynamics method" Comp. Meth. Appl. Mech. Engrg. Vol 177, 233-257.

Konishi, J., Narusi F., (1988), "A note on fabric in terms of voids", Micromechanics of Granular Materials, edited by Satake M.

Latham, J.P., & Munjiza, A., & Garzia, X., &Xiang J., & Guises, R., (2008) "Three-dimentional particle shape acquisition and shape library for DEM and FEM/DEM simulation" Mineral Engineering 21, 797-805

Nouguier-Lehon, C., (2010), “Effect of the grain elongation on the behavior of granular materials in biaxial compression”, C. R. Mécanique 338, pp. 587-595.
Voiret, C. (2008) Ph.D. thesis, Université Montpellier II.
Taylor, M.A., Garboczi, E.J., Erdogan, S.T., Fowler, D.W., 2006, “Some properties of irregular particles in 3D, Powder Technology 162, 1-15.

A GEOMETRIC PARAMETER ERROR ESTIMATION METHOD FOR INVERSE PROBLEMS

E. Imre[1,2], P.Q. Trang[2], S. Fityus[3], G. Telekes[1]
[1] *Szent Istvan University, Ybl Miklos Civil Eng. Fac., Budapest, Hungary*
[2]*Budapest University of Technology and Economics, Budapest, Hungary*
[3]*The School of Engineering, The University of Newcastle Callaghan, Newcastle, Australia*

ABSTRACT: *The steps of a general geometry-based, parameter error estimation method are summarized here. It is known that in the case of random measuring noise, the confidence domain for the parameter solution of an inverse problem (i.e. a domain where the true value of the parameter vector may be encountered with a specified probability) is generally defined by a contour of the linearized, noise-free merit function. To generalize this concept, it is suggested that the non-linearity can be taken into account when a contour of the non-linear noise-free merit function is used instead of a contour of the linearized one. It is shown that the parameter domains, so-defined, are also geometrical obstruction domains for the minimisation methods (i.e. the actual merit functions are charaterized by a 'flat, irregular' surface with a nearly uniform value and with many critical points due to the noise), irrespective of the type of the noise. Since these parameter domains are asymmetric and not necessarily connected, a method is suggested to find the connected parts and to 'measure' them. The method is illustrated by some examples.*

1 INTRODUCTION

Parameter error estimation is a part of the concept of reliability testing of non-linear inverse problem solutions. These concepts can be used beyond parameter estimation, for model validation, model discrimination or to check the "goodness" of measured data. Reliability criteria for a non-linear inverse problem solution can be formulated as follows (and some additional basic notions are explained in section 2).

Reliability criteria

In general, the solution of the inverse problem is reliable if it is unique, and if the determined parameters are acceptably precise (Imre, 1996). The uniqueness condition is met if:

(i) the solution of the noise-free inverse problem is unique (i.e. if the global minimum of the noise-free merit function is single and not degenerated, or in other words, if the derivative of the model response function has its maximum rank at the single minimiser) and,

(ii) the local minima of the noise-free merit function are not deeper than the minimum of the real-life merit function at $\boldsymbol{p}_{min}$.

The preciseness condition is met if the error domain (or confidence domain) of the solution is situated within the physically admissible parameter domain.

Parameter error estimation methods

Let us assume that the solution of the inverse problem, determined generally by minimisation, is the parameter vector $\boldsymbol{p}_{min,}$ and that the error of the solution is $\boldsymbol{d} = \boldsymbol{p}_{true} - \boldsymbol{p}_{min}$. Since $\boldsymbol{p}_{min}$ may vary as a function of the random (and deterministic) noise, the true value of the solution, $\boldsymbol{p}_{true} = \boldsymbol{p}_{min} + \boldsymbol{d}$, is generally characterized by a domain. In the simplest case a "distribution free" confidence interval can be defined for each element of the parameter vector if the standard deviation of these (which is generally not available) is known, using the Tschebiseff inequality.

A confidence domain can be determined by the Monte Carlo method as follows. A "fictitious world" is built in such a way that we repetitively generate synthetic noise, add it to some simulated noise-free data and determine a new minimizer $\boldsymbol{p}_i$ *: i=1, 2, 3…* It is assumed that the distribution of $\boldsymbol{p}_i - \boldsymbol{p}_{true}$ and $\boldsymbol{p}_i - \boldsymbol{p}_{min}$ is the same. Confidence intervals for the individual parameters or confidence regions for the joint distribution defined by the linearized merit function contours can be used (Press et al, 1986, see Figs 1 and 2).

The least-squares fitting is a maximum likelihood estimation of the parameters if the measurement error is normally distributed. Further, if the least-squares fitting is weighted with the variances of the measured data then the solution follows a χ^2 distribution.

If the measurement errors are normally distributed (which is generally the case for random errors, according to the central limit theorem of probability theory) and the model can be linearized (the uncertainties do not extend outside the region of the linearized model) then the minimum of the merit function $\chi^2(\boldsymbol{p}_{min})$ has an *N-M* degree chi-square distribution (where *N* is the number of measurements and *M* is the number of parameters). Moreover, the distribution of $\Delta\chi^2 = \chi^2(\boldsymbol{p}_{min}) - \chi^2(\boldsymbol{p}_{min})$ is with a *k* degree chi-square distribution (*k* parameters are identified). For example, if we identify *k*=1 or *k*=3 parameters with 68.3% probability, then the value of $\Delta\chi^2$ is equal to 1 or 3.53, respectively (see Table 1). Especially, the standard deviation of parameter $\sigma(p_i)$ is the half of the 68.3% confidence interval (i.e. *k*=1, the orthogonal projection of the contour value 1 of the $\Delta\chi^2$ linearized merit function, see Fig 1) which can be computed with the linearized model as follows:

$$\sigma(p_i)(\boldsymbol{p}_{min})^2 = c_{i,i}(\boldsymbol{p}_{min})F(\boldsymbol{p}_{min}) \tag{1}$$

where $F(\boldsymbol{p}_{min})$ is the minimum of the merit function (i.e. the estimated variance of the noise), $c_{i,i}$ is the element of the covariance matrix *C* which is the inverse of the matrix *Q* (the derivative of the model response function, defined and explained in section 2):

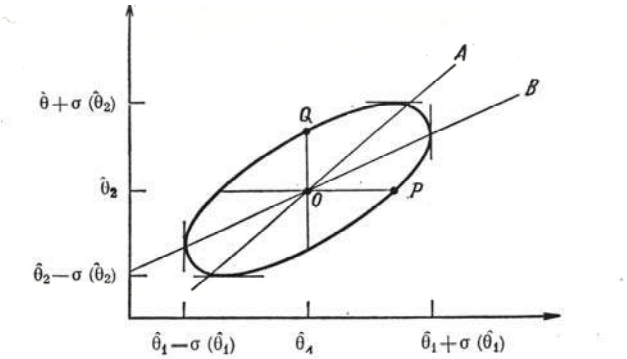

Figure 1 Confidence intervals of 68.3% with the standard deviation (after Hudson, 1970)

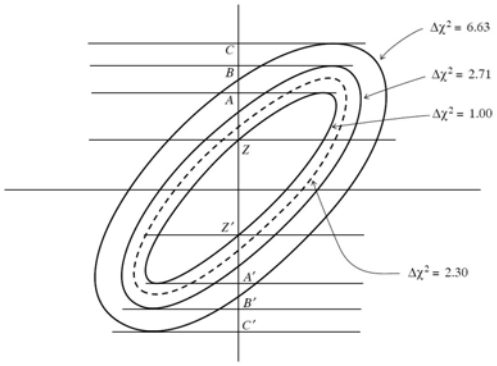

Figure 2 68.3%, 90%, 99% confidence intervals in 1 dimension (AA', BB', CC') and joint 68.3% confidence domain in 2 dimensions with dashed line (after Press et al, 1986)

Table 1 $\Delta\chi^2$ value for various parameter numbers *k* and probability *p*

	k					
p	1	2	3	4	5	6
68.3%	1.00	2.30	3.53	4.72	5.89	7.04
90%	2.71	4.61	6.25	7.78	9.24	10.06
95.4%	4.00	6.17	8.02	9.70	11.3	12.8

$$C(\boldsymbol{p}_{min}) = \left[Q^T Q\right]^{-1}(\boldsymbol{p}_{min}) \tag{2}$$

$$q_{i,j}(\boldsymbol{p}_{min}) = \frac{\partial u(t_i, \boldsymbol{p}_{min})}{p_j} \tag{3}$$

Goal and content of the paper

The generally used parameter error estimation methods are used in relation to linearized models with random (normally distributed) noise. The starting point of this paper is the suggestion that the non-linearity of the models can be taken into account when a contour of the non-linear noise-free merit function is used instead of a contour of the linearized one, to define a confidence domain. It is shown that this confidence domain may also be a geometrical obstruction domain, irrespective of the type of the noise. Moreover, a method is presented which can be used to measure the connected parts of this general shaped parameter domain, facilitating the testing of uniqueness. The method is illustrated by some examples.

2 MERIT FUNCTION GEOMETRY

Real-life merit function

The solution of the inverse problem is the global minimizer of the $F(\boldsymbol{p})$ weighed least squares merit function which is defined as follows:

$$F(\boldsymbol{p}) = \frac{1}{N-M}\sum_{i=1}^{N}\frac{\left[u_m(t_i) - u(t_i, \boldsymbol{p})\right]^2}{w_i} \tag{4}$$

where t_i are sampling times (i=1,2..N), subscript m indicates a measured value and $\boldsymbol{p}$ is the parameter vector containing M parameters which may influence (partly linearly and partly non-linearly) the solution of the model, and w_i are the weights.

In the following, the actual (noise-polluted or "real life") merit function is estimated with a noise-free merit function $F'(\boldsymbol{p})$ (also referred to as a follower merit function) which is defined as

$$F'(\boldsymbol{p}) = \sum_{i=1}^{N} h_i(\boldsymbol{p})^2 = \sum_{i=1}^{N} \left[u(t_i, \boldsymbol{p}) - u(t_i, \boldsymbol{p_{min}})\right]^2 \tag{5}$$

where the weights and multipliers are not indicated for the sake of simplicity. Using the following decomposition of the measured data

$$u_m(t_i) = u(t_i, \boldsymbol{p_{min}}) + z_i \tag{6}$$

the actual merit function can be expressed as follows with the noise-free merit function as

$$F(\boldsymbol{p}) = \sum_{i=1}^{N} \left[h_i(\boldsymbol{p}) - z_i\right]^2 = \sum_{i=1}^{N} \left[h_i(\boldsymbol{p})^2 - 2h_i(\boldsymbol{p})z_i + z_i^2\right] = F'(\boldsymbol{p}) - \sum_{i=1}^{N} \left[2h_i(\boldsymbol{p})z_i\right] + F(\boldsymbol{p_{min}}) \tag{7}$$

where $h_i(\boldsymbol{p})$ are the elements of the model response function. Using the following inequality:

$$F'(\boldsymbol{p}) - \sum_{i=1}^{N} \left[2h_i(\boldsymbol{p})z_i\right] = \sum_{i=1}^{N} h_i(\boldsymbol{p})\left[h_i(\boldsymbol{p}) - 2z_i\right] \le \sum_{i=1}^{N} \left|h_i(\boldsymbol{p})\right|\left[\left|h_i(\boldsymbol{p})\right| + 2\left|z_i\right|\right] \tag{8}$$

the actual merit function can be estimated with the noise-free merit function. We are far from the "deep" minimizers if $\left|h_i(\boldsymbol{p})\right| >> \left|z_i\right|$ and close to the global minimizer if $\left|h_i(\boldsymbol{p})\right| << \left|z_i\right|$.

Assuming $\left|h_i(\boldsymbol{p})/n\right| \approx \left|z_i\right|$, ($n$=1,2,…) and, therefore, $F'(\boldsymbol{p})/n^2 \approx F(\boldsymbol{p_{min}})$ the estimation can be written as

$$F(\boldsymbol{p}) \le F'(\boldsymbol{p})\left(1 + \frac{2}{n} + \frac{1}{n^2}\right) \tag{9}$$

It follows from this and from Equation (6) that if $n \to \infty$ then $F(\boldsymbol{p}) \approx F'(\boldsymbol{p})$, and the two kinds of merit functions are nearly the same (and far from the global (and deep) minima).

Assuming $\left|h_i(\boldsymbol{p})\right| \approx \left|z_i\right|/n$, ($n$=1,2,…) and therefore $F'(\boldsymbol{p}) \approx F(\boldsymbol{p_{min}})/n^2$ the estimation can be written as

$$F(\boldsymbol{p}) \le \left(1 + \frac{2}{n} + \frac{1}{n^2}\right) F(\boldsymbol{p_{min}}) \tag{10}$$

It follows that the two kinds of merit functions are different in the vicinity of the global (and deep) minima where the noise-free merit function may drop to zero and the actual merit function is about constant, being gradually "filled up" with noise. The "filled up" domain, corresponding to this estimation, is defined by a contour of the noise-free merit function with value equal to $F(\boldsymbol{p_{min}})/n^2$ (n=1,2,…).

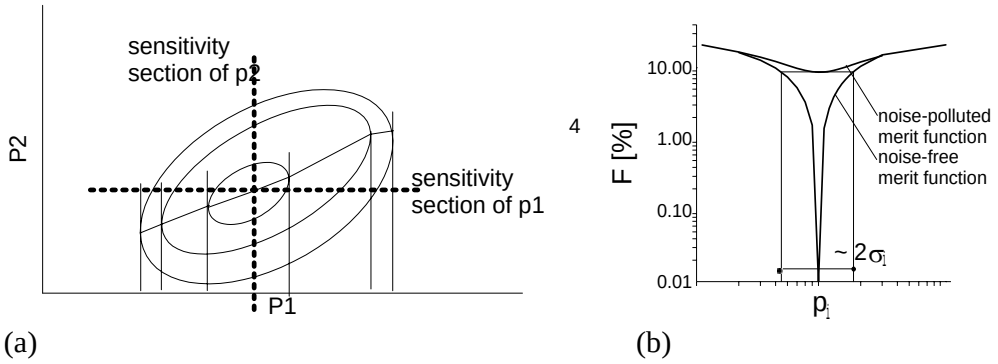

(a) (b)

Figure 3. (a) The thin line through the minimum is the minimal section of the merit function of parameter p_1 onto the parameter space, (b) The critical sensitivity sections (CSC-s) of parameter p_i, indicating the generalized standard deviation related to the noise-free merit function value $c = F(\boldsymbol{p}_{min})$.

3 MINIMAL SECTIONS

The minimal sections of the merit function

Let us assume that the parameter vector is split into two parts, $\boldsymbol{p}_1$ and $\boldsymbol{p}_2$ such that:

$$\boldsymbol{p} = [\boldsymbol{p}_1, \boldsymbol{p}_2], \qquad \boldsymbol{p}_1 \in \Re^J \ , \boldsymbol{p}_2 \in \Re^{M-J} \tag{11}$$

The solution of the following conditional minimisation where $\boldsymbol{p}_2$ is prescribed:

$$F(\boldsymbol{p}_1, \boldsymbol{p}_2) = \min!, \qquad \boldsymbol{p}_2 = \boldsymbol{p}_2^* \tag{12}$$

gives one or more J dimensional real parameter vector parts ($\boldsymbol{p}_1$). If the relationship between $\boldsymbol{p}_2$ and $\boldsymbol{p}_1$ is injective, then $F(\boldsymbol{a}(\boldsymbol{p}_2),(\boldsymbol{p}_2))$ is a M-J dimensional section of the merit function called the minimal section with respect to the parameter vector part $\boldsymbol{p}_2$.

In addition to this, if $\boldsymbol{p}_2$ is a single parameter then the 1 dimensional section is the minimal section of the merit function for parameter $\boldsymbol{p}_2$. Its projection onto the F- $\boldsymbol{p}_2$ plane is referred to as the critical sensitivity section (CSC) of parameter $\boldsymbol{p}_2$, as shown in Figure 3.

The use of the minimal sections in the reliability tests

Following from the definition, the basic characteristics of the minimal section of parameter p_i are as follows: (i) the minimal section of the merit function of parameter p_i relates the smallest merit function value to a specified value of p_i (see Fig 3), (ii) it proceeds on the 'deepest possible line' with respect to parameter p_i (iii) it crosses the global and also, the important local minima of the merit function.

It follows that the critical sensitivity section (CSC) of the merit function of parameter p_i can be used to determine the orthogonal projection of a generally-shaped parameter region, defined by the noise-free merit function contour c, onto the parameter axis p_i (Fig 3). Either the half interval or the left and the right interval-parts can be used as generalized standard deviations of parameter p_i at the noise-free merit function value of c.

Since the CSC of parameter p_i contains the global and the important local minima of the merit function, it can be used to test the uniqueness of the inverse problem solution. It is suitable to determine the CSC of parameter p_i of both the actual and the noise-free merit

functions since a deep local minimum of the noise-free merit function is an apparent solution of the actual inverse problem (see example 1, Fig 4).

Since the CSC of the merit function of parameter p_i proceeds on the 'deepest possible line' with respect to parameter p_i, even in the case of quasi-degenerated minima, it can be used to determine an approximate solution for ill-posed inverse problems, if a good value of one parameter (parameter p_i) is known. The approximate solution is such a point of the minimal section of the merit function of parameter p_i where the p_i coordinate is equal to the known or specified value.

It can be noted that the projections of any section (and therefore, of the the sensitivity sections) of the merit function onto the F- p_i plane may give an upper bound estimation for the minimal section of p_i (and a lower bound estimation of the size of the foregoing orthogonal projection). This is a useful fact since the numerical work to determine a minimal section of the merit function of parameter p_i is exponentially dependent on the number of the non-linearly dependent parameters. (The dimension of the parameter vector can be decreased in non-linear inverse problems by the number of the linearly dependent parameters.)

4 EXAMPLES

A new laboratory testing procedure, the multistage oedometric relaxation test (MRT) was described and compared with the conventional multistage oedometric compression test (MCT) in Imre, (1998). For both tests also, a new, 'quick' variant of the testing procedures is proposed as follows. The stages are generally 10 - 30 minutes long (i.e. they are interrupted well before the t_{99} dissipation time), except that the last one is longer than the t_{99} dissipation time.

Four constitutive models of differing complexity have been suggested for each case (MRT and MCT) by Imre (1995a, b, 1998). In this section, the inverse solution technique is demonstrated by validating the models against measured data. Five examples are considered: (1) the evaluation of MRT data with four models; (2) the evaluation of the short stages of the MRT test with the simplest model-version;(3) the evaluation of MCT data with four models; (4) the evaluation of MCT for a peaty soil when large modelling error occurs; and (5) a sensitivity analysis of the HBM model is mentioned.

Examples 1 and 2 (MRT)

MRT test results have been analysed using four different models. These are variants of a general model consisting of a consolidation part-model and a relaxation part-model, which entails the identification of the initial condition (Imre, 1995a, 1998). The models, in order of decreasing complexity, are referred to as follows: H>HCRT>HCR>HC. Model HC describes simple consolidation only, while models HCR, HCRT and H describe the relaxation behavior as well, but with increasing parameter numbers, as described in Table 2. In example (1), the long stages of the oedometric relaxation test data were evaluated with these models.

According to the results of an evaluation of 8 long tests with each of the four models, the CSC of c_v is generally characterized by two minima as can be seen in Figs 4 and 5. Figure 5(b) shows the initial conditions found for each of these minima. It is evident that only one of these is physically admissible (the solid line), which is the only global minimum of the noise-free merit function. Generally, the physically admissible solution can be determined only if the relaxation is taken into account. Table 3 indicates that the fitting error is reduced to about half if the relaxation is taken into account (models H, HCRT and HCR).

Table 2 The parts and parameters of MRT models H, HCRT, HCR and HC,with # of function value evaluations

c	Consolidation Part	Relaxation Part	Parameters	Non-linear dependence	# Function value evaluations
H	*yes*	*yes*	A, B, C, c_v, σ_∞, s, t_3, t_1	c_v, σ_∞, s, t_3, t_1	125,280
HCRT	*yes*	*yes*	A, B, C, c_v, σ_∞, s_k, t_3	c_v, t_3,	1044
HCR	*yes*	*yes*	A, B, C, c_v, σ_∞, s_k	c_v	36
HC	*yes*	*no*	A, B, C, c_v, σ_∞	c_v	36

Table 3 Mean fitting error [%] for 8 tests, models H, HCRT, HCR and HC (Imre, 1995a)

Model	H	HCRT	HCR	HC
Mean	1.24	1.00	1.29	2.29

Note from Table 3 that while model H is a more complex model, which identifies some additional (though relatively unimportant) parameters, the goodness of fit is not improved.

In example (2) (the evaluation of the short stages), the inverse problem is ill-posed as the minimum of the CSCs of c_v for the short stages are quasi-degenerated, as shown in Fig. 5(a). If c_v is assessed from the last (long) stage, then an approximate solution can be selected using this c_v, for the short stage CSC of parameter c_v. Fig. 7 shows that the fit between the measured and the simulated data is good even for the short stages, where the solutions of the inverse problem are only approximate.

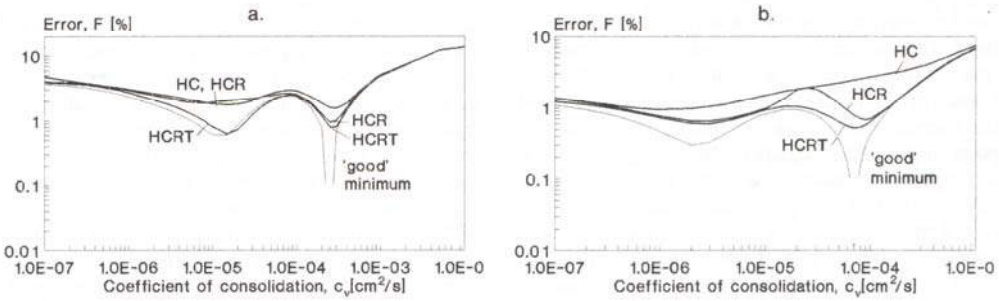

Figure 4. CSC for c_v of two clay samples, four models (Imre, 1995a)

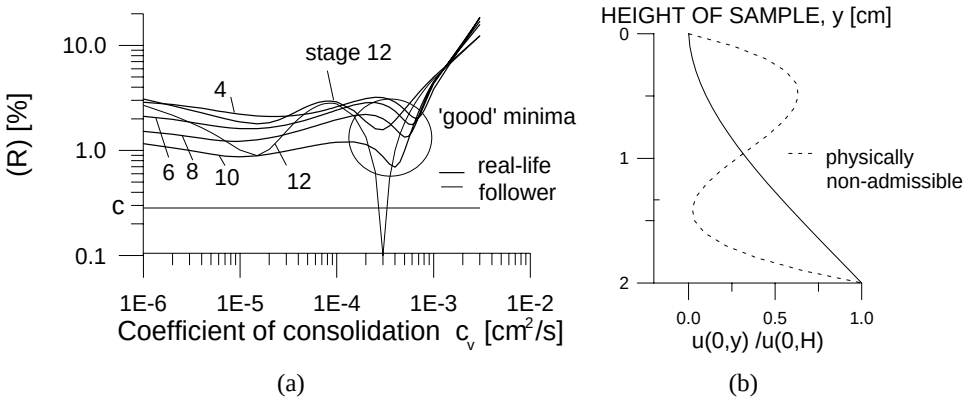

(a) (b)

Figure 5. MRT (a) CSC for c_v of a clay, model HC (b). Initial conditions for stage 12 (Imre, 1996)
(Note in (a) that the error is expressed as R[%] (cf F[%] in Fig 4) reflecting that it is an expresion of the combined error in several of the fitted variables)

The minimal section of c_v is represented together with the CSCs of the parameters A and σ_∞, in Figure 6. It can be seen that the projection of the minimal section of c_v is a good upper estimation on the whole domain for the CSC of parameter A and on a part of the domain for the CSC of parameter σ_∞.

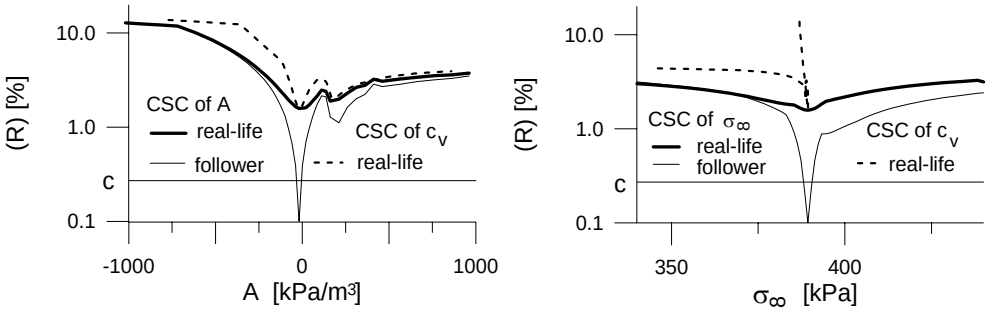

a. b.

Figure 6 a,b. CSC for two linearly dependent parameters (A, σ_∞) with the projections of the minimal section of c_v

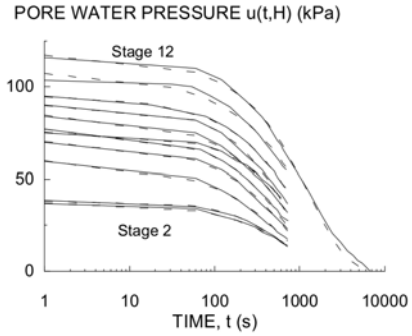

Figure 7. Comparison between MRT test results (solid lines) and computed solutions (dashedlines)

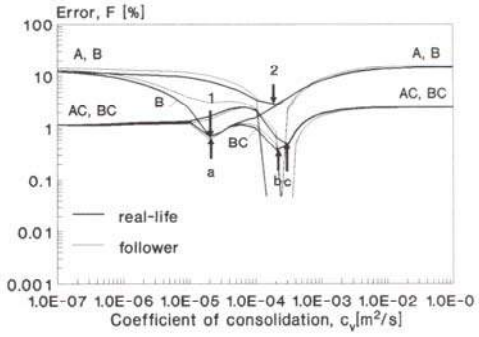

Figure 8. MCT results:, comparison of CSCs of c_v of a clay using the four models

Examples 3 and 4

The four models for MCT tests, which are variants of a general model consisting of a consolidation part-model and a creep part-model (Imre, 1995b, Fig 8, Tables 4, 5) are of complexity as follows: AC>A, BC>B, B>A. The simplest model A is the Terzaghi consolidation model including the identification of the immediate settlement h_0. Model B is the same as A except that the initial condition is also identified.

Table 4 The parts and parameters of MCT models A, AC, B and BC indicating # of function value evaluations

c	Consolidation Part	Creep Part	Parameters	Non-linear dependence	# Function value evaluations
BC	*yes*	*yes*	G', F, c_v, h_1, C_α	F, c_v	1500
B	*yes*	*no*	G', F, c_v, h_1,	F, c_v	1500
AC	*yes*	*yes*	c_v, h_0, C_α, m_v	c_v	40
A	*yes*	*no*	c_v, h_0, m_v	c_v	40

Table 5 Mean fitting error [%] for 8 tests, models A, AC, B and BC (see Fig 7, Imre, 1995b)

Model	AC	BC	B	A
Mean	0.92	0.92 (c)	2.58 (2)	2.49

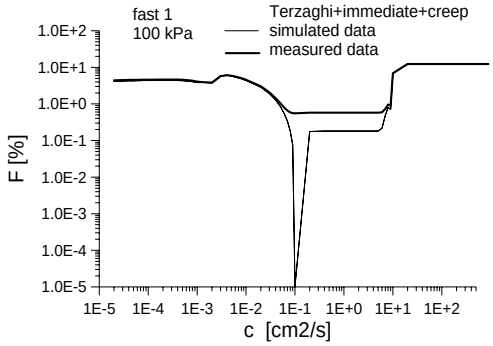

Figure 9. CSC of c_v of a peat, Bjerrum model.

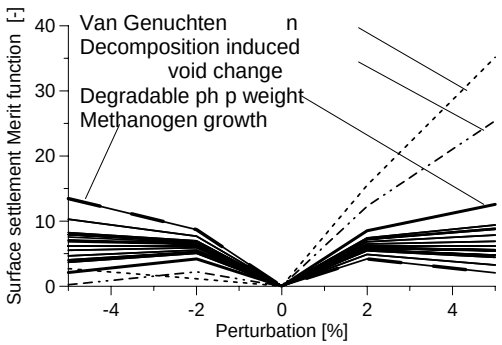

Figure 10. Sensitivity sections, HBM model.

According to the results of the evaluation 8 MCT tests made on clays (example (3)), the consideration of the creep in the model halves the fitting error, however, the identification of the initial condition (models B and BC) leads to non-unique inverse problem solutions and leads to no drop in the fitting error. A fixed initial condition (models A and AC) results in unique inverse problem solution.

Example (4) is on the evaluation of the oedometric compression tests made on peat with the model AC. According to the results in Fig 9, the CSC of the c_v shows a strong, asymmetric error domain related to the error of the consolidation modelling. The computed coefficient of variation $\sigma(p_i)/c_v$ of c_v can be as large as 80% for the AC model. The parameters of the creep part-model display much less error (this is not shown here).

Example 5

The results of the sensitivity analysis of a hydro-bio-mechanical (HBM) model for settlement and other behaviour in landfilled waste (McDougall, 2007) with 25 parameters shows on a specified example that the CSCs are generally very flat (Fig 10, Imre et al, 2009). These sections are the upper bound estimation for the CSCs, which are otherwise impossible to determine due to the large parameter number. This result indirectly but certainly indicates a huge error domain for about 14 non-controlling parameters.

5 DISCUSSION AND CONCLUSIONS

The results of the preliminary study to formulate a general parameter error estimation method can be summarized as follows.

1. In the case of general random "noise", the confidence level and the shape of the confidence region can be selected arbitrarily: the only requirement is that the region includes the stated percentage of probability. A contour of the non-linear, noise-free merit function can be used to define a confidence domain since it is is based on a similar concept as the contour of the linearized $\Delta\chi^2$ merit function.

2. A geometrical uncertainty domain (where the minimisation algorithms are less effective) can be defined by a contour of the noise-free follower merit function, as well. Further research is needed on this contour value. For example, the value used for the definition of the confidence domain might be considered. Alternatively, as a rule of thumb, a contour of $F'(\boldsymbol{p}) = F'(\boldsymbol{p}_{min})$ is suggested.

3. The fact that both the confidence domain and the geometrical uncertainty domain can be defined by a contour of the non-linear noise-free merit function - indicating that the relative size of the parameter error is basically dependent on the model - can serve as a basis

for the construction of a general parameter error estimation method for non-linear inverse problems and for any "noise" of any origin.

4. In regard to the parameter domains defined by a contour of the non-linear noise-free merit function, these are generally asymmetric and not necessarily connected. Some additional considerations may be needed to ensure that the error domain constructed at $\boldsymbol{p}_{min}$ may contain $\boldsymbol{p}_{true}$ and vice versa.

5. A method is suggested to find and 'measure' the connected parts of the general shaped parameter domains and to select the physically admissible connected parts. The method entails the determination of the 'deepest sections' of the merit function, the so called critical sensitivity sections (CSC) parameter $p_{i.}$ The well-known sensitivity sections are upper bound estimations for these). These can be used, in addition, for uniqueness testing and to find an approximate solution for ill-posed inverse problems.

6. The method is illustrated by some examples. These show that the deep local minima of the noise-free merit function may serve as apparent solutions of the actual inverse problem. The examples illustrate how the reliability criteria can be used for model discrimination and model validation.

The main results concerning the oedometric compression and relaxation tests are as follows. (i) Identifying the initial condition, the actual inverse problem has multiple solutions (with one physically admissible solution and one solution for the noise-free inverse problem). (ii) The fitting error decreases to the half if the viscous effects (creep, relaxation) are taken into account. A good solution for the relaxation test can only be determined in this way only. (iii) The inverse problem is ill-posed for short measuring periods, this can be improved with the suggested method. The result concerning the sensitivity analysis of the HBM model on a specified example indicates that only 4 to 11 parameters are important out of the 25 identified parameters, suggesting that a great number of the parameters might not need to be identified.

ACKNOWLEDGEMENT

The support of the National Research Fund Jedlik Ányos NKFP B1 2006 08 and the Norwegian research fund HU-0121 is acknowledged.

REFERENCES

Bjerrum, L.; Simmons, N.; Torblaa, A. 1958. The Effect of time on the shear strength of a soft marine clay. Publication No. 33. Norwegian Geotechnical Institute, Oslo.

Hudson D. (1970). Statistika dlja fizikov. Mir, Moszkva, 1967. p. 242.

Imre, E. (1995a). Model discrimination for the oedometric relaxation test. *Proc. of 8-th Baltic Geotechnical Conference*, 55-60.

Imre, E. (1995b). Model discrimination for conventional step-loaded oedometric test. Proc. of the Int. Symp. on Compression and Cons. of Clayey Soils, IS-Hiroshima'95, 525-530.

Imre, E. (1996). Inverse problem solution with a geometrical method. Proc. of the 2nd Int. Conf. on Inverse Problems in Engineering. Le Croisic, France.331-338.

Imre, E. (1998). Evaluation of quick multistage oedometric relaxation tests. Proc. of the XIth Danube-European Conference on SMGE, Porec. 695-702.

Imre, E., Trang, P. Q., Laufer, I., Kovács, M, Nédli, P, Firgi, T., Telekes, G. (2009) Inverse problem solution to predict long term behaviour of a landfill using short term data. Electr. Proc. of Sardinia 2009.

McDougall, J (2007) A hydro-bio-mechanical model for settlement and other behaviour in landfilled waste. COGE, Volume 34, Issue 4, July 2007, Pages 229-246

Press, W.H.; Flannery, B.P.; Teukolsky, S.A.; Wetterling, W.T. (1986): Numerical Recipes. Cambridge Univ. Press, Cambridge.

FINITE ELEMENT METHOD FOR COUPLED DYNAMIC FLOW-DEFORMATION SIMULATION

J.M. van Esch
Department of Geo-engineering, Deltares, Delft, The Netherlands

D. Stolle
Department of Civil Engineering, McMaster University, Hamilton, ON, Canada

I. Jassim
Institute of Geotechnical Engineering, Stuttgart University, Stuttgart, Germany

ABSTRACT: *This article compares a solid velocity - liquid velocity formulation and a solid velocity - liquid pressure formulation for solving the coupled flow and deformation problem in an elastic media. The finite element formulations presented here apply to small deformations, but are in the process of being extended to large deformations within a material point formulation. As the material point model uses low-order elements and forward integration in time, the finite element model has to be composed accordingly. Dynamic simulations presented in this paper focus on capturing the first compression wave, which loads the liquid phase and solid phase, and on resolving the second compression wave, which starts the consolidation process. Whereas the velocity - velocity formulation properly captures two-phase dynamic behavior including the second wave, the velocity - pressure formulation is not capable of capturing the second compression wave. With regards to implementation within a material point framework, the first formulation is more consistent in the treatment of the solid and liquid phases, providing a physically based mapping of momentum for both phases, and is preferred for this reason.*

1 INTRODUCTION

Considerable research has been carried out to address problems that involve soil-pore fluid interaction that include, for example, those dealing with consolidation, liquefaction and wave loading. The equations describing two-phase flow were originally developed by Biot (1956a), Biot (1956b), with Zienkiewicz & Shiomi (1984) and Zienkiewicz et al. (1990) investigating the numerical implementation in terms of various formulations. For a comprehensive review of the various formulations within the context of mixture theory, the reader is referred to Gidaspow (1994). A more recent contribution relevant to this paper is presented by Jeremic et al. (2008). Various simplifications have been introduced depending on the rate of loading, the dissipation time of excess pore pressure, and the speed of shear and compression waves within the media. One must however realize that each term that is eliminated introduces an error, which is spread over the other terms. As a result, certain non-physical behaviors may be captured, which in turn could lead to a misinterpretation of results and erroneous conclusions. This paper briefly reviews the two-phase flow equations and then presents a series of one-dimensional examples to demonstrate the significance of various simplifications. The emphasis is placed on use of explicit time-stepping schemes that are well-suited for implementation in material point method models.

2 MATHEMATICAL MODEL

The mathematical model provides the governing equations for coupled flow and deformation within a domain of interest Ω that is closed by its boundary Γ. Equations are given for Cartesian coordinates $x_i\,(\mathrm{m})$, with time denoted by $t\,(\mathrm{s})$. Throughout this section the index notation is used. Subscripts denote vector or tensor components in the coordinate system. Superscripts 's' and 'l' represent solid and liquid components of the variables respectively for the two-phase dynamical problem.

2.1 Balance Equations

This section presents the mass balance equations and the momentum balance equations for the liquid phase and the solid phase separately as outlined by Verruijt (2010). The equilibrium equation and the storage equation follow as a combination of the balance equations completed by constitutive laws. The mass balance equation for the solid phase reads

$$\frac{\partial}{\partial t}\left[(1-n)\,\rho^s\right] + \frac{\partial}{\partial x_i}\left[(1-n)\,\rho^s v_i\right] = 0, \tag{1}$$

where $\rho^s\,(\mathrm{kg/m^3})$ is the density of the solid phase material, $n\,(-)$ denotes porosity, which is dimensionless, and $v_i\,(\mathrm{m/s})$ represents the velocity vector of the solid phase material corresponding to the x_i direction. The momentum balance for the solid phase reads

$$(1-n)\rho^s\frac{\partial v_j}{\partial t} - \frac{\partial \sigma'_{ij}}{\partial x_i} - (1-n)\frac{\partial p}{\partial x_j} - (1-n)\rho^s g_j - n^2\mu\kappa^{-1}_{ji}\,(w_i - v_i) = 0. \tag{2}$$

Here $\sigma'_{ij}\,(\mathrm{N/m^2})$ denotes the effective stress tensor in the solid skeleton (positive for tension), $p\,(\mathrm{N/m^2})$ is the pressure in the liquid phase (positive for suction), and $g_j\,(\mathrm{m/s^2})$ indicates the gravitational acceleration vector. The dynamic viscosity of the liquid is given by $\mu\,(\mathrm{kg\,m/s^2})$, the components of the inverse of the intrinsic permeability tensor are denoted by $\kappa^{-1}_{ij}\,(\mathrm{m^2})$, and the velocity of the liquid phase is written as $w_i\,(\mathrm{m/s})$. Conservation of moment of momentum requires $\sigma'_{ij} = \sigma'_{ji}$. The mass balance for the liquid is given by

$$\frac{\partial}{\partial t}\left(n\rho^l\right) + \frac{\partial}{\partial x_i}\left(n\rho^l w_i\right) = 0, \tag{3}$$

with $\rho^l\,(\mathrm{kg/m^3})$ being the density of the pore water. The momentum balance for the liquid reads

$$n\rho^l\frac{\partial w_j}{\partial t} - n\frac{\partial p}{\partial x_j} - n\rho^l g_j + n^2\mu\kappa^{-1}_{ji}\,(w_i - v_i) = 0. \tag{4}$$

Since displacements are small and we are following the material in the material point method, time derivatives replace material derivatives in this formulation.

2.2 Equilibrium Equation

The momentum balance for the mixture follows from adding Eqs. (2) and (4) yielding

$$(1-n)\,\rho^s\frac{\partial v_j}{\partial t} + n\rho^l\frac{\partial w_j}{\partial t} - \frac{\partial \sigma_{ij}}{\partial x_i} - \gamma_j = 0, \tag{5}$$

where $\sigma_{ij}\,(\mathrm{N/m^2})$ represents the total stress tensor, and $\gamma_j\,(\mathrm{N/m^3})$ is the unit weight of the mixture. The density of the soil mixture $\rho\,(\mathrm{kg/m^3})$ reads $\rho = (1-n)\,\rho^s + n\rho^l$; thus $\gamma_j = \rho g_j$. The effective stress is related to the total stress and pore pressure by the Terzaghi decomposition according to

$$\sigma_{ij} = \sigma'_{ij} + \delta_{ij} p, \tag{6}$$

where $\delta_{ij}\,(-)$ is the Kronecker delta operator. For an elastic material the constitutive equation is defined as

$$\sigma'_{ij} = D_{ijkl}\epsilon_{kl}, \tag{7}$$

where $D_{ijkl}\,(\mathrm{N/m^2})$ represents the fourth order material stiffness tensor, and $\epsilon_{kl}\,(-)$ expresses the second order strain tensor. For an isotropic elastic material the stiffness tensor components are given by

$$D_{ijkl} = \mu^e\left(\delta_{ik}\delta_{jl} + \delta_{il}\delta_{jk}\right) + \lambda^e \delta_{ij}\delta_{kl}, \tag{8}$$

where $\mu^e\,(\mathrm{N/m^2})$ and $\lambda^e\,(\mathrm{N/m^2})$ are the Lamé constants. Assuming small deformations, the strain-displacement relation gives

$$\epsilon_{ij} = \tfrac{1}{2}\left(\frac{\partial u_i}{\partial x_j} + \frac{\partial u_j}{\partial x_i}\right). \tag{9}$$

The velocity of the solid phase relates to the displacement of the solid phase $u_i\,(\mathrm{m})$ as $v_i = \partial u_i/\partial t$.

2.3 Storage Equation

Assuming spatial variations in the liquid density and the porosity are negligible, the mass balance equation (3) for the liquid phase yields

$$n\frac{\partial \rho^l}{\partial t} + \rho^l \frac{\partial n}{\partial t} + n\rho^l \frac{\partial w_i}{\partial x_i} = 0. \tag{10}$$

Solid particles are assumed to by incompressible. Neglecting the gradient of the porosity in the mass balance equation (1) for the solid phase gives

$$\frac{\partial n}{\partial t} - (1-n)\frac{\partial v_i}{\partial x_i} = 0. \tag{11}$$

Inserting Eq. (11) into the mass balance equation (10) for the liquid phase then gives

$$\frac{n}{\rho^l}\frac{\partial \rho^l}{\partial t} + (1-n)\frac{\partial v_i}{\partial x_i} + n\frac{\partial w_i}{\partial x_i} = 0, \tag{12}$$

which is the volumetric form of the combined mass balance equation. The proposed constitutive relation for the density of the liquid reads

$$\frac{d\rho^l}{dp} = -\beta\rho^l, \tag{13}$$

where $\beta\,(\mathrm{m^2/N})$ is the compressibility of the liquid (pressure is negative for compression), which corresponds to the inverse of the compression modulus of the liquid phase. Defining specific discharge $q_i\,(\mathrm{m/s})$ as

$$q_i = n\left(w_i - v_i\right), \tag{14}$$

the mass balance equation (12) can be written as

$$n\beta\frac{\partial p}{\partial t} - \frac{\partial q_i}{\partial x_i} - \frac{\partial v_i}{\partial x_i} = 0, \tag{15}$$

with the momentum balance equation (4) reformulated as

$$q_i = \frac{\kappa_{ij}}{\mu}\left(\frac{\partial p}{\partial x_j} + \rho^l g_j - \rho^l \frac{\partial w_j}{\partial t}\right). \tag{16}$$

The storage equation then follows from Eqs. (15) and (16) as

$$n\beta\frac{\partial p}{\partial t} - \frac{\partial}{\partial x_i}\left[\frac{\kappa_{ij}}{\mu}\left(\frac{\partial p}{\partial x_j} + \rho^l g_j - \rho^l \frac{\partial w_j}{\partial t}\right)\right] - \frac{\partial v_i}{\partial x_i} = 0. \tag{17}$$

3 Solid Velocity - Liquid Pressure ($v - p$) Formulation

The $v - p$ formulation considers the relative velocity ($q \neq 0$). However the acceleration of the solid phase is assumed to equal to the acceleration of the liquid phase ($\partial v/\partial t \approx \partial w/\partial t$). The momentum balance equation (5) for the mixture then reads

$$\rho\frac{\partial v_j}{\partial t} = \frac{\partial \sigma_{ij}}{\partial x_i} + \gamma_j \qquad \text{in} \quad \Omega, \tag{18}$$

and the storage equation (17) can be written as

$$n\beta\frac{\partial p}{\partial t} = \frac{\partial}{\partial x_i}\left[\frac{\kappa_{ij}}{\mu}\left(\frac{\partial p}{\partial x_j} + \rho^l g_j - \rho^l \frac{\partial v_j}{\partial t}\right)\right] + \frac{\partial v_i}{\partial x_i} \qquad \text{in} \quad \Omega. \tag{19}$$

The effective stress increment follows from Eq. (7) and Eq. (8) as

$$\frac{\partial \sigma'_{ij}}{\partial t} = \tfrac{1}{2} D_{ijkl}\left(\frac{\partial v_k}{\partial x_l} + \frac{\partial v_l}{\partial x_k}\right) \qquad \text{in} \quad \Omega. \tag{20}$$

For this set of equations the primary variables are: velocity of the solid phase v_i, pressure in the liquid phase p, and effective stress in the solid phase σ'_{ij}. Dirichlet boundary conditions prescribe a velocity $\overline{v}_i$ for the solid phase according to

$$v_i = \overline{v}_i \qquad \text{on} \quad \Gamma_1^v, \tag{21}$$

and a pressure $\overline{p}$ for the liquid phase by

$$p = \overline{p} \qquad \text{on} \quad \Gamma_1^p \tag{22}$$

Cauchy boundary conditions for the solid phase prescribe a traction as

$$\sigma_{ij} n_j = \overline{\tau}_i \qquad \text{on} \quad \Gamma_2^v, \tag{23}$$

where $\overline{\tau}_i\,(\mathrm{N/m^2})$ denotes the traction vector components on the boundary, and $n_j\,(-)$ represents the outward pointing normal to the boundary. For the liquid phase Cauchy boundary conditions read

$$\frac{\kappa_{ij}}{\mu}\left(\frac{\partial p}{\partial x_j} + \rho^l g_j - \rho^l \frac{\partial w_j}{\partial t}\right) n_i = \overline{q}_i n_i \qquad \text{on} \quad \Gamma_2^p, \tag{24}$$

where $\overline{q}_i$ denotes the components of the outflux vector over the boundary.

The finite element method constructs the weak formulation of the given partial differential equations, and obtains the pressure in the liquid phase and the velocity of the solid phase at the nodes. In this article a Galerkin finite element discretization in space is adopted. The interpolation function $N_a\,(-)$ is used as the weighting function. An explicit finite difference time integration scheme is applied, and the mass matrices are lumped. The uncoupled set of equations are then solved sequentially. In this section discrete locations in space are indicated by the subscripts a and b. The superscript n denotes a point in time.

The discrete equilibrium equation follows from the momentum balance equation (18) of the mixture and provides the velocity increment Δv_j of the solid phase as

$$\int_\Omega \rho N_a \delta_{ab} \Delta v_{bj} d\Omega = -\Delta t \int_\Omega \frac{\partial N_a}{\partial x_i} \sigma_{ij}^n d\Omega + \Delta t \int_{\Gamma_2^u} N_a \overline{\tau}_{aj}^n d\Gamma + \Delta t \int_\Omega N_a \gamma_j d\Omega, \tag{25}$$

with the velocity of the solid phase at the next step in time following from the velocity at the current step and the velocity increment as $v_j^{n+1} = v_j^n + \Delta v_j$. The corresponding storage equation (19) discretizes to

$$\begin{aligned}\int_\Omega n\beta N_a \delta_{ab} \Delta p_b d\Omega = &-\Delta t \int_\Omega \frac{\kappa_{ij}}{\mu} \frac{\partial N_a}{\partial x_i} \frac{\partial N_b}{\partial x_j} p_b^n d\Omega - \Delta t \int_\Omega \frac{\kappa_{ij}}{\mu} \frac{\partial N_a}{\partial x_i} \rho g_j d\Omega \\ &+ \int_\Omega \frac{\kappa_{ij}}{\mu} \frac{\partial N_a}{\partial x_i} N_b \Delta v_{bi} d\Omega + \Delta t \int_{\Gamma_2^p} N_a \overline{q}_{ai}^n n_i d\Gamma + \int_\Omega N_a \frac{\partial N_b}{\partial x_i} \Delta u_{bi} d\Omega,\end{aligned} \tag{26}$$

and provides the pressure increment Δp, which increases the total stress $\Delta \sigma_{ij}$ according to

$$\Delta \sigma_{ij} = \tfrac{1}{2} \Delta t D_{ijkl} \left(\frac{\partial N_a}{\partial x_l} v_{ak}^{n+1} + \frac{\partial N_a}{\partial x_k} v_{al}^{n+1} \right) + \delta_{ij} N_a \Delta p_a. \tag{27}$$

Additionally, the Darcy velocity vector field at the next time step follows locally from

$$q_j^{n+1} = \frac{\kappa_{ji}}{\mu} \left(\frac{\partial N_a}{\partial x_j} p_a^{n+1} + \rho^l g_j - \rho^l N_a \frac{\Delta v_{aj}}{\Delta t} \right). \tag{28}$$

Stress updates $\sigma_{ij}^{n+1} = \sigma_{ij}^n + \Delta \sigma_{ij}$ and pressure updates $p^{n+1} = p^n + \Delta p$ are used to solve the set of algebraic equations sequentially.

4 Solid Velocity - Liquid Velocity ($v - w$) Formulation

The $u - w$ formulation follows the procedure outlined by Verruijt (2010), in which the increase of liquid phase velocity follows from Eq. (4) as

$$\rho^l \frac{\partial w_j}{\partial t} = \frac{\partial p}{\partial x_j} + \rho^l g_j - n\mu \kappa_{ij}^{-1} (w_i - v_i) \qquad \text{in} \quad \Omega. \tag{29}$$

Inserting this expression into Eq. (2) to obtain the solid phase velocity, yields

$$(1-n)\rho^s \frac{\partial v_j}{\partial t} = -n\rho^l \frac{\partial w_j}{\partial t} + \frac{\partial \sigma'_{ij}}{\partial x_i} + \frac{\partial p}{\partial x_j} + \rho g_j \qquad \text{in} \quad \Omega. \tag{30}$$

The pressure increase that follows from the mass balance equation (15), for the liquid phase and Eq. (14) for the relative velocity as

$$n\beta\frac{\partial p}{\partial t} = n\frac{\partial w_i}{\partial x_i} + (1-n)\frac{\partial v_i}{\partial x_i} \qquad \text{in} \quad \Omega, \tag{31}$$

with the effective stress increment follows from the velocity field of the solid phase according to

$$\frac{\partial \sigma'_{ij}}{\partial t} = \tfrac{1}{2}D_{ijkl}\left(\frac{\partial v_k}{\partial x_l} + \frac{\partial v_l}{\partial x_k}\right) \qquad \text{in} \quad \Omega. \tag{32}$$

For this set of equations the primary variables are: velocity of the solid phase v_i, velocity of the liquid phase w_i, pressure in the liquid phase p, and effective stress in the solid phase σ'_{ij}.

Dirichlet boundary conditions for the solid phase and liquid phase combine to

$$v_i = \overline{v}_i, \quad w_i = \overline{w}_i \qquad \text{on} \quad \Gamma_1. \tag{33}$$

Cauchy boundary conditions for the solid phase and for the liquid phase read

$$\sigma_{ij}n_j = \overline{\tau}_i, \quad pn_i = \overline{p}n_i \qquad \text{on} \quad \Gamma_2. \tag{34}$$

The finite element method obtains the velocity of the liquid phase and the velocity of the solid phase at the nodes. The weak form of Eq. (29) gives an expression for the velocity increment Δw_j of the liquid phase according to

$$\begin{aligned}\int_\Omega \rho^l N_a \delta_{ab}\Delta w_{bj} d\Omega = &-\Delta t\int_\Omega \frac{\partial N_a}{\partial x_j}p_a^n d\Omega + \Delta t\int_\Gamma N_a p_a^n n_j d\Gamma + \Delta t\int_\Omega \rho^l g_j N_a d\Omega \\ &- \Delta t\int_\Omega n\mu\kappa_{ij}^{-1}N_a\delta_{ab}\Delta w_{bj}^n d\Omega + \Delta t\int_\Omega n\mu\kappa_{ij}^{-1}N_a\delta_{ab}\Delta v_{bj}^n d\Omega,\end{aligned} \tag{35}$$

whereas the weak form of Eq. (30) expresses the velocity increment Δv_j of the solid phase as

$$\begin{aligned}\int_\Omega (1-n)\rho^s N_a\delta_{ab}\Delta v_{bj}d\Omega = &-\int_\Omega n\rho^l N_a\delta_{ab}\Delta w_{bj}d\Omega - \Delta t\int_\Omega \frac{\partial N_a}{\partial x_i}\sigma_{ij}^{'n}d\Omega \\ &- \Delta t\int_\Omega \frac{\partial N_a}{\partial x_j}p_a^n d\Omega + \Delta t\int_\Gamma N_a\left(\tau_{aj}^{'n} + N_a p_a^n n_j\right)d\Gamma + \Delta t\int_\Omega \rho g_j N_a d\Omega.\end{aligned} \tag{36}$$

The velocity of the solid phase at the next time step follows from the velocity at the current step and the velocity increment as $v_j^{n+1} = v_j^n + \Delta v_j$, and the same relation holds for the velocity of the liquid phase as $w_j^{n+1} = w_j^n + \Delta w_j$. In the integration points the pressure increase Δp, according to Eq. (31) is based on the liquid phase velocity at the next time step, and reads

$$n\beta\Delta p = n\Delta t\frac{\partial N_a}{\partial x_i}w_{ai}^{n+1} + (1-n)\Delta t\frac{\partial N_a}{\partial x_i}v_{ai}^{n+1}. \tag{37}$$

Finally the effective stress increase $\Delta\sigma'$ follows from Eq. (32) according to

$$\Delta\sigma'_{ij} = \tfrac{1}{2}\Delta t D_{ijkl}\left(\frac{\partial N_a}{\partial x_l}v_{ak}^{n+1} + \frac{\partial N_a}{\partial x_k}v_{al}^{n+1}\right). \tag{38}$$

Nodal velocity of the solid phase and nodal velocity of the liquid phase both follow from a forward time integration. The pressure and effective stress in the integration points follow from a backward relation with both velocities.

5 NUMERICAL SIMULATIONS

Limitations associated with various formulations have been discussed in detail in Chapter 1 of Pande & Zienkiewicz (1982). Two important factors are the period of response compared to the wave speed through a medium and the rate of drainage relative to the rate of loading. The examples given in his section are geared to specific aspects, namely the capability of capturing the second compression wave, and the impact on the solution associated with various assumptions. This section considers two cases, comparing solutions of the $v-p$ and the $v-w$ formulation for the simulation of the behavior of a confined soil column subjected to a surface load that is applied instantaneously. Since the emphasis is on wave propagation and dissipation of pore pressures the material is assumed to be linear elastic.

5.1 Case 1

For the first case a column is considered, in which the following mechanical properties apply: compression modulus of the water phase $K^l = 2000\,\text{MPa}$; bulk modulus of the skeleton $K = 2790\,\text{MPa}$ and shear modulus of the skeleton $G = 1650\,\text{MPa}$. The density of the solid phase $\rho^s = 2650\,\text{kg/m}^3$ and the density of the liquid phase $\rho^l = 1000\,\text{kg/m}^3$, with a porosity of the soil $n = 0.4$. As a result, we have an elasticity modulus of the mixture $E = K + \frac{4}{3}G + \frac{1}{n}K^l$ of $9990\,\text{MPa}$, with the speed of the compression wave given by

$$c_p = \sqrt{E/\rho}, \tag{39}$$

which for this case is $2241\,\text{m/s}$. The compression wave distributes the load over the liquid phase and the solid phase according to

$$p_0 = \frac{\alpha}{\alpha + n\beta}, \qquad \sigma_0' = \frac{n\beta}{\alpha + n\beta}, \tag{40}$$

where the compressibility of the liquid phase reads $\beta = 1/K^l$, and the compressibility of the solid phase follows from $\alpha = 1/\left(K + \frac{4}{3}G\right)$. For the parameters selected $p_0 = 0.5\sigma_0$ and $\sigma_0' = 0.5\sigma_0$.

The dynamic viscosity of the water phase μ is $1.0 \cdot 10^{-3}\,\text{Ns/m}^2$, the intrinsic permeability κ equals $1.0 \cdot 10^{-11}\,\text{m}^2$, and the gravitational acceleration g is set to $10\,\text{m/s}^2$. The hydraulic conductivity follows from the intrinsic permeability as $k = \kappa\rho^l g/\mu$. For the case at hand, as $k = 1.0 \cdot 10^{-5}\,\text{m/s}$, which applies for medium coarse sand. Given these parameters, the consolidation coefficient c_v follows from

$$c_v = \frac{k}{\rho^l g\,(\alpha + n\beta)}, \tag{41}$$

and equals $2.5\,\text{m}^2/\text{s}$.

The Courant criterion limits the time step Δt_1 for both the $v-p$ formulation and the $v-w$ formulation. As for the $v-p$ formulation a second criterion Δt_2 needs to be satisfied. Verruijt (2010) presented the time step criteria as

$$\Delta t_1 \leq \frac{1}{c_p}\Delta x, \qquad \Delta t_2 \leq \frac{1}{2c_v}\left(\Delta x\right)^2, \tag{42}$$

where Δx is the smallest element in the mesh. For a spatial discretization $\Delta x = 2.5\,\text{mm}$ the time steps should be restricted to $\Delta t_1 = 1.12 \cdot 10^{-6}\,\text{s}$ and $\Delta t_2 = 1.25 \cdot 10^{-6}\,\text{s}$.

Figure 1 compares $v-p$ simulation results to $v-w$ simulation results for the pore pressure and effective stress, in which the water pressure at the left side is set to $-1.0\,\text{Pa}$. In other words,

the increase in compressive stress at the left surface is entirely due to a water pressure change. The right side is fully fixed and impermeable. Both formulations capture the dynamic and the consolidation processes. The first process loads the liquid phase to a level of $-0.5\,\mathrm{Pa}$ and the second process gradually increases the liquid phase compressive pressure to $-1.0\,\mathrm{Pa}$, which corresponds to the total increase of the load at the boundary by raising the water level. The effective stress dissipates to its initial value of $0.0\,\mathrm{Pa}$ by consolidation. Verruijt (2010) presented the analytical solution for this problem and both $v-p$ simulation results and $v-w$ simulation results compare well to this solution.

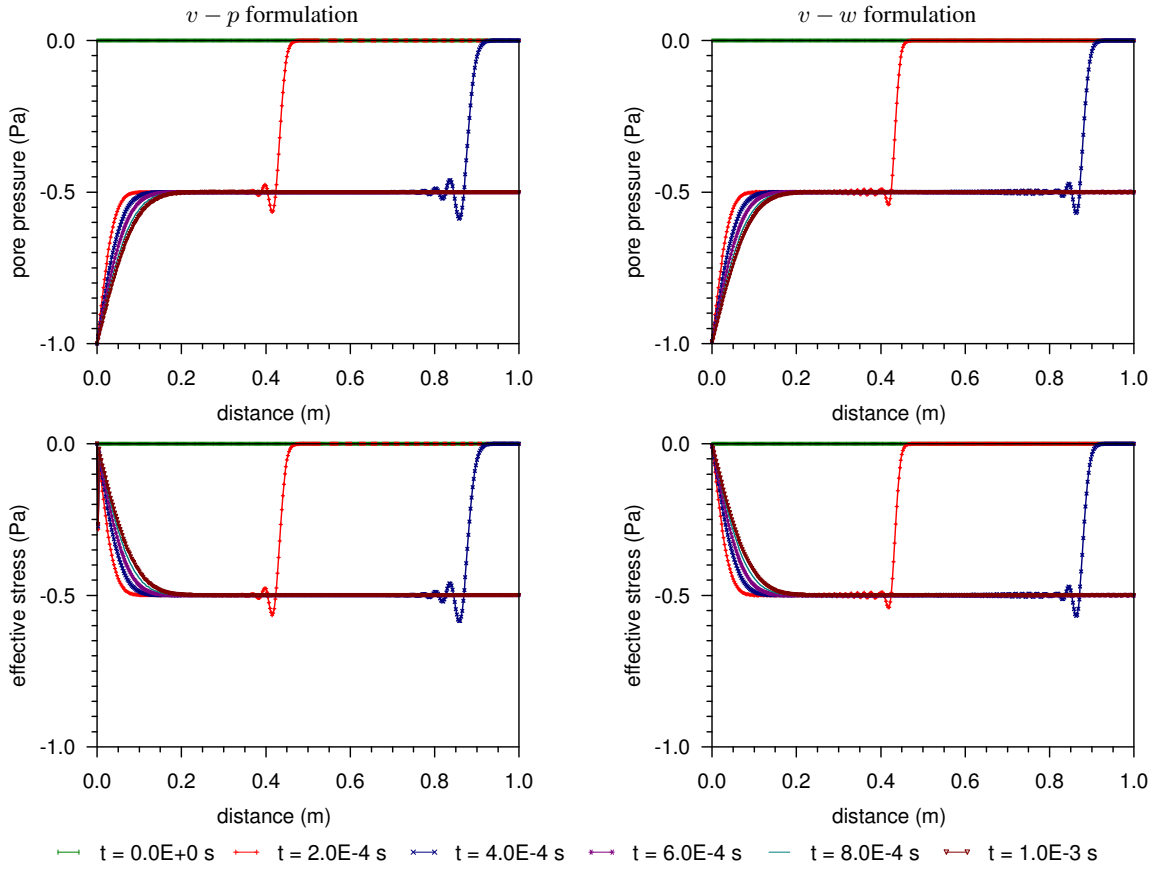

Fig. 1. Case 1, $v-p$ versus $v-w$ formulation results.

5.2 Case 2

For the second case the hydraulic conductivity is increased by a factor of 100, with the other parameters remaining the same. Owing to the increase in the hydraulic permeability, the consolidation coefficient equals $250\,\mathrm{m}^2/\mathrm{s}$. For a spatial discretization $\Delta x = 2.5\,\mathrm{mm}$ the second time step criterion becomes more restrictive: $\Delta t_2 = 1.25 \cdot 10^{-8}\,\mathrm{s}$.

Figure 2 compares $v-p$ simulation results to $v-w$ simulation results for the liquid phase and solid phase. The comparison clearly reveals a shortcoming with the $v-p$ formulation. The $v-w$ formulation is capable of capturing the first compression wave followed by a second wave that corresponds to the start of the consolidation process. The speed of the second wave is less than the speed of the first wave, and the second wave dissipates in space. Like the previous case, the first wave loads the liquid phase to a level of $-0.5\,\mathrm{Pa}$. The second wave increases the pressure

even further and decreases the effective stress as the total stress remains -1.0 Pa. The consolidation process increases the compressive water pressure to -1.0 Pa. This corresponds to the total increase of the load at the boundary by raising the water level. The effective stress dissipates to its initial value of 0.0 Pa by consolidation. Verruijt (2010) also presented the analytical solution for this problem. For this case $v-w$ simulation results compare well to the analytical solution. The $v-p$ formulation is not able to capture the second compression wave.

In order to take a closer look at what assumptions contribute to the difference, two additional simulations were performed with the $v-w$ formulation: (a) with $\partial w/\partial t \approx \partial v/\partial t$ in the momentum equation of the mixture and $\partial w/\partial t = 0$ in the momentum equation of the liquid; and (b) with $\partial w/\partial t \approx \partial v/\partial t$ in the momentum equation of the mixture only. For (a), it was found that the predictions were virtually identical to that of the $v-p$ formulation, whereas those for (b) were found to be similar to these of the full $v-w$ formulation. The peak total stress, was however found to be slightly larger. In other words, the difference between the formulations is attached to neglecting the acceleration of the fluid in the momentum balance equation of the fluid and not due to the use of a mixture acceleration.

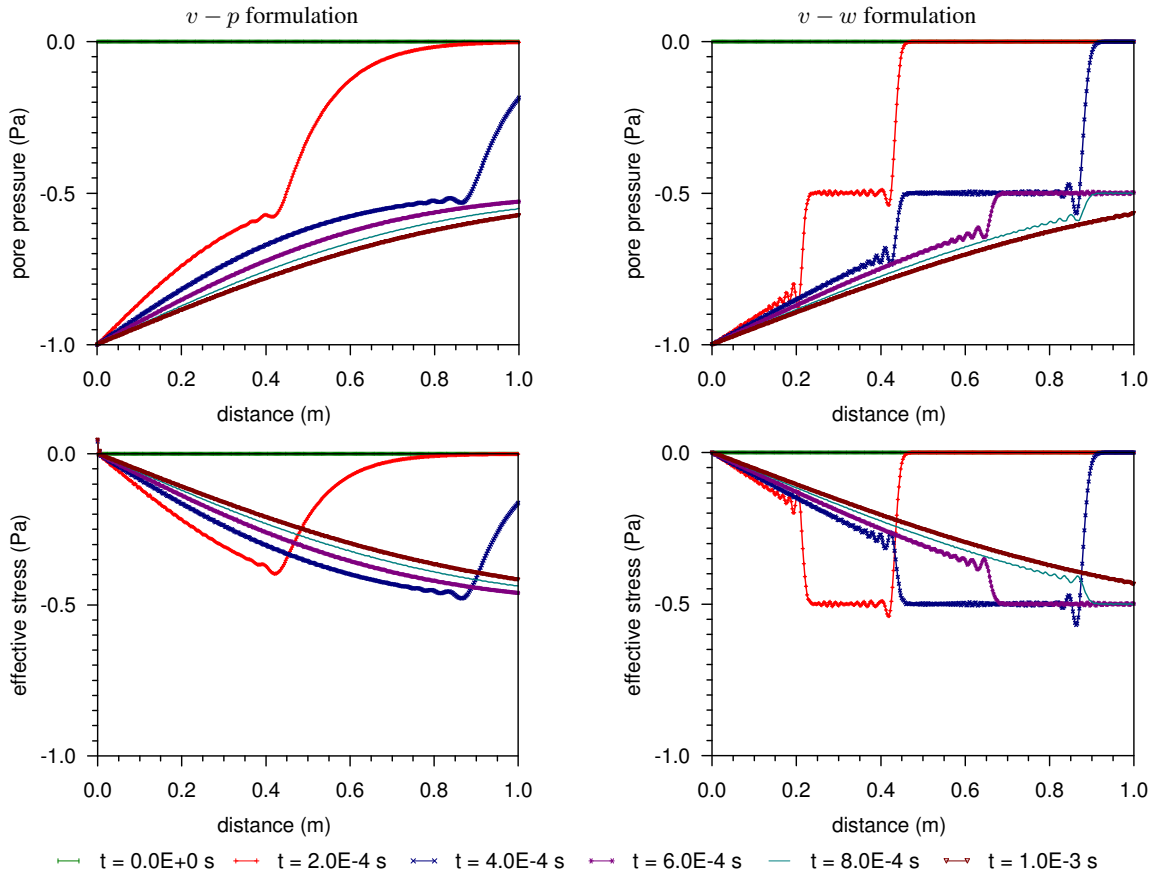

Fig. 2. Case 2, $v-p$ versus $v-w$ formulation results.

6 CONCLUSIONS

This article focused on explicit finite element models using low order elements, and being capable of properly capturing the physics of the dynamic response of a two-phase medium to dynamic loading. An important observation is that the fluid and solid velocities or displacements

are required as the degrees of freedom. For both $v-p$ and $v-w$ formulations a time stepping criterion that relates the critical time step to the spatial discretization size holds. However, for the $v-p$ formulation a second time stepping criterion has to be satisfied. This criterion relates to the square of the spatial discretization size and becomes more restrictive as the mesh size decreases. Because pressure relates to effective stress at the integration points, the $v-w$ formulations provides a more consistent form as both quantities follow as derivatives of nodal quantities. Only the $v-w$ formulation captures the second compression wave accurately.

The algorithms are being incorporated into a material point method framework. Use of fluid velocity as a primitive nodal unknown rather than pressure, which can be calculated at a material point, has the advantage that the algorithm for mapping information between the computation grid nodes and material points for the fluid is virtually identical to that for the solid phase. For example, the mapping of momentum from the material point to the nodes is tied to the physics (extensive thermodynamic property), unlike trying to map pressure (intensive thermodynamic property). There are however challenges when using low-order elements, namely mitigating locking that is associated with (near) incompressibility, and eliminating checker-boarding of the pressure field. Partial solutions to ongoing research are given by Stolle et al. (2009).

ACKNOWLEDGEMENT

This research was carried out as a part of the GEO-INSTALL project (Modelling Installation Effects in Geotechnical Engineering). It has received funding from the European Community through the program (Marie Curie Industry-Academia Partnerships and Pathways) under grant agreement no PIAP-GA-2009-230638.

REFERENCES

Biot, M. A. (1956a). Theory of propagation of elastic waves in a fluid-saturated porous solid. i. low-frequency range. *Journal of the Acoustical Society of America 28*(2), 168–178.

Biot, M. A. (1956b). Theory of propagation of elastic waves in a fluid-saturated porous solid. ii. higher frequency range. *Journal of the Acoustical Society of America 28*(2), 179–191.

Gidaspow, D. (1994). *Multiphase Flow and Fluidization Continuum and Kinetic Theory Descriptions*. Academic Press.

Jeremic, B., Cheng, Z., Taiebat, M., & Dafalias, Y. (2008). Numerical simulation of fully saturated porous materials. *International Journal for Numerical and Analytical Methods in Geomechanics 32*, 1635–1660.

Pande, G. & Zienkiewicz, O. (1982). *Soil Mechanics Transient and Cyclic Loads, Constitutive relations and numerical treatment*. John Wiley and Sons.

Stolle, D., Jassim, I., & Vermeer, P. (2009). Accurate simulation of incompressible problems in geomechanics. In M. Kuczma & K. Wilmanski (Eds.), *Lectures of the CMM 2009*, pp. 347–361. Springer Verlag.

Verruijt, A. (2010). *An Introduction to Soil Dynamics*, Volume 24 of *Theory and Applications of Transport in Porous Media*. Springer.

Zienkiewicz, O., Chan, A., Pastor, M., Paul, D., & Shiomi, T. (1990). Static and dynamic behaviour of soils: A rational approach to quantitative solutions, part i: Fully saturated problems. *Proceedings of the Royal Society 429*, 285–309.

Zienkiewicz, O. & Shiomi, T. (1984). Dynamic behavior of saturated porous media: the generalised biot formulation and its numerical solution. *International Journal for Numerical and Analytical Methods in Geomechanics 8*, 71–96.

ANALYSIS OF GAS-DRIVEN CRACK PROPAGATION AROUND A BLASTHOLE WITH THE EXTENDED FINITE ELEMENT METHOD

M. Goodarzi
Department of Mining Engineering, University of Tehran, Tehran, Iran

S. Mohammadi
School of Civil Engineering, University of Tehran, Tehran, Iran

A. Jafari
Department of Mining Engineering, University of Tehran, Tehran, Iran

ABSTRACT: *In this paper a simple model is developed to investigate the effect of gas pressure on crack propagation around a blast-hole. This process is analyzed as a quasi-static phenomenon. The gas flow through the cracks is assumed to be a one-dimensional transient flow, and its equations are governed by conservation of mass and momentum; these equations are solved with the explicit Finite Difference Method. The solid medium is modeled with the Extended Finite Element Method (XFEM) which can model the cracks without using any re-meshing algorithm. The Displacement Extrapolation method is implemented to calculate the possibility of crack propagation. The geometrical parameters of the crack are transferred to the gas subroutine and the gas pressure along the crack is given back to the XFEM code. The results are compared with available data and sensitivity analyses are performed on some of the effective parameters.*

1 INTRODUCTION

The stress wave and detonation gas both play a noticeable role in breakage of rock in a blasting operation. The effect of stress wave is to initiate cracks, while the effect of gas pressure is to extend them. Some researchers have shown that the initial stress wave only causes some cracking and crushing of the rock near the borehole and its cracks would not proceed beyond several hole diameters (Kutter & Fairhurst, 1971). In addition, in some applications, such as high energy gas fracturing and control blasting, the aim is that cracks should be extended without causing considerable damage to the wall of the hole, so the act of gas pressure can become more important than the act of stress wave.

Many efforts have been devoted to simulate the complicated process of blasting. Nilson et al. (1985) developed the equations of gas penetration into the cracks based on conservation of mass and momentum; their results were in a good agreement with available experimental data. Munjiza et al. (2000) suggested a simple model for evaluating the detonation gas pressure, within a combined finite-discrete analysis, and the gas pressure was just considered in a specific area around the source. The Nilson's equations were used by Cho et al. (2004) for analysis of dynamic fracture process of rock in a dynamic FEM code with a re-meshing algorithm to model crack growth, they also performed laboratory tests to check their results (Cho et al., 2002). Mohammadi & Bebamzadeh (2005) developed an approach to simulating gas-solid interaction. This model used two separate but coupled meshes for analysis of solid and gas phases based on mechanics of porous media.

In this paper, the second stage of blasting, gas penetration into existing cracks, is investigated. This process can be considered as a quasi-static phenomenon which allows using static algorithms (Paine & Please, 1994; Nilson et al., 1985). For analyzing the solid medium, the Extended Finite Element is implemented. This method avoids using time-consuming and technically difficult re-meshing algorithm. To consider the gas flowing through the fractures, one-dimensional transient flow, governed by the conservation of mass and momentum (Nilson et al., 1985), is used. These equations are solved with the explicit finite difference method (FDM). In each time-step, the geometrical parameters of the crack are given to the FDM code, and the calculated gas pressure is taken as boundary conditions on the solid medium. The results are compared with available experimental data with sensitivity analyses on parameters with high level of uncertainty.

2 NUMERICAL MODELING OF GAS FLOW

Around a blast-hole, a small zone with lots of cracks would appear, and just few of them can finally suppress. If intentional defects such as notches are made around the hole, they will be the preferable paths for gas flow, and as a result, those defects determine the dominating fractures.

Accordingly, in this study, the gas flow is considered only in those surpassing fractures, and the effect of gas loss due to its penetration into the rock is neglected. The gas movement through the fractures is assumed to be a one-dimensional transient flow. Moreover, because of insignificant loss of heat to the surrounding rock, it is reasonable to presume that the gas expands adiabatically (Paine & Please, 1994).

The one-dimensional equations of gas flow governed by the laws of conservation of mass and momentum can be written as (Nilson & Griffiths, 1983; Nilson et al., 1985):

$$\frac{\partial(\rho h)}{\partial t}+\frac{\partial(\rho v h)}{\partial x}=0 \tag{1}$$

$$\frac{\partial(\rho v h)}{\partial t}+\frac{\partial(\rho v^2 h)}{\partial x}=-\rho h\left(\frac{1}{\rho}\frac{\partial P}{\partial x}+\psi\right) \tag{2}$$

where ρ is the density, v is the velocity, P is the gas pressure, and ψ is the viscous shear stress which can be approximated from Eq. 3a and 3b for laminar and turbulent flow respectively.

$$\psi=\begin{cases}\dfrac{12\mu v}{\rho h^2} & \text{(3a)}\\[2ex] a\left(\dfrac{\varepsilon}{h}\right)^b\dfrac{v^2}{h} & \text{(3b)}\end{cases}$$

μ is the viscosity of fluid, h is the aperture of fracture, and based on the experimental results $a=0.1$ and $b=0.5$ (Huitt, 1956). In the present study, inertial effects are deleted from the left side of the momentum equation (Eq. 2), leaving a balance between the pressure gradient and frictional forces. This is generally permissible when the Mach number is not too large, as is expected when gases are hot and fracture speeds are moderate (Nilson et al., 1985). For the friction factor $f_t=a(\varepsilon/h)^b$, Eq. 3 can be rewritten as:

$$v = \begin{cases} \dfrac{h^2}{12\mu}\left(-\dfrac{\partial P}{\partial x}\right) & \text{(4a)} \\ \sqrt{\dfrac{h}{f_t \rho}\left(-\dfrac{\partial P}{\partial x}\right)} & \text{(4b)} \end{cases}$$

Cho et al. (2004) showed that turbulent gas flow through the fracture is much more reasonable, so Eq. 4b is chosen for the rest of this study. By substituting Eq. 4b into Eq. 1 and discretizing it on the mesh shown in Fig. 1, we have:

$$\rho_N^{t+\Delta t} - \rho_N^t = -\frac{4\Delta t}{(\Delta x_R + \Delta x_L)(h_w + h_x)}\left(h_x\sqrt{-\rho^t{}_x \frac{h_x}{f}\frac{(P^t{}_L - P^t{}_N)}{\Delta x}} - h_w\sqrt{-\rho^t{}_w \frac{h_w}{f}\frac{(P^t{}_N - P^t{}_M)}{\Delta x}}\right) \quad (5)$$

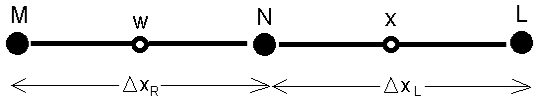

Fig. 1. The Finite Difference mesh, *w* and *x* are in the middle of the elements.

h is an constant input data along an element, and the density of elements are calculated as the average of the densities of their nodes.

To predict the detonation gas pressure, the JWL equation of state is used. This equation at the constant entropy can be written as:

$$P = A\exp^{(-R_1 V)} + B\exp^{(-R_2 V)} + CV^{-(\omega+1)} \quad (6)$$

where *A, B, C, R_1, R_2,* and ω are constant. *V* is the relative density which is defined as the ratio of initial and current densities. This equation predicts the maximum pressure of an explosive when *V*=1. The JWL parameters for the PETN explosive are defined in Table 1.

Table 1. JWL parameters for PETN explosive (Cho et al., 2004).

Parameter	value
A (GPa)	1032.158
B (GPa)	90.57
C (GPa)	3.72735
R_1	6
R_2	2.6
ω	0.57

3 THE EXTENDED FINITE ELEMENT METHOD

The Finite Element Method is one of the powerful methods in engineering analysis, frequently used to model cracks in solid medium. One of the main approaches of FEM is to use an adaptive mesh for simulating cracks physically. This re-meshing process is technically difficult and time-consuming. The Extended Finite Element Method simulates the cracks by enriching the shape functions of the elements which are involved with cracks. In this way,

after each step of crack propagation, there is no need to change the initial mesh, and just the new involved elements should be detected for proper enrichments.

There are two types of enrichments for cracked elements. When an element takes part in crack simulation, its displacement approximation can be defined as (Mohammadi, 2008):

$$u^h(x) = \sum_{j=1}^{n} N_j(x)u_j + \sum_{h=1}^{m} N_h(x)H(\xi(x))a_h + \sum_{k=1}^{mt} N_k(x)\left(\sum_{l=1}^{mf} F_l(x)b_k^l\right) \tag{7}$$

in which n is the number of the nodes of the element, m is the number of nodes which are involved with the crack length, mt is the number of nodes being related to the crack tip, mf is the number of functions that are used for enriching the crack tip element, and a and b are the additional degrees of freedom. N is the usual shape functions of FEM, H is the Heaviside function, and F is a set of functions which are obtained from analytical solution of displacement around a crack tip (Mohammadi, 2008):

$$F_\alpha(r,\theta) = \left\{\sqrt{r}\sin\frac{\theta}{2}, \sqrt{r}\cos\frac{\theta}{2}, \sqrt{r}\sin\theta\sin\frac{\theta}{2}, \sqrt{r}\sin\theta\cos\frac{\theta}{2}\right\} \tag{8}$$

The appropriate enrichment of nodes according to the crack position is schematically illustrated in Fig. 2.

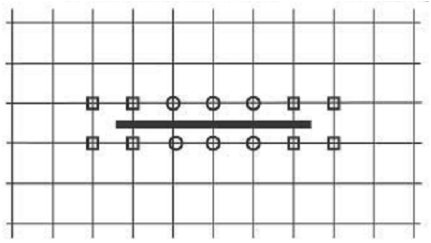

Fig. 2. The squares show the crack tip enrichment, and the circles are related to Heaviside enrichment (Mohammadi, 2008).

Due to those additional degrees of freedom, the usual FEM formulation should be updated. If the cracked solid, shown in Fig. 3, is assumed, the unknown vectors u, the global stiffness matrix K, and the external force vector f in Eq. 9, change to (QingWen et al., 2008):

$$u = Kf \tag{9}$$

$$u = \left\{u_j, a_h, b_k^1, b_k^2, b_k^3, b_k^4\right\} \tag{10}$$

$$k_{ij}^e = \begin{bmatrix} k_{ij}^{uu} & k_{ij}^{ua} & k_{ij}^{ub} \\ k_{ij}^{au} & k_{ij}^{aa} & k_{ij}^{ab} \\ k_{ij}^{bu} & k_{ij}^{ba} & k_{ij}^{bb} \end{bmatrix} \tag{11}$$

$$f_i^e = \left\{f_i^u, f_i^a, f_i^{b1}, f_i^{b2}, f_i^{b3}, f_i^{b4}\right\} \tag{12}$$

$$k_i^e = \int_{\Omega^e} \left(B_i^e\right)^T DB_j^s d\Omega \qquad (r,s = u,a,b) \tag{13}$$

$$f_i^u = \int_{\Omega} N_i b d\Omega + \int_{L_F} N_i t d\Gamma \tag{14}$$

$$f_i^a = \int_\Omega N_i H b d\Omega + \int_{L_F} N_i H t d\Gamma + 2\int_{L_c} n.N_i p d\Gamma \tag{15}$$

$$f_i^{b_l} = \int_\Omega N_i F_l b d\Omega + \int_{L_F} N_i F_l t d\Gamma + 2\int_{L_c} n\sqrt{r}.N_i p d\Gamma \qquad (l = 1-4) \tag{16}$$

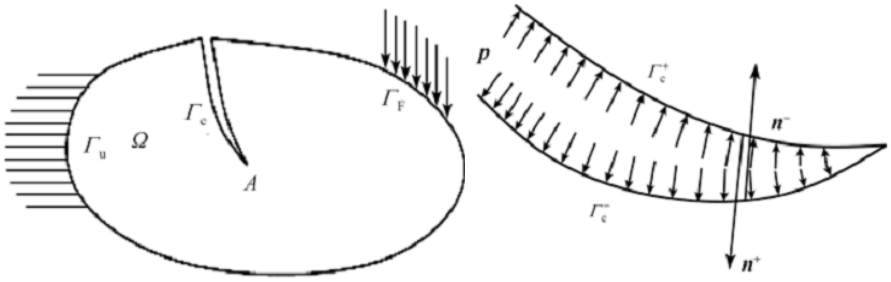

Fig. 3. A cracked solid (left) and details of the crack (right) (QingWen et al., 2008).

4 COUPLING PROCESS AND CRACK PROPAGATION

Since two different numerical methods are used, they have to be coupled. At first, an initial length for the crack should be assumed as a result of the first phase of blasting; stress wave propagation, which is not directly considered in this paper. The initial FDM mesh is generated on the existing crack and the gas flow algorithm is performed for a small time-span which is called time-step here. Then, the calculated gas pressure is applied as a boundary condition into the XFEM code. The new crack length and the crack opening displacement (COD) along the crack are imported to the gas algorithm for the next step of calculation.

A criterion is also required for crack propagation. The stress intensity factor is implemented, and compared with the critical value in each step. There are several methods for numerical calculation of SIF, but inasmuch as it is not necessary to be highly accurate, the simple thought sufficiently accurate displacement extrapolation method is adopted.

Following a liner elastic analysis, the stress intensity factors are determined by equating the numerically obtained displacements with their analytical expressions in terms of the SIF. Such a correlation is performed along a radial line emanating from the crack tip (Saouma, 2000). In addition, the crack propagation is assumed to be under pure Mode I.

5 NUMERICAL RESULTS

5.1 Loading on Crack Surface

To verify the accuracy of present XFEM codes, the results are compared with available analytical solutions. An infinite single edge notch panel with specific width and a point load on its crack surfaces has a statistical formula to calculate the produced SIF around the crack tip (Fig 4).

In this example a=0.245, c= 0.045, b=1, and P= 1e5 Pa. The available reference solution gives 4.5395e5 $Pa.m^{0.5}$ for the SIF (Tada et al., 2000). Because the panel is infinite, in one direction, the height of numerical model is selected 30 *m.* The upper and lower sides are fixed. The numerical SIF is obtained about 4.6e5 $Pa.m^{0.5}$, with the total error about 2.65 percent which is completely acceptable, as the displacement extrapolation is not an exact approach.

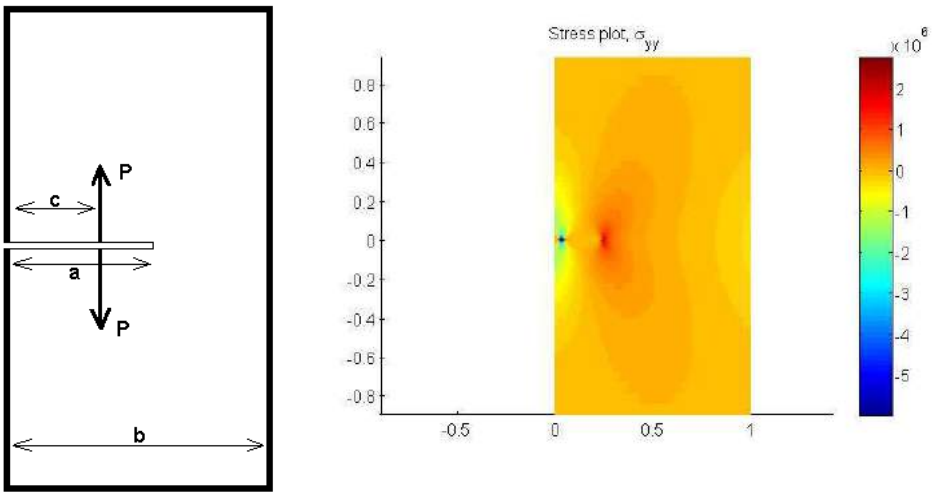

Fig. 4. The geometry of the problem (left), the numerically predicted stress around the crack tip (right).

5.2 Gas Flow

To estimate the accuracy of the algorithm of gas flow, its results are compared with available experimental tests. Cho et al. (2002) performed some experiments on blasting process and measured the gas velocity near the borehole (between 0.03-0.09 m). A detonator with 6.6 mm diameter which contained PETN (Table 1) was used, and the borehole diameter was 40 mm. It should be mentioned that the uncertainties in this kind of experimental test are high. The decoupling index (D.I.) which means the ratio of the diameter of the explosive and charge hole, is 6.06. The maximum produced pressure at borehole can then be calculated from Eq. 9. The borehole had two notches, and it was located in a cylindrical volume of rock with 40 *cm* diameter. The properties of the surrounding material are defined in Table 2.

Table 2. Material properties (Cho et al., 2004).

Parameters	Density (Kg/m^3)	P-wave Velocity (m/s)	S-wave velocity (m/s)	Poisson's ratio	Yung's modulus (GPa)	Toughness ($MPa.m^{1/2}$)
Values	2170	4000	2140	0.18	31.6	3.13

According to this study, $\varepsilon / h = 1$, and the effective time of the blasting process was about $900\,\mu s$ due to the leakage of the gas from top of the borehole or free surfaces. The average value for gas velocity in an observed point, in 0.05 m distance from the borehole, was about 178 *m/s*, and the average velocity ranged between 150-180 *m/s* for this test.

This test has been modeled by XFEM (Fig. 5); the Δt used for FDM's calculation, in Eq. 5, is $0.004\,\mu s$ and for each $20\,\mu s$ (time-step) the solid code is activated to check the crack propagation. Numerical results are shown in Table 3; the values are in a good agreement with the experimental results.

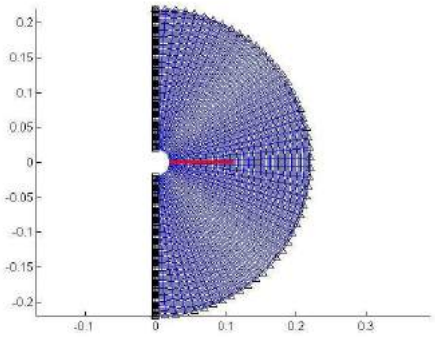

Fig. 5. The numerical model of Cho's experiment. Initial crack length is 10 *cm*.

Table 3. The numerically calculated average gas velocities.

Distance from borehole (*m*)	0.03	0.04	0.05	0.06	0.07	0.08	0.09
Values (*m/s*)	168.35	171.4	172.8	172.75	171.61	169.5	166.73

5.3 Gas-Driven Fracture Propagation

To analyze the gas-driven fracturing phenomenon, a simple model is discussed. A hole with 4 *cm* diameter, casted in a cylindrical medium with 4 *m* diameter, is considered. The explosive is PETN with 10 *mm* diameter. The properties of rock and explosive material are defined in Table 1 and 2, respectively. For considering the crack growth, a value for crack velocity should be assumed. According to Minchinton & Lynch (1996), the crack velocity in a material is about 0.38 times of the P-wave velocity, resulting to about 1500 *m/s*.

Since the first stage of blasting, the stress wave propagation, is not modeled here, an initial crack length of 11 *cm* is considered. A 2 *Mpa* hydrostatical in situ stress is applied on the outer boundary of the cylinder. σ_{yy} contours in different times around the hole are illustrated in Fig 6. The elements with maximum tensile stress show the location of crack tip. The borehole pressure drop can also be observed in these figures. This occurs just because of loss of gas mass due to its penetration into the crack. The Finial crack length is around 1.58 *m*.

In order to investigate the effect of initial crack lengths, some models, with different initial crack lengths, are carried out. The results are given in Table 4, showing the insensitivity of the finial crack length to its initial length. This result was also reported by McHugh (1983).

Table 4. Sensitivity analysis of the results with respect to the initial crack length.

Initial crack length (*m*)	0.11	0.21	0.31	0.41
Final crack length (*m*)	1.58	1.61	1.61	1.62

The second parameter that seems to be influential is the time-step which was defined previously. Table 5 shows results of final crack length with respect to the time-step, and it seems to have a small effect on the results. In addition, this parameter directly affects the run-

time of the code, and it is not reasonable to choose small time-step inasmuch as high accuracy is not necessary.

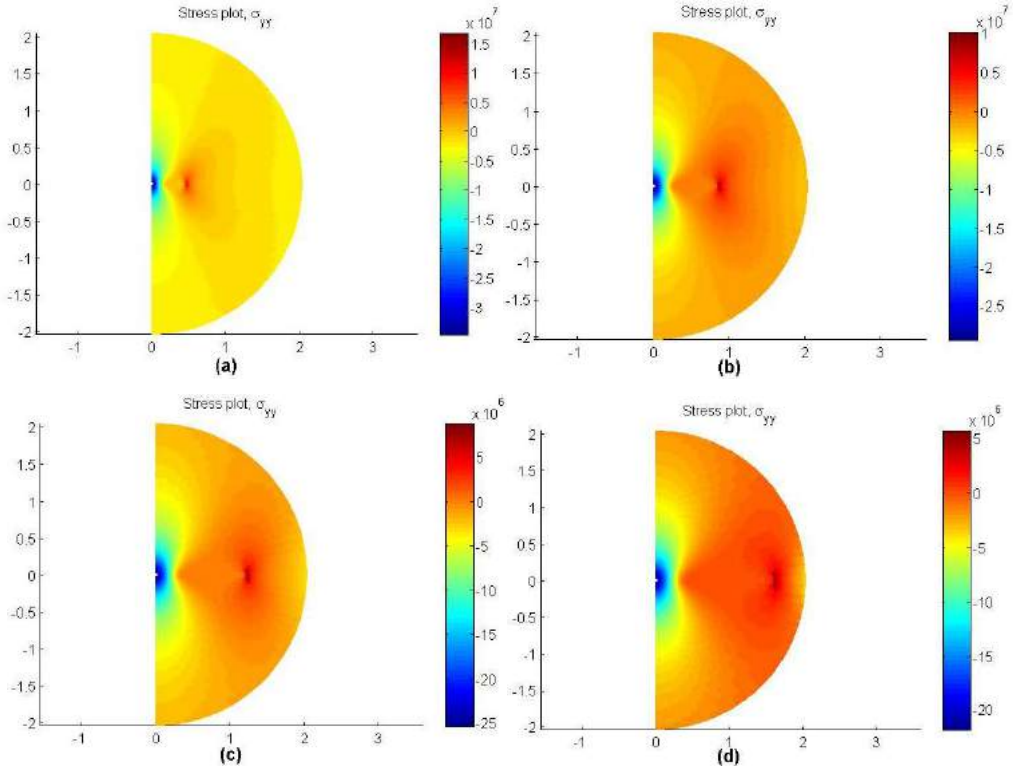

Fig. 6. The contours of σ_{yy}, (a) 250 μs, (b) 500 μs, (c) 750 μs and (d) 1000 μs.

Table 5. Sensitivity analysis of the results for the time-step.

Time-step (μs)	5	10	20	40
Final crack length (m)	1.435	1.485	1.58	1.64

The relative roughness (ε / h) of the fractures is determined by the inhomogeneity of the material. This parameter should be measured or calculated through a back analysis of the results. In Table 5, the effect of this parameter on the results is discussed. As it can be seen, by increasing the value of relative roughness, the final crack lengths reduce, which is logical because it has a negative effect on gas flow through the fractures.

Table 5. Sensitivity analysis for the relative roughness of fractures.

Relative roughness	1	2	4	6
Final crack length (m)	1.58	1.46	1.25	1.13

6 CONCLUSION

In this study, the effect of gas pressure on crack propagation has been analyzed. A simple one-dimensional gas flow through the fractures has been considered, and solved by the finite difference method, combined with a static XFEM code. For consideration of crack propagation, the stress intensity factor of the crack tip is calculated from the displacement

extrapolation and compared with its critical value. The algorithm has been evaluated, and the predicted results are in a good agreement with the available data.

Sensitivity analyses show that the final crack length does not depend on the initial length of the crack. In fact, it confirms the importance of gas pressure in the process of fracture propagation around blast-holes. The time that gas can flow through cracks for each solid calculation does not seem to be very effective, but it should be small to simulate real condition of gas-driven fracturing. The effect of relative roughness has been checked too, showing considerable influence on the results.

REFERENCES

Cho, S.H, Risei, K., Kato, M., Nakamura, Y. & Kaneko K. (2002), "Development of numerical simulatin method for dyanmic fracture propagation due to gas pressurization and stress wave". Proc. 2002 ISRM Regional Sym.(3nd Korea-Japan Joint Symposium) on Rock Engineering Problem and Approaches in Underground Construction, Jul. 22-24, Seoul, Korea, pp. 755-762.

Cho, S.H., Nakamura, Y. & Kaneko, K. (2004), "Dynamic fracture process analysis of rock subjected to stress wave and gas pressurization". Int. J. Rock Mech. Min. Sci, Vol. 41, No. 3, CD-ROM, Paper 2A20.

Huitt, J.L., (1956) "Fluid flow in simulated fractures". A.I.Ch.Jl 2(2), 259-264

Kutter, H.K. & Fairhurst, C. (1971), "On the fracture process in blasting". Int. J. Rock Mech. and Min. Sci. Vol. 8: 181-202.

McHugh, S., (1983), "Crack extension caused by internal gas pressure compared with extension caused by tensile stress". Int. J. of Fracture, Vol. 21, 163-176

Minchinton, A., Lynch, P.M. (1996), "Fragmentation and heave modellign using a coupled discrete element gas flow code". Proceeding of 5th international conference of rock fragmentation, ISBN 9054110824 X.

Mohammadi, S. & Bebamzadeh, A. (2005), "A coupled gas-solid interaction model for FE/DE simulation of explosion". Finite element in analysis and design, Vol. 41, 1289-1308.

Mohammadi, S., (2008), Extended finite element method for fracture analysis of structure, Blackwell Publishing.

Munjiza, A., Latham, J.P. & Andrews K.R.F. (2000), "Detonation gas model for combined finite-discrete element simulation of fracture and fragmentation". Int. J. for Numerical Methods in Engineering, Vol. 49, 1495-1520.

Nilson, R.H., Proffer, W.J. & Duff, R.E. (1985), "Modelling of gas-driven fractures induced by propellant combustion within a borehole". Int. J. Rock Mech. and Min. Sci. Vol. 22(1): 3-19

Nilson, R.H. & Griffiths, S.K. (1983), "Numerical analysis of hydraulically-driven fractures". Computer method in applied mechanics and engineering, Vol. 36, 359-37.

Paine, A.S. & Please, C.P. (1994), "An improved model of fracture propagation by gas during rock blasting-some analytical results," Int. J. Rock Mech. Min. Sci and Geomech, Vol. 31, 699-706.

Saouma, V.E., (2000), Lecture notes in fracture mechanics, Department of Civil Environmental and Architectural Engineering, University of Colorado.

Tada, H., Paris, P.C., & Irwin, G.R. (2000), The stress analysis of cracks handbook, Third edition, Professional Engineering Publishing.

NUMERICAL COUPLING OF GEOMECHANICS AND THERMAL RESERVOIR FLOW USING SEPARATE GRIDS

N. Guy, S. Zandi, G. Ferrer, A. Baroni, G. Renard & J.F. Nauroy
IFP Energies nouvelles, 1-4 avenue de Bois-Préau 92852 Rueil-Malmaison - France

ABSTRACT: *In this paper a numerical procedure aiming at performing thermo-hydro-mechanical simulations is proposed. This procedure relies on an iterative coupling between a reservoir simulator based on finite volume method and a geomechanical simulator based on finite element method. The coupling methodology can be used to model the mechanically induced evolution of material transport properties such as porosity and/or permeability depending on the coupling configuration. A special feature of the proposed procedure is to allow the use of different grids for reservoir and mechanical simulators. The separate grids are coupled through a field transferring technique that allows mapping fields from one grid to another by using a diffuse approximation method. The advantage of this technique is to use grids adapted to the described phenomena in both thermal fluid flow and geomechanical analysis in order to reduce computation time.*

The characteristics of the coupling procedure are studied on an artificial but realistic case describing a thermal oil recovery through Steam Assisted Gravity Drainage (SAGD) process that involves complex phenomena. The simulations are performed for various spatial discretizations and for different coupling time steps. The results show that this methodology allows both obtaining relevant results and reducing computation time.

1 INTRODUCTION

When oil recovery is implemented in a field, reservoir pore pressure and temperature eventually change, modifying the stress state in the underground. Depending on which recovery process is used, the stress state modification can lead to significant changes in rock porosity and permeability. Therefore, within some oil recovery processes, reservoir geomechanics analysis is concerned with the simultaneous study of fluid flow and the mechanical response of the reservoir.

To solve the coupling between fluid flow and geomechanics, different approaches can be used (Settari & Mourits, 1998; Longuemare et al., 2002; Jeannin et al., 2005). The fully coupled approach simultaneously solves the whole set of equations that govern the thermo-hydro-mechanical problem. It yields consistent descriptions, but the hydraulic or geomechanical mechanisms are often simplified by comparison with conventional uncoupled reservoir and geomechanical approaches. Therefore, the solution to address the coupling between fluid flow and geomechanical problems is to couple a reservoir simulator based on finite volume method and a geomechanical simulator based on finite element method. This approach, which is followed in this paper, has the advantage of benefiting from options incorporated in both finite volume based reservoir simulators and finite element based mechanical simulators. Nevertheless, performing coupled simulations instead of conventional reservoir simulations often requires a much higher computation time.

In order to reduce the coupled simulation run time, a separate-reservoir/geomechanics grid system is proposed. With this approach, geomechanics grid or reservoir grid can be refined or coarsened in different regions independently according to the scale of various physical processes of interest (Tran et al., 2008). In this paper, the procedure is used to save computation time during the geomechanical simulation by using a finite element

geomechanical grid (GG) that is coarser than the finite volume reservoir grid. In the proposed procedure the diffuse approximation method (DAM) is used to transfer the fields from one grid to another.

To illustrate the methodology, simulations describing oil recovery by steam assisted gravity drainage (SAGD) process are performed. The SAGD process is an enhanced oil recovery (EOR) process in which geomechanical effects play a significant role. The SAGD process is based on continuous steam injection and leads to changes in both pore pressure and temperature in the reservoir. The SAGD process is usually used to recover oil from oil sand reservoir. Fluid-flow related properties of oil sands are known to evolve when the rocks are submitted to variable stress. For example, laboratory tests have revealed that the permeability of oil sands can be strongly increased by shear stress modification (Touhidi-Baghini, 1998). The influence of this geomechanical phenomenon on SAGD process efficiency has been investigated through numerical simulations in numerous studies (Ito & Suzuki, 1996; Collins et al., 2002; Lerat et al., 2009a). The work presented in this paper was performed in the framework of a study on reservoir-geomechanics coupling methods conducted at IFP Energies nouvelles. SAGD coupled thermo-hydro-mechanical modeling is conducted using PumaFlow, the inner reservoir simulator of IFP Energies nouvelles, and Abaqus as the geomechanical simulator. Simulations of the SAGD process were applied on a synthetic but realistic case. The considered case (i.e., geometry, materials and fluids properties and initial conditions) has been constructed using a case that has previously been studied (Zandi et al., 2010a; Zandi et al., 2010b; Zandi et al., 2010c). Furthermore, it should be noticed that in the present work the geomechanical simulator is used with respect to the Thermo-poro-mechanics (Biot, 1941; Coussy, 1995) and that the fluids behaviors are represented in the reservoir simulator by a "Thermal-dead-oil" model already used by, as an example, Zandi et al. (2010a).

2 COUPLING APPROACH

Different approaches can be used to perform a geomechanical analysis through coupling a reservoir simulator based on finite volume method and a geomechanical simulator based on finite element method. The first one is the decoupled or "one way coupling". It is the simplest partially coupled approach in which the pore pressure history and temperature history issued from a conventional reservoir simulation is introduced as input into the geomechanical equilibrium equation to deduce the stress and deformation. This coupling is easy to implement and still includes some interesting physics (Vidal et al., 2009). The second one is the sequential coupling that can be described as "explicit" if the methodology is only performed once for each time step and "iterative" if the methodology is repeated till convergence between the two models of the calculated stress and fluid flow is reached. In this paper an iterative approach that relies on the same principle as the one of Longuemare et al. (2002) and that takes into account thermal effects is used.

2.1 Iterative coupling approach

The sequentially iterative approach is based on an external coupling between conventional reservoir and geomechanical simulators. The stress and flow equations are solved separately for each time step but information is transferred between the reservoir and geomechanical simulators. The proposed coupling approach consists in executing sequentially the two models, linked through external coupling modules (figure 1). The initialization step is performed first to evaluate consistent initial conditions. After the initialization step the fluid flow simulator is executed over a first period. Updated pore pressures and temperatures at the end of this first period are interpolated and transferred from the reservoir grid (RG) to the

geomechanical grid (GG) in the geomechanical simulator. Based on the updated producing conditions and constitutive relationships, the geomechanical simulator solves the mechanical equilibrium.

Then the results are transferred to the reservoir grid. After this step the convergence criterion is checked. In the present procedure the convergence criterion checked for every element of the reservoir simulator is:

$$\frac{\left|\phi_{g/r}(t_{i+1}) - \phi_r(t_{i+1})\right|}{\phi_0} < CRIT \qquad (1)$$

In this formula,

- $\phi_{g/r}(t_{i+1})$ is the lagrangian porosity deduced on the reservoir grid from the fields transferred by the geomechanical simulator at the end of the last iteration of the i^{th} period;
- $\phi_r(t_{i+1})$ is the lagrangian porosity evaluated by the reservoir simulator at the end of the last iteration of the i^{th} period, ϕ_0 the initial lagrangian porosity;
- *CRIT* is a user-defined value; and
- t_{i+1} is the time at the end of the i^{th} period.

If the convergence criterion is not verified the reservoir permeability is updated and the porous volume evolution is corrected in order to perform another simulation of the same period. For the studies considered in this paper, the convergence criterion has been checked with *CRIT* equal to 10^{-3}.

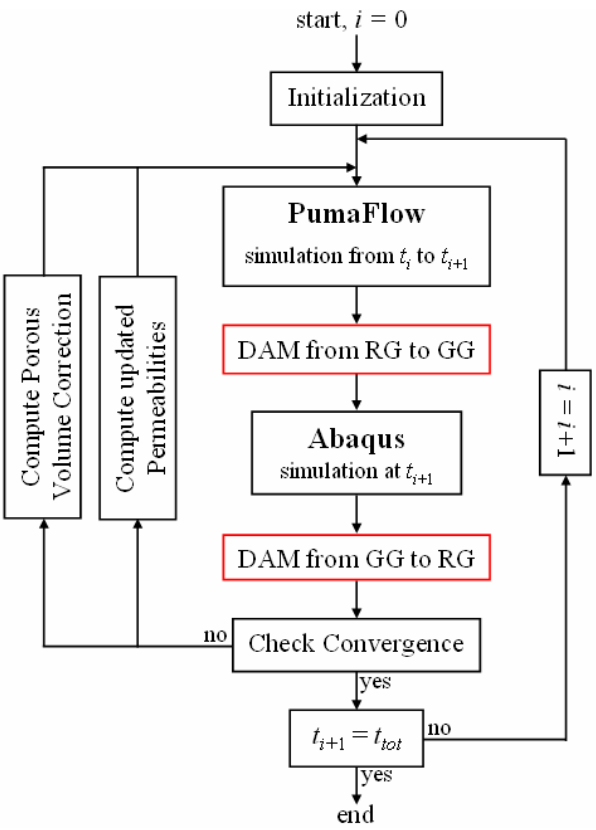

Fig. 1. Coupling procedure scheme

In the present work, the permeability is updated considering a simple and empirical relationship proposed by Touhidi-Baghini (1998). This simple relationship linking permeability changes to volumetric strain reads:

$$\ln \frac{k_1}{k_0} = \frac{c}{\phi_0} \varepsilon_v \tag{2}$$

with k_1 the updated absolute permeability, k_0 the initial absolute permeability, ε_v the volumetric strain and c a constant. According to Touhidi-Baghini (1998), the values $c = 5$ and $c = 2$ appear to be appropriate to match with vertical and horizontal permeability evolutions.

The correction of the porous volume is implicitly made. At the beginning of the new iteration of the current period, a term *DPV* traducing the evolution of porous volume due to the geomechanical phenomena is introduced in the reservoir simulator, it reads:

$$DPV = \frac{PV_{g/r}(t_{i+1}) - PV_r(t_i)}{t_{i+1} - t_i} \tag{3}$$

with t_i the time instance at the beginning of the i^{th} period, $PV_{g/r}(t_{i+1})$ the porous volume deduced on the reservoir grid from the fields transferred by the geomechanical simulator at the end of the last iteration of the i^{th} period, $PV_r(t_i)$ the porous volume evaluated by the reservoir simulator at the end of the i^{th} period. This loop is performed until convergence is reached. When the convergence is reached, the next period is simulated. This procedure is continued until the end of the simulation.

Furthermore, it should be noticed that the compressibility c_p used in the reservoir simulator PumaFlow, is linked with the geomechanical parameters using the following relation:

$$c_p = \left[\frac{b - \phi_0}{K_s} + \frac{b^2}{K_d} \right] \tag{4}$$

with b the Biot modulus, K_s the matrix bulk modulus and K_d the drained bulk modulus.

2.2 Diffuse approximation method

The fact that the grid types in reservoir simulator and geomechanical simulator are different makes the mapping process more complicated. In fact in the reservoir simulator a Finite Volume Grid discretization is used where pressures and temperatures are computed at the center of gridblocks while in the geomechanical simulator a Finite Element Grid discretization is used to compute displacements at the nodes of the grid.

Here a code named NUAGE based on diffuse approximation method (Savignat, 2000), is used for mapping the data from reservoir grid centers to geomechanics grid nodes and *vice versa*. The diffuse approximation method can be used for finding estimates of a scalar field φ from a set of nodal values (Nayroles et al., 1991). The starting point is to estimate the Taylor expansion of the studied scalar field φ at a chosen point by a weighted least squares method which uses only the values of φ at the nearest points. The main advantage of this method is that it only requires sets of discretization nodes and no geometric finite elements and that it is a local method. It has to be noticed that the diffuse approximation method can be used with

various weighting strategies that lead to different and interesting properties. Using the diffuse approximation method, when the reservoir and the geomechanics grids are distinct, reduces the simulation run time, but results remain very close to the one-grid system results. This will be shown later.

The weighting procedure used in the present scheme allows the DAM to interpolate the initial data. This scheme which is written in C language gives improved mapping for discontinuous functions. For the herein study, the data transfer is performed through a coupling module that has been developed using Fortran and Python languages. This module contains the mapping module (NUAGE) written in C language.

3 CASE STUDY

This test case has been constructed from a model that has previously been described (Zandi et al., 2010a). The reservoir is assumed homogeneous. As shown in figure 2, the top of the reservoir is 250 m deep, the initial pressure and temperature being equal to 2.4 MPa at the top of the reservoir and 10°C respectively.

The reservoir simulated domain is rectangular with its dimensions in the X, Y and Z directions respectively equal to 147, 500 and 20 meters (figure 2). The well pair is located along the Y axis and in the middle of the X axis. The distance between the two wells is 5 m. The producer is 2 m above the base of the reservoir.

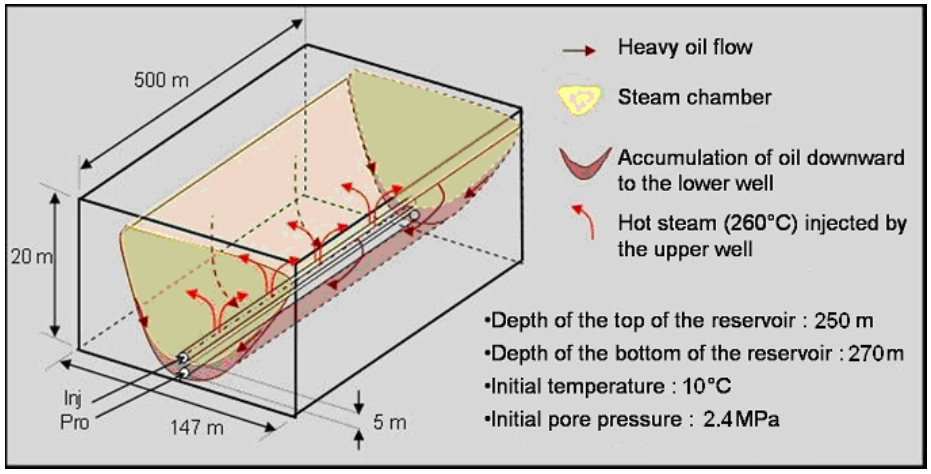

Fig. 2. Description of the case study

In the reservoir fluid flow simulator, the size of the grid cells in the X direction is equal to 1 meter near the wells and increased to 2 then 3 meters farther away. As the vertical distance between the two horizontal wells was supposed to be constant, only one cell 500 m long is used to describe the well length in the Y direction. Vertical gridding in the reservoir is constant with 40 layers 0.5 meter thick. Sideburden rocks are not modeled because the treated case is assumed geometrically periodic. This assumption corresponds to the fact that in a SAGD process, it is common to use several pairs of well that are parallel and equidistant to optimize production rates. In the model associated with the reservoir simulator, fluids cannot flow through the boundaries but heat losses by conduction through upper and lower boundaries are taken into account by a simplified and one-dimensional modeling of the overburden and underburden that is oriented in the vertical direction.

The simulations are performed over 1,440 days. As in the case presented by Zandi et al. (2010a), the first 120 days consists in pre-heating. The steam injection starts at the end of pre-

heating with a maximal pressure set to 5 MPa and the production rate is controlled in order to keep the production well temperature 20°C to 35°C lower than the injection well temperature. The production well minimal pressure is set to 0.5 MPa and the steam injection temperature is about 260°C.

In the geomechanical model, the simulated domain includes the reservoir surrounded below by underburden layers and above by overburden layers. The horizontal displacement of lateral boundaries is blocked as well as all the displacements of the lower boundary. We precise that for the reservoir the Biot coefficient is $b = 1$, the drained bulk modulus is $K_d = 4.17x10^8$ Pa and the Poisson ratio is $\nu = 0.3$. Except the reservoir depth, initial condition and drained bulk modulus, the other model properties are identical to the ones given by Zandi et al. (2010a). Initial state stresses are supposed to be isotropic.

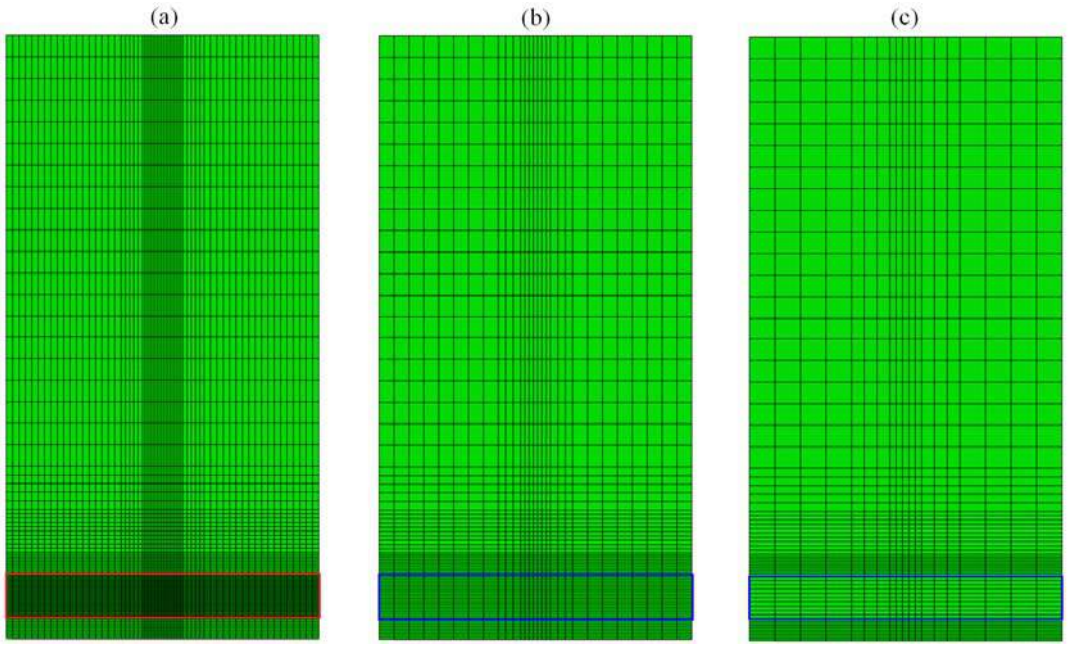

Fig. 3. The three geomechanical grids ((a) GG-1, (b) GG-2 and (c) GG-3)

In this paper we model the underground by considering a reservoir part that are modeled in both reservoir and geomechanical simulators and surrounding rocks that are only modeled in the geomechanical simulator. Recent studies based on comparable approaches have also been presented by, as examples, Lerat et al. (2009b) or Shi & Durucan (2009).

The applied coupling approach is the one described in section 2. The case study aims at comparing various simulations with the same gridding for every reservoir simulations and with different gridding for the geomechanical simulations. The geomechanical grids are described in figure 3 and are made of quadratic elements. The first geomechanical grid (GG-1), shown in figure 3(a), contains 6,175 elements. The reservoir part (delimited by a red rectangle in figure 3(a)) contains 2,600 elements and is identical to the reservoir simulator grid. The second geomechanical grid (GG-2), shown in figure 3(b), is coarser than the first one. It contains 2,175 elements and the reservoir part (delimited by a blue rectangle in figure 3(b)) contains 580 elements. The third geomechanical grid (GG-3), shown in Fig. 3(c), is even coarser than the second one. It contains 1,235 elements and the reservoir part (delimited by a blue rectangle in Fig. 3(c)) contains 190 elements. The meshes corresponding to the reservoir part of the grid GG-1, GG-2 and GG-3 can be seen in figures 5(a), 5(b) and 5(c).

Note that in the second and third cases, the geomechanics gridblocks of underburden and overburden are also resized and the number of gridblocks is less than in the first case. For each considered geomechanical grid, five simulations are performed for different coupling time steps. The studied coupling time steps are 5, 10, 20, 40 and 60 days. Also, two uncoupled reservoir simulations (namely the standard compressibility simulation and the lowered compressibility simulation) are performed in order to evaluate the contribution of both geomechanical effects and compressibility effects. The difference between the standard compressibility simulation and the lowered compressibility simulation is that the standard compressibility simulation is performed with a compressibility obtained by Eq. (4) and the second simulation is performed with a ten times lowered compressibility.

4 RESULTS

Results obtained from the fifteen coupled cases and from the two uncoupled cases are compared. First, it has to be noticed that for all the coupled simulations the coupling procedure has lead to both convergence and satisfying results.

4.1 Relevance of the results

To characterize the global response of the reservoir, cumulative oil produced at *in situ* conditions is plotted versus time on figure 4 for the various simulations. On the figure 4(a) the result obtained with the three considered geomechanical grids are compared with each other and with the results obtained with simulations in which geomechanical effects are ignored (namely the standard compressibility simulation and the lowered compressibility simulation).

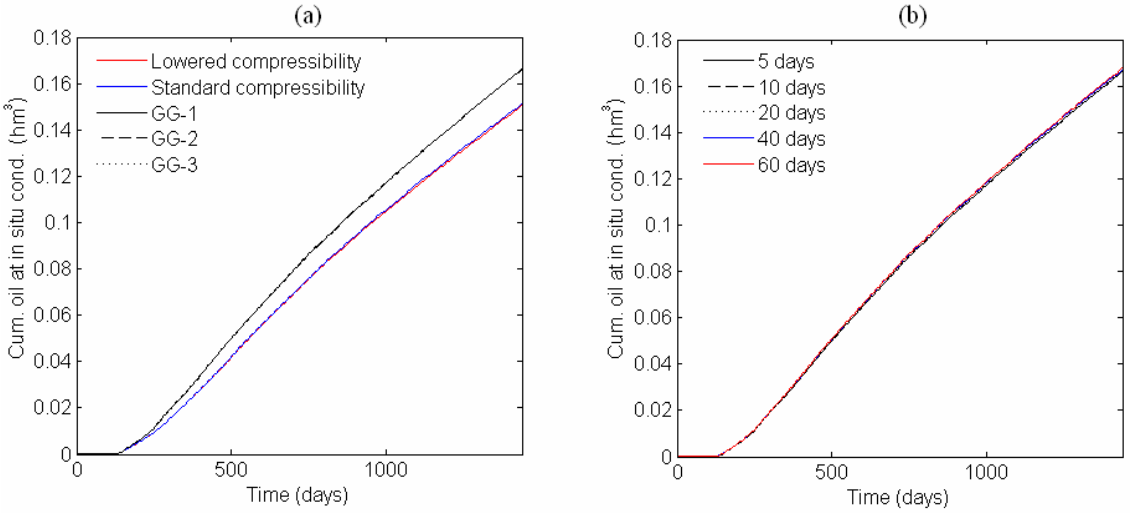

Fig. 4. Cumulative oil produced at in situ conditions versus time for different modeling and different spatial discretization with coupling time step of 5 days (a) and for different coupling time step with the geomechanical grid GG-1 (b)

On figure 4(a), the results obtained with the three geomechanical grids are superimposed. The results obtained with the two other simulations (in which geomechanical effects are ignored) are also very close with each other but are different from the results obtained with the coupled simulations using the grids GG-1, GG-2 or GG-3. This clearly shows that the geomechanical effects involved in a SAGD process cannot be represented by using a simple

compressibility factor. The gap between the coupled and uncoupled simulations in terms of produced oil at in situ conditions is of about 10%. This result is consistent with the one obtained by Collins et al. (2002). It also clearly shows that using a coarser grid for the geomechanical simulation than for the reservoir simulator with the proposed procedure allows one to obtain relevant results in terms of oil production.

On figure 4(b), the results obtained with the different coupling time steps and with the geomechanical grid GG-1 are very close. It should be noticed that even the larger coupling time steps can lead to an overestimation of the produced oil that is quite low, about 0.6%. This observation demonstrates that the results obtained through the various simulations worth computation and can legitimately be compared.

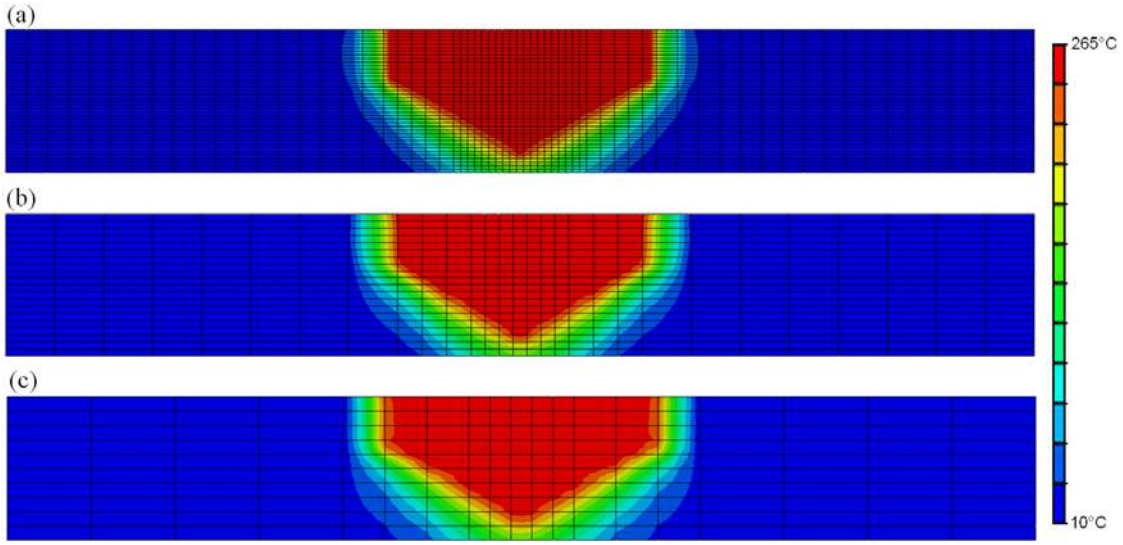

Fig. 5. Temperature field reconstructed on the geomechanical grids ((a) GG-1, (b) GG-2, and (c) GG-3) after 750 days of simulation and with a coupling time step of 5 days

Figure 5 shows the temperature field in the reservoir after 750 days of simulation and with a coupling time step of 5 days for the three geomechanical grids. As it can be seen, the temperature field resulted by the three simulations are really similar. The results plotted on figures 5(a) and 5(b) are extremely close. The results plotted on figure 5(c) that corresponds to the coarser grid are still close to the other ones. However we can see that when a part of the thermal front arrives in an area with the coarser mesh, the shape of this numerical thermal front is influenced by the considered geomechanical mesh and associated shape functions. One can suppose that the third geomechanical grid is still satisfying but represents a limit in terms of element number reduction.

4.2 Computation time of the simulations

In order to compare the computation time (CPU time) of the simulations, a normalized simulation CPU time is introduced. For each simulation and at end of a time period *i*, the normalized simulation CPU time can be estimated by considering the following expression:

$$NSC(X, Dt, i) = \frac{\sum_{k=1}^{i} (Dt + DX) \times n_k}{t_{tot}} \tag{5}$$

with X the considered grid (GG-1, GG-2 or GG-3), Dt the coupling time step, n_k the total number of iterations performed in the period k to reach convergence and DX an equivalent geomechanical simulated time associated with the geomechanical mesh X. In the present case we take DGG-1 = 30 days, DGG-2 = 8 days and DGG-3 = 3 days and t_{tot} = 1440 days.

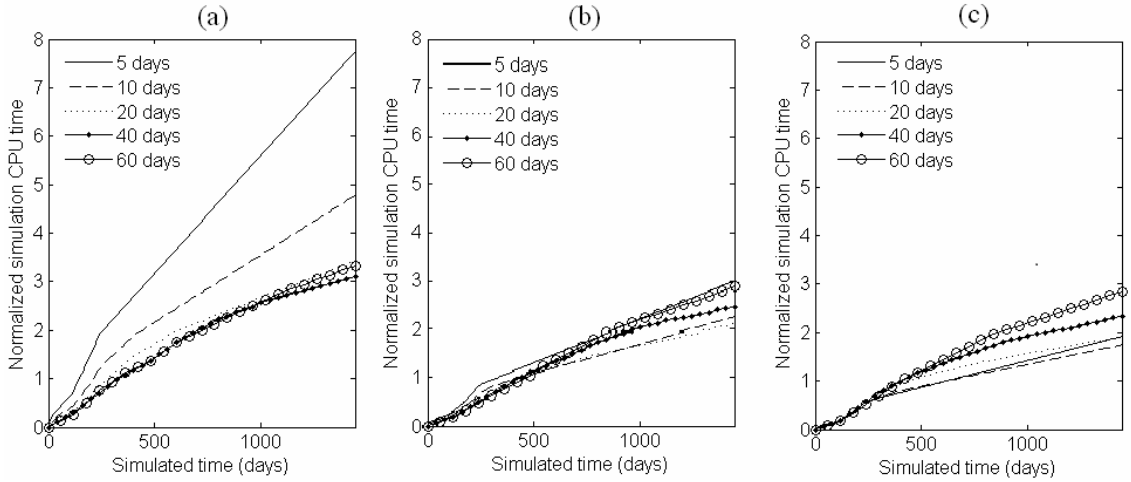

Fig. 6. Normalized simulation CPU time with simulated time for various coupling time step and for the three geomechanical grids (a) GG-1, (b) GG-2 and (c) GG-3

As an example, it means that the numerical cost of a geomechanical simulation with the GG-1 mesh is close to the numerical cost required to perform a simulation describing 30 days of fluid flow. The normalized simulation cost does not take into account the influence of data mapping from one grid to another because its numerical cost has appeared to be very low compared to the numerical cost of geomechanical simulations.

The values considered for the equivalent geomechanical simulation time show that using a coarser geomechanical grid clearly decreases the geomechanical simulation cost. Nevertheless it has to be noticed that this effect would probably be more significant for cases containing more elements and that it would probably also be more significant for a three dimensional case where the increase of element size would take place in three directions (instead of only two directions in the present case).

In figure 6, the normalized simulation costs are plotted with simulated time for the three geomechanical grids. The results obtained for the geomechanical grids GG-1, GG-2 and GG-3 are respectively plotted on the figure 6(a), 6(b) and 6(c) for the five considered coupling time steps. Figure 6 clearly shows that it leads to more important numerical cost for every time step considered. Furthermore, as it can be seen on figure 6(a), the numerical cost of the total simulation increases dramatically when the finer mesh GG-1 is used with small coupling time steps (5-10 days). For this configuration the computational time is higher than for the other configuration at every step of the simulation. Figure 6(a) also shows that to reduce the computational time with the considered configuration, it is necessary to rarely update the transport properties considered by the reservoir simulator and that even in that case the computational time is still high. As it can be seen on figure 6(c), the simulations based on the geomechanical grid GG-1 and associated with small coupling time steps (5-10 days) leads to lowest computational time of the studied cases.

As shown on figure 7 the optimal coupling time step is not the same for the three geomechanical grids. The best coupling time step appears to decrease with the number of elements, it is of 10 days for the grid GG-3, 20 days for the grid GG-2 and 40 days for the

grid GG-1. Furthermore it can be seen that with the best coupling time steps, the coarser is the geomechanical grid, the faster are the simulations.

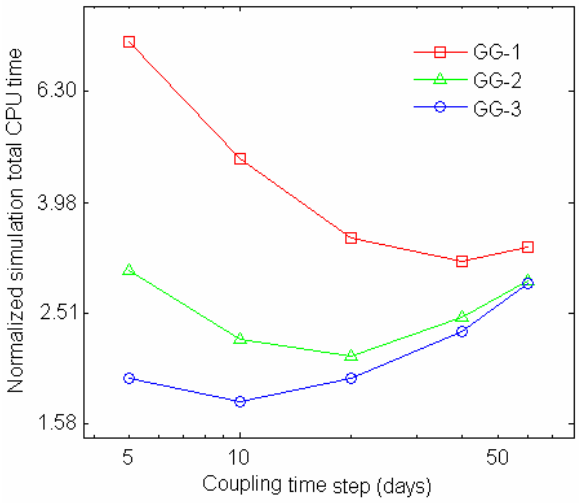

Fig. 7. Normalized simulation total CPU time versus coupling time step for the three considered geomechanical meshes

Using the proposed coupling procedure appears to be interesting because it allows performing simulations faster and updating reservoir parameters more frequently.

5 CONCLUSIONS

This paper presents a coupling procedure integrating a field transfer module (based on a diffuse approximation method). This procedure is dedicated to perform simulations coupling geomechanics and thermal reservoir flow with separate grids. The procedure ability has been evaluated on a synthetic but complex case describing a SAGD based oil recovery that involves thermo-poro-mechanical phenomena. It has been shown that the sequential iterative coupling approach combined by coincident and separate grid systems has lead to a relevant description of the considered physical phenomena. Furthermore, the presented procedure has appears to significantly reduce the computational time. It also has to be noticed that, observed reduction in computational time comes with a decrease of the optimal coupling time steps. It means that the proposed coupling method can lead to a more frequent updating of the transport properties considered by the reservoir simulator with a lower computational cost.

ACKNOWLEDGEMENT

The authors wish to thank Michel Tijani (ENSMP) who initiated this work, for his help and useful discussions.

REFERENCES

Biot, M.A. (1941), "General Theory of Three Dimensional Consolidation". J. Appl. Phys. Vol. 12, 155-164.

Collins, P.M., Carlson, M.R., Walters, D.A. & Settari, A. (2002), "Geomechanical and Thermal Reservoir Simulation Demonstrates SAGD Enhancement Due to Shear

Dilation". Proceedings of the SPE/ISRM Rock Mechanics Conference, Irving, Texas, 20-23 October.

Coussy, O. (1995), Mechanics of Porous Continua, John Wiley & Sons Ltd., New York.

Ito, Y. & Suzuki, S. (1996), "Numerical Simulation of the SAGD Process in the Hangingstone Oil Sands Reservoir". Proceedings of the 47th ATM of the Petroleum Society of CIM, Calgary, Alberta, 10-12 June.

Jeannin, L., Mainguy, M. & Masson, R. (2005), "Comparison of Coupling Algorithms for Geomechanical-Reservoirs Simulations". Proceedings of the U.S. Rock mechanics symposium, Anchorage, Alaska, USA, 25-29 June.

Lerat, O., Adjemian, F., Auvinet, A., Baroni, A., Bemer, E., Eschard, R., Etienne, G., Renard, G., Servant, G., Michel, L., Rodriguez, S., Aubin, F. & Euzen, T. (2009), "Modelling of 4D Seismic Data for the Monitoring of the Steam Chamber Growth during SAGD Process". Proceedings of the Canadian International Petroleum Conference 2009, Calgary, Alberta, Canada, 16-18 June.

Lerat, O., Adjemian, F., Auvinet, A., Baroni, A., Bemer, E., Eschard, R., Etienne, G., Renard, G., Servant, G., Rodriguez, S., Bathellier, E. & Forgues, E. (2009), "4D Seismic Modelling Applied to SAGD Process Monitoring". Proceedings of the 15th European Symposium on Improved Oil Recovery, Paris, France, 27-29 April.

Longuemare, P., Mainguy, M., Lemonnier, P., Onaisi, A., Gérard, Ch. & Koutsabeloulis, N. (2002), "Geomechanics in Reservoir Simulation: Overview of Coupling Methods and Field Case Study". Oil & Gas Science and Technology, Vol. 57(5), 471-483.

Nayroles, B., Touzot, G. & Villon, P. (1991), "The diffuse approximation". C. R. Acad. Sci. Paris, Serie II, Vol. 313, 293-296.

Savignat, J.M. (2000), Approximation Diffuse Hermite et ses Applications, PhD Dissertation, Mines Paris Tech, Paris.

Settari, A. & Mourits, F.M. (1998), "A Coupled Reservoir and Geomechanical Simulation System". SPE J. Vol. 3(3), 219-226.

Shi, J.Q. & Durucan, S. (2009), "A coupled reservoir-geomechanical simulation study of CO2 storage in a nearly depleted natural gas reservoir". Energy Procedia, Vol. 1, 3039-3046.

Touhidi-Baghini, A. (1998), Absolute Permeability of McMurray Formation Oil Sands at Low Confining Stresses, PhD dissertation, Department of Civil Engineering, University of Alberta, Alberta.

Tran, D., Buchanan, L. & Nghiem, L. (2008), "Improved Gridding Technique for Coupling Geomechanics to Reservoir Flow". Proceedings of the Annual Technical Conference and Exhibition, Denver, Colorado, USA, 21-24 September.

Vidal-Gilbert, S., Nauroy, J.F. & Brosse, E. (2009), "3D Geomechanical Modelling for CO2 Geologic Storage in the Dogger Carbonates of the Paris Basin". Int. J. of Greenhouse Gas Control, Vol. 3, 288–299.

Zandi, S., Renard, G., Nauroy, J.F., Guy, N. & Tijani, M. (2010), "Numerical Modelling of Geomechanical Effects during Steam Injection in SAGD Heavy Oil Recovery". Proceedings of the EOR Conference at Oil & Gas West Asia, Muscat, Oman, 11-13 April.

Zandi, S., Renard, G., Nauroy, J.F., Guy, N. & Tijani, M. (2010), "Numerical Coupling of Geomechanics and Fluid Flow during Steam Injection in SAGD". Proceedings of the Improved Oil Recovery Symposium, Tulsa, USA, 24-28 April.

Zandi, S., Guy, N., Ferrer, G., Renard, G. & Nauroy, J.F., (2010), "Coupled Geomechanics and Reservoir Modelling in SAGD Recovery". Proceedings of the 12th European Conference on Mathematics of Oil Recovery, Oxford, UK, 6–9 September.

DYNAMIC MATERIAL POINT METHOD WITH APPLICATIONS IN GEOMECHANICS

I. Jassim
Deltares, Delft, The Netherlands / Institute of Geotechnics, Stuttgart University, Germany

F. Hamad
Deltares, Delft, The Netherlands / Institute of Geotechnics, Stuttgart University, Germany

P. Vermeer
Deltares, Delft, The Netherlands / Institute of Geotechnics, Stuttgart University, Germany

ABSTRACT: *A dynamic Material Point Method for use in Geomechanics is presented. Soil and structural bodies are represented by (material) particles, which move inside an unstructured mesh of four-noded 3-D tetrahedral elements. As such low-order elements tend to show locking for fully developed plastic flow, a strain-enhancement remedy is described. As a first example, the penetration of a drop anchor into a Mohr-Coulomb soil is considered. As both a soil body and a metal anchor are considered, an algorithm for dynamic contact is used and described. An improved type of absorbing boundaries to avoid the reflection of stress waves is also described. The second example consists of dynamic cone penetration. Finally, the example of a collapsing tunnel is considered.*

1 INTRODUCTION

Over the last decades the Finite Element Method (FEM) has become the standard tool of analysis in the field of solid mechanics. However, due to its reliance on a mesh, the FEM is not well suited for the treatment of extremely large deformations. To overcome the mesh dependency of the FEM, meshfree methods have been developed, for example the Element-Free Galerkin Method (Belytschko et al, 1994) and the Material Point Method (MPM). The latter might be classified as a meshfree method, a Particle-in-Cell method or an Arbitrary Lagrangian-Eulerian method (Więckowski, 2004).

MPM uses two discretizations of the material, one based on a computational mesh and the other based on a collection of material points or "particles". Within the standard MPM large deformations are modeled by particles moving through a fixed mesh. The particles carry all the properties of the continuum (material properties and state of stress and strain) as well as external loads, whereas the mesh and its Gaussian integration points carry no permanent information at all. The computational grid is used to determine incremental displacements of particles by solving the governing equations. Through this approach, MPM combines the advantages of both Eulerian and Lagrangian formulations.

The early beginnings of MPM can be traced back to the work of Harlow (1964), who studied fluid flow by material points moving through a fixed grid. Sulsky et al. (1995) extended the method to the modeling of solids. It was then called the Material Point Method (Sulsky & Schreyer, 1996). Bardenhagen et al. (2000) further extended the method by including frictional contact between deformable bodies. The potential of MPM for simulating granular flow, e.g. in silo discharge, was first recognized by Więckowski et al. (1999). Coetzee et al. (2005) used the MPM for studying the large deformation problem of anchor

pull-out. All previous developments of MPM are based on dynamics, Beuth et al. (2010) were the first to develop a quasi-static MPM.

In Section 2 of this paper, the weak formulation and space integration of the momentum equation is presented. Section 3 describes integration in time. Here, explicit forward marching is used. A numerical example of a drop anchor is provided in Section 4. The formulation of a contact algorithm used to model the interaction between different bodies is explained in Section 5. In Section 6, mesh locking and strain smoothening are discussed. Absorbing boundaries and wave reflection are discussed in Section 7. A second numerical example is given in Section 8. In this example, dynamic cone penetration is investigated. Section 9 contains the example of a collapsing tunnel.

2 WEAK FORMULATION AND SPACE INTEGRATION OF EQUILIBRIUM

The Cauchy form of conservation of linear momentum is given by the equations

$$\rho\,\ddot{\mathbf{u}} = \nabla\cdot\boldsymbol{\sigma} + \rho\,\mathbf{g} \qquad \text{and} \qquad \mathbf{t} = \boldsymbol{\sigma}\cdot\mathbf{n} \tag{1}$$

where ρ is the material density, $\mathbf{u}$ is the displacement, a superposed dot denotes differentiation with time, $\boldsymbol{\sigma}$ denotes the Cauchy stress tensor and $\mathbf{g}$ is the gravitational acceleration vector. The surface traction acting on the external boundary is denoted by $\mathbf{t}$ and $\mathbf{n}$ is the outward unit normal of the boundary. Applying the virtual work principle on a domain of volume V surrounded by boundary S yields

$$\int_V \delta\mathbf{u}^T\,\rho\,\ddot{\mathbf{u}}\,dV = -\int_V \delta\boldsymbol{\varepsilon}^T\,\boldsymbol{\sigma}\,dV + \int_V \delta\mathbf{u}^T\,\rho\,\mathbf{g}\,dV + \int_S \delta\mathbf{u}^T\,\mathbf{t}\,dS \tag{2}$$

where δ implies a virtual quantity, $\boldsymbol{\varepsilon}$ is the strain tensor and the script T denotes the transpose.

For space discretisation, the displacement field $\mathbf{u}$ is approximated in terms of interpolation functions $\mathbf{N}$ and nodal displacements $\mathbf{a}$ by $\mathbf{u} = \mathbf{N}\mathbf{a}$. The strain tensor is now written in vector notation as

$$\boldsymbol{\varepsilon} = \mathbf{B}\,\mathbf{a} \qquad \text{with} \qquad \mathbf{B} = \mathbf{L}\mathbf{N} \qquad \text{and} \qquad \boldsymbol{\varepsilon} = \left(\varepsilon_{11},\ \varepsilon_{22},\ \varepsilon_{33},\ \gamma_{12},\ \gamma_{23},\ \gamma_{31}\right)^T \tag{3}$$

where $\mathbf{B}$ is the usual finite element strain-displacement matrix, as computed from the linear differential operator $\mathbf{L}$ and the shape functions $\mathbf{N}$. Substituting Eq. (3) into Eq. (2) gives

$$\delta\mathbf{a}^T\,\mathbf{M}\,\ddot{\mathbf{a}} = \delta\mathbf{a}^T\left(\mathbf{F}^{\text{ext}} - \mathbf{F}^{\text{int}}\right) \qquad \text{or} \qquad \mathbf{M}\,\ddot{\mathbf{a}} = \mathbf{F} \qquad \text{with} \qquad \mathbf{F} = \mathbf{F}^{\text{ext}} - \mathbf{F}^{\text{int}} \tag{4}$$

in which

$$\mathbf{M} = \int_V \rho\,\mathbf{N}^T\,\mathbf{N}\,dV\,, \qquad \mathbf{F}^{\text{ext}} = \int_V \rho\,\mathbf{N}^T\,\mathbf{g}\,dV + \int_S \mathbf{N}^T\,\mathbf{t}\,dS \qquad \text{and} \qquad \mathbf{F}^{\text{int}} = \int_V \mathbf{B}^T\,\boldsymbol{\sigma}\,dV \tag{5}$$

Equation (4) is identically used within FEM and MPM. However, in the Material Point Method $\mathbf{M}$ can also change in size when particles move into empty elements. In other words, the total number of degrees-of-freedom of the system can vary. A lumped-mass matrix, which offers computational and storage advantages, is used instead of the consistent-mass matrix defined in Eq. (5). On denoting the entries of the lumped-mass matrix, as m_i it yields

$$\mathbf{M}_L = \begin{bmatrix} m_1 & 0 & \dots & 0 \\ 0 & m_2 & \dots & 0 \\ \vdots & \vdots & & \vdots \\ 0 & 0 & \dots & m_n \end{bmatrix} \tag{6}$$

where n denotes the number of degrees of freedom. In order to conserve the mass of the continuum, particle-based integration is used i.e.

$$m_i \approx \sum_{p=1}^{n_p} m_p N_i^p \qquad \text{and} \qquad \mathbf{F}^{\text{int}} = \int_V \mathbf{B}^T \boldsymbol{\sigma}\, dV \approx \sum_{p=1}^{n_p} \mathbf{B}_p^T \boldsymbol{\sigma}_p V_p \tag{7}$$

where n_p denotes the number of particles, m_p is the mass of particle p, N_i^p is the shape function evaluated at particle p and V_p is the volume associated with particle p. The drawback of using a lumped-mass matrix is a slight numerical dissipation of the kinetic energy (Burgess et al, 1992).

3 TIME INTEGRATION

On applying Euler-forward time integration with lumped-mass matrix, Eq. (4) yields

$$\dot{\mathbf{a}}^{t+\Delta t} = \dot{\mathbf{a}}^t + \Delta t\, \ddot{\mathbf{a}}^t, \qquad \ddot{\mathbf{a}}^t = \left[\mathbf{M}_L^t\right]^{-1} \mathbf{F}^t \tag{8}$$

where Δt is the current time increment, $\dot{\mathbf{a}}^t$ and $\dot{\mathbf{a}}^{t+\Delta t}$ are the nodal velocities at time t, $t+\Delta t$ respectively. The incremental nodal displacement is obtained by integrating the nodal velocity by the Euler-backward rule and the position of the particles are subsequently updated, i.e.

$$\Delta \mathbf{a}^{t+\Delta t} = \Delta t\, \dot{\mathbf{a}}^{t+\Delta t}, \qquad \mathbf{x}_p^{t+\Delta t} = \mathbf{x}_p^t + \mathbf{N}_p\, \Delta \mathbf{a}^{t+\Delta t} \tag{9}$$

where $\mathbf{x}_p^t$ and $\mathbf{x}_p^{t+\Delta t}$ are the particle positions at time t and $t+\Delta t$ respectively. Strains and stresses at particles are updated using the same algorithms as for Gaussian integration points within the standard FEM. In updated Lagrangian FEM, one would use $\Delta \mathbf{a}$ to update the finite element mesh, but within the MPM only particles positions are updated. Particles eventually cross element boundaries, which entails that the new element of a crossing particle has to be detected.

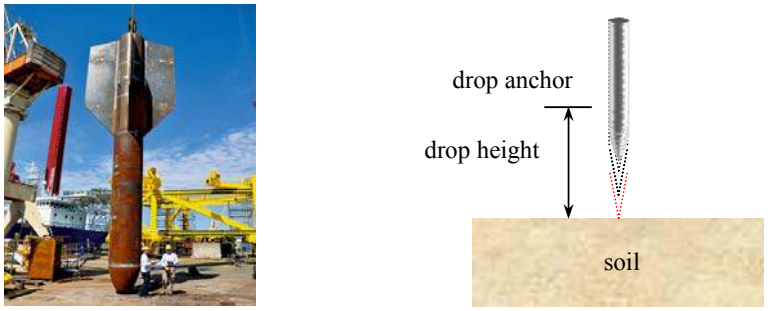

Fig. 1. A torpedo-shaped drop anchor

4 ANALYSIS OF DROP ANCHOR

The analysis of a drop anchor as shown in Figure 1 is presented in this section. These torpedo-shaped anchors are used in the offshore oil and gas industry as a cost effective anchoring solution in clays. The anchor is dropped from a particular height and penetrates the seafloor by the kinetic energy gained during its free fall (Figure 1). In the present paper, a fully dynamic penetration process is simulated. As the problem is axisymmetric, only a sector of 20^o is discretised. The drop anchor resembles a foundation pile, where soil deformations are intense around the tip. Accurate computations require a relatively dense mesh around the tip, as also shown in Figure 2a. Within the standard MPM, however, the anchor (particles) would move through the mesh and one would need mesh refinement over the complete penetration depth. In order to avoid this, we deviated from the standard MPM by using a mesh which is fixed to the anchor so that it moves into the soil. Thereby, the fine part of the mesh will always remain around the tip of the anchor. The occurrence of elements containing particles of different material is also prevented as the boundary of the anchor coincides throughout the analysis with element boundaries.

The material properties of the anchor are: Young's modulus of 50000 kPa, Poisson's ratio of 0 and unit weight of 78 kN/m³. The anchor is modeled as linear elastic. The soil is modeled by the Mohr-Coulomb model with a Young's modulus of 5000 kPa, Poisson's ratio of 0.3, cohesion of 5 kPa, friction angle of 30^o and unit weight of 18 kN/m³. Simulations were done with different friction coefficients μ of the contact surface between the anchor and the soil. Hence, we do not consider penetration in undrained clay, but in a drained sand. This is simply done because frictional sand is computationally more challenging than (undrained) cohesive clay.

Figure 3 shows the computed penetration depth for different μ-values plotted over time. For fully rough contact (μ=1), the final penetration depth is found to be 5D, where D is the diameter of the anchor. In the very beginning the anchor resistance is linear with penetration depth, but later the penetration is slowing down because the anchor looses its kinetic energy. As the anchor is penetrating deeper into the soil, the resistance is getting higher because the contact between anchor and soil is increasing and because the shear resistance of the soil increased with depth. The ultimate penetration depth obviously increases with smaller friction coefficients. The largest penetration depth obviously corresponds to the case of smooth contact. Figure 2b shows the particle distribution after a penetration of 6.5D for the case of smooth contact. It also shows soil heave around the anchor.

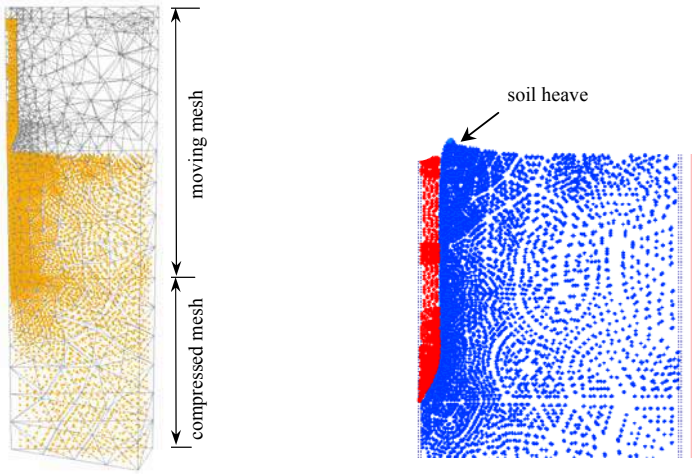

Fig. 2. Initial and final configuration of the problem

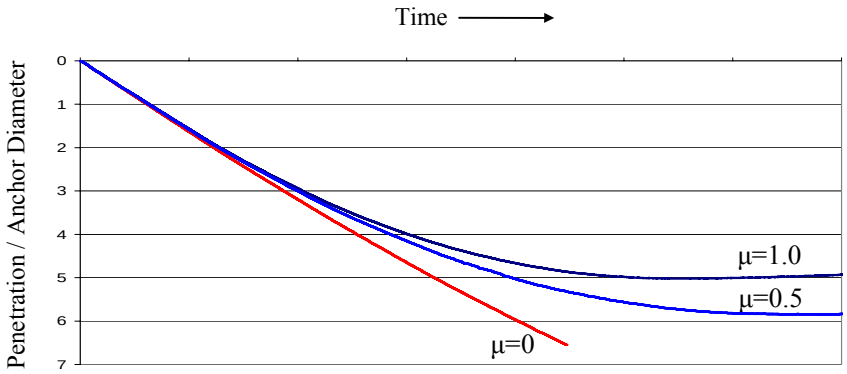

Fig. 3. Penetration depth for different values of the friction coefficient

5 CONTACT ALGORITHM

Following Bardenhagen et al. (2000), Eq. (8) is solved for the combined bodies *A* and *B* (see Figure 4) as well as for each body separately, i.e.

$$\mathbf{M}_L^A \ddot{\mathbf{a}}^A = \mathbf{F}^A, \quad \mathbf{M}_L^B \ddot{\mathbf{a}}^B = \mathbf{F}^B, \quad \mathbf{M}_L^{A+B} \ddot{\mathbf{a}}^{A+B} = \mathbf{F}^{A+B} \tag{10}$$

From these solutions, predictor velocities $\dot{\mathbf{a}}^A$, $\dot{\mathbf{a}}^B$ and $\dot{\mathbf{a}}^{A+B}$ are computed. Contact at a considered node is detected by comparing the velocity of a single body to the velocity of the combined bodies, as illustrated in the chart of Figure 5, with **n** being the outward unit normal at a considered node. When these velocities differ, the considered node is a contact node. Now we detect whether or not the contact at that node is broken (by separation) or continued (by approaching). For an approaching contact node, we check for sliding as explained in the next section.

5.1 Check for Sliding and Subsequent Correction for a Contact Node

In the following, only body *A* is considered. The relative normal and tangential velocities at a contact node are

$$\dot{\mathbf{a}}_n = \left[\left(\dot{\mathbf{a}}^A - \dot{\mathbf{a}}^{A+B}\right)\cdot\mathbf{n}\right]\mathbf{n} \quad \text{and} \quad \dot{\mathbf{a}}_t = \left(\dot{\mathbf{a}}^A - \dot{\mathbf{a}}^{A+B}\right) - \dot{\mathbf{a}}_n \tag{11}$$

The normal and tangential components of the interaction force at a contact node can then be computed from

$$\mathbf{F}_n^A = \frac{m^A}{\Delta t}\dot{\mathbf{a}}_n \quad \text{and} \quad \mathbf{F}_t^A = \frac{m^A}{\Delta t}\dot{\mathbf{a}}_t \tag{12}$$

where m^A is the mass of a contact node computed only from body *A* as in Eq. (7). In frictional contact, the tangential force is limited by

$$\left|\mathbf{F}_t^{A,max}\right| = \mu\left|\mathbf{F}_n^A\right| = \mu\frac{m^A}{\Delta t}\left[\left(\dot{\mathbf{a}}^A - \dot{\mathbf{a}}^{A+B}\right)\cdot\mathbf{n}\right] \tag{13}$$

where μ is the coefficient of friction. Sliding between the two bodies will only occur when $\left|\mathbf{F}_t^A\right| > \left|\mathbf{F}_t^{A,\max}\right|$. Thus, only then a correction of the nodal velocity is required. It can be derived that the corrected velocity of a sliding contact node is

$$\dot{\mathbf{a}}_{new}^{A} = \dot{\mathbf{a}}^{A} - \left[\left(\dot{\mathbf{a}}^{A} - \dot{\mathbf{a}}^{A+B}\right)\cdot\mathbf{n}\right](\mathbf{n} + \mu\mathbf{t}) \tag{14}$$

where **t** is the direction vector of the tangential velocity.

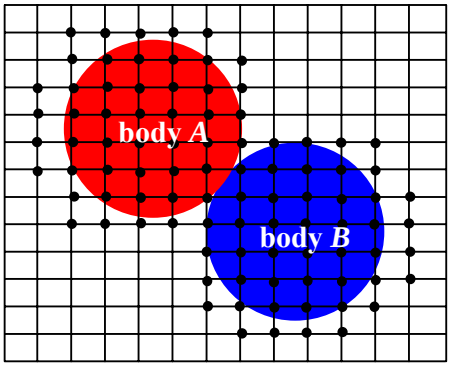

Fig. 4. Illustration of two bodies in contact for a regular mesh

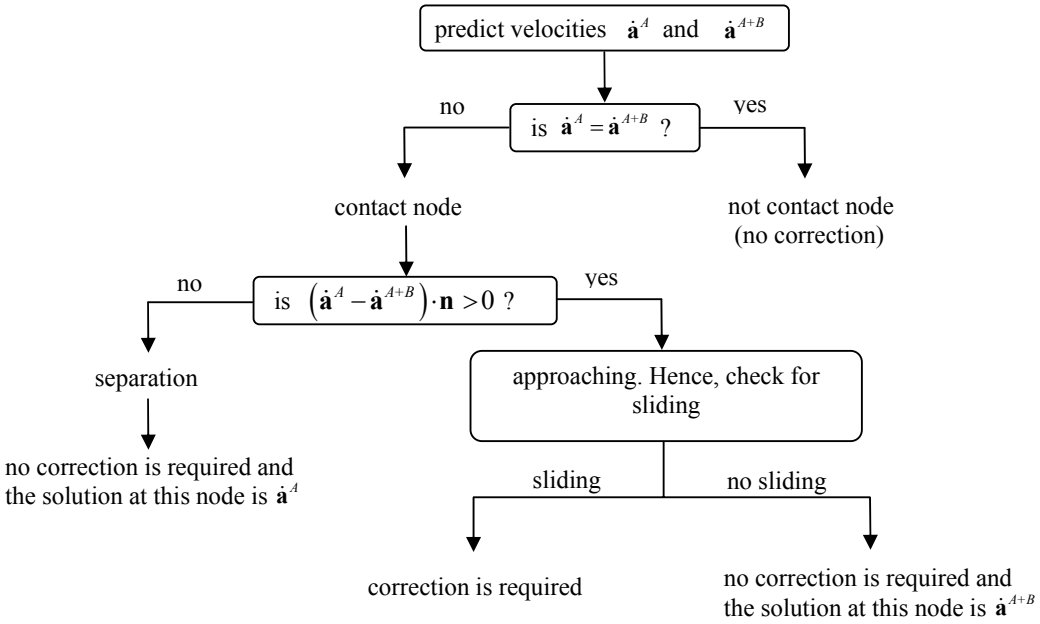

Fig. 5. Flow chart of the contact algorithm applied on body *A*

6 MESH LOCKING AND STRAIN SMOOTHENING

Difficulties arise when determining the displacement field for a solid that is nearly incompressible. For such a material, the bulk modulus is very large and small errors in strain will yield large errors in stress. Furthermore, when dealing with low-order elements the mesh may lock when incompressibility constraints from neighboring elements are imposed. For high-order elements, it is common to prevent locking by reduced integration (Bathe, 1982), but for low-order elements a kind of strain smoothening can be applied, being referred to as nodal-mixed-discretisation by Detournay and Dzik (2006). This technique involves first of all the computation of the strain rates for each element in the usual manner subsequently they are decomposed into a volumetric strain rate, $\dot{\varepsilon}_v$, and a deviatoric strain rate, $\dot{\boldsymbol{\varepsilon}}_d$. An averaged volumetric strain-rate $\bar{\dot{\varepsilon}}_v$ for an element is now defined as

$$\bar{\dot{\varepsilon}}_v = \frac{1}{4}\sum_{i=1}^{4} \bar{\dot{\varepsilon}}_{vi} \quad \text{with} \quad \bar{\dot{\varepsilon}}_{vn} = \frac{\sum_k (\dot{\varepsilon}_v \Omega)_k}{\sum_k (\Omega)_k} \tag{15}$$

where the sum is over all elements k attached to the node n. Ω is the volume of an element. The working assumption is that deviatoric strain rates need not be enhanced, only the volumetric components. As a result, the final strain rate within an element is redefined as

$$\dot{\boldsymbol{\varepsilon}} = \dot{\boldsymbol{\varepsilon}}_d + \frac{1}{3}\bar{\dot{\varepsilon}}_v \mathbf{I} \quad \text{with} \quad \mathbf{I} = (1, 1, 1, 0, 0, 0)^T \tag{16}$$

This approach is applied in all examples of the present paper.

7 ABSORBING BOUNDARIES

In numerical simulations of wave propagation, the use of finite boundaries leads to reflection of the waves upon reaching the boundary. In Geomechanics rigid boundaries are mostly numerical antifacts and reflecting waves are not physical and they will affect the solution considerably. This problem might be overcome by choosing the finite boundary of the mesh far enough so that no reflection occurs. But this is not always practical solution as it makes the mesh unnecessarily large. On top of that, the computational effort increases considerably. A partial solution to this problem was introduced by Lysmer and Kuhlemeyer (1969). They proposed a solution in which the boundary is supported on a dashpot. On denoting the normal stress at a boundary node as t_n and the shear stress as t_s, it yields

$$t_n = \alpha_n \rho V_p \dot{a}_n \quad \text{and} \quad t_s = \alpha_s \rho V_s \dot{a}_s \tag{17}$$

where $\dot{a}_n$ and $\dot{a}_s$ are the normal and tangential velocities at a boundary node respectively, ρ is the mass density of the material, α_n and α_s are dimensionless parameters, V_p and V_s are the p-wave speed and the s-wave speed of the material respectively. It yields

$$V_p = \sqrt{E_c/\rho} \quad \text{and} \quad V_s = \sqrt{G/\rho} \tag{18}$$

where E_c is the constrained modulus and G is the shear modulus. They relate to Young's modulus and Poisson's ratio by the equations

$$E_c = \frac{(1-\upsilon)E}{(1-2\upsilon)(1+\upsilon)} \quad \text{and} \quad G = \frac{E}{2(1+\upsilon)} \tag{19}$$

The drawback of supporting the boundary by dashpots is that the boundary will continuously creep as long as the dashpot will receive stresses from the soil body. In order to limit the creep of the boundary, a spring is added parallel to the dashpot to obtain a Kelvin-Voigt type of boundary response. Hence Eq. (17) is rewritten as

$$t_n = \alpha_n \rho V_p \dot{a}_n + \frac{E_c}{\delta_n} a_n \quad \text{and} \quad t_s = \alpha_s \rho V_s \dot{a}_s + \frac{G}{\delta_s} a_s \tag{20}$$

where δ is a virtual thickness being used to limit the creep of the boundary.

As a numerical example a soil layer with a thickness of 1m is considered here. The layer has a Young's modulus of 100 kPa, a Poisson's ratio of 0 and unit weight of 18 kN/m³. A uniformly distributed load of 1 kPa is applied instantaneously at the surface. Three different boundary conditions were considered at the bottom: fully fixed, dashpot and dashpot with spring in parallel. With the fully fixed boundary, the entire energy is reflected when the wave reached the bottom. Hence, the stress is doubled after reflection and oscillates later contineously. When replacing the fixities by dashpots, only a small portion of the energy is reflected, but (as explained previously), the drawback of using only dashpots is a continuous creep of the boundary.

On the other hand, the dashpot with spring in parallel will limit the creep of the boundary as shown in Figure 6. This displacement corresponds to δ_n=0.5 m and α_n=2.5. Sensitivity study showed that those are the best values for the problem considered. The final displacement of the bottom of the mesh can be calculated as $a_n=(\sigma / E_c)\ \delta_n$. For σ=1kPa and E_c=100kPa, this displacement is found to be 0.05 m. Points 1,2 and 3 of Figure 6 indicate that the wave is just reflected after reaching the bottom of the mesh. Stress fronts correspond to point 1, 2 and 3 are (1.28, 1.86 and 1.14) kPa respectively.

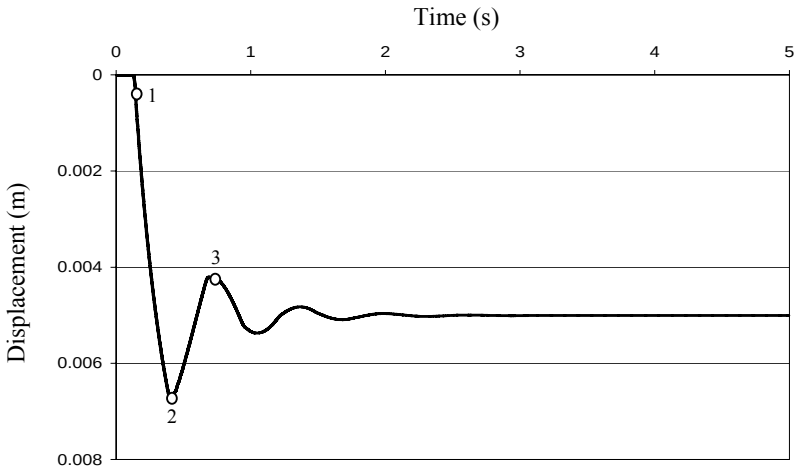

Fig. 6. Displacement of the bottom of the mesh for dashpot and spring in parallel

8 DYNAMIC PENETRATION TEST

The analysis of a cone (with a diameter of 3.57 cm) being hammered into the soil is considered in this section. Block is successively dropped from a certain height as shown in Figure 7. The maximum impulsive load, F_{max}, corresponding to the drop weight, can be calculated from the conservation of momentum i.e.

$$\int_0^{t_{pulse}} F_{\max} \sin\left(\frac{\pi t}{t_{pulse}}\right) dt = \eta m\sqrt{2gh} \tag{21}$$

where η is the hammer efficiency (fraction of energy transferred to the cone). It was chosen as 64% (Borja, 1988). The initial configuration of the problem is shown in Figure 8a. The same moving mesh technique used to simulate the drop anchor problem of Section 4 is used here. The material properties of the elastic cone are: Young's modulus of 50000 kPa, Poisson's ratio of 0 and unit weight of 78 kN/m³. Adopting the elastic-plastic Mohr-Coulomb model, the soil properties are: Young's modulus of 5000 kPa, Poisson's ratio of 0.3, cohesion of 5 kPa, friction angle of 30° and unit weight of 18 kN/m³. The dropped weight has a mass m =10 kg, the drop height h = 50 cm, t_{pulse} = 0.02 sec and t_{period} = 0.1 sec. The case of fully rough contact, μ=1, between the cone and the soil is considered. Figure 9 shows the penetration verses the number of blows. Figure 8b shows the principal stresses at the end of the penetration.

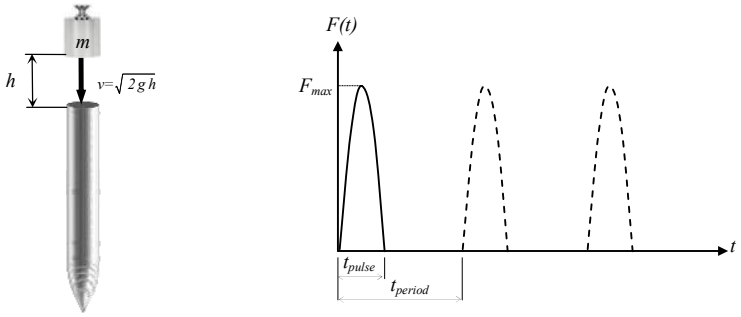

Fig. 7. Applied load of dynamic penetration test

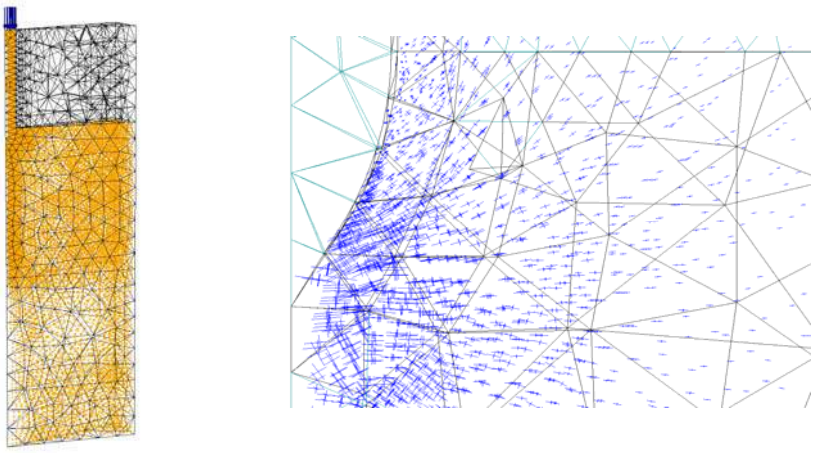

(a) Initial configuration (b) Principal stresses around the cone tip after installation

Fig. 8. Initial configuration and final state of stress

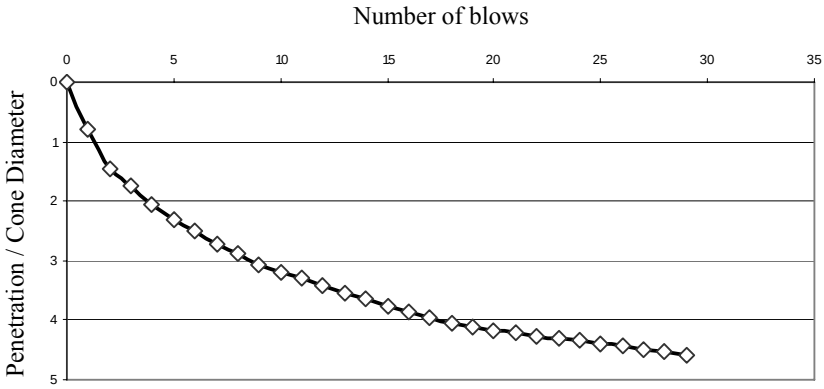

Fig. 9. Penetration as a function of number of blows

9 DYNAMIC COLLAPSE OF TUNNEL FACE

Tunnel collapse can pose a danger to life and property. Both the life of the workers standing in front of the tunnel face and individuals at the ground surface might be in danger. An example of tunnel collapse in Munich is shown in Figure 10. The aim of this analysis is to estimate the real collapse time of a tunnel and the crashing of the ground. The pattern of the tunnel face collapse is also investigated. The dimensions of the tunnel mesh are shown in Figure 11. The boundary conditions are: the upper surface is free to move, the side surfaces are roller supported, and the base is fixed.

In the first stage of the analysis, initial stresses are generated based for a K_o-value of 0.5, where K_o is the co-efficient of lateral earth pressure at rest. Adopting the elastic-plastic Mohr-Coulomb model, the soil properties are: Young's modulus of 10000 kPa, Poisson's ratio of 0.3, cohesion of 1 kPa, friction angle of 25^o and unit weight of 16 kN/m^3. A relatively fine mesh is used to discretise the material around the opening of the tunnel where the material is expected to flow. The face support pressure is removed in single step and the calculation is carried out by applying time steps of Δt=0.001 second. For time increment, the particles move due to the unbalanced forces in the system until the kinetic energy is dissipated and static equilibrium is reached. The total displacements for the final static equilibrium are shown in Figure 12a. The collapse time for the tunnel face is found to be 7 seconds. The settlement of the ground surface is shown in Figure 12b.

Fig. 10. Collapse of tunnel face Munich underground in September 1994

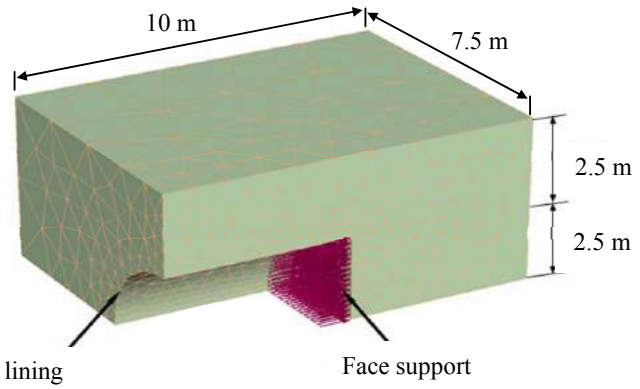

Fig. 11. Description of tunnel geometry

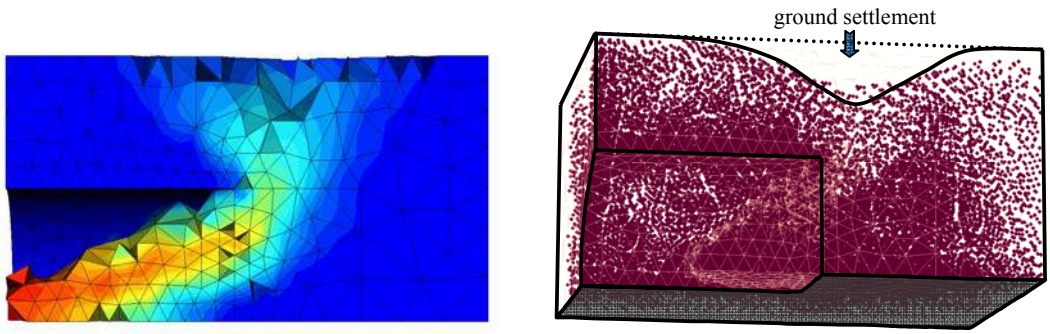

(a) Displacements after static equilibrium (b) Settlement of the ground

Fig. 12. Pattern of the tunnel face collapse

10 CONCLUSIONS

Existing dynamic MPM codes are based on a regular grid. For complex structures, being represented by a cloud of material particles, this would require a special CAD type preprocessor. On the other hand existing user-friendly preprocessors can be used in combination with non-regular and non-structured meshes. This is the main reason for the use of the non-structured meshes. Another advantage of the present non-structured mesh approach is that it allows for mesh-refinements. In this paper this has been applied for reason of achieving good accuracy in zones of intense soil deformations. For a consequent application of mesh refinement, the concept of moving mesh has been introduced.

In dynamic soil analyses one usually introduces absorbing boundaries to prevent the reflection of stress and strain waves at the more or less arbitrary bottom of the mesh. Hence, one usually employs so-called dashpots that will continually creep under load. In order to limit such non-physical displacements, the dashpot is combined with a spring to obtain a Kelvin-Voigt type of boundary response. At present the main limitations of the code is the lack of pore pressures and a soil model for cyclic loading. Meanwhile, dynamic generation and dissipation of pore pressures is nearly finished and remains to be reported. The implementation of a cyclic loading model for genuine simulations of pile driving has been planned.

ACKNOWLEDGEMENT

This research was carried out as a part of the ''GEO-INSTALL'' project (Modelling Installation Effects in Geotechnical Engineering). It has received funding from the European Community through the program (Marie Curie Industry-Academia Partnerships and Pathways) under grant agreement n^{o} PIAP-GA-2009-230638. In the framework of this project, the first and second authors are currently having a secondment at Deltares, Delft, the Netherlands. The PhD study of the first author at Stuttgart University is funded by the DAAD (German Academic Exchange Service).

REFERENCES

Bardenhagen, S.G. Brackbill, J.U. & Sulsky, D. (2000), "The material-point method for granular materials''. Computer Methods in Applied Mechanics and Engineering, Vol.(187), 529–541.

Bathe, K.J. (1982), Finite Elements Procedures in Engineering Analysis, Prentice-Hall, Inc., New Jersey.

Belytschko, T. Lu, Y. Y. & Gu, L. (1994), "Element-free Galerkin methods''. International Journal of Numerical Methods in Engineering, Vol. (37), 229-256.

Beuth, L., Więckowski, Z. & Vermeer, P. (2010), "Solution of quasi-static large-strain problems with the material point method''. International Journal of Numerical and Analytical Methods in Geomechanics, Wiley Online Library (wileyonlinelibrary.com). DOI: 10.1002/nag.965

Borja, R.I. (1988), "Dynamics of pile driving by the finite element method''. Computers and Geotechnics, Vol. (5), 39-49.

Burgess, D. Sulsky, D. & Brackbill, J.U. (1992), "Mass matrix formulation of the FLIP particle-in-cell method''. Journal of Computational Physics, Vol. (103), 1-15.

Coetzee, C.J. Vermeer, P.A. & Basson, A.H. (2005), "The modelling of anchors using the material point method''. International Journal for Numerical and Analytical Methods in Geomechanics, Vol. (29), 879-895.

Detournay, C. & Dzik E. (2006), "Nodal mixed discretization for tetrahedral elements'', Proceedinh of '4 international FLAC symposium on numerical modeling in geomechanics, Itasca Consulting Group.

Harlow, F.H. (1964), "The particle-in-cell computing method for fluid dynamics''. Methods for Computational Physics, Vol. (3), 319-343.

Lysmer, J. & Kuhlmeyer, R.L. (1969), "Finite dynamic model for infinite media''. Journal of the Engineering Mechanics Division, Vol. (95), 859-877.

Sulsky, D. Zhou, S.J. & Schreyer, H.L. (1995), "Application of a particle-in-cell method to solid mechanics''. Computer Physics Communications, Vol. (87), 236-252.

Sulsky, D. & Schreyer, H.L. (1996), "Axisymmetric form of the material point method with applications to upsetting and Taylor impact problems''. Computer Methods in Applied Mechanics and Engineering, Vol. (139), 409-429.

Więckowski, Z. Youn, S.K. & Yeon, J.H. (1999), "A particle-in-cell solution to the silo discharging problem''. International Journal for Numerical Methods in Engineering, Vol. (45), 1203-1225.

Więckowski, Z. (2004), "The material point method in large strain engineering problems''. Computer Methods in Applied Mechanics and Engineering, Vol. (193), 4417-4438.

BEARING CAPACITY OF SHALLOW FOUNDATION BY SMOOTHED PARTICLE HYDRODYNAMICS (SPH) ANALYSIS

H.H. Bui
Department of Civil Engineering, Ritsumeikan University, Japan

H.D.V. Khoa
Norwegian Geotechnical Institute (NGI), Norway

ABSTRACT: *The paper illustrates the potential of Smoothed Particle Hydrodynamics (SPH) computing technique for accurate and efficient analysis of bearing capacity and failure mechanism of shallow foundations. SPH is a meshfree particle method based on Lagrangian formulation. Since the SPH method does not possess any mesh-related difficulties, it is more suitable to deal with large geometric changes of the domain of interest than the traditional mesh-based discretisation techniques such as finite elements, finite differences or finite volumes. Although the advantages of using SPH in the field of fluid and solid mechanics have been well described by many authors, its application in geotechnical engineering is still very limited. As an application of the SPH method to geotechnical problems, deep penetration of a shallow foundation into soil is simulated under plane strain conditions. The soil behavior is modelled by the non-associated Drucker-Prager model implemented into the SPH code. The computed results in terms of bearing capacity and failure mechanism are compared with the PLAXIS finite element results and the Terzaghi limit equilibrium method. The good agreement in the results emphasizes the potential application of the SPH method to a wide range of geotechnical problems.*

1 INTRODUCTION

Smooth Particle Hydrodynamics (SPH), a meshfree particle method based on Lagrangian formulation, was introduced in 1977 (Lucy, 1977; Gingold and Monaghan, 1977). It has been successfully applied to astrophysical problems and later widely extended to solve the problems of continuum solid mechanics and fluid mechanics. The SPH method discretizes the continuum body only with a set of nodal points (particles), and so it does not possess any mesh-related difficulties. In this method, the partial differential equations for the continuum are converted into equations of motion of these particles and then solved by updated Lagrangian numerical scheme. Compared with other traditional mesh-based discretisation techniques such as finite element, finite differences or finite volumes, SPH has several advantages as follows:

- it can handle large deformation and post-failure very well thanks to its Lagrangian particle-based format and adaptive nature;
- complex free surfaces are modeled naturally without any special treatments;
- complex geometries can be handled without any difficulties and it is relatively easy to incorporate complicated physics.

Recently, Bui and his co-workers have been intensively focused on the development an SPH model for modelling large deformation problems and failure flows in geomaterials (Bui

et al., 2007; 2008; 2010). Many important geotechnical problems including granular flows, bearing capacity, slope stability, soil-water coupling, soil-structure interaction, seepage flows…etc, have been successfully analyzed using the SPH method. As an example of the application of the SPH method to geotechnical problems, this paper discusses the bearing capacity and failure mechanism analysis of deep penetration of a shallow foundation into soil. The elasto-plastic soil behavior is modelled by the Drucker-Prager model implemented into the SPH code. The computed results in terms of bearing capacity and failure mode are compared with the PLAXIS finite element (FE) solutions to validate and highlight the SPH based approach.

The rest of the paper is organized as follows. Section 2 briefly describes the smoothed particle hydrodynamics method. In Section 3, the SPH discretisation of motion equation is recalled and the technique used for improving the numerical stability is also discussed here. Section 4 focuses on description of the elastic-plastic Drucker-Prager constitutive model. The equations used for matching the Drucker-Prager model and the Mohr-Coulomb model are also presented in this section. Section 5 assesses the ability of numerical analysis using the SPH method to predict the bearing capacity and failure mechanism of a shallow foundation.

2 SMOOTHED PARTICLE HYDRODYNAMICS

In SPH, approximations for quantities of a continuum field such as density, velocity, pressure, etc., are approximated using the following integral function,

$$A(\mathbf{r}) = \int A(\mathbf{r}')\delta(|\mathbf{r}-\mathbf{r}'|)\,d\mathbf{r}' \tag{1}$$

where A is any variables defined on the spatial coordinate $\mathbf{r}$, δ refers to the Direct delta function. This integral is then approximated by replacing the delta function with a smoothing kernel W with characteristic h, such that

$$\lim_{h\to 0} W(\mathbf{r}-\mathbf{r}', h) = \delta(\mathbf{r}-\mathbf{r}') \tag{2}$$

giving

$$A(\mathbf{r}) = \int A(\mathbf{r}')W(|\mathbf{r}-\mathbf{r}'|, h)\,d\mathbf{r}' + O(h^2) \tag{3}$$

The kernel function is normalized according to,

$$\int_{\Omega} W(\mathbf{r}-\mathbf{r}', h)\,d\mathbf{r}' = 1 \tag{4}$$

The choice of kernel function directly affects the accuracy, efficiency and the stability of numerical algorithm. A number of kernel functions have been proposed in the SPH literature so far, we apply herein the most commonly used kernel function, namely cubic-spline function proposed by Monaghan & Lattanzio (1985), which has the following form,

$$W(q) = \alpha_d \times \begin{cases} 1-\frac{3}{2}q^2+\frac{3}{4}q^3 & 0 \le q < 1 \\ \frac{1}{4}(2-q)^3 & 1 \le q < 2 \\ 0 & q \ge 2 \end{cases} \tag{5}$$

where α_d is the normalization factor which is $10/7\pi h^2$ in two-dimensional problems and q is the normalized distance $q=|\mathbf{r}|/h$.

Finally, the integral (3) is discretised onto a finite set of interpolation points (the particles) by replacing the integral with a summation and the mass element ρV with a particle mass m, i.e.

$$\begin{aligned} A(\mathbf{r}) &= \int \frac{A(\mathbf{r}')}{\rho(\mathbf{r}')} W(|\mathbf{r}-\mathbf{r}'|, h)\, \rho(\mathbf{r}') d\mathbf{r}' + O(h^2) \\ &\approx \sum_{b=1}^{N} m_b \frac{A_b}{\rho_b} W(|\mathbf{r}-\mathbf{r}_b|, h) \end{aligned} \tag{6}$$

where subscript b refers to the quantity evaluated at the position of particle b. This "summation approximation" is the basis of all SPH formalisms.

The SPH approximation for the gradient terms may be calculated by taking analytical derivative of Eq. (6), giving:

$$\begin{aligned} \nabla A(\mathbf{r}) &= \frac{\partial}{\partial \mathbf{r}} \int \frac{A(\mathbf{r}')}{\rho(\mathbf{r}')} W(|\mathbf{r}\text{-}\mathbf{r}'|, h) \rho(\mathbf{r}') d\mathbf{r}' + O(h^2) \\ &\approx \sum_{b=1}^{N} m_b \frac{A_b}{\rho_b} \nabla_a W_{ab} \end{aligned} \tag{7}$$

where we have assumed that the gradient is evaluated at another particle a ($\mathbf{r} = \mathbf{r}_a$) and the remaining terms are defined by,

$$W_{ab} \equiv W(|\mathbf{r}_a - \mathbf{r}_b|, h) \quad \text{and} \quad \nabla_a W_{ab} \equiv \frac{\mathbf{r}_{ab}}{|\mathbf{r}_{ab}|} \frac{\partial W_{ab}}{\partial \mathbf{r}_a} \tag{8}$$

However, this form of gradient is not guaranteed to vanish when $A(\mathbf{r})$ is not constant. To ensure that it does, the gradient can be written as,

$$\nabla A_a \approx \sum_{b=1}^{N} m_b \frac{(A_b - A_a)}{\rho_b} \nabla_a W_{ab} \tag{9}$$

which is an estimate of

$$\nabla A(\mathbf{r}) = \nabla A - A(\nabla 1) \tag{10}$$

Alternatively, the following forms of gradient approximation which are the most commonly used to discrete the momentum equation can be written as (Monaghan, 1992; Bonet et al., 1999),

$$\nabla A_a \approx \rho_a \sum_{b=1}^{N} m_b \left(\frac{A_a}{\rho_a^2} + \frac{A_b}{\rho_b^2} \right) \nabla_a W_{ab} \tag{11}$$

$$\nabla A_a \approx \rho_a \sum_{b=1}^{N} m_b \frac{(A_b + A_a)}{\rho_a \rho_b} \nabla_a W_{ab} \tag{12}$$

These two last gradient approximations conserve linear and angular momentum (Monaghan, 1992). Further details of SPH integration scheme as well as other issues of SPH can be found in Liu & Liu (2003).

3 SPH DISCETIZATION OF MOTION EQUATION

The motion of a continuum can be described through the following equation,

$$\rho \ddot{u}^{\alpha} = \nabla_{\beta} \sigma^{\alpha\beta} + \rho g^{\alpha} \tag{13}$$

where u is the displacement; α and β denote Cartesian components x, y, z with the Einstein convention applied to repeated indices; ρ is the density; σ is the total stress tensor, taken negative for compression; and g is the acceleration due to gravity. For a soil, the total stress is normally composed of the effective stress tensor (σ') and the pore-water pressure (p_w),

$$\sigma^{\alpha\beta} = \sigma'^{\alpha\beta} + p_w \delta^{\alpha\beta} \tag{14}$$

In the current study, the pore-water pressure is not considered, thus the displacement u of soil particles relates to the effective stress in the following way,

$$\rho \ddot{u}^{\alpha} = \nabla_{\beta} \sigma'^{\alpha\beta} + \rho g^{\alpha} \tag{15}$$

Using Eq. (11), the partial differential form of Eq. (15) can be approximated in the SPH formulation in the following ways,

$$\ddot{u}_a^{\alpha} = \sum_{b=1}^{N} m_b \left(\frac{\sigma_a'^{\alpha\beta}}{\rho_a^2} + \frac{\sigma_b'^{\alpha\beta}}{\rho_b^2} + C_{ab}^{\alpha\beta} \right) \nabla_a^{\beta} W_{ab} + g_a^{\alpha} \tag{16}$$

where a indicates the particle under consideration; ρ_a and ρ_b are the densities of particle a and b respectively; N is the number of "neighbouring particles", *i.e.* those in the support domain of particle a; m_b is the mass of particle b; $C_{ab}^{\alpha\beta}$ is a stabilization term employed to remove the stress fluctuation and tensile instability (Bui et al., 2008). The stabilization term in Eq. (16) consists of two components: artificial viscosity and artificial stress, which could be computed similarly to Bui et al. (2008) except that the sound speed for the artificial viscosity term is calculated herein by,

$$c_a = \sqrt{E_a / \rho_a} \tag{17}$$

where E is Young's modulus of the soil. Eq. (16) can be integrated using the standard Leapfrog algorithm if the effective stress tensor is known. Thus, it is necessary to derive a constitutive relation for the effective stress tensor that is applicable in the SPH framework.

4 SOIL CONSTITUTIVE MODEL

A constitutive model describes the relation between stress and strain of a given material. Following the classical theory of plasticity, the total strain-rate tensor of an elasto-plastic material $\dot{\varepsilon}$ is decomposed into two parts: an elastic strain rate tensor $\dot{\varepsilon}_e$ and a plastic strain rate tensor $\dot{\varepsilon}_p$:

$$\dot{\varepsilon}^{\alpha\beta} = \dot{\varepsilon}_e^{\alpha\beta} + \dot{\varepsilon}_p^{\alpha\beta} \tag{18}$$

The elastic strain rate tensor $\dot{\varepsilon}_e^{\alpha\beta}$ is given by a generalized Hooke's law, i.e.,

$$\dot{\varepsilon}_e^{\alpha\beta} = \frac{\dot{s}'^{\alpha\beta}}{2G} + \frac{1-2\upsilon}{E}\dot{\sigma}'^{m}\delta^{\alpha\beta} \tag{19}$$

where $s'^{\alpha\beta}$ is the deviatoric effective shear stress tensor; G is the shear modulus; and σ'^{m} is the mean effective stress.

The plastic strain rate tensor $\dot{\varepsilon}_p^{\alpha\beta}$ is calculated by the plastic flow rule,

$$\dot{\varepsilon}_p^{\alpha\beta} = \dot{\lambda}\frac{\partial g_p}{\partial \sigma'^{\alpha\beta}} \tag{20}$$

where $\dot{\lambda}$ is the rate of change of plastic multiplier, and g_p is the plastic potential function. In the current study, the Drucker-Prager model with associated and non-associated plastic flow rules is applied, under the assumptions that the yield surface is fixed in stress space, and plastic deformation occurs only if the stress state reaches the yield surface. Accordingly, plastic deformation will occur only if the following yield criterion is satisfied,

$$f(I_1, J_2) = \alpha_\varphi I_1 + \sqrt{J_2} - k_c = 0 \tag{21}$$

where I_1 and J_2 are the first and second invariants of the stress tensor; and α_ϕ and k_c are Drucker-Prager constants that are calculated from the Coulomb material constants c (cohesion) and ϕ (internal friction). In plane strain, the Drucker-Prager constants are computed by,

$$\alpha_\varphi = \frac{\tan\varphi}{\sqrt{9+12\tan^2\varphi}} \quad \text{and} \quad k_c = \frac{3c}{\sqrt{9+12\tan^2\varphi}} \tag{22}$$

The associate plastic flow rule takes the same form of the yield function as the plastic potential function, while the non-associated plastic flow rule specifies the plastic potential function by,

$$g_p = \alpha_\psi I_1 + \sqrt{J_2} - \text{constant} \tag{23}$$

where α_ψ is a dilatancy factor which can be related to the dilatancy angle ψ in a fashion similar to that between α_ϕ and friction angle ϕ. Substituting Eq. (23) into Eq. (20), and then Eqs. (19-20) into Eq. (18), and additionally adopting the Jaumman stress rate for large deformation treatment, the stress-strain relation for the current soil model at particle i becomes (Bui et al., 2008),

$$\frac{d\sigma_i'^{\alpha\beta}}{dt} = \sigma_i'^{\alpha\gamma}\dot{\omega}_i^{\beta\gamma} + \sigma_i'^{\gamma\beta}\dot{\omega}_i^{\alpha\gamma} + 2G_i\dot{e}_i^{\alpha\beta} + K_i\dot{\varepsilon}_i^{\gamma\gamma}\delta_i^{\alpha\beta} - \dot{\lambda}_i\left[3K_i\alpha_{\psi i}\,\delta^{\alpha\beta} + (G/\sqrt{J_2})_i\, s_i'^{\alpha\beta}\right] \tag{24}$$

where $\dot{e}_i^{\alpha\beta} = \dot{\varepsilon}_i^{\alpha\beta} - \frac{1}{3}\dot{\varepsilon}_i^{\gamma\gamma}\delta^{\alpha\beta}$ is the deviatoric strain rate tensor; $\dot{\lambda}_i$ is the rate of change of plastic multiplier, which in SPH is specified by,

$$\dot{\lambda}_i = \frac{3\alpha_\varphi K\dot{\varepsilon}_i^{\gamma\gamma} + (G/\sqrt{J_2})_i s_i'^{\alpha\beta}\dot{\varepsilon}_i^{\alpha\beta}}{9\alpha_\varphi K_i\alpha_{\psi i} + G_i} \tag{25}$$

and $\dot{\varepsilon}_i^{\alpha\beta}$, $\dot{\omega}_i^{\alpha\beta}$ are the strain rate and spin rate tensors defined by

$$\dot{\varepsilon}_i^{\alpha\beta} = \frac{1}{2}\left(\frac{\partial \dot{u}^\alpha}{\partial x^\beta} + \frac{\partial \dot{u}^\beta}{\partial x^\alpha}\right)_i = \frac{1}{2}\left[\sum_{j=1}^{N}\frac{m_j}{\rho_j}(\dot{u}_j^\alpha - \dot{u}_i^\alpha)\frac{\partial W_{ij}}{\partial x_i^\beta} + \sum_{j=1}^{N}\frac{m_j}{\rho_j}(\dot{u}_j^\beta - \dot{u}_i^\beta)\frac{\partial W_{ij}}{\partial x_i^\alpha}\right] \tag{26}$$

$$\dot{\omega}_i^{\alpha\beta} = \frac{1}{2}\left(\frac{\partial \dot{u}^\alpha}{\partial x^\beta} - \frac{\partial \dot{u}^\beta}{\partial x^\alpha}\right)_i = \frac{1}{2}\left[\sum_{j=1}^{N}\frac{m_j}{\rho_j}(\dot{u}_j^\alpha - \dot{u}_i^\alpha)\frac{\partial W_{ij}}{\partial x_i^\beta} - \sum_{j=1}^{N}\frac{m_j}{\rho_j}(\dot{u}_j^\beta - \dot{u}_i^\beta)\frac{\partial W_{ij}}{\partial x_i^\alpha}\right] \tag{27}$$

The above soil constitutive model requires six soil parameters, which are cohesion coefficient (c), friction angle (ϕ), dilatancy angle (ψ), Young's modulus (E), Poisson's ratio (υ), and soil density (ρ). In the current paper, Eq. (25) is explicitly integrated using the standard leapfrog algorithm. A numerical error correction method proposed by Chen & Mizuno (1990) is applied to adjust stresses which exceed the yield strength of material.

5 BEARING CAPACITY ANALYSIS OF A SHALLOW FOOTING

This section discusses the potential of the SPH computing technique for accurate and efficient analyzing of bearing capacity and failure mechanism of deep penetration of a shallow foundation into soil. The material behavior is modelled by the elastic-plastic Drucker-Prager constitutive model described in Section 4. This material model was implemented into both the SPH code and the commercial finite element (FE) code PLAXIS (as a user-defined model). The SPH results in terms of bearing capacity and failure mode are compared with those computed by the FE method for two cases: the associated and non-associated flow rules. The ultimate bearing capacities predicted by the SPH and FE methods will be then compared with the well-known conventional bearing capacity solution propose by Terzaghi (1943).

5.1 Conventional design of bearing capacity using limit equilibrium method

The bearing capacity of shallow foundations is generally calculated using the Terzaghi method (Terzaghi, 1943), which is based on an approximation solution using superposition assumption to combine the effect of cohesion, overburden pressure and soil weight. For a strip footing subjected to vertical and central loading as shown in Fig. 1, the ultimate bearing capacity q_u can be expressed by Terzaghi's equation as

$$q_u = c\cdot N_c + q\cdot N_q + \frac{1}{2}\gamma\cdot B\cdot N_\gamma \tag{28}$$

where c is the cohesion intercept of soil, q the overburden pressure at foundation depth, γ the unit weight of soil, B the width of the strip footing, and N_c, N_q and N_c are non-dimensional bearing capacity factors that are functions of soil friction angle ϕ.

Fig. 1 also illustrates the general failure mechanism in soil underlying a shallow strip footing postulated by Terzaghi based on Prandlt's theory. There are three distinct failure zones of soil under the footing: a weight triangular zone (active zone), two Prandtl's radial shear zones and two Rankine passive zones.

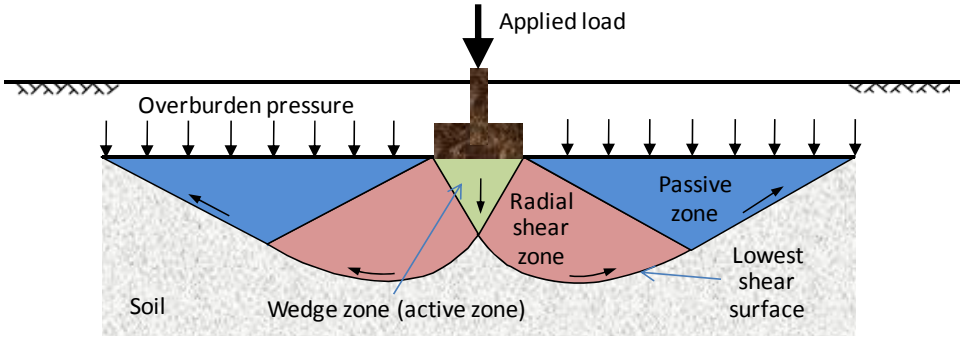

Fig. 1. General failure mechanism in soil at ultimate load for a rigid strip footing (Terzaghi, 1943).

5.2 Numerical analysis of bearing capacity using the SPH and FE methods

The bearing capacity analysis of a shallow layer of clay has been performed using a plane strain analytical model shown in Fig. 2. Its configuration is similar to those studied by Zienkiewicz et al. (1975), Chen & Mizuno (1990), except for the width of the model which is extended to 10 m from the center line. This is to allow the failure to fully develop. The foundation was assumed to be rigid and in perfect contact with the soil. This means that relative displacement between the foundation and soil is not permitted. The two vertical sides of the model have been restrained in the horizontal direction, while the base of the soil layer was not allowed to move in either the vertical or horizontal direction.

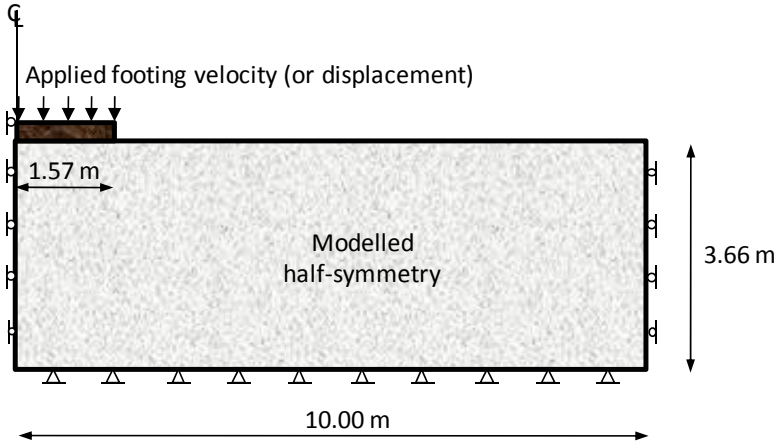

Fig. 2. Idealization of the plane strain strip foundation problem.

The soil weight effect was neglected and so initial stress state is set at the origin of the stress space. The Mohr-Coulomb constitutive model with Young's modulus E = 207 MPa, Poisson's ratio $\nu = 0.3$, cohesion c = 69 kPa and internal friction angle $\phi = 20^{o}$ was used by

Zienkiewicz et al. (1975) in order to simulate the behaviour of the soil. For plane strain conditions, the Mohr-Coulomb parameters (ϕ, c) can be exactly converted to Drucker-Prager parameters (α_ϕ, k_c) using Eq. (22) presented in Section 4.

- Description of the SPH model

For the SPH model, a total of 9900 SPH particles were arranged in a rectangular lattice to generate the modelled half-symmetry with an initial smoothing length of 0.0732 m. These particles have the same material properties as the soil model used in the FEM simulation. *Boundary particles* with no-slip boundary condition were used to model the rigid, rough base and strip footing. On the other hand, the *ghost particles* that satisfy the free-slip boundary condition were assigned to the vertical boundary. A speed of sound of 270 m/s determined based on the Young's modulus and the density of the soil was used for calculating the artificial viscosity (see Section 3). This artificial viscosity was then incorporated in the momentum equation to improve the numerical stability as well as to damp out unwanted oscillations. The gravitational force was set to zero to model the weightless soil. Even so, a reference density of 26.5 kN/m3 still need to be assigned to soil particles in order to remove the numerical divergence from the SPH momentum equation. The foundation load was applied using a constant downward velocity of 5 cm/s, which is assumed to be small enough to ensure the accurate solutions for the problem described in this paper.

- Description of the FE model

For the PLAXIS FE-model, 15-nodes triangular elements were used for the soil while the strip footing was simply modelled by the rigid beam element. The FE model composes of 1314 elements which correspond to 15768 material points (i.e. Gauss points). The foundation load was simulated by applying increments of vertical displacement to the rigid beam.

5.3 Comparison of the bearing capacity results

The bearing capacity responses of the rigid strip footing calculated by using the SPH method were compared with those calculated using the PLAXIS FE method and the Terzaghi limit equilibrium solution.

Fig. 3 plots the load-displacement responses the strip footing for both the associated and non-associated flow rules (zero dilatancy angle). It can be seen from the figure that the bearing capacities obtained with the SPH model in this paper (named current SPH model) are significantly small than those obtained with the same SPH simulation presented in the paper of Bui et al. (2008) (named SPH model 2008). This can be explained by three main effects:

- Effect of the SPH discretisation: the number of particles in the current model is larger than in the model 2008 (9900 SPH particles compared to 7371 SPH particle). This finer model can minimize the overshoot of the calculated bearing capacity caused by the "coarse" SPH discretisation used in the SPH model 2008.
- Effect of boundary: the load-displacement responses presented in Figure 10 in the paper of Bui et al. (2008) were obtained with the SPH model similar to the FE model used by Chen and Mizuno (1975). It means that its width is actually narrower than the current SPH model (7.32 m compared to 10 m). As pointed out by Bui et al. (2008) the width of 7.32 m is not sufficiently wide to avoid boundary effects, especially for the associated flow rule case;
- Effect of the artificial viscosity: as proposed by Monaghan (1992) the artificial viscosity is proportional to the sound speed of soil. In the current SPH model, the sound speed is smaller than the value used in the SPH model 2008 (270 m/s compared to 600 m/s). It is known that in the SPH method, the utilization of the artificial

viscosity is necessary to stabilize the numerical solution (see Bui et al., 2008). However, a high viscosity may result in an unrealistic stiff behaviour of the soil, and in consequence the calculated resistance of the soil can be overestimated. One other important advantage of using low sound speed is that the computational time of SPH simulation can be considerably reduced since the leapfrog time stepping scheme used in the SPH method is inversely proportional to the sound speed.

It is also obvious from Fig. 3 that both the SPH and FE methods predict almost the same ultimate bearing capacities of 1.04 MPa for the associated flow rule and 0.96 MPa for the non-associated flow rule. Note that they are significantly smaller than the bearing capacity of 1.21 MPa predicted by using Terzaghi's solution (Equation (26)). These differences can be attributed to several causes, the most important of which is that Terzaghi's method assumes the soil behaves as a rigid-perfectly plastic material which fails abruptly when the bearing capacity of the soil is reached. In contrast, the Drucker-Prager constitutive model implemented in the SPH and PLAXIS codes assumes that the soil behaves more like an elasto-plastic material which allows the soil to deform under applied loads. Furthermore, the soil can yield gradually and progressively due to the nature of the finite formulation, which means that a yielding material point can cause next to it to yield until a well-defined failure surface similar to the one shown in Fig. 2 is formed.

Fig. 4 and Fig. 5 illustrate the development of failure depicted by the shading contours of total share strains at three different stages of footing settlement (at 5 cm, 10 cm and at 30 cm) for the associated flow rule and the non-associated flow rule, respectively. It can be seen that the SPH model and the PLAXIS FE model predicts more or less the same failure surfaces for the associated and non associated flow rules. Moreover, it can be immediately noticed from Fig. 4 and Fig. 5 the presence of three major failure zones at 30 cm settlement: a triangular zone directly under the foundation, a Prandtl's radial shear zone and a Rankine passive zone, which agree very well with the general failure mechanisms assumed by Terzaghi (1943) for a rigid strip footing.

In addition, comparison of the shadings of shear strains at 30 cm settlement of the footing presented in Fig. 4 and Fig. 5 shows that the failure mechanisms obtained for the associated flow rule is larger than those for the non-associated flow rule, especially in the radial shear zone as well as in the passive zone. This is basically due to the nature of dilatancy in soil during plastic flow. It is worthwhile to recall that for the associated flow rule case, the dilatancy angle is set equal to the friction angle while it is equal to zero (no plastic volumetric strain) for the case of a non-associated flow rule in all numerical simulations presented in this paper. It is also noticed from Fig. 4 that the radial shear zone at 30 cm settlement of the foundation predicted by SPH is much smaller than that of the FE model for the associated flow case, although they are almost the same at 5 cm and 10 cm settlements of the foundation. It is probably due to too large amount of dilatancy, i.e. too large plastic volumetric strains, caused by a relatively high loading speed applied on the footing. This effect does not influence the results obtained with the non-associated since the dilatancy angle is set equal to zero.

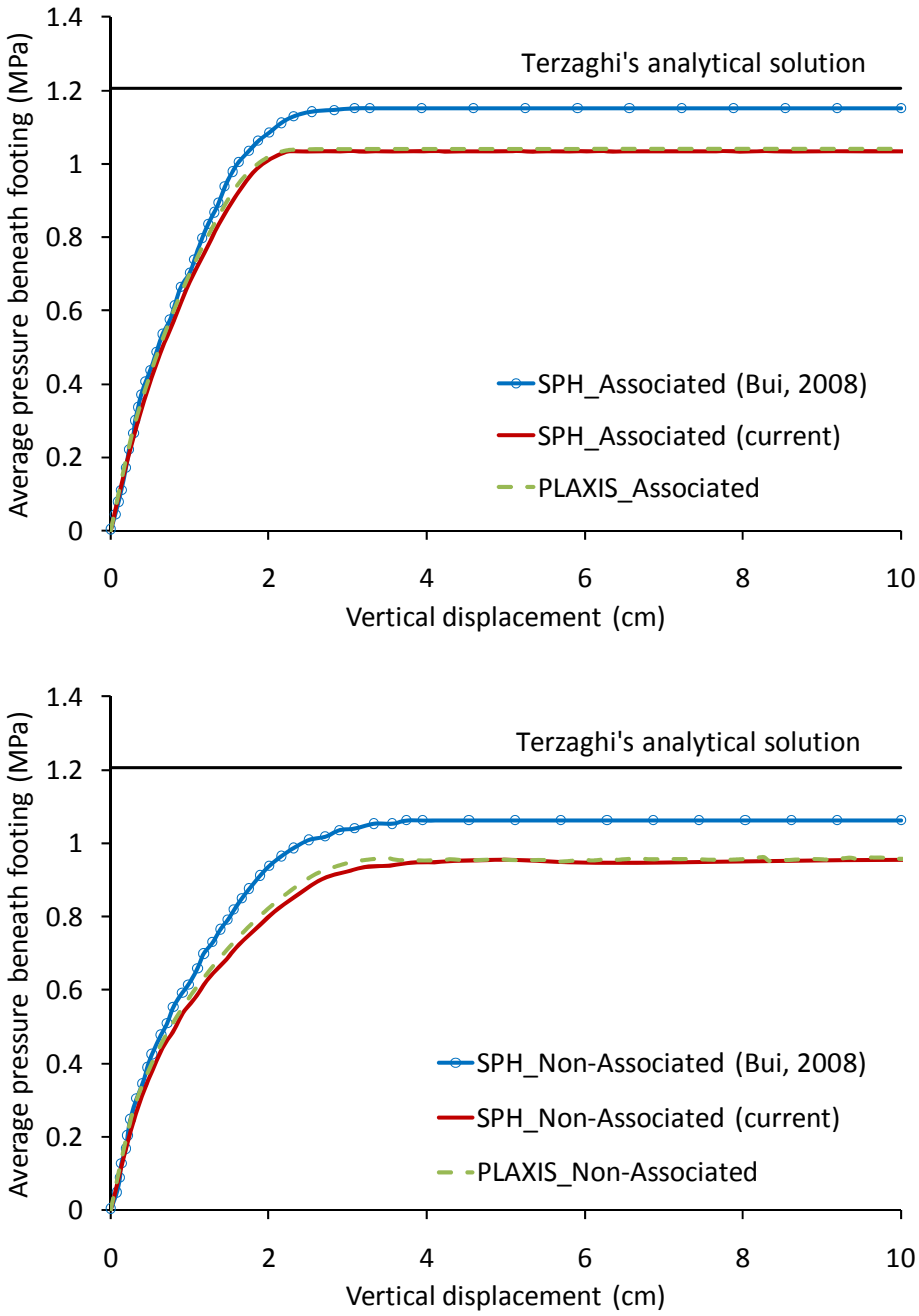

Fig. 3. Pressure-displacement curves for both the associated flow rule (top) and non-associated flow rule (bottom). Comparison of SPH results, FEM results and Terzaghi's solution.

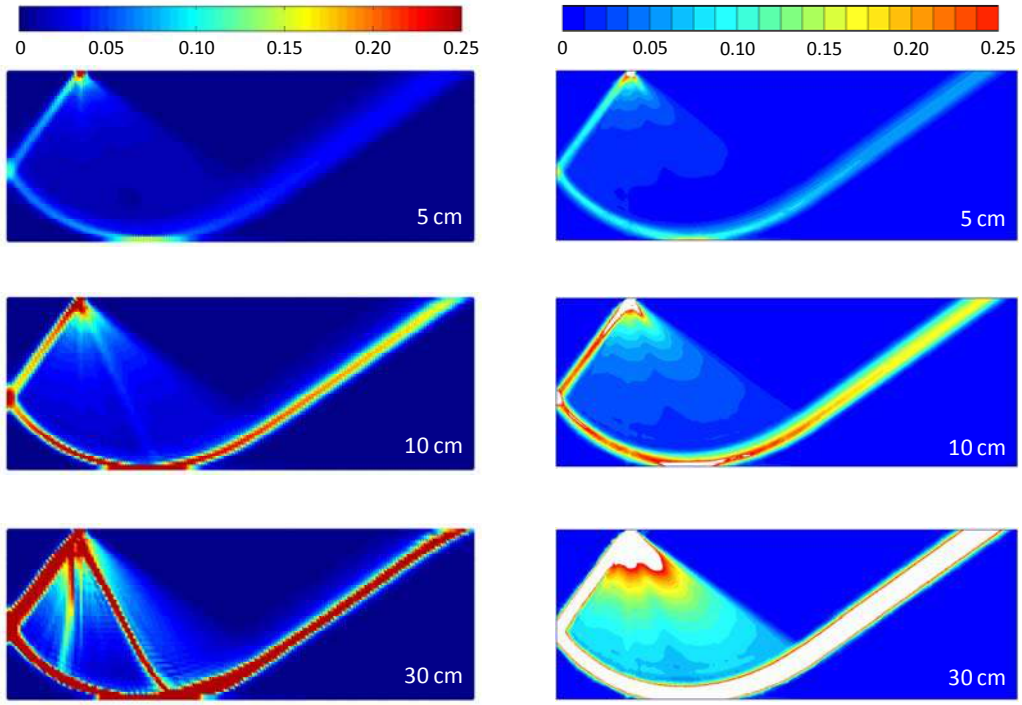

(a) SPH results for the associated flow rule (b) PLAXIS results for the associated flow rule

Fig. 4. Failure modes depicted by the shadings of shear strains at three levels of settlement of the footing: 5cm, 10 cm and 30 cm for the case of associated flow rule. (a) SPH results and (b) PLAXIS FE results.

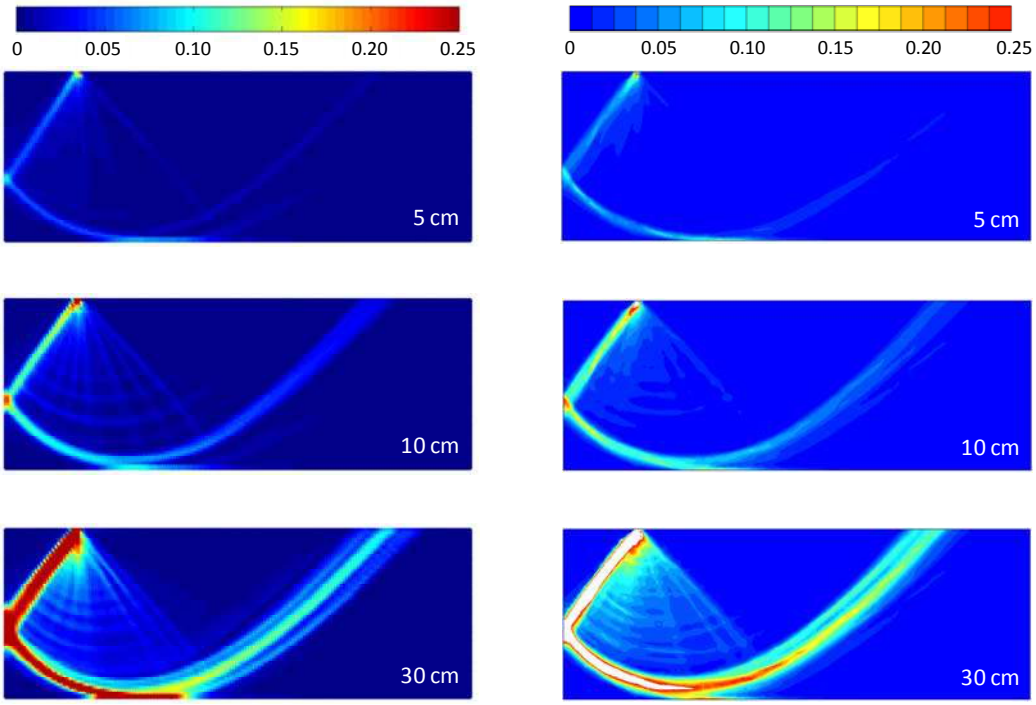

(a) SPH results for the non-associated flow rule (b) PLAXIS results for the non-associated flow rule

Fig. 5. Failure modes depicted by the shadings of shear strains at three levels of settlement of the footing: 5cm, 10 cm and 30 cm for the case of non-associated flow rule. (a) SPH results and (b) PLAXIS FE results.

6 CONCLUSIONS

The application of the smoothed particle hydrodynamics (SPH) method in conjunction with the Drucker-Prager material model in analyzing bearing capacity and failure mechanism of shallow foundation has been presented in this paper. Fairly good agreement in the computed results obtained from the SPH simulations and the finite element (FE) simulations using the PLAXIS code demonstrates the accuracy as well as the powerful capabilities of the SPH method in modelling of geotechnical problems.

7 ACKNOWLEDGEMENT

The research has been performed as a part of "GEO-INSTALL" (Modelling Installation Effects in Geotechnical Engineering) project. The work is partially funded by the European Community through the program "Marie Curie Industry-Academia Partnership and Pathways", under Contract No PIAP-GA-2009-230638, and partially supported by JSPS through Grants-in-Aid for scientific research. All these supports are gratefully acknowledged. The first author wishes to thank the Japan Society for the Promotion of Science (JSPS) for a JSPS Postdoctoral Fellowship.

8 REFERENCES

Bonet, J. and Lok, T.S.L. (1999), “Variational and momentum preservation aspects of smooth particle hydrodynamic formulations”, Computer Methods in Applied Mechanics and Engineering, 180, 97-115.

Bui, H.H., Fukagawa, R. and Sako, K. (2010), “Slope stability analysis and discontinuous slope failure simulation by elasto-plastic smoothed particle hydrodynamics (SPH)”, Géotechnique, in press.

Bui, H.H., Fukagawa, R., Sako, K. and Ohno, S. (2008), “Lagrangian mesh-free particles method (SPH) for large deformation and failure flows of geomaterial using elastic-plastic soil constitutive model”, International Journal for Numerical and Analytical Methods in Geomechanics, 32(12), 1537-1570.

Bui, H.H., Sako, K. and Fukagawa, R. (2007), “Numerical simulation of soil-water interaction using smoothed particle hydrodynamics (SPH) method”, Journal of Terramechanics, 44(5), 339-346.

Chen, W.F. and Mizuno, E. (1990), Nonlinear analysis in soil mechanics. Amsterdam: Elsevier Science Publishers.

Gingold, R.A. and Monaghan, J.J. (1977), “Smoothed particle hydrodynamics-theory and application to non-spherical stars”, Monthly Notices of the Royal Astronomical Society, 181, 375-389.

Liu, G.R. and Liu, M.B. (2003), Smoothed particle hydrodynamics: a meshfree particle method. World Scientific, Singapore.

Lucy, L.B. (1977), “A numerical approach to the testing of the fission hypothesis”, Astronomical Journal, 82(12), 1013-1024.

Monaghan, J.J. (1992), “Smoothed particle hydrodynamics”, Annual Review of Astronomy and Astrophysics, 30, 543-574.

Monaghan, J.J. and Lattanzio, J.C. (1985), “A refined particle method for astrophysical problems”, Astronomic and Astrophysics, 149-135.

Terzaghi, K. (1943), Theoretical soil mechanics, 5th ed., John Wiley & Sons Inc., New York, N.Y.

Zienkiewicz, O.C., Humpheson, C. and Lewis, R.W. (1975), “Associated and nonassociated visco-plasticity and plasticity in soil mechanics”, Géotechnique, 25(4), 671–689.

MATHEMATICAL PROGRAMMING FORMULATION OF ELASTO-PLASTO-DYNAMICS FOR GEOMATERIALS

K. Krabbenhoft, A.V. Lyamin, S.W. Sloan
Centre for Geotechnical and Materials Modelling, University of Newcastle, NSW, Australia

M. Vicente da Silva
Department of Civil Engineering, Universidade Nova de Lisboa, Portugal

ABSTRACT: *Starting from rigid-plasticity, we develop variational formulations of first incremental elastoplasticity and then elastoplastodynamics. These formulations are discretized using standard finite element techniques which results in discrete optimization problems that can be solved efficiently by modern mathematical programming methods. Finally, the extension from associated perfect plasticity to general nonassociated and hardening plasticity is detailed.*

1 INTRODUCTION

Starting from rigid-plasticity, we develop mathematical programming formulations of first incremental elastoplasticity and then elastoplastodynamics. Subsequently, the incorporation of nonassociated flow rules and the extension to hardening soil models as exemplified by modified Cam clay is detailed. The overall procedure is as follows. First a spatially continuous optimization problem (or variational principle) is postulated. By application of the methods of variation calculus, this problem is shown to yield the governing equations for the problem at hand. Next, the problem is discretized by replacing the spatially continuous variables with suitable finite element approximations. Finally, the optimality conditions for the resulting discrete problem are derived to yield the approximate, spatially discrete, governing equations.
Regarding notation, spatially continuous vector quantities are underlined while their discrete counterparts are shown in bold. For example the continuous displacement field $\underline{u} = \underline{u}(\underline{x})$ versus the nodal displacements $\boldsymbol{u}$. The same rule applies for matrices, though with double underlining for continuous quantities. Also, we use the notation $\nabla_\alpha f$ to denote the partial derivative of a function f with respect to the set of variable $\boldsymbol{\alpha}$, that is $\nabla_\alpha f(\boldsymbol{\alpha}, \boldsymbol{\beta}) = \partial f / \partial \boldsymbol{\alpha}$.

2 RIGID-PLASTICITY

We first consider the problem of rigid-plasticity, i.e. limit analysis. The aim is here to determine the magnitude of a predefined load set that leads to incipient structural collapse. This problem can be stated in terms of the following optimization problem, or variational principle,

$$\begin{aligned} &\min_{\underline{u}} \max_{\alpha, \underline{\sigma}} \quad \alpha + \int_V \underline{\sigma}^{\mathsf{T}} \underline{\nabla} \underline{u} \, \mathrm{d}V - \int_V \underline{b}^{\mathsf{T}} \underline{u} \, \mathrm{d}V - \alpha \int_S \underline{t}^{\mathsf{T}} \underline{u} \, \mathrm{d}S \\ &\text{subject to} \quad F(\underline{\sigma}) \leq 0 \end{aligned} \tag{1}$$

where $\underline{\sigma}$ are the stresses, $\underline{u}$ are the displacements (or velocities), α is load factor, $\underline{t}$ are a set of predefined tractions whose ultimate magnitude is sought, and $\underline{b}$ are constant body forces stemming for example from self weight. The yield function is given by F and $\underline{\underline{\nabla}}$ is the usual linear strain-displacement operator ($\underline{\underline{\nabla}}^{\mathsf{T}}$ being the equilibrium operator).

2.1 Euler-Lagrange equations

The governing equations associated with the above problem can be derived by means of the following procedure. First the yield inequalities are converted in equalities by addition of a positively restricted variable s:

$$\begin{aligned} &\min_{\underline{u}} \max_{\alpha,\underline{\sigma}} \quad \alpha + \int_V \underline{\sigma}^{\mathsf{T}} \underline{\underline{\nabla}} \underline{u} \, \mathrm{d}V - \int_V \underline{b}^{\mathsf{T}} \underline{u} \, \mathrm{d}V - \alpha \int_S \underline{t}^{\mathsf{T}} \underline{u} \, \mathrm{d}S \\ &\text{subject to} \quad F(\underline{\sigma}) + s = 0 \end{aligned} \tag{2}$$

Next, the following functional is defined:

$$J = \alpha + \int_V \underline{\sigma}^{\mathsf{T}} \underline{\underline{\nabla}} \underline{u} \, \mathrm{d}V - \int_V \underline{b}^{\mathsf{T}} \underline{u} \, \mathrm{d}V - \alpha \int_S \underline{t}^{\mathsf{T}} \underline{u} \, \mathrm{d}S - \int_V \lambda [F(\underline{\sigma}) + s] + \mu \ln s \, \mathrm{d}V \tag{3}$$

where λ is a Lagrange multiplier and the penalty term $\mu \ln s$, with $\mu > 0$ being a sufficiently small constant, has been introduced to effectively impose the non-negativity requirement on s. This is a common technique widely used in the optimization literature (Nash & Sofer 1996; Vanderbei 2001; Boyd & Vandenberghe 2006).
Next, taking functional derivatives (see e.g. Simo & Hughes 1998; Weinstock 1974), the following Euler-Lagrange equations appear

$$\begin{aligned} &\frac{\delta J}{\delta \underline{u}} = \begin{cases} \underline{\underline{\nabla}}^{\mathsf{T}} \underline{\sigma} + \underline{b} = 0, & \text{in } V \\ \underline{\underline{N}}^{\mathsf{T}} \underline{\sigma} = \alpha \underline{t}, & \text{on } S \end{cases} \\ &\frac{\delta J}{\delta \underline{\sigma}} = \underline{\underline{\nabla}} \underline{u} - \lambda \nabla F(\underline{\sigma}) = 0 \\ &\frac{\delta J}{\delta \alpha} = 1 - \int_S \underline{t}^{\mathsf{T}} \underline{u} \, \mathrm{d}S = 0 \\ &\frac{\delta J}{\delta \lambda} = -[F(\underline{\sigma}) + s] = 0 \\ &\frac{\delta J}{\delta s} = -\lambda + \mu s^{-1} = 0 \Longrightarrow s\lambda = \mu \end{aligned} \tag{4}$$

These equations are easily verified as being the governing equations for the problem at hand. Note that the complementarity condition $\lambda F = 0$ is recovered for $\mu \to 0$. Also, the non-negativity requirement on λ follows from μ and s both being non-negative, the former by definition and the latter by virtue of the penalty term $\mu \ln s$.

2.2 Finite element discretization

The principle (1) is discretized in terms of finite elements by postulating approximations to the state variables $\underline{\sigma}$ and $\underline{u}$. Using standard finite element notation, we have

$$\begin{aligned} &\underline{\sigma}(\underline{x}) \approx \boldsymbol{N}_\sigma(\underline{x}) \boldsymbol{\sigma} \\ &\underline{u}(\underline{x}) \approx \boldsymbol{N}_u(\underline{x}) \boldsymbol{u}, \quad \nabla \underline{u} \approx \boldsymbol{B}_u(\underline{x}) \boldsymbol{u} \end{aligned} \tag{5}$$

where $\boldsymbol{B}_u = \underline{\underline{\nabla}} \boldsymbol{N}_u$. In standard finite formulations, the stress shape functions in $\boldsymbol{N}_\sigma$ are chosen as being continuous within the elements and discontinuous between elements while $\boldsymbol{N}_u$ in addition are continuous between elements and usually one polynomial degree higher than $\boldsymbol{N}_\sigma$. Substituting the above approximations into the variational principle (1) leads to the following discrete principle

$$\begin{aligned} \min_{\boldsymbol{u}} \max_{\alpha,\boldsymbol{\sigma}} \quad & \alpha + \boldsymbol{u}^{\mathsf{T}} \boldsymbol{B}^{\mathsf{T}} \boldsymbol{\sigma} - \boldsymbol{u}^{\mathsf{T}} \boldsymbol{b} - \boldsymbol{u}^{\mathsf{T}} \boldsymbol{t} \\ \text{subject to} \quad & F_j(\boldsymbol{\sigma}) \leq 0, \;\; j = 1, \ldots, n \end{aligned} \tag{6}$$

where

$$\boldsymbol{B}^{\mathsf{T}} = \int_V \boldsymbol{B}_u^{\mathsf{T}} \boldsymbol{N}_\sigma \, \mathrm{d}V, \quad \boldsymbol{b} = \int_V \boldsymbol{N}_u^{\mathsf{T}} \underline{b} \, \mathrm{d}V, \quad \boldsymbol{t} = \int_S \boldsymbol{N}_u^{\mathsf{T}} \underline{t} \, \mathrm{d}S \tag{7}$$

and where the yield condition has been imposed at a finite number of points, often taken to coincide with the Gauss points used in the evaluation of the discrete equilibrium operator $\boldsymbol{B}^{\mathsf{T}}$. The minimization part of the above problem may be solved first to arrive at the maximization problem

$$\boxed{\begin{aligned} \underset{\alpha,\boldsymbol{\sigma}}{\text{maximize}} \quad & \alpha \\ \text{subject to} \quad & \boldsymbol{B}^{\mathsf{T}} \boldsymbol{\sigma} = \boldsymbol{b} + \alpha \boldsymbol{t} \\ & F_j(\boldsymbol{\sigma}) \leq 0, \;\; j = 1, \ldots, n \end{aligned}} \tag{8}$$

This is usually the final problem solved numerically. Although it only involves static variables (the load multiplier and the stresses), the kinematic variables (displacements and plastic multipliers) are recovered as part the solution process as discussed in the following section.

2.3 Karush-Kuhn-Tucker conditions

Solution of the above optimization problem implies satisfaction of the first-order Karush-Kuhn-Tucker conditions. These may be seen as the discrete counterpart to the Euler-Lagrange equations associated with the continuous functional. Their derivation follows a similar scheme. First include slack variables, $s_j \geq 0$, to convert the yield inequalities into equalities:

$$\begin{aligned} \underset{\alpha,\boldsymbol{\sigma}}{\text{maximize}} \quad & \alpha \\ \text{subject to} \quad & \boldsymbol{B}^{\mathsf{T}} \boldsymbol{\sigma} = \boldsymbol{b} + \alpha \boldsymbol{t} \\ & F_j(\boldsymbol{\sigma}) + s_j = 0, \;\; j = 1, \ldots, n \end{aligned} \tag{9}$$

Next, defined the Lagrangian:

$$L = \alpha + \boldsymbol{u}^{\mathsf{T}} (\boldsymbol{B}^{\mathsf{T}} \boldsymbol{\sigma} - \boldsymbol{b} - \alpha \boldsymbol{t}) - \textstyle\sum_{j=1}^{n} \{\lambda_j [F_j(\boldsymbol{\sigma}) + s_j] + \mu \ln s_j\} \tag{10}$$

The KKT conditions then follow by requiring that the Lagrangian be stationary:

$$\begin{aligned}
\frac{\partial L}{\partial \boldsymbol{u}} &= \boldsymbol{B}^{\mathsf{T}}\boldsymbol{\sigma} - \boldsymbol{b} - \alpha \boldsymbol{t} = \boldsymbol{0} \\
\frac{\partial L}{\partial \boldsymbol{\sigma}} &= \boldsymbol{B}\boldsymbol{u} - \textstyle\sum_{j=1}^{n} \lambda_j \nabla F_j(\boldsymbol{\sigma}) = \boldsymbol{0} \\
\frac{\partial L}{\partial \alpha} &= 1 - \boldsymbol{p}^{\mathsf{T}}\boldsymbol{u} = 0 \\
\frac{\partial L}{\partial \lambda_j} &= -[F_j(\boldsymbol{\sigma}) + \boldsymbol{s}_j] = 0, \quad j = 1, \ldots, n \\
\frac{\partial L}{\partial s_j} &= -\lambda_j + \mu s_j^{-1} = 0 \Longrightarrow \lambda_j s_j = \mu, \quad j = 1, \ldots, n
\end{aligned} \tag{11}$$

These conditions are easily identified as the approximate, spatially discrete, counterparts to the governing equations (4). These are the equations actually solved and as such the displacements and the plastic multipliers are recovered as the dual variables to the equilibrium and yield constraints respectively.

3 ELASTOPLASTICITY

The problem of incremental elastoplasticity may be cast in terms of the following variational statement:

$$\begin{aligned}
\min_{\underline{u}_{n+1}} \max_{(\alpha,\underline{\sigma})_{n+1}} \quad & \alpha_{n+1} + \int_V \underline{\sigma}_{n+1}^{\mathsf{T}} \Delta \underline{u}_{n+1} \,\mathrm{d}V - \int_V \underline{b}^{\mathsf{T}} \Delta \underline{u}_{n+1} \,\mathrm{d}V - \alpha_{n+1} \int_S \underline{t}^{\mathsf{T}} \Delta \underline{u}_{n+1} \,\mathrm{d}S \\
& - \tfrac{1}{2} \int_V \Delta \underline{\sigma}_{n+1}^{\mathsf{T}} \mathbb{C} \Delta \underline{\sigma}_{n+1} \,\mathrm{d}V \\
\text{subject to} \quad & F(\underline{\sigma}_{n+1}) \leq 0
\end{aligned} \tag{12}$$

where $\mathbb{C}$ is the elastic compliance modulus and $\Delta\underline{\sigma}_{n+1} = \underline{\sigma}_{n+1} - \underline{\sigma}_n$, $\Delta\underline{u}_{n+1} = \underline{u}_{n+1} - \underline{u}_n$ with subscripts n and $n+1$ referring, respectively, to the known and the new, unknown, state. Compared to the problem of limit analysis, the only essential difference is the presence of the quadratic term in the objective function which accounts for elasticity.

3.1 Euler-Lagrange equations

Following the treatment of rigid plasticity, the Euler-Lagrange equations are derived by first constructing the following functional:

$$\begin{aligned}
J = \alpha_{n+1} + \int_V \underline{\sigma}_{n+1}^{\mathsf{T}} \underline{\underline{\nabla}} \Delta \underline{u}_{n+1} \,\mathrm{d}V - \int_V \underline{b}^{\mathsf{T}} \Delta \underline{u}_{n+1} \,\mathrm{d}V - \alpha_{n+1} \int_S \underline{t}^{\mathsf{T}} \Delta \underline{u}_{n+1} \,\mathrm{d}S \\
- \tfrac{1}{2} \int_V \Delta \underline{\sigma}_{n+1}^{\mathsf{T}} \mathbb{C} \Delta \underline{\sigma}_{n+1} \,\mathrm{d}V - \int_V \lambda_{n+1}[F(\underline{\sigma}_{n+1}) + s_{n+1}] + \mu \ln s_{n+1} \,\mathrm{d}V
\end{aligned} \tag{13}$$

The governing equations then follow as

$$
\begin{aligned}
\frac{\delta J}{\delta \underline{u}_{n+1}} &= \begin{cases} \underline{\underline{\nabla}}^{\mathsf{T}} \underline{\sigma}_{n+1} + \underline{b} = 0, & \text{in } V \\ \underline{\underline{N}}^{\mathsf{T}} \underline{\sigma}_{n+1} = \alpha_{n+1} \underline{t}, & \text{on } S \end{cases} \\
\frac{\delta J}{\delta \underline{\sigma}_{n+1}} &= \underline{\underline{\nabla}} \Delta \underline{u}_{n+1} - \mathbb{C} \Delta \underline{\sigma}_{n+1} - \lambda_{n+1} \nabla F(\underline{\sigma}_{n+1}) = 0 \\
\frac{\delta J}{\delta \alpha_{n+1}} &= 1 - \int_S \underline{t}^{\mathsf{T}} \Delta \underline{u}_{n+1} \, \mathrm{d}S = 0 \\
\frac{\delta J}{\delta \lambda_{n+1}} &= -[F(\underline{\sigma}_{n+1}) + s_{n+1}] = 0 \\
\frac{\delta J}{\delta s_{n+1}} &= -\lambda_{n+1} + \mu s_{n+1}^{-1} = 0 \Longrightarrow s_{n+1} \lambda_{n+1} = \mu
\end{aligned}
\tag{14}
$$

Compared to the problem of rigid plasticity, the only essential difference is that elastic strain increments, $\mathbb{C}\Delta\underline{\sigma}_{n+1}$, are now included in the second equation.

3.2 Finite element discretization

Using the same finite element approximations (5) as before, the following discrete optimization problem appears:

$$
\begin{aligned}
\min_{\boldsymbol{u}_{n+1}} \max_{(\alpha,\boldsymbol{\sigma})_{n+1}} \quad & \alpha_{n+1} + \Delta \boldsymbol{u}_{n+1}^{\mathsf{T}} \boldsymbol{B}^{\mathsf{T}} \boldsymbol{\sigma}_{n+1} - \Delta \boldsymbol{u}_{n+1}^{\mathsf{T}} \boldsymbol{b} - \alpha_{n+1} \Delta \boldsymbol{u}_{n+1}^{\mathsf{T}} \boldsymbol{t} \\
& - \tfrac{1}{2} \Delta \boldsymbol{\sigma}_{n+1}^{\mathsf{T}} \boldsymbol{C} \Delta \boldsymbol{\sigma}_{n+1} \\
\text{subject to} \quad & F_j(\boldsymbol{\sigma}_{n+1}) \leq 0, \;\; j = 1, \ldots, n
\end{aligned}
\tag{15}
$$

where the only new quantity is the elastic compliance matrix

$$
\boldsymbol{C} = \int_V \boldsymbol{N}_\sigma^{\mathsf{T}} \mathbb{C} \boldsymbol{N}_\sigma \, \mathrm{d}V \tag{16}
$$

Also, as before, the minimization part of the problem may be solved to yield the following maximization problem

$$
\boxed{
\begin{aligned}
\underset{(\alpha,\boldsymbol{\sigma})_{n+1}}{\text{maximize}} \quad & \alpha_{n+1} - \tfrac{1}{2} \Delta \boldsymbol{\sigma}_{n+1}^{\mathsf{T}} \boldsymbol{C} \Delta \boldsymbol{\sigma}_{n+1} \\
\text{subject to} \quad & \boldsymbol{B}^{\mathsf{T}} \boldsymbol{\sigma}_{n+1} = \boldsymbol{b} + \alpha_{n+1} \boldsymbol{t} \\
& F_j(\boldsymbol{\sigma}_{n+1}) \leq 0, \;\; j = 1, \ldots, n
\end{aligned}
}
\tag{17}
$$

Again, the displacements and the plastic multipliers are recovered as part of the solution process.

3.3 Karush-Kuhn-Tucker conditions

The Karush-Kuhn-Tucker conditions again follow by first constructing the Lagrangian

$$
\begin{aligned}
L = \; & \alpha_{n+1} + \Delta \boldsymbol{u}_{n+1}^{\mathsf{T}} \boldsymbol{B}^{\mathsf{T}} \boldsymbol{\sigma}_{n+1} - \Delta \boldsymbol{u}_{n+1}^{\mathsf{T}} \boldsymbol{b} - \alpha_{n+1} \Delta \boldsymbol{u}_{n+1}^{\mathsf{T}} \boldsymbol{t} \\
& - \tfrac{1}{2} \Delta \boldsymbol{\sigma}_{n+1}^{\mathsf{T}} \boldsymbol{C} \Delta \boldsymbol{\sigma}_{n+1} - \textstyle\sum_{j=1}^{n} \lambda_{n+1}^{j} \{ F_j(\boldsymbol{\sigma}_{n+1}) + s_{n+1}^{j} + \mu \ln s_{n+1}^{j} \}
\end{aligned}
\tag{18}
$$

We then have

$$\begin{aligned}
\frac{\partial L}{\partial \boldsymbol{u}_{n+1}} &= \boldsymbol{B}^{\mathsf{T}}\boldsymbol{\sigma}_{n+1} - \boldsymbol{b} - \alpha_{n+1}\boldsymbol{t} = \boldsymbol{0} \\
\frac{\partial L}{\partial \boldsymbol{\sigma}_{n+1}} &= \boldsymbol{B}\Delta\boldsymbol{u}_{n+1} - \boldsymbol{C}\Delta\boldsymbol{\sigma}_{n+1} - \textstyle\sum_{j=1}^{n} \lambda_{n+1}^{j} \nabla F_j(\boldsymbol{\sigma}_{n+1}) = \boldsymbol{0} \\
\frac{\partial L}{\partial \alpha_{n+1}} &= 1 - \boldsymbol{p}^{\mathsf{T}}\Delta\boldsymbol{u}_{n+1} = 0 \\
\frac{\partial L}{\partial \lambda_{n+1}^{j}} &= -[F_j(\boldsymbol{\sigma}_{n+1}) + \boldsymbol{s}_{n+1}^{j}] = 0, \quad j = 1, \ldots, n \\
\frac{\partial L}{\partial s_{n+1}^{j}} &= -\lambda_{n+1}^{j} + \mu s_{n+1}^{j} = 0 \Longrightarrow \lambda_{n+1}^{j} s_{n+1}^{j} = \mu, \quad j = 1, \ldots, n
\end{aligned} \tag{19}$$

which are the discrete governing equations.

4 ELASTOPLASTODYNAMICS

The momentum conservation equations for a body subjected to a time-varying motion are given by

$$\underline{\underline{\nabla}}^{\mathsf{T}}\sigma + \underline{b} = \rho\ddot{\underline{u}} \tag{20}$$

where ρ is the material density and a superposed dot denotes differentiation with respect to time, i.e. $\ddot{\underline{u}}$ are the accelerations.

4.1 Time discretization

The momentum conservation equations may be discretized in time using the following procedure. First the equations are written in equivalent form as two first-order (in time) sets of equations:

$$\begin{aligned}
\underline{\underline{\nabla}}^{\mathsf{T}}\underline{\sigma} + \underline{b} &= \rho\dot{\underline{v}} \\
\underline{v} &= \dot{\underline{u}}
\end{aligned} \tag{21}$$

where $\underline{v}$ are recognized as the the velocities. These equations are then approximated by means of the well-known theta-method to yield

$$\begin{aligned}
\underline{\underline{\nabla}}^{\mathsf{T}}[\theta_1\sigma_{n+1} + (1-\theta_1)\sigma_n] + \underline{b} &= \rho\frac{\underline{v}_{n+1} - \underline{v}_n}{\Delta t} \\
\theta_2\underline{v}_{n+1} + (1-\theta_2)\underline{v}_n &= \frac{\underline{u}_{n+1} - \underline{u}_{n+1}}{\Delta t}
\end{aligned} \tag{22}$$

Rearranging gives the following equation in the stresses and displacements

$$\underline{\underline{\nabla}}^{\mathsf{T}}\underline{\sigma}_{n+1} + \hat{\underline{b}}_n = \hat{\rho}\frac{\Delta\underline{u}_{n+1}}{\Delta t^2} \tag{23}$$

where

$$\hat{\underline{b}}_n = \underline{b} + \frac{1-\theta_1}{\theta_1}(\underline{\underline{\nabla}}^{\mathsf{T}}\underline{\sigma}_n - \underline{b}) + \hat{\rho}\frac{\underline{v}_n}{\Delta t} \tag{24}$$

and

$$\hat{\rho} = \frac{\rho}{\theta_1 \theta_2} \tag{25}$$

After the displacements at t_{n+1} have been determined, the velocities are computed from

$$\underline{v}_{n+1} = \frac{1}{\theta_2}\left[\frac{\Delta \underline{u}_{n+1}}{\Delta t} - (1-\theta_2)\underline{v}_n\right] \tag{26}$$

The above time integration scheme is unconditionally stable for $\theta_1 = \theta_2 = \frac{1}{2}$ for which it coincides with the popular Newmark average acceleration scheme.

4.2 Variational principle

We are now in a position to postulate the following time-discrete variational principle:

$$\begin{aligned} \min_{\underline{u}_{n+1}} \max_{(\alpha,\underline{\sigma})_{n+1}} \quad & \alpha_{n+1} + \int_V \underline{\sigma}_{n+1}^{\mathsf{T}} \Delta \underline{u}_{n+1}\, \mathrm{d}V - \int_V \hat{\underline{b}}_n{}^{\mathsf{T}} \Delta \underline{u}_{n+1}\, \mathrm{d}V - \alpha_{n+1} \int_S \underline{t}^{\mathsf{T}} \Delta \underline{u}_{n+1}\, \mathrm{d}S \\ & - \tfrac{1}{2} \int_V \Delta \underline{\sigma}_{n+1}^{\mathsf{T}} \mathbb{C} \Delta \underline{\sigma}_{n+1}\, \mathrm{d}V \\ & - \tfrac{1}{2} \Delta t^2 \int_V \underline{r}_{n+1}^{\mathsf{T}} \rho^{-1} \underline{r}_{n+1} + \int_V \underline{u}_{n+1}^{\mathsf{T}} r_{n+1}\, \mathrm{d}V \\ \text{subject to} \quad & F(\underline{\sigma}_{n+1}) \leq 0 \end{aligned} \tag{27}$$

where $\underline{r} = (r_x, r_y, r_z)^{\mathsf{T}}$ is a new variable whose significance will become apparent shortly. Following the procedure detailed earlier, the solution of the above problem is realized by requiring stationarity of the following functional:

$$\begin{aligned} J = \alpha_{n+1} & + \int_V \underline{\sigma}_{n+1}^{\mathsf{T}} \Delta \underline{u}_{n+1}\, \mathrm{d}V - \int_V \hat{\underline{b}}_n{}^{\mathsf{T}} \Delta \underline{u}_{n+1}\, \mathrm{d}V - \alpha_{n+1} \int_S \underline{t}^{\mathsf{T}} \Delta \underline{u}_{n+1}\, \mathrm{d}S \\ & - \tfrac{1}{2} \int_V \Delta \underline{\sigma}_{n+1}^{\mathsf{T}} \mathbb{C} \Delta \underline{\sigma}_{n+1}\, \mathrm{d}V - \tfrac{1}{2} \Delta t^2 \int_V \underline{r}_{n+1}^{\mathsf{T}} \hat{\rho}^{-1} \underline{r}_{n+1}\, \mathrm{d}V + \int_V \underline{r}_{n+1}^{\mathsf{T}} \Delta \underline{u}_{n+1}\, \mathrm{d}V \\ & - \int_V \lambda_{n+1}[F(\underline{\sigma}_{n+1}) + s_{n+1}] + \mu \ln s_{n+1}\, \mathrm{d}V \end{aligned} \tag{28}$$

The Euler-Lagrange equations are given by

$$\begin{aligned} \frac{\delta J}{\delta \underline{u}_{n+1}} &= \begin{cases} \underline{\underline{\nabla}}^{\mathsf{T}} \underline{\sigma}_{n+1} + \hat{\underline{b}}_n = \underline{r}_{n+1}, & \text{in } V \\ \underline{\underline{N}}^{\mathsf{T}} \underline{\sigma}_{n+1} = \alpha_{n+1} \underline{t}, & \text{on } S \end{cases} \\ \frac{\delta J}{\delta \underline{r}_{n+1}} &= -\Delta t^2 \hat{\rho}^{-1} \underline{r}_{n+1} + \Delta \underline{u}_{n+1} = 0 \\ \frac{\delta J}{\delta \underline{\sigma}_{n+1}} &= \underline{\underline{\nabla}} \Delta \underline{u}_{n+1} - \mathbb{C} \Delta \underline{\sigma}_{n+1} - \lambda_{n+1} \nabla F(\underline{\sigma}_{n+1}) = 0 \\ \frac{\delta J}{\delta \alpha_{n+1}} &= 1 - \int_S \underline{t}^{\mathsf{T}} \Delta \underline{u}_{n+1}\, \mathrm{d}S = 0 \\ \frac{\delta J}{\delta \lambda_{n+1}} &= -[F(\underline{\sigma}_{n+1}) + s_{n+1}] = 0 \\ \frac{\delta J}{\delta s_{n+1}} &= -\lambda_{n+1} + \mu s_{n+1}^{-1} = 0 \Longrightarrow s_{n+1}\lambda_{n+1} = \mu \end{aligned} \tag{29}$$

The first two sets of equations give the time-discrete momentum conservation equations (23) while all other equations are identical to those of the static elastoplastic case.

4.3 Finite element discretization

In addition to stresses and displacements, the problem (27) also contains the new variables $\underline{r}$. These are approximated following the same methodology as previously:

$$\underline{r}(\underline{x}) \approx \boldsymbol{N}_r(\underline{x})\boldsymbol{r} \tag{30}$$

where $\boldsymbol{N}_r$ are a new set of finite element shape functions. Using the previously defined shape functions (5) for $\underline{\sigma}$ and $\underline{u}$, the discrete form of (27) reads

$$\begin{aligned} \min_{\boldsymbol{u}_{n+1}} \max_{(\alpha,\boldsymbol{\sigma})_{n+1}} \quad & \alpha_{n+1} + \Delta\boldsymbol{u}_{n+1}^{\mathsf{T}}\left[\boldsymbol{B}^{\mathsf{T}}\boldsymbol{\sigma} - \hat{\boldsymbol{b}}_n - \alpha_{n+1}\boldsymbol{t}\right] - \tfrac{1}{2}\Delta\boldsymbol{\sigma}_{n+1}^{\mathsf{T}}\boldsymbol{C}\Delta\boldsymbol{\sigma}_{n+1} \\ & -\tfrac{1}{2}\Delta t^2\boldsymbol{r}_{n+1}^{\mathsf{T}}\boldsymbol{A}\boldsymbol{r}_{n+1} + \Delta\boldsymbol{u}_{n+1}^{\mathsf{T}}\boldsymbol{A}^{\mathsf{T}}\boldsymbol{r}_{n+1} \\ \text{subject to} \quad & F_j(\boldsymbol{\sigma}_{n+1}) \leq 0 \end{aligned} \tag{31}$$

where

$$\boldsymbol{D} = \int_V \boldsymbol{N}_r^{\mathsf{T}}\hat{\rho}^{-1}\boldsymbol{N}_r \,\mathrm{d}V, \quad \boldsymbol{A}^{\mathsf{T}} = \int_V \boldsymbol{N}_u^{\mathsf{T}}\boldsymbol{N}_r \,\mathrm{d}V, \quad \hat{\boldsymbol{b}} = \int_V \boldsymbol{N}_u^{\mathsf{T}}\hat{\underline{b}} \,\mathrm{d}V \tag{32}$$

Solving first for $\boldsymbol{u}_{n+1}$ gives

$$\boldsymbol{B}^{\mathsf{T}}\boldsymbol{\sigma} + \boldsymbol{A}^{\mathsf{T}}\boldsymbol{r}_{n+1} = \hat{\boldsymbol{b}}_n + \alpha_{n+1}\boldsymbol{t} \tag{33}$$

which is imposed as a constraint to yield a final maximization problem given by

$$\boxed{\begin{aligned} \underset{(\alpha,\boldsymbol{\sigma},\boldsymbol{r})_{n+1}}{\text{maximize}} \quad & \alpha_{n+1} - \tfrac{1}{2}\Delta\boldsymbol{\sigma}_{n+1}^{\mathsf{T}}\boldsymbol{C}\Delta\boldsymbol{\sigma}_{n+1} - \tfrac{1}{2}\Delta t^2\boldsymbol{r}_{n+1}^{\mathsf{T}}\boldsymbol{D}\boldsymbol{r}_{n+1} \\ \text{subject to} \quad & \boldsymbol{B}^{\mathsf{T}}\boldsymbol{\sigma}_{n+1} + \boldsymbol{A}^{\mathsf{T}}\boldsymbol{r}_{n+1} = \hat{\boldsymbol{b}}_n + \alpha_{n+1}\boldsymbol{t} \\ & F_j(\boldsymbol{\sigma}_{n+1}) \leq 0, \;\; j = 1,\ldots,n \end{aligned}} \tag{34}$$

The problems of limit analysis and static elastoplasticity are both recovered by particular choices of the quantities entering into this problem. It is a rather notable, and to the authors knowledge not widely exploited, fact that inertial forces can be included in a variational formulation without making explicit reference to kinematic variables.

4.4 Karush-Kuhn-Tucker conditions

The Lagrangian associated with (34) is given by

$$\begin{aligned} L = {} & \alpha_{n+1} - \tfrac{1}{2}\Delta\boldsymbol{\sigma}_{n+1}^{\mathsf{T}}\boldsymbol{C}\Delta\boldsymbol{\sigma}_{n+1} - \tfrac{1}{2}\Delta t^2\boldsymbol{r}_{n+1}^{\mathsf{T}}\boldsymbol{D}\boldsymbol{r}_{n+1} \\ & + \Delta\boldsymbol{u}_{n+1}^{\mathsf{T}}(\boldsymbol{B}^{\mathsf{T}}\boldsymbol{\sigma}_{n+1} + \boldsymbol{A}^{\mathsf{T}}\boldsymbol{r}_{n+1} - \hat{\boldsymbol{b}}_n - \alpha_{n+1}\boldsymbol{t}) \\ & - \textstyle\sum_{j=1}^{n}\left\{\lambda_{n+1}^{j}[F_j(\boldsymbol{\sigma}_{n+1}) + s_j] + \mu\ln s_j\right\} \end{aligned} \tag{35}$$

where slack variables and penalty terms have been added following the methodology described earlier. The Karush-Kuhn-Tucker optimality conditions are given by

$$\begin{aligned}
\frac{\partial L}{\partial \boldsymbol{u}_{n+1}} &= \boldsymbol{B}^{\mathsf{T}}\boldsymbol{\sigma}_{n+1} + \boldsymbol{A}^{\mathsf{T}}\boldsymbol{r}_{n+1} - \hat{\boldsymbol{b}}_n - \alpha_{n+1}\boldsymbol{t} = \boldsymbol{0} \\
\frac{\partial L}{\partial \boldsymbol{r}_{n+1}} &= -\Delta t^2 \boldsymbol{D}\boldsymbol{r}_{n+1} + \boldsymbol{A}\Delta\boldsymbol{u}_{n+1} = \boldsymbol{0} \\
\frac{\partial L}{\partial \boldsymbol{\sigma}_{n+1}} &= \boldsymbol{B}\Delta\boldsymbol{u}_{n+1} - \boldsymbol{C}\Delta\boldsymbol{\sigma}_{n+1} - \textstyle\sum_{j=1}^{n} \lambda_{j,n+1}\nabla F_j(\boldsymbol{\sigma}_{n+1}) = \boldsymbol{0} \\
\frac{\partial L}{\partial \alpha_{n+1}} &= 1 - \boldsymbol{p}^{\mathsf{T}}\Delta\boldsymbol{u}_{n+1} = 0 \\
\frac{\partial L}{\partial \lambda^j_{n+1}} &= -[F_j(\boldsymbol{\sigma}_{n+1}) + \boldsymbol{s}^j_{n+1}] = 0, \quad j = 1, \ldots, n \\
\frac{\partial L}{\partial s^j_{n+1}} &= -\lambda^j_{n+1} + \mu s^j_{n+1} = 0 \Longrightarrow \lambda^j_{n+1} s^j_{n+1} = \mu, \quad j = 1, \ldots, n
\end{aligned} \tag{36}$$

Combining the first two optimality conditions gives the discrete momentum conservation equation in terms of stresses and displacements:

$$\boldsymbol{B}^{\mathsf{T}}\boldsymbol{\sigma}_{n+1} + \frac{1}{\Delta t^2}\left[\boldsymbol{A}^{\mathsf{T}}\boldsymbol{D}^{-1}\boldsymbol{A}\right]\Delta\boldsymbol{u}_{n+1} = \hat{\boldsymbol{b}}_n + \alpha_{n+1}\boldsymbol{t} \tag{37}$$

where the matrix $\boldsymbol{A}^{\mathsf{T}}\boldsymbol{D}^{-1}\boldsymbol{A}$ is equivalent to the mass matrix used in standard finite element formulations. In particular, if the dynamics forces $\underline{r}$ are approximated using the same shape functions as the displacements we have

$$\boldsymbol{A}^{\mathsf{T}}\boldsymbol{D}^{-1}\boldsymbol{A} = \int_V \boldsymbol{N}_u^{\mathsf{T}}\hat{\rho}\boldsymbol{N}_u \,\mathrm{d}V \tag{38}$$

This result is independent on whether $\underline{r}$ is considered to be continuous or discontinuous between elements. However, before solving programs of the type (27), the quadratic terms in the objective function are often accounted for by imposing equivalent quadratic inequalities. For this purpose the matrix square root of $\boldsymbol{D}$ is required and a discontinuous approximation of $\underline{r}$, which makes $\boldsymbol{D}$ block-diagonal, is then much more convenient although it leads to a higher number of variables in the final problem.

5 NONASSOCIATED FLOW RULES

In the previous sections, the flow rule has been associated. This is a natural consequence of the variational formulations employed. However, most frictional materials display a dilation significantly smaller than that predicted by the flow associated with the yield criterion. This would seem rule out the use of mathematical programming formulations for such materials. However, the authors have recently shown (Krabbenhoft et al. 2011) that nonassociated flow behaviour can be accommodated for incremental elastoplastic by essentially replacing the original yield function in each step, and at each yield check point, with a modified yield function that produces the desired dilation in an associated setting. The procedure is as follows. Let the original yield function to be imposed at time t_{n+1} be given by

$$F_{n+1} = q_{n+1} - Mp_{n+1} - k \leq 0 \tag{39}$$

where p and q are some measures of pressure and deviatoric stress respectively, M is friction coefficient and k is the internal cohesion. This yield condition may also be written as

$$F_{n+1} = q_{n+1} - Np_{n+1} - [k + (M - N)p_{n+1}] \leq 0 \tag{40}$$

where the term in square brackets can be interpreted as an effective pressure-dependent cohesion. This term may be evaluated explicitly so that

$$F^*_{n+1} = q_{n+1} - Np_{n+1} - [k + (M - N)p_n] \leq 0 \tag{41}$$

is imposed at t_{n+1}. Use of the associated flow rule thus gives a dilation proportional to N. This approach has proven very successful as demonstrated by the solution of a variety of complex boundary value problems involving large degrees of nonassociativity.

6 HARDENING SOIL MODELS

While the constitutive models considered so far have been of the simple rigid-plastic or linear-elatic/perfectly plastic kind, it is entirely possible to extend the basic methodology to more complex models involving hardening yield surfaces. A suitable time-discrete framework is the following problem which pertains to the material point level only (hence the use of bold rather than underlined symbols):

$$\begin{aligned} &\underset{(\boldsymbol{\sigma},\boldsymbol{\kappa})_{n+1}}{\text{maximize}} \quad \boldsymbol{\sigma}^{\mathsf{T}}_{n+1}\Delta\boldsymbol{\varepsilon}_{n+1} - \tfrac{1}{2}\Delta\boldsymbol{\sigma}^{\mathsf{T}}_{n+1}\mathbb{C}\Delta\boldsymbol{\sigma}_{n+1} - \tfrac{1}{2}\Delta\boldsymbol{\kappa}^{\mathsf{T}}_{n+1}\mathbb{H}^{-1}\Delta\boldsymbol{\kappa}_{n+1} \\ &\text{subject to} \quad F(\boldsymbol{\sigma}_{n+1}, \boldsymbol{\kappa}_{n+1}) \leq 0 \end{aligned} \tag{42}$$

where $\mathbb{H}$ is a new constitutive modulus associated with hardening, $\boldsymbol{\kappa}$ is a set of stress-like hardening variables, and the strain increment, $\Delta\boldsymbol{\varepsilon}_{n+1}$, is considered known. Following the usual procedure, we construct the associated Lagrangian:

$$\begin{aligned} L = \boldsymbol{\sigma}^{\mathsf{T}}_{n+1}\Delta\boldsymbol{\varepsilon}_{n+1} - \tfrac{1}{2}\Delta\boldsymbol{\sigma}^{\mathsf{T}}_{n+1}\mathbb{C}\Delta\boldsymbol{\sigma}_{n+1} - \tfrac{1}{2}\Delta\boldsymbol{\kappa}^{\mathsf{T}}_{n+1}\mathbb{H}^{-1}\Delta\boldsymbol{\kappa}_{n+1} \\ -\lambda_{n+1}\left[F(\boldsymbol{\sigma}_{n+1}, \boldsymbol{\kappa}_{n+1}) + s_{n+1}\right] + \mu \ln s_{n+1} \end{aligned} \tag{43}$$

for which stationarity is required:

$$\begin{aligned} &\frac{\partial L}{\partial \boldsymbol{\sigma}_{n+1}} = 0 \Longrightarrow \Delta\boldsymbol{\varepsilon}_{n+1} = \mathbb{C}\Delta\boldsymbol{\sigma}_{n+1} + \lambda_{n+1}\nabla_\sigma F(\boldsymbol{\sigma}_{n+1}, \boldsymbol{\kappa}_{n+1}) \\ &\frac{\partial L}{\partial \boldsymbol{\kappa}_{n+1}} = 0 \Longrightarrow \Delta\boldsymbol{\kappa}_{n+1} = -\lambda_{n+1}\mathbb{H}\nabla_\kappa F(\boldsymbol{\sigma}_{n+1}, \boldsymbol{\kappa}_{n+1}) \\ &\frac{\partial L}{\partial \lambda_{n+1}} = 0 \Longrightarrow F(\boldsymbol{\sigma}_{n+1}, \boldsymbol{\kappa}_{n+1}) + s_{n+1} = 0 \\ &\frac{\partial L}{\partial s_{n+1}} = 0 \Longrightarrow s_{n+1}\lambda_{n+1} = \mu \end{aligned} \tag{44}$$

The first optimality condition here comprises the usual stress-strain incorporating the additive decomposition of elastic and plastic strains while the second condition is the hardening law, i.e. the evolution law for the hardening variables κ. Note that this evolution law is similar in nature to the flow rule. We may thus classify such laws as being either associated (as in the above case) or nonassociated (in which case a variational formulation of the above kind is not possible).

6.1 Global variational principle

A global variational principle valid for solid body of a finite extent is achieved by extending the material point principle (42) to the entire domain. Moreover, the strain increment that was assumed given in this principle is related to a set of displacements which in general are unknown and are to be determined as part of the solution. The static form of the principle is given by

$$\begin{aligned} \min_{\underline{u}_{n+1}} \max_{(\alpha,\underline{\sigma})_{n+1}} \quad & \alpha_{n+1} + \int_V \underline{\sigma}_{n+1}^{\mathsf{T}} \Delta \underline{u}_{n+1} \,\mathrm{d}V - \int_V \underline{b}^{\mathsf{T}} \Delta \underline{u}_{n+1} \,\mathrm{d}V - \alpha_{n+1} \int_S \underline{t}^{\mathsf{T}} \Delta \underline{u}_{n+1} \,\mathrm{d}S \\ & - \tfrac{1}{2} \int_V \Delta \underline{\sigma}_{n+1}^{\mathsf{T}} \mathbb{C}_t \Delta \underline{\sigma}_{n+1} \,\mathrm{d}V - \frac{1}{2} \int_V \Delta \underline{\kappa}_{n+1}^{\mathsf{T}} \mathbb{H}_t^{-1} \Delta \underline{\kappa}_{n+1} \,\mathrm{d}V \\ \text{subject to} \quad & F(\underline{\sigma}_{n+1}, \underline{\kappa}_{n+1}) \le 0 \end{aligned} \tag{45}$$

which differs from the elastic/perfectly-plastic principle (12) only by the additional quadratic term in the objective function defining the hardening. A dynamic version of the principle can easily be achieved along the same lines.

6.2 Finite element discretization

The stress-like hardening variables are interpolated in a manner similar to the stresses:

$$\underline{\kappa}(\underline{x}) \approx \boldsymbol{N}_\kappa(\underline{x}) \boldsymbol{\kappa} \tag{46}$$

Inserting into the continuous variation principle shown above and pre-solving the minimization part of the problem gives the following discrete maximization problem:

$$\boxed{\begin{aligned} \underset{(\alpha,\boldsymbol{\sigma})_{n+1}}{\text{maximize}} \quad & \alpha_{n+1} - \tfrac{1}{2} \Delta \boldsymbol{\sigma}_{n+1}^{\mathsf{T}} \boldsymbol{C}_t \Delta \boldsymbol{\sigma}_{n+1} - \tfrac{1}{2} \Delta \boldsymbol{\kappa}_{n+1}^{\mathsf{T}} \boldsymbol{H}_t^* \Delta \boldsymbol{\kappa}_{n+1} \\ \text{subject to} \quad & \boldsymbol{B}^{\mathsf{T}} \boldsymbol{\sigma}_{n+1} = \boldsymbol{b} + \alpha_{n+1} \boldsymbol{t} \\ & F_j(\boldsymbol{\sigma}_{n+1}) \le 0, \;\; j = 1, \ldots, n \end{aligned}} \tag{47}$$

where

$$\boldsymbol{C}_t = \int_V \boldsymbol{N}_\sigma^{\mathsf{T}} \mathbb{C}_t \boldsymbol{N}_\sigma \,\mathrm{d}V, \quad \boldsymbol{H}_t^* = \int_V \boldsymbol{N}_\kappa^{\mathsf{T}} \mathbb{H}_t^{-1} \boldsymbol{N}_\kappa \,\mathrm{d}V \tag{48}$$

All previous results concerning duality are again valid.

6.3 Material point tests

To test the above formulations we consider two drained triaxial tests using the modified Cam clay model. The material parameters are: $\kappa^* = 0.01$, $\lambda^* = 0.03$, $M = 1.1$, $G = 5,000\,\text{kPa}$. The initial pressure is 50 kPa and two different overconsolidation ratios are used: OCR = 1.5 and OCR = 5.0.

Confining ourselves to the material point level, the problem of drained triaxial compression can be cast in terms of the following optimization problem:

$$\begin{aligned} \underset{(p,q,\kappa)}{\text{maximize}} \quad & \Delta\varepsilon_1 \alpha - \tfrac{1}{2} \Delta p^{\mathsf{T}} K_t^{-1} \Delta p - \tfrac{1}{2} \Delta q^{\mathsf{T}} (3G)^{-1} \Delta q - \tfrac{1}{2} \Delta \kappa^{\mathsf{T}} \mathbb{H}_t^{-1} \Delta \kappa \\ \text{subject to} \quad & \sigma_1 = \alpha \\ & \sigma_3 = \sigma_3^0 \\ & p = \tfrac{1}{3}(\sigma_1 + 2\sigma_3) \\ & q = \sigma_1 - \sigma_3 \\ & F(p, q, \kappa) \le 0 \end{aligned} \tag{49}$$

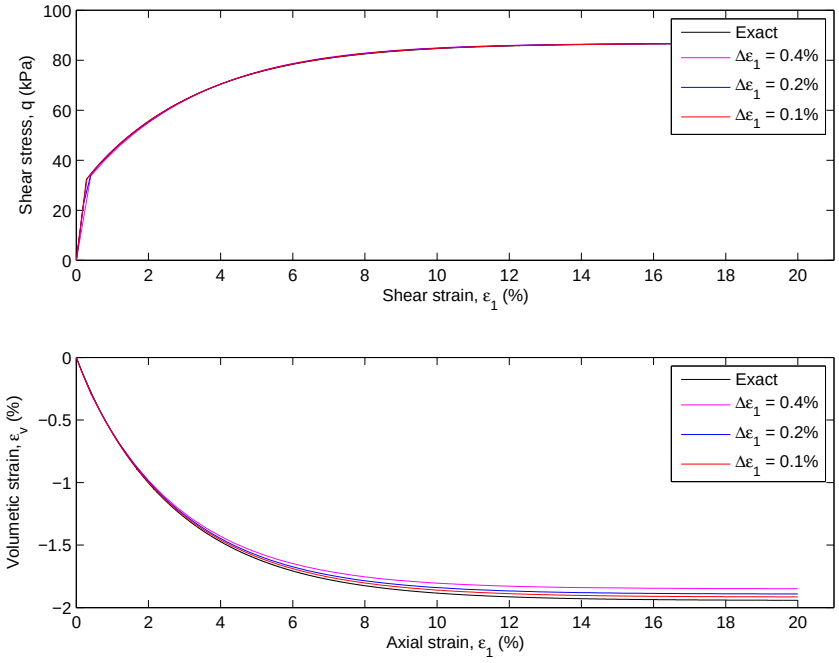

Fig. 1. Results of drained triaxial compression with OCR = 1.5.

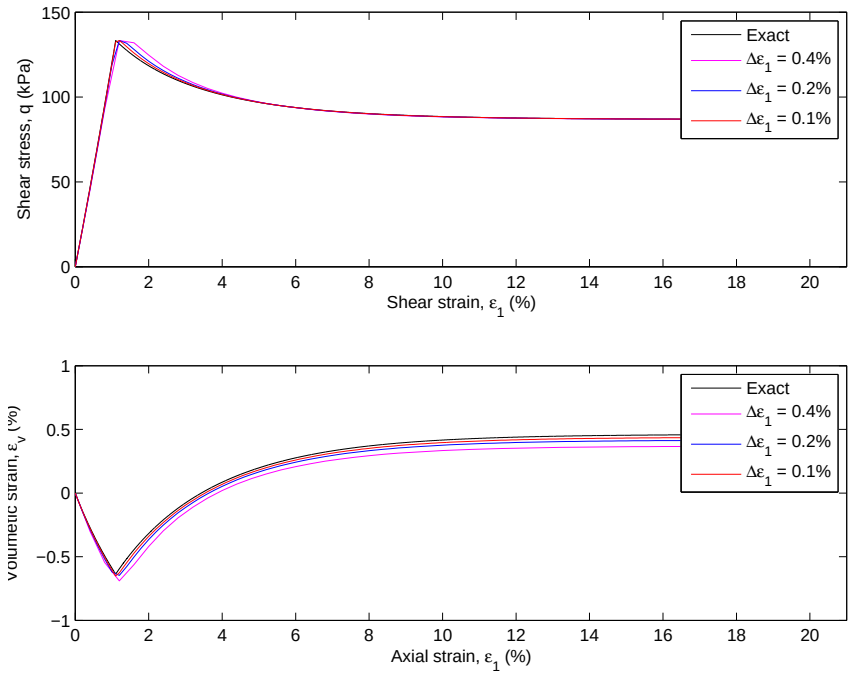

Fig. 2. Results of drained triaxial compression with OCR = 5.0.

where $\Delta\varepsilon_1$ is the prescribed axial strain increment.
The results are shown in the figures below for 50, 100, and 200 axial strain increments of equal magnitude. In both cases the performance of the mathematical programming scheme appears to

be satisfactory. In the case of softening behaviour, a new scheme which retains convexity of the problem has been used. This scheme will be detailed elsewhere.

7 CONCLUSIONS

Starting from the basic problem of rigid-plastic limit analysis, we can developed mathematical programming formulations of

- Static step-by-step elastoplasticity (Section 3)
- Dynamic elastoplasticity (Section 4)
- Nonassociated plasticity (Section 5)
- Hardening plasticity as exemplified by modified Cam clay (Section 6)

These developments showcase the significant versatility of mathematical programming as a tool for computational plasticity.

REFERENCES

Boyd, S. & Vandenberghe, L. (2006). Convex Optimization. Cambridge University Press.

Krabbenhoft, K., Lyamin, A. V., & Sloan, S. W. (2011). Associated computational plasticity schemes for nonassociated frictional materials. Int. J. Num. Meth. Engng.. Under review.

Nash, S. G. & Sofer, A. (1996). Linear and Nonlinear Programming. New York, N.Y.: McGraw-Hill.

Simo, J. C. & Hughes, T. J. R. (1998). Computational Inelasticity. Springer–Verlag.

Vanderbei, R. J. (2001). Linear Programming: Foundations and Extensions. Springer–Verlag.

Weinstock, R. (1974). Calculus of Variations with Applications to Physics and Engineering. Dover.

INTERFACE CONDITIONS MODELLING IN COMPUTATIONAL LIMIT ANALYSIS

A.V. Lyamin
Centre for Geotechnical and Materials Modelling, University of Newcastle, Australia

K. Krabbenhøft
Centre for Geotechnical and Materials Modelling, University of Newcastle, Australia

S.W. Sloan
Centre for Geotechnical and Materials Modelling, University of Newcastle, Australia

ABSTRACT: *In many geotechnical stability problems it is important to account for interface conditions between soil and structure, e.g. retaining walls and footings with no-tension contact. These interfaces can be considered as discontinuities in stress and velocity fields developed in the system undergoing plastic collapse. Discontinuous variable fields are often employed in FE lower and upper bound limit analyses to improve the performance of lower order elements used to obtain rigorous bounds on the collapse factor. Recently it was shown that these discontinuities can be conveniently represented by a patch of regular elements of zero thickness. This development opens the way for discontinuous LA formulations to be used with general yield criteria in both two- and three-dimensions to solve stability problems involving a wide variety of materials and interface conditions.*

1 DISCRETE FORMULATION OF BOUND THEOREMS

Consider a domain Ω with boundary Γ, as shown in Fig. 1. Let $\mathbf{t}$ and $\mathbf{q}$ denote, respectively, a set of fixed tractions acting on the part of the boundary Γ_t and a set of unknown tractions acting on the part of the boundary Γ_q. Similarly, let $\mathbf{g}$ and $\mathbf{h}$ be a system of fixed and unknown body forces which act, respectively, on the volume Ω. Under these conditions, the objective of a lower bound calculation is to find a stress distribution which satisfies equilibrium throughout Ω, balances the prescribed tractions $\mathbf{t}$ on Γ_t, nowhere violates the yield criterion, and maximises the integral

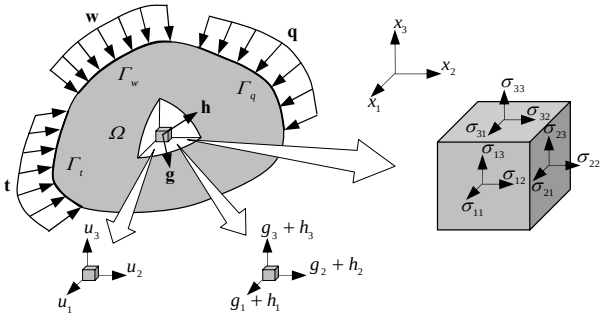

Fig. 1. A domain subject to a system of surface and body forces.

$$Q = \int_{\Gamma_q} \mathbf{q} \mathrm{d}\Gamma + \int_{\Omega} \mathbf{h} \mathrm{d}\Omega \tag{1}$$

The objective of an upper bound calculation is to find a velocity distribution **u** which satisfies compatibility, the flow rule, the velocity boundary conditions **w** on the surface area Γ_w, and minimises the integral

$$W^{internal} = \int_{\Omega} \boldsymbol{\sigma} \dot{\boldsymbol{\varepsilon}} \, \mathrm{d}\Omega \tag{2}$$

An upper bound estimate on the true collapse load can be obtained by equating $W^{internal}$ to the power dissipated by the external loads

$$W^{external} = \int_{\Gamma_t} \mathbf{t}^{\mathrm{T}} \mathbf{u} \mathrm{d}\Gamma + \int_{\Gamma_q} \mathbf{q}^{\mathrm{T}} \mathbf{u} \, \mathrm{d}\Gamma + \int_{\Omega} \mathbf{g}^{\mathrm{T}} \mathbf{u} \, \mathrm{d}\Omega + \int_{\Omega} \mathbf{h}^{\mathrm{T}} \mathbf{u} \, \mathrm{d}\Omega \tag{3}$$

To preserve the bounding properties of the numerical solutions, linear finite elements are used to discretise the continuum. In an effort to provide the best possible bounds, kinematically admissible velocity discontinuities and statically admissible stress discontinuities are permitted at all inter-element boundaries for, respectively, the upper and lower bound analyses (Sloan and Kleeman, 1995; Sloan, 1988). These discontinuities allow accurate estimates of the collapse load to be computed without using an excessive number of elements and can be efficiently implemented using the approach described in following sections.

2 VELOCITY DISCONTINUITIES AS A PATCH OF THIN ELEMENTS

A general approach for modelling a discontinuous velocity field in *D* dimensions, regardless of the yield criterion involved, can be derived by treating a discontinuity as a patch of *D* infinitely-thin elements (Krabbenhøft et al., 2005). The problem model is then simplified because the power dissipation given by (2) can be computed as the sum of contributions from all elements in the mesh. We will next show that using linear finite elements for the problem discretisation results in an a priori simplification for velocity discontinuities which are valid for general yield criteria.

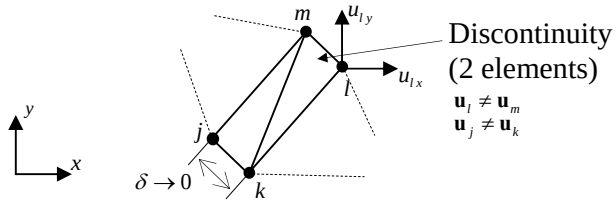

Fig. 2. Discontinuity as a patch of interconnected thin elements – upper bound.

For illustrative purposes let us consider a two-dimensional patch of interconnecting triangles shown in Fig. 2. Each triangle is a constant stress-linear velocity element with the velocity vector, **u**, varying according to

$$\mathbf{u} = \sum_i N_i(x, y) \mathbf{u}_i \,, \qquad N_i(x, y) = \frac{a_i + b_i x + c_i y}{2\Delta} \tag{4}$$

where Δ is the area of the triangle and coefficients *a*, *b*, *c* are computed from nodal

coordinates as follows

$$a_k = x_l y_m - x_m y_l\,, \quad b_k = y_l - y_m\,, \quad c_k = x_m - x_l \tag{5}$$

for node *k* and then with cyclic interchanges of indexes for nodes *l* and *m*. The compatibility matrix $\mathbf{B}$ is given by

$$\mathbf{B} = \left[\mathbf{B}_k\ \mathbf{B}_l\ \mathbf{B}_m\right] = \frac{1}{2\Delta}\begin{bmatrix} b_k & 0 & b_l & 0 & b_m & 0 \\ 0 & c_k & 0 & c_l & 0 & c_m \\ c_k & b_k & c_l & b_l & c_m & b_m \end{bmatrix} = \frac{1}{\Delta}\left[\bar{\mathbf{B}}_k\ \ \bar{\mathbf{B}}_l\ \ \bar{\mathbf{B}}_m\right] = \frac{1}{\Delta}\bar{\mathbf{B}} \quad \text{or} \quad \bar{\mathbf{B}} = \mathbf{B}\Delta \tag{6}$$

and the power dissipated in any triangular element, regardless of its area, is calculated from

$$W = \int_\Delta \boldsymbol{\sigma}\dot{\boldsymbol{\varepsilon}}\,\mathrm{d}\Delta = \int_\Delta \boldsymbol{\sigma}\mathbf{B}\mathbf{u}\,\mathrm{d}\Delta = \boldsymbol{\sigma}\bar{\mathbf{B}}\mathbf{u} = \boldsymbol{\sigma}\bar{\dot{\boldsymbol{\varepsilon}}} \tag{7}$$

The flow rule can be presented in a similar way as

$$\bar{\mathbf{B}}\mathbf{u} = \Delta \times \dot{\lambda}\nabla f(\boldsymbol{\sigma}) = \bar{\dot{\lambda}}\nabla f(\boldsymbol{\sigma}) \tag{8}$$

Considering now the case of an infinitely thin element with side *lm* being collapsed, we find that $\bar{\mathbf{B}}_k \to \mathbf{0}$ and $\bar{\mathbf{B}}_l \to -\bar{\mathbf{B}}_m$, resulting in the compatibility matrix

$$\hat{\mathbf{B}} = \left[\mathbf{0}\ -\bar{\mathbf{B}}_{lm}\ \bar{\mathbf{B}}_{lm}\right] \tag{9}$$

where $\bar{\mathbf{B}}_l$ has been replaced by $\bar{\mathbf{B}}_{lm}$ for notation convenience. It is readily seen that the strain rate in element *k*, *l*, *m* in this case can be expressed in terms of differences between velocities (velocity jumps) at nodes *l* and *m* leading to

$$\dot{\boldsymbol{\varepsilon}} = \hat{\mathbf{B}}\mathbf{u} = \bar{\mathbf{B}}_{lm}\Delta\mathbf{u}^{lm} \tag{10}$$

Krabbenhøft et al. (2005) showed that expression (10), when employed for a Mohr-Coulomb criterion, leads to the conventional expressions for the flow rule and power dissipation in the discontinuities. But modelling the discontinuities as patches of infinitely thin elements avoids any need for special treatment. Indeed, the power dissipation is computed using (7) and the flow rule constraints are given by (8). These constraints are actually obtained automatically as part of the system of optimality conditions for the upper bound optimization problem.

3 STRESS DISCONTINUITIES AS A PATCH OF THIN ELEMENTS

An efficient lower bound formulation requires statically admissible stress discontinuities between adjacent elements (Fig. 3). The constraints for these discontinuities are that only

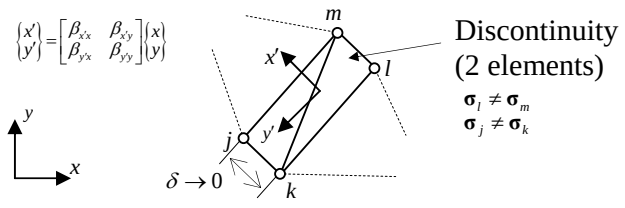

Fig. 3. Discontinuity as a patch of interconnected thin elements – lower bound.

normal and shear stresses must be continuous across the inter-element boundary. We now show that this requirement is equivalent to the element equilibrium conditions written for the discontinuity elements in the patch. Using the notation introduced in the previous section, the equilibrium conditions for element *k, l, m* can be written as

$$\mathbf{B}^{\mathrm{T}}\boldsymbol{\sigma} = \begin{bmatrix} \mathbf{B}_k^{\mathrm{T}} \; \mathbf{B}_l^{\mathrm{T}} \; \mathbf{B}_m^{\mathrm{T}} \end{bmatrix} \begin{Bmatrix} \boldsymbol{\sigma}^k \\ \boldsymbol{\sigma}^l \\ \boldsymbol{\sigma}^m \end{Bmatrix} = \frac{1}{\Delta} \begin{bmatrix} \bar{\mathbf{B}}_k^{\mathrm{T}} \; \bar{\mathbf{B}}_l^{\mathrm{T}} \; \bar{\mathbf{B}}_m^{\mathrm{T}} \end{bmatrix} \begin{Bmatrix} \boldsymbol{\sigma}^k \\ \boldsymbol{\sigma}^l \\ \boldsymbol{\sigma}^m \end{Bmatrix} = -(\mathbf{g} + \mathbf{h}) \tag{11}$$

which is equivalent to

$$\begin{bmatrix} \bar{\mathbf{B}}_k^{\mathrm{T}} \; \bar{\mathbf{B}}_l^{\mathrm{T}} \; \bar{\mathbf{B}}_m^{\mathrm{T}} \end{bmatrix} \begin{Bmatrix} \boldsymbol{\sigma}^k \\ \boldsymbol{\sigma}^l \\ \boldsymbol{\sigma}^m \end{Bmatrix} = -(\mathbf{g} + \mathbf{h})\Delta \tag{12}$$

For a zero volume element with side *lm* being collapsed, Eqn. (12) becomes

$$\begin{bmatrix} \mathbf{0} \; -\bar{\mathbf{B}}_{lm}^{\mathrm{T}} \; \bar{\mathbf{B}}_{lm}^{\mathrm{T}} \end{bmatrix} \begin{Bmatrix} \boldsymbol{\sigma}^k \\ \boldsymbol{\sigma}^l \\ \boldsymbol{\sigma}^m \end{Bmatrix} = \mathbf{0} \quad \text{or} \quad \bar{\mathbf{B}}_{lm}^{\mathrm{T}}\boldsymbol{\sigma}^l = \bar{\mathbf{B}}_{lm}^{\mathrm{T}}\boldsymbol{\sigma}^m \tag{13}$$

The last of equations (13) represents the equality of surface tractions between nodes *l* and *m*. After dividing the coefficients b_l and c_l of matrix $\bar{\mathbf{B}}_{lm}$ by the length of the discontinuity *L*, we obtain the direction cosines $\beta_{x'x}, \beta_{x'y}$ for the axis x'. Thus (11) finally leads to

$$\begin{Bmatrix} t_x^l \\ t_y^l \end{Bmatrix} = \begin{Bmatrix} t_x^m \\ t_y^m \end{Bmatrix} \tag{14}$$

Application of the conditions (14) is equivalent to setting the normal/shear stresses to be equal at nodes *l* and *m*, as these are linearly related to surface tractions by

$$\begin{Bmatrix} \sigma_n^l \\ \sigma_\tau^l \end{Bmatrix} = \begin{bmatrix} \beta_{x'x} & \beta_{x'y} \\ \beta_{y'x} & \beta_{y'y} \end{bmatrix} \begin{Bmatrix} t_x^l \\ t_y^l \end{Bmatrix} \tag{15}$$

Therefore, the approach of treating discontinuities as a patch of zero volume elements also suits the lower bound formulation, as no special "discontinuity constraints" need to be introduced. Indeed, simple application of the familiar equilibrium conditions is sufficient to ensure that the discontinuity is statically admissible.

4 INTERFACES MODELLING

4.1 Interfaces Between Material Domains

The arrangement of the elements at an interface and the locations of the stress and velocity nodes are presented in Fig. 4. Assuming an associated flow rule, the interface conditions are governed by the yield function in the zero thickness elements. For upper bound analysis, only one layer of discontinuity elements in the interface is needed as these elements have

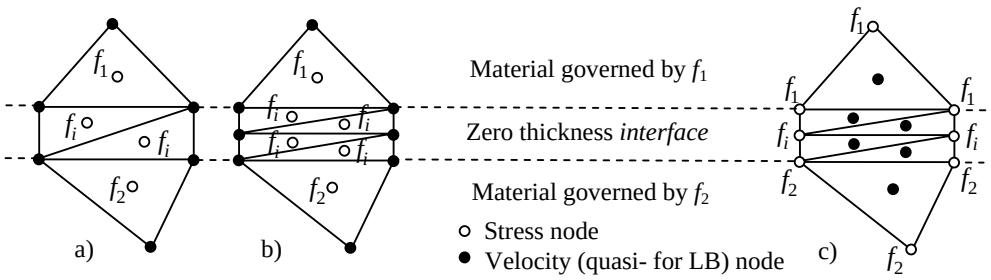

Fig. 4. Interface layout for upper (a), (b) and lower (c) bound formulations.

separate stress variables (Fig. 4a). For lower bound meshes this is not the case and two layers of zero thickness elements are essential to prescribe material properties to the stress points which are separate from the stress points of the domains adjoining the interface. To make the patch symmetric, two layers of elements are used by default for both lower and upper bound limit analysis in proposed implementation.

To demonstrate the feasibility of the approach the plane strain collapse of a surface footing on clay subjected to vertical eccentric loading (Fig. 5) is considered. Two kinds of interface conditions are modelled: full adhesion and tension cut off. The collapse mechanisms shown and corresponding bearing capacity values demonstrate the influence of the tension cut-off condition.

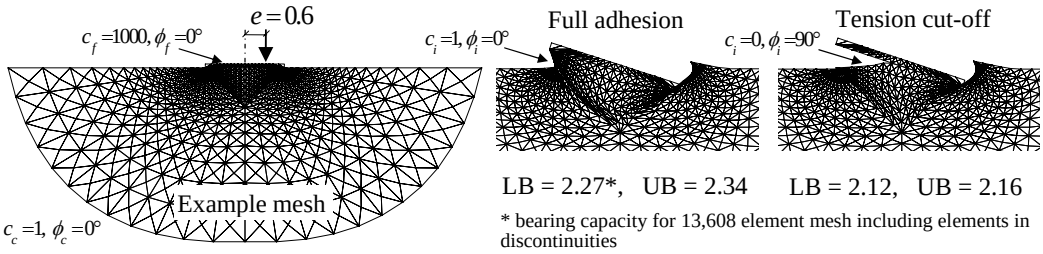

Fig. 5. Strip footing on clay subject to eccentric (e=0.6) loading with full adhesion and tension cut-off interface conditions.

4.2 Interfaces at Segments Subject to Boundary or Loading

Modelling of surface effects under applied loading or boundary conditions can proceed in the same manner as it was done for implementing the interfaces between materials. Furthermore, only one layer of zero thickness elements is sufficient in this case as we already have stress nodes which are "outside" of the domain. Therefore, for these nodes any desired yield conditions can be applied without interference with the material assumed for the domain itself (Fig. 6).

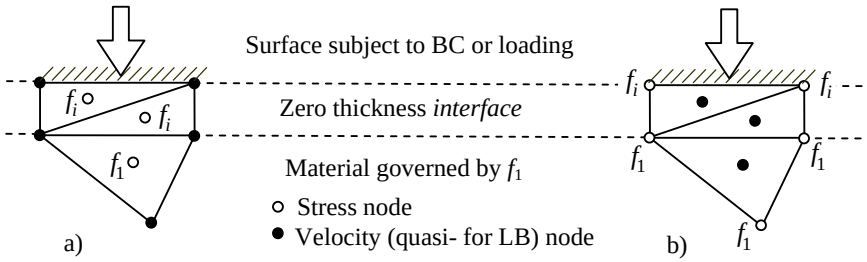

Fig. 6. Surface interface layout for upper (a) and lower (b) bound formulations.

The simple example of vertical loading of a cohesive-frictional (c=1, ϕ=20°) rectangular block laying on a flat surface is used (Fig. 7) to show a few possible scenarios of using the element patch interfaces between the applied loading or boundary and the problem domain. Three different cases of interface conditions are modeled with corresponding collapse mechanisms and limit loads shown in Fig. 7.

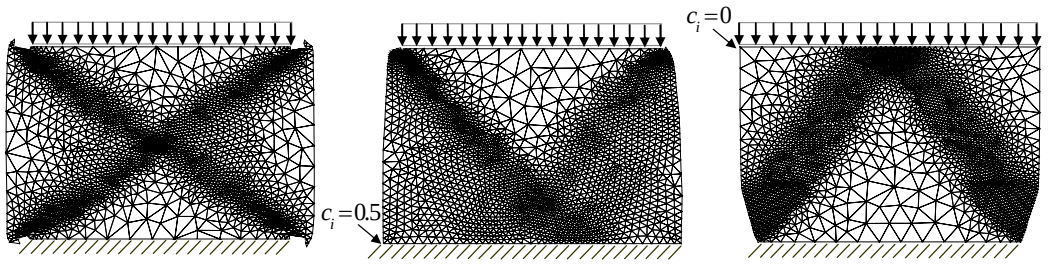

Fig. 7. Collapse of rectangular block (H/B=0.8) subject to rigid vertical loading with:
a) rough top/rough bottom; b) rough top/partially rough bottom; c) smooth top/rough bottom.

4.3 Interfaces for Overlapping Connections

Quite often in geotechnical engineering a series of plane strain stability analyses is performed on critical sections of the original 3D problem to make the case computationally feasible. This practice is common for such problems as the bearing capacity of foundations and the stability of dams, slopes and retaining walls. For anchor supported retaining walls, a problem arises in the modelling of anchors/ties without simultaneously introducing an artificial reinforcement effect. One efficient solution is to take the connection between the wall and the anchor "out" of the soil and make it overlap. This requires a special connection interface

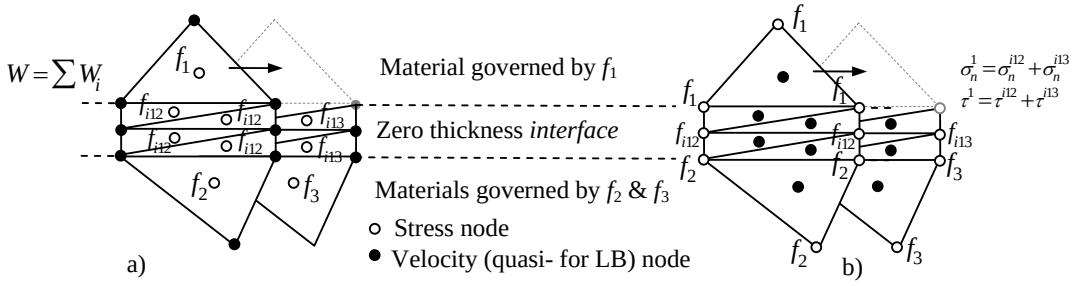

Fig. 8. Dual connection interface for upper (a) and lower (b) bound formulations.

which preserves the wall interaction with the soil and at the same time connects it to the anchor tie. Such complex connections can be modelled efficiently by using multilayered zero thickness patches of elements, as shown in Fig. 8. The upper bound implementation of multilayered interfaces is straightforward, as the power dissipated at the interface is just a sum of powers dissipated in all interface elements. For a lower bound analysis, a small adjustment is needed to the single layer implementation. In this case, the shear and normal tractions for nodes on the unsplit side must be equal to the sum of the shear and normal tractions of each of the layers (Fig. 8 b).

Fig. 9 shows an anchored sheet pile wall with the anchor tie implemented as a) interacting with the surrounding soil and b) overlapping the soil with a double-layered interface connection to the wall. The dual layer connection interface employed for this problem also includes a moment free wall/tie connection and no-tension conditions between the wall and the adjacent soil. The difference in the collapse pattern and bound values underlines the importance of selection the model appropriately.

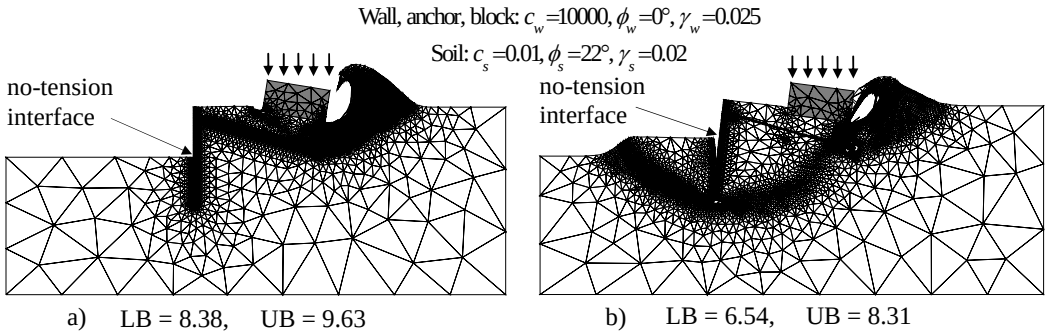

Fig. 9. Building with anchored sheet pile wall support: a) anchor tie is in contact with soil, b) anchor tie overlaps the soil and is connected to the wall using dual layer interface.

4.4 Moment-Free Interfaces for Joints Modelling

Usually structural elements have to be used to model joints with rotation. However, moment free connections can be implemented without any special elements by applying equality constraints on the stresses and velocities of the surface nodes of adjoining domains as shown in Fig. 10. These constraints ensure force and moment equilibrium across the joint for static formulations and rigid segment rotation for kinematic formulations, thus preserving the rigor of both lower and upper bound analyses.

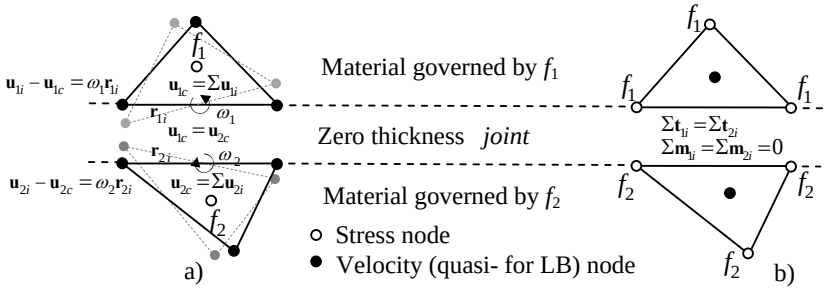

Fig. 10. Moment free joint constraints for upper (a) and lower (b) bound formulations.

The case of dual leg footing failure is used here to check the implementation of joints for limit analysis applications (Fig. 11). Two extreme cases are considered: a) the foundation panel is fully attached to the legs; b) the panel is attached to the legs via moment free joints. The load applied is inclined at 30 degrees to the horizontal, thus inducing quite distinctive

modes of collapse, namely sliding and rotational failure, as shown in Fig. 11 a) and b).

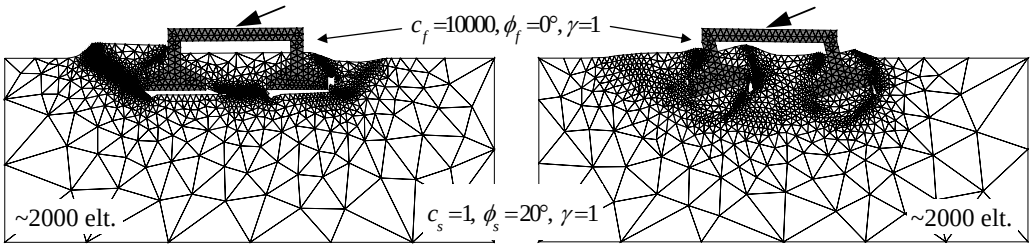

a) LB = 13.81, UB = 14.95 b) LB = 9.62, UB = 10.99

Fig. 11. Failure of panel resting on pair of footing legs and subject to inclined (30°) loading: panel is fully attached to footings, b) panel is attached via moment free joints.

CONCLUSIONS

A novel approach for modelling interface in the framework of numerical limit analysis has been presented. The method is based on a patch of zero thickness "solid" elements of regular topology with the properties of the interface material governed by the assumed yield criterion enforced at the corresponding stress points. Since all the conditions of the limit theorems are satisfied, the resultant kinematic and static formulations furnish rigorous upper and lower bounds and can be used for two- and three-dimensional stability problems with various interface conditions that are governed by general types of yield criteria.

REFERENCES

Krabbenhøft K., Lyamin A.V., Hijaj M., Sloan S.W. (2005), "A new discontinuous upper bound limit analysis formulation". Int. J. Num. Meth. Eng., Vol. 63, 1069-1088.

Lyamin A.V., Krabbenhøft K., Abbo, A.J., Sloan S.W. (2005), "General approach to modelling discontinuities in limit analysis". Proceedings of IACMAG 11, Turín.

Sloan S.W. and Kleeman P.W. (1995), "Upper bound limit analysis using discontinuous velocity fields". Comp. Meth. Appl. Mech. Eng., Vol. 127, 293-314.

Sloan S.W. (1988), "Lower bound limit analysis using finite elements and linear programming". Int. J. Num. Anal. Meth. Geomech., Vol. 12, 61–77.

APPLICATION OF h-ADAPTIVE FE METHOD FOR DYNAMIC ANALYSIS OF GEOTECHNICAL PROBLEMS

M. Nazem, M. Kardani, J.P. Carter and D. Sheng

Centre for Geotechnical and Materials Modelling
The University of Newcastle, NSW, Australia

ABSTRACT: *h-adaptive finite element procedures automatically change and optimise the density of a finite element mesh in a region to obtain a more accurate solution or to avoid mesh distortion in large deformation problems. These goals are usually achieved by generating a new finite element mesh over the integration domain based upon an error estimation or a distortion criterion. In this study an h-adaptive finite element method is suggested to solve dynamic problems of geomechanics involving large deformations. This h-adaptive technique is based upon an implicit Updated-Lagrangian method, in which mesh distortion and entanglement of elements are intrinsic pitfalls. A summary of the h-adaptive technique is presented by introducing its important aspects such as error estimation, remapping of time-dependent state variables, and dynamic equilibrium checks. The efficiency and robustness of the method is demonstrated by considering numerical examples characterised by inertia forces and large deformations.*

1 INTRODUCTION

In many problems of geomechanics, soil is subjected to dynamic or impact loads while also undergoing large deformations. Ordinary finite element methods, such as the Updated-Lagrangian method, fail to provide an accurate solution for such problems, mainly due to mesh distortion and entanglements of elements. Adaptive finite element methods have been developed to overcome the problem of mesh distortion as well as to improve the accuracy of the finite element solution. The r-adaptive finite element method, also known as the Arbitrary Lagrangian-Eulerian (ALE) method, has been established for a wide range of geotechnical applications including the static analysis of solids (Nazem et al. 2006), the analysis of consolidation of soils (Nazem et al. 2008) and dynamic analysis of soil under rapid loads and impacts (Nazem et al. 2009). The ALE method refines the spatial location of the mesh nodes, but does not change the topology of the problem domain. Although robust, the ALE method may not be efficient in problems involving localised failure or stress concentration. On the other hand, the h-adaptive finite element method regularly increases the number of the elements and the nodes by subdividing the elements to predict a more accurate solution. This method is well established in solid mechanics, but its pertinence in geotechnical engineering, particularly in large deformation problems, is yet to be investigated. One of the early applications of the h-adaptive technique in geomechanics was presented by Hu and Randolph (1998), where the analysis is performed assuming small deformations only, and is followed by remeshing the entire problem domain. In this study an

alternative h-adaptive finite element method is suggested to solve dynamic problems of geomechanics involving large deformations.

2 h-ADAPTIVE FINITE ELEMENT METHOD

The method presented here for dynamic analysis by the h-adaptive finite element technique includes four main steps. In the first step, the Updated Lagrangian (UL) method is employed to solve the global governing equations to achieve dynamic equilibrium. Secondly, a new finite element mesh is generated based on the new sizes of the elements, usually obtained by an error estimator which calculates the error in each element and determines which areas should be subdivided into smaller elements. In the third step, all nodal variables and state variables at integration points are transformed from the old mesh to the new generated mesh. Finally, an automatic procedure must be employed to check and satisfy the dynamic equilibrium at the global level as well as the principle of plasticity consistency at each integration point inside the elements. Each step is briefly explained in the following.

2.1 The Updated-Lagrangian method

In each time step of the analysis the h-adaptive procedure starts with an UL step to calculate the displacements, velocities and accelerations which satisfy the principle of virtual work according to

$$\int_V \sigma_{ij}\delta\varepsilon_{ij}dV + \int_V \delta u_i \rho \ddot{u}_i dV + \int_V \delta u_i c\dot{u}_i dV = \int_V \delta u_i b_i dV + \int_S \delta u_i q_i dS \tag{1}$$

in which δu is an arbitrary virtual displacement, σ represents the Cauchy stress tensor, $\delta\varepsilon$ is the variation of strain due to virtual displacement, u, $\dot{u}$ and $\ddot{u}$ denote displacements, velocities and accelerations, respectively, ρ and c represent the material density and damping, b is the body force, q is the surface load acting on area S of volume V. Linearisation of equation (1) provides the matrix form of equilibrium equation as in the following

$$\mathbf{M}\ddot{\mathbf{u}}^{t+\Delta t} + \mathbf{C}\dot{\mathbf{u}}^{t+\Delta t} + \mathbf{F}_{int}^{t+\Delta t} = \mathbf{F}_{ext}^{t+\Delta t} \tag{2}$$

where **M** is the mass matrix, **C** represents the damping matrix, $\mathbf{F}_{int}$ and $\mathbf{F}_{ext}$ are the internal and external force vectors, respectively, **u** is the displacement vector, and a superimposed dot represents the time derivative of a variable.

2.2 Error estimator and mesh generation

Boroomand and Zienkiewicz (1999) presented an error estimator for nonlinear elasto-plastic materials based on the energy norm, which is adopted in this study. The error in each element, e_{el}, is obtained by

$$\|e_{el}\| = \int \left| \left(\sigma^* - \hat{\sigma}\right)^T \left(\Delta\varepsilon^* - \Delta\hat{\varepsilon}\right) \right| dV_{el} \simeq \sum_{i=1}^{ngp} w_i \left(\sigma_i^* - \hat{\sigma}_i\right)\left(\Delta\varepsilon_i^* - \Delta\hat{\varepsilon}_i\right) \tag{3}$$

where σ^* and $\Delta\varepsilon^*$ are recovered stresses and incremental strains, respectively, $\hat{\sigma}$ and $\Delta\hat{\varepsilon}$ represent the corresponding finite element approximations, V_e is the domain of the element, w is the Gauss quadrature weight, and *ngp* indicates the total number of integration points in the element. With the knowledge of the error in each element we can calculate the error in the finite element domain, estimate the relative error of each element, and obtain the new size of

each element. In two-dimensional problems the new area of each element, A_{new}, is calculated by

$$A_{new} = A_{old}\left(\frac{\bar{\eta}\sqrt{\sum_{j=1}^{N}\sum_{i=1}^{ngp} w_i \sigma_{ji}^{*T}\Delta\varepsilon_{ji}^{*}}}{\|e_{el}\|\sqrt{N}}\right)^{\frac{1}{p}} \tag{4}$$

where A_{old} is the old area of the element, p is the polynomial order of the shape functions, N represents the total number of elements and $\bar{\eta}$ is a prescribed accuracy.

After calculating the new area of each element, a mesh generation algorithm, based on the Delaunay triangulation, generates a new mesh for the entire domain of the problem.

2.3 Remapping of variables

The state variables in the newly generated finite element mesh must be calculated based on their old values using a robust remapping scheme. Note that this procedure is only required for the new nodal points as well as the new elements. Nodal variables, such as displacements, velocities and accelerations, can be remapped from the old mesh to the new mesh by a direct interpolation using the displacement shape functions. Remapping of the variables at Gauss points, on the other hand, is more challenging. First, the variables in a patch are computed using the super convergent patch recovery technique (Zienkiewicz and Zhu, 1992). This method estimates the quantities in a patch using a polynomial of the same order as the displacements, and uses the least square technique to find the unknown coefficients of the polynomial. Then, the state variables at all new Gauss points are obtained by substituting their coordinates in the polynomial describing the distribution of the variables over the patch.

2.4 Retrieving dynamic equilibrium

After remapping the state variables, the equilibrium in the new mesh is yet to be satisfied. Moreover, for elastoplastic soil models, the principle of plasticity consistency may be violated due to some stress points lying outside the yield surface. In this study, we use the Newmark's integration scheme to conduct further iterations to guarantee equilibrium as well as plasticity consistency. Employing the Newton-Raphson method, the following equation needs to be solved in each iteration

$$\begin{aligned}\left[\frac{\mathbf{M}}{\beta\cdot\Delta t^2}+\frac{\mathbf{C}}{\beta\cdot\Delta t}+\mathbf{K}_{(i-1)}\right]\cdot\Delta\mathbf{u}_{(i)} &= \Delta\mathbf{F}_{ext}^{t+\Delta t}-\Delta\mathbf{F}_{int(i-1)}^{t+\Delta t}-\mathbf{M}\left[\frac{\mathbf{u}_{(i-1)}^{t+\Delta t}-\mathbf{u}^{t}}{\beta\cdot\Delta t^2}-\frac{\dot{\mathbf{u}}^{t}}{\beta\cdot\Delta t}-\frac{(1-2\beta)\ddot{\mathbf{u}}^{t}}{2\beta}\right]\\ -\mathbf{C}\left[\frac{\delta\left(\mathbf{u}_{(i-1)}^{t+\Delta t}-\mathbf{u}^{t}\right)}{\beta\cdot\Delta t}+\frac{(\beta-\delta)\dot{\mathbf{u}}^{t}}{\beta}+\Delta t\left(1-\frac{\delta}{2\beta}\right)\ddot{\mathbf{u}}^{t}\right]&\end{aligned} \tag{5}$$

where β and δ are the Newmark integration parameters, Δt represents the time step, and $\mathbf{K}$ is the tangential stiffness matrix.

3 NUMERICAL EXAMPLES

The h-adaptive finite element described in Section 2 has been implemented in SNAC, the finite element code developed by the Geotechnical research group at the University of Newcastle, Australia. SNAC was used to analyse the numerical example in this section.

3.1 Undrained behaviour of a soil layer under dynamic pressure

To demonstrate the ability and accuracy of the h-adaptive method presented here we consider an undrained layer of soil under a rough rigid footing to which a uniform pressure is applied dynamically at a uniform rate with time. The footing, the soil layer, the material properties, and the boundary conditions are shown in Figure 1. Note that G, s_u, ϕ_u, ρ and ν in Figure 1 represent the elastic shear modulus, undrained shear strength, undrained friction angle, unit mass density and Poisson's ratio of the soil, respectively. The material damping of the soil is assumed to be zero, and the soil is modelled as a Tresca material, and any increase in the shear strength due to strain rate effects is neglected, in order to avoid further complexities. Nazem et al. (2009) studied the behaviour of such a soil layer for pressure loads applied at rates of $2s_u$ and $20s_u$ per second, using the ALE method. In this paper we study the soil behaviour for a load rate of $10s_u$ per second, i.e., a total pressure $10s_u$ is applied in 1 s. The problem is analysed using three different finite element meshes, as shown in Figure 2. All three meshes are composed of 6-node triangular elements. As depicted in Figures 2a and 2b, Mesh A includes 1817 nodal points and 872 elements while Mesh B is composed of 7903 nodes and 3884 elements. Both meshes A and B are analysed by the ALE method proposed by Nazem et al. (2009). Figure 2c shows Mesh C, which includes 1040 nodes and 487 elements at the beginning of the analysis, and is analysed by the h-adaptive FE method described in this paper.

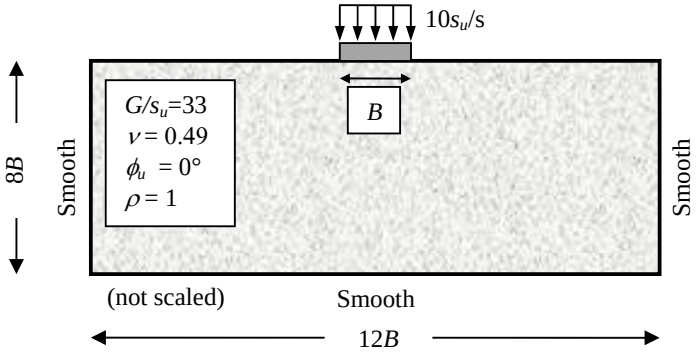

Figure 1. An undrained layer of soil under a rigid footing.

The deformed meshes at the end of each analysis are shown in Figure 3. The analyses using meshes A, B and C predicted that the final displacements of the footing are 0.278B, 0.322B and 0.318B, respectively. Note that the mesh analysed by the h-adaptive finite element method includes 8683 nodal points and 4268 elements at the end of the analysis. The predicted vertical displacement of the footing normalised by its width, versus the applied dynamic pressure normalised by the shear strength of the soil, is plotted in Figure 4 for Meshes A, B and C. The results obtained by the h-adaptive FE method are in good agreement with the results obtained by the ALE method using Mesh B. Note that the topology of the mesh does not change during the ALE analysis whilst the h-adaptive method regularly changes the number of the nodal points as well as the number of elements. For the h-adaptive method, the change in topology is plotted versus time in Figure 5.

4 CONCLUSIONS

An h-adaptive finite element method for dynamic analysis of geotechnical problems was presented in this study. The error in each element was measured based on the energy norm. For the footing problem studied in this paper, it is shown that this type of error estimator

a. Mesh A, 1817 nodes and 872 6-node triangular elements.

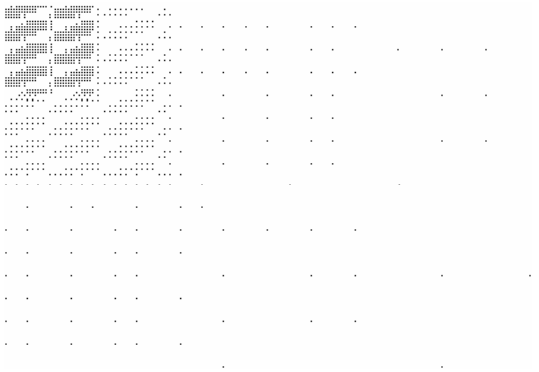

Mesh B. 7903 nodes and 3884 6-node triangular elements.

Mesh C. 1040 nodes and 487 6-node triangular elements, beginning of the analysis.

Figure 2. Finite element meshes.

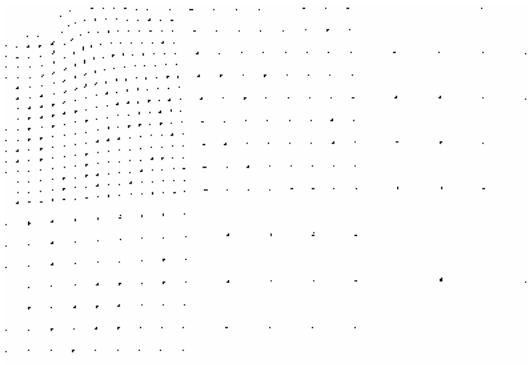

a. Mesh A, total displacement of the footing predicted by the ALE method = 0.278*B*.

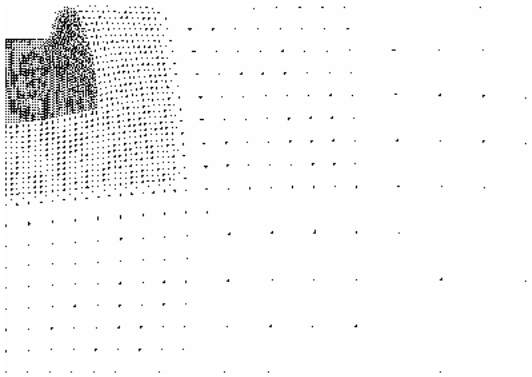

b. Mesh B, total displacement of the footing predicted by the ALE method = 0.322*B*.

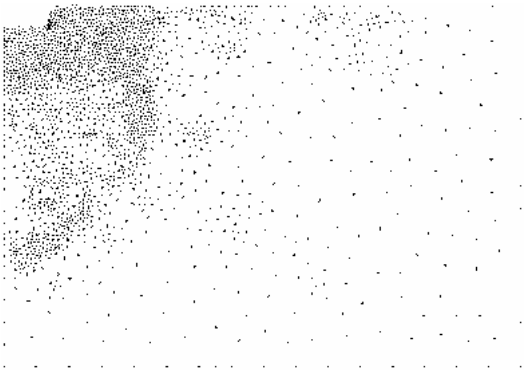

c. Mesh C, total displacement of the footing predicted by the h-adaptive FE method = 0.318*B*.

Figure 3. Deformed meshes at the end of the analysis.

provides results which are in good agreement with the results obtained by the analysis of a relatively fine mesh. The main challenge noticed in this study is tendency for violation of dynamic equilibrium as well as the plasticity consistency after remapping of the state variables from the old mesh to a newly generated mesh. Unfortunately, there is no explicit solution for this problem in the literature to date. Nonetheless, the results show that a few further Newton-Raphson iterations based on Newmark's method will guarantee that equilibrium and the principle of consistency are both satisfied to acceptable tolerances.

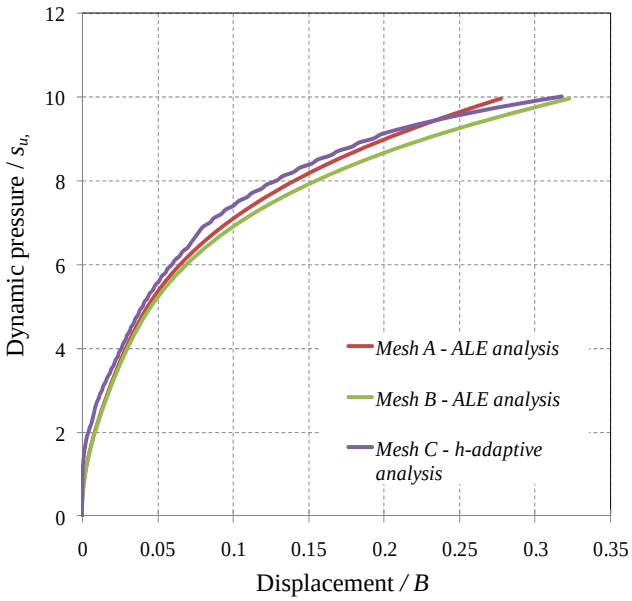

Figure 4. Normalised displacement of the footing versus normalised applied dynamic pressure.

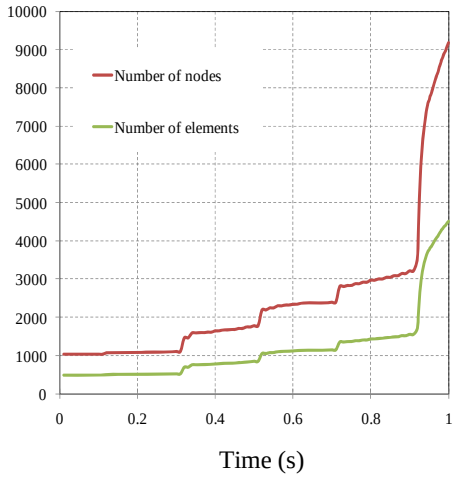

Figure 5. Change in topology versus time.

REFERENCES

Boroomand, B. & Zienkiewicz, O.C., (1999), “Recovery procedures in error estimation and adaptivity, Part II: adaptivity in nonlinear problems of elasto-plasticity behaviour”, Comp. Meth. Appl. Mech. Eng., Vol. 176, 127-146.

Hu, Y. & Randolph, M.F. (1998), "A practical numerical approach for large deformation problems in soils", Int. J. Num. Anal. Meth Geom., Vol. 22, 327-350.

Nazem, M., Sheng, D. & Carter J.P. (2006), "Stress integration and mesh refinement in numerical solutions to large deformations in geomechanics", Int. J. Num. Meth. Eng., Vol 65, 1002-1027.

Nazem, M., Sheng, D., Carter, J.P. & Sloan S.W. (2008), "Arbitrary Lagrangian-Eulerian method for large-strain consolidation problems", Int. J. Num. Anal. Meth. Geom., Vol. 32, 1023-1050.

Nazem, M, Carter, J.P. & Airey, D. (2009), "Arbitrary Lagrangian-Eulerian Method for dynamic analysis of Geotechnical Problems", Comp. Geotech. Vol. 36, 549-557.

Zienkiewicz, O.C. & Zhu, J.Z. (1992), “The superconvergent patch recovery and a posteriori error estimate. Part I: The recovery technique”, Int. J. Num. Meth. Eng., Vol. 33, 1331-1364.

A FAST ALGORITHM FOR FINDING THE FIRST INTERSECTION WITH A NON-CONVEX YIELD SURFACE

Daichao Sheng
Centre for Geotechnical and Materials Modelling, the University of Newcastle, Australia

Charles E Augarde
School of Engineering and Computing Sciences, Durham University, UK

Andrew J Abbo
Centre for Geotechnical and Materials Modelling, the University of Newcastle, Australia

ABSTRACT: *A major task in the numerical modeling of soils using complex elasto-plastic models is stress updating. This paper proposes a fast and robust numerical algorithm for locating the first intersection between a non-convex yield surface and an elastic trial stress path. The intersection problem is cast into a problem of finding the smallest positive root of a nonlinear function. Such a function may have multiple roots within the interval of interest. The method is based on the Modified Steffensen method, with important modifications to address the issues arising from the non-convexity. Numerical examples demonstrate that the proposed M^2 Steffensen method is indeed computationally efficient and robust.*

1 INTRODUCTION

Implementation of complex elasto-plastic constitutive models for soils into finite element codes requires development of robust procedures for stress updating, the integration of the constitutive model. While many constitutive models lead to convex yield surfaces there are certain cases where the yield surface of a soil model is non-convex. For example, the yield surface for an unsaturated soil model is non-convex, if both saturated and unsaturated states of the soil are considered. Because both partial and full saturation are only different states of a soil, a single constitutive model should be expected to work for both states. As such, the non-convexity becomes inevitable. Wheeler et al. (2002) pointed out the possible non-convexity of the most widely used model for unsaturated soils, the Barcelona Basic Model (BBM, Alonso et al. 1990) in the unsaturated zone. Sheng (2003) argued that this non-convexity in BBM is inevitable if the pore water pressure is allowed to vary between positive and negative values. The non-convexity exists irrespective of the stress state variable used to formulate the constitutive model, as illustrated in Figure 1. Some researchers have also argued that suction should be treated as a hardening (internal) variable instead of an additional variable in the stress space. However, this argument does not alter the fact that the size of the yield surface in stress space varies with suction and this variation does not necessarily result in plastic deformation. Another example of non-convexity appears when the Hvorslev envelope is added to the Mohr-Coulomb envelope in a Mohr-Coulomb type model. The Hvorslev envelope is usually used for low stress levels and is flatter than the Mohr-Coulomb envelope in the space of normal (or mean) stress versus shear (or deviator) stress, leading to a non-convex elastic zone around the transition.

A closely related problem arises when the elastic behaviour inside the yield surface is nonlinear. In this case, even if the yield surface is convex, the elastic trial stress path may cross the yield surface more than once. In other words, the elastic trial stress path is a curve

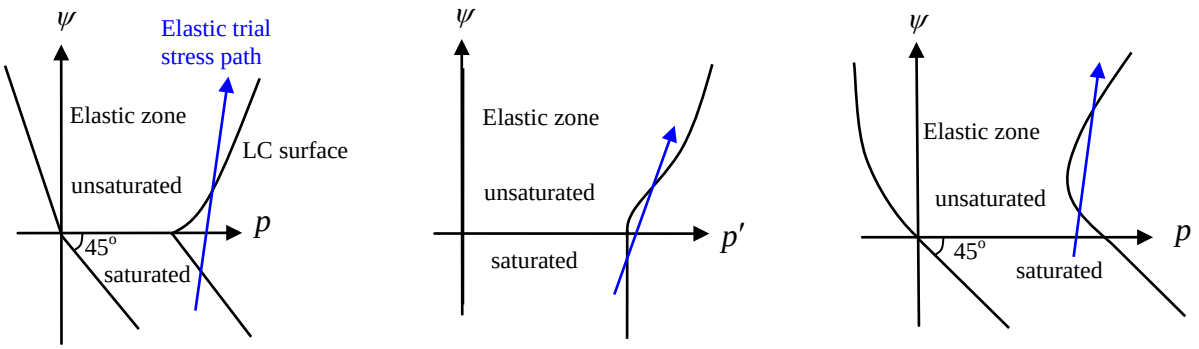

(a) net stress (Alonso *et al.*, 1990) (b) effective stress (Sheng *et al.*, 2004) (c) net stress (Sheng *et al.*, 2008a)

Figure 1. Non-convexity of yield surfaces in unsaturated soil models in the suction-stress space (ψ: suction, $\overline{p}$: net and p' effective mean stress respectively.

instead of a straight line in the stress space. As such, a stress path that starts and ends inside the yield surface can still intersect with the yield surface (Figure 2). In general, a convex elastic zone enclosing nonlinear behaviour is mathematically equivalent to a non-convex zone enclosing linear behaviour.

One of the main challenges in integrating constitutive models with non-convex yield surfaces or nonlinear elasticity is that the elastic trial stress path may cross the initial yield surface more than once, as illustrated in Figure 1 for unsaturated soil models. Furthermore, the number of times the yield surface is crossed remains unknown, for a given strain increment and an initial stress state. In such circumstances, only the first intersection is of interest, as the stress path is likely to cause an initial elastoplastic loading followed by an elastic unloading. This leads to the key issue in solving non-convex models: to find the first intersection between the elastic trial stress path and the initial yield surface.

Integration of rate-type constitutive equations can be carried out in an implicit or explicit manner. In implicit schemes, all gradients and functions are evaluated at advanced unknown stress states and the solution is achieved by iteration. These methods do not usually involve a procedure to find the intersection between the elastic trial stress path and the yield surface. However, when the yield surface is non-convex, the knowledge of the first intersection seems to be a prerequisite for making these schemes work. Otherwise, a trial stress path that starts and ends in the initial elastic zone would be assumed to cause only elastic deformation. For unsaturated soil models, where the location of non-convexity is known, implicit schemes may work if the strain increments are kept sufficiently small (Borja 2004). The difficult question is: what is sufficiently small? On the other hand, explicit schemes estimate the gradients and functions at the current known stress states and proceed in an incremental fashion. These schemes invariably need to determine the intersection and substepping methods have been developed to control the integration error (Sloan 1987; Sloan *et al.* 2001). Therefore, it seems necessary for both implicit and explicit methods to find the first intersection between the current yield surface and the elastic trial stress path.

There is very little discussion in the literature about integrating non-convex soil models. Pedroso *et al.* (2008) proposed a novel method for bracketing the intersection between the elastic trial stress path and a non-convex yield surface. Finding this intersection can be cast into a problem of finding the multiple roots of a nonlinear equation:

$$f(\alpha) = f(\mathbf{s}_\alpha, \mathbf{h}) = 0 \tag{1}$$

where $0 \le \alpha \le 1$, $f(\mathbf{s}, \mathbf{h})$ is the yield function, $\mathbf{s}$ is a set of external variables such as stress

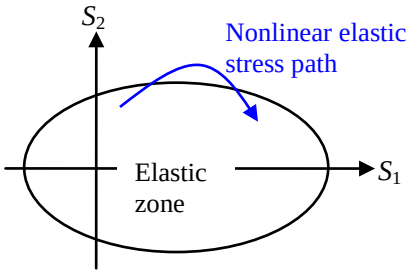

Figure 2. Multiple intersection problem due to nonlinear elasticity (S_1 and S_2 are two stress variables).

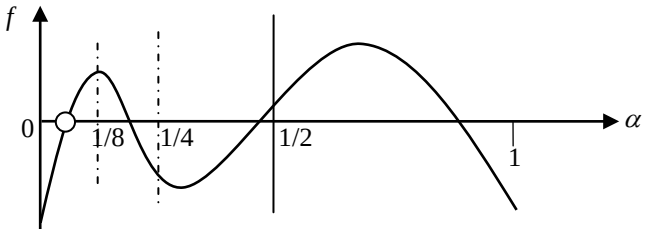

Figure 3. Bracketing the roots for nonlinear function according to Pedroso *et al.* (2008).

and suction, **h** is a set of internal variables, typically plastic strain or hardening parameters, subscript α indicates that the quantity is evaluated at strain increment $\alpha\Delta\boldsymbol{\varepsilon}$, the strain increment $\Delta\boldsymbol{\varepsilon}$ is assumed to be known, and the variable $\mathbf{s}_\alpha$ is assumed to be fully determined for given strain increment $\alpha\Delta\boldsymbol{\varepsilon}$, for example using elasticity theory.

The method proposed by Pedroso *et al.* (2008) for bracketing the roots (α) is illustrated in Figure 3. For a given increment (α = 1), the number of roots of $f(\alpha)$ is first computed. If there is more than one root, the increment is divided into two equal sub-increments. The number of roots of each sub-increment is then computed. If the first sub-increment contains more than one root, it is further divided into two sub-increments. This process is repeated until the first sub-increment contains at most one root (Figure 3). Once the roots are bracketed, the solution of the first root can be found by using numerical methods such as the Pegasus method (Sloan *et al*. 2001).

Sheng *et al.* (2008b) applied the method by Pedroso *et al.* (2008) to integrate an unsaturated soil model described by Sheng *et al.* (2008a) and found that the method can provide an accurate solution of the intersection problem. However, this approach was found to be computationally extremely expensive. It should be realised that the root-finding procedure must be applied for all strain increments at all Gauss points, irrespective of the starting and ending stress states. Pedroso's formula requires both the first and second orders of gradients of the yield function and also complex numerical integration to compute the number of roots, leading to high computational expense.

The objective of this paper is to propose a fast and robust numerical algorithm that can be used to find the first intersection between a non-convex yield surface and an elastic trial stress path. This problem is further cast into a problem of finding the smallest positive root of a nonlinear function that has multiple roots.

2 M^2 STEFFENSEN'S METHOD

The problem of finding the first intersection between a non-convex yield surface and an elastic trial stress path can be reformulated into a problem of finding the smallest positive root of a nonlinear function that has multiple roots:

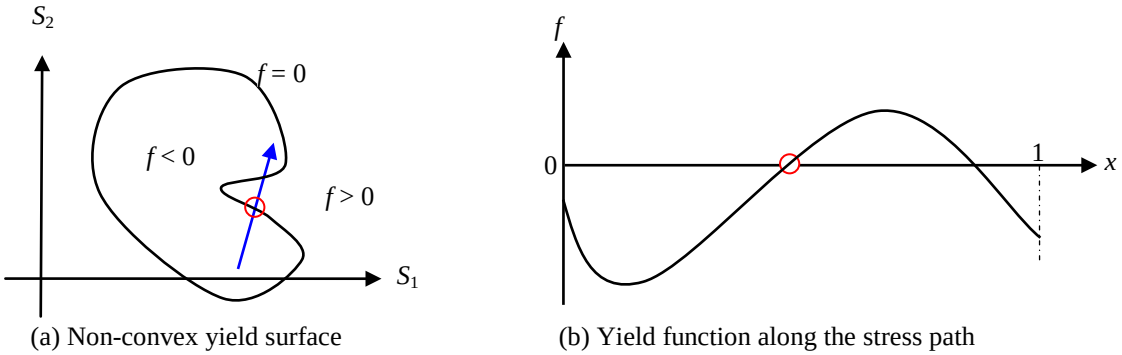

(a) Non-convex yield surface (b) Yield function along the stress path

Figure 4. Casting the stress integration into a root finding problem.

$$f(x) = 0 \qquad 0 \le x \le 1 \tag{2}$$

Furthermore, for elastoplastic problems, the initial stress state must be inside or on the initial yield surface, and hence the following is generally true:

$$f(0) \le 0 \tag{3}$$

Due to the non-convex yield surface, function $f(x)$ does not necessarily vary monotonically between x=0 and the smallest positive root. A typical case is shown in Figure 4. For the nonlinear equation shown in Figure 4b, most existing algorithms, including the bisection-type methods, secant-type methods and Newton-type methods, will not work. One would argue that the Newton-type methods would work if a better starting point was located. However, finding a better starting stress state can not be achieved in a general manner and is indeed part of the solution of the problem we are seeking.

The method proposed to solve the nonlinear equation illustrated in Figure 4b is based on the modified Steffensen method (Esser 1976 in Engeln & Uhlig 1996; Dehghan & Hajarian 2010) which solves a nonlinear equation via the following iteration:

$$x_{n+1} = x_n - j\frac{\left(f(x_n)\right)^2}{z} \tag{4}$$

with

$$z = f(x_n) - f\left(x_n - f(x_n)\right) \tag{5}$$

and

$$j = \frac{z^2}{z^2 + f(x_n)\left(z + f(x_n) - f\left(x_n + f(x_n)\right)\right)} \tag{6}$$

The parameter j converges to the multiplicity of the root. Compared with Newton's method, the modified Steffensen method approximates the derivative of the function by

$$f' \approx \frac{f(x) - f\left(x - f(x)\right)}{f(x)} \tag{7}$$

for simple roots. It is thus clear that the function itself is used as an increment in the method.

The modified Steffensen method has to be further modified to be useful for the nonlinear equation shown in Figure 4b. In this paper the following M^2 Steffensen method is proposed:

$$x_{n+1} = x_n + \zeta \left| j \right| \frac{\left(f(x_n) \right)^2}{\left| z \right|} \tag{8}$$

with

$$z = f(x_n) - f\left(x_n - \zeta f(x_n) \right) \tag{9}$$

and

$$j = \frac{z^2}{z^2 + f(x_n)\left(z + f(x_n) - f\left(x_n + \zeta f(x_n) \right) \right)} \tag{10}$$

where ζ is a constant used to adjust the increment size in the approximation (7) whichdepends on the relative magnitude of function $f(x)$ compared with unknown x. This parameter is further discussed below, in conjunction with numerical examples.

Equation (7) is designed for functions in the form of equations (2) and (3). It may overshoot the solution near the desired root so that $f(x_{n-1}) f(x_n) < 0$. In this case, the iteration can be carried out in the following form:

$$x_{n+1} = x_n - \zeta j \frac{\left(f(x_n) \right)^2}{z} \qquad f(x_{n-1}) f(x_n) < 0 \tag{11}$$

The M^2 Steffensen method involves the evaluation of the function only, not its derivatives. It needs only one case of exception handling, i.e. equation (11). The method can be implemented with a few lines of coding.

3 NUMERICAL EXAMPLES

To assess the performance of the proposed method a number of numerical examples are now presented. In the first three cases, simple functions are used which nevertheless possess features which are challenging for root-finding, and which represent different features of non-convex yield surfaces. The final example presented here is for a yield surface from an unsaturated soil model.

3.1 The first root of $f(x) = -\sin(8x) = 0$

The M^2 Steffensen method is first used to find the root of the following cyclic function:

$$f(x) = -\sin\left(8x\right) \qquad 0 \le x \le 1$$

The function is illustrated in Figure 5. The function has three roots within the interval [0, 1]. In the context of elastoplastic models, the root (x=0) means that the starting stress point is on the yield surface and hence is not of interest here. The objective is to find its smallest positive root (x_s) for an arbitrary starting point between $0 < x < x_s$.

The performance of the proposed M^2 Steffensen method to find the smallest positive root

(x_s) for the function is shown in Table 1 which shows the convergence for two arbitrary starting points: x_0=0.3 and x_0=0.0001. The method is able to locate the correct root for these starting points. Indeed, the starting point can be very close to zero, i.e. x_0=0.0001. It generally takes more iterations to find the correct root when the starting point is close to zero. The solution converges quadratically towards the desired root (at least asymptotically). Parameter ζ also affects the convergence rate, as shown in Table 2. As mentioned above, ζ is used to control the increment size ($\zeta f(x)$) and hence depends on the relative magnitude of the function. The maximum value of ζ can be approximated by:

$$\zeta \le \frac{\left|x_{\max} - x_{\min}\right|}{\left|f_{\max} - f_{\min}\right|} \tag{12}$$

In this example, the above condition leads to $\zeta \le 0.5$.

Table 1. Convergence of M^2 Steffensen method for –sin(8x)=0.

x	ζ	$f(x)$	$f(x+\zeta f(x))$	$f(x-\zeta f(x))$	z	j
0.3	0.3	-0.675463181	-0.70249	0.770432	-1.4459	0.68567
0.364908703	0.3	-0.220496073	-0.68275	0.302074	-0.52257	0.953557
0.391523606	0.3	-0.009403667	-0.03197	0.013165	-0.02257	0.999912
0.392698987	0.3	-7.53898E-07	-2.6E-06	1.06E-06	-1.8E-06	1
0.392699082	0.3	-1.22515E-16	-5.7E-16	3.22E-16	-4.4E-16	1
0.0001	0.3	-0.0008	0.00112	-0.00272	0.00192	0.999999
0.0002	0.3	-0.0016	0.00224	-0.00544	0.00384	0.999997
0.000400001	0.3	-0.003200002	0.00448	-0.01088	0.00768	0.99999
0.000800008	0.3	-0.006400021	0.00896	-0.02176	0.015358	0.999959
0.001600065	0.3	-0.01280017	0.017919	-0.04351	0.030707	0.999836
0.003200521	0.3	-0.025601374	0.035831	-0.08694	0.061336	0.999343
0.006404174	0.3	-0.051210983	0.071612	-0.17326	0.12205	0.997351
0.012833386	0.3	-0.102486822	0.142811	-0.34162	0.239129	0.989064
0.025866544	0.3	-0.205458667	0.282279	-0.64424	0.438784	0.950354
0.05329519	0.3	-0.413560793	0.536416	-0.98849	0.574926	0.680619
0.114037602	0.3	-0.790913762	0.833765	-0.32508	-0.46583	0.116017
0.160775692	0.3	-0.959776624	0.85067	0.433233	-1.39301	0.386928
0.237536228	0.3	-0.946206351	0.36218	0.857089	-1.8033	0.52482
0.315705617	0.3	-0.577732332	-0.90825	0.696573	-1.27431	0.748627
0.374531252	0.3	-0.144831461	-0.47322	0.200877	-0.34571	0.979439
0.39235974	0.3	-0.002714729	-0.00923	0.003801	-0.00652	0.999993
0.392699079	0.3	-1.81395E-08	-6.2E-08	2.54E-08	-4.4E-08	1
0.392699082	0.3	-1.22515E-16	-5.7E-16	3.22E-16	-4.4E-16	1

Table 2. Performance of M^2 Steffensen method in solving $-\sin(8x) = 0$.

ζ	Starting point	Number of Iterations	x_s	$f(x_s)$
0.1	0.0001	21	0.392699082	-1.22515x10^{-16}
	0.1	10	0.392699082	-1.22515x10^{-16}
	0.3	5	0.392699082	-1.22515x10^{-16}
0.3	0.0001	18	0.392699082	-1.22515x10^{-16}
	0.1	8	0.392699082	-1.22515x10^{-16}
	0.3	5	0.392699082	-1.22515x10^{-16}
0.5	0.0001	16	0.392699082	-1.22515x10^{-16}
	0.1	5	0.392699082	-1.22515x10^{-16}
	0.3	3	0.392699082	-1.22515x10^{-16}

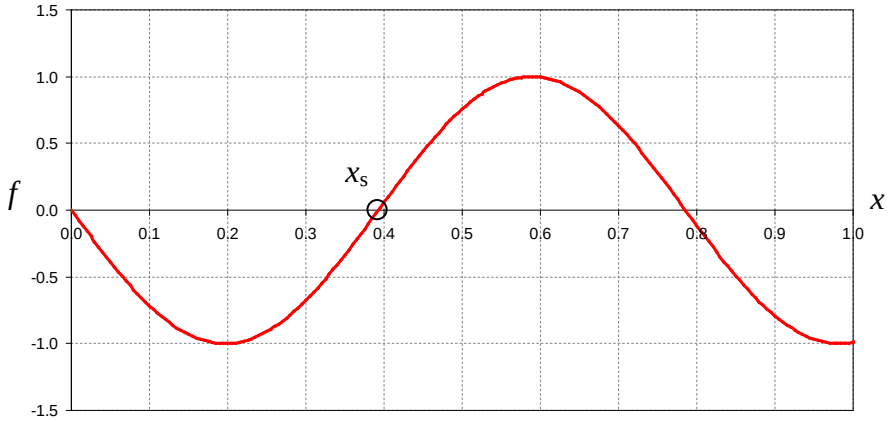

Corresponding stress integration problem:

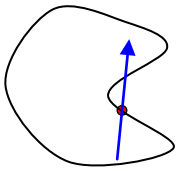

Figure 5. Equation -sin(8x)=0 and its roots between [0, 1].

The cyclic function in the first example has constant amplitude and frequency. In this case, the desired root is approached monotonically from the left on the x axis and equation (11) is not evoked.

3.2 The first root of $f(x) = -\dfrac{\cos(10x - 1.5)}{1 + 10x} = 0$

In the second example, the M^2 Steffensen method is used to find the root for the following function:

$$f(x) = -\frac{\cos(10x - 1.5)}{1 + 10x} \qquad 0 \le x \le 1$$

The function is illustrated in Figure 6. The function has three roots in the interval [0, 1], but only the smallest root is of interest. Again, the starting stress point can be arbitrary, within the interval $0 < x < x_s$.

It is found that $\zeta \le 1.6$ for this example, using equation (12). The performance of the method is shown in Table 3. The method again has an asymptotically quadratic convergence rate. For x_0=0.0001 or x_0=0.1, only 7 iterations are required to find the root. It should be noted that the function changes signs near the desired root and hence equation (11) has to be evoked. Table 3 also shows that the three function values at the root become equal, z becomes zero and j becomes undefined.

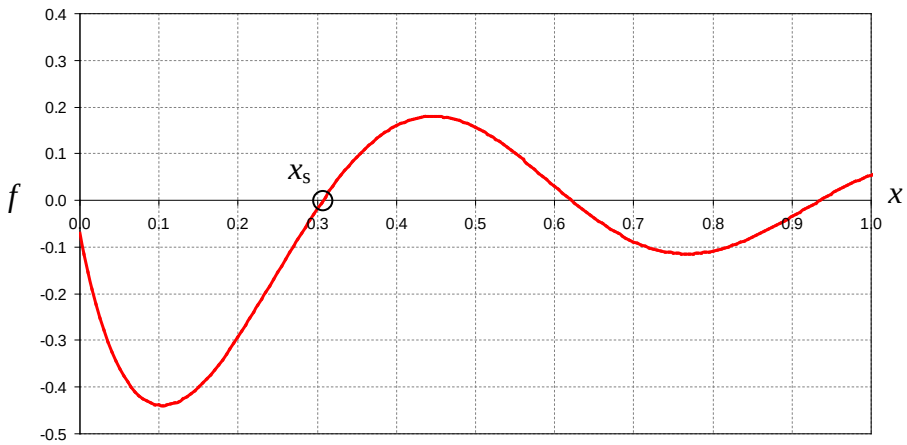

Corresponding stress integration problem:

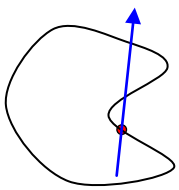

Figure 6. Equation $-\dfrac{\cos(10x - 1.5)}{1 + 10x} = 0$ and its roots between [0, 1].

Table 3. Convergence of M^2 Steffensen method for $-\frac{\cos(10x-1.5)}{1+10x}=0$.

x	ζ	$f(x)$	$f(x+\zeta f(x))$	$f(x-\zeta f(x))$	z	j
0.0001	1.5	-0.071662998	-11.40264186	-0.439042446	0.367379448	-0.191886658
0.004123566	1.5	-0.107370293	-1.751899777	-0.372767816	0.265397523	-0.523166999
0.038211683	1.5	-0.316606253	0.271646783	0.143937738	-0.460543991	0.389779009
0.165467476	1.5	-0.372196889	0.224121055	-0.103772382	-0.268424507	0.182915938
0.307068412	1.5	-2.75657E-05	-0.000129155	7.40031E-05	-0.000101569	1.000055131
0.307079634	1.5	3.56011E-09	1.66783E-08	-9.55813E-09	1.31182E-08	0.999999993
0.307079633	1.5	-1.5048E-17	-1.5048E-17	-1.5048E-17	0	#DIV/0!
0.1	1.5	-0.438791281	0.152263232	-0.114171428	-0.324619853	0.207777411
0.284854697	1.5	-0.057274657	-0.295241294	0.126322101	-0.183596758	1.101786011
0.314383681	1.5	0.017610625	0.07505586	-0.048962198	0.066572823	0.9650003
0.3076404	1.5	0.001375634	0.006404424	-0.003704914	0.005080548	0.997249145
0.307083226	1.5	8.82801E-06	4.13557E-05	-2.37018E-05	3.25298E-05	0.999982344
0.307079633	1.5	3.65093E-10	1.71038E-09	-9.80195E-10	1.34529E-09	0.999999999
0.307079633	1.5	-1.5048E-17	-1.5048E-17	-1.5048E-17	0	#DIV/0!

The function in this example has a decreasing amplitude with increasing x. The root is approached from both right and left (Table 3), and equation (11) has been evoked.

3.3 The Intersection of SFG Model

In the last example, we study the performance of the proposed M^2 Steffensen method in integrating a yield surface for an unsaturated soil model, the SFG model (Sheng *et al.* 2008a). The SFG model features a non-convex elastic zone in the space of suction versus net mean stress. The yield function is given as follows:

$$f = q^2 - M^2\left(p - p_0\right)\left(p_c - p\right) \tag{13}$$

where q is the deviator stress, p is the net mean stress, M is the slope of the critical state line in the $q-p$ space, and p_0 and p_c are two yield stresses when q is zero. Both yield stresses are functions of suction (ψ):

$$p_0 = \begin{cases} -\psi & \psi \le \psi_{sa} \\ -\psi_{sa} - \psi_{sa}\ln\dfrac{\psi}{\psi_{sa}} & \psi > \psi_{sa} \end{cases} \tag{14}$$

$$p_c = \begin{cases} p_{c0} - \psi & \psi \le \psi_{sa} \\ p_{c0} - \psi + \dfrac{p_{c0}}{\rho}\left(\psi - \psi_{sa} - \psi_{sa}\ln\dfrac{\psi}{\psi_{sa}}\right) & \psi > \psi_{sa} \end{cases} \tag{15}$$

where ψ_{sa} is the transition suction between saturated and unsaturated states and is assumed to be a constant in this paper, p_{c0} is the yield stress when q=0 and ψ=0, and ρ is a material constant depending on the stress history of the soil and can not be greater than p_{c0}. The yield stress (p_0) usually remains stationary in the stress space. However, the yield stress (p_c) can evolve in the stress space due to plastic strain and as such hardening and softening occur. Two examples of the SFG yield surface are shown in Figure 8: one for an air-dry unsaturated soil and the other for a compacted soil. In both cases, the yield surfaces are non-convex.

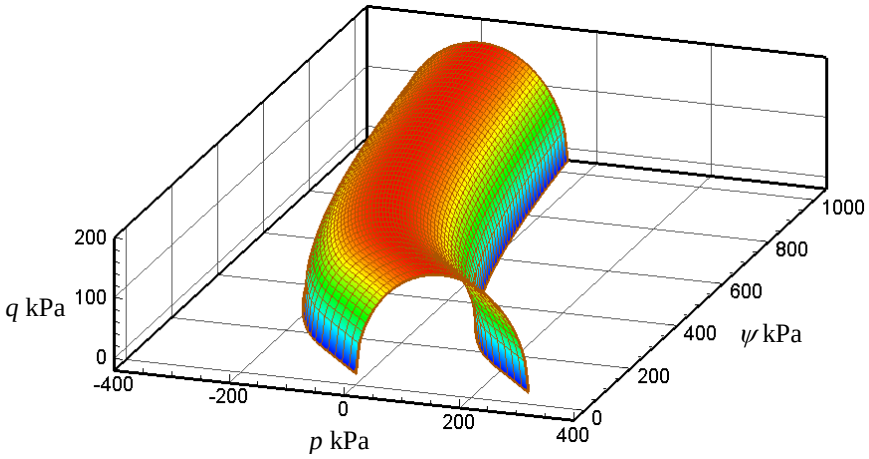

(a) Yield surface for unsaturated soil air-dried from slurry (p_{c0}=30 0kPa, ρ=p_{c0}, s_{sa}=100 kPa).

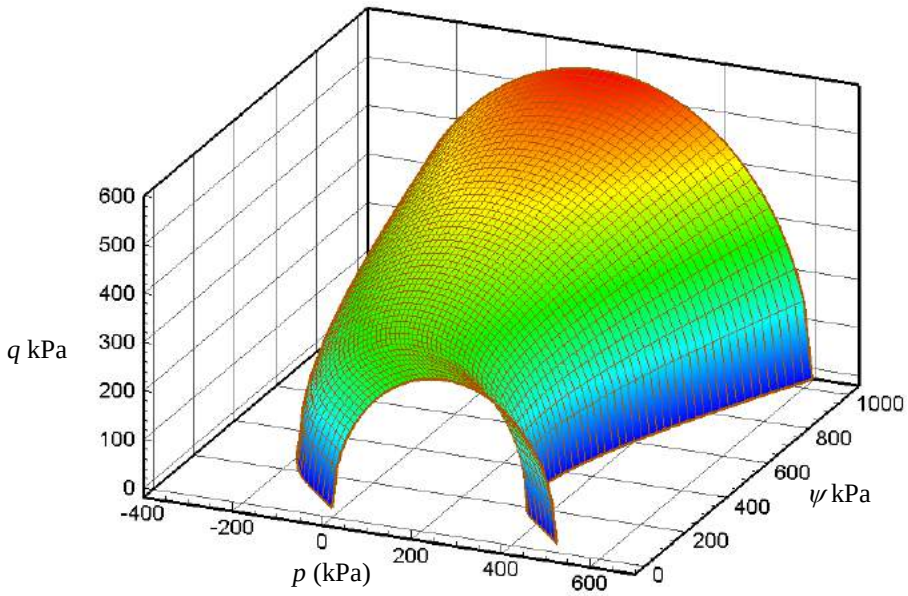

(b) Yield surface for compacted soil (p_{c0}=500 kPa, ρ=300 kPa, ψ_{sa}=100 kPa).

Figure 8. SFG yield surfaces for different soil types (M=1.2).

The M^2 Steffensen method is now used to find the intersection between a known initial yield surface (p_{c0}) and a given trial stress increment (dq, dp, dψ). The initial stress state (q, p, ψ) is also assumed to be known. Furthermore, without losing generality, the deviator stress q is assumed to remain zero. The problem is illustrated in Figure 9, where ρ is set to 300 kPa and ψ_{sa} to 100 kPa. The stress increment spans from the initial stress state (p = 300 kPa, ψ = -200 kPa) to the trial stress state (p = 500 kPa, ψ = 900 kPa). The problem can be cast into a specific root-finding problem as follows:

$$f(\alpha) = -\left(300 + 200\alpha - p_0\right)\left(p_c - 300 - 200\alpha\right) = 0$$

with

$$p_0(\alpha) = \begin{cases} -200 - 1100\alpha & 0 \le \alpha \le \dfrac{3}{11} \\ -100 - 100\ln\dfrac{1100\alpha - 200}{100} & \dfrac{3}{11} < \alpha \le 1 \end{cases}$$

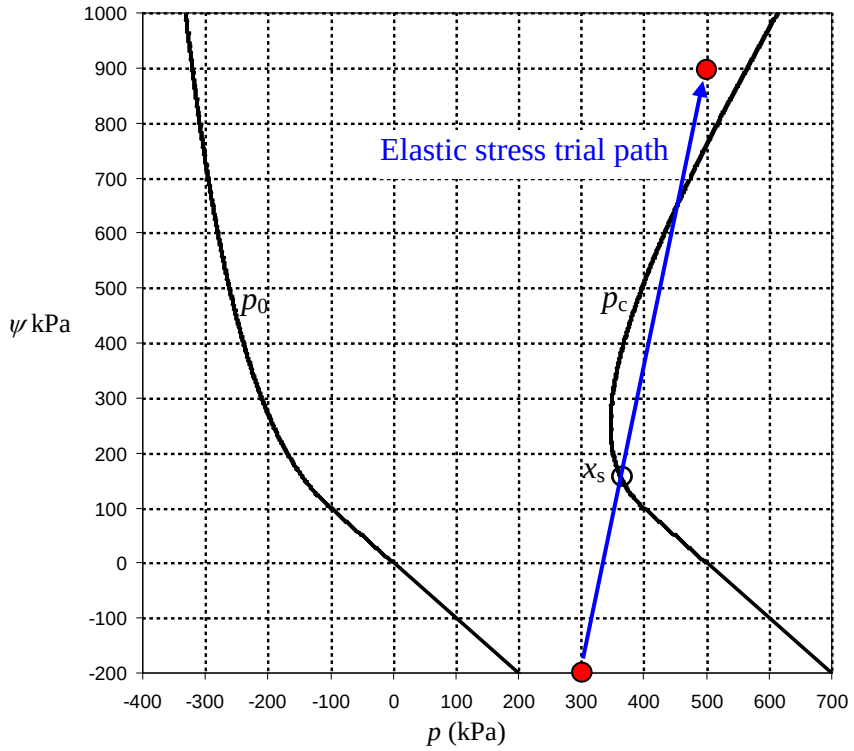

Figure 9. Yield surfaces and trial stress path (p_{c0}=500 kPa, ρ=300 kPa, ψ_{sa}=100 kPa).

$$p_c(\alpha) = \begin{cases} 700 - 1100\alpha & 0 \le \alpha \le \dfrac{3}{11} \\ 700 - 1100\alpha + \dfrac{5}{3}\left(1100\alpha - 300 - 100\ln\dfrac{1100\alpha - 200}{100}\right) & \dfrac{3}{11} < \alpha \le 1 \end{cases}$$

and α is a fraction of the stress increment and varies between 0 and 1. Figure 9 shows that the given elastic stress path crosses the yield surface (p_c) twice. Therefore, plastic hardening occurs and the yield surface (p_c) evolves. In this case, it is necessary to find the first intersection (x_s) to make a stress integration scheme work, no matter if it is implicit or explicit.

Parameter ζ is set to 0.000002, according to expression (12) and Figure 10. Table 5 lists the convergence performance of the M^2 Steffensen method from which it can be seen that only 5 iterations are required to locate the first root (s=153.45 kPa, p=364.26 kPa) to a yield function accuracy of 10^{-9}. The method again provides a quadratic convergence rate near the root. Figure 10 shows the yield function values along the stress path shown in Figure 9. Due to the cyclic behaviour of the function, any Newton-type or bisection-type iterations would not be able to locate the desired root or the correct intersection for this problem. Newton-type iterations (e.g. Newton method, modified Newton method, Steffensen method, modified Steffensen method) would work only if the starting stress point was sufficiently close the desired root (x_s). On the other hand, bisection-type methods (e.g. bisection method, Regula Falsi method and Pegasus method) require that the starting and ending points are on different sides of the yield surface and there is only one root within the interval. The M^2 Steffensen method presented here will always locate the desired root, irrespective of the starting and ending stress states. Furthermore, no derivatives of the yield function are required and the method is computationally very robust and efficient.

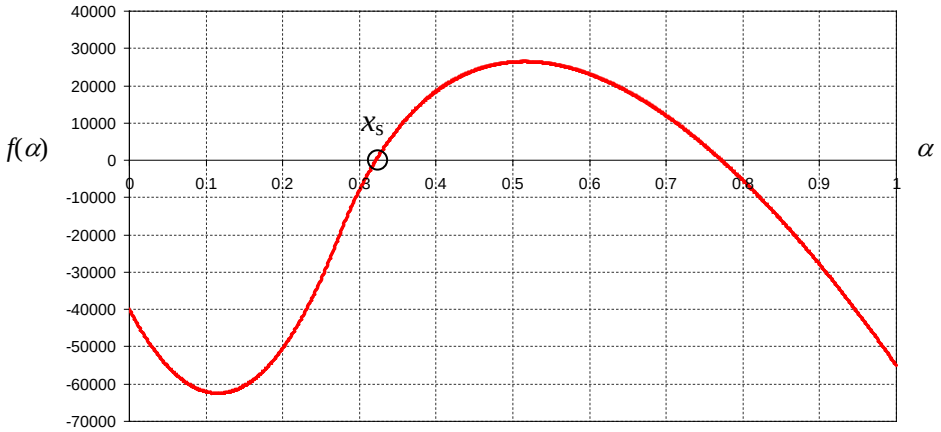

Figure 10. The SFG yield function along the elastic trial stress path.

Table 5. Convergence of M^2 Steffensen method for the SFG model.

α	$f(\alpha)$	z	j	ψ	p
0.0000000000000000	-40000	20384.000000000	0.324415620	-200.000000000	300.000000000
0.1569858712715860	-59575.17701	-40696.950026594	0.367073967	-27.315541601	331.397174254
0.3314068887386640	3227.894546	2031.035361293	0.914572041	164.547577613	366.281377748
0.3211467983473340	-58.67427575	-39.398755012	1.001634482	153.261478182	364.229359669
0.3213215587240660	-0.015713086	-0.010539637	1.000000450	153.453714596	364.264311745
0.3213216055759780	-1.09533E-09	-7.49439E-10	0.94677871	153.453766134	364.264321115
0.3213216055759810	2.88246E-11	2.88246E-11	0.5	153.453766134	364.264321115
0.3213216055759810	0	0	#DIV/0!	153.453766134	364.264321115

Application of the proposed method to general three-dimensional stress – strain equations in boundary-value problems requires a complete implementation of the method into the finite element method. The above examples only demonstrate the efficiency of the method in finding the first positive root of cyclic functions or to locating the intersection between the elastic trial stress path and the yield surface. This intersection-finding method can be incorporated into both explicit and implicit stress integration methods.

4 CONCLUSIONS

Certain constitutive models for geo-materials feature non-convex elastic zones. A typical example is an unsaturated soil model, where the non-convexity occurs along the suction axis. As a consequence, the elastic trial stress path may cross the yield surface more than once. The same problem can happen when nonlinear elastic behaviour is considered. To integrate these models in the finite element method, an essential step is to find the first intersection between the elastic trial stress path and the current yield surface. This paper presents a simple numerical method for locating this intersection. The method is based on the Modified Steffensen method, with important additional modifications to address the issues arising from the non-convexity. The numerical method is then used to find first roots for a number of nonlinear functions that have multiple roots within the interval of interest. The numerical examples demonstrate that the proposed M^2 Steffensen method is indeed computationally efficient and robust. Application of the proposed method for integrating general three-dimensional stress – strain equations in boundary-value problems requires a complete implementation of the method into the finite element method.

REFERENCES

Alonso, E.E., Gens, A. & Josa A. (1990). “A constitutive model for partially saturated soils”. Géotechnique, Vol. 40, 405-430.

Borja, R.I. (2004), “Cam clay plasticity, Part V: A mathematical framework for three phase deformation and strain localization analysis of partially saturated porous media”. Computer Methods in Applied Mechanics and Engineering, Vol. 193, 5301–38.

Dehghan, M. & Hajarian, M. (2010), “Some derivative free quadratic and cubic convergence iterative formulas for solving nonlinear equations”. Computational & Applied Mathematics, Vol. 29, 19-30.

Engeln-Müllges, G. & Uhlig, F. (1996), Numerical Algorithms with Fortran, Springer, Germany.

Esser, H. (1975), “Eine stets quadratisch konvergente Modifikation des Steffensen-Verfahrens“. Computing, Vol. 14, 367-369.

Pedroso, D.M., Sheng, D. & Sloan, S.W. (2008), “Stress update algorithm for elastoplastic models with non-convex yield surfaces”. International Journal for Numerical Methods in Engineering, Vol. 76, 2029-2062.

Sheng, D. (2003), “Non-convexity of the Barcelona Basic Model - Comment on SJ Wheeler, D Gallipoli & M Karstunen (2002; 26:1561-1571)”. International Journal for Numerical and Analytical Methods in Geomechanics, Vol. 27, 879-881.

Sheng, D., Sloan, S.W. & Gens, A. (2004), “A constitutive model for unsaturated soils: thermomechanical and computational aspects”. Computational Mechanics, Vol. 33, 453-465.

Sheng, D., Fredlund, D.G. & Gens, A. (2008a), “A new modelling approach for unsaturated soils using independent stress variables”. Canadian Geotechnical Journal, Vol. 45, 511–534.

Sheng, D., Pedroso, D.M. & Abbo, A.J. (2008b). “Stress path dependency and non-convexity of unsaturated soil models”. Computational Mechanics, Vol. 42, 685-695.

Sloan, S.W. (1987), “Substepping schemes for the numerical integration of elastoplastic stress-strain relations”. International Journal for Numerical Methods in Engineering. Vol. 24, 893-911.

Sloan, S.W., Abbo, A.J. & Sheng, D. (2001), “Refined explicit integration of elastoplastic models with automatic error control”. Engineering Computations, Vol. 18, 121–54. Erratum: Engineering Computations, Vol. 19, 594-594 (2002).

Wheeler, S.J., Gallipoli, D. & Karstunen, M. (2002), “Comments on use of the Barcelona Basic Model for unsaturated soils”. International Journal for Numerical and Analytical Methods in Geomechanics, Vol. 26, 1561-1571.

IMPACT OF THE INTEGRATION OF A HILL CLIMBING PROCEDURE ON THE PERFORMANCE OF A GENETIC ALGORITHMS-BASED SOFTWARE

D. M. G. Taborda
Geotechnical Consulting Group, London, UK

A. Pedro
Department of Civil and Environmental Engineering, Imperial College London, London, UK

P. A. L. F. Coelho
Department of Civil Engineering, University of Coimbra, Coimbra, Portugal

D. Antunes
Critical Software SA, Coimbra, Portugal

ABSTRACT: *The large number of operations typically involved in the application of Genetic Algorithms may result, for certain types of problems, in substantial computation times. With the objective of improving its efficiency, this paper analyses the impact of coupling this optimisation technique with a local search method, namely Hill Climbing. In this paper, the formulation of the latter component is described in detail and its implementation into a Genetic Algorithms-based code is presented. The results of comprehensive computational studies focussing on the relevance of the introduced parameters – step size, number of climbing steps and frequency of evaluation of the objective function – are discussed and conclusions are drawn on the potential advantages of adopting local search techniques in conjunction with Genetic Algorithms.*

1 INTRODUCTION

The use of Genetic Algorithms in the solution of optimisation problems commonly encountered in Geotechnical Engineering has demonstrated the efficacy and flexibility of this technique. However, in certain situations, such as those requiring the execution of complex numerical analysis (e.g. Finite Element models), the iterative nature of this method may lead to prohibitive computation times.

In this paper, the possibility of increasing the efficiency of Genetic Algorithms by adding a local search technique to its structure, such as Hill Climbing, is considered. The adopted formulation for extending the applicability of this method to the analysis of general search areas is presented in detail and the procedure followed for its implementation into a Genetic Algorithms-based software is described. Subsequently, the impact of coupling the two methods is assessed by conducting computational studies focussing on the calibration of the Modified Cam-Clay (MCC) model. The obtained results clearly demonstrate that the benefit in terms of reduction in computation time of introducing a local search technique may be substantial, even though a considerable dependency on the control parameters (e.g. step size and frequency of evaluation of the objective function) is evident.

2 OPTIMISATION METHODS

2.1 Genetic Algorithms

Briefly, a Genetic Algorithm (GA) is a technique which employs concepts from the theory of natural evolution, such as selection, mutation, inheritance and crossover, to solve

optimisation problems. Accordingly, a candidate solution is represented by the "genes" of an "individual" and can either be defined in binary or real format. The various individuals compose the analysed "population", which is randomly generated from within a previously defined search area at the beginning of the optimisation process. Each of the individuals is sequentially tested in a series of numerical procedures representing mathematically the studied problem. The behaviour yielded by this component of the algorithm (e.g. stress paths, stress-strain curves, settlement troughs, bending moment distributions, etc.) is subsequently compared to the reference input data (e.g. laboratory testing results, monitoring data, etc.) and their quality is assessed by a "fitness function". Naturally, this expression can either provide a measure of the "error", in which case the lower the value, the better the individual, or the "merit", meaning that better solutions are associated to larger magnitudes of this quantity. Once the fitness of the whole population has been determined, the stopping criteria are tested and, if satisfied, the procedure is terminated.

Clearly, the procedure described above resembles an automated trial-and-error procedure and, consequently, very large populations are required for its application to be effective. Therefore, GAs employ a set of techniques designed to enhance the performance of the abovementioned process: "selection", which focuses on determining whether a given individual is to be discarded or transferred to the subsequent generation; "crossing", which consists of defining which characteristics (i.e. genes) of the parent individuals ("ancestors") are to be transmitted to the offspring ("descendants") and "mutation", which introduces minor adjustments to the genes during the crossing procedure. Once these operations have been carried out, a new generation of the population is obtained and the previously described assessment process is repeated. Indeed, given the evolutionary features of the GAs, it is expected that the best individual of the new generation is better than that of the previous one, eventually fulfilling the selected termination criteria.

Interesting examples of the application of this technique to problems encountered in Geotechnical Engineering include the identification of failure surfaces in slopes (Goh, 1999; McCombie, 2009), the analysis of discontinuities in rock masses (Simpson & Priest, 1993) and the calibration of constitutive models (Pat et al., 1996; Levasseur et al., 2008). In the present case, the research carried out at the University of Coimbra, Portugal, may be included in the latter group, even though the developed software, *genUC*, is a generic platform allowing the application of GAs to any given problem (Taborda et al., 2008). In its current version, the abilities of the computer code *genUC* are restricted to the determination of the parameters required by the Modified Cam-Clay (MCC) model in its constant Poisson's ratio version (Potts & Zdravković, 1999), based on the results of any combination of undrained and drained triaxial compression tests and oedometer tests (Taborda et al., 2010).

2.2 Hill Climbing

Hill Climbing is a direct search optimisation technique which, starting from a given initial solution to the problem, $\mathbf{p_0}$, attempts to improve it by randomly altering its characteristics (Weise, 2009). Naturally, should the new solution be worse, the performed adjustment is discarded and the previous state is retained as the best known solution to the analysed problem. These operations are repeated until a specified stopping condition (i.e. number of failed attempts, value of the objective function, etc.) is satisfied.

Clearly, the greatest advantages of Hill Climbing are its simplicity and the fact that, unlike gradient and Newton search methods, it requires solely the evaluation of the objective function (Schwefel, 1995). However, in the abovementioned form, the algorithm is inherently local and its ability is, therefore, restricted to determining local maxima or minima of the selected function. Indeed, to overcome this limitation, it is often suggested that either the

quality of the solution should be allowed to decrease, or the optimisation procedure should be randomly restarted, thus allowing a wider search area to be explored (Weise, 2009).

Based on the principles described above, a Hill Climbing procedure was devised for implementation into a Genetic Algorithms-based software. The formulated algorithm relies greatly on three fundamental quantities, which require appropriate definition: Δ_{max}, N_{steps} and N_{climb}. Indeed, the first of these parameters determines the size of the step in relation to the extent of the search area, thus establishing the distance between the current and the ensuing solutions. Additionally, N_{steps} defines the number of Hill Climbing steps carried out prior to re-evaluating the objective function, while the number of times this procedure is repeated is controlled by N_{climb}. Therefore, each individual is altered $N_{steps} \cdot N_{climb}$ times, with the objective function being calculated every N_{steps}. Indeed, the introduction of two distinct types of steps (i.e. with and without calculation of the value of the objective function) guarantees greater flexibility when coupling this method with Genetic Algorithms, as the majority of the computational resources required by the latter technique are typically utilised on the evaluation of the error or fitness of each individual.

In terms of the operations executed within any given adjustment step, the relative change for each of the N_p components of the solution, Δp_i, is firstly obtained by randomly generating values ranging from -1.0 to 1.0:

$$\Delta p_i = 2.0 \cdot \left(X_{random} - 1.0 \right), \; 0.0 \le X_{random} \le 1.0, \quad i = 1, N_p \tag{1}$$

Subsequently, the resulting vector is normalised, thus guaranteeing that, for every Hill Climbing step, a vector of constant magnitude is employed:

$$\left\| \boldsymbol{\Delta p} \right\| = \sqrt{\sum_{i=1}^{N_p} \left(\Delta p_i \right)^2} \tag{2}$$

$$\Delta p_{i,corrected} = \frac{\Delta p_i}{\left\| \boldsymbol{\Delta p} \right\|}, \quad i = 1, N_p \tag{3}$$

Lastly, the variation of the solution is evaluated based on the normalised incremental vector, $\boldsymbol{\Delta p}_{\mathbf{corrected}}$, the Hill Climbing parameter, Δ_{max}, and the extent of the search area prescribed for each component, $(p_{i,max} - p_{i,min})$:

$$\Delta p_{i,final} = \Delta p_{i,corrected} \cdot \left(p_{i,max} - p_{i,min} \right) \cdot \Delta_{max}, \; i = 1, N_p \tag{4}$$

Note that the inclusion of the latter quantity – $(p_{i,max} - p_{i,min})$ – is of extreme importance when analysing problems where the components of the solution are described in substantially different scales (e.g. λ and ϕ_{CS}' in the Modified Cam-Clay model). Indeed, the abovementioned procedure ensures that the variation of an element of the solution within a step is proportional to the corresponding range of possible values, which is typically compatible with the expected magnitude of each component.

Furthermore, it can be concluded that the maximum possible change for any given component of the solution is limited to $\pm(p_{i,max} - p_{i,min}) \cdot \Delta_{max}$, and can only occur if the remaining values are kept constant (i.e. $\Delta p_{j,final} = 0$, for $j \neq i$). In fact, due to the normalisation proposed in Eq. (3), should more than one component suffer alterations, the maximum admissible variations will be reduced accordingly.

Once the operations described above have been repeated N_{steps} times, the accumulated incremental values for each parameter, $\mathbf{\Delta p_{final}}$, which aggregates the changes computed in each of the steps, is calculated. Subsequently, designating by $\mathbf{p}$ and $\mathbf{p} + \mathbf{\Delta p_{final}}$ the solutions at the beginning of the first step and at the end of the last step, respectively, and by F the objective function being minimised (i.e. measuring the current error of the solution), the criterion establishing the acceptance of the performed adjustments can be defined by:

$$\Delta F_{norm} = \frac{F(\mathbf{p} + \mathbf{\Delta p_{final}}) - F(\mathbf{p})}{F(\mathbf{p})} < Error_{\lim} \tag{5}$$

where $Error_{\lim}$ is the maximum normalised decrease in the quality of the solution, arising from the execution of the Hill Climbing steps. Clearly, if a value of 0.0 is adopted for this quantity, solely the individuals which have improved during the adjustment procedure are accepted. Conversely, if the condition defined in Eq. (5) is not satisfied, the changes defined in $\mathbf{\Delta p_{final}}$ are rejected and the vector containing the best known solution to the problem is reset to $\mathbf{p}$. Lastly, as previously mentioned, the specification of a positive, non-zero value for $Error_{\lim}$ may allow a wider search area to be explored by preventing an excessively quick convergence of the solution to the numerous local minima or maxima likely to be encountered when analysing complex objective functions (Weise, 2009).

To demonstrate the meaning of the previously introduced concepts, the presented algorithm was employed in the minimisation of the function described by Eq. (6) and depicted in Fig. 1(a). Clearly, as the graph illustrates, a unique global minimum exists at $x = 0$ and $y = 0$, for which the function assumes a value of $F = 0.0$. Furthermore, given that the coefficient of y^2 is larger than that of x^2, a proportionally smaller search interval needs to be specified for the former, as changes in this variable affect the analysed function to a greater extent. In the present case, the selected search area is defined by the conditions $-2.0 < x < 2.0$ and $-1.0 < y < 1.0$. For this situation, due to the proposed formulation for the Hill Climbing method – in particular, Eq. (4) –, the step size is inherently dependent on the direction along which the solution is altered, as demonstrated in Fig. 1(b) for $\Delta_{max} = 5\%$ (i.e. $|\Delta x|_{max} = 5\% \cdot (x_{max} - x_{min}) = 0.2$ and $|\Delta y|_{max} = 5\% \cdot (y_{max} - y_{min}) = 0.1$).

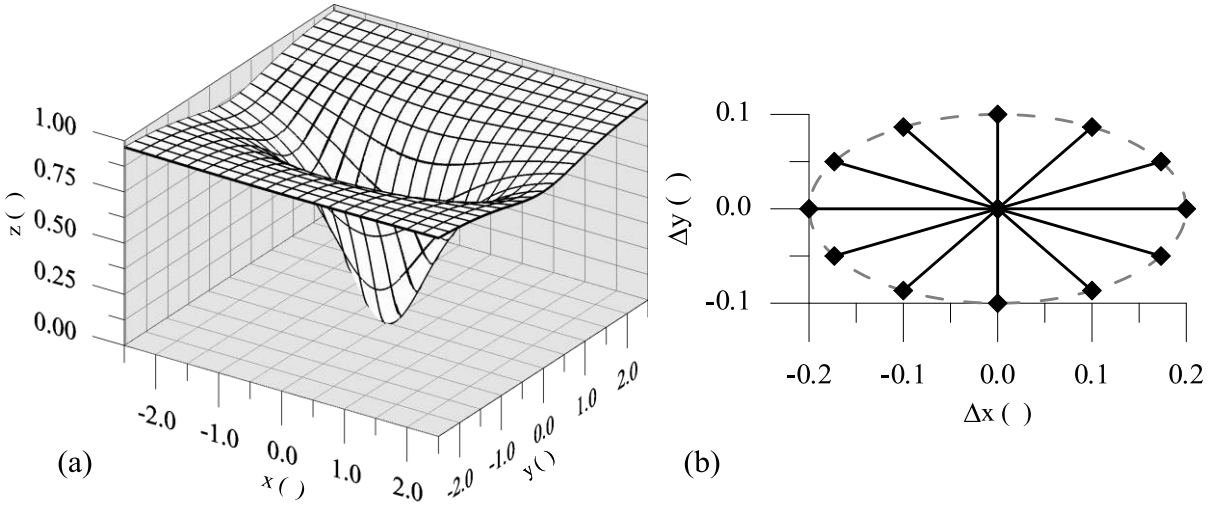

Fig. 1. (a) Three-dimensional representation of the selected function and (b) directionality of step size.

$$F(x,y) = 1.0 - \frac{1.0}{1.0 + x^2 + 4.0 \cdot y^2} \tag{6}$$

The obtained trajectories in $x - y$ space for two different initial solutions located at the border of the search area – $x_{0,1}$ = -2.0, $y_{0,1}$ = -1.0 and $x_{0,2}$ = 2.0, $y_{0,2}$ = 1.0 – are illustrated in Fig. 2, together with contours corresponding to various magnitudes of the analysed function. Furthermore, F = 0.10 was employed as a stopping criterion, while a value of N_{steps} = 3.0 was specified, meaning that the acceptance or rejection of the performed steps is determined once three successive adjustments have been carried out. Additionally, $Error_{\lim}$ was set to 0.0, implying that new solutions are only accepted when the corresponding value of F decreases. Lastly, in order to improve the readability of the figure, only the valid steps are depicted.

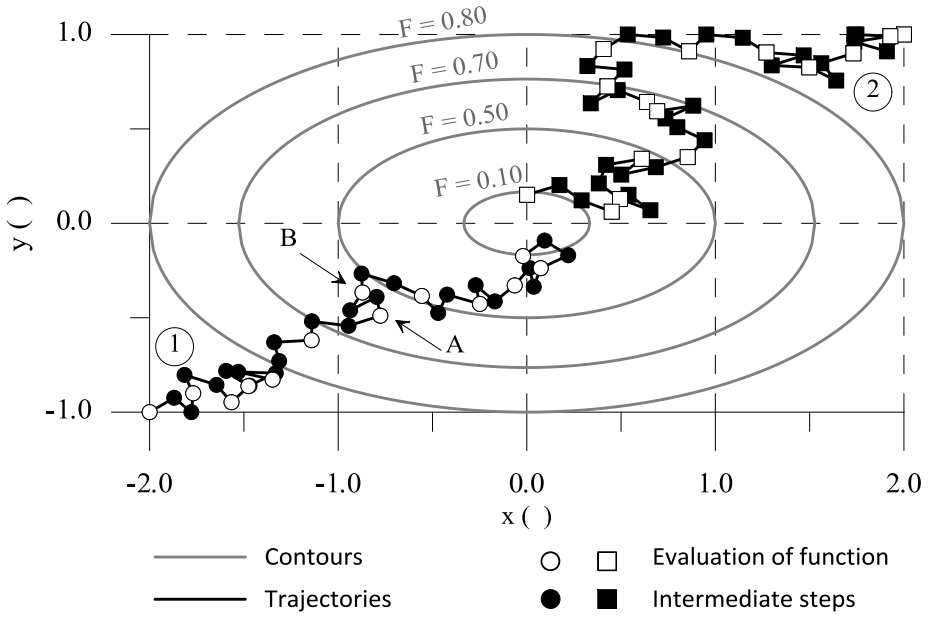

Fig. 2. Application of a hill climbing procedure to the minimisation of the function defined in Eq. (6).

In the presented figure, both the directionality of the steps (i.e. larger when aligned with the x axis) and the effect of evaluating the objective function solely after multiple adjustments have been performed are noticeable. Indeed, the latter aspect is particularly evident between the solutions indicated as A and B, for which a slight decrease in the function is determined at the end of the three steps, even though a considerable increase in the magnitude of F was obtained for the second adjustment.

2.3 Coupling of Optimisation Methods

The formulation of the Hill Climbing technique presented in the previous section was introduced in the Genetic Algorithms-based code *genUC* as an additional set of instructions to be carried out prior to the execution of the crossing and mutations procedures. A simplified diagram illustrating the implementation process is depicted in Fig. 3, where the relationship between the number of evaluations of the fitness of the population and the control quantities N_{steps} and N_{climb} is clearly indicated.

Indeed, according to Renders & Bersini (1994), the adopted structure suggests that the Hill Climbing procedure simulates individual learning (i.e. the independent life of each individual), while the Genetic Algorithm focuses on the evolution of the population as a whole. Therefore, this configuration attempts to combine the strength of the former technique

as a local search method with the ability of the latter to explore large search areas. Lastly, as a possible alternative to this coupling strategy, Renders & Bersini (1994) propose the introduction of new genetic operators – crossing and mutation procedures – formulated based on Hill Climbing principles.

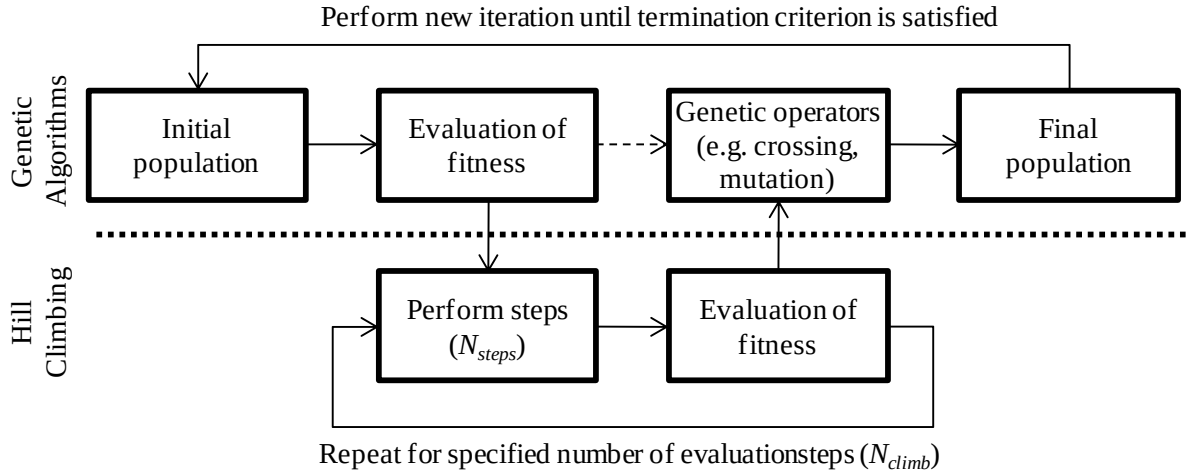

Fig. 3. Adopted scheme for implementing a hill climbing procedure into the genetic algorithms-based software.

3 COMPUTATIONAL STUDY

3.1 Methodology and Analysed Problem

The objective of the conducted computational studies is to evaluate the effect of introducing a Hill Climbing procedure on the performance of the Genetic Algorithms-based software *genUC*, when employed to determine the parameters required by the MCC model (Potts & Zdravković, 1999). Naturally, to eliminate the influence of the limitations of the selected constitutive relationship when reproducing real soil behaviour, the input data supplied to the code consisted of pseudo-experimental test results obtained using expressions identical to those implemented into *genUC*. Therefore, the computer software should be able to fit perfectly the MCC model to the chosen curves, while the proximity to the known solution (Table 1) can be used to assess the global accuracy of the method.

Table 1. Modified Cam-Clay model parameters employed in the generation of the input data.

κ	λ	ν_1	ϕ_{CS} (º)	ν
0.05	0.20	3.0	32.0	0.25

The employed pseudo-experimental tests, which are characterised in detail in Table 2, comprised undrained triaxial compression (UTXC), drained triaxial compression (DTXC) and one-dimensional consolidation (1-DC) tests. This combination of tests, as demonstrated by the results of the analyses performed by Taborda et al. (2010), ensures that a unique solution to the problem exists, with the error of the parameters estimated by the optimisation technique depending solely on the strictness of the selected stopping criterion. In the present case, the calculation was terminated once a mark of 10 was obtained for the best individual (Azeiteiro et al., 2009), which, according to Taborda et al. (2010), should guarantee an average error in the computed solution below 0.5%.

Table 2. Characteristics of the selected pseudo-experimental tests.

Reference	Type	$p'_{init.}$ (kPa)	OCR ( )	p'_{final} (kPa)
UD.1	UTXC	100.0	6.0	Critical state
UD.2	UTXC	500.0	1.2	Critical state
DR.1	DTXC	100.0	1.5	Critical state
OE.1	1-DC	100.0	1.5	1000.0

In terms of search area, the limit values for the different parameters are defined in Table 3. It has to be noted that, although the reliability of the Genetic Algorithms are thought to be essentially independent of the extent of the search area (Azeiteiro et al., 2010), reasonable limits are required, since the proposed formulation of the Hill Climbing procedure assumes a constant relationship between the step size and the range of possible values for each parameter.

Additionally, in all the analyses presented in the subsequent sections, the dimension of the employed population is $2^6 = 64$ individuals, while a variable probability alternate crossing process and a continuous mutation scheme (with a relative change of +/- 5%) have been chosen based on the results of previous studies (Azeiteiro et al., 2009). Lastly, due to the large number of random operations included in the global formulations of Genetic Algorithms (e.g. generation of initial population, crossing and mutation schemes, etc.) and Hill Climbing, it is necessary to repeat each analysis several times in order to draw meaningful conclusions. Indeed, as demonstrated by Taborda et al. (2010), the average error, computation time and number of iterations determined based on the results of 200 identical calculations are practically unaffected by the random nature of the various components of the algorithm. Therefore, a similar procedure was followed in the present situation, with each analysed case being defined by the average results of 200 calculations.

Table 3. Limits of the searched area.

Limit	κ	λ	ν_1	ϕ_{CS} (º)	ν
Min.($p_{i,min}$)	0.02	0.10	2.5	25.0	0.15
Max.($p_{i,max}$)	0.08	0.30	3.5	42.0	0.35

3.2 Influence of Proportion of Evaluation Steps

The first factor to be analysed is the frequency with which the population is evaluated during the application of the Hill Climbing procedure. Naturally, this aspect of the algorithm is directly controlled by the relation between N_{climb} and N_{steps}. Furthermore, to allow direct comparisons to be carried out, the product $N_{climb} \cdot N_{steps}$ must remain constant as it determines the total number of adjustments applied to each individual at the end of an iteration of the Genetic Algorithm. As a result, in addition to the basic situation for which the Hill Climbing component is not invoked, three cases were selected: $N_{climb} = 1$ and $N_{steps} = 9$; $N_{climb} = 3$ and $N_{steps} = 3$; $N_{climb} = 9$ and $N_{steps} = 1$. Briefly, the first of these combinations corresponds to evaluating the population solely after performing 9 consecutive adjustments, while the latter situation is characterised by the assessment of the quality of the solution at the end of each of the 9 steps, which clearly involves the execution of a significantly larger number of operations.

The results obtained for $\Delta_{max} = 5.0$ %, in terms of number of iterations and computation time, are illustrated in Fig. 4(a) and Fig. 4(b), respectively. As it can be seen, although the inclusion of Hill Climbing reduces significantly the amount of iterations necessary to reach the desired solution, the introduction of additional operations leads to a substantial increase of the total duration of the calculation with the number of evaluation steps. Thus, based on these

observations, it can be concluded that the Hill Climbing procedure, for the adopted parameters, affects negatively the global performance of the coupled optimisation technique.

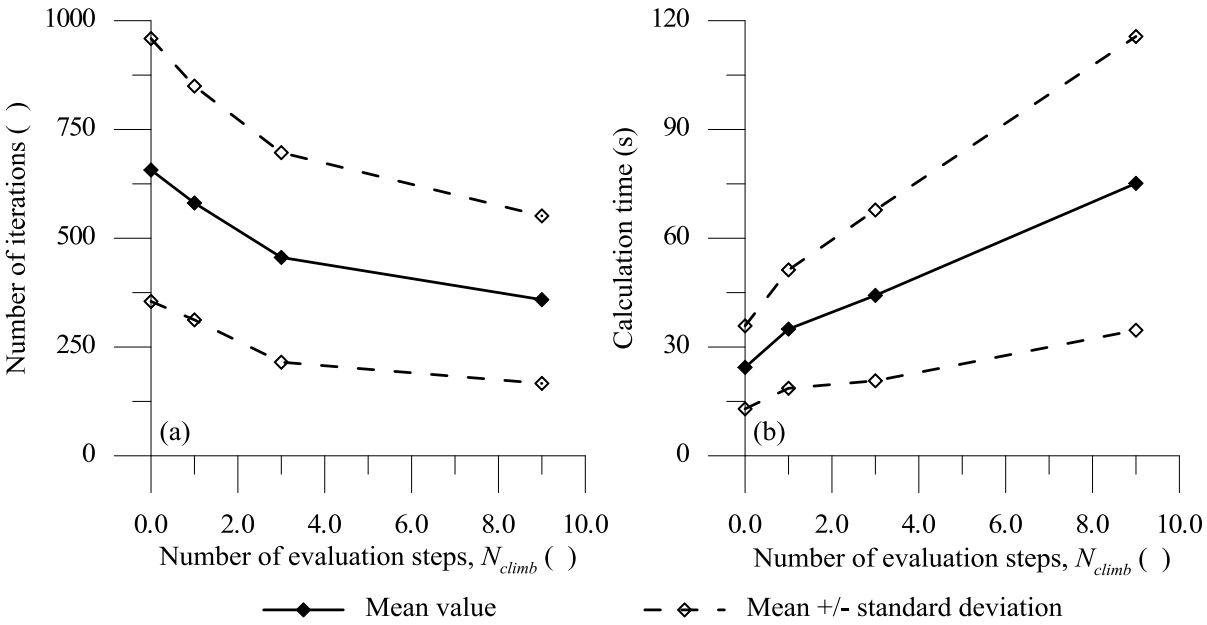

Fig. 4. Influence of evaluation steps on (a) number of iterations and (b) calculation time (Δ_{max} = 5%).

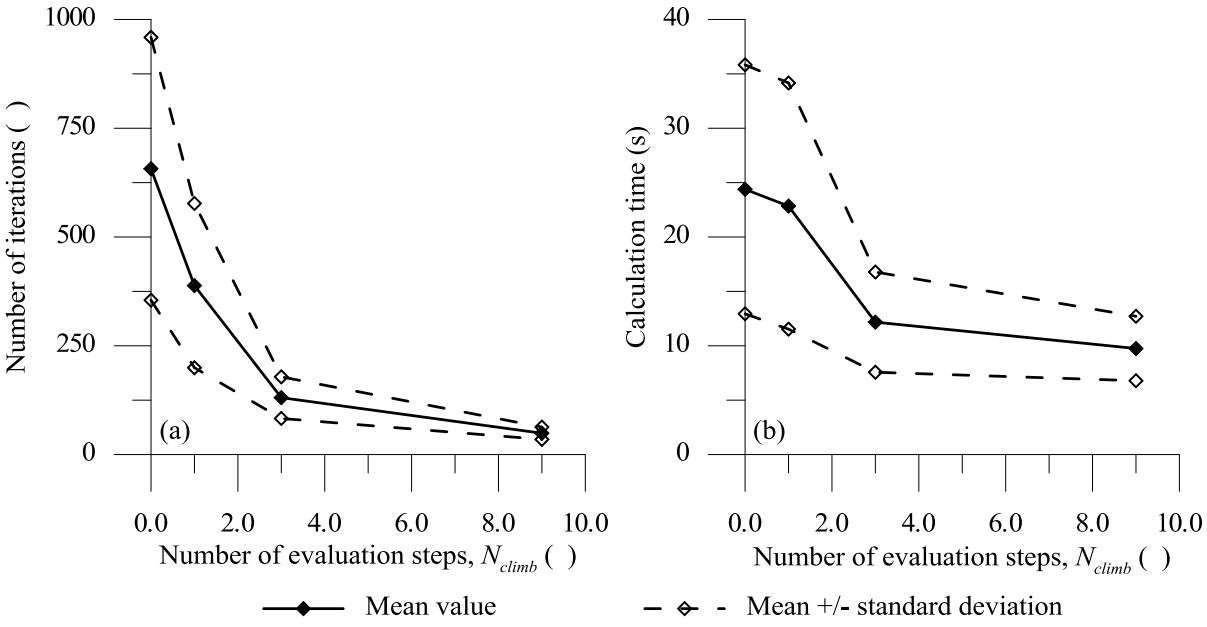

Fig. 5. Influence of evaluation steps on (a) number of iterations and (b) calculation time (Δ_{max} = 0.5%).

Subsequently, an identical study was conducted for Δ_{max} = 0.5 %, the results of which are presented in terms of number of iterations and computation time in Fig. 5(a) and Fig. 5(b), respectively. As it can be seen, similarly to the trend observed in the previous set of analyses, the number of iterations required to achieve the desired solution decreases significantly with the frequency of evaluation of the population. Indeed, the reduction is sufficiently sharp to compensate for the increase in the number of performed operations, thus leading to a decrease in the overall calculation time. Hence, in the present case, the introduction of Hill

Climbing resulted in a clear increase in the computational efficiency of the global optimisation procedure.

Lastly, the impact of the Hill Climbing component of the adjustment procedure on the time taken to carry out a single iteration of the Genetic Algorithm is depicted on Fig. 6. Clearly, there is a linear relationship between the proportion of evaluation steps and the measured computational effort, which is undoubtedly associated to the increase in the number of performed operations. Moreover, as expected, no discernible effect of the step size on this aspect of the calculation can be observed.

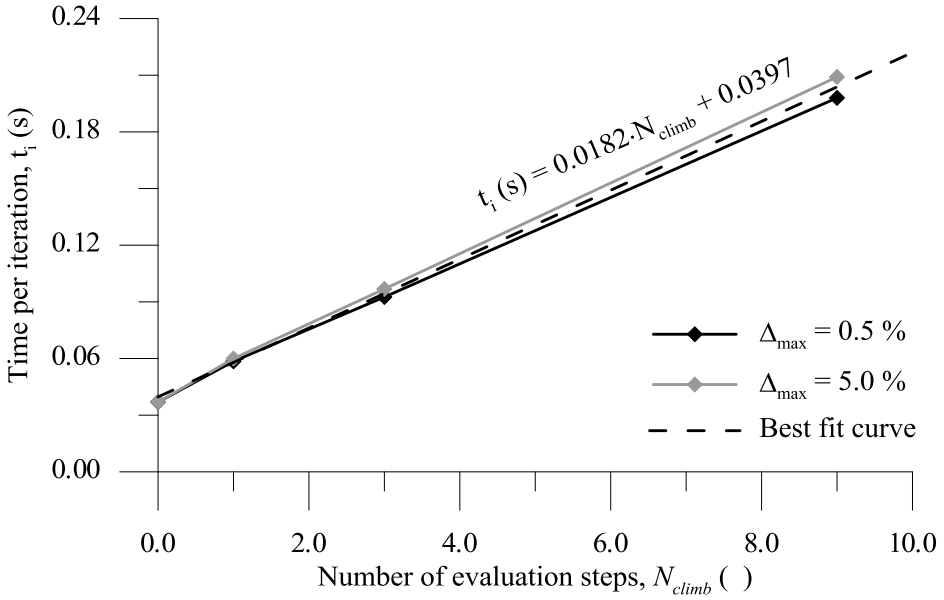

Fig. 6. Influence of evaluation steps on the time taken for each iteration for Δ_{max} of 0.5% and 5.0%.

3.3 Influence of Step Size

Given the conclusions of the previous analyses, the second computational study focused on the impact of the step size on the performance of the optimisation procedure. As a result, 16 different calculations were carried out for magnitudes of Δ_{max} varying between 1×10^{-4} % and 10 %, while assuming N_{steps} = 3 and N_{climb} = 3. The results in terms of number of iterations and total computation time are depicted in Fig. 7(a) and Fig. 7(b), respectively. Note that the values obtained without Hill Climbing are represented in the figures by the dashed line.

As it can be seen, independently of the step size, the introduction of Hill Climbing always leads to a decrease in the average number of iterations. However, in accordance with the conclusions drawn for the study presented in the previous section, this reduction is not always sufficient to result in a decrease of the calculation time, since a larger number of operations is executed when the Hill Climbing component of the algorithm is active. Moreover, it is interesting to note that the range of values of Δ_{max} leading to an increase in the efficiency of the optimisation procedure is considerably narrow – between 1×10^{-2} % and 1 % –, thus demonstrating the importance of specifying an adequate magnitude for this parameter. Indeed, for Δ_{max} = 0.2 %, savings of about 60 % on the overall calculation time were obtained, while for both $\Delta_{max} = 1\times10^{-4}$ % and Δ_{max} = 10 %, the introduction of Hill Climbing led to a duplication of the computational effort.

Naturally, although the drawn conclusions are likely to retain their validity for other combinations of N_{steps} and N_{climb}, additional analyses are required to establish a general relationship between Δ_{max} and the performance of the presented method.

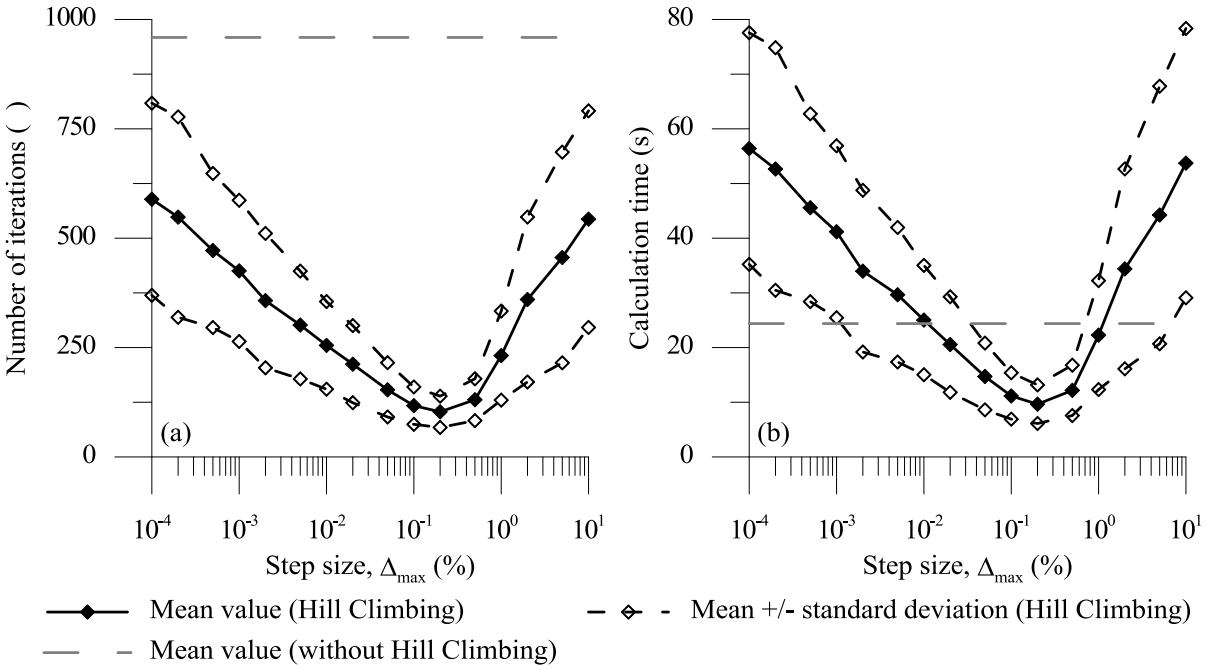

Fig. 7. Influence of step size on (a) number of iterations and (b) calculation time.

4 CONCLUSIONS

The general principles of Genetic Algorithms as a global search method and of Hill Climbing as a local search technique were briefly presented, giving particular emphasis to the formulation and application of the latter. Furthermore, a possible form of integrating the two methods, based on the notion that Hill Climbing could represent individual learning in the context of an evolutionary framework, was described.

The impact of the frequency with which the objective function is evaluated during the Hill Climbing part of the devised algorithm was assessed in the first of two detailed computational studies. Indeed, for a relatively large step size (5% of the extent of the search area), the introduction of Hill Climbing led to a considerable decrease in the required number of iterations. However, due to the associated increase in performed operations, the overall total computation time was observed to increase considerably with the number of evaluation steps. Conversely, when a smaller step size (0.5 % of the extent of the search area) was employed, the sharper reduction in the number of iterations compensated the increase in the number of operations, resulting in smaller calculation times for larger numbers of evaluation steps. Therefore, in this case, the inclusion of Hill Climbing clearly enhanced the efficiency of the Genetic Algorithm.

Subsequently, since two contradictory trends were observed in the first set of analyses, an additional computational study was carried out, in order to clarify the importance of the magnitude of the parameter controlling the step size. The obtained results indicated that, independently of the value adopted for this quantity, the introduction of Hill Climbing led to a reduction in the number of required iterations, when compared to the performance of a simple Genetic Algorithm. However, this observation was only accompanied by a decrease in computation time for a reasonably narrow interval of magnitudes of step size. Indeed, for step sizes either below the lower limit or above the upper limit of the identified interval, the inclusion of the Hill Climbing procedure resulted in a substantial increase in the duration of the optimisation process.

In conclusion, the coupling of Genetic Algorithms with local search techniques, such as the simple Hill Climbing procedure described in this paper, has the potential to reduce significantly the required computational effort. Moreover, a considerable dependency of the global performance of the algorithm on the respective control parameters (i.e. number of evaluation steps and step size) was observed, highlighting the necessity for further research on this subject.

REFERENCES

Azeiteiro, R.N., Coelho, P.A.L.F., Taborda, D., Pedro, A. & Antunes, D. (2009), "Computational study of the performance of a genetic algorithms-based software", Proceedings of the 1st International Symposium on Computational Geomechanics – COMGEO I, Juan-les-Pins, France.

Azeiteiro, R. N., Coelho, P. A. L. F., Taborda, D., Pedro, A. & Antunes, D. (2010) "Study on the multiplicity of solutions when calibrating geotechnical constitutive models using genetic algorithms", Proceedings of the 12h National Conference in Geotechnics – XII CNG, Guimarães, Portugal, 87-96 (in Portuguese).

Goh, A.T.C. (1999), "Genetic algorithm search for critical slip surface in multiple-wedge stability analysis". Can. Geotech. J., Vol. 36, 382-391.

Levasseur, S., Malécto, Y., Boulon, M. & Flavigny, E. (2008), "Soil parameter identification using a genetic algorithm". Int. J. Numer. Anal. Meth. Geomech., Vol. 32, 189-213.

McCombie, P. (2009), "Critical failure surface location using simple genetic algorithm and multiple wedge slope stability", Proceedings of the 1st International Symposium on Computational Geomechanics – COMGEO I, Juan-les-Pins, France.

Potts, D.M. & Zdravković, L. (1999) Finite element analysis in geotechnical engineering: theory, Thomas Telford, London.

Pal, S., Wathugala, G.W. & Kundu, S. (1996), "Calibration of a constitutive model using genetic algorithm". Comp. Geotech., Vol. 19(4), 325-348.

Renders, J. M. & Bersini, H. (1994) "Hybridizing genetic algorithms with hill-climbing methods for global optimization: Two possible ways", Proceedings of the First IEEE Conference on Evolutionary Computation, Orlando, FL, USA. Vol. 1, 312-317.

Schwefel, H.-P. (1995) Evolution and optimum seeking, Wiley Intersience, New York, NY.

Simpson, A.R. & Priest, S.D. (1993), "The application of genetic algorithms to optimization problems in geotechnics". Comp. Geotech., Vol. 15, 1-19.

Taborda, D., Coelho, P.A.L.F., Antunes, D. & Pedro, A. (2008), "Genetic algorithms as a calibration method for constitutive models", Proceedings of the 11th National Conference in Geotechnics – XI CNG, Coimbra, Portugal (in Portuguese).

Taborda, D., Pedro, A., Coelho, P.A.L.F. & Antunes, D. (2010), "Impact of input data on soil model calibration using genetic algorithms", Proceedings of the 7th European Conference on Numerical Methods in Geotechnical Engineering – NUMGE2010, Trondheim, Norway, 69-74.

Weise, T. (2009), Global optimization algorithms – theory and application, Self-published e-book, http://www.it-weise.de/projects/book.pdf (accessed 20/12/2010).

ON INTEGRATING BARODESY FOR PATHS STARTING FROM ZERO STRESS

Wolfgang Fellin
Division of Geotechnical and Tunnel Engineering, University of Innsbruck, Austria

Dimitrios Kolymbas
Division of Geotechnical and Tunnel Engineering, University of Innsbruck, Austria

ABSTRACT: *Barodesy is a new approach to constitutive modelling of soil based on two principles of* GOLDSCHEIDER*: (i) proportional strain paths starting from a stress free state lead to proportional stress paths and (ii) any stress path associated to a proportional strain path starting from a nonzero stress state will eventually approach the corresponding proportional stress path of (i). Barodesy, being inherently related and close to hypoplasticity, faces the same problem with stress rates calculated for any stretching applied to states with zero stress. This makes numerical integration impossible in this case. However, an incremental solution of this special loading case can be found analytically due to the simple mathematical structure of Barodesy, which is consistent with the rate formulation. This paper presents the analytical calculation of a stress increment for loading from a stress-free state, which can be implemented together with any standard numerical integration scheme in Finite-Element codes. The performance of this approach is checked by means of a one-dimensional compression test. Its benefit refers to problems where sand is considered near to free surfaces.*

1 INTRODUCTION

One of the main characteristics of granulates is that their stiffness increases with mean stress, i.e. with $|\mathrm{tr}\,\mathbf{T}|$.[1] This fact, called barotropy, was early recognised in Soil Mechanics and expressed e.g. with OHDE's relation $d\sigma/d\varepsilon \propto \sigma^{c_4}$ (Jefferies & Been 2000; Pestana & Whittle 1995). Adapting the exponent c_4 to oedometric tests with Hostun sand yields $c_4 = 0.5519$ (Kolymbas 2009). This value complies with early results in Soil Dynamics, according to which soil stiffness is proportional to the square root (i.e. $c_4 = 0.5$) of the stress (Hardin & Richart Jr 1963). An implication of this relation is that the stiffness of granulates vanishes at zero stress. The phenomenon of liquefaction is but a consequence of this effect. In gravity conditions, zero stress is encountered at the surface of soil deposits, and stress increases linearly with depth. From the view of numerics, however, the stress is nearly zero near to the surface, and this gives rise to numerical problems. A way to overcome such problems is to assume there a cohesion, which implies a non-vanishing stiffness. This assumption is physically justified in case of soils with silty and/or clayey components but not for cohesionless soils and/or granulates. The present paper aims at exploiting the mathematical structure of Barodesy, which is a new hypoplastic (Kolymbas 1985) approach to constitutive modelling of granulates, towards obtaining numerically sound solutions for loading paths starting from nearly stress-free states.

[1] $\mathbf{T}$ is the Cauchy stress, σ its value, $\sigma = |\mathbf{T}|$.

2 A SHORT OUTLINE OF BARODESY

As Barodesy is a quite new approach to model the behavior of cohesionless soil, we give here a short outline.

Barodesy is based on two rules of GOLDSCHEIDER that refer to proportional paths[2] applied to dry sand (Goldscheider 1976):

1. Proportional strain paths ($P\varepsilon P$) starting from the stress $\mathbf{T} = \mathbf{0}$ are associated to proportional stress paths ($P\sigma P$).
2. Proportional strain paths starting from $\mathbf{T} \neq \mathbf{0}$ lead asymptotically to the corresponding proportional stress paths obtained when starting at $\mathbf{T} = \mathbf{0}$.

The main concept of Barodesy is already published in (Kolymbas 2009), especially the implementation of the first rule, which is studied here in detail. The actual final version of modelling the second rule has changed a little bit and is briefly presented below.

The first rule is modelled by means of a function which relates the stretching $\mathbf{D}$ to a stress-like tensor $\mathbf{R}$ pointing in the direction of the corresponding proportional stress path (Kolymbas 2009)

$$\mathbf{R}(\mathbf{D}) = (\operatorname{tr}\mathbf{D}^0)\mathbf{I} + c_1 \exp(c_2\mathbf{D}^0) \,, \tag{1}$$

wherein the streching $\mathbf{D}$ is the symmetric part of the velocity gradient, and c_1, c_2 are material constants. The exponent 0 denotes the normalisation of a tensor $\mathbf{X}$, i.e. $\mathbf{X}^0 := \mathbf{X}/|\mathbf{X}|$ with $|\mathbf{X}| = \sqrt{\operatorname{tr}\mathbf{X}^2}$. A representation of this function for isochoric stretchings is given in Fig 1.

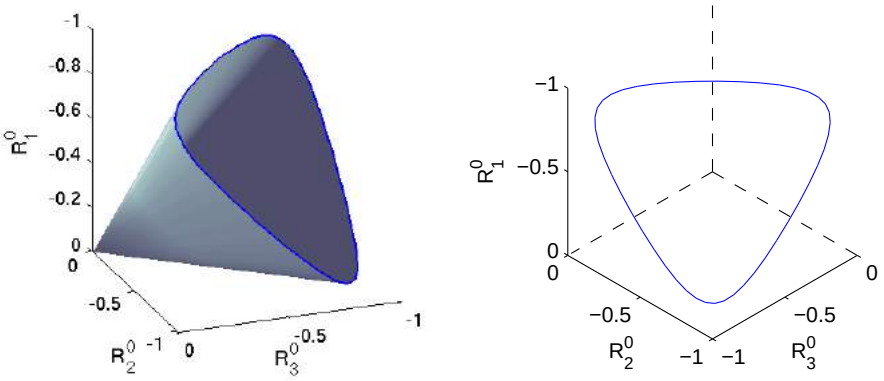

Fig. 1. Fan of stress directions $\mathbf{R}^0$ for isochoric stretchings ($\operatorname{tr}\mathbf{D} = 0$) in principal stress space: surface representation (left), cross section with a deviatoric plane at $\operatorname{tr}\mathbf{R}^0/\sqrt{3} = -1$ (right); $\mathbf{R}^0 = \mathbf{R}/|\mathbf{R}|$, $\mathbf{R}$ from Eq. 1, material parameters from Tab. 1.

The second rule implies an evolution equation of the Jaumann objective stress rate of the type

$$\mathring{\mathbf{T}} = (\hat{f}\mathbf{R}^0 + \hat{g}\mathbf{T}) \,. \tag{2}$$

The functions $\hat{f}$ and $\hat{g}$ are chosen (Kolymbas subm)

$$\hat{f} := f \cdot \dot{\varepsilon} \cdot h(\sigma) \tag{3}$$

$$\hat{g} := g \cdot \dot{\varepsilon} \cdot h(\sigma)/\sigma \tag{4}$$

[2] Proportional stress and strain paths are characterized by constant ratios of the principal values $T_1 : T_2 : T_3$ and $\varepsilon_1 : \varepsilon_2 : \varepsilon_3$, respectively.

to preserve homogeneity of the first degree with respect to $\mathbf{D}$, wherein $\sigma := |\mathbf{T}|$ and $\dot{\varepsilon} := |\mathbf{D}|$

$$\mathring{\mathbf{T}} = h(\sigma) \cdot [f\mathbf{R}^0 + g\mathbf{T}^0)] \cdot \dot{\varepsilon} \ . \tag{5}$$

This evolution equation enforces $\mathbf{T}^0$ to approach $\mathbf{R}^0$ for constant stretching, i.e. the stress direction $\mathbf{R}^0$ acts as attractor.

The function $h(\sigma)$ is set to

$$h(\sigma) := c_3 \sigma^{c_4} \ , \tag{6}$$

with $c_4 < 1$ to take barotropy into account. The critical state concept is implemented via assuming $f = f(e)$ and $g = g(\sigma)$

$$f(e) = \frac{1 + e_{c_0}}{1 + e} - c_5 \mathrm{tr}\,\mathbf{D}^0 \tag{7}$$

$$g(\sigma) = -\exp\left(\frac{\sigma^{1-c_4}}{c_3 c_5 (1 - c_4)}\right) \ , \tag{8}$$

with e_{c_0} being the critical void ratio at zero pressure.

When the stress state reaches the critical state the stress rate vanishes, $\mathring{\mathbf{T}} = \mathbf{0}$, and the stress direction meets the direction of $\mathbf{R}$, $\mathbf{R}^0 = \mathbf{T}^0$. It follows from (5) that

$$f(e) + g(\sigma) = 0 \tag{9}$$

for critical states, which is the equation of the critical state line. For non-isochoric proportional paths and incrompressible grains a generalised critical state relation

$$f(e) + g(\sigma) = c_5 \mathrm{tr}\,\mathbf{D}^0 \tag{10}$$

results from (7) and (8) (Kolymbas subm).

The material parameters for Hostun RF Sand (Desrues, Zweschper, & Vermeer 2000) are given in Tab. 1. Exemplary numerical results of element tests are shown in Figs. 2 and 3

Table 1. Material parameters of Barodesy for Hostun RF Sand.

e_{c_0}	c_1	c_2	c_3	c_4	c_5
1.0	-1.7637	-1.0246	2358 kPa$^{1-c_4}$	0.5519	0.5080

3 NUMERICAL INTEGRATION

The equations of motion together with the constitutive equations form a coupled system embedded into an initial-boundary value problem. A solution of this system is usually obtained by co-simulation: the equations of motion are solved with the help of a finite-element package, and the constitutive equations by a solver for ordinary differential equations in a so called material subroutine. The material subroutine is usually supplied by a rotation-free strain increment $\Delta\boldsymbol{\epsilon}$ along with a time increment Δt and the state variables (i.e. stress and additional material variables) at $t = 0$. It has to return the stress increment and the derivative of the stress increment with respect to the strain increment. The latter is not discussed here, however a general approach

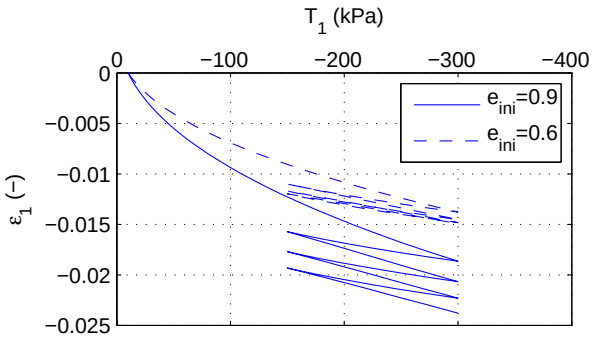

Fig. 2. Oedometric compression: initial stress $T_1 = -10$ kPa, $T_2 = T_3 = K_0 T_1$ with $K_0 = R_2/R_1 = 0.4672$; initial void ratio $e_{\text{ini}} = 0.6$, to represent a dense specimen and $e_{\text{ini}} = 0.9$, to represent a loose specimen; material parameters from Tab. 1.

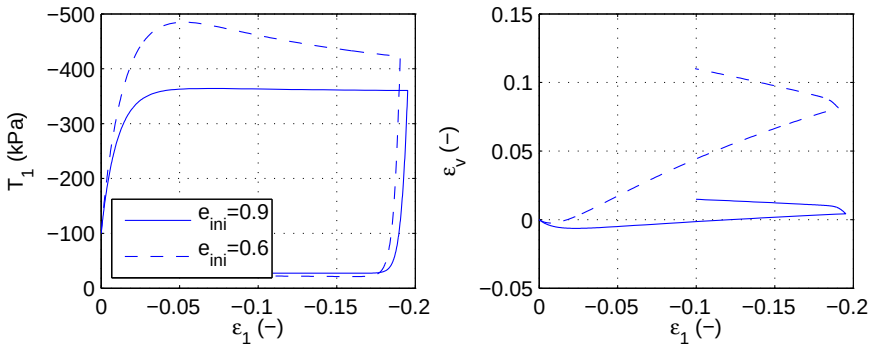

Fig. 3. Triaxial compression: initial stress $T_1 = T_2 = T_3 = -100$ kPa; initial void ratio $e_{\text{ini}} = 0.6$, to represent a dense specimen and $e_{\text{ini}} = 0.9$, to represent a loose specimen; material parameters from Tab. 1.

to tackle constitutive models of the rate type has already been worked out (Fellin & Ostermann 2002). The stretching is assumed to be constant during the integration window Δt

$$\mathbf{D} = \frac{\Delta \boldsymbol{\epsilon}}{\Delta t} \,, \tag{11}$$

which yields a $P\varepsilon P$ for the time integration.

Some error-controlled sub-stepping must be applied to get reliable results (Fellin & Ostermann 2002; Fellin, Mittendorfer, & Ostermann 2009). Let us denote this adaptive time sub-step with τ_n, i.e $\mathbf{T}_{n+1} = \mathbf{T}_n + \dot{\mathbf{T}}\,\tau_n$.

For $\mathbf{T}_n = \mathbf{0}$, Barodesy (5) will yield $\mathbf{T}_{n+1} = \mathbf{T}_n$. However, the simple mathematical structure of Barodesy allows an analytical time integration along proportional stress paths. Goldscheider's first rule postulates that $P\varepsilon P$ starting from a stress state $\mathbf{T} = \mathbf{0}$ are associated with $P\sigma P$, i.e. $\mathbf{T}^0 = \mathbf{R}^0$ along the whole path. In turn, for a given stretching any stress path will be a proportional one, when we start at $\mathbf{T} = \mathbf{0}$.

We obtain for a $P\varepsilon P$ from (5) with $\mathbf{T}^0 = \mathbf{R}^0$ and (10)

$$\dot{\mathbf{T}} = -c_5 h(\sigma) \mathbf{T}^0 \operatorname{tr} \mathbf{D}^0 \dot{\varepsilon} \,, \tag{12}$$

which can be simplified with $\operatorname{tr} \mathbf{D} = \dot{e}/(1+e)$ and $\dot{\mathbf{T}} = \dot{\sigma}\mathbf{T}^0$ to

$$\dot{\sigma} = -c_5 h(\sigma) \frac{\dot{e}}{1+e} \,. \tag{13}$$

Introducing (6) and integrating yields

$$\sigma = \left(c_3 c_5 (1 - c_4) \ln \frac{1+e_0}{1+e} \right)^{\frac{1}{1-c_4}} \tag{14}$$

with e_0 being the (initial) void ratio at $\sigma = 0$.

We investigate now the first time sub-step and will drop the index n for simplicity. The given stretching (11) will cause a change of the void ratio

$$\dot{e} = (1 + e_0)\mathrm{tr}\,\mathbf{D} \; . \tag{15}$$

in the case of incompressible grains. The increment of the void ratio is

$$\Delta e = \dot{e}\,\tau = (1 + e_0)\mathrm{tr}\,\mathbf{D}\,\tau \; . \tag{16}$$

With this (14) results in the stress increment

$$\Delta\sigma = \left(c_3 c_5 (1 - c_4) \ln \frac{1 + e_0}{1 + e + \Delta e} \right)^{\frac{1}{1-c_4}} \tag{17}$$

We know that $\dot{\mathbf{T}} = \dot{\sigma}\mathbf{T}^0$, which is for a $P\sigma P$ also $\dot{\mathbf{T}} = \dot{\sigma}\mathbf{R}^0$, where $\mathbf{R}^0$ is known from the given stretching and constant throughout the integration. The stress increment is then

$$\Delta\mathbf{T} = \dot{\mathbf{T}}\,\tau = \dot{\sigma}\mathbf{T}^0\,\tau = \Delta\sigma\mathbf{R}^0 \; , \tag{18}$$

in this time sub-step. The updated stress will, thus, differ from zero, therefore the subsequent integration can be performed using (5).

This approach is meaningful for compressive stretchings ($\mathrm{tr}\,\mathbf{D} < 0$) only. The stress should not change for expansions ($\mathrm{tr}\,\mathbf{D} < 0$) starting from zero stress.

4 EXAMPLE

We collect the components of the stress tensor $\mathbf{T}$ and the additional state variable e in a vector $\mathbf{y} = [T_{11}, T_{22}, T_{33}, T_{12}, T_{13}, T_{23}, e]$ for the numerical integration and obtain a nonlinear system of differential equations

$$\mathbf{y}'(t) = \mathbf{f}(\mathbf{y}(t)) \tag{19a}$$

$$\mathbf{y}(0) = \mathbf{y}_0 \; , \tag{19b}$$

with $m = 7$ components, wherein the function $\mathbf{f}$ is a vector version of (5) for the stress components and (15) for the void ratio.

We use the *Richardson extrapolation* of the explicit Euler method, which is a second order method allowing adaptive sub-step sizes. We give a short outline of the method below, details see e.g. (Fellin & Ostermann 2002; Fellin, Mittendorfer, & Ostermann 2009).

4.1 Richardson extrapolation

Let $\widetilde{\mathbf{y}}_n$ be the numerical approximation to the exact solution of (19) at time t_n. To obtain a numerical approximation at time $t_{n+1} = t_n + \tau_n$, we perform one Euler step of size τ_n

$$\mathbf{v} = \widetilde{\mathbf{y}}_n + \tau_n \mathbf{f}(\widetilde{\mathbf{y}}_n) \; , \tag{20a}$$

as well as two Euler steps of size $\tau_n/2$

$$\mathbf{w} = \widetilde{\mathbf{y}}_n + \frac{\tau_n}{2}\mathbf{f}(\widetilde{\mathbf{y}}_n) + \frac{\tau_n}{2}\mathbf{f}\Big(\widetilde{\mathbf{y}}_n + \frac{\tau_n}{2}\mathbf{f}(\widetilde{\mathbf{y}}_n)\Big) \; . \tag{20b}$$

Their combination

$$\widetilde{\mathbf{y}}_{n+1} = 2\mathbf{w} - \mathbf{v}\ , \tag{21}$$

is a second order approximation to the solution. The difference of the auxiliary values (20)

$$\text{EST} = \|\mathbf{w} - \mathbf{v}\| \tag{22}$$

is an asymptotically correct estimate for the error. If the estimated error EST is below a user-supplied tolerance TOL, the step is accepted and the new step size

$$\tau_{\text{new}} = \tau_n \cdot \min\left(\kappa_{\text{I}},\ \max\left(\kappa_{\text{D}},\ 0.9 \cdot \sqrt{\frac{\text{TOL}}{\text{EST}}}\ \right)\right) \tag{23}$$

is chosen for the next step (Hairer, Nørsett, & Wanner 1993). If the estimated error EST is larger than TOL, however, we reject the step and redo it with a smaller step size, given again by (23).

The factor 0.9 in (23) is a safety factor that accounts for the neglected higher order terms of (22). The other two constants κ_{D} and κ_{I} limit the step size change (maximum decrease and increase, respectively). A typical choice is $\kappa_{\text{D}} = 0.2$ and $\kappa_{\text{I}} = 2$.

In order to obtain a reliable error estimate, it is common to use a scaled maximum norm in (22)

$$\|\mathbf{v} - \mathbf{w}\| = \max_{i=1,\ldots,m} \left| \frac{v_i - w_i}{s_i} \right| \tag{24}$$

with the scaling factors

$$s_i = a_i + r_i \cdot \max\bigl(|(\widetilde{\mathbf{y}}_n)_i|\,, |(\widetilde{\mathbf{y}}_{n+1})_i|\bigr)\ .$$

The parameters a_i and r_i are used to fine-tune the error estimate. Taking $a_i = 0$ and $r_i = 1$ results in a relative error estimate. This is important when the absolute value of the corresponding quantity (a stress component, e.g.) gets considerably larger than 1. On the other hand, this choice is dangerous whenever the solution gets close to zero. In the latter case, the absolute error should be controlled.

Let AERR_i be the largest absolute error of component i accepted by the user. Then the choice

$$a_i = \frac{\text{AERR}_i}{\text{TOL}} \tag{25}$$

enforces that steps with errors larger than AERR_i (in component i) will be rejected. A one-dimensional example illustrating the effect of AERR on the step size selection is given in Table 2.

Table 2. One-dimensional example ($m = 1$) of error control with TOL $= 10^{-3}$ and $r = 1$: the step is accepted or rejected depending on the size of AERR.

v	w	AERR= 10	AERR= 1
100,005	100,000	accepted	accepted
10,005	10,000	accepted	accepted
1,005	1,000	accepted	*rejected*
105	100	accepted	*rejected*

The following values for the tolerances are used in all numerical experiments: $\text{TOL} = 5 \cdot 10^{-4}$, $\text{AERR}_{\mathbf{T}} = \text{AERR}_e = \text{TOL}/10$. We choose $r_i = 1$.

4.2 One-dimensional compression

We use the above derived closed-form integral expression of Barodesy (18) in rate form, i.e. $\dot{\mathbf{T}} = \Delta\mathbf{T}/\tau$ instead of the rate equation (5) for stresses $\sigma < \text{AERR}_{\mathbf{T}}$ to be consistent with the tolerances of the adaptive numerical integrator. The result of a one-dimensional (oedometric) compression starting with $\mathbf{T}_0 = \mathbf{0}$ is shown in Fig. 4. The first integration sub-step was performed using the rate form of (18) for calculating $\mathbf{v}$ and the first half step of $\mathbf{w}$,[3] compare (20), and the original Barodesy equation (5) for the second half step of $\mathbf{w}$. The further integration was performed using the original Barodesy equation (5) only. The first numerical solution $\widetilde{\mathbf{y}}_1 = 2\mathbf{w} - \mathbf{v}$ and the error estimate $\text{EST} = \|\mathbf{w} - \mathbf{v}\|$ include both the analytical and rate expression of berodesy. As the analytic version is consistent to the rate form, the first step size is similar to the following step-sizes of integrating the original barodetic equations to fullfill the accuracy requirement $\text{EST} = \|\mathbf{w} - \mathbf{v}\| < \text{TOL}$.

As comparison we decided to use Elasticity ($E = 500\,\text{kPa}$, $\nu = 0.3$) for $\sigma < \text{AERR}_{\mathbf{T}}$. The result is shown in the right plot of Fig. 4: One can clearly see that the adaptive integrator needs much more sub-steps in the beginning. This is due to the inconsistency between Elasticity and Barodesy, which forces the integrator to perform very small sub-steps to achieve the desired accuracy.

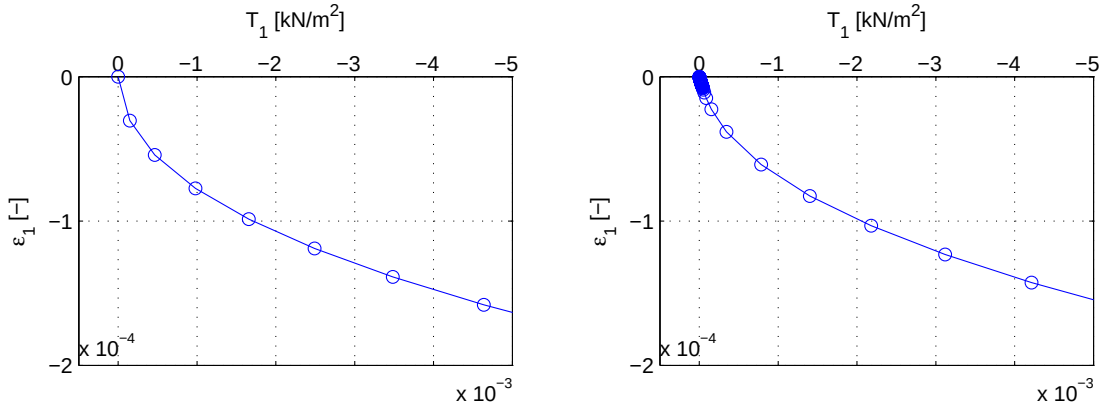

Fig. 4. One-dimensional compression with initial stress $\mathbf{T}_0 = \mathbf{0}$ (material parameters from Tab. 1): (left) presented approach, (right) elastic behaviour for $\sigma < \text{AERR}_{\mathbf{T}}$; circles denote time sub-steps. Note, that the adaptive integrator needs much more sub-steps in the latter case due to the inconsistency between Elasticity and Barodesy.

5 CONCLUSION

The constitutive equations of Barodesy, a new hypoplastic model for soils, cannot be integrated numerically for stretchings applied to states with zero stress, which occurs at (and near to) free surfaces of a cohesionless soil. This applies also to former versions of hypoplasticity, but in contrary to these versions the simple mathematical structure of Barodesy allows an analytical integration in this situation. This analytical solution can be implemented in a standard adaptive time integration scheme. Simple work-arounds, like using elastic constitutive equations for zero stress states, increases the number of required sub-steps considerably, which enlarges the computational costs.

[3] $\sigma > \text{AERR}_{\mathbf{T}}$ for $t = \tau_1/2$

REFERENCES

Desrues, J., Zweschper, B., & Vermeer, P. (2000). Database for tests on hostun rf san. Institutsbericht 13, Institut für Geotechnik, Universität Stuttgart.

Fellin, W., Mittendorfer, M., & Ostermann, A. (2009). Adaptive integration of constitutive rate equation. *Computers and Geotechnics 36*, 698–708.

Fellin, W. & Ostermann, A. (2002). Consistent tangent operators for constitutive rate equations. *International Journal for Numerical and Analytical Methods in Geomechanics 26*, 1213–1233.

Goldscheider, M. (1976). Grenzbedingung und Fließregel von Sand. *Mechanics Research Communication 3*, 463–468.

Hairer, E., Nørsett, S., & Wanner, G. (1993). *Solving Ordinary Differential Equations I. Nonstiff Problems* (2 ed.). Berlin: Springer.

Hardin, B. & Richart Jr, F. (1963). Elastic wave velocities in granular soils. *Journal of the Soil Mechanics and Foundation Division, ASCE 89*(1), 33–65.

Jefferies, M. & Been, K. (2000). Implications for critical state theory from isotropic compression of sand. *Géotechnique 50*(4), 419–429.

Kolymbas, D. (1985). A generalized hypoelastic constitutive law. In *Proc. XI Int. Conf. Soil Mechanics and Foundation Engineering, San Francisco*, Volume 5, Rotterdam, pp. 2626. Balkema.

Kolymbas, D. (2009). Sand as an archetypical natural solid. In D. Kolymbas & G. Viggiani (Eds.), *Mechanics of Natural Solids*, pp. 1–26.

Kolymbas, D. (subm). Barodesy: A new hypoplastic approach. *International Journal for Numerical and Analytical Methods in Geomechanics*.

Pestana, J. & Whittle, A. (1995). Compression model for cohesionless soil. *Géotechnique 45*(4), 611–631.

HETEROGENEOUS SEDIMENT TRANSPORT MODEL APPLIED TO TAILINGS DAMS

A.L.B. Cavalcante
Department of Civil Engineering and Environmental, University of Brasilia, Brasilia, Brazil

M.M. de Farias
Department of Civil Engineering and Environmental, University of Brasilia, Brasilia, Brazil

ABSTRACT: *This paper presents an alternative method to solve the system of equations that represent the phenomenon of the bed load transport in tailings dams. The field conditions that govern this problem include Navier-Stokes equations for the fluid and the mass balance of sediments, besides a constitutive relation for rate of transported sediments is also required. The Navier-Stokes equations include an advective term. If these equations are solved using traditional approximation techniques, such as the Finite Differences Method (FDM), the numerical solution generates spurious dissipations that are not related to the real physical phenomenon. In order to solve this problem, the equations are split into non-advective and advective parts and the so-called Cubic Interpolated Pseudo-Particle Method (CIP) is applied to solve the advective phase. The numerical scheme is then used to perform a few parametric anlyses in order to gain further insight of the mechanisms that rule the bed load transport in tailings dams. The solution was also compared to experimental data obtained both from laboratory and in situ tests, and the model could adequately reproduce the actual deposition phenomenon.*

1 INTRODUCTION

Tailings dams built using hydraulic fill technique normally present geotechnical deficiencies related to construction aspects and safety. The material is placed randomly and the physical variables which affect the hydraulic deposition process normally change considerably during construction. The hydraulic problem must satisfy field equations related to equilibrium, water and solid mass continuity, as well as a constitutive relation for the rate of transport. Cavalcante (2004) presented a 2D model to simulate the bed load transport of heterogeneous sediments. This model couples Navier-Stokes equations, representing continuity and equilibrium of the fluid phase, with the equation for the conservation of mass of the solid sediments. Besides, a constitutive relation that describes the rate of transported sediments should also be adopted. This paper extends the model to a 3D case, considering all the conditions above. The model also incorporates the properties of the tailings (mean diameter and percentage of iron) and of the pumping process (flow rate and slurry concentration). The problem is transient, coupled and non-linear, and it may be solved either analytically or numerically depending on the boundary conditions.

Heterogeneous sediments or tailings, comprising iron and quartz particles, are commonly produced during the extraction and concentration of iron. The bed load transport phenomenon, in which the particles roll when carried by a thin film of water, is the most

representative of the actual condition that is observed during the construction of tailings dams using hydraulic deposition techniques. Despite some engineering drawbacks, mainly if the upstream construction method is used, this is the solution for waste disposal generally adopted by most mining industries, due to its relatively low costs.

The coupled model for the conditions of equilibrium and continuity of the fluid phase, plus the continuity of the solid sediments, results in a system of hyperbolic equations. In this kind of problem the material is transported without dissipation. Nevertheless, if this system of equation is solve using classic techniques, such as the explicit Finite Differences Method (FDM), the solution introduces spurious dissipations that are purely numerical without any relation with the real physical problem. In order to overcome this problem, another technique known as the Cubic Interpolated Pseudo-particle method (CIP) is adopted in this paper.

2 COUPLED MODEL

In this section, a mathematical model for the bed load transport of heterogeneous sediments is presented (Figure 1). The model couples the behavior of the fluid phase and the sediments, composed of particles of quartz and iron. The objective when developing this model was to devise a mathematical and numerical tool that could help to forecast the profile of hydraulic deposition, including segregation, in tailings dams. Parametric analyses using this model, are very useful to gain further insight about the mechanisms involved during the deposition process, such as the distribution of density, porosity and grain sizes along the profile, as a function of the production variables (discharge and pulp concentration).

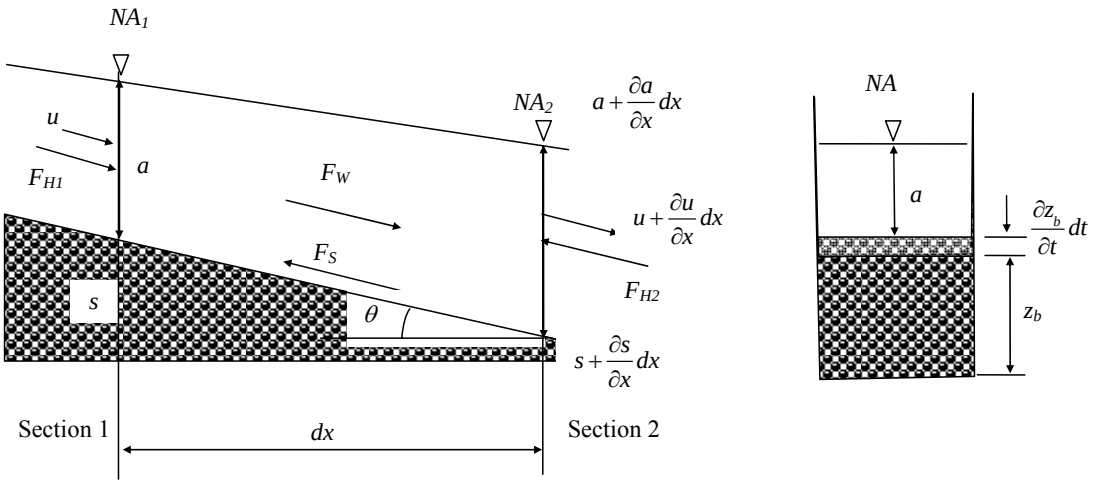

Fig. 1. Details of an infinitesimal element in the upstream slope.

Considering the continuity of the fluid phase, equilibrium in the fluid, continuity of transported sediments and a relation for the rate of sediment transport, respectively, one can deduce the following equations:

$$a_t + ua_x + va_y = -a\left(u_x + v_y\right) \tag{1}$$

$$\left(ua\right)_t + u\left(ua\right)_x + v\left(ua\right)_y = ga\left(-z_{bx} - a_x\right) - gu\sqrt{u^2+v^2}\,/\left(C_h^2 a\right) - ua\left(u_x + v_y\right) \tag{2a}$$

$$\left(va\right)_t + u\left(va\right)_x + v\left(va\right)_y = ga\left(-z_{by} - a_y\right) - gv\sqrt{u^2+v^2}\,/\left(C_h^2 a\right) - va\left(u_x + v_y\right) \tag{2b}$$

$$z_{b_t} + \left(s_x\right)_x + \left(s_y\right)_y = 0 \tag{3}$$

$$s_x = \sum_k m_k u^{n_K} \tag{4a}$$

$$s_y = \sum_k m_k v^{n_K} \tag{4b}$$

in which u is the velocity of transport of sediments in x direction, v is the velocity of transport of sediments in y direction, a is the film of water above the bed of the deposition profile, z_b is the height of deposited sediments, s_x is the rate of transported sediments composed of particles of two types k (quartz, Qz and iron, Fe) in x direction, s_y is the rate of transported sediments composed of particles of two types k (quartz, Qz and iron, Fe) in y direction, C_h is the coefficient of Chèzy, m_k and n_k are empirical constants dependent on the properties of the sediments, x and y are the system of coordinates, as illustrated in Fig. 1, and t is time.

One can deduce a numerical solution for the system of equations (1)-(4), based on the Finite Differences Method using advanced differences in time and central differences in the space domain. The resulting explicit algorithm is summarized as follows:

$$\begin{aligned} a_{k,l}^{n+1} = a_{k,l}^{n} &- \frac{\Delta t}{2\Delta x}\left\{a_{k,l}^{n}\cdot\left(u_{k+1,l}^{n}-u_{k-1,l}^{n}\right)+u_{k,l}^{n}\cdot a_{k+1,l}^{n}-a_{k-1,l}^{n}\right\} \\ &- \frac{\Delta t}{2\Delta y}\left\{a_{k,l}^{n}\cdot\left(v_{k,l+1}^{n}-v_{k,l-1}^{n}\right)-v_{k,l}^{n}\cdot\left(a_{k,l+1}^{n}-a_{k,l-1}^{n}\right)\right\} \end{aligned} \tag{5}$$

$$\begin{aligned} (u\cdot a)_{k,l}^{n+1} = (u\cdot a)_{k,l}^{n} &- \frac{\Delta t}{2\Delta x}\cdot u_{k,l}^{n}\cdot\left\{(u\cdot a)_{k+1,l}^{n}-(u\cdot a)_{k-1,l}^{n}\right\}-\frac{\Delta t}{2\Delta x}\cdot u_{k,l}^{n}\cdot a_{k,l}^{n}\cdot\left(u_{k+1,l}^{n}-u_{k-1,l}^{n}\right) \\ &- \frac{\Delta t}{2\Delta y}\cdot v_{k,l}^{n}\cdot\left\{(u\cdot a)_{k,l+1}^{n}-(u\cdot a)_{k,l-1}^{n}\right\}-\frac{\Delta t}{2\Delta y}\cdot u_{k,l}^{n}\cdot a_{k,l}^{n}\cdot\left(v_{k,l+1}^{n}-v_{k,l-1}^{n}\right) \\ &- \frac{g\cdot\Delta t}{2\Delta x}\cdot a_{k,l}^{n}\cdot\left(z_{bk+1,l}^{\ n}-z_{bk-1,l}^{\ n}+a_{k+1,l}^{n}-a_{k-1,l}^{n}\right)-\frac{g\cdot\Delta t}{C_h^2}\cdot\frac{u_{k,l}^{n}\cdot\left(\left[u_{k,l}^{n}\right]^2+\left[v_{k,l}^{n}\right]^2\right)^{1/2}}{a_{k,l}^{n}} \end{aligned} \tag{6a}$$

$$\begin{aligned} (v\cdot a)_{k,l}^{n+1} = (v\cdot a)_{k,l}^{n} &- \frac{\Delta t}{2\Delta x}\cdot u_{k,l}^{n}\cdot\left\{(v\cdot a)_{k+1,l}^{n}-(v\cdot a)_{k-1,l}^{n}\right\}-\frac{\Delta t}{2\Delta x}\cdot v_{k,l}^{n}\cdot a_{k,l}^{n}\cdot\left(u_{k+1,l}^{n}-u_{k-1,l}^{n}\right) \\ &- \frac{\Delta t}{2\Delta y}\cdot v_{k,l}^{n}\cdot\left\{(v\cdot a)_{k,l+1}^{n}-(v\cdot a)_{k,l-1}^{n}\right\}-\frac{\Delta t}{2\Delta y}\cdot v_{k,l}^{n}\cdot a_{k,l}^{n}\cdot\left(v_{k,l+1}^{n}-v_{k,l-1}^{n}\right) \\ &- \frac{g\cdot\Delta t}{2\Delta y}\cdot a_{k,l}^{n}\cdot\left(z_{bk,l+1}^{\ n}-z_{bk,l-1}^{\ n}+a_{k,l+1}^{n}-a_{k,l-1}^{n}\right)-\frac{g\cdot\Delta t}{C_h^2}\cdot\frac{v_{k,l}^{n}\cdot\left(\left[u_{k,l}^{n}\right]^2+\left[v_{k,l}^{n}\right]^2\right)^{1/2}}{\left(a_{k,l}^{n}\right)} \end{aligned} \tag{6b}$$

$$z_{bk,l}^{\ n+1} = z_{bk,l}^{\ n} - \frac{\Delta t}{2\cdot\Delta x}\left(s_{xk+1,l}^{\ n}-s_{xk-1,l}^{\ n}\right)-\frac{\Delta t}{2\cdot\Delta y}\left(s_{yk,l+1}^{\ n}-s_{yk,l-1}^{\ n}\right) \tag{7}$$

$$s_{xk}^{\ n+1} = m_{Qz}\left[u_k^n\right]^{n_{Qz}} + m_{Fe}\left[u_k^n\right]^{n_{Fe}} \tag{8a}$$

$$s_{yk}^{\ n+1} = m_{Qz}\left[v_k^n\right]^{n_{Qz}} + m_{Fe}\left[v_k^n\right]^{n_{Fe}} \tag{8b}$$

Cavalcante et al. (2003 and 2007) compared the solution obtained with the Finite Differences algorithms in equations (5)-(8) with the experimental data obtained by Ribeiro (2000) from laboratory hydraulic deposition tests for the two-dimensional method. The numerical and empirical results were also compared with analytical solutions obtained by Cavalcante (2004) for simplified boundary conditions, expressed as follows:

$$z_b(x,t) = A\cdot\left\{\sqrt{Bt}\cdot\exp\left(-E\frac{x^2}{t}\right)-D\cdot x\cdot\operatorname{erfc}\left(\sqrt{E}\frac{x}{t}\right)\right\} \tag{9}$$

$$A = \frac{z_b(0,t)}{\sqrt{Bt}}, \quad B = \frac{60 \cdot s_0 \cdot i_0}{\pi \cdot a_0}, \quad D = \frac{3 \cdot i_0}{a_0} \quad \text{and} \quad E = \frac{9 \cdot i_0}{60 \cdot a_0 \cdot s_0} \tag{10}$$

$$\operatorname{erfc}(x) = 1 - \frac{2}{\sqrt{\pi}}\left(x - \frac{x^3}{3 \cdot 1!} + \frac{x^5}{5 \cdot 2!} - \frac{x^7}{7 \cdot 3!} + \cdots \right) \tag{11}$$

When comparing the analytical solution and the FDM solution in equations (5)-(8), the numerical results were satisfactory only for a time-space discretization with a Courant number (C=u_0.Δt/Δx) equal to one. However, for C values less than unit the numerical solutions showed spurious dissipation and the results did not converge to those obtained analytically and empirically. This numerical error is investigated by Cavalcante & Farias (2007) and in this present paper. The solution to such numerical problem may be achieved using the so-called Cubic Interpolated Pseudo-particle (CIP) method (Cavalcante et al., 2007).

3 COUPLED METHOD SOLVED BY CIP

The CIP method is efficient to solve advection problems, which results in hyperbolic equations for which dissipation phenomena are not present or may be disregarded. In order to use the CIP method, according to an algorithm known as particle-in-cell (Nishiguchi & Yabe, 1983), the transport model in equations (1)-(4), must be split in two parts: an advective (Lagrangian) phase, and a non-advective (Eulerian) phase.

The non-advective equations governing the model are the following:

$$a_t = -a\left(u_x + v_y\right) \tag{12}$$

$$\left(ua\right)_t = ga\left(-z_{bx} - a_x\right) - gu\sqrt{u^2 + v^2} \,/\left(C_h^2 a\right) - ua\left(u_x + v_y\right) \tag{13a}$$

$$\left(va\right)_t = ga\left(-z_{by} - a_y\right) - gv\sqrt{u^2 + v^2} \,/\left(C_h^2 a\right) - va\left(u_x + v_y\right) \tag{13b}$$

$$z_{bt} + \left(s_x\right)_x + \left(s_y\right)_y = 0 \tag{14}$$

$$s_x = \sum_k m_k u^{n_K} \tag{15a}$$

$$s_y = \sum_k m_k v^{n_K} \tag{15b}$$

The advective equations of the problem are as follows:

$$a_t + ua_x + va_y = 0 \tag{16}$$

$$\left(ua\right)_t + u\left(ua\right)_x + v\left(ua\right)_y = 0 \tag{17a}$$

$$\left(va\right)_t + u\left(va\right)_x + v\left(va\right)_y = 0 \tag{17b}$$

Therefore the equation governing continuity of the fluid phase, equation (1), was divided into a non-advective part in equation (12) and an advective part in equation (16). The same process was applied to the equation governing equilibrium of the fluid phase, equations (2a and 2b), which was split into equations (13a and 13b) and (17a and 17b).

The CIP method is applied only to the advective equations, thus avoiding the introduction of spurious numerical dissipations in the solution. The method can be described by taking the function f (Yabe & Takei, 1988; Yabe & Aoki, 1991):

$$f_k^{n+1} = F\left(-u\Delta x\right) = a\xi^3 + b\xi^2 + f_{x,i}\xi + f_i \tag{18a}$$

$$a = \frac{1}{\Delta x^2}\left(f_{x,k}^{n} + f_{x,k-1}^{n}\right) - \frac{2}{\Delta x}\left(f_{k}^{n} - f_{k-1}^{n}\right); \quad b = \frac{1}{\Delta x}\left(2f_{x,k}^{n} + f_{x,k-1}^{n}\right) - \frac{3}{\Delta x^2}\left(f_{k}^{n} - f_{k-1}^{n}\right) \tag{18b}$$

$$f_{l}^{n+1} = F\left(f^{n}, f_{x}^{n}\right)\left(-u\Delta t\right) = a\xi^3 + b\xi^2 + f_{x,l}\xi + f_{l} \tag{19a}$$

$$a = \frac{1}{\Delta x^2}\left(f_{x,l}^{n} + f_{x,l-1}^{n}\right) - \frac{2}{\Delta x}\left(f_{l}^{n} - f_{l-1}^{n}\right); \quad b = \frac{1}{\Delta x}\left(2f_{x,l}^{n} + f_{x,l-1}^{n}\right) - \frac{3}{\Delta x^2}\left(f_{l}^{n} - f_{l-1}^{n}\right) \tag{19b}$$

$$f_{x,l}^{n+1} = F_{x}\left(f^{n}, f_{x}^{n}\right)\left(-u\Delta t\right) = 3a\xi^2 + 2b\xi + f_{x,l} \tag{20}$$

$$f_{y.l}^{n+1} = F\left(f_{y}^{n}, f_{xy}^{n}\right)\left(-v\Delta t\right) = c\xi^3 + d\xi^2 + f_{xy,l}^{n}\xi + f_{y,l}^{n} \tag{21a}$$

$$c = \frac{1}{\Delta x^2}\left(f_{xy,l}^{n} + f_{xy,l-1}^{n}\right) - \frac{2}{\Delta x}\left(f_{y,l}^{n} - f_{y,l-1}^{n}\right); \quad d = \frac{1}{\Delta x}\left(2f_{xy,l}^{n} + f_{xy,l-1}^{n}\right) - \frac{3}{\Delta x^2}\left(f_{y,l}^{n} - f_{y,l-1}^{n}\right) \tag{21b}$$

$$f_{xy.l}^{n+1} = F_{x}\left(f_{y}^{n}, f_{xy}^{n}\right)\left(-v\Delta t\right) = 3c\xi^2 + 2d\xi + f_{xy,l}^{n} \tag{22}$$

The non-advective equations may be solved using the Finite Differences Method (FDM). In this case the correspondent non-advective equations (12)-(15), may be re-written as:

$$a_{k,l}^{n+1} = a_{k,l}^{n} - \frac{\Delta t}{2\Delta x}\left\{a_{k,l}^{n} \cdot \left(u_{k+1,l}^{n} - u_{k-1,l}^{n}\right)\right\} - \frac{\Delta t}{2\Delta y}\left\{a_{k,l}^{n} \cdot \left(v_{k,l+1}^{n} - v_{k,l-1}^{n}\right)\right\} \tag{23}$$

$$\begin{aligned}\left(u \cdot a\right)_{k,l}^{n+1} &= \left(u \cdot a\right)_{k,l}^{n} - \frac{\Delta t}{2\Delta x} \cdot u_{k,l}^{n} \cdot a_{k,l}^{n} \cdot \left(u_{k+1,l}^{n} - u_{k-1,l}^{n}\right) - \frac{\Delta t}{2\Delta y} \cdot u_{k,l}^{n} \cdot a_{k,l}^{n} \cdot \left(v_{k,l+1}^{n} - v_{k,l-1}^{n}\right) \\ &- \frac{g \cdot \Delta t}{2\Delta x} \cdot a_{k,l}^{n} \cdot \left(z_{b\,k+1,l}^{\ n} - z_{b\,k-1,l}^{\ n} + a_{k+1,l}^{n} - a_{k-1,l}^{n}\right) - \frac{g \cdot \Delta t}{C_h^2} \cdot \frac{u_{k,l}^{n} \cdot \left(\left[u_{k,l}^{n}\right]^2 + \left[v_{k,l}^{n}\right]^2\right)^{1/2}}{a_{k,l}^{n}}\end{aligned} \tag{24a}$$

$$\begin{aligned}\left(v \cdot a\right)_{k,l}^{n+1} &= \left(v \cdot a\right)_{k,l}^{n} - \frac{\Delta t}{2\Delta x} \cdot v_{k,l}^{n} \cdot a_{k,l}^{n} \cdot \left(u_{k+1,l}^{n} - u_{k-1,l}^{n}\right) - \frac{\Delta t}{2\Delta y} \cdot v_{k,l}^{n} \cdot a_{k,l}^{n} \cdot \left(v_{k,l+1}^{n} - v_{k,l-1}^{n}\right) \\ &- \frac{g \cdot \Delta t}{2\Delta y} \cdot a_{k,l}^{n} \cdot \left(z_{b\,k,l+1}^{\ n} - z_{b\,k,l-1}^{\ n} + a_{k,l+1}^{n} - a_{k,l-1}^{n}\right) - \frac{g \cdot \Delta t}{C_h^2} \cdot \frac{v_{k,l}^{n} \cdot \left(\left[u_{k,l}^{n}\right]^2 + \left[v_{k,l}^{n}\right]^2\right)^{1/2}}{\left(a_{k,l}^{n}\right)}\end{aligned} \tag{24b}$$

$$z_{b\,k,l}^{\ n+1} = z_{b\,k,l}^{\ n} - \frac{\Delta t}{2 \cdot \Delta x}\left(s_{x\,k+1,l}^{\ n} - s_{x\,k-1,l}^{\ n}\right) - \frac{\Delta t}{2 \cdot \Delta y}\left(s_{y\,k,l+1}^{\ n} - s_{y\,k,l-1}^{\ n}\right) \tag{25}$$

$$s_{x\,k}^{\ n+1} = m_{Qz}\left[u_{k}^{n}\right]^{n_{Qz}} + m_{Fe}\left[u_{k}^{n}\right]^{n_{Fe}} \tag{26a}$$

$$s_{y\,k}^{\ n+1} = m_{Qz}\left[v_{k}^{n}\right]^{n_{Qz}} + m_{Fe}\left[v_{k}^{n}\right]^{n_{Fe}} \tag{26b}$$

After solving the non-advective equations, these solutions are used as initial conditions for the advective equations. The advective phase, equations (16) and (17), is solved using the CIP method as described in equations (18) to (22).

4 EXPERIMENTAL SIMULATION AND MODEL VALIDATION

The general mathematical formulation of an advective problem, in one-dimensional space, is described by the following hyperbolic equation:

$$u_t + v \cdot u_x = 0 \tag{27}$$

in which $v > 0$ is the advection velocity and $v.u_x$ is the so called advective term. The independent variable u is function both of space x and time t; u_x and u_t denote its derivatives.

Equation (27) represents the transport of u along axis x towards the right-hand side when v > 0. Since this equation does not contain a dissipative term, u_{xx}, then the value of u should just be transported along x, without undergoing any alteration, between time t_0 and $t_0 + \Delta t$. The absence of dissipative phenomena implies that any discontinuity in the initial conditions should propagate to the solution at any time $t > 0$. This implies that hyperbolic equation admits discontinuous solutions, and the numerical method adopted to solve these equations should be able to deal with such discontinuities efficiently.

The initial value problem, or Cauchy problem, for the advection equation consists in finding a function $u(x, t)$ in the semi-space $D = \{(x,t)/\, t \geq 0, -\infty < x < \infty\}$, that satisfies both Equation (27) and a particular initial condition. In general the solution is continuous and sufficiently differentiable, but this is not always the case.

As an example, consider the phenomenon of a wave propagating to the right hand side with the particular initial condition described in Figure 2. In Figure 2, the solution for the advection problem, was obtained using the Finite Differences and CIP methods for a Courant number C=0.5. These solutions are shown for time equal to 3 s. Notice that the initial solution propagated in time without any loss of information, dissipation or oscillations for the CIP method.

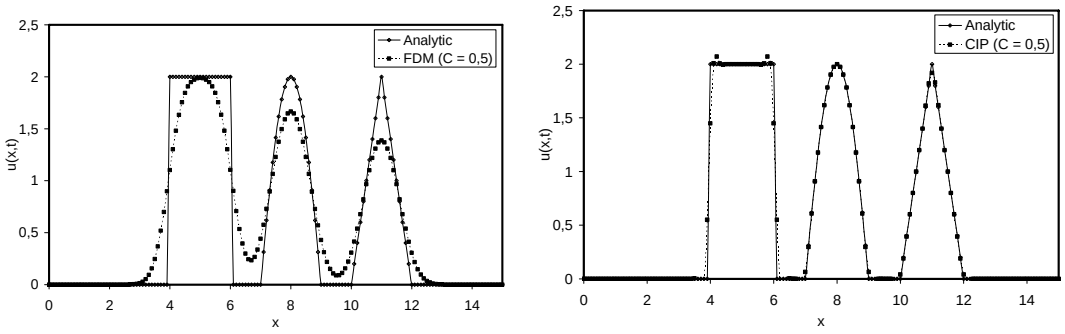

(a) (b)

Fig. 2. Solution for the Advection Problem using (a) FDM and (b) CIP methods for a Courant number C=0.5.

Considering the importance of predicting the behaviour of hydraulic fill structures in the field and afterwards analyzing the performance of different kinds of laboratory simulation tests, a hydraulic deposition simulation apparatus was developed at the University of Brasilia (Ribeiro, 2000). The apparatus consists of a depositional channel, 6.0 m long, 0.4 m wide and 1.0 m high. The channel was built using steel profiles and panels of tempered glass. This kind of wall permits the observation of the evolution of the deposition process during the entire test. Figure 3 shows a general view of hydraulic deposition simulation tests (HDST), developed at the University of Brasilia.

Fig. 3. General view of the HDST equipment developed at the University of Brasilia.

A series of comparisons were made between the HDST results obtained by Ribeiro (2000) and those forecasted by the coupled model solved by analytical, FDM and CIP techniques, for different Courant numbers. According to Ribeiro (2000), the main characteristics of the material used in the HDST are those presented in Tables 1 and 2. In Tables 1 and 2, *Fe* is the percentage of iron particles, C_w is the concentration of solid particles (quartz and iron) in the slurry, *Q* is the slurry flow rate and im is the average (global) beach slope.

Figures 4 and 5 present comparisons between the results obtained from tests HDST 1 and 6 by Ribeiro (2000) and those obtained analytically using the mathematical model proposed by Cavalcante et al. (2002), and numerically using the FDM as obtained by Cavalcante et al. (2003) and using the CIP technique describe in Cavalcante & Farias (2007) for a Courant number equal to 0.5. Axis *x* (abscissas) represents the distance from the discharge point and axis *y* (ordinates) gives the normalized height of the deposited beach.

From Figures 4 and 5, one can notice that the mathematical model is not able to describe the successive erosion and deposition processes, which are clearly observed in the HDST beaches. However, the model describes quite well the basic geometric characteristics of the deposited beaches, such as global slope inclination. The numerical solution using the Finite Differences Method differs drastically from the experimental and analytical solution for the adopted time-space discretization with *C*=0.5. This is due to spurious dissipation introduced by the numerical solution scheme as explained in Cavalcante & Farias, 2007. This problem is solved when the mixed CIP-FDM scheme is adopted and the numerical solution matches satisfactorily the experimental and analytical results for any Courant number, as illustrated in figures 4(b) and 5(b) for *C*=0.5.

Table 1. Average physical characteristics of the tailings used in the hydraulic deposition simulation test HDST (Ribeiro, 2000).

	Quartz	Iron
D_{50} (mm)	0.265	0.240
D_{90} (mm)	0.645	0.640
Gs	2.65	5.50

Table 2. HDST controlled variables and final slope inclination of the hydraulically deposited beach (Ribeiro, 2000).

	HDST 1	HDST 6
C_w (%)	8.9	20.4
Fe (%)	23.0	23.0
Q (l/min)	4.8	5.9
i_m (%)	7.7	9.2

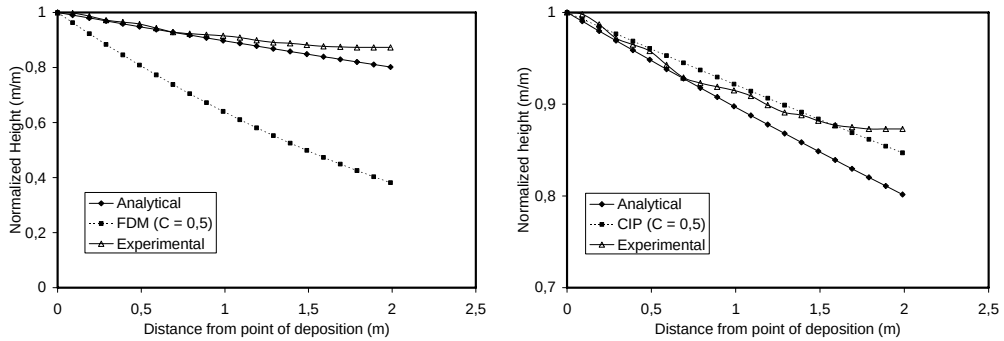

(a) (b)

Fig. 4. Comparisons between experimental data for test HDST 1 (Ribeiro, 2000) and numerical results using: (a) Finite Differences; and (b) CIP method for Courant number C=0.5.

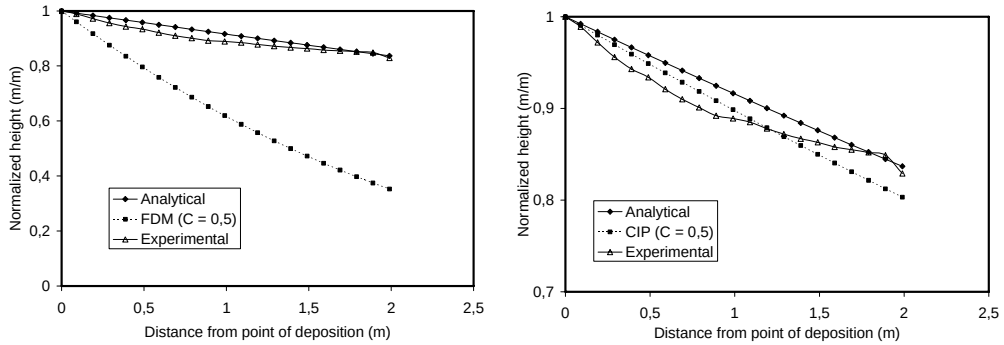

(a) (b)

Fig. 5. Comparisons between experimental data for test HDST 6 (Ribeiro, 2000) and numerical results using: (a) Finite Differences; and (b) CIP method for Courant number C=0.5.

5 THREE-DIMENSIONAL ANALYSES

Figure 6 presents comparisons about the results obtained numerically using the FDM and using the CIP technique as proposed in this paper for a Courant number equal to 0.5. Axis *x* and *y* represent the distance from the discharge point and axis *z* gives the normalized height of the deposited beach. In these analysis were used the dates obtained from tests HDST 1 by Ribeiro (2000)

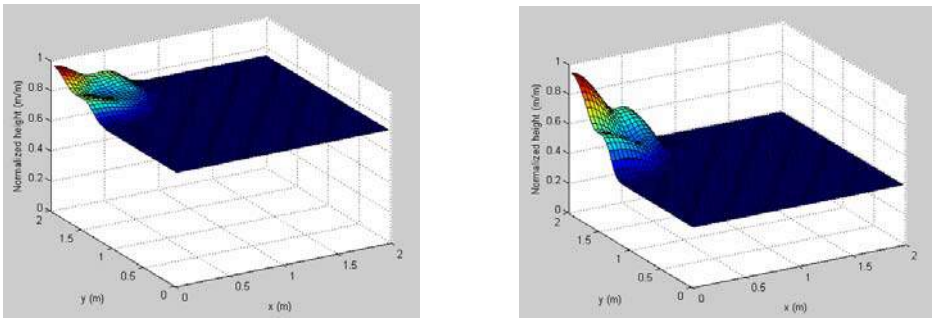

(a) (b)

Fig. 6. Comparisons between numerical results using: (a) CIP method; and (b) Finite Differences for Courant number C=0.5.

Figure 7 presents the time evolution about the results obtained numerically using the CIP technique as proposed in this paper for a Courant number equal to 0.5. Axis *x* and *y* represent the distance from the discharge point and axis *z* gives the normalized height of the deposited beach. In these analysis were used the dates obtained from tests HDST 1 by Ribeiro (2000)

6 CASE-STUDY: MONJOLO DAM (VALE CO.)

After properly checked, the bed load transport model was used to simulate a real case of the construction of a tailings dam. The geotechnical data from the Monjolo Dam (Vale Co.) was used. The construction of this dam started in 1997 and a general view is shown in Figure 8. The dam accumulated tailings produced by spiral separators, and the grain size of the solids were in the range of fine to medium sand (diameter < 1.0 mm). According to Esposito and Assis (1997), the average grain density was 3.12 g/cm3 and the chemical composition of the solids comprised 23% of iron (Fe), 65% of silicon dioxide or silica (SiO2) and 0.4% of aluminium oxide (Al2O3). The tailings were transported and deposited hydraulically, and the fill was lifted using the upstream method.

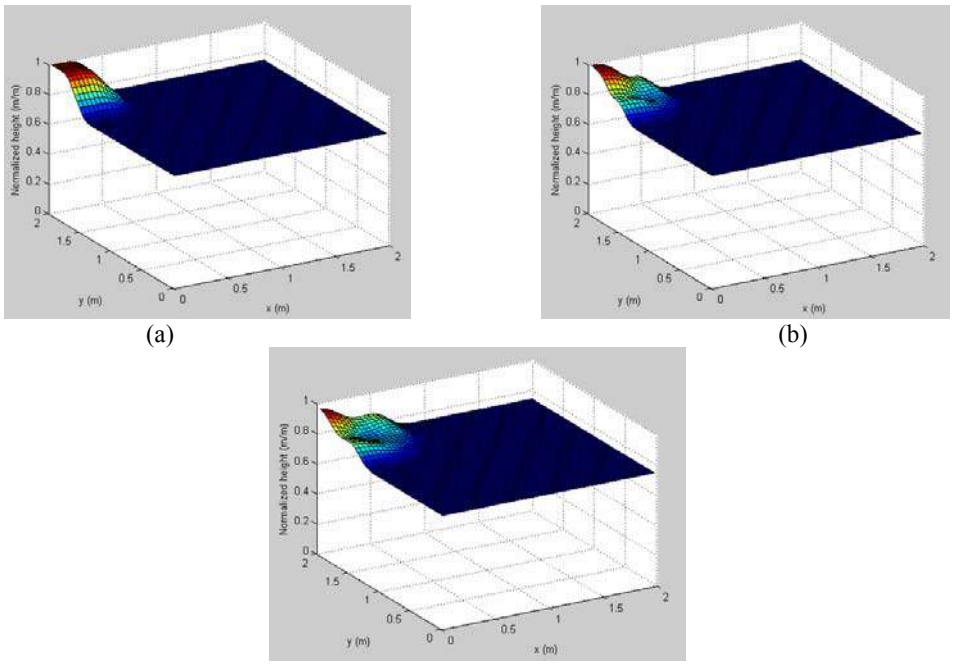

(a) (b)

(c)

Fig. 7. Comparisons between time evolution about the numerical results using CIP method for Courant number C=0.5: (a) 25 minutes; (b) 50 minutes and (c) 75 minutes.

Fig. 8. General view of Monjolo Dam (2000)

The dam construction began with a start dike with a toe rockfill at elevation 800 m, then it was successively lifted by every 10 m using the deposited tailings. The fill should reach elevation 860 m in the 2000, with a height of 60 m and a total volume of 6 million cubic meters including the dam and the reservoir as illustrated in Figures 9 and 10. In the year 2002, the fill was expected to reach elevation 875 m, with 75 m in height and a total volume of 10 million cubic meters according to the designers (Geoconsultoria, 1997).

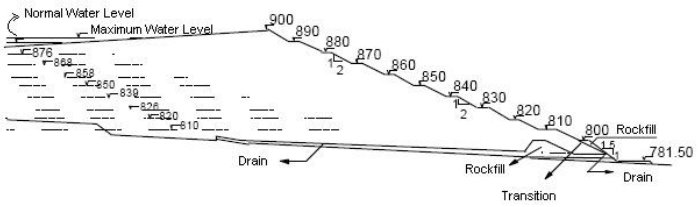

Fig. 9. Beach profile, including designers prediction up to year 2002 (modified – Geoconsultoria, 1997).

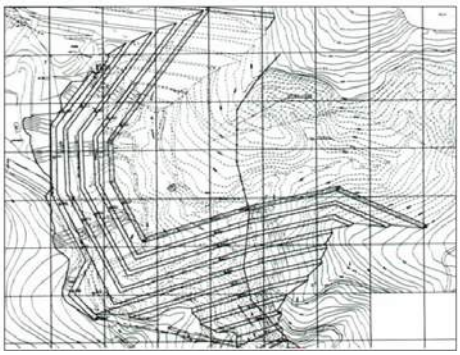

Fig. 10. Final plan view of Monjolo Dam. (modified – Geoconsultoria, 1997).

Table 3 presents a comparison between measured and computed heights of the dam in different times. The height simulated by the Mathematical Sediment Transport Model for the year 2000, 3 years after construction, was 59.6 m, which compares very well with the real observed height of 60 m. For year 2002, 5 years after construction, the model predicted a height of 76.9 m against a measured value of 75 m.

Table 3. Comparision between observed and computed fill high.

	2000	2002
Time since start of construction (year)	8.9	20.4
Height of dam measured in field (m)	23.0	23.0
Height of dam simulated by the model (m)	4.8	5.9

Figure 11 presents the predicted profile of hydraulic deposition for Monjolo Dam using the Mathematical Sediment Transport Model and deposition times of 3 and 5 years. Two points, illustrating the observed heights at the discharged point x=0 in years 2000 and 2002, were also included in the figure for comparison. The beach profile observed in field has similar concavity as that obtained analytically. Besides, the inclination has the same order of magnitude (1 V: 40 H to 1 V: 50 H).

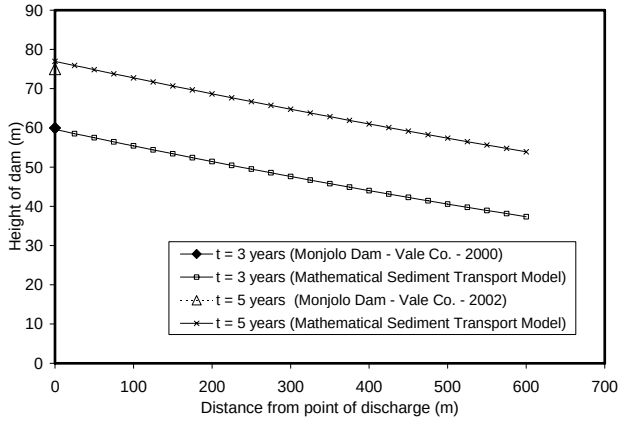

Fig. 11. Predicted profile of hydraulic deposition for Monjolo Dam.

7 CONCLUSIONS

A coupled system of equations representing the bed load transport of heterogeneous sediments in hydraulically deposited tailings dams was described. This model is governed by

the field equations for equilibrium and continuity of the fluids and the condition of continuity of the solid particles. A constitutive model must also be assumed for the rate of transport of the sediments.

The overall system of equations governing the problem may be split in a sub-system of advective equations and a sub-system of non advective equations. Advective equations do not exhibit dissipation during the transport phenomena; however spurious numerical dissipations are introduced in the solution when classical schemes, such as the Finite Differences Method (FDM), are used to solve this kind of hyperbolic equations.

The solution for the unrealistic numerical dissipation problem may be achieved by adopting the so-called CIP (Cubic Interpolated Pseudo-particle) method to solve the advective part of the equations governing the overall problem. The remaining equations may be solved using any other method, such as the FDM, without undesirable numerical problems.

ACKNOWLEDGEMENT

The authors acknowledge the support of the following institutions: Brazilian National Research Council (CNPq), University of Brasilia, UPIS University and FINATEC. The authors are also indebted to Dr. Shuji Moriguchi and Professor Takayuki Aoki from Tokyo Institute of Technology, Japan, for their kindness in teaching us the details of the CIP method.

REFERENCES

Cavalcante, A.L.B. Modeling and Simulation of Bed Load Transport of Heterogeneous Sediments Coupling Stress-Strain-Porepressure Applied to Tailings Dams. (In Portuguese) PhD Thesis, Department of Civil and Environmental Engineering, University of Brasilia, Brazil, 313 p, (2004).

Cavalcante, A.L.B; Assis, A.P. and Farias, M.M. Numerical Sediment Transport Model of Heterogeneous Tailings. Proc. 5th European Conference on Numerical Methods in Geotechnical Engineering, 5th NUMGE, Paris, France, pp. 491-496, (2002).

Cavalcante, A.L.B., Assis, A.P. & Farias, M.M. Bed Load Transport in Tailings Dams – Analytical and Numerical View. Proc. of the 4th International Workshop on Applications of Computational Mechanics in Geotechnical Engineering, Brasil, pp. 103-113, (2003).

Cavalcante, A.L.B, Farias, M.M & Assis, A.P. Heterogeneous Sediment Transport Model Solved by CIP Method. Proc. of the 5th Int. Workshop on Applications of Computational Mechanics in geotechnical Engineering, Guimarães, Portugal, pp. 429-437, (2007).

Cavalcante, A.L.B & Farias, M.M. Numerical Schemes for the Solution of Advection Problems. Proc. of the 5th Int. Workshop on Applications of Computational Mechanics in geotechnical Engineering, Guimarães, Portugal, pp. 417-427, (2007).

Nishiguchi, A. & Yabe, T. Second order fluid particle scheme. J. Comput. Phys. Vol. 52, pp. 390-, (1983).

Ribeiro, L.F.M. Physical Simulation of the Process of Formation of Hydraulic Fills Applied to Tailings Dams. (In Portuguese) PhD Thesis, Department of Civil and Environmental Engineering, University of Brasilia, Brazil, 232 p., (2000).

Yabe, T. & Takei, E. A New Higher-Order Godunov Method for General Hyperbolic Equations. Journal of the Physical Society of Japan. Vol. 57, No. 8, pp. 2598-2601, (1988).

Yabe, T. & Aoki, T. A Universal Solver for Hyperbolic Equations by Cubic Polynomial Interpolation. Comput. Phys. Commun. Vol. 66, pp. 219-232, (1991).

MODELLING THERMAL IMPACTS ON REACTIVE TRANSPORT PROCESSES RELATED TO MULTICOMPONET CHEMICALS IN COMPACTED CLAYS

M. Sedighi
Geoenvironmental Research Centre, Cardiff University, Cardiff, UK

H.R. Thomas
Geoenvironmental Research Centre, Cardiff University, Cardiff, UK

P.J. Vardon
Geoenvironmental Research Centre, Cardiff University, Cardiff, UK

ABSTRACT: *This paper presents some aspects of recent developments to the chemical module of a coupled numerical model for thermal, hydraulic, chemical and mechanical behaviour in porous media (COMPASS). Developments to the theoretical formulation of multicomponent chemical transport due to combined electrochemical and thermal potentials are provided. The model proposes an explicit theoretical form of approximation for thermal diffusion, i.e. Soret effect, coupled with electrochemical diffusion in multi-ionic systems. The chemical module has been further enhanced through the inclusion of an advanced geochemical model.*

1 INTRODUCTION

Clays in geoenvironmental applications may be exposed to a variety of physical, chemical and mechanical conditions. In particular, in the case of deep geological disposal of high level radioactive waste, where compacted clay has been suggested as a buffer material, the clay is exposed to coupled thermal, hydraulic, chemical and mechanical (THCM) conditions. The transport process of chemical ions in compacted clays is dominated by the diffusion mechanism which is highly affected by the specific microstructure evolution and surface electrostatic forces of the clay minerals (Pusch & Yong, 2006). As the result, the diffusion rate of ionic species varies with the type of moving ion in the system, which requires modelling the process under different apparent diffusion coefficients for different ions (Appelo & Wersin, 2007).

The variation in the effective rate of diffusion for different cations and anions in multiple ionic systems affects the condition of electro-neutrality of the aqueous system and causes an electrical field. Therefore, the diffusion rate of each ion may deviate from that calculated by Fick's diffusion law (Lasaga, 1979).

It is also well established that under non-isothermal conditions, the temperature gradient can induce a mass flow due to a thermal diffusion phenomenon (i.e., Soret-Ludwig effect or Soret effect). Although the contribution of thermally induced diffusion in diffusive transport is reported to be small in geological materials compared to diffusion due to the chemical potential, a quantitative consideration of the effect is required for the precise analysis of mass transport, especially in cases where long term impacts are considered in modelling investigations. Therefore, electrochemical diffusion is coupled here with the thermal diffusion potential or Soret effect in order to obtain an overall understanding of the combined effects.

This paper presents therefore recent advances in the chemical reactive transport module of the coupled THCM model. Developments to the theoretical formulation of multicomponent chemical diffusion are presented. A formulation of diffusion of multicomponent chemicals due to coupled electrochemical and thermal diffusion potentials is provided. In addition, a theoretical approach is incorporated for estimating the thermal diffusion coefficient or the Soret coefficient, to complement limited experimental data in clays. The developed model incorporates an advanced geochemical model, PHREEQC version 2, (Parkhurst & Appelo, 1999) for calculating the chemical reactions.

An example simulation of coupled thermal, hydraulic and chemical behaviour is provided to demonstrate the contribution of thermal diffusion.

2 BACKGROUND OF THE COUPLED THCM MODEL

The basis for the work presented is a THM model, developed by Thomas and co-workers (e.g. Thomas & He, 1995) based on a mechanistic approach. The model was extended to THCM form, by Seetharam (2003); to include chemical behaviour. The chemical module of the coupled model included multicomponent reactive chemical transport incorporating an equilibrium geochemical model. In terms of physical processes, moisture flow including liquid water and vapour is considered in the model. Dry air flow is also considered as bulk air and dissolved air. The model considers heat transfer via the mechanisms of conduction, convection and latent heat of vaporisation transfer. The mechanical behaviour can be modelled based on an appropriate constitutive relationship. Detailed information about the thermal, hydraulic and mechanical behaviour can be found in Thomas & He (1995).

The governing equation for reactive transport of multicomponent chemicals developed by Seetharam (2003) considers the transport of dissolved chemicals due to advective, dispersive and diffusive mechanisms (molecular and thermal). The associated geochemical reactions under equilibrium condition are calculated via coupling the transport module with an equilibrium geochemical model. Diffusive flux in the formulation of the reactive transport of chemicals is expressed based on Fick's law of diffusion. If ions move with a different rate of diffusion, the aqueous system becomes electrically imbalanced.

In order to incorporate the electro-neutrality condition in both molecular and thermal diffusion, the general derivation of diffusion flux under coupled chemical, electrical and thermal potentials was revisited by Sedighi et al. (2010) and Thomas et al. (2011). The formulation developed for coupled electrochemical and thermal diffusion is presented below. In addition, the components of the geochemical sink/source term in the governing chemical transport equation are calculated using a geochemical model, PHREEQC version 2 (Parkhurst & Appelo, 1999). Detailed information about the theoretical and numerical formulations of the geochemical model can be found in Parkhust & Appelo (1999).

3 THE DIFFUSIVE REACTIVE TRANSPORT OF MULTICOMPONENT CHEMICALS

Following an approach proposed by Lasaga (1979) for the diffusion of multicomponent chemicals under isothermal condition, Sedighi et al. (2010) and Thomas et al. (2011) presented the derivation of the governing equations for the diffusion of multicomponent chemicals under coupled electrochemical and thermal potentials. The thermal diffusion potential was included as an additional component of diffusion flux. Accordingly, the general diffusive flux of a chemical component in an aqueous solution due to electrochemical and thermal potentials can be described as follows:

$$\mathbf{J_i^{Diff}} = \begin{Bmatrix} -D_i^0\left(1+\dfrac{\partial \ln \gamma_i}{\partial \ln c_i}\right)\nabla c_i + \dfrac{z_i D_i^0 c_i}{\sum_{k=1}^{nc} z_k^2 D_k^0 c_k}\sum_{j=1}^{nc} z_j D_j^0\left(1+\dfrac{\partial \ln \gamma_j}{\partial \ln c_j}\right)\nabla c_j \\ -D_i^0 c_i \dfrac{Q_i^*}{RT^2}\left(1+\dfrac{\partial \ln \gamma_i}{\partial \ln c_i}\right)\nabla T + \dfrac{z_i D_i^0 c_i}{\sum_{k=1}^{nc} z_k^2 D_k^0 c_k}\sum_{j=1}^{nc} z_j D_j^0 c_j \dfrac{Q_j^*}{RT^2}\left(1+\dfrac{\partial \ln \gamma_j}{\partial \ln c_j}\right)\nabla T \end{Bmatrix} \quad (1)$$

where c_i represents the dissolved concentration of the i^{th} chemical component in the aqueous solution. D_i^0, z_i and γ_i stands for the tracer diffusion coefficient in water, charge and the activity coefficient of the i^{th} ion component. T is the absolute temperature and R is the gas constant. Q_i^* is the heat of transport of the i^{th} ion in a dilute solution. The degree of coupling of thermal diffusion with the overall mass diffusion is determined by this coefficient.

The heat of transport and the Soret coefficient are related to each other. For a dilute solution the heat of transport (Q_i^*) for a charged ion is related to the Soret coefficient (Agar et al., 1989) via:

$$\frac{Q_i^*}{RT^2} = S_i^T \quad (2)$$

where S_i^T stands for the Soret coefficient of the i^{th} component in a dilute solution.

To the authors' knowledge, only a few experimental studies have been reported on thermal diffusion in clays (Tornton & Seyfried, 1983; Rosanne et al., 2006). Thornton & Seyfried (1983) reported an average value for the Soret coefficient of around 4×10^{-3} (1/K) for multi-ion sediment-sea water. Rosanne et al. (2006) found that the Soret coefficients for mica and glass powder are very close to the values reported for the Soret coefficient of NaCl in an aqueous solution while the corresponding value for argillite clay was found to be five times larger than that in free water. Given the limited experimental data on the Soret coefficient in clays and multiple-ionic systems, a theoretical approach is suggested in this paper for the assessment of the overall effects of thermal diffusion in modeling studies.

Agar et al. (1989) provided a theoretical interpretation for standard heat of transport in an infinite dilute electrolyte solution at a temperature of 25 °C based on a hydrodynamic approach. Using the approach proposed by Agar et al. (1989), the heat of transport of the i^{th} component in a dilute solution can be obtained according to the ion tracer diffusion and its valence.

$$Q_i^* = A z_i^2 D_i^0 \quad (3)$$

where A is a constant value depending on the hydrodynamic boundary condition (i.e. 2.48×10^{12} and 2.20×10^{12} for two different hydrodynamic boundary conditions.

The general governing equation for reactive transport of each component in a multicomponent chemical system of clay comprising the effects of electrochemical and thermal diffusion potentials is given as (Sedighi et al., 2010; Thomas et al., 2011):

$$\frac{\partial(\theta_l c_i)}{\partial t}+\frac{\partial(\theta_l s_i)}{\partial t}=-\nabla\cdot(\mathbf{v_l}c_i)+\nabla\cdot(\mathbf{D}_m\nabla c_i)+\nabla\cdot\left(\sum_{j=1}^{nc}\tau_i\theta_l D_{ij}^0\nabla c_j\right)+\nabla\cdot\left(\tau_i\theta_l D_i^T\nabla T\right) \quad (4)$$

where θ_l stands for the volumetric liquid content and s stands for the sink/source term due to homogenous and heterogeneous geochemical reactions at which the i^{th} component is produced or depleted by the chemical reactions. The terms at the right hand side of the chemical transport equation represent the components of the total chemical flux comprising advective flux, dispersive flux, diffusive flux due to chemical concentration potential, and diffusive flux due to temperature gradients or Soret effect. $\mathbf{v_l}$ represents the velocity of liquid and $\mathbf{D}_m$ is the coefficient of mechanical dispersion. τ_i is the tortuosity factor of the porous medium which can be different for different ions in clays. D_{ij}^0, and D_i^T represent the molecular diffusion and thermal diffusion coefficient for the i^{th} component, respectively. The molecular and thermal diffusion coefficients can be represented based on Eq. (1) as follows (Sedighi et al., 2010; Thomas et al., 2011):

$$D_{ij}^0=\delta_{ij}D_i^0\left(1+\frac{\partial\ln\gamma_i}{\partial\ln c_i}\right)-\frac{z_i D_i^0 c_i}{\sum_{k=1}^{nc}z_k^2 D_k^0 c_k}z_j D_j^0\left(1+\frac{\partial\ln\gamma_j}{\partial\ln c_j}\right) \quad (5)$$

$$D_i^T=D_i^0 c_i S_i^T\left(1+\frac{\partial\ln\gamma_i}{\partial\ln c_i}\right)-\frac{z_i D_i^0 c_i}{\sum_{k=1}^{nc}z_k^2 D_k^0 c_k}\sum_{j=1}^{nc}z_j D_j^0 c_j S_j^T\left(1+\frac{\partial\ln\gamma_j}{\partial\ln c_j}\right) \quad (6)$$

where δ_{ij} is the Kronecker's delta function.

Overall charge conservation, i.e., the electro-neutrality condition, is provided through charge conservation in the transport module following Lasaga (1979). The later modification leads to the elimination of the concentration of an arbitrary component from the diffusion flux. The concentration of *nc-1* components is calculated using the governing equation for mass conservation whereas the concentration of a selected component is simply calculated from charge conservation. The geochemical reaction module conserves the charge in the reaction sink/source term separately. PHREEQC considers the charge conservation in the reactions by adjusting the concentration of an arbitrary ion or pH in the solution.

In order to solve the set of governing equations for the coupled transport processes the Galerkin weighted residual method is employed to formulate the finite element spatial discretisation. The spatially discretised equations are time discretised by the application of a fully implicit mid-interval backward difference time-stepping algorithm. Detailed information about governing equations and numerical implementation can be found in Thomas & He (1995) and Seetharam et al. (2007). The THCM model (COMPASS) and the geochemical model (PHREEQC version 2) are linked together incorporating a sequential non-iterative approach. The formulation was verified for both isothermal and non-isothermal conditions for an aqueous system by Sedighi et al. (2010) and Thomas et al. (2011).

4 NUMERICAL SIMULATION

The simulation considers a 2D (0.1 m long and 0.01 m wide) clay domain subjected to heating and hydration. Figure 1 provides a schematic diagram of the thermo-hydraulic cell and the boundary conditions. Deionised water at a pressure of 1.5 MPa is injected at the hydration end and the hot end is assumed to be impervious to flow. A temperature gradient of 1.5 °C/cm is applied across the length of the domain by fixing the temperature at 25 °C at the hydration end and at 40 °C at the opposite end. The domain is discretised into 100 equally sized 4-noded quadrilateral elements. The numerical simulation is performed for a period of 200 days with an initial time-step of 360 seconds that is allowed to increase to 360000 seconds, depending on the convergence rate.

The clay physical properties, including moisture-suction relationship, hydraulic and thermal conductivity relationship are adopted from experimental data provided by Huertas et al. (2000) for compacted swelling clay. The initial porosity of the clay is considered as 0.352. The system is initially unsaturated with a degree of saturation equal to 65%. The physical properties of material for the thermal and hydraulic analysis are given in Table *1*.

Boundary conditions:	Unsaturated clay Initial conditions:	Boundary conditions:
T = 25 °C (Fixed) *u_l=1.5 MPa (Fixed)* *$Ca^{2+} = SO_4^{2-} = 0$* *Distilled water*	*T = 25 °C* *u_l = -100 MPa* *$Ca^{2+} = 14.25\times10^{-3}$ mol/l* *$SO_4^{2-} = 14.25\times10^{-3}$ mol/l*	*T = 40 °C (Fixed)* *Impermeable for moisture and chemicals transport*

Fig. 1. Schematic representation of the simulation example and boundary conditions

The pore water contains two dissolved chemical species, Ca^{2+} and SO_4^{2-}, in equilibrium with the anhydrite mineral ($CaSO_4 = Ca^{2+} + SO_4^{2-}$). The initial concentration of dissolved chemicals is 14.25×10^{-3} mol/l. The equilibrium constant of the anhydrite mineral precipitation/dissolution reaction are adopted from the database of PHREEQC version 2 (*log* K_{eq}= -4.637 at 25 ^{o}C and ΔH=-3.769 kcal, from *minteq.dat*).

Table 1. Physical properties/relationships of the simulated material

Physical properties	Relationship
Degree of saturation versus suction relationship:	$S_l = S_{l_0} + (S_{l_{\max}} - S_{l_0})[1+(\frac{s}{p_0})^{(1-\alpha)^{-1}}]^{-\alpha}$ $S_{l_{max}} = 1.0,\ S_{l_0} = 0.0001,\ p_0 = 14.5,\ \alpha = 0.17$
Hydraulic conductivity relationship:	$K = K_{sat}(S_l)^3 \quad K_{sat} = 10^{-13}(m/s)$
Thermal conductivity relationship:	$\lambda = A_2 + (A_1 - A_2)\left[1+\exp(\frac{S_l - x_0}{d_x}\right]^{-1}$ $A_1 = 0.57,\ A_2 = 1.28,\ x_0 = 0.65,\ d_x = 0.10$

In this test, different diffusion coefficients are considered for the chemical components and the effects of thermal diffusion are also investigated. The tracer diffusion coefficient in water for Ca^{2+} and SO_4^{2-} is assumed as 7.9×10^{-10} and 10.6×10^{-10} m^2/s. Different tortuosity factors for chemical diffusion are considered for anionic and cationic chemical components.

The tortousity factor is calculated based on the proposed relationship by Millington & Quirk (1961), considering an additional modification factor (κ), in order to include different effective diffusion coefficients for ionic components as:

$$\tau_i = \kappa_i \frac{(nS_l)^{7/3}}{n^2} \tag{7}$$

κ is assumed to be 10^{-1} for the anionic component (SO_4^{2-}) and 1 for the cationic component (Ca^{2+}). The temperature dependency of the tracer diffusion coefficient is calculated using the Stokes-Einstein relationship.

The effect of thermal diffusion, i.e. the Soret effect, is considered using the theoretical approach explained in Eq. (2).

Figure 2 shows transient profiles of temperature in the domain. Steady-state temperature profile is achieved across the domain within a few hours. Achieving the final steady state of the temperature profile is coupled to the moisture fields, and it is affected, in particular, by the dependence of the thermal conductivity on the degree of saturation. Figure 3 also presents the transient profile of degree of saturation in the domain. During the initial stages, up to approximately 2 days, the moisture content of the soil is reduced at the hot end due to vapour flow away from the heater. After 2 days, the model predicts that the water front has reached the hot end and the moisture content gradually increases in whole domain. The resaturation of the whole domain is completed after 50 days.

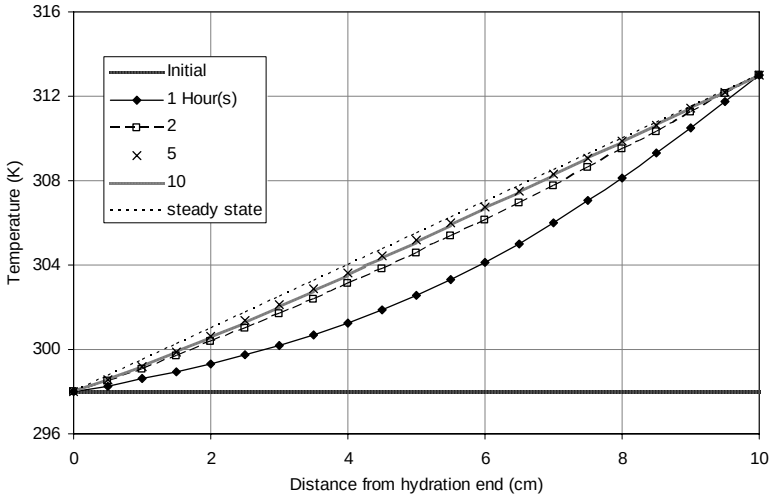

Fig. 2. Transient profile of temperature in the analysing domain

Figure 4 shows transient profiles of the dissolved ion concentrations and figure 5 presents the pattern of the dissolution-precipitation behaviour of anhydrite mineral. The model predicts identical results for the concentration of the calcium and sulphate although different effective diffusion coefficients were used in the simulation. This is attributed to the overall charge neutrality condition which was adopted in the formulation of the multicomponent reactive transport.

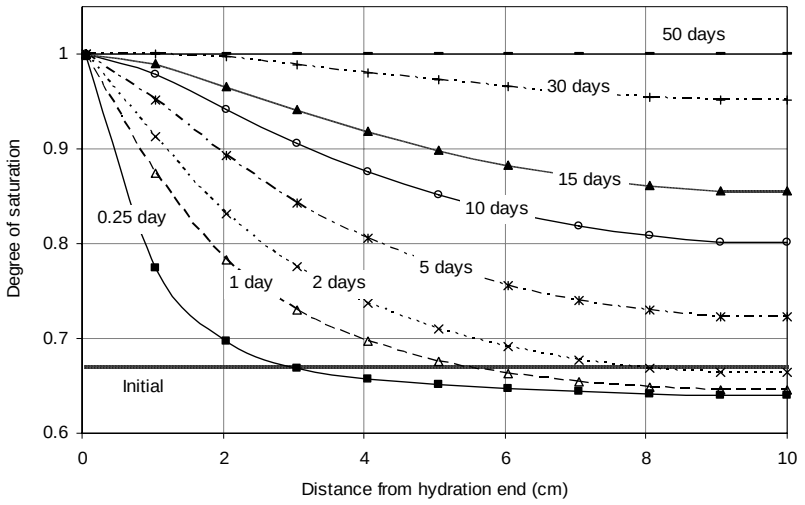

Fig. 3. Transient profile of degree of saturation in the analysing domain

During the initial stages, the model predicts a reduction in the dissolved ion concentrations and anhydrite mineral concentration near the hydration end. This is due to the advective flow toward the hot end which leads to the dissolution of anhydrite mineral to maintain the equilibrium condition between solid and aqueous phases. The drop in the dissolved chemical concentrations at the hot end can be attributed to the precipitation of the mineral caused by the higher temperature and decreasing moisture content due to vapour flow. Due to the migration of dissolved ions to the hot end by the advection process and temperature dependency of the equilibrium constant of anhydrite dissolution, the amount of precipitate anhydrite increases towards the hot end in the regions beyond the dissolution front up to about 30 days. After 30 days, the system is almost saturated and the dissolved ions tend to move towards lower concentrations. Thermal diffusion effects decrease the rate of precipitation of migrated dissolved ions at vicinity of the hot region and the subsequent increase in the precipitate amount of mineral near the heater.

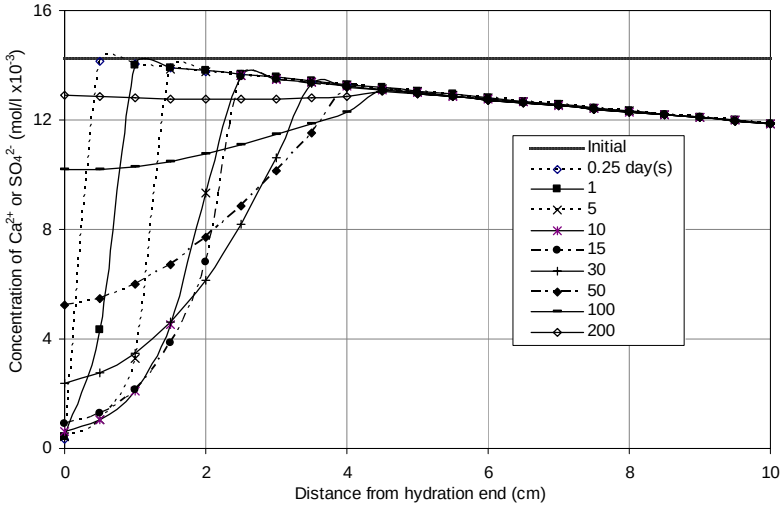

Fig. 4. Transient profiles of the dissolved ion concentrations

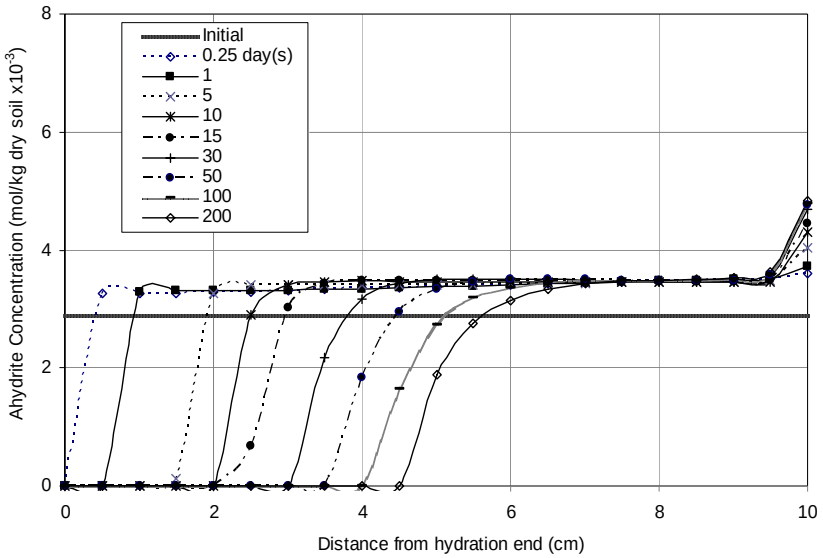

Fig. 5. Transient profiles of the precipitate amount of anhydrite mineral

In order to demonstrate the magnitude of the thermal diffusion effects, the simulation is repeated but without considering thermal diffusion effects, i.e. $S^T=0$. Figure 6 shows the transient profile of the distribution of precipitate anhydrite mineral for the analysis. In the early stages of resaturation, up to about 15 days, the distribution pattern is similar to that presented in figure 5. Thermal diffusion has a greater effect as the degree of saturation increases towards full saturation. Comparison of results with and without Soret effects shows that the effects of thermal diffusion are highlighted at the hot end where the amount of precipitate is about 40% less that the amount obtained from the analysis without considering thermal diffusion effects after 200 days of analysis.

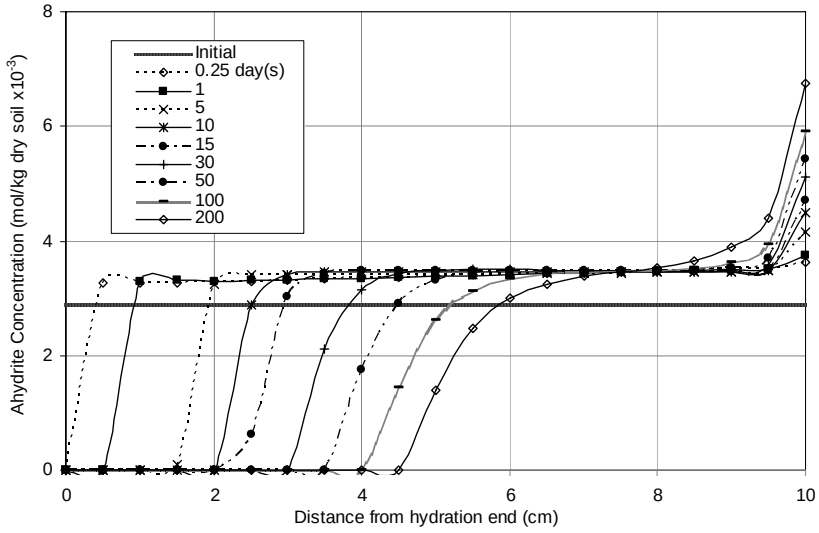

Fig. 6. Transient profiles of the precipitate amount of anhydrite mineral without considering Soret effect

5 CONCLUSIONS

Advances to a coupled thermal, hydraulic and chemical model for unsaturated soil are presented. The development includes a theoretical formulation for reactive transport of multicomponent chemicals considering combined electrochemical and thermal diffusion potentials. The proposed formulation also provides a theoretical approximation for the Soret coefficient. In addition, the transport module of the coupled model incorporates an advanced geochemical model (PHREEQC version 2) in order to consider the effects of equilibrium and kinetically controlled chemical reactions in soil system. The behaviour of the developed model was investigated via a simulation of the reactive transport of chemicals under THC conditions in unsaturated compacted clay. The results demonstrated the effects of the coupled electrochemical and thermal diffusion potentials on the behaviour of a binary ionic system in equilibrium with a mineral under THC conditions.

REFERENCES

Agar, J.N., Mou, C.Y., & Lin, J. (1989), "Single-ion heat of transport in electrolyte solutions. A hydrodynamic theory". Journal of Physical Chemistry, Vol. 93, 2079-2082.

Appelo, C.A.J. & Wersin, P. (2007), "Multicomponent diffusion modeling in clay systems with application to the diffusion of tritium, iodide and sodium in Opalinus clay". Environmental Science and. Technology, Vol. 41, 5002-5007.

Huertas, F. et al. (2000), Full-scale engineered barriers experiment for a deep geological repository for high-level radioactive waste in crystalline host rock-FEBEX project, Euratom.

Lasaga, A.C. (1979), "The treatment of multicomponent diffusion and ion pairs in diagenetic fluxes". American Journal of Science, Vol. 279, 324-346.

Millington, R.J. & Quirk, J.M. (1961), "Permeability of porous solids". Transaction Faraday Society, Vol. 57, 1200–1207.

Parkhurst, D.L. & Appelo, C.A.J. (1999), User's guide to PHREEQC (version 2), U.S. Geological Survey, Water Resource Investigation Report 99-4259.

Pusch, R. & Yong, R.N. (2006), Microstructure of Smectite Clays and Engineering Performance, Taylor and Francis.

Rosanne, M., Paszkuta M. & Adler, P.M. (2006), "Thermodiffusional transport of electrolytes in compact clays". Journal of Colloid Interface Science, Vol. 299, 797-805.

Sedighi, M., Thomas, H.R., Vardon, P.J. & Seetharam, S.C. (2010), "Advances in modelling the non-isothermal behaviour of multicomponent chemicals in unsaturated soils". 6th International Congress on Environmental Geotechnics, New Delhi, India.

Seetharam, S.C. (2003), "An investigation of the thermo/hydro/chemical/mechanical behaviour of unsaturated soils". Ph.D. Thesis, Cardiff University, UK.

Seetharam, S.C., Thomas, H.R. & Cleall, P.J. (2007), "Coupled thermo-hydro-chemical-mechanical model for unsaturated soils-Numerical algorithm". International Journal of Numerical Methods in Engineering, Vol. 70, 1480-1511.

Thomas, H.R. & He, Y. (1995), "Analysis of coupled heat, moisture, and air transfer in a deformable unsaturated soil". Géotechnique, Vol. 45, 677-689.

Thomas, H.R., Sedighi, M. & Vardon, P.J. (2011), "Diffusive reactive transport of multicomponent chemicals under coupled thermal, hydraulic, chemical and mechanical conditions", submitted to the International Journal of Geomechanics.

Thornton, E.C. & Seyfried, W.E. (1983), "Thermodiffusional transport in pelagic clay: implications for nuclear waste disposal in geological media". Science, Vol. 220, 1156-1158.

HYDROMECHANICALLY COUPLED ANALYSIS OF TRANSIENT PHENOMENA IN A RAINFALL-INDUCED LANDSLIDE

J. Eichenberger[1]

M. Nuth[1]

L. Laloui[1]

Laboratory of Soil Mechanics, Ecole Polytechnique Fédérale de Lausanne, EPFL, Lausanne, Switzerland

ABSTRACT: *Heavy rainfall can lead to shallow slips in slopes that are initially in a state of partial water saturation. Multiphysics numerical modelling approaches taking into account the involved physical key processes in variably saturated soils during rainfall events could help in understanding the main slip mechanisms. The concerned processes are related to water flow through the solid matrix, soil water retention behaviour and the effects of matric suction on the mechanical behaviour. In this paper, the elasto-plastic constitutive model ACMEG-s that captures some key features of the behaviour of variably saturated soils is used in a fully coupled hydromechanical finite element analysis for the assessment of destabilizing, transient processes in a steep slope during rain infiltration. It is shown that at the onset of failure, wetting pore collapse and plastic shear strains occur in the lower part of the slope and develop upwards towards the slope surface to delimit a probable failure mechanism.*

1 INTRODUCTION

Rainfall-induced landslides are mostly superficial and are triggered in soil slopes where a permanent groundwater table is often absent due to slope steepness and generally dry environmental conditions. Soils in such slopes are most of the time in a state of partial water saturation. The failure surface of shallow slips is commonly situated between 0.5 and 3 meters in soil depth and runs subparallel to the slope surface along an interface between soil cover and bedrock. The whole sliding mass is often several meters to tens of meters wide, several tens of meters long and sums up to a couple of hundred to thousand cubic meters in volume (Dai et al. 1999). Shallow slides in steep (30 to 40°), loose colluvial deposits are mostly translational and mobilize completely to form debris flows. Actually, flow-type failures such as debris flows and flowslides are reported to result most often from shallow slips (Iverson et al. 1997). Although landslides under the action of variations of positive (compressive) pore pressures are well documented and probably most recurrent, they may also happen in unsaturated conditions. Such is the case for slopes where the substratum is not in particular less permeable than the soil cover and the contribution of capillary forces to slope stability is substantial (Godt et al. 2009).

In order to perform a geomechanical analysis of shallow landslide phenomena, the numerical model has to be capable of reproducing the physical processes during rain infiltration and failure initiation in variably saturated soils. Within the framework of an elasto-plastic constitutive model for unsaturated soils, results from a time-dependent, hydromechanical finite element analysis of a rainfall-induced landslide are presented in this paper. The considered case study is inspired from a real test-site slope in partially saturated

conditions subjected to rain infiltration (Springman et al. 2009). The simulation results show the usefulness of considering partial saturation in hydraulic and mechanical terms for the modelling of the predominant transient processes and key physical mechanisms, such as soil hardening effect of matric suction, wetting pore collapse and plastic shearing.

2 PHYSICAL PROCESSES IN UNSATURATED SOIL SLOPES

Commonly, two flow regimes are encountered in natural slopes: a deep flow regime, most often parallel to the slope surface with possible complex bedrock interactions and a superficial flow regime with capillary pressures or positive, compressive pore water pressures controlled by rainfall. The slope response to a rainfall event depends mainly on rainfall intensity and duration, on soil hydraulic characteristics, on the thickness of the sliding mass and on antecedent weather conditions (Klubertanz et al. 2009). The occurrence and type of landslide triggering mechanism depends strongly on hydraulic predisposition factors, but also on slope angle and mechanical soil characteristics. Shallow slope failures are often reported to occur along an interface between soil deposits and underlying bedrock under fully saturated conditions due to a build-up of positive pore water pressures and subsequent loss in soil shear strength (Johnson and Sitar 1990). This is especially the case for slopes where the effective internal friction angle of the soil is close to the slope angle. Slopes with an angle much steeper than the soil's internal friction angle rely on suction stresses and/or root reinforcement in order to be stable. In the case presented in this paper, the average slope angle is noticeably higher (α=38°) than the effective internal friction angle (φ'=33°) determined in the laboratory. A real-scale slope failure has been triggered artificially by sprinkling the test-site with water (Springman et al. 2009).

During a rainfall event, water infiltrates predominantly vertically under the influence of gravity and capillary forces into the soil. Several hydromechanical processes act in a destabilizing sense on the slope during and after rain infiltration:

- The degree of saturation of the upper soil layer increases, thereby reducing the capillary tension between the soil particles, which weakens in most cases the slope.
- Deposited soils, as well as heavily weathered residual soils are susceptible to a collapse of the loose soil matrix upon wetting. The wetting pore collapse in parts of the slope can lead to differential settlements (Jia et al. 2009). At high degrees of saturation, the rapid volume reduction may be a cause for debris flow initiation.
- A slope-parallel flow regime installs itself after the rainfall event in the upper partially saturated soil layer when the volume of infiltrated water is large enough. Water is consequently carried to the toe region. Upon that, due to the mobilized fluid flow inside the soil matrix, the fluid exerts a destabilizing, downhill frictional drag.

Unsaturated zone physical processes govern the time-dependent response of soil slope to a rainfall event. Considering that they take place in a timescale relevant to a single rainfall event, their identification and integration in the modelling process is necessary in order to perform an analysis of the onset of failure. This can be achieved with a hydromechanically coupled approach and an adequate constitutive model for variably unsaturated-saturated soils.

3 THEORETICAL FRAMEWORK FOR UNSATURATED SOILS

In order to capture the main features of soil slope behaviour in unsaturated conditions for modelling purpose, an elasto-plastic constitutive model including the soil water retention behaviour is used in the framework of hydromechanically coupled porous media. The principal model concepts are reviewed in this section.

The Advanced Constitutive Model for Environmental Geomechanics (ACMEG-s) (Nuth & Laloui 2007; Nuth & Laloui 2008a) is a Cam-Clay-type elasto-plastic model (Schofield & Wroth 1968) and is based on the so-called initial Hujeux's model (Hujeux 1985). The increment of strain $d\varepsilon_{ij}$ is decomposed into:

$$d\varepsilon_{ij} = d\varepsilon_{ij}^{e} + d\varepsilon_{ij}^{p} \tag{1}$$

Where $d\varepsilon_{ij}^{e}$ is the elastic strain increment and $d\varepsilon_{ij}^{p}$ the plastic strain increment. The elastic deformation can be expressed as:

$$d\varepsilon_{ij}^{e} = C_{ijkl} d\sigma'_{kl} \tag{2}$$

The tensor C_{ijkl} is the mechanical elastic tensor and is composed of non-linear elastic moduli. The elastic strain increment $d\varepsilon_{ij}^{e}$ can be decomposed in volumetric and deviatoric increments which are related to mean effective, respectively deviatoric stress by means of spherical stress-dependent elastic moduli. σ'_{kl} in Eq. (2) is the effective stress for unsaturated soils (Laloui & Nuth, 2009):

$$\sigma'_{kl} = \left(\sigma_{kl} - u_a \delta_{kl}\right) + S_r \left(u_a - u_w\right) \delta_{kl} \tag{3}$$

Where σ_{kl} is the total stress, u_a is the air pressure, u_w is the water pressure, S_r is the degree of saturation and δ_{kl} is the Kronecker's delta. The difference between the total stress σ_{kl} and the air pressure u_a is called the net stress $\sigma_{kl\,net}$. The difference between u_a and u_w is defined as the matric suction s.

The critical state line is defined in the plane of deviatoric stress q versus mean effective stress p', with a slope M. The slope of the critical state line in the plane volumetric plastic strain vs. mean effective stress $\left(\varepsilon_v^p - \ln p'\right)$ is β, p'_{CR0} being the initial critical state pressure:

$$\ln \frac{p'_{CR}}{p'_{CR0}} = \beta \varepsilon_v^p \tag{4}$$

In the ACMEG-s model, the plastic irreversible strain increment $d\varepsilon_{ij}^{p}$ is induced by two coupled dissipative processes: an isotropic and a deviatoric plastic mechanism. The yield limits of each mechanism, bounding the elastic domain in the effective stress space, can be written as:

$$\tilde{f}_{iso}(p', \varepsilon_v^p, r_{iso}) = p' - r_{iso}.d.p'_{CR} \tag{5}$$

$$\tilde{f}_{dev}(p', q, r_{dev}, \varepsilon_v^p, \varepsilon_d^p) = q - Mp'\left(1 - b \ln \frac{p'}{p'_{CR}}\right) r_{dev} \tag{6}$$

Where p'_{CR} is the critical state pressure. d, b, r_{iso} and r_{dev} are material parameters. ε_v^p and ε_d^p are respectively the volumetric plastic strain and the deviatoric plastic strain. The critical

state pressure in Eq. (4) can be related to the preconsolidation pressure $p_c^{'}$ using the material parameter *d*, that represents the distance in the volumetric plane between the normally consolidated line and the critical state line:

$$p'_c = d.p'_{CR} \tag{7}$$

Using the space of triaxial stress variables *q* and *p'*, the elastic domain is enclosed by an ellipsoidal surface which is cut by the isotropic yield limit (see Figure 1). Adding the suction s as a third axis of the space, Figure 1 shows that the elastic domain gets larger with suction. This accounts for the fact that a dryer material will have higher strength and stiffness. Eq. (8) gives the mathematical formulation of the contribution of the capillary effects to the mechanical behaviour. The principle is to introduce a dependency of the preconsolidation pressure p'_c on the level of suction s and using a material parameter γ_s:

$$p'_c = \begin{cases} p'_{c0} & \text{if } s \le s_e \\ p'_{c0}\left[1+\gamma_s \log\left(s/s_e\right)\right] & \text{if } s \ge s_e \end{cases} \tag{8}$$

p'_{c0} is the initial preconsolidation pressure at zero suction and s_e is the suction air entry.

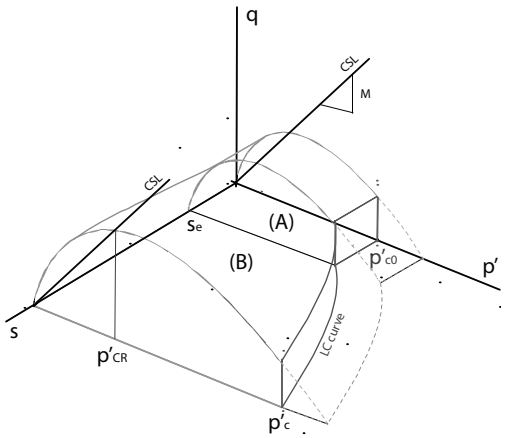

Figure 1. Yield surface shape and critical state line (CSL) in a $\left(p',q,s\right)$ space.

Modelling the evolution of the degree of saturation S_r with respect to suction s is also taken into account in the model (Nuth & Laloui 2008b). The increment of the degree of saturation dS_r is decomposed into an elastic part and a plastic part and is written:

$$dS_r = \frac{ds}{K_H \times \left(s/s_e\right)} + \frac{ds_D}{\beta_H \times \left(s_D/s_{D0}\right)} \tag{9}$$

K_H is the elastic slope and β_H is the plastic slope defined in Figure 2. s_e represents the limit below which the degree of saturation remains equal to one. s_e depends on the void ratio (i.e. the density of the material). If the suction remains lower than the air entry value, the degree of saturation equals one and there is no elastic increment. If the residual state is reached ($S_r = S_{res}$, where S_{res} is the residual degree of saturation), then the elastic increment becomes null too. s_D is the drying yield suction, which is the maximum suction ever

experienced by the material along a drying path. s_{D0} is the initial value of the drying yield suction.

The process of drying and wetting is not fully reversible and the $(S_r - s)$ data usually show the existence of a capillary hysteresis. A given level of suction can indeed correspond to different degrees of saturation. The way chosen to reproduce the retention hysteresis is to make the yield surface evolves by means of kinematic hardening. The elastic domain is delimited by the following yield limit:

$$f = \left\| \ln(s) - \ln(s_D) + \frac{1}{2}\left[\ln(s_{D0}) - \ln(s_e)\right] \right\| - \frac{1}{2}\left[\ln(s_{D0}) - \ln(s_e)\right] \tag{10}$$

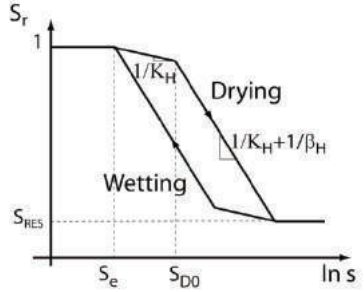

Figure 2. Modelling of the soil water retention curve.

For the flow problem, the generalized Darcy's law is used to describe the relative velocity of the fluid with respect to the solid skeleton. The permeability tensor $\mathbf{K}_w$ depends in general on the degree of saturation S_r. Assuming hydraulic isotropic conditions, the water relative permeability coefficient k_{rw} is defined according to the following relationship, CKW1 being a material parameter:

$$k_{rw} = \sqrt{S_r}\left[1 - \left(1 - S_r^{\frac{1}{CKW1}}\right)^{CKW1}\right]^2 \tag{11}$$

The constitutive model presented above is implemented into the finite element code called LAGAMINE (Charlier 1987; Collin 2003). The code features hydro-mechanically coupled finite elements.

4 NUMERICAL MODELLING OF AN UNSATURATED SOIL SLOPE SUBJECTED TO RAINFALL INFILTRATION

As a generic case study, the hydromechanically coupled analysis is inspired from realistic geometrical (Askarinejad 2009) and material parameters (Eichenberger et al., 2010) close to those of a real test-site case study in Rüdlingen, Switzerland (Swiss Competence Center Environment and Sustainability, project TRAMM). A detailed description of this landslide triggering experiment is presented by Springman et al. (2009). It is not intended here to reproduce the in-situ experiment neither to compare the performance of the model with the measured in-situ data. The material parameters for the ACMEG-s model were calibrated on the basis of triaxial, oedometer and retention tests carried out at the Laboratory of Soil Mechanics, EPFL (Table 1). The geometry of the slope is presented in Figure 3. The steep slope of 38° is composed of silty sand deposits (soil cover) of 2 to 5m thickness and a beneath laying, fractured bedrock. The principal objective of this study is to show the effect of rain infiltration on the stability of a partially saturated slope and its failure mechanisms.

4.1 Definition of the Geomechanical Model and the Calculation Procedure

The finite element mesh presented in Figure 3 is composed of 4672 six-noded quadratic triangles. The ACMEG-s constitutive model is applied to both, bedrock and soil cover, using the parameters of table 1. The behaviour of the bedrock is assumed elastic. Its saturated soil water permeability is set equal to that of the soil cover in order to focus the study solely on the effect of vertical rain infiltration and not on eventual hydraulic heterogeneities. The mesh is strongly refined in the upper soil layer in order to properly model the transient hydromechanical processes and the development of plastic zones during rain infiltration. Conventional kinematic boundary conditions are imposed to the box model.

Table 1. Parameters for the elasto-plastic ACMEG-s and water retention model.

		Symbol	Description	Value
Stress-strain model	Elastic parameters	K_{ref}	Bulk modulus	$1*10^9$ Pa
		G_{ref}	Shear modulus	$6*10^8$ Pa
		n^e	Elastic exponent	0.1
	Plastic parameters	φ'	Friction angle	33°
		β_0	Compressibility coefficient	30
		*α	Dilatancy coefficient	0.7
		*a		0.05
		b	see equation (5)	0.1
		*c		0.08
		d	see equation (4)	1.3
	Limits of elastic domain	r^e_{dev}	Initialisation of deviatoric mechanism	0.3
		r^e_{iso}	Initialisation of isotropic mechanism	0.3
Capillary effects		γ_s	Coefficient of LC curve	0.78173
		*Ω	Coef. var. compressibility	$2*10^{-5}$
		s_e	Air entry value	3000 Pa
Retention model		K_h	Elastic coefficient	8.8
		β_h	Plastic coefficient	10
		s_{D0}	Drying yield suction	6000 Pa
		S_{res}	Residual degree of saturation	0.3
Permeability		$k_{w,sat}$	Intr. water permeability	10^{-5} m/s
		CKW1	Parameter for the water rel. perm. function	0.55

*see Nuth & Laloui 2007 for explanation of parameters.

Initially, two calculations are run which consist of a gravity loading phase and a coupled flow and deformation analysis for the determination of the water table position and distribution of matric suction in the vadose zone. The resulting water table runs inclined from the top left to the bottom right model boundary. Matric suction is distributed hydrostatically in the partially saturated zone above the water table and the degree of saturation reaches its residual value of $S_r = 0.3$ along the slope surface, see Figure 3.

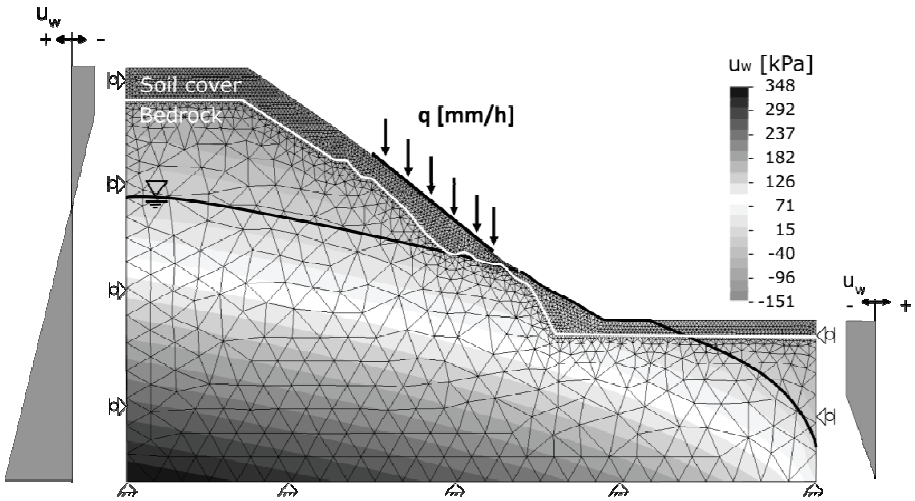

Figure 3. Finite element mesh, boundary and initial conditions.

In a final step, rain infiltration is simulated by means of an imposed boundary flux of 15mm/h for 3.5 days (the rain input is virtual and does not correspond to the real experiment). The water saturation contours in Figure 4a show clearly that the superficial soil layer has been quasi completely saturated. The soil water retention curve in Figure 4b indicates for 3 points at different depths that the matric suction has decreased to reach zero or close to zero values.

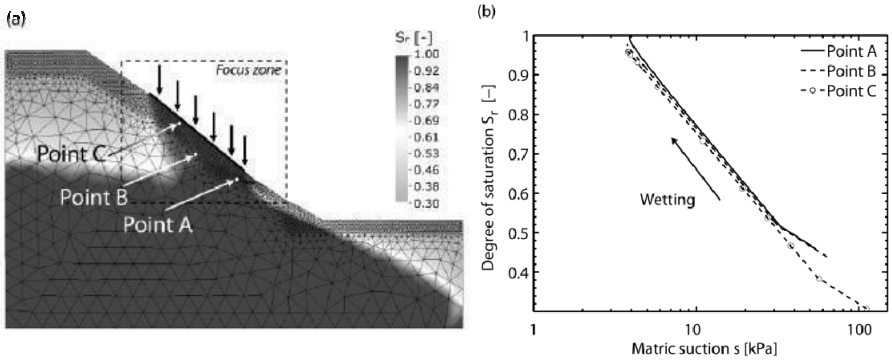

Figure 4. Rain infiltration in a partially saturated slope: spatial distribution of the degree of saturation (a); Soil water retention curve (b).

4.2 Plastic Mechanisms during Rain Infiltration

The supply of water in a partially saturated slope acts negatively on its stability. With increasing water content, the capillary forces reigning between the soil particles decrease. This de-bonding effect of wetting is taken into account in the model through the effective stress (Eq. (3)), which decreases during rain infiltration. The soil loses strength in classical soil mechanics terms.

In Figure 5, the contours of deviatoric strains are shown for the ”focus zone” indicated in Figure 4. Shear strains are localized along the interface between bedrock and soil layer for the lower and middle part of the slope and run up biased to the slope surface in the upper part. The extent of the shear zone coincides with the zone of increased degree of saturation (Figure 4a), showing clearly a localized effect of the infiltrated water.

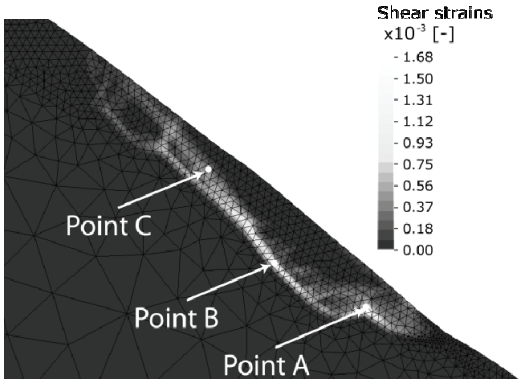

Figure 5. Contour of deviatoric strains after 3.5 days of rain infiltration. Light zones indicate a concentration of shear strains.

The deformation history of three selected points A, B and C defined in Figure 5 indicate which plastic mechanism, among the isotropic (Eq. (5)) and deviatoric (Eq. (6)), is predominant in different parts of the slope at different instants in time. The soil in the vicinity of point A above the bedrock abutment was almost normally consolidated prior to infiltration. In this zone, water infiltration is at the origin of strong shearing associated with noticeable positive (compressive) plastic volumetric deformations (Figure 6).

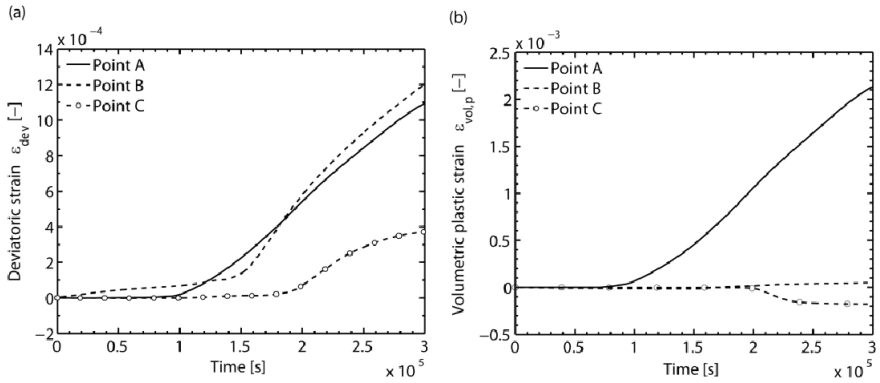

Figure 6. Evolution of deviatoric (a) and plastic volumetric (b) deformations.

Compared to the other observation points, the volumetric behaviour in point A is clearly distinguished. Point B situated in the middle part of the slope undergoes strong shearing of the same order of magnitude as for point A. The compressive plastic volumetric deformation at point B is however negligible. Point C located in the shearing zone running up to the slope surface reacts only after $2*10^5$ seconds. In accordance with the other observation points this suggests that the shearing mechanism starts in the lower part of the slope, above the abutment, then moves upwards along the bedrock interface and finally runs up to the slope surface, delimiting consequently a potentially unstable soil mass. The plastic volumetric strains in point C are negative in the sense of extension and are associated to the occurrence of plastic deviatoric strains. The extension of the soil can be either due to dilatancy during shearing, considering that the soil is overconsolidated, or due to a downwards movement of the potentially unstable soil mass leading to the formation of a tension crack in the upper part of the slope.

The almost normally consolidated soil in the lower part of the slope is a priori susceptible to plastic deformations in the sense of a wetting pore collapse. The wetting pore collapse is the property of the soils to get denser when soaked under a sufficient mechanical load. As shown in Figure 7a for points A and B the stress paths during wetting remain at first within

their respective elastic domains. The isotropic yield limits are reached at lower values of matric suction. The stress paths then follow the current isotropic yield surfaces without moving them noticeably. Yet, this process corresponds to soil hardening and generation of compressive volumetric plastic strains. This behaviour was experimentally observed in confined testing conditions and is coherent with the simulated conditions in the soil slope. There is a considerable loss in mean effective stress associated to the wetting pore collapse in point A after $7*10^4$ seconds which indicates a strength decrease in the lower part of the slope (Figure 7b). The mean effective stress reaches a constant value of around 60kPa after $1.5*10^5$ seconds. Matric suction decreases to a steady constant value of around 5kPa.

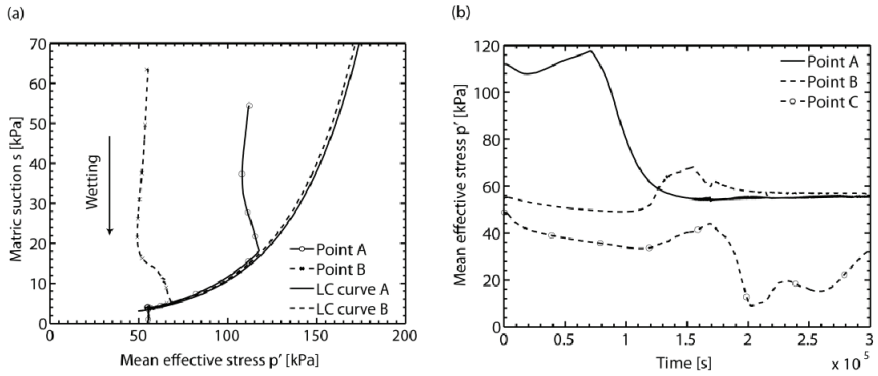

Figure 7. Stress paths and loading collapse curves (isotropic yield loci) for two points (a); Evolution of mean effective stresses (b).

To summarize, the deviatoric plastic mechanism is clearly predominant in the upper and middle part of the slope while in the lower part of the slope the isotropic plastic mechanism governs the behaviour.

5 CONCLUSIONS

Rainfall-induced shallow landslides often take place in slopes which are most of the time in a state of partial saturation. Although these failures take place rapidly, precursor signs in terms of surface settlements exist and have been observed in laboratory and field experiments (Take et al. 2004; Jia et al. 2009; Springman et al. 2009). In order to model numerically the onset of rainfall-induced landslides in variably saturated-unsaturated conditions, a consistent stress framework needs to be chosen. For this purpose, the generalized effective stress framework has been used. It allows on one hand a smooth transition between saturated and unsaturated states, and on the other an explicit hydromechanical coupling between the soil's effective stress and the evolution of matric suction and degree of saturation. The ACMEG-s model is capable of reproducing some of the major features of unsaturated soil behaviour, such as wetting pore collapse, soil shear strength and stiffness variation with matric suction. Its use for the transient finite element analysis of a partially saturated slope subjected to rain infiltration revealed interesting results on the actual onset of failure. The analysis gave detailed information on the active physical mechanisms during rain infiltration. The most probable failure mechanism develops in the lower part of the slope as a consequence of a wetting pore collapse and then spreads upwards along the bedrock and through the soil cover to the slope surface as a predominant shear mechanism. The volumetric compaction in the lower part of the slope is accompanied by important shear strains which indicate that both, isotropic and deviatoric plastic mechanisms are active. The increasing degree of saturation and the simultaneous volumetric compaction can also be interpreted as indicators for an increased susceptibility for flow mobilization in the post-failure stage.

ACKNOWLEDGEMENT

This work was supported by Swiss Competence Center Environment and Sustainability, TRAMM project and the European Commission, FP7 project SafeLand. Special thanks are addressed to Dr. F. Collin and Prof. R. Charlier from Université de Liège for their support in numerical issues.

REFERENCES

Askarinejad, A. (2009), "A method to locate the slip surface and measuring subsurface deformations in slopes". Proc. 4th Intern. Young Geotechnical Engineers' Conf., Alexandria.

Charlier, R. (1987), "Approche unifiée de quelques problèmes non linéaires de mécanique des milieux continus par la méthode des éléments finis". PhD thesis, Université de Liège.

Collin, F. (2003), "Couplages thermo-hydro-mécaniques dans les sols et les roches tendres partiellement saturés". PhD thesis, Université de Liège.

Dai Fuchu, Lee, C.F., and Wang Sijing (1999), "Analysis of rainstorm-induced slide-debris flows on natural terrain of Lantau Island, Hong Kong". Engineering Geology. 51 (4), 279–290.

Eichenberger, J., Nuth, M., Laloui, L. (2010), "Modeling landslides in partially saturated slopes subjected to rainfall infiltration". Chapter of the book "Mechanics of unsaturated geomaterials", pp.235-250, Eds. L. Laloui, John Wiley & Sons.

Godt J.W., Baum R.L., Lu N. (2009), "Landsliding in partially saturated materials". Geophysical Research Letters. 36, L02403, 1-5.

Hujeux, J. (1985), "Une loi de comportement pour le chargement cyclique des sols". Génie Parasismique. Paris, Les éditions de l'E.N.P.C.: 287-353.

Iverson, R.M., Reid, M.E., LaHusen, R.G. (1997), "Debris-flow mobilization from landslides". Annual Review of Earth and Planetary Sciences. 25, 85-138.

Jia, G.W., Zhan, T.L.T., Chen, Y.M., Fredlund, D.G. (2009), "Performance of a large-scale slope model subjected to rising and lowering water levels". Engineering Geology. 106, 92-103.

Johnson, K.A., Sitar, N. (1990), "Hydrologic conditions leading to debris flow initiation". Canadian Geotechnical Journal. 27 (6): 789-801.

Klubertanz, G., Laloui, L., Vulliet L. (2009), "Identification of mechanisms for landslide type initiation of debris flows". Engineering Geology. 109 (1-2), 114-123.

Laloui, L., Nuth, M. (2009), "On the use of the generalised effective stress in the constitutive modelling of unsaturated soils". Computer and Geotechnics. 36 (1-2): 20-23.

Nuth, M., Laloui, L. (2007), "New insight into the unified hydro-mechanical constitutive modelling of unsaturated soils". Proc. Unsat Asia 2007. Nanjing, 109-125.

Nuth, M., Laloui, L. (2008a), "Effective stress concept in unsaturated soils: Clarification and validation of a unified framework". International journal for numerical and analytical methods in Geomechanics. 32, 771-801.

Nuth, M., Laloui, L. (2008b), "Advances in modelling hysteretic water retention curve in deformable soils". Computers and Geotechnics. 35 (6), 835-844.

Schofield, A.N., Wroth, C.P. (1968), Critical state soil mechanics, McGraw-Hill, London.

Springman, S.M., Kienzler, P., Casini, F., Askarinejad, A. (2009), "Landslide triggering experiment in a steep forested slope in Switzerland". 17th Intern. Conf. of Soil Mech. & Geot. Eng., Alexandria.

Take, W.A., Bolton, M.D., Wong, P.C.P., Yeung, F.J. (2004), "Evaluation of landslide triggering mechanisms in model fill slopes". Landslides. 1 (3), 173-184.

ON THE ESTIMATION OF EFFECTIVE PERMEABILITY OF HETEROGENEOUS GEOMATERIALS

P.A. Selvadurai
Department of Civil and Environmental Engineering, University of California, Berkeley, CA, USA

A.P.S. Selvadurai
Department of Civil Engineering and Applied Mechanics, McGill University, Montréal, QC, Canada

ABSTRACT: *The paper presents the mathematical, computational and experimental approaches that have been developed recently to estimate the effective permeability of a heterogeneous porous medium. The procedures available for estimating effective permeability are assessed in relation to experimental results derived from steady state fluid flow conducted on a cuboidal specimen of Indiana Limestone that displays heterogeneous properties. The computational developments are then applied to evaluate the effective permeability of a cuboidal region with a lognormal distribution of permeability.*

1 INTRODUCTION

Naturally occurring geomaterials are invariably inhomogeneous. Such heterogeneity translates to geomaterial properties, with scalar and tensor descriptions, that can be functions of position and orientation. Problems dealing with flow in naturally occurring porous media therefore have to incorporate descriptions of permeability that are both anisotropic and inhomogeneous. Such definitions are compounded by the fact that permeability in particular is highly dependent on scale. These can vary from regional scales of 0.5 km to 5 km, borehole scales ranging from 30m to 300m and laboratory scales of 5 cm to 15 cm. (Selvadurai et al., 2005). Ultimately, the objective of permeability measurement is to use accurate estimates of permeability at the laboratory scale to generate estimates that are applicable for regions of larger dimensions. This process of upscaling is not without its limitations particularly in relation to capturing the influence of geological defects such as vugs, cracks, inclusions and other inhomogeneities that can significantly affect the estimation of permeabilities at larger scales. Furthermore, the role of an inhomogeneity at one scale could contribute to anisotropy at a larger scale, which is characteristic of naturally occurring geologic media. The pioneering contributions of Henry Darcy (1856) focused mainly on the measurement of permeability characteristics of granular materials used primarily in applications to filter materials used for water purifications, which unfortunately do not possess the spatial and directional inhomogeneities associated with naturally occurring geologic media. The permeability of a geomaterial is the property with the largest variability. Harr (1987) indicates that permeability can have coefficients of variation that depend on the degree of saturation (around 240% for 80% saturation and around 90% for full saturation). In the fields of environmental geoscience and environmental geomechanics, permeability is a parameter that can have a significant influence on processes such as subsurface movement of groundwater, advection-dominated transport of contaminants in the geosphere, deep injection of fluidized hazardous materials, geologic sequestration of carbon dioxide in fluidized

supercritical form, ground subsidence due to water extraction, migration of fines in porous media, aquifer contamination due to salt water intrusion, etc. In many geoenvironmental problems involving groundwater flow, the accurate estimation of the permeability characteristics of a geologic medium is therefore critical to the evaluation quantities of geoenvironmental interest.

The classical treatments of flow in porous media are documented in a number of classical treatises on the subject including those of Polubarinova-Kochina (1962), Harr (1962), Bear (1972), Verruijt (1982), de Marsily (1986), Philips (1991) and further developments and advances are summarized in many recent works including those by Strack (1989), Selvadurai (2000a, 2007, 2010), Zijl and Nawalany (2000) and Bear and Cheng (2009). The conventional approach to the specification of the law of groundwater movement pre-supposes the applicability of hydraulic homogeneity (and hydraulic isotropy) without a clear specification of the regions over which such assumptions are applicable. In this paper we examine the role of scale in the definition of effective permeability of a heterogeneous porous medium. The estimation of effective permeability is demonstrated by examining patch permeability experiments conducted on the six surfaces of a cuboidal block of Indiana Limestone measuring 508mm. The hydraulic behaviour of the patch permeameter is examined using both analytical and computational methods. These surface estimates of permeability are used in conjunction with a kriging technique to develop the distribution of permeabilities within the cuboidal specimen. The spatial distribution of permeabilities is then used to estimate the effective permeability of the block as a whole. The conformity of the spatial variation of permeability to a lognormal distribution enables the application of theoretical relationships for the estimation of effective permeability. Several such estimates are available in the literature and the predictive capabilities of the estimates are examined computationally through one-dimensional potential flows induced along three orthogonal directions. The results of the research are also used to propose a measure of effective permeability that is based on the *geometric mean* of permeabilities determined by establishing one-dimensional flow in a region along any three orthogonal directions. The accuracy of the effective permeability based on the geometric mean is also examined via computational modelling of complex flow patterns within a cuboidal region.

2 SPATIAL VARIATIONS AND SCALE-DEPENDENCY OF PERMEABILITY

Naturally occurring porous geomaterials are rarely homogeneous and this invariably leads to permeability measures that are representative volume element-dependent. As an example consider the elementary problem of the estimation of the permeabilities of a stratified medium with strata thicknesses t_i and assume that effective permeabilities K_i can be assigned to all the individual strata. The effective permeability normal to the stratifications is given by the *weighted harmonic mean*

$$K_n = \left(\sum_{i=1}^{n} t_i \right) \Big/ \left(\sum_{i=1}^{n} \frac{t_i}{K_i} \right) \tag{1}$$

and the effective permeability along the stratifications is given by the *weighted arithmetic mean*

$$K_t = \left(\sum_{i=1}^{n} K_i t_i \right) \Big/ \left(\sum_{i=1}^{n} t_i \right) \tag{2}$$

Consider the problem of a stratified porous medium where the permeability distribution of the individual strata of equal thickness corresponds to a *random sequence* with permeabilities

varying between $(10, 20)\times10^{-15}\,\mathrm{m}^2$. We consider the permeability estimates that are determined from (1) and (2) corresponding to this random sequence of permeabilities and select the number of layers of equal thickness as an integer number (n) varying between 2 and 40. The effective permeabilities K_n and K_t can be calculated using the random permeability distribution, obtained using the random number generator provided in MATHEMATICA™. The permeabilities K_n and K_t calculated for the different layer numbers n is shown in Figure 1. If we interpret the number of layers as a measure of the volume of material used in the estimation of permeability, it is clearly evident that the effective permeabilities in directions normal to and along the stratifications are dependent on n and consequently on the volume of region considered. Large fluctuations in the estimated permeabilities are observed as n decreases and, as the volume of the region examined increases, the fluctuations diminish and the permeabilities approach steady values. Similar calculations can be performed for permeabilities determined from other statistical distributions of permeabilities assigned to the various strata and the thicknesses of the layers themselves could be considered to be varying randomly. Also in these circumstances, the estimates of the effective permeabilities K_n and K_t will depend on the representative volume element used in the calculations.

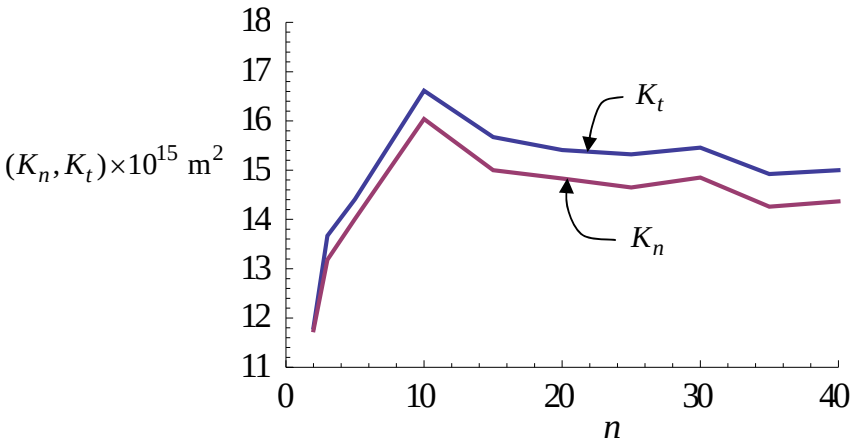

Fig. 1. Influence of layer number on the effective permeabilities of a stratified porous medium where layers of equal thickness have isotropic permeabilities that are randomly distributed in the range $(10, 20)\times10^{-15}\,\mathrm{m}^2$

3 EXPERIMENTAL DETERMINATION OF HYDRAULIC HETEROGENEITY

The dependency of the effective permeability on scale requires that estimates are derived using a technique that can account for the spatial variations in the permeability properties at the scale of the element being tested. The steady state permeability tests conducted on the large cuboidal block of Indiana Limestone measuring 508 mm was an attempt to determine, in a laboratory context, the spatial variability of permeability of the block. In conventional laboratory permeability testing, one-dimensional flow is induced on cylindrical samples that have substantially smaller dimensions (maximum 10 cm in diameter and 20 cm in length) in comparison with the dimensions of the geomaterial volume it is expected to represent in a groundwater flow situation. Larger specimens can eliminate some of the drawbacks of conventional small-scale testing but the use of conventional axial or radial flow tests with large samples is non-routine. When there is access to large samples, alternative methods can

be developed to estimate the variation of permeability within the tested region (Selvadurai and Selvadurai, 2007). Studies by P.A. Selvadurai (2010) illustrate the use of surface permeameter techniques to estimate the permeability of a cuboidal sample of Indiana Limestone; novel experimental techniques and analytical and computational procedures were needed for the estimation of the surface permeability characteristics. The experimental technique involved the use of an annular patch to seal a part of the surface being tested and steady state flow was initiated by pressurizing the interior of the annular region. The experimental arrangement of the annular patch permeability test is shown in Figure 2 and full details of the experimental procedures are given by Selvadurai (2010b).

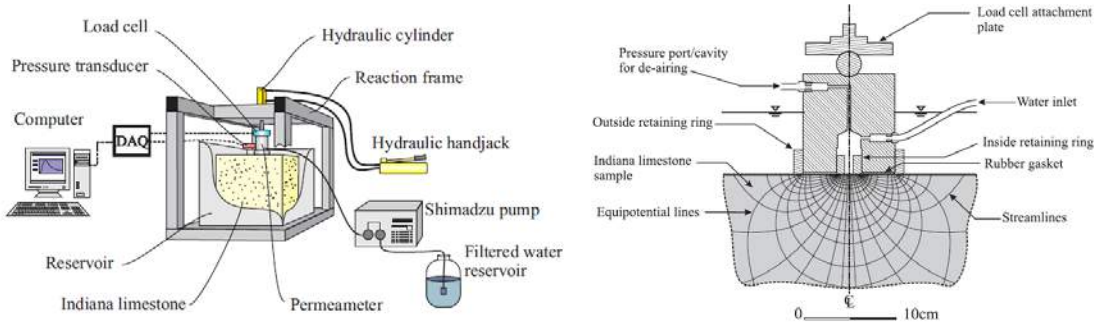

Fig. 2. The experimental arrangement for the annular sealed patch measurement of the surface permeability of the block of Indiana Limestone

In order to estimate the surface permeability of the block of Indiana Limestone, we make the assumption that in the region of the surface location of the annular permeameter, the porous medium exhibits local hydraulic homogeneity and isotropy. Darcy's law for the velocity vector $\mathbf{v}(\mathbf{x})$ takes the form

$$\mathbf{v}(\mathbf{x}) = -\frac{K\,\gamma_w}{\mu}\nabla\Phi \tag{3}$$

where K is the permeability, γ_w is the unit weight of water, μ is the dynamic viscosity, Φ is the reduced Bernoulli potential and ∇ is the gradient operator. The mass conservation equation during flow through the porous medium is given by

$$\nabla\cdot\mathbf{v}(\mathbf{x}) = 0 \tag{4}$$

Considering (3) and (4), the axisymmetric potential satisfies Laplace's equation, which, in cylindrical polar coordinates suitable for modelling the axisymmetric problem of fluid flow in the vicinity of the annular permeameter, takes the form

$$\left(\frac{\partial^2}{\partial r^2}+\frac{1}{r}\frac{\partial}{\partial r}+\frac{\partial^2}{\partial z^2}\right)\Phi(r,z) = 0 \tag{5}$$

where (r,θ,z) is the cylindrical polar coordinate system. The annular permeameter of inner radius a and outer radius b is sealed in the region $r\in(a,b);\ z=0$ and assuming that the dimensions of the sealed region permit the local region to be modelled as a semi-infinite domain, the mixed boundary value problem associated with the annular permeameter takes the form

$$\Phi(r,0) = \Phi_0\ \ ;\ \ r\in(0,a) \tag{6}$$

$$\left(\frac{\partial\Phi}{\partial z}\right)_{z=0} = 0\ \ ;\ \ r\in(a,b) \tag{7}$$

$$\Phi(r,0)=0 \;\; ; \;\; r\in(a,\infty) \tag{8}$$

The three-part mixed boundary value problem defined by (6)-(8) can be solved using a Hankel transform development of (5) (Selvadurai, 2000b). The details are given in Selvadurai and Selvadurai (2010) and the steady flow rate q from the central aperture that is subjected to the potential Φ_0 is given by

$$q=a\,\Phi_0\left(\frac{K\gamma_w}{\mu}\right)F(c) \tag{9}$$

where

$$F(c)=4\left\{\begin{array}{l}1+\left(\dfrac{4}{\pi^2}\right)c+\left(\dfrac{16}{\pi^4}\right)c^2+\left(\dfrac{64}{\pi^6}+\dfrac{8}{9\pi^2}\right)c^3+\left(\dfrac{64}{9\pi^4}+\dfrac{256}{\pi^8}\right)c^4+\\ \left(\dfrac{92}{225\pi^4}+\dfrac{384}{9\pi^6}+\dfrac{1024}{\pi^{10}}\right)c^5+\mathrm{O}(c^6)\end{array}\right\} \tag{10}$$

and $c=(a/b)<<1$ is the aperture ratio. Selvadurai and Selvadurai (2010) have shown that the approximate analytical result (9) is in excellent agreement with results obtained by Goggin et al. (1988), Tidwell and Wilson (1997) and Tartakovsky et al. (2000) using numerical solutions of the system of triple integral equations. Steady flow tests were conducted at nine locations on each of the six surfaces of the cuboidal block of Indiana Limestone, to generate surface estimates of permeability. The surface point estimates are used to generate, via a kriging procedure, estimates for the distribution of permeabilities at the interior of the cuboidal block of Indiana Limestone (Figure 3).

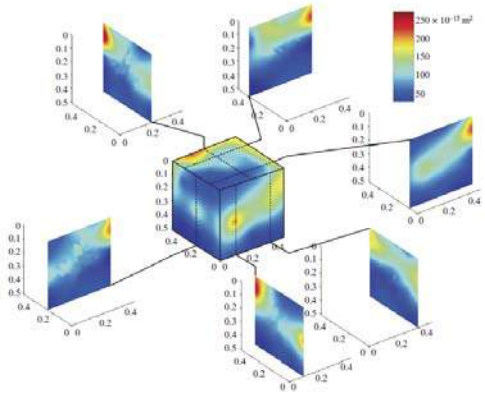

Fig. 3. Permeability inhomogeneity within the cuboidal block of Indiana Limestone.

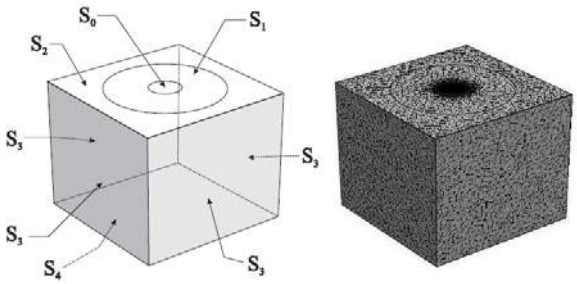

Fig.4. Computational modelling of a sub-cube region

As is evident, the permeability exhibits spatial inhomogeneity, even though the local evaluations that use the result (9) assume permeability homogeneity in the vicinity of the annular sealed region. To establish the influence of the permeabilities of the surrounding regions on the interpretation of the annular patch permeameter, a sub-cube region containing the annular patch permeameter was computationally modelled, varying the boundary conditions on the surfaces S_3 and S_4 to mimic either null Dirichlet or null Neumann conditions, representing either completely pervious or completely impervious conditions(Figure 4). i.e.

$$\Phi = \Phi_0, \mathbf{x} \in S_0\ ; \quad \frac{\partial \Phi}{\partial n} = 0, \quad \mathbf{x} \in S_1\ ; \quad \Phi = 0, \mathbf{x} \in S_2 \cup S_3 \cup S_4 \tag{11}$$

$$\Phi = \Phi_0, \mathbf{x} \in S_0\ ; \quad \frac{\partial \Phi}{\partial n} = 0, \ \mathbf{x} \in S_1, \mathbf{x} \in S_3 \cup S_4\ ; \quad \Phi = 0, \ \mathbf{x} \in S_2 \tag{12}$$

Computations indicate that the differences between the local permeability estimates for the extreme types of boundary conditions defined by (11) and (12) are less than 5.3%. In the experiments, the interpreted permeability has an order of magnitude difference over the entire block and the variation between the extremes is gradual. This is an acceptable justification for the assumption of local homogeneity.

4 ESTIMATION OF EFFECTIVE PERMEABILITY OF THE HYDRAULICALLY HETEROGENEOUS POROUS MEDIUM

The surface permeability values can now be used to predict, through a kriging procedure, the distribution of permeability at the interior of the cuboidal sample of Indiana Limestone. The details of the kriging procedures used are given by Selvadurai (2010b) and Selvadurai and Selvadurai (2010). The availability of a spatial distribution of permeabilities provides an opportunity to investigate the various approaches that are available for deducing the effective permeability of inhomogeneous porous media.

(i) Wiener (1912) bounds. If the isotropic permeability of an inhomogeneous porous medium has a variation $K(\mathbf{x})$ within a region V_0, the effective isotropic permeability K_{eff} of the region is always bounded by the inequality

$$K_{\text{h}} \le K_{\text{eff}} \le K_{\text{a}} \tag{13}$$

where K_{h} and K_{a} are, respectively, the harmonic mean and the arithmetic mean defined by

$$K_{\text{h}} = \frac{\iiint_{V_0} dV}{\iiint_{V_0} [K(\mathbf{x})]^{-1}\, dV}; \ K_{\text{a}} = \frac{\iiint_{V_0} K(\mathbf{x})\, dV}{\iiint_{V_0} dV} \tag{14}$$

(ii) Matheron (1967) suggests that the effective permeability is a weighted average of the Wiener bounds according to the dimension D of the space; i.e.

$$K_{\text{eff}}^{\text{M}} = K_{\text{a}}^{\alpha} K_{\text{h}}^{(1-\alpha)} \tag{15}$$

where $\alpha \in [0,1]$ and $\alpha = (D-1)/D$.

(iii) Journel et al. (1986) propose the following result for the effective permeability, which can be derived by considering the *power average* (or an average of order $p \in (-1,1)$ depending on the spatial distribution of permeabilities: i.e.

$$K_{\text{eff}}^{\text{J}} = \left(\frac{\iiint_{V_0} [K(\mathbf{x})]^p\, dV}{\iiint_{V_0} dV} \right)^{1/p} \tag{16}$$

It may be noted that in the limit $p = -1$, (16) corresponds to the harmonic mean, $p \to 0$ corresponds to the geometric mean and $p = 1$ corresponds to the arithmetic mean. For a statistically homogeneous and isotropic medium, $p = 1 - (2/D)$.

(iv) King (1989) proposes a perturbation technique, which indicates that the effective permeability can be estimated from the result

$$K_{\text{eff}}^{\text{K}} = K_a\left(1-\frac{\sigma^2}{D\,K_{\text{a}}^2}\right) \tag{17}$$

where σ^2 is the permeability variance. Another estimate by King (1987), based on a conjecture of Landau and Lifshitz (1960) and on methods that rely on field theory gives

$$K_{\text{eff}}^{\text{LL}} = K_{\text{g}}\exp\left(\tilde{\sigma}^2\left\{\frac{1}{2}-\frac{1}{D}\right\}\right) \tag{18}$$

where $\tilde{\sigma}^2$ is the variance in the logarithm of permeability and K_{g} is the geometric mean.

(v) Dagan (1993) proposes an estimate that takes into consideration higher-order terms in the variance and has the form

$$K_{\text{eff}}^{\text{D}} = K_g\left\{1+\left(\frac{1}{2}-\frac{1}{D}\right)\sigma^2+\frac{1}{2}\left(\frac{1}{2}-\frac{1}{D}\right)^2(\sigma^2)^2\right\} \tag{19}$$

(vi) Selvadurai and Selvadurai (2011) have proposed an estimate that is based on the *geometric mean of permeabilities* determined by considering one-dimensional flow along three arbitrarily oriented orthogonal directions. Consider a region V_0, with a permeability distribution $K(\mathbf{x})$, which is lognormal and such that the one-dimensional permeabilities measured along any three orthogonal directions do not display any evidence of marked orthotropy. If the permeabilities in the three orthogonal directions are K_1, K_2 and K_3, the effective permeability can be estimated from the geometric mean. i.e.

$$K_{\text{eff}}^{\text{SS}} = \sqrt[3]{K_1K_2K_3} \tag{20}$$

The data for the spatial distribution of permeability within the cuboidal block of Indiana Limestone and the results (13) to (20) were used to determine the effective permeability of the specimen. The results obtained were as follows (the actual estimate for the permeability can be obtained by multiplying the values by 10^{-15} m^2):

$$\begin{aligned}
&(K_{\text{eff}}^{\text{W}})_{\text{LB}} = 62.16 \quad ; \quad (K_{\text{eff}}^{\text{W}})_{\text{UB}} = 80.10 \\
&K_{\text{eff}}^{\text{M}} = 73.79\,; \quad K_{\text{eff}}^{\text{J}} = 74.08\,; \quad K_{\text{eff}}^{\text{K}} = 74.05 \\
&K_{\text{eff}}^{\text{LL}} = 71.65\,; \quad K_{\text{eff}}^{\text{D}} = 71.08\,; \quad K_{\text{eff}}^{\text{SS}} = 73.75
\end{aligned} \tag{21}$$

The results of the computations indicate that the Wiener bounds are the extreme limits for estimating the permeability of the inhomogeneous domain and all other measures for the effective permeability give relatively similar estimates. In particular the estimate based on the geometric mean provides a satisfactory estimate of the effective permeability of the inhomogeneous porous medium.

5 VALIDATION OF ESTIMATES FOR THE EFFECTIVE PERMEABILITY

The accuracy of the various relationships presented previously for estimating the effective permeability of a heterogeneous porous medium can also be validated by performing computational simulations where the permeability distribution within the region is assumed to be lognormal. We consider a cuboidal region of a porous medium which contains 1000 sub-cubes of equal volume that are hydraulically homogeneous and isotropic (Figure 5). Figure 5 also shows the typical inhomogeneous nature of an argillaceous limestone

encountered in a potential site for a deep geologic repository for storage of low and intermediate level nuclear waste.

The permeabilities of the 1000 sub-domains conform to a lognormal distribution (Figure 6) and satisfy the Kolomogorov-Smirnov criterion applicable to such distributions. Computations were performed using the COMSOL™ Multiphysics Code for the finite element solution of the potential problem. The accuracy of the mesh refinement is established through comparison with known analytical results for hydraulically homogeneous domains. The details of the modelling will be presented elsewhere (Selvadurai and Selvadurai, 2011) and in this section we present the basic results that pertain to the estimation of the effective permeability based on the concept of the *geometric mean*.

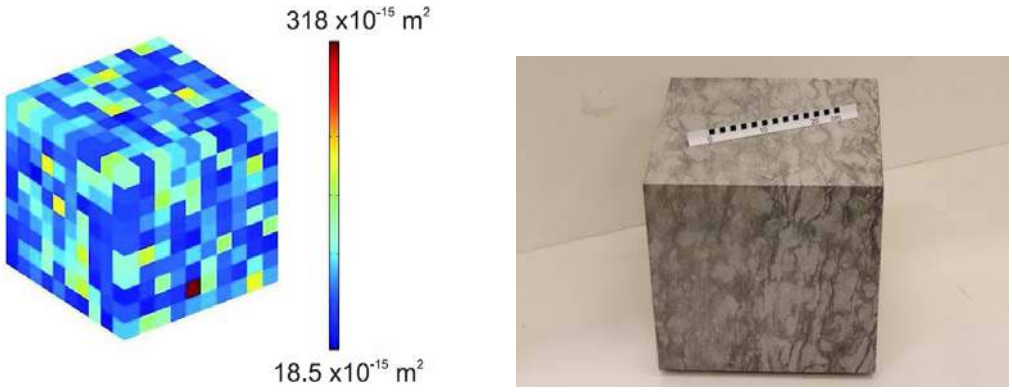

Fig. 5. Heterogeneous permeability distribution in a cuboidal region

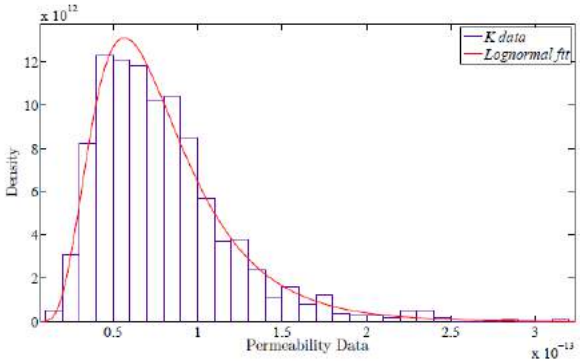

Fig. 6. Lognormal permeability distribution in the 1000 sub-cubes of the cuboidal region

The effective permeability for the inhomogeneous region shown in Figure 5 is computed using the expressions (14) and (20). These yield the following:

$$(K_{\text{eff}}^{\text{W}})_{\text{LB}} = 63.39 \quad ; \quad (K_{\text{eff}}^{\text{W}})_{\text{UB}} = 79.79 \quad ; \quad K_{\text{eff}}^{\text{SS}} = 73.96 \qquad (22)$$

Computations were also performed to determine the effective permeability of a cuboidal region that is situated within the 1000 element cuboidal region. The orientation of this sub-region is arbitrary and schematically indicated in Figure 7. It can be shown that the permeability within the sub-cube region also conforms to a lognormal distribution. The effective permeability for the inhomogeneous sub-cube region shown in Figure 7 is computed using the expressions (14) and (20). These yield the following:

$$(K_{\text{eff}}^{\text{W}})_{\text{LB}} = 63.39 \quad ; \quad (K_{\text{eff}}^{\text{W}})_{\text{UB}} = 79.54 \quad ; \quad K_{\text{eff}}^{\text{SS}} = 73.98 \tag{22}$$

Figure 7. Sub-cuboidal region with permeability inhomogeneity

6 CONCLUDING REMARKS

The property of permeability is central to many geoenvironmental applications involving groundwater movement. Naturally occurring geologic formations are heterogeneous and this aspect needs to be addressed in the specification of flow characteristics of geologic media. From a practical point of view, the modelling of fluid flow in naturally occurring geologic media can be simplified if a convenient measure of effective permeability can be developed to account for hydraulic heterogeneity. This paper approaches the problem of estimating hydraulic heterogeneity in a porous medium through the combination of experimental techniques, mathematical models and computational procedures. The experimental data is used to estimate the effective permeability of a large cuboidal specimen of Indiana Limestone, employing the theoretical relationships proposed by Wiener, Matheron, Journel, King, Landau and Lifshitz and Dagan. The present research also proposes the use of the geometric mean as a measure of the effective permeability of a heterogeneous porous medium. It is shown that many of the theoretical relationships provide close estimates for the permeability of the heterogeneous medium and that the Wiener bounds for the permeability correspond to the extreme limits.

ACKNOWLEDGEMENT

The work described in this paper was initiated through the research support provided by the *2003 Max Planck Research Prize in the Engineering Sciences* and through an *NSERC Discovery Grant* awarded to the second author.

REFERENCES

Bear, J. (1972), Dynamics of Fluids in Porous Media, Dover Publications, NY.

Bear, J. & Cheng, A.H.-D. (2009), Modeling Groundwater Flow and Contaminant Transport, Springer-Verlag, Berlin.

Dagan, G. (1993), Higher-order correction of effective permeability of heterogeneous isotropic formations of log normal conductivity distributions. Transp. Porous Media, Vol. 12, 279–290.

Darcy, H. (1856), Les Fontaines Publiques de la Ville de Dijon, Dalmont, Paris.

de Marsily, G. (1986), Quantitative Hydrogeology. Groundwater Hydrology for Engineers, Academic Press Inc., San Diego.

Goggin, D.J., Thrasher, R.I. & Lake, L.W. (1988), “Theoretical and experimental analysis of mini-permeameter response including gas slippage and high velocity flow effects”. In Situ, Vol. 12, 79-116.
Harr, M.E. (1962), Groundwater and Seepage. McGraw-Hill, New York.
Harr, M.E. (1987), Reliability-Based Design in Civil Engineering, McGraw-Hill, New York.
Journel, A. G., C.V. Deutsch, C. V. & Desbrats, A. (1986), “Power averaging for block effective permeability”, Technical Report. Society of Petroleum Engineers.
King, P.R. (1987), “The use of theoretic methods for the study of flow in a heterogeneous medium”, J. Phys A: Math. Gen. Vol. 20, 3935–3947.
King, P.R. (1989), “The use of renormalization for calculating effective permeability”. Transport in Porous Media, Vol.4, 37–58.
Landau, L. D. & Lifshitz, E.M. (1960), Electrodynamics of Continuous Media, Pergamon Press Oxford, UK.
Matheron, G. (1967), Eléments pour une théorie des milieux poreux, Masson, Paris, France.
Philips, O.M. (1991), Flow and Reactions in Permeable Rocks, Cambridge Univ. Press, Cambridge.
Polubarinova-Kochina, P.Y. (1962), Theory of Groundwater Movement (Translated by J.M.R. de Wiest), Princeton University Press, Princeton, New Jersey.
Selvadurai, A.P.S. (2000a), Partial Differential Equations in Mechanics, Vol.1. Fundamentals, Laplace’s Equation, Diffusion Equation, Wave Equation, Springer-Verlag, Berlin.
Selvadurai, A.P.S. (2000b) Partial Differential Equations in Mechanics, Vol.2. Biharmonic Equation, Poisson’s Equation, Springer-Verlag, Berlin.
Selvadurai, A.P.S. (2007), “The analytical method in geomechanics”, Appl. Mech. Rev., Vol. 60, 87-106.
Selvadurai, A.P.S. (2010), “On the hydraulic intake shape factor for a circular opening located at an impervious boundary: Influence of inclined stratification”. Int. J. Num. Analyt. Meth. Geomech., doi: 10.1002/nag.915
Selvadurai, P. A. (2010), Permeability of Indiana limestone: Experiments and theoretical concepts for interpretation of results. M. Eng. Thesis, McGill University, Canada.
Selvadurai, A.P.S. & Selvadurai, P.A. (2010), “Surface permeability tests: Experiments and modelling for estimating effective permeability”, Proc. Roy. Soc., Ser A, Math. Phys. & Engng. Sci., Vol. 466, 2819-2846.
Selvadurai, P.A. & Selvadurai, A.P.S. (2007), “On cavity flow permeability testing of a sandstone”, Groundwater, Vol. 45, 93-97.
Selvadurai, P.A. & Selvadurai, A.P.S. (2011), “Effective permeability: A strategy for representing hydraulic heterogeneity”, (In preparation).
Selvadurai, A.P.S., Boulon, M.J. & Nguyen, T.S. (2005), “The permeability of an intact granite”, Pure Appl. Geophys., Vol.162, 373-407.
Strack, O.D. (1989), Groundwater Mechanics, Prentice-Hall, New Jersey.
Tartakovsky, D.M., Moulton, J.D. & Zlotnik, V.A. (2000), “Kinematic structure of minipermeameter flow”, Water Resources Research, Vol. 36, 2433-2442.
Tidwell, V.C. & Wilson, J.L. (1997), “Laboratory method for investigating permeability upscaling”, Water Resources Research, Vol. 33, 1607-1616.
Verruijt, A. (1982), Theory of Groundwater Flow, Macmillan, London.
Wiener, O. (1912), “Die Theorie des Mischkörpers für das Feld des stationaären Strömung. ErsteAbhandlung die Mittelswertesätsze für Kraft, Polarisation und Energie”. Abh. Math.-Physischen Klasse Königl. Säcsh Gesell. Wissen, Vol. 32, 509–604.
Zijl W. & Nawalany, N. (2000), Natural Groundwater Flow, Lewis Publishers, CRC Press, Boca Raton, Florida.

SIMULATION OF A GAS INJECTION TEST IN A LAYERED ARGILLACEOUS ROCK

T.S. Nguyen, G. Su
Canadian Nuclear Safety Commission, Ottawa, ON, Canada

M. Fall, E. Evgin
University of Ottawa, Ottawa, ON, Canada

ABSTRACT *A laboratory gas injection test in an unsaturated Opalinus Clay sample was performed. The rate of gas flow shows a substantial increase when the injection pressure is higher than the confining stress, and thus indicates that damage has been possibly induced in the rock sample resulting in an important increase in permeability. In order to simulate the experiment, we developed a poro-elastic model, with the consideration of two compressible pore fluids (water and gas). The bulk movement of the pore fluids is assumed to obey the generalized Darcy's law, and their respective degree of saturation is represented by the Van Genuchten's functions. The solid skeleton is assumed to obey Hooke's law, with degradation of the elastic moduli accompanied by an increase in permeability. Argillaceous rocks, such as Opalinus Clay, are characterized by bedding planes that result in anisotropy in its hydraulic and mechanical properties. That anisotropy is taken into account by the use of orthotropic stiffness and permeability tensors in the formulation of Hooke's and Darcy's laws. The model can predict the three distinct flow regimes found in the experiment: a low flow regime where gas movement is restricted to the injection zone, a moderate flow regime when damage is limited, and a high flow regime when damage induces a substantial increase in the permeability.*

1 INTRODUCTION

The understanding of multiphase flow in porous media is important in many industrial and environmental projects, such as the extraction of oil and natural gas, the sequestration of CO_2 in geological formations, and the disposal of radioactive wastes in deep geological repositories (DGR).

A research project has been initiated by the Canadian Nuclear Safety Commission (CNSC) to study the influence of gas generation and migration on the long term safety of DGRs for radioactive wastes. Such facilities rely on multiple barriers to isolate and contain the wastes. Depending on the level of radioactivity of the wastes, those barriers include: corrosion and structurally resistant containers, low permeability seals around the emplacements rooms, galleries and shaft, and finally the host rock formations. Large quantities of gas may be generated from the degradation of the waste forms or the corrosion of the containers. The generated gas pressures, if sufficiently large, can induce cracks and microcracks in the engineered and natural barriers and affect their containment functions. The CNSC in collaboration with the University of Ottawa has developed a mathematical model to simulate the above effects. The model must be calibrated and validated with laboratory and field experiments in order to provide confidence in its future use for assessing the effects of gas on

the long term safety of typical nuclear wastes repositories. The present paper describes the model and its use in the simulation of a laboratory gas injection test in a sample of layered argillaceous rock, known as Opalinus clay, from Mont Terri, Switzerland. Opalinus clay is stiff overconsolidated clay of Middle Jurassic age found in the Jura Mountains. This formation, due to its low permeability, high sorption capacity and lack of valuable natural resources is being considered by Switzerland as a potential host for the disposal of radioactive wastes. Numerous laboratory and field programs have been performed at the Underground Research Laboratory in Mont Terri to characterize the properties of the clay. These properties have been compiled by Gens et al. (2007) among others. Many of these properties reflect the anisotropy due to bedding. For example, the elastic modulus in the bedding direction is of the order of 10 GPa while it is of the order of 4 GPa in the perpendicular direction. On the other hand, the permeability in the bedding direction is about ten times higher than the permeability in the perpendicular direction (Popp et al., 2008).

2 EXPERIMENTAL SETUP

Laboratory gas injection tests were performed at the ifG laboratory in Germany. Opalinus clay samples were emplaced in a triaxial pressure device (Popp et al., 2008) shown in Fig. 1. Each sample was subjected to a confining pressure and also possibly to an axial load before gas was injected through it.

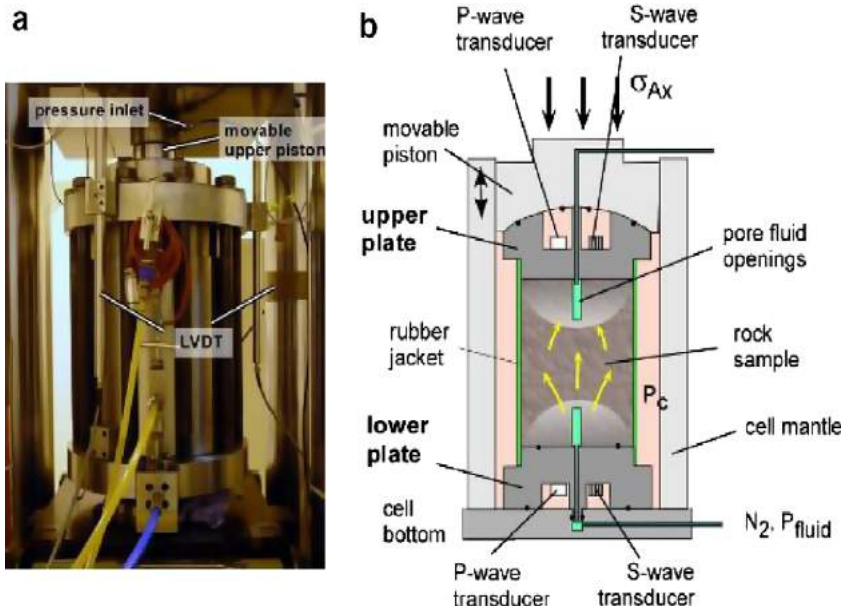

Fig. 1 Experimental setup for gas injection test in Opalinus Clay
(From Popp et al.2008)

For the test considered in this paper, the sample had a diameter of 73.6 mm and a length of 150.5 mm and was partially saturated, with an initial degree of saturation of approximately 90%. It was subjected to a confining pressure of 3 MPa, before nitrogen was injected at controlled pressure (Fig. 2) in a central borehole located at the bottom of the sample. The gas outflow rate from a similar borehole at the top of the sample was continuously monitored.

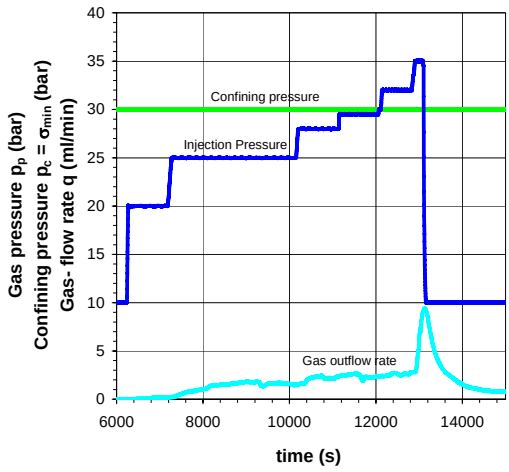

Fig. 2 Experimental results for gas injection test in Opalinus clay at controlled injection pressures

3 MATHEMATICAL MODEL

Conceptually, the clay medium consists of solid particles and pores filled with a mixture of water and gas. As gas is injected into the pores, a net increase in the average pore pressure occurs, resulting in a rearrangement of the solid skeleton. When that pressure is sufficiently high, the bonds that exist between the solid particles could break, leading to an increase in the pore space for gas and water flow. Macroscopically, a substantial increase in permeability could occur with a corresponding increase in gas flow, as shown in Fig.2.

A mathematical model was developed based on the above conceptualization. The governing equations of the model were derived from the consideration of mass balance of the water, the gas and the solid; and momentum balance of the bulk medium. In addition, the following main assumptions were adopted:

i) Flow of gas and water are advective. We neglect the diffusive flow components of gas and water vapour. The generalized Darcy's law is thus adopted:

$$V_{iw} - V_{is} = -\frac{k_{ij}k_{rw}}{n\mu_w}\left(\frac{\partial p_w}{\partial x_j} + \rho_w g_j\right) \tag{1.a}$$

$$V_{ig} - V_{is} = -\frac{k_{ij}k_{rg}}{n\mu_g}\left(\frac{\partial p_g}{\partial x_j} + \rho_g g_j\right) \tag{1.b}$$

In equation (1), the subscript *s*, *w*, *g* stand for solid, water and gas, respectively; V_{is}, V_{iw}, V_{ig} are the velocities of the different phases; p_w, p_g are the pressures of the corresponding phase; k_{ij} is the intrinsic permeability of the porous medium; n is the porosity; k_{rg} and k_{rw} are the relative permeability for the corresponding phases; ρ_g and ρ_w are the densities; μ_g and μ_w are the viscosities, and g_j is the acceleration of gravity.

ii) Bishop's principle of effective stress applies:

$$\sigma_{ij} = \sigma'_{ij} + \alpha\bar{p}\delta_{ij} \tag{2}$$

In equation (2) σ'_{ij} is the effective stress tensor, δ_{ij} is the Kronecker delta; α is Biot's coefficient and the average pore fluid pressure is given by:

$$\bar{p} = (Sp_w + (1-S)\,p_g) \tag{3}$$

where S is the degree of water saturation.

iii) Hooke's law of elasticity for an anisotropic material applies. In tensorial notation, the effective stress tensor is related to the strain tensor as follows:

$$\sigma_{ij}^{'} = C_{ijkl}\varepsilon_{kl} \tag{4}$$

where ε_{kl} is the strain tensor and C_{ijkl} is the stiffness tensor. When written in matrix notation, for an elastic layered material, equation (4) becomes:

$$\begin{pmatrix} \sigma_{xx}^{'} \\ \sigma_{yy}^{'} \\ \sigma_{zz}^{'} \\ \sigma_{xy} \\ \sigma_{yz} \\ \sigma_{xz} \end{pmatrix} = [D] \begin{pmatrix} \varepsilon_{xx} \\ \varepsilon_{yy} \\ \varepsilon_{zz} \\ \varepsilon_{xy} \\ \varepsilon_{yz} \\ \varepsilon_{xz} \end{pmatrix} .....and.....[D]^{-1} = \begin{bmatrix} 1/E_x & -\nu_{yx}/E_y & -\nu_{zx}/E_z & 0 & 0 & 0 \\ & 1/E_y & -\nu_{zy}/E_z & 0 & 0 & 0 \\ & & 1/E_z & 0 & 0 & 0 \\ & & & 1/G_{xy} & 0 & 0 \\ & & & & 1/G_{yz} & 0 \\ & & & & & 1/G_{xz} \end{bmatrix} \tag{5}$$

The matrix [D] is symmetric. If the bedding planes are parallel to x-y, then: $E_x=E_y= E_b$ is the Young's moduli in the direction of the bedding; $E_z=E_p$ is the Young's modulus in the perpendicular direction to bedding; ν_{yx}, $\nu_{zx}=\nu_{zy}$ are the Poisson's ratios; and G_{xy}, $G_{yz}=G_{xz}$ are the shear moduli.

iv) Breaking of the bonds between the solid particles results in a degradation of the Young's moduli and an increase in the intrinsic permeability. Similarly to Shirazi and Selvadurai (2004), we assume that a measure of that damage is the equivalent deviatoric strain:

$$\varepsilon_d = \frac{\sqrt{2}}{3}\sqrt{(\varepsilon_{xx}-\varepsilon_{yy})^2 + (\varepsilon_{yy}-\varepsilon_{zz})^2 + (\varepsilon_{xx}-\varepsilon_{zz})^2 + 6\varepsilon_{xy}^2 + 6\varepsilon_{xz}^2 + 6\varepsilon_{yz}^2} \tag{6}$$

Evolution functions of the Young's moduli and the permeability versus the damage coefficient will be assumed as follows:

$$E_b = E_{b0}/(1-D_b) \tag{7.a}$$

$$E_p = E_{p0}/(1-D_p) \tag{7.b}$$

$$k_b = k_{b0}(1+\beta_b D_d{}^2) \tag{8.a}$$

$$k_p = k_{p0}(1+\beta_p D_p{}^2) \tag{8.b}$$

where E_{b0} and E_{p0} are the initial Young's moduli, k_{b0} and k_{p0} are the initial permeability coefficients, in the parallel and perpendicular directions; β_b and β_p are empirical coefficients; and D_b, D_p are the damage coefficients, which for simplicity are assumed to be equal (isotropic damage) and to follow the following evolution function (similar to Shirazi and Selvadurai, 2004):

$$D = 1 - \exp(\eta\varepsilon_d) \tag{9}$$

where η is an empirical coefficient.

The final governing equations are:

$$\frac{\partial}{\partial x_i}\left[\rho_g k_{ij}\left(\frac{k_{rg}}{\mu_g}\left(\frac{\partial p_g}{\partial x_j} + \rho_g g_j\right) + H\frac{k_{rw}}{\mu_w}\left(\frac{\partial p_W}{\partial x_j} + \rho_W g_j\right)\right)\right] = \rho_g[n(H-1)(\frac{dS}{dp_c})\frac{\partial p_c}{\partial t} + \frac{n(1-S+HS)}{K_g}\frac{\partial p_g}{\partial t} - (1-S+HS)(\frac{n+\alpha}{K_s})\frac{\partial \bar{p}}{\partial t} + \alpha(1-S+HS)\frac{\partial^2 u_k}{\partial t \partial x_k}] \tag{10}$$

$$\frac{\partial}{\partial x_i}\left[\rho_w k_{ij}\frac{k_{rw}}{\mu_w}\left(\frac{\partial p_w}{\partial x_j}+\rho_w g_j\right)\right]=\rho_w\left[n(\frac{dS}{dp_c})\frac{\partial p_c}{\partial t}+\frac{nS}{K_w}\frac{\partial p_w}{\partial t}-S(\frac{n+\alpha}{K_s})\frac{\partial \overline{p}}{\partial t}+\alpha S\frac{\partial^2 u_k}{\partial t\partial x_k}\right] \quad (11)$$

$$\frac{1}{2}C_{ijkl}\left(\frac{\partial^2 u_k}{\partial x_j\partial x_k}+\frac{\partial^2 u_l}{\partial x_i\partial x_l}\right)+\alpha\frac{\partial \overline{p}}{\partial x_i}=0 \quad (12)$$

Equation (10) expresses conservation of gas mass; equation (11), conservation of water mass; and (12) conservation of momentum. The primary unknowns are: displacement u_i, gas pressure p_g and water pressure p_w. H is Henry's coefficient of dissolution for gas in water; K_w, K_s, and K_g are the bulk moduli of the water, the solid material and the gas, respectively.

4 NUMERICAL SIMULATION OF THE GAS INJECTION TEST

The governing equations of the above mathematical model, along with applicable initial and boundary conditions were numerically solved using the finite element method to simulate the laboratory injection test.

5.1 Finite element model and boundary conditions

The finite element mesh with the boundary conditions is shown in Fig.3. Due to radial symmetry, only half of a cross-section through the sample was represented. All boundaries of the model were assumed to be impermeable to porewater. A constant confining pressure of 3 MPa was applied on the top and right boundaries. An injection gas pressure was prescribed at the lower borehole, as shown in Figure 2, while the upper borehole was maintained at atmospheric pressure (0.1 MPa).

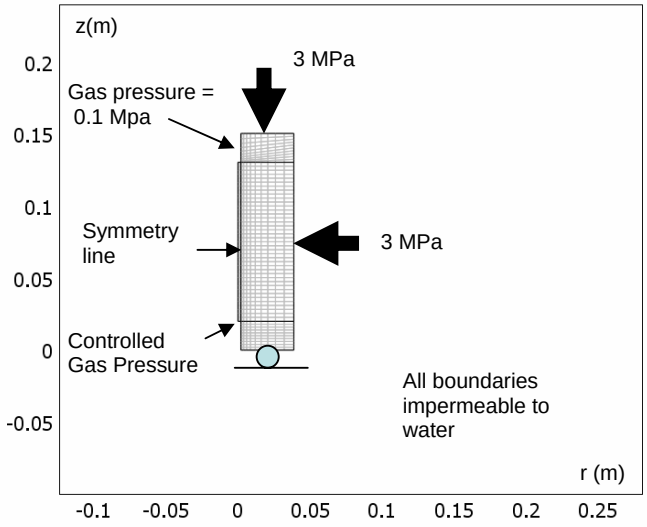

Fig.3 Finite element model of gas injection test

5.2 Input properties

The following input properties were derived from published data from Popp et al. (2009) and Gens et al. (2008).

Initial intrinsic permeability: $k_{b0}=2 \times 10^{-17}$ m$^2=10 \times k_{p0}$

Coefficients of equation 8: $\beta_b=\beta_p=200000$

Initial Young's moduli: E_{b0}=10GPa; E_{p0}=4GPa

Coefficient of equation (9): η=250

The water retention curves of the Opalinus clay were represented with the Van Genuchten's models:

$$S = \frac{1}{\left[1+\left|aH_c\right|^n\right]^m} ...if ..H_c > 0 \qquad (13)$$

$$S = 1 ...if ...H_c \le 0$$

$$k_{rw} = S^L\left[1-\left(1-S^{1/m}\right)^m\right]^2 ...if ...H_c > 0 \qquad (14)$$

$$k_{rw} = 1 ....if ...H_c \le 0$$

$$k_{rg} = \left(1-S\right)^L\left(1-S^{1/m}\right)^{2m} \qquad (15)$$

where H_c is the suction head given by:

$$H_c = \frac{p_g - p_w}{\rho_w g} \qquad (16)$$

The initial porosity of the sample was 16% and its initial degree of saturation was 87.8%. The following parameters were used in the Van Genuchten relations:

L=0.5; m=$(n$-1$)/n$=0.5; 1/a= 2.5 MPa.

1/a is known as the apparent air entry pressure. Other input parameters are related to the physical properties of gas and water, such as density and compressibility, and Henry's coefficient of dissolution *H*. We neglected *H* and the compressibility of the water and the solid phases. The compressibility and density of gas were derived from the ideal gas law, under assumed adiabatic conditions:

$$K_g = 1.4 p_g$$

$$\rho_g = 1.28 p_g / p_{atm} \qquad (17)$$

where p_{atm} is the atmospheric pressure.

5.3 Simulation results

The calculated gas outflow is compared to the measured outflow in Fig.4.

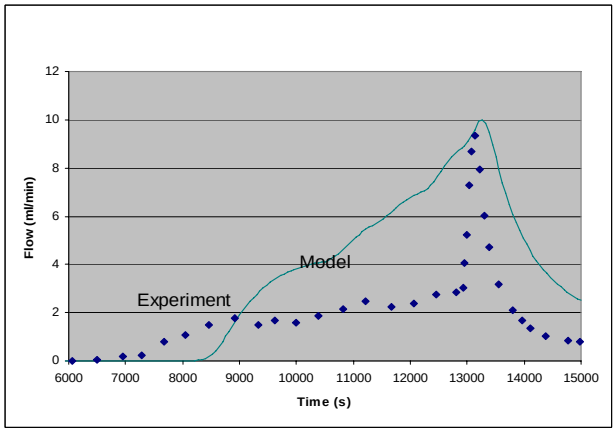

Fig.4 Predicted versus measured gas outflow rate

Four distinct flow regimes could be seen.

i. In the first flow regime, gas flow is limited by the gas entry pressure and the compressibility of the gas. No gas outflow is detected during that regime. The model correctly predicts the above threshold for outflow, although it over predicts the time for that threshold (8000 s versus 7000s). The calculated gas flow pattern and redistribution of water saturation are shown in Fig.5, at a typical time during that first flow regime. The gas flow velocities, shown in Fig.5, indicate that flow takes place in the immediate vicinity of the injection borehole, and no gas has reached the outlet. Due to the anisotropy of the permeability, gas flow occurs in a direction sub-parallel to the bedding planes around the injection borehole. The gas pushes the porewater in an outward radial direction, resulting in a decrease in the degree of saturation in the immediate vicinity of the injection borehole. The deformed shape of the model shows that, due to the anisotropy of the stiffness tensor, displacement occurs mainly in the vertical direction, perpendicular to the bedding planes.

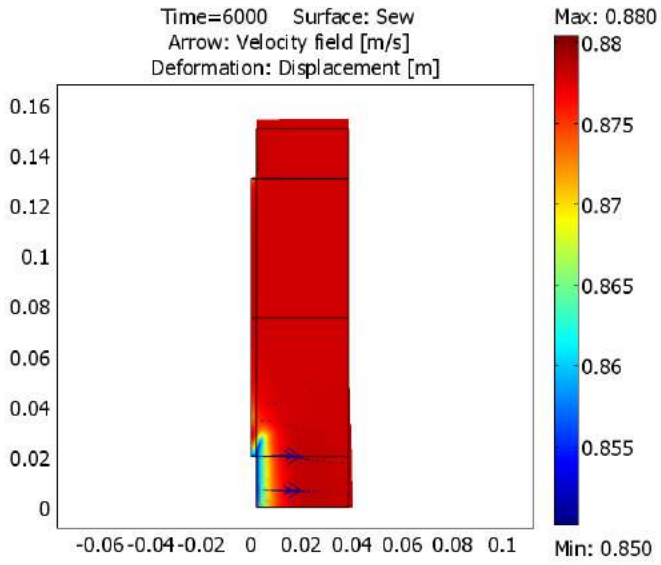

Fig. 5 Gas flow pattern and porewater saturation distribution at 6000s.
(The arrows represent the gas velocity vectors; the colour shading represents the water saturation. The deformed shape of the sample is also shown.)

ii. The second regime prevails when the injection pressure is lower than the confining pressure, and is governed by two-phase flow behaviour. Limited increase in permeability due to mechanical effects would be found during this regime. The model correctly predicts the occurrence of that regime (up to 12500s), although it overpredicts the mechanical and damage effects that result an increase in the permeability (cf. eqs. 7, 8 and 9), and consequently an overprediction of the flow rate. Fig.6 shows the gas flow pattern and water saturation at a typical time in this second flow regime. It could be seen that outflow is predicted to occur; the pore water is redistributed in such a way that

drying occurs near the injection borehole, and wetting (increase in saturation) occurs near the outlet.

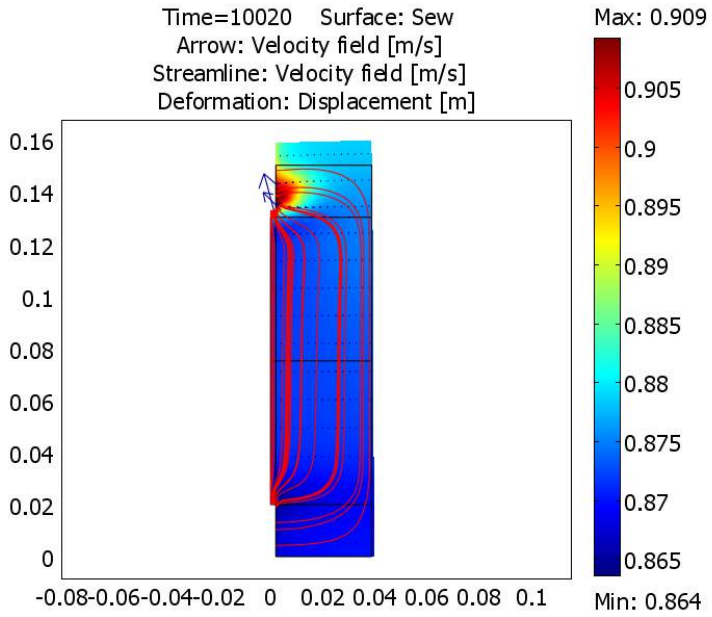

Fig. 6 Gas flow pattern at 10020 s.
(The arrows represent the gas velocity field; the gas streamlines are also shown. The colour shading represents the water saturation.)

iii. The third regime is characterized by a substantial increase in permeability due to damage, and a corresponding sharp increase in the flow rate. The model predicts that effect, however the predicted transition from the two-phase flow regime to dilation flow is not as abrupt as indicated by the experimental data. In order to better calibrate the experimental data, one would need to use a function of permeability (equation 8) with a sharper rate of increase; however this creates convergence problems with the numerical solution. The gas flow pattern and the saturation distribution (Fig. 7) are similar to the previous flow regime; however a significant increase in the gas outflow rate is predicted. This is caused by the permeability increase due to damage. Fig.8 shows that the permeability is predicted to increase by many orders of magnitude at the injection and outlet boreholes, where the most damage is predicted. Throughout the rest of the sample, permeability is predicted to increase by one order of magnitude.

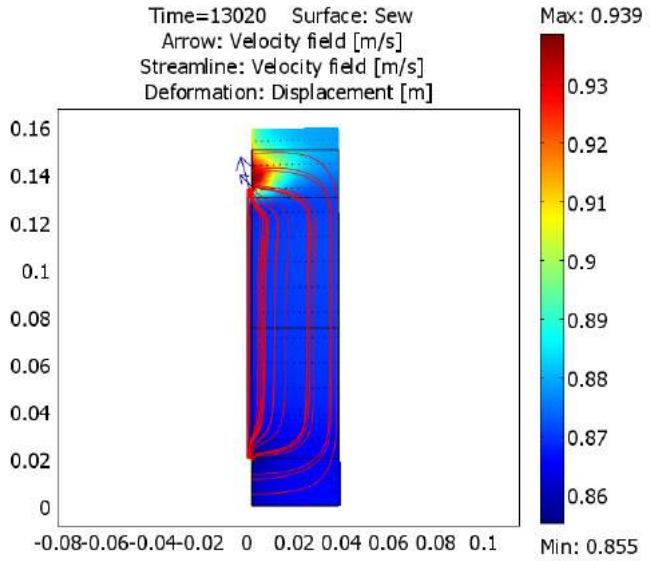

Fig.7 Gas flow pattern and saturation distribution at 13020 s

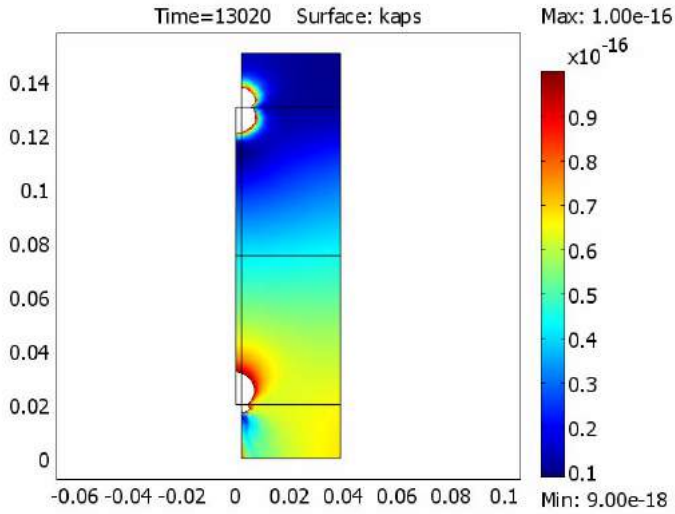

Fig.8 Permeability distribution at 13020 s.
(Around the injection and outlet boreholes, damage results in an increase in permeability by many orders of magnitude (shaded in white). Throughout the rest of the sample, the increase is lower than a factor of ten.)

iv. The fourth flow regime prevails after the sudden decrease of the injection pressure that triggers a more gradual decrease in the outflow. Figure 9 shows that due to high zones of gas pressure that subsist in the middle of the sample, some backflow towards the injection borehole could occur.

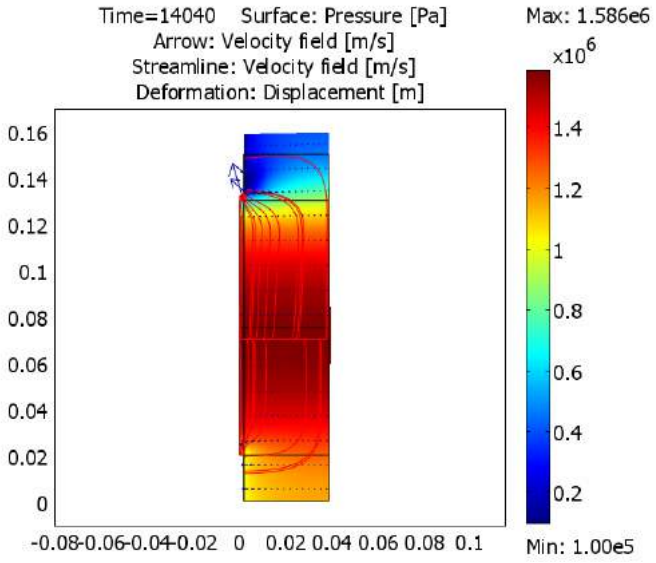

Fig. 9 Gas flow pattern at 14040 s
(The colour shading represents the gas pressure. Around the middle of the sample, zones of high gas pressure subsist after the end of injection, and trigger backflow towards the injection borehole.)

5 CONCLUSIONS

In the gas injection experiment considered in this paper, it is seen that the simultaneous flow of gas and water in porous media follows three distinct regimes, depending on the gas pressure. The above observation is consistent with the conceptual model proposed by Marshall et al. (2005). At low pressures, gas flow is limited by the air entry pressure and the compressibility of the gas. At intermediate pressures, gas and water simultaneously move through the pore space, with limited dilation of the flow paths. At high pressures, mechanical effects can lead to damage and increase in permeability, resulting in substantially higher flow rates. The mathematical model presented in this paper takes into account the anisotropy of the sample, and damage due to poro-mechanical effects. The model can correctly simulate the above flow regimes. However, the predicted transition between the second and third flow regimes is not as sharp as observed in the experiment. Further work is underway to develop damage relationships that can better capture that transition. Additionally, pure damage behaviour is applicable to brittle materials. Opalinus clay, on the other hand, is a semi-brittle material, and we will need to develop a coupled damage-plasticity model to better represent its mechanical behaviour. The model will also be used to simulate an in-situ gas injection test performed at the Mont Terri underground research laboratory.

ACKNOWLEDGEMENT

The CNSC is gratefully acknowledged for its financial support. The views expressed in this paper are the authors' and do not necessarily reflect the views and opinions of the CNSC. Dr. Shao Hua and Dr. Till Popp, respectively from the BGR and the ifG, Germany, are also specially thanked for providing the experimental data.

REFERENCES

Gens, A., Vaunat, J., Garitte, B. and Wileveau, Y. (2007). In situ behaviour of a stiff layered clay subject to thermal loading: observations and interpretation. Geotechnique, Vol. 57(2), 207-228.

Marschall, P., Horseman, S. and Gimmi, T. (2005). "Characterization of gas transport properties of the Opalinus Clay, a potentialhost rock formation for radioactive waste disposal". Oil and Gas Science, Vol. 60 (1), 1211-139.

Popp, T., Salzer, K. and Minkley, W. (2008). "Influence of bedding planes to EDZ-evolution and the coupled HM properties of Opalinus Clay". Physics and Chemistry of the Earth, Vol. 33, 374-387.

Selvadurai, A.P.S. and Shirazi, A. (2004). "Poroelastic damage resulting from an in-plane loaded disc anchor", Proceedings of the 9th symposium on numerical models in geomechanics – NUMOG IX, Ottawa, Canada.

MODELLING OF BIOGROUT PROPAGATION IN SOILS

S. Fauriel
L. Laloui
Laboratory of Soil Mechanics, Swiss Federal Institute of Technology EPFL, Lausanne, Switzerland

ABSTRACT: *Bacterial strains producing urease can have a major impact on the natural calcite precipitation process if they are supplied with nutrients and urea. In Microbial Induced Calcite Precipitation (MICP) process, the precipitated calcite acts as a cementing agent in the soil, offering an alternative sustainable and cost-effective grouting technique. The miscible and reactive biogrout injection in saturated, deformable soils need however to be better understood and described to more effectively design the grouting technique. A research work is therefore carried out on this topic. The field equations for biogrout transport are established based on the understanding of the complex involved processes. The related constitutive equations for stress-strain relationship and fluid flow are considered. The resulting set of field equations is discretized and implemented into an advanced finite element code. Finite element modelling of column injection tests is carried out to validate the mathematical formulation and to demonstrate the potentiality of the developed model.*

1 INTRODUCTION

Following the global increase of infrastructure needs, innovative construction techniques are sought and alternative soil improvement methods are developed. Usually, chemical and cement based grouting products are indeed used for soil improvement; however, they lead to permanent soil pollution or emission of carbon dioxide. More environmentally friendly grouting products such as biogrouting are therefore in demand.

In the frame of sustainable development, biogrouting is a revolutionary technique based on the injection of a biological solution in soil. There is in such a context, a need to develop a comprehensible and highly coupled bio-hydro-mechanical mathematical model able to realistically predict the behaviour of biogrouted saturated soils. The presented work contributes to this topic.

2 MICROBIALLY INDUCED CALCITE PRECIPITATION

In natural environments, the primary means by which microorganisms promote calcium carbonate precipitation is by metabolic processes that increase alkalinity. The crystals formed by bacterially promoted precipitation cement the soil matrix, increasing the mechanical strength of the material.

In MICP, bacteria use urea $(NH_2)_2CO$ as an energy source and produce ammonia NH_4^+, which increases pH in the proximal environment, and carbonate ions CO_3^{2-} (reaction 1a).

This hydrolysis is promoted by the enzyme urease which is widespread among bacteria. The released carbonate ions CO_3^{2-} react with calcium ion Ca^{2+}, which should also be present. Calcium $CaCO_3$ carbonate hence precipitates (reaction 1b):

$$\left(NH_2\right)_2 CO + 2H_2O \xrightarrow{urease} CO_3^{2-} + 2NH_4^+ \quad (1a)$$

$$Ca^{2+} + CO_3^{2-} \rightarrow CaCO_{3(s)} \quad (1b)$$

Sporosarcina pasteurii are producers of a great number of extracellular enzymes. They exhibit a high area/volume proportion and they have the capacity to generate biofilms. Also, they have a high potential for nucleation and growth of calcite crystals, making them an excellent candidate for MICP.

3 MODELLING A TRANSPORT PROCESS IN SOILS

3.1 Transport models

In the context of advanced grouting fluid transport analysis, among the most relevant works from the last decade are those presented by Bouchelaghem et al. (2001), Saada et al. (2005) and Chupin et al. (2009). Their mathematical formulations account for the following phenomena: transport (advection, diffusion and dispersion), miscibility, filtration and hydro-mechanical coupling.

From another side, when considering the transport of a living organism, the phenomena to be considered are also governed by a number of strictly biological processes affecting their transport (Sen et al., 2005). Bacteria enriched fluid transport models such as Li et al. (1996), Sen et al. (2005) and Tufenkji (2007) therefore additionally consider factors and mechanisms which influence microbial transport and removal in saturated porous media, such as: bacterial transport (random motility and chemotaxis) and growth/decay, but they usually lack the miscibility and the effect of the fluid flow and the porosity variation characterizing advanced grouting fluid transport models.

Advanced pollutant transport models such as the one developed by Biver (1993) consider many of the above listed processes: transport, filtration, miscibility and growth/decay. This literature constitutes the starting point of the analysis presented in this paper in which also the processes accounting for the effect of bacterial communities on the elastic strains are taken into account (Figure 1).

3.2 Phases and species

The concept of continuous porous media used herein is based on the notion of a Representative Elementary Volume (REV) that allows establishing balance equations at the macroscale. Assuming that the porous medium is saturated, it is composed of two phases:

- the solid phase *s* consisting of the solid matrix; and
- the fluid phase *f* corresponding to the pore fluid.

As the biogrout is injected into the medium, the composition of the phases is altered. Bacteria can indeed attach to the solid or stay suspended in the fluid and, as a result, be considered as two distinguished species. We define herein also two other species, leading to the four following species:

- the attached bacteria *sb* belong to the solid phase;
- the suspended bacteria *fb* to the fluid phase;
- the solid grains *sg* belong to the solid phase; and

- the pore water *fw* belongs to the fluid phase.

The injected solution is supposed to be a part of the pore fluid. Both attached and suspended bacteria can be referred to as biomass and belong to a same component (bacteria).

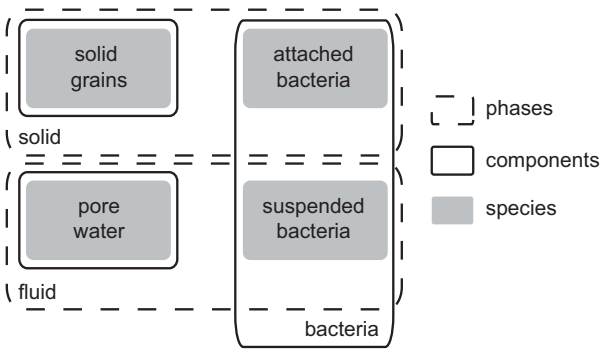

Fig 1. Phases, components and species

4 THEORETHICAL FRAMEWORK

4.1 Assumptions

A series of assumptions are made in the development of the balance equations:

- the porous media is saturated by one fluid phase;
- the dispersive and diffusive fluxes are neglected for the phases as spatial variations in the phases density are small (the fraction of bacteria within the fluid and solid phases is assumed to be small in comparison to the homogeneously distributed pore water and solid grains);
- the dispersive and diffusive fluxes are neglected for the attached bacteria; iv. no internal production of solid grains or pore water occurs;
- a linear equilibrium isotherm is assumed between the concentration of attached and suspended bacteria;
- growth and decay rates are considered equal in both solid and fluid phases; and
- random mobility and chemotaxis are neglected for both attached and suspended bacteria.

4.2 Bio-hydro-mechanical mechanisms

Biogrout transport in porous media is concerned with a number of bio-hydro-mechanical mechanisms involving numerous couplings as illustrated in Figure 2.

The mechanisms considered in the theoretical formulation of the present model are the following:

- the advective, the dispersive and the diffusive transport of bacteria in the porous media; a hydro-biological coupling needs to be considered as the fluid flow affects the transport of bacteria;
- the biogrout is considered perfectly miscible in the pore-water;
- the hydro-mechanical interactions are important as a coupling exists between pressure and concentration fields;
- the attachment and the detachment of bacteria to the solid grains contribute to modify the thickness of the biofilm, and hence the microscopic geometry of the pore space (bio-hydraulic interaction); porosity and permeability are therefore affected by biofilm

increase or decrease (Taylor and Jaffé, 1990); also, as the biofilm is modified, a slight deformation of the media is expected (bio-mechanical interaction); and

- the growth and the decay of bacteria are functions of time and availability of nutriments; as growth or decay occur, the biofilm thickness changes, affecting the porosity and the permeability of the porous media; these processes can also cause a deformation of the media, contributing to the bio-hydraulic and bio-mechanical interactions.

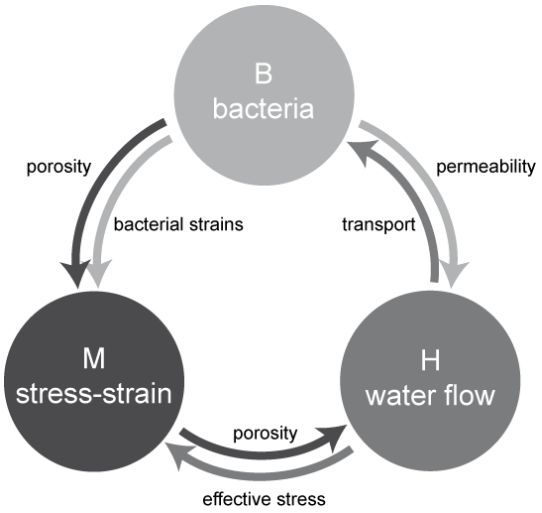

Fig 2. Considered interactions in the bio-hydro-mechanical model

4.3 Compositional approach

The velocity distribution within the fluid phase is needed as input information for the bacteria component transport problem. Also, interactions between the hydraulic flows and the mechanical behaviour of the solid matrix are taken into account. Therefore, the mass balance of the fluid and solid phases carrying the bacteria and the momentum balance of the mixture need to be solved along with the mass balance of the bacteria. The balance equations needed in the development of the model are consequently the following:

- *solid phase and fluid phase mass balances* to evaluate the velocity distribution through a flow equation;
- *total momentum balance* to evaluate the hydro-mechanical coupling; and
- *bacteria mass balance* to derive a transport equation.

Mass balance of each species composing the porous media is first expressed, adopting the compositional approach (Panday & Corapcioglu, 1989). From these, all needed equations are derived.

In addition to the balance equations, constitutive equations are needed to complete the description of the material behaviour.

5 BIO-HYDRO-MECHANICAL MODEL

5.1 Balance equations

Mass balance equations are derived respectively for solid and fluid phases considering the assumptions listed in paragraph 4.1:

$$\frac{\partial}{\partial t}\left((1-n)\rho^s\right) = -\nabla\cdot\left((1-n)\left(\rho^s \boldsymbol{V}^s\right)\right) + k_{att}(nC) - k_{det}\left(\rho^b S\right) + k_g\left(\rho^b S\right) - k_d\left(\rho^b S\right) \quad (2)$$

$$\frac{\partial}{\partial t}\left(n\rho^f\right) = -\nabla\cdot\left(n\left(\rho^f \boldsymbol{V}^f\right)\right) - k_{att}(nC) + k_{det}\left(\rho^b S\right) + k_g(nC) - k_d(nC) \quad (3)$$

Momentum balance is established for the mixture:

$$\nabla\cdot\boldsymbol{\sigma} + \rho\boldsymbol{F} = 0 \quad (4)$$

Mass balance is finally established for the transported component bacteria, combining mass balance of attached and of suspended bacteria:

$$\frac{\partial}{\partial t}\left(\rho^b S + nC\right) = -\nabla\cdot\left(\left(\rho^b S + nC\right)\boldsymbol{V}^s\right) - \nabla\cdot\left(n\left(C\boldsymbol{V}^r - \boldsymbol{D}\nabla C\right)\right) + \left(k_g - k_d\right)\left(\rho^b S + nC\right) \quad (5)$$

with n the porosity; ρ^s the solid phase density; $\boldsymbol{V}^s$ the macroscopic velocity of the solid phase; C the suspended bacteria concentration; S the attached bacteria density; ρ^b the dry bulk density of the porous media; k_{att}, k_{det} respectively the attachment and detachment rates of bacteria; k_d, k_g respectively the growth and decay rates of bacteria; ρ^f the fluid phase density; $\boldsymbol{V}^f$ the macroscopic velocity of the fluid phase; $\boldsymbol{\sigma}$ the volume averaged stress; $\rho\boldsymbol{F}$ the total body force per unit volume of porous medium at a macroscopic point; $\boldsymbol{V}^r$ the macroscopic relative velocity of the liquid phase with respect to the solid phase; and D the hydrodynamic dispersion tensor.

5.2 Constitutive Equations

In the solid skeleton constitutive model, a biologically induced deformation is introduced in addition to the mechanical one. This biological deformation is linked to the amount of attached bacteria on the grain surface through a biological expansion coefficient, similarly to the way thermal deformation is conventionally conceptualized:

$$\boldsymbol{\sigma}' = \boldsymbol{D}^e : \boldsymbol{\varepsilon}^e = \boldsymbol{D}^e : \left(\boldsymbol{\varepsilon}^e_{mec} + \boldsymbol{\varepsilon}^e_{bio}\right) = \boldsymbol{D}^e : \left(\boldsymbol{\varepsilon}^e_{mec} - \alpha_{bio}\Delta S\boldsymbol{I}\right) \quad (6)$$

The soil is expected to expand upon arrival and growth of bacteria and the biological expansion coefficient α_{bio} is defined as positive. Therfore, a minus sign is necessary on the right hand side of equation (6) as compressive strains are considered as positive in this formulation.

The relative fluid-solid velocity is governed by Darcy's law:

$$n\boldsymbol{V}^r = n\left(\boldsymbol{V}^f - \boldsymbol{V}^s\right) = -K\left(\nabla p^f + \rho^f \boldsymbol{g}\right) \quad (7)$$

with $\boldsymbol{D}^e$ the elastic tensor; $\boldsymbol{\varepsilon}^e$ the solid elastic strain with a mechanical part $\boldsymbol{\varepsilon}^e_{mec}$ and a biological part $\boldsymbol{\varepsilon}^e_{bio}$; α_{bio} the biological expansion coefficient of the solid grains due to the attachment of bacteria; K the permeability defined as $K = k/\mu$ with k the intrinsic permeability and μ the dynamic viscosity.

Following the assumptions, linear equilibrium attachment/detachment is assumed in the developments. We consider that the kinetic attachment/detachment processes are active during a very short duration of time only and that apparent equilibrium or steady-state is reached quasi instantaneously. Such processes are indeed very fast compared to flow and deformation processes. A linear relation is hence assumed at all times between the concentration of attached bacteria S and the concentration of suspended bacteria C.

Finally, an equilibrium relation between S and C can be derived from mass balance:

$$S = \frac{n}{\rho^b}\frac{k_{att}}{k_{det}}C = K_d C \tag{8}$$

with $K_d = (n/\rho^b)*(k_{att}/k_{det})$ the partition coefficient.

5.3 Field Equations

The field equations are obtained by combining the mass balance equations and introducing the related constitutive equations.

Upon combining mass balance equations for solid and fluid phases and introducing Darcy's law, the following flow equation is obtained:

$$\nabla\cdot\boldsymbol{V}^s - \nabla\cdot\left(K\left(\nabla p^f + \rho^f \boldsymbol{g}\right)\right) + n\beta_f \frac{\partial p^f}{\partial t} = \left(k_g - k_d\right)\left(\frac{1}{\rho^f}n + \frac{1}{\rho^s}\rho^b K_d\right)C \tag{9}$$

with β_{fw} the fluid compressibility defined by $\partial_t \rho^{fw}/\rho^{fw} = \beta_{fw}\,\partial_t p^f$.

Considering Terzaghi's effective stress, the following equation accounting for the hydro-mechanical coupling is derived from momentum balance of the mixture:

$$\nabla\left(\boldsymbol{D}^e : \left(\boldsymbol{\varepsilon}^e_{mec} - \alpha_{bio}K_d\Delta C\boldsymbol{I}\right) - p^f\boldsymbol{I}\right) + \rho\boldsymbol{g} = 0 \tag{10}$$

The sign convention is the usual convention of soil mechanics in which compressions are positive.

Mass balance of bacteria is developed considering Darcy's law. This yields the following transport equation:

$$\begin{aligned}&\frac{\partial}{\partial t}\left(\left(\frac{\rho^b}{n}K_d + 1\right)C\right) = -\nabla\cdot\left(\left(\frac{\rho^b}{n}K_d + 1\right)C\boldsymbol{V}^s\right) - \nabla\cdot\left(-C\frac{K}{n}\left(\nabla p^f + \rho^f\boldsymbol{g}\right)\right)\\ &+\nabla\cdot\left(\boldsymbol{D}\nabla C\right) + \left(k_g - k_d\right)\left(\frac{\rho^b}{n}K_d + 1\right)C\end{aligned} \tag{11}$$

5.4 Final system

The final system is composed of the three previous equations that allow determining the three main unknowns (solid displacement $\boldsymbol{u}^s$, pore water pressure p^f and bacteria concentration in the fluid phase C):

$$\begin{cases}\nabla\cdot\dfrac{\partial\boldsymbol{u}^s}{\partial t} - \nabla\cdot\left(K\left(\nabla p^f + \rho^f\boldsymbol{g}\right)\right) + n\beta_f\dfrac{\partial p^f}{\partial t} - \left(k_g - k_d\right)\left(\dfrac{1}{\rho^f}n + \dfrac{1}{\rho^s}\rho^b K_d\right)C = 0\\ \nabla\left(\boldsymbol{D}^e : \left(\dfrac{1}{2}\left(\nabla\boldsymbol{u}^s + \nabla\boldsymbol{u}^{sT}\right) - \alpha_{bio}K_d\boldsymbol{I}\Delta C\right) - p^f\boldsymbol{I}\right) + \rho\boldsymbol{g} = 0\\ \dfrac{\partial}{\partial t}\left(R_d C\right) + A_d C + \nabla\cdot\left(R_d C\dfrac{\partial\boldsymbol{u}^s}{\partial t}\right) - \nabla\cdot\left(C\dfrac{K}{n}\left(\nabla p^f + \rho^f\boldsymbol{g}\right)\right) + \nabla\cdot\left(-\boldsymbol{D}\nabla C\right) = 0\end{cases} \tag{12}$$

with $R_d = (\rho^b K_d/n + 1)$ the retardation factor; and $A_d = (k_d - k_g)R_d$.

These equations are implemented in the finite element code LAGAMINE (Charlier, 1987 and Collin, 2003). For such a coupled problem, a two-step method is applied; the transport problem is solved for each step and the obtained bacteria concentration in the fluid phase values are injected in the flow and equilibrium equations.

6 NUMERICAL SIMULATIONS

To test the validity of the developed biogrout transport model, numerical simulations of column injection tests are carried out. The geometrical model of the column injection test consists of a vertical straight pipe (Figure 3). Results are given for a drained column with free concentration at its top under rapid injection (increase of concentration from 0 to 1 kg/m^3 during 10 s followed by constant injection during 2000 s). The column is considered packed with Jossigny silt (Cui & Delage, 2009 and Nuth, 2009) and all bacterial parameters are based on the literature data.

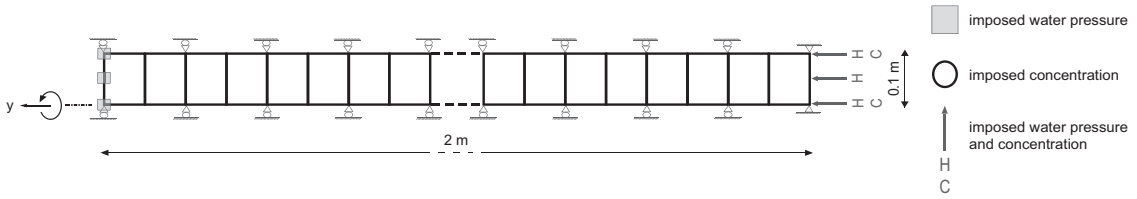

Fig 3. Column used for injection tests

Figure 4a presents the evolution of the front of concentration along the column. The short injection duration results in a fast propagation of the concentration. In the formulation, the propagation of the concentration is a combination of advection, dispersion and diffusion. The variation of the dispersivity and of the diffusivity and the relative correlation between water flow and biogrout transport lead to the conclusion that the transport of biogrout is mainly managed by the advective process.

The evolution of the porosity along the column is presented in Figure 4b (the initial porosity of 0.5 is uniform throughout the column). It can be noticed that the porosity profile is quite symmetrical to the concentration profile (Figure 4a). The main part of the porosity variations can therefore be attributed to bio-affected porosity variations, in addition to those attributed to the flow.

Biological induced stresses are finally presented in Figure 4c. As the lateral dilatation is prevented and a bio-elastic model is considered, an increase in biogrout concentration leads to an increase of lateral compressive stresses. Axial displacements on the other hand are free as the top of the column is not blocked. Therefore, no variations of axial effective stresses are observed due to the injection.

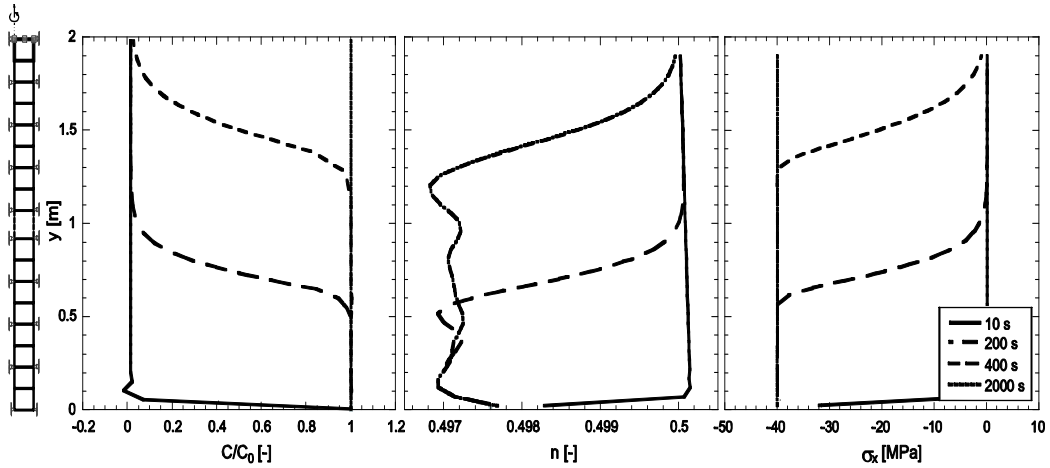

Fig 4. (a) Biogrout concentration profile, (b) porosity profile and (c) biologically induced stresses profile

7 CONCLUSION

A bio-hydro-mechanical model for the case of miscible and reactive biogrout propagation in a saturated and deformable porous media is developed. The framework of these developments is built on the conceptual understanding of the processes involved in biogrout transport and their interactions. Conventional hydro-mechanical coupling is for example supplemented by a bio-mechanical and bio-hydrological couplings as attached bacteria modify the porosity and induce bio-elastic deformations.

The bio-hydro-mechanical model is implemented in a finite element code. Modelling of column injection tests is carried out to demonstrate the potentiality of the developed formulation. The bio-hydro-mechanical model will be further used to design foreseen laboratory tests and also for in-situ injections.

ACKNOWLEDGMENTS

The authors are indebted especially to master student Thibaud Meynet for his work on the model development. The authors are also grateful for the help of Dr. Frederic Collin and his coworkers at the University of Liège regarding the numerical implementation of the model in LAGAMINE.

REFERENCES

Biver, P. (1993). "Modélisation du transport de polluant". PhD thesis, Université de Liège.

Bouchelaghem, F., Vulliet, L., Leroy, D., Laloui, L. & Descoeudres, F. (2001). "Real scale miscible grout injection experiment and performance of Advection-Dispersion-Filtration Model". Intl. J. of Numerical and Analytical Methods in Geomechanics, Vol. 25(12), 1149-1173.

Charlier, R. (1987). "Approche unifiée de quelques problèmes non linéaires de mécanique des milieux continus par la méthode des éléments finis". PhD thesis, Université de Liège.

Chupin, O., Saiyouri, N. & Hicher, P.Y. (2009). "Modeling of a semi-real injection test in sand." Computers and Geotechnics, Vol. 36**(**6**),** 1039-1048.

Clement, T.P., Hooker, B.S. & Skeen, R.S. (1996). "Macroscopic modes for predicting changes in saturated porous media properties caused by microbial growth". Ground Water, Vol. 34(5), 934-942.

Collin, F. (2003). "Couplages thermo-hydro-mécaniques dans les sols et les roches tendres partiellement saturés". PhD thesis, Université de Liège.

Corapcioglu, M.Y. & Haridas, A. (1984). "Transport and fate of microorganisms in porous media: a theoretical investigation". J. of Hydrology, Vol. 72(1-2), 149-169.

Cui, Y. & Delage, P. (2009). "Yielding and plastic behaviour of an unsaturated compacted silt". Géotechnique, Vol. 46(2), 291-311.

Li, B.-L., Loehle, C. & Malon, D. (1996). "Microbial transport through heterogeneous porous media: random walk, fractal and percolation approaches". Ecological Modelling, Vol. 85(2-3), 285-302.

Nuth, M. (2009). "Constitutive modelling of unsaturated soils with hydro-geomechanical couplings". PhD thesis, EPFL.

Panday, S. & Corapcioglu, M.Y. (1989). "Reservoir transport equations by compositional approach". Transport in Porous Media, Vol. 4, 369-393.

Saada, Z., Canou, J., Dormieux, L., Dupla, J.C. & Maghous, S. (2005). "Modelling of cement suspension flow in granular porous media". Intl. J. for Numerical and Analytical Methods in Geomechanics, Vol. 29(7), 691-711.

Sen, T.K., Das, D., Khilar, K. C. & Suraishkumar, G.K. (2005). “Bacterial transport in porous media: New aspects of the mathematical model”. Colloids and Surfaces A: Physicochemical and Engineering Aspects, Vol. 260(1-3), 53-62.

Terzaghi, K. (1936). “The shearing resistance of saturated soils and the angle between the planes of shear”. Proceedings of 1st Intl. Conference on Soil Mechanics and Foundation Engrg., Vol. 1, 54-56.

Tufenkji, N. (2007). “Modeling microbial transport in porous media: Traditional approaches and recent development”. Advances in Water Resources, Vol. 30(6-7), 1455-1469.

ANALYSIS OF THE EXCAVATION OF A DEEP DRIFT IN A TERTIARY CLAY

J. Vaunat
Department of Geotechnical and Geosciences, Technical University of Catalonia (UPC), Barcelona, Spain, E-08034
A. Gens
Department of Geotechnical and Geosciences, Technical University of Catalonia (UPC), Barcelona, Spain, E-08034
R. de Vasconcelos
Department of Geotechnical and Geosciences, Technical University of Catalonia (UPC), Barcelona, Spain, E-08034
X.-L. Li
EIG Euridice, Mol, Belgium, BE-2400

ABSTRACT: *This paper tackles the issues related to the excavation of a horizontal gallery carried out in Boom clay, a tertiary clay that hosts the Underground Laboratory of the Belgium Nuclear Agency (SCK-CEN). The gallery is 85 m long, 5 m wide and connects one of the laboratory access shafts to a horizontal drift drilled from the second access shaft. Displacement and pore water pressure sensors installed from both gallery ends allowed for a detailed monitoring of the hydro-mechanical response of the clay rock before, during and after gallery excavation. A striking feature of the response concerns the strong changes measured in pore water pressure at distances as large as 60m from the excavation front. To explore and discriminate the mechanisms controlling such pore pressure changes, 2D axisymmetric Finite Element hydro-mechanical calculations have been carried out. An elastoplastic constitutive law based on Mohr-Coulomb criterion has been considered for the material. Several types of analyses have been performed: a) material and stress state are isotropic; b) material is isotropic but stress state is orthotropic and, c) material and stress state are orthotropic. Results allow for explaining the field measurements and identifying the key variables that control the clay response around the drift.*

1 INTRODUCTION

Burial of nuclear waste at high depths (several hundreds of meters) is one of the solution contemplated for a safe storage of radioactive elements along their whole life. The construction of such deep repositories requires the realization of many excavations: access shafts, access galleries, operation galleries and alveoli to store waste containers. In soft argillaceous formations, the high stress release occasioned by excavation works is the cause for the development of significant hydro-mechanical perturbed zones, whose size, continuity and characteristics are of highest importance for the safety of the whole storage.

In Underground Research Laboratories constructed in argillaceous rocks, there is therefore a strong effort devoted to the assessment of the impact of excavations on the surrounding displacement and pore pressure fields. As well, development of fissures and fractures in the Excavation Damaged Zone and its consequences for the value of the host rock permeability is carefully monitored, as the latter parameter controls in a large part the sealing capability of the whole storage scheme. Experiments like MODEX-REP (Su, 2007) at Meuse/Haute Marne Underground Research Laboratory – France, ED-B (Corkum & Martin, 2007) at Mont Terri laboratory – Switzerland, and CLIPEX experiment (Bernier et al., 2007)

at HADES URL – Belgium, are examples of highly instrumented full scale tests designed to this aim (see Table 1).

Table 1. Examples of full-scale tests designed to monitor the hydro-mechanical response of argillaceous rocks around excavations.

Test label	Argillaceous formation	Characteristics of the material	Characteristics of the excavation
MODEX-REP	Callovo-Oxfordian mudstone	Porosity: 0.17 $CaCO_3$ content: 20-40% UCS: 10 MPa Permeability: 1-5 10^{-13} m/s Bedding: sub-horizontal (1-2º)	Diameter: 6.1 m Vertical shaft
ED-B	Opalinus clay	Porosity: 0.13-0.17 $CaCO_3$ content: 6-22% UCS: 4-22 MPa (anisotropic) Permeability: 1-5 10^{-13} m/s Bedding: inclined (40º)	Diameter: 3.6 Horizontal drift
CLIPEX	Boom clay	Porosity: 0.39 $CaCO_3$ content: 0-3% UCS: 1-2 MPa Permeability: 2-4.5 10^{-12} m/s Bedding: sub-horizontal (1-2º)	Diameter: 4.8-4.9 m Horizontal gallery

Although carried out in different formations, the three tests provided measurements qualitatively very similar. Particularly, all evidenced large changes in pore pressure in the near field (typically between 0.5 MPa and 1 MPa) as well as a large extension of the zone of pore pressure perturbations (more than 10 diameters). As an example, Figure 2 shows pore pressures measured during the ED-B test. Within a zone of two diameters, pore pressure increased up to 0.5 to 0.7 MPa at time of the reach of the instrumented section by the excavation front. When left in place after the experiment, pore pressure sensors further recorded changes in pore pressure during excavation of farther galleries. The high sensitivity of pore pressures to excavation has also been observed during borehole drilling operations in small scale in situ tests.

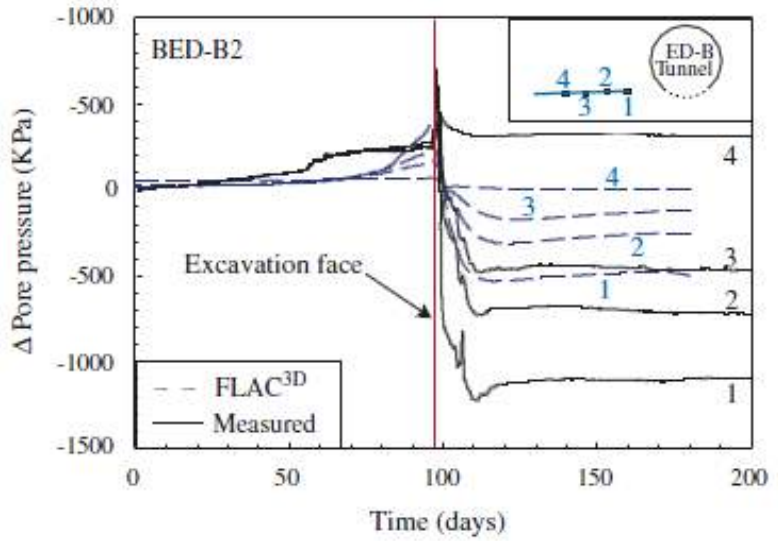

(from Corkum & Martin, 2007)

Fig. 1. Pore pressures measured during ED-B experiment.

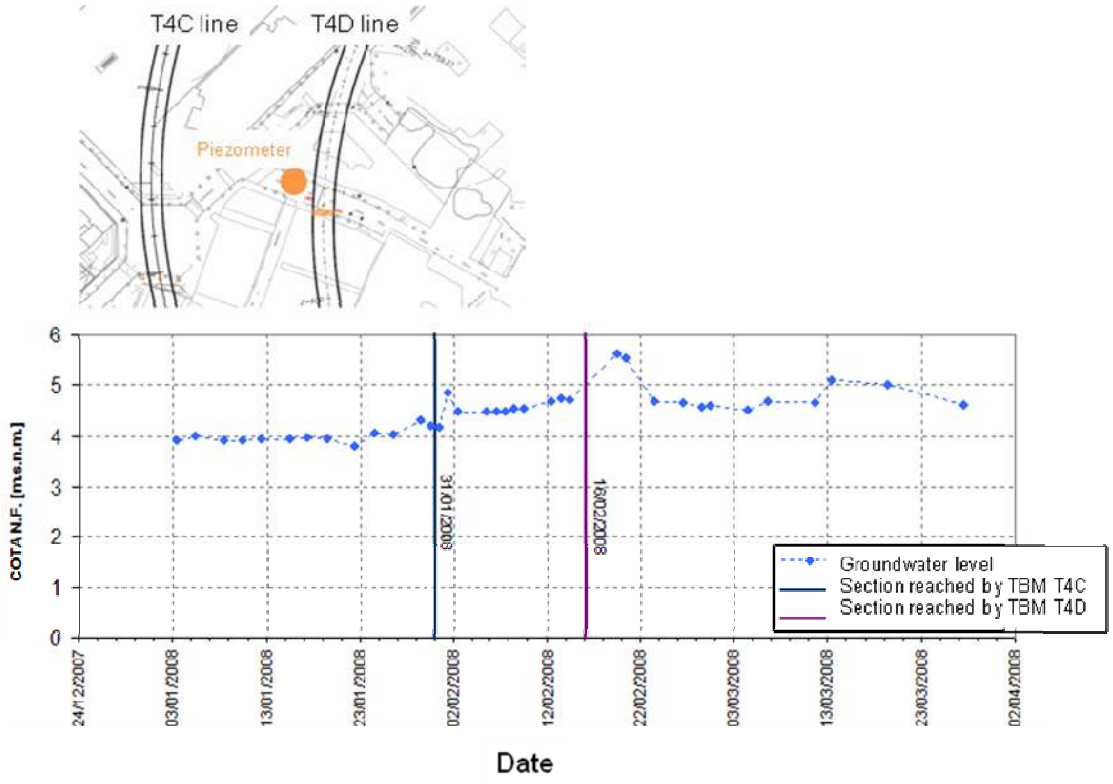

Fig. 2. Pore pressures measured during excavation of two drifts of the new Barcelona metro line.

Similar effect is detectable for excavations at much lower depths, typical of civil engineering works. Fig 2. shows for example the groundwater level registered in an open piezometer during excavation, in a layer of tertiary clay, of two drifts of the new Barcelona metro line. An increase of approximately 1 m is registered when the first tunnelling machine crosses the instrumented section, followed by a second increase of the same order at time of arrival of the second machine. Measured change in pore pressure is however much lower than in Fig. 1 as the result of the much lower release in stress.

All these observations indicate that underground excavations in stiff and low permeable materials causes a rearrangement of stress that traduces into pore pressure changes. Explanation to this effect has to be looked for in the undrained conditions that prevail in such material during short term excavation, in the anisotropy of the stress state (see for example Alonso et al., 2005) and in the anisotropy and non linearity of material behaviour. In this paper, Finite Element modeling of CLIPEX experiment is used to provide keys about the main factors controlling pore pressure changes during excavation in Boom clay formation.

2 CLIPEX EXPERIMENT

2.1 Experimental setup

Figure 3 shows a general picture of HADES underground Research Laboratory. Construction of the URL starts in 1980 by the excavation of the first access shaft and the realization of a gallery at 224 m to host several experimental works during the years 1983-1984. In 1987, a second gallery (Test drift) has been excavated next to his zone. Ten years after, excavation of

the second shaft is started. Works have been completed by the drilling of the connecting gallery in 2001-2002.

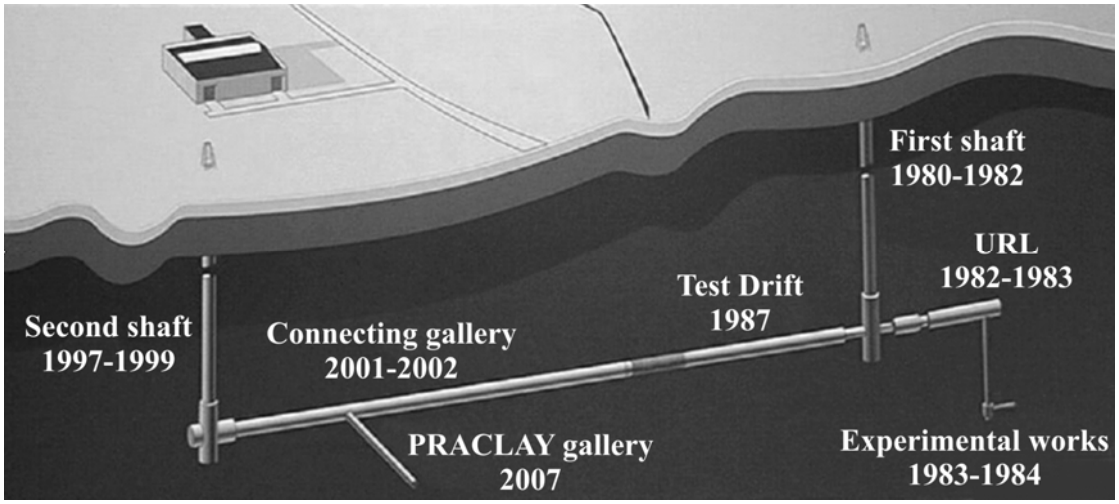

Fig. 3. Location of the connecting gallery at HADES Underground Research Laboratory.

A tunneling machine equipped with a road header sheltered by a tunneling shield has been used for the excavation of the connecting gallery. The tunneling machine was mounted in a chamber close to the second shaft and advanced at a rate above 2 m/day to connect finally to the Test Drift.

The gallery is 85 m long and 5 m wide. Concrete lining was installed behind the shield as excavation progressed, using the wedge-block technique to limit to the minimum the convergence of the clay. Excavation works were completed in 37 days.

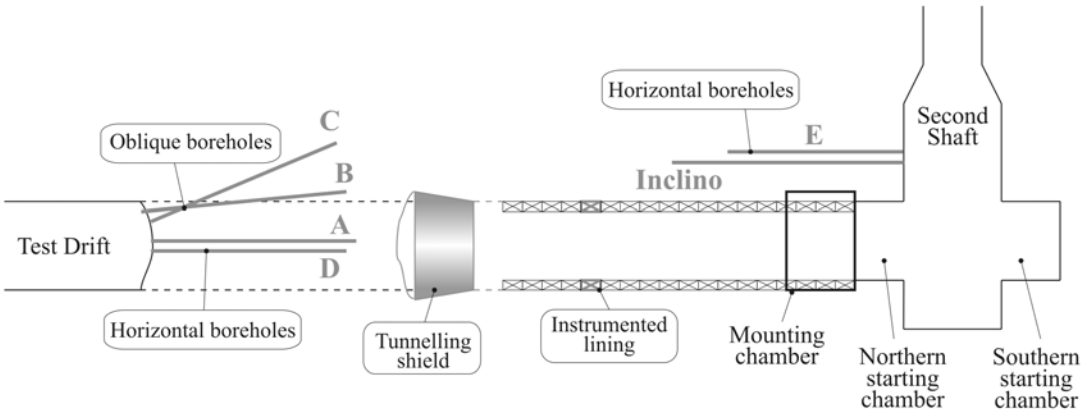

Fig. 4. Detail of instrumentation around the connecting gallery.

Figure 4 show the detail of the instrumentation around the connecting gallery. Eight thirty meter long boreholes (A1, A2, B1, B2, C1, C2, D1 and D2) were drilled behind the front of the Test drift. A1 host a six anchors extensometer, B1 and C1 two ten-segments inclinometers and D1 one deflectometer composed by eleven segments. Borehole A2 to D2 were equipped with piezometers (six filters for A2, B2 and D2 and eight filters for C2). A1 and A2 are oriented along the centerline of the gallery to be excavated. B1, B2, C1 and C2 are inclined in the vertical plane passing through gallery centerline while D1 and D2 are inclined in the horizontal plane. In addition, two horizontal boreholes (E1 and E2) were drilled from the

second access shaft, nearby the beginning of the connecting gallery. E1 is five meter long and has been instrumented with displacement measurements. E2 is 6.5 meters long and were equipped with pore pressure sensors. Instrumentation is completed by strain gauges embedded in lining panels. Convergences during excavation were also measured.

2.2 Material properties

Boom clay is a formation of the Rupelian Period (Tertiary age) period. It is a stiff silty clay of marine origin characterized by intercalations of layers of tens centimetres thick with different clay, silt, carbonate and organic matter contents, reflecting cyclical deposition periods. At HADES site, the formation has a thickness of 100 m and its roof culminates at a depth of 190 m. At the depth of CLIPEX experiment, the plasticity index is equal to 50%, the porosity to 0.39 and the uniaxial compressive strength ranges between 1 and 2 MPa (Bastiaens et al., 2006). Pore pressure and vertical stress are equal to 2.2 and 4.5 MPa, respectively.

Several studies on natural Boom clay have been conducted in the laboratory during the last decades (Horseman et al., 1987; Baldi et al., 1991; Mair et al. 1992; Djéran Maigre et al., 1995; Delage et al. 1999; Coll, 2005; Lima, 2011). On the basis of the oedometer test results presented by Horseman, Burland (1990) indicates that the behaviour of the material is consistent with that of a structured clay with apparent preconsolidation caused by creep and diagenesis. The preconsolidation pressure is close to 6 MPa and the OCR to 2.4. Bernier et al. (2007) pointed out the highly non linear response of the material. In light of this and with the objective of using simple linear elastic-plastic model, they propose to use a drained tangent Young modulus E' = 300 MPa, which provides a reasonable value of the deviatoric strain at failure. From resonant column measurements, Lima (2011) forwards values between 700 and 900 MPa for the small strain Young modulus and a ratio between the horizontal and vertical component equal to 1.2. Lower values (250 and 500 MPa) were however provided by the back-analysis of a thick hollow cylinder test. As far as concerns failure parameters, Bernier et al. (2007) propose to use a Mohr Coulomb type of failure locus with value of friction angle and cohesion equal to 18º and 300 kPa for stress level close to the in situ value. Dilation angle is between 0 and 10º. Finally, Lima (2011) backanalysed the pore pressure evolution measured in the laboratory during a heating experiment. She found a value equal to 7.4 10-12 m/s.

Field measurements are also available for some engineering properties. Seismic measurements realized in the vicinity of the 2nd shaft give values between 1800 and 1900 m/s for the P-wave velocity. These values allow to bracket the Young modulus between 700 MPa and 1600 MPa (depending of the value of Poisson's ratio – considered between 0.125 and 0.3). Pulse test performed in two boreholes nearby the Praclay gallery gives in situ values equal, respectively, to 4 and 6 10-12 m/s for the horizontal and vertical components of the saturated permeability.

3 NUMERICAL MODEL

3.1 Field and constitutive equations

The solution of the coupled hydro-mechanical problem requires the simultaneous solution of the mass balance of water and stress equilibrium. In absence of water vapour (saturated problem), the water mass balance reduces to:

$$\frac{\partial}{\partial t}(\rho_l \phi) + \nabla \cdot (\mathbf{j}_l) = f_l \tag{1}$$

where ϕ is the porosity, ρ_l the density of the liquid phase, $\mathbf{j}_l$, the mass flux of water and f_l an eventual source/sink term of liquid. The stress equilibrium reads:

$$\nabla \cdot \boldsymbol{\sigma} + \mathbf{b} = \mathbf{0} \tag{2}$$

where $\boldsymbol{\sigma}$ is the stress tensor and **b** body forces.

Field equations are completed by Darcy law that relates the Darcy flux to the gradient of water head, the state equation for water density and the mechanical law of the material.

In this work, an elastoplastic law based on linear elasticity and Mohr Coulomb yield criterion is used to represent the behaviour of Boom clay. The flow rule is considered non-associated and governed by the dilation angle of the material. The elastic law can be either isotropic or orthotropic.

Material properties have been defined according to the lower values of in situ measurements described in paragraph 2.2. They are summarized in Table 2.

Table 2. Parameters of Boom clay used in the simulations.

Law	Parameter	Component	Symbol	Value
Elasticity	Drained Young modulus	Horizontal (or isotropic)	E'_h	700 (MPa)
		Vertical (if anisotropy is considered)	E'_v	300 (MPa)
	Drained Poisson's ratio	Horizontal (or isotropic)	ν_h	0.125
		Cross (if anisotropy is considered)	ν_{hv}	0.125
	Shear modulus	Vertical (if anisotropy is considered)	G_v	222 (MPa)
Plasticity	Drained cohesion	Isotropic	c'	0.3 (MPa)
	Drained Friction angle	Isotropic	ϕ'	18 (°)
	Dilation angle	Isotropic	y	0-18 (°)
Darcy	Saturated Permeability	Horizontal (or isotropic)	K_{wh}	$6\ 10^{-19}$ (m/s)
		Vertical (if anisotropy is considered)	K_{wv}	$3\ 10^{-19}$ (m/s)

3.2 Geometry and mesh

With the objective to prepare the full 3D analysis of CLIPEX experiment, a series of pseudo 3D computations (2D axisymmetric) were carried out. Axisymmetry is set around the centreline of the connecting gallery. Pore pressure is set initially to 2.2 MPa in the whole mesh and maintain constant at 50 m from gallery axis. On the lateral boundary, conditions of null displacement and null wall flow have been imposed.

Four main stages are considered in the analysis: an initial stage to insure equilibrium, a stage for the excavation of the test drift excavation (realized in 1987 and left open 14 years), a stage for the step-by-step excavation of the connecting gallery (whole duration 35 days) and one final stage from the end of the excavation of the connecting gallery. Excavation of test

drift is considered instantaneous. Excavation of the connecting gallery is divided into 28 steps defined in accordance with the real advance of the front. The average rate of advance is 3m/d.

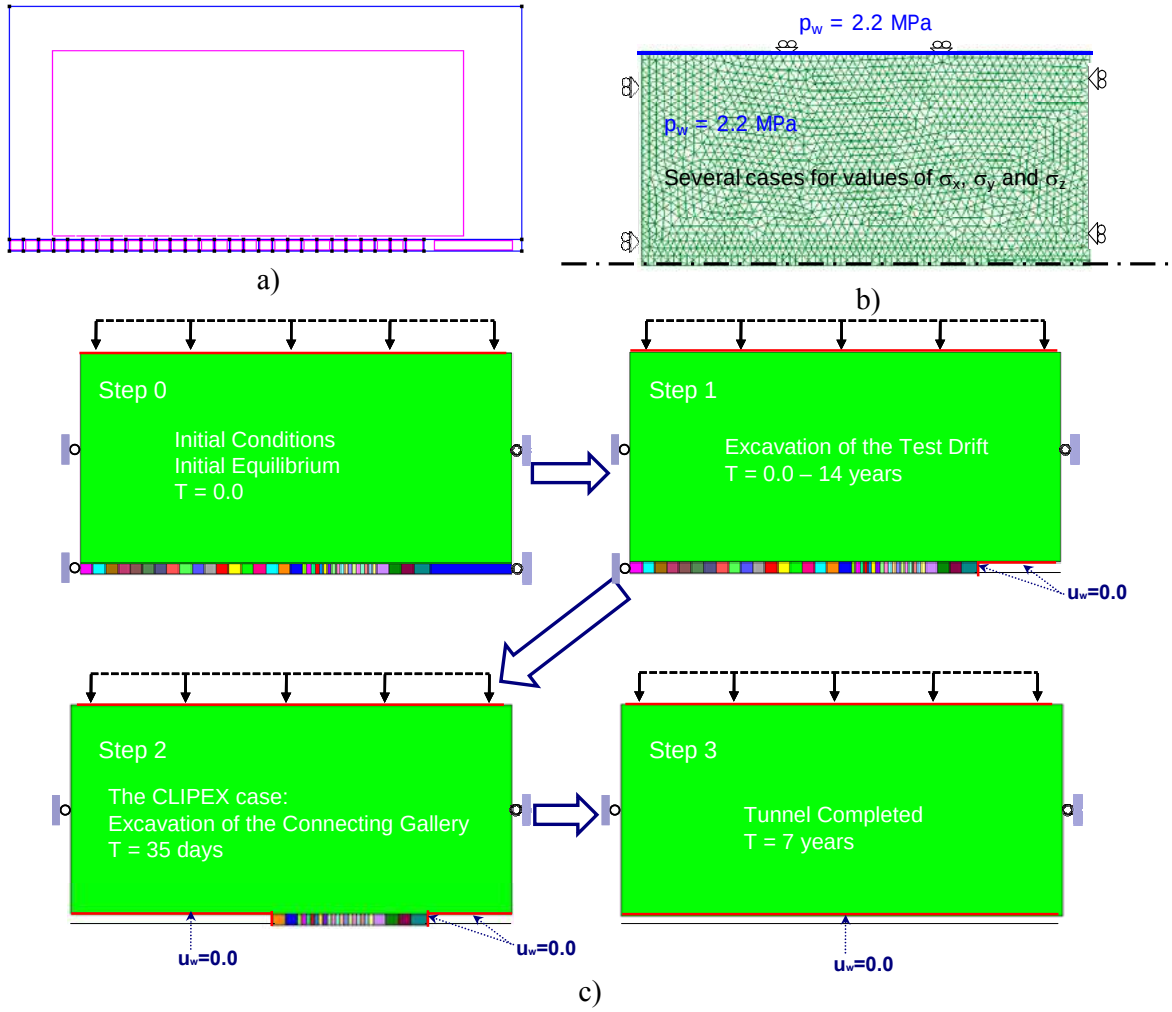

Fig. 5. Characteristics of the numerical model: a) geometry; b) mesh, boundary and initial condition, and c) main stages of excavation process.

In order to study the effect of different factors of anisotropy (in permeability, stress state of stiffness), eight cases – labeled form I to VIII - have been simulated. Factor(s) of anisotropy considered in each case are described in Table 3.

Table 3. Factor(s) of anisotropy considered in the different simulations.

Computation number →	**I**	**II**	**III**	**IV**	**V**	**VI**	**VII**	**VIII**
Isotropic	X							
Anisotropy in permeability		X			X	X		X
Anisotropy in stress state			X		X		X	X
Anisotropy in stiffness				X		X	X	X

4 RESULTS AND DISCUSSION

Figure 6 shows a comparison between the pore overpressure due to excavation, computed by the full anisotropic model (case VIII of Table 42) and the isotropic model (case I) for one sensor located in borehole. It evidences the capability of the anisotropic model to capture the peak in pore pressure as the front approaches the sensors. This is due to the loading originated by the redistribution farther ahead the front of the lateral stress released by the excavation. When the front goes closer to the sensor (less than 6 m), a sudden decrease in pore pressure is observed caused by axial unloading. The effect on pore pressure of the two last steps of excavation before the reach of the sensor can be clearly observed in the Figure. To the opposite, the isotropic model captures only the pore pressure decrease by axial unloading but not the previous peak by lateral loading.

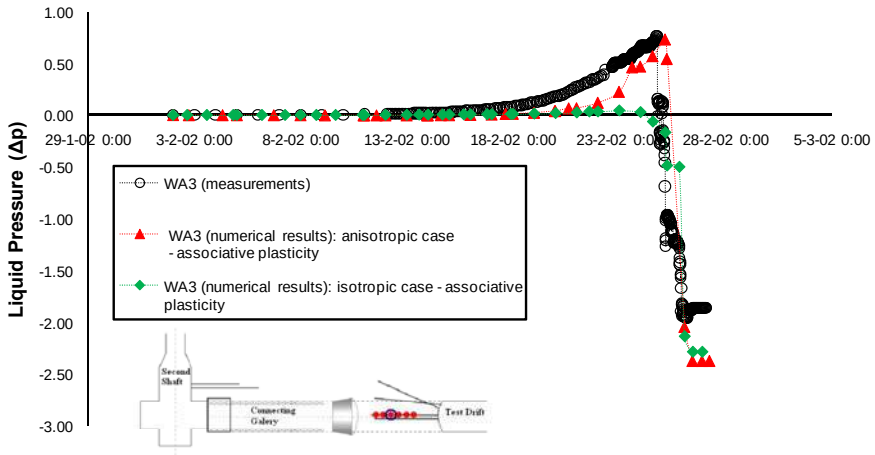

Fig. 6. Computed pore pressure vs measurement at sensor A3 for the isotropic and full anisotropic model.

In Figure 7, pore pressures computed by the full anisotropic model are further compared with pore pressure measurements at sensors located on the sides of the excavation. Agreement is good for sensors close to the gallery wall (borehole B). For sensors farther in the rock (borehole C), the trend of evolution, characterized by a cycle of increase/decrease in pore pressure, is well reproduced but the magnitude of change in pore pressure is not totally captured.

Results of a sensitivity analysis on the value of dilatancy angle are also reported in the Figure 7. Whatever is the value of ψ (ψ = 0 – red symbols, 3.6º – in blue, 9º – in green, 18º – full dilatancy in yellow), the computed evolutions of pore pressure almost identical. This has been confirmed by comparison of pore pressure maps around the excavation at different times (not presented here). The dilatancy angle appears thus to have little influence on the hydraulic field around CLIPEX experiment.

A final analysis was performed to identify whether anisotropy in permeability, stress state or moduli control mainly the pore pressure field. As a representative example, comparison between computed pore pressures and measurements at sensor A4 is reported in Figure 8 for three models: the full anisotropic model, the model considering anisotropy only in elastic moduli and the model considering anisotropy in all variables (permeability, stress state) but in elastic moduli. The figure indicates that the peak in pore pressure ahead the front is controlled almost exclusively by the anisotropy in moduli.

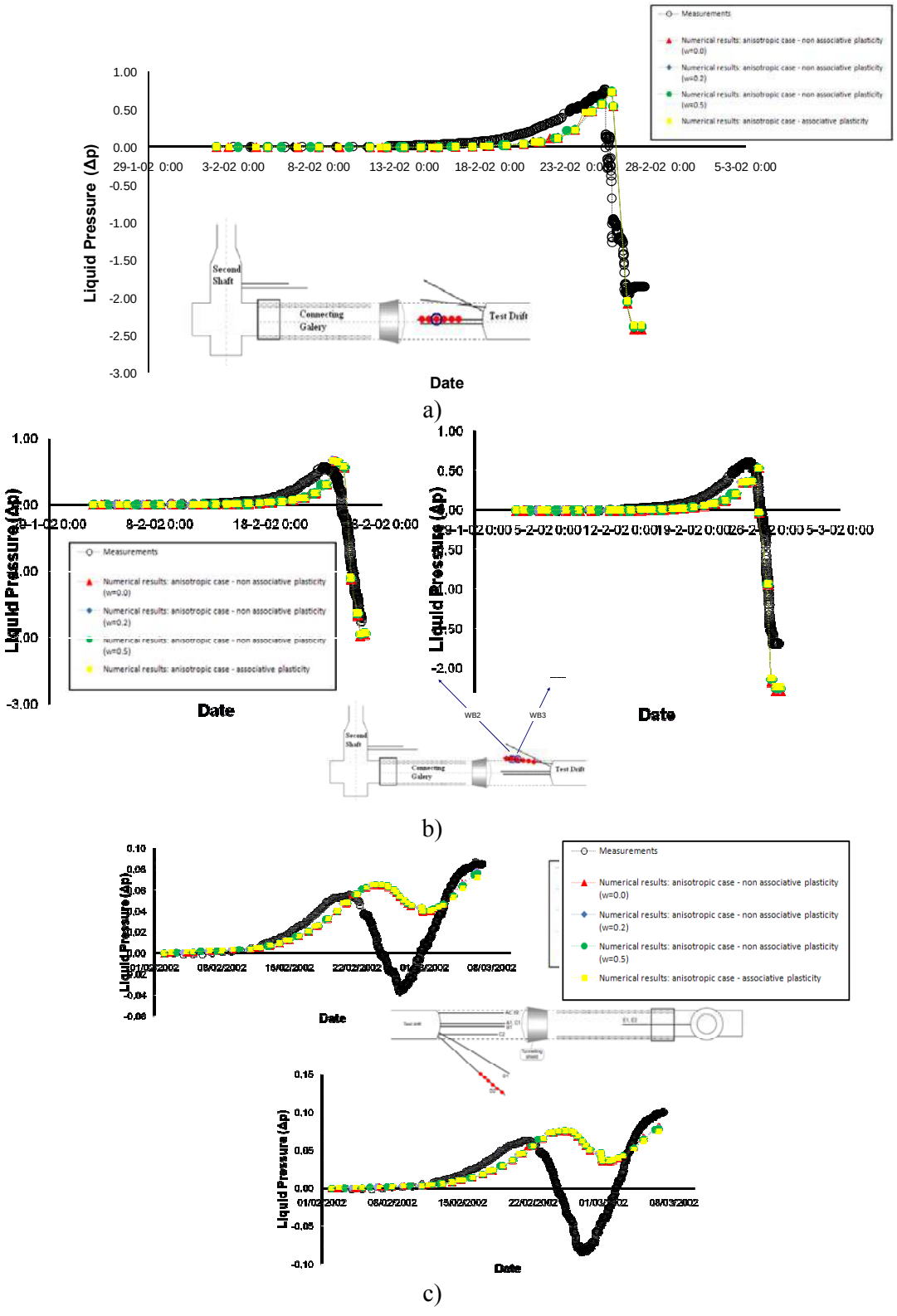

Fig. 7. Computed pore pressure vs measurement at five sensors along borehole a) A, b) B and c) C for the full anisotropic model and three values of dilatancy.

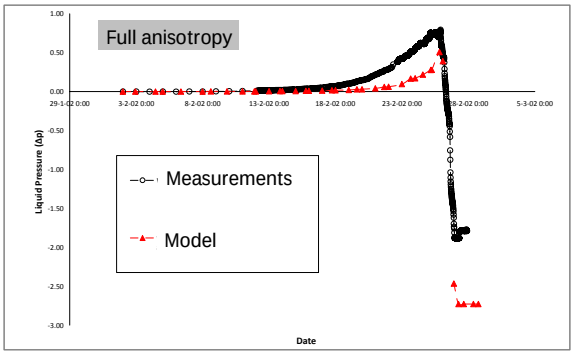

a)

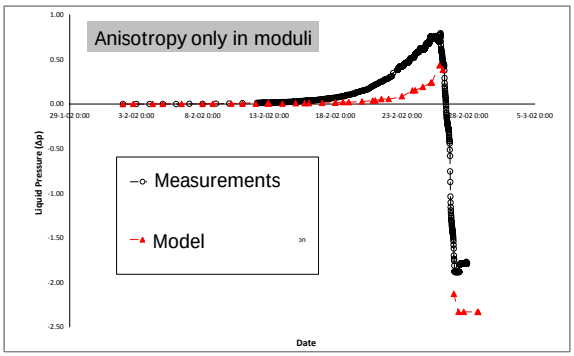

b)

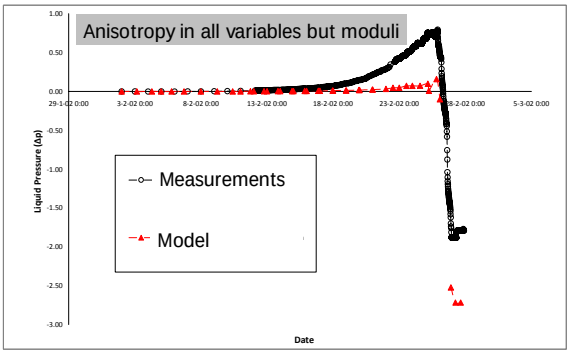

c)

Figure 8: Computed pore pressure vs measurement at sensor A4 for a) the full anisotropic model b) model with anisotropy only in moduli and c) model with anisotropy in all variables but in moduli.

Fig. 9 shows a comparison between displacements computed by the full anisotropic model and measurements at sensors A1 and A4. Agreement is reasonable although the magnitude of displacement provided by the model appears to be lesser that the measured one. It is however difficult to put forward reasons for such a discrepancy because of the possible sliding of the extensometer chain during excavation (Bastiaens et al, 2003).

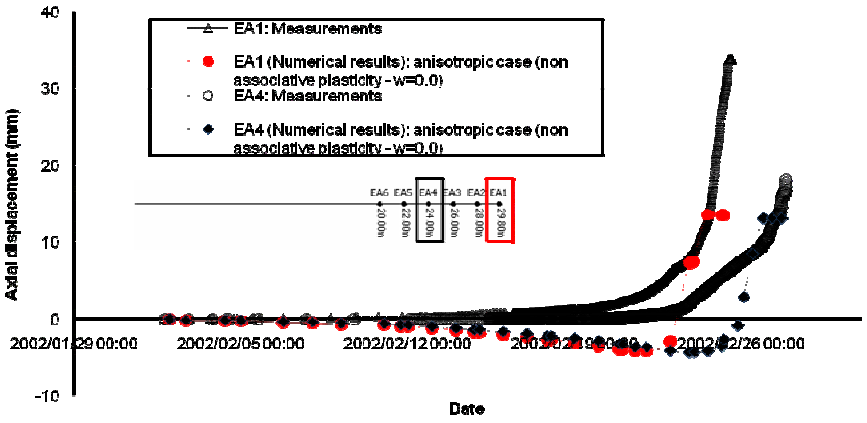

Figure 9: Comparison between displacement computed by the full anisotropic model and measurements at sensor A1 and A4.

5 CONCLUDING REMARKS

Underground excavations in stiff, low permeable and saturated clayey materials evidence strong variations of pore pressure along long distances because of the stress rearrangement around the cavities. While the underlying mechanism may be qualitatively understood as the undrained response of anisotropic geological formations, the quantitative reproduction of the magnitude and spatial extension of pore pressure variations is still a challenging issue for numerical modellers. In this paper, experimental results obtained in a full scale Mine-by Test experiment performed at high depths in Boom clay formation are used to analyze the possible effects of different factors of anisotropy (anisotropy in stress state, permeability and stiffness) on the hydraulic response. It appears that, in this case, the anisotropy in stiffness is the main controlling factors of pore pressure variations.

ACKNOWLEDGEMENT

This work has been developed as a part of the European project TIMODAZ (Contract Number: FI6W-CT-2007-036449).

REFERENCES

Alonso E.E., Alcoverro J., Coste F., Malinsky L., Merrien Soukatchoff V., Kadiri I., Nowak T., Shao H., Nguyen T.S., Selvadurai A.P.S., Armand G., Sobolik S.R., Itamura C.M., Stone C.M., Webb S.W., Rejeb A., Tijani M., Maouche Z., Kobayashi A., Kurikami H., Ito A., Sugita Y., Chijimatsu M., Börgesson L., Hernelind J., Rutqvist J., Tsang C.F. and Jussila P. (2005). "The FEBEX Bechmark test. Case Definition and comparison of modelling approaches", Int. J. Rock Mech. & Min. Sci,, Vol. 42, 611-638.

Baldi G., Hueckel T., Peano A. and Pellegrini R. (1991). Developments in modelling of thermo-hydro-geomechanical behaviour of Boom Clay and clay-based buffer materials, ISMES, Final report, EUR 13365/1, 134 p.

Bastiaens, W., Bernier, F. & Li, X. L. (2006). "An overview of long-term HM measurements around HADES URF". Proceedings of the international symposium on multiphysics coupling and long term behaviour in rock mechanics, Liège, pp. 15–26.

Corkum, A.G. & Martin, C.D. (2007). “Modelling a mine-by test at the Mont Terri rock laboratory, Switzerland”, International Journal of Rock Mechanics & Mining Sciences, Vol. 44, 846–859.

Djéran-Maigre, I., Bazargan, B., Giraud, A. & Rousset, G. 1994. Étude expérimentale du comportement thermo-hydro-mécanique de l’argile de Boom. Rapport No. 94-002. Mol: SCK.CEN.

Horseman S.T., Winter M.G. and Entwistle D.C., 1987, Geotechnical characterization of Boom clay in relation to the disposal of radioactive waste, Commission of the European Communities, EUR 10987, 87 p.

Lima, A. (2011). Thermo-hydro-mechanical behaviour of natural Boom clay: an experimental study. PhD thesis, Universitat Politècnica de Catalunya, Spain (in preparation).

Mair, R. J., Taylor, R. N. & Clarke, B. G. (1992). Repository tunnel construction in deep clay formations: Final report, EUR 13964. Luxembourg: Commission of the European Communities.

Neerdael, B., Beaufays, R., Buyens, M., De Bruyn, D., and Voet, M. 1992. Geomechanical behaviour of Boom clay under ambient and elevated temperature conditions. Commission of the European Communities, Nuclear Science and Technology, EUR 14154.

Su, K. 2007. Development of Hydro-mechanical Models of the Callovo-Oxfordian Argillites for the Geological Disposal of Radioactive Waste (MODEX-REP), Final report EUR 20844, European Commission.

COUPLED CHEMO-MECHANICS OF EVOLVING PERMEABILITY IN GEOMATERIALS

L. B. Hu
College of Engineering, University of Vermont, Burlington, VT 05405, USA

T. Hueckel
Department of Civil and Environmental Engineering, Duke University, Durham, NC 27708, USA

ABSTRACT: *Flow of fluids in geomaterials may be strongly affected by chemo-mechanical processes, which are either externally induced or spontaneous. This is the case when dissolution, transport of the dissolved mineral and its precipitation in the neighborhood pore space causes a decrease of what is upscaled as Darcian permeability. Factors affecting the process are studied at the micro-scale using a model of a system of vessels of variable length and opening formed in the neighborhood of a stressed contact between two damage-affected grains. It appears that permeability is mildly affected by the contact area increase, and for most of the duration, by the precipitation of the mineral solute, until the inter-grain pores are almost completely clogged by the precipitate, when the permeability decreases very fast by orders of magnitude. Rigid chemo-plasticity model is employed to simulate the enhancement to dissolution induced by formation of new inter-phase interfaces at the walls of micro-cracks, represented by dilatant plastic strain. Such a process is widely believed to occur in oil/gas bearing sediments. Dissolution leads to chemo-plastic softening of the material. Couplings, feedbacks and feedforwards between mechanical, transport and geochemical processes caused by intergranular damage and dissolution are discussed.*

1 INTRODUCTION

Geomaterials respond to some environmental circumstances through generation of a series of self-regulatory mechanisms of damage, deformation, erosion, and chemical processes or reactions: e.g. osmosis, dissolution and precipitation. These mechanisms are coupled at different scales. Several natural geomechanical processes, as sediment compaction, rock weathering or landsliding appear to include such sequences of mechanisms. A better understanding of the involved processes will improve the chances to control and/or engineer better the geo-materials and geo-structures subject to such processes.

We investigate mechanisms that control the rate of damage to geomaterials induced by geochemical processes at the level of intergranular contact in sediment compaction eventually critically affecting its permeability. Our focus is on irreversible changes expressed via chemo-plasticity studied numerically at three scales: those of grain, grain- assembly- and continuum-scale. The proposed scenario includes: damage in the near-contact area via microfracturation; activation of the microfracture wall surfaces as sites for dissolution of minerals entering in contact with permeating water; mass removal due to dissolution causing material softening; diffusion and advection of the dissolved mineral across the grain toward the external pore space; diffusion within the pore fluid of the dissolved minerals; and finally precipitation of minerals onto free grain surfaces. This paper presents an extension of our previous work (Hu and Hueckel, 2007) to the effect of the above processes on sediment fluid

transmissibility. Such effects are crucial in petroleum extraction engineering and compaction of clay barriers.

Rigid chemo-plasticity is used to simulate the contact phenomena in the grain at the microscale, coupled with the reactive-diffusive transport of the dissolved mineral across the grain. Upscaled variables at mesoscale simulate the change of permeability of the grain system as a result of the mineral precipitation. The resulting redistribution of mass within the pore space is controlled by microscopic and mesoscopic chemical gradients, which in turn are controlled by microscopic damage variables. Partial masses of the same mineral are shown to play a different role in the sediment stiffness changes, changes in porosity and in permeability at the macro- and meso-scale requiring them to be linked to different processes (dissolution and precipitation) derivable only at the microscale. Self-regulation is exercised via stress reduction by the increasing contact surface area, and possibly by the generation of pore pressure, due to the dissolution flux via the increasing reaction site area controlled by damage and eventually a permeability decrease.

2 OUTLINE OF BASIC MECHANICAL, HYDRAULIC AND GEOCHEMICAL PROCESSES

The natural process of normal consolidation of sediments is believed to be a superposition of several coupled processes regarding the sediment solid matrix and pore fluids. The processes involved are: defromation of sediment grains, including plastic deformation, especially near contact between grain asperities and corresponding locally smooth surface of another grain; dilatant damage induced by the plastic yielding; infiltration of the dilatant zone by pore water; activation of damage (microcracking) related internal interfaces between pore liqid and solid; dissolution of minerals at these interfaces; diffusion of the dissolved species within the grain away from the reaction sites; intergrain diffusion of the dissolved minerals in the pore water and precipitation of those on the free surface of adjacent or remote grains.

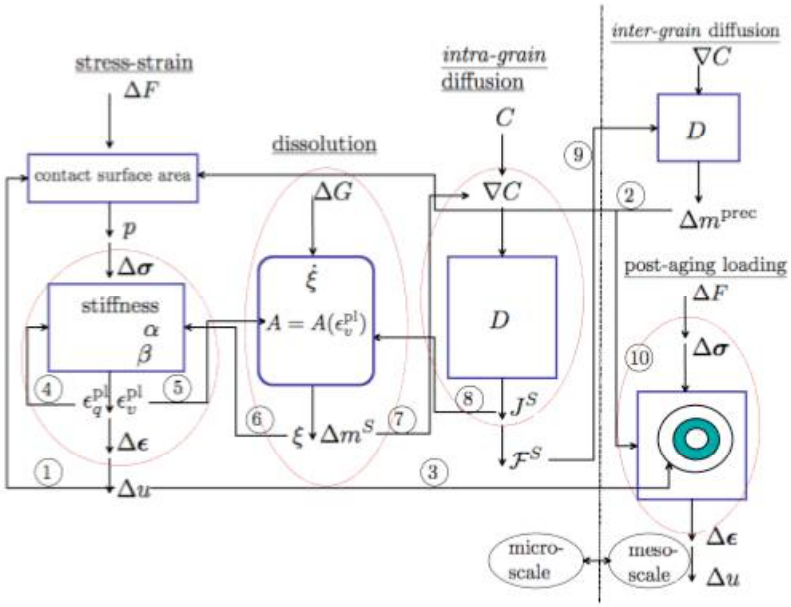

Fig. 1: Schematic of feedbacks and feedforwards in coupled processes of mineral reaction assisted sediment compaction and stiffening (for idetification labels see Hueckel and Hu, 2009)

The above sequence of processes is common to other phenomena such as aging (see Mitchell and Solymar, 1984; Hueckel et al., 2001; Hueckel et al., 2005), or pressure solution

in petroleum reservoir modeling (Rutter, 1976; Lehner, 1995). Hu and Hueckel (2007) have developed a sequence of three-scale models to simulate aging, and identified leading feedbacks and feedforwards of intersacale coupling to evaluate the evolution of meso-scale stiffness. A summary of the feedbacks and feedforwards are redrawn in Fig. 1. In this paper we apply that model to address the evolution of permeability, and feedbacks involved in it.

The three-scale model of sediment compaction is described in detail by Hu and Hueckel (2009). In what follows only main concepts are presented. The models at the microscale include stress-strain relationship, dissolution law, and intra-grain diffusion. At the meso-scale the models include intergranular diffusion with precipiation and a resulting increase of material stiffness. The macro-scale is not shown in the figure. The micro-scale medium is a porous material of the solid grain minerals. Its porosity is the internal grain porosity, and the mechanical properties of the material are those of the solid grain mineral. Stress and strain (positive in compression) are microstress and microstrain at the scale of a fraction of the grain (Fig. 2).

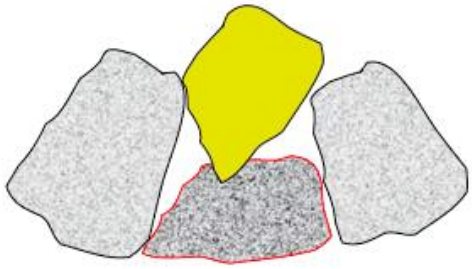

Fig. 2. Schematic of a rigid grain indentation into an adjacent rigid-plastic grain

The material of individual grain is taken as rigid plastic. To describe mathematically a near contact failure one needs to identify a micro-stress (σ_{ij}) yield locus, $f(\sigma_{ij}) \le 0$, within which no strain (ε_{ij}) occurs, whereas at yielding, the strain rate is entirely irreversible

$$\begin{aligned} &f < 0, \text{ and for } f = 0, \dot{f} < 0: \ \dot{\varepsilon}_{ij} = 0; \\ &\text{whereas for } f\left[\sigma_{ij}, p_c\right] = 0 \text{ and } \dot{f}\left(\dot{\sigma}_{ij}, \dot{p}_c\right) = 0: \ \dot{\varepsilon}_{kl} = \dot{\varepsilon}_{kl}^{irr} \neq 0 \end{aligned} \tag{1}$$

The superimposed dot over a symbol denotes a time rate.

Dilatancy-damage at the sub-grain scale is a critical variable for the entire concept as a vehicle of the chemo-mechanical coupling. It is linked to micro-cracking, which plays multiple roles. First, it provides a connected network across the damaged part of the grain that becomes instantly permeated with water as a result of suction induced by dilatancy. Second, micro-crack walls form new solid-fluid interface, which constitutes a source of dissolution of mineral species, that is solid mass removal. Third, irreversible micro-slips occur across micro-cracks. As a result of micro-slips and mass removal, the yielding behavior of the material is affected by two competing plastic hardening mechanisms: deviatoric strain-hardening and mass removal softening. Hence, p_c which is the apparent preconsoliation stress, i.e. isotropic size characteristics of the yield locus, depends on two hardening parameters, which are mechanical (ε_q^{irr}) or chemical (ξ) in nature (Hueckel, 2002).

$$p_c = p_c(\varepsilon_q^{irr}, \xi)\text{, where } \dot{\varepsilon}_q^{irr} = \left| \left(\frac{2}{3} \dot{e}_{ij}^{irr} \dot{e}_{ij}^{irr} \right)^{1/2} \right| \text{ and } \dot{e}_{ij}^{irr} = \dot{\varepsilon}_{ij}^{irr} - \frac{1}{3} \dot{\varepsilon}_{kk}^{irr} \delta_{ij} \tag{2}$$

Chemical softening parameter ξ is an accumulated relative mass removal of a single mineral species that dominates the material strength, computed with respect to the original total mass of that particular species. The relationship between change in the apparent preconsoliation stress p_c and a reaction progress variable is established empirically. A mineral in the example, dominating the strength of quartz sand is silica. Dissolution reaction of silica in water may be measured through a change in activity of its product which is silicic acid H_4SiO_4 formed in the aqueous solution. The rate of silica dissolution is determined by Rimstidt and Barnes (1980) formula as proportional to the specific surface area of the solid-fluid interface *A,* normalized with respect to *1* m^2 to yield a non-dimensional quantity $\tilde{A}$

$$\frac{da_{\mathrm{H_4SiO_4}}}{dt} = \tilde{A}\gamma_{\mathrm{H_4SiO_4}} \left(k_+ a_{\mathrm{SiO_2}} a_{\mathrm{H_2O}}^2 - k_- a_{\mathrm{H_4SiO_4}} \right) \tag{3}$$

where *ai* are activities, and γ_i, activity coefficients, of *i*-th species, while k_+ and k_- are rate constants of respectively forward and backward reactions. $\tilde{A}$ is a dimensionless specific interfacial surface area, as above, per unit mass of pore fluid. For details see Hu and Hueckel, 2007). ξ is a reaction progress $\xi = 1$ variable constrained by the inequalities: $0 \le \xi \le 1$; when, the reaction is completed, that is all silica is removed from the material.

In the current context the damage occurs within a single grain and consists in opening of microcracks. A new scalar variable, $\tilde{a}$, represents the amount of the added interface surface area per unit volume of the grain medium. It is linked to the relative reaction area, $\tilde{A}$, $\tilde{a} = \tilde{A} \frac{n_g \rho_w}{\rho^0}$, where ρ^0= 1 kg/m3, ρ_w is the density of water, n_g is porosity of the grain solid. The new internal interface surface area generated by the micro-cracking per unit volume is proposed to be proportional to the volumetric strain. Hence,

$$\tilde{A} = \tilde{A}\left(\varepsilon_v^{irr}\right) = \phi \left| \varepsilon_v \right| + \phi_c; \quad \varepsilon_v < 0 \tag{4}$$

where ϕ is a constant, whereas ϕ_c represents the specific surface area of pre-existing voids. For $\varepsilon_v > 0$, $\phi = 0$, which aims at excluding the compressive strain for which there are no micro-cracks and hence no change in the dissolution surface area. Therefore

$$\dot{\xi} = \left(\Xi \left| \varepsilon_v \right| + \Xi_o \right) \gamma_{\mathrm{H_4SiO_4}} k_+ a_{\mathrm{SiO_2}} a^2{}_{\mathrm{H_2O}}; \quad \Xi = s\phi \left| \varepsilon_v \right|; \Xi_o = \mathrm{const}; \quad \varepsilon_v < 0 \tag{5}$$

Notably, precipitation at the dissolution site is neglected.

The irreversible strain rate mode is determined by the associated flow rule, whereas its magnitude by the plastic multiplier $\dot{\lambda}$ resulting from the extended Prager's consistency condition, $\dot{f}(\dot{\sigma}_{ij}, \dot{\varepsilon}_q^{irr}, \dot{\xi}) = 0$ (see e.g. Hueckel, 2002). Therefore, the strain rate is a function of the rates of stress and reaction progress

$$\dot{\varepsilon}_{ij}^{irr} = \frac{1}{H}\left(\frac{\partial f}{\partial \sigma_{mn}}\dot{\sigma}_{mn} + \frac{\partial f}{\partial \xi}\dot{\xi}\right)\frac{\partial f}{\partial \sigma_{ij}};\ \ H = -\frac{\partial f}{\partial \varepsilon_q^{irr}}\left[\frac{2}{3}\frac{\partial f}{\partial s_{ij}}\frac{\partial f}{\partial s_{ij}}\right]^{\frac{1}{2}};\ s_{ij} = \sigma_{ij} - \frac{1}{3}\sigma_{kk}\delta_{ij} \tag{6}$$

In particular, at constant stress, an irreversible strain rate is generated proportional to the reaction rate. The yield locus in the form of a set of linear functions for single principal stress components has the advantage of a very simple kinematics, yet capturing the essence of straining,

$$\frac{\sigma_1}{\sigma_{01}} = 1 + \alpha\varepsilon_q - \beta\xi \geq 0,\ \ \frac{\sigma_2}{\sigma_{02}} = 1 + \alpha\varepsilon_q - \beta\xi \geq 0;\ \ \sigma_{01} \geq 0;\ \ \sigma_{02} \leq 0 \tag{7}$$

where α and β are constants, σ_3 remains undetermined. As discussed earlier, ξ is the relative mass removal (its rate is described by eq. (5)). At this point the precipitation term is ignored, as it would lead to a constitutive non-linearity, making it impossible to solve the equation system semi-analytically.

The intra-grain diffusion of silicic acid is limited to the damaged zone, as shown in Fig. 3a. It is described (in radial coordinates with axial symmetry here) by a linear reactive diffusive transport law combined with a mass balance law, with a reaction term (last term of the RHS) through which transport is coupled to deformation via eq. (6):

$$\frac{\partial x_{H_4SiO_4}}{\partial t} = D\left(\frac{\partial^2 x_{H_4SiO_4}}{\partial r^2} + \frac{1}{r}\frac{\partial x_{H_4SiO_4}}{\partial r}\right) + \frac{k_+\left(\Xi\varepsilon_v + \Xi_0\right)}{s} \tag{8}$$

where $x_{H_4SiO_4}$ is molar fraction of aqueous silica in the fluid phase within the grain. Assuming the pore fluid to be a dilute solution, the molar fraction of any of its species *k,* has mass content $m_{kF} = M_{kF}/V_0$, linked to molar fraction, x_{kF} through V_0 which is the reference volume of the entire grain medium. D is the solute diffusion coefficient.

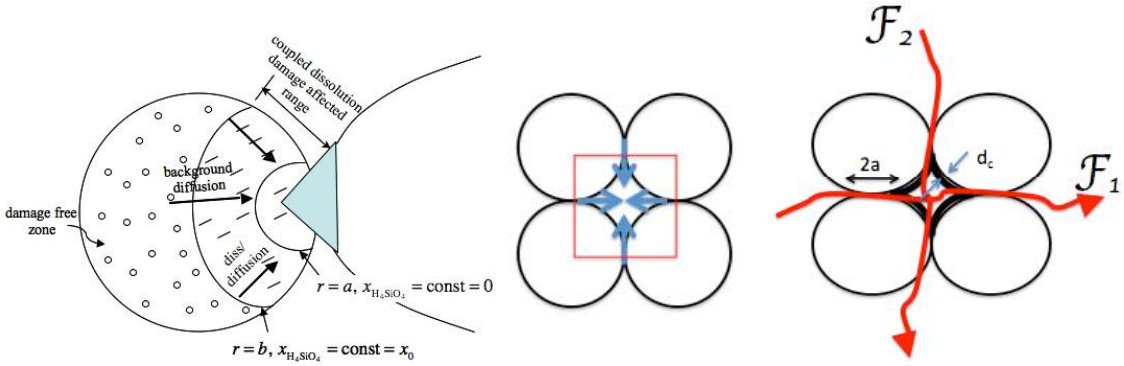

Figure 3. (a) A cartoon showing intra-grain diffusion of the dissolved species; (b) iner-grain pore with the flux of the dissolved silica; (c) pore fluid flow through a dissolution altered meso-scale inter-grain pore system

The above system of constitutive equations is to be supplemented by equilibrium equations and kinematics expression to yield displacements. Hu and Hueckel (2007) provided a solution to the coupled chemo-mechanical deformation-diffusion using an axisymmetrical approximation proposed for the contact problem by Johnson (1985).

3 CHEMO-MECHANICALLY INDUCED EVOLUTION OF PERMEABILITY

In a similar way to the evolution of stiffness, the evolution of permeability is evaluated at the meso-scale, at which we consider as a REV a quadruplet of 1/4th grains, with equal radiuses, *R,* as shown in Fig. 3b.

There are two processes that affect the inter-grain pore system as shown in Fig. 3b: the increase of the contact size between two stressed grains due to chemo-plastic deformation of the grain and the precipitation of the solute within the pore. In terms of porosity variation, the effect of contact area increase is more significant, as seen in Fig. 4a. However, it is an open question if the same is true for the permeability evolution.

The current radius of contact may be approximated as $a=a_0+u_a$ here a_0 is the initial radius of the contact, while u_a is the vertical indentation advancment. Fig. 5 shows the evolution of the radius a in terms of its variable part of u_a as a function of time depending on the dissolution rate constant k_+.

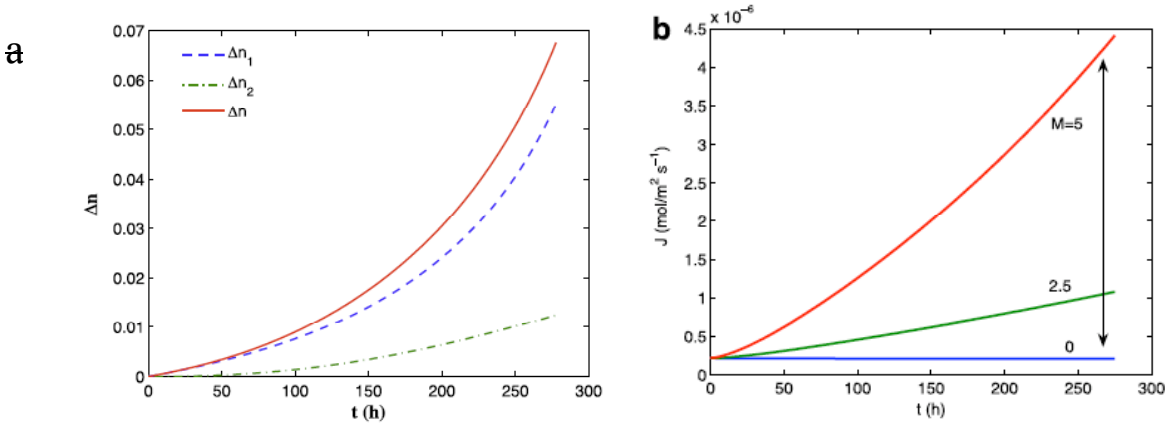

Figure 4. (a) Inter-grain porosity change (Δn), originated from deformation of the grain (Δn_1) and from precipitation induce grain coating; (b) Flux of dissolved silica from a grain as a function of intra-grain mass transfer coefficient $M = \Xi k_+ a^2/Dx_0$, where x_0 is the initial concentration of silicic acid within the grain

The rate of the formation of coating can be calculated as a change in the coating thickness, $\dot{d}_c$ over an area, dS of the free surface, as certain number of moles of silica are precipitated in the water volume, dV,

$$\dot{d}_c = \frac{VOL_{\text{pre}}}{dS} = \frac{MOL_{\text{pre}}\upsilon_{SiO_2}}{dS} = \frac{k\_x_{H_4SiO4}\cdot dV\cdot\upsilon_{SiO_2}}{\upsilon_{H_2O}dS} = \frac{k\_x_{H_4SiO4}\varpi_p\upsilon_{SiO_2}}{\upsilon_{H_2O}} \tag{9}$$

where $\varpi_p = V_{\text{void}}/S_{\text{free}} = (2/\pi - 1/2)R$, υ_{SiO2} and υ_{HO2} are the molar mass of SiO_2 and H_2O, respectively. $x_{H_4SiO_4}(\theta,t)$ is the distribution of precipitating silica determined from a steady state solution of diffusion-precipitation transport eqution, where θ, $-\pi/4<\theta<\pi/4$ is an angular coordinate along the grain surface, with a grain mineral mass flux $\pm f_p(t) = \mp J_a \pi a/4\varpi_p$, as a boundry conditions at the contact points, while J_a *(t)* is the mass flux across the inner boundary of the grain, $r = a$ (see Hu and Hueckel, 2007 for details). As a result of linearization of eq. (9), the coating rate becomes uniformly distributed, i.e. independent of θ.

$$\dot{d}_c = \frac{J_a a \upsilon_{SiO_2}}{R \upsilon_{H_2O}} \tag{10}$$

The relative coating rate $\dot{d}_c$/R is plotted against time in Fig.5b.

The two variables shown in Fig. 5 control the overall change in permeability of the pore system as visualized in Fig. 4c. Notably their dependence with time is different. The change in the contact area appears to accelerate with time, whereas the coating rate increases nearly linearly, after an initial period.

To evaluate the effect of the two factors, a simple formula based on Poisseuille flow through two connected in-series planar tubes of different thickness, will be studied following Hueckel et al. (1997) by examining meso-scale structural changes. Given, that gravity plays an essential role in stress pattern, in which horizontal contacts are usually acted upon by twice as big grain force than the vertical contacts, we shall limit our consideration to conduit denoted as $\mathcal{F}_1$. Explicit data are needed to calculate the permeability evolution as listed in Table 1.

Table 1: Characteristic dimensions of the flow conduit

name	symbol	value
grain size	R	1mm
maximum damage zone	b	0.7mm
size of the indent radius	a_0=b/10	0.07mm
asperity size=contact slit	δ_c	0.05mm
initial (nominal) pore opening	δ_{p0}	0.86mm

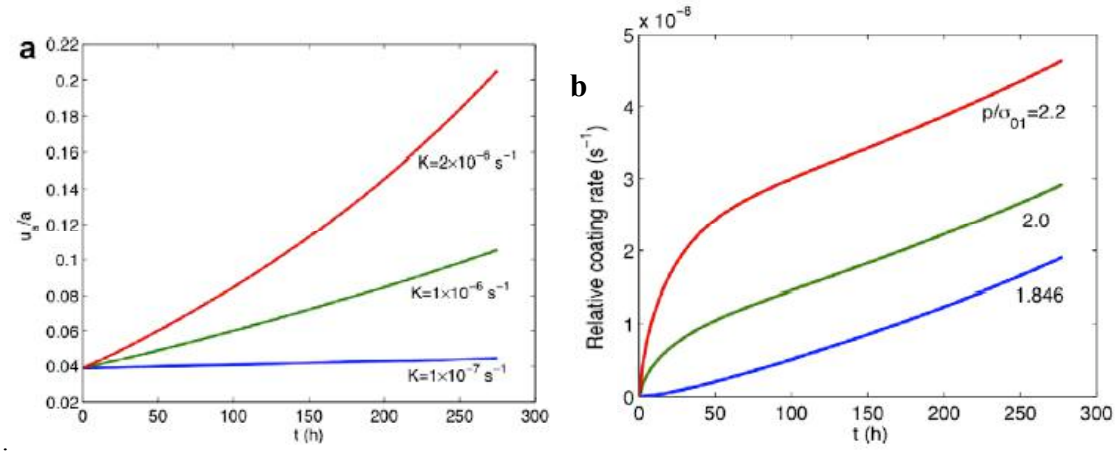

Fig. 5: (a) Increment of the contact area (also grain penetration) as function of time and rate constant; (b) relative coating rate of the walls of inter-grain pore (also of free surfaces of grains) for different values of constant inter-grain pressure. Normalized with respect to grain size, R (calculated for k_+=1x10^{-12}s^{-1}).

The flow is envisioned as occurring through a 2D flat vessel composed of the intergranular slit communicating with the adjacent inter-grain pore, as shown in Fig. 6. The intergrain slit has a very limited opening, equivalent to a size of an asperity, or a piece of mineral depris locked in the contact space. As such it will be assumed not to change during the process of deformation, and enlarging of the contact extent.

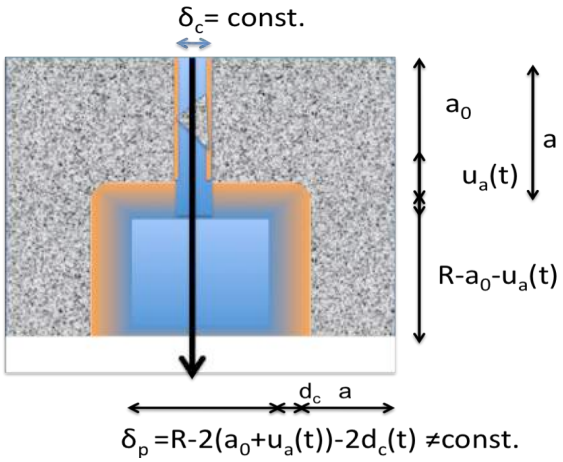

Fig. 6. Schematic of idealized flow conduit F_1 across the inter-grain pore space

Clearly the vessel is a very simplistic representation of the conduit. Especially the shape of the portion representing the iner-grain pore, with its initial size taken as an average between the pore entrance and its maximum, is a major simplification. However, as our goal is to capture main features of the evolution of the flow, following the earlier experience with such models (Hueckel et al., 1997) these simplifications seem acceptable. The specific discharge of the two conduits connected in series, per unit area over which the vessel is the only conduit, in this case 2Rx1, is obtained from the rules of a series connection, which are

$$v_c\delta_c = v_p\delta_p = 2qR; \quad \Delta p = \Delta p_c + \Delta p_p \tag{11}$$

where $\Delta p, \Delta p_c$ *and* Δp_p, are total, contact and pore fluid pressure difference between the exit and entrance to the respective segment of the conduit, where the flow velocities in the contact portion and pore portion, and the one with respect to the entire cross section area, are respectively equal to

$$v_c = -\frac{\delta_c^2}{12\mu}\frac{\Delta p_c}{a_0 + u_a}; \quad v_p = -\frac{\delta_p^2}{12\mu}\frac{\Delta p_p}{R - a_0 - u_a}; \quad \mathrm{q} = -\frac{K^s}{\mu}\frac{\Delta p}{R} \tag{12}$$

where μ is dynamic viscosity of the pore fluid, and K^s is a resultant intrinsic permeability of the medium. Combining (11) and (12) one arrives at the expression for evolution of the specific discharge of the medium expressed in terms of a variable resultant intrinsic permeability, $K^s = \frac{\delta_c^3}{24R}K^t(t)$

$$q = -\frac{\delta_c^3}{24\mu R^2}K^t\Delta p; \qquad K^t(t) = \frac{1}{a(t)/R + (1 - a(t)/R)\left(\frac{\delta_c}{\delta_p(t)}\right)^3} \tag{13}$$

$$a = a_0 + u_a(t); \ \delta_p(t) = R - 2\left(a_0 + u_a(t)\right) - 2d_c(t); \ \dot{d}_c = \frac{J_a(t)a(t)\upsilon_{SiO_2}}{R\upsilon_{H_2O}} \tag{14}$$

where K^t is a coefficient describing the evolution of the intrinsic permeability due to chemo-mechanical coupling in the medium, υ_i denote the molar mass of species "i". As may be easily anticipated from the form of the expression for K^t, the evolution of the permeability will be not much sensitive to the effect of pore coating, until well into an advanced stage when the size of the pore approaches the size of the contact slit, as seen in Fig. 7.

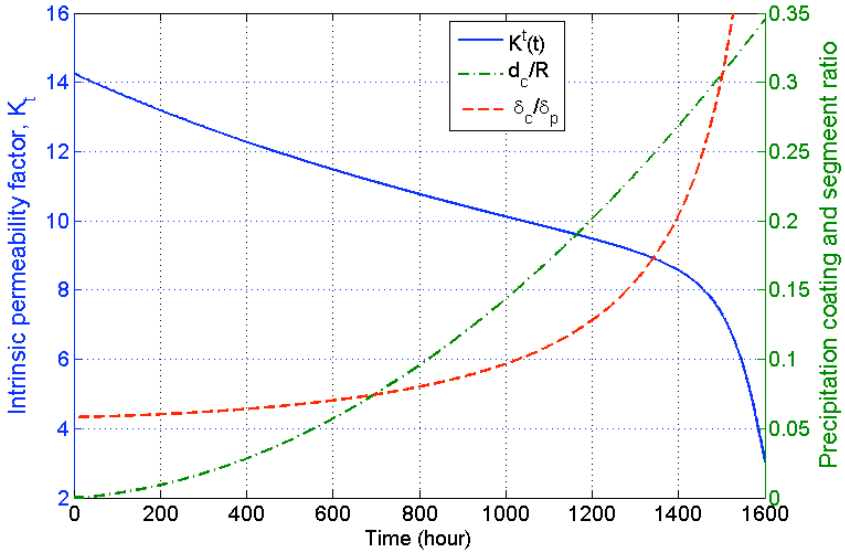

Fig.7: Evolution of permeability: $K^t(t)$-intrinsic permeability factor (left scale); ratio of the thickness of contact slit to the pore size, δ_c/δ_p (right scale); integrated precipitation pore coating d_c/R

The intrinsic permeability factor (time dependent) is seen to decline slightly (30%) in the first 1400 hours mainly due to the increase of the contact area, whereas it seems to be unaffected by the pore wall coating by precipitating mineral. This abruptly changes in a short time, when the pore is practically clogged by the precipitate, and hence its size becomes of the order, and then even smaller than the intergranular contact slit. So, within a few days the permeability drops over one order of magnitude, and more. It is therefore concluded that precipitation is felt very quickly as far as the increase of stiffness is concerned (Hu and Hueckel[6]), while it is not felt in terms of permeability until it reaches a critical moment when permeability drastically drops in a short time. A practical conclusion from the simulation concerns the critical time to clogging that may be easily estimated from the mass dissolution rate needed to produce a solute to fill almost completely the pore.

4 CONCLUSIONS

From the presented analysis it can be seen that the strongest feedforward to permeability evolution is provided by dissolution and damage, hence the chemo-plastic process. Notably, another implication of feedback (1), Fig. 1, regarding the increase of the contact area is not as significant (at least if the hypothesis of asperity is valid). Nevertheless, its effect on reducing the contact stress (not quantified here), may lead to a retardation of the dissolution enhancement. Further reduction of stress may come from generation of a substantial pore pressure, as permeability drastically decreases. Pore pressure, at a constant overburden, reduces the effective stress, and hence the intergranular forces. This slows the process of the mass removal and therefore of chemical softening. In particular circumstances lowering of the effective stress may interrupt temporarily the plastic yielding, introducing elastic pauses,

during which however the dissolution continues, until the decreasing yield limit reaches anew the effective stress state. This feedback mechanism is not included in Fig. 1, which is limited to micro- and meso-scale feedbacks. The presented model is clearly idealized, many constitutive functions are taken as linear, so the actual processes may be oversimplified. Nevertheless, the discussed feedbacks and feedforwards capture the essence of the coupled processes in their basic properties.

In regard to the permeability evolution it is found that while precipitation affects the increase of stiffness relatively early in the process (Hu and Hueckel, 2007), it does not affect permeability until the process reaches a critical moment when permeability drastically drops in a short time. A practical conclusion regards the critical time to clogging that may be easily estimated from the mass dissolution rate needed to produce a solute to fill the pore.

ACKNOWLEDGEMENT

This work was partially supported by US NSF grant CMMI-07-00294.

REFERENCES

Hu, L.B. & Hueckel, T. (2007). "Coupled chemo-mechanics of intergranular contact: toward a three-scale model". Comput Geotech, 34(4):306-327.

Hueckel, T. (2002). "Reactive plasticity for clays during dehydration and rehydration. Part I: Concepts and options". Int. J. Plasticity,18:281-312

Hueckel, T., Kaczmarek, M. & Caramuscio, P. (1997). "Theoretical assessment off fabric and permeability changes in clays affected by organic contaminants". Canadian Geotechnical J., 34:588-603.

Hueckel, T., Cassiani, G., Fan, T., Pellegrino, A.& Fioravante, V. (2001). "Effect of aging on compressibility of oil/gas bearing sediments and their subsidence". J. of Geotechncal and Geoenv. Eng, ASCE, 127(11):926-938.

Hueckel, T., Cassiani, G., Prévost, J.H. & Walters, D.A. (2005). "Field derived compressibility of deep sediments of Northern Adriatic". Proceedings of Seventh International Symposium on Land Subsidence, Shanghai, China, Special Volume, F.B.J. Barends et al. (eds.), 35-50.

Hueckel, T. & Hu, L.B. (2009). "Feedback mechanisms in chemo-mechanical multi-scale modeling of soil and sediment compaction". Computers and Geotechnics, 36:934-943.

Johnson, K.L. (1985). Contact Mechanics. Cambridge University Press, Cambridge, UK.

Lehner, F.K. (1995). "A model for intergranular pressure solution in open systems" Tectonophys., 245:153-70.

Mitchell, J. K., & Solymar, Z.V. (1984). "Time-dependent strength gain in freshly deposited or densified sand". J. Geotech. Engrg., ASCE, 110(11):1559-1576.

Rimstidt, J.D.& Barnes, D.L. (1980). "The kinetics of silica water reaction". Geochim Cosmoch. Acta; 44:1683-1699.

Rutter, E.H. (1976). "The kinetics of rock deformation by pressure solution" Phil. Trans. R. Soc. A, 283:203–219.

A FULLY COUPLED THERMO-HYDRO-MECHANICAL ANALYSIS FOR UNSATURATED SOILS

V. Galavi
Plaxis bv, Delft, the Netherlands

ABSTRACT: *Finite element formulation of thermo-hydro-mechanical analysis is presented in this study. The governing equations are derived for saturated and partially saturated soils. Flow of water in both liquid and gas phase as well as heat flow are considered. The study is based on the assumption that the air pressure is constant and therefore air flow is ignored. A fully implicit scheme is used to solve the problem. Finally, an example is presented to show the capability of the formulation to simulate non-isothermal consolidation.*

1 INTRODUCTION

The need for thermo-hydro-mechanical (THM) codes in civil engineering has kept increasing in the recent years as the technology involving THM processes is expanding continuously. From deep storage of nuclear wastes to geothermal energy management, temperature has become an important part of civil engineering. It has been observed for long time that the hydro-mechanical properties of soils are affected by temperature. Temperature gradient is one of the main causes for movement of heat and water in soil which leads to shrinkage or swelling in soils as the water content changes. For time dependent applications, temperature, pore water pressure and displacements have to be calculated simultaneously in a proper manner. Due to elastoplastic behaviour of soil skeleton and also suction and temperature dependency of parameters (such as saturation, permeability, stiffness and strength), all coefficients of the global stiffness matrix in the finite element formulation of THM analysis are non-linear. Therefore efficient numerical procedures are required, as implemented in PLAXIS 2D (Brinkgreve et al 2010). Accuracy, robustness and efficiency of the calculation depend on the method that selects the time increments. In the THM formulation presented here, a fully implicit scheme is used which has been proven to be unconditionally stable (Booker & Small, 1975).

A key issue in the modelling of the mechanical behaviour of unsaturated soils in a THM analysis is the constitutive model which considers the effect of temperature and suction on the elastic and plastic behaviour of soils. A conceptually similar model to the well-known Barcelona Basic Model (BBM) (Alonso et al., 1990) has been implemented in Plaxis 2D via user defined soil model option which includes suction in irreversible strains (Galavi et al., 2009). However, in this paper only the effect of temperature and suction on the elastic behaviour of soils is considered.

An example for application of this implementation, a non-isothermal consolidation, is presented. The purpose is to measure the influence of ground surface temperature on the

consolidation, in terms of time and changes in suction and water content. This example shows the robustness of the code and its ability to model practical applications

2 GENERAL EQUATIONS

Governing equations of fully coupled thermo-hydro-mechanical (THM) analysis is briefly described for deformable porous media. This is an extension to the previous work (Galavi et al. 2009) in which a fully coupled hydro-mechanical analysis based on Biot's consolidation theory has been developed for saturated and partially saturated soils. Here, non-isothermal saturated and partially saturated water flow (water and vapour) due to the water pore pressure gradients (or capillary pressure above the phreatic line), heat transport due to multiphase advection and conduction and deformation due to change in stresses, pore pressures and temperature are considered. Gas pressure is assumed to be constant in entire domain and the air flow is therefore neglected. This assumption leads to have only one independent unknown in the fluid mass balance equation which is pore water pressure (or capillary pressure). This study is based on the assumption of local thermodynamic equilibrium which means that all phases have the same temperature at a point of the multiphase porous medium.

In the following the governing equations required to describe the THM model, namely water mass balance, heat transport and balance of momentum (equilibrium) equations, are described. Note that the mechanical sign convention is used, i.e. compressive stresses (in the solid and the fluid) are considered to be negative.

2.1 Mass balance equation

The water mass balance can be written in the following form (Rutqvist et al., 2001):

$$n\frac{\partial}{\partial t}\left(S\rho_w+(1-S)\rho_v\right)+\left(S\rho_w+(1-S)\rho_v\right)\left[\frac{\partial\varepsilon_v}{\partial t}+\frac{(1-n)}{\rho_s}\frac{\partial\rho_s}{\partial t}\right]=-\nabla\cdot\left(\underline{J}_w+\underline{J}_v\right) \qquad (1)$$

where ρ_s, ρ_w and ρ_v are the solid, the water and the vapour densities, n is porosity, S is water saturation and ε_v is volumetric strain. $\underline{J}_w$ and $\underline{J}_v$ are the mass flux of water in water phase and in gas phase (vapour), respectively. The definition of the advective mass flux of water $\underline{J}_w$ is based on Darcy's law as:

$$\underline{J}_w=-\rho_w\left(\frac{k_{rel}}{\mu}\underline{\underline{\kappa}}^{\text{int}}\left(\nabla p_w+\rho_w\,\underline{g}\right)\right) \qquad (2)$$

where μ is the dynamic viscosity of the fluid and $\underline{\underline{\kappa}}^{int}$ is the intrinsic permeability of the porous medium. The dynamic viscosity depends on the type of fluid and temperature and the intrinsic permeability is a function of porous structure. In an unsaturated state the coefficient of permeability depends on the soil saturation. The relative permeability $k_{rel}(S)$ is defined as the ratio of the permeability at a given saturation to the permeability in saturated state. $\underline{g} = (0, -g, 0)^T$ is the vector of gravitational acceleration.

The non-advective mass flux of water in gas (vapour flux), $\underline{J}_v$, is computed based on Fick's law as:

$$\underline{J}_v=-\rho_g D_v\nabla\left(\frac{\rho_v}{\rho_g}\right) \qquad (3)$$

where ρ_g is the gas density and D_v is the molecular vapour diffusion coefficient in the porous media. The vapour density ρ_v is related to the temperature dependent saturated vapour density ρ_{vS} via the psychrometric law (Gens et al., 1998):

$$\rho_v = \theta \rho_{vS} \tag{4}$$

where ρ_{vS} is the saturated vapour density which is the density of vapour at phreatic level. The relative humidity θ is defined by:

$$\theta = \exp\left(\frac{p_g - p_l}{\rho_w RT}\right) \tag{5}$$

where T is local equilibrium temperature of the porous medium (K), p_g and p_l are gas and liquid pressures, respectively. By the assumption of atmospheric pressure, $p_w = p_g - p_l$. R is the specific gas constant for water vapour (461.5 J/kgK).

The saturated vapour density is a temperature dependent parameter which can be obtained from empirical relationships. Here the following empirical function (Wang et al., 2009) is adopted:

$$\rho_{vS} = 10^{-3} \exp(19.891 - 4974/T) \tag{6}$$

in which ρ_{vS} is in Kg/m^3.

By the assumption that the gas density is constant in Eq. (3) and substituting Eq. (4) and Eq. (5) into Eq. (3), the mass flux of water in air phase is found:

$$\underline{J}_v = -\left(D_{pv}\nabla p_w + D_{Tv}\nabla T\right) = -\left(\frac{D_v \rho_v}{\rho_w RT}\nabla p_w + f_{Tv} D_v \left(\theta \frac{\partial \rho_{vS}}{\partial T} - \frac{\rho_v p_w}{\rho_w RT^2}\right)\nabla T\right) \tag{7}$$

f_{Tv} is a thermal diffusion factor which is introduced to control effect of temperature on the non-advective water mass flux.

By expanding Eq. (1), the water mass balance equation is derived:

$$\begin{aligned}
&\left[n(\rho_w - \rho_v)\frac{\partial S}{\partial p_w} - nS\rho_w \beta_{wP0} - n(1-S)\frac{\rho_v}{\rho_w RT}\right]\frac{\partial p_w}{\partial t} \\
&+\left[n(\rho_w - \rho_v)\frac{\partial S}{\partial T} - nS\rho_w \beta_{wT0} + n(1-S)\left(\theta \frac{\partial \rho_{vS}}{\partial T} - \frac{\rho_v p_w}{\rho_w RT^2}\right)\right]\frac{\partial T}{\partial t} \\
&-\left[(S\rho_w + (1-S)\rho_v)(1-n)\beta_{sT}\right]\frac{\partial T}{\partial t} \\
&+(S\rho_w + (1-S)\rho_v)\frac{\partial \varepsilon_v}{\partial t} + \nabla \cdot (\underline{J}_w + \underline{J}_v) = 0
\end{aligned} \tag{8}$$

where β_{wP0} and β_{wT0} are the reference compressibility and volumetric thermal expansion of water. The volumetric thermal expansion of water at 293.15 K is 2.1×10^{-4} (1/K). β_{sT} is the volumetric thermal expansion coefficient of soil grains.

2.2 Balance of momentum

For a representative elemental volume of the soil the linear momentum balance is given by:

$$\nabla \cdot (\underline{\sigma}) + \rho \underline{g} = \underline{0} \tag{9}$$

where

$$\rho = (1-n)\,\rho_s + n S\,\rho_w \tag{10}$$

In Eq. (9) $\underline{\sigma}$ is the total stress. For partially saturated soils the total stress can be written in the following form:

$$\underline{\sigma} = \underline{\sigma'} + P\,\underline{m} \tag{11}$$

where $\underline{m}$ = $(1,1,1,0,0,0)^T$ is the identity vector, $\underline{\sigma}'$ is the effective stress and P is the average pore pressure:

$$P = S p_w + (1-S) p_g \tag{12}$$

By substituting the average pore pressure into Eq. (11) we have:

$$\underline{\sigma} = \underline{\sigma'} + \left(S p_w + (1-S) p_g\right)\underline{m} \tag{13}$$

If the degree of saturation is replaced by the matric suction coefficient χ, the well-known Bishop's stress (Bishop & Blight, 1963) is obtained:

$$\underline{\sigma} = \underline{\sigma'} + \left(\chi p_w + (1-\chi) p_g\right)\underline{m} \tag{14}$$

χ is an experimentally determined factor which depends on degree of saturation, porosity, and the matric suction. As the pore gas pressure is assumed to be constant and equal to the atmospheric pressure, the pore gas pressure can be neglected. Therefore the Bishop's stress (average stress) can be simplified as:

$$\underline{\sigma} = \underline{\sigma'} + \chi p_w \underline{m} \tag{15}$$

The constitutive relation using the effective stress $\underline{\sigma}'$ is written in the following form:

$$d\underline{\sigma'} = \underline{\underline{M}}\left(d\underline{\varepsilon} - d\underline{\varepsilon}_T\right) \tag{16}$$

$\underline{\underline{M}}$ represents the material stress-strain matrix. $\underline{\varepsilon}$ is the total strain of the skeleton and $\underline{\varepsilon}_T$ is thermal strain caused by temperature increase. The thermal strain can be found from:

$$d\underline{\varepsilon}_T = \underline{\underline{B}}_{DT}\,\underline{m}\cdot dT = \begin{bmatrix} \beta_{DT,x} & 0 & 0 & 0 & 0 & 0 \\ 0 & \beta_{DT,y} & 0 & 0 & 0 & 0 \\ 0 & 0 & \beta_{DT,z} & 0 & 0 & 0 \\ 0 & 0 & 0 & 0 & 0 & 0 \\ 0 & 0 & 0 & 0 & 0 & 0 \\ 0 & 0 & 0 & 0 & 0 & 0 \end{bmatrix} \underline{m}\cdot dT \tag{17}$$

where $\beta_{DT,x}$, $\beta_{DT,y}$ and $\beta_{DT,z}$ are the drained linear thermal expansion coefficient of soil skeleton (1/K) in x, y and z directions, respectively, which vary between 0.5×10^{-6} and 12×10^{-6} (1/K) depending on the type of the soil or rock. Khalili et al. (2010) showed that the thermal expansion coefficient of soils grains is the same as the skeletal thermal expansion coefficient of homogenous porous media. Therefore:

$$\beta_{sT} = \beta_{DT,x} + \beta_{DT,y} + \beta_{DT,z} \tag{18}$$

The constitutive relation (16) can be written as:

$$d\underline{\sigma}' = \underline{\underline{M}}\left(d\underline{\varepsilon} - \underline{\underline{B}}_{DT}\,\underline{m}\cdot dT\right) \tag{19}$$

The governing equation for the deformation model is then obtained:

$$\nabla\cdot\left[\underline{\underline{M}}\left(d\underline{\varepsilon} - \underline{\underline{B}}_{DT}\,\underline{m}\cdot dT\right) + \chi\, dp_w\,\underline{m}\right] + d\left(\rho\underline{g}\right) = 0 \tag{20}$$

2.3 Heat transport

The heat balance equation for the porous medium can be written in the following form (i.e. Rutqvist et al., 2001):

$$C\rho\frac{\partial T}{\partial t} = \nabla\cdot\left(\underline{J}_c + \underline{J}_{Aw}\right) + Q_T \tag{21}$$

in which $\underline{J}_{\mathrm{Aw}}$ and $\underline{J}_{\mathrm{c}}$ are the advective internal energy flux in water and the conductive heat flux in the porous medium, respectively. Q_T is the heat source term, i.e. heat generation rate per unit volume. $\mathrm{C}\rho$ is the heat capacity of the porous medium:

$$C\rho = (1-n)C_s\rho_s + nSC_w\rho_w + n(1-S)C_v\rho_v \tag{22}$$

where C_s, C_w and C_v are the solid, the water and the vapour specific heat capacities.

The conductive heat flow is assumed to be governed by Fourier's law:

$$\underline{J}_c = -\lambda\nabla T \tag{23}$$

where λ is the thermal conductivity of the porous medium:

$$\lambda = (1-n)\lambda_s + nS\lambda_w + n(1-S)\lambda_v \tag{24}$$

where λ_s, λ_w and λ_v are the solid, the water and the vapour thermal conductivities.

The advective internal energy flux in water is:

$$\underline{J}_{Aw} = C_w T \underline{J}_w = -\rho_w C_w T \left(\frac{k_{rel}}{\mu} \underline{\underline{\kappa}}^{\text{int}} \left(\nabla p_w + \rho_w \underline{g} \right) \right) \tag{25}$$

By expanding Eq. (21) and considering air temperature at the ground surface as boundary conditions, the governing equation on heat transport can therefore be written as:

$$\begin{aligned} & C\rho \frac{\partial T}{\partial t} + \nabla \cdot (\lambda \nabla T) + \rho_w C_w \left[\frac{k_{rel}}{\mu} \underline{\underline{\kappa}}^{\text{int}} \left(\nabla p_w + \rho_w \underline{g} \right) \right] \cdot \nabla T \\ & + \rho_w C_w T \left[\nabla \cdot \left(\frac{k_{rel}}{\mu} \underline{\underline{\kappa}}^{\text{int}} \left(\nabla p_w + \rho_w \underline{g} \right) \right) \right] - Q_T + C_{as} (T - T_a) = 0 \end{aligned} \tag{26}$$

where T_a is the air temperature and C_{as} (W/m^{2}K) is the convective heat transfer coefficient at the surface in contact with air (Al-Khoury et al., 2005).

3 FINITE ELEMENT FORMULAITON

3.1 Discretization in space

The finite element formulation of thermo-hydro-mechanical analysis, as implemented in PLAXIS 2D, is obtained by applying Galerkin's procedure of weighted residuals to Eq. (8), Eq. (20) and Eq. (26). The spatial discretization yields the following system of equations, Eq. (27). The unknowns are displacements of the solid skeleton ($\underline{v}$), pore water pressure (p_w) and temperature (T).

$$\begin{bmatrix} \underline{\underline{K}}_{vv} & \underline{\underline{K}}_{vP} & \underline{\underline{K}}_{vT} \\ \underline{\underline{C}}_{Pv} & \underline{\underline{C}}_{PP} & \underline{\underline{C}}_{PT} \\ 0 & 0 & \underline{\underline{C}}_{TT} \end{bmatrix} \begin{bmatrix} \frac{d\underline{v}}{dt} \\ \frac{dp_w}{dt} \\ \frac{dT}{dt} \end{bmatrix} = \begin{bmatrix} 0 & 0 & 0 \\ 0 & \underline{\underline{K}}_{PP} & \underline{\underline{K}}_{PT} \\ 0 & \underline{\underline{K}}_{TP} & \underline{\underline{K}}_{TT} \end{bmatrix} \begin{bmatrix} \underline{v} \\ p_w \\ T \end{bmatrix} + \begin{bmatrix} \frac{d\,\underline{f}_u}{dt} \\ \underline{G}_p + \underline{q}_p \\ \underline{G}_T + \underline{q}_T + \underline{Q}_T \end{bmatrix} \tag{27}$$

In general, the interpolation functions $\underline{\underline{N}}$ for displacements, pore water pressure and temperature can be considered to be different. However, in the formulation presented here, the same interpolation functions are used for displacements, pore water pressure and temperature. The matrices in Eq. (27) are listed as follows:

$$\underline{\underline{K}}_{vv} = \int_V \underline{\underline{B}}^T \underline{\underline{\underline{M}}}\, \underline{\underline{B}}\, dV \tag{28}$$

$$\underline{\underline{K}}_{vP} = \int_V \chi \underline{\underline{B}}^T \underline{m} \underline{\underline{N}} dV \tag{29}$$

$$\underline{\underline{K}}_{vT} = -\int_V \underline{\underline{B}}^T \underline{\underline{\underline{M}}}\, \underline{\underline{\underline{B}}}_{DT}\, \underline{m} \underline{\underline{N}}\, dV \tag{30}$$

$$\underline{f}_u = \int_V \underline{\underline{N}}^T \Delta \underline{b}\, dV + \int_S \underline{\underline{N}}^T \Delta \underline{t}\, dS \tag{31}$$

$$\underline{\underline{C}}_{Pv} = \int_V \underline{\underline{N}}^T \left(S\rho_w + (1-S)\rho_v\right)\underline{\underline{L}}\,\underline{\underline{N}} dV \tag{32}$$

$$\underline{\underline{C}}_{PP} = \int_V \underline{\underline{N}}^T \left[n(\rho_w - \rho_v)\frac{\partial S}{\partial p_w} - nS\rho_w\beta_{wP0} - n(1-S)\frac{\rho_v}{\rho_w RT}\right]\underline{\underline{N}} dV \tag{33}$$

$$\underline{\underline{C}}_{PT} = \int_V \underline{\underline{N}}^T \left[\begin{array}{l} n(\rho_w - \rho_v)\dfrac{\partial S}{\partial T} - nS\rho_w\beta_{wT0} + n(1-S)\left(\theta\dfrac{\partial \rho_{vS}}{\partial T} - \dfrac{\rho_v p_w}{\rho_w RT^2}\right) \\ -\left(S\rho_w + (1-S)\rho_v\right)(1-n)\beta_{sT} \end{array}\right]\underline{\underline{N}} dV \tag{34}$$

$$\underline{\underline{K}}_{PP} = \int_V (\nabla \underline{\underline{N}})^T \rho_w \frac{k_{rel}}{\mu}\underline{\underline{\kappa}}^{\text{int}} \nabla \underline{\underline{N}}\, dV + \int_V (\nabla \underline{\underline{N}})^T \frac{D_v \rho_v}{\rho_w RT}\nabla \underline{\underline{N}}\, dV \tag{35}$$

$$\underline{\underline{K}}_{PT} = \int_V (\nabla \underline{\underline{N}})^T f_{Tv} D_v \left(\theta\frac{\partial \rho_{vS}}{\partial T} - \frac{\rho_v p_w}{\rho_w RT^2}\right)\nabla \underline{\underline{N}}\, dV \tag{36}$$

$$\underline{G}_p = \int_V (\nabla \underline{\underline{N}})^T \rho_w \frac{k_{rel}}{\mu}\underline{\underline{\kappa}}^{\text{int}}\, \rho_w\, \underline{g}\, dV \tag{37}$$

$$\underline{q}_p = -\int_\Gamma \underline{\underline{N}}\ \hat{J}_w \underline{n} dS \tag{38}$$

$$\underline{\underline{C}}_{TT} = \int_V \underline{\underline{N}}^T C\rho \underline{\underline{N}} dV \tag{39}$$

$$\underline{\underline{K}}_{TP} = -\int_V (\nabla \underline{\underline{N}})^T \left(\rho_w C_w T \frac{k_{rel}}{\mu}\underline{\underline{\kappa}}^{\text{int}}\right)\nabla \underline{\underline{N}} dV \tag{40}$$

$$\underline{\underline{K}}_{TT} = -\int_V (\nabla \underline{\underline{N}})^T \lambda \nabla \underline{\underline{N}}\, dV - \int_V \underline{\underline{N}}^T \left[\rho_w C_w \frac{k_{rel}}{\mu}\underline{\underline{\kappa}}^{\text{int}}(\nabla p_w + \rho_w \underline{g})\right]\nabla \underline{\underline{N}} dV - \int_S \underline{\underline{N}}^T C_{as}\underline{\underline{N}} T dS \tag{41}$$

$$\underline{G}_T = -\int_V (\nabla \underline{\underline{N}})^T \rho_w C_w T \frac{k_{rel}}{\mu}\underline{\underline{\kappa}}^{\text{int}}\rho_w\, \underline{g} dV \tag{42}$$

$$\underline{q}_T = \int_S \underline{\underline{N}}^T J_T \underline{n} dS + \int_S \underline{\underline{N}}^T C_{as} T_a dS \tag{43}$$

$$\underline{Q}_T = \int_V \underline{\underline{N}}^T Q_T dV \tag{44}$$

3.2 Discretization in time

Discretization in the time domain is performed by using a fully implicit finite difference scheme. Equation (27) can be integrated in time, using a first order finite difference method. Application of this procedure yields:

$$\left[\begin{array}{ccc} \underline{\underline{K}}_{vv} & \underline{\underline{K}}_{vP} & \underline{\underline{K}}_{vT} \\ \underline{\underline{C}}_{Pv} & \underline{\underline{C}}^*_{PP} & \underline{\underline{C}}^*_{PT} \\ 0 & -\Delta t\underline{\underline{K}}_{TP} & \underline{\underline{C}}^*_{TT} \end{array}\right]^{i+1}\left[\begin{array}{c} \Delta \underline{v} \\ \Delta p_w \\ \Delta T \end{array}\right] = \left[\begin{array}{ccc} 0 & 0 & 0 \\ 0 & \Delta t\underline{\underline{K}}_{PP} & \Delta t\underline{\underline{K}}_{PT} \\ 0 & \Delta t\underline{\underline{K}}_{TP} & \Delta t\underline{\underline{K}}_{TT} \end{array}\right]^{i+1}\left[\begin{array}{c} \underline{v}^i \\ p_w{}^i \\ T^i \end{array}\right] + \left[\begin{array}{c} \Delta \underline{f}_u \\ \Delta t(\underline{G}_p + \underline{q}_p) \\ \Delta t(\underline{G}_T + \underline{q}_T + \underline{Q}_T) \end{array}\right] \tag{45}$$

where

$$\underline{\underline{C}}^*_{PP} = \left(\underline{\underline{C}}_{PP} - \Delta t\underline{\underline{K}}_{PP}\right) \tag{46a}$$

$$\underline{\underline{C}}^*_{PT} = \left(\underline{\underline{C}}_{PT} - \Delta t\underline{\underline{K}}_{PT}\right) \tag{46b}$$

$$\underline{\underline{C}}^{*}_{TT} = \left(\underline{\underline{C}}_{TT} - \Delta t \underline{\underline{K}}_{TT}\right) \tag{46c}$$

where Δt is the time step. $\underline{v}^i$, ${p_w}^i$ and T^i denote values at the beginning of a time step.

The system of equation presented in equation 45 is highly non-linear due to suction dependent degree of saturation, suction and temperature dependent permeability, elastoplastic behaviour of soil skeleton and pore pressure and temperature dependent density of vapour.

4 RETENTION CURVE

To describe the hydraulic behaviour of unsaturated soils, the well-known Van Genuchten model (Van Genuchten, 1980) is used. Van Genuchten function is a three-parameter equation and relates saturation to suction head:

$$S = S_{res} + (S_{sat} - S_{res})\left[1 + \left(g_a \frac{p_w}{\gamma_w}\right)^{g_n}\right]^{g_c} \tag{47}$$

where g_a, g_n and g_c are fitting parameters, which have to be measured for a specific material by fitting the experimentally obtained water-suction retention curve. g_c is often used as $(1/g_n – 1)$. S_{res} is the residual degree of saturation at very high value of suction and S_{sat} is the degree of saturation of saturated soil. In general at saturated conditions the pores will not be completely filled with water, therefore S_{sat} can be less than 1.

The relative permeability (k_{rel}) is related to suction pore pressure by:

$$k_{rel} = (S_e)^{g_l}\left(1 - \left[1 - S_e^{\left(-\frac{1}{g_c}\right)}\right]^{(-g_c)}\right)^2 \tag{48}$$

where g_l is a fitting parameter and S_e is called effective saturation and is obtained by

$$S_e = \frac{S - S_{res}}{S_{sat} - S_{res}} \tag{49}$$

In this study the matric suction coefficient χ is assumed to be equal to the effective saturation.

It should be noted that the effect of temperature on the retention curve is not considered in this study.

5 EXAMPLE

In this section one-dimensional non-isothermal consolidation of partially saturated soil is simulated with the proposed formulations. An elastic material is used in this example and therefore the effect of temperature on the stiffness is ignored. To show the effect of phase change two cases are considered. In *case a*, phase change is ignored while in *case b* this phenomena is considered. Figure 1 shows the geometry and the boundary conditions of the model. The example consists of a column which is 10 m high (Figure 1). All boundaries excepting the top boundary are closed for heat flow.

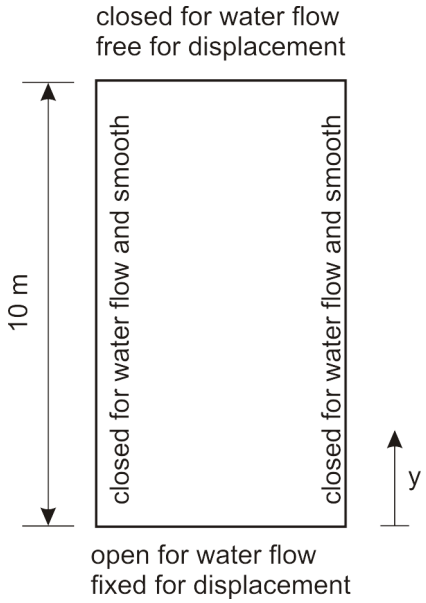

Fig. 1. Geometry and boundary conditions for one dimensional non-isothermal consolidation

The initial temperature is 293.15 K. A linear distribution of suction is assumed in the column as initial condition for water pore pressure (100 kPa at the top of the model and 0 at the bottom). Table 1 gives the material properties. To describe the mechanical behaviour of soil, a linear elastic constitutive model is utilised.

To simulate this example, the initial pore pressure is applied to calculate the initial stresses. This phase is performed by an uncoupled plastic calculation. To simulate the non-isothermal consolidation, the temperature of top boundary is suddenly set to 343.15 K. The consolidation is calculated for 100 days.

Table 1. Material data used for non-isothermal consolidation

parameter		Unit	Value
γ_{sat}	Saturated soil weight	[kN/m^3]	18.0
γ_{dry}	Dry soil weight	[kN/m^3]	16.0
k_x & k_y	Permeability	[m/day]	0.04752
ν	Poisson's ratio	[-]	0.2
E	Young's modulus	[kPa]	5000
n	Porosity	[-]	0.5
β_{wP0}	Compressibility of water	[kPa^{-1}]	9.76×10^{-6}
C_s	Solid heat specific capacity	[kJ/kgK]	0.718
C_w	Water heat specific capacity	[kJ/kgK]	4.1813
C_v	Vapour heat specific capacity	[kJ/kgK]	1.0035
λ_s	Solid thermal conductivity	[W/mK]	1.5
λ_w	Water thermal conductivity	[W/mK]	0.6
λ_v	Vapour thermal conductivity	[W/mK]	0.025
β_{DT} (x,y,z)	Linear thermal expansion of grains	[1/K]	1×10^{-6}
D_v	Vapour diffusion coefficient	[m^2/day]	1×10^{-11}
f_{Tv}	Thermal diffusion factor	[-]	1.0
g_a	Retention curve fitting parameter	[1/m]	0.8
g_n	Retention curve fitting parameter	[-]	1.09
g_l	Retention curve fitting parameter	[-]	0.5
S_{res}	Residual saturation	[-]	0.179

Figure 2 and 3 show the distribution of water pore pressure and degree of saturation for cases a and b, respectively. Figure 4 shows the settlement of a node at the top of the column for both cases. It follows from the curves that when water changes into vapour, water saturation decreases and suction increases. This leads to have more settlement in this case because of increase in effective stresses.

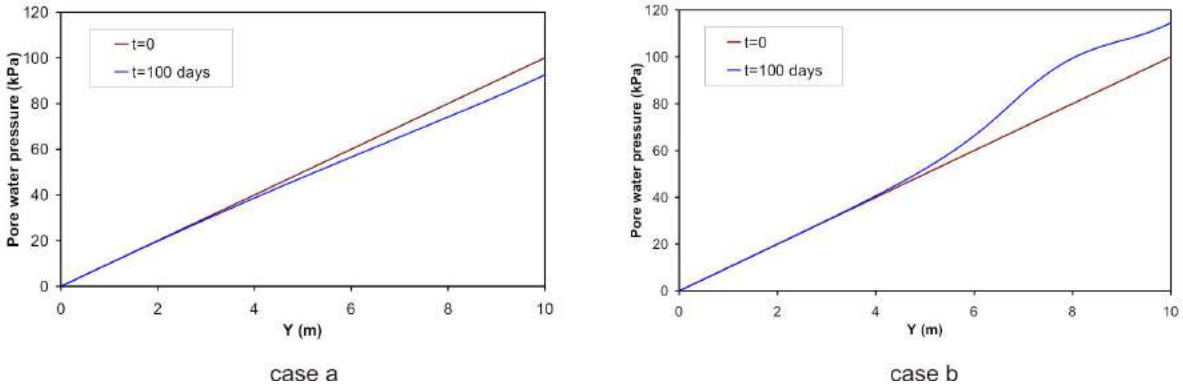

Fig. 2. Distribution of pore water pressure for cases a and b

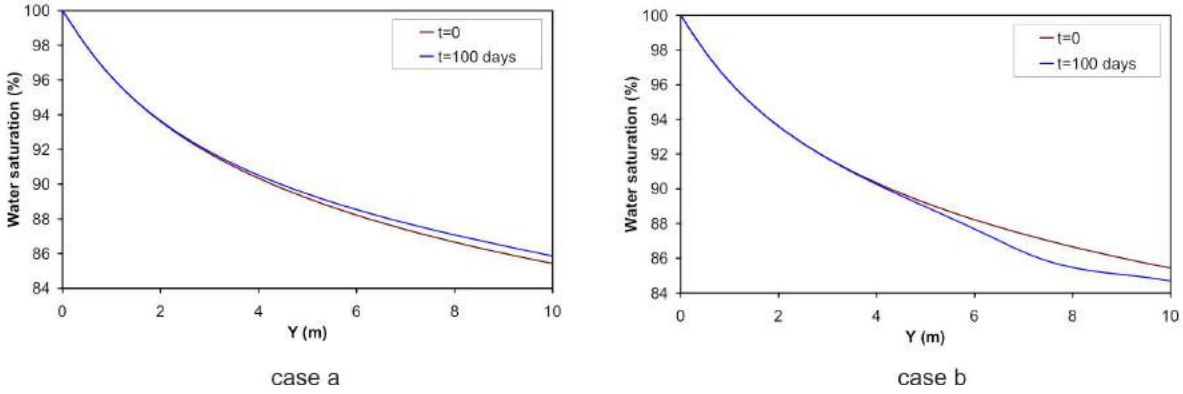

Fig. 3. Distribution of degree of saturation for cases a and b

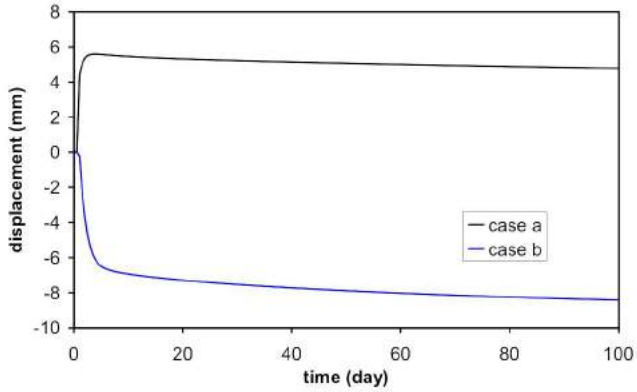

Fig. 4 Displacement at the top of the column during consolidation

6 CONCLUSION

Formulations of fully coupled thermo-hydro-mechanical analysis for saturated and partially saturated soils have been presented. It has been shown that the model is able to take into account the effects of suction and temperature on the mechanical behaviour of soils. The model is capable of considering phase change (water to vapour) which has been illustrated by means of an example. As illustrated, for the particular soil, the effect of phase change can be significant.

ACKNOWLEDGEMENT

The author would like to thank Dr. Paul G. Bonnier and Dr. A. Haxaire, Plaxis BV, for their valuable suggestions during the implementation of the THM code in PLAXIS 2D code.

REFERENCES

Al-Khoury, R., Bonnier, P.G. & Brinkgreve, B.J. (2005), "Efficient finite element formulation for geothermal heating systems. Part I: Steady state". Int. J. Numer. Meth. Engng, 63, 988-1013.

Alonso, E.E.; Gens, A. & Josa, A. (1990), "A constitutive model for partially saturated soils". Géotechnique, 40, 405-430.

Bishop, A.W. & Blight, A.K.G. (1963), "Some aspects of effective stress in saturated and partially saturated soils". Géotechnique, 13, 177-197.

Booker, J.R. & Small, J.C. (1975), "An investigation of the stability of numerical solutions of Biot's equations of consolidation". Int. J. Solids Struct., 11, 907-917.

Brinkgreve, R.B.J; Engin, E. & Swolfs, W. M. (2010), PLAXIS 2D, Finite element code for soil and rock analyses, users manual. The Netherlands.

Galavi, V., Brinkgreve, R.B.J., Bonnier, P.G. & Gonzalez, N.A. (2009), "Fully coupled hydro-mechanical analysis of unsaturated soils", Proceeding of Computational Geomechanics I (ComGeo I), Juan-les-Pins, France, 486-495, IC2E International Center for Computational Engineering, Rhodes, Greece.

Gens, A., Garcia-Molina, A. J., Olivella, S., Alonso, E. E. & Huertas, F. (1998), "Analysis of a full scale in situ test simulating repository conditions". International Journal for Numerical and Analytical Methods in Geomechanics, 22: 515-548.

Khalili, N., Uchaipichat, A. & Javadi, A.A. (2010), "Skeletal thermal expansion coefficient and thermo-hydro-mechanical constitutive relations for saturated homogeneous porous media". Mechanics of Materials, 42: 593-598.

Rutquist, J., Borgesson, L., Chijimatsu, M., Kobayashi, A., Jing, L., Nguyen, T.S., Noorishad, J. & Tsang, C.-F. (2001), "Thermohydromechanics of partially saturated geological media: governing equations and formulation of four finite element models". International Journal of Rock Mechanics & Mining Sciences, 38: 105-127.

Van Genuchten, M.T. (1980), "A closed-form equation for predicting the hydraulic conductivity of unsaturated soil". Soil Science Society of America Journal, 44, 892-898.

Wang, W., Kosakowski, G. & Kolditz, O. (2009). "A parallel finite element scheme for thermo-hydro-mechanical (THM) coupled problems in porous media". Computers and Geotechnics, 35: 1631-1641.

MULTI-SCALE MODELING OF PERMEABILITY EVOLUTION IN THE EXCAVATION DAMAGED ZONE AROUND TUNNELS

Séverine Levasseur, Frédéric Collin, Robert Charlier
Department ArGEnCo, Université de Liège (ULg), Liège, Belgium

Djimédo Kondo
Institut d'Alembert, Université Pierre et Marie Curie (UPMC), Paris, France

ABSTRACT: *A zone with significant irreversible deformations and significant changes in flow and transport properties is expected to be formed in indurated clay around underground excavations. The stress perturbation around the excavation could lead to a significant increase of the permeability, related to diffuse and/or localized crack propagation in the material. The main objective of the study is to model these processes at large scale with a micromechanical damage approach, based on the Ponte-Castaneda and Willis approximation (PCW) in the presence of initial stress, in order to assess the crack impacts on the performance of radioactive waste geological repositories. Combined with this model, permeability tensor is described as a function of micromechanical damage that is generated during the excavation. Advantages and drawbacks of this approach are described thanks to the results on Opalinus Clay and of the Selfrac long term dilatometer experiment.*

1 INTRODUCTION

Excavation of underground structures in rock masses creates a perturbed zone, named Excavation Damaged Zone (EDZ), where geotechnical and hydro-geological properties are altered. These perturbations correspond to significant changes in flow and transport properties (one or more orders of magnitude increase in flow permeability) resulting in macro and micro-fracturing and a rearrangement of rock structures. In the context of radioactive waste disposal, as the potential host rocks must be characterized by a very low hydraulic conductivity, EDZ has the main implications for the operation and long term performance of underground repository and its behavior needs to be well understood. The general hydro-mechanical behavior of host rocks like over-consolidated clay depends mainly on the stress history, the stiffness, the strength and its undisturbed structure. But it is also influenced by the presence and the orientation of discontinuities or micro-cracks, which result in elastic stiffness reduction and variations of permeability. Modeling of such behavior is generally performed by considering purely macroscopic models (see for instance Levasseur et al. 2010). However, as recent developments in homogenization of microcracked media provides now physical and mathematical models for the description of damage induced anisotropy, as well as cracks closure effects (Dormieux et al. 2006; Dormieux & Kondo 2009; Zhu et al. 2009; Levasseur et al. 2010), the idea of this study is to test the performance of this method for EDZ modeling. Behavior of this zone is mainly considered in this paper through the formulation of a micromechanical anisotropic damage model; illustration focuses on the indurated Opalinus Clay of Mont Terri underground research laboratory in

Switzerland. The micromechanical anisotropic damage model is based on Ponte-Castaneda and Willis homogenization scheme (Ponte-Castaneda & Willis 1995), which takes into account initial stresses and ensures a good compromise between mechanics and transport characteristics in cracked media. The paper is organized as follows. In Section 2, the basic principles of the micromechanical modeling, applied to the case of an elastic matrix weakened by an arbitrary distribution of microcracks, are presented. Later, a constitutive law for anisotropic microcracked media taking into account initial stresses is developed. An estimation of permeability evolution in EDZ is also proposed, based on micromechanical considerations. In Section 3, identification of Opalinus Clay parameters from some triaxial tests is discussed and the framework is then applied to model the in situ experiment SELFRAC. Finally, a discussion on the reliability of micromechanical modeling of the behavior of Opalinus Clay is provided.

2 MICROMECHANICAL MODELING OF DAMAGE PROCESS AND TRANSPORT PROPERTIES

2.1 Principle of the micromechanical modeling of damage

The proposed micromechanical modeling including initial stresses is based on a representative elementary volume (*rev*, Ω) made up of a solid matrix s (occupying a domain Ω^s) and an arbitrary system of inhomogeneous inclusions; each inclusion family is denoted I and occupies a domain Ω^I. The matrix and the inclusions behaviors are supposed elastic whereas an initial uniform stress field $\boldsymbol{\sigma_0}$ is assumed in the solid matrix occupying a domain Ω^s. The *rev* is subjected to uniform strain boundary conditions :

$$\partial\Omega \ : \ \underline{\xi} = \mathbf{E} \cdot \underline{z} \tag{1}$$

where the quantity $\underline{z}$ denotes the vector position, $\underline{\xi}$ the displacement vector, and $\mathbf{E}$ the macroscopic strain tensor. Following the ideas developed in Levasseur et al. (2010), it is convenient to formulate the problem of homogenization with initial stresses in a unified way by considering the stress tensor field $\boldsymbol{\sigma}(\underline{z})$, everywhere in the *rev*, in an affine form:

$$(\underline{z} \in \Omega) \quad \boldsymbol{\sigma}(\underline{z}) = \mathbb{C}(\underline{z}) : \boldsymbol{\varepsilon}(\underline{z}) + \boldsymbol{\sigma}^p(\underline{z}) \tag{2}$$

where $\mathbb{C}(\underline{z})$ is a heterogeneous stiffness, and $\boldsymbol{\sigma}^p(\underline{z})$ a prestress tensor such as:

$$\mathbb{C}(\underline{z}) = \begin{cases} \mathbb{C}^I & in \ \ (\Omega^I) \\ \mathbb{C}^s & in \ \ (\Omega^s) \end{cases} \quad \boldsymbol{\sigma}^p(\underline{z}) = \begin{cases} \boldsymbol{\sigma_0} & in \ \ (\Omega^s) \\ 0 & in \ \ (\Omega^I) \end{cases} \tag{3}$$

This problem can be solved by using the classical Levin's theorem ((Levin 1967) and (Laws 1973)). It results the first state law:

$$\boldsymbol{\Sigma} = (\mathbb{C}^s : \mathbf{E} + \boldsymbol{\sigma_0}) : \left[\mathbb{I} + \mathbb{C}^{s^{-1}} : (\mathbb{A} + \mathbb{A} : \mathbb{B} : \mathbb{A})\right] \tag{4}$$

and the PCW scheme-based estimate of the energy potential takes the form:

$$\Psi = \frac{1}{2}\mathbf{E} : \mathbb{C}^s : \mathbf{E} + \boldsymbol{\sigma_0} : \mathbf{E} + \left(\frac{1}{2}\mathbf{E} + \boldsymbol{\sigma_0} : \mathbb{C}^{s^{-1}}\right) : (\mathbb{A} + \mathbb{A} : \mathbb{B} : \mathbb{A}) : \mathbf{E} \tag{5}$$

with $\mathbb{A}$ is a localization tensor derived from the dilute approximation (Levasseur et al. 2010):

$$\mathbb{A} = -\sum_{r=1}^{N} \varphi^r \mathbb{C}^s : (\mathbb{I} - \mathbb{S}^r)^{-1} \tag{6}$$

$\mathbb{S}^r$ the Eshelby tensor and $\varphi^r = \frac{4\pi}{3} w_r d^r$, in which w_r being radius of cracks belonging to the r^{th} family. $|\Omega|$ being the volume of the *rev* and a^r the crack length, the quantity $d^r = \frac{(a^r)^3}{|\Omega|}$ represents the cracks density parameter already introduced by Budiansky & O'Connell (1976).
$\mathbb{B}$ is a 4^{th} order tensor which characterized the effect of the crack spatial distribution:

$$\mathbb{B} = \mathbb{P}_d : (\mathbb{I} - \mathbb{A} : \mathbb{P}_d)^{-1} \tag{7}$$

with $\mathbb{P}_d$ for a spherical distribution of cracks is given by the isotropic tensor:

$$\mathbb{P}_d = \frac{\alpha}{3k^s}\mathbb{J} + \frac{\beta}{2\mu^s}\mathbb{K} \quad \text{with } \alpha = \frac{3k^s}{3k^s + 4\mu^s} \text{ and } \beta = \frac{6(k^s + 2\mu^s)}{5(3k^s + 4\mu^s)} \tag{8}$$

The damage yield function is written by considering the thermodynamical force $\mathcal{F}^{d^r}$ associated to each d^r (obtained as the negative of the derivative of Ψ with respect to d^r):

$$\mathcal{F}^{d^r} = -\frac{\partial \Psi}{\partial d^r} = -\left(\frac{1}{2}\mathbf{E} + \boldsymbol{\sigma_0} : \mathbb{C}^{s^{-1}}\right) : \frac{\partial \mathbb{C}^{hom}}{\partial d} : \mathbf{E} \tag{9}$$

where:

$$\mathbb{C}^{hom} = \mathbb{C}^s + \mathbb{A} + \mathbb{A} : \mathbb{B} : \mathbb{A} \tag{10}$$

Considering this simple damage criterion:

$$f^r(\mathcal{F}^{d^r}, \underline{d}) = \mathcal{F}^{d^r} - \mathcal{R}(d^r) \leq 0 \tag{11}$$

where $\mathcal{R}(d^r) = h_0(1 + \eta d^r)$ is the local resistance to the damage propagation, the damage evolution law reads by assuming a damage normality rule $\dot{f}^r = 0$. It results, like in the dilute scheme (Levasseur et al. 2010), the rate form of the constitutive damage law:

$$\dot{\boldsymbol{\Sigma}} = \mathbb{C}_t^{hom} : \dot{\mathbf{E}} \tag{12}$$

with

$$\mathbb{C}_t^{hom} = \mathbb{C}^{hom} - \sum_{r=1}^{N} H^r \frac{\left[(\mathbf{E} + \boldsymbol{\sigma_0} : \mathbb{C}^{s^{-1}}) : \dfrac{\partial \mathbb{C}^{hom}}{\partial d^r}\right] \otimes \left[(\mathbf{E} + \boldsymbol{\sigma_0} : \mathbb{C}^{s^{-1}}) : \dfrac{\partial \mathbb{C}^{hom}}{\partial d^r}\right]}{h_0\eta + \left(\dfrac{1}{2}\mathbf{E} + \boldsymbol{\sigma_0} : \mathbb{C}^{s^{-1}}\right) : \dfrac{\partial^2 \mathbb{C}^{hom}}{\partial d^2} : \mathbf{E}} \tag{13}$$

where

$$H^r = \begin{cases} 0 \text{ if } f^r < 0 \text{ or if } f^r = 0 \text{ and } \dot{f}^r < 0 \\ 1 \text{ if } f^r = 0 \text{ and } \dot{f}^r = 0 \end{cases} \tag{14}$$

2.2 Coupling between damage and permeability evolutions

To determine the macroscopic permeability evolution, we follow here an approach proposed by Dormieux & Kondo (2004) and then by Barthélémy (2009). The upscaling problem to solve on the *rev*, Ω, is similar to the mechanical elliptic problem:

$$\begin{cases} \text{div}\underline{q} = 0 & (\Omega) \\ \underline{q} = -\dfrac{\mathbf{K^s}}{\mu} \cdot \underline{\text{grad}}\, p & (\Omega^s) \\ \underline{q} = -\dfrac{\mathbf{K^i}}{\mu} \cdot \underline{\text{grad}}\, p & (\Omega^i) \\ p = \underline{\nabla} P \cdot \underline{x} & (\partial\Omega) \end{cases} \tag{15}$$

where $\underline{\nabla}\, P$ corresponds to the macroscopic pressure gradient linked to the microscopic one by:

$$\forall \underline{x} \in \Omega,\ \underline{\text{grad}}\, p(\underline{x}) = \mathbf{A}(\underline{x}) \cdot \underline{\nabla} P \tag{16}$$

The macroscopic permeability is then given by:

$$\underline{Q} = < \underline{q} >_{\Omega} = -\frac{\mathbf{K^{hom}}}{\mu} \cdot \underline{\nabla} P \tag{17}$$

with

$$\mathbf{K^{hom}} = < \mathbf{K} \cdot \mathbf{A} >_{\Omega} = \mathbf{K^s} + \sum_{i=1}^{N} \varphi_i \left(\mathbf{K^i} - \mathbf{K^s} \right) \cdot \boldsymbol{\alpha_i} \tag{18}$$

in which $\varphi_i = \frac{4\pi}{3} d_i w_i$, $\mathbf{K^s} = K^s \mathbf{I}$ and $\mathbf{K^i} = K_t^i (\mathbf{I} - \underline{n}_i \otimes \underline{n}_i) - K_n^i \underline{n}_i \otimes \underline{n}_i$. $\boldsymbol{\alpha_i}$ depends on the homogenization scheme (Levasseur et al. 2011) and is equal for the Ponte-Castaneda and Willis approximation scheme to:

$$\begin{aligned} \boldsymbol{\alpha_i^{pcw}} &= \left[\mathbf{I} - \mathbf{P_0^i} (\mathbf{K^i} - \mathbf{K^s}) \right]^{-1} \\ &\quad \cdot \left\{ \mathbf{I} + \sum_{j=1}^{N} \varphi_j \left[\mathbf{I} + (\mathbf{P_0^j} - \mathbf{P^d}) \cdot (\mathbf{K^j} - \mathbf{K^s}) \cdot \left(\mathbf{I} - \mathbf{P_0^j} (\mathbf{K^j} - \mathbf{K^s}) \right)^{-1} \right] \right\}^{-1} \qquad (19) \\ &= \boldsymbol{\alpha_i^{esh}} \cdot \left\{ \mathbf{I} + \sum_{j=1}^{N} \varphi_j \left[\mathbf{I} + (\mathbf{P_0^j} - \mathbf{P^d}) \cdot (\mathbf{K^j} - \mathbf{K^s}) \cdot \boldsymbol{\alpha_i^{esh}} \right] \right\}^{-1} \qquad (20) \end{aligned}$$

where $\boldsymbol{\alpha_i^{esh}} = \left[\mathbf{I} - \mathbf{P_0^i} (\mathbf{K^i} - \mathbf{K^s}) \right]^{-1}$ and $\mathbf{P^d} = \frac{1}{3K^s}\, \mathbf{I}$ represents the spherical distribution of cracks of the PCW scheme (Dormieux et al. 2006). According to Barthélémy (2009), the vector $\mathbf{P_0^i}$ is equal to:

$$\mathbf{P_0^j} = \frac{\underline{n}_i \otimes \underline{n}_i}{K^s} + w_i \frac{\pi}{4K^s} (\mathbf{I} - 3\underline{n}_i \otimes \underline{n}_i) \tag{21}$$

then,

$$\boldsymbol{\alpha_i^{esh}} = \frac{1}{1 + \frac{\pi w_i}{4K^s}(K_t^i - K^s)} (\mathbf{I} - \underline{n}_i \otimes \underline{n}_i) + \frac{1}{1 + \frac{2 - \pi w_i}{2K^s}(K_n^i - K^s)} \underline{n}_i \otimes \underline{n}_i \tag{22}$$

In the following, we neglect the effect of the normal component of the permeability vector $K_n^i \approx 0$ and the tangential component is evaluated by Poiseuille solution $K_t^i = \dfrac{c_i^2}{12}$ with $c_i = a^i w_i$ the crack opening (Barthélémy 2009). This opening is linked to the deformation at microscopic scale by Deudé et al. (2002):

$$c_i = c_{i_0} + \delta c_i = c_{i_0} (1 + \underline{n}_i \cdot \boldsymbol{\varepsilon_i} \cdot \underline{n}_i) = c_{i_0} \left(1 + \underline{n}_i \cdot (\mathbb{A}^i : \mathbf{E}) \cdot \underline{n}_i \right) \tag{23}$$

3 APPLICATIONS

3.1 Opalinus Clay parameter calibration on triaxial tests

Located in the Jura Mountains of the north-western Switzerland, Mont Terri research laboratory is located within the Opalinus Clay unit, which is mainly an overconsolidated claystone. This

clay exhibits at its natural state very favorable conditions for the disposal of radioactive wastes thanks to low and uniform hydraulic conductivity, low diffusion coefficients and good retention capacity for radionuclides. To characterize its behavior, we proposed to calibrate some triaxial compression tests by the previous model based on micromechanical modeling, through PCW approximation. These triaxial tests (compiled by Laloui & Francois (2008)) compare three different inclinations of the bedding plane with respect to the loading direction: bedding planes parallel (P-Sample, α_σ= 90°), perpendicular (S-Sample, α_σ= 0°) and with an inclination of 45° (Z-Sample, α_σ= 45°) with respect to the loading direction (figure 1). Calibration results provide the geomechanical characteristics presented in Table 1. The comparison between experimental results and numerical simulations is made in figure 2.

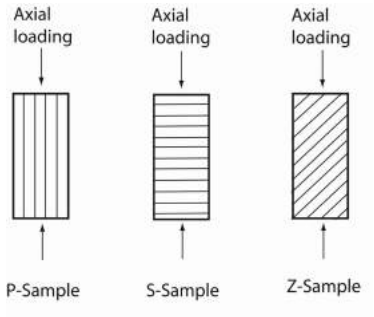

Fig. 1. Orientation of bedding with respect to the loading direction in P-, S- and Z- samples

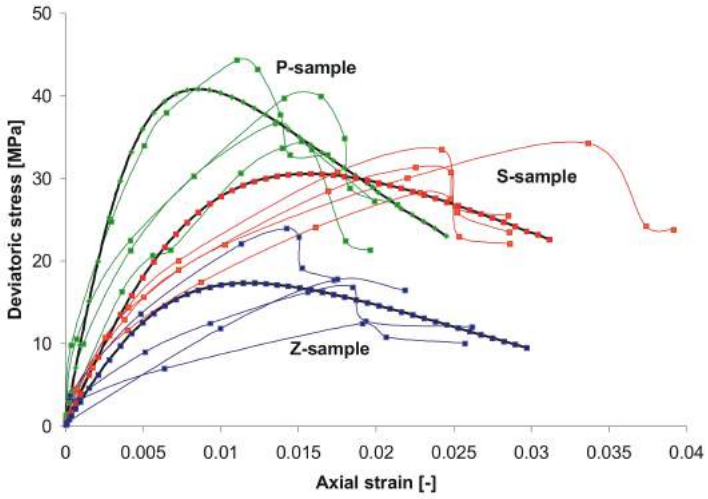

Fig. 2. Comparison between numerical simulations and experimental results of triaxial compression tests with a confining pressure of 15 MPa and three different orientation of bedding with respect to axial loading (thin lines: experimental results – thick lines: PCW modelling)

The elastic stiffness and the shear strength are clearly affected by the direction of loading with respect to the bedding plane. The elastic rigidity of the Z-sample is included between the rigidity of P- and S- samples which is characteristic of cross-anisotropic behavior. Nevertheless, the calibrated values satisfy the values classically admitted for this material in literature (Gens et al. 2007; Wileveau 2005; Martin & Lanyon 2003). Concerning the damage parameter values, the

Table 1. Geomechanical characteristics of Opalinus Clay according to bedding orientation

Bedding orientation			$\parallel$	$\perp$	$45°$
Young elastic modulus	E	[GPa]	10	4	4
Poisson ratio	υ	[-]	0.24	0.33	0.33
damage coefficient	h_0	[J/m^2]	100	100	100
damage coefficient	η	[-]	2500	3500	1500

values of η used in the three approaches are quite different in order to capture different responses and different crack propagation modes following the inclination of the bedding plane. This difference can be partly explained by the fact that some phenomena are not taken into account in our model, as for instance the coupling between damage and frictional sliding which are neglected here. As this coupling plays an important role in the propagation of closed microcracks under compressive stresses (Zhu et al. 2008; Barthélémy et al. 2003), the use of a unique value of η could not capture large differences in responses between each case in the present model.

3.2 SELFRAC Experiment

Design of the experiment The SELFRAC project aimed to understand and to quantify the EDZ fracturing in clay and its evolution with time (sealing process) in order to assess its impact on the performances of radioactive waste geological repositories. The general concept of this experiment, presented in figure 3, was to combine dilatometer tests and numerous hydraulic tests with multi-packer system to test the influence of bentonite swelling pressure on the axial transmissivity of the Excavation Damaged Zone (EDZ) (Bernier et al. 2007; Levasseur et al. 2010). The pressure in the dilatometer probe, which has modeled the effect of the bentonite swelling pressure, was increased stepwise and hydraulic tests were periodically performed under different dilatometer pressures. Active hydraulic tests were carried out periodically in the deepest interval of the borehole. The pressure responses were observed in the test interval as well as in the interval above the dilatometer. It can be assumed that pressure changes were preferably transmitted through the EDZ along the borehole. So, the problem was to know if the inflation pressure of the dilatometer can influence flows in EDZ. Then, by modeling this experiment, our main objective in this paper is to check if the hydraulic conductivity of the EDZ can be seen as a function of the dilatometer pressure.

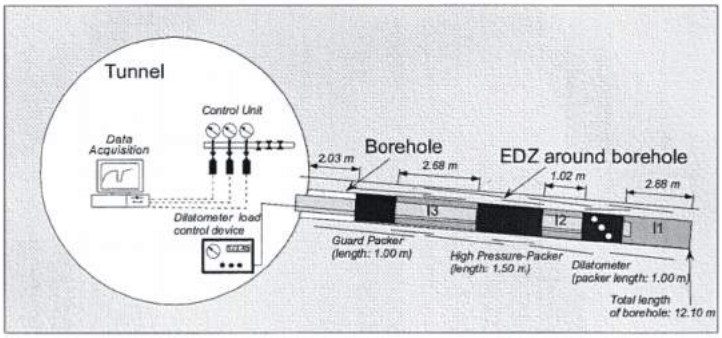

Fig. 3. Long-term dilatometer experiment, SELFRAC: Experiment layout

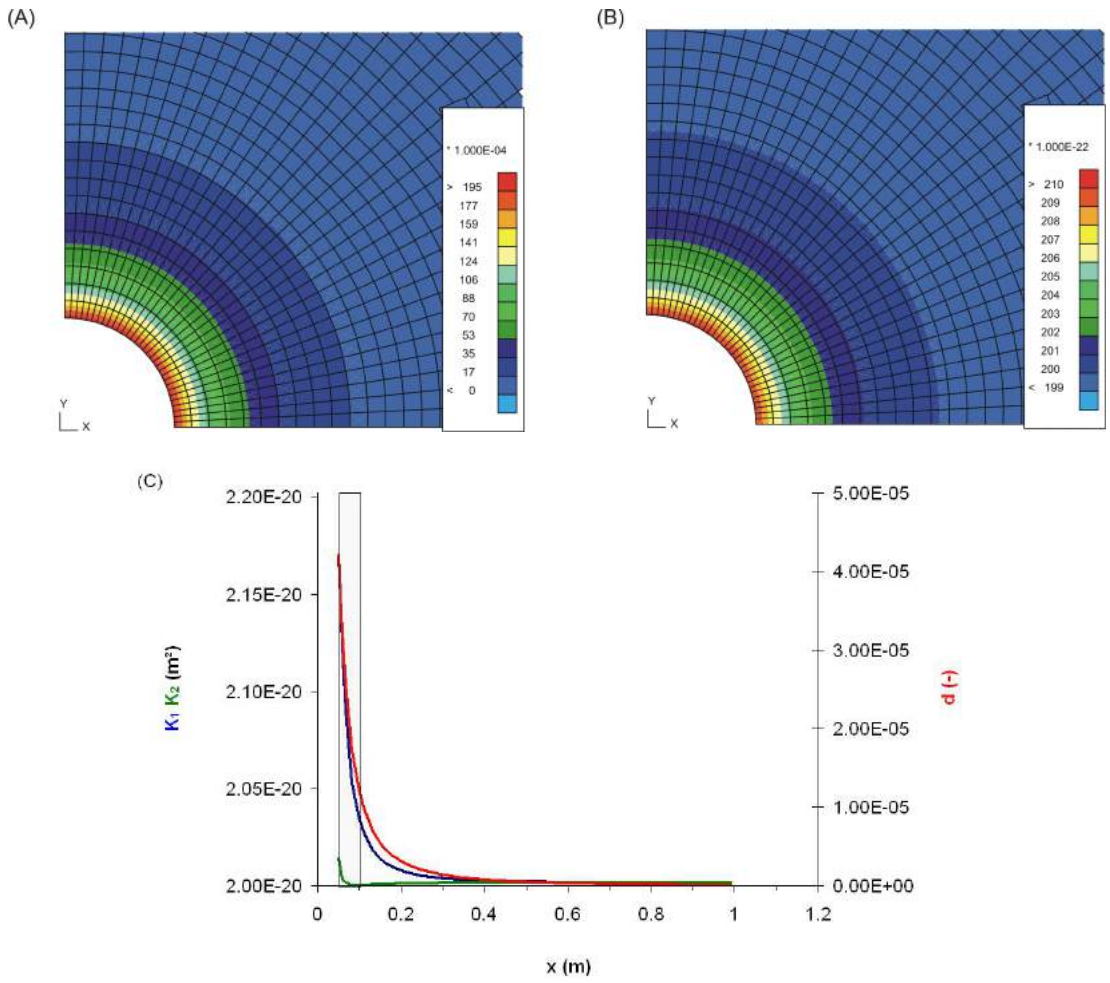

Fig. 4. SELFRAC experiment modelling: (A) EDZ, Damage evolution; (B) Permeability evolution; (C) cross section of evolution of damage variable d (-) and permeability tensor variables in main axes (K_1 and K_2)

Modeling results As a first approximation in this paper, the SELFRAC experiment is simplified. Only the excavation process of the borehole is modeled through a 2D-plane strain modeling, in a section perpendicular to the dilatometer probe, defined in the Finite Element Code LAGAMINE from Liège University. Soil behavior anisotropy is neglected, initial stresses are supposed as isotropic. It will permit to test the validity of the proposed model. More complex initial and boundary conditions will be taken into account in a further paper (Levasseur et al. 2011).

As expected, modeling comparisons between multi-scale damage model and elastoplastic one (performed in Levasseur et al. (2010)) shows that stress and strain evolutions around tunnel excavation are similar. Multi-scale damage model permits to described an EDZ shape around excavation which extends for around 1 tunnel radii from the excavation periphery. In this zone, permeability tensor evolves as illustrated in figure 4. This permeability is defined by an anisotropic tensor established from the open cracks which develop around the excavation. The anisotropic properties of the permeability tensor is directly obtained from the multi-scale approach definition. Compare to the elastoplastic approach proposed by Levasseur et al. (2010) where permeability tensor anisotropy is deduced from the main strain tensor directions, it presents a big advantage.

4 DISCUSSION

This study on multi-scale anisotropic modeling of damage and permeability evolution around tunnels based on Ponte-Castaneda and Willis homogenization scheme which takes into account initial stresses is very promising. Its application on problems performed on Opalinus Clay shows that the material behavior is well described. Compare to experimental results, as Bossart et al. (2002) defined the EDZ shape around excavation closed to 0.5-1 tunnel radii from the excavation periphery in Opalinus Clay, the damage zone numerically obtained is relevant. Crack processes and EDZ shape are well capture. Permeability evolution qualitatively follows the good tendency. Unfortunately, the degree of damage evaluated by multi-scale modeling does not permit to reproduce the good degree of magnitude of the permeability increase observed in SELFRAC experiment after excavation. It means that some ingredients are missing in our model in order to reproduce all the phenomena; the model and how it has to be put into action probably need some adjustments.

ACKNOWLEDGEMENTS

The authors would like to thank the F.R.S.-FNRS, the national funds of scientific research in Belgium, for their financial support in the FRFC project.

REFERENCES

Barthélémy, J.-F. (2009). Effective permeability of media with a dense network of long and micro fractures. *Transport in porous media 76*, 153–178.

Barthélémy, J.-F., Dormieux, L., & Kondo, D. (2003). Détermination du comportement macroscopique d'un milieu à fissures frottantes. *Comptes rendus de mécanique 331*, 77–84.

Bernier, F., Li, X., Bastiaens, W., Ortiz, L., Van Geet, M., Wouters, L., Frieg, B., Blumling, P., Desrues, J., Viaggiani, G., Coll, C., Chanchole, S., De Greef, V., Hamza, R., Malinsky, L., Vervoort, A., Vanbrabant, Y., Debecker, B., Verstraelen, J., Govaerts, A., Wevers, M., Labiouse, V., Escoffier, S., Mathier, J., Gastaldo, L., & Bhler, C. (2007). Fractures and self-healing within the excavation disturbed zone in clays (selfrac). Final report, 5th EURATOM Framework Programme (1998-2002).

Bossart, P., Meier, P., Moeri, A., Trick, T., & Mayor, J. (2002). Geological and hydraulic characterization of the excavation disturbed zone in the opalinus clay of the mont terri rock laboratory. *Engineering Geology 66*, 19–38.

Budiansky, B. & O'Connell, R. (1976). Elastic moduli of a cracked solid. *Int. J. Solids Struct. 12*, 81–97.

Deudé, V., Dormieux, L., Kondo, D., & Maghous, S. (2002). Micromechanical approach to non linear poroelasticity: application to cracked rocks. *Journal of engineering mechanics 128(8)*, 848–855.

Dormieux, L. & Kondo, D. (2004). Approche micromécanique du couplage permeabilité-endommagement. *C.R. Mecanique 332*, 135–140.

Dormieux, L. & Kondo, D. (2009). Stress-based estimates and bounds of effective elastic properties : the case of cracked media with unilateral effects. *Computational Materials Science 46(1)*, 173–179.

Dormieux, L., Kondo, D., & Ulm, F.-J. (2006). *Microporomechanics*. Wiley.

Gens, A., Vaunat, J., Garitte, B., & Wileveau, Y. (2007). In situ behaviour of a stiff layered clay subject to thermal loading: observations and interpretation. *Geotechnique 57(2)*, 207–228.

Laloui, L. & Francois, B. (2008). Benchmark on constitutive modeling of the mechanical behaviour of opalinus clay. Mont terri project, technical report, NAGRA.

Laws, N. (1973). On the thermostatics of composite materials. *J. Mech. Phys. Solids 21*, 9–17.

Levasseur, S., Charlier, R., Frieg, B., & Collin, F. (2010). Hydro-mechanical modelling of the excavation damaged zone around an underground excavation at mont terri rock laboratory. *Int. J. Rock Mech. Min. Sci. 47(3)*, 414–425.

Levasseur, S., Collin, F., Charlier, R., & Kondo, D. (2010). A two scale anisotropic damage model accounting for initial stresses in microcracked materials. *Engineering Fracture Mechanics accepted*.

Levasseur, S., Collin, F., Charlier, R., & Kondo, D. (2011). Micromechanical modelling of damage coupled with permeability evolution. *in preparation*.

Levin, V. (1967). Thermal expansion coefficient of heterogeneous materials. *Mekh. Tverd. Tela 2*, 83–94.

Martin, C. & Lanyon, G. (2003). Measurement of in situ stress in weak rocks at mont terri rock laboratory, switzerland. *Int. J. Rock Mech. Mining Sci. 40(7-8)*, 1077–1088.

Ponte-Castaneda, P. & Willis, J. (1995). The effect of spatial distribution on the effective behavior of composite materials and cracked media. *J. Mech. Phys. Solids 43(12)*, 1919–1951.

Wileveau, Y. (2005). Thm behaviour of host rock (he-d) experiment: Progress report. Mont Terri Project, Technical Report TR 2005-03, NAGRA.

Zhu, Q., Kondo, D., & Shao, J. F. (2008). Micromechanical analysis of coupling between anisotropic damage and friction in quasi brittle materials: role of the homogenization scheme. *International Journal of Solids and Structures 45*, 1385–1405.

Zhu, Q., Kondo, D., & Shao, J. F. (2009). Homogenization-based analysis of anisotropic damage in brittle materials with unilateral effect and interactions between microcracks. *Int. J. Num. Anal. Meth. Geomech. 33*, 749–772.

IMPROVEMENT OF THE INTERPRETATION OF PULSE TEST THROUGH FULLY COUPLED PORO-MECHANICAL ANALYSIS

R. Giot, A. Giraud, C.Auvray
LAEGO – ENSG – Nancy Université, 54501 Vandoeuvre-Lès-Nancy, France

T. Guillon
ANDRA, Parc de la Croix-Blanche, 1-7 rue Jean Monnet, F-92298 Châtenay-Malabry Cedex, France

ABSTRACT: *The pulse test is a laboratory test which permits the assessment of the intrinsic permeability of weakly permeable rock in fully saturated conditions. It is generally interpreted by comparison of experimental and theoretical curves obtained by a simplified 1D analytical solution. In this work, we shall propose several improvements for the interpretation which permit the assessment of intrinsic permeability, mechanical and poro-mechanical coupling parameters. The main improvements concern the fully coupled numerical modelling of the pulse test and accounting for the anisotropy (transverse isotropy) of the material. 3D numerical modelling is required to account for all possible orientations of the samples and the analysis is coupled with an inverse method of a probabilistic type. The full method is implemented in the finite element code Code_Aster (EDF). Different hypotheses were used and compared with results of laboratory tests on argillites. The inversion based on poro-mechanical 2D modelling of pulse test shows that the classical interpretation, although it does not account for the true physics of the test, gives a fair estimation of the intrinsic permeability. The 3D transverse isotropic modelling provides more coherent values of the parameters than the 2D modelling, particularly for the mechanical parameters.*

1 FRAMEWORK OF THE RESEARCH

The permeability of a rock controls liquid and gas transfers. Consequently, assessment of permeability is of fundamental importance in projects such as nuclear waste storage management. In weakly permeable porous rocks, such as argillite, measuring techniques based on a steady state flow are not suitable for the assessment of permeability with lower values ranging between 10^{-22} and 10^{-20} m^2 since it is quasi-impossible, in practical terms, to conduct drained tests for this range of permeability values. This means transient flow methods must be used. Among the possibilities there is the pulse test, as proposed by Brace et al. (1968), which permits the determination both of the intrinsic permeability and of specific storage. The latter is defined as the volume of water, per unit volume of saturated rock, injected into the pores when it is exposed to a unit decrease of pore fluid pressure. During the pulse test, the intrinsic permeability controls the transient evolution while the specific storage controls the final equilibrium. The pulse test is usually interpreted as a one-dimensional pore pressure diffusion problem in the axial direction while also considering simplifying assumptions, such as constant mean stress, constant strain or uniaxial strain. The analysis is based on the solution of a hydraulic diffusion equation assuming no coupling between hydraulic and mechanical behaviour. For example, Hsieh et al. (1981) solved the problem

with the hypothesis of constant mean stress by a Laplace transform method and provided an analytical solution for the pulse test. Based on this solution, Neuzil et al. (1981) developed a graphical method to carry out tests of both the permeability and the specific storage. Homand et al. (2004) applied the pulse test to argillites, using the analytical solution for the constant mean stress combined with an inverse method. However, Wang (2003) and Adachi (1997) demonstrated that the pulse test is a fully coupled problem with poroelastic strains coupled with the pore pressure field while Walder et al. (1986) showed that neglecting poro-mechanical couplings could result in errors in the assessment of permeability. Due to this coupling between hydraulic and mechanical behaviours, the problem can be considered overall as being 3D or 2D with axial symmetry. Thus a fully accurate solution of the pulse test would entail coupled hydromechanical modelling requiring a numerical code. Here, we opted to interpret the pulse test by combining fully coupled finite element modelling of this test with an inversion algorithm, to identify intrinsic permeability and parameters influencing specific storage.

Figure 1 shows the experimental apparatus detailed by Escoffier et al. (2005). A thin cylindrical rock sample is placed in a load cell and connected to two fluid reservoirs, an upstream and a downstream reservoir. The circumference of the sample is wrapped in a viton jacket to prevent it from radial flow at its lateral boundary. Figure 2 illustrates the principle of the test. After sample saturation and pore pressure homogenization, the pressure is suddenly increased in the upstream reservoir. The evolution of the pressure in both reservoirs is then measured.

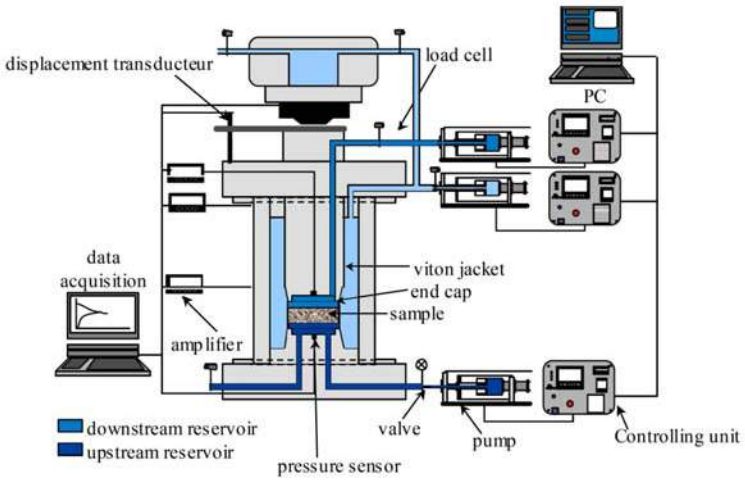

Fig. 1. Experimental apparatus for the pulse test

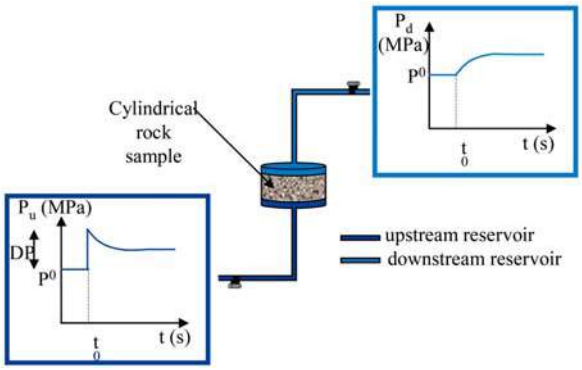

Fig. 2. Principle of the pulse test

2 FULLY COUPLED CONSTITUTIVE EQUATIONS FOR THE PULSE TEST

Pulse tests are conducted in saturated conditions. In this section we shall therefore state once again the constitutive equations of the poroelastic model for the saturated case which were already detailed by Giot et al. (2009). This is based on Biot's mechanics for fluid saturated porous media (Coussy, 2004) and is available in the finite element code Code_Aster (Edf) (Chavant, 2001; Granet, 2009). In addition to those equations, we shall present further modifications to the equations corresponding to the case of the material being transverse isotropic rather than isotropic.

We considered a porous medium composed of a deformable matrix and fully saturated by an incompressible liquid (subscript lq). We took Darcy's law into account to model the diffusion of the liquid. Assuming isothermal conditions, the linear porous elastic model is composed of one balance equation for liquid mass and linear momentum of the media.

2.1 Constitutive equations for the fully saturated medium

The non-linear poroelastic constitutive equations for the fully saturated media can be written incrementally:

$$d\sigma_m = K_o d\varepsilon_v - b dp_{lq} \tag{1a}$$

$$d\sigma_m = K_{un} d\varepsilon_v - bM \frac{dm_{lq}}{\rho_{lq}} \tag{1b}$$

$$ds_{ij} = 2G de_{ij} \tag{2}$$

$$dp_{lq} = M\left(-b d\varepsilon_v + \frac{dm_{lq}}{\rho_{lq}} \right) \tag{3}$$

In those equations, σ_m, $\mathbf{s}$, ε_v, $\mathbf{e}$, m_{lq}, ρ_{lq} and p_{lq} respectively stand for the mean stress, the deviatoric stress tensor, the volumetric strain, the deviatoric strain tensor, the liquid mass supply, the liquid density and the liquid pressure. K_o and K_{un} respectively refer to the drained ($\mathrm{d}p_{lq} = 0$) and undrained ($\mathrm{d}m_{lq} = 0$) bulk moduli, b and M respectively to the Biot coefficient and modulus of the saturated poroelastic medium. Inverting the equation (3) allows the liquid mass supply to be expressed as a function of liquid pressure and volumetric strain:

$$\frac{dm_{lq}}{\rho_{lq}} = b d\varepsilon_v + N dp_{lq} \tag{4}$$

with $N = 1/M$. The deviatoric behaviour equation (2) is not coupled to the volume change behaviour equation (1).

2.2 Conduction equations

By applying Darcy's generalized law in a fully saturated medium and neglecting gravity, the velocity of liquid is controlled by:

$$\frac{\mathbf{M_{lq}}}{\rho_{lq}} = -\lambda_{lq} \nabla \mathbf{p_{lq}} \tag{5}$$

where λ_{lq} designates Darcy's conductivity for liquid and is linked, for the fully saturated porous medium, to the intrinsic permeability k_{int} through:

$$\lambda_{lq} = \frac{k_{\text{int}}}{\mu_{lq}} \tag{6}$$

μ_{lq} stands for the liquid dynamic viscosity.

2.3 Momentum and diffusion equation

If we leave gravity out, the linear momentum equation is written as follows:

$$\nabla.\boldsymbol{\sigma} = \mathbf{0} \tag{7}$$

The mass conservation equation for the liquid is expressed as:

$$\frac{\partial m_{lq}}{\partial t} = -\nabla.\mathbf{M_{lq}} \tag{8}$$

The field equation may be obtained by inserting Darcy's conduction law and the constitutive poroelastic equations into (8):

$$b\frac{\partial \varepsilon_v}{\partial t} + N\frac{\partial p_{lq}}{\partial t} = \lambda_{lq}\nabla^2 p_{lq} \tag{9}$$

or, in terms of mean stress σ_m:

$$\frac{b}{K_o}\frac{\partial \sigma_m}{\partial t} + \left(N + \frac{b^2}{K_o}\right)\frac{\partial p_{lq}}{\partial t} = \lambda_{lq}\nabla^2 p_{lq} \tag{10}$$

In these equations ∇^2 stands for the Laplacian operator.

2.4 Initial and boundary conditions

A cylindrical sample of radius R and height L was submitted to a hydrostatic stress state. The sample was initially fully saturated and both the liquid pressure and the mean stress inside the sample were homogeneous:

$$p_{lq}(\mathbf{x}, t=0) = p_{lq}^0 \tag{11a}$$

$$\sigma_m(\mathbf{x}, t=0) = \sigma_m^0 \tag{11b}$$

where $\boldsymbol{x}$ represents the position vector. The lateral surface Γ_R of the sample was insulated:

$$\mathbf{M_{lq}}.\mathbf{n} = \mathbf{0} \text{ on } \Gamma_R \tag{12}$$

The liquid pressure was assumed to be homogeneous in both the upstream ($z = 0$) and downstream ($z = L$) reservoirs, z referring to the axial coordinate:

$$p_{lq}(\mathbf{x}, t) = p_{re}^u(t) \text{ on } \Gamma_0 \tag{13a}$$

$$p_{lq}(\mathbf{x}, t) = p_{re}^d(t) \text{ on } \Gamma_L \tag{13b}$$

The liquid pressure was suddenly increased in the upstream reservoir:

$$p_{re}^{u}\left(0^{+}\right)=p_{lq}^{0}+\Delta p \tag{14}$$

The conservation of liquid mass gave the two boundary conditions between the sample and the reservoirs:

$$\frac{\partial \xi^{u}}{\partial t}=\int_{\Gamma_0}-\lambda_{lq}\nabla\mathbf{p_{lq}}\left(\mathbf{x},t\right).\mathbf{n}da \tag{15a}$$

$$\frac{\partial \xi^{d}}{\partial t}=\int_{\Gamma_L}-\lambda_{lq}\nabla\mathbf{p_{lq}}\left(\mathbf{x},t\right).\mathbf{n}da \tag{15b}$$

$$\xi^{u}=\frac{M_{lq}^{u}}{\rho_{lq}}\qquad \xi^{d}=\frac{M_{lq}^{d}}{\rho_{lq}} \tag{15c}$$

M_{lq}^{u}, M_{lq}^{d}, ξ^{u} and ξ^{d} respectively refer to the mass and volume of liquid contained in the upstream and downstream reservoirs. We may assume that there is a linear relation between the volume of liquid content in the reservoirs and the liquid pressure which means that the following equations can be written:

$$\xi^{u}=\frac{p_{re}^{u}}{C_{re}^{u}}\qquad \xi^{d}=\frac{p_{re}^{d}}{C_{re}^{d}} \tag{16}$$

The two coefficients C_{re}^{u} and C_{re}^{d} are the compressibilities of the reservoirs and can be linked to the reservoir storage coefficients S_{re}^{u} and S_{re}^{d} through:

$$C_{re}^{u}=\frac{\gamma_{lq}}{S_{re}^{u}}\qquad C_{re}^{d}=\frac{\gamma_{lq}}{S_{re}^{d}} \tag{17}$$

γ_{lq} denotes the volumetric weight of liquid. The boundary conditions between the reservoirs and the rock sample may be expressed as:

$$\int_{\Gamma_0}-\lambda_{lq}\nabla\mathbf{p_{lq}}\left(\mathbf{x},t\right).\mathbf{n}da=\frac{1}{C_{re}^{u}}\frac{\partial p_{lq}\left(\mathbf{x},t\right)}{\partial t}\qquad p_{lq}\left(\mathbf{x},t\right)=p_{re}^{u}\left(t\right)\qquad \text{on } \Gamma_0 \tag{18a}$$

$$\int_{\Gamma_L}-\lambda_{lq}\nabla\mathbf{p_{lq}}\left(\mathbf{x},t\right).\mathbf{n}da=\frac{1}{C_{re}^{d}}\frac{\partial p_{lq}\left(\mathbf{x},t\right)}{\partial t}\qquad p_{lq}\left(\mathbf{x},t\right)=p_{re}^{d}\left(t\right)\qquad \text{on } \Gamma_L \tag{18b}$$

The boundary conditions were implemented within the finite element code Code_Aster (Edf) through the development of Fortran routines. An explicit time integration scheme was employed for the implementation of the boundary conditions (18):

$$p_{re}^{u}\left(t_{n+1}\right)=p_{re}^{u}\left(t_{n}\right)+C_{re}^{u}\Delta t\int_{\Gamma_0}-\lambda_{lq}\nabla\mathbf{p_{lq}}\left(\mathbf{x},t_{n}\right).\mathbf{n}da \tag{19a}$$

$$p_{re}^{d}(t_{n+1}) = p_{re}^{d}(t_n) + C_{re}^{d}\Delta t\int_{\Gamma_L} -\lambda_{lq}\nabla \mathbf{p_{lq}}(\mathbf{x},t_n).\mathbf{n}da \tag{19b}$$

2.4 Transverse isotropy

With anisotropy, the constitutive and conduction equations presented previously are modified. For the material under study, argillites, we focused on the particular case of transverse isotropy. The axis of revolution is denoted as O_{x3} and the behaviour is supposed isotropic in the plane O_{x1x2}. It is assumed that the porous medium (skeleton) and the matrix are transverse isotropic elastic with the same axis of revolution O_{x3}.

The constitutive equation must then be written under tensorial form and equations (1) to (3) which thus gives:

$$\mathbf{d\sigma} = \mathbf{C} : \mathbf{d\varepsilon} - \mathbf{B}dp_{lq} \tag{20}$$

$$\frac{dm_{lq}}{\rho_{lq}} = \mathbf{B} : \mathbf{d\varepsilon} + \left(\frac{1}{M_\phi} + \frac{\phi}{K_{lq}}\right)dp_{lq} \tag{21}$$

In those equations, $\boldsymbol{\sigma}$ and $\boldsymbol{\varepsilon}$ respectively stand for the second rank stress and strain tensors. $\mathbf{C}$ is the fourth rank elasticity tensor, characterized by two Young moduli, two Poisson coefficients and a shear coefficient. M_ϕ is the pore compressibility and ϕ is the lagrangian porosity. $\mathbf{B}$ refers to the second rank tensor of Biot coefficients, which can be written as follows:

$$\mathbf{B} = b_1(\mathbf{e_1}\otimes\mathbf{e_1} + \mathbf{e}_2\otimes\mathbf{e}_2) + b_3\mathbf{e}_3\otimes\mathbf{e}_3 \tag{22}$$

In the conduction equations, the intrinsic permeability, and thus Darcy's conductivity, must also be written as second rank tensors:

$$\mathbf{K^{int}} = K_1^{\text{int}}(\mathbf{e_1}\otimes\mathbf{e_1} + \mathbf{e}_2\otimes\mathbf{e}_2) + K_3^{\text{int}}\mathbf{e}_3\otimes\mathbf{e}_3 \tag{23}$$

$$\boldsymbol{\lambda}^{\mathbf{lq}} = \lambda_1^{lq}(\mathbf{e_1}\otimes\mathbf{e_1} + \mathbf{e}_2\otimes\mathbf{e}_2) + \lambda_3^{lq}\mathbf{e}_3\otimes\mathbf{e}_3 \tag{23}$$

The conduction equation (5) then becomes:

$$\frac{\mathbf{M_{lq}}}{\rho_{lq}} = -\boldsymbol{\lambda}^{\mathbf{lq}}.\nabla\mathbf{p_{lq}} \tag{24}$$

This fully coupled transverse isotropic elastic constitutive law was implemented in the finite element code Code_Aster (Edf) on the basis of an existent isotropic behaviour law (Granet, 2009).

3 NUMERICAL MODELLING OF THE PULSE TEST

The numerical calculations were performed using the finite element code Code_Aster (Edf). During our first approach, the material was considered to be isotropic and thus would show the effects of poro-mechanical couplings. The geometrical model was thus 2D-axisymmetrical and represents half a sample with the symmetry axis being vertical. When

investigating the effects of anisotropy, the whole sample was considered and the geometrical model was fully 3D.

Numerical modelling (Giot et al., 2010) has shown that the pulse test is affected by 3D, or 2D-axisymmetrical effects, and cannot be fully and accurately interpreted only by considering 1D axial effects. Thus pore pressure is a function of both the axial and radial coordinates. An illustration of this would be that the liquid pressure along a horizontal profile in the middle of the sample is homogeneous before the pressure increment in the upstream reservoir. At the beginning of the test, just after the pressure increase in the upstream reservoir, the pressure decreased along that line, exhibiting the presence of a region of negative pore pressure variations. After this transient decrease, the pressure then increased until the end of the test and finally became homogeneous once more. The pressure was not homogeneous during the transient evolution, and particularly early in the test process, while the pressure was not constant along the profile, exhibiting radial effects on pore pressure.

Concerning the displacements and strains, an initially horizontal line does not remain horizontal during the transient phase of the test as Wang (2003) have previously noted. Also, the profile of radial displacements on the lateral boundary of the sample is not linear at all during the transient evolution. To illustrate the effects of the displacements on the sample, figure 3 shows the deformed mesh at different times during the test, with a factor of amplification for better viewing. The sample was again undistorted at the end of the test but expanded because of the free strain. The distortion of the sample is obvious and clearly confirms that the problem is 2D-axisymmetrical rather than 1D axial.

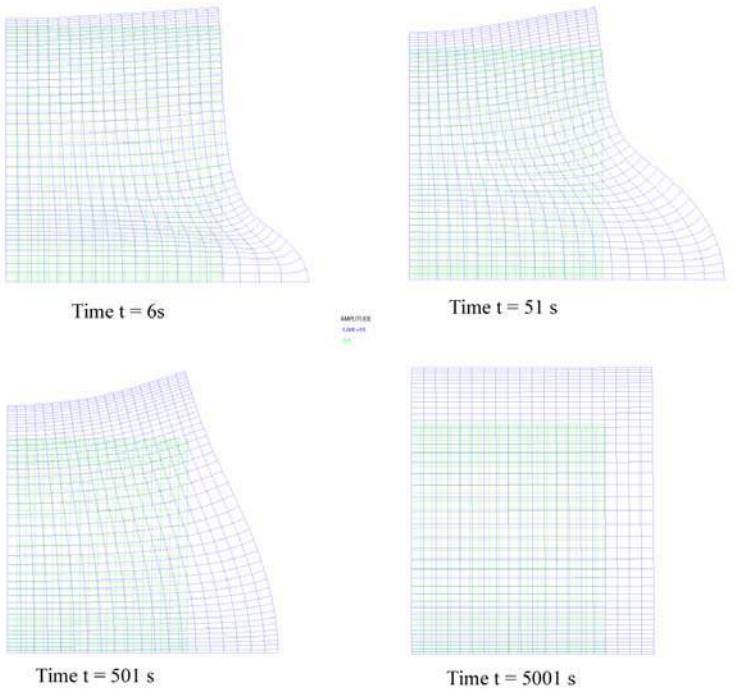

Fig. 3. Evolution of the deformed mesh during the test (amplification factor of 10^5)

It should also be noted that the profile of axial displacements on the lateral boundary of the sample was not linear from the beginning of the test to the end. More specifically, at early times during the test, the displacement was greater near the base of the sample, in a region that corresponds to the region of increased pore pressure. That means that the increase of pore pressure due to the pulse expands the base of the cylinder which resulted in the expansion and distortion of the whole sample. These phenomena were previously observed by Wang (2003)

and illustrate the poromechanical coupling since the increased pore pressure results in a deformation of the sample. Finally, at the end of the test, the profile of the displacements was linear in the sample.

So, the evolution of the stresses, strains and displacements in the whole sample can be explained by the poromechanical couplings through equations (1) and (3). At the beginning of the test, the passage of the pulse pore pressure front induced a pore pressure increase in the base of the sample. It resulted in the swelling of the base of the sample thus inducing compressive effective stress variations in the zone ahead of the base, namely in the middle of the sample. This is a poromechanical coupling effect. These compressive effective stresses led to negative strains meaning that the sample shrank locally. When the pore pressure front arrived at the middle of the sample, the pore pressure then increased, the effective strain variations and indeed the strains themselves were positive and the sample swelled locally.

In conclusion, the numerical modellings of the pulse test in 2D-axisymmetrical hypothesis show that the pulse test is a fully coupled problem. As a consequence of this poromechanical coupling, the pulse test is not 1D, but rather 2D-axisymmetrical. Although analyzing the test under a 1D hypothesis provides good results considering the constant mean stress assumption, we may conclude that this method is not thorough or accurate enough and indeed could lead to badly estimated parameters.

4 APPLICATION TO THE INTERPRETATION OF LABORATORY TESTS

4.1 Inverse method

The pulse test interpretation consists of combining the numerical modelling (direct problem) with an inversion algorithm (inverse problem) to identify liquid transport parameter (intrinsic permeability) and poromechanical coupling parameters influencing the specific storage (Biot coefficients, Young moduli). This identification problem was thus brought back to an optimisation problem consisting of minimizing a cost-functional quantifying the differences between experimentally measured pressures and numerically calculated pressures. This is an inversion problem and was detailed by Giot et al. (2010). The cost-functional is of the least-squares type:

$$\chi[\mathbf{c}] = \frac{1}{2}\sum_{i=1}^{Nmes}\omega_i\left(\gamma[\mathbf{c},t_i]-\gamma_{mes}[t_i]\right)^2 + \frac{1}{2}\sum_{j=1}^{Npar}\upsilon_i\left(c_j - c_j^{prior}\right)^2 \tag{25a}$$

$$\gamma_{mes}[t_i] = p_{re}^{mes}[t_i] \tag{25b}$$

$$\gamma[\mathbf{c},t_i] = p_{re}^{u}[t_i] \quad \text{or} \quad \gamma[\mathbf{c},t_i] = p_{re}^{d}[t_i] \tag{25c}$$

In equations (25) γ_{mes}, γ, $Nmes$, ω_i and υ_j respectively stand for measured and calculated pressure levels in the (upstream and downstream) reservoirs (the pore pressures at the base and the top of the sample) the total number of measured data points, and weighting coefficients on measurements and a priori information. γ is a function of the parameters to be identified which are stored in vector $\boldsymbol{c}$ and depend on which type of interpretation (2D or 3D). $\boldsymbol{c}^{prior}$ is made of prior values of the parameters, inferred from previous knowledge of those parameters. For example from a 1D analysis of the pulse test. p_{re}^{u} and p_{re}^{d} were calculated by finite element resolution of equations (1)-(3), (7), (9)-(10), (18).

As a consequence, the inverse problem of the pulse test may be formulated as follows:

$$\mathbf{c}^{\mathbf{identified}} = \arg\min[\chi[\mathbf{c}]] \tag{26}$$

The inverse method is of the probabilistic type. The minimization algorithm is derived from Levenberg-Marquardt and is of the gradient type. It requires the assessment of the derivatives of the pressures calculated with respect to the parameters to be identified, which was achieved using a finite differences method.

4.2 Example application

The inverse method based on numerical modelling of the pulse test was applied to the interpretation of laboratory tests on 4 samples on Meuse / Haute-Marne argillites, which is a transverse isotropic material. Two of the samples were axial, by which we mean cylindrical samples with the axis of the sample parallel to the isotropy plane. 2 samples were transverse samples, or cylindrical samples with the axis of the sample perpendicular to the isotropy plane. The tests were interpreted using both 2D numerical modelling, which neglects the effects of anisotropy, and 3D numerical modelling which means anisotropy may be taken into account.

In all cases, there was a fair level of compliance between numerical and experimental curves and a meaning set of parameters was identified. Figure 4 gives an example of this kind of compliance for an axial sample, with the 3D transverse isotropic interpretation. Table 1 sums up the parameters that were identified in each case. It should be noted that for the 3D interpretation, on the basis of a sensitivity analysis, we focused on the parameters in the direction of the axis of the sample.

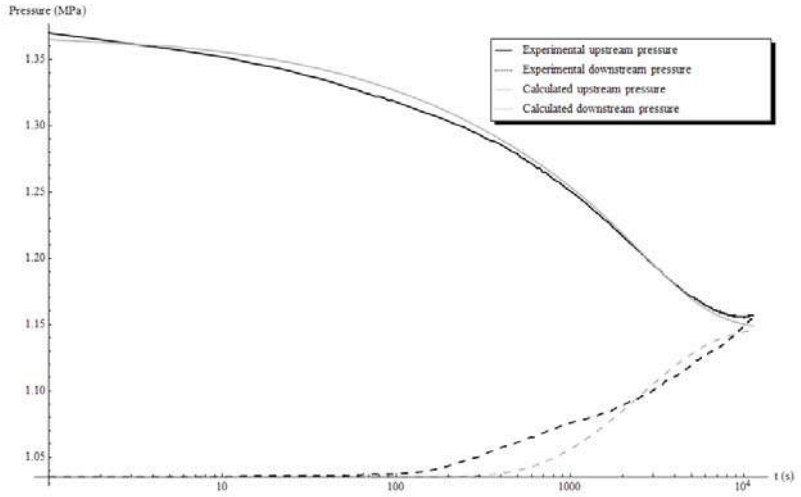

Fig. 4. Example of the fitting of experimental and calculated curves on an axial sample

Table 1. Identified values of the parameters for 2D and 3D interpretations

Sample	1-28396_6	1-28396_7	1-28591_6	1-28591_7
Orientation 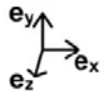	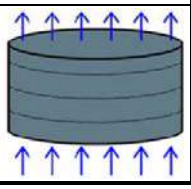	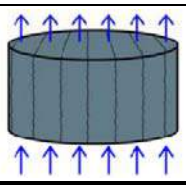	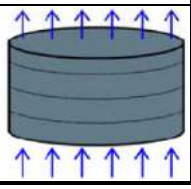	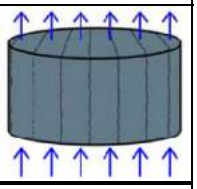
2D isotropic interpretation				
K_{int} [m^2]	3.36 10^{-20}	5.12 10^{-20}	5.45 10^{-20}	8.78 10^{-20}
b [-]	0.817	0.870	0.810	0.905
E_O [GPa]	2.14	4.29	2.09	0.8
3D transverse isotropic interpretation				
K_{int} [m^2]	k_3 = 2.97 10^{-20}	k_1 = 8.01 10^{-20}	k_3 = 4.24 10^{-20}	k_1 = 4.21 10^{-20}
E_O [GPa]	E_3 = 1.41	E_1 = 5.34	E_3 = 2.22	E_1 = 2.30

The main finding of this work is that 2D-axisymmetrical interpretation is more accurate than classical no-coupled 1D interpretation even if this method does give good approximate parameters and may be used with a posteriori validation for common engineering applications. Another important result is that the 3D interpretation which takes anisotropy into account, the values of the parameters, particularly Young moduli, are much more meaningful than if anisotropy is neglected as with 2D-axisymmetrical modelling.

ACKNWLEDGEMENT

This work was supported by ANDRA, Scientific Division, 1/7 rue Jean Monnet, Châtenay-Malabry – F-92290. The author expresses sincere gratitude to the organization.

REFERENCES

Adachi J.I. & Detournay E. (1997), “A poroelastic solution of the oscillating pore pressure method to measure permeabilities of tight rocks”. Int. J. Rock Mech. Min. Sci. Geomech. Abstr., Vol. 34(3-4) : paper 062.

Brace W.F., Walsh J.B. & Frangos W.T. (1968), “Permeability of granite under high pressure”. J. Geophys. Res; Vol. 73(2), 2225-2236.

Chavant C. (2001), Modélisations THHM, généralités et algorithmes, Official Documentation of Code_Aster, R7.01.10a, www.code-aster.org.

Coussy O. (2004), Poromechanics, John Wiley and Sons, ISBN 0 470 84920 7.

Escoffier S., Homand F., Giraud A., Hoteit N. & Su K. (2005), “Under stress permeability determination of the Meuse / Haute-Marne argillite”. Engineering Geology, Vol. 81(3), 329-340.

Giot R., Giraud A., Auvray C., Homand F. & Guillon T. (2009), “Fully coupled poromechanical back analysis of the pulse test by inverse method”. Int. J. Numer. Anal. Methods Geomech., DOI: 10.1002/nag.897.

Granet S. (2008), Modèles de comportement THHM, Official Documentation of Code_Aster, R7.01.11c, www.code-aster.org.

Homand F., Giraud A., Escoffier S., Koriche A. & Hoxha D. (2004), “Permeability determination of a deep argillite in saturated and partially saturated conditions”. Int. J. Heat Mass Transfer, Vol. **47,** 3517-3531.

Hsieh P.A., Tracy J.V., Neuzil C.E., Bredehoeft J.D. & Silliman S.E. (1981), “A transient laboratory method for determining the hydraulic properties of tight rocks. I. Theory”. Int. J. Rock Mech. Min. Sci. Geomech. Abstr., Vol. 18, 245-252.

Neuzil C.E., Cooley C., Silliman S.E., Bredehoeft J.D. & Hsieh P.A. (1981), “A transient laboratory method for determining the hydraulic properties of tight rocks. II. Application”. Int. J. Roch Mech. Min. Sci. Geomech. Abstr., Vol. 18, 253-258.

Walder J. & Nur J. (1986), “Permeability measurement by the pulse decay method: effect of poroelastic phenomena and non linear pore pressure diffusion”. Int. J. Rock Mech. Min. Sci. Geomech. Abstr., Vol. 23(3), 225-232.

Wang H.F. (2003), Theory of linear poroelasticity. Princeton University Press, Princetown and Oxford.

NUMERICAL STUDY OF PRACLAY SEAL TEST IN MOL, BELGIUM

G. J. Chen
European Underground Research Infrastructure for Disposal of Nuclear Waste in Clay Environment (EURIDICE),Mol, Belgium

X. L. Li
European Underground Research Infrastructure for Disposal of Nuclear Waste in Clay Environment (EURIDICE),Mol, Belgium

ABSTRACT: *The paper gives first an overview on the PRACLAY project, which includes the PRACLAY seal test, in Underground Research Facility (URF) in Mol, Belgium. The PRACLAY Seal Test is performed to examine the feasibility of hydraulically sealing the heated part of the PRACLAY gallery from the rest of the gallery. The annular seal is horizontally installed, and it is mainly composed of compacted MX80 bentonite and steel structure. The PRACLAY Seal Test is a complex system with coupled THM processes. Prior to installation of the PRACLAY seal, feasibility analyses were performed to provide support to the decision made for PRACLAY seal: especially to optimize the initial state of the bentonite (dry density, water content, saturation degree, etc.), the technological voids as well as the hydration strategy. Numerical simulations are based on the finite element code, and several models (1D, 2D axisymmetric and 2D plane strain) were studied. A large number of THM parameters for bentonite used in the calculations are carefully determined based on the extensive literature review and the latest laboratory experiments.*

1 PRACLAY PROJECT

For more than 30 years Belgium has been actively studying the long-term management of high-level and/or long-lived radioactive waste. A research programme has been launched by the Belgian Nuclear Research Centre (SCK●CEN) at Mol in the early 1970's. This programme followed international recommendations to isolate radioactive waste from humans and the environment by geological disposal. SCK●CEN chose to concentrate its efforts on investigating the poorly-indurated Boom Clay layer beneath its own site at a depth of some 200 metres as a potential host formation, where the underground research facility HADES (High-Activity Disposal Experimental Site) was constructed since 1980 (Figure 1).

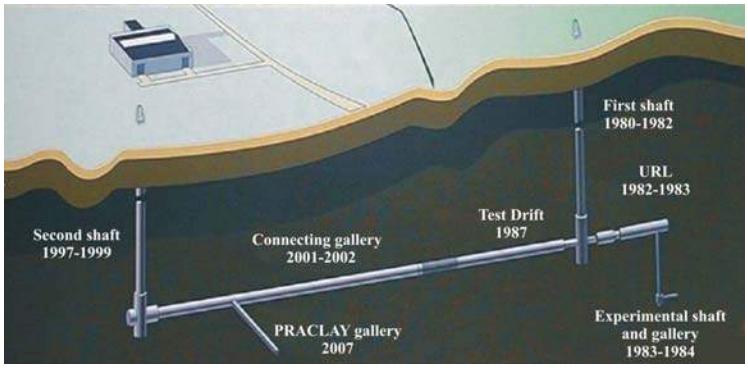

Figure 1: Construction history and layout of the underground research facility HADES

In 1985 ONDRAF/NIRAS, the Belgian Agency for Radioactive Waste and Fissile Materials, took over the R&D programme for the disposal of radioactive waste from SCK●CEN. An expert assessment in the late 1980's confirmed that the poorly-indurated clays, and in particular the Boom Clay under the Mol site, could be considered for the disposal of high-level and/or long-lived waste, since they are able to offer effective protection in the very long term. The Boom Clay had been found to have a very low hydraulic conductivity, a plastic character that gives it good self-sealing properties and a high capacity to fix radionuclides and, hence, to delay their migration towards the biosphere. These encouraging results prompted ONDRAF/NIRAS and SCK●CEN to launch an ambitious demonstration project: the PRACLAY project (NIROND, 1997). The PRACLAY project is to be managed by EURIDICE (European Underground Research Infrastructure for Disposal of nuclear waste In Clay Environment), an economic interest grouping between SCK•CEN and ONDRAF/NIRAS. This PRACLAY project comprises three large in-situ tests (Figure 2):

(1) The Gallery and Crossing Test: to further examine and demonstrate the construction of an underground repository by industrial method and to examine the feasibility to construct a crossing between galleries.

(2) The Heater Test: to study the responses of the Boom Clay to a thermal impact.

(3) The Seal Test: to examine the feasibility of hydraulically sealing the heated part of the PRACLAY gallery from the rest of the gallery.

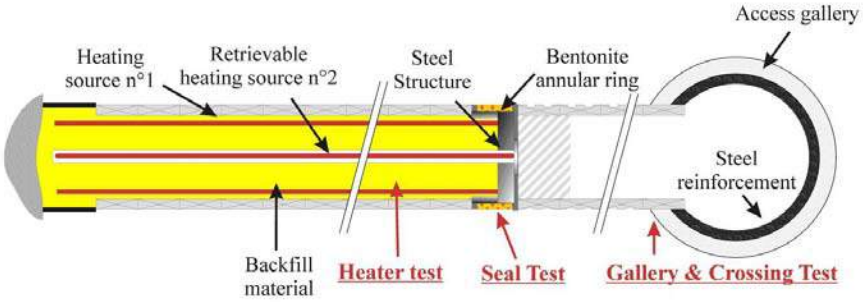

Figure 2: The PRACLAY project comprises three in-situ tests: the Gallery & Crossing Test, the Seal Test and the Heater Test

2 PRACLAY SEAL TEST

The PRACLAY heater test is designed in such a way that it will impose to the clay conditions that are more penalizing than a real repository. In terms of hydraulic boundary condition, the PRACLAY heater test is going to be performed under an undrained boundary within the limits of what is reasonable achievable. This "undrained" boundary condition will be realised by backfilling the heated part of the gallery with saturated high permeable material, which allows to easily build-up the higher pore water pressure as expected by the undrained boundary condition, and by installation of a hydraulic Seal at the intersection between the heated and the non-heated part of the gallery. The hydraulic seal does not only have to close the PRACLAY gallery, but it also has to hydraulically cut off the preferential pathway to the main gallery through the excavation disturbed zone around the gallery. The hydraulic seal consists of a steel structure and an annular ring of bentonite placed against the clay (Figure 2).

The hydraulic seal is located at a distance of 10 m from the Connecting Gallery to limit the mutual interaction between the Heater Test and the Connecting Gallery. As the length of the heater was already set at 30 m, the minimum length of the PRACLAY gallery was fixed at 40 m.

To maintain the accessibility of the clay sidewall at the location of the hydraulic seal, an alternative lining was installed (Figure 3). The alternative lining consisted of four steel ribs making up of the permanent part of the lining and the wood placed behind these steel ribs as a temporary component of the lining which was removed before the erection of the hydraulic seal.

The installation of the hydraulic seal started on 13.01.2010 and finished on 11.02.2010.

(a) (b)

Figure 3: Alternative lining before the hydraulic seal is erected: (a) the lining consists of a permanent part (4 steel ribs) and a temporary part (wood placed between the steel ribs); (b) the segments making up of the steel ribs are connected by a pin-hole connection in the steel plates between the ribs

Figure 4 presents a schematic view of the layout of the seal. MX-80 bentonite fills the major space encompassed by Boom clay, steel structure and four steel ribs, and there are two main technological voids inside the seal.

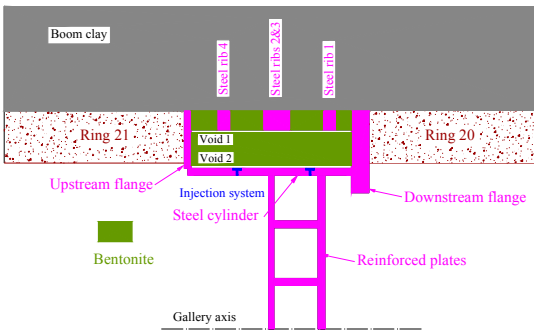

Figure 4: Schematic view of the PRACLAY Seal

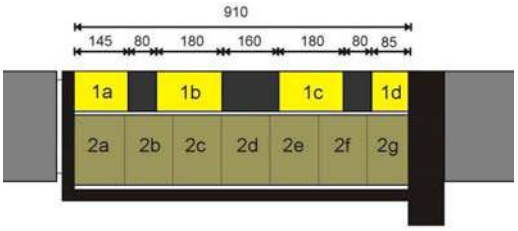

Figure 5: Layout of the bentonite blocks

The steel structure consists of the downstream flange, the upstream flange, the steel cylinder and the reinforced plates. The downstream flange is 100 mm thick, the upstream flange is 40 mm thick, and the cylinder has a thickness of 40 mm, an external diameter of 1840 mm and an internal diameter of 1760 mm.

The MX-80 bentonite is compacted into blocks that are assembled into different rings of bentonite. The layout of these bentonite rings is shown in Figure 5. Four rings of bentonite form the outer layer, and seven rings form an inner layer. Between the inner and outer layer and between the steel cylinder and inner layer there are two main technological voids. The technological void ratio is defined as the initial void volume over the initial bentonite volume.

In the extrados of the steel cylinder, two rings of filters are placed for the artificial hydration of the bentonite. The filters are 50 mm wide and 3 mm thick. The filters are SIKA-

R1 AX having a grade efficiency of 1.8 µm. Such a high grade efficiency is required to avoid clogging of the filters by the bentonite particles.

To be able to follow the behaviour of the seal test during its installation, both natural and artificial hydration, sand backfilling in PRACLAY gallery and PRACLAY heater test etc., sensors have been installed inside and around the bentonite. Figure 6 shows the layout of the instrumentation in the three different sections.

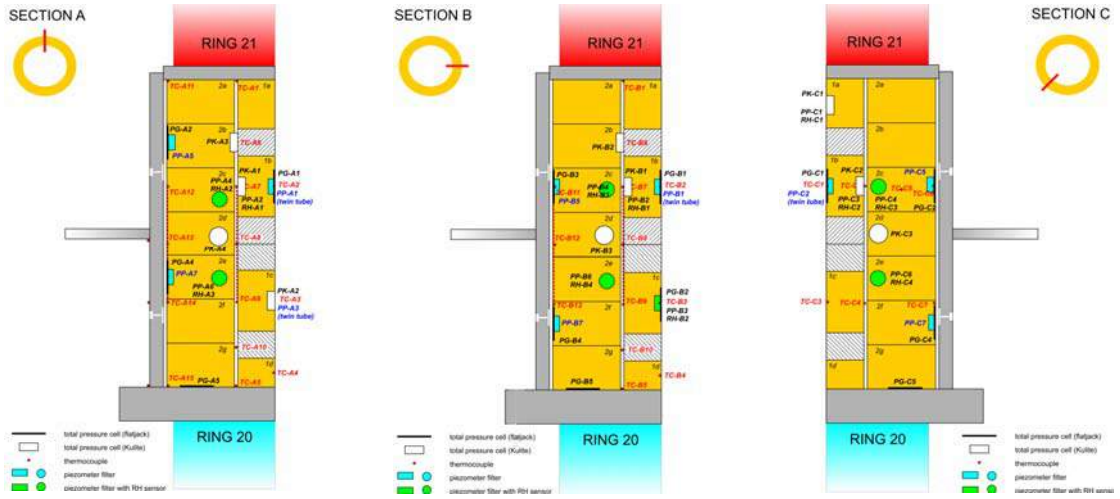

(a) Section A-A (b) Section B-B (c) Section C-C

Figure 6: Instrumentation in the three different sections

3 FEASIBILITY ANALYSIS

The objectives of the calculations are to design the initial dry density of MX80 bentonite, the technological void ratio, the artificial injection strategy, and to check the interaction between PRACLAY Seal Test and PRACLAY Heater Test etc.. When designing the seal, two main criteria are followed: The maximum swelling pressure between the bentonite and Boom clay should be 4~5 MPa (large enough to "re-seal" the EDZ of host formation, but should not too large to avoid re-damage the host formation), value and the magnitude of the hydraulic conductivity of bentonite at saturated state is 1~2 orders lower than that of undisturbed Boom Clay.

The basic theory for the coupled thermo-hydro-mechanical (THM) analysis considered in this paper has been presented elsewhere (Olivella et al., 1994; Gens et al., 1998; Rutqvist et al., 2001), based on which CODE_BRIGHT (Olivella et al., 1996), a finite element code, was developed by Technical University of Catalonia (UPC) and Centre for Numerical Methods in Engineering (CIMNE). The code has been used in many research projects in the context of radioactive waste disposal, and it is well known in the scientific and technical community dealing with this kind of applications. This code was here used to carry out the numerical simulation.

3.1 THM parameters

MX80 bentonite was selected mainly based on the literature data on its swelling capacity, water retention potential and permeability. Furthermore it is a Na-bentonite which makes it chemically compatible with the Boom Clay water. Finally, the relevant experience and information with this type of bentonite is documented widely from its use in other

experiments in different underground research facilities (Mont Terri, Bure, ASPO, AECL's URL) and in different on surface laboratories (CEA, CIEMAT, CERMES and SKB).

Clay Technology in Sweden (Borgesson & Hernelind, 1999) has done some tests to measure the variation of the thermal conductivity of MX80 bentonite with saturation degree, see Figure 7. The following model is used to fit the measured data (Chen & Ledesma, 2009)

$$\lambda = \lambda_{dry} \cos^2\left(\frac{\pi S_l}{2}\right) + \lambda_{sat} \sin^2\left(\frac{\pi S_l}{2}\right) \tag{1}$$

where λ_{dry}, λ_{sat} are the thermal conductivity at dry and full saturation condition, and S_l is the saturation degree.

A large number of laboratory measured permeability for MX80 bentonite with different dry density are shown in Figure 8 (Borgesson & Herlineid, 1999; Krohn, 2004; Villar, 2005; Gatabin et al., 2007). Kozeny´s law is used to relate the intrinsic permeability to the porosity, and this model fits the measurement from CEA (Gatabin et al., 2007) quite well.

$$k_i = k_0 \frac{\phi^3}{(1-\phi)^2} \frac{(1-\phi_0)^2}{\phi_0^3} \tag{2}$$

where k_0 is the intrinsic permeability at reference porosity ϕ_0.

The retention capacity of MX80 bentonite has been measured to relate the saturation degree to the suction. The modified van Genutchen model is used to fit the measured data for bentonite of dry density around 1700kg/m^3 and 1800kg/m^3.

$$S_l = \left[1 + \left(\frac{P_g - P_l}{P_0}\right)^{\frac{1}{1-\beta}}\right]^{-\beta} \left(1 - \frac{P_g - P_l}{S_m}\right)^m \tag{3}$$

where $P_g - P_l$ is the matric suction, and P_0, β, S_m, m are the parameters of the modified van Genutchen model.

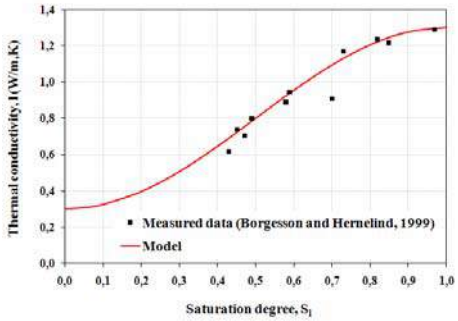

Figure 7 Thermal conductivity of MX80 bentonite

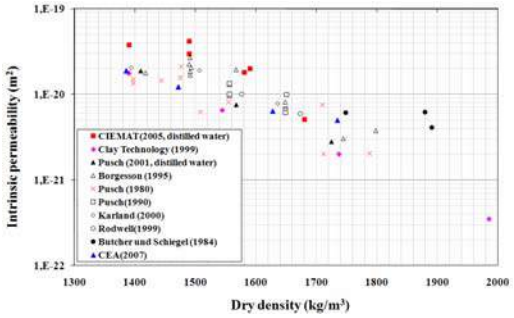

Figure 8 Intrinsic permeability of MX80 bentonite

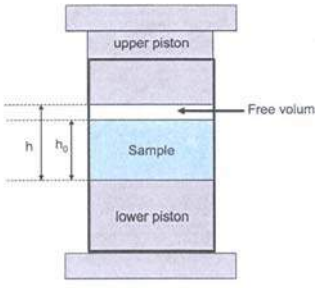

(a) Test cell

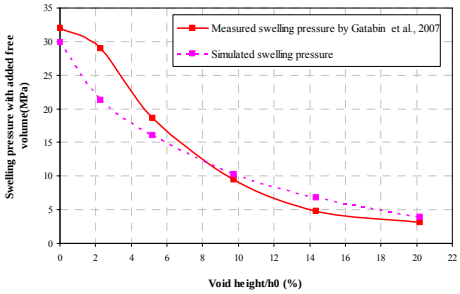

(b) Comparison between measured data and modeled results

Figure 9: Swelling pressure test with different free swelling volume on MX80 bentonite

Barcelona Basic Model (BBM, Alonso et al., 1990) is employed as the mechanical model for unsaturated bentonite, which can well represent the wetting expansion and drying shrinkage behaviors in a consistent and unified manner. Tang (2005) has done some laboratory tests to investigate the mechanical behavior of MX80 bentonite, from which elastic stiffness coefficient for changes in net mean stress, κ; stiffness parameter for changes in net mean stress for virgin states, λ; and preconsolidation pressure, p_0 at different controlled suction can be obtained. Two suction controlled oedometer tests were carried out for MX80 bentonite of dry densities $1790\,kg/m^3$ and $1690\,kg/m^3$ to obtain the relationship between the void ratio and the suction, the tests were performed at constant loading 0.1 MPa, from which variation of elastic stiffness parameter for changes in suction, κ_s for two initial dry density $1790\,kg/m^3$ and $1690\,kg/m^3$ are obtained (Villar, 2005).

Table 1 Thermo-hydraulic parameters

Material	Thermal conductivity (W/mK)		Specific heat	Intrinsic permeability	Initial Porosity	Retention curve			
	λ_{dry}	λ_{sat}	$c(J/kgK)$	$k_0\,(m^2)$	ϕ_0	P_0 (MPa)	β	S_m	m
Boom clay	1.35	1.35	769	4.5×10^{-19} (constant)		20.36	0.378		
Bentonite	0.3	1.3	800	5.0×10^{-21} * 3.5×10^{-21} **	0.388* 0.353**	32.30* 25.17**	0.306* 0.261**	600* 800**	1.1 1.1
Sand	2.54	2.54	900	10^{-13}	0.434				
Concrete liner	1.5	1.5	770	4.5×10^{-18}	0.1				
Steel	50.16	50.16	460	10^{-30}	0.001				

*: for bentonite of dry density of 1700 kg/m^3;
**: for bentonite of dry density of 1800 kg/m^3.

Table 2 Mechanical model and parameters

Material	Model	Parameters
Boom clay	Cam-clay	$\kappa = 0.025, \nu = 0.2, \lambda = 0.13, M = 0.814, p_s = 0.7815MPa, p_{0*} = 6MPa$
Bentonite	BBM	$\kappa_{i0} = 0.032; \alpha_i = -0.008; \alpha_{il} = -0.002;$ $\rho_d = 1700kg/m^3 : \kappa_{s0} = 0.185, \alpha_{ss} = -0.085;$ $\rho_d = 1800kg/m^3 : \kappa_{s0} = 0.2; \alpha_{ss} = -0.065;$ $K_{\min} = 0.35MPa; \nu = 0.2;$ $\lambda = 0.15; r = 0.4; \beta = 0.032MPa^{-1};$ $M = 0.780; p_c = 0.05MPa; p_{0*} = 0.22MPa$
Sand	Linear Elasticity	$E = 10MPa, \nu = 0.3$
Concrete Liner		$E = 30GPa, \nu = 0.15$
Steel		$E = 2.06\times10^5 MPa, \nu = 0.3$

Note: κ_i: elastic stiffness parameter for changes in net mean stress; κ_s: elastic stiffness parameter for changes in suction; $K_{\min}$: minimum bulk modulus; p_{0*}: preconsolidation stress for saturated conditions; ν: Poisson's ratio; $\lambda(s) = \lambda(0)\left[(1-r)\exp(-\beta s) + r\right]$ is stiffness parameter for changes in net mean stress for virgin states of the soil; and M is the slope for critical state lines.

Dependence of the swelling pressure on dry density has been found to be quite stable from a large number of laboratory tests on MX80 bentonite. Aforementioned mechanical parameters are validated by simulating the swelling pressure tests with dry density of both

$1700\,kg/m^3$ and $1800\,kg/m^3$. Gatabin et al. (2007) have recently carried out some laboratory tests on MX80 bentonite to simulate the PRACLAY Seal test in a simple way, different free swelling volumes (simulating the technological voids in the seal) are allowed for the different samples with initial dry density of around 1820 kg/m^3 (Figure 9a). The variation of measured swelling pressure with added free volume is used to further check the parameters for MX80 bentonite. The good agreement between measurement and simulation (see Figure 9b) proves again the reliability of the set of BBM parameters for MX80 bentonite.

The main THM parameters used for the scoping calculation are summarized in Tables 1~2.

3.2 2D axisymmetric modeling

Coupled Thermo-Hydro-Mechanical (THM) modeling with two dimensional axisymmetric geometry is performed for the seal test. The numerical simulation procedure follows the actual and planned procedures of the PRACLAY tests: (1) Excavation of the PRACLAY gallery and installation of the lining; (2) Equilibrium and drainage period (after excavation and before installation of seal); (3) Installation of PRACLAY seal (removal of the wood, installation of bentonite and steel structure); (4) Artificial injection (about 1 year) into bentonite; (5) Backfill and saturate the sand in the gallery; (6) Heating phase: stepwise increase of the temperature to 80 °C (at the interface "Boom clay/liner") within half a year, then keeping the temperature constant during 10 years. Many cases are modeled for the seal test to check the influences of (1) the initial dry density of MX80 bentonite (1700 kg/m^3 and 1800 kg/m^3), (2) the technological void ratio, (3) the artificial injection pressure and duration time, (4) the Connecting Gallery (CG), and (5) the intrinsic permeability of bentonite etc. on (1) the swelling pressure at the interface "Boom clay/bentonite", (2) the swelling pressure at the interface "confining structure/bentonite", (3) the recompression of Boom clay due to swelling of bentonite, (4) the saturation process of the bentonite, and (5) the pore water pressure field within Boom clay around PRACLAY Heater test etc.. The main interesting modeling results are shown in Figures 10~12.

By summarizing the swelling pressures at the interface "bentonite/Boom clay" under many cases, Figure 10 gives the relationship between the steady swelling pressure and the technological void ratio (initial void volume over the initial volume of bentonite blocks) for bentonite of two initial dry densities of 1700kg/m^3 and 1800kg/m^3. Linear lines could well fit the modeled results. From this figure, we can see that if we select bentonite of initial dry density of 1800kg/m^3, and if the technological void ratio can be controlled to be 6 ~10 %, the target steady swelling pressure of 4~5 MPa can be reached.

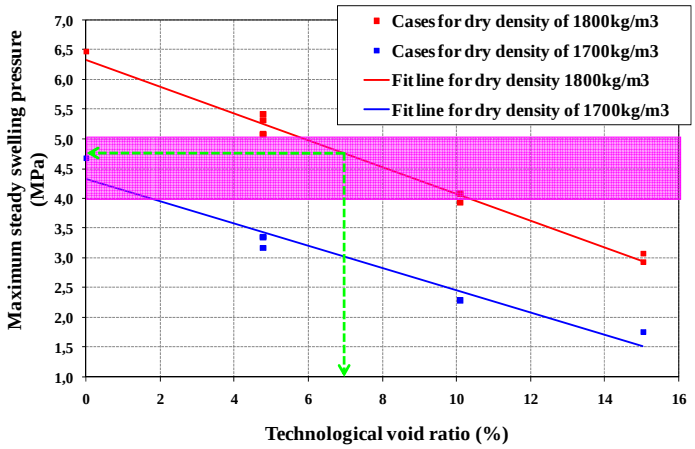

Figure 10 Steady swelling pressure profiles under different technological void ratios (ρ_d=1800kg/m^3)

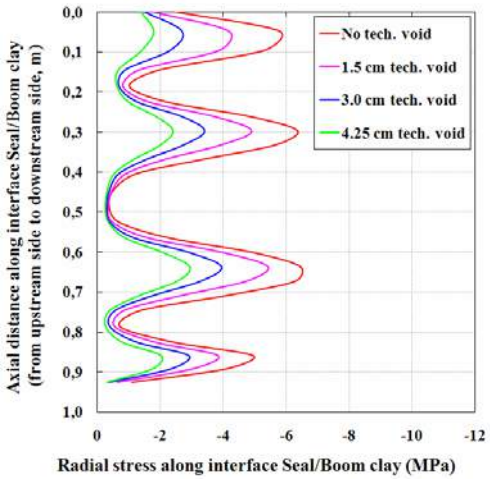

Figure 11 Steady swelling pressure profiles under different technological void sizes (ρ_d=1800kg/m^3)

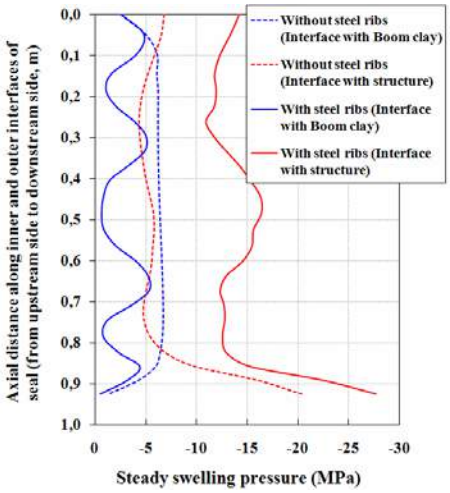

Figure 12 Steady swelling pressure profiles at two interfaces (tech. void size is 1.5 cm, ρ_d=1800kg/m^3)

Figure 11 shows the final steady swelling pressure along the interface "Boom clay/bentonite & steel ribs" for bentonite of initial dry density of 1800kg/m^3. It is observed that with the increase of the technological void sizes (It should be noted that in the modeling, the two technological voids shown in Figure 4 are simplified into one void concentrated at the intrados of the seal with the equivalent volume), the swelling pressure decreases, and the distribution of the swelling pressure is quite inhomogeneous due to the existence of the steel ribs. Figure 12 presents the final steady swelling pressure along both the interface "Boom clay/bentonite & steel ribs" and the interface "bentonite/steel cylinder" for the bentonite of initial dry density of 1800kg/m^3 and the technological void size of 1.5 cm. It is more clearly demonstrated that the existence of steel ribs makes the swelling pressure towards the Boom clay inhomogeneous and increases the swelling pressure towards the steel cylinder.

To investigate the saturation time of the bentonite, the minimum saturation degree within bentonite, $S_{r\text{-}min}$, is defined. Based on the results of many cases, it was found that: (1) After 1-year artificial injection, $S_{r\text{-}min}$=95% in the bentonite has not been reached yet; (2) It takes much time for $S_{r\text{-}min}$ to increase from 99% to 100%, which indicates that the full saturation condition of bentonite before heating test is difficult to reach; (3) Saturation process is mainly controlled by the relative permeability of bentonite and water retention properties ; (4) The presence of steel ribs also makes the saturation process inside the bentonite inhomogeneous, because the steel ribs hinder the water flow from the host Boom clay into bentonite.

3.3 2D plane strain modeling

Coupled THM modeling results of PRACLAY Seal Test using 2D axisymmetric model presented in section 3.2 shows that the existence of the steel ribs induces inhomogeneous swelling pressure towards both Boom clay and confining structure and, much higher swelling pressure is applied on the confining structure.

As shown in Figure 4, the 4 steel ribs remained in place are composed of segments. The neighboring segments of the first and the second and of the third and fourth rib are connected by two lateral plates placed between them. These plates are fixed by "pin-hole connection". This connection prevents the segments of the steel ribs to move outwards during the swelling of the bentonite and a rather heterogeneous pressure distribution exerted by the bentonite on the clay massif is obtained.

The objective of this modeling is to simulate the effect of unlocking the connection between the segments of the steel ribs on the swelling pressure. 2D coupled THM plane strain

models are considered to investigate the efficiency of unlocking of the steel ribs. Two cross-sections of the seal perpendicular to the axis of PRACLAY gallery are employed as the geometries, one crosses both steel rib and bentonite (Model 1), and the other is through only bentonite (Model 2) (see Figure 13).

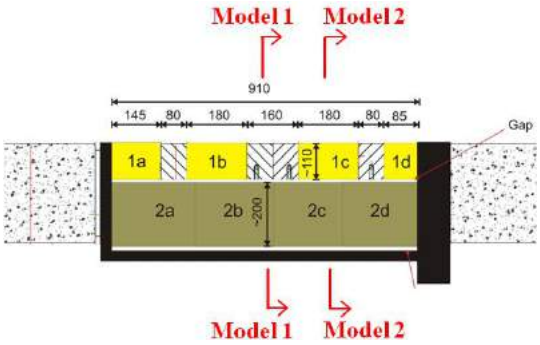

Figure 13: Two cross-sections of the seal employed in Model 1 and Model 2

Results shown in Figures 14 and 15 clearly indicate that unlocking the steel ribs makes the swelling pressure distribution more homogeneous, and it decreases the swelling pressure applied on the confining steel cylinder.

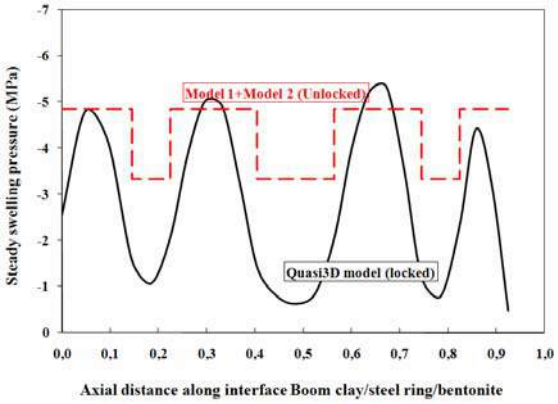

Figure 14 Swelling pressures at the interface "Seal/Boom clay" for both Model 1 and Model 2, with the tech. void being 1.5 cm and ρ_d=1800kg/m^3

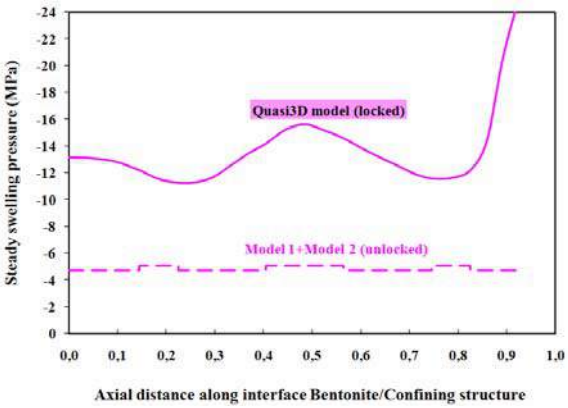

Figure 15 Swelling pressures at the interface "Bentonite/steel cylinder" for both Model 1 and Model 2, with the tech. void being 1.5 cm and ρ_d=1800kg/m^3

4 CONCLUSIONS AND DISCUSSION

Based on the scoping calculations, if the bentonite of initial dry density of 1800kg/m^3 is selected, and the technological void ratio can be controlled to be 6 ~10 %, the target steady swelling pressure of 4~5 MPa would be reached. The intrinsic permeability of MX80 bentonite of initial dry density 1800kg/m^3 is 2 orders lower than that of the Boom clay, and even at the final state after saturation and swelling, the estimated intrinsic permeability of MX80 bentonite is about 6~10×10^{-21}m^2, being nearly 2 orders lower than that of Boom clay. Finally MX80 bentonite of initial dry density of 1800kg/m^3 is selected, which could satisfy the two criteria for the seal design.

The steel ribs are unlocked to release the heterogeneity of the swelling pressure towards the Boom clay, to reduce the swelling pressure applied on the steel cylinder.

The seal test was installed in Feb. 2010, the first measured data and observations are obtained, and the numerical modeling is being updated and improved for the interpretation based on the real test conditions and the measured data.

REFERENCES

Alonso, E.E. Gens, A. & Josa, A. (1990), "A constitutive model for partially saturated soils". Geotechnqiue , Vol. 40(3), 405~430.

Borgesson, L. & Hernelind, J. (1999), "Coupled thermo-hydro-mechanical calculations of the water saturation phase of a KBS-3 deposition hole". Technical Report TR-99-41.

Chen, G.J. & Ledesma, A. (2009), "Coupled thermo-hydro-mechanical modeling of the full scale in-situ test 'Prototype Repository'". Journal of Geotechnical and Geoenvironmental Engineering, ASCE, Vol. 135(1), 121-132.

Dang, K.D. & Robinet, J.C. (2004), "Thermo-hydro-mechanical behaviour of MX80 bentonite for temperature ≥ 100ºC". Final Report. ANDRA report C.RP.0EUG.02.008m.

Gatabin, C. Touze, G. Billaud, P. Imbert, C. & Guillot, W. (2006), "ESDRED PROJECT-MODULE 1, Selection and THM characterisation of the buffer material". Technical Report.

Gens, A. Garcia-Molina, A.J. Olivella, S. Alonso, E.E. & Huertas, F. (1998), "Analysis of a full scale in situ test simulating repository conditions". Int. J. Numer. Analyt. Meth. Geomech., Vol. 22, 515-548.

Krohn, K.P. (2004), "Modelling the re-saturation of bentonite in final repositories in crystalline rock". Final report.

NIROND, (1997), "The PRACLAY Demonstration Test". NIROND report 97-06.

Olivella, S. Carrera, J. Gens, A. & Alonso, E.E. (1994), "Non-isothermal multiphase flor of brine and gas through saline media". Transp. Porous Media, Vol. 15, 271-293.

Olivella, S, Gens, A, Carrera, J, and Alonso, EE: (1996), "Numerical formulation for a simulator (CODE_BRIGHT) for the coupled analysis of saline media". Eng. Comput., Vol. 13, 87-112.

Rutqvist, J. Borgesson, L. Chijimatsu, M. Kobayashi, A. Jing, L. Nguyen, T.S. Noorishad, J. a& Tsang, C.F. (2001), "Thermohydromechanics of partially saturated geological media: governing equations and formulation of four finite element codes". Int. J. Rock Mech. Mining Sciences, Vol. 38, 105-127.

Tang, A.M. (2005), "Effect de la temperature sur le comportement des barrieres de confinement", PhD thesis.

Villar, M.V. (2005), "MX-80 bentonite, thermo-hydro-mechanical characterisation performed at CIEMAT in the context of the Prototype project", CIEMAT Technical Report.

HYDROMECHANICAL BEHAVIOUR OF CALLOVO-OXFORDIAN ARGILLITES DURING DESATURATION/RESATURATION CYCLES

T. Guillon
French National Agency for the Nuclear Waste Management, Châtenay-Malabry, France

R. Giot
Laboratoire Environnement, Géomécanique et Ouvrage, Vandoeuvre-lès-Nancy, France

A. Giraud
Laboratoire Environnement, Géomécanique et Ouvrage, Vandoeuvre-lès-Nancy, France

G. Armand
French National Agency for the Nuclear Waste Management, Bure, France

ABSTRACT: *The French Agency for Nuclear Waste Management (ANDRA) is currently studying the Callovo-Oxfordian argillites (COxA) as a possible repository for nuclear wastes. The aim of this work is to focus on the hydromechanical unsaturated response of the COxA subjected to hydraulic loading. A coupled model is proposed, and is enhanced with a plastic part. First, the mechanical behaviour of the rock is obtained from triaxial tests. The observed inelastic strains are attributed to plasticity (Chiarelli et al., 2003) and a non-associated plastic law is proposed. Later, drying tests are performed to estimate poroelastic parameters. These tests are interpreted using EDF's Code_Aster finite element software as the model involves highly non-linear equations.*

1 OVERALL FRAMEWORK

Deep geological storage seems to be a serious solution for the management of radioactive wastes. The embedding geological layer must exhibit properties in agreement with long term safety. The French Agency for Nuclear Waste Management (ANDRA) is currently studying the COxA as a possible repository for nuclear wastes. The Underground Research Laboratory, located 490 meters below the ground surface within the COxA, is equipped with hundreds of sensors acquiring various kinds of data. Mechanical, hydrodynamical and chemical models should be identified, and parameters should be estimated in order to best fit the experimental results. Particularly, the COxA displays a quite high mechanical strength and a low permeability. Those properties are degraded in the vicinity of the galleries (Bossart et al., 2004; Levasseur et al., 2010), where drilling damaged the rock and climatic conditions are impressed thereafter. An accurate modelling of the hydromechanical coupling is 'crucial' to correctly investigate possible effect of mechanical and hydraulic loading on transfer properties of such rocks around galleries.

2 COUPLED HYDROMECHANICAL MODEL

2.1 Unsaturated mechanics

The equations governing the poromechanical modelling are derived from Coussy's extended work on porous media. The various assumptions are not detailed here, as they can be found in Coussy (2004). The non-linear isothermal isotropic poroelastic constitutive law is obtained extending Biot's theory for partially saturated media (Homand et al., 2004).

2.2 Non-associated plastic law

The COxA exhibits inelastic strains (Chiarelli et al., 2003; Shao et al., 2006). This irreversible behaviour can stem from matrix damage and/or plasticity. Those processes are *a priori* intricate and their separate influences can't be easily quantified. As a first approach, we focused on plasticity in this work.

The plastic law is an extention of Hoxha's work (Hoxha et al., 2007). It is characterized by a non associated deviatoric plastic mechanism combined with an isotropic non-kinematic hardening expressed in terms of mean and equivalent deviatoric effective stresses:

$$\begin{cases} f\left(\boldsymbol{\sigma},\gamma_p\right)=\sigma_{eq}^{'}+\alpha\left(I_1^{'}\right)I_1^{'}-R\left(\gamma_p\right)=0 \\ \alpha\left(I_1\right)=\alpha_\infty+\left(\alpha_0-\alpha_\infty\right)e^{I_1^{'}/I_1^0} \\ R\left(\gamma_p\right)=\left(R_0+H\gamma_p\right)\left(1-\omega e^{-\gamma_p/\gamma_p^0}\right) \end{cases} \quad (1)$$

where $\sigma_{eq}^{'}=\sqrt{3/2\mathbf{s}:\mathbf{s}}\ [Pa]$ is the equivalent deviatoric effective stress, $\mathbf{s}'=\boldsymbol{\sigma}'-I_1^{'}/3\boldsymbol{\delta}\ [Pa]$ the deviatoric effective stress, $I_1^{'}=Tr\left(\boldsymbol{\sigma}'\right)[Pa]$ the mean effective stress, $\gamma_p=\sqrt{3/2\mathbf{e}^p:\mathbf{e}^p}\ [-]$ the plastic shear strain, $\mathbf{e}^p=\boldsymbol{\varepsilon}^p-\varepsilon_v^p/3\boldsymbol{\delta}\ [-]$ the deviatoric plastic strain, $\varepsilon_v^p=Tr\left(\boldsymbol{\varepsilon}^p\right)[-]$ the volumetric plastic strain, $\alpha_0,\alpha_\infty\ [-]$ the internal friction angle coefficients, $R_0,H\ [Pa]$ the cohesion parameters and $\omega,\gamma_p^0,I_1^0\ [-]/[-]/[Pa]$ smoothing parameters. The plastic yield function may be seen as a generalized non linear model, schematically intermediate between Drucker-Prager type model and parabolic type model.

A non-associated model is introduced and the form of the plastic potential is similar to that of the yield surface:

$$\begin{cases} g\left(\boldsymbol{\sigma},\gamma_p\right)=\sigma_{eq}^{'}+\psi\left(I_1^{'}\right)I_1^{'}=0 \\ \psi\left(I_1\right)=\psi_\infty+\left(\psi_0-\psi_\infty\right)e^{I_1^{'}/I_1^0} \end{cases} \quad (2)$$

where $\psi_0,\psi_\infty\ [-]$ are the dilatancy angles.

The plastic model can account for the plastic hardening and the progressive degradation of the tangent modulus observed on the COxA (Jia et al., 2010). Moreover, using opposite signs for ψ_0 and ψ_∞ enables to take into account a dilatancy-contractancy transition.

3 FLOW EQUATIONS

In the following section, equations are not listed. One should refer to Coussy (2004) and Gray et al. (2010) for detailed relationships.

Let us consider a porous medium, where the porosity is saturated with two fluids: liquid water and a gas, perfect mixture of dry air and water vapour. The advection of the two fluids is expressed thanks to the generalized Darcy's law. In addition, the diffusion of vapour in dry air is taken into account through Fick's law. The mass balance is also included, constraining the fluids mass supplies. Two thermodynamical relations complete the description. First, the dry air and vapour are seen as perfect gases, and second the water balance leads to the Kelvin relation (providing that the liquid/gas phase transition is instantaneous).

The advection equations display the intrinsic and relative permeabilities. Some empirical models have been suggested to express the relation between the medium permeability and its saturation (see Chen et al. (1999) for a short review). Among others, Van Genuchten (1980) proposed a statistical model correlating the saturation with the capillary pressure and integrated it in Mualem's permeability relation. The Van Genuchten-Mualem's model gives good agreements with geomaterials (Dai et al., 2008; Hwang and Powers, 2003; Leij et al., 1997) while offering a quite simple form based on 4 parameters only:

$$\begin{cases} S_{le}\left(p_c\right) = \left(1+\left(p_c / p_r\right)^n\right)^m \\ K_l^{rel}\left(S_l\right) = \sqrt{S_{le}}\left(1-\left(1-S_{le}^{\ 1/m}\right)^m\right)^2 \\ K_g^{rel}\left(S_l\right) = \sqrt{1-S_{le}}\left(1-S_{le}^{\ 1/m}\right)^{2m} \end{cases} \tag{3}$$

where $S_{le} = \left(S_l - S_{lr}\right)/\left(1-S_{lr}\right)\left[-\right]$ is the reduced saturation, $K_i^{rel}\left[-\right]$ the relative permeability to liquid or gaz ($i = l/g$), $S_{lr}\left[-\right]$ the residual saturation, $p_r\left[Pa\right]$ the residual capillary pressure and $n, m\left[-\right]$ dimensionless coefficients.

m is often considered as equal to $1-1/n$, but those two parameters can be uncoupled. Mixing the mass balance equations, the advection and diffusion relations yield the non-linear field equations to be solved within the porous medium (Giraud et al., 2009):

$$\begin{cases} C_{l\varepsilon}\dfrac{\partial \varepsilon_v}{\partial t} + C_{lc}\dfrac{\partial p_c}{\partial t} + C_{\mathrm{lg}}\dfrac{\partial p_g}{\partial t} = \nabla.\left[K_{lc}\nabla p_c + K_{\mathrm{lg}}\nabla p_g\right] \\ C_{g\varepsilon}\dfrac{\partial \varepsilon_v}{\partial t} + C_{gc}\dfrac{\partial p_c}{\partial t} + C_{gg}\dfrac{\partial p_g}{\partial t} = \nabla.\left[K_{gc}\nabla p_c + K_{gg}\nabla p_g\right] \end{cases} \tag{4}$$

where $K_{ii}\left[kg.m^{-1}.s^{-1}.Pa^{-1}\right]$ are non-linear coefficients (Giraud et al., 2009).

4 DRYING TEST

4.1 Test principle

The drying test is based on the mass variation of a sample subjected to a certain Relative Humidity (RH) change. In order to balance with the atmosphere, heat and mass transfers occur within the sample. In particular at the beginning of the test, evaporation rate is high and the drying process requires a huge amount of energy. The former is provided by the sample itself through heat transfers and is accompanied by a temperature variation (Gerard et al., 2009). However, as far as weakly permeable materials are concerned, heat transfers happen quasi-instantaneously (compared to those of mass) and the slowness of the humidity transport hinders the evaporation. The latent heat of vaporization of water required during the drying is hence provided by the atmosphere, making the temperature variation in the sample negligible (Mainguy et al., 2001). The drying test can therefore be considered as isothermal. The mass loss/gain kinetic is due to the water exchanges with the atmosphere and is mostly controlled by the sample transport properties. By modifying the porous medium, the mechanics also plays a (much lower, see below) role. Model parameters can be retrieved by fitting the mass and strains data recorded during the test.

4.2 *Experimental set-up*

A rock sample ($\phi = 38\,mm$ diameter and $h = 57\,mm$ height) is placed within a hermetic chamber in which a saline solution enables a constant RH to be maintained (see Figure 1). Once the equilibrium with the atmosphere is reached, the saline solution is changed. According to Kelvin's relation, a capillary pressure is impressed at the sample's boundaries and triggers water transport within it. The sample mass is measured regularly (every 2 to 8 days) until a plateau is noticed. Moreover, gauges are glued at the sample's mid-height, acquiring the axial strains continuously (once every ten minutes).

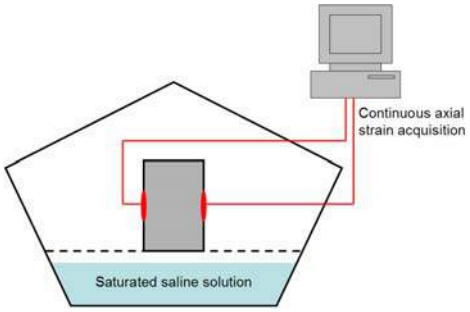

Figure 1 : Experimental set-up for the drying test

4.3 *Initial and boundary conditions*

The sample is assumed to be initially in equilibrium with the atmosphere (RH of h_r^0). The capillary, gas and vapour pressures as well as the stress state are assumed to be homogeneous within the sample:

$$\begin{cases} p_c\left(x,t=0\right) = -\left(\rho_l RT\right)/M_v \ln\left(h_r^0\right) \\ p_g\left(x,t=0\right) = p_{atm} \\ p_v\left(x,t=0\right) = p_v^{sat}\left(T\right)h_r^0 \\ \sigma_{ij}\left(x,t=0\right) = -p_{atm}\delta_{ij} \end{cases} \tag{5}$$

where $p_{atm}\left[Pa\right]$ is the atmospheric pressure, $p_v^{sat}\left[Pa\right]$ the vapour pressure in a water saturated air, $M_v\left[kg.mole^{-1}\right]$ the molar mass of vapour, $\mathrm{R}\left[J.K^{-1}.kg^{-1}\right]$ the universal gas constant, $\mathrm{T}\left[K\right]$ the absolute temperature and $\rho_l\left[kg.m^{-3}\right]$ the liquid density.

At time 0^+, the saline solution is changed (RH of h_r^{imp}) and the capillary pressure is modified. According to RH monitoring, the RH stabilization requires less than $t_m = 5h$. In this paper, a progressive step loading is imposed between 0^+ and t_m, and a constant capillary pressure is then maintained. The capillary pressure on the boundary $\partial\Omega$ of the sample is assumed to be uniform:

$$\begin{cases} p_c\left(x \in \partial\Omega, t > 0\right) = -\left(\rho_l RT\right)/M_v \ln\left(h_r^{imp}\right) \\ p_g\left(x \in \partial\Omega, t > 0\right) = p_{atm} \\ \sigma_n\left(x \in \partial\Omega, t > 0\right) = -p_{atm} \end{cases} \tag{6}$$

where $\sigma_n\,[Pa]$ is the normal part of the stress tensor.

The initial (5) and boundary (6) conditions along with the field equations (4) give the fully coupled poroplastic model to be solved within the sample. The equations are highly non-linear, and the problem is therefore solved using a Finite-Elements Method through the Code_Aster (EDF) code. According to the structural and loading symmetries, the resolution is achieved on a quarter of the sample, meshed with quadratic edged quadrangles (see Figure 2). The mesh is refined close to the outer boundaries.

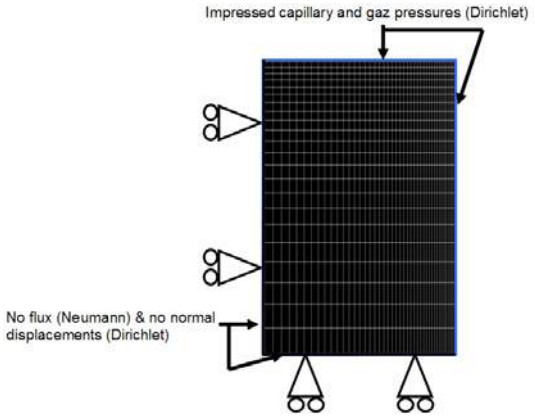

Figure 2 : Sample meshing and boundary conditions for the modelling of drying tests

5 RESULTS

5.1 Plastic parameters fitting

The elastoplastic law involves 2 elastic and 9 plastic parameters: respectively (E,ν) and $(\alpha_0,\alpha_\infty,R_0,H,\omega,\gamma_p^0,I_1^0,\psi_0,\psi_\infty)$, where $E[Pa]$ and $\nu[-]$ are the undrained Young modulus and Poisson coefficient. These parameters were assessed through a triaxial test. Each parameter can be best fitted on a particular part of triaxial tests stress-strains curves. The elastic parameters can be determined from the initial linear part of these curves. As for the plastic ones, they can be inferred from the non-linear parts. R_0 yields the plasticity threshold, while H fits an asymptotic linear behaviour. α_0 and α_∞ constrain the initial and final shape of the axial and radial strains, with I_1^0 controlling the fastness of the in-between transition. ω accounts for the non-linear part of the hardening, and γ_p^0 for its curvature. ψ_0 and ψ_∞ suit to the initial and final shape of the volumetric strains.

In this work, no degradation of the elasto-plastic parameters was considered. That is, the model can't fit either the post-peak behaviour, or the stiffness deterioration indicated by the unloading-loading cycles. As a first approach, those were not modeled at all. The parameters are fitted according to triaxial test results. The test was carried out on a Cox argillite cylindrical sample, with a $\phi = 38\,mm$ diameter and a $h = 76\,mm$ height. The sample was first subjected to a progressive hydrostatic stress up to a final compressive state of $p_{conf} = -12\,MPa$. An axial displacement (at a constant velocity) was then impressed at the top of the sample, while a p_{conf} confining pressure was maintained. In order to experimentally assess the stiffness deterioration, unloading-reloading cycles were performed.

Relaxation plateaus were observed. Axial and radial strains were acquired at the mid-height of the sample, all along the test. Figure 3 gives the comparison between experimental and numerical results, according to the parameters set obtained in Table 1. On Figure 3, compressive strains are positives.

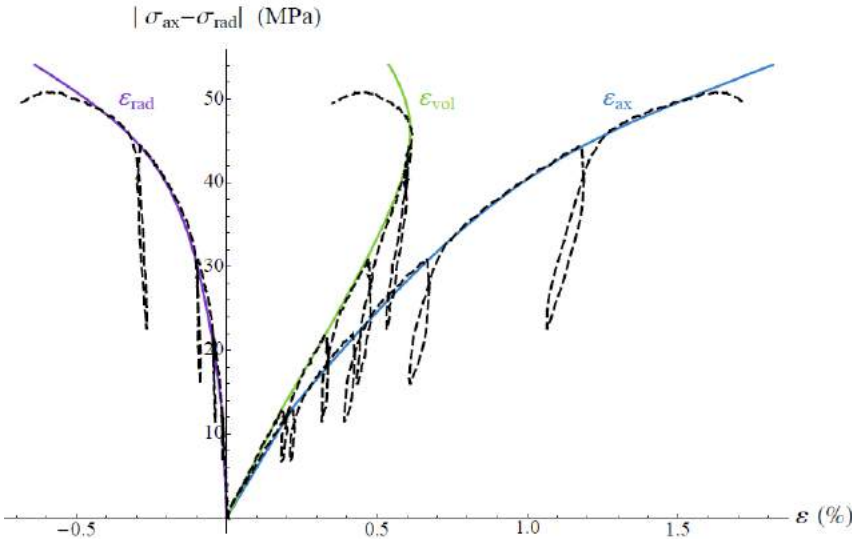

Figure 3 : Equivalent deviatoric stress versus axial, radial and volumetric strains (dashed lines: experiment; continuous colored lines: simulation)

Table 1 : Estimated plastic parameters

Parameters	$\alpha_0[-]$	$\alpha_\infty[-]$	$R_0[MPa]$	$H[MPa]$
Values	0.3	0.1	20	1200

$\omega[-]$	$\gamma_p^0[-]$	$I_1^0[MPa]$	$\psi_0[-]$	$\psi_\infty[-]$
0.97	0.0015	270	-0.6	0.85

Figure 4 points out the hardening of the material.

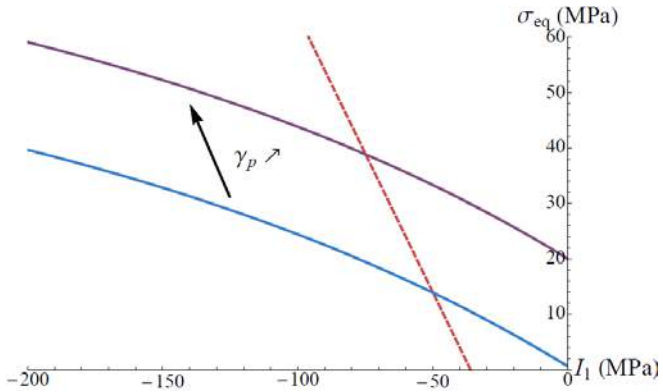

Figure 4 : Initial (blue) and final (purple) yield surfaces, and triaxial test loading path (red dotted)

5.2 Mechanical response to drying tests

Two drying tests were carried out, each one starting from $h_r^0 = 85\%$. The samples EST32883-2 and EST32883-3 were loaded with $h_r^{imp} = 94\%$ and $h_r^{imp} = 98\%$ respectively. So far, the RH amplitudes were to small to enable inelastic strains. Indeed, the elastic model was sufficient to retrieve the experimental mass variations and axial strains (see Figures 5 and 6).

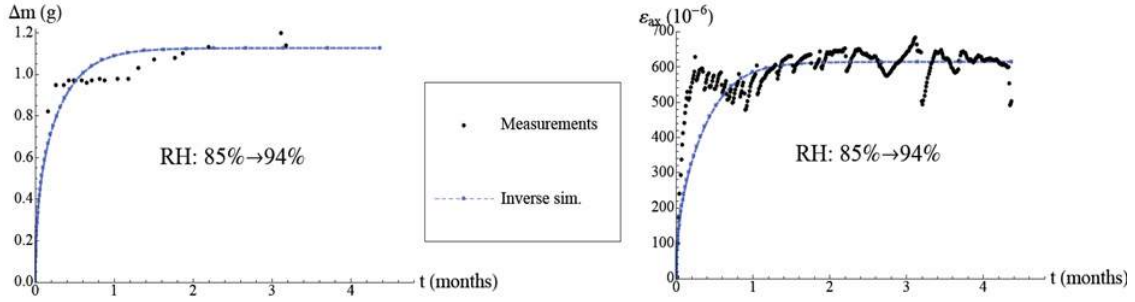

(a) (b)

Figure 5 : Mass variations (a) and strains (b) versus time, EST32883-2 sample

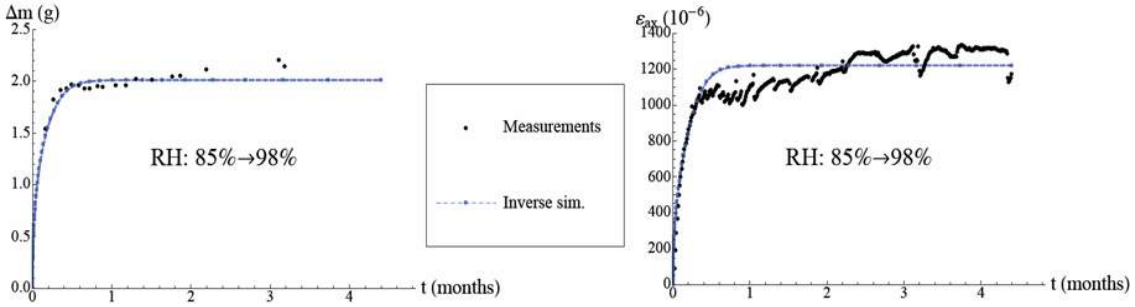

(a) (b)

Figure 6 : Mass variations (a) and strains (b) versus time, EST32883-3 sample

The parameters were fitted following an inverse approach, according to a Newton-Raphson method modified with a Levenberg-Marquardt algorithm (Giot et al., 2010). Final results were quite close to direct simulations. Initial parameters (stemming from direct calculations) are close to the solution and avoid discrepancies of a badly conditioned problem (see Table 2). The inversions were performed on 4 parameters: $\mathbf{c} = (b, n, m, p_r)$.

Table 2 : Estimated poroelastic parameters

Parameters	$E[MPa]$ (fixed)	$b[-]$	$n[-]$	$m[-]$	$p_r[MPa]$	$S_{lr}[-]$ (fixed)
Initial values (sample 2)	6000	0.65	1.2	$1-1/n$	9	0
Final values (sample 2)	6000	0.64	1.16	0.17	9.4	0
Initial values (sample 3)	5000	0.75	1.22	$1-1/n$	8.5	0
Final values (sample 3)	5000	0.73	1.2	0.17	8.9	0

Model relative sensitivities were calculated around the optimal parameter values. The mass variations were quite insensitive to E and b. The plateau is sensitive to n, while a sensitivity peak for m and p_r was observed during the transient phase. The strains however show a sensitivity peak to n, m and p_r during the transient phase and are much more sensitive to E and b. Also, the sensitivities to these two parameters were always of the same order of magnitude but with opposite signs. This highlights the correlated influence of E and b, and justifies fixing one of them during inversions. As attention was brought to hydromechanical coupling, E was fixed during computations.

A third drying test was carried out, under greater RH amplitude ($h_r^0 = 54\%, h_r^{imp} = 94\%$). Two results were obtained, whether the solid matrix was considered elastic or plastic. The elastic as well as the plastic model gave satisfying mass variations, but overestimated about twice the axial strains (see Figure 7). Little difference was noticed between the elastic and plastic results (Figure 7.b). If further investigations confirm this observation, it could be concluded that the elastic part would account for almost all the strains occurring during drying tests.

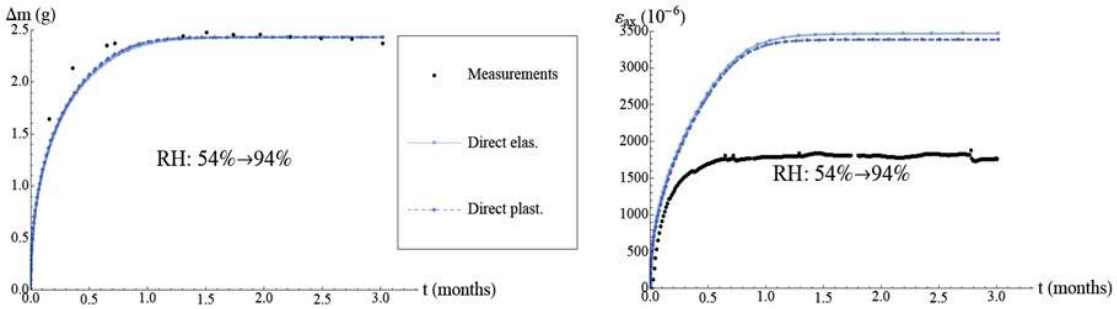

(a) (b)

Figure 7 : Mass variations (a) and strains (b) versus time, EST32887-12 sample

The discrepancy between measured and modelled strains may result from the transversely isotropic structure of the COxA. Their deposit conditions led to transport and mechanical anisotropies (Delay et al., 2006; Zhang and Rothfuchs, 2004). The elasto-plastic parameters were first obtained on a sample whose axis was perpendicular to the isotropic planes, whereas the drying samples' axes were parallel. E and ν are particularly sensitive to orientation (Sarout et al., 2007). According to the results, the values of E and ν seemed to be of relatively little importance for samples bearing small RH amplitudes. In this case, strains could be retrieved with biased elastic parameters. When the RH amplitude, and thus strains, was increased, the error in the parameters values did not allow to fit experimental strains. Due to argillaceous sheets, the rock exhibits a much softer behavior in the perpendicular orientation. That is, estimating parameters from a "parallel" sample should bring more acceptable results. Ongoing calculations should help validate this assumption.

6 CONCLUDING REMARKS

Firstly, a plastic model was proposed and applied to the COxA. The plastic yield surface and potential can take into account hardening and progressive degradation of the tangent modulus, as well as a dilatancy-contractancy transition. The 11 elasto-plastic parameters can be fitted on different parts of the stress-strains curves, enabling their fast identification.

Nevertheless, the results presented in this paper consist in a first approach. Further investigations are still carried out, such as proper identification based on back and sensitivity analysis. In order to fully describe the stress-strains curves, a post-peak part and stiffness deterioration should be added. Moreover, more tests under various confining pressures should be involved.

Secondly, a poro-mechanical coupled description of drying tests was put forward. The model is derived from Biot's theory and the partially saturated flow is based on the Van Genuchten-Mualem relations. Hydromechanical coupling was observed, as hydraulic loading resulted in mechanical response. The mass variations and axial strains could be satisfactorily retrieved for two samples. However, discrepancies were noticed between the measured and simulated strains of the third sample, raising the issue of mechanical anisotropy in COxA. Elasto-plastic parameters estimated from samples whose axes are parallel to bedding planes should give better results. In addition, samples subjected to drying paths should give information on the hysteretic behaviour of argillites. The model lacks description of observed phenomena, such as mechanical and transport anisotropies or drying-induced damage. The latter modifies the poral network, and thus the permeability. Those features should be integrated in the model, so that the simulations can better fit the reality.

The main objectives were to introduce a coupled hydromechanical model able to reproduce the mass variations and strains occurring during drying test of samples, and to enhance the initial elastic model thanks to a plastic non-associated law. Only tests with great RH loading amplitudes involved plasticity with respect to the model, and made use of the fully poroplastic description. The first results seemed to show that the impact of this plasticity is not significant but it needs to be confirmed. Current work is focused on coupled numerical modelling as well as further development of the plastic model.

ACKNOWLEDGEMENTS

The authors would like to thank the ANDRA for their financial support and their sample providing.

REFERENCES

Bossart, P., Meier, P.M., Moeri, A., Trick, T. & Mayor, J.-C. (2002), "Geological and hydraulic characterisation of the excavation disturbed zone in the Opalinus Clay of the Mont Terri Rock Laboratory". Eng. Geol., Vol. 66(1-2), 19-38.

Chen, J., Hopmans, J.W. & Grismer, M.E. (1999), "Parameter estimation of two-fluid capillary pressure-saturation and permeability functions". Adv. Water Resour., Vol. 22(5), 479-493

Chiarelli, A.S., Shao, J.F., & Hoteit, N. (2003), "Modeling of elastoplastic damage behaviour of a claystone". Int. J. Plasticity, Vol. 19(1), 23-45

Coussy, O. (2004), Poromechanics, John Wiley & Sons Ltd, The Atrium, Southern Gate, Chichester, England

Dai, Z., Semper, J., Wolfsberg, A. & Levitt, D. (2008), "Identification of relative conductivity models for water flow and solute transport in unsaturated bentonite". Phys. Chem. Earth, Vol. 33(1), S177-S185

Delay, J., Trouiller, A. & Lavanchy J.-M. (2006), "Hydrodynamical properties of the Callovo-Oxfordian argillites: comparisons of results obtained according to different methods". C.R. Geosci., Vol. 338(12-13), 892-907 *[french + english abridged version]*

Gerard, P., Léonard, A., Masekanya, J.-P., Charlier, R. & Collin, F. (2010), “Study of the soil-atmosphere moisture exchanges through convective drying tests in non-isothermal conditions”. Int. J. Numer. Anal. Meth. Geomech., Vol. 34(12), 1297-1320

Giot, R., Giraud, A., Auvray, C., Homand, F. & Guillon T. (2010), “Fully coupled poromechanical back analysis of the pulse test by inverse method”. Int. J. Numer. Anal. Meth. Geomech, DOI: 10.1002/nag.897

Giraud, A., Giot, R. & Homand, F. (2009), “Poromechanical modelling and inverse approach of drying tests on weakly permeable porous rocks”. Transp. Porous Media, Vol. 76(1), 45-66

Gray, W.G., Schrefler B.A. & Pesavento, F. (2010), “Work input for unsaturated elastic porous media”. J. Mech. Phys. Solids, Vol. 58(5), 752-765

Hoxha, D., Giraud, A., Homand, F. & Auvray, C. (2007), “Saturated and unsaturated behaviour modelling of Meuse-Haute/Marne argillite”. Int. J. Plasticity, Vol. 23(5), 733-766

Homand, F., Giraud, A., Escoffier S., Koriche, A. & Hoxha D. (2004), “Permeability determination of a deep argillite in saturated and partially saturated conditions”. Int. J. Heat Mass Trans., Vol. 47(14-16), 3517-3531

Hwang, S.I. & Powers S.E. (2003), “Estimating unique soil hydraulic parameters for sandy media from multi-step outflow experiments”. Adv. Water Resour. , Vol. 26(4), 445-456

Jia, Y., Bian, H.B., Su, K., Kondo, D. & Shao J.F. (2010), “Elastoplastic damage modelling of desaturation and resaturation in argillites”. Int. J. Numer. Anal. Meth. Geomech., Vol. 34(2), 187-220

Leij, F.J., Russell, W.B. & Lesch, S.M. (1997), “Closed-Form Expressions for Water Retention and Conductivity Data”. Ground Water, Vol. 35(5), 848-858

Levasseur, S., Charlier, R., Frieg, B. & Collin, F. (2010), “Hydro-mechanical modelling of the excavation damaged zone around an underground excavation at Mont Terri Rock Laboratory”. Int. J. Rock Mech. Min. Sci., Vol. 47(3), 414-425

Mainguy, M., Coussy, O. & Baroghel-Bouny, V. (2001), “Role of air pressure in drying of weakly permeable materials”. J. Eng. Mech., Vol. 127(6), 582-592

Sarout, J., Molez, L., Guéguen Y. & Hoteit N. (2007), “Shale dynamic properties and anisotropy under triaxial loading: Experimental and theoretical investigations”. Phys. Chem. Earth, Vol. 32(8-14), 896-906

Shao, J.F., Jia, Y., Kondo, D. & Chiarelli, A.S. (2006), “A coupled elastoplastic model for semi-brittle materials and extension to unsaturated conditions”. Mech. Mater., Vol. 38(3), 218-232

Van Genuchten, M.T. (1980), “A closed-form equation for predicting the hydraulic conductivity of unsaturated soils”. Soil Sci. Soc. Am. J., Vol. 44(5), 892-898

Zhang, C. & Rothfuchs T. (2004), “Experimental study of the hydro-mechanical behaviour of the Callovo-Oxfordian argillite”. Appl. Clay. Sci., Vol. 26(1-4), 325-336

REACTIVE TRANSPORT IN GRANULAR MEDIA: HEAVY METAL TRANSPORT MODELING

T. Khalil , N. Sayouri, P-Y.Hicher
Research Institute of Civil Engineering and Mechanics(GeM), UMR CNRS 6183, Ecole Centrale de Nantes, 1 Rue de la Noë BP 92101, Nantes cedex 3, France

ABSTRACT: *This study is aimed at developing a better understanding of the mechanisms of coupled particle (eroded)-pollutants migration in porous materials. The transport of eroded particles has an important role in the transport of pollutants. In fact, in presence of soil particles (e.g. sandy soils) in underground aqueous medium, the pollutants are adsorbed and desorbed by the mobile and immobile soil particles. The erosion of the particles adsorbing the heavy metal will be considered in our model. Heavy metals have a high affinity to attach themselves to particles. Thus, particle-bounded metals are supposed to simply undergo the erosion of the rigid medium and filtration of the transported particles which are computed first. The pollutants transport changes the concentration of heavy metals in the eroded particles, the filtered particles and the rigid granular skeleton. Therefore, the model equations of the general nonlinear and coupled problem are solved numerically with a finite element code. This model is based on the adsorption data of batch-tests on metals such as Cu, Zn and Pb. These experimental data will give us the values of kinetic constants of adsorption and desorption of these metals for various materials such as kaolinte, bentonite, etc.*

1 INTRODUCTION

Soils and sub-soils can be affected by various pollutants in urban space. In fact, due to demographical increases and growing urbanization, new studies are required of sustainable management of soils and sub-soils. During infiltration of water in soils, the pollutants can be transported within the aqueous phase through saturated and unsaturated zones, towards the groundwater. Therefore, it is necessary to understand the mechanism of the pollutants migration in soils and to predict it in the long term i.e. to study the influence of the internal erosion (IE) of soil particles on the pollutants migration.

Erosion is ubiquitous in the natural and urban environments. Surface soils of the earth have been continuously changing as erosion sculpts the landscape (e.g. carving out valleys and canyons between cliffs) and works to flatten it (e.g. reducing the mountains to a fraction of their original size).

In the present study, we employed a mathematical 1-D model that simulates the experiments in order to monitor bulk changes in the effective porosity (n), intrinsic permeability (k), pore pressure (denoted by P), concentrations of erodible (denoted by C) and fluidized (denoted by χ) particles. The model is based on the continuum description of a multi-phase system, as detailed in Bear and Bachmat (1991).

As a result of the variables' mutual relationships and the high sensibility to initial conditions, a coupled and nonlinear model is unavoidable (Bonelli and Marot, 2008). Current models that treat IE focus on dislodgement and/or transport of particles that occur during water seepage into soils or sands (Vardoulakis et al., 1996, 2001; Papamichos et al., 2001; Wan and Wang, 2002; Papamichos and Vardoulakis, 2005), whereas, to our knowledge, no data is available on the topic of coupled internal flow effects on void network of reinforced materials. The present work lies within the scope of a larger research effort intended to probe the mechanisms inherent to IE and ultimately minimize its destructive consequences.

The erosion of particles of soil adsorbing the heavy metal will be considered in our model. Heavy metals have a high affinity to attach themselves to particles. Thus, particle-bounded metals are supposed to simply undergo the erosion of the rigid medium and the filtration of the transported particles which are computed first. The equations for the transport control and the partition of heavy metals are used within the framework of a model that simulates injection tests. In a first approach, we do not consider the exchanges between the pollutants and the granular skeleton.

2 MODEL DESCRIPTION

A mathematical model is presented to simulate experimental erosion test. The model depends on two erosion parameters, namely the erosion coefficient (λ) and the damage coefficient (β). These erosion parameters are assumed to be constant. During the erosion simulations, we investigated the evolution of: P (in Pa), C (in kg m^{-3}), k (in m^2) and χ (in kg m^{-3}).

2.1 Mathematical formulation

The saturated porous medium is considered to consist of a rigid skeleton (i.e. the Fontainebleau sand and ultrafine sand) and a fluid phase (i.e. the injected water and fluidized particles). In this approach, the fluidized particles were supposed miscible with the existing fluid medium. In order to treat erosion and transport of eroded fine particles within soil, the following must be considered: the poral pressure, the concentration of erodible and fluidized of the eroded soil particles through the soil pores and the increase in the porosity of soils owing to the erosion. This permitted us to formulate the concentration of fluidized particles on the basis of a mass balance including advection-dispersion equation.

$$\frac{\partial (n\chi)}{\partial t} + \nabla (\chi \mathbf{q}) - \nabla (\mathbf{D} \nabla \chi) = \lambda \| \mathbf{q} \| C \tag{1}$$

where $\mathbf{q}$ is the Darcy flux (in m s^{-1}; boldface denotes that $\mathbf{q}$ is a vector and $\| \mathbf{q} \|$ is its norm) and $\mathbf{D}$ is the hydrodynamic dispersion tensor (including the molecular diffusion coefficient, the longitudinal and transversal dispersion coefficients and the tortuosity of the porous medium) (Bear, 1972). The evolution of the concentration of erodible particles,

$$\frac{\partial [(1-n)C]}{\partial t} = -\lambda \| \mathbf{q} \| C \tag{2}$$

is set proportional to the erosion coefficient and is expressed as a linear function of the Darcy velocity of the fluid and erodible particles. If the porosity of the material and the fluid

velocity remain relatively unchanged, the concentration of erodible particles would in time decrease exponentially. Yet, IE affects the rigid skeleton in such a way that dislodgement of erodible particles increases the local of volume of voids. The model was implemented in order to take into account the variation of porosity in time. Many equations based on theoretical work or determined in experiments are used allowing the estimation of the variations of porosity starting from the permeability and screw poured. In our study, porosity is connected to the variation of the density of the erodible particle in the material, which is calculated preliminarily. In other words, the mechanisms of internal erosion affect the rigid skeleton of material in such way that the wrenching of particles increases the volume of the vacuums locally. Thus the evolution of effective porosity

$$n = n_0 + (1 - n\ )\frac{(C_0 - C)}{\rho_m} \tag{3}$$

is formulated as a linear function of the concentration of eroded particles. The subscript "0" indicates that the quantities under consideration are taken at the initial time, t = 0 s. ρ_m is the density of eroded materials (1,300 kg m^{-3}, ESEM observations showed that eroded particles from the effluents mostly consist of silica gel moieties) and $(1-n)(C_0-C) \mid \rho_m$ ratio represents the volume of eroded particles per unit of total volume. The fluid velocity is related to the Darcy law

$$\mathbf{q} = -\frac{\mathbf{k}}{\mu_f}\left(\nabla P + \rho_f \mathbf{g}\right) \tag{4}$$

where μ_f is the viscosity of the fluid phase, ρ_f is the density of the fluid and **g** the gravity. Higher μ_f and ρ_f values tend to lower the mean velocity of the fluid phase. Hence, without precise information about the evolution laws of both variables with regard to P and χ, two linear functions were proposed:

$$\mu_f = (\mu_0 - \mu_w)\frac{\chi}{\rho_0} + \mu_w \tag{5}$$

$$\rho_f = \rho_0\left[1 + \varepsilon_P(P - P_0) + \varepsilon_\chi(\chi - \chi_0)\right] \tag{6}$$

where μ_w is the viscosity of water at 20 °C (1.00 10^{-3} Pa s). The initial viscosity (measured with a rheometer; μ_0 1.10 10^{-3} Pa s) and density (ρ_0 1.050 kg m^{-3}) of the fluid phase were assessed in the absence of imposed flow. The experimentally determined ε_P (3.8 10^{-8} Pa^{-1}) and ε_χ (2.9 10^{-4} m^3 kg^{-1}) coefficients introduce the effect of density change of the fluid as a result of changes in P and χ, respectively. They also allowed to formulate the fluid mass balance equation.

$$\frac{\partial n}{\partial t} + \varepsilon_P\frac{\partial(nP)}{\partial t} + \varepsilon_\chi\frac{\partial(n\chi)}{\partial t} + \nabla\mathbf{q} = 0 \tag{7}$$

Finally, due to the drain of erodible materials, the intrinsic permeability of the porous medium is increased during the passing-through of the fluid, and thus modelled by the linear function below:

$$\mathbf{k} = \mathbf{k}_0\left[1 + \beta(C_0 - C)\right] \tag{8}$$

Eq. (8) depends on the initial permeability ($\mathbf{k}_0$), initial concentration of erodible particles, and is proportional to the damage coefficient.

The main parameters used for erosion simulations by means of the previously described model (see Section 2.1) are showed in Table 1.

Table 1. Parameter used in the numerical simulation of internal erosion mechanism

	Notation	Value of ultrafine sand test
Sample size (diameter, height)	(∅, H)	(0.1 m, 0.1m)
Initial content of erodible particles	C_0	1959 kg m^{-3}
Initial concentrations of fluidizes particles	χ_0	0 kg m^{-3}
Initial effective porosity	n_0	0.242
Initial intrinsic permeability	k_0	3 10^{-13} m^2
Gravity	g	9.81 m^2 s^{-1}
Inflow	Q	0.1 L min^{-1}
Coefficient of longitudinal dispersion	a_L	0.02 m
Coefficient of molecular diffusion	D_d	10^{-10} m^2 s^{-1}
Viscosity of injected water	μ_w	1.00 10^{-3} Pa s
Initial viscosity of poral water	μ_0	1.10 10^{-3} Pa s
Initial density of poral water	ρ_0	1,050 kg m^{-3}
Pressure coefficient	ε_P	3.8 10^{-8} Pa^{-1}
Concentration coefficient	ε_χ	2.9 10^{-4} m^3 kg^{-1}
Density of eroded materials	ρ_m	1,300 kg m^{-3}
Erosion coefficient	λ	1.08 10^{-2} m^{-1}
Damage coefficient	β	1.1 10^{-3} m^3 kg^{-1}

2.2 Calibration and limitations of the model

The proposed IE model depends on two experimentally determined parameters: λ and β (Table 1). The calibration procedure is detailed elsewhere in Chupin et al., 2007. In sum, λ values, which determine, the IE kinetics, were approached (at constant fluid phase viscosity and without dispersion) from Eq. 9 and the monitored mass losses ($\Delta m / \Delta t$) after saturation, i.e., when the mass variations are primarily driven by the dislodgement and transport of particles.

$$\frac{\Delta m}{\Delta t} = \frac{V_{CSC} \| \mathbf{q} \| C_b}{L} \left(1 - \frac{\rho_w}{\rho_m} \right) \left[1 - exp(-\lambda L) \right] \tag{9}$$

λ (in m^{-1}) is the only unknown of Eq. 9 where V_{CSC} is the total volume (rigid skeleton + pores) of the CSC, $C_b = C(0,t)$ ($\sim C_0$ at early IE stages) is the boundary condition, L is the height of the column (0.1 m), ρ_w is the density of injected water. To calculate β, we used the experimental slope of the hydraulic head ($\Delta P / \Delta t$) with the integrated Darcy law (over [0, L], Eq. 10).

$$\frac{\Delta P}{\Delta t} = \frac{\mu_f \| \mathbf{q} \|^2 C_b \beta}{(1-n) \| \mathbf{k}_0 \|} \left[1 - exp(-\lambda L) \right] \tag{10}$$

As far as λ is determined first, β (in m^3 kg^{-1}) is the only unknown of Eq. 10. Overall, while λ controls the amount of eroded particles, β modulates the passing-through of the eroding fluid.

In reality, an important proportion of the eroded particles does not make it to the sample outlet as a result of granular filtration mechanisms. The sizes of constrictions in the void network may be smaller than some of the fluidized particles, preventing these particles to be flushed out by seepage. However, when calculating the fate of eroded particles in the granular matrix, the experimentally determined λ and β parameters factor, at least partly, the overall filtration effects take place on the inside.

2.3 The numerical algorithm

The algorithm used to numerically solve the set of nonlinear and coupled equations is detailed in Kolditz et al., 1998 and in Chupin et al., 2007. The coupled problem is solved by a Gauss-Seidel type method for nonlinear partial differential equation (PDE) systems as explained in (Langtangen, 1999). In brief, the equations of flow and transport with viscosity and density effects are implemented in finite elements codes. This code is computed using the Diffpack software. The problem is discretized in time by finite differences using a classical trapezoidal rule (or θ-rule) and in space by finite element method. The discretized system is solved in sequences with an outer iteration. It consists in solving the initial system within an iterative procedure for each state variable separately, leading to a decoupled resolution. The pressure equation is first solved with respect to P. The pressure equation is still nonlinear and is solved by successive substitutions. Therefore the transport equation is solved with respect to χ, using the most recently computed P values. The attractive feature of the Gauss-Seidel iteration approach to the nonlinear problem is that we only need to solve standard scalar PDEs. For instance, if i denotes the iterative index, Eq. 7 is first solved with respect to $P^{i,j+1}$ (where j represents the time level) considering the other state variables at the previous iteration, i-1. Once $P^{i,j+1}$ is known, the transport and the erosion equations are solved with respect of $C^{i,j+1}$ and $\chi^{i,j+1}$, respectively. Iterations stop when a convergence criterion is fulfilled.

2.4 Results of the erosion model

Simulated data of mass losses, injection pressure, Porosity and permeability have been confronted to experimental results. The resulting curves are presented in Figs. 1A, B, C and D, respectively. The presented erosion simulations were obtained using the experimentally determined values for λ and β. The simulations exhibit evolutions close to experimental data, thereby indicating that model overall reproduces well the IE effects. Indeed, since bulk filtration of fluidized particles has not explicitly been taken into account, the proposed model tends to overestimate the experimental values. Furthermore, local shifts, like the mass loss episode, which correspond to brutal releases of fine Fontainebleau sand grains, were neglected and therefore consist of a limit to the model. Hence, numerical data provide an upper limit of the amplitude of structural changes (e.g. n, p increases) and, when combined to the experimental values for unstable materials, can be used to predict a minimum IE time for reinforced material to reach the final step to failure.

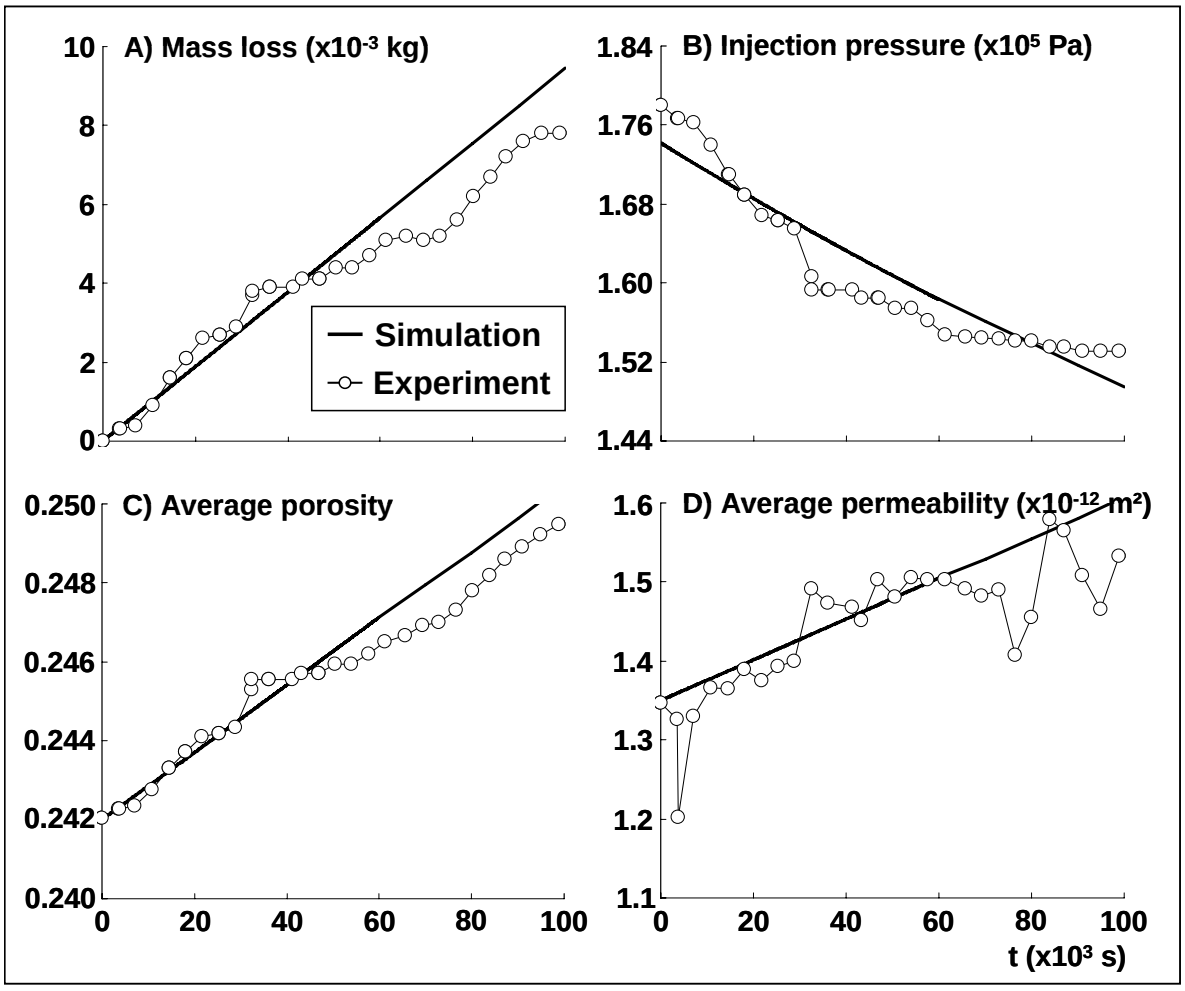

Fig. 1. Comparisons between the evolutions of modelled and experimental with Fontainebleau sand A) mass losses, B) injection pressure, C) average porosity and D) average permeability (t = 0 s denotes the beginning of the mass loss episode)

3 COUPLED EROSION-HEAVY METAL DISTRIBUTION AND TRANSPORT

The transport of eroded particles has an important role in the transport of pollutants. In fact, in presence of soil particles in underground aqueous medium, the pollutants are adsorbed and desorbed by the mobile and immobile soil particles.

The exchanges of heavy metals (e.g. Zn, Cu, Hg) between a fluid (the aqueous phase) and solid phases (the conveyed particles and the rigid granular skeleton of the medium) will be described in terms of kinetic transfer coefficients. Therefore, assuming that adsorption / desorption reactions are governed by a single reversible reaction, a coefficient k_1 controls the transport from the aqueous phase of the fluid to the miscible suspension or the solid phases and a coefficient k2 controls the inverse process. The erosion of the particles adsorbing the heavy metal will be considered in our model. Heavy metals have a high affinity to be fixed to particles. Thus, particle-bounded metals are supposed to plainly undergo the erosion of the rigid medium and the filtration of the transported particles which are computed first. In a first approach, one does not consider the exchange surface between the pollutants and the granular skeleton.

3.1 Mass balance equations

The equation that gives the time evolution of heavy metal concentration in the aqueous phase of the fluid, C_{aq}, is:

$$\frac{\partial\left(\mathrm{n}C_{aq}\right)}{\partial \mathrm{t}}+\nabla\left(\mathbf{q}C_{aq}\right)-\nabla\left(\mathbf{D}\nabla C_{aq}\right)=-K_1C_{aq}+K_2C_m\times\chi \tag{11}$$

where C_m is the concentration of heavy metals on the eroded particles of soil. The second part of the Eq. (11) has a loss term and a gain term. The loss term (the adsorption of the pollutant on the particles; $-K_1C_{aq}$) is formulated product of kinetic adsorption coefficient and concentration of pollutants in water. The term gain (desorption of the pollutant on the particles; $K_2C_m\times\chi$) is the product of kinetic desorption coefficient and tenneur each pollutant particles multiplied by the concentration of the eroded particles (kinetic order 1).

The equation that gives the time evolution of metal concentration on the eroded particles is:

$$\frac{\partial\left((1-\mathrm{n})\chi C_m\right)}{\partial \mathrm{t}}+\nabla\left(\mathbf{q}\chi C_m\right)-\nabla\left(\mathbf{D}\nabla\chi C_m\right)=K_1C_{aq}-K_2C_m\times\chi \tag{12}$$

The presented equations that control the transport and the partition of heavy metals are fated to be used within the framework of the model that simulates erosion mechanism. The model equations of the general nonlinear and coupled problem are solved numerically. Numerically obtained partitions of the probed heavy metals will be compared to that observed from the injection tests.

3.2 Results erosion-heavy metal transport model

The obtained results for the model evolution of concentration of heavy metals on soil particles were presented as function of time and distance from the water injection point. The time step was 10 s. Here we present the model concentration of the transport of heavy metals erosion (Figure 2) and without erosion (Figure 3).

The simulation results clearly indicated an increase of concentration with increasing time of injection (Figure 2). The initial concentration of heavy metals on the soil particles was set to $1.5\text{x}10^{-4}$ g/kg. It is possible that the transport of particles near the point (z=0.01m) move faster than particles near the point (z=0.05) of the column. This indicates that particle dislodgement and ensuing formation of cavities or channels firstly occurred near the input of the sample. Overall, C_m increased with increasing erosion time. Further more researches are needed to probe the migration of eroded particles into porous media during internal erosion.

As for Figure 2, the modelling of Figure 3 used a time step of 10 s. Here we present the modelled evolution of the concentration of heavy metals on soil particles without erosion as function of time and at different point of column. The obtained results clearly indicated an increase of concentration of heavy metal on soil particles with increasing of time injection. However, while expecting upper C_m values near the top of the column, the concentration of heavy metals reached a minimum (Figure 2).

The developed model can reproduce the mechanisms of pollutant transfer in saturated soils coupled with the erosion of fine soil particles. In particular, this model allows us to clearly show the accelerating effect of the migration of pollutant through erosion (figure 4).

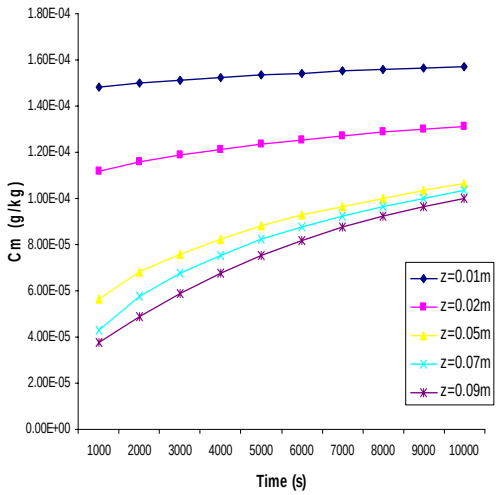

Fig. 2 Concentration of heavy metals on soil particles with erosion at different point of column and as functions of the time.

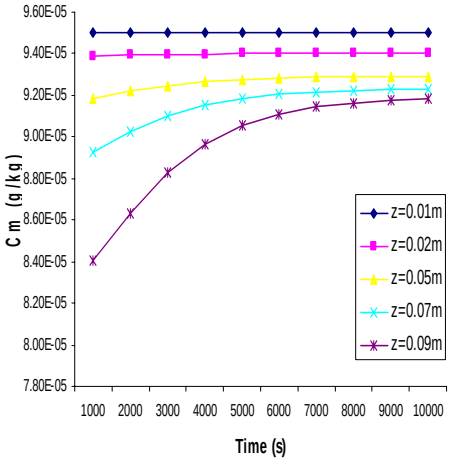

Fig 3. Concentration of heavy metals on soil particles without erosion at different point of column and as functions of the time.

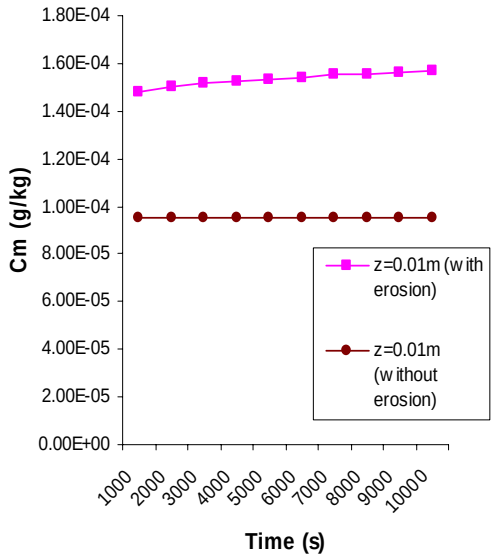

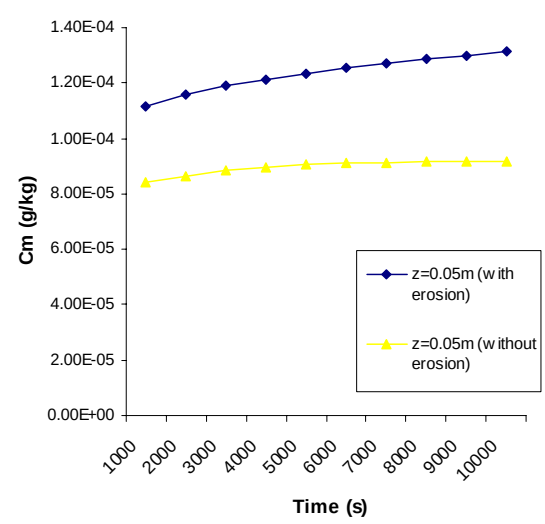

Fig. 4 Comparison between the simulation of concentrations of the pollutant on the particles with and without erosion at different point of column as functions of the time.

4 CONCLUSIONS

The aim of this paper was to improve our understanding of the mechanism of transport of fluids in granular media affected by coupled particle (eroded) - pollutants migration. Here we proposed a model which described the evolution of key parameters of transport of heavy metals and erosion. During the internal erosion, it highlighted the existence of large variations in pore pressure, particle concentrations, porosity and permeability along with their transport. We also demonstrated that the erosion mechanisms play a major role in accelerating the pollutant distribution. The mathematical model reproduces well the internal erosion effects. It enables interpretation of the distribution of structural changes and seepage stresses.

REFRENCES

Bear J., Bachmat Y. (1991). Introduction to modeling phenomena of transport in porous media. Kluwer Academic publishers, Dordrecht, 554 pp.

Donatella.Sterp (2003), Effects of the erosion and transport of fine particules due to seepage flow. International Journal of Geomechanics. Vol. 3, pp.111-122

Damien Lachouette. et al. (2008), One-dimensional modeling of piping flow erosion. Computes Rendus Mecanique. Vol. 336, pp.731–736

Reddi et al., (2000), Comparison of internal and surface erosion using flow pump tests on a sand-kaolinite mixture. Geotechnical Testing Journal. Vol. 23(1), pp. 116-122

I. Vardoulakis, M. Stavropoulou, P. Papanastasiou (1996), Hydromechanical aspects of sand production problem, Transport in Porous Media. Vol. 22, pp. 225–244.

I. Vardoulakis, P. Papanastasiou, M. Stavropoulou (2001), Sand erosion in axial flow conditions, Transport in Porous Media. Vol. 45, pp. 267–281.

Minh Nguyen, Stefan Dultz, Jorn KAsbohm (2009), Simulation of retention and transport of copper, lead and zinc in a paddy soil of the Red River Delta, Vietnam, Agriculture, Ecosystems and Environment 129 (2009) 8–16

Papamichos E., Vardoulakis I. (2005). Sand erosion with a porosity diffusion law. Computers and geotechnics, 32(1): 47–58.

Wan R.G., Wang J. (2002). Modelling sand production within a continuum mechanics framework. Journal of canadian petroleum technology, 41(4): 46–52.

Bonelli S., Marot D. (2008). On the modelling of internal soil erosion. The 12 International conference of international association for computer methods and advances in geomechanics (IACMAG) 1-6 October, Goa, India.

NUMERICAL ANALYSIS OF A NEAR-TO-REAL SCALE IN-SITU EXPERIMENT OF A DEEP GEOLOGICAL REPOSITORY

F. Dupray
Soil Mechanics Laboratory (LMS), School of Architecture, Civil and Environmental Engineering (ENAC), Ecole Polytechnique Fédérale de Lausanne (EPFL), Switzerland

B. François
Building, Architecture & Town Planning Department (BATir), Université Libre de Bruxelles, Belgium

L. Laloui
Soil Mechanics Laboratory (LMS), School of Architecture, Civil and Environmental Engineering (ENAC), Ecole Polytechnique Fédérale de Lausanne (EPFL), Switzerland

ABSTRACT: *Deep geological repository involving a multi-barrier system constitutes one of the most promising options to isolate high-level radioactive waste from the human environment. In order to certify the efficiency of waste isolation, it is essential to understand the behaviour of the confining geomaterials under a variety of environmental conditions. The efficiency of Engineered Barrier Systems (EBS) is highly based on the complex behaviour of bentonite. To improve the understanding of the processes involved in the EBS, results from a near-to-real scale experiment, the FEBEX experiment, are studied by means of a thermo-hydro-mechanical (THM) finite element approach including a consistent thermo-plastic constitutive model for unsaturated soils. The model also features a coupled THM approach of the water retention curve. The extended literature available on the behaviour of the FEBEX bentonite is used to calibrate the parameters. The results of the numerical simulations are compared with sensor measurements and show the ability of the model to reproduce the main features of the mechanical behaviour of the system. The hydraulic and thermal response is also realistically described by the model. The link between the confined swelling behaviour as tested in laboratory and the results of the real-scale experiment is clearly established by this simulation.*

1 INTRODUCTION

Over the coming years, definitive solutions will likely be available for the management of large quantities of high-level radioactive waste that mainly stem from the production of nuclear electricity. Deep geological repositories constitute one of the most promising options for isolating such waste from the human environment. In this context, the highly coupled thermo-hydro-mechanical (THM) phenomena that occur in engineered and geological barriers must be captured adequately by means of numerical analysis (Laloui et al., 2008). To validate and calibrate the mathematical models, numerical simulations of in-situ experiments reproducing comparable studies have to be performed. In such a way, the results of the experiment may be interpreted within the constitutive framework of the chosen models which in turn may improve the understanding of the phenomena involved.

The FEBEX (Full-scale Engineered Barriers EXperiment in crystalline host rock) in-situ test is a near-to-real experiment carried out in the underground laboratory at Grimsel (Switzerland). It uses the Spanish disposal concept for underground nuclear waste storage in granitic formations as its reference. The gallery, excavated in the granitic rock of the Aare Massif in central Switzerland, has a diameter of 2.28 m and a length of 71.4 m. Two heaters (0.95 m in diameter and 4.54 m long, the same dimensions as the canisters of the reference

disposal concept) were placed in the axis of the gallery at a 1 m distance from each other. The free space between the heaters and the granite was filled with compacted bentonite blocks for the last 17 m of the gallery. The 17 m long test zone was sealed by a concrete plug (Figure 1) (Lloret et al., 2004). During this in-situ experiment direct measurements, in terms of temperature, fluid pressure, humidity, total stresses and deformation of the confining structure, provided worthwhile information for the verification and the validation of mathematical models aimed at predicting the coupled THM processes occurring in such disposal. Several numerical predictions, or validations, have already been reported in the literature by Gens et al. (1998) and Alonso et al. (2005), among others. Gens et al. (2009) recently published a comprehensive paper on this in-situ heating test including observations, numerical analysis and interpretation. Experimental aspects considering the system of sensors were especially detailed in this paper and will not be further reviewed here. The present study brings additional information on various aspects of the problem, in particular the role of the irreversible straining of the bentonite, related to its thermo-plasticity and suction-induced hardening, is highlighted. In the present paper, the use of a constitutive model that considers the thermal and suction plasticities in a unique theoretical framework offers a unified constitutive approach for the modelling of the bentonite response. By doing so, the focus is made on the various thermo-hydro-mechanical couplings including important plastic mechanisms in the behaviour of bentonite.

Predictions of the THM behaviour of compacted bentonite and host rock have been performed by means of finite element simulations. These numerical analyses provide accurate information on the mechanical effects of temperature and suction evolution in the confining materials. To carry out the numerical analysis, the ACMEG-TS elasto-thermoplastic constitutive model for unsaturated soils (François & Laloui, 2008) has been implemented in the finite element code LAGAMINE (Charlier et al., 2001; Collin et al., 2002).

First, the paper presents a brief summary of the capabilities of the constitutive model and numerical tools used. Then, calibration and features of the numerical analysis performed are presented. Finally, the comparison between the results obtained and in-situ measurements is discussed, in terms of irreversible strains, coupling between mechanical, thermal and water retention responses and diffusion processes.

2 THEORETICAL APPROACH

The ACMEG-TS model (Advanced Constitutive Model in Environmental Geomechanics – Thermal and Suction effects) considers the material as a composition of a solid matrix and two species, in that case water and air. In order to uniquely describe the state of the material, four primary state variables are needed: gas pressure p_g, water pressure p_w, temperature T and solid displacement vector $\mathbf{u}$. The solid phase component is assumed to be incompressible, whereas the liquid phase is slightly compressible. The kinematics of fluid diffusion being slow with respect to thermal diffusion, the solid, liquid and gas phases are assumed to be in thermal equilibrium.

The model therefore uses three phases and models the three thermal, hydraulic and mechanical processes in a coupled way. Mass balances equations are written for the species rather than for the phases. The equilibrium equations, as well as water and heat flows, are described in a Lagrangian actualised formulation. Further details on these aspects can be found in other studies (Collin et al., 2002; Collin, 2003)

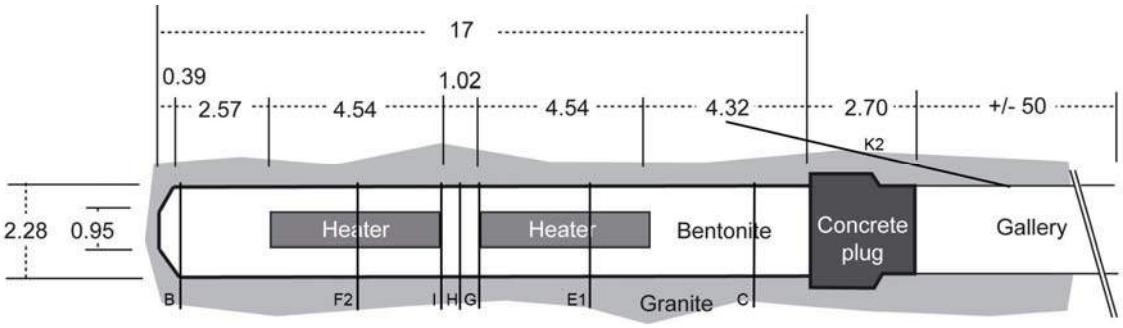

Figure 1: Layout of the FEBEX in-situ test, with localisation of the sections and boreholes (adapted from Gens *et al.* (2009)). Lengths in meters.

THM field equations

The mass conservation equations for the water and gas species are, respectively:

$$\underbrace{\frac{\partial}{\partial t}\left(\rho_w n S_r\right)+div\left(\rho_w \mathbf{f_l}\right)-Q_w}_{\text{Liquid water}}+\underbrace{\frac{\partial}{\partial t}\left(\rho_v n\left(1-S_r\right)\right)+div\left(\mathbf{i_v}+\rho_v \mathbf{f_g}\right)-Q_v}_{\text{Water vapour}}=0 \tag{1}$$

$$\underbrace{\frac{\partial}{\partial t}\left(\rho_a n\left(1-S_r\right)\right)+div\left(\rho_a \mathbf{f_g}+\mathbf{i_a}\right)-Q_a}_{\text{Dry air in gas phase}}+\underbrace{\frac{\partial}{\partial t}\left(\rho_a H_s n S_r\right)+div\left(\rho_a H_s \mathbf{f_l}\right)-Q_{da}}_{\text{Dissolved air in water}}=0 \tag{2}$$

where ρ_w, ρ_v and ρ_a are the bulk density of liquid water, water vapour, and dry air. $\mathbf{f_l}$ and $\mathbf{f_g}$ are the macroscopic velocity of the liquid and gas phases, respectively. $\mathbf{i_v}$ and $\mathbf{i_a}$ are the non-advective flux of water vapour and dry air. S_r is the degree of saturation. The Henry's coefficient, H_s, defining the proportion of dissolved air in the liquid phase, is taken to be equal to 0.017. Q_w, Q_v, Q_a and Q_{da} are volume sources of liquid water, water vapour, dry air and dissolved air in water, respectively.

The energy balance equation of the mixture has the following form:

$$\underbrace{\frac{\partial S_T}{\partial t}+L\frac{\partial}{\partial t}\left(\rho_v n\left(1-S_r\right)\right)}_{\text{Heat storage}}+\underbrace{div\left(\mathbf{f_T}\right)+L\cdot div\left(\mathbf{i_v}+\rho_v \mathbf{f_g}\right)}_{\text{Heat transfer}}-Q_T=0 \tag{3}$$

where $\mathbf{f_T}$ is the heat flow and Q_T is a volume heat source. L is the latent heat of water vaporisation. The enthalpy of the system S_T is given by:

$$S_T=\rho C_p\left(T-T_0\right) \tag{4}$$

where ρ and C_p are the density and the specific heat of the mixture (solid matrix with voids filled by gas and liquid), respectively. Those parameters are deduced from the properties of each phase:

$$\rho C_p=nS_r\rho_w c_{p,w}+\left(1-n\right)\rho_s c_{p,s}+n\left(1-S_r\right)\rho_a c_{p,a}+n\left(1-S_r\right)\rho_v c_{p,v} \tag{5}$$

where ρ_s is the soil grain bulk density and $c_{p,w}$, $c_{p,s}$, $c_{p,a}$ and $c_{p,v}$ are the specific heat of liquid water, solid, dry air and water vapour, respectively.

The soil equilibrium equation is given by:

$$div(\boldsymbol{\sigma}) + \mathbf{b} = 0 \tag{6}$$

where $\boldsymbol{\sigma}$ is the total (Cauchy) stress tensor, with compressive stress taken as positive and $\mathbf{b}$ is the body force vector which is equal to $\rho\mathbf{g}$ if the only body force is gravity.

3 ACMEG-TS: A SOIL CONSTITUTIVE MODEL

The behaviour of the solid matrix is assumed to be governed by the generalized effective stress tensor $\boldsymbol{\sigma}'$ through combinations of mechanical stresses and fluid pressures (Schrefler, 1984; Nuth & Laloui, 2008):

$$\boldsymbol{\sigma}' = \boldsymbol{\sigma} - p_g \mathbf{I} + S_r \left(p_g - p_w \right) \mathbf{I} \tag{7}$$

The term $(\boldsymbol{\sigma} - p_g \mathbf{I})$ is called the net stress, while $\left(p_g - p_w \right)$ is the matrix suction.

Mechanical behaviour

The mechanical model (François & Laloui, 2008), is based on an elasto-plastic framework, the total strain increment $d\boldsymbol{\varepsilon}$ being decomposed into non-linear, thermo-elastic, $d\boldsymbol{\varepsilon}^{\mathbf{e}}$ and plastic, $d\boldsymbol{\varepsilon}^{\mathbf{p}}$, components. The elastic part of the deformation is expressed as follows:

$$d\boldsymbol{\varepsilon}^{\mathbf{e}} = \mathbf{E}^{-1} d\boldsymbol{\sigma}' - \boldsymbol{\beta}_{\mathbf{T}} dT \tag{8}$$

The first term of Equation (8) is the contribution of the effective stress increment $d\boldsymbol{\sigma}'$ to the total elastic strain increment, through the non-linear elastic tensor $\mathbf{E}$. This tensor depends on the effective pressure. According to Equation (7), this part may follow from total stress or fluid pressure variations. The second term of Equation (8) is related to the thermo-elastic strain of the material, through the thermal expansion coefficient matrix, $\boldsymbol{\beta}_{\mathbf{T}} = (1/3)\beta_s' \mathbf{I}$.

The plastic mechanism of the material is induced by two coupled hardening processes: an isotropic and a deviatoric one. Using the concept of multi-mechanism plasticity, both mechanisms may induce volumetric plastic strain (Hujeux, 1979). Therefore the total volumetric plastic strain rate $d\varepsilon_v^p$ is the coupling variable linking the two hardening processes. The yield functions of the two mechanical plastic mechanisms have the following expressions (see Figure 2):

$$f_{iso} = p' - p_c' \, r_{iso} \quad ; \quad f_{dev} = q - Mp' \left(1 - b \, Log \frac{d \, p'}{p_c'} \right) r_{dev} = 0 \tag{9}$$

where p' is the mean effective stress, q the deviatoric stress and p_c' the preconsolidation pressure. b, d and M are material parameters. In addition to the volumetric plastic strain, ε_v^p, p_c' depends on temperature T and suction s, what introduces thermo-plasticity and suction-induced plasticity (Salager et al., 2008):

$$p_c' = \begin{cases} p_{c0}' \exp\left(\beta \ \varepsilon_v^p\right) \left\{ 1 - \gamma_T \log\left[T / T_0 \right] \right\} & \text{if } s \le s_e \\ p_{c0}' \exp\left(\beta \ \varepsilon_v^p\right) \left\{ 1 - \gamma_T \log\left[T / T_0 \right] \right\} \left\{ 1 + \gamma_s \log\left[s / s_e \right] \right\} & \text{if } s \ge s_e \end{cases} \tag{10}$$

where p'_{c0} is the initial preconsolidation pressure at ambient temperature T_0 and for suction lower than the air-entry value s_e. β is the plastic compressibility modulus and γ_T and γ_s are material parameters.

r_{iso} and r_{dev} are the degree of mobilization of the isotropic and the deviatoric mechanisms and are hyperbolic functions of the plastic strain induced by the isotropic and the deviatoric mechanisms, respectively (Hujeux, 1979; Laloui & Francois, 2009). This enables a progressive evolution of the yield limit during loading and a partial release of this limit during unloading.

Water retention behaviour

In terms of water retention response, desaturation is also a yielding phenomenon. Hysteresis in water retention behaviour is modelled as a plastic process. As long as the soil is drying, suction increases, and the degree of saturation, S_r, tends to decrease mainly when the air-entry suction s_e is reached. Under re-wetting, a hysteretic phenomenon occurs, also represented by a yielding process (Figure 3). A wetting-drying cycle activates two successive yield limits in the $(S_r - s)$ plane (f_{dry} and f_{wet}, along the drying and wetting paths, respectively):

$$f_{dry} = s - s_d = 0 \quad ; \quad f_{wet} = s_d s_{hys} - s = 0 \tag{11}$$

where s_d is the drying yield limit and s_{hys} a material parameter considering the size of the water retention hysteresis. Because air-entry suction of the materials depends on temperature and dry density, sd is a function of temperature T and volumetric strain ε_v (François & Laloui, 2008) :

$$s_d = s_{d0}\left\{1 - \theta_T \log\left[T/T_0\right] - \theta_e \log\left[1-\varepsilon_v\right]\right\} \tag{12}$$

where θ_T and θ_e are material parameters describing the evolution of air-entry suction with respect to temperature and volumetric strain, respectively. If the initial state is saturated, the initial drying limit s_{d0} is equal to air-entry suction s_e and increases when suction overtakes s_e as follows:

$$s_{d0} = s_e \exp\left(-\beta_h \, \Delta S_r\right) \tag{13}$$

where β_h is the slope of the desaturation curve in the $\left(S_r - \ln s\right)$ plane (see Figure 3). The evolution of s_d with respect to T and ε_v is described by Equation (12).

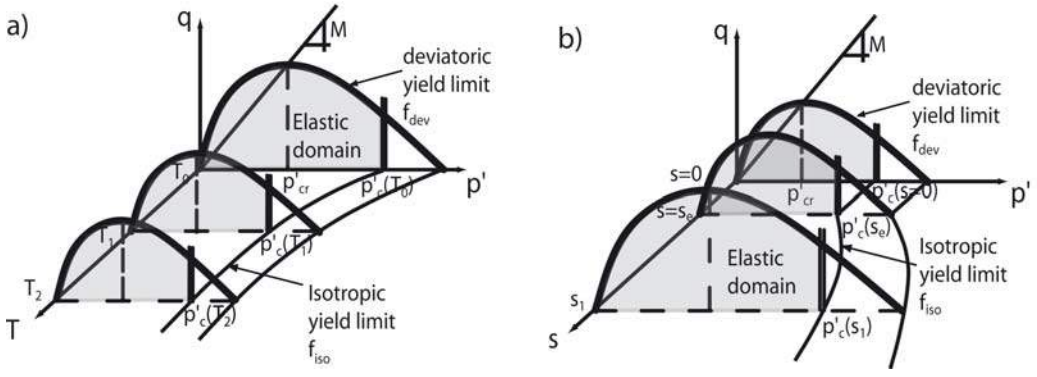

Figure 2: ACMEG-TS: Effect of (a) temperature and (b) suction on the shape of mechanical yield limits.

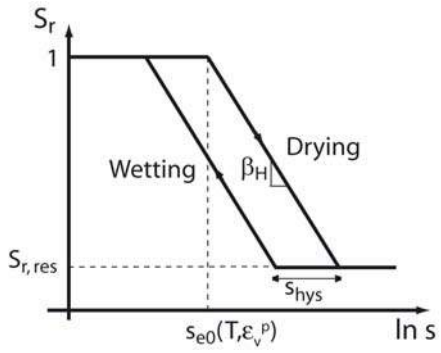

Figure 3: ACMEG-TS: Schematic representation of water retention curve modelling.

4 MATERIAL CHARACTERISTICS

FEBEX bentonite

The clay barrier was constructed with highly compacted FEBEX bentonite blocks with an initial void ratio of 0.6 and an initial water content comprised between 12.5 % and 15.5 %, corresponding to an initial suction of 110 to 130 MPa (Lloret et al., 2004). This corresponds to an initial dry density of the blocks of around 1700 kg.m^{-3}, and a degree of saturation between 35 and 45 %. The THM properties of the FEBEX bentonite have been extensively investigated over the last decade. Its mechanical behaviour under non-isothermal and unsaturated conditions has been characterised by means of several experimental programs by Villar, Lloret, Romero et al. (ENRESA, 2000; Villar, 2002; Lloret et al., 2003; Lloret et al., 2004; Villar et al., 2005).

The results of these studies have shown that, on the mechanical side of the problem, the simulation of the confined swelling behaviour of bentonite is the most important feature to reproduce. Pintado et al. (2002) performed swelling pressure tests in oedometric conditions on samples of FEBEX bentonite that were less compacted than the blocks used in the in-situ experiment. Depending upon density and suction, swelling pressures ranged from 3 to 8 MPa. Due to the difference in initial dry density between the experiment and the emplaced bentonite blocks, it has been decided to calibrate the model with a 10 MPa swelling pressure, which corresponds to the initial dry density of the blocks, i.e. 1700 kg.m^{-3}, according to the trend reported by Lloret et al. (2004).

Another important feature in the simulated scenario is the thermal response of the materials. Reference ENRESA (2000) provides the necessary information concerning the thermal expansion of compacted FEBEX bentonite. A conservative value has been chosen according to this document of 2.1×10^{-4} K^{-1} (volumetric coefficient), in order to mitigate the absence of gaps in the simulation whereas some construction gaps exist in the actual experiment.

A range of experiments and choices enabled calibration of the model with parameters defining the mechanical and water retention behaviour, as presented in Table 1. It should be noted that due to the lack of information on the shear behaviour of the material, the deviatoric mechanical parameters have been assigned with usual values for such a kind of clay.

The parameters governing the thermal and hydraulic diffusion in FEBEX bentonite are established from a review of the literature. Villar (2002) reported the saturated hydraulic conductivity as a function of the dry density. The thermal diffusion of each phase has been calibrated to reproduce the experimental evolution of the thermal diffusion of the bentonite

with respect to its degree of saturation (as reported in (Gens et al., 1998)) yielding the following parameters $(\lambda_s\ ;\ \lambda_w\ ;\ \lambda_a) = (0.7\ ;\ 2.1\ ;\ 0)\ \left[W/(m°C)\right]$. The heat capacity of the solid matrix is $c_s = 1091\ J/(kg°C)$ (Gens et al., 1998).

Table 2 reports the material parameters of FEBEX bentonite in relation to the thermal and hydraulic diffusion processes. The parameters of the water retention curve have been previously defined in Table 1.

Elastic parameters		
E_{ref}, ν, p_{ref}, n^e, β'_s	[MPa], [-], [MPa], [-], [°C^{-1}]	48, 0.3, 1, 1, 2.1×10^{-4}
Isotropic plastic parameters		
β, γ_s, γ_T, r^e_{iso}, p'_c	[-], [-], [-], [-], [-], [MPa] , [-]	10, 10, 0.2, 0.7, 2.2
Deviatoric plastic parameters		
b, d, M, g, α, a, r^e_{dev}	[-], [-], [°], [-], [-], [-], [-]	1, 1.5, 1.2, 0, 1, 0.001, 0.8
Water retention parameters		
s_{e0}, β_h, θ_T, θ_e, s_{hys}	[MPa], [-], [-], [-], [-]	4, 6.33, 0.1, 5, 0.9

Table 1: Set of FEBEX bentonite parameters for ACMEG-TS model.

Granite and other materials

The Grimsel test site has been excavated in a predominately granite and granodiorite rock. Hydraulic and mechanical properties of the Aare massif granite have been compiled in several internal reports and have been partially reported by Alonso et al. (2005) and Gens et al. (1998). The mechanical behaviour of the granite is modelled by an elastic model and is assumed to be fully saturated even under negative pore water pressure.

The material parameters of the steel of the heaters, as well as the concrete of the plug, have been chosen in the range of usual parameters for those types of material. Their mechanical behaviours have been assumed to be linear elastic. The steel is considered as impervious and the concrete plug as fully saturated. Table 2 reports the chosen parameters for the three materials.

5 FEATURES OF THE ANALYSIS OF FEBEX IN-SITU EXPERIMENT

The problem is treated under axisymmetric conditions around the y-axis, which is the axis of the test drift (Figure 4) and consequently gravity is not considered. The distance of the external boundary to the engineered barrier is the same (60 m) in both the axial and radial directions. The modelled domain is sufficiently large to avoid the undesired effects of the imposed boundary conditions in the far-field and to model the dissipation of pore water pressure during the excavation stage. The first stage of the simulation is a preliminary hydro-mechanical calculation of the excavation phase. The goal is to obtain the initial pore water pressure in the host granite, during the ventilation of the drift, and also to get realistic stresses in the host rock, while keeping the radial stress along the drift at zero. An initial isotropic total stress of 28 MPa is imposed on the granite. The water pressure is initially equal to 0.7 MPa over the whole domain, and is brought to the atmospheric pressure on the drift surface for 1000 days. Due to the phasing of construction, the bentonite, canisters and plug elements are not included in the mesh during this first stage, as they are not present during the excavation and ventilation phase. The second stage begins with the introduction of these three elements.

Thermal parameters			Bentonite	Granite	Concrete	Canister
Solid thermal conductivity	λ_s	[W/(m.°C)]	0.7	-	-	-
Water thermal conductivity	λ_w	[W/(m.°C)]	2.1	-	-	-
Air thermal conductivity	λ_a	[W/(m.°C)]	0	-	-	-
Global thermal conductivity	Γ	[W/(m.°C)]	-	3.34	1.7	-
Solid heat capacity	$c_{p,s}$	[J/(kg.°C)]	1091	-	-	-
Water heat capacity	$c_{p,w}$	[J/(kg.°C)]	4200	-	-	-
Gas heat capacity	$c_{p,a}$	[J/(kg.°C)]	1000	-	-	-
Global heat capacity	C_p	[J/(kg.°C)]	-	1000	750	-
Liquid thermal expansion coefficient	β'_w	[°C^{-1}]	4 10^{-4}	4 10^{-4}	4 10^{-4}	-
Solid thermal expansion coefficient	β'_s	[°C^{-1}]	2.1 10^{-4}	2.5 10^{-5}	1 10^{-5}	2.5 10^{-5}
Hydraulic parameters						
Intrinsic water permeability	$k_{w0,sat}$	[m^2]	4 10^{-21}	4.5 10^{-19}	1 10^{-19}	
Kozeny-Carman coefficient 1	$EXPM$	[-]	6.5	0	0	-
Kozeny-Carman coefficient 2	$EXPN$	[-]	6.5	0	0	-
Relative permeability coefficient	$CKW1$	[-]	2.9	-	-	-
Volumetric parameters						
Initial porosity	n_0	[-]	0.4	0.01	0.15	0
Tortuosity	τ	[-]	0.5	0.6	0.6	
Solid specific mass	ρ_s	[kg/m^3]	2700	2660	2500	7800
Water specific mass	ρ_w	[kg/m^3]	1000	1000	1000	-
Air specific mass	ρ_a	[kg/m^3]	1.18	-	-	-
Liquid compressibility	$1/\chi_w$	[Pa^{-1}]	3.33 10^{-10}	3.33 10^{-10}	3.33 10^{-10}	-
Mechanical parameters						
Young elastic modulus	E	[MPa]	See	5000	3000	20000
Poisson ratio	υ	[-]	Table 1	0.35	0.2	0.3

Table 2: Parameters of the various materials involved in the simulation of the FEBEX in-situ experiment.

In the bentonite, suction of 114 MPa is considered as the initial hydraulic condition. The external total stress is initially equal to zero at the beginning of the second stage. This corresponds to a generalised mean effective stress of 53.9 MPa, equal to the product $S_r \times s$ at the initial temperature (Equation 7). The bentonite is assumed to be normally consolidated ($p'_{c0} = 2.2MPa$; $\gamma_s = 10$; $s_0 = 114MPa$). The canister and the concrete plug are also under zero stress. The air pressure has been fixed to atmospheric pressure over the entire unsaturated domain.

In the computation, the construction gap, evaluated as 5.53 % of the emplacement volume (Alonso et al., 2005), has not been considered. This implies that the swelling pressure predicted by the numerical simulations will be overestimated. This swelling caused by progressive wetting starts with this second stage and lasts four months before heating begins.

In the experiment, the temperature ramp was imposed with a controlled power (1200 W per heater for 20 days and 2000 W per heater over the following 33 days until reaching the desired temperature of 100 °C). The same scheme has been reproduced in the simulation. Due to the insulating air gaps, the power applied in the simulation is only 85 % of the real power, with the same ramp up, and the centre of the heaters reaches 100 °C at the correct time. The temperature on all heater nodes is then kept constant for the rest of the simulation. The simulation has been performed on the total time of operation (i.e. 5 years). For all subsequent graphs, zero-time corresponds to the start of the heating (February 27th 1997).

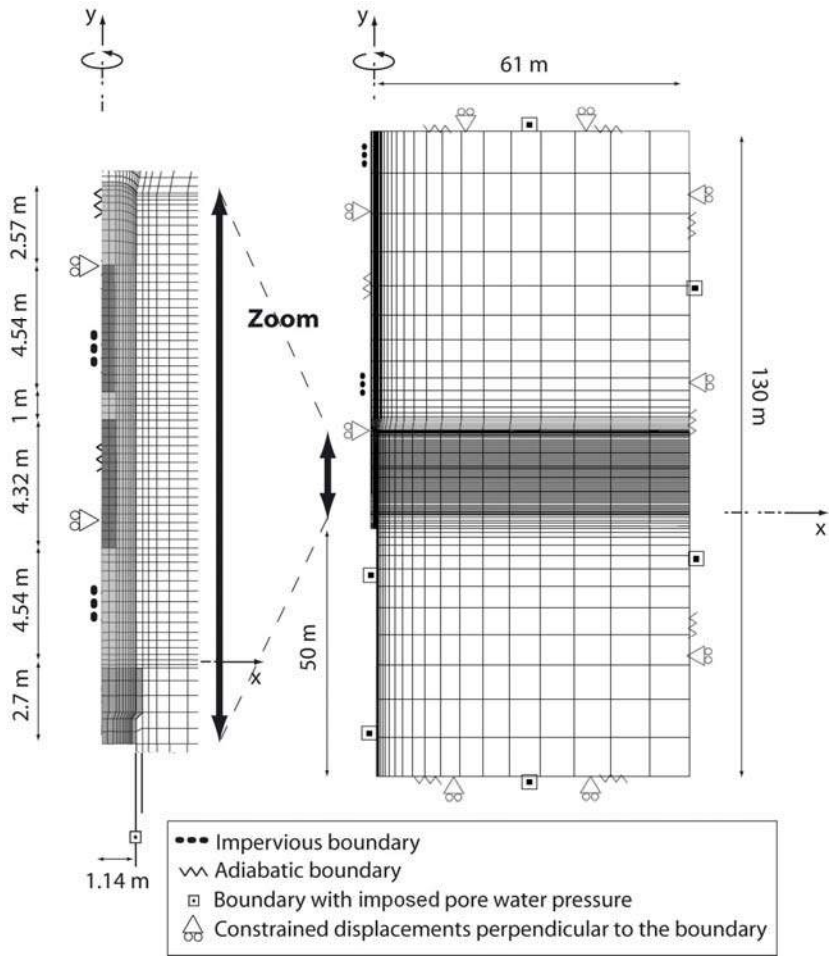

Figure 4: Finite element mesh used in the simulation of the in-situ FEBEX experiment. The y axis is the axis of symmetry of revolution (y=0 corresponds to the bentonite/plug contact).

6 RESULTS OF SIMULATION COMPARED WITH MEASUREMENTS

Figure 5 to Figure 7 compare numerical results to experimental measurements at various locations. The indicated letters in figures correspond to sections, and are shown in Figure 1. The associated number corresponds to the radial rank of the node: 0 is for the centre of the tunnel, 2 for the heater radius, 10 for the frontier between the bentonite and granite, and higher numbers are located in the granite. The nodes are chosen for their proximity to actual sensors.

Figure 5 presents the evolution of temperature over time in three sections of the engineered barrier and in one borehole in the rock mass. Points F2-2 and I-2 being on the heater surface, their temperatures remain constant in the last phase, but there is a clear difference in their temperature. In section I, we observe a steady thermal gradient of about 60 °C across 66 cm after 500 days (from 95°C at x = 0.48 m to 45 °C at x = 1.14 m). On the other hand, far away from the heater (section B2, Figure 5 left, and boreholes K1 and K2, Figure 5 right), the temperature continuously increases, even after five years of heating. The results of the simulation show good agreement with in-situ measurements.

The relative humidity in the bentonite is obtained in the simulation from the temperature and suction through Kelvin's law. Figure 6 displays the comparison between the measured

and the computed values in two different sections of the engineered barrier. The simulated processes are also presented before zero-time, so that one can see why both the zero-time experimental and simulated fields are not uniform. The simulation starts from a homogeneous relative humidity field of about 40% (corresponding to s = 114 MPa and T = 12°C), and in the simulation wetting starts immediately at the frontier between the granite and bentonite, because of the water flow from the saturated granite to the unsaturated bentonite. The sensor measurements show an initial gradient of relative humidity in each section, which is closely matched by the simulations. Close to the heater, the bentonite is dried due to thermally-induced water evaporation (Figure 6, left, point E1-2). Vapour arising from that drying diffuses outwards and condensates in the cooler region, causing accelerated wetting of the bentonite in the central part. In addition the more heated bentonite initially dilates and pressurises the more central one, therefore increasing the relative humidity at the centre. This effect is clearly visible in the wetting rate at point F2-6 (Figure 6, left), before and after the heating. A rapid increase from 40 to 60 % is observed, while the trend before heating indicated a very slow increase. Close to the granite the effect of temperature on the resaturation of bentonite is not so obvious, as its evolution does not seem to be affected by heating at time t_0 (Point C-9).

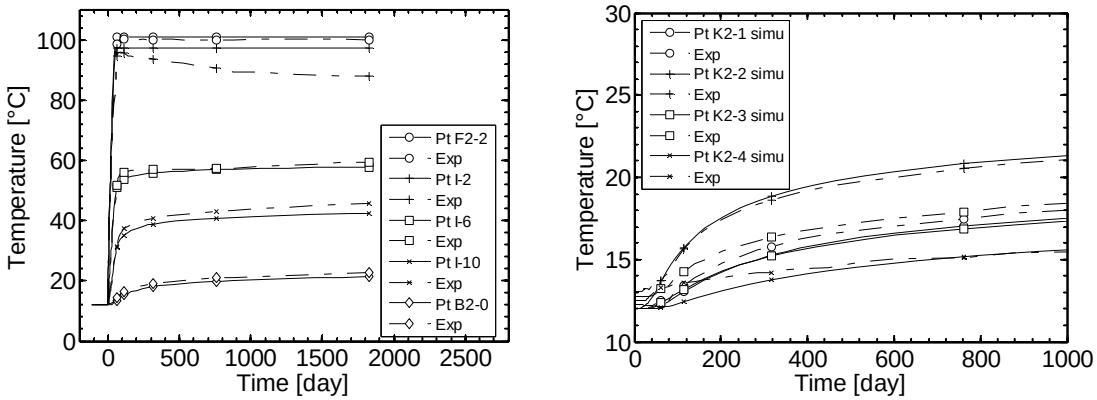

Figure 5: Variation of temperature with time at five points (distributed in three sections) of the engineered barrier, and in one borehole in the host rock. Comparison between numerical simulation (full lines) and experimental measurements (dashed lines).

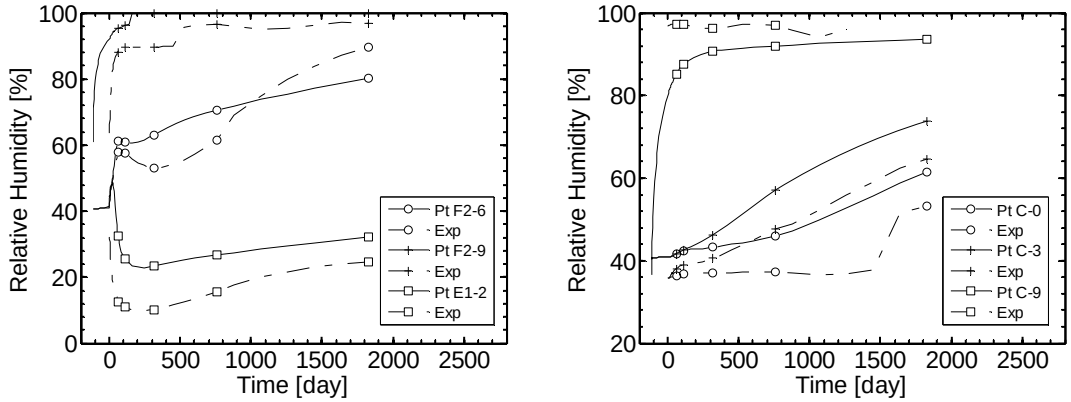

Figure 6: Variation of relative humidity with time at nine points distributed between heater and host rock (left graph) and in a section far from the heaters (right graph). Comparison between numerical predictions (full lines) and experimental measurements (dashed lines).

Figure 7 (left) displays the evolution of total mean stress along a borehole in section G, at radial distances of 2.2, 3.3 and 7.1 m. The simulation shows relatively good agreement with the sensors, given the mechanical assumptions made in the simulation (no construction gap allowing some free swelling of the bentonite). The most important difference comes from the peak in net mean stress that is observed experimentally in the most central sensor. This peak is only observed in the radial component of the stresses in the simulation. This can be more clearly seen in Figure 7 (right), which represents the radial displacements in a radial borehole, reset to zero at zero-time. The peak in displacement induced by the peak in the swelling pressure of bentonite is clearly visible in both the simulation and experiment, and was not observed in previous studies. Although its magnitude is greater than the experimental measurement, this is a very interesting feature of this model, which clearly reproduces the trend observed in reality.

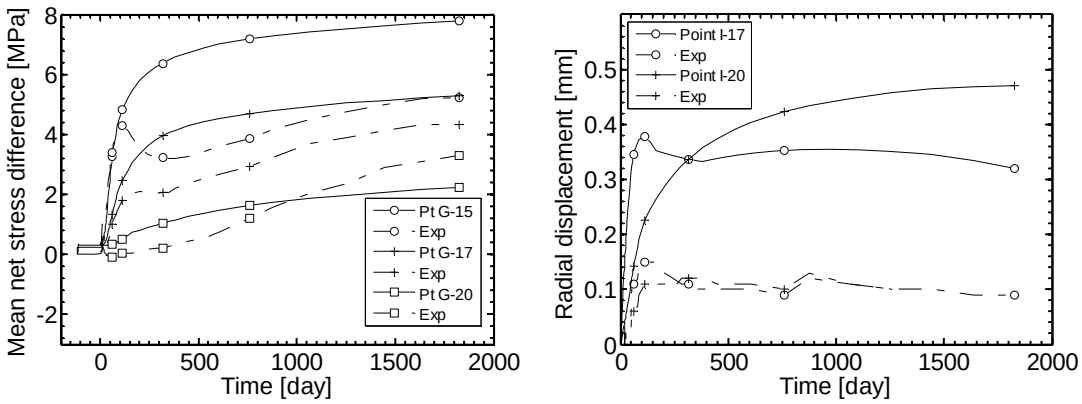

Figure 7: (left) Variation with time of mean net stress in a radial borehole in the middle section of the experiment, at radial distances 2.2, 3.3 and 7.1 m. The reference state is that of granite after the excavation of the drift. Comparison between numerical predictions (full lines) and experimental measurements (dashed lines). (right) Variation with time of radial displacement (outwards positive) in a radial borehole in section I. Comparison between numerical predictions (full lines) and experimental measurements (dashed lines).

7 CONCLUSIONS

Facing the need to analyse and predict the long-term behaviour of underground disposal facilities for nuclear waste, the primary aim of this numerical analysis is to provide a means for assessing and understanding the thermal, hydraulic and mechanical responses of bentonite and the surrounding rock involved in a multi-barrier system. The interpretation of the THM processes requires comprehensive constitutive models and numerical tools in order to incorporate most of the material behavioural features.

The FEBEX in-situ test is a near-to-real experiment of nuclear waste disposal in a granitic formation. The THM behaviour of the buffer material (made of FEBEX bentonite) and the surrounding host rock (granite), encountering many complex and interconnected THM phenomena, has been modelled by means of finite element simulations.

The parameters of the thermo-plastic constitutive model used for saturated and unsaturated materials, named ACMEG-TS, have been defined after a thorough review of the literature and the choice of the confined swelling pressure as the main feature.

The features of the numerical analysis have been presented. Subsequently, the obtained results have been compared with the available sensors measurements in both the engineered barrier and the granite. The results of the simulations show good agreement with the

experiment. The confined swelling behaviour of highly compacted bentonite is well reproduced by the constitutive model, in terms of both magnitude and behaviour. It is an important feature of the ACMEG-TS model, and is directly obtained from the introduction of a wetting collapse mechanism in the framework of generalised effective stress.

The use of a performant finite element code, coupled with an advanced thermo-plastic constitutive model using an unsaturated formalism, significantly advances the knowledge of the highly coupled processes occurring in a clayey formation, initially unsaturated, in the near field of a heat-emitting radioactive waste.

ACKNOWLEDGMENTS

The authors would like to acknowledge NAGRA for funding and supporting this research, and also wish to thank Prof. R. Charlier and Dr. F. Collin for their collaboration and their advice regarding the implementation of the model in the LAGAMINE finite element code.

REFERENCES

Alonso, E.E., Alcoverro, J., Coste, F., Malinsky, L., Merrien-Soukatchoff, V., Kadiri, I., Nowak, T., Shao, H., Nguyen, T.S., Selvadurai, A.P.S., Armand, G., Sobolik, S.R., Itamura, M., Stone, C.M., Webb, S.W., Rejeb, A., Tijani, M., Maouche, Z., Kobayashi, A., Kurikami, H., Ito, A., Sugita, Y., Chijimatsu, M., Börgesson, L., Hernelind, J., Rutqvist, J., Tsang, C.F. & Jussila, P. (2005). "The FEBEX benchmark test: case definition and comparison of modelling approaches." Int. J. Rock Mech. Min. Sc. Vol. 42(5-6), 611-638.

Charlier, R., Radu, J.-P. & Collin, F. (2001). "Numerical modelling of coupled transient phenomena." Rev. Fr. Génie Civ.

Collin, F. (2003). "Couplages thermo-hydro-mécaniques dans les sols et les roches tendres partiellement saturés." Department ArGEnCo. Liège, Belgium, Université de Liège. PhD.

Collin, F., Li, X.L., Radu, J.P. & Charlier, R. (2002). "Thermo-hydro-mechanical coupling in clay barriers." Eng. Geol. Vol. 64(2-3), 179-193.

ENRESA (2000). "Febex Project: Full-scale engineered barriers experiment for a deep geological repository for high level radioactive waste in crystalline host rock." Publicación técnica. Madrid, Spain, ENRESA**:** 354.

François, B. & Laloui, L. (2008). "ACMEG-TS: A constitutive model for unsaturated soils under non-isothermal conditions." Int. J. Numer. Anal. Meth. Vol. 32(16), 1955-1988.

Gens, A., Garcia-Molina, A.J., Olivella, S., Alonso, E.E. & Huertas, F. (1998). "Analysis of a full scale in situ test simulating repository conditions." Int. J. Numer. Anal. Meth. Vol. 22(7), 515-548.

Gens, A., Sánchez, M., Guimarães, L.d.N., Alonso, E.E., Lloret, A., Olivella, S. & Villar, M.V. (2009). "A full-scale in situ heating test for high-level nuclear waste disposal: observations, analysis and interpretation." Géotechnique Vol. 59(4), 377-399.

Hujeux, J.-C. (1979). "Calcul numérique de problèmes de consolidation élastoplastique." Paris, France, Ecole Centrale. PhD.

Laloui, L. & Francois, B. (2009). "ACMEG-T: Soil Thermoplasticity Model." J. Eng. Mech. Vol. 135(9), 932-944.

Laloui, L., François, B., Nuth, M., Péron, H. & Koliji, A. (2008). "A thermo-hydro-mechanical stress-strain framework for modeling the performance of clay barriers in deep geological repositories for radioactive waste." 1st European Conf. on Unsaturated Soils. Durham, UK.

Lloret, A., Romero, E. & Villar, M.V. (2004). “FEBEX II Project: Final report on thermo-hydro-mechanical laboratory tests.” Publicación técnica. Madrid, Spain, ENRESA**:** 165.

Lloret, A., Villar, M.V., Sánchez, M., Gens, A., Pintado, X. & Alonso, E.E. (2003). “Mechanical behaviour of heavily compacted bentonite under high suction changes.” Géotechnique Vol. 53(1), 27-40.

Nuth, M. & Laloui, L. (2008). “Effective stress concept in unsaturated soils: Clarification and validation of a unified framework.” Int. J. Numer. Anal. Meth. Vol. 32(7), 771-801.

Pintado, X., Ledesma, A. & Lloret, A. (2002). “Backanalysis of thermohydraulic bentonite properties from laboratory tests.” Eng. Geol. Vol. 64(2-3), 91-115.

Salager, S., François, B., El Youssoufi, S., Laloui, L. & Saix, C. (2008). “Experimental investigations on temperature and suction effects on compressibility and pre-consolidation pressure of a sandy silt.” Soils Found. Vol. 48(4), 453-466.

Schrefler, B.A. (1984). “The finite element method in soil consolidation (with applications to surface subsidence).” Swansea, UK, University College. PhD.

Villar, M.V. (2002). “Thermo-hydro-mechanical characterisation of a bentonite from Cabo de Gata: A study applied to the use of bentonite as sealing material in high level radioactive waste repositories.” Publicación técnica. Madrid, Spain, ENRESA.

Villar, M.V., García-Siñeriz, J.L., Bárcena, I. & Lloret, A. (2005). “State of the bentonite barrier after five years operation of an in situ test simulating a high level radioactive waste repository.” Eng. Geol. Vol. 80(3-4), 175-198.

EFFECTS OF PAST GLACIATION ON THE HYDROGEOLOGY OF THE MICHIGAN BASIN

O. Nasir, M. Fall, E.Evgin
Department of Civil Engineering Ottawa University, Ottawa, ON, Canada

T. S. Nguyen
Canadian Nuclear Safety Commission, Ottawa, ON, Canada

ABSTRACT: *The Northern hemisphere was subjected to more than ten cycles of glaciation-deglaciation during the last million years. The last cycle started approximately 120,000 years ago. At its peak, the continental ice cap that covered all of Canada and part of the United States had a maximal thickness of 3km and imposed a pressure of 30 MPa on the earth surface. Such a pressure caused significant disturbances in the hydraulic and mechanical regimes in the earth crust. In Canada, a deep geological repository for low and intermediate level radioactive wastes is currently being proposed at a depth of 680m in a clayey limestone of the Michigan Basin. Borehole investigations at the site of the proposed repository show zones of overpressure and under pressure with respect to hydrostatic at different depths of the sedimentary rock formations. In addition, at depths of more than 300 m, very saline water, with total dissolved solid concentrations of up to 300g/l was found. In this work, we tested the hypothesis that the above water pressure could be attributed to past glaciation-deglaciation cycles. We developed a coupled Hydraulic-Mechanical-Chemical (HMC) model based on a generalization of Biot's theory of poroelasticity in order to simulate the effects of past glaciation cycles on the Michigan Basin. The results show that past glaciation could be a plausible explanation for the pressure anomalies. Despite the tremendous hydraulic disturbances caused by these cycles, due to the very low permeability of the rock at depths, the salinity profile did not change significantly; in particular the brine found at great depths is shown to remain virtually stagnant.*

1 INTRODUCTION

The Earth's climate during the Quaternary period has dynamical characteristics, represented by periodic glaciation-deglaciation cycles. The dynamic features of the Earth's climate can be attributed to the Earth's response to the external and/or internal forcing mechanisms such as orbital forcing, tectonic, volcanic, oceanic and atmospheric circulation, and anthropogenic activities (Lowe and Walker, 1997; Maslin et al., 2007). Glaciation is associated with the development of a large continental ice sheet in many parts of the world, particularly, in the Northern hemisphere. The Northern hemisphere was subjected to more than ten cycles of glaciation-deglaciation during the last million years. The last cycle started approximately 120,000 years ago. At its peak, the continental ice cap that covered all of Canada and part of the United States had a maximal thickness of 3km and imposed a pressure of 30 MPa on the earth surface. The ice load caused significant disturbances in the hydraulic and mechanical regimes in the earth crust, as well as its surface topography (Vidstrand et al., 2008).

Deep geological repositories (DGR) for nuclear wastes are currently being proposed in many countries, such as Canada, Finland and Sweden. For those Northern countries, glaciation-deglaciation cycles similar to the ones that occurred in the past are predicted to recur (Vidstrand et al., 2008). These cycles are identified as external events that could significantly affect the performance of the host rock formations for the long term isolation and containment of the wastes (Nguyen et al. 1993, Chan et al., 2005). In order to predict the impact of future glaciations on the stability of such DGRs, the authors have developed Thermo-Hydro-Mechanical-Chemical (THMC) mathematical models. However, before such models could be used with confidence for the prediction of the effects of future glaciation-deglaciation cycles, they need to be calibrated with field evidence reflecting the possible effects of past glaciations. Such a calibration is illustrated in this paper.

2 DESCRIPTION OF THE STUDY AREA

In Canada, a DGR for low and intermediate wastes is currently proposed at a depth of 680m in a clayey limestone of the Michigan Basin (Figure 1). The DGR would be located near the NE edge of the Basin. The lowermost strata of the Basin started deposition more than 500 million years ago. The groundwater in the area can be classified into three zones: shallow, intermediate and deep (Sykes et al., 2008). The intermediate and deep zones are mainly characterized by high total dissolved solids of up to 300 g/L (Sykes et al., 2008) while the shallow zone contains fresh to brackish water. Moreover, field measurements of pore water pressures showed anomalous water pressures, with under pressure within the Middle and Upper Ordovician Formations and over pressure within the Cambrian Formation (Jensen et al., 2009).

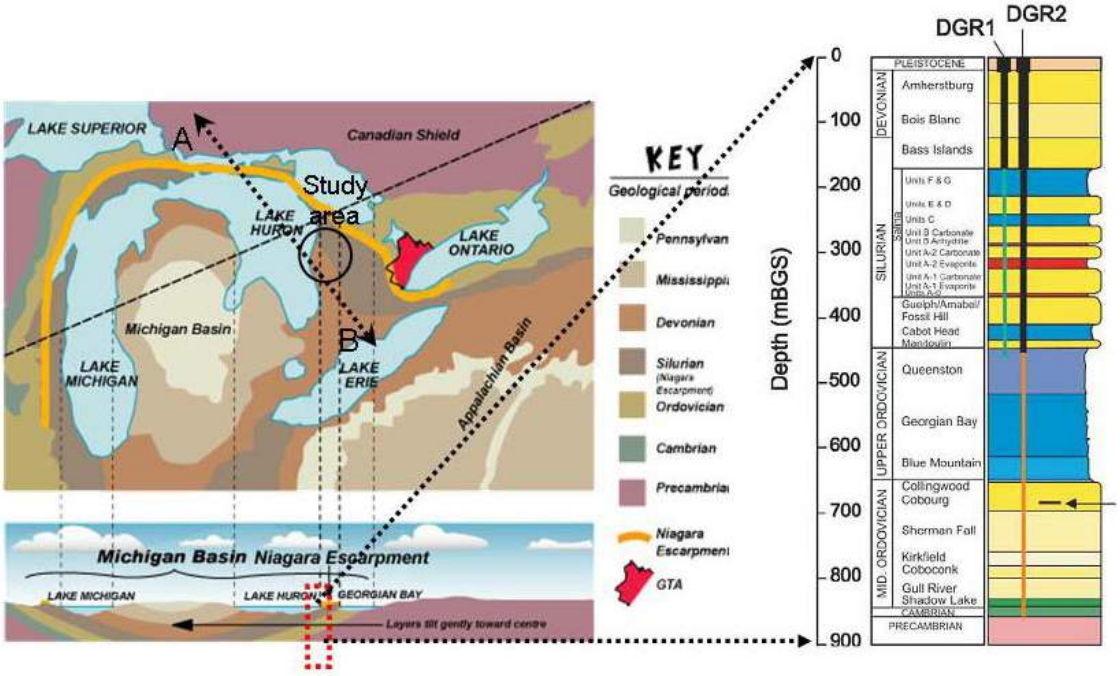

Figure 1. Michigan basin and location of the study area (sources, left: geological survey of Canada, right DGR Phase 2 Geoscientific Characterization plan).

Based on the available geological information, a two dimensional NW-SE cross section A-B is constructed. The direction of the cross section is chosen parallel to the direction of the ice sheet advance and retreat during the last ice ages which was observed through the geomorphologic records (Lowe and Walker, 1997) as shown in Figure 2. Within the cross section A-B, a column domain of 1653m depth x 200m width, including the depth of a potential DGR at the Mid-Ordovician of 680 m depth is used for the HMC numerical model.

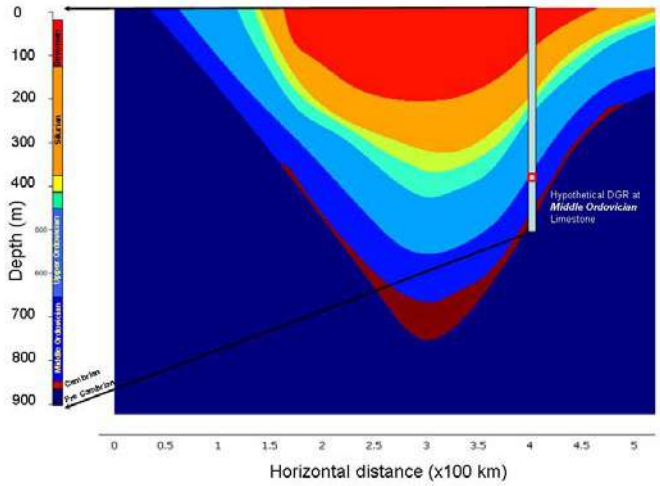

Figure 2. Geological cross section in the study area showing the location of the potential DGR.

3 PAST GLACIATION CYCLES

The coupled HMC model that we developed is used to simulate the effect of past glaciation cycles on the sedimentary rocks of the study area. The ice sheet loading and temperature history are adopted from the University of Toronto Glacial Systems Model (GSM), "Peltier's Model" realization scenario nn9930 (Peltier, 2008), illustrated in Fig. 3.

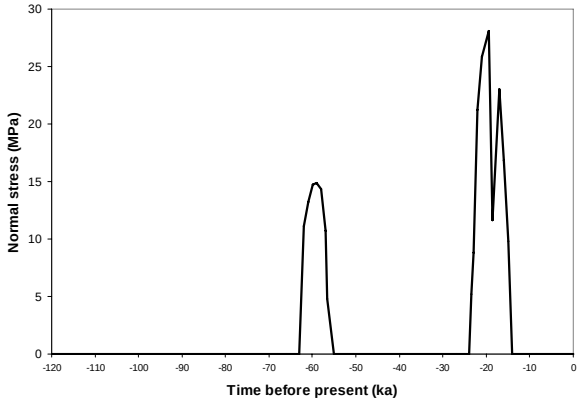

Figure 3. Ice loading (interpolated from The University of Toronto Glacial Systems Model (GSM) "Peltier's Model" model nn9930 (Peltier, 2008)).

4 SURFACE BOUNDARY CONDITIONS

Cyclic and transient climate change leads to the accumulation and melting of snow and ice. This results in growth and decay in ice sheet thicknesses, accompanied by temporal and spatial variations in the glacier hydrology and basal hydraulic boundary conditions. Jansson et al. (2009) have investigated this phenomenon by field works in Storglaciären, Northern Sweden. .They performed in-situ measurements that include subglacial water pressure measurements. The measured pressures can attain values equivalent to 90% of the weight of the ice. However, based on the location of sensors used for this specific field work, these pressure measurements seem to apply to the ablation zone of the Ice Sheet only. Depending on locations, the basal thermal regime can result in a warm base where large quantities of melt water is present, or a cold base where the glacier is frozen to its bed. Consequently, the hydraulic pressures under the ice sheet might be much less than the values measured in the above field investigation.

In order to take this variation in boundary conditions into account, different scenarios are used in this work by implementing four sets of boundary conditions (B.Cs), including: hydraulic, mechanical and chemical are used to simulate the effect of past glaciation. The assumed B.Cs can be divided into two groups: the first group is fixed B.Cs; and the second group is transient B.Cs. Table 1 shows the boundary conditions used in this study.

Table 3. HMC boundary conditions used for the simulation.

B.Cs	Top	Bottom	Sides
Mechanical	Free deformation Transient loading[a]	Roller	Roller
Hydraulic	Free drainage Transient Pressure[b]	No flow	No flow
Chemical	Zero concentration	150 kg/m3	Insulation
a: transient loading derived from Peltier's Climate change model b: transient pressure is taken different as a percentage of ice loading derived from Climate change model			

Transient HMC B.Cs are mainly adopted from the results of Peltier's Climate change model (Peltier, 2008), which includes the variation of ice sheet thickness during the past 120,000 year. The glaciation cycle is repeated 9 times to represent glaciations cycles during the past one million years.

5 MODEL DEVELOPMENT

A set of governing equations is developed to simulate coupled solute and fluid transfer in deformable porous media. The governing equations are derived based on the basic laws of force equilibrium and mass conservation. The governing equations presented describe three phenomena: (i) mass conservation of the pore fluid, (ii) mass conservation of the solute, and (iii) conservation of momentum. A number of assumptions have been made in the formulation of the governing equations. These assumptions are: (i) the host rock is considered

as a continuous porous medium made of two constituents, a solid (s) and a liquid (l); (ii) the liquid moves in the connected voids of the medium. The liquid phase is composed of liquid water; (iii) the deformations are small; (iv) Local thermal equilibrium is assumed for the two-phase system; (v) the constituents of the porous medium are not reactive. For the sake of brevity, only the final form of the governing equations is given below.

The governing equations are derived below. Although isothermal conditions are assumed in the application illustrated in this paper, the general case of non-isothermal conditions is included in the following derivation of the governing equations. Equations 1 and 2 express the conservation of mass for both fluid and solid, respectively, which can be written as (De Marsily, 1986):

$$\nabla \cdot \left(\rho_f U_f\right) + \frac{\partial}{\partial t}\left(\rho_f n\right) + \rho_f q = 0 \tag{1}$$

$$\nabla \cdot \left(\rho_s U_s\right) + \frac{\partial}{\partial t}\left(\rho_s (1-n)\right) + \rho q = 0 \tag{2}$$

where ρ is density, U are fictitious velocities, t is time, n is porosity, q is mass source, s is the solid and f is the fluid.

In the above equations, the mean velocities for fluid and solid can be defined as:

$$u = \frac{U}{n} \text{ , and } u_s = \frac{U_s}{(1-n)} \tag{3}$$

Darcy's law can be expressed in terms of the mean velocities as:

$$\left(u - u_s\right) = -\frac{\kappa}{\eta}\left(\nabla p + \rho_f g \nabla D\right) \tag{4}$$

where κ is permeability, η is dynamic viscosity, p is pressure and D is the direction of gravitational acceleration (g).

Combining Equations 2 and 3, and using Darcy's law we obtain (De Marsily, 1986):

$$\nabla \cdot \left[\rho_f \frac{\kappa}{\eta}\left(\nabla p + \rho_f g \nabla D\right)\right] = n\frac{\partial \rho_f}{\partial t} + \frac{\rho_f}{1-n}\frac{\partial n}{\partial t} - \frac{\rho n}{\rho s}\frac{d\rho_S}{dt} \tag{5}$$

Based on the compressibility of fluid, solid and skeleton of the rock components, the term $\frac{\partial n}{\partial t}$ (time variation in porosity) can be represented with:

$$\frac{dn}{dt} = \left(\left((\alpha - n)\frac{de_{ff}}{dt} + \frac{(\alpha - n)}{K_s}\frac{dp}{dt}\right) + \left(-(\alpha - n)\beta + (1-n)(\beta - \beta_S)\right)\frac{dT}{dt}\right) \tag{6}$$

As well, Equation 5 can be written as:

$$\nabla\cdot\left[\rho_f\frac{\kappa}{\eta}\left(\nabla p+\rho_f g\nabla D\right)\right]=(n\gamma)\frac{\partial C}{\partial t}+\rho_f\alpha'\frac{de_{ff}}{dt}+\rho_f\left(\frac{\alpha'}{K_s}-\frac{n}{K_S}+\frac{n}{K_f}\right)\frac{dp}{dt}$$
$$+\rho_f\left(n\beta_S-\alpha'\beta+(\beta-\beta_S)-n\beta_f\right)\frac{dT}{dt} \tag{7}$$

where $\alpha'=\frac{(\alpha-n)}{(1-n)}$, $\alpha=1-\frac{K_D}{K_S}$, K_D , K_S and K_f are the bulk moduli of the solid matrix, solid grains and water fluid, respectively, β , β_s and β_f are thermal expansion coefficients for the solid matrix, solid grains and water fluid, respectively.

Equation 7 includes the concentration (C) of dissolved solids in the pore fluid and the local average temperature (T) of the porous medium. The density of the pore fluid is assumed to vary with dissolved solid concentration according to the following equation:

$$\rho_f=\rho_{fo}+\gamma C \tag{8}$$

where ρ_{fo} is the initial fluid density, and γ is a concentration–density coefficient. The numerical values of both ρ_{fo} and γ are taken to be 1000 kg/m3 and 2/3 for a range of C from 0 to 300 kg/m3 (Sykes et al., 2008).

Solute transport is modeled by single species transport that represents the total dissolved solid in the porous media by advection-dispersion. The governing equation (Fetter, 1999) for saturated porous media and entirely fluid or solid systems is:

$$\theta_s\frac{\partial c}{\partial t}+\nabla.\left[-\theta_s D_L\nabla c+\mathrm{u}c\right]=S_c \tag{9}$$

where θ_s is porosity; DL is the hydrodynamic dispersion tensor, u is vector of pore fluid velocities, and Sc is the solute source. In this work, it is assumed that the solute transport is diffusion dominated.

Assuming linearly elastic rocks, the mechanical part is included by taking the equation of momentum conservation, coupled with the water pressure using Terzaghi's effective stress principle (Nguyen, 1995):

$$G\frac{\partial^2 u_i}{\partial x_j\partial y_j}+(G+\lambda)\frac{\partial^2 u_j}{\partial x_i\partial y_j}-\alpha\frac{\partial p}{\partial x_i}-\beta K_D\frac{\partial T}{\partial x_i}+F_i=0 \tag{10}$$

where u is the displacement, G is the shear modulus, λ is Lamé's first parameter, α is Biot coefficient, and T is the temperature.

Mechanical deformation is an important process because it can affect the porosity and the intrinsic permeability, hence the hydraulic conductivity of sedimentary rocks. In this work, the change in intrinsic permeability due to change in porosity is modeled using the Carman–Kozeny relationship (Kozeny, 1927; Carman, 1937):

$$k^t = \left[\frac{n^3}{(1-n^2)}\right]^t \left[\frac{(1-n^2)}{n^3}\right]^{initial} k^{initial} \tag{11}$$

where k^t [L2] represents permeability at time t, and and $k^{initial}$ [L2] represents the initial permeability. In this work, initial porosity and permeability are assumed to be equal to the current field values.

6 MATERIAL PROPERTIES

The hydraulic conductivity and elastic modulus of the rock formations for the model are shown in Figures 4 and 5. Data used for the graphs are inferred from Jensen et al. (2009), Sykes et al. (2008), and Gaerner Lee Ltd. (2008).

Figure 4 shows the profile of the horizontal hydraulic conductivity (Kh) at the study area. The value of Kh shows that three main levels can be identified: the first level (0-170 m in depth which includes the Devonian and part of Silurian formations) with a high Kh of 10^{-7} m/s to, the second level (170-750 m in depth which includes the Silurian Upper-Ordovician and part Mid-Ordovician formations) with a Kh range from 10^{-14}m/s to $5x10^{-13}$m/s, and the third level (750-1000 m in depth which includes Mid-Ordovician and the pre- Cambrian formation) with Kh about $5x10^{-11}$m/s to 10^{-12}m/s. In addition, there are three layers with high Kh at depth of about 330m, 370m (within the Silurian formations) and 850m (within the Cambrian formations)

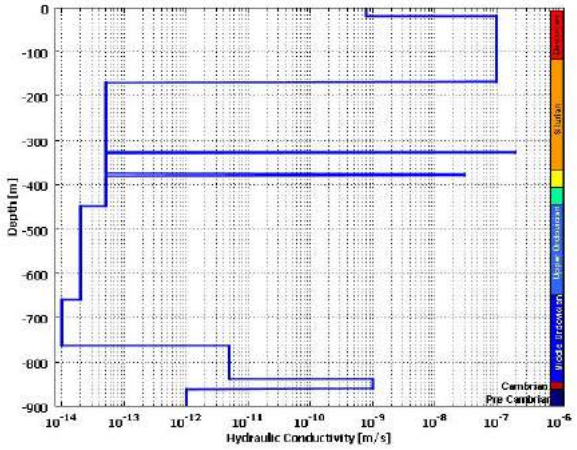

Figure 4. Variation of hydraulic conductivity with depth.

Figure 5 shows the profile of the modulus of elasticity (E) at the study area. Three main groups of values can be recognized: the first group (20-175, 330-400 and 660-690 m in depth which includes the Devonian, part of Silurian and Mid-Ordovician formations) with an E-value of about 40 GPa, the second group (175-330, 410-660 and 690-860 m in depth which includes the Silurian, Upper and Mid-Ordovician formations) with an E-value of about 5-25 GPa, and the third group is (900-1000 m depth which includes the Cambrian formation) with an E-value of about 60 GPa.

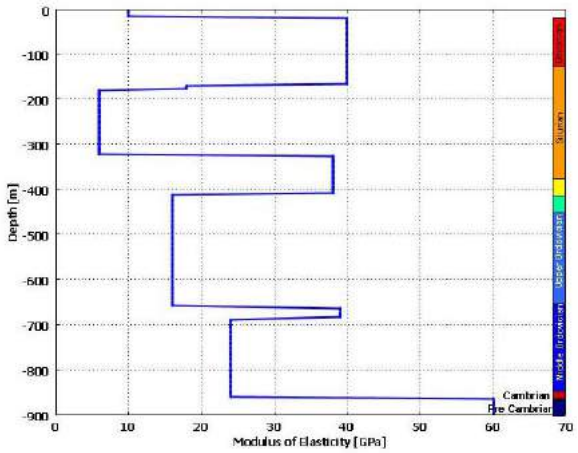

Figure 5. Variation of elastic modulus with depth used in the model.

Figure 6 shows the profile of the initial total dissolved solids (TDS) in the water for depth from surface to 1000m, values of TDS adopted from field measurements (Jensen et al., 2009). After 9 cycles of glaciation-deglaciation, the calculated final profile is not changed significantly indicating that solute transport is diffusion dominated.

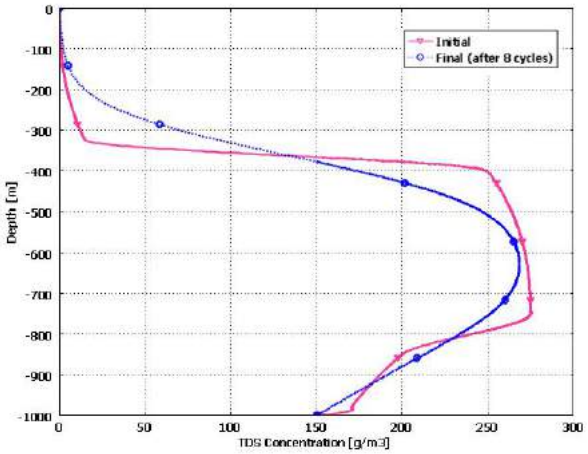

Figure 6. Initial and final TDS profile.

7 RESULTS

Figures 7 shows the pore water pressure profile in the study area for a depth of 0-1000 m using three different scenarios of surface hydraulic boundary conditions, including: zero pressure, 30% of ice load and 80% of ice load. The results are compared with both field data (Jensen et al., 2009) as well as with theoretical hydrostatic pore water pressure for water (for both fresh and saline water). The trends for the pressure profiles for the zero and 30% scenarios are consistent with the field data: a hydrostatic profile changing to under pressure and then overpressure with increasing depths. The predicted values of overpressure at depths of approximately 800m compare well with the field data; however, the values of under pressure were under predicted. The scenario of 80% ice base pressure did not give the trend of field pressure change, and did not give any under pressure values.

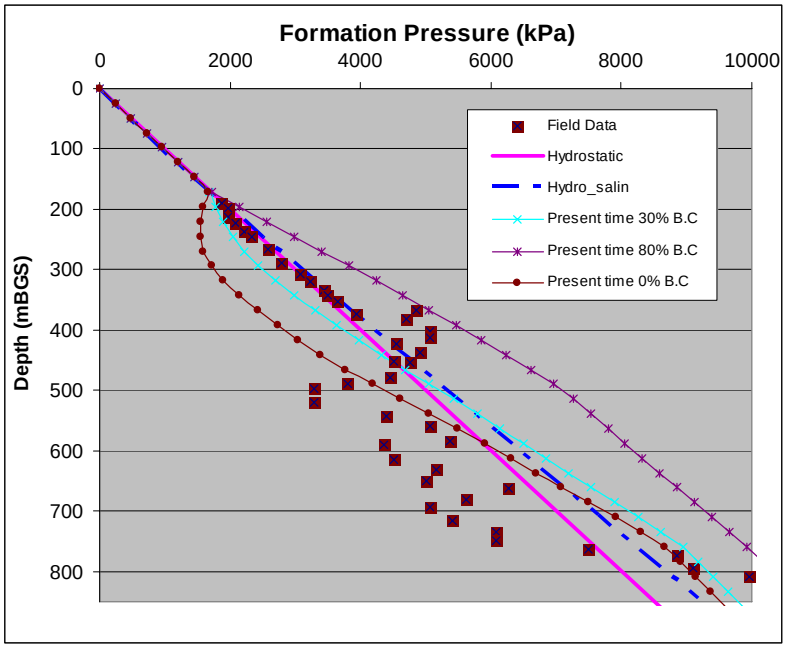

Figure 7. Field, hydrostatic (fresh and saline water) and predicted pore water pressure profile of three hydraulic boundary conditions; (i): free draining conditions (0 p,); (ii) hydraulic head equal to 30% of the ice thickness at the surface; and (iii) hydraulic head equal to 80% of the ice thickness at the surface.

8 CONCLUSIONS

In this paper, the HMC processes under the impact of glaciation cycles in sedimentary rocks in southern Ontario using a column model are investigated. The governing coupled HMC equations are derived from the poroelasticity framework, with the additional consideration of solute transport. Nine cycles of glaciation, including ice and water pressure loading with different surface hydraulic boundary conditions is applied on the surface using the University of Toronto Glacial Systems Model (GSM). Based on the results obtained from this study, the following conclusions can be drawn. First, the pore water pressure distribution is significantly influenced by the glaciation-deglaciation cycles, with the occurrences of zones of over and

under pressure at depths greater than 200m. These anomalous pressure zones are predicted to subsist until present time, when patterns of pressure distribution are consistent with the field observations when the basal water pressure is assumed to be less than 30% of the weight of the ice. For these cases, the values of overpressure compare well with the field values. However, the values of under pressure are under predicted. This under prediction could be attributed to phenomena not included in the study, such as gas pressure or somatic pressure. Second, although glaciation-deglaciation cycles can dramatically increase the hydraulic gradients in the host rock of a deep geological repository, the TDS profile is predicted to remain largely unchanged. In particular the brine that exists in the Ordovician formations at the depth of the proposed repository is predicted to remain virtually stagnant during the nine glaciation-deglaciation cycles. This is due to the very low permeability of the host rock layers at these depths.

ACKNOWLEDGEMENT

The authors sincerely thank the the Canadian Nuclear Safety Commission (CNSC) and the University of Ottawa (UO) for their financial support. The opinions expressed in this paper are the authors' and does not necessarily reflect the CNSC's or UO's.

REFERENCES

Carman, P.C., (1937). "Fluid flow through granular beds", Transactions, Institution of Chemical Engineers, London., Vol. 15 (1937) 150_166.

Chan, T., Christiansson, R., Boulton, G. S., Ericsson, L. O., Hartikainen, J., Jensen, M. R., Mas Ivars, D., Stanchell, F. W., Vistrand, P., and . Wallroth, T. (2005). "DECOVALEX III BMT3/BENCHPAR WP4: The thermo-hydro-mechanical responses to a glacial cycle and their potential implications for deep geological disposal of nuclear fuel waste in a fractured crystalline rock mass". International Journal of Rock Mechanics and Mining Sciences Vol. 42, (5-6 SPEC. ISS.): 805-827.

Comsol Multiphysics 3.5a. (2009). http://www.comsol.com.

De Marsily, G., 1986. "Quantitative Hydrogeolcgy" . p. 100-101. Acad. Press, New York.

Gartner Lee Limited. (2008). "Phase I Regional Geology, Southern Ontario". Supporting technical report. OPG 00216-REP-01300-00007-R00.

INTERA Engineering Limited. (2008). "DGR Phase 2 Geoscientific Characterization plan". OPG 00216-PLAN-03902-00002-R00

Jansson P, Näslund J-O, Rodhe L, AB S K. (2009). "Spatial and temporal variations in glacier hydrology on Storglaciären". Sweden. SKB, Stockholm, Technical Report, TR-09-13.

Jensen, M., Lam, T., Luhowy, D., McLay, J., Semec, B and Frizzel, R. (2009). "Ontario Power generation's Proposed L&ILW Deep Geologic Repository: An Overview of Geoscientific Studies". Canadian Geotechnical Conference, Halifax, Canada.

Kozeny, J. (1927). "Uber Kapillare Leitung Des Wassers in Boden", Wien, Akad. Wiss. 136 (1927) 271.

Lowe, J.J. & Walker, M.J.C. (1997). "Reconstructing Quaternary Environments". Second Edition, Longman Group Ltd., London and New York, 446 pp.

Maslin, M. A., & Christensen, B. (2007). "Tectonics, orbital forcing, global climate change, and human evolution in Africa". Introduction to the african paleoclimate special volume. Journal of human evolution 53, (5): 443-464.

Mazurek, M. (2004). "Long-term used nuclear fuel waste management - Geoscientific review of the sedimentary sequence in southern Ontario". Technical Report TR 04-01, Institute of Geological Sciences, University of Bern, Switzerland.

Natural Resources Canada. “http://geoscape.nrcan.gc.ca/toronto/escarp_e.php”

Nguyen, T.S., Poliscuk, V.& Selvadurai, A.P.S. (1993), “Effects of glaciation on a nuclear fuel waste repository”, 46th Canadian Geotechnical Conference, Toronto.

Nguyen, Thanh Son. (1995). “Computational modeling of thermal-hydrological mechanical processes in geological media”. Ph.D Thesis, McGiIl University, Montreal, Quebec.

Paterson, W. S. B. (1994). “The physics of glaciers”. 3rd edition. P. 241-242, PERGAMON.

Peltier, W.R. (2008). “Phase I long term climate change study”. Supporting technical report. OPG 00216-REP-01300-00004-R00.

Rasilainen, K., Luukkonen, A., Niemi, A., Olin, M. & Pöllä J. (1999). ”The feasibility of modelling coupled processes in safety analysis of spent nuclear fuel disposal”. Espoo: VTT Technical Research Centre of Finland.

Sykes, J.F., Sykes, E.A., Normani, S.D., Yin, Y., Park, Y.J. (2008). “Phase I Hydrogeologic modeling”. Supporting technical report. OPG 00216-REP-01300-00009-R00.

Vidstrand, P., Wallroth, T., & Ericsson, L.O. (2008), “Coupled HM effects in a crystalline rock mass due to glaciation: Indicative results from groundwater flow regimes and stresses from an FEM study”. Bulletin of Engineering Geology and the Environment, Vol. 67(2), 187-197.

Vugrinovich, R. (1989). “Subsurface temperatures and surface heat flow in the Michigan Basin and their relationships to regional subsurface fluid movement”. Marine and Petroleum Geology, Volume 6(1), 60-70.

SIMULATION OF DILATANCY-CONTROLLED GAS MIGRATION PROCESS IN SATURATED ARGILLACEOUS ROCK

W.J. Xu[1,4], H. Shao[1], J. Hesser[1], W.Q. Wang[2], O. Kolditz[2,4] & T. Popp[3]
[1]*Federal Institute for Geosciences and Natural Resources (BGR), Hanover, Germany*

[2]*Helmholtz Center for Environmental Research (UFZ), Leipzig, Germany*

[3]*Institute for Rock Mechanics (IfG), Leipzig, Germany*

[4]*Technical University of Dresden, Dresden, Germany*

ABSTRACT: *A coupled hydro-mechanical model has been developed to simulate the gas injection tests with increasing gas pressure in saturated argillaceous rock. In the model, the gas migration in porous medium is assumed to be controlled by the gas pressure, the hydro-mechanical states (saturation, stress), and the material properties (permeability, porosity, deformation behaviour). Based on the model, laboratory gas injection tests on a rock specimen of Opalinus Clay have been simulated with the FEM program OpenGeoSys (OGS). The rock specimen is modelled as a continuum anisotropic porous medium. The effective stress is defined by using the saturation as weighting functions for the gas and water pressures. The relationship between capillary pressure and water saturation is described by the van Genuchten function based on laboratory data and the relative permeabilities to gas and water by the approach of Mualem. A modified Drucker-Prager elasto-plastic model, which contains a tensile yield function with associated flow rule, is applied. The simulated gas flow rate evolutions under different gas injection pressures agree very well with the experimental measurement data. Low gas flow rates can be simulated by using a coupled multiphase flow and an elastic model for the rock specimen if the gas injection pressure is higher than the gas entry pressure. If the gas injection pressure is higher than minimal principle stress, a plastic zone with micro fissures may be generated which leads to an increase in permeability of several orders of magnitude.*

1 INTRODUCTION

Gas transport and migration in an engineered barrier system and in the host rock is an important issue for management of final disposal of radioactive waste in deep geological underground. In the post closure phase of a nuclear waste disposal system gases can be produced as a result of corrosion of metal canister, degradation of organic matter and radiolysis of water (NAGRA 2004). Due to gas generation the pressure in a repository will be increased and it has large influence on the mechanical stability of the host rock and barrier system. Therefore, thermo-hydro-mechanical analysis is required to evaluate the long-term safety of a disposal system.

The gas transport mechanisms depend strongly on the gas pressure and hydro-mechanical state of the rock. The gas transport process in argillaceous rock can be described in four parts according to the different controlled criteria (NAGRA, 2002). Under a gas pressure, which is lower than the gas entry pressure of the rock mass, the transport process is controlled by advection and diffusion of dissolved gas in water. Once the gas pressure exceeds the entry pressure of the rock mass, the transport process is mostly controlled by visco-capillary two-

phase flow. Advection and diffusion of dissolved gas exist at any level of gas pressure, but its contribution for the total gas migration in comparison to the visco capillary two-phase flow process is very small. Because of the relative low tensile strength of argillaceous rocks micro-fissure will be occurred when the gas pressure is higher than the minimum principal stress. The pore space and permeability will be increased due to micro-fracture. After that if the gas pressure keeps on increasing the macroscopic fractures will be formed. This process can cause the extremely high transport capacity of the host rock and destroy the barrier system.

In this paper numerical simulations using a finite element model for non-isothermal multiphase elasto-plastic porous medium are presented. The numerical code OGS is used. The material is modelled as a porous continuum with gas and water flow. Only the gas phase is assumed compressible. A mechanic model with a modified Drucker-Prager yield surface is applied and the return mapping algorithm is used.

In order to investigate the gas transport mechanisms and to determinate the hydraulic properties of clay stone a series of experiments have been carried out in the laboratory of IfG. In this paper the focus is on two gas injection experiments.

2 GOVERNING EQUATIONS

Multi-phase flow and elasto-plastic deformation are included. The primary variables are capillary pressure p_c, gas pressure p_w and displacement vector **u**. Gas phase is assumed to be compressible and obeys the ideal gas low. Liquid and solid are defined as incompressible phase. The whole medium is continuum and homogeneous.

The linear momentum balance equation of the porous medium is given as

$$\nabla\left(\boldsymbol{\sigma} - \alpha\left(p_g - S_w p_c\right)\mathbf{I}\right) + \rho\mathbf{g} = 0 \tag{1}$$

where $\boldsymbol{\sigma}$ is the effective stress, α is the Biot coefficient. The water saturation S_w is used as weighting factor for the modified effective stress in unsaturated porous medium. ρ is the density of the medium, which is composed by solids, liquid and gas and can be written as

$$\rho = (1-\phi)\rho_s + \phi S_w \rho_w + \phi(1-S_w)\rho_g \tag{2}$$

where ϕ is the porosity of the porous medium.

The flow rate of gas phase and fluid phase is described in form of Darcy law as

$$v_\gamma = \frac{k_{rel}^\gamma \mathbf{k}}{\mu_\gamma}\left(\nabla p_\gamma - \rho_\gamma \mathbf{g}\right), \quad \gamma = \mathrm{w, g} \tag{3}$$

where k_{rel}^γ is the relative permeability of the phase, which can be defined as a function of saturation in multi-phase flow, $\mathbf{k}$ is the intrinsic permeability tensor of the medium, μ_γ is the viscosity of the phase, ρ is the density and $\mathbf{g}$ is the gravity acceleration.

The mass balance equations for the solid and the water (Eq. 4a) and for the gas phase (Eq. 4b) are

$$\phi\rho_w\left(\frac{\partial S_w}{\partial p_c}\frac{\partial p_c}{\partial t}\right)+\rho_w S_w\nabla\left(\frac{\partial \mathbf{u}}{\partial t}\right)+\nabla\left(\rho_w\frac{k_{rel}^w\mathbf{k}}{\mu^w}\left[-\nabla p_g+\nabla p_c+\rho_w\mathbf{g}\right]\right)$$
$$+\nabla\left(\rho_g\frac{k_{rel}^g\mathbf{k}}{\mu^g}\left[-\nabla p_g+\rho_g\mathbf{g}\right]\right)=0 \tag{4a}$$

and

$$\phi\rho_g\left(\frac{\partial S_w}{\partial p_c}\frac{\partial p_c}{\partial t}\right)+\rho_g(1-S_w)\nabla\left(\frac{\partial \mathbf{u}}{\partial t}\right)+\phi(1-S_w)\left(\frac{\partial \rho_g}{\partial p_c}\frac{\partial p_c}{\partial t}+\frac{\partial \rho_g}{\partial p_g}\frac{\partial p_g}{\partial t}\right)$$
$$+\nabla\left(\rho_g\frac{k_{rel}^g\mathbf{k}}{\mu^g}\left[-\nabla p_g+\rho_g\mathbf{g}\right]\right)=0 \tag{4b}$$

The relationship between capillary pressure p_c, gas pressure p_g and water pressure p_w is defined by the sorption equilibrium equation.

$$p_c = p_g - p_w \tag{5}$$

The relative permeability k_{rel} of liquid and gas phase can be determined with approach of Mualem (Mualem, 1976)

$$k_{rel}^g = (1-S_e)^{1/2}\left(1-S_e^{\frac{n}{n-1}}\right)^{2(1-1/n)} \tag{6a}$$

$$k_{rel}^w = S_e^{1/2}\left[1-\left(1-S_e^{\frac{n}{n-1}}\right)^{\frac{n-1}{n}}\right]^2 \tag{6b}$$

with

$$S_e = \frac{S_w - S_{wr}}{1-S_{gr}-S_{wr}} \tag{6c}$$

where S_{wr} and S_{gr} are the residual water and gas saturation, n is the shape factor.

The dependence of the water saturation and capillary pressure can be described with an empirical function. The relationship between water saturation and capillary pressure is characterized by the van Genuchten model as followed

$$p_c = p_0\left(S_e^{\frac{n}{n-1}}-1\right)^{\frac{1}{n}} \tag{7}$$

where p_0 is the gas entry pressure of the porous medium.

3 MODIFIED DRUCKER-PRAGER MODEL

The mechanical behaviour of the solid skeleton is assumed to be perfect elasto-plastic. The Drucker-Prager yield surface is applied and modified with an extra yield surface in order to take tensile failure into account. The return mapping algorithm is used for the numerical simulation. The hardening/softening effect is not considered in this model.

Two yield functions are defined in form as

$$F^s = \alpha_\theta I_1 + \sqrt{J_2} - k_\theta \tag{8a}$$

$$F^t = \frac{1}{3} I_1 - \sigma^t \tag{8b}$$

where F^s is the yield function of commonly Drucker-Prager model for the shear failure criterion, F^t is the yield function for tensile failure criterion, I_1 is the first stress invariant and J_2 is the second invariant of the deviatoric stress, α_θ and k_θ are material parameters, which can be defined with the inner adjustment of Mohr-Coulomb pyramid (Itasca, 2009).

For the general return mapping algorithm the increment of stress can be calculated in form as

$$\Delta\boldsymbol{\sigma} = \Delta\boldsymbol{\sigma}^e - \Delta\boldsymbol{\sigma}^p = \mathbf{D}^e\left(\Delta\boldsymbol{\varepsilon} - \Delta\lambda\frac{\partial G}{\partial\boldsymbol{\sigma}}\right) \tag{9a}$$

with

$$\Delta\lambda = \frac{\left(\partial F/\partial\boldsymbol{\sigma}\right)^T \mathbf{D}^e \Delta\boldsymbol{\varepsilon}}{\left(\partial F/\partial\boldsymbol{\sigma}\right)^T \mathbf{D}^e \left(\partial G/\partial\boldsymbol{\sigma}\right)} \tag{9b}$$

where $\mathbf{D}^e$ is the elastic constitutive tensor and G is the potential function. A non-associative plasticity for F^s and associative plasticity for F^t is assumed.

$$G^s = \alpha_\psi I_1 + \sqrt{J_2} \tag{10a}$$

$$G^t = \frac{1}{3} I_1 \tag{10b}$$

The parameter α_ψ has the same form as α_θ but using dilation angle ψ instead of inner friction angle θ. The yield surface can be defined in the I_1-$\sqrt{J_2}$ coordinate system in Fig. 1.

If the elastic predictor stress satisfies the failure criteria it must be returned to the yield surface with corresponding potential function. Stress region is introduced by Clausen (2007) to determine to which plane, line or point the stress should be returned. The stress space is separated in three parts for the modified Drucker-Prager model. For stress region 1 or 2, it will be replaced to plane $F^s(\boldsymbol{\sigma}) = 0$ or $F^t(\boldsymbol{\sigma}) = 0$ using plastic potential function $G^s(\boldsymbol{\sigma})$ or $G^t(\boldsymbol{\sigma})$.

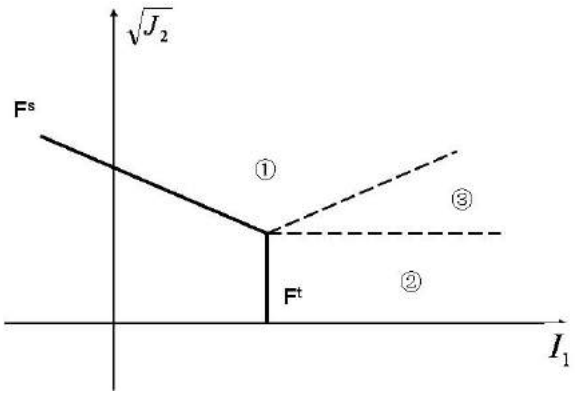

Fig. 1. Failure criterion of modified Drucker-Prager model in I_1-$\sqrt{J_2}$ coordinate system

For stress region 3, both of the two failure criteria are active and the returned stress is located at the intersection of two yield planes. This is assumed when the two yield criteria are both active, the total plastic corrector stress $\Delta\boldsymbol{\sigma}^p$ is composed by $\Delta\boldsymbol{\sigma}^{p,s}$ and $\Delta\boldsymbol{\sigma}^{p,t}$, which are plastic corrector stresses for return to the corresponding yield surface $F^s(\boldsymbol{\sigma})=0$ and $F^t(\boldsymbol{\sigma})=0$. During the return mapping the direction of the stress is assumed to be constant. It can be written as

$$\Delta\boldsymbol{\sigma}^p = m_s\Delta\boldsymbol{\sigma}^{p,s} + m_t\Delta\boldsymbol{\sigma}^{p,t} \tag{11}$$

where $\Delta\boldsymbol{\sigma}^{p,s}$ and $\Delta\boldsymbol{\sigma}^{p,t}$ can be calculated using Eq. (9), m_s and m_t are constant parameters. Because the updated stress satisfies both yield functions, m_s and m_t can be easily solved from the equation system in form as

$$\begin{cases} F^s\left(\boldsymbol{\sigma}^0 + \mathbf{D}^e\Delta\boldsymbol{\varepsilon} - m_s\Delta\boldsymbol{\sigma}^{p,s} - m_t\Delta\boldsymbol{\sigma}^{p,t}\right)=0 \\ F^t\left(\boldsymbol{\sigma}^0 + \mathbf{D}^e\Delta\boldsymbol{\varepsilon} - m_s\Delta\boldsymbol{\sigma}^{p,s} - m_t\Delta\boldsymbol{\sigma}^{p,t}\right)=0 \end{cases} \tag{12}$$

4 THE LABORATORY GAS INJECTION EXPERIMENTS

To investigate the gas transport in argillaceous rocks a series of gas injection experiments with rock salt and clay stone specimens were carried out in IfG. Two experiments of Opalinus Clay are discussed in this paper. The specimens are from the Mont Terri Rock Laboratory in Switzerland.

Fig. 2 is a sketch of the experiment concept for axial injection geometry. A cylinder specimen with 150.45 mm height and 73.59 mm diameter was prepared. Two boreholes with 30 mm length and 4 mm diameter were drilled at the top and the bottom surface. Nitrogen was used as test gas and injected from the bottom borehole. The flowing through gas was collected from the suction borehole at the top surface. The cylinder specimen was bonded between two metal plates and sealed with a rubber jacket. A hydrostatical or deviatoric loading condition can be provided.

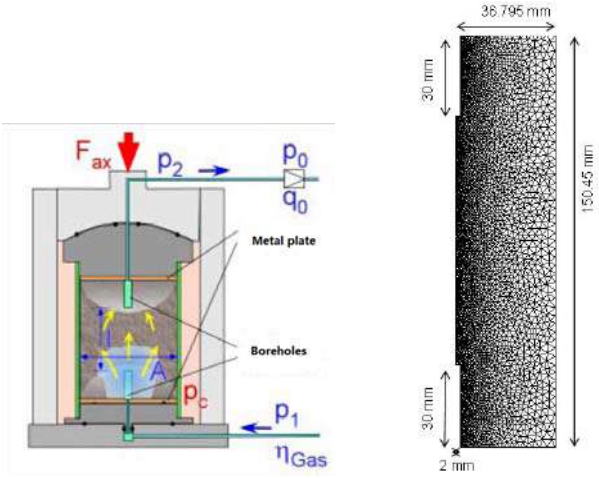

Fig. 2. Sketch of the laboratory experiment in axial injection geometry (left) and numerical model (right)

Both experiments were carried out under similar conditions. In the first test with a constant confining pressure of 1 MPa, gas injection pressure was increased stepwise. The confining pressure was always higher than the gas pressure. After the gas injection pressure reached 0.9 MPa the confining pressure started to raise step by step and had an end level of 5 MPa. The process of this experiment is depicted in Fig. 3. During the other experiment the gas pressure was increased from 1 MPa to 3.5 MPa, which is higher than the confining pressure with a value of 3 MPa. After significant increase of measured gas flow rate the gas injection pressure was decreased to 1 MPa. The test history is shown in Fig. 4.

Opalinus Clay from Mont Terri has apparent anisotropic structure. The specimens of both experiments were prepared concerning the orientation of the bedding plane perpendicular to gas injection direction.

5 NUMERICAL RESULTS

The specimens (chapter 4) are modelled with an axial symmetry geometry and 8078 triangular elements, as shown in Fig. 2.

Initial gas pressure was set to 0.1 MPa. During the experiment no water draining was observed (Popp et al. 2004), so the value of initial saturation was varied between 0.7 and 0.9. The measured gas injection pressure was used as boundary condition in the injection borehole and the gas pressure kept constant with 0.1 MPa in the suction borehole. The symmetric axis and the bottom edge were fixed as no displacement boundaries. Hydrostatic confining pressure state was applied at the top and outer edge.

The experiments were simulated as isothermal multi-phase flow with elasto-plastic mechanical behaviour using modified Drucker-Prager model. All the material parameters are listed in Table 1 (NAGRA, 2002, Popp et al., 2004). The specimen is assumed to be homogenous and isotropic for mechanical behaviour. Because of the orientation of the bedding plane structure in the specimens the hydraulic behaviour was modelled as anisotropic porous media and the permeability in horizontal direction is assumed 10 times higher than that in vertical direction.

The numerical results of gas flow rate are compared with the measurement results of both laboratory experiments.

Table 1. Material parameters used for experiment 1 and 2.

Parameter	Unit	Experiment 1	Experiment 2
Initial gas pressure	Pa	1.0E+5	1.0E+5
Initial water saturation	-	0.7	0.9
Gas entry pressure	Pa	9E+4	2.5E+6
Water residual saturation	-	0.5	0.5
Gas residual saturation	-	0	0
Shape factor	-	2	2
Intrinsic permeability //	m^2	2.1E-16	3.7E-17
Intrinsic permeability $\perp$	m^2	2.1E-17	3.7E-18
Biot coefficient	-	1.0	1.0
Porosity	-	0.16	0.16
Solid density	kg/m^3	2450	2450
Young modulus	Pa	2.5E+9	2.5E+9
Poisson ratio	-	0.27	0.27
Cohesion	Pa	4.5E+5	4.5E+5
Internal friction angle	°	30	30
Dilatancy angle	°	20	20
Tensile strength	Pa	2.33E+5	2.33E+5

5.1 Experiment 1

In experiment 1 with constant confining pressure and stepwise increase of injection pressure, the gas flow rate was observed. The permeability change due to the deformation change was different by compaction and tension process. The different behaviour of compaction and tension is observed not only in the laboratory but also in the in-situ experiments, e.g. the in-situ-ventilation experiment in Mont Terri (Zhang & Rothfuchs, 2005). During the experiment the gas pressure was always lower than the confining pressure. There was no damage in form as micro-fracture due to tensile failure. Empirical functions for permeability change (Eq. 13) were applied to consider the change of permeability caused by deformation as

$$\mathbf{k} = f\left(\Delta\varepsilon_{vol}\right) e^{4000\Delta\bar{\varepsilon}^{p}} \mathbf{k}_{\text{int}} \tag{13a}$$

and

$$f\left(\Delta\varepsilon_{vol}\right) = \begin{cases} 10^{600\Delta\varepsilon_{vol}}, & \textit{compaction} \\ 10^{50\Delta\varepsilon_{vol}}, & \textit{tension} \end{cases} \tag{13b}$$

where $f\left(\Delta\varepsilon_{vol}\right)$ describes the different behaviour of permeability change due to compaction and tension, $\mathbf{k}_{\text{int}}$ is the intrinsic permeability and $\Delta\bar{\varepsilon}^{p}$ is the equivalent plastic strain.

The results of numerical simulation and laboratory measurements are depicted in Fig. 3. The calculated gas flow rate matches the measured rate very well. The calculated gas flow rate increases with the gas injection pressure. When the confining pressure starts to rise the gas flow rate is reduced. Because of the time independent mechanical behaviour the decreasing of gas flow rate from the numerical results is immediately reacted with the change of the confining pressure. Another explanation for this phenomenon is the change of porosity, which was not considered in this model. When the specimen was compressed the porosity was decreased and in the pore space stored gas was squeezed out. Therefore the measured gas flow rate should be higher.

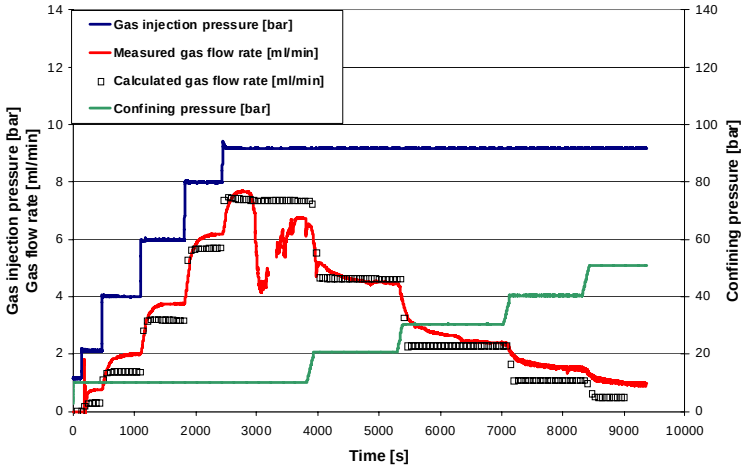

Fig. 3. Numerical results of gas flow rate and laboratory measured data

5.2 Experiment 2

Before the second experiment was carried out the specimen was compressed by a deformation experiment, therefore the material properties are quite different from the first experiment, e.g. permeability, gas entry pressure and initial saturation. During this experiment the gas flow rate had a significant increasing when gas injection pressure reached the highest value. This phenomenon is well known for Opalinus Clay not only from the laboratory but also from in-situ experiments.

To deal with the gas injection in the saturated clay stone, quite often a two-phase flow model with pressure dependent permeability is used. Similar to the modelling of experiment 1, an empirical function was implemented to consider the change of permeability due to gas pressure (Eq. 14).

$$\mathbf{k} = f\left(p_g\right)\mathbf{k}_{\text{int}} = \begin{cases} \left(1+0.0125\,p_g\right)\mathbf{k}_{\text{int}} & , \quad p_g \le 3.2 \quad MPa \\ \left(15.2\,p_g - 485\right)\mathbf{k}_{\text{int}} & , \quad p_g > 3.2 \quad MPa \end{cases} \tag{14}$$

Therefore this laboratory experiment was simulated using two different models. One of them is a two-phase flow model taking the permeability change into consideration (Eq. 14). The other one is a fully coupled hydro-mechanical model using Eq. (13) to describe the relationship between permeability and mechanical behaviour.

It is considered that the pore spaces of the specimen were extended during the gas pressure increasing but there were no interconnections among pore space under a lower gas pressure. That's why the permeability had only small increase. When the gas pressure exceeds the threshold pressure the extended pore spaces were connected and permeability significantly increased. This process can be described by the correction functions in Eq. (13) and Eq. (14). Eq. (14) defines directly the threshold pressure and applies a linear relationship between gas pressure and permeability. Using Eq. (13) in the HM coupled model the permeability increases significantly when effective stress reaches tensile strength and plastic strain occurs.

The numerical results from the H and coupled HM modelling are depicted in Fig. 4. The application of the empirical function in the H model gives results that match the measurement data very well. With the increased gas injection pressure until 32 bar the calculated gas flow rate of H and HM model are similar. The significant increase of gas flow rate can be

simulated with both models. When the gas injection pressure falls to 10 bar, the gas flow rate of HM model decreases instantly. It's similar as the results of experiment 1 in chapter 5.1. The time independent mechanical behaviour and the neglecting of porosity change is a possible cause for this phenomenon.

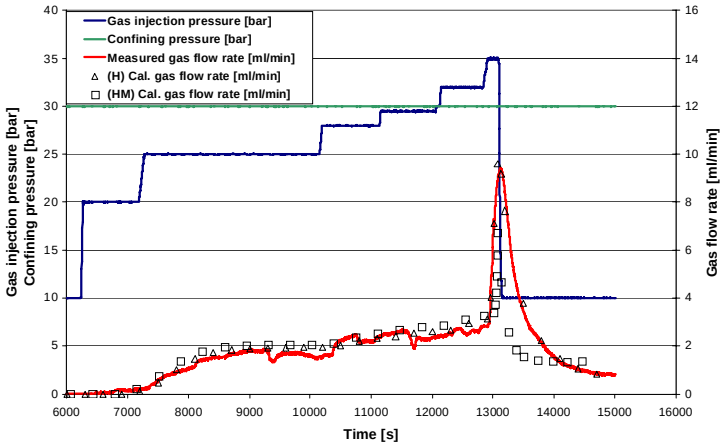

Fig. 4. Numerical results of not coupled and coupled simulation in comparison to laboratory data

Fig. 5 shows the calculated equivalent plastic strain, permeability correction factor and gas pressure with gas flow vectors when the gas injection pressure reaches 35 bar using the HM coupled model. Because of the effective stress concept, which uses the saturation as weighting factor, the higher plastic strain occurs not only in the near field of the end of the injection borehole but also at the outer edge. The highest gas flow rate appears at the end of the injection borehole and its direction is dominated by horizontal direction due to the anisotropic permeability.

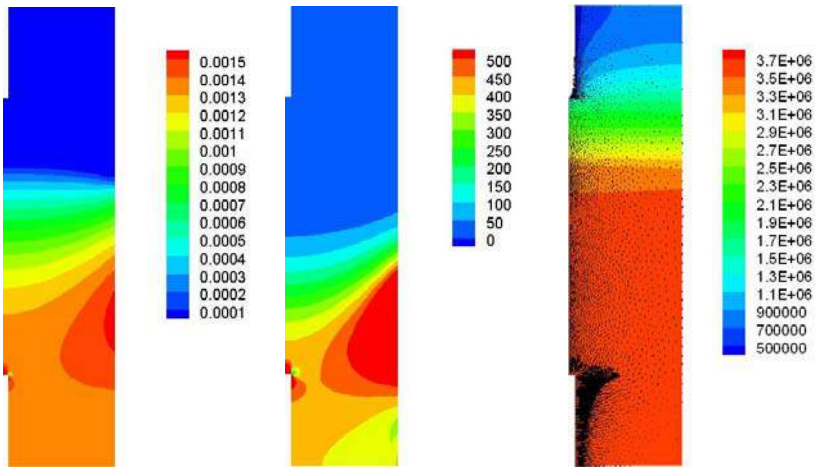

Fig. 5. Distribution of equivalent plastic strain (left), permeability correction factor (middle) and gas pressure with gas flow vectors (right) at 13040 s

With the assumption of the permeability dependence on mechanical behaviour the laboratory experiments can successfully be simulated. With the well matched measurement data by the numerical results, the applied correction function Eq. (13) describing the hydro-mechanical coupled relationship between permeability and deformation is acceptable. This

function can be treated as a general equation to modify the permeability for elastic and elasto-plastic deformation.

6 CONCLUSIONS

A hydro-mechanical coupled model for partially saturated porous media has been presented. The development of permeability due to deformation and tensile failure is considered, and such development is described by using correction functions. Two laboratory gas injection experiments are simulated and numerical results of gas flow rate have been presented. The numerical results have a good agreement with the measurement data. The applied hypotheses for the permeability dependence on mechanical behaviour are appropriate for the visco-capillary two-phase flow and dilatancy-controlled gas flow by gas migration in argillaceous rocks.

The immediate decrease of gas flow rate from the simulation of both experiments is different to the laboratory measurements. To consider this phenomenon the change of porosity during the simulation has to be taken into account. For Opalinus clay with obvious bedding plane not only the hydraulic but also the mechanical properties are anisotropic. Therefore, a model with anisotropic mechanical behaviour is required for further study of the pressure problems. In fact, the pore spaces extension and micro fissures are also directional and depend on the mechanical state.

AKNOWLEDGEMENTS

This work was supported by BMWi (Bundesministerium für Wirtschaft und Technologie, Berlin). We thank S. Nguyen (CNSC), M. Fall and E. Evgin (University of Ottawa) for the cooperative discussions.

REFERENCES

Clausen, J. (2007), Efficient non-linear finite element implementation of elasto-plasticity for geotechnical problems. Ph.D. thesis, Esbjerg institute of technology, Aalborg University

Itasca Consulting Group, Inc. (2009), FLAC3D (Fast Lagrangian Analysis of Continua in 3 Dimensions), Version 4.0, Minneapolis.

Mualem, Y. (1976), “A new model for predicting the hydraulic conductivity of unsaturated porous media”. Water Resour. Res. 12/6, 539-542.

NAGRA (2002), “Entsorgungsnachweis für abgebrannte Brennelement, verglaste hochaktive sowie langlebige mittelaktive Abfälle”. Nagra Tech. Rep. 02-03.

NAGRA (2004), “Effects of Post-disposal Gas Generation in a Repository for Spent Fuel, High-level Waste and Long-lived Intermediate Level Waste Sited in Opalinus Clay”. Nagra Tech. Rep. 04-06.

Popp, T., Wiedemann, M., Böhnel, H. & Minkley, W. (2007), “Untersuchungen zur Barriereintegritaet im Hinblick auf das Ein-Endlager-Konzept”.

Van Genuchten, M.Th. (1980), “A closed-form equation for predicting the hydraulic conductivity of unsaturated soils”. Soil Sci. Soc. Am. J., Vol.44.

Wang, W. Kosakowski, G. & Kolditz, O. (2009), “A parallel finite element scheme for thermo- hydro-mechanical (THM) coupled problems in porous media”. Computers & Geosciences, Vol. 35(8), 1631-1641.

Zhang, C.-L. & Rothfuchs, T., (2005), Determination of material parameters for the Opalinus Clay. NF-Pro RTDC4 – WP 4.3: EDZ long term evolution. Deliverable 4.3.4. GRS Braunschweig.

DESIGN OF PILED-RAFT FOUNDATIONS BY MEANS OF A MULTI-PHASE MODEL ACCOUNTING FOR SOIL-PILE INTERACTIONS

G. Hassen, P. de Buhan
Université Paris-Est, UR Navier (ENPC-LCPC-CNRS), Ecole des Ponts ParisTech, Marne-la-Vallée, France

E. Bourgeois
Université Paris-Est, LCPC-MACS, Paris, France

ABSTRACT. *The settlement behavior of a pile-raft foundation is analyzed with the help of a multiphase model aimed at describing the overall response of the reinforced ground. According to this model, the group of piles is treated as a homogenized continuous medium in interaction with the soil along the pile length, as well as at their lower tips. These two kinds of interaction, which play a decisive role in the way the piles are actually working as strengthening elements, are described by specific constitutive laws which can be directly introduced in the general governing equations of the multiphase model. Thus improved, the multiphase model can then be incorporated in a finite element code developed in the context of an elastoplastic behavior of the soil, provided that the constitutive parameters of the interaction laws have been previously identified. This identification procedure is performed through numerical simulations of the simple problem of a single pile, loaded at its top. The global response of vertically loaded piled-raft foundations, expressed in the form of load settlement curves, is finally presented, clearly highlighting the decisive influence of the mobilized pile shaft friction and tip resistance on the foundation settlement reduction.*

1 INTRODUCTION

The setup of rational and reliable design methods for piled-raft foundations still remains a major computational challenge. Indeed, referring for instance to a finite element simulation of this kind of geotechnical structures, a fully three-dimensional analysis is required, with a locally refined mesh discretization in order to capture with sufficient accuracy the complex interactions prevailing between the piles, the surrounding soil and the raft. This leads to the elaboration of a complex and sophisticated computational tool, the use of which remains limited to rather simple configurations, such as purely vertical loading (Lee et al., 2010). Conceived as an improved homogenization procedure, a so-called “multiphase model” has been proposed, which can easily be implemented in a f.e.m.-based numerical code, thus leading to a considerable simplification of the initial design problem and to dramatically reduced computational times (Sudret & de Buhan, 2001).

The present contribution is focused on extending the range of applicability of the model, in order to account for soil-pile interactions taking place not only along the pile length (mobilized “shaft or skin friction”), as already developed in (Bourgeois et al., 2011), but also at the lower ends of the piles (mobilized “tip resistance”), both kinds of interactions being captured through specific laws expressed in the formalism of the multiphase model. The analysis is carried out following two successive steps. First, appropriate values for the constitutive stiffness and strength parameters of the above interaction laws are identified from

numerical simulations performed on a representative volume of pile-reinforced ground. These parameters are then incorporated in the multiphase model and implemented in a finite element code, allowing to investigate the behavior of pile-reinforced foundations and thus provide insight into the way the foundation settlement is actually reduced by the incorporation of piles.

2 PRINCIPLE OF THE MULTIPHASE APPROACH

2.1 Problem statement

The typical engineering problem to be dealt with is that of a shallow strip footing of width B resting upon a soft clay which has been previously reinforced by a group of piles of length L placed just beneath the raft. The latter is subject to a purely vertical loading characterized by a linear density Q along the raft's axis Oz, as sketched in Figure 1(*a*). Denoting by ρ the pile's radius and by s the spacing between two adjacent piles assumed to be distributed in the soil mass following a regular square pattern, a key parameter of such a reinforcement scheme is the *reinforcement volume fraction* defined as:

$$\eta = \pi \frac{\rho^2}{s^2} \tag{1}$$

which is generally small. Our objective is to investigate through numerical simulations the actual settlement reduction provided by the piles.

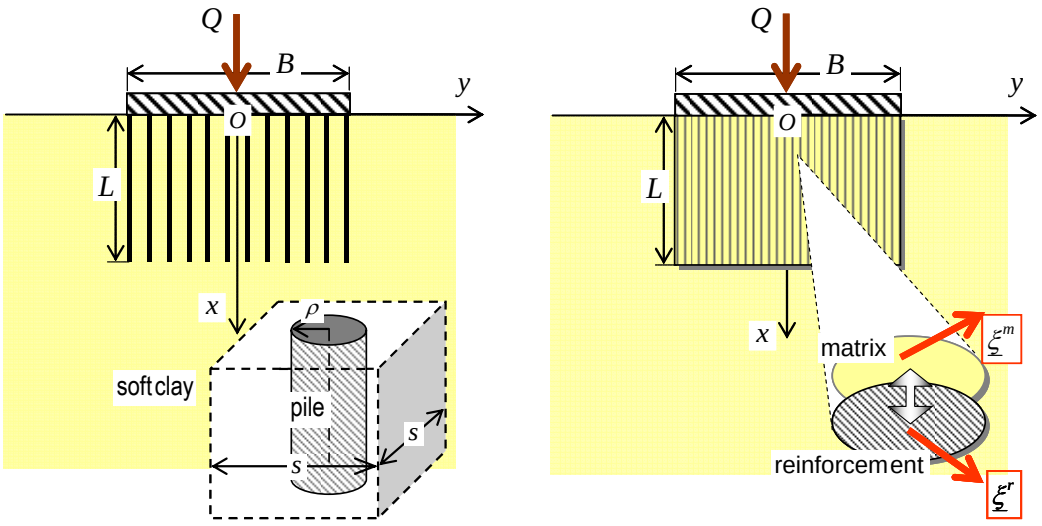

Fig. 1. Piled raft under vertical loading: (*a*) initial problem and (*b*) multiphase description

2.2 Outline of the multiphase model

The multiphase approach consists in replacing the composite pile-strengthened zone of height L and width B located beneath the raft, not by one single equivalent medium as in the traditional homogenization approach, but by *two superposed interacting continua*, called "phases". According to this model, a detailed presentation of which may be found in (Sudret & de Buhan, 2001), the soil is represented by a *matrix phase*, while the group of piles is represented by a *reinforcement phase*. More precisely, two coincident particles are located at

any geometrical point of the reinforced zone; each particle is attributed its own kinematics, namely a displacement vector $\underline{\xi}^m$ for the matrix phase particle and $\underline{\xi}^r$ for the reinforcement phase particle.

The matrix phase is a classical continuous medium where the stress at any point is defined by a tensor $\underline{\underline{\sigma}}^m$, whereas the stress in the reinforcement phase occupying the domain V is defined by a uniaxial tensor $n^r \underline{e}_x \otimes \underline{e}_x$ along the vertical pile orientation, where n^r can be interpreted as the axial force in the piles per unit cross sectional area of reinforced soil. The equilibrium equations, expressed for each phase separately, may be written as:

$$\begin{aligned} &\mathrm{div}\underline{\underline{\sigma}}^m + I\underline{e}_x = 0 \qquad &&\text{for the matrix phase} \\ &\mathrm{div}(n^r \underline{e}_x \otimes \underline{e}_x) - I\underline{e}_x = 0 \qquad &&\text{for the reinforcement phase} \end{aligned} \tag{2}$$

where, for the sake of simplicity, the external body forces (gravity) have been omitted. In the above equations, I is a body force volume density, which represents, at the macroscopic scale of the multiphase model, the action of the piles on the soil along their length ("shaft or skin friction").

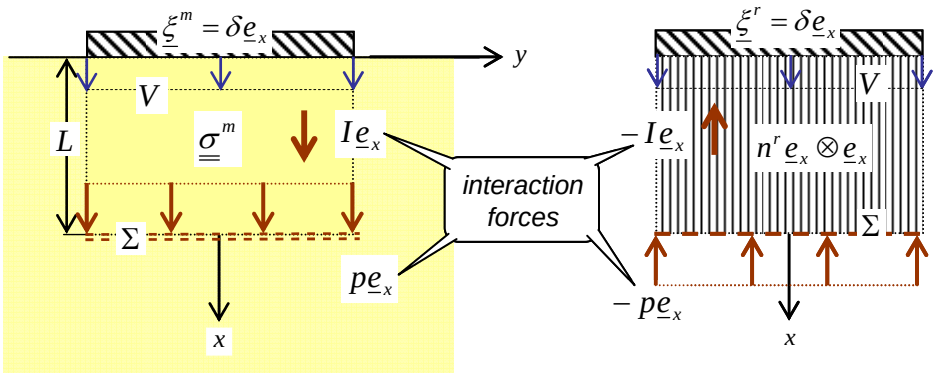

Fig. 2. Statics of the piled raft foundation modelled as a system made of two mutually interacting phases

A second kind of soil-pile interaction should be taken into account, corresponding to the action exerted by the pile lower tips onto the soil. This interaction takes place on the horizontal surface Σ located at a depth L from the surface, as shown in Figure 2, in the form of a surface density $p\underline{e}_x$, while the matrix phase exerts on the lower boundary surface Σ of the reinforcement phase an opposite surface density $-p\underline{e}_x$ (right hand side of Figure 2). The existence of such an interaction surface density, associated with the "pile tip resistance", implies the following condition on the lower boundary of the reinforcement phase:

$$n^r(x = L) = -p \tag{3a}$$

It generates at the same time in the matrix phase a *discontinuity of the vertical stress component* across Σ:

$$\sigma^m_{xx}(x = L^+) - \sigma^m_{xx}(x = L^-) = -p \tag{3b}$$

Besides, it should be noted that the same uniform displacement boundary condition is imposed by the rigid raft on top of both phases (Figure 2):

$$\underline{\xi}^m(x=0) = \underline{\xi}^r(x=0) = \delta \underline{e}_x \tag{4}$$

where δ is the foundation surface settlement.

2.3 Constitutive equations of the multiphase model

Assuming that the piles remain elastic, the constitutive equation of the reinforcement simply writes:

$$n^r = \alpha \varepsilon^r \tag{5}$$

where $\varepsilon^r = \partial \xi_x^r / \partial x$ is the *axial strain* of the reinforcement phase, while α is the *axial stiffness of the piles per unit transverse area*, which can be evaluated as the product of the reinforcement volume fraction η by the Young's modulus E^p of the pile constituent material:

$$\alpha = \eta E^p \tag{6}$$

On the other hand the matrix phase constitutive relations are simply identified with those of the soil, modelled as a linear elastic perfectly plastic, purely cohesive material, with a cohesion *C*.

Furthermore, the above described soil-pile interactions are governed by specific constitutive laws which can be written as follows.

- The first kind of interaction ("shaft friction") is formulated by means of a relationship linking the interaction force *volume* density *I* to the relative axial displacement between the reinforcement and the matrix phases, defined as:

$$\Delta = \xi_x^r - \xi_x^m \tag{7}$$

  In the context of an elastic perfectly plastic behavior, such a constitutive law takes the following form:

$$I = c^I(\Delta - \Delta^p) \quad \text{with} \quad \dot{\Delta}^p = \begin{cases} 0 \text{ if } |I| \le I^0 \\ \ge 0 \text{ if } I = +I^0, \dot{I} = 0 \\ \le 0 \text{ if } I = -I^0, \dot{I} = 0 \end{cases} \tag{8}$$

  where Δ^p is the plastic component of the relative displacement, while c^I and I^0 are coefficients describing the stiffness of the interaction and the threshold value of the interaction force density for which an irreversible relative displacement between the matrix and reinforcement phases occurs. The latter parameter can for instance be related to the maximum skin friction between the piles and the ground (Bourgeois et al., 2011).
- Similarly, the second type of interaction, associated with the "pile tip resistance", will be expressed by a relation between the interaction force *surface* density *p* and the

axial reinforcement/matrix relative displacement on $\Sigma(x=L)$. Adopting an elastoplastic framework, we thus obtain:

$$p = c^p\left(\Delta(L) - \Delta^{\mathrm{p}}(L)\right) \text{ with } \dot{\Delta}^{\mathrm{p}} = \begin{cases} 0 \text{ if } |p| \le p^0 \\ \ge 0 \text{ if } p = +p^0, \dot{p} = 0 \\ \le 0 \text{ if } p = -p^0, \dot{p} = 0 \end{cases} \tag{9}$$

Both interaction constitutive laws are represented in Figure 3 below, in the form of classical stress-strain diagrams.

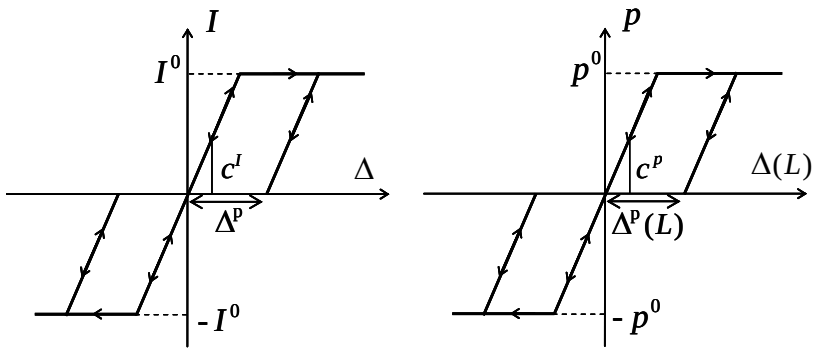

Fig. 3. Stress-strain diagrams for (*a*) the "shaft friction" and (*b*) "tip resistance" interaction laws

These interaction constitutive laws are strongly reminiscent of load-transfer curves ("*t-z*" curves) classically introduced for designing the load bearing capacity of individual piles driven in a soil (see among the most recent references: Ashour et al., 2010). It should be emphasized that an important difference between the above interaction laws and the usual load-transfer curves, is that the relevant kinematic variable associated with the pile-ground interaction forces is the relative displacement (Δ) between the matrix and reinforcement phases and not the absolute settlement (z) of the pile.

3 IDENTIFYING THE CONSTITUTIVE PARAMETERS OF THE MULTIPHASE MODEL

The key ingredient to the application of the multiphase approach to the simulation of the piled-raft settlement behavior lies in the identification of the different constitutive parameters introduced above.

3.1 Matrix and reinforcement phases

The identification of the constitutive stiffness and yield strength parameters of both phases is very straightforward. Owing to the fact that the reinforcement volume fraction introduced in Eq. (1) is small, and consequently the soil volume fraction is close to unity, the matrix phase is assigned the same elastoplastic characteristics as the purely cohesive soft clayey soil, namely:

$$E^m = 45\,\mathrm{MPa}\,,\ \nu^m = 0.3,\ \ C^m = 30\,\mathrm{kPa} \tag{10}$$

As regards the reinforcement phase, assumed to remain elastic as the (concrete) piles, the axial elastic stiffness density is simply calculated from Eqs. (1) and (6). Thus:

$$\rho = 0.25\text{m}, s = 2\text{m} \rightarrow \eta = 4.9\%$$
$$E^p = 12500\ \text{MPa} \rightarrow \alpha = 613\ \text{MPa} \tag{11}$$

3.2. Elastic interaction parameters

The determination of the interaction stiffness parameters c^I and c^p is based upon the same procedure as that used for piled-embankments (Hassen et al., 2009), which can be briefly described as follows. Considering the representative elementary volume of reinforced ground comprising one single pile surrounded by the soil, subject to a laterally constrained compressive loading, as pictured in Figure 4, the numerical simulation of this auxiliary problem (performed by means of a standard finite element code) is compared with the solution derived from the multiphase description of the same problem, which may be expressed analytically in the context of linear elasticity.

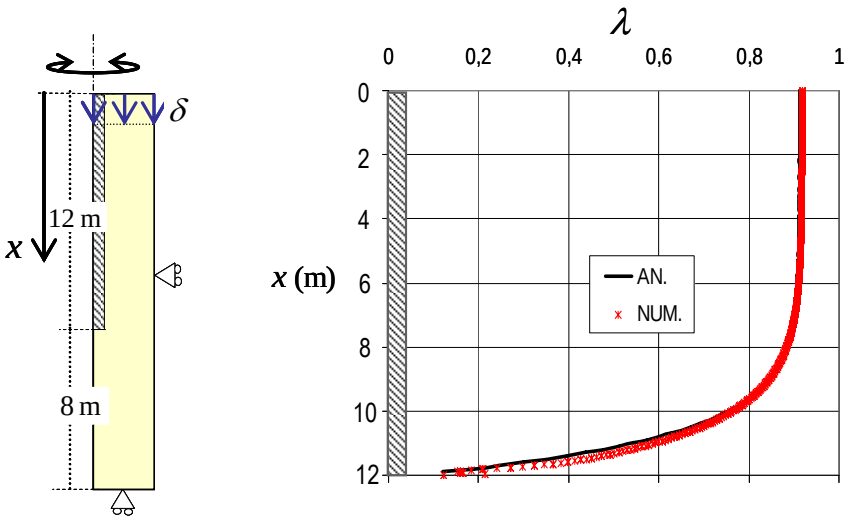

Fig. 4. Identification of the interaction stiffness parameters

More precisely, the identification is realized from fitting the numerical and analytical curves giving the variation with depth of the proportion λ of the total loading supported by the reinforcing pile. In the present configuration, the values of the interaction coefficients associated with the best fitting of these curves (Figure 4) are:

$$c^I = 40\ \text{MPa.m}^{-2}, \quad c^p = 5\ \text{MPa.m}^{-1} \tag{12}$$

3.2. Yield strength interaction parameters

The parameters governing the strength of the interaction laws (i.e. I^0 and p^0) can also be very simply evaluated on the basis of the numerical solution to the auxiliary problem, the loading being applied up to obtaining a complete plastification of the soil surrounding the pile. Figure 5 displays the corresponding axial load distribution along the pile length, expressed in terms of (compressive) stress n^r in the reinforcement phase, which turns out to vary linearly from -204 kPa at the pile head (x=0m) to -32 kPa at the pile tip (x=12m).

Such a result can be interpreted as follows in the framework of the multiphase model, assuming that both interaction forces have reached their yield values:

$$I = I^0 \text{ and } p = p^0 \tag{13}$$

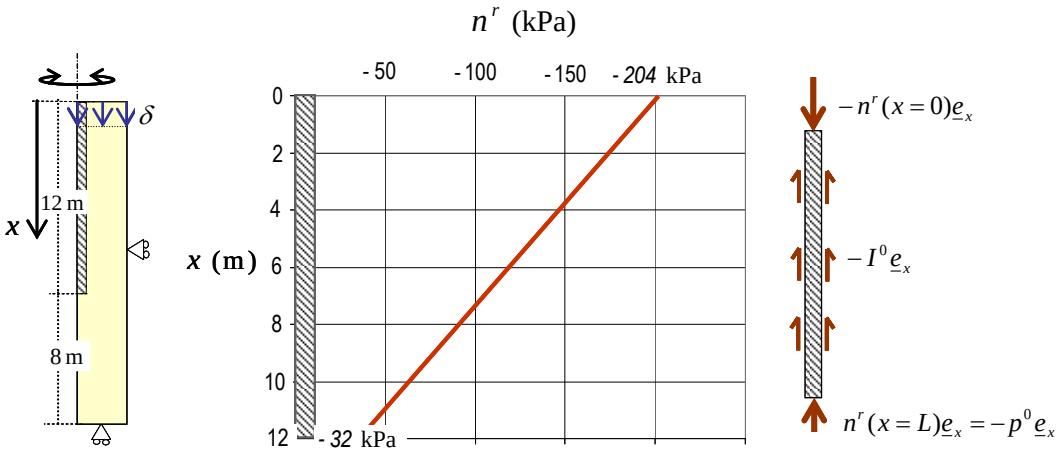

Fig. 5. Axial load distribution along the reinforcement for a fully plastic surrounding soil in the auxiliary problem

Indeed, it follows immediately from combining the above equalities with the equilibrium equation of the reinforcement phase (second equation in (2)), along with the boundary condition (3a) that:

$$n^r(x) = \overbrace{n^r(L)}^{-p^0} - I^0(L-x) \tag{14}$$

so that:

$$p^0 = -n^r(L) = 32\,\text{kPa} \text{ and } I^0 = \frac{n^r(L) - n^r(0)}{L} = 14.33\,\text{kPa.m}^{-1} \tag{15}$$

4 EXAMPLE OF NUMERICAL SIMULATION

Due to the symmetry with respect to the vertical plane passing through the footing axis, only one half of the piled raft foundation to be analyzed as a plane-strain problem, is represented in Figure 6, with its corresponding finite element mesh of 1,732 triangular elements and 3,542 nodes. The total width of the rigid footing acting on top of the pile-reinforced is equal to 12 m, so that the reinforcement scheme consists in six rows of 12m piles regularly spaced by a distance of 2m. All the other geometrical and geotechnical characteristics adopted in the following simulations are the same as those previously introduced.

It should be pointed out that the refinement of the mesh in the reinforced zone is the same as for a non reinforced, and thus homogeneous, soil. The only significant difference lies in the fact that three degrees of freedom (instead of two in the case of homogeneous soil) are attached to each node, namely the two components of the matrix phase displacement along with the axial relative displacement between phases Δ.

The numerically computed load-settlement curves are displayed in Figure 7. The four curves drawn up to the ultimate bearing capacity of the structure (vertical branch of the curves) correspond to the following four different situations.

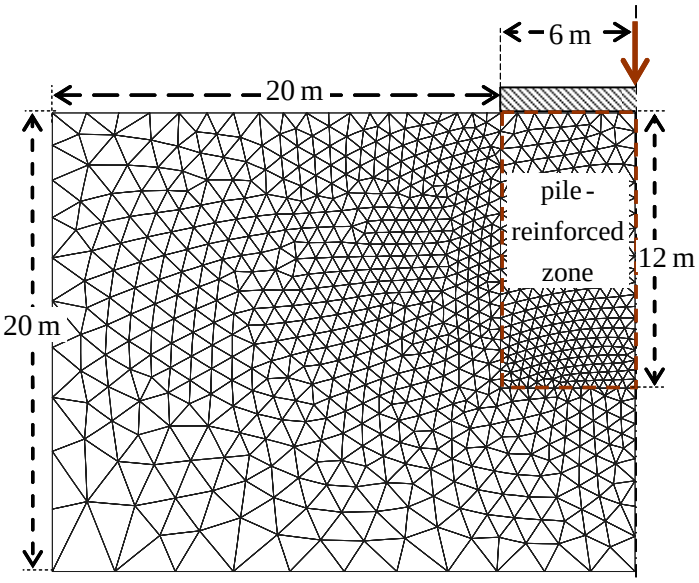

Fig. 6. Finite element discretization of the piled-raft foundation

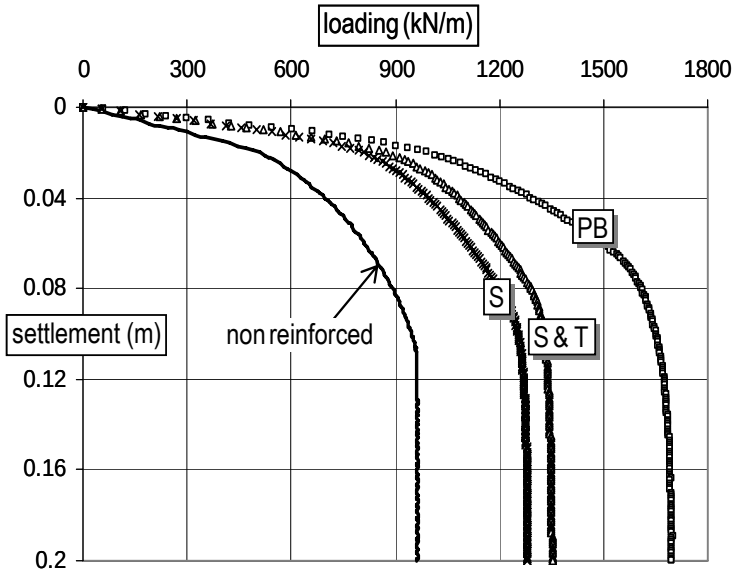

Fig. 7. Load-settlement curves of the piled and unpiled-raft foundation under different assumptions

- First, the foundation without any pile (*non reinforced case*) for which the ultimate bearing capacity is equal to 960 kN/m, that is slightly above the classical value predicted by the Prandtl's failure mechanism ($(\pi+2)CB/2 \cong 930$ kN/m).
- The case of the piled-raft foundation, where the condition of *perfect bonding* (PB) between phases has been assumed, which can be enforced by assigning very high

values to the interaction stiffness (c^I, c^p) and strength (I^0, p^0) parameters. The corresponding ultimate bearing capacity is equal to almost twice as much as that of the un-piled raft: 1700 kN/m.

- The two remaining cases considered in the analysis are those where only the "side" interaction law is taken into account (S) and when both "side" and "tip" interactions are accounted for (S&T). The corresponding ultimate bearing capacity is equal to 1350 kN/m in the latter case, 1280 kN/m in the former one.

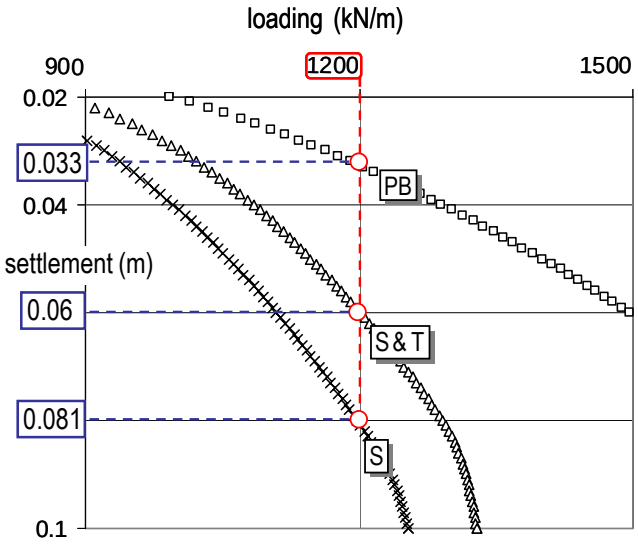

Fig. 8. Load-settlement curves of the piled and unpiled-raft foundation under different assumptions

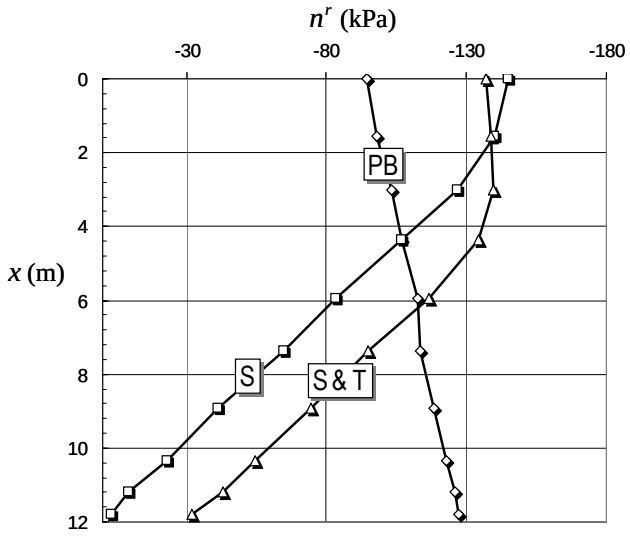

Fig. 9. Force distributions along the central pile for different interaction laws

Figure 8 represents a detailed picture of the load-settlement curves in the vicinity of a working load level of 1200kN/m, which exceeds the ultimate bearing capacity of the non reinforced foundation. Notable differences can be observed for the corresponding settlements

evaluated on the basis of the above mentioned hypotheses: 3.3cm for the perfect bonding assumption, 8.1cm and 6cm for the "side interaction only" and "side and tip interaction" assumptions, respectively.

This influence is confirmed in Figure 9, showing the corresponding variations of forces along the pile located in the middle of the reinforce zone, expressed in terms of stress distributions n^r along the corresponding vertical line in the reinforcement phase. The most striking difference between the three profiles is the value of the reinforcement stress at the tip of the piles (x=12m), which vanishes when no tip interaction is taken into account, takes the maximum value of -127kPa when perfect bonding is assumed and the intermediate value of -32kPa (that is $-p^0$) when tip interaction is also considered in the analysis.

5 CONCLUSION

It has been shown in this contribution how it was possible to incorporate specific soil-pile interaction laws in a multiphase model developed for the numerical simulation of piled-raft foundations. The important role played by such so-called "side and tip" interaction laws on the ultimate bearing capacity of the foundation, as well as on its settlement under working load conditions, has been clearly assessed in the analysis performed above.

Reliable predictions of piled-raft behaviour are therefore strongly dependent on the possibility of identifying appropriate values for the stiffness and yield strength interaction parameters to be introduced in the multiphase numerical calculations. The identification procedure proposed in this contribution, based on the numerical simulation of an auxiliary problem, should be used in a more systematic way, in order to produce closed-formed expressions giving the interaction parameters as functions of geometric (pile diameter and spacing) as well as constitutive soil and pile parameters, as it has been already done in the context of a linear elastic behaviour (Cartiaux et al., 2007).

REFRERENCES

Ashour, M., Norris, G.M., Elfass S. & Al-Hamdan, A.Z. (2010), "Mobilized side and tip resistances of piles in clay". Computers & Geotechnics, 37, 858-866.

Bourgeois, E., Hassen G. & de Buhan P. (2011), "Finite element simulations of the behaviour of piled-raft foundations using a multiphase model". To appear in Int. Journal of Geomechanics.

Cartiaux, F.-B., Gellée, A., de Buhan, P. & Hassen, G. (2007), A multiphase model for the design of soils reinforced by rigid inclusions (in French). Revue Française de Géotechnique, N°118, pp. 43-52.

Hassen, G., Dias, D. & de Buhan, P. (2009), "Multiphase constitutive model for the design of piled-embankments: comparison with three-dimensional simulations". Int. Journal of Geomechanics, Vol. 9, No. 6, 258-266.

Lee, J., Kim, Y. & Jeong S. (2010), "Three-dimensional analysis of bearing behavior of piled raft on soft clay". Computers and Geotechnics, 37, pp.103-114.

Sudret, B. & de Buhan, P. (2001), "Multiphase model for inclusion-reinforced geostructures. Application to rock-bolted tunnels and piled raft foundations". Int. J. Numer. Anal. Meth. Geomech., n°25, pp. 155-182.

A STUDY OF GRAIN CRUSHING AROUND PENETRATING PILES USING A MICROMECHANICS-BASED CONTINUUM MODEL

Chunshun Zhang, Itai Einav, Giang D Nguyen
School of Civil Engineering, The University of Sydney, Sydney, NWS, 2006, Australia

ABSTRACT: *The effects of grain crushing during pile penetration into crushable granular media are studied using a novel constitutive model (Einav, 2007b). This model is developed using clear micromechanics-based links between an internal variable, called breakage, and the evolving grain size distribution (gsd) due to grain crushing. In particular, using a Finite Element implementation of this breakage model, we now have more rigorous access to many field quantities that have been difficult to quantify/predict using previous continuum models. For example, in this paper we combine the breakage model with an Eulerian Finite Element (FE) method to predict the evolution of gsd surrounding penetrating piles, followed by the calculation of the associated permeability reduction. We address the importance of faithfully predicting the permeability reduction due to grain crushing, as this crushing is found to be the dominant mechanism governing the permeability change of the material in pile penetration. The results are assessed against experimental counterparts to demonstrate the capabilities of our model in this particular geotechnical application.*

1 INTRODUCTION

Grain crushing is an important issue in geomechanics, which has been studied using both discrete (e.g. discrete element method (DEM)) and continuum approaches. Tremendous DEM-based research has been carried out to explore the physical behaviour of crushable media under high pressure (Lobo-Guerrero & Vallejo, 2005; Ben-Nun et al, 2010). Apparently, DEM provides a good access to micromechanics; however it is still not capable of tackling engineering problems due to requirements of extremely huge computational resources.

A practical approach to engineering issues relevant to grain crushing would be better based on continuum models that include the effect of grain sizes. Although the gsd has been commonly measured and its importance in governing the mechanical response of granular materials is now well appreciated (McDowell & Bolton, 2000; Lade, 1996; Hardin, 1985), its introduction into continuum models is still not popular. Many continuum models devoted to modelling grain crushing are still based on plasticity theory without taking into account the evolving gsd as an internal variable. Yasufuku and Hyde (1995) developed a formula to calculate the pile end-bearing capacity in crushable sand with cavity expansion theory. The results seem good in predicting the tip resistance; however, for the absence of gsd as an internal variable, this model is unable to account for the crushing condition surrounding the pile. An interesting model example relating to gsd was proposed by Indraratna and Salim (2002). They extended Ueng and Chen's approach (2000) by linking the energy consumption

due to crushing linearly with the Marsal's (1973) breakage index. However, this brought additional phenomenological parameters from curve-fitting tests, which replaced the role of the breakage index as an independent state parameter. Therefore, this model did not provide the required solution: a model dependent only on physically understood parameters, which is able by itself to predict the evolving gsd.

Einav (2007) developed a novel continuum theory which is the first constitutive model able to predict and thus include the effect of the evolving gsd on the model responses. This theory possesses a micromechanics-based link between the evolving gsd and an internal variable, called breakage *B*, of the continuum models. Statistical homogenization and micromechanics were used to link the underlying micromechanics of grains and macroscopic responses of the models. Models based on breakage theory have been assessed against experimental data of crushable granular materials (Nguyen & Einav, 2009).

In this paper, we used a continuum model based on breakage mechanics theory to explore the penetration-induced grain crushing problems, probing the evolution and distribution of the crushing zone surrounding the pile. Particular focus will be given to the crushing induced permeability reduction around the penetrating pile. In all simulation, an idealized steady ground conditions at different deep depths during the penetration were realized by the Eulerian Finite Element method.

2 FUNDAMENTAL EQUATIONS OF BREAKAGE MODEL

The stress-strain relationship in triaxial space of a linear-elasticity-based model of breakage mechanics (Einav, 2007c) can be written as:

$$p = \partial \Psi / \partial \varepsilon_v^e = (1 - \vartheta B) K \varepsilon_v^e \tag{1}$$

$$q = \partial \Psi / \partial \varepsilon_s^e = 3(1 - \vartheta B) G \varepsilon_s^e \tag{2}$$

where K and G are the bulk and shear modulii; ε_v^e and ε_s^e are the elastic volumetric and shear strains in triaxial conditions; p and q are volumetric stress and shear stress in triaxial conditions; B is the breakage internal variable on the basis of current ($g(x)$), initial ($g_0(x)$) and ultimate ($g_u(x)$) accumulative gsd (Einav, 2007a): $g(x) = g_0(x)(1-B) + g_u(x)B$; ϑ is the criticality proximity index of the gsd, that in effect weighs how far the initial gsd is from the ultimate gsd.

After some derivation it can be shown that in stress-space the yield function of this model can be expressed in terms of the breakage as:

$$y = \frac{\vartheta}{2E_c}\left(\frac{p^2}{K} + \frac{q^2}{3G}\right)\left(\frac{1-B}{1-\vartheta B}\right)^2 + \left(\frac{q}{Mp}\right)^2 - 1 \le 0 \tag{3}$$

where $M=q_f/p_f$, defines the friction coefficient at critical state with volumetric and shear stresses at failure, p_f and q_f. An example of the yielding evolutions in p-q-B space is plotted in Fig. 1. The flow rules of the model can eventually be written as:

$$\delta \varepsilon_v^p = \delta \lambda \frac{2E_B (1-B)^2 \sin^2 \omega}{pE_c} \tag{4}$$

$$\delta\varepsilon_s^p = \delta\lambda \frac{2q}{(Mp)^2} \tag{5}$$

$$\delta B = \delta\lambda \frac{2(1-B)^2 \cos^2 \omega}{E_c} \tag{6}$$

in which $\delta\lambda$ is a non-negative multiplier; ω is a parameter controlling the coupling between breakage and plastic strains; E_B is the thermodynamic energy conjugate to the breakage internal variable; E_c is the critical breakage energy (Einav, 2007b).

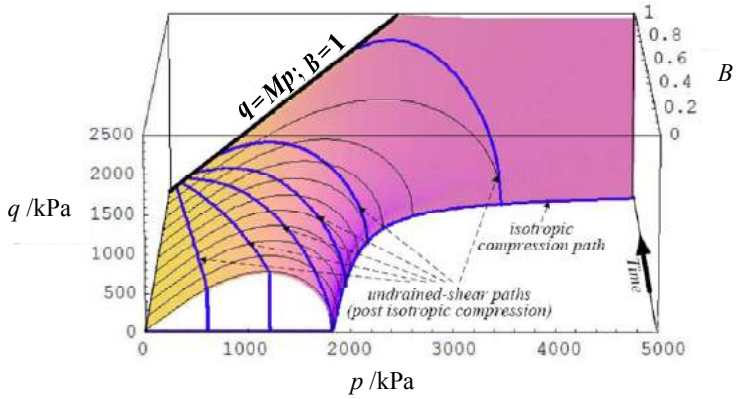

Fig. 1 An example of *p*-*q*-*B* yielding space based on linear elasticity (Einav, 2007d)

3 PERMEABILITY REDUCTION USING BREAKAGE MECHANICS

The grain crushing would cause the reduction of permeability k for the increase of particle surface, S which can be represented in terms of the harmonic mean grain size D_H: $S=6/D_H$, for spherical grains. Using the modified Kozeny-Carman equation (Nguyen & Einav, 2009), the permeability k is expressed as:

$$k = \frac{1}{c_1} \frac{n^3}{(1-n)^2} D_H^{\,2} \tag{7}$$

where c_1 is the so-called Kozeny-Carman constant (Matyka et al, 2008); n is current porosity, which is calculated from: $n = e/(1+e)$; the void ratio, e, ignoring the solid elastic volume change, is updated using $de \approx -d\varepsilon_v^p(1+e)$. The harmonic mean grain size, D_H, as a function of gsd is defined by:

$$D_H^{\,-1} = \int_{D_m}^{D_M} g(x) \frac{dx}{x} = (1-B) D_{H0}^{\,-1} + B D_{Hu}^{\,-1} \tag{8}$$

in which D_{H0} and D_{Hu} are initial and ultimate harmonic mean grain sizes, corresponding to $g_0(x)$ and $g_u(x)$ that can be practically assumed power functions in the absence of experimental data. The permeability reduction, R_k, is here defined as follows:

$$R_k = \log(k_0 / k) \tag{9}$$

where k_0 is the permeability corresponding to the initial values in Eq. (7) (i.e. with $n = n_0$ and $D_H = D_{H0}$).

4 FINITE ELEMENT MODEL BY EULERIAN METHOD

We use the above model to study the grain crushing during pile penetration into crushable media. To preserve the quality of the mesh during penetration, the Eulerian method is employed, which involves a fixed mesh through which the material flows, as seen in Fig. 2. The model parameters are mainly from Kuwajima et al (2009) and Coop et al (2004): bulk modulus, K=17,800kPa; shear modulus G=14,500kPa; ultimate friction parameter M=1.78; grading index ϑ=0.2; critical breakage energy constant E_c=9.5kPa and coupling angle ω=30^0. Other necessary parameters include: the unit weight of the sand γ =20kN/m^3; pile's radius r=0.2m; and the initial porosity n_0=0.6. The shear stress at the interface is calculated using the Coulomb friction model, with a friction coefficient μ=0.4. Note that the pile tip position is represented implicitly, through the initially specified vertical stress. Only a 4m section of the pile is described, while the analysis focuses on the steady state behavior of breakage around the pile.

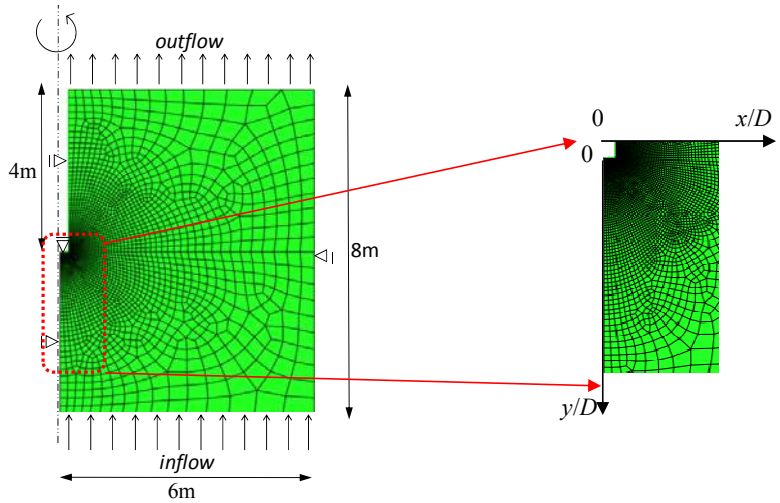

Fig. 2 Axisymmetric Eulerian FE models and boundary conditions, in which (i) the rigid pile is fixed; (ii) inflow material velocity is 0.01m/s; (iii) initial vertical and horizontal stresses are defined by nominating σ_{v0} and σ_{H0} (x/D and y/D indicate the normalized distance from the centre of pile and from the pile tip, respectively.)

5 RESULTS AND DISCUSSION

The simulated tip resistance, q_p, against penetration depths, S, normalized by pile diameter, D, is compared with an experiment performed by Kuwajima et al (2009) in Fig. 3. Close agreement is found. The contours of the breakage and permeability reduction around the pile, due to grain crushing and porosity reduction, are presented in Fig. 4, which reveals the formation of crushing zone. The most serious crushing (B≈1) apparently is found clinging to the pile, indicating an impermeable barrier (red adjacent to the pile) where the current permeability, k is 4 orders less than the original value. The trends towards steady states around the pile are illustrated in Figs. 5–6, regarding to 2 typical zones, respectively, surrounding the shaft and beneath the pile tip. We can see that the soil beneath the pile tip is easier to reach a steady state than that surrounding the pile shaft. Comparing Figs. 5a and 5b or Figs. 6a and 6b, it is noted that small amount of crushing can lead to significant permeability reduction.

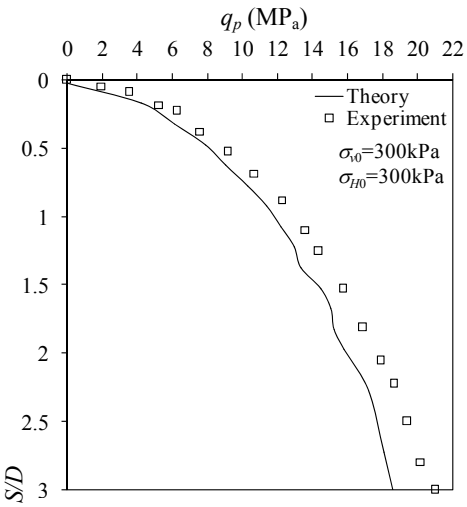

Fig. 3 Pile end bearing capacity under large deformation for Chiishibi sand (experimental data from Kuwajima et al, 2009)

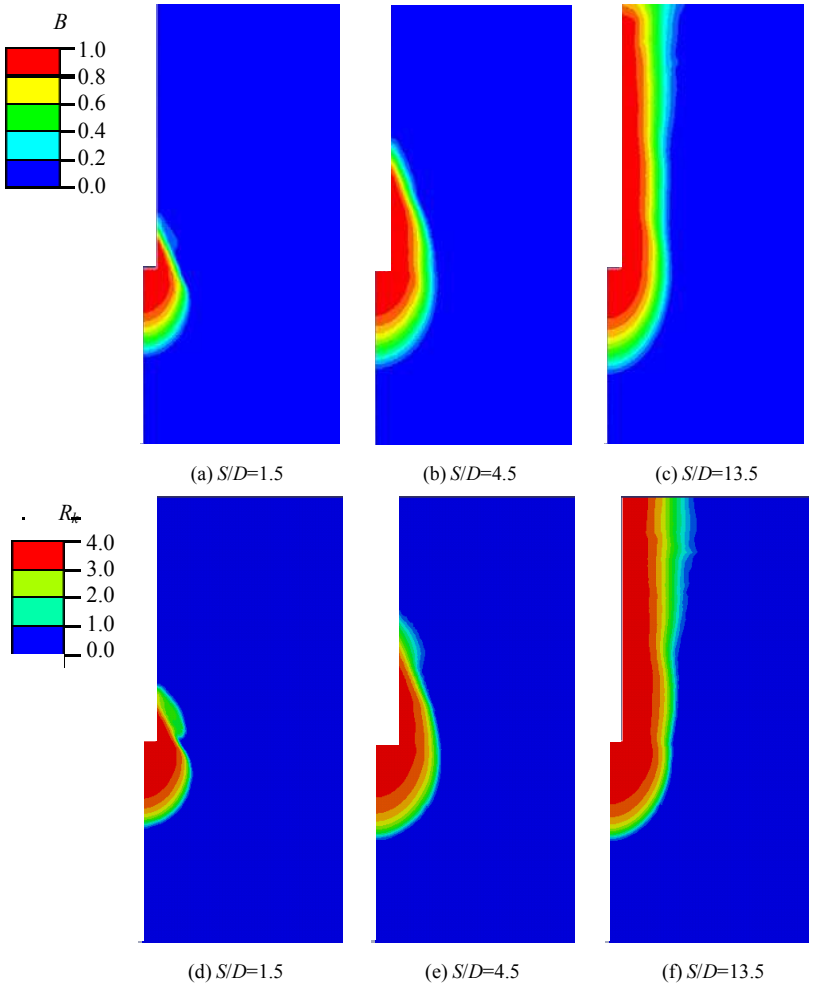

Fig. 4 Contours of evolution of breakage, B (a–c) and permeability reduction, R_k (d–f) in terms of different penetration depths

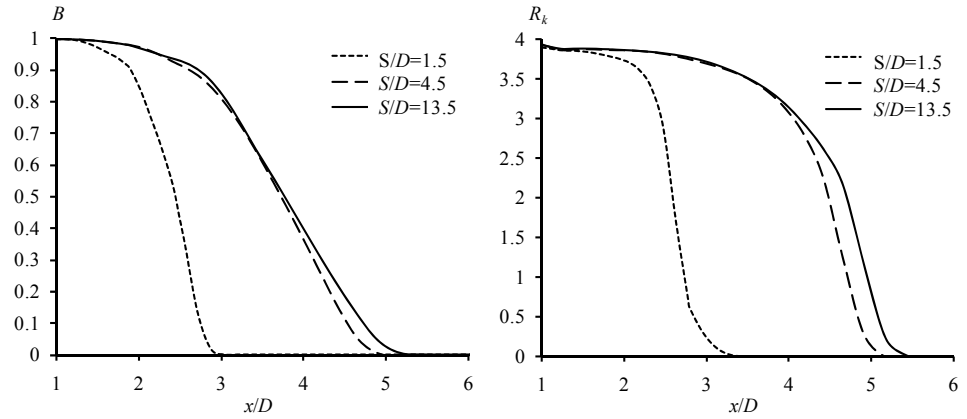

Fig. 5 Distribution of breakage and permeability reduction along the normalized radial distance from the centre of pile (see x/D in Fig. 2)

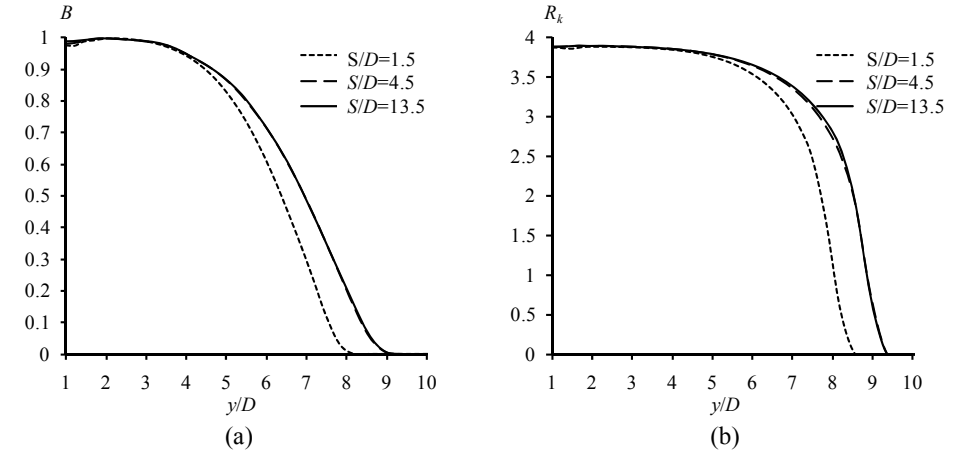

Fig. 6 Distribution of breakage and permeability reduction along the normalized distance from the pile tip (see y/D in Fig. 2)

6 CONCLUSIONS

A continuum model has been applied for the analysis of grain crushing around penetrating piles. The predicted tip resistance is largely consistent with the experimental one, showing capability of the breakage model. Intrinsic links between the gsd and the internal variable gives the model capability of tracking changes in the gsd due to grain crushing. This is a unique feature of this novel model, which could be highlighted against the many plasticity-based continuum models. Thanks to this feature, the effects of grain crushing on the permeability reduction in the vicinity of the pile can be quantified by using a modified Kozeny-Carman formula. This highlights the advantages of using our micromechanics–based constitutive model to capture grain crushing phenomena and the related physics in geotechnical applications.

ACKNOWLEDGEMENTS

The authors would like to acknowledge the Australian Research Council through the ARC *Discovery Projects* funding scheme (project number DP0986876). The third author wishes to thank the University of Sydney for support through the Postdoctoral Fellowship scheme.

REFERENCES

Ben-Nun, O., Einav, I. & Tordesillas, A. (2010), "Force attractor in confined comminution of granular materials". Phys. Rev. Lett., 104, 108001–108004.

Coop, M.R., Sorensen, K. K, Bodas-Freitas, T., & Georgoutos, G. (2004), "Particle breakage during shearing of a carbonate sand". Géotechnique, 54(3):157–163.

Einav, I. (2007a), "Breakage mechanics–Part I: Theory". Journal of the Mechanics and Physics of Solids 55(6)**,** 1274–1297.

Einav, I. (2007b), "Breakage mechanics–Part II: Modelling granular materials". Journal of the Mechanics and Physics of Solids, 55(6), 1298–1320.

Einav, I. (2007c), "Fracture propagation in brittle granular matter". Proceedings of the Royal Society A: Mathematical, Physical and Engineering Sciences, 463(2087)**,** 3021–3035.

Einav, I. (2007d), "Soil mechanics: breaking ground". Philosophical Transactions of the Royal Society A: Mathematical, Physical and Engineering Sciences, 365(1861), 2985–3002.

Hardin, B.O. (1985), "Crushing of soil particles". ASCE Journal of Geotechnical and Geoenvironmental Engineering, 111(10), 1177–1192.

Indraratna, B. & Salim, W. (2002), "Modeling of particle breakage in coarse aggregates in corportating strength and dilatancy". Geotech. Eng., 155(4), 243–252.

Kuwajima, K., Hyodo, M. & Hyde. A.F.L. (2009), "Pile bearing capacity factors and soil crushability". J. Geotech. and Geoenvir. Engng., 135(7), 901–913.

Lobo-Guerrero, S. & Vallejo, L.E. (2005), "DEM Analysis of Crushing Around Driven Piles in Granular Materials". Geotechnique, 55(8), 617–623.

Lade, P.V., Yamamuro, J.A. & Bopp, P.A. (1996), "Significance of Particle Crushing in. Granular Materials". J. of Geotech. Eng., ASCE, 122(4), 309–316.

Marsal, R.J. (1973), "Mechanical properties of rockfill". In: Hirschfield, R.C., Poulos, S.J. (Eds.), Embankment Dam Engineering. Wiley, NY, PP. 109–200.

McDowell, G.R. & Bolton, M. D. (2000), "Effect of particle size distribution on pile tip resistance in calcareous sand in the geotechnical centrifuge". Granular Matter, 2, No. 4, 179–187.

Matyka, M., Khalili, A. & Koza, Z. (2008), "Tortuosity–porosity relation in porous media flow". Physical Review E, 78: 026306-1–026306-8.

Nguyen, G.D. & Einav, I. (2009), "The energetics of cataclasis based on breakage mechanics". Pure Appl. Geophys., 166, 1–32.

Ueng, T.-S. & Chen, T.-J. (2000), "Energy aspects of particle breakage in drained shear of sands". Géotechnique, 50(1), 65–72.

Yasufuku, N. & Hyde, A.F.L. (1995), "Pile end-bearing capacity in crushable sands". Géotechnique, 45(4), 663–676.

A HYPOPLASTIC MACROELEMENT FOR SHALLOW FOUNDATIONS SUBJECT TO SIX-DIMENSIONAL LOADING PATHS

Diana Salciarini
Dipartimento di Ingegneria Civile e Ambientale, University of Perugia, Italy

Britta Bienen
Centre for Offshore Foundation System, University of Western Australia, Perth, Australia

Claudio Tamagnini
Dipartimento di Ingegneria Civile e Ambientale, University of Perugia, Italy

ABSTRACT: *In this work, the hypoplastic macroelement model for shallow foundations proposed by Salciarini & Tamagnini (2009) is extended to six–dimensional loading conditions, including torsional moments and rotations. In addition, a new hardening law for the vertical bearing capacity V_f is adopted to include the effects of accumulated displacements and rotations. As pointed out in Bienen et al. (2006), the extension to six–dimensional loading conditions is of great importance in the analysis of foundations for offshore structures. The incrementally non–linear constitutive equations of the macroelement are formulated in terms of normalized generalized forces and displacements and are constructed based on the general approach proposed by Niemunis (2002). A suitable vectorial internal variable (internal displacement) is employed to provide the model sufficient memory of past displacement history to be able to reproduce the observed behavior under cyclic loading paths such as those associated with wind or wave loading. The model performance has been evaluated by comparing the model predictions with available experimental results from a series of small–scale model tests with complex loading paths reported by Bienen et al. (2006). The model parameters have been calibrated using independent experimental data for more conventional loading conditions. As compared to similar macroelements based on the theory of kinematic hardening elastoplasticity, the proposed approach has the advantage of a much simpler mathematical structure, which allows a straightforward implementation in existing structural analysis FE codes.*

1 INTRODUCTION

Shallow foundation behaviour is often analyzed by independently considering the issues related to (1) the serviceability limit states and (2) the ultimate limit states. Recently, the need for proper design of foundations for special structures such as high–rise towers, tall bridge piers and offshore structures has led to an increased interest towards alternative approaches which consider the complete soil–structure interaction (SSI) in an integrated manner, from installation to ultimate failure. This is particularly important for structures such as offshore wind turbines or mobile offshore jack–up platforms, where the response is load path dependent and second order effects need to be taken into consideration.

Macroelements that encapsulate the footing–soil load-displacement behaviour in a single point element represent significant progress in this respect. These can be incorporated into structural analyses, enabling an efficient computational approach to SSI problems without oversimplification of the non–linear foundation behaviour (Thompson 1996; Williams et al. 1998; Cassidy 1999; Martin & Houlsby 1999; Bienen & Cassidy 2006; Bienen & Cassidy 2009). In the past 20 years, a number of macroelements have been developed (including Nova & Montrasio 1991, Gottardi et al. 1999, Martin & Houlsby 2000, Martin & Houlsby 2001, Byrne & Houlsby 2001, Houlsby & Cassidy 2002, Bienen et al. 2006, Grange et al. 2008, Grange et al. 2009), all of which are based on classical elasto-plasticity theory.

A different approach was recently followed by Salciarini & Tamagnini (2009), which developed a macroelement framed in the theory of hypoplasticity – originated in Karlsruhe (Kolymbas 1991) and Grenoble (Chambon et al. 1994). In contrast to elasto-plasticity, the hypoplastic approach features incrementally nonlinear response, without the existence of a large elastic domain. The hypoplastic macroelement model was shown to be able to predict the relevant features of the experimentally observed response of a foundation–soil system even under rather complex loading paths, including a limited number of load reversals.

In their work, Salciarini & Tamagnini (2009) considered only 5 degrees of freedom for the footing, namely vertical displacement, horizontal displacements in two orthogonal directions and rocking motions in two orthogonal vertical planes. While this can be considered appropriate under many circumstances (see, *e.g.*, Grange et al. 2010), the extension of the macroelement formulation to six–dimensional loading conditions – including the torsional rotation and moment – can be necessary in the analysis of offshore structures such as wind turbines or mobile jack–up platforms.

In this work, a new hypoplastic macroelement model is introduced which can account for general loading conditions, including out-of-plane and torsional components. The model is formulated in the 6–dimensional loading space and incorporates the major features of the elasto-plastic formulation of Bienen et al. (2006), such as the failure locus, the plastic potential and the hardening law for the bearing capacity failure under vertical centered loads. In addition, the absence of a large elastic domain in the loading space, the incrementally non–linear character of the material response and the incorporation of a suitable vectorial internal variable to describe the effects of past displacement history make the proposed formulation suitable to reproduce the observed behavior under cyclic loading paths such as those associated with wind or wave loading. A description of the relevant constitutive equations of the macroelement is given in Sect. 2.

The model performance is evaluated through comparison with experimental data from an extensive series of model tests performed at Oxford University on a small–scale shallow footing on sand under complex loading paths (Bienen et al. 2006). Some details of the the experimental equipment and testing program are provided in Sect. 3. In particular, two separate subsets of model tests performed at $1g$ have been used to calibrate and evaluate the hypoplastic macroelement. Results of horizontal, rocking and torsional swipe tests served for calibration purposes (Sect. 4), while the data of more complex experiments involving two different loading phases have been considered in the model evaluation of model performance (Sect. 5). Some concluding remarks are finally provided in Sect. 6.

2 MODEL DESCRIPTION

2.1 General principles

In the macroelement approach, the incremental response of a rate–independent soil–foundation system is provided by a global constitutive equation of the form:

$$\dot{\boldsymbol{T}} = \boldsymbol{\mathcal{K}}_t(\boldsymbol{T}, \boldsymbol{Q}, \boldsymbol{\eta})\, \dot{\boldsymbol{U}} \tag{1}$$

in which the generalized force vector rate:

$$\dot{\boldsymbol{T}} := \left\{ \dot{V}\,,\, \dot{H}_x\,,\, \dot{M}_y/\ell\,,\, \dot{H}_y\,,\, \dot{M}_x/\ell,\, \dot{Q}/\ell \right\}^T \tag{2}$$

is expressed as a function of the generalized velocity vector:

$$\dot{\boldsymbol{U}} := \left\{ \dot{U}_z\,,\, \dot{U}_x\,,\, \dot{\Theta}_y\ell\,,\, \dot{U}_y\,,\, \dot{\Theta}_x\ell,\, \dot{\Omega}\ell \right\}^T \tag{3}$$

via a tangent stiffness matrix $\boldsymbol{\mathcal{K}}_t$, depending, in general, on the current loading state $\boldsymbol{T}$, on the previous loading history, accounted for by the internal variables stored in vector $\boldsymbol{Q}$, and on the current loading direction $\boldsymbol{\eta} := \dot{\boldsymbol{U}}/\|\dot{\boldsymbol{U}}\|$. In eqs. (2) and (3), ℓ represents a suitable length scale which, for a circular foundation, can be set equal to the foundation diameter d. The meaning of the components of the vectors $\boldsymbol{U}$ and $\boldsymbol{T}$ is shown in Fig. 1.

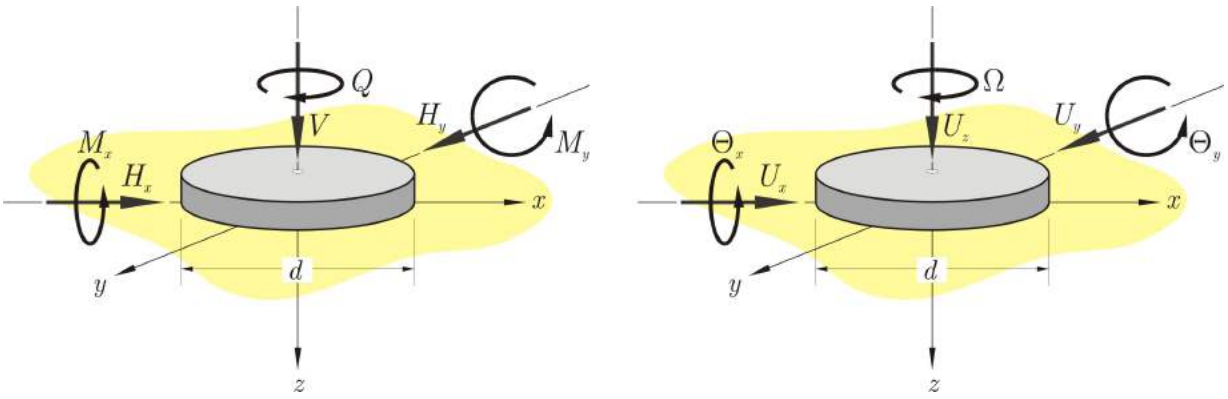

Fig. 1. Reference frame and notation adopted for generalized forces and displacements.

According to Salciarini & Tamagnini (2009), in the framework of the theory of hypoplasticity with internal variables, the set $\boldsymbol{Q} = \{\boldsymbol{q}, \boldsymbol{\delta}\}$ contains a vectorial internal variable $\boldsymbol{\delta}$ (the internal displacement) which records the previous displacement history and plays the role of the back–stress in the kinematic hardening elastoplastic models (Grange et al. 2009). The tangent stiffness matrix then assumes the following general format:

$$\boldsymbol{\mathcal{K}}_t\left(\boldsymbol{T}, \boldsymbol{q}, \boldsymbol{\delta}\right) := A_1(\rho)\boldsymbol{\mathcal{L}}(\boldsymbol{T}, \boldsymbol{q}) + \boldsymbol{\mathcal{N}}\left(\boldsymbol{T}, \boldsymbol{q}, \boldsymbol{\delta}\right) \tag{4}$$

where:

$$\boldsymbol{\mathcal{N}}\left(\boldsymbol{T}, \boldsymbol{q}, \boldsymbol{\delta}\right) := \begin{cases} A_2(\rho)\boldsymbol{\mathcal{L}}(\boldsymbol{T}, \boldsymbol{q})\boldsymbol{\eta}_\delta\boldsymbol{\eta}_\delta^T + A_3(\rho)Y(\boldsymbol{T}, \boldsymbol{q})\boldsymbol{m}(\boldsymbol{T}, \boldsymbol{q})\boldsymbol{\eta}_\delta^T & (\boldsymbol{\eta}_\delta \cdot \boldsymbol{\eta} > 0) \\ A_4(\rho)\boldsymbol{\mathcal{L}}(\boldsymbol{T}, \boldsymbol{q})\boldsymbol{\eta}_\delta\boldsymbol{\eta}_\delta^T & (\boldsymbol{\eta}_\delta \cdot \boldsymbol{\eta} \leq 0) \end{cases} \tag{5}$$

In eqs. (4) and (5), the matrix $\boldsymbol{\mathcal{L}}$ is related to the stiffness matrix upon full displacement reversal (pseudo–elastic stiffness); the unit vector $\boldsymbol{m}$ provides the velocity direction $\boldsymbol{\eta}$ under collapse conditions; the scalar function Y is a dimensionless measure of the distance of the current loading state from the failure locus (FL); ρ denotes a scaled norm of the internal displacement vector $\boldsymbol{\delta}$, and the unit vector $\boldsymbol{\eta}_\delta := \boldsymbol{\delta}/\|\boldsymbol{\delta}\|$ is the internal displacement direction. Any specific hypoplastic macroelement model is constructed by providing suitable expressions for the functions $\boldsymbol{\mathcal{L}}$, $\boldsymbol{m}$, Y and A_k ($k = 1, \ldots, 4$).

2.2 Constitutive equations in dimensionless form

In the development of a hypoplastic version of the 6–dimensional model proposed by Bienen et al. (2006) it proves useful to recast the constitutive equation (1) in the following dimensionless form:

$$\dot{\boldsymbol{t}} = \boldsymbol{\mathcal{D}}_t\,(\boldsymbol{t}, \boldsymbol{q}, \boldsymbol{d})\,\dot{\boldsymbol{u}} \tag{6}$$

where:

$$\boldsymbol{t} := \frac{1}{V_{f0}}\boldsymbol{T} \qquad \boldsymbol{d} := \frac{1}{d}\boldsymbol{\delta} \qquad \boldsymbol{u} := \frac{1}{d}\boldsymbol{U} \qquad \boldsymbol{\mathcal{D}}_t = \frac{d}{V_{f0}}\boldsymbol{\mathcal{K}}_t \tag{7}$$

and V_{f0} is a force scaling factor, chosen in this case as a reference value for the bearing capacity of the foundation under centered vertical loading conditions.

2.3 Scalar functions ρ and A_k

The scaled norm ρ of the internal displacement $\boldsymbol{\delta}$ is given by the following expression:

$$\rho = \frac{1}{R}\sqrt{\boldsymbol{d}^T\boldsymbol{\mathcal{W}}\boldsymbol{d}} \qquad \boldsymbol{\mathcal{W}} = \mathrm{diag}\left\{1\ ,\ w_h\ ,\ w_m\ ,\ w_h\ ,\ w_m\ ,\ w_q\right\} \tag{8}$$

where R is a model constant defining the size of the *pseudo–elastic* domain in the normalized displacement space, and the weighting coefficients w_h, w_m and w_q are given by:

$$w_h = \frac{16}{h_0^2} \qquad w_m = \frac{16}{m_0^2} \qquad w_q = \frac{16}{q_0^2} \tag{9}$$

in which h_0, m_0 and q_0 are three model constants controlling the shape of the failure locus of the foundation, see Sect. 2.5. As in Salciarini & Tamagnini (2009), the role of the weighting matrix $\boldsymbol{\mathcal{W}}$ is to transform the pseudo–elastic domain taking into account the actual shape of the FL.

Following the original proposal of Niemunis & Herle (1997), the scalar functions $A_k(\rho)$, with $k = 1, \ldots, 4$ are defined as follows:

$$A_1 = \rho^\chi m_T + (1 - \rho^\chi) m_R\ , \quad A_2 = \rho^\chi (1 - m_T)\ , \quad A_3 = \rho^\chi\ , \quad A_4 = \rho^\chi (m_R - m_T) \tag{10}$$

For proportional loading paths of sufficient length (Swept Out of Memory, or SOM state), $\rho \to 1$ and eqs. (10) yield: $A_1 = m_T$, $A_2 = 1 - m_T$, $A_3 = 1$ and $A_4 = m_R - m_T$. When $\rho = 0$, $A_1 = m_R$ and $A_2 = A_3 = A_4 = 0$.

2.4 Stiffness matrix $\boldsymbol{\mathcal{L}}$

The role of the matrix $\boldsymbol{\mathcal{L}}$ appearing in (4) can be clarified considering that, under a complete loading direction reversal from a SOM state ($\boldsymbol{\eta} = -\boldsymbol{\eta}_\delta$ and $\rho = 1$), eqs. (4),(5)and (10) yield:

$$\dot{\boldsymbol{T}} = m_R \boldsymbol{\mathcal{L}}\,\dot{\boldsymbol{U}} \tag{11}$$

Since under such conditions the incremental response of the foundation can be considered to be elastic, the matrix $m_R\boldsymbol{\mathcal{L}}$ can be identified with the elastic tangent stiffness $\boldsymbol{\mathcal{K}}^e$ of the circular soil–foundation system, an expression for which is provided, *e.g.*, by Bienen et al. (2006).

2.5 *Loading function Y*

The function Y controls the degree of nonlinearity of the system response and, as such, it increases monotonically with decreasing distance from the FL. Adopting the expression provided by Martin (1994)for the FL in the 6–dimensional loading space, we have:

$$f(\boldsymbol{t}, v_f) = \left(\frac{t_2}{h_0 v_f}\right)^2 + \left(\frac{t_3}{m_0 v_f}\right)^2 + \left(\frac{t_4}{h_0 v_f}\right)^2 + \left(\frac{t_5}{m_0 v_f}\right)^2 + \left(\frac{t_6}{q_0 v_f}\right)^2 - 2a\left(\frac{t_4 t_5 - t_2 t_3}{h_0 m_0 v_f^2}\right) - \beta_{12}\left(\frac{t_1}{v_f}\right)^{2\beta_1}\left(1 - \frac{t_1}{v_f}\right)^{2\beta_2} = 0 \quad (12)$$

where $v_f = V_f / V_{f0}$ is a normalized measure of the failure load under pure vertical compression, and h_0, m_0, q_0, β_1, β_2 and β_{12} are model constants (Martin 1994; Bienen et al. 2006).

For any (stable) loading state $\boldsymbol{t}$ strictly inside the FL, it is possible to define an *image* state $\bar{\boldsymbol{t}} = \xi \boldsymbol{t}$ on the FL, such that:

$$f(\bar{\boldsymbol{t}}, v_f) = f(\xi \boldsymbol{t}, v_f) = 0 \qquad (\xi \geq 1) \quad (13)$$

The scalar ξ, which can be easily determined by solving eq. (13) for given $\boldsymbol{t}$ and v_f, provides a suitable measure of the distance of the current state from the FL, so that the loading function Y can be defined as:

$$Y(\boldsymbol{t}, v_f) = \left\{\frac{1}{\xi(\boldsymbol{t}, v_f)}\right\}^{\kappa} \quad (14)$$

where κ is a model constant.

2.6 *Flow direction $\boldsymbol{m}$*

As in Salciarini & Tamagnini (2009), the flow direction vector given by:

$$\boldsymbol{m} = \frac{1}{\|\nabla g\|} \nabla g \quad (15)$$

where the potential function g is assumed identical to the plastic potential adopted by Bienen et al. (2006):

$$g(\boldsymbol{t}) = \left(\frac{t_2}{\alpha_h h_0 v_g}\right)^2 + \left(\frac{t_3}{\alpha_m m_0 v_g}\right)^2 + \left(\frac{t_4}{\alpha_h h_0 v_g}\right)^2 + \left(\frac{t_5}{\alpha_m m_0 v_g}\right)^2 + \left(\frac{t_6}{\alpha_q q_0 v_g}\right)^2 - 2a\left(\frac{t_4 t_5 - t_2 t_3}{\alpha_h h_0 \alpha_m m_0 v_g^2}\right) - \beta_{34}\left(\frac{t_1}{v_g}\right)^{2\beta_3}\left(1 - \frac{t_1}{v_g}\right)^{2\beta_4} = 0 \quad (16)$$

In eq. (16), α_h, α_m, α_q, β_3, β_4 and β_{34} are model constants, and $v_g(\boldsymbol{t})$ a dummy parameter to be determined from the condition $g(\boldsymbol{t}, v_g) = 0$.

2.7 *Evolution equations for the internal variables*

As shown, *e.g.*, by Bienen et al. (2006), the size of the FL, V_f, can change due to accumulated irreversible displacements. Starting from the evolution equation suggested by Bienen et al. (2006), we adopt the following evolution equation for the normalized size of the FL, v_f:

$$\dot{v}_f = \hat{k}_1 \left(\frac{1 + \zeta/\hat{w}_1}{1 + \zeta/\hat{w}_2}\right)\left\{1 + \frac{1}{(1 + \zeta/\hat{w}_1)}\,\frac{\zeta}{\hat{w}_1} - \frac{1}{(1 + \zeta/\hat{w}_2)}\,\frac{\zeta}{\hat{w}_2}\right\}\dot{\zeta} \quad (17)$$

where ζ is a normalized measure of the accumulated displacement, the rate of which is given by:

$$\dot{\zeta} = \dot{u}_1 + c_1\sqrt{\dot{u}_2^2 + \dot{u}_4^2} + c_2\sqrt{\dot{u}_3^2 + \dot{u}_5^2} + c_3\,|\dot{u}_6| \tag{18}$$

and $\hat{k}_1$, $\hat{w}_1$, $\hat{w}_2$, c_1, c_2 and c_3 are model constants controlling the influence of the different components of the generalized displacement on the internal variable v_f. It is worth noting that total displacement rates appear in the definition (18), as in hypoplasticity no distinction is made between reversible and irreversible displacement rates, and most of the accumulated displacements are irreversible in nature, due to the incrementally non–linear character of the constitutive equation.

As for the internal displacement, the following evolution law is adopted, as in Salciarini & Tamagnini (2009):

$$\dot{\boldsymbol{d}} = \begin{cases} \left(\boldsymbol{\mathcal{I}} - \rho^{\beta_r}\boldsymbol{\eta}_\delta\boldsymbol{\eta}_\delta^T\right)\dot{\boldsymbol{u}} & (\boldsymbol{\eta}_\delta \cdot \boldsymbol{\eta} > 0) \\ \dot{\boldsymbol{u}} & (\boldsymbol{\eta}_\delta \cdot \boldsymbol{\eta} \leq 0) \end{cases} \tag{19}$$

in which β_r is a model constant controlling the rate at which $\dot{\boldsymbol{d}}$ decreases with increasing ρ.

3 EXPERIMENTAL PROGRAM

The experiments were performed at Oxford University using a unique testing apparatus with individual control of all six displacement degrees of freedom (Byrne & Houlsby 2005, Fig. 2). All experiments considered in this study are presented in Bienen et al. (2006) and were performed on dry yellow Leighton Buzzard silica sand, which was prepared at a relative density D_r of 5%. A rough flat circular footing of 150 mm diameter was subject to a variety of load paths, with the experimental programme designed to provide information about the combined load capacity as well as the flow direction at shallow embedment depths.

The former was investigated through a series of displacement–controlled "swipe" tests. In this type of experiment, the footing is first penetrated into the soil. In a subsequent step, the vertical displacement is held constant while a displacement or rotation is imposed along one of the remaining degrees of freedom. The resulting load path is thought to closely trace the combined load capacity corresponding to the footing embedment. Proportional displacement tests were performed to gather data regarding the flow direction. In these tests, a combination of displacement components in two or more degrees of freedom was applied to the footing at a constant ratio. These types of tests have been widely used to investigate foundation response, both experimentally (Tan 1990; Gottardi et al. 1999; Martin & Houlsby 2000; Byrne & Houlsby 2001) and numerically (Gourvenec & Randolph 2003; Yun & Bransby 2007; Zhang et al. 2010).

4 MODEL CALIBRATION

The details of the calibration tests are provided in Tab. 1. Before the swipe phase, the model footing was penetrated into the sand to an embedment depth U_z, which corresponds to the initial vertical bearing capacity V_{f0} of the footing measured in the tests, except for test BB32, in which the shape of the loading path in the Q:V plane suggests that the soil could have been slightly preconsolidated before the torsional swipe phase. To account for this effect, the value of V_{f0} has been increased by 10% with respect to the initial vertical load V_0.

In order to simplify the calibration process, the constants controlling the quasi–elastic stiffness of the system upon full load reversal ($\boldsymbol{\mathcal{K}}^e$), and the shape of the FL (h_0, m_0, q_0, a, β_1 and

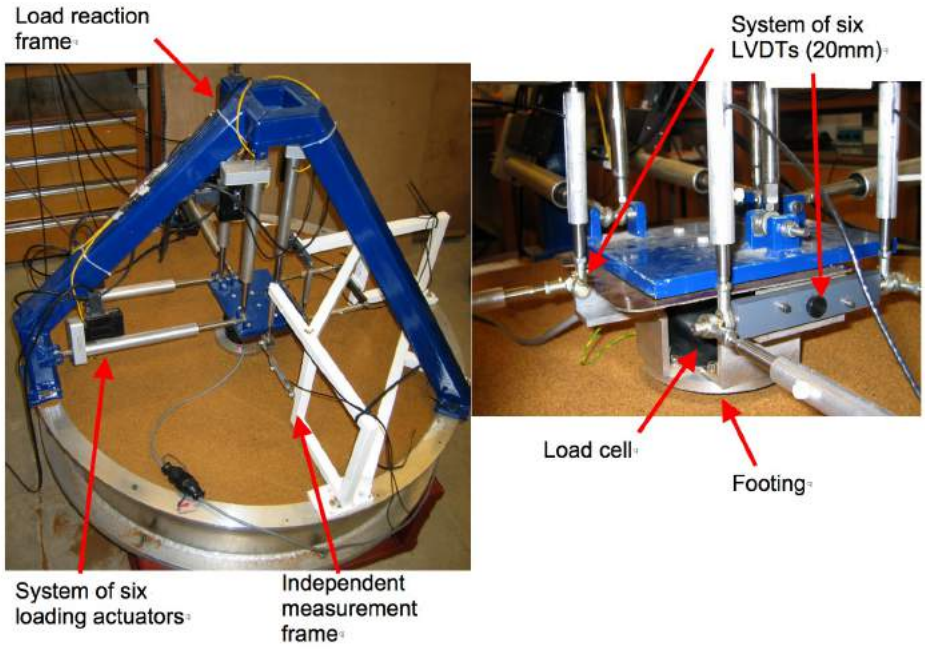

Fig. 2. Experimental set–up for small scale footing tests: a) general arrangement; b) close–up of footing; c) details of the 6 degree of freedom load cell (after Byrne & Houlsby 2005).

Table 1. Calibration test details.

Test number in Bienen et al. (2006)	Test type	V_0 (N)	V_{f0} (N)	ΔU_x, $\Delta \Theta_y d$ or $\Delta \Omega d$ (mm)
BB16	Horizontal swipe	568.5	568.5	1.90
BB10	Rocking swipe	496.6	496.6	2.20
BB32	Torsional swipe	603.9	667.8	2.40

β_2) have been taken – with only minor changes – from Bienen et al. (2006), while the constants controlling the stiffness at small displacement increments and the effects of the recent loading history (m_R, m_T, R, β_r and χ) have been assumed as in Grange et al. (2010). As for the constants appearing in the evolution equation for v_f (k_1, w_1, w_2, c_1, c_2, c_3) they have been estimated starting from the values provided by Bienen et al. (2006); in any case, their influence on the results is relatively limited, as the total displacement accumulated during the swipe phases is small, and v_f changes only very slightly during the loading process.

In the calibration process, the attention has thus been focused on the parameters controlling the flow direction vector $\boldsymbol{m}$ (α_h, α_m, α_q β_3, β_4) and on the exponent κ of the loading function Y. The full set of model constants adopted in all the numerical simulations is given in Tab. 2.

The comparison between the observed and predicted responses for calibration tests BB16 and BB32 is given in Figs. 3 and 4. Figs. 3a,b show the horizontal load *vs.* horizontal displacement curves and the loading path in the H_x:V plane for the horizontal swipe test BB16. Figs. 4c,d show the torsional moment *vs.* axial rotation curves and the loading path in the Q:V plane for the torsional swipe test BB32.

In both the tests considered, the vertical load decreases during the swipe phase, at constant U_z, due to the tendency of the footing to accumulate irreversible vertical displacements. A very

Table 2. Model constants adopted in the numerical simulations.

k_v (–)	k_h (–)	k_m (–)	k_q (–)	k_c (–)	G (MPa)	h_0 (–)	m_0 (–)	q_0 (–)	a (–)
2.904	2.901	0.548	0.100	-0.208	12.7	0.122	0.075	0.026	-0.112
β_1 (–)	β_2 (–)	α_h (–)	α_m (–)	α_q (–)	β_3 (kPa)	β_4 (–)	k_1 (–)	w_1 (mm)	w_2 (mm)
0.76	0.76	1.50	1.60	2.30	0.25	0.25	10.0	20.5	8.0
c_1 (–)	c_2 (–)	c_3 (–)	κ (–)	m_R (–)	m_T (kPa)	R (mm)	β_r (–)	χ (–)	
1.07	0.62	1.09	14.00	1.10	1.05	0.001	1.00	1.50	

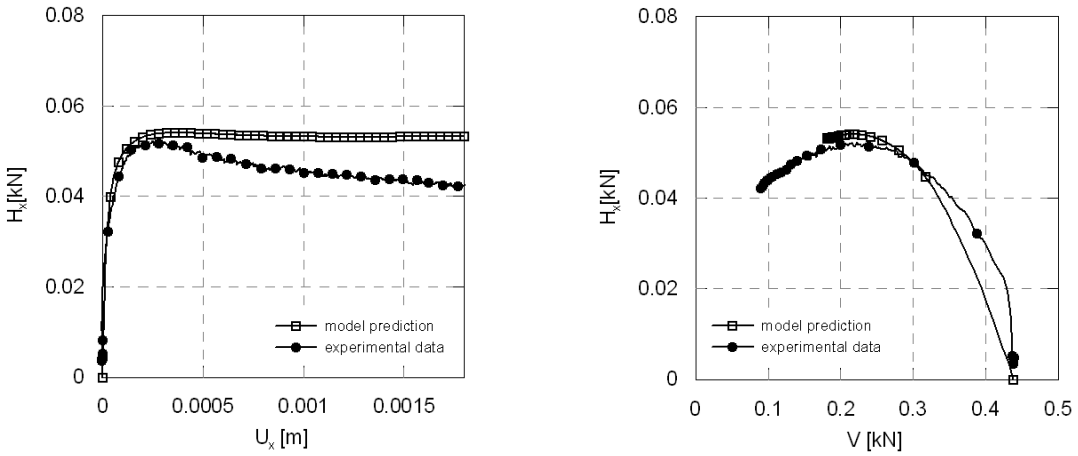

(a) (b)

Fig. 3. Results of the model calibration for tests BB16

small displacement/rotation is required to mobilise the peak bearing capacity of the footing. The comparison shows that the model is capable to capture correctly the coupling between the vertical load and horizontal or torsional loads under fixed vertical displacements, both from a qualitative and a quantitative point of view.

5 SIMULATION OF COMPLEX LOADING PATHS

More complex load paths, with two swipe loading phases of different type have been used to assess the predictive capabilities of the hypoplastic macroelement model. The details of the evaluation tests are given in Tab. 3.

In test BB16 an initial horizontal swipe loading phase along the x direction ($\dot{U}_x > 0$) is followed by a second horizontal swipe loading phase along the y direction ($\dot{U}_y > 0$). During the second swipe phase, all the other displacement components should have been kept constant. However, a small horizontal displacement U_x, of the order of 10% of the imposed horizontal displacement U_y has been recorded by the displacement transducer. This additional small displacement in the x direction has also been taken into account in the simulation.

In test BB27 an initial horizontal swipe loading phase along the x direction ($\dot{U}_x > 0$) is followed by a torsional swipe loading phase ($\dot{\Omega} d > 0$). Again, a small horizontal displacement

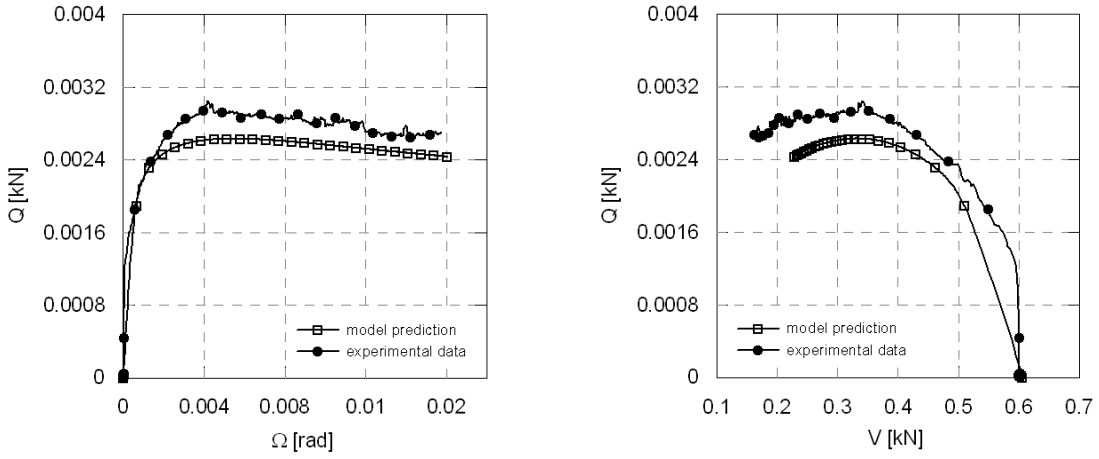

Fig. 4. Results of the model calibration for tests BB32

Table 3. Evaluation test details.

Test number in Bienen et al. (2006)	Test type	V_0 (N)	V_{f0} (N)
BB19	H_x–H_y swipe	753.3	753.3
BB27	H_x–Q swipe	524.0	524.0

U_x has been recorded by the displacement transducer during the second swipe stage, but it has not been taken into account in the simulation.

The results of the complex tests BB19 and BB27 are shown in Figs. 5 and 6, in terms of load–displacement curves and loading paths, together with the corresponding model predictions. In both tests, the general response of the footing is similar to those observed in the single swipe phase tests used for calibration. In particular, a steady decrease in the vertical load V is observed, due to the coupling existing between the vertical degree of freedom and the mobilized one. The change in displacement direction during the swipe stage (*i.e.*, from U_x to Ωd) gives rise to a change in the loading path, which, for sufficiently large displacements tends to align to the imposed displacement direction.

The prediction of the hypoplastic macroelement for test BB19, shown in black in Fig. 5, captures reasonably well the observed response of the footing both in terms of load–displacement curves and loading paths. The model significantly overestimates the stiffness of the footing and the peak horizontal load during the U_x swipe phase and the transition between the two swipe phases is too fast, as in the test, much larger displacements along the y direction are required for H_x to approach zero. However, it has to be noted that the observed footing response during this loading phase is quite close, in terms of peak load and peak displacement, to the one obtained in calibration test BB16, in spite of the much larger initial vertical load (and, hence, size of the failure locus). The model is therefore not capable of obtaining accurate predictions for both tests unless the shape of the FL is changed with increasing v_f.

The model prediction for test BB27 is also close to the observed response, and captures reasonably well the main features of the footing behavior, such as the coupling between the vertical, horizontal and torsional degrees of freedom. Again, the prediction of the transition between the

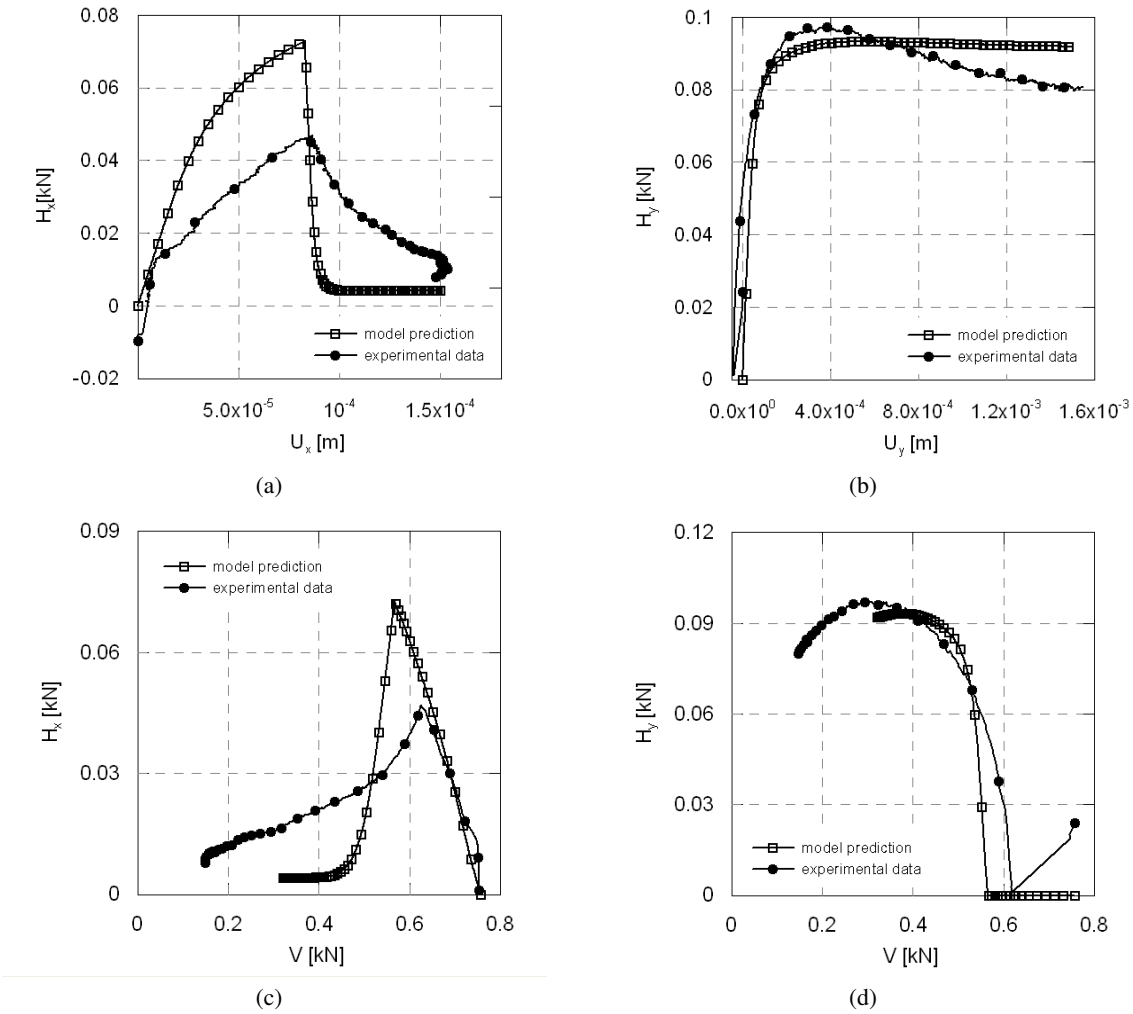

Fig. 5. Results of the simulation of the complex load path BB19.

horizontal and torsional swipe phases is correct from a qualitative point of view but tends to be too fast with respect to the actual measurements.

6 CONCLUDING REMARKS

The predictive capabilities of the hypoplastic macroelement model proposed in this work have been evaluated by comparing its predictions with experimental results obtained in a number of $1g$ small–scale model tests, specifically designed to investigate features such as the geometry of the failure locus and the flow direction under general loading conditions.

The comparison between model predictions and experimental observations under complex loading paths indicates that the model is capable to capture – both from a qualitative and a quantitative point of view – the main features of the observed response, under both monotonic loading paths and loading paths with sharp bends.

In this respect, the model can be considered equivalent to the elastoplastic macroelement proposed by Bienen et al. (2006). The main differences with the elastoplastic formulation can be found in:

i) the absence of a large elastic domain in the loading space;
ii) the incrementally non–linear character of the constitutive equations;

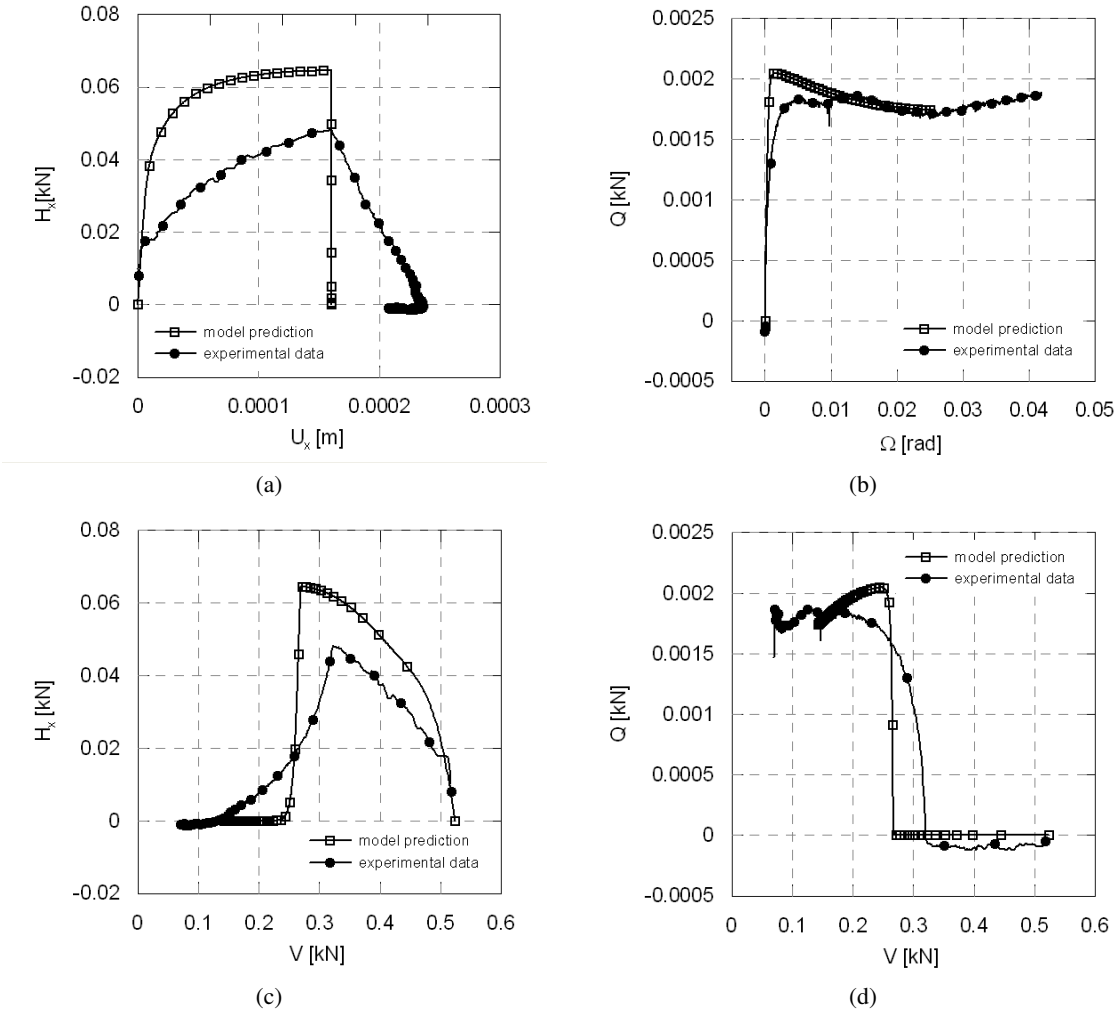

Fig. 6. Results of the simulation of the complex load path BB27.

iii) the incorporation of a suitable vectorial internal variable (the internal displacement $\boldsymbol{\delta}$), in addition to the scalar V_f, to describe the effects of recent displacement history.

In addition, the proposed approach has the advantage of a simple mathematical structure of the constitutive equations, which allows a straightforward implementation in existing structural analysis FE codes.

Further research is currently ongoing for the assessment of the model performance for footings tested at stress levels similar to offshore field installations (Bienen et al. 2007), and including load paths relevant to these particular structures (Bienen et al. 2009) rather than those aimed at macroelement development. The features of the hypoplastic model are expected to enable realistic prediction of the behavior of shallow footings under cyclic loading paths, such as those associated with wind and wave actions.

ACKNOWLEDGEMENTS

The work described here forms part of the activities of the Centre for Offshore Foundation systems (COFS) and the Australian Research Council (ARC) Centre of Excellence in Geotechnical Science and Engineering. The second author acknowledges the support of the ARC through her Australian Postdoctoral Fellowships (DP110101603).

REFERENCES

Bienen, B., Byrne, B. W., Houlsby, G. T., & Cassidy, M. J. (2006). Investigating six–degree–of–freedom loading of shallow foundations on sand. *Géotechnique 56*, 367–379.

Bienen, B. & Cassidy, M. (2006). Advances in the three-dimensional fluid-structure-soil interaction analysis of offshore jack-up structures. *Marine Structures 19*, 110–140.

Bienen, B. & Cassidy, M. (2009). Three–dimensional numerical analysis of centrifuge experiments on a model jack-up drilling rig on sand. *Canad. Geotech. Journal 46*, 208–224.

Bienen, B., Cassidy, M. J., & Gaudin, C. (2009). Physical modelling of the push-over capacity of a jack-up structure on sand in a geotechnical centrifuge. *Canad. Geotech. Journal 46*(2), 190–207.

Bienen, B., Gaudin, C., & Cassidy, M. J. (2007). Centrifuge tests of shallow footing behaviour on sand under combined vertical-torsional loading. *Int. J. Phys. Modelling in Geotechnics 7*, 1–21.

Byrne, B. W. & Houlsby, G. T. (2001). Observations of footing behaviour on loose carbonate sands. *Géotechnique 51*, 463–466.

Byrne, B. W. & Houlsby, G. T. (2005). Investigating 6 degree-of-freedom loading on shallow foundations. In S. Gourvenec & M. J. Cassidy (Eds.), *Proc. Int. Symposium Frontiers in Offshore Geotechnics (ISFOG)*, Perth, Australia, pp. 477–482. Taylor & Francis.

Cassidy, M. J. (1999). *Non–Linear analysis of jack-up structures subjected to random waves*. Ph. D. thesis, University of Oxford.

Chambon, R., Desrues, J., Hammad, W., & R., C. (1994). CLoE, a new rate–type constitutive model for geomaterials. theoretical basis and implementation. *Int. J. Num. Anal. Meth. Geomech. 18*, 253–278.

Gottardi, G., Houlsby, G. T., & Butterfield, R. (1999). The plastic response of circular footings on sand under general planar loading. *Géotechnique 49*, 453–470.

Gourvenec, S. & Randolph, M. (2003). Effect of strength non-homogeneity on the shape of failure envelopes for combined loading of strip and circular foundations on clay. *Géotechnique 53*, 575–586.

Grange, S., Kotronis, P., & Mazars, J. (2008). A macro–element for a circular foundation to simulate 3d soil–structure interaction. *Int. J. Num. Anal. Meth. Geomech. 32*, 1205–1227.

Grange, S., Kotronis, P., & Mazars, J. (2009). A macro–element to simulate 3d soil–structure interaction considering plasticity and uplift. *Int. Journal of Solids and Structures 46*, 3651–3663.

Grange, S., Salciarini, D., Kotronis, P., & Tamagnini, C. (2010). A comparison of different approaches for the modelling of shallow foundations in seismic soil-structure interaction problems. In T. Benz & S. Nordal (Eds.), *Numerical Methods in Geotechnical Engineering NUMGE 2010*. Trondheim, June 2010.

Houlsby, G. T. & Cassidy, M. J. (2002). A plasticity model for the behaviour of footings on sand under combined loading. *Géotechnique 52*, 117–129.

Kolymbas, D. (1991). An outline of hypoplasticity. *Archive of Applied Mechanics 61*, 143–151.

Martin, C. & Houlsby, G. (1999). Jackup units on clay: Structural analysis with realistic modelling of spudcan behaviour. In *Offshore Technology Conference (OTC) Houston, Texas, OTC 10996*.

Martin, C. M. (1994). *Physical and numerical modelling of offshore foundations under combined loads*. Ph. D. thesis, University of Oxford.

Martin, C. M. & Houlsby, G. T. (2000). Combined loading of spudcan foundations on clay: laboratory tests. *Géotechnique 50*, 325–338.

Martin, C. M. & Houlsby, G. T. (2001). Combined loading of spudcan foundations on clay: numerical modelling. *Géotechnique 51*, 687–700.

Niemunis, A. (2002). *Extended Hypoplastic Models for Soils*. Habilitation Thesis, Bochum University.

Niemunis, A. & Herle, I. (1997). Hypoplastic model for cohesionless soils with elastic strain range. *Mech. Cohesive–Frictional Materials 2*, 279–299.

Nova, R. & Montrasio, L. (1991). Settlements of shallow foundations on sand. *Géotechnique 41*, 243–256.

Salciarini, D. & Tamagnini, C. (2009). A hypoplastic macroelement model for shallow foundations under monotonic and cyclic loads. *Acta Geotechnica 4*(3), 163–176.

Tan, F. S. C. (1990). *Centrifuge and numerical modelling of conical footings on sand*. Ph. D. thesis, University of Cambridge.

Thompson, R. S. G. (1996). *Development of non-linear numerical models appropriate for the analysis of jackup units*. Ph. D. thesis, University of Oxford.

Williams, M. S., Thompson, R. S. G., & Houlsby, G. T. (1998). Non–linear dynamic analysis of offshore jack-up units. *Computers and Structures 69*, 171–180.

Yun, G. & Bransby, M. F. (2007). The horizontal-moment capacity of embedded foundations in undrained soil. *Canad. Geotech. Journal 44*(4), 409–424.

Zhang, Y., Bienen, B., Cassidy, M. J., & Gourvenec, S. (2010). Numerical study of the undrained bearing capacity of deeply embedded foundations under combined loading. In S. Gourvenec & D. White (Eds.), *Proc. 2nd Int. Symposium Frontiers in Offshore Geotechnics (ISFOG)*, Perth, Australia, pp. 691–696. CRC Press.

SHEAR BEHAVIOUR OF EXPANSION ANCHORS

M. M. El Sharnouby
Department of Civil and Environmental Engineering, The University of Western Ontario, London, ON, Canada

M. H. El Naggar
Department of Civil and Environmental Engineering, The University of Western Ontario, London, ON, Canada

ABSTRACT

The upgraded seismic loading proposed in the revised national building code (NBCC 2005) postulates an increased seismic hazard in Canada. Existing structures were designed and constructed prior to these new design guidelines and are still susceptible to earthquake damage; these structures have to adhere to the new seismic loading provisions. The helical pile is a foundation system that is used to support new residential and commercial buildings. It also represents an attractive retrofitting tool to upgrade the seismic resistance of existing foundations. This study is aimed at assessing the lateral performance of the specialized connectors, connecting the pile shaft to the concrete foundation. The helical pile connectors are attached to existing foundations using mechanical expansion anchors. A non-linear finite element analysis was conducted to determine the failure mechanism and the ultimate capacity of the connectors in the lateral direction. The numerical study was conducted using a three-dimensional finite element model based on the plastic-damage model available in ABAQUS software. Initially, the effects of different modeling techniques are briefly investigated. Subsequently, the shear capacity of a single anchor subjected to shear loads, simulating lateral loading conditions, was evaluated. It was found that the anchor behaviour was dominated by the steel failure mode.

Keywords: Helical pile, specialized connector, finite element, concrete, cracking, anchor bolts, ABAQUS.

1 INTRODUCTION AND RESEARCH MOTIVATION

Helical screw piles are used as an efficient retrofit technique for moderately loaded buildings (Carville & Walton, 1995). A typical helical pile consists of a steel shaft and a number of helical plates welded to it. Helical piles are attached to the existing foundation using a two-piece specialized connector. Typically, two 1/2 in. (12.7 mm) wedge-type expansion anchors are used to attach the connector (bracket) to the foundation.

The capacity of the helical pile connectors under lateral loads is expected to be dependent on the shear capacity of the wedge-type anchors (El Naggar et al., 2007). Anchors subjected to shear loads can experience four different failure modes: steel failure, concrete edge failure, concrete pry-out failure, and pull-out failure. Figure 1 shows possible failure modes for expansion anchors. The failure mode and the ultimate capacity depend on the anchor configuration including the embedment depth, anchor diameter, and the edge distance towards and parallel to the loading direction.

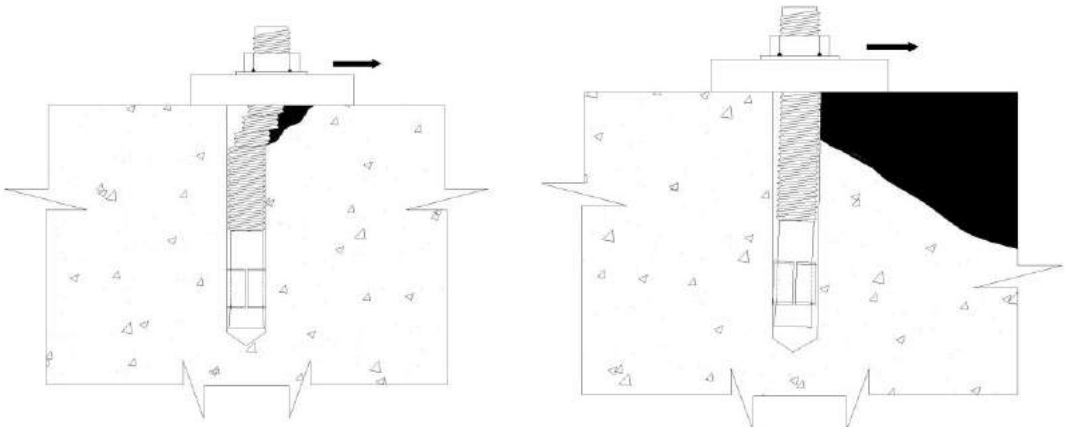

a) Steel failure preceded by concrete spall

b) concrete edge breakout

Fig. 1. Failure modes of expansion anchors under shear loading (after ACI 355.2-01).

El Sharnouby & El Naggar (2009) studied the performance of wedge-type expansion anchors under tensile loads. In this study, non-linear finite element analysis is conducted to simulate wedge-type anchor installed in uncracked concrete and subjected to shear loading. The influence of different modeling techniques on the anchor's response is investigated. In addition the performance characteristics and the ultimate capacity are examined.

2 ANCHORS AND PARAMETERS STUDIED

The connector is typically attached to the concrete foundation using the "WS-G Hot-Dipped Galvanized" anchor type shown in Fig. 2. It is composed of an anchor shaft, an expansion sleeve and a conical end. Key dimensions of the anchor are shown in Table 1.

It is made of steel with yield strength, f_y = 380 MPa and tensile strength, f_{ut} = 517 MPa (ICC, 2007). The connector design allows the installation of anchors with diameters 12.7 mm (1/2 in.) and 15.9 mm (5/8 in.). In the following sections, anchors will be identified based on their size. In this paper, results for the 12.7 mm anchor are presented.

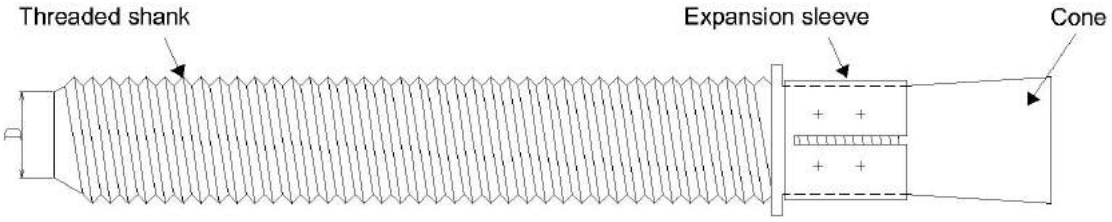

Fig. 2. Wedge-type expansion anchor.

Table 1. Key dimensions of the 12.7mm (1/2 in.) anchor.

D		d_1		d_2		l_s	
mm	in.	mm	in.	mm	in.	mm	in.
12.7	1/2	12.7	1/2	11.35	0.47	12.5	0.492

The expansion anchors are typically installed with an embedment depth, $h = 6\ d$ (d is its diameter). El Sharnouby & El Naggar (2010) showed that under horizontal loading conditions, installing the two wedge-type expansion anchors with an embedment depth of 9 times the anchors diameter, and an edge distance of 120 mm would preclude failure in the concrete foundation. In the current investigation, the embedment depth was 9 *d*. The edge distance parallel to the loading direction was taken c_1 = 120 mm (as in typical anchor installation). The edge distance in the direction perpendicular to the loading direction, c_2, depends on the foundation size and piles spacing. It was taken c_2 = 215 mm (see Fig. 3).

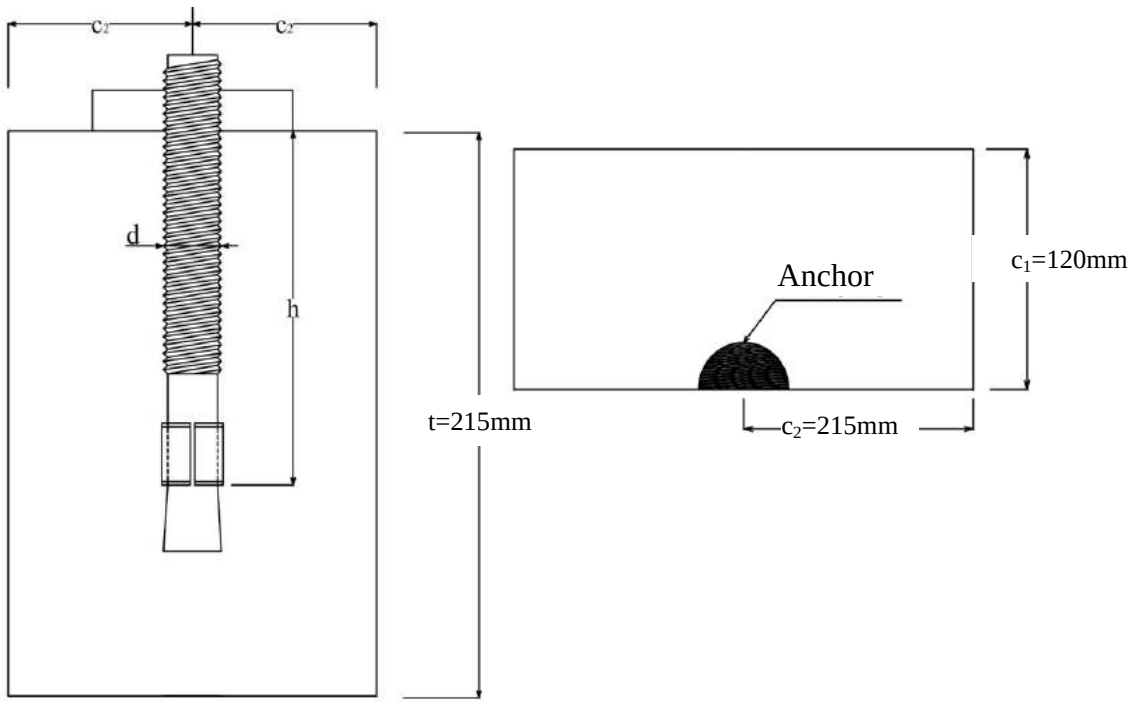

Fig. 3. Edge and spacing distances for typical anchor installation.

3 NUMERICAL INVESTIGATION

The ABAQUS software was used to conduct the analysis. The anchorage system was simulated using a 3-D FE model comprising eight-nodded hexahedron elements, C38DR, to represent the concrete foundation, the anchor (shaft and nut) and the sleeve. The interfaces between different parts were modelled using surface-based interactions. Loading was applied in a displacement controlled fashion. Reduced integration elements were chosen to overcome the volumetric locking effect of the fully integrated elements when material model is almost incompressible (Cook et al., 2002). A staged mesh refinement was conducted to optimize the solution. In order to accurately capture the geometry of anchor, the average aspect ratio of elements was kept below 1:4. In high stress concentration regions, the aspect ratio was kept close to unity. No yielding is expected in the connector itself, therefore it was treated as rigid.

In order to reduce the computational time and effort, with acceptable accuracy, the anchorage system was simplified to rectangular half symmetric model as shown in Fig. 4. A fully fixed boundary condition was applied to the base of the foundation. In addition, symmetry boundary conditions were employed, i.e., only half of the system is modeled. A typical finite element mesh is shown in Fig. 4.

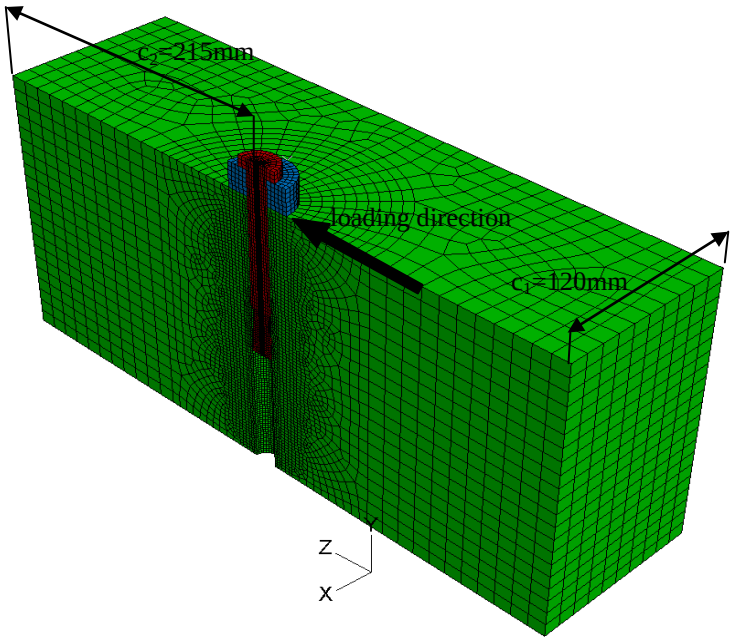

Fig. 4. Typical finite element mesh for single anchorage system.

The Von-Mises plasticity criterion was used to define the yield and post yield behaviour of steel. A multi-linear stress-strain relationship was used in this analysis to describe the behaviour of the anchor and the sleeve (Fig. 5). The steel parameters were taken as: Young's modulus E_s = 200 GPa, Poisson's ratio v_s = 0.3, yield stress f_y = 380 MPa, ultimate strength f_{ut} = 517 MPa (ICC, 2007). Coefficient of friction between steel and steel, μ_s, was assumed 0.16, and between hardened concrete and steel μ_c = 0.43 (Cook & Kinlgner, 1989).

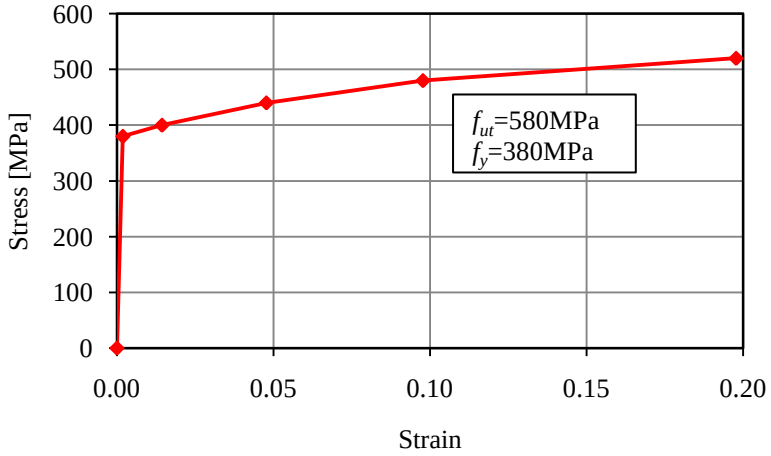

Fig. 5. Stress-strain model for anchor and sleeve (steel).

The concrete behaviour is described using a plastic-damage model for concrete developed by Lubliner et al. (1989) and later modified by Lee and Fenves (1998). The model incorporates a non-associative flow rule, i.e. the potential function differs from the yield function, and crushing and cracking of concrete are represented by two isotropic (scalar) damage variables, one for compressive damage and one for tensile damage.

Concrete parameters used are: compressive strength f_c' = 25 MPa, compression modulus of elasticity E_c = 4800 $\sqrt{f_c'}$ MPa, Poisson's ratio v_c = 0.2, yield limit f_{cy} = 0.5 f_c', strain at ultimate stress ε_{cu} = 0.0015, tensile strength f_t = 0.1 f_c', biaxial to uniaxial compressive ratio f_{bu}/f_{cu} =1.16 (Kupfer et al., 1969), and the ratio of the second stress invariant on the tensile meridian to that on the compressive meridian for a given value of the first stress invariant K_C = 2/3

(Lubliner et al., 1989). Compressive behaviour was described by a Tri-linear stress-strain relationship, as shown in Fig. 6, with compressive damage parameter equal to 0.4. The tensile behaviour was described by a linear stress-strain curve till cracking considering the tension modulus of elasticity $E_t = E_c$ and damage parameter assumed $d_t = 0.75$. Post cracking behavior was described by a stress-cracking displacement relationship *(σ-w).* The equations proposed by Bazant & Becq-Giraudon (2002) were used to evaluate fracture energy (G_F) and was found to be $G_F = 0.093$ N/mm. Exponential stress-cracking displacement relationships was considered as recommended by El Sharnouby & El Naggar (2010) as shown in Fig. 7. The formula proposed by Eligehausen et al. (2006) was adopted (Fig. 7), and, the displacement corresponding to $\sigma(w) = 0$, w_c = 0.14-0.2 mm (Reinhardt, 1997-according to Eligehausen et al., 2006). Anchors were pre-tensioned to 8 kN then shear load was applied incrementally in a displacement controlled fashion on the back side of the fixture.

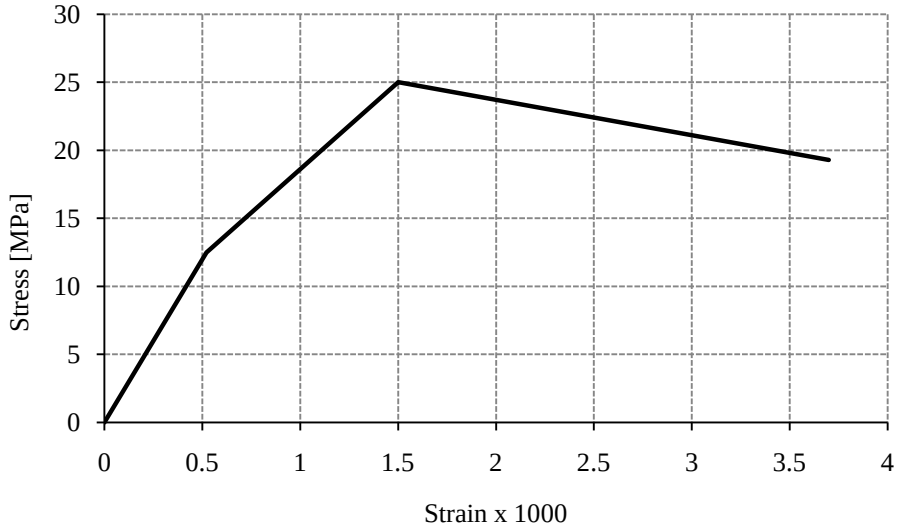

Fig. 6. Concrete model in compression for lateral loading case.

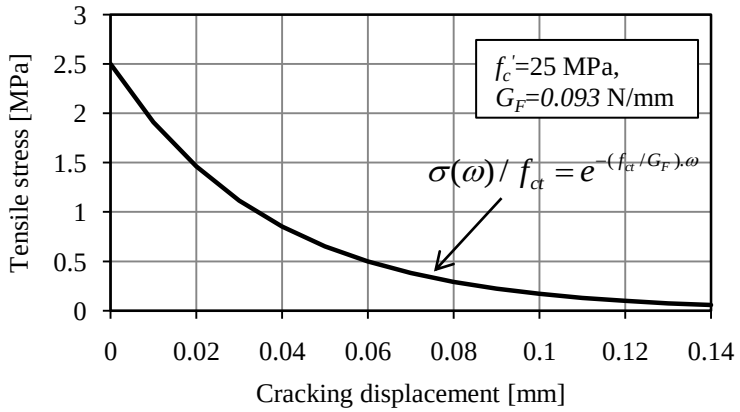

Fig. 7. Concrete stress-cracking displacement model.

4 NUMERICAL RESULTS

The finite element model was verified by comparing its results with those obtained from an experimental study performed by Cattaneo (2007) that involved single wedge-type expansion anchors subjected to tensile loading embedded in unreinforced concrete (see El Sharnouby & El Naggar 2009).

4.1 Influence of Modelling Techniques

There are two possible modelling techniques to simulate the anchorage components. The first possibility is to model the anchor and the fixture as one part (see Fig. 8a). The second technique is to model the anchor and the fixture as separate parts (see Fig. 8b). The first technique is expected to simplify the analysis and reduce the computational time. However, it implies that the anchor is restrained to rotate in the fixture hole (the anchor is welded to the fixture plate). To check the validity of such an approach, a set of analysis was carried out to compare both techniques.

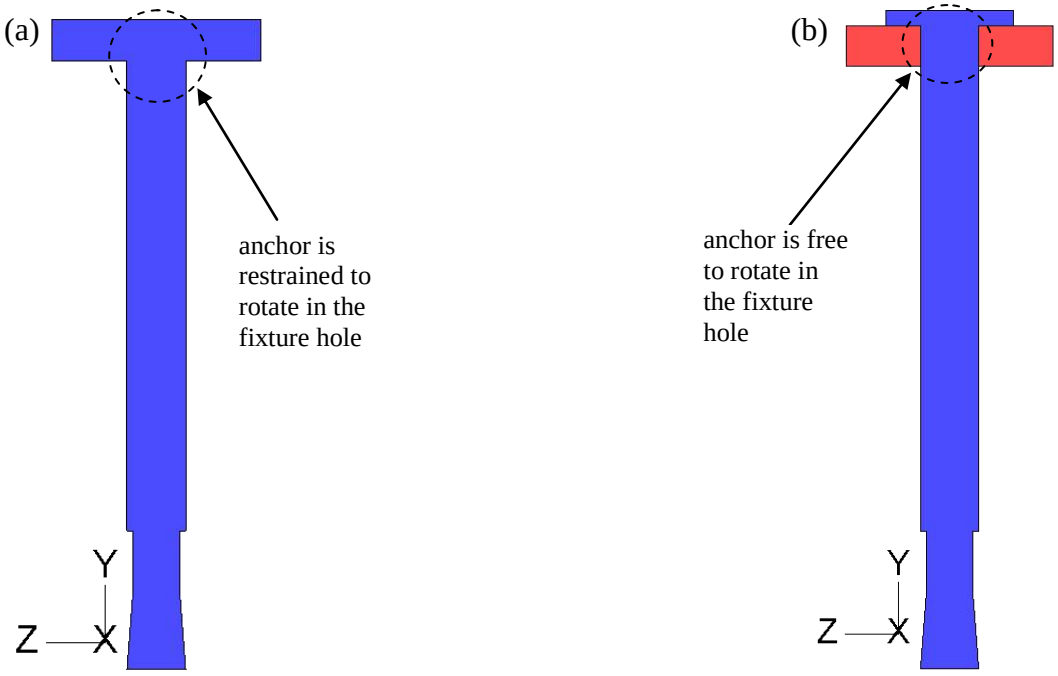

Fig. 8. Different modelling techniques (a) anchor and fixture as one part and (b) anchor and fixture hole as separate parts.

Figure 9 shows the load-displacement curves for both modelling techniques considered for the 12.7 mm anchor. It can be seen that both techniques yield approximately the same response up to the "yield point". Afterwards, the first approach predicted a stiffer response. This is attributed to allowing the anchor to rotate in the fixture hole (as considered in modelling technique 'b') generated bending stresses, in addition to the shear loads, and therefore reduced the ultimate capacity of the anchor bolt. The ultimate load predicted when the anchor was restrained in the fixture hole (modelling technique a) is 11.4 % higher than that predicted when the anchor was free to rotate in the fixture hole (modelling technique b). Meanwhile, the displacement at failure in technique (a) was 85.5% of that predicted by technique (b). Therefore, restraining the anchor in the fixture hole slightly overestimates the ultimate capacity and predicts a more brittle behaviour. It is worth noting that the first modelling approach is valid for welded studs.

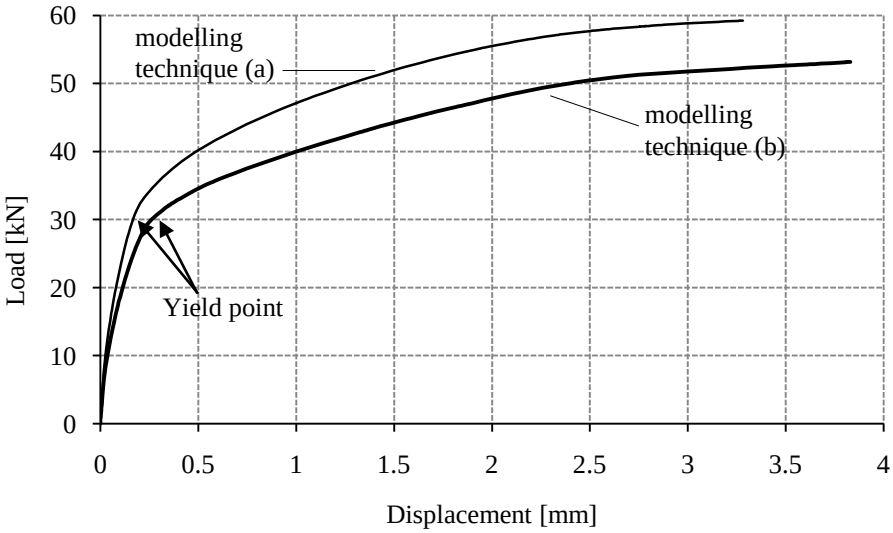

Fig. 9. Load-displacement curves for different modelling techniques.

4.2 Failure Modes and Mechanism

In all cases considered, the anchors exhibited steel failure. Fig. 10 depicts the deformed shape and the Mises stress distribution. As it can be seen, the stresses in all elements along the anchor cross-section reached their ultimate strength. The shear load generated high compressive stresses in front of the anchor resulting in a conical-shaped fracture surface as can be seen in Fig. 11. During load application, radial and circumferential cracks are generated at the concrete surface. In addition, splitting cracks are formulated along the edge distance parallel to the loading direction as shown in Fig. 12. However, the anchor bolt failed before the splitting forces reach the splitting resistance of the concrete.

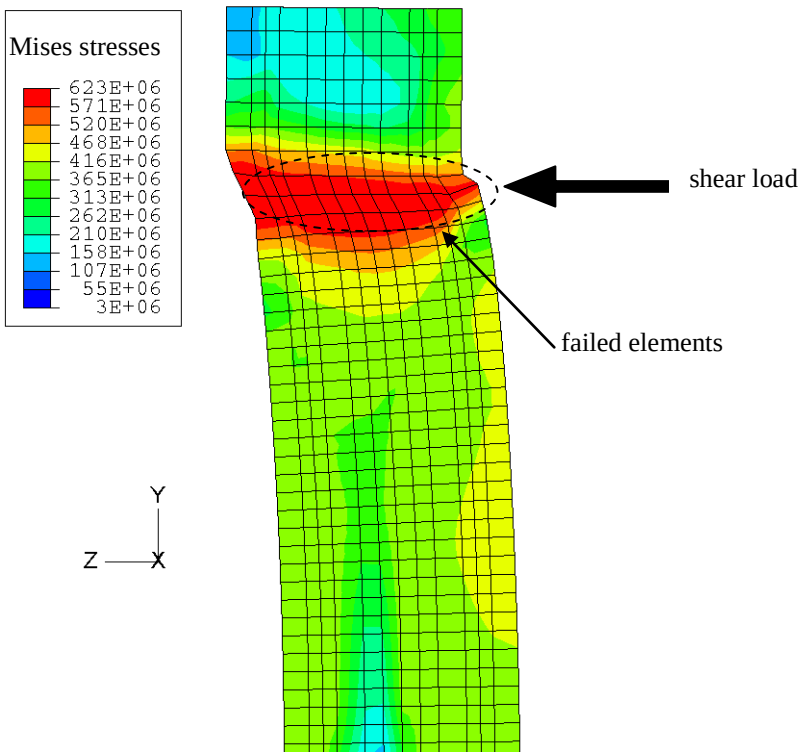

Fig. 10. Deformed shape and Mises stress distribution at failure.

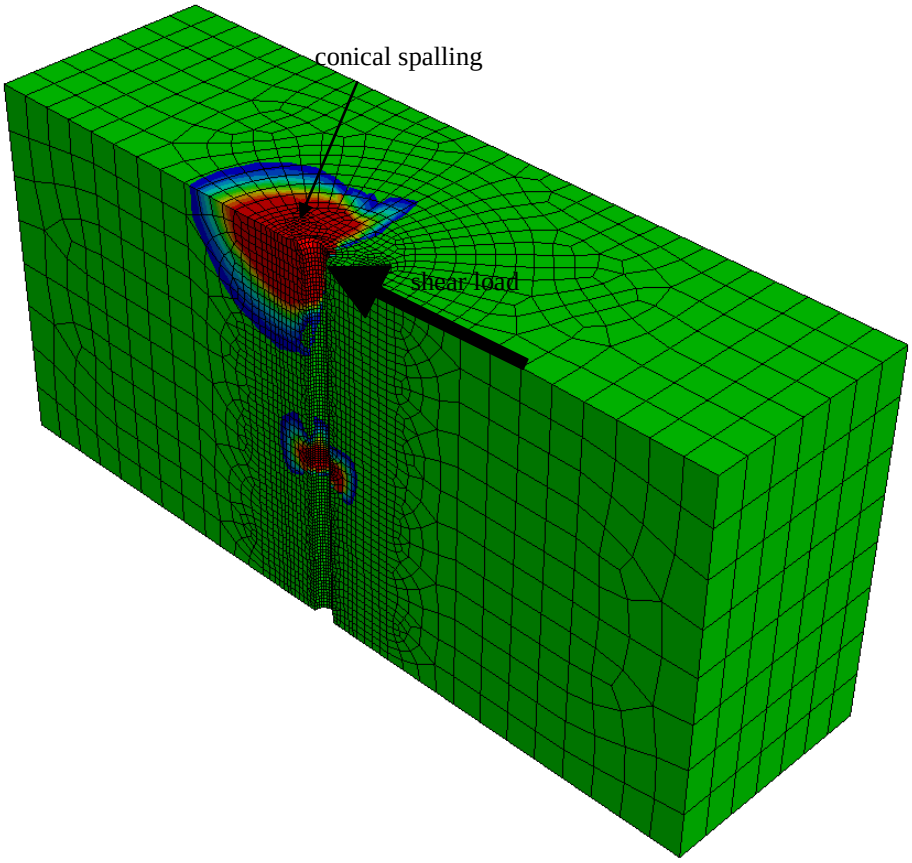

Fig. 11. Conical-shaped concrete spalling in front of the anchor at failure (red zones=damaged elements).

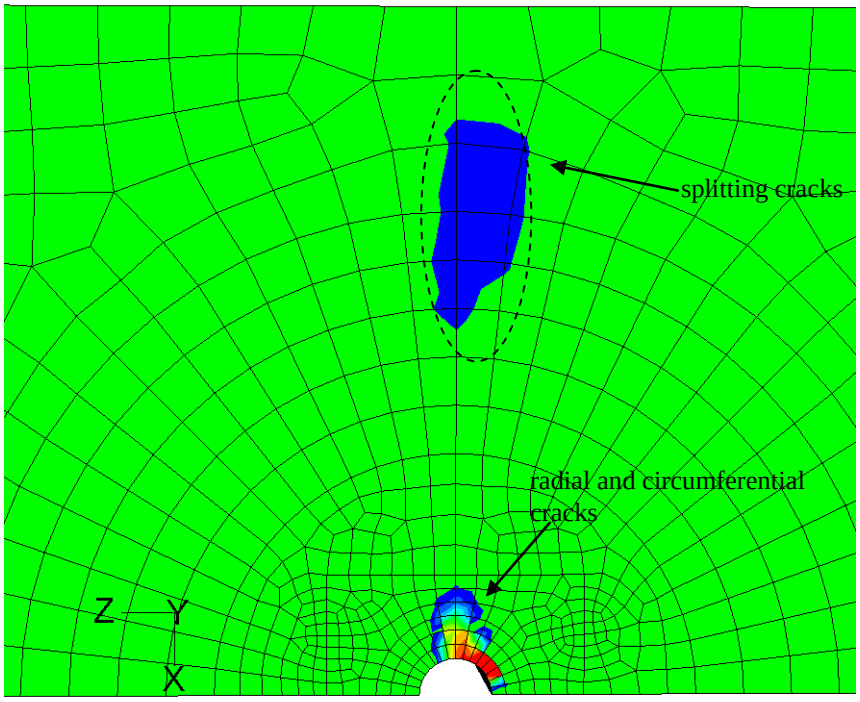

Fig. 12. Crack pattern at failure (red zones=damaged elements).

A typical load-displacement curve corresponding to the steel failure mode is shown in Fig. 13. As the loading started, the shear force was transferred through friction yielding a steep initial response. When the applied shear exceeded the available friction, the shear load was transferred through bearing of the fixture onto the anchor bolt and accordingly bearing of the anchor bolt onto the concrete. As the shear load was increased, the anchor bolt yielded and some damage in front of the anchor was observed. Further increase in the load resulted in the formation of the conical shaped fracture surface (see Fig. 11) in front of the anchor. The size of this conical shape increased with further increase in the load until failure occurred in the anchor bolt. The failure load was considered as the load at which the load-displacement response becomes flat indicating complete loss of stiffness. The ultimate capacity of the 12.7 mm anchor for the case under consideration was found to be 53 kN at a displacement of 3.5 mm.

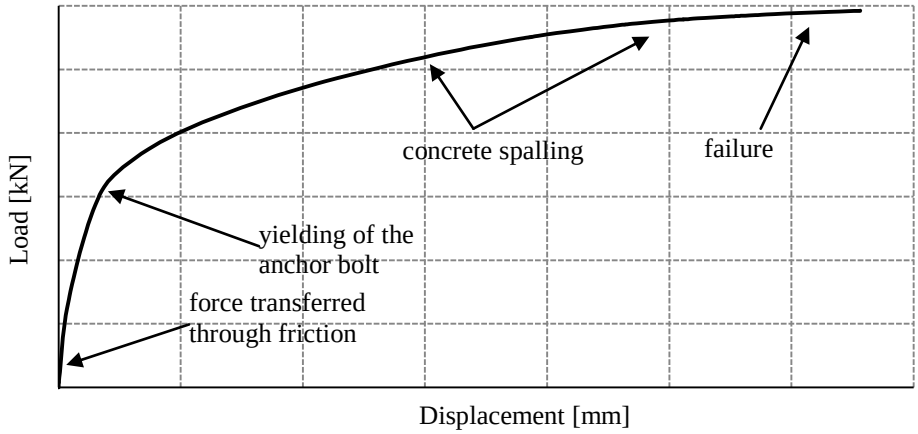

Fig. 13. Load-displacement curve for steel failure mode.

5 CONCLUSIONS

In this paper, the shear capacity of a single anchor subjected to shear loads, simulating lateral loading conditions for helical pile connectors, has been evaluated.

- Techniques in modeling the interaction between the anchorage system components may have an influence on the prediction of the performance and of the ultimate capacity of these anchors.
- The ultimate capacity of the 12.7 mm anchor for the case under consideration was found to be 53 kN at a displacement of 3.5 mm.
- Failure of the connector under lateral loads is expected to be governed by steel rupture.
- Further analysis is needed for connectors installed in cracked concrete.

ACKNOWLEDGMENTS

The authors would like to thank EBS Engineering & Construction Limited for their continuous support throughout this research program**.**

REFERENCES

ACI Committee 355. (2001), "Evaluating the Performance of Post-Installed Mechanical Anchors in Concrete (ACI 355.2-01)". American Concrete Institute, Farmington Hills, Mich.

Bazant, Z.P. & Becq-Giraudon, E. (2002), "Statistical prediction of fracture parameters of concrete and implications for choice of testing standard". Cement and Concrete Research, Vol. 32(4), 529-556.

Cattaneo, S. (2007), "Wedge-type expansion anchors in high-performance concrete". ACI Structural Journal, Vol. 104 (2), 191-198.

Carville, C.A. & Walton, R.W. (1995), "Foundation repair using helical screw anchors", Proceedings of the Conference of the Geotechnical Engineering Division of the ASCE in Conjunction with the ASCE Convention San Diego, CA, USA, 56-75.

Cook, R. A. & Klingner, R. E. (1989), "Behavior and design of ductile multiple-anchor-to-concrete connections". Research report No. 1126-3, Centre for Transportation Research, University of Texas at Austin, Mar.

Cook, R. D., Malkus, D. S, Plesha, M. E. & Witt, R. J. (2002), Concepts and applications of finite element analysis, John Wiley & Sons. Inc, USA.

Eligehausen, R., Mallee, R. & Silva, J. F. (2006), Anchorage in concrete construction, Ernst & Sohn, Berlin.

El Naggar, M.H., Youssef, M.A. & Ahmed, M. (2007), "Monotonic and cyclic lateral behaviour of helical pile specialized connectors". Engineering Structures, Vol. 29(10), 2635-2640.

El Sharnouby, M. M. & El Naggar, M. H. (2009), "Numerical Analysis of Expansion Anchors", The First International Symposium on Computational Geomechanics, France.

El Sharnouby, M. M. & El Naggar, M. H. (2010), "Numerical investigation of the response of expansion anchors used to attach helical pile connectors to concrete foundations". Canadian Journal of Civil Engineering, Vol. 37(6), 866-877.

Hibbitt, H.D., Karlsson, B.I., & Sorensen, E.P. (2007), "ABAQUS standards user's manual 2007", version 6.7. Habbitt, Karlsson & Sorensen, Inc., Pawtucket, R.I.

Hubbell Power Systems, Inc. (2003), "Helical Screw Foundation System Design Manual for New Construction", Centralia, Missouri, USA.

ICC Evaluation Service, Inc. (2007), "ITW red head trubolt carbon steel wedge anchors in concrete", Report No. ESR-2251, Whittier, California, USA.

Kupfer, H., Hilsdorf, H.K. & Rusch, H. (1969), "Behavior of concrete under biaxial stress". ACI Journal, Vol. 66(8), 656-66.

Lee, J. & Fenves, L.G. (1998), "Plastic-damage model for cyclic loading of concrete structures". Journal of Engineering Mechanics, Vol. 27(9), 937-956.

Lubliner, J., Oliver, J., Oller , S. & Onate, E. (1989), "Plastic-damage model for concrete". International Journal of Solids and Structures, Vol. 124(8), 892-900.

Reinhardt, H.-W. (1997), "Werkstoffe des bauwesens (Building materials)". In: Der Ingenieurbau, Editor: Mehlhorn, G., Ernst & Sohn, Berlin, 1-163 (in German).

NUMERICAL ANALYSIS OF INSTALLATION EFFECTS OF PILE JACKING IN SAND

H.K. Engin
Geo-Engineering Section, Delft University of Technology, Delft, Netherlands

R.B.J. Brinkgreve
Geo-Engineering Section, Delft University of Technology / Plaxis b.v., Delft, Netherlands

A.F. van Tol
Geo-Engineering Section, Delft University of Technology / Deltares, Delft, Netherlands

ABSTRACT: *In this study installation effects of a jacked pile in sand is modelled using a simplified finite element technique: The 'Press-Replace' technique. The main goal is to find out a trend of installation effects by modelling the jacking by piece-wise updated geometry and discarding distortion problems. To model sand Hypoplasticity with intergranular strain is used. A robust version (Masin, 2010), which is based on Runge-Kutta-Fehlberg explicit integration, is employed. A 0.40m diameter, 4m length pile geometry is used and the 'Press-Replace' technique is employed to model the penetration process in various types of sands based on hypoplastic parameters as reported by several authors. For each different type of sand, three relative densities (RD) are investigated, namely, 20%, 40% and 75%, to describe very loose, medium and dense cases. Average behaviour as well as standard deviations and variation percentages are calculated. It is shown that Press-Replace technique can be used efficiently for the modelling of pile jacking. A good correlation for the void ratio changes is obtained. On the other hand higher variation is observed for the stress states.*

1 INTRODUCTION

Recent developments in pile jacking techniques have increased the preference of this method due to its benefits (minimal noise, vibration and pollution) compared to hammering and vibratory driving, especially in urban environment (Basu et al., 2010). Besides its environmental merits, pile jacking has better performance due to reduced friction fatigue and residual base load (Deeks et al., 2005). Moreover, better predictions of pile shaft and base capacities can be obtained for this method (Yang et al., 2006).

The behaviour of jacked piles has been studied by several researchers both experimentally (Aranov & Gudakov, 1977; White, 2002; Dijkstra et al., 2006) and numerically (Mahutka et al., 2006; Broere & van Tol, 2006; Pham et al., 2010; Sheng et al., 2007; Said et al., 2008; Vermeer et al., 2008; Henke & Grabe, 2009). However, knowledge of the effect of jacking process on the soil is still quite limited. Besides this, the Finite Element (FE) modelling of pile installation effects is also a difficult task due to lack of knowledge on soil behaviour during the installation process (Dijkstra et al., 2007).

It is known that due to mesh distortion, it is not possible to model the pile installation process using regular FE Analysis (FEA). Some simple techniques like imposing some boundary conditions (BC's) at the pile soil interface (Broere & van Tol, 2006; Said et al., 2008; Pham et al., 2010) using small deformation theory avoid this problem. However the solutions cannot be generalized for all pile jacking cases.

In this perspective, the 'Press-replace' technique is introduced, providing simplicity, robustness, applicability in simple FE codes and generalization as compared to aforementioned small deformation solutions. In this study this technique is employed to investigate installation effects due to pile jacking. A robust version of hypoplasticity with intergranular strain (Masin, 2010) is used as the constitutive model. This version is based on the Von Wolffersdorff (1996) hypoplastic model with improved Runge-Kutta-Fehlberg explicit integration algorithm. Hypoplasticity is chosen as constitutive model because of the dependency of stiffness and strength properties on the void ratio. The limiting values of the void ratio are defined with an exponential function of the mean effective stress and granular stiffness (Bauer, 1996). This feature makes hypoplasticity quite suitable for the modelling of Boundary Value Problems in cases where the material density changes significantly, like in the case of pile installation in sand.

The purpose of this study is to quantify the installation effects after pile jacking, which is of interest for the geotechnical engineering practice. Hence, we focus on the final (relaxed) state, and not in the changes during the jacking phase.

As an initial attempt to quantify installation effects, a 0.40m diameter, 4m (20·D) length pile geometry is used and the 'Press-Replace' technique is employed to model the penetration process in various types of sands based on hypoplastic parameters as reported by several authors. For each sand, three relative densities (*RD*) are investigated, namely, 20%, 40% and 75%, to describe very loose, medium and dense cases. Results for mean values, as well as standard deviations are presented and discussed for each *RD* case.

In the conclusions, the applicability of the technique and quantification of installation effects based on relative densities are discussed. Finally, future plans for the improvement of the technique and quantification of installation effects are given.

2 FE ANALYSIS OF INSTALLATION EFFECTS OF PILE JACKING

In this part first the technique used in the analysis is explained in details. Later analyses details of the several cases and the base FE model is explained. Material properties are summarized; triaxial and oedometer responses of the sands modelled are also shown.

2.1 Press-replace technique

For the modelling of the jacking of a pile in sand, a small deformation, step-wise updated FE mesh, 'Press-Replace' technique is employed (Figures 1&2). A similar technique has been employed previously by Andersen et al. (2004) to model penetration of a suction pile in clay.

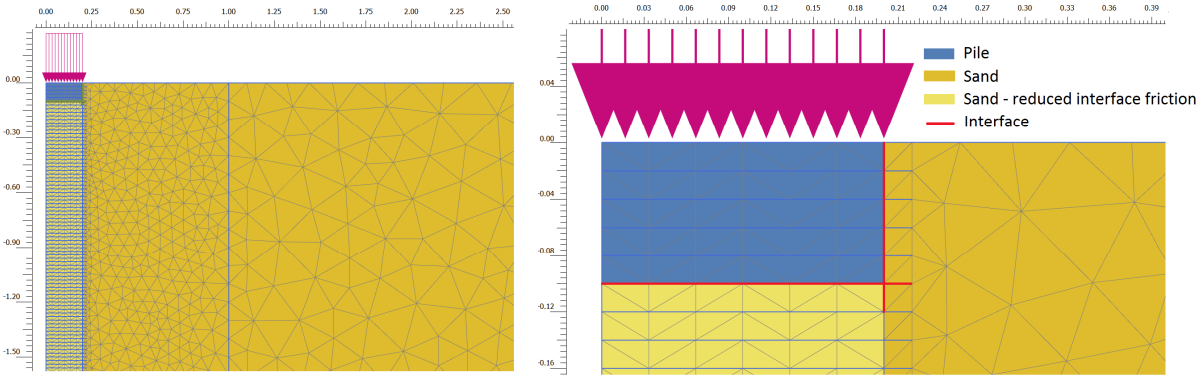

Figure 1. Details on the Press-Replace modelling technique.

The technique involves a (vertical) displacement phase (coaxial with the direction of penetration) followed by a phase in which material exchanged by pile material (concrete). These phases are repeated until the desired level of penetration is achieved. To model pile soil interaction and reduce concentrations on the corner zero-thickness interfaces with small extensions into the soil are employed. In order to reduce high shear stresses under the tip residual (critical) strength parameters are assigned for the interfaces at the tip. The resolution of stresses and other state variables increases with finer step size and mesh fineness (Engin & Andresen, 2011). On the other hand there is a lower limit for the smallest step size as the purpose is to model continuous failure. It is important to note that the model does not capture the flow mechanism under the pile tip.

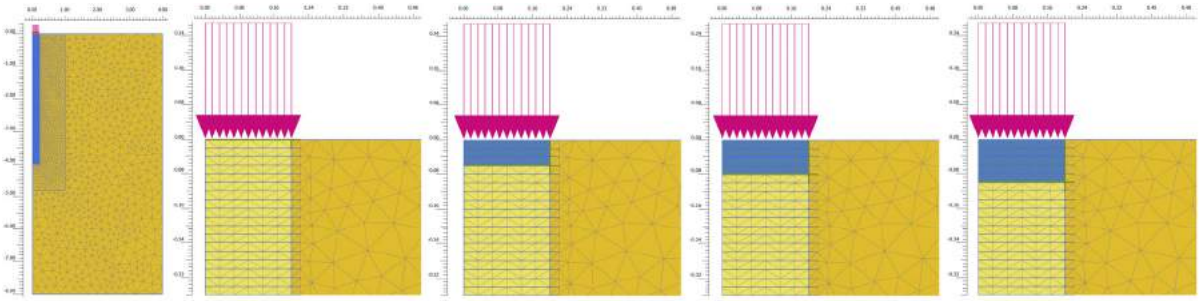

Figure 2. FE mesh and illustration of 'Press-Replace' technique.

2.2 FE analysis of pile jacking

In Figure 3 the FE mesh used throughout the analyses is shown. A 0.40m diameter, 4m (20·D) length pile geometry is used and the 'Press-Replace' technique is employed to model the penetration process in various types of sands based on hypoplastic parameters as reported by several authors (Johansson & Konagai, 2007; Rondón et al., 2007; Henke & Grabe, 2009; Masin, 2010; Pham et al., 2010). For the missing intergranular strain parameters a common parameter set for sand (Niemunis & Herle, 1997) is used. The hypoplastic parameters used for these materials are summarized in Table 1.

The hypoplastic model used in the calculations is the Von Wolffersdorff (1996) version incorporating the Matsuoka-Nakai failure criterion, with Runge-Kutta-Fehlberg explicit time integration with substepping (Masin, 2010).

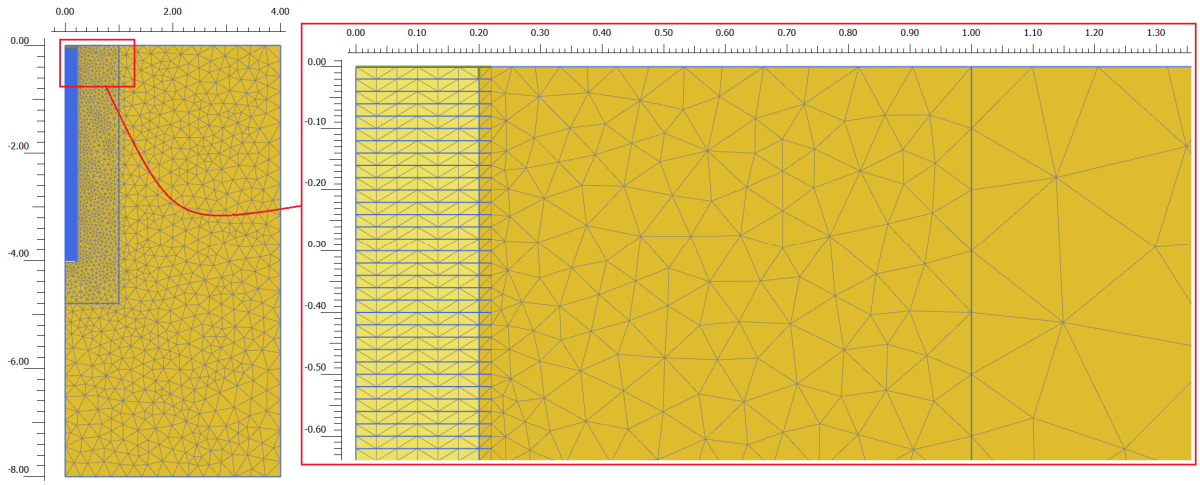

Figure 3. FE mesh used in the pile jacking analyses.

As can be seen from Table 1, each soil type is analysed for three relative densities, *RD* of 20%, 40%, 75 %, to account for very loose, medium and dense conditions, respectively. The initial void ratios, e_0 are calculated using:

$$e_0 = e_{c0} - RD \cdot \left(e_{c0} - e_{d0}\right) \tag{1}$$

where e_{d0} is the possible densest state and e_{c0} is the critical state density both at $p'=0\ kN/m^2$.

Table 1. Hypoplastic soil model parameters used in the analyses

Parameter	Unit	Karlsruhe[1, 2, 3]	Hochstetten[1, 4]	Toyoura[1, 4]	Hostun[1, 4]	Lausitz[1, 4]	Mai-Liao[2, 4]	Bremerhaven[3]
ϕ_c	°	30	33	30	31	33	31.5	30
h_s	GPa	5.8	1.5	2.6	1.0	1.6	0.032	4.1
n	-	0.28	0.28	0.27	0.29	0.19	0.32	0.20
e_{d0}	-	0.530	0.550	0.610	0.610	0.440	0.570	0.490
e_{c0}	-	0.840	0.950	0.980	0.960	0.850	1.040	0.830
e_{i0}	-	1.000	1.050	1.100	1.090	1.000	1.200	0.996
α	-	0.13	0.25	0.18	0.13	0.25	0.40	0.05
β	-	1.00	1.50	1.10	2.00	1.00	1.00	1.50
m_R	-	5	5	5	5	5	5	5
m_T	-	2	2	2	2	2	2	2
R_{max}	-	$1\cdot10^{-4}$	$1\cdot10^{-4}$	$1\cdot10^{-4}$	$1\cdot10^{-4}$	$1\cdot10^{-4}$	$1\cdot10^{-4}$	$3\cdot10^{-4}$
β_R	-	0.50	0.50	0.12	0.50	0.50	0.50	0.50
χ	-	2	6	1	6	6	6	1
e_0	-	0.778 0.716 0.608	0.870 0.790 0.650	0.906 0.832 0.703	0.890 0.820 0.698	0.768 0.686 0.543	0.946 0.852 0.688	0.762 0.694 0.575
RD	%	0.20 0.40 0.75	0.20 0.40 0.75	0.20 0.40 0.75	0.20 0.40 0.75	0.20 0.40 0.75	0.20 0.40 0.75	0.20 0.40 0.75

1 Masin (2010)
2 Johansson & Konagai (2007)
3 Henke (2010)
4 Rondón et al. (2007)

2.3 *Oedometer and triaxial response of the sands*

The oedometer and triaxial responses of the sands used in the analyses with relative densities of 20%, 40% and 75% are given in Figures 4 & 5.

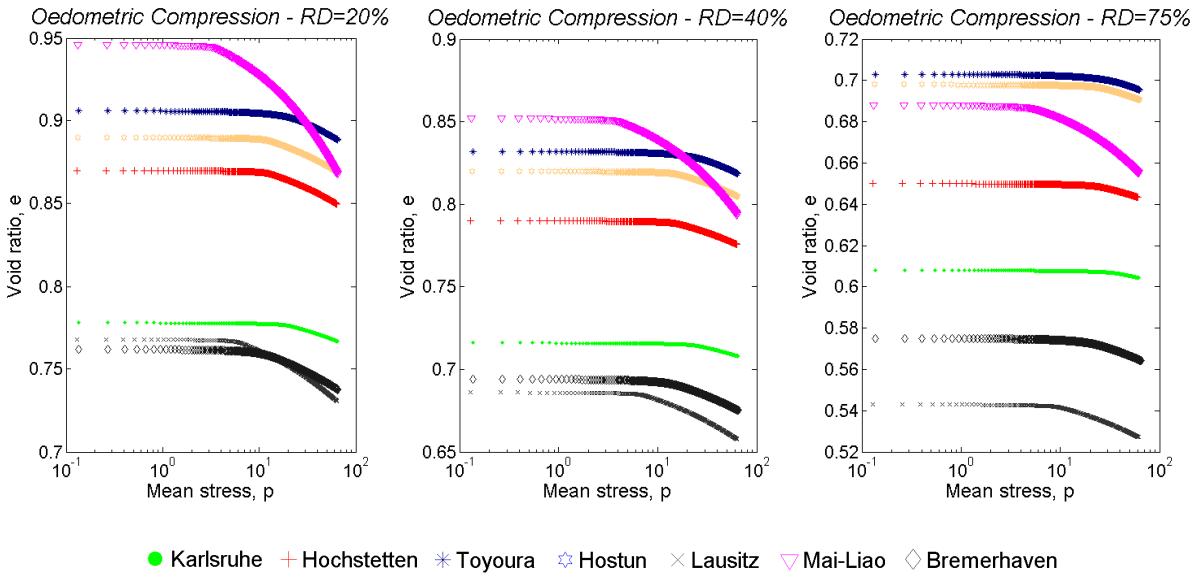

Figure 4. Oedometric response of the sands for very loose, medium and dense (left to right) cases

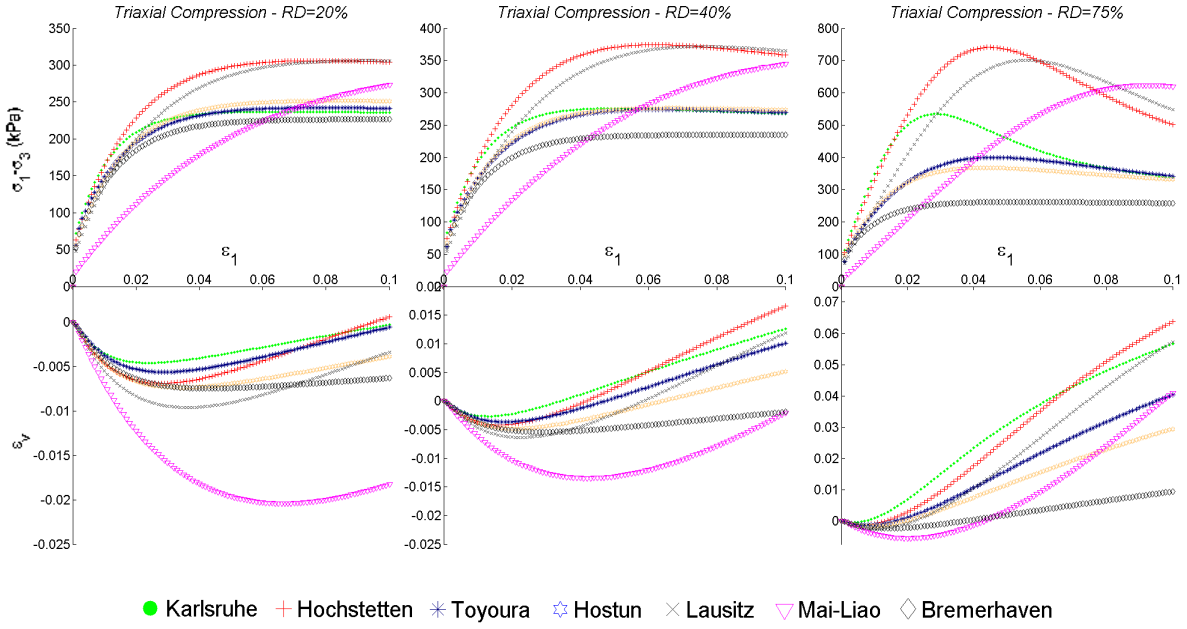

Figure 5. Triaxial compression response of the sands for very loose, medium and dense (left to right) cases

3 RESULTS

In this part average values of *ratios* (normalized values) of the final state to initial state for void ratio (R_e, Eq. (2a)), horizontal (R_{xx}, Eq. (2b)) and vertical stresses (R_{yy}, Eq. (2c)), as obtained for loose, medium and dense cases (RD = 20%, 40% & 75%), are shown in Figures 4, 6 and 8, respectively.

$$R_e = \frac{e^f}{e^{K_0}} \tag{2a}$$

$$R_{xx} = \frac{\sigma_{xx}{}^f}{\sigma_{xx}{}^{K_0}} \tag{2b}$$

$$R_{yy} = \frac{\sigma_{yy}{}^f}{\sigma_{yy}{}^{K_0}} \tag{2c}$$

where f denotes the final state and K_0 denotes the initial state.

The standard deviation distributions for all these cases are shown in Figures 5, 7 and 9. The aim here is to identify variations obtained from analysis of different type of soils and to investigate the possibility to generalize changes in states for particular relative densities (RD) for a particular pile geometry (D = 0.40m) and penetration depth ($L_{pen} = 20 \cdot D$ = 4m).

As $R_e < 1$ indicates compaction and $R_e > 1$ indicates dilation, it can be seen from Fig.4a for average of very loose cases (RD = 20%) that there is only compaction in the pile vicinity. A higher compaction is obtained under the pile tip for this case. For an average behaviour of medium dense (RD = 40%) cases, there is still, but less compaction under the pile tip; very little dilation close to pile shaft and some compaction in the close vicinity (up to $7.5 \cdot D$ from the shaft and ~ $6 \cdot D$ from the tip). Lastly for an average of dense cases (RD = 75%) there is very little compaction $5 \cdot D$ away from shaft and elsewhere dilation. The dilation is pronounced near the pile shaft. Interestingly there is dilation under the pile tip (also observed by Dijkstra, 2009) for the latter one.

Standard deviations of R_e's are given in Figure 5. It can be seen that the standard deviation values increase near the pile vicinity and higher for denser cases. That means the void ratio distribution can be generalized for different RD's with a good confidence.

Horizontal stress ratios, R_{xx} are given in Fig. 6 and one can easily point out that the highest stress increase is under the pile tip for all cases. For very loose cases, under the pile tip, an average horizontal stress increase of $\sim 15 \cdot \sigma_{xx}$ exists, which decays somewhat exponentially with distance from the tip. This distribution is quite similar to medium case except the increase is $\sim 20 \cdot \sigma_{xx}$ and therefore the values in the near field are slightly higher. And for the dense case it is $\sim 25 \cdot \sigma_{xx}$. Close to the shaft there are some fluctuations but as a general trend an average horizontal stress increase of $\sim 1.5 \cdot \sigma_{xx}$ is observed for very loose and medium cases and $\sim 2.5 \cdot \sigma_{xx}$ for the dense case.

Standard deviations for the R_{xx} are given in Fig. 7. The higher values are observed especially under the tip (~4 for very loose and medium, ~10 for dense cases). These values seem to decrease, like the stress distribution, exponentially. These values can be normalized with the stress ratios and hence percent variations, which are more comprehensible, can be obtained. For example, the percent variations for the very loose case vary between ~26% (under the tip) to ~2%, for medium case ~20% to ~2% and for dense case ~40 to ~5%. It can be seen that the variation is much more for the dense case. Therefore generalization of the R_{xx} values for different RD's involves lower confidence as compared to R_e values.

Vertical stress ratios, R_{yy} are given in Fig. 8. Similar to the R_{xx} distributions, higher values are obtained under the pile tip. Under the pile tip, average vertical stress increases of ~$8\cdot\sigma_{yy}$ for the very loose case, ~$10\cdot\sigma_{yy}$ for the medium and ~$15\cdot\sigma_{yy}$ for the dense case are obtained. There is again a rapid decay with increasing distance and is more in horizontal direction. On the other hand there is a stress decrease observed near the pile shaft for all cases but more for the very loose case (~$0.4\cdot\sigma_{yy}$). This value is ~$0.6\cdot\sigma_{yy}$ for medium and ~0.6 to $0.8\cdot\sigma_{yy}$ for dense cases.

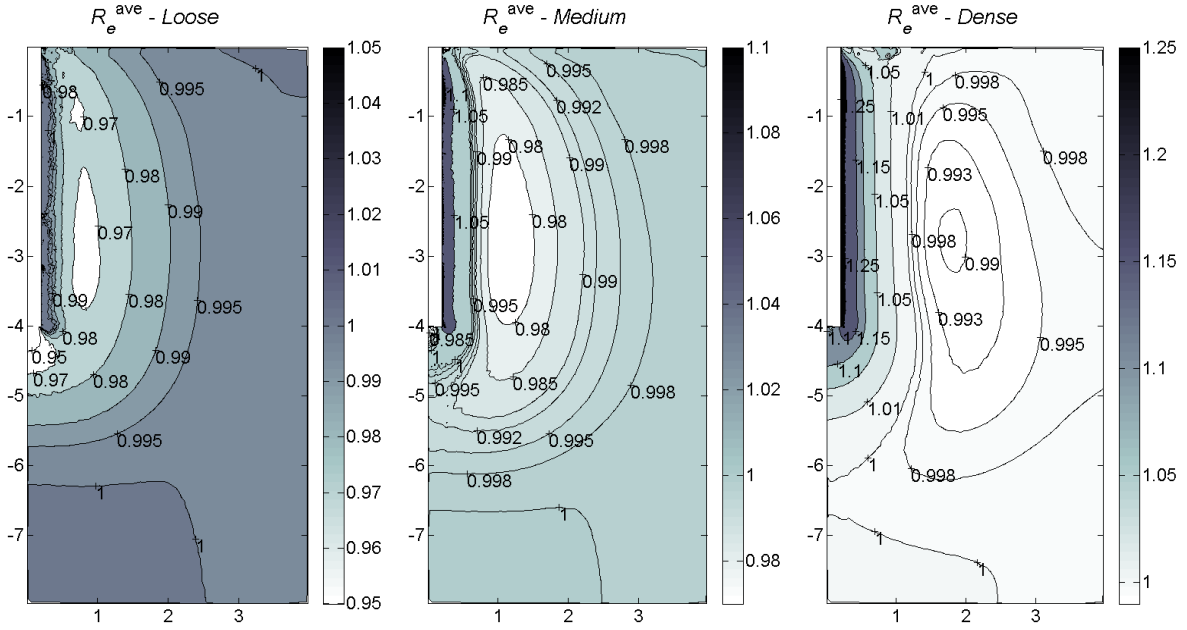

Figure 4. Average R_e contours for very loose, medium and dense cases.

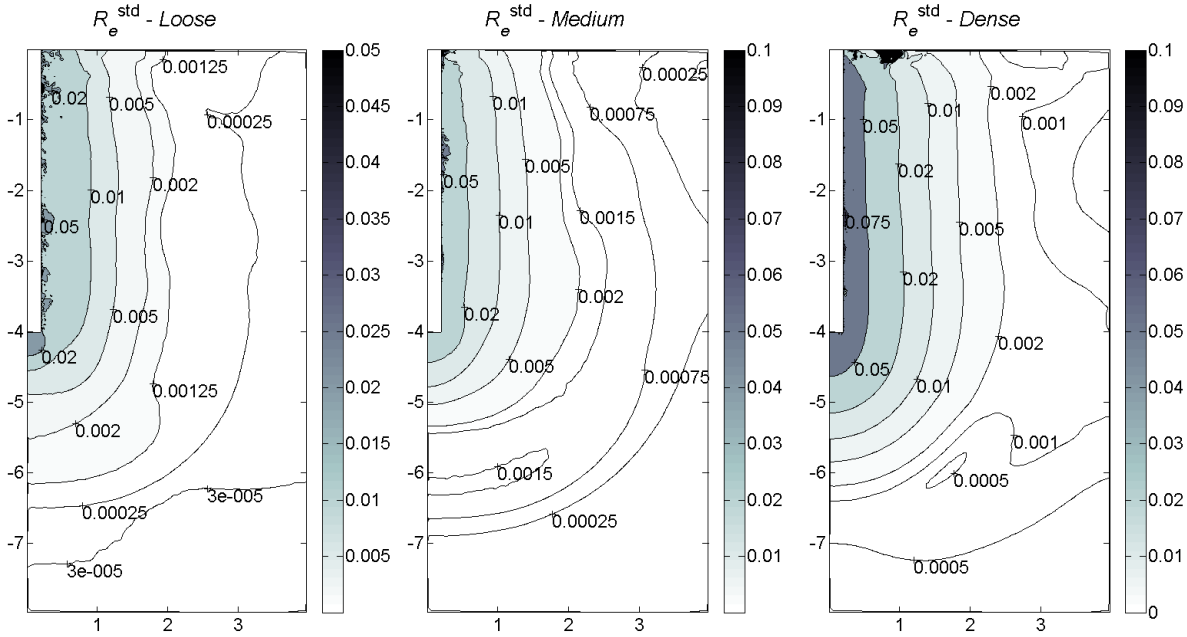

Figure 5. Standard deviation contours of R_e for very loose, medium and dense cases.

Standard deviations for the R_{yy} are given in Fig. 9. Again, highest values can be recognized under the tip (~1.5 for very loose and medium, ~3 for dense cases). These values decrease with distance rapidly to a value as low as ~0.01. In terms of percentages, a variation as high as ~19% ,~15% and ~20% for very loose, medium and dense cases, respectively. The generalization of the R_{yy} values for different *RD*'s involves lower confidence as compared to R_e, but better than R_{xx} values.

These interesting results will be discussed in the next chapter.

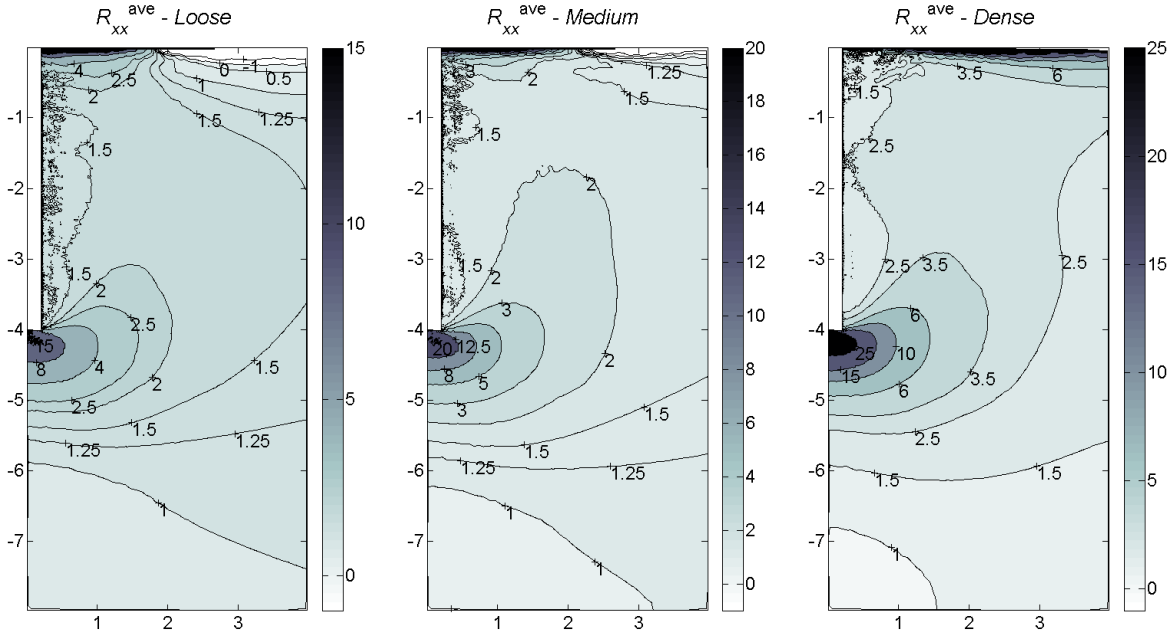

Figure 6. Average R_{xx} contours for very loose, medium and dense cases.

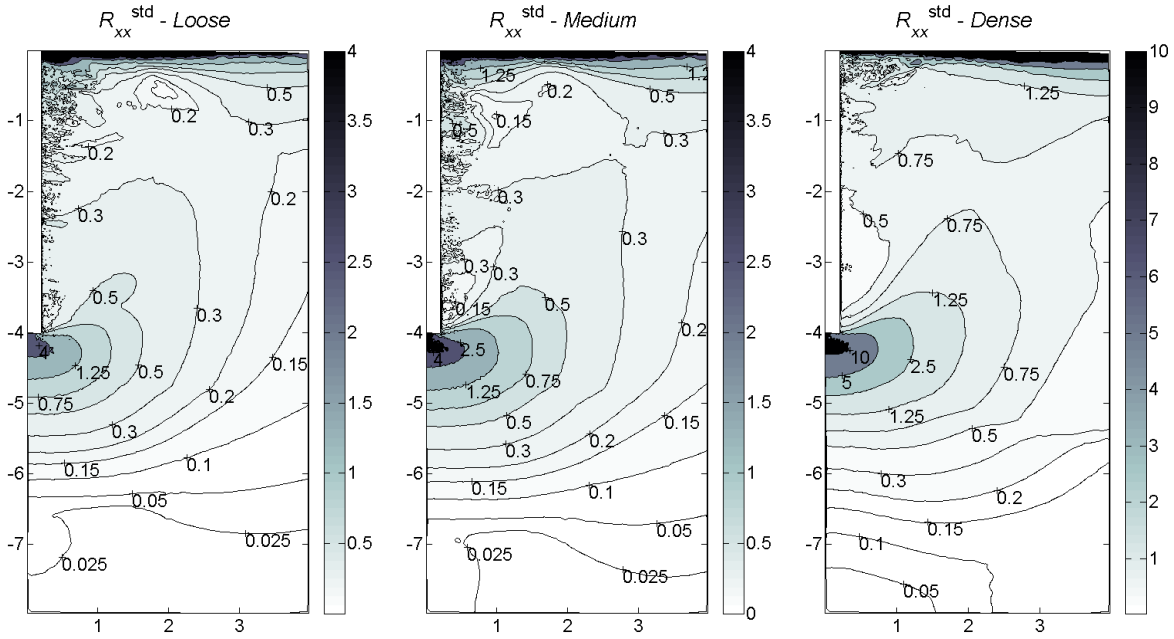

Figure 7. Standard deviation contours of R_{xx} for very loose, medium and dense cases.

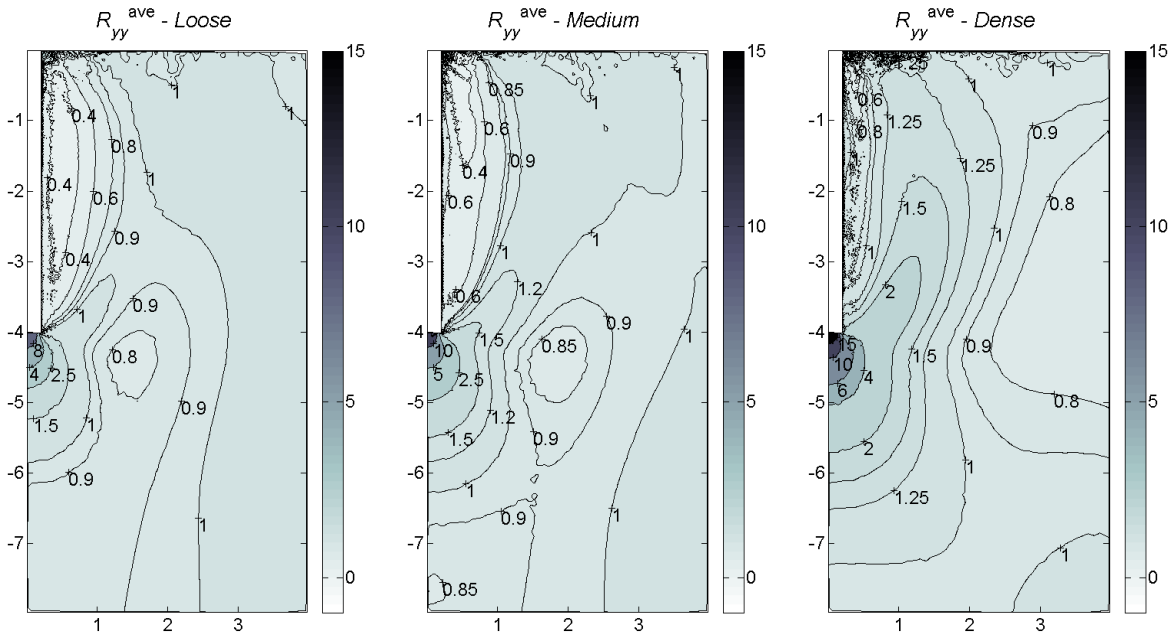

Figure 8. Average R_{yy} contours for very loose, medium and dense cases.

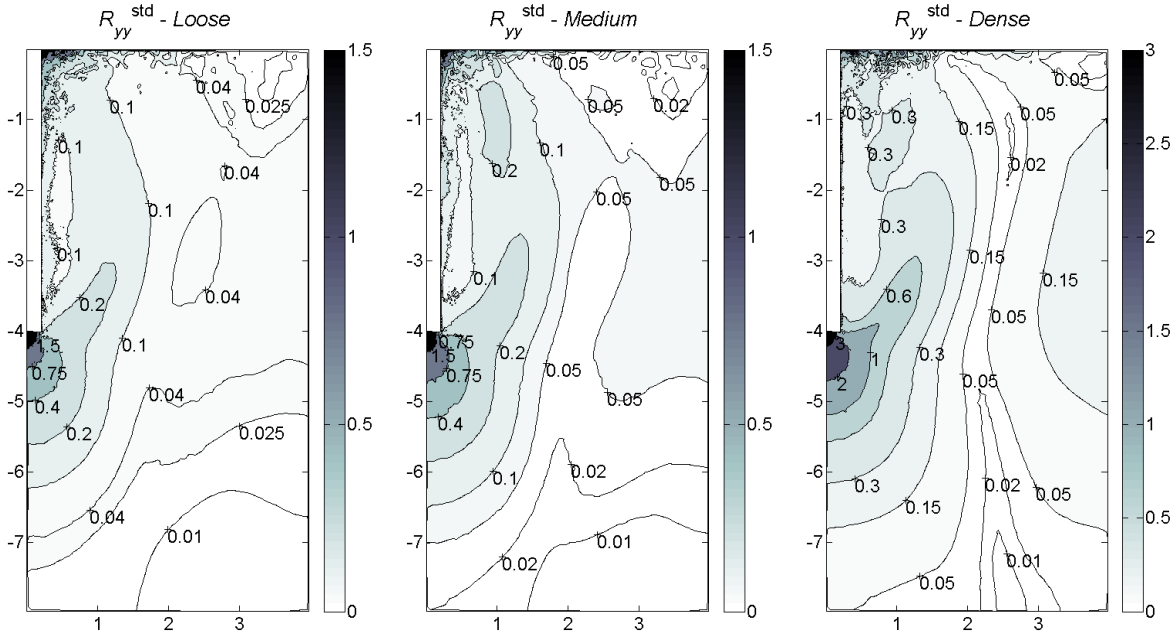

Figure 9. Standard deviation contours of R_{yy} for very loose, medium and dense cases.

4 DISCUSSION OF RESULTS

In the previous part contour plots of average states as well as the variations due to pile installation in seven different sands with different densities were given. Considering the purpose of this study, a general trend for each relative density, *RD* was investigated.

In a first glance the general behaviour obtained for horizontal (R_{xx}) and vertical (R_{yy}) stress changes and especially the density changes (R_e) seem to be consistent with literature. The aim, qualifying and quantifying installation effects for different relative densities seem to be

convenient especially for the density changes (R_e) as the variation is quite low for all three densities. However higher variations obtained for horizontal (R_{xx}) and vertical (R_{yy}) stress changes. This makes the generalization probably be less accurate if relative density would be chosen as the only variable affecting stress changes due to pile installation. The cases will be discussed separately and in details in coming paragraphs. We would like to mention that peak values are obtained especially in the near stress free surface, which is more of a numerical issue (due to zero or very low mean stress levels). Therefore the discussions will be focused on the changes near the pile and the deeper levels.

It can be seen from Figure 4. that there is more or less pure compaction for the average behaviour of the very loose cases (RD=20%). This behaviour is quite clear as the shearing will not be enough to cause dilation. For denser cases (RD=40% & 75%) dilation is observed near the pile shaft, which is well expected. For the dense case dilation is also observed under the tip, which is already reported by a set of centrifuge experiments with density measurements by Dijkstra (2009). Similar trend is observed by numerical simulations (Henke, 2010; Pham et al., 2010).

Higher stress increase is observed under the tip for all relative densities (Figs. 6 & 8). These values are higher for dense cases. The variations in stresses also increase with higher relative density (Figs. 7 & 9). This can be attributed to the influence of stiffness. The stiffness values, which can be quantified easily from the oedometric (Fig. 4) and triaxial compression responses (Fig. 5), vary and are not well distributed for all seven cases. Horizontal stress increase near the pile is not as much as the tip (Fig. 6) and decrease is observed for vertical stresses (Fig. 8). During the penetration process, the principle stresses near the pile shaft rotate (Lehane, 1992; Chow, 1996), which give in return a vertical stress reduction near the pile shaft.

As can be seen from all contour plots there are some concentrations especially near the pile and also near the surface. These are mainly numerical issues and for the pile, interface elements are employed to reduce these effects. However, unlike several numerical simulations based on contact and/or Arbitrary Lagrangian-Eulerian (ALE) techniques (Mahutka et al., 2006; Sheng et al., 2007; Henke & Grabe, 2009) or Material Point Method (MPM) techniques (Vermeer et al., 2008), the pile tip is flat here and with sharp corner towards the shaft; therefore concentrations near this region could not be avoided.

The results encourage the idea of generalization of installation effects and further elaborations on this modelling technique.

5 CONCLUSIONS

In this study sets of sand parameters have been analysed for three different densities to with the purpose to quantify pile installation effects in an attempt to find a trend for different state variables, namely void ratio, horizontal and vertical stress changes. The final purpose is to be able to generate the 'installation state' after pile installation without actually simulating the penetration process itself. This way the installation field will be generated and the performance in practical applications (in terms of pile and soil behaviour) can be further improved, e.g. for piled foundations, piled rafts, etc.

The results seem to be promising especially for void ratio changes since the variation is quite low for this parameters. Even though the variation for the horizontal and vertical stress changes is higher as compared to void ratio changes, they can still be used to estimate these changes in real pile penetration problems at least as a first estimate. The results would possibly be improved by considering the stiffness, e.g. granular hardness, h_s, and strength parameters, e.g. critical state friction angle, ϕ_c, etc. besides the relative density.

The prediction of jacked piles has been always a challenge and many researchers investigated different cases to model the process and hence changes of the soil properties

involved. In this study a simple numerical small deformation ('Press-Replace') technique is explained and used to investigate the installation effects due to pile jacking in sand. We are aware of the limitations of the model used to investigate installation effects. However, despite the limitations, the method enables us to make a further step in attempt to come up with a general solution to the generation of pile installation effects for practical applications.

ACKNOWLEDGEMENTS

The authors would like to thank to Dr. Paul Bonnier for his sincere help and support throughout the numerical study. This research is supported by the Dutch Technology Foundation STW, which is the applied science division of NWO, and the Technology Programme of the Ministry of Economic Affairs."

REFERENCES

Andersen, K. H., Andresen, L., Jostad, H. P., & Clukey, E. C. (2004), "Effect of Skirt-Tip Geometry on Set-Up Outside Suction Anchors in Soft Clay", ASME Conference Proceedings' 04(37432), 1035-1044.

Aranov, A. M., & Gudakov, Y. S. (1977), "Evaluating the bearing capacity of driven piles in sandy soils", Soil Mechanics and Foundation Engineering, 14(1), 28-30.

Basu, P., Loukidis, D., Prezzi, M., & Salgado, R. (2010), "Analysis of shaft resistance of jacked piles in sands", International Journal for Numerical and Analytical Methods inGeomechanics, Early View, Article first published online: 22/09/10, DOI: 10.1002/nag.968, http://dx.doi.org/10.1002/nag.968.

Bauer, E. 1996. "Calibration of a comprehensive hypoplastic model for granular materials", Soils and Foundations 36(1):13-36.

Broere, W., & van Tol, A. F. (2006), "Modelling the bearing capacity of displacement piles in sand", Proceedings of the ICE - Geotechnical Engineering, 159(3), 195-206.

Chow, F. C. (1996) Investigations into the behaviour of displacement piles for offshore foundations, PhD Dissertation, University of London, London, UK.

Deeks, A. D., White, D. J., & Bolton, M. D. (2005), "A comparison of jacked, driven and bored piles in sand", Proceedings of the 16th International Conference on Soil Mechanics and Geotechnical Engineering, Vols 1-5, 2103-2106.

Dijkstra, J. (2009), On the Modelling of Pile Installation, PhD Dissertation, Delft University of Technology, Delft, The Netherlands, ISBN:978-90-8570-432-4.

Dijkstra, J., Broere, W., & Van Tol, A. F. (2006), "Experimental investigation into the stress and strain development around displacement pile", In Proceedings of the Tenth International Conference on Piling and Deep Foundations, pp. 252–259.

Dijkstra, J., Broere, W., & Van Tol, A. F. (2007), "Numerical investigation into stress and strain development around a displacement piles in sand", In Proc. of 10th Int. Symp. on Numerical Models in Geomechanics, NUMOG X, Rhodes, pp. 461–466.

Engin, H. K., & Andresen, L. (2011), "Comparison of zipper type techniques for finite element analysis of pile penetration problem", Proc. of 13th International Conference of the International Association for Computer Methods and Advances in Geomechanics, Melbourne, Australia, accepted for publication.

Henke, S. (2010). "Influence of pile installation on adjacent structures". International Journal for Numerical and Analytical Methods in Geomechanics, 34(11), 1191-1210.

Henke, S., & Grabe, J. (2009). "Simulation of pile driving by 3-dimensional finite element analysis". International Journal for Numerical and Analytical Methods in Geomechanics, Early View, Article first published online: 26/10/09, DOI: 10.1002/nag.859, http://dx.doi.org/10.1002/nag.859

Johansson, J., & Konagai, K. (2007). “Fault induced permanent ground deformations: Experimental verification of wet and dry soil, numerical findings' relation to field observations of tunnel damage and implications for design”. Soil Dynamics and Earthquake Engineering, 27(10), 938-956.

Lehane, B. (1992), “Experimental investigations of pile behaviour using instrumented field piles”, PhD Dissertation, University of London, London, UK

Mahutka, K.-P., König, F., & Grabe, J. (2006), “Numerical modelling of pile jacking, driving and vibratory driving”. In Proc. of Int. Conf. on Numerical Simulation of Construction Processes in Geotechnical Engineering for Urban Environment (NSC06), Triantafyllidis T (ed.). Bochum, Balkema: Rotterdam, 2006; 235–246.

Masin, D. (2010), “PLAXIS implementation of hypoplasticity”, Delft, The Netherlands.

Niemunis, A., & Herle, I. (1997), “Hypoplastic model for cohesionless soils with elastic strain range”, Mechanics of Cohesive-Frictional Materials 2, pp. 279-299.

Pham, H. D., Engin, H. K., Brinkgreve, R. B. J., & van Tol, A. F. (2010), “Modelling of installation effects of driven piles using hypoplasticity”, In Proc. of the 7th NUMGE Numerical Method in Geotechnical Engineering, Trondheim, Norway.

Rondón, H., Wichtmann, T., Triantafyllidis, T., & Lizcano, A. (2007), “Hypoplastic material constants for a well-graded granular material for base and subbase layers of flexible pavements”. Acta Geotechnica, 2(2), 113-126.

Said, I., De Gennaro, V., & Frank, R. (2008), “Axisymmetric finite element analysis of pile loading tests”. Computers and Geotechnics, 36(1-2), 6-19.

Sheng, D., Wriggers, P., & Sloan, S. W. (2007), “Application of Frictional Contact in Geotechnical Engineering”. International Journal of Geomechanics, 7(3), 176.

Vermeer, P. A., Beuth, L., & Benz, T. (2008), “A Quasi-Static Method for Large Deformation Problems in Geomechanics”, In Proc.of the 12th International Conference of International Association for Computer Methods and Advances in Geomechanics (IACMAG), 1-6 October 2008, Goa, India, pp. 55-63.

von Wolffersdorff, P. A. (1996), “A hypoplastic relation for granular materials with a predefined limit state surface”. Mechanics of Cohesive-frictional Materials, 1(3), 251-271.

White, D. J. (2002), “An investigation into the behaviour of pressed-in piles”, PhD Dissertation, Univesity of Cambridge, Churchill College, Cambridge.

Yang, J., Tham, L. G., Lee, P. K. K., Chan, S. T., & Yu, F. (2006), “Behaviour of jacked and driven piles in sandy soil”. Geotechnique, 56(4), 245-259.

UPPER BOUND ANALYSIS FOR PLATE ANCHORS BASED ON BLOCK SET MECHANISM

M.S. Huang, S.B. Yu
Department of Geotechnical Engineering, Tongji University, Shanghai, China

Y.L. Liu
Research Institute of Highway Ministry of Communications, Beijing, China

ABSTRACT: *Plate anchors are employed in the foundation systems for structures requiring uplift resistance, such as transmission tower, retaining wall and mooring system for offshore floating oil and gas facilities. Although many researchers have proposed approximate techniques to estimate the ultimate pullout capacity of plate anchors in various soil types, the failure mechanism for anchors in cohesive soils remains unclear. In this paper, a novel mechanism for constructing kinematically admissible velocity fields in the upper bound limit analysis, entitled the Block Set Mechanism, is introduced to examine the pullout capacity and failure mechanism of strip anchors in clay. It is based on a basic block set, which is formed by a number of triangular rigid wedges, and the construction of admissible velocity fields can be simplified to a combination of several basic block sets. An application to upper bound analysis of shallow strip anchor in clay is given to illustrate the utility and effectiveness of the proposed mechanism. Detailed comparisons with results obtained from other approaches are presented. The aim of this research is to obtain the failure surface of plate anchor at different embedment depth and to develop pullout capacity solutions for plate anchors that can be used by design engineers. The Block Set Mechanism is based on a very simple concept and can be a reference for the practical design.*

1 INTRODUCTION

Plate anchors are employed in the foundation systems for structures requiring uplift resistance such as transmission towers, retaining wall and mooring system for offshore floating oil and gas facilities. Most of the early research on plate anchors used limit equilibrium (Meyerhof and Adams 1968) and empirical methods from laboratory model tests (Das 1980; Murray and Geddes 1987; Das and Puri 1989). Although the limit equilibrium method provides a simple and useful way of analyzing the stability of geotechnical structures, an arbitrary failure surface must be assumed *a priori* to calculate the limit bearing capacity.

Alternatively, other solutions were obtained using finite element analysis (Rowe and Davis 1982; Thorne et al. 2004; Yu et al. 2009) and limit analysis. There are two main approaches that have been followed so far in the limit analysis to improve the calculation of the pullout capacity of anchors in clay. One approach is to combine the limit analysis with finite element method and linear/nonlinear programming (Sloan and Kleeman 1995; Merifield et al. 2001; Merifield et al. 2005). It provides a useful way of analyzing the pullout capacity of plate anchors, but instead of the explicitly assumed failure surface, velocity vector field can only be given after optimization. The other approach is to use a multi-rigid-block mechanism (Rowe 1978; Gunn 1980) to obtain an upper bound solution. Due to the difficulty

in manually constructing kinematically admissible velocity fields, the multi-rigid-block method is often difficult to obtain a solution with sufficient accuracy.

In the present study, a novel mechanism for constructing kinematically admissible velocity fields in the upper bound limit analysis, entitled the Block Set Mechanism, is introduced to examine the pullout capacity and failure mechanism of strip anchors in clay. It is based on a basic block set, which is formed by a number of triangular rigid wedges, and the construction of admissible velocity fields can be simplified to a combination of several basic block sets. The failure surface and upper bound solution obtained in this study not only provide the engineer with a physical feeling for how the soil mass may fail, but also provide a useful check on the collapse load obtained from numerical finite element schemes. The aim of this research is to obtain explicit failure surface and to develop pullout capacity solutions for plate anchors that can be used by design engineers.

An application to upper bound analysis of shallow strip anchor in clay is given to illustrate the utility and effectiveness of the proposed mechanism. Detailed comparisons with results obtained from other approaches are presented. The Block Set Mechanism is based on a very simple concept and can be a reference for the practical design.

2 BASIC BLOCK SETS

The basic block sets with a polar coordinate system in the clockwise or counterclockwise direction shown in Fig. 1 is considered, where the point *O* is the pole and ρ_i is the radius. To facilitate presentation, the triangle wedges are numbered as ①,②,③,④…; and θ_1 and θ_2 are the start angle and stop angle of the basic block set. Thus, the swept area of basic block set is confined to the range θ_1 to $2\pi - \theta_2$. Now consider the case in the clockwise direction which is shown in Fig. 1(b). In this case, the parameters of the triangle wedge numbered *i* are given in Fig. 2, where α_i, β_i and $\delta\theta_i$ are the three angles of the triangle wedge *i*; d_i, ρ_i and ρ_{i+1} are the three sides respectively; ξ_{i+1} is the angle between d_i and d_{i+1}; v_i is the velocity of triangle wedge *i*; and $v_{r(i+1)}$ is the relative velocity of the triangle wedge *i+1* with respect to the triangle wedge *i*. According to the normality rule, the velocity jump on every discontinuity surface should be inclined at an angle φ with the surface, where φ is the friction angle of the soil in which the discontinuity surface lays.

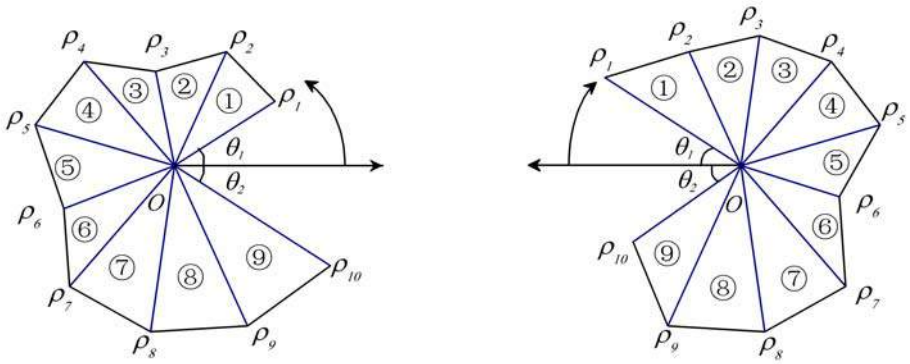

（a）Counterclockwise （b）Clockwise

Fig. 1 Schematic view for basic block sets

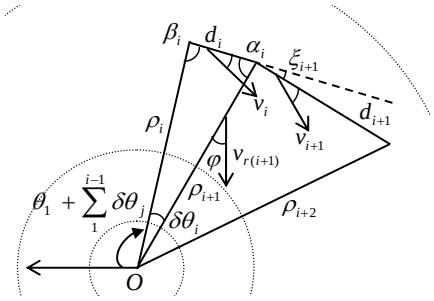

Fig. 2 Parameters of triangular wedge *i*

Geometrical characteristics of the triangular wedge *i* are presented in the following equations:

$$d_i = \sqrt{\rho_i^{\,2} + \rho_{i+1}^{\,2} - 2\rho_i\rho_{i+1}\cos\delta\theta_i} \tag{1}$$

$$\alpha_i = \arccos\left(\frac{d_i^{\,2} + \rho_{i+1}^{\,2} - \rho_i^{\,2}}{2d_i\rho_{i+1}}\right) \tag{2}$$

$$\beta_i = \pi - \alpha_i - \delta\theta_i \tag{3}$$

$$\xi_i = \pi - \alpha_{i-1} - \beta_i \tag{4}$$

$$\zeta_{i+1} = \zeta_i + \xi_{i+1} \tag{5}$$

where ζ_i is the azimuth of velocity v_i in the polar coordinate system, and $\zeta_1 = \theta_1 + \pi - \beta_1 + \varphi$.

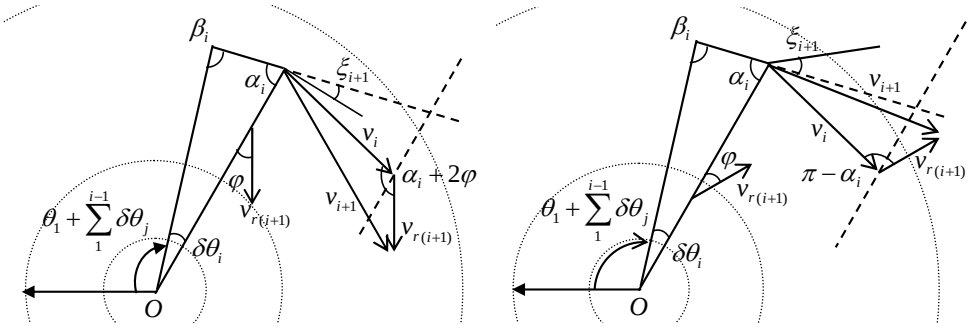

(a) $\xi_{i+1} \geq 0$ (b) $\xi_{i+1} < 0$

Fig. 3 Velocity hodograph

As shown in Fig. 3, the velocity hodograph for two adjacent wedges can be divided into two cases. The velocity of each triangle rigid wedge in the basic block set can be determined in a certain order.

Case 1: $\xi_{i+1} \geq 0$

From the velocity hodograph of Fig. 3(a), the angle between v_i and v_{i+1} is ξ_{i+1}; and the angle between v_i and $v_{r(i+1)}$ is $\alpha_i + 2\varphi$. Thus, the velocities v_{i+1} and $v_{r(i+1)}$ can be calculated from the velocity v_i as follows

$$v_{i+1} = \frac{\sin(2\varphi + \alpha_i)}{\sin(\beta_{i+1} - 2\varphi)} v_i \tag{6}$$

$$v_{r(i+1)} = \frac{\sin(\alpha_i + \beta_{i+1})}{\sin(\beta_{i+1} - 2\varphi)} v_i \tag{7}$$

where *i* takes values from 1 to *N-1* and *N* is the total number of triangular rigid wedges used in the basic block set.

Case 2: $\xi_{i+1} < 0$

From the velocity hodograph of Fig. 3(b), the angle between v_i and v_{i+1} is $-\xi_{i+1}$; the angle between v_i and $v_{r(i+1)}$ is $\pi - \alpha_i$. Thus, the velocities v_{i+1} and $v_{r(i+1)}$ are

$$v_{i+1} = \frac{\sin \alpha_i}{\sin \beta_{i+1}} v_i \tag{8}$$

$$v_{r(i+1)} = -\frac{\sin(\alpha_i + \beta_{i+1})}{\sin(\beta_{i+1})} v_i \tag{9}$$

For the basic block set, the total internal energy dissipated on the velocity discontinuities is given by the sum of the product of cohesion of soil *c*, relative velocity, length of each discontinuity and $\cos\varphi$.

$$E = \sum_1^N c d_i v_i \cos\varphi + \sum_2^N c \rho_i v_{r(i)} \cos\varphi \tag{10}$$

and the total work done by the weight of soil is

$$W = -\sum_1^N \gamma \frac{1}{2} \rho_i \rho_{i+1} \sin(\delta\theta_i) v_i \sin\zeta_i \tag{11}$$

where *c* and φ is the cohesion and internal friction angle of soil; and γ is the unit weight of soil.

Since the directions of weight for both the clockwise and counterclockwise cases are the same as $3\pi/2$, Eqs. (10) and (11) are also applicable in the case of counterclockwise order.

3 PULLOUT CAPACITY OF SHALLOW ANCHOR

3.1 Definition of Problem

Typically, soil anchors are used to transmit tensile forces from a structure to the soil. The analysis of anchor behavior can be divided into two distinct categories, immediate breakaway and no breakaway (Rowe and Davis 1982). Depending on their mode of failure, anchors can be further classified as shallow or deep ones. In the present paper, the immediate breakaway case where no suction forces exist between the anchor and soil was studied, which is illustrated in Fig. 4. Since the most of plate anchors are very stiff, a rigid plate anchor without thickness was assumed. In Fig. 4, *B* is the anchor size, *H* is the embedment depth of anchor, and Q_u is the ultimate load of plate anchor. The direction of pullout is perpendicular to the anchor face.

The ultimate pullout capacity of plate anchors in purely cohesive soil is usually expressed as a function of the undrained shear strength in the following form

$$q_u = \frac{Q_u}{A} = c_u N_c \tag{12}$$

where A is the area of anchor plate, c_u is the undrained shear strength of soil, and N_c is the pullout factor of plate anchor.

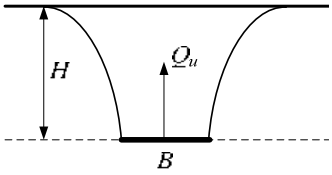

Fig. 4 Problem notation: shallow horizontal strip anchors

3.2 Admissible Velocity Fields of Shallow Anchor

According to the basic block set described above, the admissible velocity fields of shallow anchors can be constructed by a type of combination as shown in Fig. 5 and Fig. 6. Part ① and Part ② shown in Fig. 5(a) are the basic block sets, while Part ③ and Part ④ are the triangle rigid blocks. A continual curve was adopted here to indicate the swept area of basic block set. From the velocity hodograph of Fig. 5(b), v_3 and v_4 denote the velocities of blocks ③ and ④, v_1^0 and v_1^1 denote the velocities of start and end wedges of Part ①, and v_2^0 and v_2^1 are the velocities of start and end wedges of Part ②. v_{13} and v_{14} denote the relative velocities between Part ① and triangle block ③, and between Part ① and triangle block ④. v_{23} and v_{24} are the relative velocities between Part ② and triangle block ③, and between Part ② and triangle block ④. A detailed velocity hodograph is given in Fig. 7.

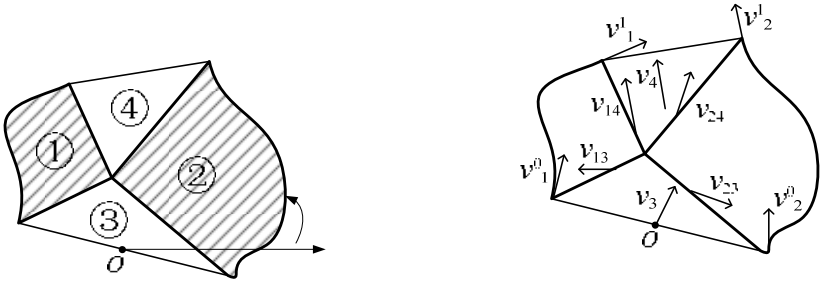

(a) Schematic view of the combination of block sets (b) Velocity hodograph

Fig. 5 Combination of basic block sets (Combination set A)

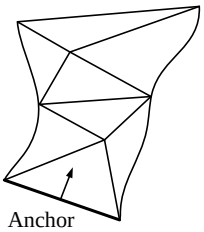

Fig. 6 Construction schematics of admissible velocity fields for shallow strip anchors

Hence, the unknown quantities can be solved by two vector identities shown in the following equations:

$$\overrightarrow{v_3} + \overrightarrow{v_{13}} = \overrightarrow{v_1^0} \tag{13a}$$

$$\overrightarrow{v_1^1} + \overrightarrow{v_{14}} = \overrightarrow{v_2^1} + \overrightarrow{v_{24}} = \overrightarrow{v_4} \tag{13b}$$

Note that Eq. (13b) may give two reasonable solutions. For the reason that the goal of upper bound analysis is to find the minimum solution, we just compare and choice the minimum one.

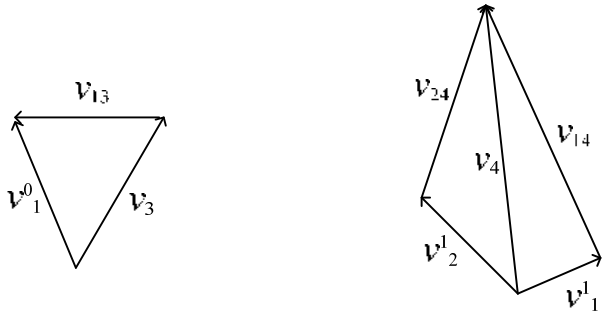

(a) Part ① and Block ③ (b) Block ④

Fig. 7 Velocity hodograph of Combination Set A

The total internal energy dissipation of Combination Set A from Part ①, Part ② and conjunctions of four parts is

$$E = E_1 + E_2 + c\rho_1^0 v_{13}\cos\varphi + c\rho_1^1 v_{14}\cos\varphi + c\rho_2^0 v_{23}\cos\varphi + c\rho_2^1 v_{24}\cos\varphi \tag{14}$$

where E_1 and E_2 can be given by Eq. (10).

The work done by the weight of soil in the four parts is

$$W = W_1 + W_2 + W_3 + W_4 \tag{15}$$

where W_1 and W_2 can be given by Eq. (11).

Construction of admissible velocity fields for shallow horizontal strip anchors is shown in Fig. 6, in which two combination sets A were adopted. According to the upper bound theorem (Chen 1975), the following inequality must be satisfied:

$$N_c \le \left(E' + E'' - W' - W''\right)/B\nu_0 c_u \tag{16}$$

where E' and E'' are the total internal energy dissipation in each combination set A，and it can be given by Eq. (14); W' and W'' are the total works done by the weight of soil in each combination set A, and it can be given by Eq. (15).

The initial shape of block set was randomly generated. Then the Optimization is required to find the minimum pullout factor of plate anchor, as well as corresponding failure surface. After the optimization was performed for specified number of triangle rigid wedges, more wedges were adopted by interpolation in order to provide greater accuracy in the

determination of pull out capacity and failure surface. In the present study, the final mechanism may contain more than three hundreds rigid wedges.

3.3 Results and Discussions

To illustrate the combination set A, the failure surface of shallow horizontal strip anchor after optimization is shown in Fig. 8, in which the detail of each combination set A is presented. The rigid wedges of each basic block set are schematically denoted by little circles and stars. The horizontal line in Fig. 8 is a borderline between two combination sets, and is indeed not a velocity discontinuity after optimization.

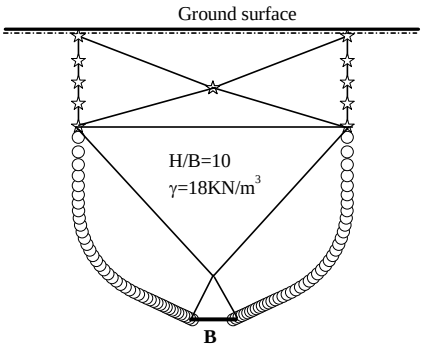

Fig. 8 Failure surface of shallow horizontal strip anchor after optimization (H/B=10)

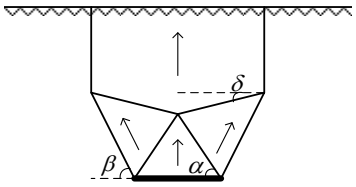

Fig. 9 Gunn's upper bound mechanism

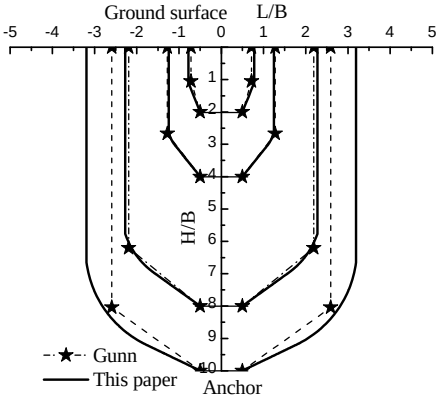

Fig.10 Comparison of failure surfaces at different embedment ratios

Gunn (1980) used the bound theorems to produce solutions for the case of a horizontal strip anchor and trapdoor respectively. The three-variable block mechanism proposed by Gunn (1980) is shown in Fig. 9. For comparison purposes, the failure surfaces at different embedment ratios (H/B) obtained by the proposed Block Set Mechanism and Gunn's solution

are shown in Fig. 10. It can be seen that the greatest improvement on the failure surface for greater embedment ratios (H/B>8) is provided by the Block Set Mechanism. Since the more blocks were adopted in the present study, the failure surface obtained in this paper is more precise than Gunn's.

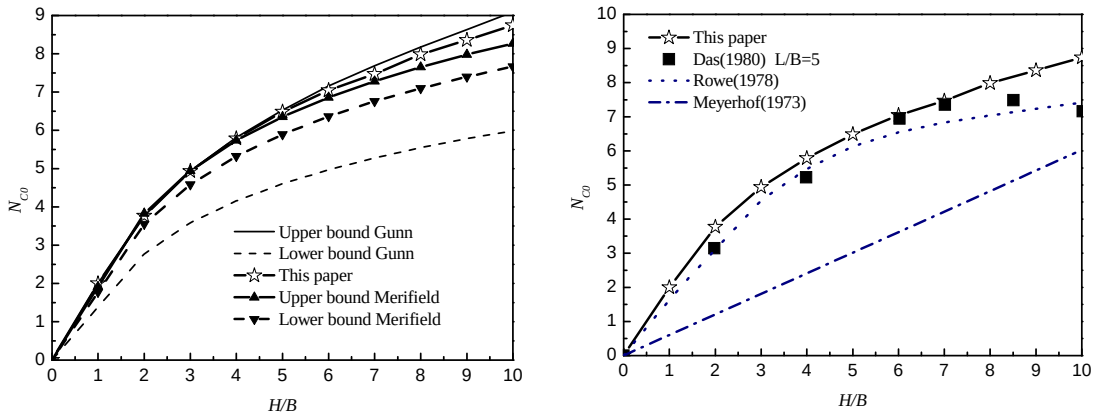

(a) Comparison with existing upper bound solutions (b) Comparison with existing laboratory test results

Fig. 11 Comparison of pullout capacity with existing solutions

Fig. 11(a) compares the solutions from the Block Set Mechanism with existing upper bound solutions. Here N_{c0} is the pullout factor of plate anchor without considering soil weight. It can be seen that the solutions of this paper is between the solutions of Gunn (1980) and the finite element limit analysis (Merifield et al. 2001). For anchors at small embedment ratios (H/B<4), these upper bound solutions are plot very close to each other.

The results considering soil weight show that the following equation representing the principle of superposition is valid:

$$N_c = N_{c0} + \gamma H / c_u \tag{17}$$

Values of the break-out factor N_{c0} obtained from the Block Set Mechanism can be approximated by the following equations:

$$N_{c0} = \frac{\pi}{2}\ln[\frac{3\pi}{4}(\frac{H}{B})^2 + 1] \tag{18}$$

4 CONCLUSIONS

Upper bound solutions based on the so-called Block Set Mechanism for the ultimate capacity of horizontal strip anchors have been presented. Emphasis has been given to the horizontal strip anchors in purely cohesive soil. Consideration has been given to the effect of anchor embedment depth, soil weight. A significant improvement on the failure surface for greater embedment ratios over that of Gunn (1980) has been achieved by the proposed mechanism. A relationship between the pullout capacity of plate anchors and simple parametric equations was developed to facilitate the use in solving practical design problems. The failure surfaces and upper bound solutions obtained in this study not only provide the engineer with a physical feeling for how the soil mass may fail, but also a reference for the practical design.

ACKNOWLEDGEMENTS

This research is supported by the National Science Fund for Distinguished Young Scholars of China through Grant No. 50825803.

REFERENCES

Chen, W. (1975), Limit analysis and soil plasticity, Elsevier Science & Technology.

Das, B. (1980). "A procedure for estimation of ultimate uplift capacity of foundations in clay". Soils and Foundations, Vol. 20(1): 77-82.

Das, B. & Puri, V. (1989), "Holding capacity of inclined square plate anchors in clay." Soils and Foundations, Vol. 29(3): 138-144.

Gunn, M. (1980), "Limit analysis of undrained stability problems using a very small computer", Proc. Symposium on Computer Applications to Geotechnical Problems in Highway Engineering, Cambridge University.

Merifield, R. S., Lyamin, A. V. & Sloan, S. W. (2005), "Stability of inclined strip anchors in purely cohesive soil". Journal of Geotechnical and Geoenvironmental Engineering, ASCE, Vol.131(6): 792-799.

Merifield, R. S., Sloan, S. W. & Yu, H. S. (2001), "Stability of plate anchors in undrained clay". Geotechnique, Vol.51(2): 141-153.

Meyerhof, G. & Adams, J. (1968), "The ultimate uplift capacity of foundations." Canadian Geotechnical Journal 5(4): 225-244.

Murray, E. & Geddes, J. (1987), "Uplift of anchor plates in sand." Journal of Geotechnical Engineering, ASCE, Vol.113(3): 202-215.

Rowe, R. (1978), Soil Structure Interaction Analysis and Its Application to the Prediction of Anchor Plate Behaviour. PhD thesis, University of Sydney.

Rowe, R. & Davis, E. (1982), "Behaviour of anchor plates in clay". Geotechnique, Vol.32: 9-23.

Sloan, S. W. & Kleeman, P. W. (1995), "Upper Bound Limit Analysis Using Discontinuous Velocity-Fields". Computer Methods in Applied Mechanics and Engineering 127(1-4): 293-314.

Thorne, C. P., Wang, C. X. & Carter, J. P. (2004), "Uplift capacity of rapidly loaded strip anchors in uniform strength clay." Geotechnique 54(8): 507-517.

Yu, L., Liu, J., Kong, X. J. & Hu, Y. X. (2009), "Three-dimensional numerical analysis of the keying of vertically installed plate anchors in clay". Computers and Geotechnics, Vol.36(4): 558-567.

A NUMERICAL STUDY OF FEASIBILITY OF USING STONE COLUMNS UNDER LOW-RISE BUILDINGS

D. Kamrat-Pietraszewska
Department of Civil Engineering, University of Strathclyde, Glasgow, United Kingdom

M. Karstunen
Department of Civil Engineering, University of Strathclyde, Glasgow, United Kingdom

ABSTRACT: *The paper considers the settlement and consolidation time reduction of a low-rise building foundation constructed on the soft soil deposit improved with floating stone columns. Coupled 3D FE analyses of the undrained construction and consolidation behaviour of the soft soil improved with columns have been performed with the advanced elasto-plastic S-CLAY1 model to account for the complexity of soft soil behaviour.*

1 INTRODUCTION

The case study considers a soft soil improved by floating stone columns under a residential building. In order to fulfil the project's requirements, special attention has been put on the performance of the stone columns after first three years of service. The granular columns are proposed as a support of a footing (raft foundation) in order to reduce the total and differential settlements, as well as to reduce the consolidation time required for full dissipation of the excess pore water pressures. The case study demonstrates a typical application for the stone columns for settlement reduction in geotechnical engineering.
To represent ground conditions for this case study, soil profile found on site of Bishopton, Scotland, is considered. Formerly location to an explosive-manufacturing Royal Ordnance Factory (ROF Bishopton), due to decontamination and remediation issues Bishopton site was for many years omitted in council's plans for residential and business development. In 2008 new planning consent has been granted, allowing for a redevelopment scheme and the construction of a motorway junction (Motorways A8/M8), BBC (2008).

2 SITE CHARACTERIZATION

Area of Bishopton is situated in approximately 15 km outside Glasgow in north-west direction on the estuary of River Clyde, see Fig. 1a. Recently, local council granted planning consent for residential and business development. The redevelopment on one of Europe's largest brownfield sites proposes construction of approximately 2000 homes, a community woodland park and facilities, as well as a business park. Moreover, construction of the new motorway function (Motorways A8/M8) has been planned, which elevates the significance of Bishopton site in Scotland.
A notable amount of ground investigation has been done in the area considered, including cone penetration tests (CPT), standard penetration tests, standard drilling using cable percussion method, piezometric measurements, particle size distribution analysis and laboratory triaxial compression and oedometer tests. Site investigation data has been available thanks to courtesy of Keller Foundation (UK). The data review indicated that the

soil profile consists of a layer of dry crust, which overlays a maximum of 6.7 m and 7 m of silty clay and soft clay, respectively. Below the clay layer a sandstone stratum is found, which forms a natural boundary for the geometry of considered in the case study. The groundwater table is located at a depth of 1.3 m. The soil profile assumed in the case study is shown in Fig. 1b.
Given the thickness of the clay layers, a scheme like this would typically involve piled foundations under all building structures in order to mitigate problems related total and differential settlements. This is not particularly environmentally friendly, sustainable and adaptable solution. Hence, for settlement reduction of the raft footing during construction and serviceability period, the use of floating stone columns have been investigated. Length and diameter of the granular columns have been selected to be 5.5 m (from footing level) and 0.6 m, respectively.

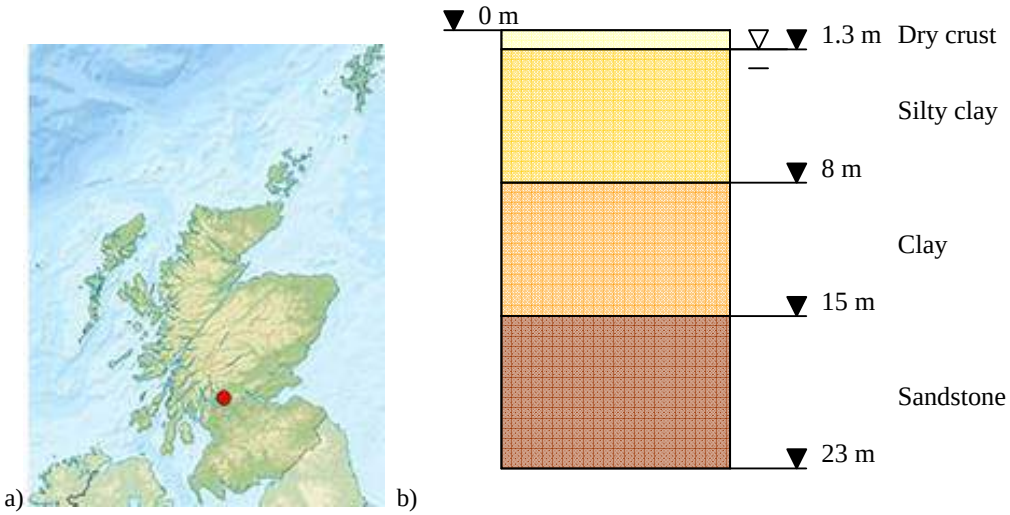

Fig. 1. Bishopton site: a) localisation b) assumed soil profile.

3 NUMERICAL MODEL

For all simulations PLAXIS 3D Foundation v.2.2 finite element has been used, taking advantage of three-dimensional modelling. A mesh with 8800 tetrahedral elements and approximately 960000 degrees-of-freedom has been used in simulations, see Fig. 2. At first, two-dimensional mesh with triangular elements has been created. Next, the mesh has been extended in depth direction forming three-dimensional shape. Mesh sensitivity studies have been done before performing the case study in order to reduce the influence of the mesh on the results of the simulations. The computational time required to calculate considered case study is approximately one day due to the great number of degrees-of-freedom in each of simulations. The soil is allowed to consolidate through the bottom and top boundaries of the model. In order to exclude any influences of the lateral boundary, the geometry model has been extended in both horizontal planes (X and Z) by approximately 2B laterally from the symmetry axis of the footing and 2B beneath the footing, where B is the footing width in X direction. Depth of the geometry model extends up to 23 m, see Fig. 2.

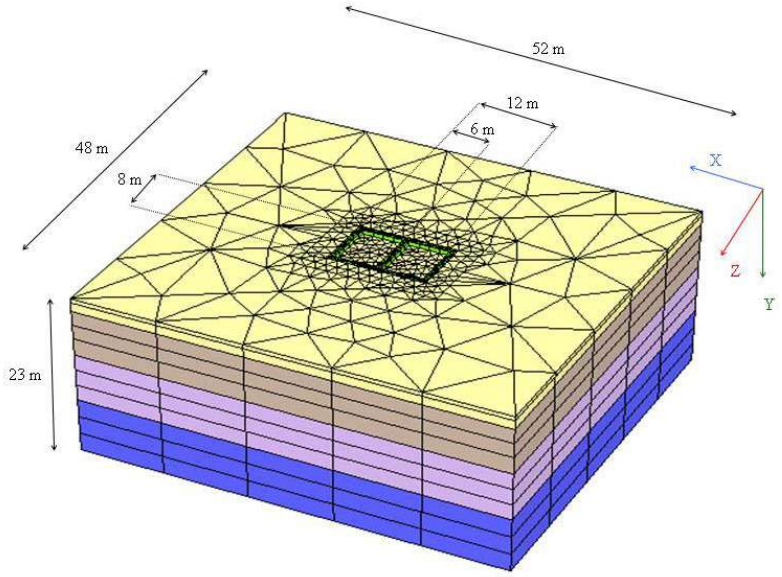

Fig. 2. Mesh and geometry of the problem.

3.2 Constitutive models used to represent soil deposit and stone column material

In order to simulate the complexity of the materials involved, three different constitutive models have been used in the finite element analyses. Each soil layer has been analysed using an appropriate constitutive model, in order to realistically represent the mechanical behaviour of the constituent. Both standard and advanced constitutive models are used for three-dimensional analysis of case study, taking advantage of the implementation of the S-CLAY1 model (Wheeler *et al.*, 2003) as a user-defined formulation in the commercial code PLAXIS 3D Foundation.

The slightly over-consolidated silty clay and clay layers, which are overlain by a dry crust, represent soft recently deposited marine sediments. Below the clay layer, a sandstone stratum forms a natural boundary for the soft deposit on Bishopton site. The dry crust material, sandstone and stone column material are simulated using the Hardening Soil (HS) model (Schanz, 1998). The behaviour of the materials is considered fully drained and material parameters are listed in Tab. 1-2.

The soft soil found at depth of 1.3 to 8 m at Bishopton site is classified as silty clay. The soil stratum lying below silty clay is classified as slightly sandy clay. Undrained shear strength is estimated to be in the range of 10-55 kPa based on undrained triaxial tests and CPT testing. One-dimensional compression tests on samples from the depth of 2.1-9.5 m allowed for study of the loading-unloading response of the soil and the yield stresses. Careful inspection of laboratory tests results showed unexpectedly low compressibility of the soft soil layers and low values of preconsolidation pressure, indicating high disturbance of the soil samples. Based on a desk study, soft soil at Bishopton site is expected to be in over-consolidated state with compressibility parameters similar to the soft clay from Bothkennar (for more information about Bothkennar clay please see Géotechnique 1992), although the Bishopton clay layers would be expected to be less homogeneous and structured than Bothkennar clay due to the differences in sedimentation environment. Given the difficulty in estimating the in-situ compressibility and the apparent OCR (over-consolidation ratio) of the soil at Bishopton, due to sample disturbance, for these preliminary analyses the soil is modelled as a normally consolidated and fully destuctured material. Hence, the compressibility values are assumed to correspond to the intrinsic compressibility λ_i. As Fig. 3 suggests, this can be considered as a very conservative assumption. For the sake of simplicity, the in-situ coefficient of the earth

pressure at rest K_0 is based on the equation given by Jaky (1948) and calculated to be equal to 0.5. Soil constants and variables describing soft soil deposit are listed in Tab. 3-4. Because the exact location of residential buildings is not yet known, the simulations consider the worst scenario from total settlement point of view (thickest clay layer).

Tab. 1. Stiffness parameters: HS model.

Material	γ	ν'_{ur}	$E_{50}^{ref} = E_{oed}^{ref}$	E_{ur}^{ref}
	[kN/m^3]	[-]	[kN/m^2]	[kN/m^2]
Dry crust	19.0	0.2	1720	5160
Sandstone	22.0	0.2	100000	200000
Stone column	19.0	0.3	80000	260000

Tab. 2. Additional parameters: HS model.

Material	k	c'	φ'	ψ	K_0	m
	[m/s]	[kN/m^3]	[^{o}]	[^{o}]	[-]	[-]
Dry crust	3.35x10^{-9}	0.1	27	12	0.700	0.55
Sandstone	2.31x10^{-8}	200	27	12	0.530	0.3
Stone column	1.97x10^{-4}	0.1	42	12	0.331	0.3

Tab. 3. Standard soil constants: S-CLAY1 model.

Material	γ	k	ν'	M	κ	λ_i
	[kN/m^3]	[m/s]	[-]	[-]	[-]	[-]
Silty clay	18.0	2.2x10^{-10}	0.2	1.2	0.015	0.133
Clay	18.0	2.5x10^{-10}	0.2	1.2	0.015	0.125

Tab. 4. Advanced soil constants and state variables: S-CLAY1 model.

Material	β	μ	e_0	K_0	OCR	α_0
	[-]	[-]	[-]	[-]	[-]	[-]
Silty clay	0.76	90	0.790	0.5	1.0	0.46
Clay	0.76	110	0.844	0.5	1.0	0.46

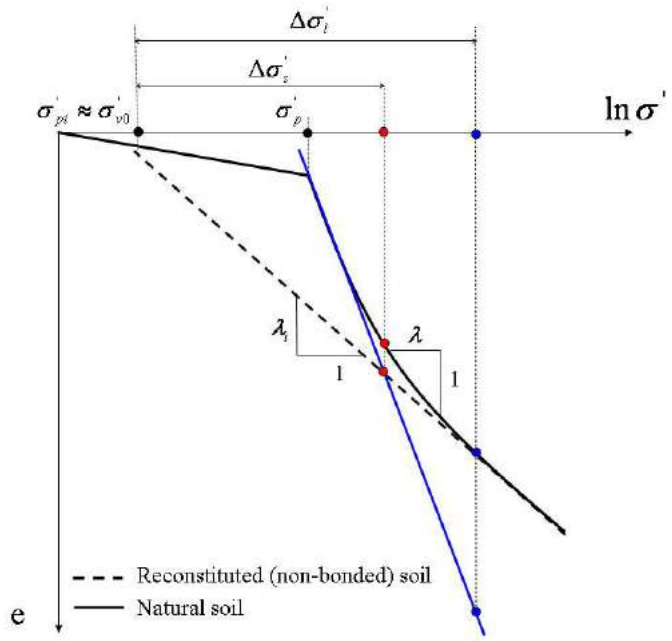

Fig. 3. Compressibility parameter for natural and reconstituted soil.

4 NUMERICAL PREDICTIONS

Numerical simulations consider a raft footing assumed the following sequence of site works: i) undrained construction of stone columns and footing with application of loading on top of raft footing, ii) consolidation (first period of service 3 years and consolidation until full dissipation, where the excess pore pressures are equal or less to 1 kPa). Construction of foundation is followed by application of distributed load on top of raft footing of 71.43 kN/m^3, which corresponds to 50 kN/m run of line load. For comparison, the analyses are also done for the case with no stone columns. One should note that floating stone columns in these analyses are simply 'wished-in-place' and that no installation effects are considered in this study. In fact, the installation of stone columns on structured soils not only results in increase of the excess pore pressures, but also reduces the amount of bonding (and sometimes also strength of the soil) next to the columns, as well as changes the anisotropy and the coefficient of earth pressure at rest, as shown by Castro & Karstunen (2010). Assuming the soil to be fully destructured, as done in these analyses, could be argued to represent to some extent the installation effects around the stone columns, but the areas below and outside the columns would not be influenced.

4.1 Vertical displacement and differential settlement

The plot of vertical displacements in respect to time needed for full dissipation of the excess pore pressures is shown in Fig. 4 for 4 selected points at foundation level. One can see that installation of floating stone columns reduces the total settlements by approximately factor of 1.5. In fact, the settlement reduction ratio s_r (defined as ratio between the settlement value with and without stone columns) varies with time, resulting in the lowest value after loading on top of footing is applied (simulated as undrained) and reaching value of 0.6703 after dissipation of the excess pore pressures. Additionally, one can see that the time required for full dissipation of the excess pore pressures is reduced by 40 % when floating stone columns are constructed in site of Bishopton. If no ground improvement is used, the time required for reaching excess pore pressure value equal or less 1 kPa is approximately 50 years and, with

stone columns in place, it reduces to approximately 30 years. As the soil deposit under the footing has been assumed homogeneous, differential settlements are not an issue, and even the predicted total settlements are small. The main advantage of the floating stone columns is that they virtually eliminate any ongoing settlements after the 3 year service period, whilst in the case with no columns about 40 mm is predicted.
The plots of the predicted settlement versus horizontal profile for cross-section A-A' and B-B' at the foundation level after the consolidation phase are shown in Fig. 5. In grey and red the outlines of the foundation and stone columns in both cross-sections are shown. One can see that in the cross-section A-A' underneath footing, where a row of six columns supports the raft foundation, almost uniform settlement is predicted for both cases (with and without floating columns). The differential settlement of raft foundation in cross-section A-A' after construction is found to be negligible in both cases, about 1/4000, and well within acceptable limits for British housing, which is equal to 1/500, NHBC (2010). Inspection of the Fig. 4b for cross-section B-B' shows how well floating stone columns carry the load applied and reduce the vertical displacements, leading to reduction of the settlements in between the footing slabs by 14 %. The differential settlement of raft foundation in cross-section B-B' is found to be negligible (1/1500) and well in acceptable differential settlements for housing, see NHBC (2010).

4.2 Effective stress distribution

Vertical effective stress contours along horizontal profile for the cross-section A-A' after construction and consolidation are plotted in Fig. 6 and 7, respectively for the case with stone columns. Detailed inspection of the improved zone reveals that the stress level attracted by stone columns is much greater than that attracted by the surrounding soil. As floating stone column are considered, the granular columns do not transfer the load into rigid stratum but into surrounding soil as a part of load transfer process along their shaft. This process can be seen on each figure: in upper part of plot granular material transfers more load than the surrounding soil. Then, at column tip level the load is transferred by columns to the soil underneath are equal to the stresses transferred between the columns. The 'neutral point', where the amount of load held by column and surrounding soil is of the same value, is found to be at depth of approximately 4 m.
In order to fully investigate the influence of the stone column on the stress-strain behaviour of the soil deposit, the incremental vertical effective stresses for cross-section A-A' are plotted along the horizontal profile, where the stress increment is defined between the stages of 3 years into consolidation process (first 3 years of foundation service) and the initial phase of the FE calculations, see Fig. 8. A positive incremental stress value means that after first 3 years of service the vertical effective stress found in soil mass is greater than generated initial stresses, whereas a negative value indicates that after consolidation the vertical effective stress is reduced in respect to initial vertical stresses. Some small negative values are predicted due to numerical round-off errors. The installation of the stone columns affects the area directly underneath the footing only. As expected, due to the high stiffness of the granular material the columns attract more vertical effective stress than the surrounding soil.

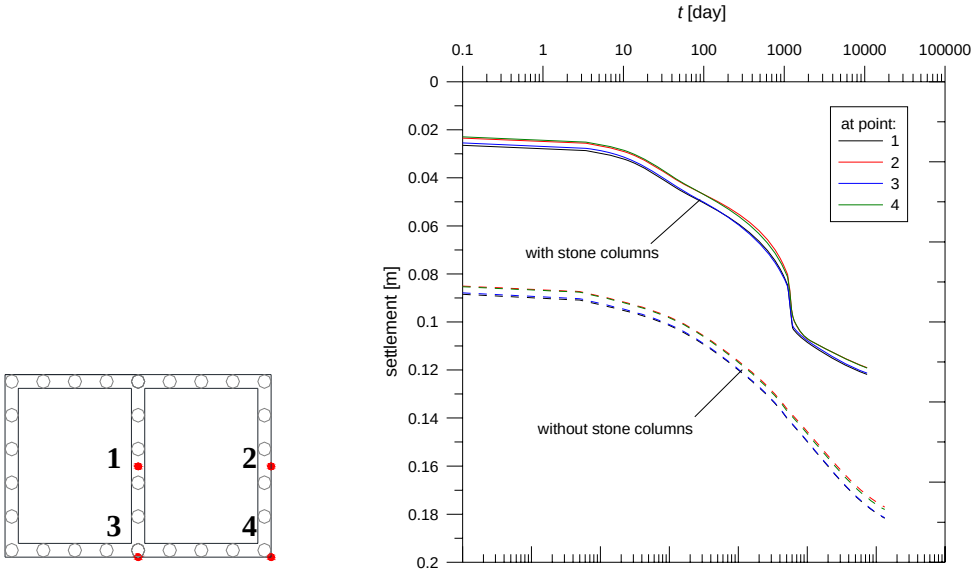

Fig. 4. Evolution of settlement with time.

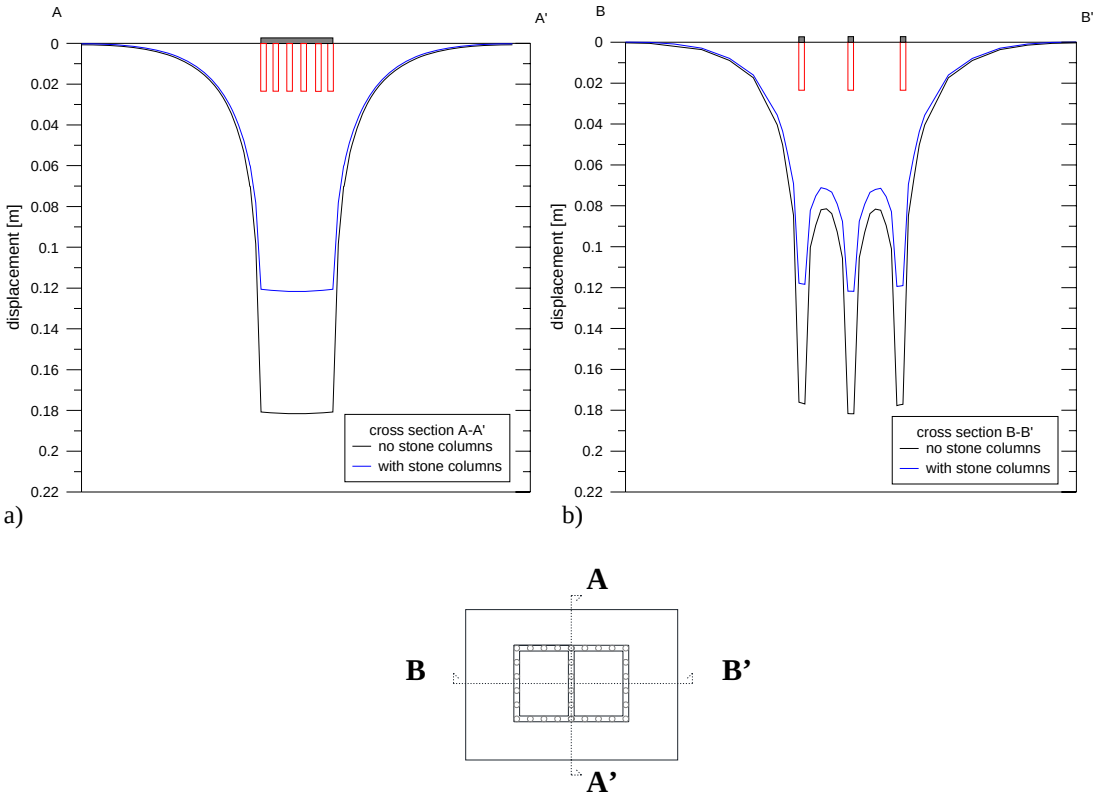

Fig. 5. Settlement at the foundation level at the end of consolidation for cross-section: a) AA' b) BB'.

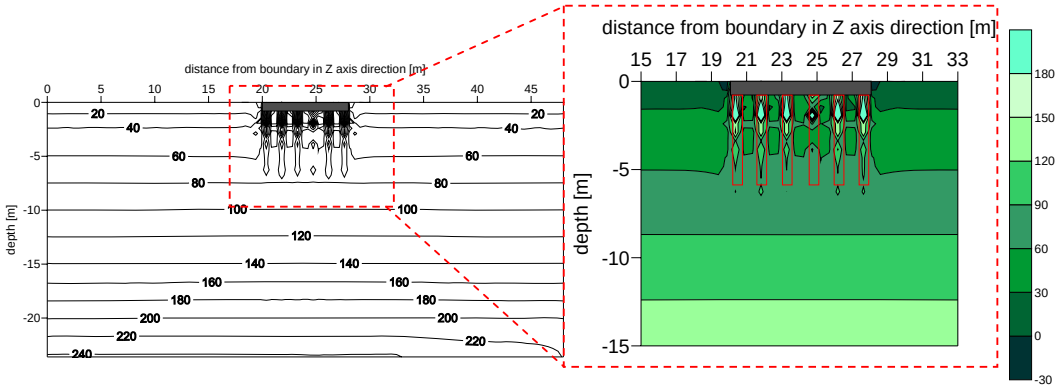

Fig. 6. Vertical stress contours after construction, cross-section A-A'.

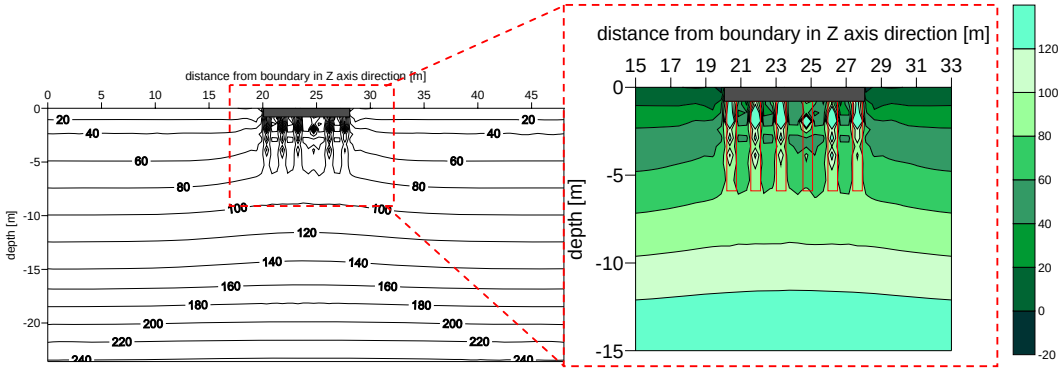

Fig. 7. Vertical stress contours at the end of consolidation, cross-section A-A'.

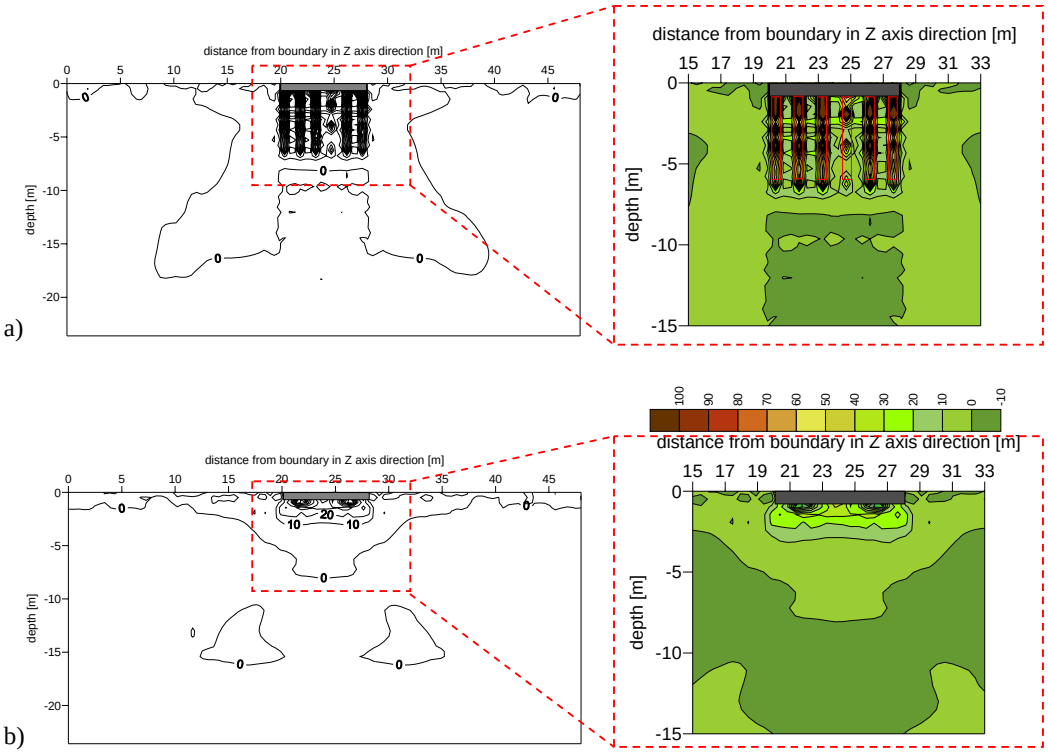

Fig. 8. Incremental vertical effective stress contours (3 years), cross-section A-A': a) with b) without columns.

4.3 Excess pore pressures and time of consolidation

The excess pore pressures contours after 3 years of consolidation along the cross-section A-A' for case with and without stone columns are plotted in Fig. 9. Again, geotechnical sign convention has been applied for those plots and due to space saving plots are limited to improved area only. As the top consolidation boundary remained open during the consolidation phase, the lowest excess pore pressure values are found at the top of the geometry model. One can see that the effect of the stone columns in reduction of the excess pore pressure value is significant. The excess pore pressure value is reduced by approximately 2 times during the considered serviceability period (3 years into consolidation) in the area where stone columns are installed. Some excess pore pressures concentration in the untreated area is evident, see Fig. 9. Below the tips of the stone columns (and also in close vicinity) and in improved area the excess pore pressures decay so efficiently that the zero value is registered.

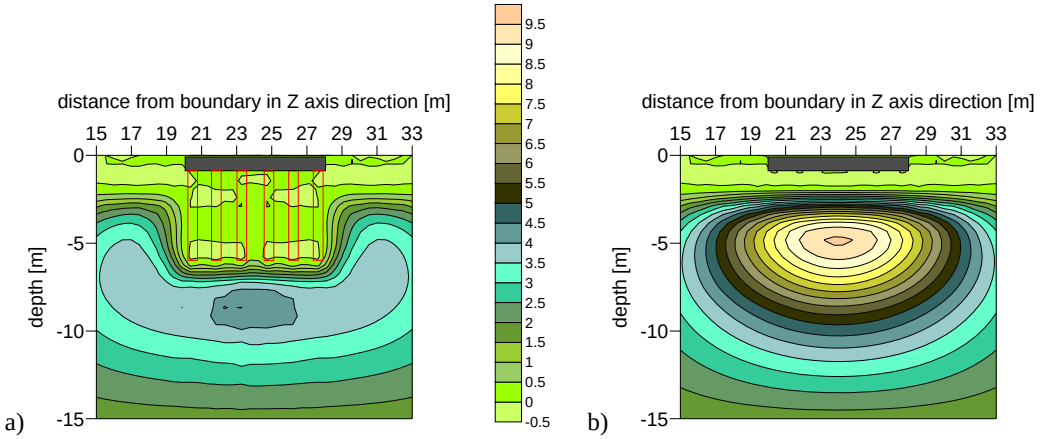

Fig. 9. Excess pore pressure contours for cross-section A-A' 3 years into consolidation: a) with b) without columns.

5 CONCLUSIONS

Feasibility of using floating stone columns settlement reduction of a foundation is studied, considering a soft soil stratum on a site in Bishopton site (Scotland). Due to the thick clay layers, any residential buildings on the site considered would typically have piled foundations. In current case study, floating stone columns, which have been simply 'wished-in-place', are considered as a more sustainable alternative than piling. Providing that the excess pore pressures created by the stone columns installation are allowed to dissipate before construction of the buildings commences, it is recognised that the installation effects are likely to be very beneficial. Application of the stone columns in Bishopton case study resulted in predictions of the settlement reduction by approximately 50 % and speeding up of the excess pore pressure dissipation process by a factor of approximately 1.6. Moreover, it has been demonstrated that floating stone columns are very effective in reducing the ongoing settlements after the three year serviceability period, which is important from the point of view of contractors' liability. The simulations suggest that in the case of Bishopton, despite of rather thick clay layers involved, piling is not necessary.

Simulations have been performed using advanced constitutive S-CLAY1 model (accounting for plastic anisotropy) implemented in the three-dimensional commercial finite element code. Due to poor quality and high disturbance of the soil samples, an assumption of normally consolidated and fully destructured soft soil deposit has been made. This can be considered as

conservative, given that any apparent over-consolidation is ignored. However, natural soft soils tend to have a very high compressibility and creep rate at the onset of yielding. As a result, in the case of no ground improvement for a lightly over-consolidated soil notably larger deformations than estimated by the current simulations would be predicted. In the area with stone columns, the assumption of full destructuration can be justified, but in parallel, there would be expected to be a total rotation of anisotropy due to stone columns installation, as demonstrated by Castro & Karstunen (2010), which would also influence the stress-strain response. This will be subject of further numerical studies. Furthermore, is the case of floating stone columns, it would be extremely important to estimate accurately the compressibility of the natural clay layers underneath the stone columns. For more detailed and reliable numerical modelling of this case study, further site investigation and sampling with highest possible sample quality is strongly recommended. It is essential to ensure high sample quality in order to minimise the soil disturbance. In particular this is important, if a case that no ground improvement is used is considered.

ACKNOWLEDGEMENT

The research leading to these results has been partly funded from the 7th Framework Programme (FP7/2007-2013 under grant agreement PIAG-GA-2009- 230638). The findings reflect only the authors' views and the EC is not liable for any use that may be made of the information contained therein.

REFERENCES

BBC (2008). http://news.bbc.co.uk/go/pr/fr/-/1/hi/scotland/glasgow_and_west/7784474.stm, Published 15 December 2008, Accessed 20 September 2010.

Castro J. & Karstunen M. (2010). Numerical simulations of stone column installation. Can. Geotechnical J. 47(10), pp. 1127-1138.

Géotechnique 42(2), 1992. Bothkennar soft clay test site: characterization and lessons learned, *Symposium in print, Institution of Civil Engineers, London.*

Jaky J. (1948) Pressure in soils, *2nd ICSMFE*, London, Vol. 1, pp. 103-107.

National House Building Council Standards NHBC (2010). *Efficient design of piled foundations for low-rise housing. Design guide.* Building Research Establishment Ltd. Press.

Schanz, T. (1998). Zur Modellierung des Mechanischen Verhaltens von Reibungsmaterialen, Habilitation, Univertity of Stuttgart, Germany.

Wheeler, S. J., Näätänen, A., Karstunen, M. & Lojander, M. (2003). An anisotropic elastoplastic model for soft clays. *Can. Geotechnical Journal 40*, pp. 403-418.

APPLICATION OF PARTIAL FACTORS OF SAFETY IN NUMERICAL ANALYSIS OF BEARING CAPACITY

D.M. Potts
Department of Civil and Environmental Engineering, Imperial College London, UK

L. Zdravkovic
Department of Civil and Environmental Engineering, Imperial College London, UK

ABSTRACT: *One of the issues that arise when using numerical analysis in accordance with Eurocode 7 is how to account for partial factors of safety on material strength. Namely, Eurocode 7 implies that strengths to be used in an analysis should be based on a design value, but reduced by partial factors. This can be done in two ways, but Eurocode 7 gives no guidance as to which one is more appropriate. This paper examines the application of partial factors of safety in a bearing capacity problem. Finite element analyses are performed using both a simple Tresca and a more advanced Modified Cam Clay models to represent soil behaviour, and both approaches for the application of partial factors of safety.*

1 INTRODUCTION

As of 2010 Eurocode 7 (EC 7) has become the primary geotechnical design code in Europe, thus effectively replacing the existing national codes. One of the main novelties in EC 7 has been the introduction of partial factors of safety, as opposed to the previous single global factors of safety, which has also led to the development of three different design approaches within the EC 7. Where and how the partial factors of safety are applied in the design of geotechnical structures has been discussed, amongst others, by Simpson (2000), Bauduin et al. (2003), Simpson (2007), Cheung et al. (2010).

Furthermore, compared to previous codes, EC 7 is not as prescriptive of the type of geotechnical analysis to be performed for a certain problem and encourages the use of numerical analysis (e.g. finite elements, finite differences). However, it does not provide any guidance as to how the partial factors of safety should be applied in conjunction with numerical analysis. Some work in this area has been done by Bauduin et al. (2000), Schweiger (2005), Schweiger et al. (2010).

Application of partial factors of safety implies that the material strength used in an analysis is based on the design strength, but reduced by partial factors of safety. For analyses based on undrained strength, S_u, the strength used in an analysis, $S_u^{analysis}$, is estimated as:

$$S_u^{analysis} = \frac{S_u^{design}}{F_s} \tag{1}$$

whereas for analyses based on drained strength, ϕ', the strength used in an analyses, $\phi'^{analysis}$, is estimated as:

$$\phi'^{analysis} = \arctan\left(\frac{\tan\left(\phi'^{design}\right)}{F_s}\right) \tag{2}$$

In the above equations F_s is the factor of safety, whereas S_u^{design} and ϕ'^{design} are the characteristic values of soil strength, estimated from the available site investigation data.

The strength reduction in Eqs. (1) and (2) can be achieved in two ways in a numerical analysis. The first approach is to use the design strength (S_u^{design} or ϕ'^{design}) directly, without modification, in an analysis and then at relevant stages of this analysis to gradually increase the factor of safety (i.e. to reduce the strength) until failure occurs. This approach has the advantage in that a single analysis could be used to investigate both the serviceability and ultimate limit states for the problem being analysed. However, a great disadvantage of this approach is that there is no agreed unique way of how the strength reduction should be numerically implemented and different software does this in different ways. Additionally, some software can only perform such reductions if simple constitutive models are used in the analysis.

The second approach is to start the analysis with the factored strength ($S_u^{analysis}$ or $\phi'^{analysis}$) and continue until failure occurs. The advantage of this approach is that no modification to the analysis software is needed, which makes it an easier option and can be used with most constitutive models. However, the disadvantage is that such a reduced strength may require initial stresses that are not consistent with those in-situ (e.g. K_o could be reduced). As a consequence, smaller structural forces could be calculated in, for example, a retaining wall or a tunnel lining that are present in the analysis.

Another issue with the two approaches is whether they produce the same result for a given problem (i.e. the same limit state). In this respect, using the example of the bearing capacity of a strip footing, this paper examines this issue through analyses using a simple Tresca and a more advanced Modified Cam Clay (MCC) constitutive models.

2 THE FINITE ELEMENT MODEL

Fig.1 shows the finite element mesh for a vertically loaded 2m wide strip footing. Due to symmetry only half of the domain has been discretised with a single soil layer. As the footing is considered to be rigid, the loading of the footing is simulated by application of increments of uniform vertical displacements at nodes along the footing-soil interface. The vertical load on the footing is then obtained as the reaction to the applied vertical displacements. The soil-footing interface is considered to be rough and this is achieved by prescribing zero horizontal displacements at the nodes along the soil-footing interface. The remaining boundary conditions are those of zero vertical and horizontal displacements along the bottom boundary, zero horizontal displacement and zero vertical force on the vertical boundaries and a stress-free top boundary away from the footing.

In the first set of analyses the application of partial factors in undrained bearing capacity of the above strip footing is investigated, modelling the soil with a simple elastic-perfectly plastic Tresca constitutive model. The undrained strength S_u^{design} =100kPa is assumed uniform with depth, with K_o=1 on total stresses, an undrained Young's modulus of 10^5kPa and a Poisson's ratio of 0.499.

In the second set of analyses the same problem is considered, but the soil is modelled with a form of the Modified Cam Clay (MCC) model (Potts & Zdravkovic, 1999), which is a strain-hardening/softening critical state type model. As this is an effective stress model, the undrained conditions were imposed by assigning a large value of the bulk compressibility of the pore fluid, see Potts & Zdravkovic (1999). The relevant strength parameter is the angle of shearing resistance, ϕ', and therefore ϕ'^{design} =30° is assumed for these analyses, resulting in K_o=1−sinϕ' =0.5 (according to Jaky, 1948). The soil is assumed to be normally consolidated, with an inclination of the virgin compression line λ=0.16, an inclination of the swelling lines

κ=0.02, the specific volume at unit mean effective stress on the isotropic compression line v_1=3.2 and the Poisson's ratio μ=0.3.

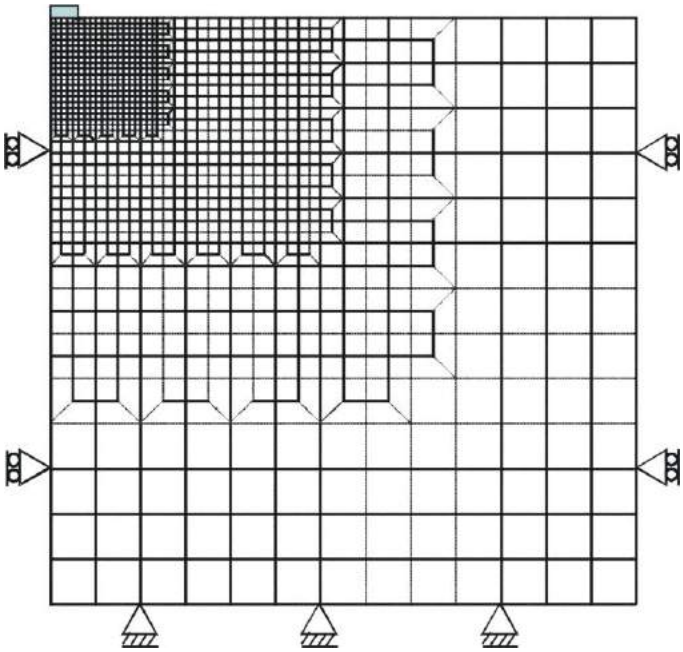

Fig. 1. Finite element mesh for footing analyses

All analyses presented here have been performed with the Imperial College Finite Element Program (ICFEP), which employs a modified Newton-Raphson non-linear solver with an error-controlled sub-stepping stress-point algorithm (see Potts & Zdravkovic, 1999).

3 RESULTS WITH THE TRESCA MODEL

Fig. 2 shows load-displacement curves from the set of analyses where the soil was simulated with a Tresca constitutive model. The solid line (A) in the figure presents the result from an analysis with an unfactored undrained strength, S_u^{design} =100kPa. The bearing capacity of the footing is 519kN/m, which is within 1% of the theoretical value of 514kN/m for this footing and is therefore considered sufficiently accurate for present purposes.

The line with symbols (B) is the result of an analysis in which the first approach for strength reduction (described in Section 1) was applied. The footing was first loaded to a working load of 273kN/m, which results in a load factor, L_f, of 1.9 with respect to the design bearing capacity (i.e. L_f =519/273=1.9). This load was then maintained while the factor of safety on soil strength was incrementally increased (i.e. the strength was reduced) until failure occurred. The resulting factor of safety on undrained strength was 1.9, which is identical to the above calculated load factor for working load, as would be expected.

The final analysis utilised the second approach (described in Section 1) for strength reduction. Namely, the factor of safety of 1.9, calculated in the second analysis, was applied to the design value of undrained strength at the beginning of analysis, according to Eq. (1), resulting in $S_u^{analysis} = S_u^{design} / F_s$ =100/1.9=52.6kPa. The analysis of the footing bearing capacity with this initial strength was then performed, resulting in the limit value of 273kN/m, as shown by the dashed line (C) in Fig. 2.

Consequently, with the Tresca constitutive model, both options for incorporating partial factors in numerical analysis resulted in an identical failure loads for the same factor of safety.

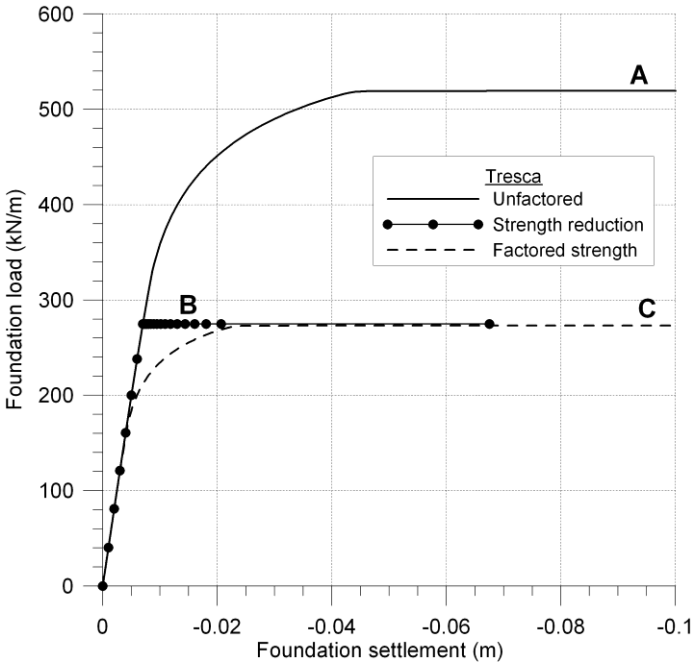

Fig. 2. Load-displacement curves for undrained footing capacity using Tresca model

4 RESULTS WITH THE MODIFIED CAM CLAY MODEL

An effective stress model is applied in modelling undrained soil behaviour when it is necessary to monitor the changes in both the pore pressures and effective stresses in the ground, which is not possible with a simple, total stress based Tresca model. As mentioned in Section 2, the approach for simulating undrained soil behaviour with such a model, adopted in the analyses presented here, is that of prescribing a large value for the compressibility of the pore water (as explained in Potts & Zdravkovic, 1999).

Fig. 3 shows load-displacement curves from analyses performed to investigate the application of partial factors on the undrained bearing capacity of the same footing (shown in Fig. 1), using the MCC soil constitutive model. As before, the solid line (A) in Fig. 3 is the result of the bearing capacity obtained with an unfactored strength ϕ'^{design} =30° and a K_o of 0.5, resulting from Jaky (1948) expression for K_o. The ultimate footing capacity so obtained is 29kN/m.

A second analysis was then performed in which the footing was initially loaded to a working load of 14.5kN/m, in the same initial ground conditions (i.e. ϕ'^{design} =30° and K_o=0.5) and with the same model parameters as described in Section 2. This load was then maintained, while the factor of safety on soil strength was gradually increased (i.e. the strength reduced) until failure occurred, resulting in a factor of safety F_s=2.25 (line B, with symbols). As in the above Tresca case, this analysis corresponds to the first approach for application of partial factors described in Section 1.

In the second approach for application of partial factors the soil strength was reduced at the beginning of the analysis by applying the F_s=2.25, calculated from the second analysis, to the tan(ϕ'^{design}), according to Eq. (2). This resulted in the $\phi'^{analysis}$ =14.4° (i.e. $\phi'^{analysis}$ = arctan(tan(30°)/2.25)). An issue now arises as to which K_o value should be used to calculate the initial stresses at the beginning of the analysis: the original value of 0.5 (=1−sin30°), corresponding to the unfactored strength; or a value that corresponds to the reduced strength, which equals 0.751 (=1−sin14.4°). It should be noted that this issue did not

arise in the case of a simple Tresca model, as the value of K_o does not affect the ultimate bearing capacity of a surface footing on such a soil.

The third analysis performed for this case adopted the $\phi'^{analysis}$ =14.4° and K_o=0.751, with all other model parameters as described in Section 2 and again assuming that the soil was normally consolidated. This analysis resulted in the load-displacement curve C (dashed line) in Fig. 3 and the ultimate bearing capacity of 17.1kN/m. This is clearly different from 14.5kN/m (line B) obtained by applying the first approach for strength reduction.

The fourth analysis adopted the alternative combination of $\phi'^{analysis}$ =14.4° and K_o=0.5, with all other model parameters as described in Section 2 and also assuming the soil to be normally consolidated. This analysis produced the load-displacement curve D (dash-dotted line) in Fig. 3 and ultimate bearing capacity of 27.6kN/m, which is also different from 14.5kN/m obtained from the first approach for strength reduction.

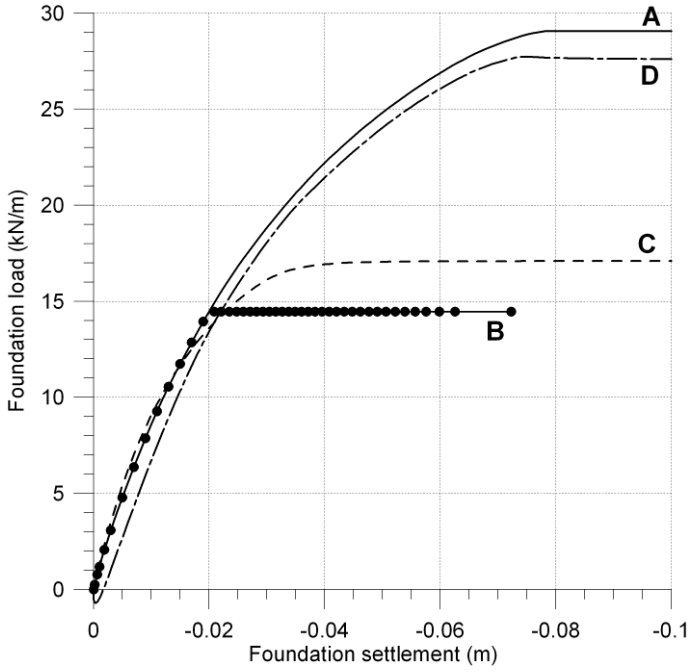

Fig. 3. Load-displacement curves for undrained footing capacity using the MCC model

5 DISCUSSION OF NUMERICAL RESULTS

The above results have shown that the two approaches for application of partial factors of safety in numerical analysis of undrained bearing capacity of a strip footing may result in the same limit state if a simpler, Tresca, constitutive model is used, but that this is not the case with a more complicated MCC model.

The differences in ultimate loads obtained with the MCC model can be fully explained by the different undrained strength profiles that arise in the four different analyses performed for this footing. Namely, although the S_u profile is not an input parameter for the model, this can be calculated from the model input parameters described in Section 2 and initial stresses in the ground, according to the following equation (see Potts & Zdravkovic (1999) for its derivation):

$$S_u = \sigma'_{vi}\ g(\theta)\cos\theta\frac{(1+2K_o)}{3}\left(\frac{1+B^2}{2}\right)^{1-\kappa/\lambda} \qquad (3)$$

where

$$B = \frac{\sqrt{3}(1-K_o)}{g(-30^o)(1+2K_o)} \qquad \text{and} \qquad g(\theta) = \frac{\sin\phi'}{\cos\theta + \frac{\sin\theta\,\sin\phi'}{\sqrt{3}}}$$

In addition to the parameters described in Section 2, θ is the Lode's angle in the deviatoric plane and σ'_{vi} is the initial vertical effective stress in the ground. It is clear from Eq. (3) that the S_u profile depends on the value of K_o and Fig. 4 shows the S_u profiles for the four analyses performed with the MCC model.

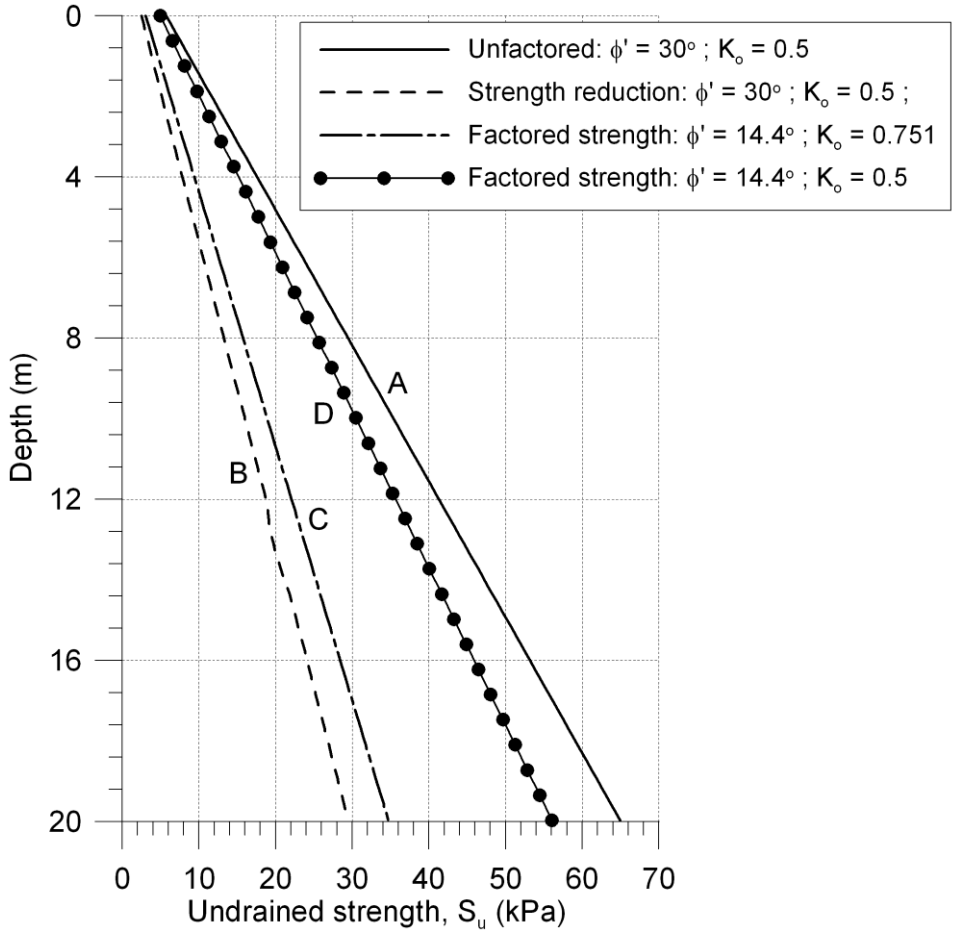

Fig. 4. Undrained strength profiles for analyses performed with the MCC model

The solid line (A) is the initial undrained strength profile for the unfactored soil strength and the corresponding value of K_o applied in the first analysis using the MCC model. When this strength is reduced by applying the first approach for strength reduction, the dashed line (B) is obtained for the S_u profile in the second analysis. In the second approach for strength reduction, when the drained strength is factored at the beginning of the analysis, the two different values of K_o in the initial stresses result in two different S_u profiles C and D (in the third and fourth analysis respectively). Consequently, different S_u profiles have resulted in different bearing capacity values in Fig. 3.

Additionally, an unusual behaviour of the load-displacement curve D can be seen in Fig. 3 at the beginning of loading (initial negative load). This is fully explained by noting that if K_o=0.5 and $\phi'^{analysis}$ =14.4°, the initial stress state for a normally consolidated clay occurs on the yield surface on the dry side of the critical state. Therefore, on initial loading there is

some undrained softening. This situation may be viewed as unrealistic, but is a consequence of the mismatch between the $\phi'^{analysis}$, K_o and the assumption of normal consolidation.

6 CONCLUSIONS

The above example clearly illustrates some of the difficulties that may arise when attempting to include partial factors of safety on soil strength into a numerical analysis. For more complex boundary value problems and/or when using advanced constitutive models, these difficulties may increase. Very little work has been done to date by the geotechnical community in addressing these problems. Clearly, to avoid considerable confusion and to enable numerical analysis to fulfil its enormous potential as a design tool, as intended by EC 7, a rational set of guidelines must be developed on how to safely apply the partial factors in numerical analysis.

REFERENCES

Bauduin C., De Vos M. & Simpson B., (2000), "Some considerations on the use of finite element methods in ultimate limit state design", Proc. Int. Workshop on Limit State Design in Geotechnical Engineering, Melbourne, Australia.

Bauduin C., De Vos M. & Frank R. (2003), "ULS and SLS design of embedded walls according to Eurocode 7; Proc. XIII ECSMGE, Prague, Czech Republik; Vol. 2: 41-46.

Cheung K., West K., Yeow H. & Simpson B. (2010), "Do Eurocodes make a difference?", Geomechanics and Tunnelling, 3 (1): 35-47.

Jaky, J. (1948), "Pressure in soils", Proceedings of 2nd ISSMFE, London, Vol. 1: 103-107.

Potts, D.M. & Zdravkovic, L. (1999), Finite element analysis in geotechnical engineering: theory, Thomas Telford, London.

Schweiger H. (2005), "Application of FEM to ULS design (Eurocodes) in surface and near surface geotechnical structures"; Proc. 11th Int. Conf. of IACMAG, Turin, Italy; Bologna, Patron-Editore: 419-430.

Schweiger H., Marcher T. & Nasekhian A. (2010), "Nonlinear FE analysis of tunnel excavation – comparison of EC7 design approaches"; Geomechanics and Tunnelling, 3 (1): 61-67.

Simpson B. (2000), "Partial factors: where to apply them?"; Proc. Int. Workshop on Limit State Design in Geotechnical Engineering, Melbourne, Australia.

Simpson B. (2007), "Approaches to ULS design – The merits of Design Approach 1 in Eurocode 7"; 1st Int. Symp. on Geotechnical Safety and Risk, Shanghai, Tongji University, China.

MODELLING OF FRICTIONAL SOIL DAMPING IN FINITE ELEMENT ANALYSIS

S. Van Baars
Department of Science, Technology and Communication, University of Luxembourg, Luxembourg

ABSTRACT: *In soil dynamics, the soil is often described as a viscous material. In a viscous material however, the dissipated energy is assumed to be proportional to the wave frequency, which is absolutely not applicable to soils. It is therefore better to use a concept of damping based on dry particle friction. A non-viscous model based on this concept results in a damping ratio that becomes constant for small deformations for both sand and clay, and is also independent of frequency or shear strain amplitude. This behaviour corresponds with laboratory measurements and requires only one damping parameter which can be obtained from laboratory tests.*
This model is implemented in Plaxis as a User-Defined Soil Model to analyse the problem of a strip footing subjected to a dynamic load. The initial results are rather remarkable. . For example, a Power Spectral Density plot of the velocities shows that not all frequencies seem to be damped equally and at some distance the input frequency is not even present.

1 INTRODUCTION

The accuracy of predictions with Finite Element Models for Geotechnical Engineering can be rather good for stiffness and in strength calculations. In the field of soil dynamics however, the quality of the predictions is often disappointingly low. Therefore the hypothesis will have to be evaluated that the current method of dynamic modelling neglects several fundamental geotechnical aspects such as non-viscous damping, inhomogeneity, anisotropy, variable degree of saturation and others. Aspects, which obviously do not hinder the other well-known applications (such as settlement and stability calculations), but might explain the unexpected deviations of the vibration predictions. In this article the effect of the first aspect, i.e. the non-viscous damping, will be investigated.

In soil dynamics the simplest way of calculating the energy dissipation during the wave propagation is to describe the soil as a Kelvin-Voigt material, which means as a viscous material. For example in Plaxis the material damping is programmed as a Rayleigh Damping. Unfortunately this method holds two large problems:

1. With viscous models like these, the dissipated energy is assumed to be proportional to the wave frequency, which is absolutely not applicable to soils (damping is rather constant with frequency).
2. Therefore there is no laboratory test to obtain the two necessary material parameters of this method; the mass factor α and the stiffness factor β.

Since a viscous model does not reflect a correct soil behavior, it is better to use a concept of damping based on dry particle friction.

2 VISCOUS DAMPING

One of the best known ways in soil dynamics for calculating the wave propagation and the energy dissipation is to describe the soil as a Kelvin-Voigt material. This model can be represented by a parallel combination of a purely viscous damper and a purely elastic spring. Fig. 1 shows a mass connected to this spring and damper combination.

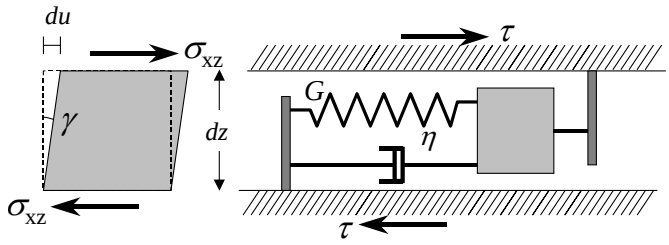

Fig. 1. Kelvin-Voigt model with mass

Since this visco-elastic model shows harmonic shear strains and stresses of the form:

$$\begin{aligned} \gamma &= \hat{\gamma} \sin \omega t \\ \tau &= G\hat{\gamma} \sin \omega t + \omega \eta \hat{\gamma} \cos \omega t \end{aligned} \tag{1}$$

there will be an elliptical stress-strain loop with an energy dissipation per wave cycle of:

$$\Delta W = \int_{t_o}^{t_o + 2\pi/\omega} \tau \frac{\partial \gamma}{\partial t} = \pi \eta \omega \hat{\gamma}^2 \tag{2}$$

leading to the damping ratios ζ, ξ or D of :

$$\begin{aligned} \zeta &= \frac{\Delta W}{W} \quad \text{with} \quad W = \tfrac{1}{2} G \hat{\gamma}^2 \\ \xi &= D = \frac{1}{4\pi} \zeta = \frac{\eta \omega}{2G} \end{aligned} \tag{3}$$

This indicates that for a Kelvin-Voigt material the dissipated energy is proportional to the frequency of the loading, which is not the case for soils. Solving this problem by using an equivalent viscosity such as:

$$\eta = \frac{2G}{\omega} \xi \tag{4}$$

is not only scientifically incorrect (Kramer, 1996), but is also unusable for numerical implementation. The problem is illustrated by considering a superposition of waves with multiple frequencies, for which there can be no equivalent viscosity for all waves at the same time.

3 FRICTIONAL DAMPING

The shear displacement u_s can be used to relate the shear velocity v_s to the shear strain γ

$$
\begin{aligned}
u_s &= \hat{u}_s \sin(\omega t + kx) \\
v_s &= \frac{\partial u_s}{\partial t} = \hat{u}_s \omega \cos(\omega t + kx) \Rightarrow \hat{v}_s = \hat{u}_s \omega \\
\gamma &= \frac{\partial u_s}{\partial x} = \hat{u}_s k \cos(\omega t + kx) \Rightarrow \hat{\gamma} = \hat{u}_s k \\
\hat{\gamma} &= \hat{u}_s k = \frac{\hat{v}_s}{\omega} k = \frac{\hat{v}_s}{2\pi f} \frac{2\pi}{\lambda} = \frac{\hat{v}_s}{\lambda f} = \frac{\hat{v}_s}{c_s}
\end{aligned}
\tag{5}
$$

According to the Dutch vibration standards, the human amplitude perception threshold is at a velocity of 0.4 mm/s and the plaster damage threshold for houses is at 4.0 mm/s. A strong shear wave with a lateral velocity amplitude of even $\hat{v}_s$ = 10 mm/s in clay with a wave speed of c_s = 100 m/s, will therefore result in a shear deformation amplitude no greater than $\hat{\gamma} = \frac{\hat{v}_s}{c_s} = 0.01\%$.

Various research results (Kokusho, Yoshida, and Esashi ,1982; Vucetic and Dobry, 1991; Wang and Kuwano, 1999; Okur and Ansal, 2007) have shown that the damping ratio is nearly constant up to a deformation of this magnitude ($\hat{\gamma} < 0.01\%$).

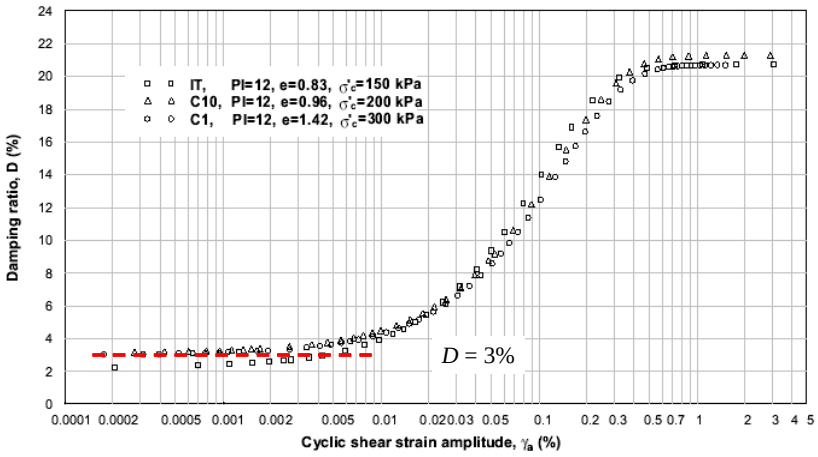

Fig. 2. Damping versus shear strain amplitude (Okur and Ansal)

These results are for both sand and clay, and also for slow movements (viz. 0.5 Hz or 1.0 Hz). This almost constant damping ratio is about D = 3% (or ζ = 38%), see Fig. 2. The added dashed line shows the result of the theory to be presented below.

Since the damping in this range is related not to frequency, but to shear strain, it is better to use the concept of damping based on dry particle friction. Shear deformation will always be accompanied by some dry shear movement between two adjacent particles. The energy absorbed in this dry friction is independent of particle velocity. A possible dynamic soil

model that embodies this concept can be based on a force-displacement curve that has an exponential distribution. Then the shear stress can be written in the form:

$$\tau' = G_0 \left(\gamma'\right)^X \tag{6}$$

with G_0 and X as material parameters; G_0 with the dimension of a stress and X dimensionless. The zero stresses and strains are defined from a turning point in the cycle, see also Fig. 3, so the peak-to-peak shear strain amplitude is $\widehat{\gamma}' = 2\hat{\gamma}$.

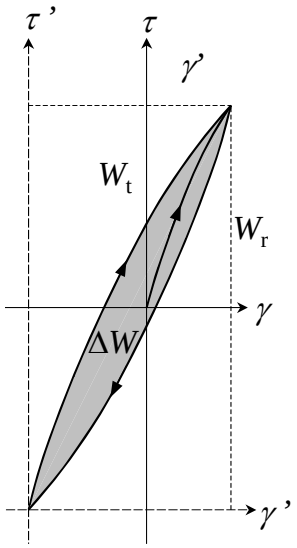

Fig. 3. Energy loss of stress-strain cycle.

The area of the ellipse representing the energy dissipation per cycle is defined by ΔW. The area below the upper line is (including ellipse and the “triangle” below) is defined by:

$$\begin{aligned} W_t &= \int_{\gamma'} \tau' \partial \gamma' \\ &= \frac{1}{\left(X+1\right)} G_0 \, \widehat{\gamma}'^{(X+1)} \end{aligned} \tag{7}$$

The energy dissipation of the ellipse is therefore:

$$\begin{aligned} \Delta W &= 2W_t - \widehat{\tau}'\widehat{\gamma}' \\ &= \frac{2}{X+1} G_0 \, \widehat{\gamma}'^{(X+1)} - G_0 \, \widehat{\gamma}'^{(X+1)} \\ &= \frac{1-X}{1+X} G_0 \, \widehat{\gamma}'^{(1+X)} \end{aligned} \tag{8}$$

The peak energy stored in the cycle is:

$$W = \tfrac{1}{2}\hat{\tau}\hat{\gamma} = \tfrac{1}{2}(\tfrac{1}{2}\hat{\tau}')(\tfrac{1}{2}\hat{\gamma}') = \tfrac{1}{8}\hat{\tau}'\hat{\gamma}' = \tfrac{1}{8}G_0\,\hat{\gamma}'^{(1+X)} \tag{9}$$

With this we find a damping ratio of:

$$\zeta = \frac{\Delta W}{W} = 8\frac{1-X}{1+X} \quad \Rightarrow \quad X = \frac{8-\zeta}{8+\zeta} \tag{10}$$

Thus, by calculating X with eq.(10) and by using a certain input damping ratio D or ζ, eq. (6) will always result in a damping ratio which is equal to the input ratio. So, the chosen exponential distribution is such that the damping ratio is constant for all shear strain amplitudes.

In order to verify this constant damping behaviour, eq. (6) has been used to calculate the stress-strain cycles for a range of different shear strains. The power is assumed to be $X = 0.91$ (so $D = 3\%$ or $\zeta = 38\%$ according to eq.(10)). The damping was calculated for each cycle. The results are plotted as a dashed line in Fig. 2. It shows that the damping ratios, resulting from eq. (6), are indeed independent from the shear strain amplitude.

Because of the exponential behaviour of this damping model, the corresponding shear modulus is not automatically comparable with the shear modulus of the normal Mohr-Coulomb model. So, in order to make the shear moduli comparable, there has to be a correction factor, which depends on the maximum shear strain:

$$f = \frac{\hat{\tau}_{MC}}{\hat{\tau}_{DMC}} = \frac{G\,\hat{\gamma}'}{G\,\hat{\gamma}'^{X}} = \hat{\gamma}'^{(1-X)} \tag{11}$$

Another way of writing the damping model could therefore be:

$$\tau' = f\,G(\gamma')^{X} \quad \text{with:} \quad f = \hat{\gamma}'^{(1-X)} = \hat{\gamma}'^{\left(\frac{2\pi D}{2+\pi D}\right)} \tag{12}$$

In that case the shear modulus G is more comparable with the Mohr-Coulomb model, but the correction factor f is for the relative large damping of granular materials not fully constant, as can be seen in the table below.

Table 1. Correction factor versus maximum shear strain

$\hat{\gamma}$	$f_{D=3.0\%}$	$f_{D=3.6\%}$
0.01%	0.44	0.37
0.001%	0.35	0.29
0.0001%	0.29	0.23

4 FRICTIONAL DAMPING THEORY VERSUS MEASUREMENTS

Besides the correct modelling of the damping ratio, it is also important to verify the total stress-strain path. The stress-strain path of Fig. 4 has been measured by Okur and Ansal (2007). The measured damping ratio of this cycle is $D = 3.6\%$ (so, $X = 0.89$).

The dashed cycle in the figure is the reproduced stress-strain path based on the proposed concept of dry particle friction formulated in eq. (6). The reproduced data fits almost exactly the measured data.

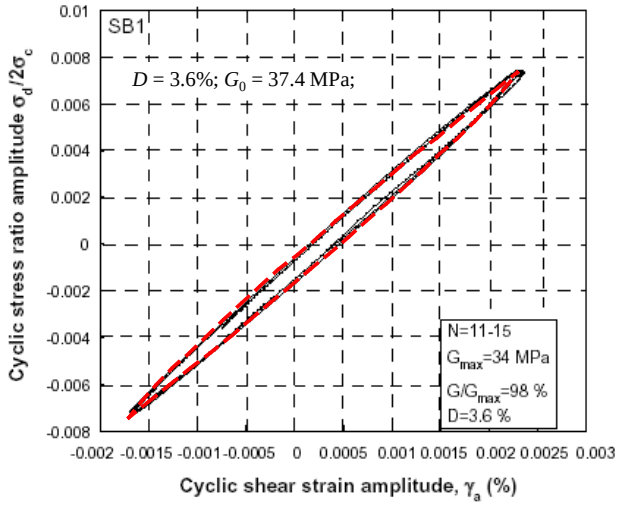

Fig. 4. Cyclic behaviour and damping; proposed method versus data from Okur and Ansal (2007)

5 FRICTIONAL DAMPING AND FINITE ELEMENT MODELLING

In order to study the effect of this frictional damping, a finite element calculation with this model has been made. Verruijt et al. (2008) has showed that the numerical results of the dynamical calculations with Plaxis give the same result as the analytical solution found by Verruijt for the elasto-dynamic strip load problem. This is an important validation.

Therefore a similar type 2D-calculation with a strip load on a half-space has been made. The soil is assumed to behave as a Mohr-Coulomb material with a Young Modulus of E = 10.000 kPa and a Poisson's ratio of $\nu = 0.25$.

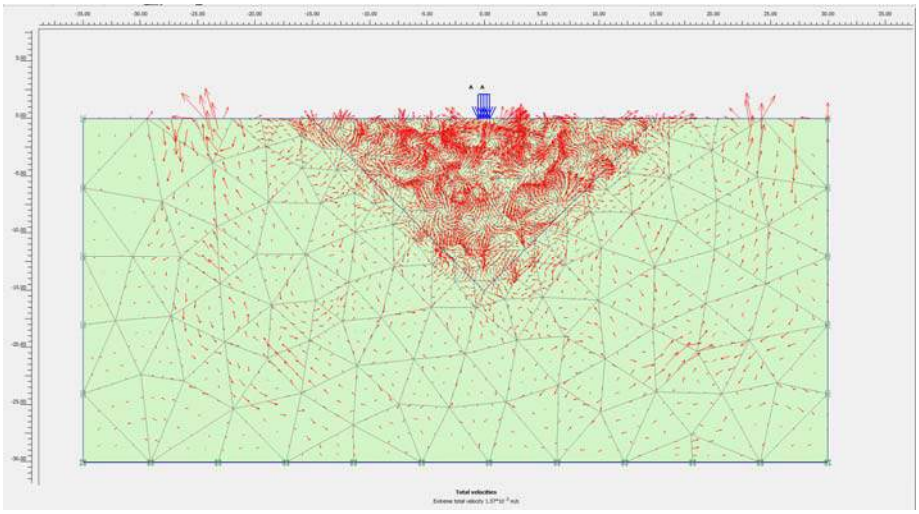

Fig. 5. Cyclic strip load on a half-space

The load is a sinusoidal load with amplitude of 10 kPa applied to a strip of 1 m width. The frequency is 50 hz and there are 3 load cycles. This means there is also tension. Therefore the soil is programmed to be strongly cohesive in order to avoid plasticity.

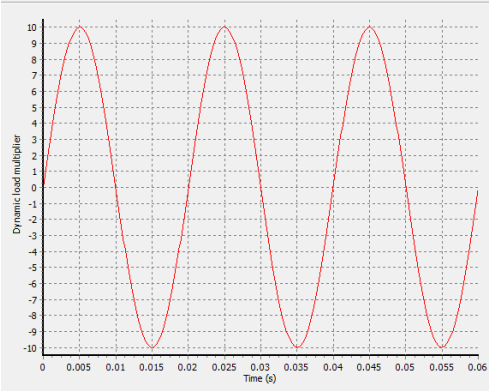

Fig. 6. Cyclic load of three cycles

After the three load cyles, the half-space is free to move. The calculation is made both with the normal Mohr-Coulomb model and with the Damping Mohr-Coulomb model, with a damping of D = 3.6%, which is a normal value for frictional soil materials. This frictional damping model is implemented in Plaxis with the help of the User-Defined Soil Model option of Plaxis. This means that for the Damping Mohr-Coulomb model a Dynamic Link Library (DLL) has been programmed and compiled, in this case in Delfi, and added to the source code of Plaxis. Of course for values of D = 0%, exactly the same values are found for this model as for the Mohr-Coulomb model of Plaxis.

At a distance of 10 m from the center, the absolute velocities were recorded numerically. This can be found in Fig. 7. The first waves which arrive are the compression waves. After these the other waves (shear waves and surface waves) pass by.

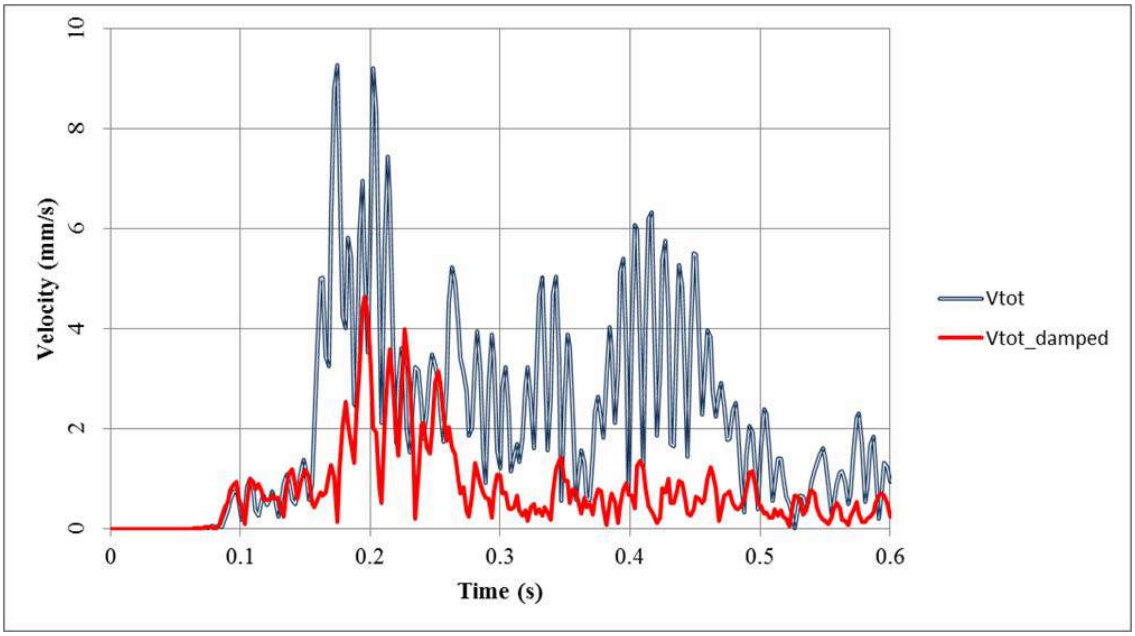

Fig. 7. Absolute velocity at 10 m distance

Several conclusions can be drawn from the figure:

- The sinusoidal input load is not found back in the output recordings; these waves are strongly deformed, both for the undamped and damped waves.
- The compression waves in the start do not create the largest velocities.
- Since these compression waves have mainly a compression component and hardly a shear component, there is hardly any damping.
- The waves after the first compression waves have mainly a shear component and are strongly damped.

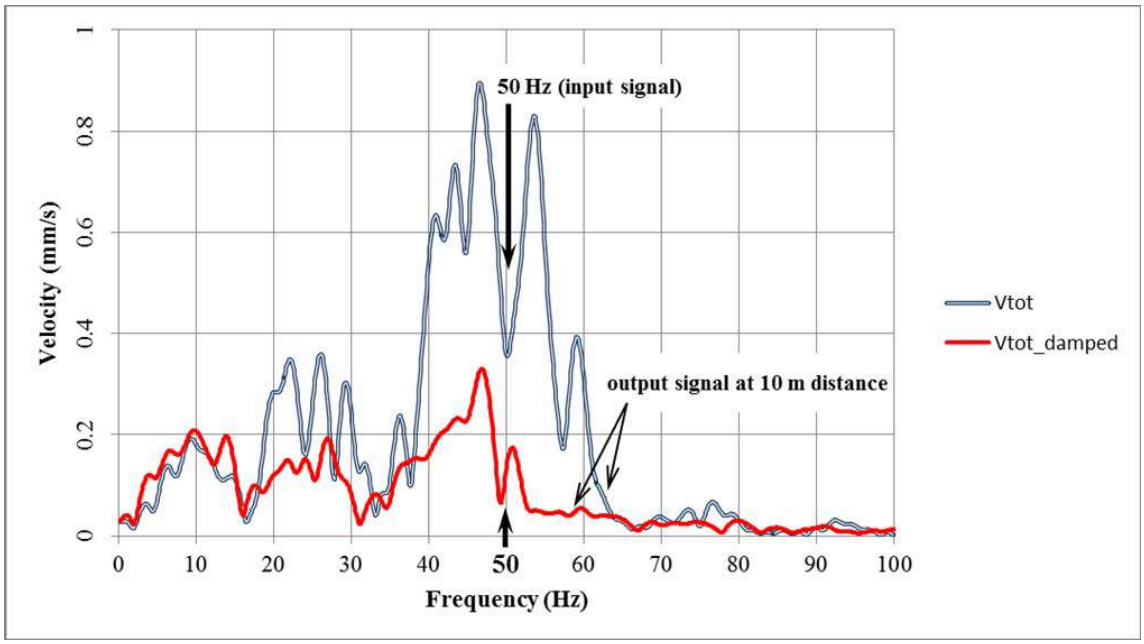

Fig. 8. Power Spectral Density plot of velocity

Fig. 8 shows the Power Spectral Density plot, obtained through a Fourier transformation of the recorded velocities of Fig. 7. This PSD plot shows some remarkable points:

- The effect of the damping is very strong, but especially the larger peaks are damped.
- The damping does not damp all frequencies equally.
- Although the input frequency is 50 Hz, the output signal shows a gap (relatively low average velocity) for this frequency of 50 Hz (see graph near arrow in Fig. 8.). In fact it is even less than the average velocity of the surrounding frequencies between 40 and 55 Hz.

The reason for these findings is unknown but, since the damping is implemented correctly, it might lead to an explanation of the unexpected deviations of the vibration predictions. That means that the first step of this research, finding unexpected vibration behavior, is successful.

6 CONCLUSIONS

Based on the measured constant damping ratio at small shear deformations, it must be concluded that a visco-elastic model like Kelvin-Voigt is inappropriate for a correct modeling of the energy dissipation of granular materials. The proposed spring-slider mass model however, correctly reproduces the cyclic stress-strain behaviour and the corresponding damping, independent of frequency or shear strain amplitude. A non-viscous damping model

based on this dry-friction concept corresponds with laboratory measurements and requires only one damping parameter which can be obtained from laboratory tests

This model is implemented in Plaxis as a User-Defined Soil Model. First results of a dynamical strip footing are remarkable. For example a Power Spectral Density plot of the velocities shows that the damping does not damp all frequencies equally and the input frequency is not found back at some distance, there is even a gap at this frequency. That means that the first steps of this research, modelling and finding unexpected vibration behavior, are successful.

References

Journal

Salvadori, C.K. & Martin, S.H. (1989), "Coupled use of reduced integration and nonconforming modes in improving quadratic plate element". Int. J. Num. Meth. Eng., Vol. 28(4), 1909-1928.

Kokusho, T.,Yoshida, Y. & Esashi, Y. (1982), "Dynamic properties of soft clays for wide strain range". *Soils and Foundations*, Volume 22, Issue 4, 1–18.

Vucetic, M. & Dobry, R. (1991) "The effect of soil plasticity on cyclic response". ASCE Journal of Geotechnical Engineering, Vol. 117, No. 1., 89-107.

Wang, G. X. & Kuwano, J. (1999) "Modelling of strain dependency of shear modulus and damping of clayey sand", *Soil Dynamics and Earthquake Engineering*, Volume 18, Issue 6, August 1999, pp. 463-471

Okur, D.V. & Ansal (2007) "Stiffness degradation of natural fine grained soils during cyclic loading", *Soil Dynamics and Earthquake Engineering*, Volume 27, 843–854

Verruijt, A. & Brinkgreve, R.B.J. & Li, S., „Analytical and numerical solution of the elastodynamic strip load problem", Int. J. Numer. Anal. Meth. Geomech. 2008; 32:65–80

Book

Kramer, S. L. (1996) Geotechnical Earthquake Engineering, Prentice Hall, New Jersey. ISBN-10: 0133749436, ISBN-13: 9780133749434, pp176-177

NUMERICAL MODELING OF TENSION PILES UNDER AXIAL CYCLIC LOADING

K. Abdel-Rahman
M. Achmus
Institute of Soil Mechanics, Foundation Engineering & Waterpower Engineering,
Leibniz University of Hannover, Germany

ABSTRACT: *Cyclic axial loading of piles often occurs, in particular in offshore engineering applications. Although it is known that a decrease of ultimate skin friction occurs with cyclic pre-loading, no general calculation approach yet exists. A numerical method is presented which is capable to assess stress changes in the soil around a pile due to cyclic axial loading and to figure out the post-cyclic pullout-capacity of the pile with respect to the magnitude of cyclic axial load and the number of load cycles. The method is a numerical realization of an analytical approach of Richter & Kirsch (2010). Here, the volume compaction due to cyclic shearing is assessed empirically dependent on the cyclic shear strains and is then applied to the pile-soil system. First results for rigid piles in homogeneous medium dense sand are presented. The method gives a prediction of post-cyclic pile capacities and is thus a promising tool to assess cyclic load effects on the behavior of axially loaded piles.*

1 INTRODUCTION

The behavior of piles under cyclic loading is an important research issue. In particular offshore piles are often subject to intensively cyclic loads due to the strong wind and wave actions. Regarding axial cyclic loading, it is known that the pile capacity is in general decreasing with increasing number of load cycles. This occurs mainly due to a decrease of ultimate skin friction, whereas the tip resistance is believed to remain almost unchanged.

Although a numerous studies have been carried out regarding pile capacity under cyclic loading, no calculation approach yet exists to determine the decrease of capacity dependent on cyclic load magnitude and number of load cycles. The question has recently become very important, since numerous wind farms shall be erected in the North Sea and the Baltic Sea in the near future. In many cases, the foundations of the wind energy converters will consist of jacket and tripod structures, which are supported by steel pipe piles located at the edges of the foundation area. These piles will have diameters between 1.5 and 3m and are loaded by cyclic compression and tension loads. For the economic design of the required pile length the decrease of pile capacity with number of load cycles must be assessed.

Recently, Richter & Kirsch (2010) proposed a method to calculate the decrease of skin friction in sand soil, applying approaches for the calculation of the shear strains in the soil beneath a pile and for the estimation of volume contraction of sand soil due to cyclic shearing. At the institute of the authors, an attempt is made to transfer this method in a numerical scheme based on a finite element simulation of the pile behavior under tensile loading. This method is described in this paper, and first results are presented.

2 OVERVIEW OF PREVIOUS WORK

Under cyclic axial loads, degradation of ultimate skin friction and with that a decrease of the pile capacity is to be expected. Different studies on steel pipe piles in non-cohesive soils have been carried out. Some investigations were made at a test field in Dunkirk under the supervision of the Imperial College in London (Jardine & Standing 2000). It has been shown that degradation of skin friction due to axial cyclic loading leads to accumulating displacements and a severe reduction in pile capacity.

Due to experience, no pile capacity reduction is to be expected if a certain magnitude of the cyclic load portion is not exceeded. The threshold value is termed the critical level of repeated loading (CLRL):

$$CLRL = \frac{E_{cycl}}{R_k} \tag{1}$$

Here E_{cycl} is the cyclic load amplitude and R_k is the static pile capacity. From an evaluation of literature results, Schwarz (2002) reported the *CLRL*-values given in Table 1. The table shows clearly that piles in non-cohesive soils are more sensitive to cyclic axial loading than piles in cohesive soils.

Table 1. Critical level of repeated loading according to Schwarz (2002)

Soil type	*CLRL*
Sand	0.1 – 0.4
Silt	0.4 – 0.6
Clay, normally consolidated	0.3 – 0.55
Clay, overconsolidated	0.85 – 1.0

Poulos (1988) presented a cyclic stability diagram for axially loaded piles (Fig. 1). Based on several model and field tests, the load cycle numbers leading to pile failure are given dependent on the normalized mean load E_0/R_k and the cyclic load amplitude E_{cycl}/R_k. A "stable" region is defined here with $E_{cycl}/R_k \leq 0.2$ (i.e. $CLRL = 0.2$) for $E_0 \leq 0.6\ R_k$.

From this diagram, critical cyclic load amplitudes (leading to failure) can be obtained dependent on the mean axial load and the number of load cycles. Mittag & Richter (2005) derived the following calculation approach based on the stability diagram of Poulos:

$$\frac{E_{cycl}}{R_k} \leq \kappa \left(1 - \left(\frac{E_0}{R_k} \right)^2 \right) \tag{2}$$

Here, the factor κ accounts for the number of load cycles by $\kappa = 0.5 - 0.05 \log_{10} N$. The stability curves corresponding to this approach are also shown in Fig. 1.

Kempfert (2009) evaluated pile test results in cohesive and non-cohesive soils separately and proposed the following approach to determine the critical cyclic load amplitude:

$$\frac{E_{cycl}}{R_k} \leq \kappa^* \left(1 - \left(\frac{E_0}{R_k} + 0.65 - \kappa^* \right)^4 \right) \tag{3}$$

The factor κ^* is dependent on the number of load cycles and the type of soil and is given in Table 2.

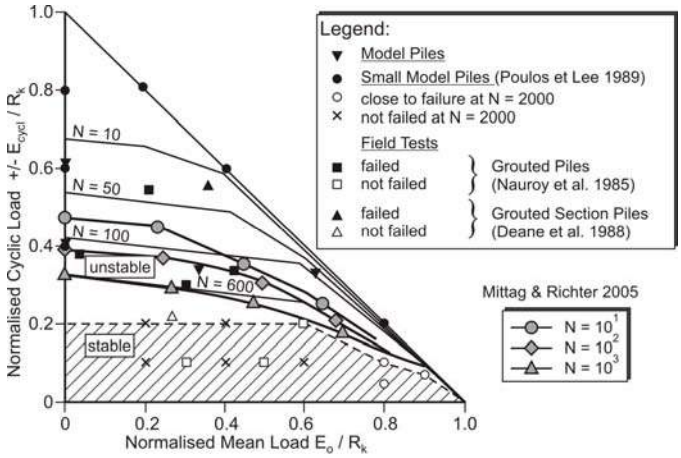

Fig. 1. Stability diagram of Poulos (1988) and approach of Mittag & Richter (2005)

Table 2. κ^*-value dependent on the number of load cycles and soil type (Kempfert 2009)

Number of load cycles N	10^1	10^2	10^3	10^4	10^5	10^6
κ^* non-cohesive	0.43	0.38	0.33	0.28	0.23	0.18
κ^* cohesive	0.48	0.43	0.38	0.33	0.28	0.23

It is generally assumed that the reason for the decrease of skin friction is the compaction of the sand directly beneath the pile shaft due to cyclic shearing. The compaction induces a relaxation of the radial horizontal stress σ_r and thus, since the ultimate skin friction in sand is proportional to the normal stress acting on the pile shaft, also of ultimate skin friction τ_{ult}:

$$\Delta\tau_{ult} = \Delta\sigma_r \, \mu \tag{4}$$

Here, μ is the friction coefficient between pile and soil.

According to Randolph (2009), who evaluated cyclic interface tests on sand, the soil compaction occurs mainly within a small shear band around the pile. In a model proposed by Richter & Kirsch (2010), compaction occurs up to a distance at which a threshold value of cyclic shear strain in the soil is reached. The latter model is used for the numerical approach and is described more detailed below.

3 DESCRIPTION OF THE RICHTER & KIRSCH APPROACH

Kirsch & Richter developed a calculation method for the decrease of ultimate skin friction on cyclic axially loaded piles. In a first step, the distribution of shear stresses along the pile under the cyclic load portion has to be determined. At a certain depth, the attenuation of shear stresses τ with increasing distance r from the pile axis is described by Eq. (5):

$$\tau(r) = \tau \frac{r_0}{r} \tag{5}$$

Here r_0 is the pile radius. A cyclic shear modulus $\widetilde{G}$, which can be calculated from the maximum shear modulus as a function of cyclic shear strain (Kirsch & Richter 2010), is used to calculate the cyclic shear strain amplitude $\widetilde{\gamma}$.

$$\widetilde{\gamma}(r) = \frac{\tau(r)}{\widetilde{G}} \tag{6}$$

The compaction effect due to application of 10 cycles of shear strain was investigated previously by Silver & Seed (1971) by performing cyclic simple shear tests on sand. Their results can be presented as a relationship between the volume reduction due to compaction (ε_{ii}) and the cyclic shear strain $\tilde{\gamma}$ (see Fig. 2). Richter & Kirsch assumed a logarithmic dependence of volume compaction and number of cycles and thus extended the equation by introducing $\log_{10}N$:

$$\varepsilon_{ii} = 0.5\left(\tilde{\gamma} - \alpha \cdot \gamma_{\lim}\right) I_d^{-2.32} \log_{10} N \tag{7}$$

Here I_d is the relative density of the sand specimen. By integrating the volumetric strain due to compaction (ε_{ii}), a radial displacement u_r can be calculated. The integration is carried out up to a limiting distance r_{limit}, at which the cyclic strain amplitude becomes smaller than a threshold value $\gamma_{\lim}$. This threshold value $\gamma_{\lim}$ can be derived from Vucetic (1994). For non-cohesive soil, $\gamma_{\lim}$ can be set to 0.01%. The factor α in the Eq. (7) is a parameter introduced by Richter & Kirsch (2010), which can be derived from cyclic simple shear test. Silver & Seed (1971) reported a value of $5 \cdot 10^{-5}$ for $\alpha \cdot \gamma_{\lim}$, which leads to α=0.5. Interpreting u_r as an expansion of the pile diameter and applying the elastic solution of cavity expansion problem, the corresponding change of radial soil stress ($\Delta\sigma_r$) and with that of ultimate skin friction ($\Delta\tau_{ult}$) can be calculated:

$$\Delta\tau_{ult} = \Delta\sigma_r \, \mu = 2 G_w \frac{u_r}{r_0} \mu \tag{8}$$

Here G_w is the reloading shear modulus of the soil. For more details refer to Richter & Kirsch (2010).

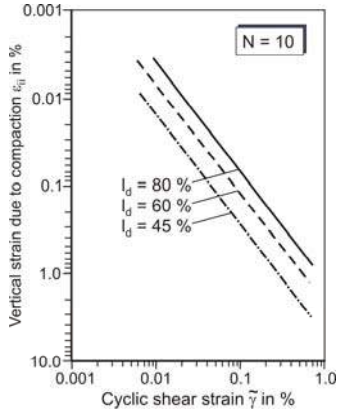

Figure 2. Cyclic vertical compaction of sand after 10 cycles (Silver & Seed 1971)

4 NUMERICAL ANALYSIS

In the numerical approach, the basic idea of Richter & Kirsch is adopted by using Eq. (7) to determine volumetric compaction of the soil induced by cyclic shear strain. However, the shear stress and shear strain distributions in the soil beneath the pile and also the stress changes due to the volumetric compaction are calculated by means of a finite element model of the pile-soil system. The computations were carried out using the finite element program system ABAQUS (Abaqus 2010).

4.1 Mesh Design

A two-dimensional (2D-axisymmetric) finite element model to investigate the axial deformation response of a pile in sandy soil in this study was established. The finite element mesh used in the analysis is shown in Fig. 3. The elements used to model the soil are 4-noded axisymmetric elements. Close to the pile, a very fine discretization was applied in order to get

accurate results. The boundaries of the mesh were at a radius of 25m and 15m below the base of the pile. It was verified that with the model dimensions used the calculated behavior of the pile is not affected by the boundary conditions.

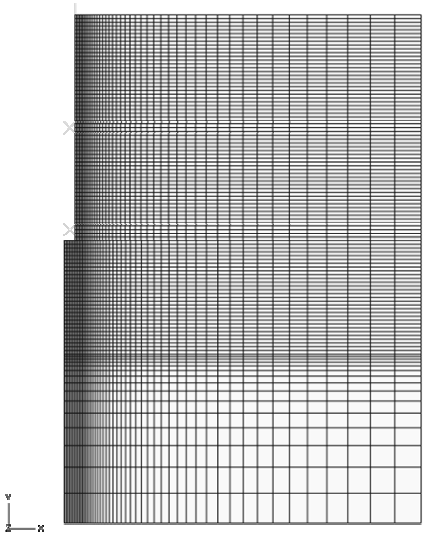

Figure 3. Finite element mesh

The piles were assumed to be rigid (non-deformable) and were modeled using the "rigid body" option in ABAQUS. Different pile dimensions (diameter and length) were used in order to perform a parametric study to examine the overall behavior of tension piles. Three different pile diameters (D=2m, 2.5m and 3m) and three different embedded lengths (L=20m, 25m and 30m) were modeled.

4.2 Constitutive Model

To account for the non-linear soil behavior, soil elements were simulated as elasto-plastic material with Mohr-Coulomb failure criterion. A stress dependency of the oedometric stiffness modulus was implemented as follows:

$$E_s = \kappa \sigma_{at} \left(\frac{\sigma_m}{\sigma_{at}} \right)^{\lambda} \tag{9}$$

Here $\sigma_{at} = 100$ kN/m^2 is a reference (atmospheric) stress and σ_m is the current mean principal stress in the considered soil element. The parameter κ determines the soil stiffness at the reference stress state and the parameter λ rules the stress dependency of the soil stiffness. The material parameters used here are given in Table 3.

Table 3. Material parameters used for medium dense sand.

Unit buoyant weight γ'	11.0 kN/m^3
Oedometric stiffness parameter κ	600
Oedometric stiffness parameter λ	0.55
Poisson's ratio ν	0.25
Internal friction angle φ'	35.0°
Dilation angle ψ	5.0°
Cohesion c'	0.1 kN/m^2

4.3 Contact Behavior

For the contact behavior of the surface between pile (rigid body) and soil an elasto-plastic model was used. The maximum frictional shear stress $\tau_{fric,max}$ is dependent on the normal stress σ_n and a coefficient of friction μ. In the numerical simulations presented here $\mu = 0.431$ was assumed ($\mu = tan\ (2/3\varphi)$). In order to describe the frictional behavior between the pile and the surrounding soil realistically, the maximum frictional shear stress was limited to a value of 80 kN/m^2, which is approximately the value for medium dense sand recommended in the API design guidelines (API 2000).

For full mobilization of the limit frictional stress the relative displacement (elastic slip) between the pile and the surrounding soil was set to $\Delta u_{el,slip}$ = 0.005 m. The stiffness of the contact (k_τ) before reaching the maximum frictional stress is thus defined as shown in Fig. 4.

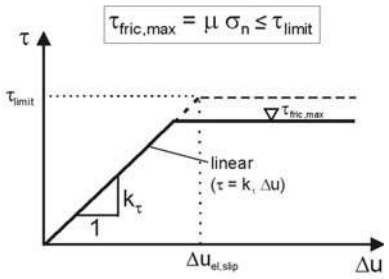

Figure 4. Modeling of contact behavior

4.4 Modeling procedure

The numerical modeling was performed in three stages. In the first stage the static pull-out capacity of the pile was calculated by increasing the tensile load until failure occurred. In a second stage a certain tensile load – in the investigations presented here about 40% of the static pull-out capacity – was applied and the resulting stress-strain behavior of the system was assessed. In a third stage, the volume compactions determined from the results of the second stage and for a certain number of load cycles were applied to the pile-soil system and subsequently the pile load was increased to failure in order to obtain remaining pile capacity after cyclic loading.

The first step was the initialization of geostatic stresses in the soil mass by activating the soil's weight. Afterwards, the soil elements located at the pile position were removed and replaced by the rigid pile body and the contact conditions were activated. In the first stage calculation, the static pile capacity was determined subsequently.

In the second stage calculation, the initial shear strains in the soil elements γ_0 were calculated. As a measure of shear strain, the value proposed by Wegener & Herle (2010) was used:

$$\gamma = \sqrt{\frac{2}{3}\left[(\varepsilon_1 - \varepsilon_2)^2 + (\varepsilon_2 - \varepsilon_3)^2 + (\varepsilon_1 - \varepsilon_3)^2\right]} \tag{10}$$

Then the cyclic load portion was applied and the shear strains in all soil elements were assessed again, yielding the values γ_1. The cyclic shear strain portion is then

$$\tilde{\gamma} = (\gamma_1 - \gamma_0)/2.0 \tag{11}$$

Using Eq. (7), the volumetric strain for each soil element was determined. For elements in which the cyclic shear strain was smaller than the threshold value $\alpha\,\gamma_{lim}$, the volumetric strain was set to zero. In the calculations presented here, $\alpha\,\gamma_{lim}=5\cdot10^{-5}$ was used.

In the third stage, the degradation behavior under cyclic loading was modeled as follows:

i) To apply the volumetric strain to the pile-soil system, a temperature field was established and applied to the system. The temperature difference and the respective material parameter (temperature expansion coefficient) were chosen such that the resulting shrinkage of an element was identical to the demanded volumetric compaction.
ii) The application of the temperature fields induces stress redistribution in the systems. Thus, the reduction of normal stress acting on the pile is obtained directly by the model.
iii) Finally, the pile was pulled out and the post-cyclic pile capacity was determined.

The steps ii) and iii) were repeated to simulate different number of load cycles (here ranging from 10 to 10,000).

5 NUMERICAL RESULTS

5.1 General remarks

In this study, first results regarding the stress changes in sand soil due to cyclic axial (tensile) pile loading and the resulting post-cyclic pile capacities are presented. In order to investigate the effect of cyclic loading, the number of load cycles was varied from N=1 (static loading) until N=10,000.

Stiff piles in medium dense sand with the parameters given in Table 3 were considered. Regarding the soil compaction due to cyclic shearing, Eq. (7) was applied with $\alpha\,\gamma_{lim}=5\cdot10^{-5}$. For this first approach, no distinction was made between soil stiffness values under first time loading and reloading.

5.2 Post-cyclic pile capacity

In Fig. 5 the post-cyclic load-displacement relationships for two different pile geometries are shown. Once a pile with diameter D=2m and length L=30m and once a pile with D=3m and L=20m was considered.

Static pullout-capacities of about 5.75 MN (D=2m, L=30m) and 3.75 MN (D=3m, L=20m) were obtained. The considered cyclic loads were pure swell-loads with amplitude of 40% of the obtained static capacities. Assessing the volume compaction dependent on the calculated shear strains and the number of load cycles, these values were applied to the model and afterwards pullout was modeled.

As to be expected, a decrease of post-cyclic capacity with the number of load cycles was obtained and can be seen in absolute values in Fig. 5 and as a degradation factor dependent on number of load cycles in Fig. 6. Since the dependence of the volume compaction on the number of load cycles is assumed to be logarithmic, also the decrease of post-cyclic capacity depends on the logarithm of load cycles. Very similar degradation factors were found for the two cases considered. The factors vary from about 8% for N=10 until about 30% for N=10,000. Similar results were also obtained with other pile dimensions. Thus, the results are valid for almost rigid piles with lengths of 20m to 30m under cyclic amplitude of 40% of the static pile capacity.

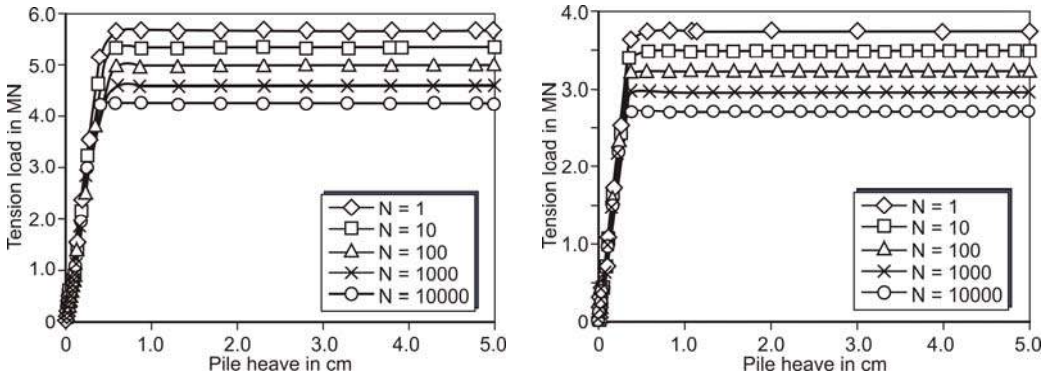

Figure 5. Numerically obtained post-cyclic tensile pile capacities (left: D=2m, L=30m, right: D=3m, L=20m)

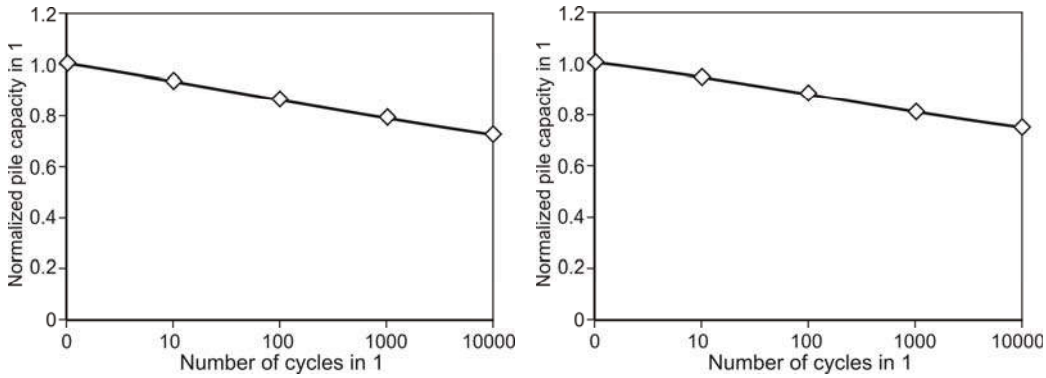

Figure 6. Pile capacity degradation due to cyclic pre-loading (left: D=2m, L=30m, right: D=3m, L=20m)

5.3 Skin friction distribution under cyclic loading

The decrease of the horizontal stress ($\Delta\sigma_r = \Delta\sigma_{11}$) around a pile with a diameter D=2.5m and length L=25m after 100 cycles is shown in Figure 7. The contour plot shows the effect of the cyclic loading on the horizontal stress and consequently on the ultimate skin friction between the pile and the soil. A decrease occurs up to a certain distance from the pile, which is consistent with the theoretical assumptions. This decrease of the horizontal stress is mainly concentrated in the soil beneath the lower part of the pile.

Figure 8 shows the distribution of ultimate skin frictions along the piles after different numbers of load cycles. For the rigid piles in sand considered here, a triangular distribution of ultimate skin friction is obtained for static load condition, as it also can be found in design guidelines (e.g. API 2000). Fig. 8 shows that after cyclic pre-loading this linear distribution changes to a non-linear distribution. The larger the depth, the larger the skin friction degradation becomes. In the first upper meters there is almost no degradation in the skin friction, because the cyclic shear strains in these depths are smaller than the threshold value above which volume compaction occurs. But below, the degradation starts and becomes maximal at the pile tip. This result is valid for rigid piles in homogeneous soil, since here the actual skin friction monotonically increases with depth and thus also the cyclic shear strain amplitudes become larger with depth.

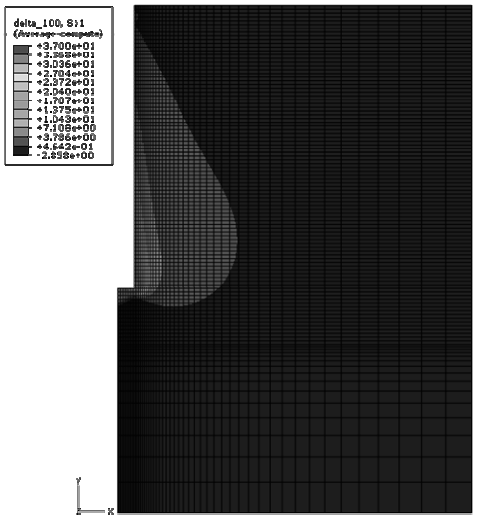

Figure 7. Decrease of the horizontal stress under cyclic loading (D=2.50, L=25.0m, N=100)

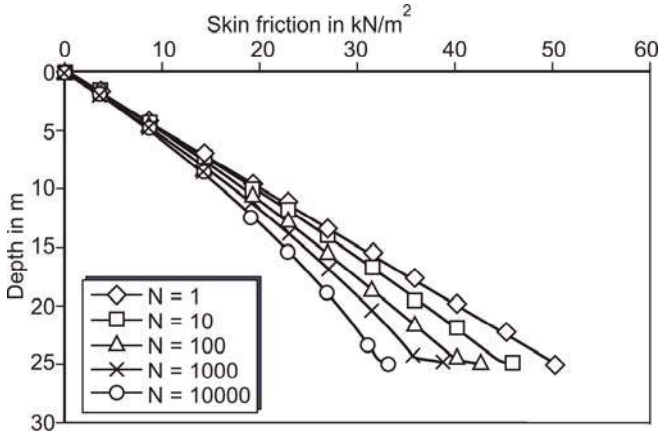

Figure 8. Skin friction degradation under cyclic loading (D=2.50, L=25.0m)

6 SUMMARY AND CONCLUSIONS

A numerical method was developed which is capable to assess stress changes in the soil around a pile due to cyclic axial loading and to figure out the post-cyclic pullout-capacity of the pile with respect to the magnitude of cyclic axial load and the number of load cycles. The method is a numerical realization of an analytical approach of Richter & Kirsch (2010). Here, the volume compaction due to cyclic shearing is assessed empirically dependent on the cyclic shear strains and is then applied to the pile-soil system.

In the paper in hand, mainly the idea and the way of realization of the method are described. First results for rigid piles in homogeneous medium dense sand are presented. The method gives a prediction of post-cyclic pile capacities and is thus a promising tool to assess cyclic load effects on the behavior of axially loaded piles.

In subsequent investigations, further parametric studies will be carried out with non-rigid piles, different relative densities of the sand soil, layered soils and different cyclic load magnitudes. A further refinement of the method is also highly desirable. In particular, consideration of small strain stiffness effects and distinction between first time loading and cyclic un- and reloading is foreseen.

ACKNOWLEDGEMENT

The results presented in this paper were obtained as part of the GIGAWIND ALPHA VENTUS research group project funded by the Federal Ministry for the Environment, Natural Conservation and Nuclear Safety, Germany. The support is thankfully acknowledged.

REFERENCES

ABAQUS User's Manual, Version 6.7. (2008). Simulia, Providence, RI, USA.

API (2000), "API Recommended Practice 2A-WSD", Recommended Practice for Planning, Designing, Constructing Fixed Offshore Platforms - Working Stress Design; 21st edition, Dallas.

API (2007). Errata and Supplement 3 - API Recommended Practice 2A-WSD, Recommended Practice for Planning, Designing, Constructing Fixed Offshore Platforms - Working Stress Design.

Jardine, E. & Standing (2000), "Pile Load Testing Performed for HSE". Cyclic Loading Study at Dunkirk, Volume 1 und 2. In: Offshore Technology Report, HSE Health & Safety Executive.

Kempfert, H.-G. (2009). Pfahlgründungen; in: Grundbau-Taschenbuch Teil 3, ed. K.J. Witt, Ernst & Sohn.

Mittag, J. & Richter, T. (2005), „Beitrag zur Bemessung von vertikal zyklisch belasteten Pfählen". Festschrift zum 60. Geburtstag von Herrn Prof. H.-G. Kempfert. Schriftreihe Geotechnik Universität Kassel, Heft 18.

Poulos, H.G. (1988), "Cyclic Stability Diagram for axially loaded piles". ASCE Journal of Geotechnical Engineering Vol. 114, No. 8.

H. Randolph, M. (2009), "Mechanical behaviour of soils under environmentally induced cyclic loads". Lecture at the International Centre for Mechanical Sciences (CISM), Udine.

Richter, T. & Kirsch, F. (2010),"Ein analytisch-empirischer Ansatz zur Bestimmung der Tragfähigkeit und der Verformungen von axial zyklisch belasteten Pfählen". Workshop Offshore-Gründungen von Windkraftanlagen, Karlsruhe.

Schwarz, P. (2002), "Beitrag zum Tragverhalten von Verpresspfählen mit kleinem Durchmesser unter axialer zyklischer Belastung". Lehrstuhl und Prüfamt für Bodenmechanik und Felsmechanik der Technischen Universität München, Schriftenreihe Heft 33.

Silver, L. & Seed, B. (1971), "Volume Changes in Sands during Cyclic Loading". In: Proceedings of the American Society of Civil Engineers, Vol. 97, No. SM9,1171-1182.

Wegener, D. & Herle, I (2010), "Zur Ermittlung von Scherdehnungen unterhalb von dynamisch belasteten Flächen", Geotechnik, Vol. 33, No. 1., 12-18.

Vucetic, M. (1994), „Cyclic Threshold Shear Strains in Soils", Journal of Geotechnical Engineering, Vol. 120, No.12, 2208-2228.

ANALYSIS OF LARGE DIAMETER MONOPILE FOR OFFSHORE WIND TURBINES

S.S. Jeong & Y.M. Kim
Department of Civil and Environmental Engineering, Yonsei University, Seoul, Korea

ABSTRACT: *The load distribution and deflection of large diameter monopile is investigated by lateral load transfer method (p-y curve). Special attention is given to the p-y characteristics using three-dimensional finite element analysis. A series of numerical studies are conducted on clay and sandy soil to determine the influence factors of monopile design. Based on the results, the modulus of subgrade reaction (K) and the ultimate soil resistance (p_u) increase linearly with an increase in pile diameter, while pile-toe conditions exert no significant influence on the p-y characteristics. Moreover, it is also found that for flexible piles the effect of pile diameter on K is more significant than for rigid piles.*

1 INTRODUCTION

According to the increasing demand for green energy from renewable sources, the application of offshore wind turbines is becoming an important issue in the alternative energy field. Although early offshore wind turbines were located in shallow waters, recent developments in the foundation engineering indicate that it would be possible to place the wind turbines in water depths of 30 to 40m. A monopile has been widely used as a foundation system to support the offshore wind turbines. It has diameters up to 4m with a wall thickness of as much as 150mm and slenderness ratios (*L/D*) around 5. The maximum forces acting at the foundation for typical offshore wind turbines are: 4MN in horizontal and 6MN in vertical directions, respectively, and 120MNm in overturning moment (Ubilla et al., 2006). Thereby, offshore wind turbines foundations are subjected to high lateral loads and bending.

Though axial loading and bending are major consideration in designing such structures, large lateral loads necessitate the use of large diameter piles. Therefore, lateral force-resistance in a large diameter monopile is complex and requires three-dimensional analyses.

Laterally loaded piles are traditionally designed based on a load transfer curve method (*p-y* curve). The *p-y* curves have been studied for many applications in engineering practice. This method is based on a numerical solution of a physical model based on a beam on a Winkler foundation. The offshore design regulations such as DNV (1992) and API (1993) also recommend using the *p-y* curve in practical design. The confidence in this method is derived from the fact that the p-y curves employed have been obtained (back calculated) from a few full-scale field tests. However, most *p-y* curves used in practice are based on the results of lateral load test on relatively small diameter piles (e.g., Matlock: 0.33 m diameter steel-pipe piles, four cases; Reese and Welch: 0.76 m diameter drilled shaft, one case; Reese et al.: 0.64 m diameter drilled shaft, three cases). Thus, there is a lack of well verified *p-y* curve for monopiles which have large diameter of around 3 to 4m.

The overall objective of this study is to verify *p-y* characteristics for applications to large diameter monopile under lateral loading. Therefore, a series of three dimensional Finite Element (FE) analyses were performed for lateral soil resistance.

2 3D FINITE ELEMENT MODELING OF THE MONOPILE

2.*1 Model description*

A 3D FE model to simulate the response of a monopile subjected to lateral loads using PLAXIS 3D Foundation (2008) is presented here. The typical 3D FE mesh used to analyze a monopile is shown in Figure 1. The overall dimensions of the model boundaries comprise a width of 11 times the pile diameter (D) from the pile center and a height equal to the pile length (L) plus a further 0.7L below the pile-toe level. These dimensions were considered adequate to eliminate the influence of boundary effects on the pile performance (Kim, 2010). The mesh consists of fifteen-node wedge elements. The outer boundary of the mesh is fixed against displacement. The monopile and soil are modeled with finite element, which allows for rigorous treatment of soil-structure interaction. Here, the analysis of a monopile is conducted under undrained conditions.

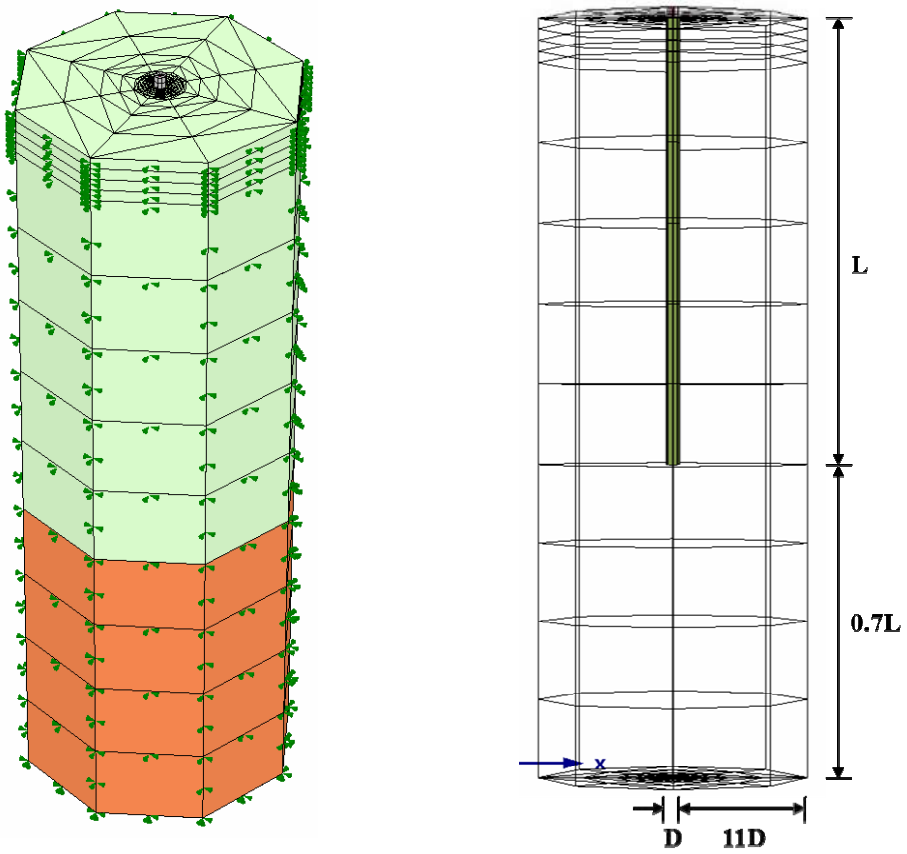

(a) 3-D view (b) Plan view

Fig. 1. Typical 3D model for FE analysis

2.2 *Material parameters and interface modeling*

The monopiles are considered as linear-elastic material with the parameters E_p=200GPa and v=0.25, while for the surrounding soil layer the Mohr-Coulomb model with non-associated flow rule is adopted. Here, the pile is modeled as a solid cylinder rather than an open tubular pile considering internal soil plugging effect. The interface element modeled by the bilinear Mohr-Coulomb model is employed to simulate the pile–soil interface. The interface element is treated as a zone of virtual thickness. It behaves as an element with the same material properties as the adjacent soil elements before slip occur. A decreased value of shear modulus is assigned to the interface element when a slip mode occurs in the interface element. The decrease of strength for the interface element is represented by a strength reduction factor R_{inter} in PLAXIS. The interface properties are calculated from following equation:

$$c_{\text{int}er} = R_{\text{int}er} c_{soil}, \quad \tan\phi_{\text{int}er} = R_{\text{int}er} \tan\phi_{soil} \tag{1}$$

where $c_{\text{int}\,er}$ and $\varphi_{\text{int}\,er}$ are the cohesion and friction angle of the interface, and c_{soil} and φ_{soil} are the cohesion and friction angle of the soil mass.

In numerical analysis, the initial equilibrium state is important. The specified initial stress distributions should match with a calculation based on the self-weight of the material. After the initial step, the applied loading was simulated by the application of a lateral load at the top of the pile. The modeling of the pile installation process is rather complicated, so that pile is assumed to be in a stress-free state at the beginning of the analysis, and the effect of the pile installation is ignored.

2.3 *Determination of soil response in FE analysis*

The soil resistance for a pile subjected to lateral loads is computed directly by integrating the stresses in the soil elements around the circumference of the pile. Fan & Long (2005) have reported that using soil element around the pile is an effective way to predict the lateral soil resistance (p). Based on this concept, the stresses in the soil elements at the Gauss points closest to the pile are taken as the soil stresses between the pile and soil. A cross-section of a pile–soil system with a lateral load applied in the x-direction is shown in Figure 2. The closest Gauss points to the pile in the soil elements are on the dashed circumference. The soil resistance per unit length along the pile is the x-component of the total stress acting on the dashed circumference. The x-component stresses at a point in a soil element can be represented by a traction vector, T_x, as follows:

$$T_x = \sigma'_{xx} n_x + \sigma'_{xy} n_y + \sigma'_{xz} n_z \tag{2}$$

where n_x, n_y, and n_z are the components of the unit normal along the x-, y-, and z-direction at the gauss point, respectively. The component n_y is zero because the unit normal is along horizontal plane. To calculate the total soil resistance p_x per unit length along the pile, the soil resistance is integrated over the dashed circumference, and p_x is expressed as:

$$p_x = \int T_x dL \tag{3}$$

where L is the circumference of the closest Gauss points in the soil elements adjacent to the pile. The p–y relationship at a given depth is obtained by relating the soil resistances p to the corresponding lateral deflections y of the pile at that depth.

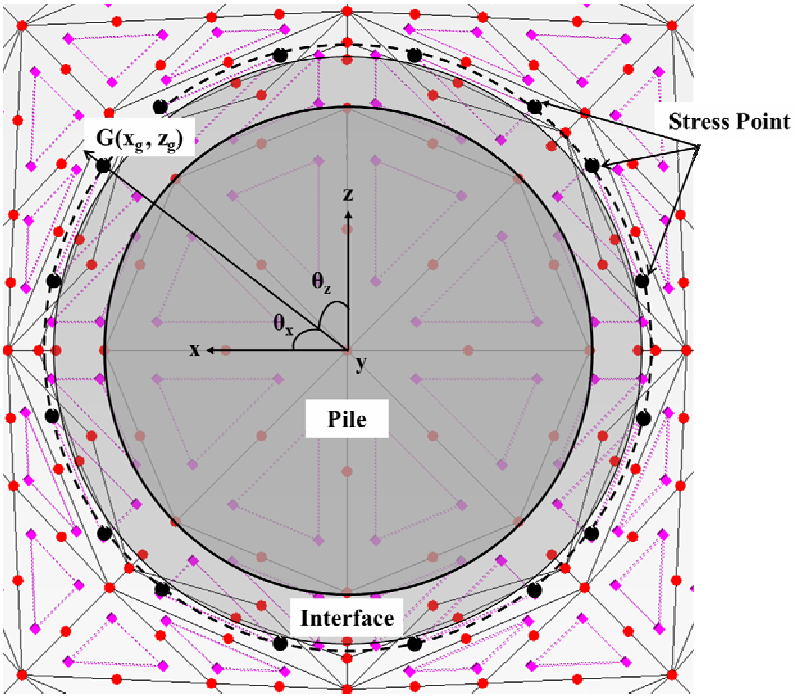

Fig. 2. Cross-section of a pile-soil system in the horizontal-direction

3 PARAMETRIC STUDY

To examine the influencing factor of a lateral load transfer, a series of FE analyses on monopile(steel pile) were performed based on the major influencing parameters, such as the pile diameters (D), the pile length (L), the soil type and the bearing layer. Table 1 summarizes the configuration and material properties used in the analysis.

3.1 Effect of soil-pile rigidity

Based on the soil-pile rigidity criterion (Randolph, 1981), the soil-pile rigidity is a direct function of the pile characteristic (β) and pile length (L). In order to verify the effect of lateral soil-pile rigidity, the Broms criterion is applied to the piles. The value of pile characteristic (β) can be assessed from the following equation.

$$\beta = \sqrt[4]{\frac{K_{ave}}{4E_pI_p}} \qquad (4)$$

where K_{ave} is the average value of the modulus of subgrade reaction (K) and is the flexural rigidity of the pile. To obtain detailed information on the pile behaviors based on soil-pile rigidity, piles with the same elastic modulus, (E_p) but different pile diameters (D) and embedment lengths (L) were employed as shown in Figure 3.

The effects of pile diameter and embedment length at a certain depth are shown in Figure 4. There are so many researches about the effect of the pile diameter and the pile length on the modulus of subgrade reaction (K, Initial slope of p-y curve). Terzaghi (1955) and Vesic (1961) concluded that the diameter and length of piles have no effect on the modulus of subgrade reaction. Additionally, Ashford and Juirnarongrit (2003) indirectly verified that the modulus of subgrade reaction is independent of pile diameter when examining full-scale

vibration tests results on drilled shaft in a sand deposit. However, Carter (1984) found from his own field test data that the diameter and the length of piles exerted significant effect on modulus of subgrade reaction. From the present studies, it is found that the lateral load transfer was highly influenced by the pile diameter as the characteristic length increased (belong to flexible pile category). Similar results concerning the effect of soil-pile rigidity on K were found previously by Guo (2001) in his numerical study. Therefore, the initial slope of p-y curve increases linearly with the increase of the pile diameter when the pile is designed to be flexible pile.

Table 1. Summary of material properties

Type	Model	L (m)	D (m)	E (MPa)	μ_s	γ_{sat} (kN/m^3)	c_u (kPa)	φ (°)
Pile	Elastic	8 25 40	1 2 3 4	200,000	0.20	23.0	-	-
Clay	M.C.[a]	-	-	3-15	0.49	17.5	15-25	-
Sand	M.C.	-	-	40-80	0.49	18.5	-	34
Rock	Elastic	-	-	8,000	0.25	20.2	-	-

[a] *Note*: M.C. is Mohr-Coulomb model.

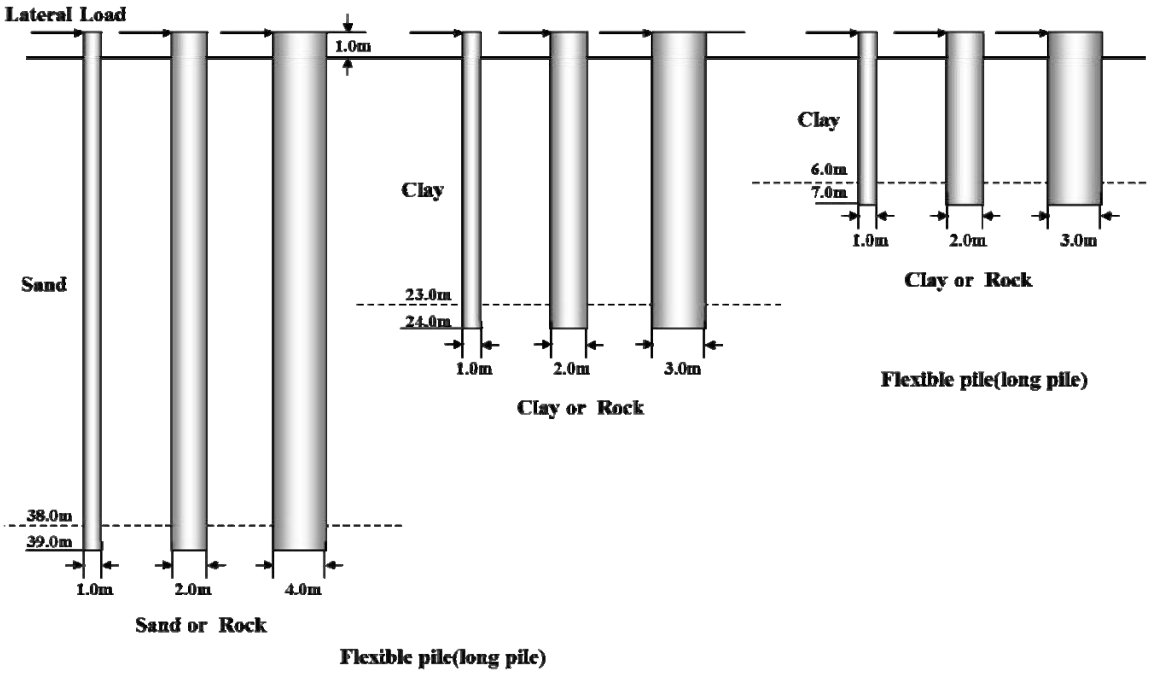

Fig. 3. Subsurface profile and pile embedments

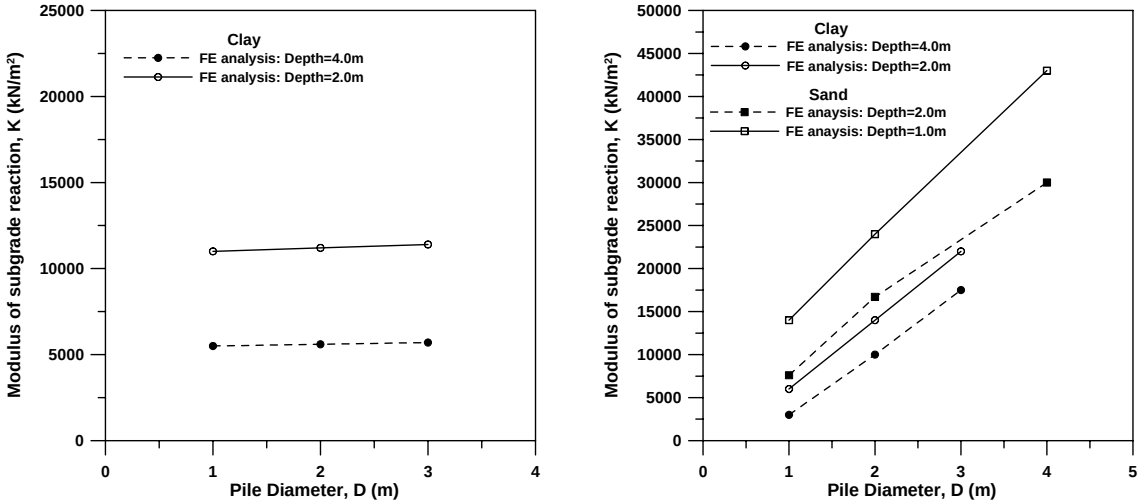

(a) Rigid pile (b) Flexible pile

Fig. 4. Initial slope of p-y curves for various pile diameter

3.2 Effect of Bearing Layer

In order to investigate the effect of bearing layer, additional FE analyses are conducted in single clay and sand soil. Both the rigid and flexible piles have the toe embedded in the same soil layer as used in the previous parametric cases. Again, the *p-y* curve is generated for a depth of 1m in clay and 1-2m in sand. The comparison results according to existence of bearing layer are shown in Figure 5-6. Based on the results, it is found that the ultimate soil resistance of rigid pile only has increased by approximately 5%, while the *p-y* characteristics of the flexible pile have no effect on bearing conditions. However, this increasing rate in rigid pile does not seem to be having much effect on the nonlinear pile analysis. Ashour & Norris (2000) and Kim et al. (2009) have reported comprehensive studies of pile-soil interaction. They conclude that the magnitude and distribution of the *p-y* curves are hardly influenced by the shear resistance at the base of the shaft when the pile is rigid.

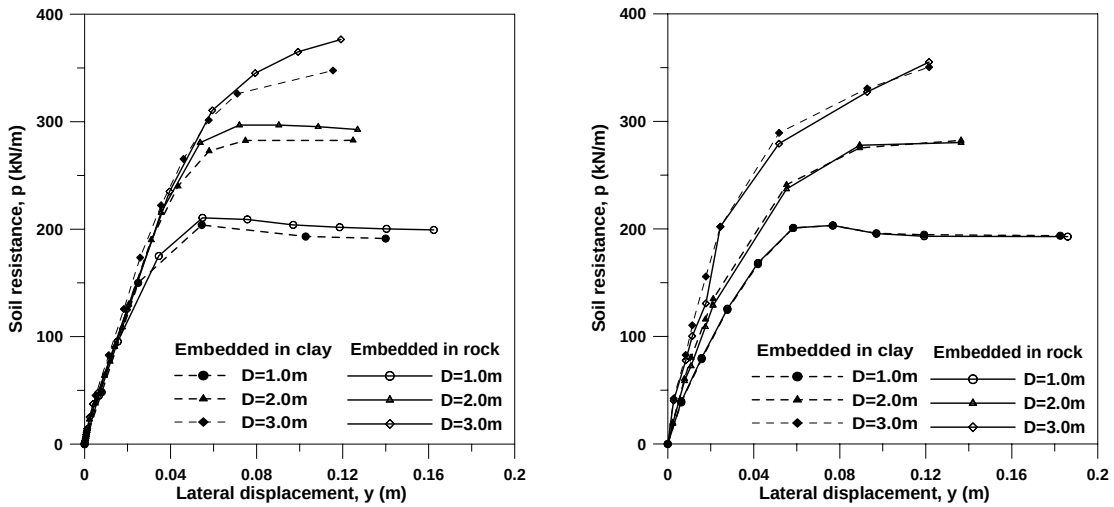

(a) Rigid pile (b) Flexible pile

Fig. 5. Comparison of p-y curves for various bearing conditions in clay

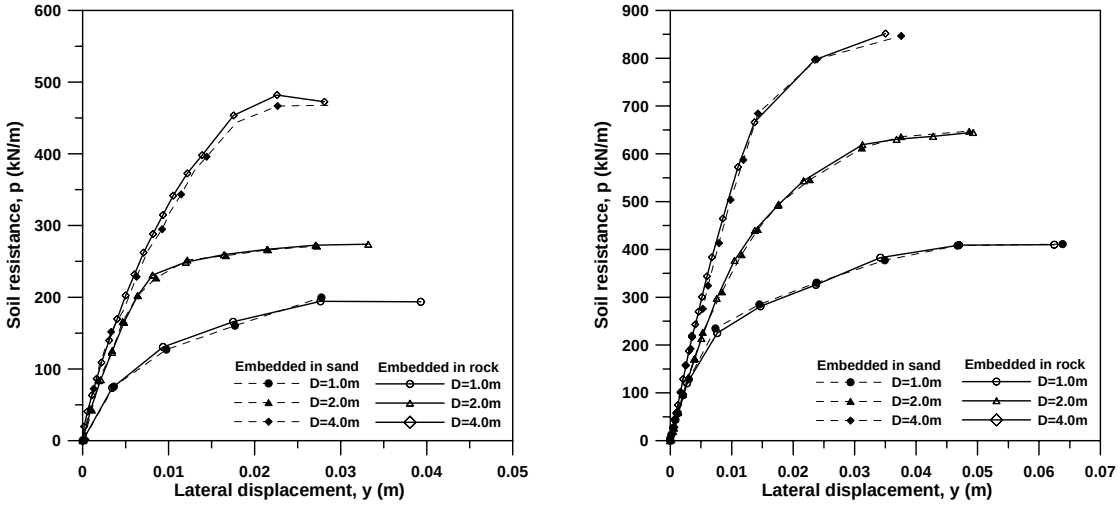

(a) Depth 1.0m (b) Depth 2.0m

Fig. 6. Comparison of p-y curves for various bearing conditions in sand

4 CONCLUSIONS

The main objective of this study is to investigate numerically lateral load transfer curve with respect to monopile, which are constructed on offshore deposits. For this work, the nonlinear 3D finite element modeling has been presented and discussed by taking into account the soil-pile continuity. To examine the influencing factor of a lateral load transfer, a series of parametric studies were performed. Based on the findings of this study, the following conclusion can be drawn:

1. The modulus of subgrade reaction (K) and the ultimate soil resistance (p_u) increase linearly with an increase in pile diameter, while pile-toe conditions exert no significant influence on the p-y characteristics
2. Moreover, it also found that for flexible piles the effect of pile diameter on K is more significant than for rigid piles.

REFERENCES

API. (1993), Recommended practice for planning, designing, and constructing fixed offshore platforms-Working stress design, API RP2A-WSD, American Petroleum Institute, Washington D.C., 21. edition.

Ashford, S.A. & Teerawut Juirnarongrit (2003). “Evaluation of pile diameter effect on initial modulus of subgrade reaction.” J. Geotech. Geoenvir. Eng., Vol. 129(3), 234-242.

Ashour, M. & Norris, G. (2000). “Modelling Lateral Soil-Pile Response Based on Soil-Pile Interaction.” J. Geotech. Geoenvir. Eng., Vol. 126(5), pp. 420-428.

Carter, D.P. (1984). “A nonlinear soil model for predicting lateral pile response.” Rep. No. 359, Civil Engineering Dept., Univ. of Auckland, New Zealand.

Cox, W.R., Reese, L.C. & Grubbs, B.R. (1974). “Field testing of laterally loaded piles in sand.” In Proc. of the 6th Annual Offshore Technology Conference, Houston, Texas, USA, OTC 2079, pp.459-472.

DNV. (1992), Foundation-Classification Notes No. 30.4, Det Norske Veritas, Det Norske Veritas Classification A/S.

Fan, C.C. & Long, J.H. (2005). “Assessment of existing methods for predicting soil response of laterally loaded piles in sand.” Computers and Geotechnics, Vol. 32, 274-289.

Guo, W.D. (2001). “Subgrade modulus for laterally loaded piles.” Proceedings of the Eighth International Conference on Civil and Structural Engineering Computing, Vienna, Austria.

Kim, Y.H. (2010), “Improved lateral load transfer (p-y) curves for large diameter piles based on 3D wedge failure method”. PhD thesis, Yonsei University

Kim, Y.H., Jeong, S.S., & Won, J.O. (2009). “Effect of lateral rigidity of offshore piles using proposed p-y curves in marine clay.” J. Marine Georesources and Geotechnology, 27(1), 53-77.

Matlock, H. (1970), “Correlations for design of laterally loaded piles in clay.” Proc. of Second Annual Offshore Technology Conference, Houston, Texas, USA, Vol. 1, pp. 577-594.

PLAXIS 3D Foundation. (2008), PLAXIS 3D foundation user manual, Version 2.0, Brinkgreve, R.B. and Swolfs, W. M., PLAXIS Inc.

Randolph, M.F. (1981), “The response of flexible piles to lateral loading.” Geotechnique, Vol. 31(2), pp. 247-259.

Reese, L.C., Cox, W.R. & Koop, F.D. (1974), “Analysis of laterally loaded piles in sand.” In Proc. of the 6th Annual Offshore Technology Conference, Houston, Texas, USA, OTC 2080, pp.473-484.

Reese, L.C. & Welch, R.C. (1975), “Lateral loading of deep foundations in stiff clay.” J. Geotech. Geoencir. Eng., Vol. 101(7), pp.633-649.

Terzaghi, K. (1955). “Evaluation of Coefficients of Subgrade Reaction.” Geotechnique, Vol. 5, pp 297-326.

Ubilla, J., Abdoum, T. & Zimmie, T. (2006), “Application of in-flight robot in centrifuge modeling of laterally loaded stiff pile foundations”. Physical Modeling in Geotechnics., Taylor & Francis Group, London, 259-264

Vesic, A.S. (1961). “Bending of beams resting on isotropic elastic solids.” J. Engrg. Mech. Div., ASCE, 87(2), 35-53.

ON THE FINITE ELEMENT STABILITY ANALYSIS OF SLOPES UNDER INCREASING PORE WATER PRESSURE

A. Cividini, G. Gioda
Department of Structural Engineering, Politecnico di Milano, Milan, Italy

M. Redaelli
Halcrow Group Ltd., London, UK

ABSTRACT: *A discussion is presented of the influence of the hydraulic boundary conditions on the finite element stability analysis of a river levee. The problem concerns an embankment built on a low-permeability soil layer overlying a coarse-grained deposit. It is shown that the finite element calculations could predict stable or unstable conditions of the levee depending on the assumed distance between the river and the external boundary of the mesh where the water table is assumed undisturbed. The causes of this notable drawback are discussed, showing that they derive from the marked influence that the mentioned distance has on the calculated pore pressure distribution below the embankment. The calibration of a proper numerical seepage model, based on the back analysis of piezometer measurements, is suggested as a possible way to limit the observed boundary effects*.

1 INTRODUCTION

The finite element analyses involving unbounded domains often require the introduction of external boundaries that limit the discretized portion of the medium. In geotechnical engineering, depending on the nature of the problem being analyzed, the stresses (total or neutral) and/or the displacements are constrained on these boundaries. Unless specific geometric or hydraulic conditions are present, their location and the consequent size of the mesh depend on the judgment of the analyst.

The influence of the location of the abovementioned boundaries has been discussed by Cividini & Gioda (2007) with reference to seepage problems, showing that they strongly influences the back analysis of the coefficients of hydraulic conductivity based on in-situ pumping tests. Here the discussion is extended to the influence of the hydraulic boundary conditions on the stability of river levees considering a problem frequently met in practice. It concerns an embankment built on low-permeability, fine-grained soil overlying a coarse-grained deposit with much larger coefficient of hydraulic conductivity (see Fig. 1).

The adverse hydraulic effects on the stability of the embankment can lead to two main failure modes. The first one is due to under-piping and is related to the development of excessive gradients in the covering layer at the ground surface. This can produce sand boils and subsurface erosion that could compromise the integrity of the levee, leading eventually to its failure. Studies on this process and practical tools for the prediction of the exit gradient have been proposed by Wolff (1989) and Gabr et al. (1996).

It is also believed that the stability of landward slope in dikes and levees can be affected by uplift forces developing at the base of the upper impervious layer that, in turn, are related

to the pore pressure increase in presence of high water levels (Cooling & Marsland, 1954; Marsland, 1961; Bauduin et al., 1989; Van, 2001; Ozkan et al., 2008).

The uplift induced failure of a levee is discussed here based on a series of finite element analyses. The numerical results demonstrate the influence of the distance between the draining boundary of the mesh and the levee. It is shown that, depending on this distance, the calculations could predict failure of the levee, under moderate water levels in the river, or stable conditions also in the presence of high water levels.

Possible reasons for this unexpected result are discussed and calibration of predictive numerical seepage models is suggested that could mitigate the mesh dependence of the numerical analyses.

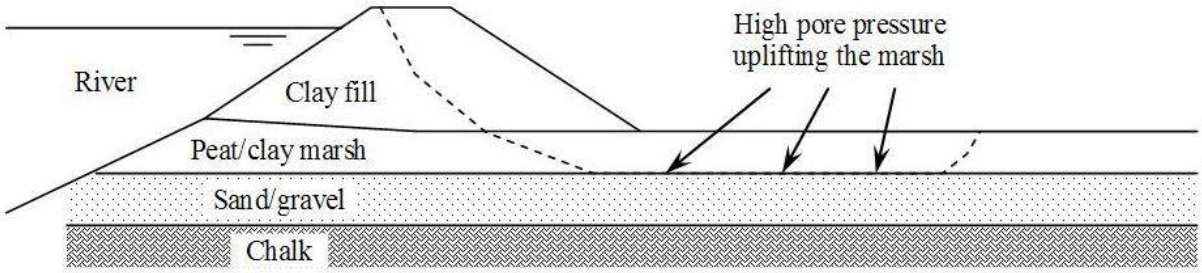

Fig. 1. Scheme of the uplift mode of failure.

2 PREVIOUS STUDIES

The uplifting mechanism was introduced to explain the bank failure that occurred in the Thames Estuary during the 1953 North Sea flood, resulting in a major breach. The levee at Dartford Lock was built on a peat/clay marsh overlying a stratum of gravel which, outcropping in the riverbed, was in direct hydraulic communication with the body of water.

Cooling & Marsland (1954) and Marsland (1961) suggested that the marsh acted as an impervious boundary, favoring the build up of high pore pressure in the underlying gravel. The resulting uplifting forces induced the floatation of the low density marsh; the slope was then deprived of the lateral support initially provided by the marsh and, consequently, it failed.

Hird et al. (1978) investigated the effects of hydraulic uplift through centrifuge tests on model levees. Some of the tests were heavily influenced by the rigid boundaries of the model. In a subsequent centrifuge testing program Padfield & Schofield (1983) further investigated the possibility that a mechanism different from the usual rotational failure could be triggered by high pore pressure at the base of the top layer.

A circular slip surface, not intersecting the layer interface, was observed under increasing gravity only when no uplift pressure was applied. On the contrary, when the uplift pressure was increased holding the gravitational acceleration constant the observed slip surface started in the levee body and then run along the layers interface, without returning to the surface.

Finally when the gravitational acceleration was increased keeping the uplift pressure constant a hybrid type of failure occurred, with the slip surface following the interface, significantly deviating from a purely rotational mechanism, but finally re-emerging (Padfield & Schofield, 1983).

The unexpected collapses of some dams during the 1980s in the Netherlands were explained as uplift-induced failures (Bauduin et al., 1989). The subsequent research led to an analytical method (Van, 2001; Van et al., 2005) for the stability analysis of dikes subject to uplifting. This method follows a modified limit equilibrium approach and introduces a longer

slice, representing the uplifted zone, the length of which depends on the pore pressure acting at its bottom (Barends, 1988; 2003).

It is worth noting that when the fine grained top layer is uniform, the calculations lead to a factor of safety for the uplift-induced failure higher than that resulting for the purely rotational failure. This fact has also been noted by Padfield & Schofield (1983) who, having observed the non-emergent failure surface in their centrifuge tests, suggested that the uplift-induced failure mechanism could be influenced by the lateral deformation of the top layer.

Since this deformation cannot be introduced in a limit equilibrium approach, a non-linear finite element analysis is attempted here that accounts for its influence. The calculations showed an unexpectedly large effect of the pore pressure and displacement boundary conditions, as discussed in the following.

3 NUMERICAL MODEL

The finite element mesh of eight-node isoparametric elements adopted in this study is shown in Fig. 2 and derives from the scheme in Fig.1. The selected geometry and material properties do not refer to a specific case history but could reasonably represent conditions frequently met in river levees.

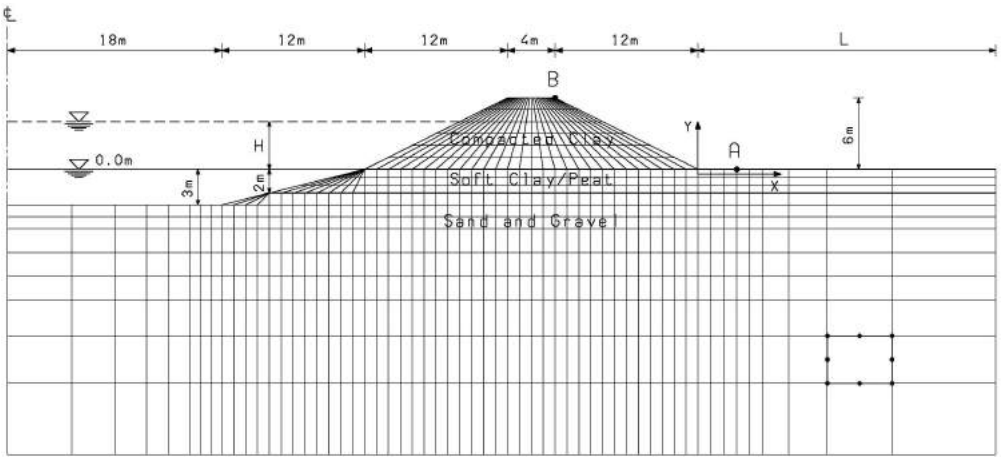

Fig. 2. Finite element mesh of quadrilateral eight node isoparametric elements.

The embankment and the soil layers are assumed to be fully saturated. A coupled approach is adopted in the calculations, where the displacement components of the soil skeleton and the pressure of the liquid phase represent the nodal variables.

To avoid inconsistencies between the effective and neutral stress distributions, the two fields should be interpolated within the elements through polynomials having similar degree. Consequently, while the displacements are defined at all nodes of the element, the pore pressure is defined only at its four corner nodes.

The stability problem is addressed through a sequence of seepage and elastic-plastic analyses. The effective stress state prior to the construction of the levee is first determined subjecting the mesh to the total self-weight of soil (soft layer and sand) and to the buoyancy forces at each node that correspond to the hydrostatic condition when the river level coincides with the ground surface. This first analysis, where the embankment is not introduced, is carried out in drained conditions and smooth boundaries are assumed, in terms of nodal displacements, for the vertical and bottom sides of the mesh.

According to the formulation of coupled two-phase problems (see e.g. Sandhu & Wilson, 1969; Ghaboussi & Wilson, 1973; Zienkiewicz, 1985), the buoyancy forces $\underline{f}_p$ are derived from the nodal pore pressures $\underline{p}$ through the following relationships:

$$\underline{f}_p = \underline{C}\,\underline{p} \quad , \tag{1}$$

$$\underline{C} = \sum_e \int_{V_e} \underline{B}_e^T \cdot \underline{m} \cdot \underline{g}_e^T dV \quad . \tag{2}$$

Here $\underline{C}$ is the so called coupling matrix of the assembled mesh; $\underline{B}_e$ is the displacement-strain matrix containing the derivatives of the displacement interpolation functions of the e-th element, having volume V_e; $\underline{g}_e$ is the vector of its pore pressure interpolation functions; $\underline{m}$ is a vector whose entries are equal to 1 if they correspond to normal stresses, 0 otherwise.

The analysis then proceeds with the simulation of the levee construction. This is done in six steps adding each time a row of elements 1 m in height. The total weight of the compacted clay is applied to these elements and again an elastic-plastic analysis is carried out in drained conditions. The water table and the river level still coincide with the original ground surface. No appreciable plastic strains were observed at the end of the levee construction.

Having evaluated the initial effective stress distribution by means of the abovementioned analyses, the river level is increased in steps of 1 m each until the levee crest is reached. Considering the relatively short time during which this process takes place, and the low hydraulic conductivity of both compacted clay and soft layer, undrained conditions were assumed for these materials during each step. Drained conditions were assigned to the underlying granular deposit instead.

At the beginning of each step a confined seepage analysis is performed to evaluate the pore pressure within the coarse-grained layer depending on the current river level. In this simulation the left vertical boundary of the mesh, which corresponds to the river centerline, is impervious. The same condition is also imposed on the mesh bottom. On the contrary, a hydrostatic pore pressure distribution is applied to the (pervious) right boundary of the mesh were the water table coincides with the ground surface. The distance L in Fig. 2 denotes the location of this boundary and it can be referred to as the "hydraulic radius" of the problem.

The increment of pore pressure in the granular deposit with respect to the previous river level is then evaluated and the equivalent nodal forces $\underline{f}_p$ are computed through Eq. (1). These forces and those equivalent to the increase of the water load on the river contour provide the load vector $\underline{f}$, which is applied in subsequent small increments to the mesh.

Each increment requires an elastic-plastic stress analysis where undrained conditions are assumed only for the embankment and the soft clay/peat layer. This analysis involves an iterative process (Zienkiewicz et al., 1969) that provides the vectors of incremental nodal pore pressures $\underline{p}^*$, for the undrained elements only, and displacements $\underline{u}$ on the basis of the current increment of nodal forces $\underline{f}$.

Note that while $\underline{f}$ depends on the pore pressures $\underline{p}$ (cf. Eq. 1) in the granular deposit (obtained from the previous seepage analysis), $\underline{p}^*$ is the unknown pore pressure increment that develops in the undrained elements when the forces $\underline{f}$ are applied to the mesh.

In the elastic-plastic stress analyses both vertical and horizontal displacements of the nodes belonging to the right and bottom boundaries of the grid are constrained, while only the horizontal component is constrained on the left vertical boundary that coincides with the river centerline (see Fig. 2).

4 SOIL PROPERTIES

An elastic perfectly plastic behavior obeying Mohr-Coulomb yield criterion with a non-associated flow rule was adopted for the levee and for the soil layers. The values of the relevant material constants are listed in Table 1.

Table 1. Soil properties

Soil type	γ_{sat} **(kN/m^3)**	E' **(MPa)**	ν' **(-)**	c' **(kPa)**	ϕ' **(°)**	c_u **(kPa)**
Compacted clay	18.	50.	0.25	10.0	28	100.
Soft clay/peat layer	16.	10.	0.25	0.1	20	25.
Sand/gravel deposit	19.	200.	0.25	0.0	32	--

As to the non associated flow rule, the plastic potential coincides with Mohr-Coulomb criterion and is characterized by a dilation angle $\psi = \alpha \cdot \phi'$. Different values of coefficient α, namely 0.3, 0.2 and 0.1, were used respectively for the sand deposit, for the embankment and for the soft clay layer. The calculations were also repeated using the same coefficient α=0.3 for the three materials without observing appreciable changes in the results.

A marginal observation concerns the ultimate shear resistance τ_{lim} of soil. Consider two elastic-plastic analyses carried out in undrained conditions: the first based on a total stress c_u approach; the second one based on the coupled two-phase approach and on the effective parameters c' and ϕ'. Obviously the two calculations should lead to the same result, hence,

$$\tau_{\lim} = c_u = c' + \sigma' \cdot \tan\phi' \quad . \tag{3}$$

A simple way to fulfill Eq. (3) and, hence, to obtain from the two analyses the same overall shear resistance, consists of introducing in the effective stress calculation a "built in" effective stress σ^* such that,

$$\sigma^* = \frac{c_u - c'}{\tan\phi'} \quad . \tag{4}$$

Considering the parameters listed in Table 1 for the embankment clay being considered, the stress σ^* is found to be about 170 kN/m^2. The ratio between σ^* and the maximum vertical effective stress σ_v' at the embankment base at the end of construction, is about σ^*/σ_v'=1.6. As to the soft clay layer the ratio σ^*/σ_v' slightly exceeds 2.

Based on the above observations, and taking into account that the moderate mechanical compaction of the embankment during construction could increase the abovementioned "built in" stress, a ratio σ^*/σ_v' equal to 2 was adopted for both clays.

Consequently, the volumetric part of the effective stresses of the two clay zones at the end of the embankment construction was doubled before simulating the rising of the river. Note that the "built in" stress affects only the elastic-plastic calculations but it does not enter into the global equilibrium of the relevant elements.

5 RESULTS OF CALCULATIONS

Initially the calculations have been based on a mesh (cf. Fig. 2) having a distance L=25 m between the land toe of the levee and the right vertical boundary. The boundary effects observed by Hird et al. (1978) in their centrifuge tests suggested using also meshes with

increasing L, namely 50, 100 and 200 m. They were obtained introducing additional elements on the right side of the grid with L=25 m. The largest mesh, with L=200 m, has 2893 nodes and 916 eight node elements.

It turned out that L had an unexpectedly large influence on the numerical results, as shown by the diagrams in Fig. 3. The first two diagrams report the displacements of points A and B in Fig. 2 during the rising of the river level H. Fig. 3c reports the water level at collapse as a function of L. Note that this level varies from less than 2 m to more than 5 m with increasing L.

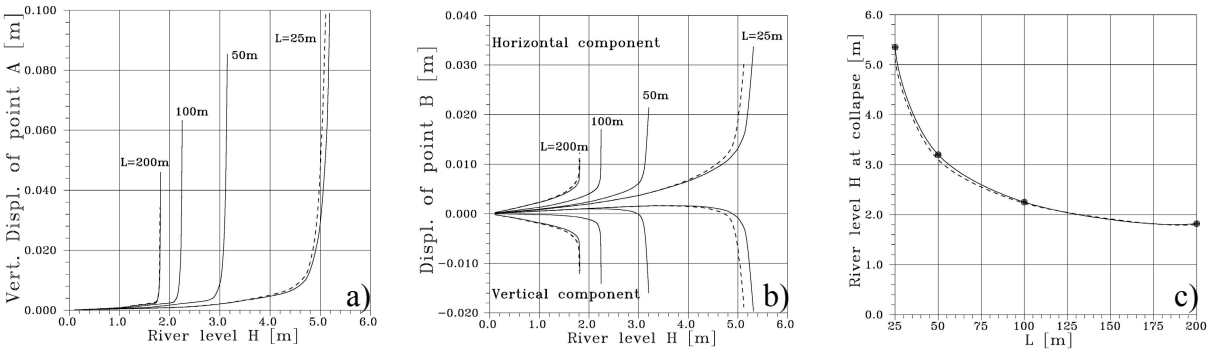

Fig. 3. a,b) Displacements of points A and B in Fig. 2 vs. river level H; c) river level at collapse vs. geometrical parameter L. The dashed lines refer to the analyses with pore pressure tension cut off.

The solid lines in the above figures refer to analyses in which no limits were introduced to the pore pressure within the undrained region (embankment and soft fine-grained layer). Additional analyses were carried out (dashed lines) introducing a tension cut off on the pore pressure to avoid the attainment of pore pressures smaller than the atmospheric one. This provision, in fact, has some influence when dealing with the analysis of shallow excavation and retaining structures (Cividini & Gioda, 2004). For the problem at hand, however, this effect appeared quite marginal.

The large influence of L on the numerical results depends on the fact that the pore pressure distribution at the base of the soft layer is governed by the location of the right vertical boundary where the undisturbed water table level is imposed. To gain some insight into this influence, Fig. 4a shows the different uplift pore pressure distributions underneath the soft layer that develop at the onset of embankment collapse. Figs. 4b,c report the corresponding diagrams of the vertical effective stress. Note that tensile neutral and effective stresses are assumed as positive.

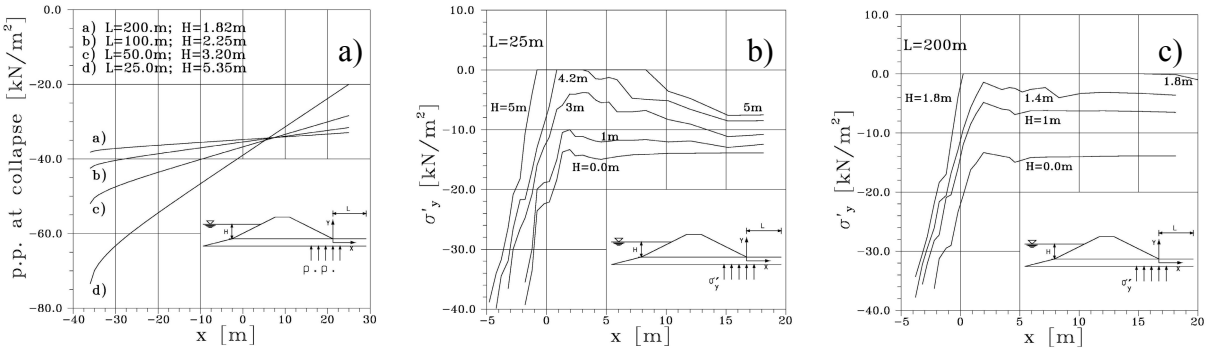

Fig. 4. a) Uplift water pressures and b,c) vertical effective stresses acting at collapse at the base of the landward toe of the embankment.

Small values of L, e.g. curve (d) in Fig. 4a, lead to a rapid decrease of the pore pressure in the coarse-grained deposit from the river bed towards the right draining boundary. As a consequence, a relatively high river level is necessary to reach the floatation of the low density marsh and the collapse of the earth embankment. Note that the effective vertical stress at the base of the soft layer vanishes at collapse (see Figs. 4b,c).

On the contrary, an almost constant distribution of the uplift pressure is obtained for large values of L, e.g. curve (a) in Fig. 4a, which for $L \to \infty$ tends to the hydrostatic water pressure exerted by the river.

In other words, the numerical evaluation of the river level that could involve a failure of the levee depends on the arbitrary choice of the horizontal length L of the finite element mesh.

The mesh size also influences the spreading of the plastic region. Figs. 5 and 6 show the contour lines of the square root of the second invariant of the deviatoric plastic strains for L=25 m and 200 m, respectively. These diagrams correspond to the load increment immediately preceding failure that in the elastic-plastic analyses involves non-convergence of the iterative solution process.

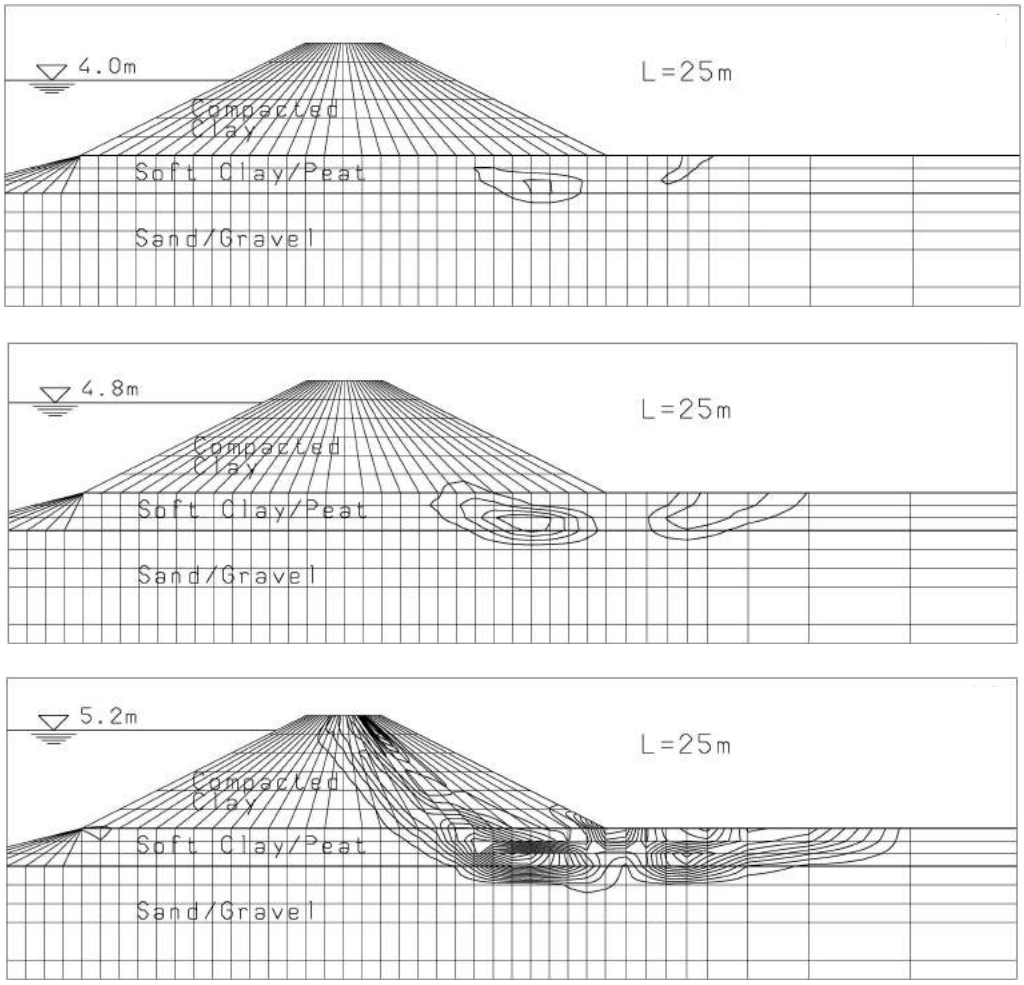

Fig. 5. Horizontal size of the mesh L=25 m: contour lines of the square root of the second invariant of deviatoric plastic strains during the river rising..

Two plastic regions initiate within the soft layer when L=25 m: the first one underneath the landward toe of the embankment; the second on at the right of the embankment. Collapse occurs when the two zones meet with each other and the first one suddenly spreads within the river bank. This collapse mechanism seems similar to a circular mode of failure.

On the contrary, the onset of only one plastic zone is observed for L=200 m. This zone develops in the soft layer underneath the embankment and spreads within it. In the condition immediately preceding collapse, no appreciable plastic region can be observed in the soft layer on the right of the levee. This second behavior presents some similarities with the non-emerging failure surface experimentally observed by Padfield & Schofield (1983).

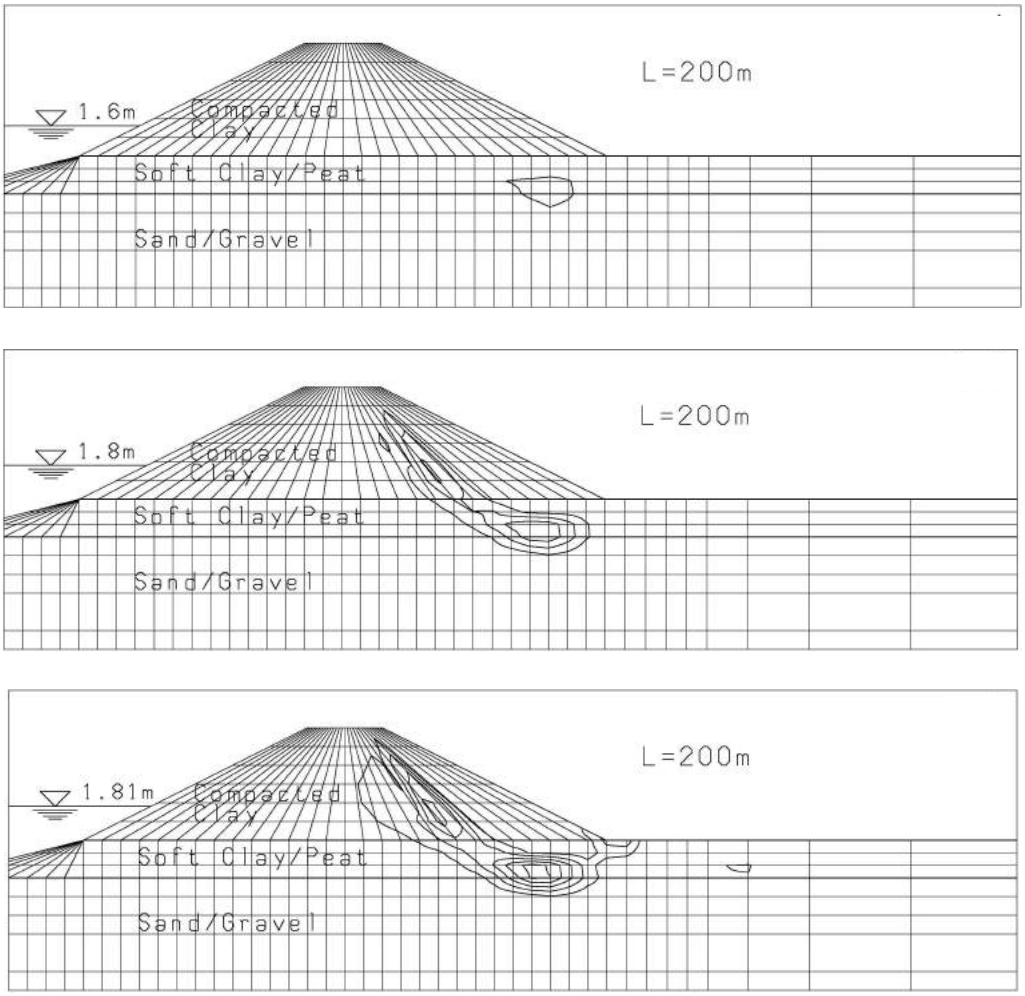

Fig. 6. Horizontal size of the mesh L=200 m: contour lines of the square root of the second invariant of deviatoric plastic strains during the river rising.

6 CONCLUDING REMARKS

The finite element stability analysis of a river levee has been discussed considering the increase of the uplift water pressure as the driving force. It was shown that the numerical results are governed by the distance L between the embankment and the boundary of the mesh where the undisturbed water level is assumed and the displacements are constrained.

This influence is similar to that of the so-called hydraulic radius on the evaluation of the coefficient of hydraulic conductivity based on field pumping tests. In that case the equation

that relates the inflow of water within the well to the coefficient of permeability of the surrounding soil contains the hydraulic radius, i.e. the distance between the well and the location of the undisturbed water table. Consequently this quantity influences the coefficient of hydraulic conductivity derived from the interpretation of field data.

Similarly, in the problem analyzed here the arbitrary length L governs the distribution of the uplift water pressure and, hence, the calculated river level at collapse.

In both cases the problem solution depends on the location of the boundary where the water table reaches its undisturbed level. Unless specific hydrogeological information is available, the position of this boundary is often left to the judgment of the engineer. Consequently the results of the finite element analyses depend on an arbitrary geometrical choice and can lead to quite different and contradictory results.

The application of back analysis procedures, frequently employed in geotechnical engineering practice today, could represent a possible way to overcome this notable drawback.

In the context of the problem at hand, a series of piezometers could be installed in the vicinity of the levee toe. The pore pressure variation recorded during the fluctuations of the river level would allow for the calibration of a proper predictive model (numerical or analytical) of the hydraulic regime in the sand and gravel underlying the soft upper layer. This model could subsequently provide reliable pore pressure data for estimating the behavior of the embankment under particularly severe increases of the river level.

REFERENCES

Barends, F.B.J. (1988), "Uplift in the hinterland at high water levels", (in Dutch). Report No. CO-290831/2, GeoDelft, Delft, The Netherlands.

Barends, F.B.J. (2003), "Groundwater mechanics and flood risk management", Proceedings of the International Symposium on Groundwater Problems related to Geo-Environment, Okayama (Japan), 53-66.

Bauduin, C.M.H., Moses, C.J.B. & Van Baalen, M. (1989), "The influence of uplift pressure on the deformations and stability of flood embankments", Proceedings of the 12th International Conference on Soil Mechanics and Foundation Engineering, Rio de Janeiro (Brazil), 3, 1713-1716.

Cividini, A. & Gioda, G. (2004), "Pore pressure tension cut-off in two-phase finite element analyses". Computers and Geotechnics, 31(8), 613-624.

Cividini, A. & Gioda, G. (2007), "Back-analysis approach for the design of drainage systems". International Journal of Geomechanics ASCE, 7(5), 325-332.

Cooling, L.F. & Marsland, A. (1954), "Soil mechanics studies of failures in the sea defence banks of Essex and Kent", Proceedings of the Conference on the North Sea Floods, Institution of Civil Engineers, 58-73.

Gabr, M.A., Wolff, T.F., Brizendine, A.L. & Taylor, H.M. (1996), "Underseepage analysis of levees on two-layer and three-layer foundation". Computers and Geotechnics, 18(2), 85-107.

Ghaboussi, J. & Wilson, E.L. (1973), "Flow of compressible fluid in porous elastic media". International Journal for Numerical Methods in Engineering, 5, 419-442.

Hird, C.C., Marsland, A. & Schofield, A.N. (1978), "The development of centrifugal models to study the influence of uplift pressure on the stability of a flood bank". Géotechnique, 28(1), 85-106.

Marsland, A. (1961), "A study of a breach in an earth embankment caused by uplift pressure", Proceedings of the 5th International Conference on Soil Mechanics and Foundation Engineering, Paris (France), 2, 663-668.

Ozkan, S., Adrian, D.D., Sills, G.L. & Singh, V.P. (2008), "Transient Head Development due to Flood Induced Seepage under Levees". Journal of Geotechnical and Geoenvironmental Engineering ASCE, 134(6), 781-789.

Padfield, C.J. & Schofield, A.N. (1983), "The development of centrifugal models to study the influence of uplift pressure on the stability of a flood bank". Géotechnique, 33(1), 57-66.

Sandhu, R.S. & Wilson, E.L. (1969), "Finite element analysis of seepage in elastic media". Journal of Engineering Mechanics ASCE, 95(3), 641-652.

Van, M.A. (2001), "New approach for uplifting induced slope failure", Proceedings of the 15th International Conference on Soil Mechanics and Foundation Engineering, Istanbul (Turkey), 3, 2285-2288.

Van, M.A., Koelewijn, A.R. & Barends, F.B.J. (2005), "Uplift phenomenon: model, validation and design". International Journal of Geomechanics ASCE, 5(2), 98-106.

Wolff, T.F. (1989), "Levee Underseepage Analysis for Special Foundation Conditions", Technical Report REMR-GT-11, U.S. Army Corps of Engineers Waterways Experiment Station, Vicksburg (Miss.), U.S.A.

Zienkiewicz, O.C. (1985), "The coupled problem of soil-pore fluid-external fluid interaction – Basis for a geomechanics code", Proceedings of the 5th International Conference on Numerical Methods in Geomechanics, Nagoya (Japan), 1731-1740.

Zienkiewicz, O.C., Valliappan, S. & King, I.P. (1969). "Elastoplastic solution of engineering problems. Initial stress: finite element approach". International Journal for Numerical Methods in Engineering, 1, 75-100.

A SIMPLIFIED APPROACH FOR THE ANALYSIS OF DYNAMIC SLOPE STABILITY

F. Pisanò
Department of Structural Engineering, Politecnico di Milano, Milan, Italy

C. di Prisco
Department of Structural Engineering, Politecnico di Milano, Milan, Italy

M. Pastor
Department of Applied Mathematics, ETS de Ingenieros de Caminos, Madrid, Spain
Centro de Estudios y Experimentación de Obras Públicas, Madrid, Spain

ABSTRACT: *In this paper the problem of simulating the dynamic/seismic performance of 1D dry earth slopes is tackled. Since in the Seismic Engineering practice the use of both sophisticated constitutive models and non-linear finite element computations are not yet widespread, in this paper a sort of condensation procedure for lumping the full set of static and kinematical variables into an equivalent 1D-shear formulation, where a simpler shear stress-strain relationship is accounted for, is proposed. This introduces a first bridge between standard 1D linear elastic/viscoelastic and elastoplastic dynamic analyses. Indeed, the use of plasticity is essential in slope analysis, to predict permanent displacements and, in many cases, the occurrence of failure (strain localization).*
The condensation procedure is developed with reference to non-associated Mohr-Coulomb perfectly viscoplastic materials loaded in simple shear conditions, by considering the fact that the lateral confinement severely influences failure conditions and induces "pseudo-hardening" pre-failure responses.
The proposed approach aims at reducing the number of unknowns and, therefore, the computational costs. Its effectiveness is pointed out with reference to virgin slopes, while, in the case of highly overconsolidated strata, some difficulties arise because of the marked brittle behavior induced both by previous loading histories and non-associativeness.

1 INTRODUCTION

Nowadays, one-dimensional approaches for predicting the seismic performance of earth slopes under shear disturbances are widespread in the field of Geotechnical Earthquake Engineering (GEE). From a mechanical standpoint, their employment is appropriate whenever the sloping soil deposit is sufficiently shallow. Even though 1D schemes cannot capture some aspects of the dynamic response (such as topographic amplification), they can be however employed to derive, in many cases, reasonable results at low computational costs. In the last years, the suitability of 1D approaches for seismic slope problems has been increasingly recognised and some numerical codes for non-linear dynamic analyses have been developed (e.g. Yang & Elgamal, 2002; Pestana & Nadim, 2000).

However, even in the context of geometrically 1D models, several approaches can be distinguished, especially in terms of static/kinematical assumptions. In this work two different 1D schemes – henceforth referred to as "simple shear" and 1D shear" – are compared: in the former, the problem is properly interpreted as a special plane strain, this implying a three-dimensional stress state and multi-axial constitutive relationships to be considered; in the latter, equilibrium, compatibility and constitutive equations are formulated

solely in terms of shear variables, so that the soil volumetric behavior under shear loading is disregarded.

In GEE, the latter approach is widely adopted because of its computational convenience, but it is here shown not to be equivalent to the simple shear scheme, which is more "consistent" from a mechanical viewpoint. For this reason, the authors propose a 1D shear model capable of reproducing the dynamic response of simple shear systems, at least for the case of elasto-perfectly viscoplastic soils. A theoretically based procedure for condensing the main features of the simple shear multi-axial behavior into the constitutive parameters of a simpler 1D shear hardening model is illustrated. From this perspective, the paper has to be interpreted as an attempt at conciliating the concepts from theoretical Geomechanics with the necessity of providing the technical community with inexpensive but reliable numerical tools.

2 STATIC/KINEMATIC ASSUMPTIONS FOR 1D DYNAMIC ANALYSES

The initial boundary value problem (IBVP) under examination is represented in Fig. 1. It concerns a dry "infinite" stratum resting on an inclined rigid bedrock and shaken at the bottom by a shear seismic input (Fig. 2). α and H are the inclination and the thickness of the slope, respectively, while the soil is assumed to be characterized by a Mohr-Coulomb (MC) elasto-perfectly viscoplastic behavior.

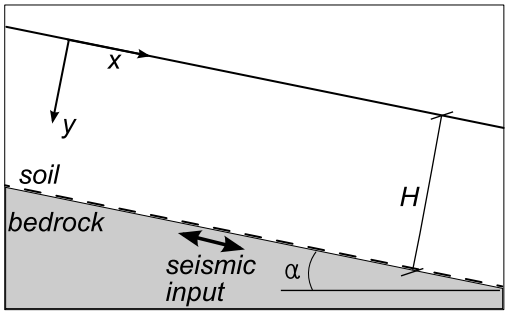

Fig. 1. Geometrical scheme of the IBVP

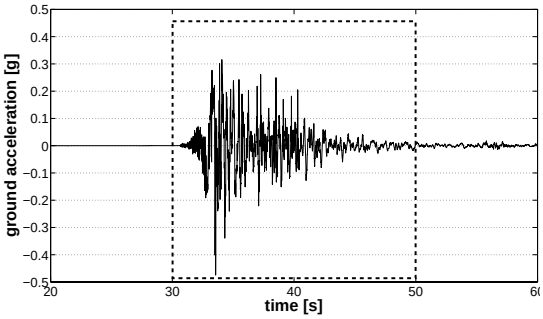

Fig. 2. The input excitation employed for the seismic analyses. Accelerometric record from the L'Aquila earthquake (Italy, 2009-04-06).

Assuming a 1D geometry implies all the field variables to depend only on time t and depth coordinate y, while their number can be reduced by introducing further static and kinematical assumptions.

At any rate, the equations governing the dynamic response of homogeneous viscoplastic strata can be cast, in general, as a first-order hyperbolic system:

$$\frac{\partial \boldsymbol{\varphi}}{\partial t} + \frac{\partial \mathbf{F}}{\partial y} = \mathbf{S} \tag{1}$$

describing the advective propagation of $\boldsymbol{\varphi}$ due to the flux $\mathbf{F}$ in the presence of the source term $\mathbf{S}$. The components of vectors $\boldsymbol{\varphi}$, $\mathbf{F}$ and $\mathbf{S}$ are determined by the variables employed to represent the motion and the local stress-strain state; hereafter, they are specified according to the aforementioned "simple shear" (SS) and "1D-shear" (1DS) assumptions.

2.1 The simple shear assumption

The infinite slope problem in Fig. 1 can be formulated by properly reducing a general 3D problem in the light of simple symmetry arguments. In particular, due to the infinite extension along both the x and z (out-of-plane) directions, any soil element is laterally constrained and lies in the same stress/strain conditions that geotechnicians try to reproduce through the simple shear apparatus (hence the term "simple shear assumption"). Despite the 1D geometry, the local stress vector $\boldsymbol{\sigma}$ is characterized by four non-nil components, while the two non-nil velocities – $v_x(y)$ and $v_y(y)$ – determine uniquely the strains ε_y and γ_{xy}. Thus, the dynamic SS problem can be considered as a special plane strain, and system (1) is specified as follows:

$$\boldsymbol{\varphi} = \begin{bmatrix} \sigma_x & \sigma_y & \tau_{xy} & \sigma_z & v_x & v_y \end{bmatrix}^T \tag{2a}$$

$$\mathbf{F} = -\begin{bmatrix} D_{12}v_y & D_{22}v_y & D_{33}v_x & D_{42}v_y & \tau_{xy}/\rho & \sigma_y/\rho \end{bmatrix}^T \tag{2b}$$

$$\mathbf{S} = \begin{bmatrix} -D_{11}\dot{\varepsilon}_x^{vp} - D_{12}\dot{\varepsilon}_y^{vp} - D_{14}\dot{\varepsilon}_z^{vp} \\ -D_{21}\dot{\varepsilon}_x^{vp} - D_{22}\dot{\varepsilon}_y^{vp} - D_{24}\dot{\varepsilon}_z^{vp} \\ -D_{33}\dot{\gamma}_{xy}^{vp} \\ -D_{41}\dot{\varepsilon}_x^{vp} - D_{42}\dot{\varepsilon}_y^{vp} - D_{44}\dot{\varepsilon}_z^{vp} \\ b_x/\rho \\ b_y/\rho \end{bmatrix} \tag{2c}$$

where ρ is the soil density, **b** is the vector of body forces (own weight), D_{ij} are elastic stiffness coefficients and the superscript *vp* denotes the viscoplastic strain rates. As is evident, system (1) is formed in this case by four constitutive relationships and two equilibrium equations (compatibility has been accounted for by expressing the rates of total strains in terms of velocity components). It should be noted that σ_x and σ_z are not determined by equilibrium, but by the compatibility requirements ε_x=ε_z=0.

Viscoplastic strain rates are instead expressed according to the Perzyna's approach (Perzyna, 1963):

$$\frac{\partial \boldsymbol{\varepsilon}^{vp}}{\partial t} = \eta \left\langle \frac{f}{|p|} \right\rangle^m \frac{\partial g/\partial \boldsymbol{\sigma}}{\left|\partial g/\partial \tau_{xy}\right|} \tag{3}$$

where f and g are the yield locus and plastic potential, η (fluidity parameter) and m the viscous parameters (later set equal to 1), p the isotropic mean pressure and the brackets ⟨ ⟩ denote the "positive part function" of the inner argument. A general multi-axial expression is employed for the MC yield locus:

$$f = \left(\cos\theta - \frac{\sin\theta \sin\phi'}{\sqrt{3}} \right) \sqrt{J_2} + \frac{1}{3} I_1 \tag{4}$$

in which I_1 is the first stress invariant (tensile stresses are here positive), J_2 the second deviatoric stress invariant, θ the Lode angle ($-\pi/6 \le \theta \le \pi/6$), while ϕ' is the friction angle; the plastic potential g is obtained from (4) by substituting ϕ' with the dilatancy angle ψ.

2.2 The 1D-shear assumption

According to the 1DS assumption, the shear problem is decoupled from the volumetric response (as it is for elastic analyses), and the soil mechanical behavior is described by means of a simpler τ-γ relationship. As a consequence, the problem becomes "twice" one-dimensional, i.e. both for geometry and constitutive equation.

As is well known, the 1DS approach is commonly employed in GEE, e.g. to evaluate the non-linear site response of layered deposits (Idriss and Seed, 1968) and, in the last years, to predict the seismic deformation of slopes as well (Rathje & Bray, 2000). For these purposes, an "equivalent linear viscoelastic" soil behavior is usually adopted, implying a dependence both of the shear modulus and the damping ratio on the shear strain (Hardin & Drnevich, 1972).

Hereafter, the elasto-viscoplastic 1DS problem is formulated by introducing in system (1):

$$\boldsymbol{\varphi} = \begin{bmatrix} \tau_{xy} & v_x \end{bmatrix}^T \tag{5a}$$

$$\mathbf{F} = -\begin{bmatrix} G v_x & \tau_{xy}/\rho \end{bmatrix}^T \tag{5b}$$

$$\mathbf{S} = \begin{bmatrix} -G\dot{\gamma}_{xy}^{vp} & b_x/\rho \end{bmatrix}^T \tag{5c}$$

being G the elastic shear modulus. In this case, the problem is governed by only two equations, the former constitutive and the latter for the shear dynamic equilibrium.

The 1DS counterparts of Eq. (3-4) are in this case:

$$\frac{\partial \gamma_{xy}^{vp}}{\partial t} = \eta \left\langle \frac{f}{|\sigma_y|} \right\rangle^m sign\left(\tau_{xy}\right) \tag{6}$$

$$f = \left|\tau_{xy}\right| + \sigma_y \tan\phi \tag{7}$$

where ϕ is the 1DS friction angle, while the normal stress σ_y is statically determined and unaffected by the shear excitation.

The 1DS approach implies a lower number of unknowns but, as it will be illustrated in section 3, it cannot capture some essential features of the SS mechanical response.

3 STATIC SIMPLE SHEAR RESPONSE OF PERFECTLY PLASTIC MATERIALS

Before tackling dynamic conditions, in this section some introductory theoretical concepts, already discussed in di Prisco & Pisanò (2010), are summarized. These concern the SS response of perfectly plastic materials with reference to static slope stability problems.

As far as the failure condition is concerned, in the aforementioned paper the authors have derived, by following the strain localization analysis by Borré & Maier (1989) and by using a MC elasto-plastic constitutive model, the condition here below:

$$\frac{\partial g}{\partial \sigma_x} \cdot \frac{\partial f}{\partial \sigma_x} \leq 0 \Leftrightarrow \left(\underbrace{\frac{\sigma_x}{\sigma_y}}_{k_0} - \underbrace{\frac{1+\sin\psi\sin\phi'}{1-\sin\psi\sin\phi'}}_{k_0^g} \right) \cdot \left(\underbrace{\frac{\sigma_x}{\sigma_y}}_{k_0} - \underbrace{\frac{1+\sin^2\phi'}{1-\sin^2\phi'}}_{k_0^f} \right) \leq 0 \tag{8}$$

Condition (8) clearly shows that shear banding is governed by the $k_0=\sigma_x/\sigma_y$ ratio, while the bifurcation limits k_0^g and k_0^f depend both on friction and dilatancy angles.

Consider a material point "extracted" at a depth y of an ideal virgin infinite slope, and then subjected to a SS load path, in which, starting from the *in situ* stresses, σ_y is kept constant and τ_{xy} increased. In Fig. 3, the SS responses (y=5 m and α=10°) numerically simulated for two dilatancy values ($\psi = \phi' = 40°$ and $\psi = 0°$) are plotted in terms of the friction mobilized along the x-z plane (ϕ_{mob}=atan(τ_{xy}/σ_y)). In these simulations, the elastic Young modulus E and Poisson's ratio ν are set equal to 117 MPa and 0.3, respectively.

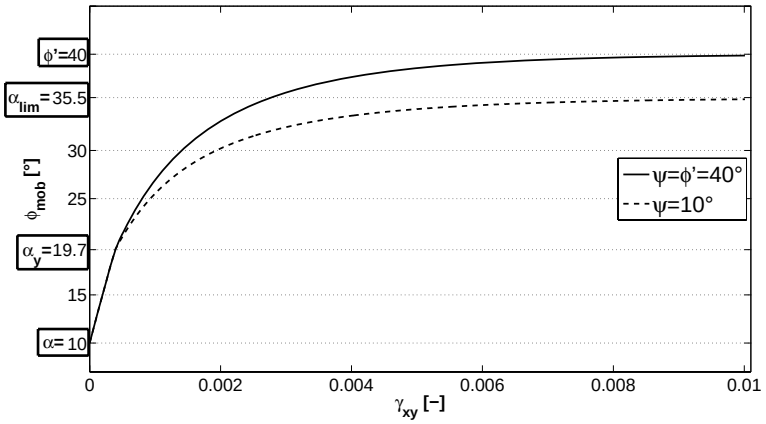

Fig. 3. Comparison between the SS responses obtained by imposing $\psi = \phi' = 40°$ and $\psi = 10°$

From Fig. 3 it is possible to infer that: (i) as long as angle α is "sufficiently" small, the mechanical response is initially elastic (in Fig. 3 α_y corresponds with the ϕ_{mob} yielding value, which is independent on the plastic flow rule); (ii) although the constitutive model is perfectly elasto-plastic, the ϕ_{mob}-γ_{xy} curves are characterized by a *pseudo-hardening* branch, this being basically due to the static redundancy of the constrained soil element; (iii) ϕ_{mob} tends to a limit value α_{lim}, which is affected by dilation. In the case of MC perfect plasticity, α_y and α_{lim} can be analytically determined:

$$\alpha_y = \tan^{-1}\left\{\sqrt{\left[4\nu(1-\nu)-\cos^2\phi'\right]}\Big/2(1-\nu)\right\} \tag{9}$$

$$\alpha_{\lim} = \tan^{-1}\left[(\cos\psi\sin\phi')/(1-\sin\phi'\sin\psi)\right] \le \phi' \tag{10}$$

Eq. (10) shows the influence of dilatancy on the limit obliquity α_{lim}, whose achievement in Fig. 3 can be proven to coincide with the fulfillment of the localization condition $k_0 = k_0^g$.

The simulation of the SS response for overconsolidated deposits gives rise to more complex results. Overconsolidation, here assumed to be the consequence of surface erosion, produces non uniform k_0 profiles, with local values larger than those corresponding with the virgin case. This is exemplified in Fig. 4 for a 30°-inclined stratum, whose final height H is equal to 5 m. Three different eroded thicknesses have been considered (1 m (a), 3 m (b), and 5 m (c); the constitutive parameters are listed in Table 1). As long as $\alpha>\alpha_y$, the thicker is the eroded stratum, the higher is k_0 at any point of the deposit.

To clarify the mechanical consequences of previous loading history, that is of the material overconsolidation, in Fig. 4, the range of admissible k_0 values is subdivided into three distinct

zones (H, S and HS), characterized by three sign combinations for the two factors in product (8). If one material point is now "extracted" from each k_0-zone (points P1, P2 and P3 belonging to curve b) and subjected to the same SS loading illustrated in Fig. 3, the three SS responses plotted in Fig. 5 result. In particular, the deepest point P1 (placed in zone H) still shows a pseudo-hardening response, while points P2 (zone S) and P3 (zone HS) exhibit a pseudo-softening and a pseudo-hardening-softening behavior, respectively. It is worth noting that the residual ϕ_{mob} value equals α_{lim} in all the three cases.

The assumption of non-associativeness is essential for pseudo-softening and pseudo-hardening-softening responses to take place (Vermeer, 1990). Indeed, when $\psi = \phi'$ the localization zone S vanishes and a pseudo-hardening response always results. In the case of dynamic/seismic problems, a pseudo-brittle response may occur even for initially virgin slopes, because of a sort of "transient overconsolidation" induced by the seismic cyclic loading.

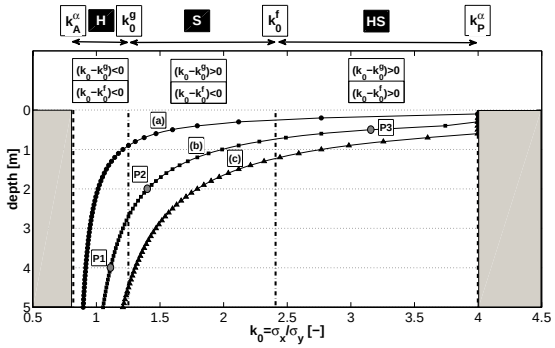

Fig. 4. Spatial distribution of the k_0 ratio for three different eroded thicknesses (5 m, 3 m, and 1 m)

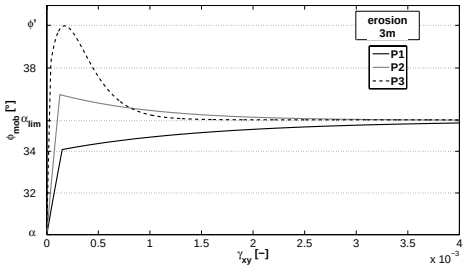

Fig. 5. SS response of points P1, P2 and P3 of Fig. 4

4 DEFINITION OF A "SIMPLE SHEAR EQUIVALENT" 1D SHEAR MODEL

As is intuitive, a perfectly plastic 1DS model cannot capture the variety of SS mechanical effects discussed above, as, in particular, the influence of dilatancy on the failure condition and the occurrence of pseudo-hardening/softening shear responses.

Suppose an essential mechanical characterization to be available for the soil (elastic parameters, friction and dilation angles), sufficient to calibrate a MC SS model. However, for the sake of simplicity, a 1DS approach may be preferred for the seismic analysis of the slope. As a consequence, a calibration of the 1DS model capable of providing results similar to the SS one becomes necessary.

In the case of virgin slopes, the theoretical observations summarized in section 3 suggest the use of a strain-hardening 1DS model for better approximating the SS perfectly plastic dynamic response. In particular, a best fitting can be obtained, for instance, by introducing in Eq. (7) the following hardening rule for the friction angle:

$$\tan\phi = \tan\phi_l + \left(\tan\phi_y - \tan\phi_l\right)e^{-h\kappa},\ \kappa(t) = \int_0^t \left|\frac{d\gamma_{xy}^{vp}}{dt'}\right| dt' \tag{11}$$

in which ϕ_y and ϕ_l are the mobilized friction angles at first yielding and failure respectively, h is the hardening constitutive parameter and κ quantifies the cumulated viscoplastic shear strain.

Based on the above analytical relationships, a "SS equivalent" 1DS hardening model (henceforth 1DSh) can be set up as follows (di Prisco et al., 2010):

(1) the same elastic shear modulus and viscous parameters of the SS model are employed for the 1DSh one. In the lack of *ad hoc* data for the calibration of the viscous parameters, sufficiently high values are suggested to obtain a nearly elasto-plastic response;

(2) ϕ_y and ϕ_l in (11) are set equal to α_y and α_{lim} in (9) and (10), respectively. If $\alpha>\alpha_y$ then $\phi_y=\alpha$ is set, implying an inelastic response since the beginning of the dynamic loading;

(3) it could be shown that it is not possible to reproduce at any depth y the pseudo-hardening SS response through a unique hardening parameter h, as the local hardening branch saturates more and more rapidly for the most shallow points. Therefore, the use of a depth-dependent hardening constitutive parameter $h=h_{ref}y_{ref}/y$ is proposed, in which h_{ref} is the reference parameter calibrated to match the SS τ_{xy}-γ_{xy} curve at a given reference depth y_{ref} (e.g. at the bottom of the stratum).

The above procedure allows to lump into the 1DSh constitutive parameters the effects of structural redundancy and non-associativeness characterizing the SS response of virgin slopes. For the sake of simplicity, the brittleness induced by overconsolidation has been not incorporated into the condensation procedure, as this would require the hardening parameter to be history-dependent as well.

5 NUMERICAL VALIDATION OF THE CONDENSATION PROCEDURE

The effectiveness of the above condensation procedure is numerically demonstrated with reference to the seismic excitation in Fig. 2. Several analyses have been performed by adopting (i) the "consistent" SS approach, (ii) a simple 1DS (non-hardening) model in which $\phi=\phi'$, and (iii) the 1DSh model set up as detailed in section 4. The constitutive parameters employed for the three models are listed in Table 1.

Table 1. Constitutive parameters for SS, 1DS and 1DSh analyses

SS		**1DS**		**1DSh**			
ELASTIC							
E [MPa]	υ [-]	G [MPa]		G [MPa]			
117	0.3	45		45			
PLASTIC							
ϕ' [°]	ψ [°]	ϕ [°]		ϕ_y [°]	ϕ_l [°]	h_{ref} [-]	y_{ref} [m]
40	10	40		19.7, 30	35.5	730	5
VISCOUS							
η [s^{-1}]	m [-]	η [s^{-1}]	m [-]	η [s^{-1}]		m [-]	
20	1	20	1	20		1	

The numerical results have been obtained by means of a two-step Taylor-Galerkin FEM algorithm coupled with a Runge-Kutta-type source integrator (the so-called "Jameson's multistage method"). This algorithm allows to effectively deal with dynamic problems in

viscoplastic solids, also in the presence of the strong source terms induced by weakly rate-sensitive geomaterials (Mabssout & Pastor, 2006; di Prisco et al., 2010).

First, two virgin slopes have been considered: the former (Fig. 6a-b) characterized by α=30° and H=5, the latter (Fig. 6c-d) by α=10° and H=5 m (different inclinations are associated with different non-linear effects in the dynamic response). The numerical results are presented in terms of permanent displacement U_x^{irr} at the surface of the slope (Fig. 6a-c) and final profile of the viscoplastic shear strain γ_{xy}^{vp} (Fig. 6b-d).

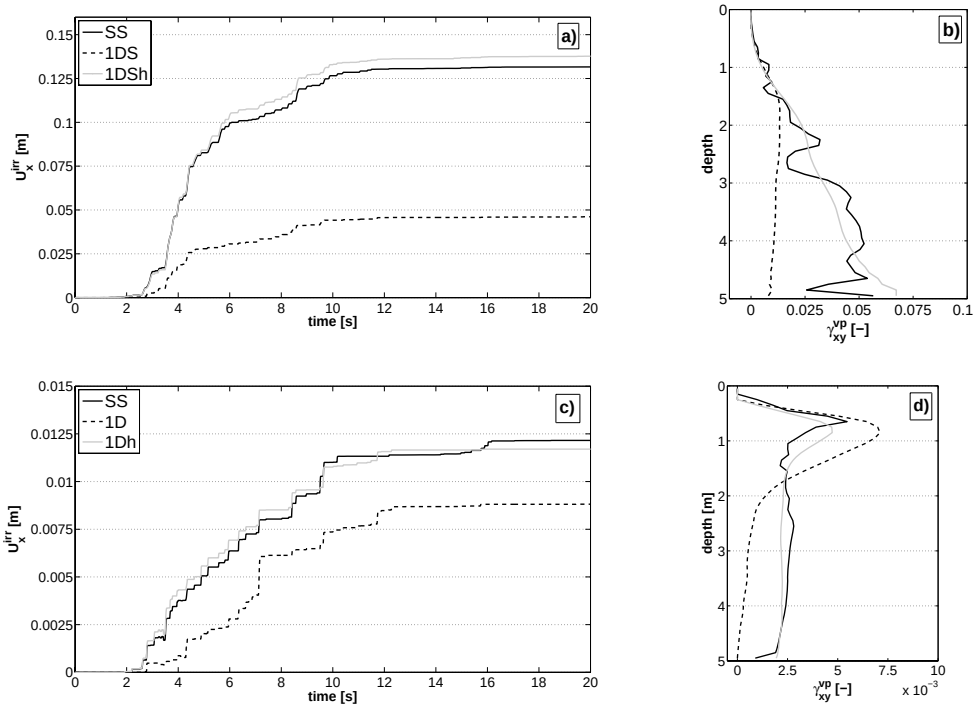

Fig. 6. Comparison among SS, 1DS and 1DSh results in terms of surface permanent displacement and final profiles of viscoplastic shear strain. α=30° and H=5 m in (a-b), α=10° and H=5 m in (c-d)

While the SS and 1DS results differ substantially, the SS-1DSh agreement is satisfactory for α equal both to 30° (highly inelastic response) and 10° (weak non-linearity). The 1DSh γ_{xy}^{vp} profiles interpolate "on average" the SS outcome, this being the reason for the good matching in terms of irreversible displacement. However, especially in Fig. 6b, the SS profile is more "irregular" than the 1DS and 1DSh ones: indeed, even though an initially virgin slope is considered, the cyclic seismic loading can induce that "transient overconsolidation" mentioned at the end of section 3, giving rise to some brittleness in the shear response and, therefore, to a "slight structural localization".

The effectiveness of the condensation procedure is further corroborated for different values of geometrical (Fig. 7, α=30° and H=10 m) and constitutive parameters (Fig. 8, α=30°, H=5 m and η=0.02 s^{-1}). In particular, despite the analytical relationships in section 3 have been derived in the framework of inviscid elasto-plasticity, the outcomes of the 1DSh model are satisfactory for highly rate-sensitive materials as well (i.e. for low viscous parameters, Fig. 8).

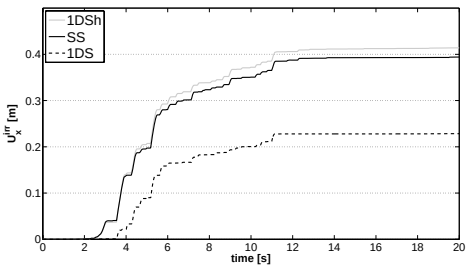

Fig. 7. SS, 1DS and 1DSh comparison for α=30° and H=10 m

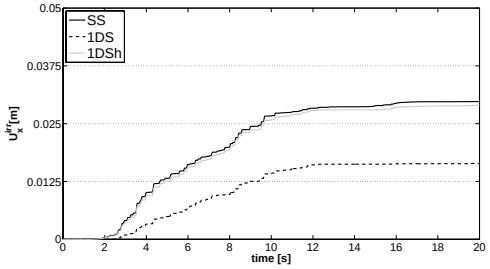

Fig. 8. SS, 1DS and 1DSh comparison for α=30°, H=5 m and η=0.02 s^{-1}

The influence of structural brittleness is even more evident when an initial overconsolidation is considered. To stress this point, the seismic SS performances of three overconsolidated slopes are illustrated in Fig. 9, characterized by the initial states in Fig. 4 (eroded thicknesses 5, 3 and 1 m) and shaken by the seismic input of Fig. 2.

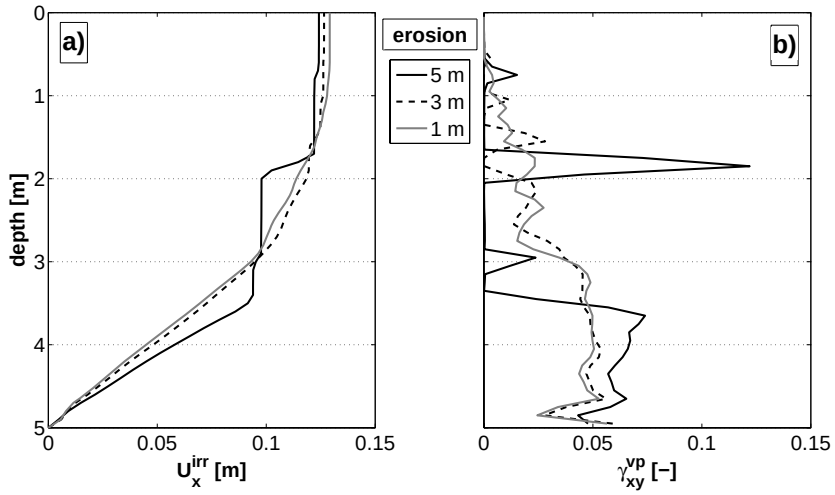

Fig. 9. SS seismic response for three overconsolidated slopes. Final profiles of permanent (a) displacement and (b) shear strain (constitutive parameters from Table 1)

As is evident, the initial overconsolidation can cause a clear "structural strain localization". The effects of its occurrence get more and more pronounced as the eroded thickness (i.e. the OCR) gets larger, because of an increasingly marked pseudo-softening behavior. Conversely, such effects vanish when weakly non-associated flow rules are considered, since the softening zone S in Fig. 4 tends to disappear.

6 CONCLUDING REMARKS

The use of geometrically 1D models for predicting the seismic response of earth slopes has been theoretically/numerically discussed, by assuming for the soil an elasto-perfectly viscoplastic behavior. Two different static/kinematical assumptions to characterize the mechanics of the system have been compared: (i) the simple shear (SS) assumption, in which a three-dimensional stress state and a multi-axial constitutive relationship are considered; (ii)

the 1D shear (1DS) assumption, in which the dynamic problem is formulated only in terms of shear variables and a 1D τ-γ constitutive model is introduced.

Despite the numerical model is geometrically 1D in both cases, substantial differences between the two approaches have been put in evidence and interpreted in the light of a preliminary static analysis. In particular, in the SS case, the "structural redundancy" of the system along with the soil non-associativeness determines a pseudo-hardening shear response and a marked influence of dilation on the failure conditions (strain localization). In contrast, the 1DS approach, suitable from a computational standpoint, disregards all the aforementioned structural effects.

With the aim of relating the two approaches, a hardening 1DS model (1DSh) has been introduced, by accounting for: (i) the dependence of the limit mobilized friction angle both on the internal friction and the dilatancy angles; (ii) the "depth dependent" structural hardening induced by redundancy. The condensation procedure of passing from the SS to the 1DSh model has been validated by considering different geometries and constitutive parameters.

It has been also pointed out that the procedure proposed by the author can be satisfactorily applied in the case of virgin deposits, while, in the case of overconsolidated, it cannot capture the marked structural brittleness and the occurrence of strain localization. This would require a 1DSh model capable of reproducing both strain-hardening and strain-softening responses, depending on depth and previous loading history.

REFERENCES

Borré, G. & Maier, G. (1989), "On linear versus non linear flow rules in strain localization analysis". Meccanica, Vol. 24, 36-31.

di Prisco, C. & Pisanò, F. (2010), "An exercise on slope stability and perfect elastoplasticity". Accepted for publication in Géotechnique.

di Prisco, C., Pastor, M. & Pisanò, F. (2010), "Shear wave propagation along infinite slopes: a theoretically based numerical study". Accepted for publication in Int. J. Anal. Num. Meth. Geomech.

Hardin, B.O. & Drnevich, V.P. (1972), "Shear modulus and damping in soils: measurement and parameter effect". ASCE J. Soil Mech. Found. Div., Vol. 98(6), 603-624.

Idriss, I.M. & Seed, H.B. (1968), "Seismic response of horizontal soil layers". J. Soil Mech. Found. Div. ASCE, Vol. 94(4), 1003-1031.

Mabssout, M. & Pastor, M. (2006), "A Runge-Kutta, Taylor-Galerkin scheme for hyperbolic systems with source terms. Application to shock wave propagation in viscoplastic geomaterials". Int. J. Anal. Num. Meth. Geomech., Vol. 30, 1337–1355.

Perzyna, P. (1963), "The constitutive equations for rate sensitive plastic materials". Quart. Appl. Math., Vol. 20, 321-332.

Pestana, J.M. & Nadim, F. (2000), "Nonlinear site response analysis of submerged slopes". Technical Report UCB/GT/2000-04, Department of Civil and Environmental Engineering, University of California at Berkeley.

Rathje, E.M., & Bray, J.D. (2000), "Nonlinear coupled seismic sliding analysis of earth structures". ASCE J. Geotech. Geoenv. Eng., Vol. 126(11), 1002–1014.

Vermeer, P.A. (1990), "The orientation of shear bands in biaxial tests". Géotechnique, Vol. 40(2), 223–236.

Yang, Z. & Elgamal, A. (2002), "Influence of permeability on liquefaction-induced shear deformation". ASCE J. Eng. Mech., Vol. 128(7), 720-729.

MIXED FINITE ELEMENT ANALYSIS OF A TRIAL EMBANKMENT AT THE COASTLAND OF VENICE, ITALY

Nicola Castelletto
Department of Mathematical Methods and Models for Scientific Applications, University of Padova, Padova, Italy

Pietro Teatini
Department of Mathematical Methods and Models for Scientific Applications, University of Padova, Padova, Italy

Massimiliano Ferronato
Department of Mathematical Methods and Models for Scientific Applications, University of Padova, Padova, Italy

Giuseppe Gambolati
Department of Mathematical Methods and Models for Scientific Applications, University of Padova, Padova, Italy

Luigi Tosi
Institute of Marine Sciences, National Research Council, Venice, Italy

ABSTRACT: *In the safeguard works currently under way at the inlets of the Venice Lagoon, an instrumented trial embankment was built with the aim of investigating the lagoon subsoil response to loading/unloading and assessing the relevant geomechanical parameters. A 20 m radius, 6.7 m high vertically-walled sand cylinder was constructed on the Venice littoral from September 2002 to March 2003, and removed in June 2007. The movements of the ground surface were accurately monitored at the center and side of the embankment, as well as at a reference benchmark 100 m apart by leveling, GPS, and persistent scatterer interferometry. Moreover, cone and standard penetration tests, geotechnical borings, and standard lab tests were performed to characterize the soil below the embankment. This large amount of information is used to set-up a fully coupled three-dimensional (3D) mixed finite element (MFE) model based on the Biot consolidation equations. Linear piecewise polynomials and the lowest order Raviart-Thomas mixed space are selected to approximate the medium displacement and the fluid flow rate, respectively. The approach ensures an element-wise mass conservative formulation while preserving the practical advantage of low-order interpolation elements. This helps to stabilize the numerical solution and obtain a more accurate calculation of the flow field. A finite difference scheme is used for the integration in time. The model is implemented over the actual lithostratigraphy of the subsurface down to 60 m depth by prescribing the surface loading vs time as a forcing factor. A small adjustment of the geomechanical and hydrological parameters allows for a satisfactory reproduction of most of the observed displacements both in the vertical and horizontal directions despite the simple linear elastic constitutive law used in the modelling approach.*

1 INTRODUCTION

The city of Venice and its lagoon represent a unique natural environment and an important historical heritage that are experiencing a progressive deterioration due to relative sea level rise (RSLR). The lagoon originated during the Holocene transgression of the Adriatic Sea onto the

Late Pleistocene Po Plain and its evolution has been subject to a complex combination of natural processes and human intervention such as land subsidence, eustacy, river diversions, and inlet and channel dredging. The 25 cm RSLR occurred at Venice over the 20th century, consisting of about 12 cm of land subsidence and 13 cm of sea level rise, has significantly increased the frequency of the city flooding due to high tide (Carbognin et al. 2010).

Starting from the beginning of the 1990s, a huge government project was undertaken to protect the city of Venice and the lagoon from the periodic flooding by the construction of mobile gates located at the three lagoon inlets (Fig. 1). In normal tidal conditions, the gates rest on the floor of the inlets while during high water they raise to prevent the tide from entering the lagoon (Gentilomo & Cecconi 1997).

Although the gates construction was officially approved in May 2003 only, a preliminary geotechnical characterization of the lagoon subsoil by standard methodologies started in the 1990s to help design the foundations of the mobile gates (Simonini & Cola 2000; Cola & Simonini 2002). More recently, a field-scale geotechnical experiment was initiated in September 2002 at Treporti, a lagoon island located a few kilometers north of the Lido inlet (Fig. 1(a)). A large cylindrical embankment was constructed to measure in-situ the stress/strain behavior of the subsoil at a scale comparable with the dimension of the mobile gates (Simonini 2004). Several equipments have been installed below the embankment to monitor the stress, strain, and pressure generated by the surficial load.

The measurements at the embankment test site have been recently used by Berengo et al. (2008) to develop and calibrate a geomechanical finite element (FE) model intended to reproduce the observed displacements. The model implements the Soft Soil Creep relationship (Vermeer & Neher 1999) and the Anisotropic Creep constitutive law (Leoni et al. 2008).

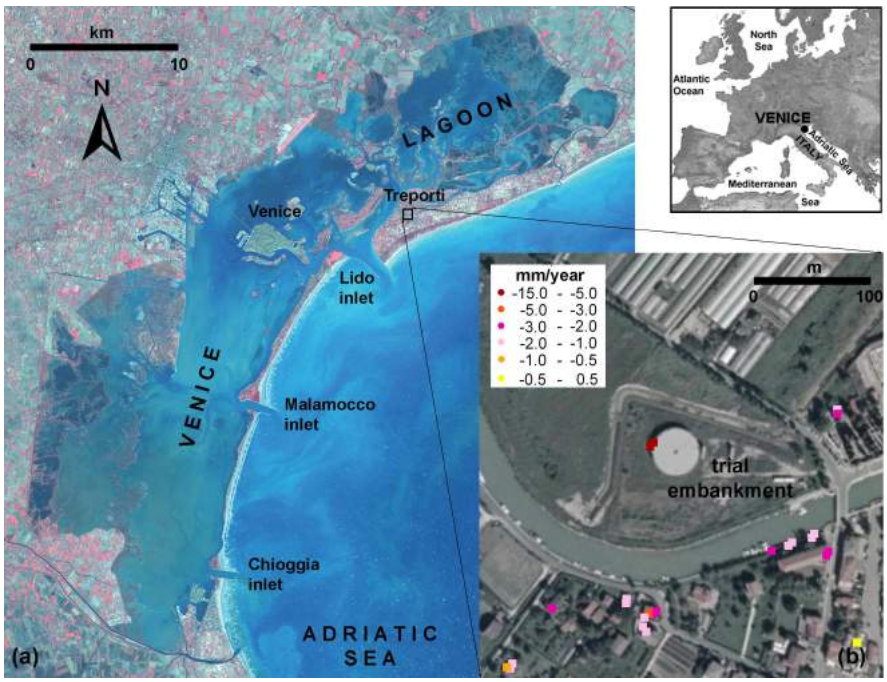

Fig. 1. (a) Satellite image of the Venice Lagoon, Italy. The black box highlights the location of the trial embankment. (b) Aerial photo of the trial embankment on which the mean displacement rates (March 2003 – May 2007) as detected by persistent scatterer interferometry (PSI) are superposed (after Bincoletto et al. (2011)).

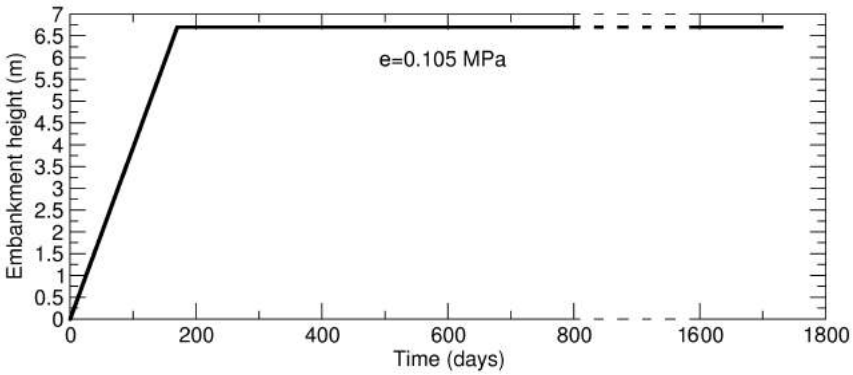

Fig. 2. Time evolution of the embankment height (after Simonini et al. (2007)).

As this test site represents a unique example because of the comprehensive characterization of the geological and geotechnical environment, in the present contribution we test the capability of a numerically advanced mixed finite element (MFE) code (Ferronato et al. 2010) to predict the measured displacements with a simple isotropic elastic constitutive model. The model solves the stress equilibrium equations fully coupled to a fluid mass balance equation, with Terzaghi's relationship between the intergranular stress and the fluid pore pressure.

2 THE TREPORTI TRIAL EMBANKMENT

A 20 m radius, 6.7 m high vertically-walled reinforced embankment was constructed at Treporti from September 12, 2002, to March 10, 2003, and was kept in the northern Venice littoral till June 2007. A number of 3 m long vertical drains were first established in the shallower silty clay unit to accelerate the overpressure dissipation. The cylinder was composed of geogrid-reinforced 0.5 m thick sandy layers, which were dynamically compacted to have an average 15.6 kN/m^3 dry weight. The time evolution of the load distribution e on the ground surface was recorded by load cells (Fig. 2), with e after the construction completion amounting to 0.105 MPa.

A thorough characterization of the subsoil was carried out by in-situ tests and laboratory experiments on undisturbed samples. The results show that silt is the prevailing facies within a highly heterogeneous porous medium. A schematic soil profile down to a 60 m depth is summarized in Table 1.

The induced displacements were carefully monitored in time, at different depths and distances form the embankment center. GPS, topographical levelling, extensometers, inclinometers, and micrometers were used. Moreover, PSI on the images acquired by the ENVISAT satellite has provided meaningful information on a couple of persisted radar reflectors located at the embankment side (Fig. 1(b)). For a detailed description of the embankment structure, lithostratigraphy, instrumentations, and available measurements, see Simonini et al. (2007) and Jamiolkowski et al. (2009).

3 MODELLING APPROACH

The equilibrium equation for an isotropic poro-elastic medium incorporating Terzaghi's effective stress concept reads:

$$\mu\nabla^2\hat{\mathbf{u}} + (\lambda+\mu)\,\nabla(\nabla\cdot\hat{\mathbf{u}}) = \alpha\nabla p + \mathbf{b} \tag{1}$$

Table 1. Schematic soil profile down to -60 m below msl and hydrological and geomechanical properties as implemented into the model simulations.

Soil type	Depth (m below msl)	$k_x = k_y = k_z$ (m/s)	ϕ -	E (Mpa)	ν -
silty clay with drains	0 – 3	10^{-9}	0.40	2	0.15
silty sand	3 – 7	10^{-9}	0.45	9	0.20
clay with sand lenses	7 – 20	5×10^{-10}	0.40	4	0.15
silty sand	20 – 22	10^{-9}	0.45	9	0.20
sandy silt	22 – 32	10^{-10}	0.40	18	0.15
silty clay	32 – 33	10^{-10}	0.40	8	0.15
sandy silt	33 – 45	10^{-10}	0.40	18	0.15
fine sand	45 – 55	10^{-9}	0.45	36	0.20
silty clay	55 – 60	10^{-10}	0.40	8	0.15

where $\lambda = \nu E/\left[(1+\nu)(1-2\nu)\right]$ and $\mu = E/\left[1+\nu\right]$ are the Lamé constants, with E Young's modulus and ν Poisson's ratio, α is the Biot coefficient, **b** the body forces, $\hat{\mathbf{u}}$ the medium displacements, p the fluid pore pressure, ∇ and $\nabla\cdot$ the gradient and the divergence operator, respectively. The fluid mass balance is prescribed by the continuity equation:

$$\nabla \cdot \mathbf{v} + \frac{\partial}{\partial t}\left(\phi\beta p + \alpha\, \nabla \cdot \hat{\mathbf{u}}\right) = f \tag{2}$$

where ϕ is the medium porosity, β the fluid compressibility, t time, f a flow source or sink, and **v** the Darcy velocity. In equation (2) **v** is given by:

$$\overline{\boldsymbol{\kappa}}^{-1}\mathbf{v} + \nabla p = 0 \tag{3}$$

with $\overline{\boldsymbol{\kappa}} = \overline{\mathbf{k}}/(\rho g)$, $\overline{\mathbf{k}}$ the hydraulic conductivity tensor and (ρg) the fluid specific weight.

Equations (1) through (3) form a coupled partial differential system defined on a 3-D domain Ω bounded by the frontier Γ with $\hat{\mathbf{u}}$, **v** and p as unknowns. This system is solved by prescribing appropriate boundary (BCs) and initial (ICs) conditions:

$$\text{BCs: } \begin{cases} \hat{\mathbf{u}}\left(\mathbf{x},t\right) = \hat{\mathbf{u}}_D\left(\mathbf{x},t\right) & \text{over } \Gamma_D \\ \overline{\boldsymbol{\sigma}}_{\text{tot}}\left(\mathbf{x},t\right)\mathbf{n}\left(\mathbf{x}\right) = \mathbf{t}_N\left(\mathbf{x},t\right) & \text{over } \Gamma_N \\ p\left(\mathbf{x},t\right) = p_D\left(\mathbf{x},t\right) & \text{over } \Gamma_p \\ \mathbf{v}\left(\mathbf{x},t\right)\cdot\mathbf{n}\left(\mathbf{x}\right) = q_N\left(\mathbf{x},t\right) & \text{over } \Gamma_q \end{cases} \qquad \text{ICs: } \begin{cases} \hat{\mathbf{u}}\left(\mathbf{x},0\right) = \hat{\mathbf{u}}_0\left(\mathbf{x}\right) \\ p\left(\mathbf{x},0\right) = p_0\left(\mathbf{x}\right) \end{cases} \tag{4}$$

with $\Gamma_D \cup \Gamma_N = \Gamma_p \cup \Gamma_q = \Gamma$, $\overline{\boldsymbol{\sigma}}_{\text{tot}}$ the total stress tensor, **n** the outer normal to Γ and **x** the position vector in R^3, while the right-hand sides are known functions.

Approximate the medium displacement in space with continuous piecewise linear polynomials ℓ_i, $i = 1,\ldots,n_n$, with n_n the number of FE nodes in Ω:

$$\hat{\mathbf{u}}\left(\mathbf{x},t\right) \simeq \left[\sum_{i=1}^{n_n}\ell_i\left(\mathbf{x}\right)u_{x,i}\left(t\right), \sum_{i=1}^{n_n}\ell_i\left(\mathbf{x}\right)u_{y,i}\left(t\right), \sum_{i=1}^{n_n}\ell_i\left(\mathbf{x}\right)u_{z,i}\left(t\right)\right]^T = N_u\left(\mathbf{x}\right)\mathbf{u}\left(t\right) \tag{5}$$

The fluid pore pressure and Darcy's flux are discretized in space with piecewise constant polynomials and in the lowest order Raviart-Thomas space (Raviart & Thomas 1977), respectively.

Denoting by n_e and n_f the number of elements and faces, respectively, p and $\mathbf{v}$ are approximated as:

$$p(\mathbf{x},t) \simeq \sum_{j=1}^{n_e} h_j(\mathbf{x})\, p_j(t) = \mathbf{h}^T(\mathbf{x})\,\mathbf{p}(t)\,, \quad h_j(\mathbf{x}) = \begin{cases} 1\,, \mathbf{x} \in T^{(j)} \\ 0\,, \mathbf{x} \in \Omega \setminus T^{(j)} \end{cases} \tag{6}$$

$$\mathbf{v}(\mathbf{x},t) \simeq \sum_{k=1}^{n_f} \mathbf{w}_k(\mathbf{x})\, q_k(t) = W(\mathbf{x})\,\mathbf{q}(t)\,, \;\; \mathbf{w}_k(\mathbf{x}) = \begin{cases} \pm \frac{(\mathbf{x}-\mathbf{x_k})}{3\left|V\left(T^{(j)}\right)\right|}\,, \mathbf{x} \in T^{(j)} \\ \mathbf{0} \qquad\qquad\;\; , \mathbf{x} \in \Omega \setminus T^{(j)} \end{cases} \tag{7}$$

In equations (6) and (7) $T^{(j)}$ denotes the j-th tetrahedron, V its volume and $\mathbf{x}_k$ the position vector of the node opposite to the k-th face in $T^{(j)}$. The $\pm$ sign in (7) identifies a conventional face orientation such that $\mathbf{w}_k$ points outward the element $T^{(j)}$ with the smallest index j. This gives rise to a unitary flux through the k-th face and a zero flux through all other edges. The vectors $\mathbf{u}(t)$, $\mathbf{p}(t)$ and $\mathbf{q}(t)$ whose components are the nodal displacements $u_{x,i}$, $u_{y,i}$, $u_{z,i}$, the elemental pressures p_j and the edge normal fluxes q_k, respectively, are the discrete unknowns of the variational problem.

The governing equations are solved by the Galerkin method of weighted residuals, leading to the following semi-discrete MFE expressions of (1), (2) and (3):

$$K\mathbf{u} - Q\mathbf{p} = \mathbf{f}_1 \tag{8}$$

$$B^T\mathbf{q} + P\dot{\mathbf{p}} + Q^T\dot{\mathbf{u}} = \mathbf{f}_2 \tag{9}$$

$$A\mathbf{q} - B\mathbf{p} = \mathbf{f}_3 \tag{10}$$

where:

$$\begin{array}{ll} A = \int_\Omega W^T \overline{\boldsymbol{\kappa}}^{-1} W \,\mathrm{d}\Omega & B = \int_\Omega \boldsymbol{\omega}\mathbf{h}^T \mathrm{d}\Omega \\ K = \int_\Omega B_u^T D_e B_u \,\mathrm{d}\Omega & P = \int_\Omega \phi\beta\mathbf{h}\mathbf{h}^T \,\mathrm{d}\Omega \\ Q = \int_\Omega \alpha B_u^T \mathbf{i}\mathbf{h}^T \,\mathrm{d}\Omega & \mathbf{f}_1 = \int_\Omega N_u^T \mathbf{b} \,\mathrm{d}\Omega + \int_{\Gamma_N} N_u^T \mathbf{t}_N \,\mathrm{d}\Gamma \\ \mathbf{f}_2 = \int_\Omega \mathbf{h} f \,\mathrm{d}\Omega & \mathbf{f}_3 = -\int_{\Gamma_p} p_D W^T \mathbf{n} \,\mathrm{d}\Gamma \end{array} \tag{11}$$

with B_u and D_e the strain-displacement and the elastic moduli matrix, respectively, $\mathbf{i}$ the Kronecker delta in vectorial form, and $\boldsymbol{\omega}$ a vector whose components are equal to div($\mathbf{w}_k$), $k = 1, \ldots, n_f$. The system of differential-algebraic equations (8), (9) and (10) is numerically integrated in time by a finite difference scheme, with the resulting algebraic linear system solved by a specific block version of a preconditioned Krylov subspace method. As to the preconditioner, a variant of the block constraint approach successfully applied to standard FE consolidation models, e.g. (Ferronato et al. 2009), is applied in order to accelerate the Symmetric Quasi-Minimal Residual solver (Freund & Nachtingal 1994) which has proved a robust and efficient algorithm for sparse symmetric indefinite problems. A detailed description of the algorithm is provided in Ferronato et al. (2010).

4 MODEL SET-UP

The 3D MFE model described above has been used to predict the displacement and pressure fields induced by the Treporti embankment. The model domain is formed by a cylindrical stratified porous volume with a 100-m radius, made of a sequence of alternating sandy, silty and clayey layers down to 60 m depth according to the lithostratigraphy provided in Table 1. The axial symmetry of the model geometry allows for the discretization of one fourth only of the overall porous volume (Fig. 3) with zero flux and horizontal displacement prescribed on the inner boundaries. The following additional boundary conditions apply: the outer boundary is fixed

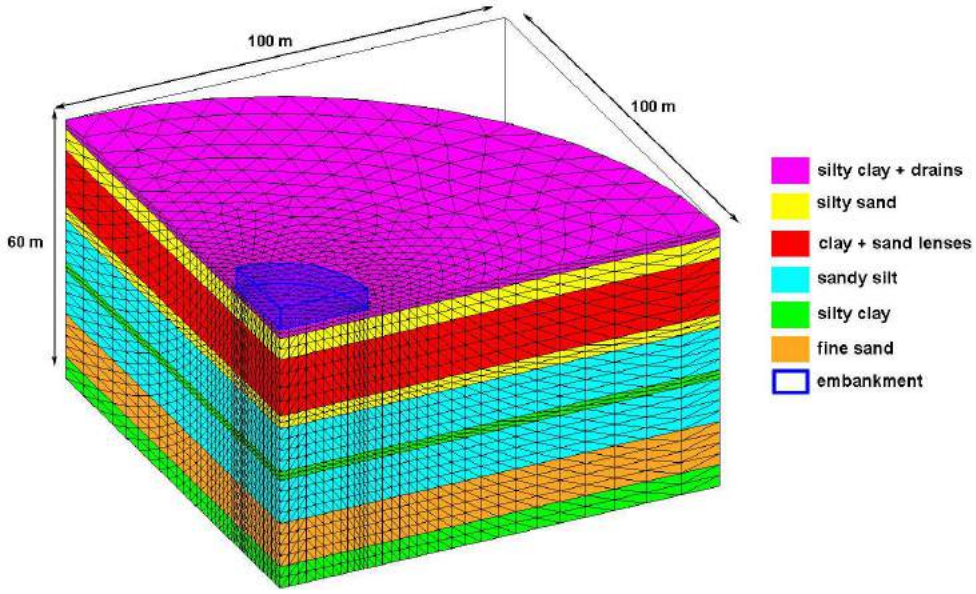

Fig. 3. Axonometric view of the finite element grids. The colors indicate the different lithologies.

and drained, the bottom is fixed and impervious, the top is traction-free and drained. As shown in Figure 3, a regularly refined FE grid is used totaling $n_n = 15,606$ nodes, $n_e = 83,304$ elements, and $n_f = 169,912$ faces with an overall model size equal to 300,034.

A uniform surface load distributed over a circular area centered on the domain top with a 20-m radius is applied. The load is time dependent from an initial zero value up to 0.105 MPa according to the embankment height as shown in Figure 2. Concerning the other hydro-geomechanical data, α=1 and $\beta = 4.32 \times 10^{-4}$ Mpa^{-1} have been used.

5 NUMERICAL RESULTS

The model has been initially run in steady state, i.e. only equation (1) has been solved assuming that the overpressure generated by the embankment load is fully dissipated. Given a preliminary distribution of the Young modulus according to the geotechnical characterization and using the compaction of each layer measured below the embankment center as of June 2007, i.e. just before the embankment removal, the steady state simulation has allowed for a quick calibration of the geomechanical parameters to be subsequently implemented into the more CPU-time consuming transient simulations. A slight modification of the E values initially prescribed has been needed.

The calibration of the hydraulic conductivity (assumed to be isotropic) has been carried out in transient conditions by matching the time behavior of the vertical land displacement u_z as measured below the cylinder center. One-order of magnitude difference has been generally assumed between the silty/sandy and silty/clayey units. The shallower fine-soil layer has been characterized by a higher conductivity to take into account the effect of the artificial drainage. An intermediate value has been used for the clayey layer located between 7 and 20 m depth below msl due to the presence of intervening thin sandy lenses. The E and $k_x = k_y = k_z$ values obtained from the calibration are provided in Table 1.

Fig. 4 shows a comparison between the measured and the predicted ground vertical displacements u_z versus time at the embankment center and toe. The records have been measured by leveling and PSI, respectively. The settlement behavior is well captured at both locations, al-

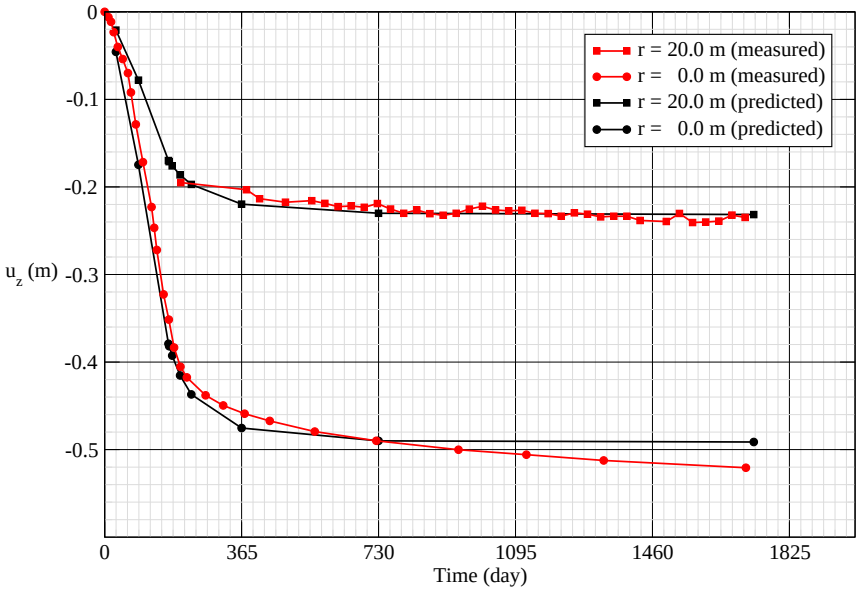

Fig. 4. Measured (after Jamiolkowski et al. (2009)) and predicted vertical displacements u_z of the ground surface versus time at the embankment center ($r = 0$ m) and toe ($r = 20$ m).

though the linear elastic model slightly underestimates the long-term movement that, according to Berengo et al. (2008), is mainly due to creep of the fine-grained units.

The satisfactory reproduction of the observed vertical displacements at different depths below the embankment center is emphasized in Fig. 5. The figure shows that, according to the available measurements, the largest deformations occur in the silty and clayey layers close to the land surface and between 7 and 20 m depth.

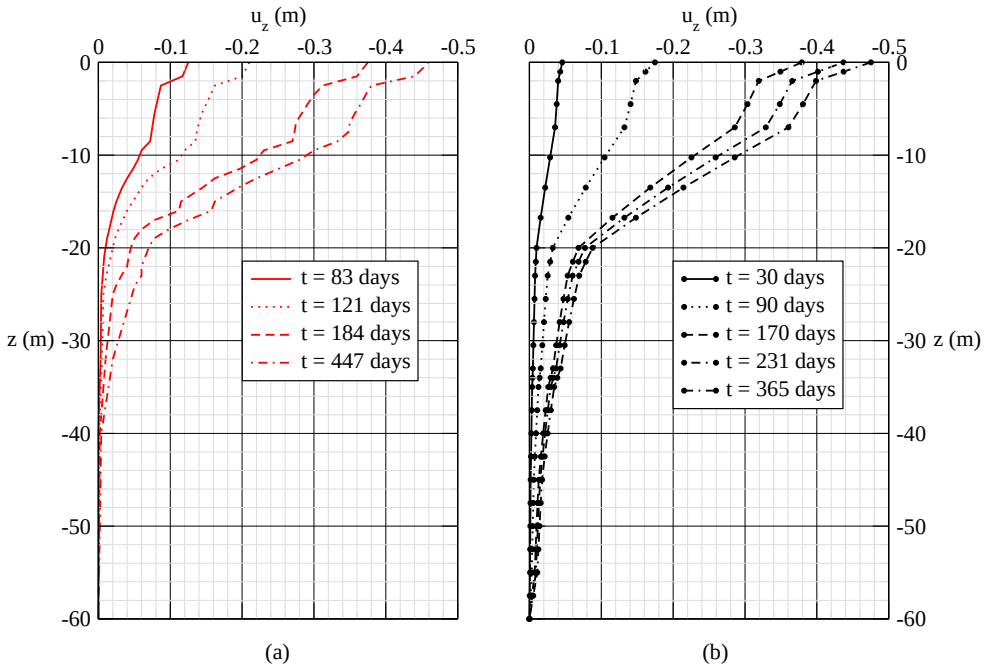

Fig. 5. (a) Measured (after Jamiolkowski et al. (2009)) and (b) predicted vertical displacements u_z versus depth below the embankment center ($r = 0$ m) for a few times after the beginning of the cylinder construction.

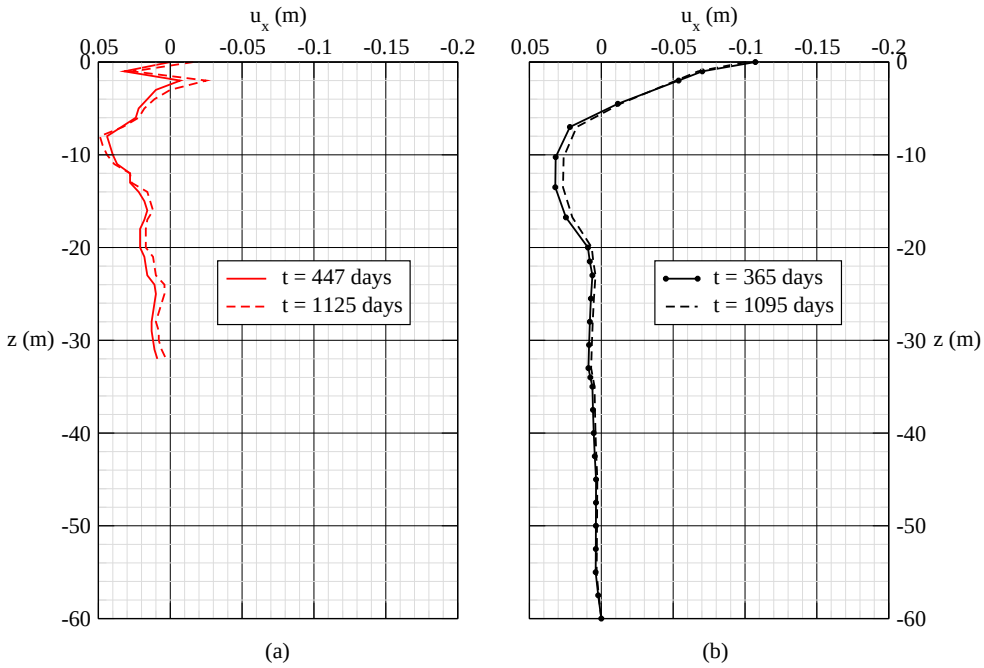

Fig. 6. (a) Measured (after Simonini et al. (2007)) and (b) predicted radial displacements u_x versus depth below the embankment toe ($r = 20$ m) for a couple of times after the beginning of the cylinder construction.

Also the order of magnitude of the horizontal displacement u_x at the embankment toe is well predicted, in particular below 5 m depth (Fig. 6). In the shallower soil, the modeling result overestimates the measurements. Possible reasons for that include the larger rigidity of the upper silty layer in the horizontal direction due to the presence of the vertical drains and the constraint exerted on the ground surface by the embankment itself and its containment structure.

Finally, Fig. 7 provides the evolution of the pore overpressure during the embankment built-up and 6 months after the construction completion, i.e. t=365 days. According to the available data, a relatively small overpressure developed, mainly during the first half of the construction phase, and quickly dissipated after the load e attained the final value.

6 CONCLUSIONS

A MFE model based on the classical Biot equations is developed to simulate the displacement and pore overpressure generated by a large cylindrical embankment constructed over the past decade at the Venice coastland. The field-scale test was designed so as to comprehensively characterize the geotechnical response of the lagoon subsoil in view of the construction of the mobile gates at the lagoon inlets. Despite the simple elastic constitutive relationship used in the modeling approach, the numerical model is capable to satisfactorily reproduces the majority of the measured vertical and horizontal displacements below the embankment. A creep model appears to be in order to capture the small long-term consolidation as observed after the completion of the embankment construction.

REFERENCES

Berengo, V., Leoni, M., & Simonini, P. (2008). Numerical modelling of the time-dependent behaviour of Venice lagoon silts. In Singh (Ed.), *Proc. 12th Int. Conf. of the International Association for Computer Methods and Advances in Geomechanics*, pp. 929–936.

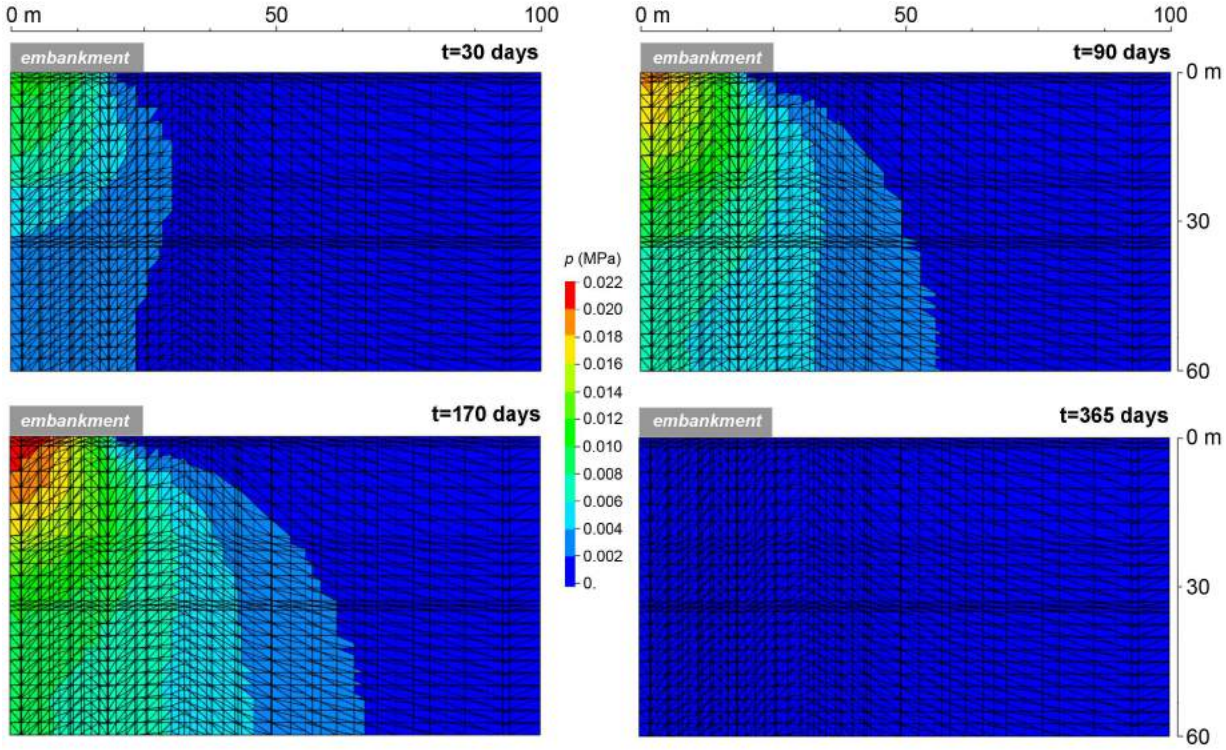

Fig. 7. Predicted overpressure versus time on a vertical cross section of the simulation domain.

Bincoletto, L., Simonini, P., Strozzi, T., Teatini, P., & Tosi, L. (2011). Assessment of soil long-term compression by PSI on Venice coastland structures. *Coast. Eng.*, submitted.

Carbognin, L., Teatini, P., Tomasin, A., & Tosi, L. (2010). Global change and relative sea level at Venice: what impact in term of flooding. *Climate Dynamics 35*, 1039–1047.

Cola, S. & Simonini, P. (2002). Mechanical behaviour of silty soils in the Venice lagoon as a function of their grading properties. *Canadian Geotech. J. 39(4)*, 879–893.

Ferronato, M., Castelletto, N., & Gambolati, G. (2010). A fully 3-d mixed finite element model of Biot consolidation. *J. Comp. Physics 229*, 4813–4830.

Ferronato, M., Pini, G., & Gambolati, G. (2009). The role of preconditioning in the solution to FE coupled consolidation equations by Krylov subspace methods. *Int. J. Num. Anal. Meth. Geomech. 33*, 405–423.

Freund, R. W. & Nachtingal, N. M. (1994). A new Krylov-subspace method for symmetric indefinite linear systems. In *Proc. 14th IMACS World Congress on Computational and Applied Mathematics*, pp. 1253–1256.

Gentilomo, G. & Cecconi, G. (1997). Flood protection system designed for Venice. *Hydropower & Dams 2(IV)*, 46–52.

Jamiolkowski, M., Ricceri, G., & Simonini, P. (2009). Safeguarding Venice from high tides: site characterization & geotechnical problems. In *Proc. 17th ICSMGE Int. Conf. on Soil Mechanics and Geotechnical Engineering*.

Leoni, M., Karstunen, M., & Vermeer, P. A. (2008). Anisotropic creep model for soft soils. *Géotechnique 58(3)*, 215–226.

Raviart, P. A. & Thomas, J. M. (1977). *A Mixed Finite Element Method for Second Order Elliptic Problems*. Lecture Notes in Mathematics. Springer Verlag, New York.

Simonini, P. (2004). Characterization of the Venice lagoon silts from in-situ tests and the performance of a test embankment. In da Fonseca & Mayne (Eds.), *Geotechnical and Geophysical Site Characterization*, pp. 187–207. Millpress, Rotterdam.

Simonini, P. & Cola, S. (2000). Use of piezocone to predict maximum stiffness of Venetian soil. *J. of Geotech. and Geoenv. Engng., ASCE 126(4)*, 378–381.

Simonini, P., Ricceri, G., & Cola, S. (2007). Geotechnical characterization and properties of Venice lagoon heterogeneous silts. In T. et al. (Ed.), *Characterization and Engineering Properties of Natural Soils*, pp. 2289–2328. Taylor & Francis, London.

Vermeer, P. A. & Neher, H. P. (1999). A soft soil model that accounts for creep. In Brinkgreve (Ed.), *Beyond 2000 in Computational Geotechnique*, pp. 249–261. Balkema, Rotterdam.

USE OF ADVANCED CONSTITUTIVE MODELS IN NUMERICAL ANALYSIS OF EMBANKMENT DAMS

N. Kovacevic
Geotechnical Consulting Group, London, UK

D.M. Potts
Department of Civil and Environmental Engineering, Imperial College, London, UK

ABSTRACT: *Although the main concern when designing or analysing embankment dams is their stability, assessing their deformation pattern is also important. This paper describes the recent use of advanced numerical analysis to predict the latter, and examples of its use in assessing likely movements of a series of embankment dams constructed in the UK are provided. Various phases in dam life are considered: embankment construction, first reservoir impounding, subsequent reservoir operation and raising the dam crest level. The use of adequate constitutive laws and, in particular, the importance of modelling the pre-peak (and post-peak) plastic behaviour of in-situ and embankment fill materials during loading, unloading and re-loading is clearly demonstrated.*

1 INTRODUCTION

The finite element (FE) method is a powerful tool to predict the behaviour of embankment dams. A large number of FE analyses of actual dams have been reported in the literature and these have been extensively summarised by Duncan (1994).

The FE analysis of stresses and movements in embankment dams is a complex problem. The techniques for modelling construction, first impounding and subsequent operation are covered in various publications (see e.g. Naylor, 1991). Many factors should be considered, such as construction in layers, the stiffness of the simulated layer, compaction stresses, etc. However, the most influential factor is the modelling of the stress-strain behaviour of the fill by an appropriate constitutive law (Duncan, 1994). Both elastic and elasto-plastic formulations have been used in the past. The former are simpler to use, but the latter are superior.

Soils are far from being either linear or elastic. Nevertheless, because of simplicity, the idealized models of linear isotropic elasticity were used in the past to characterize behaviour of real soils. Stress conditions in rockfill dams are usually far away from failure, and thus it is not surprising that linear elasticity has been successful in a number of cases (see e.g. Charles, 1976).

One of the most important characteristics of soil stress-strain behaviour is a lack of a linear relationship between stresses and strains. The 'layered' analysis of embankment dams permits straightforward simulation of the non-linear and stress dependent behaviour of fill materials, and so called 'variable' elastic constitutive laws have been widely used in numerical analyses of dams. However, some problems have been experienced with this approach, both in deriving model parameters from available tests data and in producing displacement patterns which agree with field measurements.

It is well known that elasto-plastic stress-strain relationships are capable of modelling the behaviour of real soils more closely. Plastic strain increments depend not only on stress increments but also on the state of stress and stress history. Thus the soil deformation depends on the direction in which the soil is loaded (stress path dependency) and whether principal stresses (and their increments) are rotating. There is no doubt that elasto-plastic FE analyses should provide a better prediction of stresses and especially movements in embankment dams. Unfortunately, they have not been widely used in practice. One reason for this might be the considerable complexity of such analyses. Another is related to the difficulties connected with testing of fill materials, particularly rockfills, because of their coarse grained nature, and consequently a lack of the experimental data required to determine model parameters.

2 CONSTITUTIVE MODELS USED

The constitutive models used in the numerical analysis of the various embankment dams described in this paper are briefly described below. The available space does not allow for a detailed description of the available laboratory test data and the models' parameters derivation. However, references are provided wherever appropriate.

2.1 Generalised Mohr Coulomb model

A generalised non-linear elastic perfectly plastic model incorporating a Mohr-Coulomb yield criterion given by the apparent cohesion, c', and the angle of shearing resistance, ϕ', is described by Potts & Zdravkovic (1999).

In the form of the model used here, the Young's modulus, E, and Poisson's ratio, ν, vary according to the mean effective stress, p', and shear stress level, S, according to the following relationships

$$E = E_i \, (1 - A \, B \, S)/(1+B \, S)$$
$$E_i = E_0 \, [(p' + p_a)/p_a]^C$$
$$E_u = H \, E_i$$
$$\nu = \{I - L \log [(p' + p_a)/p_a]\} \, (1 - S) + 0.49 \, S$$

where E and E_u are the Young's moduli on first loading and unloading/re-loading, p_a is the atmospheric pressure, E_0, A, B, C, H, I and L are model parameters.

The yield function is given by:

$$F(s') = S - 1$$

and the shear stress level, S, is defined as:

$$S = J/[(p' + a) \, g(\theta)]$$

where

$$p' = (\sigma'_1 + \sigma'_2 + \sigma'_3)/3$$
$$J^2 = [(\sigma'_1 - \sigma'_2)^2 + (\sigma'_2 - \sigma'_3)^2 + (\sigma'_3 - \sigma'_1)^2]/6$$
$$g(\theta) = \sin \phi'/(\cos \theta + \sin \theta \sin \phi'/ \sqrt{3})$$
$$\theta = \tan^{-1} [(2b - 1)/ \sqrt{3}]$$
$$b = (\sigma'_2 - \sigma'_3)/(\sigma'_1 - \sigma'_3).$$

a is the intercept of the yield surface on the mean effective stress, p', axis and is given by:

$$a = c'/g(\theta = 0) = c'/\sin \phi'$$

where c' is the cohesion intercept with Lode angle $\theta = 0$, i.e. $\sigma'_2 = (\sigma'_1 + \sigma'_3)/2$.

The plastic potential is also defined in the same way as the yield function, but with the angle of shearing resistance, ϕ', replaced by the angle of dilation, ψ.

2.2 Lade's double hardening model

This model is described in detail by Lade (1977). Elastic behaviour is assumed to be isotropic with a constant value of Poisson's ratio, ν, and a Young's modulus, E, which varies according to the following equation:

$$E = K_i\, p_a\, (\sigma'_3/p_a)^n$$

where σ'_3 is the minimum principal effective stress, p_a is the atmospheric pressure, and K_i and n are model parameters.

Plastic behaviour is controlled by two sets of yield surfaces, plastic potentials and hardening laws.

Yield Surface 1 - Conical surface

Yield surface:

$$F_1 = (I_1^3/I_3 - 27)\, (I_1/p_a)^m - H_1 = 0$$

where $I_1 = \sigma'_1 + \sigma'_2 + \sigma'_3$ and $I_3 = \sigma'_1\, \sigma'_2\, \sigma'_3$ are the first and third invariants of the effective stress tensor and H_1 is the hardening parameter. At failure $H_1 = \eta_1$, and η_1 and m are the model parameters defining the Lade's (1977) three-dimensional failure criterion.

Plastic potential:

$$G_1 = I_1^3 - [27 + \eta_2\, (p_a/I_1)^m]\, I_3$$

$$\eta_2 = s\, H_1 + r\, (\sigma'_3/p_a)^{1/2} + t$$

where s, r and t are model parameters.

Hardening law:

$$H_1 = a \exp(-b\, W_{p1})\, (W_{p1}/p_a)^{1/q}\ ,\ q \geq 1$$

$$a = \eta_1\, (e\, p_a/W_{p1,peak})^{1/q}$$

$$b = 1/(q\, W_{p1,peak})$$

$$q = \alpha + \beta\, (\sigma'_3/p_a)\ ,\ q \geq 1$$

$$W_{p1,peak} = P\, p_a\, (\sigma'_3/p_a)^l$$

where W_{p1} is the plastic work associated with the conical yield surface, and α, β, P and l are model parameters.

Yield Surface 2 - Spherical Cap

Yield surface and plastic potential:

$$F_2 = I_1^2 + 2\, I_2 - H_2 = 0$$

where H_2 is the hardening parameter, and $I_2 = -(\sigma'_1\, \sigma'_2 + \sigma'_2\, \sigma'_3 + \sigma'_3\, \sigma'_1)$ is the second invariant of the effective stress tensor.

Hardening law:

$$H_2 = p_a^2\, [W_c/(C\, p_a)]^{1/p}$$

where W_c is the plastic work associated with the spherical yield surface, and C and p are model parameters.

2.3 Lade's single hardening model

This model is described in detail by Lade & Kim (1998). Elastic behaviour is defined as above for the double hardening model, whereas the yield surface, plastic potential and hardening law are defined below.

Yield surface:

$$F = (\psi_1\, I_1^3/I_3 - I_1^2/I_2)\, (I_1/p_a)^h\, e^q - H = 0$$

$$\psi_1 = 0.00155\, m^{-1.57}$$

$$q = (\alpha\, S)/[1 - (1 - \alpha)\, S]$$

$$S = \eta/\eta_1 = (1/\eta)\, (I_1^3/I_3 - 27)\, (I_1/p_a)$$

where H is the hardening parameter, and h, m and α are model parameters.

Plastic potential:

$$G = (\psi_1 I_1^3/I_3 - I_1^2/I_2 + \psi_2) (I_1/p_a)^{\mu}$$

where ψ_2 and μ are model parameters.

Hardening law:

$$H = (27 \psi_1 + 3) [W_p/(C p_a)]^{h/p}, \text{ during hardening}$$

$$H = A \exp[-B (W_p/p_a)], \text{ during softening}$$

$$A = (27 \psi_1 + 3) [(e W_{p,peak})/(C p_a)]^{h/p}$$

$$B = (h/p) (p_a/W_{p,peak})$$

where W_p is the plastic work, and h and p are model parameters.

2.4 Kinematically hardening 'bubble' model

The model of Al-Tabbaa & Wood (1989) has been generalised by Grammatikopoulou at al. (2006). It uses the elliptical yield surface of the modified Cam Clay model to represent the bounding surface defined by:

$$(p'-p'_0/2)^2 + (\mathbf{s} : \mathbf{s})/[2 g^2(\theta_b)] - (p'^2_0/4) = 0$$

and employes an inner kinematic yield surface ('bubble', see Figure 1) given by:

$$(p'-p'_\alpha)2 + (\mathbf{s}-\mathbf{s}_a):(\mathbf{s}-\mathbf{s}_a)/[2 g^2(\theta_y)] - R^2 (p'^2_0/4) = 0$$

assuming it to have the same shape but to be smaller in size than the bounding surface. p'_α and $\mathbf{s}_a$ are the mean effective stress and the deviatoric stress tensor (tensor quantities are represented by bold type) at the centre of the bubble and R is the ratio of the bubble size to that of the bounding surface. The functions $g(\theta_b)$ and $g(\theta_y)$ define the shape of the bounding and kinematic surface in the deviatoric plane where θ_b and θ_y are the values of the Lode's angle for the bounding and kinematic surface respectively defined as:

$$g(\theta) = \sin\varphi'/(\cos\theta + \sin\theta \sin\varphi'/\sqrt{3})$$

where φ' is the critical state angle of shearing resistance.

Within the kinematic yield surface the behaviour is assumed to be elastic with a constant Poisson's ratio, μ, and a variable bulk stiffness given by:

$$K = p'/\kappa^*$$

where κ^* is the gradient of the elastic swelling line in $\ln \nu$ - $\ln p'$ space where ν is the specific volume. Otherwise, the behaviour is elasto-plastic with non-associated plasticity assumed and a hardening/ softening law which depends on the experimentally determined parameter α.

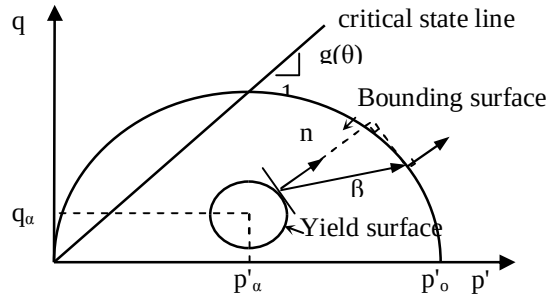

Figure 1. Representation of bounding and kinematic yield surfaces in triaxial stress space.

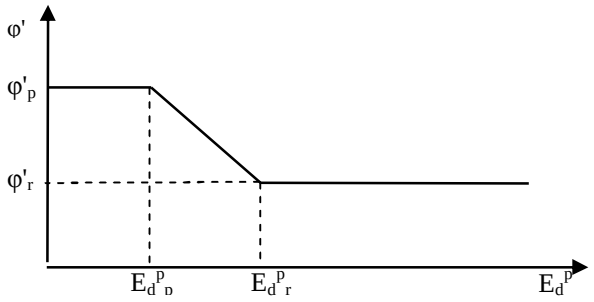

Figure 2.Variation of the angle of shearing resistance, φ', with the deviatoric plastic strain invariant, E_d^p.

The parameters required by the model are: λ^* (the gradient of the virgin compression line), κ^*, μ, φ', R and α (the parameter in the modified hardening modulus). An additional

parameter, *N*, is also usually adopted in order to fix the model in ln ν - ln p' space, taken here as the specific volume of the isotropic compression line at p' = 1kPa.

In the extension of the model (Grammatikopoulou at al., 2010), strain-softening is achieved by allowing the critical state angle of shearing resistance, φ', to vary with the plastic deviatoric strain, $E_d{}^p$, from a peak value, φ'_p, to a residual value, φ'_r, as shown in Figure 2. The deviatoric plastic strain invariant $E_d{}^p$ is defined as follows:

$$E_d{}^p = 2\,[(\varepsilon_1 - \varepsilon_2)^2 + (\varepsilon_2 - \varepsilon'_3)^2 + (\varepsilon_3 - \varepsilon_1)^2]/3$$

In the 'new' model, the peak angle of shearing resistance, φ'_p, replaces the angle of shearing resistance, φ', as an input parameter. The additional parameters required are the residual angle of shearing resistance, φ'_r, the plastic deviatoric strain at peak, $E_d{}^p{}_p$, and the plastic deviatoric strain at residual, $E_d{}^p{}_r$.

3 FINITE ELEMENT ANALYSES

All FE analyses described in this paper were carried out using the finite element code ICFEP (Potts and Zdravkovic, 1999). The analyses were plane strain and used eight noded isoparametric quadrilateral elements with 2x2 integration. A modified Newton-Raphson scheme, with an error controlled sub-stepping algorithm, was used as the non-linear solver.

3.1 Roadford Dam

Roadford Dam is a homogeneous 41m high rockfill dam (Figure 3) completed in 1990. The properties of the Carboniferous rockfill used in dam construction were measured in 250mm diameter triaxial and 1m diameter oedometer laboratory cells. Results of a suite of drained triaxial tests in compression at different confining stresses are shown in Figure 4. The fill was initially characterised by the non-linear elastic Mohr-Coulomb model which only accounts for the plastic behaviour when the peak strength is mobilised (Figure 4a). As a research exercise (Kovacevic at al., 1994), the rockfill behaviour was also predicted (Figures 4b and 4c) by using two more complex elasto-plastic models of the Lade's type both of which account for the plastic behaviour before and after the peak strength of the rockfill is mobilised.

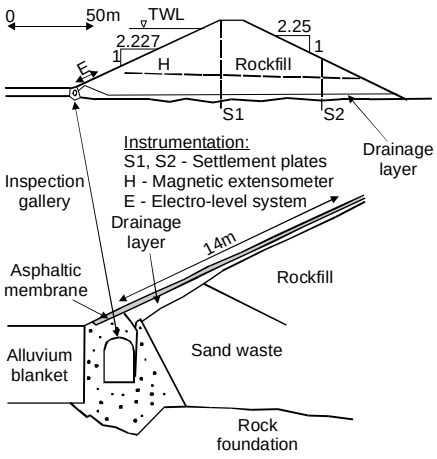

Figure 3. Cross-section of Roadford Dam.

The measured settlements near the dam centre line (position S1 in Figure 3) and mid-downstream slope (position S2 in Figure 3) during construction are presented in Figure 5. The magnitude of the predicted settlements is in reasonable agreement with the measurements. Whereas the non-linear elastic Mohr-Coulomb model overpredicted the settlements slightly, the Lade's elasto-plastic models underpredicted them.

The measured and predicted lateral movements along the extensometer H (see Figure 3) during construction are shown in Figure 6. The non-linear elastic Mohr-Coulomb model overpredicted lateral movements by a factor of two. The prediction could have been improved but only by using soil parameters which no longer fitted the triaxial test results. However, both Lade's elasto-plastic models predicted the horizontal movements reasonably well, so the behaviour of the embankment was recovered from the available laboratory data. The likely cause for the difference between the above predictions is the ability of the Lade's elasto-plastic models to account for plastic strains pre-peak, which are qualitatively quite different from the elastic strains predicted by the non-linear elastic model.

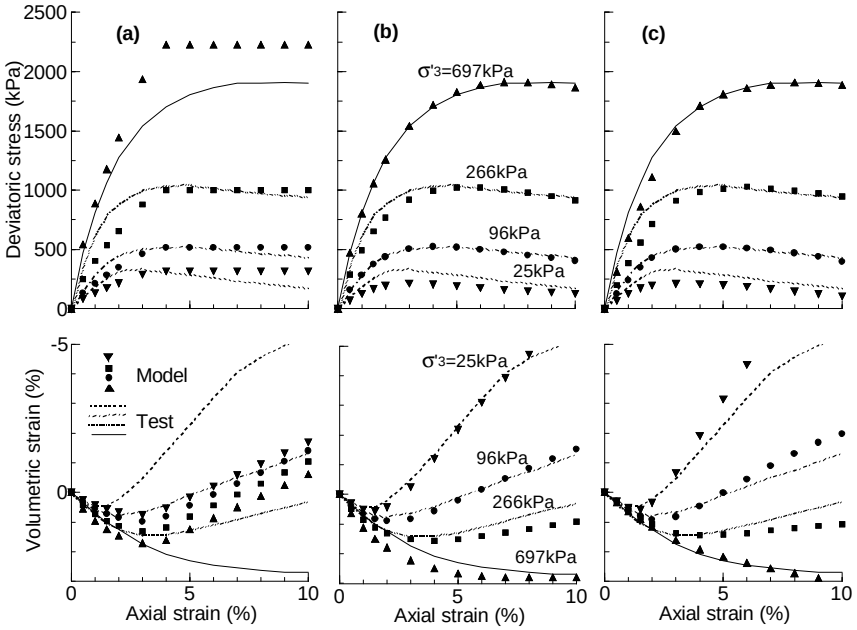

Figure 4. Predicted and measured behaviour in triaxial tests by (a) the nonlinear elastic Mohr Coulomb, (b) Lade's double and (c) single hardening models – Roadford Dam.

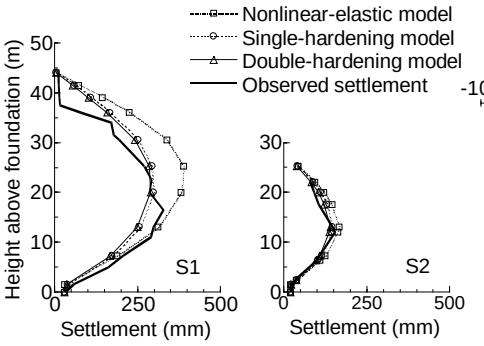

Figure 5. Predicted and observed settlements during construction - Roadford Dam.

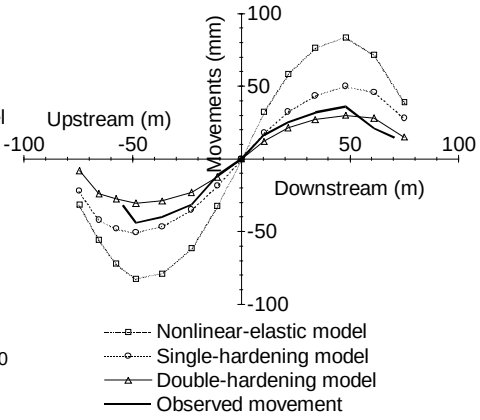

Figure 6. Predicted and observed lateral movements during construction - Roadford Dam.

3.2 Winscar Dam

A similar exercise was carried out on the 53m high Winscar Dam (Figure 7); however, this time the emphasis was on predicting the upstream asphaltic concrete membrane movements during the first reservoir impounding (Kovacevic et al., 2002). Three horizontal plate gauges were installed in the 50m high section of the dam during construction at positions A, B and C to measure dam deformations during its construction and first impounding.

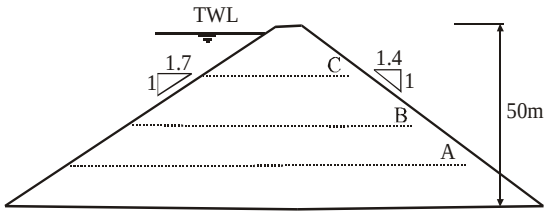

Figure 7. Cross-section of Winsacr Dam.

A comparison of the predicted and observed deflections of the upstream membrane during reservoir impounding is shown in Figure 8. Predictions presented in Figure 8a were made by Penman & Charles (1985) using a 'simple' linear elastic FE analysis. Initially, they significantly over predicted the membrane movements. Subsequently, they modified the model parameters in their analysis to simulate the stress changes during reservoir impounding more closely and, as a result, smaller and more realistic membrane movements were obtained. However, the 'new' parameters could not then recover the observed movements during dam construction any longer. No such 'problems' were encountered in the ICFEP analysis using the Lade's elasto-plastic constitutive models (Figure 8b) which were able to predict reasonably well dam movements during both construction and reservoir impounding without adjusting the input parameters derived from the available laboratory tests.

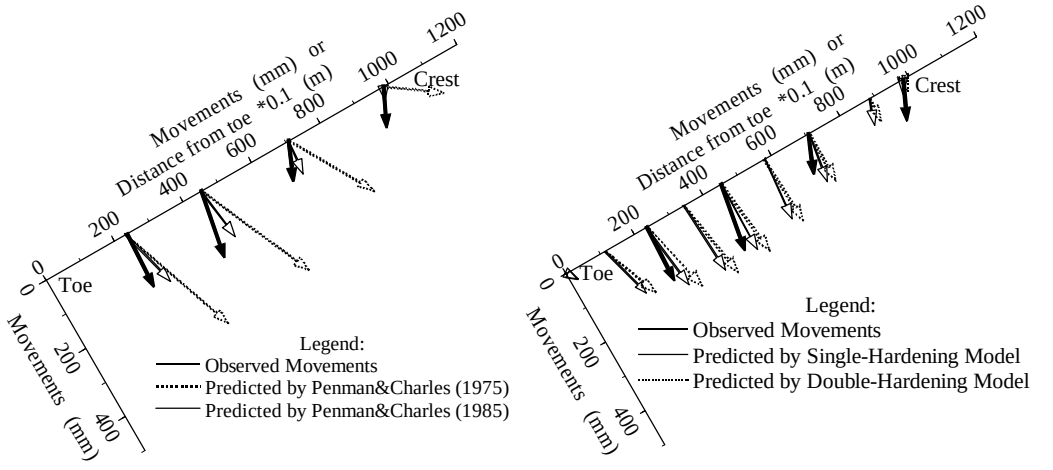

a) predictions by Penman & Charles (1975, 1985)

b) predictions by ICFEP using Lade's elasto-plastic models

Figure 8. Predicted and observed movements of upstream membrane during first reservoir impounding of Winscar Dam.

3.3 Ramsden Dam

The 25m high Ramsden Dam is an old embankment dam with a central puddle clay core and a concrete filled cut-off trench (Figure 9a). Given the previous success in reproducing the rockfill behaviour both during dam construction and first reservoir impounding, it was analysed using the Lade's single hardening model (Kovacevic at al., 1997). The results of cyclic loading in an oedometer test on the dam shoulder fill are presented in Figure 10a. In order to account for the observed permanent deformation after each operational cycle of draw-down and re-impounding, the non-linear elastic moduli in the Lade's model during unloading were made to be stiffer than during reloading (Figure 10b).

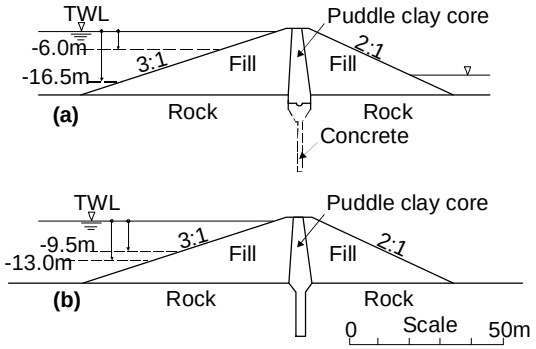

Figure 9. Cross-sections of (a) Ramsden and (b) Walshaw Dean Lower Dam.

The predictions were in reasonable agreement with observations during two reservoir draw-downs, particularly the smaller second one (Figure 11). However, the analysis showed that there was a tendency for the predicted permanent displacements to be towards upstream, rather than downstream as the observations suggest. It was suspected that a part of the problem was in the inability of the Lades's elasto plastic models to account for the hysteretic behaviour during unloading/re-loading cycles (Figure 10b).

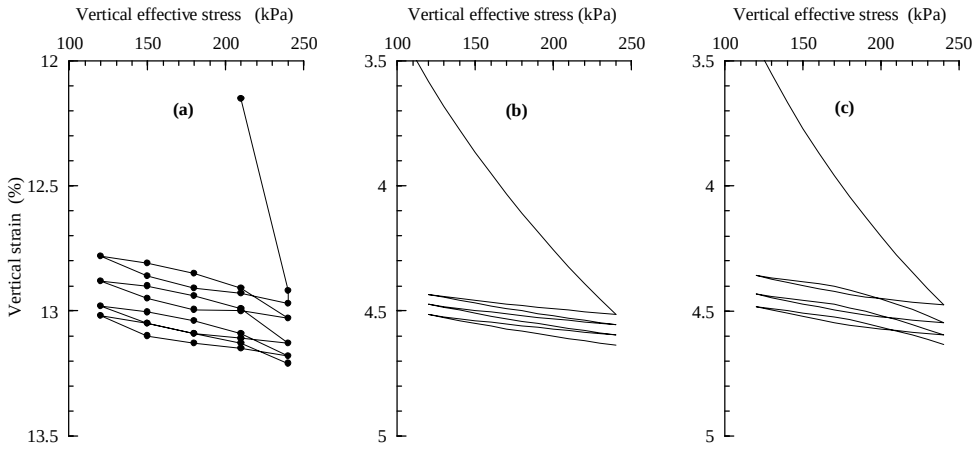

Figure 10. Behaviour of shoulder fill during cyclic loading in oedometer test: (a) observed and predicted by (b) Lade's single hardening and (c) 'bubble' model.

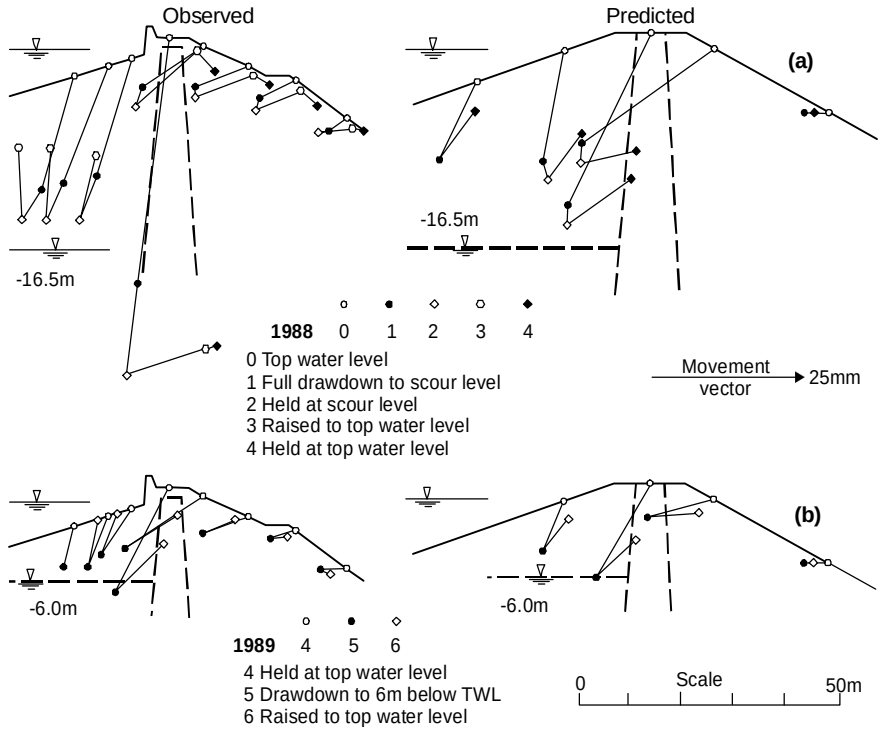

Figure 11. Observed and predicted behaviour of Ramsden Dam during (a) 1988 and (b) 1989 drawdowns by Lade's single hardening model.

3.4 Walshaw Dean Lower Dam

To account for the above hysteretic behaviour during unloading/re-loading cycles, another old British dam, the 22m high Walshaw Dean Lower Dam (Figure 9b), was analysed using both Lades' single hardening model and the kinematically hardening 'bubble' model (Kovacevic et al., 2004). The latter successfully predicted the observed fill behaviour in the oedometer test as shown in Figure 10c.

The measured horizontal and vertical displacements at the dam crest are compared with those predicted by the two models in Figure 12. It can be seen that, whereas the settlements were reasonable predicted by both models, only the 'bubble' model successfully predicted the observed movements downstream. Thus, it appears that an overall downstream movement of the dam crest is a result of the plastic behaviour during unloading/re-loading loops which the Lade's models cannot account for.

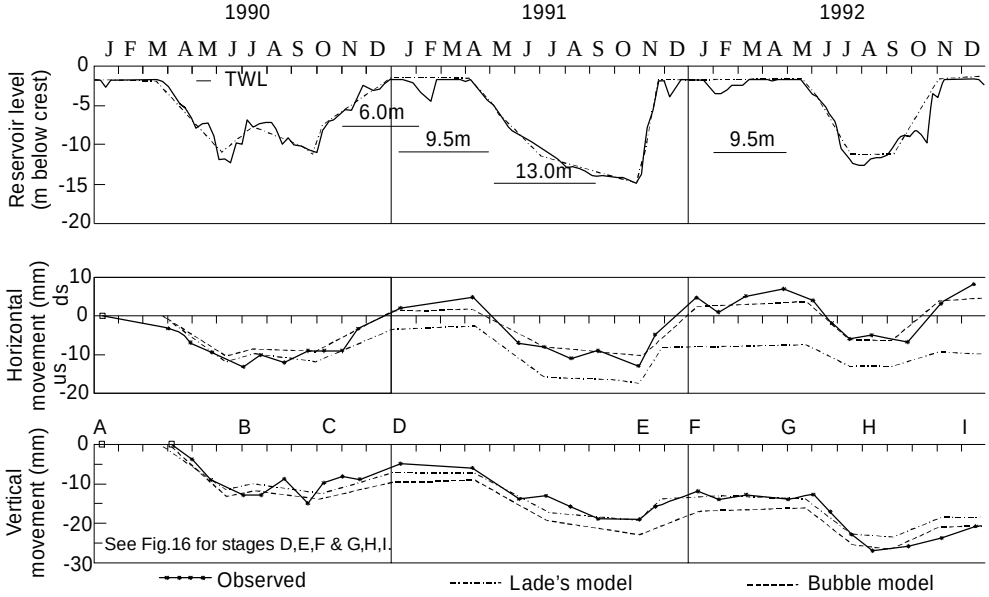

Figure 12. Observed and predicted displacements of the crest during three drawdowns – Walshaw Dean Lower Dam.

3.5 Ladybower Dam

The Lade's single hardening and kinematically hardening 'bubble' models were also used during the recent raising of the 43m high Ladybower Dam (Figure 13) which was originally built during the Second World War (Kovacevic et al., 2009).

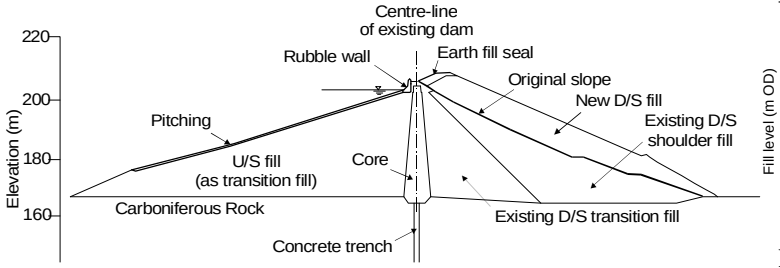

Figure 13. Typical cross-section of 'original' and 'raised' Ladybower Dam.

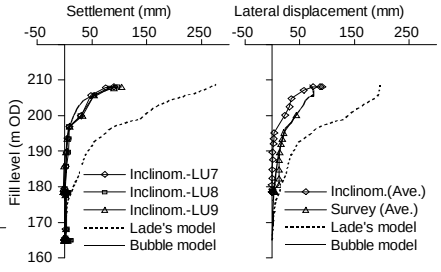

Figure 14. Observed and predicted (a) settlements and (b) lateral displacements of the crest of the 'original' dam.

Observed settlements and lateral displacements of the crest of the 'original' dam are plotted against the level (height) of the 'new' fill in Figure 14. The observed movements only started to develop after 30m of fill had been placed. However, rather unexpectedly, the crest of the original dam moved down-stream, being dragged down by the new fill. The 'before-the-event' prediction using the Lade's single hardening model overpredicted the observed movements by a factor of 3. The 'after-the-event' prediction by the 'bubble' model was quite reasonable. This was a surprising result, bearing in mind that the parameters for both models were derived using the same available laboratory tests. Nevertheless, it proved that the 'bubble' model can be successfully used in characterising the behaviour of dams not only during operational cycles of draw-dawn and re-impounding but also crest raising.

3.6 Empingham Dam

The examples of FE analyses of embankment dams presented so far have largely involved the modelling of free draining rockfill materials. Thus, it was decided to test the capabilities of the 'bubble' model in characterizing the behaviour of modern, compacted clay fills (and even of in-situ clays in a dam's foundation) which, because of their low permeability, behave largely in an undrained manner, at least during dam construction.

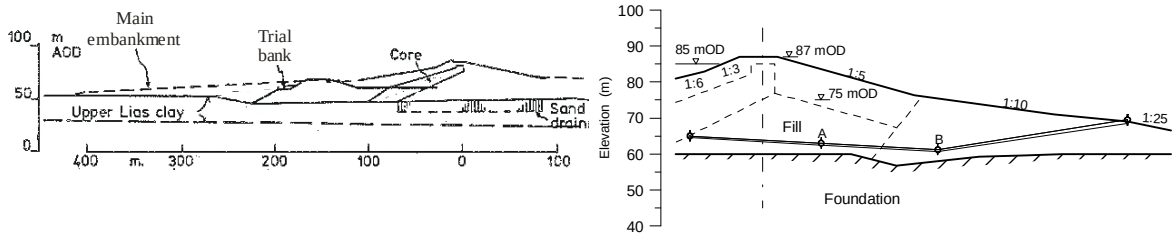

Figure 15. (a) Tipical cross section of Empingham dam showing location of trial bank, and (b) 'north section' of main embankment with position of rod gauges.

The 37m high Emingham Dam was built in the early 1970s. It is a 'modern' zoned earthfill dam founded on the stiff plastic Upper Lias Clay (ULC) which was also used as a fill in its construction (Kovacevic et al., 2007a). The 20m high instrumented trial bank was built inside the footprint of the dam (Figure 15) to examine and prove the undrained strength of the ULC in the dam foundation. The FE analyses of the trial bank using the 'bubble' model to characterise the behaviour of both the in-situ ULC and the fill derived from it were reported by Kovacevic et al (2007b).

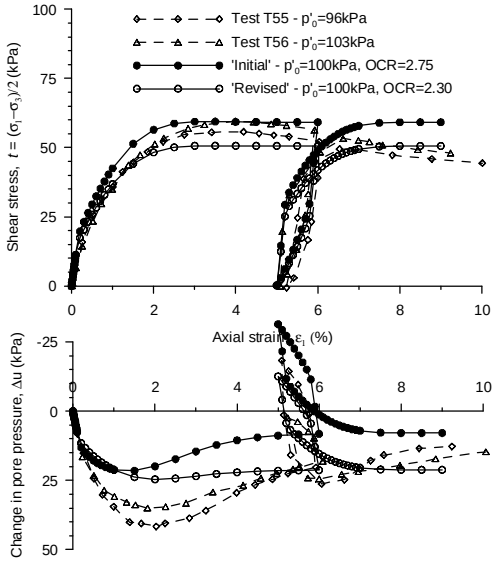

Figure 16. Observed and predicted behaviour of the in-situ ULC in undrained triaxial compression tests.

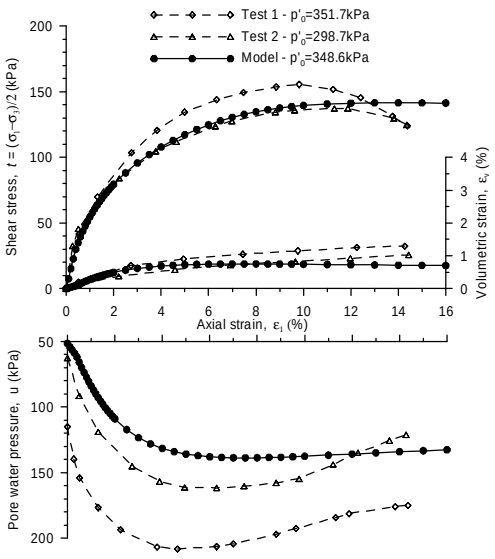

Figure 17. Observed and predicted behaviour of the ULC fill in undrained triaxial compression tests.

The model parameters for the ULC in the foundation were estimated from slow undrained triaxial tests on 260mm diameter samples. The results of two such tests involving post-peak unload/ re-load loops are shown in Figure 16 where they are compared with predictions from the 'bubble' model. Initially, the model could not allow for strain-softening due to dislocation, shear surface formation and particle orientation at large strains; however, the observed non-linearity of the stress-strain response during initial loading and subsequent unloading/re-loading is predicted reasonably well.

The results obtained during undrained triaxial compression tests on the 100mm diameter field compacted samples of the ULC are shown in Figure 17, where they are compared with the predictions from the 'bubble' model. The matching of the observed behaviour is reasonable. In particular, the compressibility of the pore fluid was introduced in the model resulting in a realistic pore water pressure response and agreement with the volumetric strain changes observed in the laboratory tests.

The behaviour of the trial embankment was reproduced successfully by FE back-analyses (Kovacevic et al., 2007b) by the 'bubble' model which did not account for strain-softening. However, when the same constitutive model was used in the back-analysis of the 'north section' of the main embankment, the observed sudden increase in movements as dam filling approached the crest level (Figure 18) could not be observed (Kovacevic et al., 2007a). Grammatikopoulou et al. (2010) extended the 'bubble' model to account for the post-peak strain softening (Section 2.4, Figure 19) and showed that the sudden increase in the horizontal movements (Figure 18) seems to be a consequence of the low undrained shear strength at the top of the ULC foundation combined with strain-softening (Figures 20 and 21).

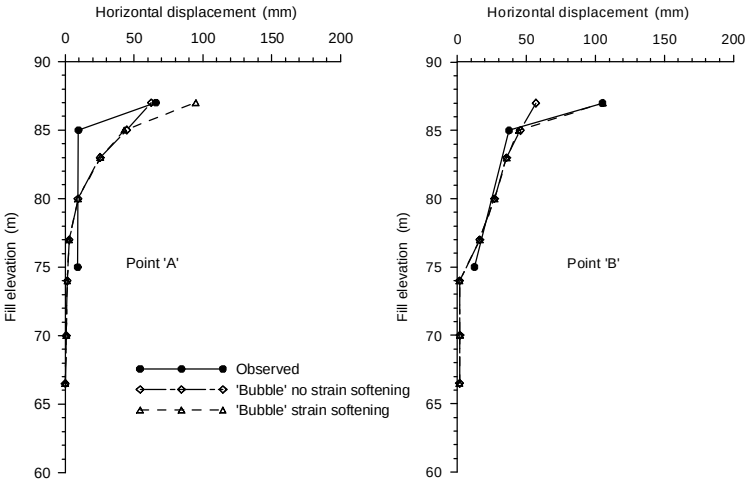

Figure 18. Observed and predicted horizontal movement of 'north section' of main dam at (a) rod gauge point A and (b) rod gauge point B.

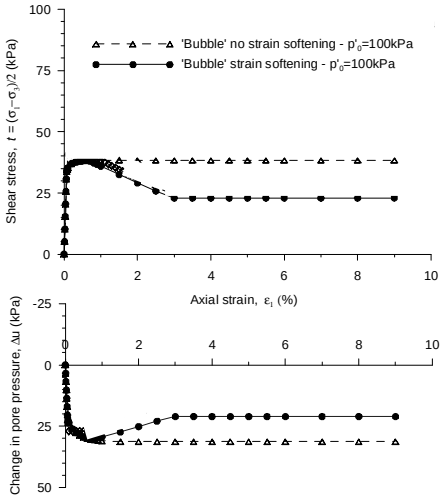

Figure 19. Predicted behaviour of ULC foundation in undrained triaxial compression.

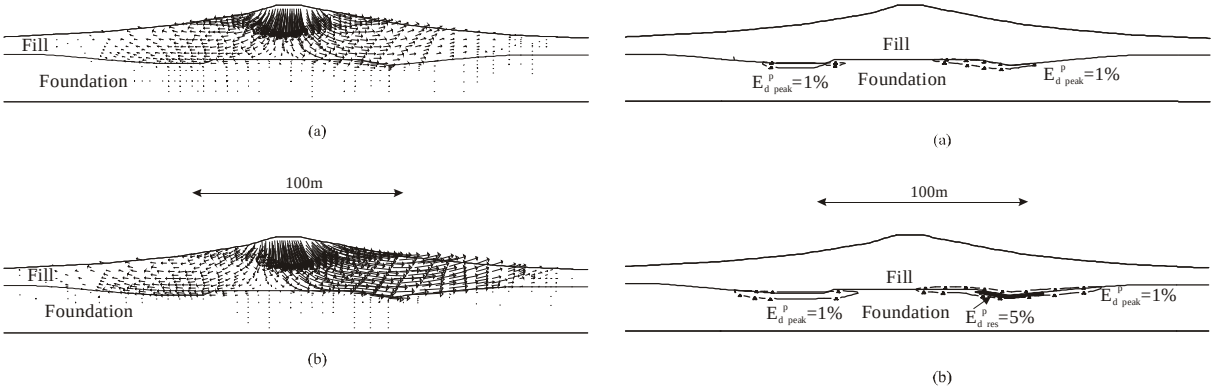

Figure 20: Predicted incremental displacement vectors and contours of plastic shear strain of 'north section' of main dam due to last 2m of fill placing: (a) analysis without strain-softening and (b) with strain-softening.

4 CONCLUSIONS

Embankment dams are important geotechnical structures which have often been analysed using advanced numerical analyses. However, to obtain predictions of deformation which

agree well with those observed in the field, it is necessary to characterise the behaviour of the various fill (and foundation) materials using advanced constitutive models based on elasto-plastic theory. It has been shown that such models with their parameters derived from the available laboratory test data are capable of reproducing the full range of the observed behaviour of a series of embankment dams constructed in the UK. From all the elasto-pastic models considered in this study, the latest form of the kinematically hardening 'bubble' model with its ability to account for non-linearity and both pre- and post-peak plasticity has proved to be particularly versatile and successful in characterising the behaviour of dams during various phases of their life, such as construction, first reservoir filling, operational cycles of draw-dawn and re-impounding and also crest raising.

REFERENCES

Al-Tabbaa, A. and Wood, D.M. (1989), "An experimentally based 'bubble' model for clay", Proc. 3rd Int. Conf. Numerical Models Geomechanics, Niagara Falls, Canada, 91-99.

Charles, J.A. (1976), "The use of one-dimensional compression tests and elastic theory in predicting deformations of rockfill embankments", Can. Geotech. J., Vol.13, No.3, 189-200.

Duncan, J.M. (1994), "The role of advanced constitutive relations in practical applications", Proc. 13th Int. Conf. Soil Mechs & Found. Eng., New Delhi, India, Vol.5, 31-48.

Grammatikopoulou, A., Zdravkovic, L. and Potts, D.M. (2006), "General formulation of two kinematic hardening constitutive models with a smooth elasto-plastic transition", International Journal of Geomechanics, ASCE, Vol.6, No.5, 291-310.

Grammatikopoulou, A., Kovacevic, N., Zdravkovic, L. and Potts, D.M. (2010), "Finite element analysis of the main embankment at Empingham", Proc. 7th European Conf. Num. Methods in Geotech. Engng, Trondheim, Norway, 557-562.

Kovacevic, N., Potts, D.M. and Vaughan, P.R. (1994), "Finite element analysis of a rockfill dam. Proc. 8th Int. Conf. Computer Methods & Advances in Geomechs", Morgantown, West Virginia, Vol.3, 2459-64.

Kovacevic, N., Potts, D.M., Vaughan, P.R., Charles, J.A. and Tedd, P. (1997), "Assessing the safety of old embankment dams by observing and analysing movement during reservoir operation", Trans. 19th Int. Cong. Large Dams, Florence, Q.73, R.34, 551-566.

Kovacevic, N., Vaughan, P.R. and Potts, D.M. (2002) "A comparison between observed and predicted deformations of Winscar dam", Proc. 8th Int. Conf. Numerical Models in Geomechanics, Rome, Italy, 565-571.

Kovacevic, N., Vaughan, P.R. and Potts, D.M. (2004), "A comparison between observed and predicted deformations of an old dam during reservoir operation", Proc. 9th Int. Conf. Numerical Models in Geomechanics, Ottawa, Canada, 587-593.

Kovacevic, N., Higgins, K.G., Potts, D.M. and Vaughan .P.R. (2007a), "Undrained behaviour of brecciated Upper Lias Clay at Empingham Dam, Geotechnique, Vol.57, No.2, 181-195.

Kovacevic, N., Higgins, K.G. and Potts, D.M. (2007b), "Finite element back analysis of trial bank at Empingham Dam", Proc. 10th Int. Conf. Num. Models in Geomechanics, Rhodes, Greece, 587-593.

Kovacevic, N., Vaughan, P.R. and Potts, D.M. (2009), "Finite element analysis of Ladybower Dam: Long-term operation and dam raising", Proc. 2nd Int. Conf. Long term behaviour of dams, Graz, Austria, 808-813.

Lade, P.V. (1977), "Elasto-plastic stress-strain theory for cohesionless soil with curved yield surface", Int. Jour. Solids & Structures, Vol.13, 1019-35.

Lade, P.V. and Kim, M.K. (1988), “Single hardening constitutive model for frictional materials, III: Comparisons with experimental data”, Computers & Geotechnics, Vol.6, 31-47.

Naylor, D.J. (1991), “Finite element methods for fills and embankment dams”, Advances in Rockfill Structures, 291-340.

Penman, A.D.M. and Charles, J.A. (1985), “Behaviour of rockfill dam with asphaltic memebrane”, Proc. 11th Int. Conf. Soil Mechs. Found. Eng., San Francisco, Vol.4, 2011-2014.

Potts, D.M. and Zdravkovic, L. (1999), Finite element analysis in geotechnical engineering: theory, Thomas Telford, London.

COMPUTATION OF THE SAFETY FACTORS OF GEOTECHNICAL STRUCTURES

G. J Machado
Mathematics Centre, Universidade do Minho, 4800-058 Guimarães, Portugal

D. F. Costa
Civil Engineering Department, Universidade do Minho, 4800-058 Guimarães, Portugal

J. M. Silva
Civil Engineering Department, , Universidade do Minho, 4800-058 Guimarães, Portugal

H. J. C. Ribeiro
Comunications Engineering, Universidade do Minho, 4800-058 Guimarães, Portugal

J. B. Martins
Department of Civil Enginearing, Universidade do Minho, 4800-058 Guimarães, Portugal

ABSTRACT:
The paper discusses the methods for the calculation of the factor of safety, Fs, of a nonhomogenious loaded soil (and/or rock) mass in relation to Limit Equilibrium (EQU) and refers to the senior author's own computer programs to solve these problems involved in Engineering Design Practice. To complement general programs for the traditional slices methods, new methods are presented and programmed: The "Rigid Blocks Methods" (RBM) for 2D and 3D situations. RBM are based on the creation of self-equilibrating structural systems inside the sliding ground mass. This generalization allows the treatment of problems such as the stability of excavations for tunnels in addition to the stability of slopes. A number of examples are presented using the authors PC MATLAB programs based on the generalized method of slices and on the new RBM Methods. Comparisons of results with published Fs obtained by other authors and those obtained by FEM are provided. The Rigid Blocks Method gave values for Fs close to published values. However, many more tests and comparisons are needed. Also, the 3D Rigid Blocks Method is promising, mainly for 3D situations such as the stability of the front face in tunnels excavations.

1 INTRODUCTION

The calculation of the safety factor F_s in the limit equilibrium analysis of ground (soil, or soil and fissured rock) of any type is today, as always, fundamental for geotechnical ultimate limit design. F_s can be calculated by elastic-plastic numerical methods (Finite Elements, Finite Differences and Boundary Elements). The mechanism of collapse is not explicit in these methods. Also, convergence is not assured "a priori". The mechanism of collapse may not be unique. To find it the least F_s must be searched for. In the Rigid Blocks Method presented here the mechanism of collapse is explicit "a priori": This is a kind of non-linear programming method where the optimization to obtain the minimum F_s is done iteratively. The rigid-plastic methods for the calculation of F_s (Coulomb (1776) and Rankine (1857)) precede the elastic-plastic ones.

On the other hand, since the elastic component of the deformation is irrelevant at rupture, the F_s obtained by elastic-plastic methods should, theoretically, be equal to that obtained by rigid-plastic methods.

For the calculation of F_s by rigid-plastic methods there are several PC programs, but they are only applicable to the stability of slopes (including earth dams). However, earth pressure, the

bearing capacity of footings and piled foundations and the stability of tunnels are not considered in those PC programs.
The work to be presented is a comparison between the F_s calculated using a PC program for the general calculation of F_s by various slices methods (Martins 2006). These include the particular cases of Fellenius (1936) and Bishop's (1955) circular surfaces of sliding methods and those of Morgenstern & Price (1965) and Correia (1988) for non-circular surfaces of sliding. Furthermore, the F_s calculated by the Rigid Blocks Method is also compared for the case of a shallow tunnel.
The Slices Methods Program is inspired by the work of Zhu et al. (2003). Starting with an arbitrary but realistic initial Fs the equilibrium equations for every slice are combined with the Mohr-Coulomb yield equations. Since there are more known than equations a linear relationship $T(x)= G_1(x).E(x)+ G_2(x)$ between the vertical and the horizontal forces at each vertical interface can be established.
Morgenstern and Price (1965) stated $T(x)/ E(x)= \lambda .f(x)$, where f(x) is a prescribed function having zero values at the end points of the sliding mass. Numerical experiments show that both a linear and a sine function give essentially the same results.
Correia (1988) stated that $T(x)= \lambda .f(x)$, Martins (1979) and Martins & Marques (1984) that $\Delta T(x)= \lambda .f(x)$, where $\Delta T(x)$ is the difference in shear force on the vertical joints on either side of a slice.
Together with these assumptions, an initial distribution of normal stresses on the sliding surface must be assumed. After this, a system of –n- non linear equations with n unknowns, including Fs and λ, is set up and solved by iteration. The calculation stops when the absolute value of the difference between the Fs in a cycle of that calculations and the previous one is of the order of 0.001.

2 RIGID BLOCKS METHOD

A computer program has been put forward for the calculation of F_s by the 2D Blocks Method in the following way:
1 - The most unfavourable noncircular sliding surface is found by the general method of slices referred above.
2 - The soil sliding mass, defined by that most unfavorable noncircular sliding surface ("critical" ground mass), is divided into blocks (triangular and/or quadrilateral). A joint is assumed between adjacent blocks (and at the external contacts). At the mid point of each joint an hinge is considered. The network of blocks is designed in such a way to form a stable self equilibrating structure.
3 - The normal and tangential internal forces at each joint due to external forces (self weight of the blocks, external loads, if any, etc.) are calculated.
4 - The tangential internal forces so calculated are compared with the resistance available at each joint, according to the Mohr-Coulomb yield criteria.
Resistance available at joint k is

$$R(k)=Q(n,k)*(\tan\phi'/Fs)+ LJ(k)*c'/Fs \quad (1)$$

where Q(n,k) is the normal internal force at joint k; and LJ(k) is the length of joint.
From the differences in the forces

$$r(k)=R(k)-Q(t,k) \quad (2)$$

F_s is calculated at each joint and the minimum found.

This minimum is on the safe side (see discussion below). If the difference is significant then a new network of blocks must be designed in such a way to transfer internal loads for the joints with larger available resistance. So, by iteration, final Fs can be found.

3 EXAMPLE 1: SHALLOW TUNNEL - LATERAL STABILITY

This shallow tunnel was excavated in decomposed and weathered granite. It is about 134 m long and has a cross section of about 95 m^2. Its depth varies between 5 and 13 m. The New Austrian Tunnelling Method (NATM) was used in the excavation. The mechanical characteristics and the parameters adopted to define the initial stresses were obtained from Martins et al. (2003) and are presented in Table 1.
Furthermore, in the FEM elastic-plastic calculations of Fs, K_0 was assumed equal to 0.4 for all materials. Also, linear elastic perfectly plastic behaviour was assumed throughout. The pre-yield elastic modulus was assumed independent of stress and strain. Failure was controlled by the Mohr-Coulomb yield criterion.

Table 1. Ground characteristics

Soils	E' (MPa)	ν'	c' (kPa)	ϕ' (º)	γ (kN/m^3)
Fill	20	0,35	0	30	19
Granite W5	1000	0,35	10	38	19
Granite W3 "Rigid stratum"	6000	0,20	300	52	25

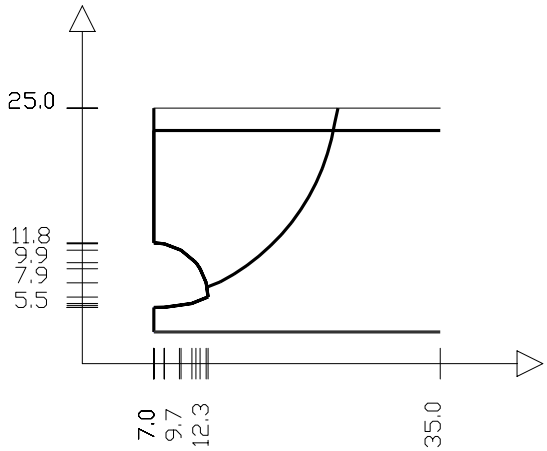

Figure 1 Shallow tunnel. Lateral Stability

The general program of Martins (2006) was used to search for the most unfavorable non circular sliding surface (a plane instead of the circle in Figure 1). The results presented in Table 2 were obtained by two different methods.

Table 2: F_s for lateral rupture (non circular sliding surface)

Morganstern & Price method	Correia method
1.33	1.33

These values compare well with those obtained from Fellenius as well as Bishop Method (Table 3):

Table 3: F_s for lateral rupture (circular sliding surface)

Fellenius	Bishop
1.20	1.36

The same problem has been solved by the 2D Blocks Method referred above in section 2. The result, for a division of the sliding mass into 8 quadrilateral blocks, was F_s =1.38. The resistance of the lining and that of the applied passive anchors were not taken into account in all cases, however, these can be included.

4 THE RIGID BLOCKS-SLICES METHOD

In this method the soil sliding mass is divided into slices comprising rigid blocks with vertical joints. On each slice there is a normal and tangential force at the center of the base and a net horizontal and shear force on one of the vertical faces, the other having horizontal force, only. Since there are 3*n equilibrium equations (n= number of slices), there must be a total of 3*n unknowns. These are 2*n normal and tangential forces at the base of the slices, n-1 normal forces inter-slices and 1 tangential force at one vertical joint. So a self-equilibrating structural system is created inside the soil sliding mass.
Computer programs in MATLAB (and FORTRAN) have been written for this method. The thickness of the slices can be either fixed (constant) or variable. The program has been applied to the first example presented by Zhu et al., (Figs. 2a and 2b)

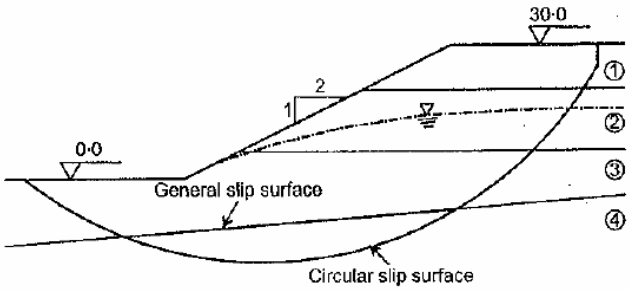

Fig. 2a . 1st. example of Zhu et al.

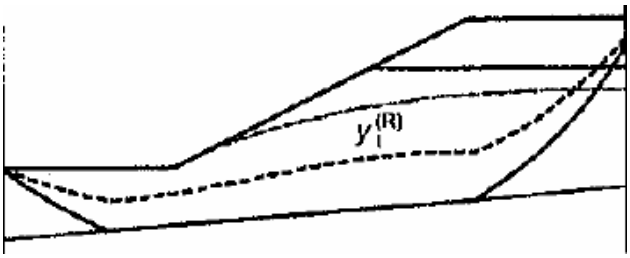

Fig. 2b. Non circular surface of sliding

Table 4 shows the values of F_s obtained by various methods as reported by :-i) Zhu et al; ii) Martins (2006) Circular and Noncircular surfaces of sliding: Morgenstern & Price's and Rui Correia,-iii) Rigid blocks-slices method.

Table 4. Comparisons of the results for safety factor Fs with the various programs. Pore pressures given by the "Zhu et al" piezometric line

Programs Matlab	Zhu et al. Circular Sliding	Zhu et al. Non-circular Sliding	Martins Circular Sliding	MartinsNon-circular Sliding	Martins Bloks Slices_LS	Martins Bloks FDL
Factor of Safety Fs	Fellenius =1.07-1.30 Bishop=1.07-1.29	Morgenstern & Price =1.12 Correira=1.12	Fellenius=1.54 Bishop=1.56	Morgenstern & Price =1.36 Correira=1.38	1.01-1.37	0.95-1.10

5 CONCLUSIONS

5.1 The most rigorous methods for the calculation of the limit equilibrium (EQU) safety factors for loaded earth masses (and any structure) are those based on non linear programming.

5.2 .However, it is known that mathematical programming can produce one, several or no solutions.

5.3 In the case of the calculation of the EQU safety factors, the kind of solution depends on the way the problem is posed. Since in practice the earth masses are heterogeneous and with a complicated geometry the calculation of the safety factors requires the masses to be divided into blocks. The Fs obtained with any stable isostatic system of blocks inside the "critical" ground mass, will be a "lower bound" solution, i.e., a value on the safe side. Since the calculation takes only a few seconds, a large number of stable systems can be tested. In the case of rock masses the user must choose the system of joints between blocks such that it matches the system of joints existing in nature. In the case of soil masses the user must divide the masse with a system of block joints which include the weaker soils.

5.4 The slices method, programmed for general situations, give results that, in practice, are very much near those of mathematical programming. Nevertheless some precautions must be taken: -i) the sliding surfaces must be chosen satisfying the nº4.3 above. –ii) Several reasonable values for the starting Fs0 must be chosen and a list of the corresponding final Fs must be written. From the list of calculated values for Fs, the final Fs is obtained.

5.5 The "most" unfavorable mechanism of failure was always obtained in the following ways

(i) By obtaining the Fs of Fellenius and Bishop for five circles chosen by experience from a scale drawing, to give the minimums Fs. However, many more sliding circles could be tested.

(ii) By approximating the circular sliding surface which gives the minimum F_s by an inscribed polygon. Using this sliding surface F_s is obtained for the Fellenius, Bishop, Morgenstern & Price and Correia methods, by means of the general program used here. These results are compared with the minima obtained by the classical methods of those authors.

(iii) By choosing a few polygonal sliding surfaces which bracket the initial - perhaps passing through the weaker layers of soil - the F_s for the methods of slices is obtained for the "most" unfavourable sliding surface. The methods of Fellenius, Bishop, Morgenstern & Price and Correia are used for this.

(iv) For the case of the tunnel considered above the "most" unfavourable sliding surface defines a "critical" sliding mass of soil and/or rock mass. Inside this mass an isostatic system of 8 blocks was defined. In the middle of each joint, whether internal or external, a double connection with a normal and a shear force is assumed. This isostatic system is then solved; the loads being the self weight of the blocks and any other external loads (live loads, seismic loads, hydraulic loads). In this way the normal and shear forces at the joints are obtained.

(v) From equation (2) the available resistance at each joint is obtained. Then the value F_s at each joint is increased by small increments (0.001), until, at least, in one joint there is no residual force, and the structural system becomes hypostatic. Therefore, in this way one can trace the joint that slips first. In the proposed problem this joint was always near the cavity of the tunnel which is in the plastification zone shown in the elastic-plastic solution obtained with a FEM (PLAXIS, program), not presented in this work.

5.6 The Rigid Blocks-Slices Method gave values for Fs near those obtained by Zhu et al. However, many more tests and comparisons are needed.

5.7 The 3D Rigid Blocks Method is promising, mainly for 3D situations such as the stability of the front face in tunnels excavations.

ACKNOWLEDGEMENT

Thanks are due to David Naylor, retired Senior Lecture from Swansea University, UK, for revising the English.

REFERENCES

Bishop, A. W. (1955). "The Use of the Circle Slip Surface in the Stability Analysis of Earth Slopes.". Géotechnique 5, Nº.1,. 7-17.

Chen J., Yin, J-H & Lee C. F. A. (2005), "Three-Dimensional Upper-bound Approach to Stability Analysis based on RFEM". ", Géotechnique 55, Nº.7, 549-556.

Correia, R. M. (1988), "A Limit Equilibrium Method of Slope Stability Analysis". Proceedings of 5th Int. Symp. Landslides. Lausanne, . 595-598.

Coulomb, C.A. (1776), "Essais sur une Application des Regles des Maximis et Minimis a Quelques Problems de Statique Relatives à l'Arquitecture" Memoirs Academie Royal Press Division Sav.7, Paris.

Fellenius, W. (1936), "Calculation of the stability of earth dams". Proceedings of 2nd Cong. Large Dams, Washington, 4, pp. 445-462.

Martins, J. B. (1979), "State of the art of the methods to solve the problem of the limit equilibrium of earth and rock masses with joints. (in Portuguese)". I.U.T.A.M National Congress, Lisbon, LNEC, October.

Martins, J. B. (2006), "Limit equilibrium of ground loaded masses. a general PC program for the factor of safety by rigid-plastic methods" Proceedings of 5th Int. Conf Mech.&M.Design, FEUP July, OPorto.

Martins, F. F., da Costa F. & Almeida e Sousa, J. (2003), "Túnel 4 (Porto) – Análise tridimensional por elementos finitos", Geotecnia, n.º 99, pp.65-80.

Martins, J. B. & Marques, P. S. (1984), "Calcul par Programmation Linéaire des Murs de Soutènement Renforcés".in Colloque "Renforcement en place des sols et des roches, ENPC, DFCAI (Direction de la Formation Continue et de l'Action Internacional), Oct. Paris, 9-11.

Morgenstern, N. R. and Price, V. E. (1965), "The Analysis of the Stability of General Slip Surfaces". Géotechnique 15, Nº.1, 79-93.

Rankine, W. J. M. (1857), "Earth Pressure Theory", Phil. Trans. of the Royal Soc..

Zhu, D. Y., Lee C. F. & Jiang H. D.(2003), " Generalized Framework of Limit Equilibrium Methods for the Stability Analysis". , Géotechnique 53, Nº.4, 377-395.

SEISMIC ANALYSIS OF NUCLEAR STRUCTURES AFFECTED BY CHEMICAL DEGRADATION

R. Ushaksaraei
Department of Civil Engineering, McMaster University, Hamilton, ON, Canada

S. Pietruszczak
Department of Civil Engineering, McMaster University, Hamilton, ON, Canada

V. Gocevski
Hydro-Quebec, Montreal, QC, Canada

ABSTRACT: *This paper deals with application of a non-linear continuum model for reinforced concrete affected by alkali-aggregate reaction (AAR) to analysis of some nuclear structures. The macroscopic behaviour of the material affected by AAR is described by incorporating a homogenization/averaging procedure. The formulation addresses the main stages of the deformation process, i.e. a homogeneous deformation mode as well as that involving localized deformation, associated with formation of macrocracks. The formulation is applied to examine the mechanical behaviour of some reinforced concrete structures in nuclear power facilities located in Quebec (Canada). First, a containment structure is analyzed subjected to 45 years of continuing AAR. Later, an inelastic analysis is carried out for the spent fuel exchange room in the nuclear reactor building subjected, once again, to continuing AAR followed by a seismic event.*

1 INTRODUCTION

The durability of concrete and reinforced concrete structures is often significantly impaired by the alkali-aggregate reaction (AAR). The product of the reaction is a gel that forms around the aggregate particles; it imbibes water from the pore fluid and expands triggering a progressive damage of the material. The rate of expansion depends primarily on the available alkali content of concrete. Other factors influencing the kinetics of the reaction are the relative humidity, temperature and the confining stress.

This work is primarily concerned with application of a non-linear continuum model which was recently developed for the description of mechanical behaviour of reinforced concrete subjected to AAR (Winnicki & Pietruszczak, 2008). The model is an extension of the framework presented earlier by Pietruszczak & Winnicki (2003), in which the reinforced concrete is considered as a composite medium comprising concrete matrix and two orthogonal families of reinforcement. The latter formulation is generalized to incorporate the chemo-mechanical interaction associated with continuing AAR.

The mechanical behaviour of reinforced concrete affected by AAR is described by employing a non-linear continuum theory that incorporates a chemo-mechanical coupling. In general, the most efficient way of analysing heavily reinforced large concrete structures is to use a homogenization technique. In this approach, the reinforced concrete is considered as a composite medium comprising the concrete matrix and a set of families of reinforcement. The overall macroscopic behaviour is then defined by employing suitable averaging procedures. In the framework employed here, the concrete is assumed to be strengthened with two orthogonal sets of reinforcing steel bars. The formulation addresses the main stages of

the deformation process, i.e. a homogeneous deformation mode as well as that involving localized deformation, associated with formation of macrocracks. In the former case, i.e. prior to cracking, the problem is formulated by invoking a volume averaging procedure. After the onset of localization, the representative volume incorporates the fractured zone and the adjacent 'intact' material, both reinforced with steel bars. In this case, the stiffness of the reinforcement network and the criterion of yielding are both assessed in a discrete sense, by considering the bending characteristics of individual bars rigidly embedded in the adjacent intact material. The concrete itself is assumed to suffer from continuing alkali-aggregate reaction. The mathematical description of the effects of the reaction is based on chemo-plasticity and invokes the assumption that the formation of expansive phases results in progressive degradation of both strength and deformation properties of the material.

In what follows, the governing constitutive relations, which have been incorporated in a finite element code, are first reviewed. Later, the results of numerical studies are presented. First, the mechanical response of a containment structure of a nuclear facility located near the community of Trois-Rivières in Québec is examined. Subsequently, an inelastic analysis is carried out for a spent fuel exchange room in the nuclear reactor building subjected to continuing AAR followed by a seismic event typical for the region.

2 MATHEMATICAL FORMULATION

The specific form of the constitutive relation for describing the AAR-affected reinforced concrete is that proposed in a recent paper by Winnicki & Pietruszczak (2008). In this approach, the material is treated as a composite medium comprising the AAR-affected concrete matrix (*m*) and two orthogonal families of reinforcement (sets *1* and *2*, respectively).

For concrete matrix, the formulation incorporates a scalar parameter ζ which is a measure of the continuing reaction and is defined as

$$\zeta(t)=\frac{\in(t)}{\bar{\in}}; \qquad \bar{\in}=\in(t\to\infty) \tag{1}$$

Here, $\in(t)$ is the volumetric expansion of concrete and $\bar{\in}$ is a material parameter that defines the maximum value of $\in$, for a given alkali content, in the stress free state. The evolution law is assumed in a simple linear form

$$\dot{\zeta}=\gamma(\bar{\zeta}-\zeta) \quad \text{for } t\geq t_0 \;\Rightarrow\; \zeta=\bar{\zeta}(1-e^{-\gamma\langle t-t_0\rangle}); \qquad \zeta=0 \quad \text{for} \quad t<t_0 \tag{2}$$

where $\bar{\zeta}$ can be interpreted as a value of the state variable ζ associated with the chemical equilibrium, γ is a material constant describing rate of the reaction, and t_0 is the initiation time. The closed form integration for ζ in Eq. (2) is based on a constant value of $\bar{\zeta}$, where <…> are Macauley brackets. The value of $\bar{\zeta}$ depends, in general, on the confining pressure, temperature and relative humidity.

The formulation of the constitutive relation that governs the chemo-mechanical interaction follows the framework established in an earlier article by Pietruszczak and Gocevski (2002). In the *elastoplastic* range, the additivity of elastic and plastic strain rates leads to

$$\dot{\boldsymbol{\varepsilon}}=[C^e]\dot{\boldsymbol{\sigma}}+\mathbf{b}\dot{\zeta}+\dot{\boldsymbol{\varepsilon}}^p \quad\Rightarrow\quad \dot{\boldsymbol{\sigma}}=[D^e](\dot{\boldsymbol{\varepsilon}}-\dot{\boldsymbol{\varepsilon}}^p-\mathbf{b}\dot{\zeta}); \qquad \mathbf{b}=\frac{\partial}{\partial\zeta}[C^e]\boldsymbol{\sigma}+\frac{1}{3}\bar{\in}\,\boldsymbol{\delta} \tag{3}$$

in which $[D^e]=[C^e]^{-1}$, where $[C^e]$ is the elastic compliance. In order to define the plastic strain rates, the functional form of the yield criterion f=0 is assumed to be affected by the progress in the reaction, i.e. $f = f(\boldsymbol{\sigma}, \boldsymbol{\varepsilon}^p, \zeta)$. Following a standard plasticity procedure, the constitutive relation can be obtained as

$$\dot{\boldsymbol{\varepsilon}} = [C]\dot{\boldsymbol{\sigma}} + \boldsymbol{\Gamma}\dot{\zeta}; \quad \boldsymbol{\Gamma} = \mathbf{b} + \frac{1}{H}\frac{\partial f}{\partial \zeta}\frac{\partial Q}{\partial \boldsymbol{\sigma}} = \frac{\partial}{\partial \zeta}[C^e]\boldsymbol{\sigma} + \frac{1}{H}\frac{\partial f}{\partial \zeta}\frac{\partial Q}{\partial \boldsymbol{\sigma}} + \frac{1}{3}\in \boldsymbol{\delta} \tag{4}$$

where

$$[C] = [C^e] + \frac{1}{H}\frac{\partial Q}{\partial \boldsymbol{\sigma}}\left(\frac{\partial f}{\partial \boldsymbol{\sigma}}\right)^T; \quad H = -\left(\frac{\partial f}{\partial \boldsymbol{\varepsilon}^p}\right)^T \frac{\partial Q}{\partial \boldsymbol{\sigma}} \tag{5}$$

In the equations above, $[C]$ is the elastoplastic compliance operator, H is the plastic hardening modulus and $\boldsymbol{\delta}$ is the Kronecker's delta.

For reinforced concrete, the problem is formulated in two stages (Pietruszczak & Winnicki, 2003). Stage I deals with the homogeneous deformation mode prior to cracking of the concrete matrix, whereas stage II involves a localized deformation associated with formation of macrocracks.

2.1 Stage I (prior to cracking)

The problem is referred to the frame of reference $\mathbf{x}^*$, such that x_2^* and x_3^* are along the axes of reinforcement. The average macroscopic stress/strain rates for the composite body are defined through the volume averaging procedure (Hill, 1963), i.e.

$$\dot{\boldsymbol{\sigma}}^* = \eta_1\dot{\boldsymbol{\sigma}}_1^* + \eta_2\dot{\boldsymbol{\sigma}}_2^* + (1-\eta_1-\eta_2)\dot{\boldsymbol{\sigma}}_m^*; \quad \dot{\boldsymbol{\varepsilon}}^* = \eta_1\dot{\boldsymbol{\varepsilon}}_1^* + \eta_2\dot{\boldsymbol{\varepsilon}}_2^* + (1-\eta_1-\eta_2)\dot{\boldsymbol{\varepsilon}}_m^* \tag{6}$$

where η_1 and η_2 represent the volume fractions of the respective sets of reinforcement, whereas $\dot{\boldsymbol{\sigma}}_k^*, \dot{\boldsymbol{\varepsilon}}_k^*$ $(k = 1, 2, m)$ are the averages of stress/strain rates in the constituents involved. Both these local fields are assumed to be homogeneous within themselves, so that

$$\dot{\boldsymbol{\varepsilon}}_1^* = [C_1^*]\dot{\boldsymbol{\sigma}}_1^*; \quad \dot{\boldsymbol{\varepsilon}}_2^* = [C_2^*]\dot{\boldsymbol{\sigma}}_2^*; \quad \dot{\boldsymbol{\varepsilon}}_m^* = [C_m^*]\dot{\boldsymbol{\sigma}}_m^* + \boldsymbol{\Gamma}^*\dot{\zeta} \tag{7}$$

where $[C^*]$'s are the compliance operators. The reinforcing steel is considered to be an elastic–perfectly plastic von Mises material obeying an associated flow rule, while the behaviour of concrete matrix is governed by eq.(4).

The local stress rate averages can be related to the overall macroscopic measure $\dot{\boldsymbol{\sigma}}^*$ viz.

$$\dot{\boldsymbol{\sigma}}_1^* = [B_1]\dot{\boldsymbol{\sigma}}^* + [\bar{B}_1]\boldsymbol{\Gamma}^*\dot{\zeta}; \quad \dot{\boldsymbol{\sigma}}_2^* = [B_2]\dot{\boldsymbol{\sigma}}^* + [\bar{B}_2]\boldsymbol{\Gamma}^*\dot{\zeta}; \quad \dot{\boldsymbol{\sigma}}_m^* = [B_m]\dot{\boldsymbol{\sigma}}^* + [\bar{B}_m]\boldsymbol{\Gamma}^*\dot{\zeta} \tag{8}$$

The details on the specification of operators $[B]$ and $[\bar{B}]$, based on imposing some explicit kinematic constraints, are provided in the original reference.

Combining the above equations, the macroscopic constitutive relation can be established

$$\begin{aligned} &\dot{\boldsymbol{\varepsilon}}^* = [C^*]\dot{\boldsymbol{\sigma}}^* + [\bar{C}^*]\boldsymbol{\Gamma}^*\dot{\zeta}; \quad [C^*] = \{\eta_1[C_1^*][B_1] + \eta_2[C_2^*][B_2] + (1-\eta_1-\eta_2)[C_m^*][B_m]\}; \\ &[\bar{C}^*] = \{\eta_1[C_1^*][\bar{B}_1] + \eta_2[C_2^*][\bar{B}_2] + (1-\eta_1-\eta_2)([C_m^*][\bar{B}_m] + [I])\} \end{aligned} \tag{9}$$

Apparently, the macroscopic stress/strain rates can be transformed to an arbitrarily chosen global Cartesian system by following the standard transformation rules.

The above equation defines the response of the composite prior to formation of macrocracks in the concrete matrix. In reinforced concrete structures, the cracking is typically associated with the *tensile* stress regime. Once a macrocrack forms, the formulation of the problem follows the procedure outlined below.

2.2 Stage II (after formation of a macrocrack)

The representative volume of the material comprises now the 'intact' reinforced concrete intercepted by a macrocrack of a given orientation $\boldsymbol{n}$. The latter represents a composite medium within itself as it consists of a zone of fractured concrete reinforced with steel bars. A volume averaging procedure can be used again for specifying the macroscopic rates, i.e.

$$\dot{\boldsymbol{\sigma}} = \mu_i \dot{\boldsymbol{\sigma}}_i + \mu_f \dot{\boldsymbol{\sigma}}_f ; \quad \dot{\boldsymbol{\varepsilon}} = \mu_i \dot{\boldsymbol{\varepsilon}}_i + \mu_f \dot{\boldsymbol{\varepsilon}}_f \tag{10}$$

Here, *i* refers to the intact material outside the localization zone, *f* denotes the material in the fractured zone and μ's represent the corresponding volume fractions. All quantities are referred to the global coordinate system **x.** The strain rate in the fractured zone can be expressed in terms of velocity discontinuities $\dot{\boldsymbol{g}}$. Thus, the constitutive relations governing the behaviour of the intact material and the interface are as follows

$$\dot{\boldsymbol{\varepsilon}}_i = [C]\dot{\boldsymbol{\sigma}}_i + [\bar{C}]\boldsymbol{\Gamma}\dot{\zeta} ; \quad \dot{\boldsymbol{\varepsilon}}_f = \frac{1}{h}[N]\dot{\boldsymbol{g}} ; \quad \dot{\boldsymbol{g}} = [K]^{-1}\dot{\boldsymbol{t}} ; \quad \dot{\boldsymbol{t}} = [N]^T \dot{\boldsymbol{\sigma}}_i \tag{11}$$

where [*K*] denotes the stiffness of the fractured zone, $\boldsymbol{t}$ is the traction vector, and *h* denotes the thickness of the cracked zone. Noting that $\mu_f \ll \mu_i$ and employing eq.(10), the average macroscopic response of the composite can be defined as

$$\dot{\boldsymbol{\varepsilon}} \simeq ([C] + \mu[N][K]^{-1}[N]^T)\dot{\boldsymbol{\sigma}} + [\bar{C}]\boldsymbol{\Gamma}\dot{\zeta} \tag{12}$$

Here, $\mu = \mu_f / h$ represents the ratio of the area of the fractured zone to the representative volume of the sample. Thus μ is, in fact, independent of *h*.

The approach outlined above requires an assessment of the mechanical properties of the fractured zone, viz. operator [*K*]. This zone is composed of the damaged concrete and the network of reinforcement. The details on the description of mechanical characteristics are provided in the article by Pietruszczak & Winnicki (2003).

The particular formulation employed here to describe the nonlinear behaviour of concrete matrix is similar to that outlined by Pietruszczak et al. (1988). It invokes a non-associated flow rule and the yield surface is expressed in a functional form

$$f = \bar{\sigma} - \alpha(\zeta)\beta(\xi)k(\theta)\bar{\sigma}_c = 0; \quad \dot{\xi} \propto (\frac{1}{2}\dot{e}^p_{ij}\dot{e}^p_{ij})^{1/2}; \quad \bar{\sigma}_c = \frac{-a_1 + \sqrt{a_1^2 + 4a_2(a_3 + I/f_c)}}{2a_2} f_c \tag{13}$$

In the equations above *a*'s are material constants normalized with respect to axial compressive strength (f_c); $I = -I_1, \bar{\sigma} = (J_2)^{1/2}, \theta = \frac{1}{3}\sin^{-1}(3\sqrt{3}\,J_3 / 2\bar{\sigma}^3)$, where I_1 and (J_2, J_3) are the basic invariants of the stress tensor and stress deviator, respectively. The degradation of strength properties is governed here by the variable $\alpha(\zeta)$. In general, all degradation functions, for elastic moduli as well as strength, are assumed in a simple linear form

$$E = E_0\left[1-(1-B_1)\zeta\right]; \qquad \nu = \nu_0\left[1-(1-B_2)\zeta\right]; \qquad \alpha = 1-(1-B_3)\zeta \tag{14}$$

where B's are material parameters. Finally, in the simulations presented below, the parameter $\overline{\zeta}$ is taken as a function of the confining pressure only, and its evolution is described via an exponential form

$$\overline{\zeta} = e^{-A_1\sqrt{\frac{\langle -tr(\boldsymbol{\sigma})\rangle}{3f_c}}} \tag{15}$$

where A_1 is a material constant.

3 NUMERICAL ANALYSIS

In this section, the results of some numerical simulations are provided. In particular, the framework described in Section 2 is applied to examine the mechanical behaviour of some structural elements within the Gentilly-2 (G2) nuclear powerplant, situated near the community of Trois-Rivières in Quebec.

The surface cracking of concrete at G2 powerplant started during the construction stage and gradually worsens over time due to the effects of AAR and the continuing thermal cycles typical for the Canadian climate. The propagation of cracks (now penetrating, on average, about 100mm into the walls) and the changes of pre-stressing over time are continuously influencing the structural behaviour. The main issue, after 27 years of operation, is the ultimate pressure capacity (UPC) and the air tightness of the reinforced concrete envelope, which depend mainly on the losses/gains of post-tensioning forces. The latter are due to AAR-effects as well as the damage that can be attributed to shrinkage and aging of concrete caused by freeze-thaw cycles (Gocevski 2003, 2010). In what follows, the results of numerical simulations performed to evaluate the UPC and the air tightness of the containment building (without considering the penetration seals) under own weight, post-tensioning and AAR are presented first. Then, the results of FE analysis of the spent fuel exchange room in the nuclear reactor building, under self-weight, 30 years of continuing AAR, and seismic load are discussed.

3.1 Containment structure

The evolution of damage within the concrete walls of the containment structure of G2 is examined first. The ultimate pressure capacity is directly affected by the formation and a slow propagation of micro and macrocracks. Therefore, it is important to predict the time-history of their occurrence in order to assess the need for implementing some remedial measures to maintain the air tightness of the building, as imposed under the requirements of the Canadian Commission of Nuclear Safety (CCNS). The structure, shown in Fig.1, was analyzed using the constitutive model for AAR-affected reinforced concrete, as discussed earlier. The analysis was conducted using the primary set of material properties specified in Table 1. The values of parameters governing the kinetics of AAR were taken as

$$\overline{\in} = 0.01704 \ ; \ \gamma = 0.092 \ (1/day) \ ; \ B_1 = 0.7 \ ; \ B_2 = 0 \ ; \ B_3 = 0.9 \ ; \ A_1 = 8.3$$

The perimeter wall has circumferential post-tensioning tendons and vertical tendons while the upper dome consists of three layers of superimposed tendons, the latter placed in such a way that the tendons form spherical equilateral triangles. The equivalent initial compressive stresses in the concrete sections were evaluated based on spacing of the cables in the structural elements. The average values were estimated as: 10.7 MPa for the two

perpendicular principal components in spherical plane of the superior dome, 5.9 MPa for circumferential and 3.5 MPa for vertical direction of the wall, and finally 4.4 MPa and 2.3 MPa for the inferior and superior part of the ring beam, respectively.

An important component in determining the state of the structure at the present time and in the future (year 2035) is the evaluation of the rate of free expansion in concrete. This has been assessed based on the results of some laboratory tests as well as the strain measurements obtained from the strain gages placed in concrete during the construction of the containment.

The results describing the response of the structure under own weight, post-tensioning, and the continuing AAR are shown in Figs. 2-4. Fig. 2 presents the distribution of damage factor, β, eq.(13), after 12, 17, and 32 years of ongoing reaction. Note that the values of $\beta > 1$ are indicative of an unstable response associated with formation of macrocracks. The evolution of the distribution of damage factor in the horizontal section of the wall opposite the opening is shown in Fig. 3. The results indicate the presence of a damage zone, which at some locations penetrates through the entire thickness of the wall. However, the macrocracks are not more than 0.15mm wide. Fig. 4 shows the distribution of damage factor β at the connection of perimeter wall with the base slab. In general, the extent of damage after 45 years of continuing AAR is not very significant. The containment is structurally sound and only minor refurbishment from inside the building may be required to ensure adequate air tightness.

Table 1. Material properties

Concrete Elastic Properties	E = 34.5 GPa; υ = 0.2
Concrete Compressive Strength (nominal) (actual)	 f_{co} = 35 MPa f_{c2035} = 58 MPa
Concrete Tensile Strength (nominal) (actual)	 f_{to} = 2.72 MPa f_{c2035} = 1.5 MPa
Post-tensioning	1.06 nominal
Reinforcement	E=200 GPa; υ = 0.3; σ_y = 400 MPa

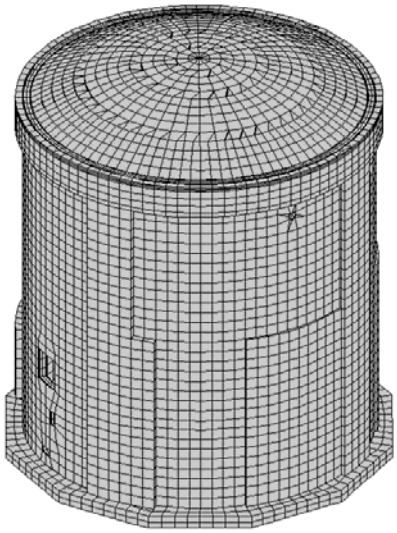

Fig. 1. Discretization of the containment structure

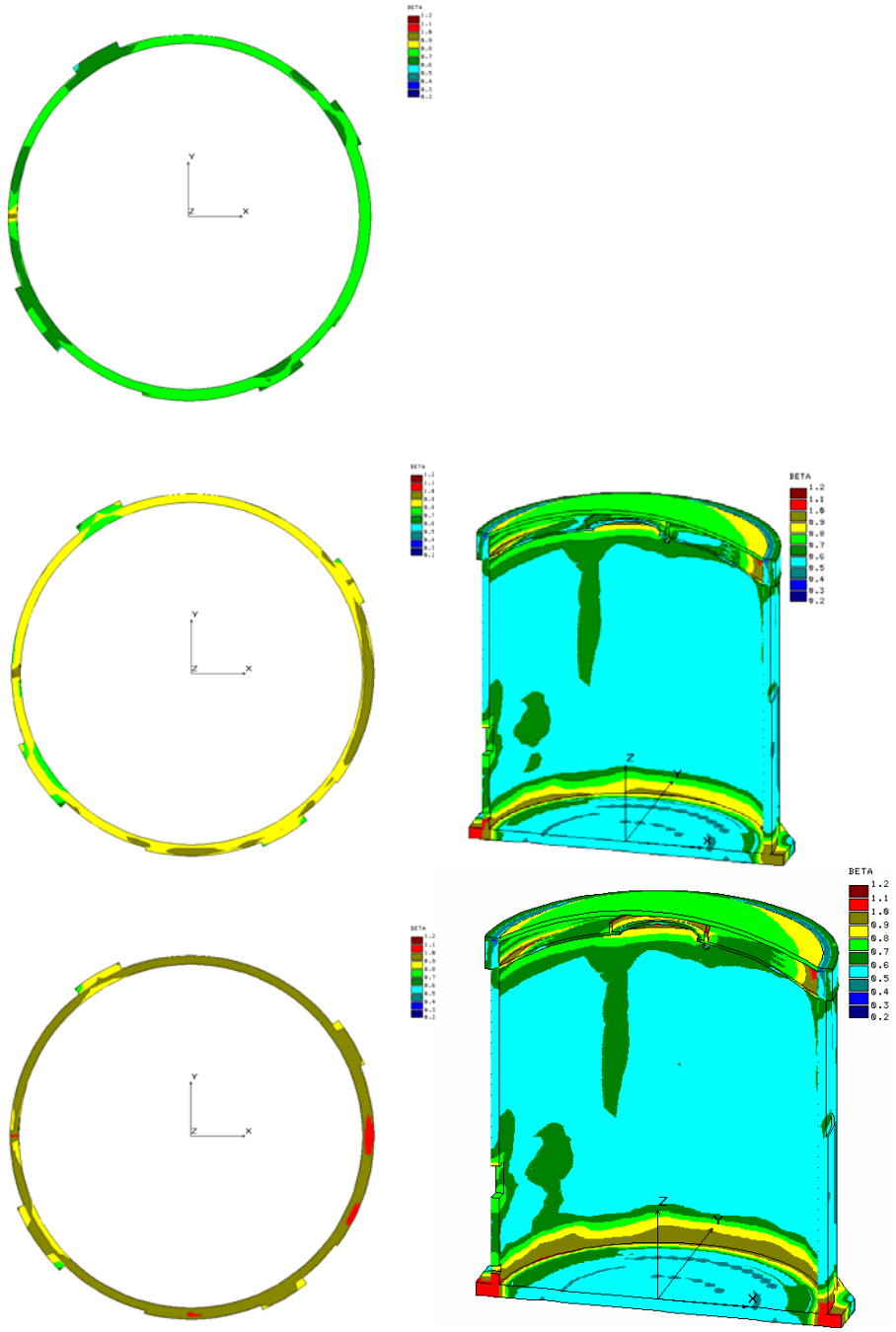

Fig. 2. Distribution of damage factor, β, due to work load and the AAR continuing for 12 years (onset of micro-cracking), 17 years, and 32 years from top to bottom, respectively); horizontal section at z=1.41m

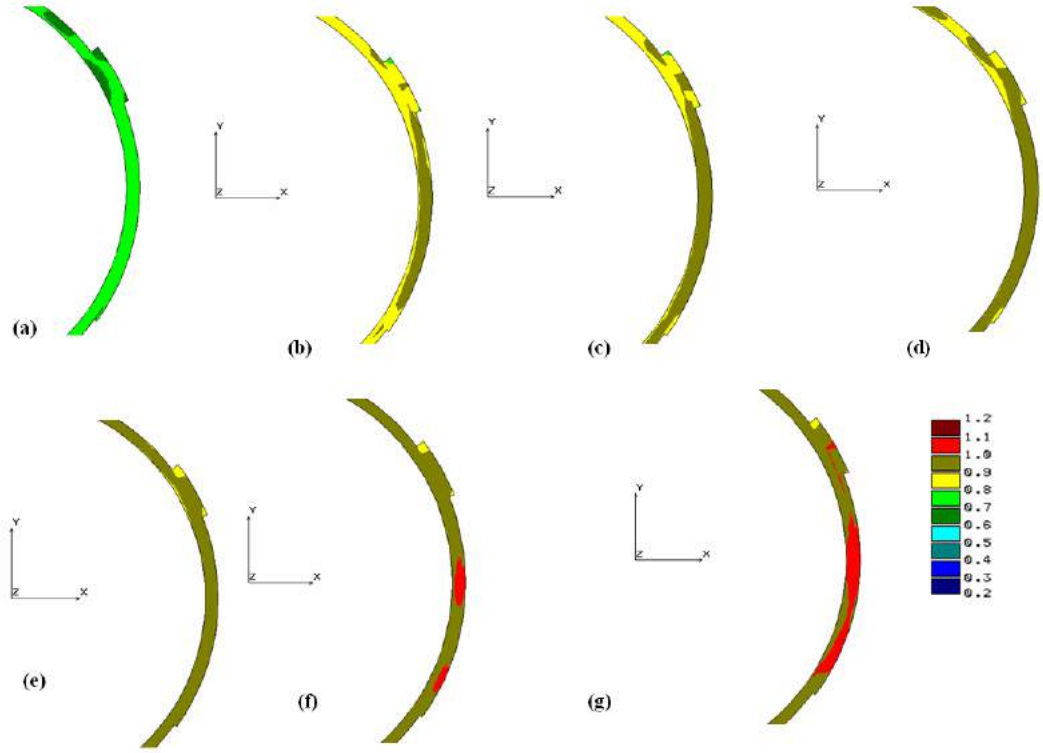

Fig. 3. Distribution of damage factor, β , due to work load and the AAR continuing for a) 12, b) 17, c) d) 20, e) 25) f) 32**,** g) 35 years; horizontal section at z=1.41m. Detail of the wall opposite of the opening

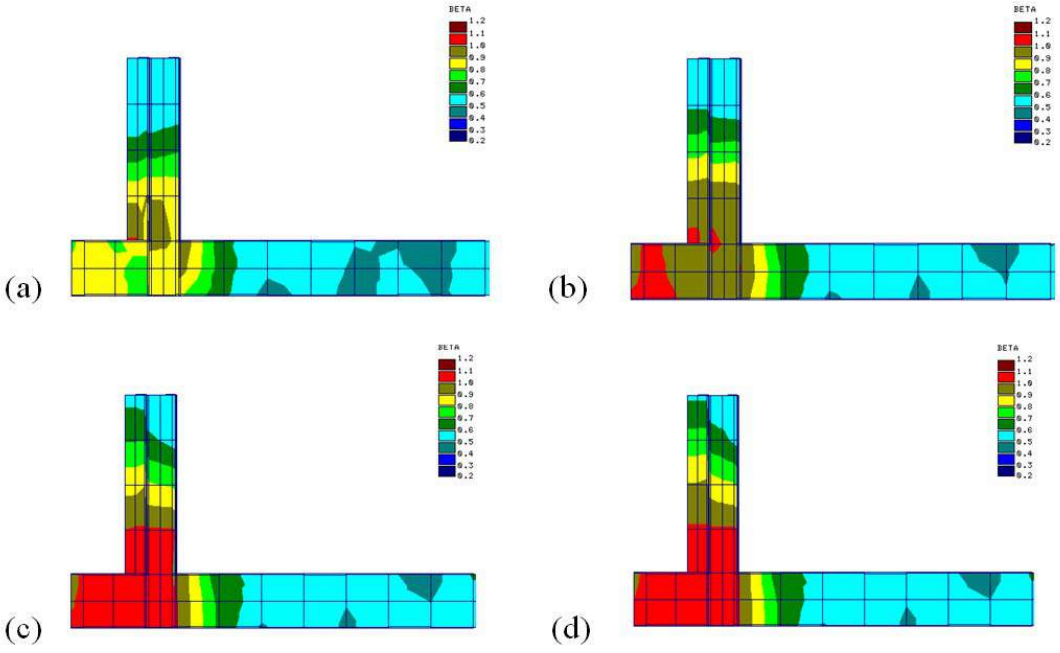

Fig. 4. Distribution of damage factor β at the connection of perimeter wall with base slab due to work load and AAR continuing for : a) 20 , b) 30 ,c) 40 , d)45 years

3.2 Spent fuel exchange room in the nuclear reactor building

In this section the results of FE analysis of the spent fuel exchange room in the nuclear reactor building, under self-weight, 30 years of continuing AAR, and the seismic load are presented. The FE discretization of the structure, which employs 8-noded solid elements, is shown in Fig. 5. The AAR-affected parts of the structure, with different ultimate free expansions due to AAR, are also shown in this figure. The rest of the structure is assumed to consist of reinforced concrete exhibiting an elastic behaviour. Fig. 6 presents the contours of displacement field within the structure under self-weight and 30 years of continuing AAR. Fig. 7 shows the distribution of damage factor after 30 years of AAR. In this figure, the cracked regions, i.e. those for which the damage factor β exceeds one, are marked in dark red. It is evident here that the damaged zones appear on the wall surfaces, where the expansion of concrete due to AAR is high. The cracking through the wall cross-sections is not very significant however. In general, additional studies combined with in-situ tests are required for a better calibration of the numerical model in order to assess whether the local cracking has an effect on air tightness of the concrete. The concrete aging management program presently under preparation will insure that adequate repairs are undertaken, if needed, so that the plant safety is never compromised.

Fig. 8 shows the location of nodal points that have been selected to monitor the displacement histories in x, y, and z directions, under self-weight and continuing AAR. The displacement histories themselves are depicted in Fig. 9. Installation of displacement monitoring devices in these points is planned. This additional information will provide the data for a better calibration of the numerical model and will allow for a much closer monitoring of the AAR-induced degradation process.

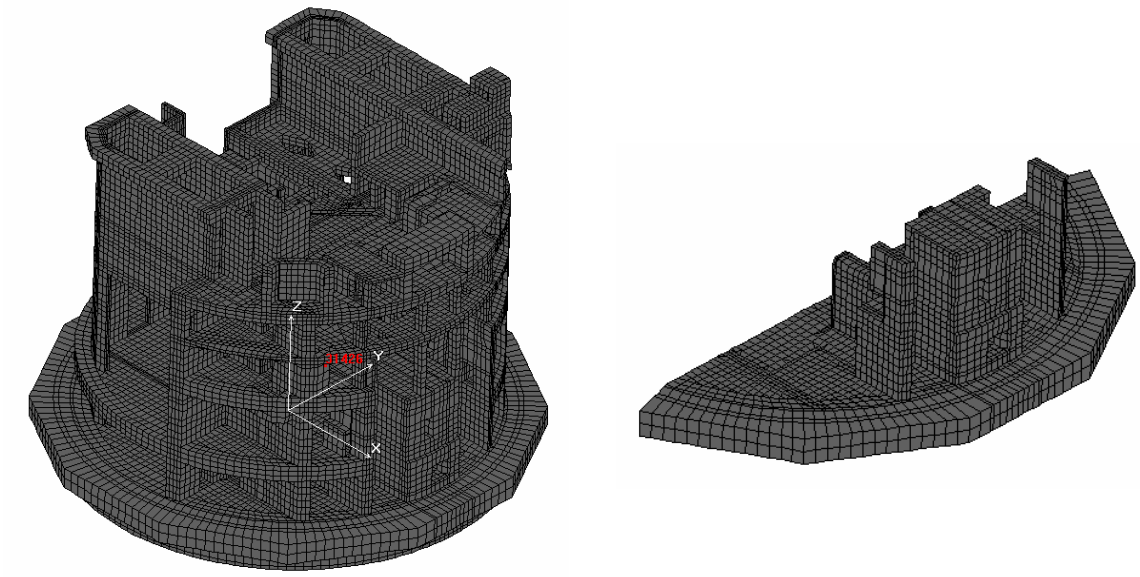

Fig. 5. FE discretization of the interior of G2: entire structure (left);
AAR-affected parts (right)

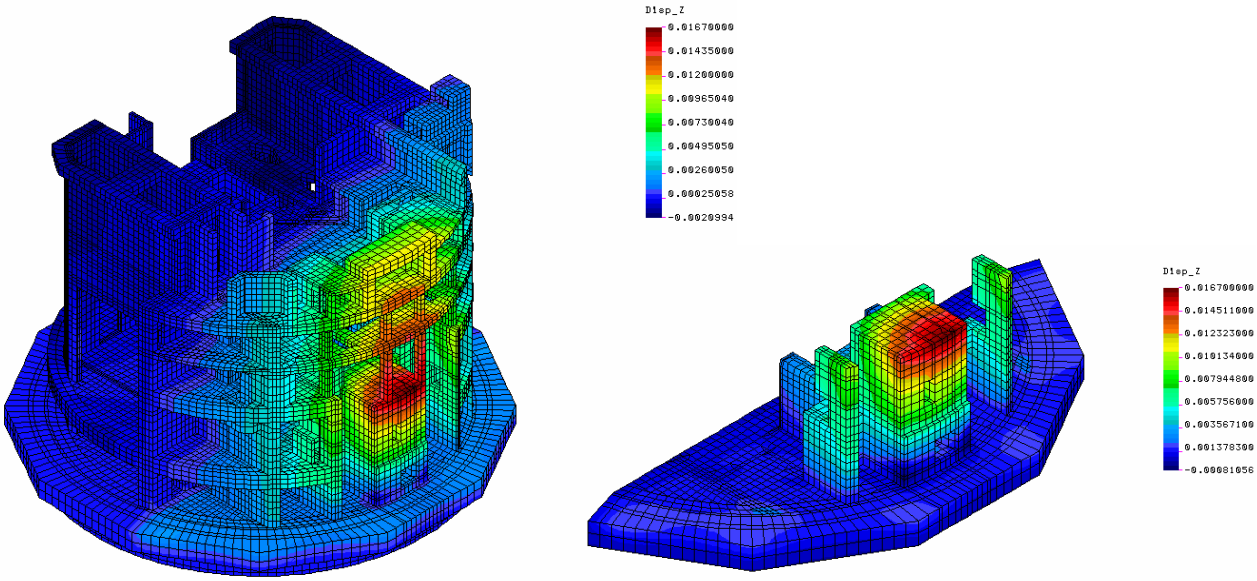

Fig. 6. Distribution of vertical displacements (in z direction) after 30 years of AAR

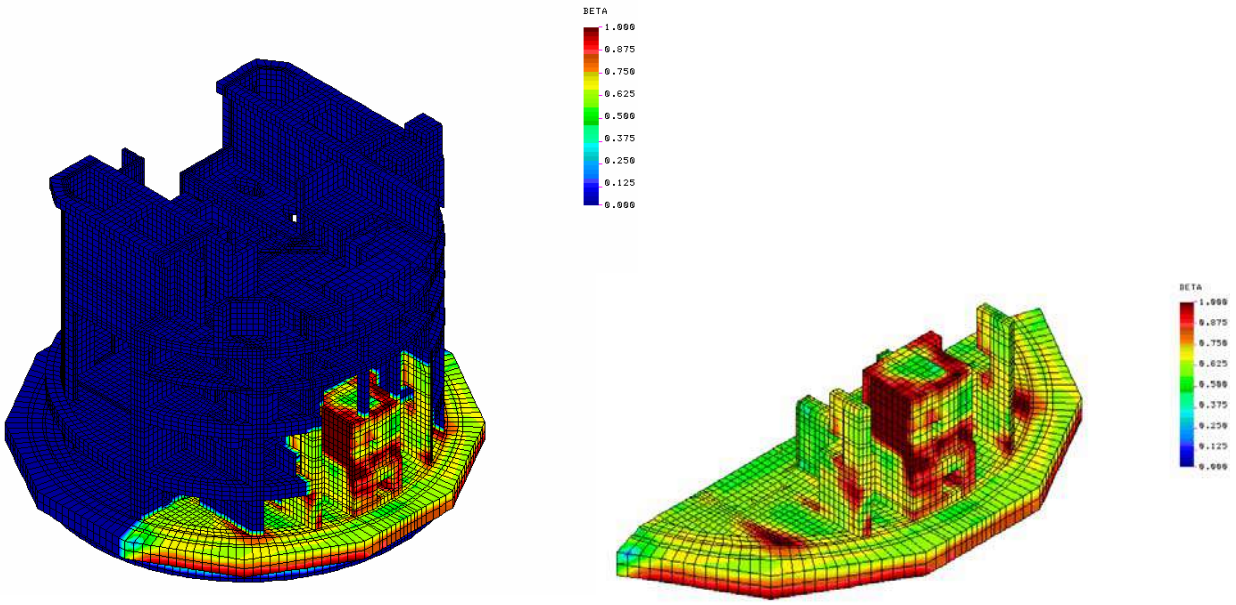

Fig. 7. Distribution of damage factor, β, after 30 years of AAR

Fig. 8. Location of the selected nodes

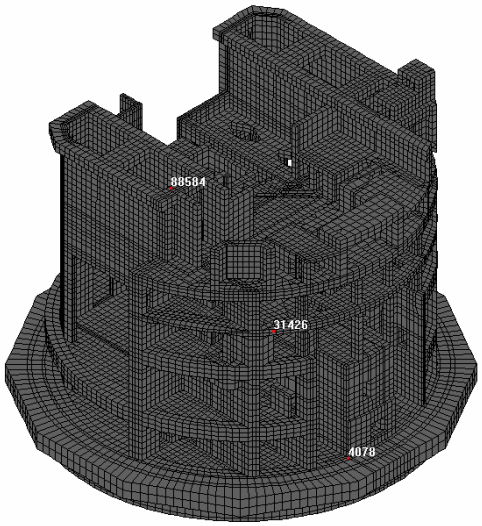

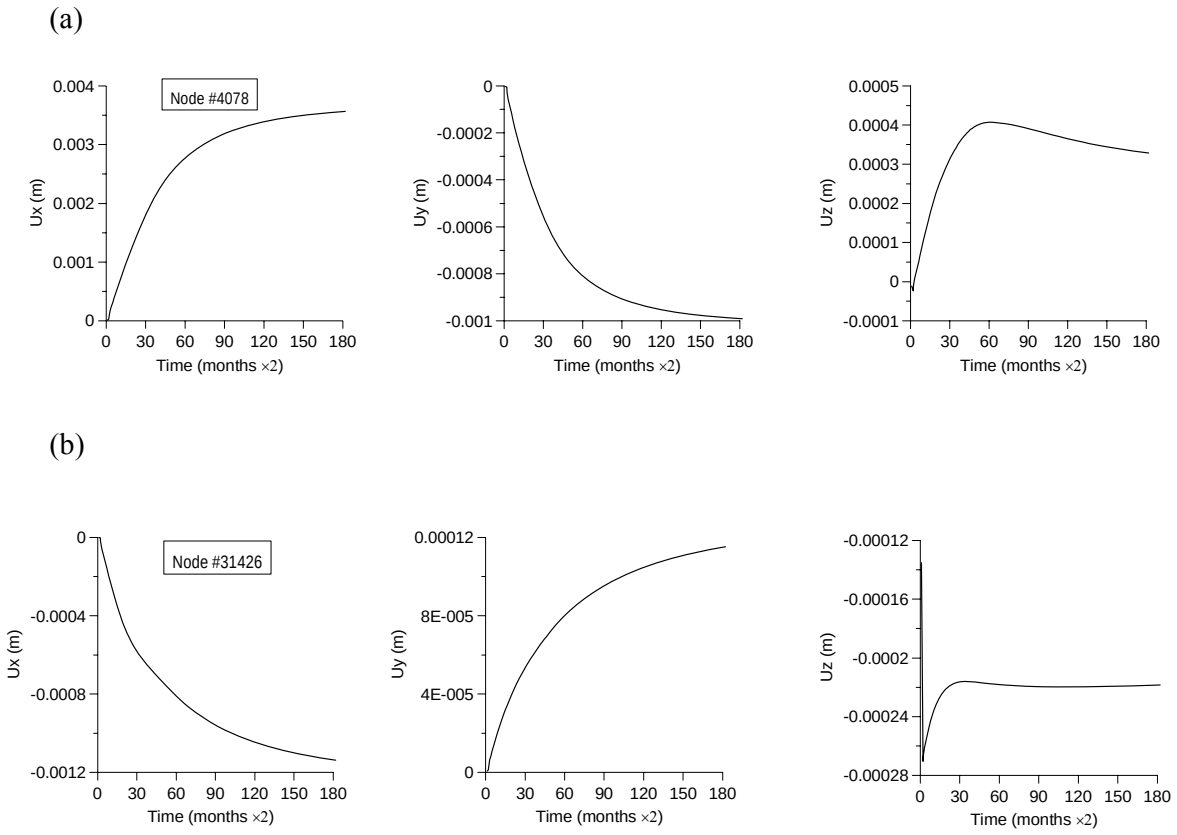

Fig. 9. Displacement histories for (a) node #4078 and (b) node #31426, under self-weight and AAR

In the final stage, the response of the structure under a seismic excitation, typical for the region, has been examined. The predicted displacement histories for the selected node are shown in Fig. 10. The figure presents the response for the first 25 seconds of the seismic event, which is the most critical part of the typical spectrum. Finally, it should be mentioned that the distribution of damage factor during the seismic activity is virtually the same as that corresponding to 30 years of AAR, Fig. 7. This indicates that the predominant source of damage is the 30 years of continuing AAR.

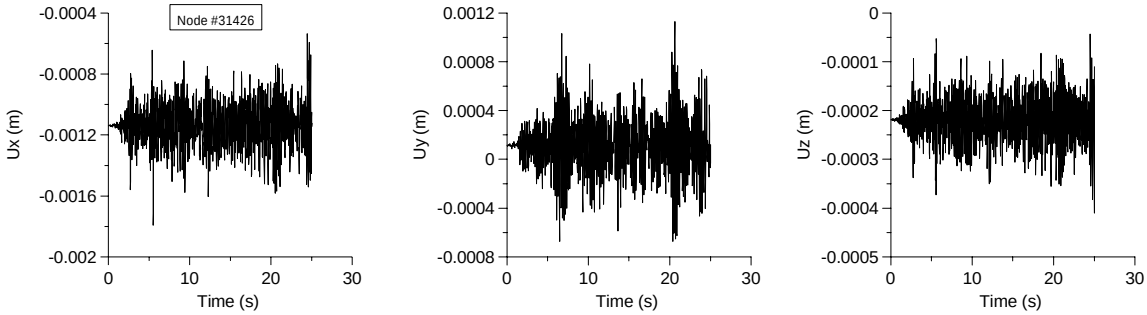

Fig. 10. Displacement histories during seismic excitation; node #31426

4 CONCLUSIONS

A meso-scale approach has been outlined for describing the chemo-mechanical interaction in reinforced concrete. The formulation has been incorporated in a finite element code to examine the mechanical behaviour of some reinforced concrete structures in nuclear power facilities located in Quebec, Canada. First, the response of a containment structure under self-weight, post-tensioning, and continuing AAR was examined. A formation of some zones of micro/macro-cracking was predicted in the walls of the containment building over 45 years of reaction. Subsequently, finite element simulations were carried out to examine the response of a spent fuel exchange room in the nuclear building under self-weight, 30 years of AAR, and a seismic load typical for the region. For the spent fuel room, it has been concluded that the predominant source of damage is the 30 years of AAR and there is no extensive damage that can be attributed to the seismic activity.

ACKNOWLEDGEMENT

The collaborative effort in conducting the numerical simulations, and the financial support provided by Hydro-Quebec is acknowledged.

REFERENCES

Gocevski, V. 2003. “Centrale nucléaire de Gentilly-2; analyse du comportement du bâtiment du réacteur“, Volume 1 du Rapport Final, Hydro-Québec TAYAA-12242-001, avril 2003.

Gocevski, V. 2010. “Gentilly 2 NPP - concrete aging effects on long term pre-stress losses and propagation of concrete cracking due to pressure testing”, International Symposium, Fontevraud-7, SFEN French Nuclear Energy Society, Paper A158-T10, 26-30 September 2010, Avignon, France.

Hill, R. (1963), “Elastic properties of reinforced solids: some theoretical properties”. J. Mech. Phys. Solids, 11, 357–372.

Pietruszczak, S., & Gocevski, V. (2002), “On rehabilitation of concrete structures affected by alkali-silica reaction”. Int. J. Comp. Civil & Struct. Eng., 1(3), 182-197.

Pietruszczak, S., Jiang, J., & Mirza, F.A. (1988), “An elastoplastic constitutive model for concrete”. Int. J. Solids Struct., 24(7), 70 –722.

Pietruszczak, S., & Winnicki, A. (2003), “Constitutive model for concrete with embedded sets of reinforcement”. J. Eng. Mech., ASCE, 129(7), 725–738.

Winnicki, A. & Pietruszczak, S. (2008), “On mechanical degradation of reinforced concrete affected by alkali-silica reaction”. J. Eng. Mech., ASCE, 134(8), 611–627.

SIMULATION OF MECHANICAL AND THERMAL BEHAVIOR OF SYNTHETIC ROCK AROUND AN OPENING USING BONDED PARTICLE MODEL

C. Lee, S. Jeon
Department of Energy Systems Engineering, Seoul National University, Seoul, Korea

Y. Lee
Department of Coastal Construction Engineering, Kunsan National University, Kunsan, Korea

ABSTRACT: *Laboratory experiment and numerical simulation were carried out in order to investigate the influence of an EDZ, Excavation Damage Zone, on the mechanical and thermal behavior of synthetic rock. The EDZ was artificially made at around an opening in the synthetic rock by repeating loading and unloading cycles. The specimen was 300×300×75 mm in size with a circular opening at the center. By applying biaxial load on the surfaces of the specimen with and without EDZ, we monitored displacements around an opening. The results showed that the tangential displacements were significantly different in the two cases, i.e. specimens with and without EDZ. It was thought that the difference in the mechanical behavior was a clear evidence of the formation of EDZ around the opening. The influence of the EDZ on the temperature distribution in the specimen was also examined. The influence of the EDZ observed in the laboratory test was demonstrated by DEM simulation using Particle Flow Code 2D. The results of the simulation also revealed that the presence of EDZ around an opening has a significant effect on the mechanical and thermal behavior of the synthetic rock.*

1 INTRODUCTION

Excavation Damaged Zone (EDZ) is inevitably produced in the process of rock excavation regardless of the excavation method. EDZ is the zone in the vicinity of excavation where the thermal, mechanical, and hydraulic properties of rock mass are changed due to the excavation damage or stress redistribution (Martino and Chandler, 2004). A repository facility for high-level nuclear waste that is usually planned in depth (Min et al., 2005; Kwon and Cho, 2008), is a good example where the occurrence of EDZ is a matter of considerable concern. Many recent studies on EDZ were carried out at underground research laboratories, i.e. KAERI Underground Research Tunnel (KURT) in Korea (Kwon et al., 2009), Tono Mine in Japan (Sato et al., 2000), Underground Research Tunnel (URL) in Canada (Cai and Kaiser, 2005), Hard Rock Laboratory (HRL) in Sweden (Emsley et al., 1997), Mont Terri in Switzerland (Bossart et al., 2002), Yucca Mountain in the USA (Price and Bauser, 1985), and so forth. In those studies, many attempts have been made to characterize the extent and behavior of EDZ in the context of mechanical and hydraulic responses.

This study intends to examine the influence of EDZ on the mechanical and thermal behavior of synthetic rock. In the study, laboratory experiments were carried out along with the numerical simulation using PFC^{2D} (Itasca, 2008). The experimental evidence of the influence of an EDZ on the mechanical and thermal behavior was demonstrated by the results from the numerical simulation.

2 METHODOLOGY

Experimental plan for the study of the influence of EDZ on mechanical behavior consists of three loading steps in two different loading scenarios as shown in Fig. 1. In the first loading step, uniaxial loading of 6.33 MPa was applied to get the mechanical behavior at EDZ free condition. In the second step, the specimen was loaded biaxially to an extent sufficient to induce EDZ around the opening by repeating loading and unloading cycles. It should be noted that we decided the stress level considering the stress concentration around the circular opening and the uniaxial strength of the synthetic rock of 30 MPa.

In the two different loading scenarios, EDZs in asymmetric and symmetric shape were assumed to be created as shown in Fig. 1. In the last step, the same magnitude of uniaxial stress as in the first step was applied to the specimen and the tangential strains were monitored at the four points A1, B1, C1, and D1 in Fig. 3. The measured strains were compared with those measured in the first loading step. Assuming that the difference in the strain measurements reflects the presence of an EDZ, the influence of the stress-induced EDZ on the mechanical behavior was investigated.

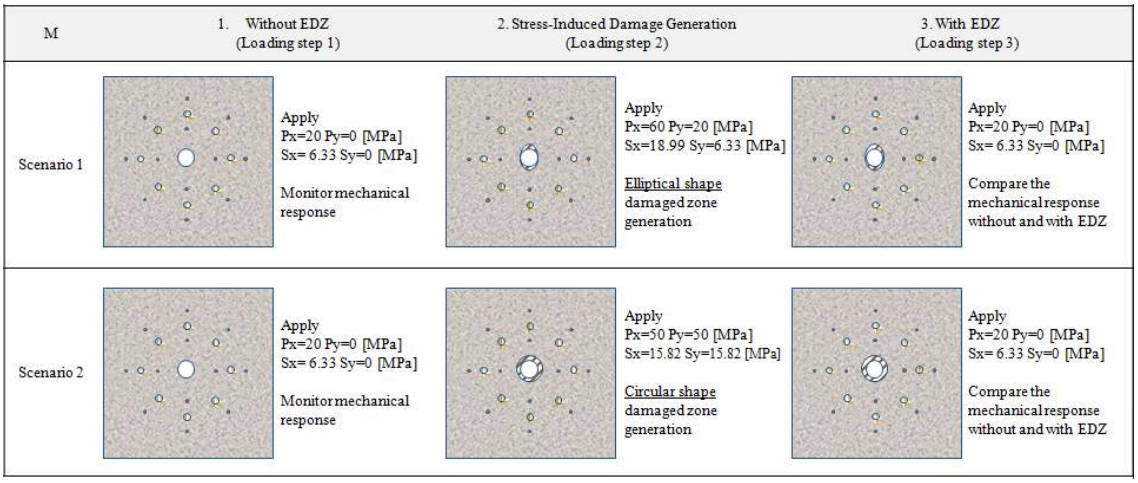

Fig. 1. Experimental plan for the study of the influence of EDZ on mechanical behavior

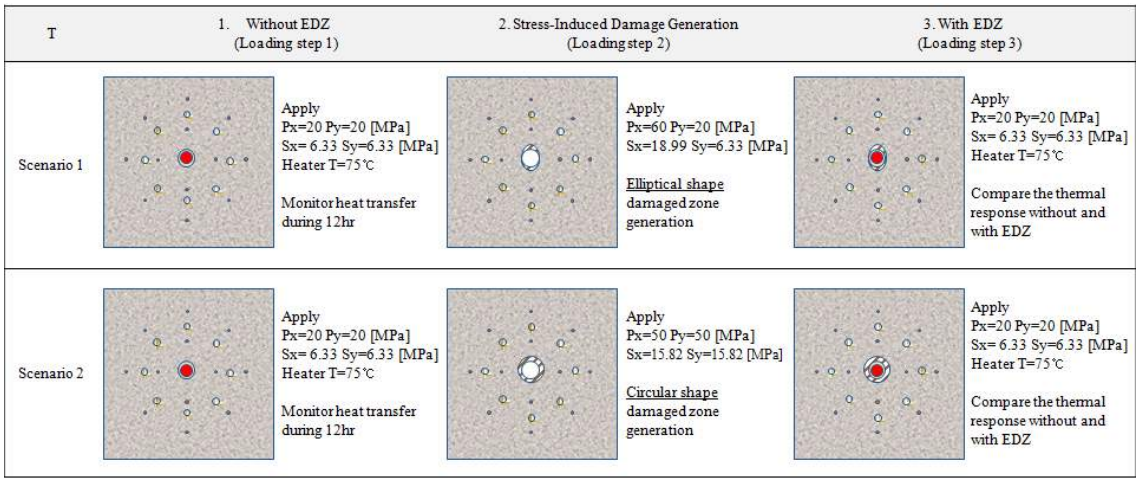

Fig. 2. Experimental plan for the study of the influence of EDZ on thermal behavior

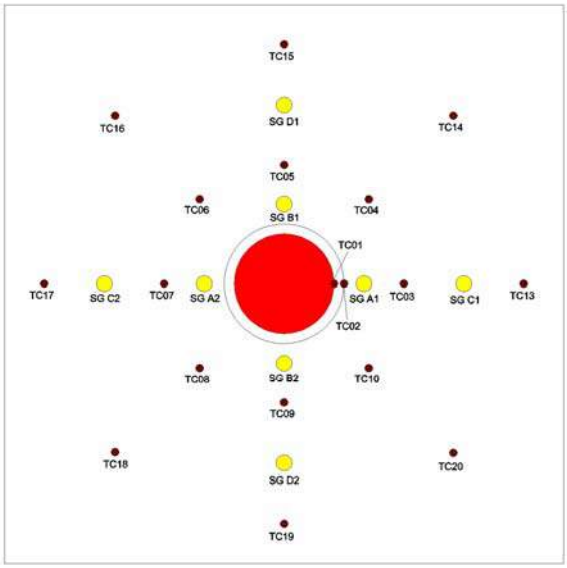

Fig. 3. Locations of thermocouples (TCs) and strain gages (SGs) on the surface of the specimen

The influence of EDZ on thermal behavior was also examined in the same manner as shown in Fig. 2. Engineering heater of 25 mm in diameter was placed in the central opening of the specimen. The empty space between the wall of the circular opening and the heater was filled with compacted Kyeongju bentonite powder. Temperature of the heater was kept constant at 75°C during the tests.

Thermocouples and strain gauges were installed at the locations shown in Fig. 3. The thermocouple TC01 was attached on the surface of the heater and TC02 was placed at the interface between the specimen and bentonite infilling. TC03, TC04, and TC05 were located at 30 mm away from the center, while TC13, TC14, and TC15 were at 60 mm away.

The laboratory experiments were simulated by the distinct element modeling code, PFC^{2D}, to demonstrate the reliability of the experiments. In the corresponding numerical experiments, four additional strain gauges (A2, B2, C2, D2) and ten additional thermocouples (TC06-10 and TC16-20) were installed. Table 1 shows the material properties obtained from the laboratory test, where the synthetic rock has the mixing ratio of sand : cement : water = 0.54 : 0.27 : 0.19. The properties of bentonite were referred to the previous studies (Kwon et al., 2002; Chun et al., 1998).

3 DEM MODEL AND MICRO-PARAMETERS

PFC^{2D} is widely used in micromechanical analysis of geomaterials. The thermal option of PFC^{2D} can be used in simulating transient heat conduction and storage in materials consisting of particles. The general heat-conduction equation is given by Equation (1) (Carslaw, 1959).

$$-\frac{\partial q_i}{\partial x_i} + q_v = \rho C_v \frac{\partial T}{\partial t} \tag{1}$$

where q_i is the heat-flux vector [W/m^2], q_v is the volumetric heat-source intensity or power density [W/m^3], ρ is the mass density [kg/m^3], C_v is the specific heat at constant volume [J/kg°C], and T is the temperature [°C]. Fourier's law for a continuum defines the relation between the heat-flux vector and the temperature gradient as

Table 1. Mechanical and thermal properties of the mortar specimen and Kyeongju bentonite

Properties	Mortar	Kyungju bentonite
Young's modulus (GPa)	11.0	1.27
Poisson's ratio	0.20	0.20
UCS (MPa)	31.9	8.83
Density (kg/m^3)	1900	1775
Thermal conductivity (W/m·K)	1.5	1.59
Specific heat capacity (J/kg·K)	960	830
Thermal expansion coefficient (1/°C)	8.0×10^{-6}	3.1×10^{-4}

$$q_i = -k_{ij}\frac{\partial T}{\partial x_j} \tag{2}$$

where k_{ij} is the thermal-conductivity tensor [W/m°C].

The PFC^{2D} thermal model consists of a network of heat reservoirs (associated with each particle) and thermal pipes (associated with the contacts). Heat flow only occurs via conduction in the active pipes that connect the reservoirs. Properties characterizing the heat reservoir include temperature, mass, volume, specific heat, and coefficient of linear thermal expansion. The thermal pipe is related with a power (Q) and thermal resistance (η). All the pipes are regarded as one-dimensional objects with a thermal resistance per unit length of η. So, the power, Q, in a pipe is given as Equation (3).

$$Q = -\frac{\Delta T}{\eta L} \tag{3}$$

where, ΔT is the temperature difference between the two reservoirs, and L is the pipe length.

The thermal micro-parameters required in the model are the specific heat (C_v), the linear thermal expansion coefficient (α_t), and the thermal resistance (η). C_v of each ball can be set equal to the value for a solid continuum. α_t of solid material (macro property) is almost the same with α_t of each ball (ITASCA, 2008). In other words, for thermally heterogeneous rock specimens, the C_v and α_t can be easily generated with changing the micro-parameters of particles (ITASCA, 2008; Wanne &Young, 2008). On the other hand, the same value of the thermal resistance, which is calculated by Equation (4), is assigned to all pipes in the specimen. Wanne & Young (2008) used this approach to model a thermally homogeneous material, Lac du Bonnet granite.

$$\eta = \frac{1}{2VK}\sum_{i=1}^{N} l_i \tag{4}$$

where, K is thermal conductivity, V is the volume of interest and l is the length of thermal pipe over the area.

Numerical simulation using PFC^{2D} requires proper selection of micro-parameters. Mechanical and thermal micro-parameters for the synthetic rock were carefully calibrated from the laboratory test data. A total of 164,187 particles, which have micro-parameters shown in Table 2, were generated and packed into a 300 × 300 mm area.

Table 2. Micro-parameters used to represent synthetic rock specimen

Micro-parameters	Value
Minimum ball radius (mm)	0.5
Ratio of maximum ball radius / minimum ball radius	1.66
Ball to ball contact modulus (GPa)	7.25
Ball stiffness ratio	1.37
Ball friction coefficient	0.5
Ball density (kg/m^3)	1900
Parallel - bond modulus (GPa)	7.25
Parallel - bond stiffness ratio	1.37
Parallel - bond normal strength, mean (MPa)	20.0
Parallel - bond normal strength, std. dev (MPa)	6.0
Parallel - bond shear strength, mean (MPa)	36.0
Parallel - bond shear strength, std. dev (MPa)	10.8
Specific heat at constant volume (J/kg°C)	960.0
Coefficient of linear thermal expansion (10^{-6}/°C)	8.0
Thermal resistance (°C /Wm)	1157.33

4 MECHANICAL BEHAVIOR AROUND A CIRCULAR HOLE

4.1 Mechanical behavior around a circular hole without EDZ generation

Fig. 4 shows the tangential strains monitored at different eight positions during loading up to 6.33 MPa in the loading step 1 in Fig. 1. The solid lines present the strains obtained from the numerical simulation while the dotted lines present the results from laboratory test. Since only the horizontal load is applied, the strains at the points B and D are compressive, whereas the strains at the points A and C are tensile. The numerical results are quite consistent with those from the laboratory test.

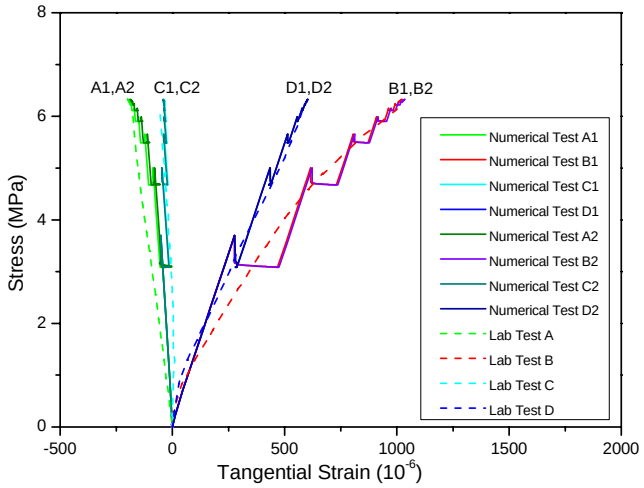

Fig. 4. Stress-strain behaviors at different positions on the surface of the specimen without EDZ generation

4.2 Mechanical behavior around a circular hole with EDZ generation

Fig. 5 shows the crack distributions resulting from the two different damage generation processes considered in the numerical experiment. For the loading scenario 2, the cracks are evenly distributed around the hole perimeter as shown in Fig. 5(b). On the other hand, for the loading scenario 1, the cracks are concentrated in the two opposite regions perpendicular to the direction of the load, which coincide with the highly compressed regions as shown in Fig. 5(a).

The stress-strain curves obtained from the numerical simulation in the loading step 1 and 2 are presented in Fig. 6 and Fig. 7, respectively, together with the curves from the laboratory tests. The two corresponding curves obtained at the opposite points are almost coincident in Fig. 7. In Fig. 6, larger strain is obtained at the point B2 than in the point B1, which suggests that the damage generation process can influence on the mechanical behavior. Consequently, Figs. 4-7 provide the strong evidence of the formation of stress-induced EDZ in the region adjacent to the opening.

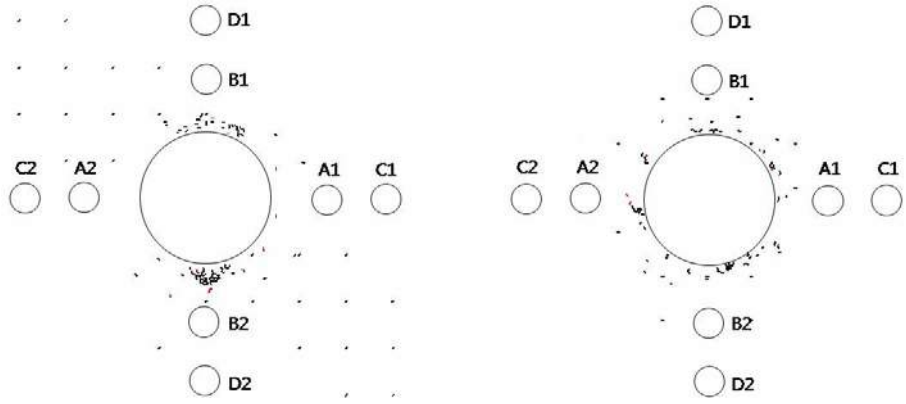

(a) Crack distribution in loading scenario 1 (b) Crack distribution in loading scenario 2

Fig. 5. Crack distribution resulting from the two different damage generation processes in the numerical simulation

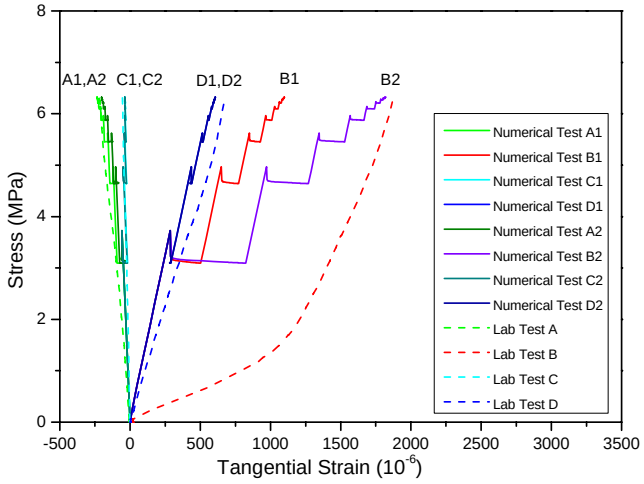

Fig. 6. Stress-strain curves for the loading scenario 1 at different positions of the numerical specimen with and without EDZ generation

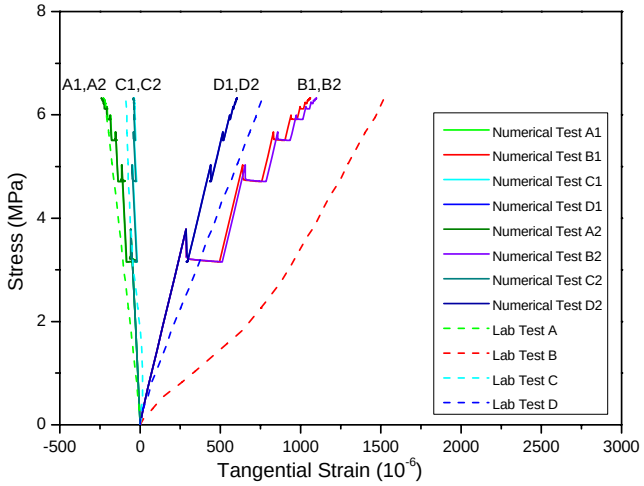

Fig. 7. Stress-strain curves for loading scenario 2 at different positions of the numerical specimen with and without EDZ generation

5 THERMAL BEHAVIOR AROUND A CIRCULAR HOLE

5.1 Thermal behavior around a circular hole without EDZ generation

The influence of an EDZ on thermal behavior was examined in the same way as for the mechanical behavior. A heater test was carried out for a specimen and numerical simulation was performed as well. During the laboratory test, the temperatures at eight different positions were recorded for 18 hours. The temperature of the heater was set at 75°C. However, the temperature at the interface, TC02, between the opening wall and the bentonite powder was measured to be 43.8-49.4°C. The average temperature, 46.6°C, at the TC02 was used as an input parameter in the numerical simulation. The boundary temperature was fixed at room temperature of 21.5°°C.

Fig. 8 shows the temperature change of "without EDZ" laboratory test and numerical simulation at the thermocouples located at 30 mm from the center. The temperature gets constant in the range of 37.7-38.7°C (39.1-39.3°C) at the locations TC03, TC04, and TC05. From the results of laboratory test and numerical simulation, the temperature gets constant at about 29.5°C (31.8-32.0°C) at TC13, TC14, and TC15. The values in parentheses refer to the results from the numerical simulation. From the test, it was confirmed that the temperature distribution is only dependent on the distance from the heat source. The temperature fluctuation decreased at remote positions from the heat source.

5.2 Thermal behavior around a circular hole with EDZ generation

In order to examine the influence of an EDZ induced by the damage generation process on thermal behavior, heater test was carried out. The boundary conditions are shown in Fig. 2. Different temperature distributions were expected for the loading scenarios 1 and 2, because the size and shape of the EDZ induced by the damage generation process were not the same.

The temperature change in scenario 1 is shown in Fig. 9. From the experimental and numerical tests, the temperatures at TC03, TC04 and TC05 were 36.7-37.6°C (TC03: 39.1°C, TC07: 39.2°C), 35.8-36.7°C (TC04 and TC08: 39.0°C), and 35.0-35.8°C (TC05: 39.0°C, TC09: 38.4°C), respectively. The values in parentheses refer to the results from the numerical simulations. The temperature at TC05 shows the lowest value at 30 mm away from the center

of the specimen. This is because the EDZ, which was expected to be generated around the TC05 dominantly, prevented heat transfer toward TC05. Compared with “without EDZ” result in Fig. 8, temperatures at the three (eight in the numerical simulation) thermocouples decreased by 1.2-1.4°C (0.1 - 0.9°C).

For scenario 2, experimental and numerical test “with EDZ” presents uniform temperature at TC03, TC04, and TC05 as shown in Fig. 10. The temperatures at the three (eight in the numerical simulation) thermocouples were recorded to be 36.5-37.3°C (38.9-39.2°C) after 6 hours. Compared with “without EDZ” result in Fig. 8, overall temperature at the three (eight in the numerical simulation) thermocouples decreased by 1.2-1.4°C (0.0-0.4°C). Because an EDZ was expected to be generated with a uniform thickness around the hole, the three thermocouples showed a little bit lower temperature than the “without EDZ” case.

From the “with EDZ” experimental heater test, it could be concluded that there was a tendency for EDZ to block heat transfer. These findings coincide with the former research conclusion that thermal conductivity decreased by generated cracks (Hasselman, 1978).

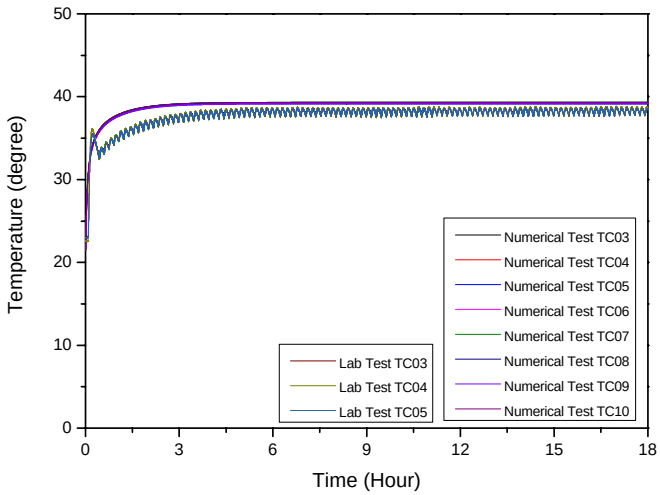

Fig. 8. Temperature versus time at different positions located at 30 mm from the center (without EDZ)

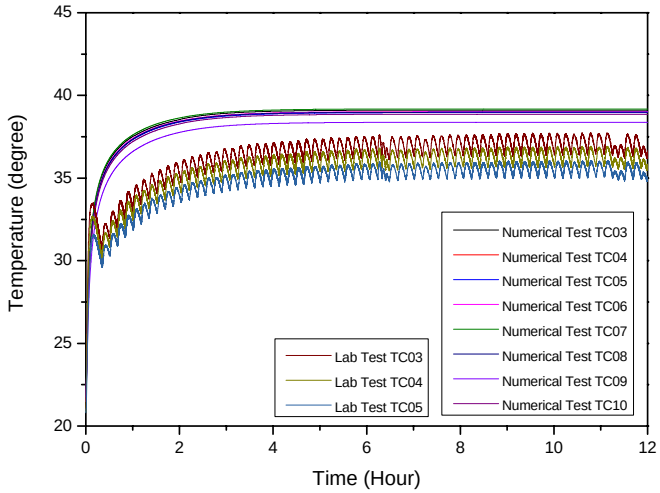

Fig. 9. Temperature versus time relation at TC3, TC4, and TC5 (with EDZ generation, scenario 1)

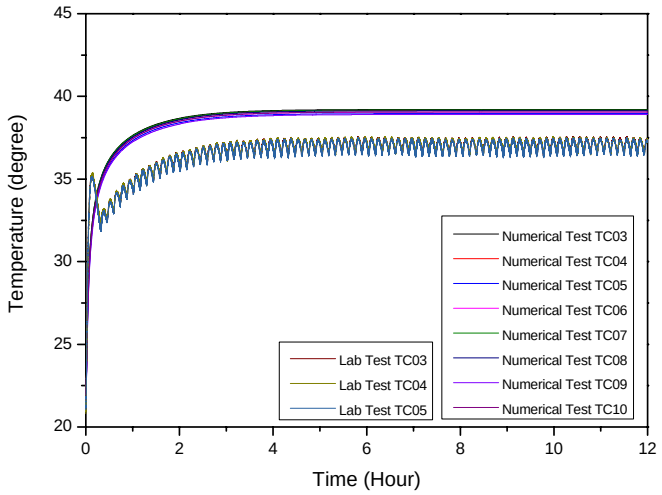

Fig. 10. Temperature versus time relation at TC3, TC4, and TC5 (with EDZ generation, scenario 2)

6 CONCLUSIONS

In this study, the influence of an EDZ (Excavation Damaged Zone) on the mechanical and thermal behavior around an opening was analyzed in laboratory experiment and numerical simulation. An EDZ was induced by damage generation process of biaxial loading. Comparing the experimental results from "without EDZ" and "with EDZ" test, we could observe the influence of the induced EDZ on the mechanical and thermal behavior. In order to demonstrate the EDZ effect, numerical experiment was carried out using PFC^{2D}. The following conclusions could be drawn from this study.

Two different EDZs were induced around an opening during damage generation process adopting two different loading scenarios. In the laboratory experiment of damage generation, failure or macro cracks were not observed at the surface of the opening. However, the influence of induced EDZ was observed in terms of mechanical and thermal behavior.

When the experimental results from "without EDZ" and "with EDZ" test are compared, in loading scenario 1, tangential strain in the area where EDZ is induced increased up to 64% (75% in the numerical simulation), and temperature decreased down to 2.8°C (0.8°C in the numerical simulation). For the loading scenario 2, the tangential strain in the EDZ increased up to 17% (6% in the numerical simulation), and temperature decreased down to 0.85°C (0.4°C in the numerical simulation).

As result of the numerical simulation, the influence of an EDZ on the mechanical and thermal behavior observed in the laboratory experiment could be successfully reproduced. In particular, numerical simulation showed that the generated cracks, which were resulted from a damage generation procedure, similarly increase the deformation and block the heat transfer.

REFERENCES

Bossart, P., Meier, P. M., Moeri, A., Tric, T., Mayor, J. (2002), "Geological and hydraulic characterization of the excavation disturbed zone in Opalinus Clay of the Mont Terri Rock Laboratory". Engineering Geology, Vol. 66, 19-38.

Cai, M. & Kaiser, P.K. (2005), "Assessment of excavation damaged zone using a micromechanics model". Tunnelling and Underground Space Technology, Vol. 20, 301-310.

Carslaw, H. S. & Jaeger, J.C. (1959), Conduction of Heat in Solids, 2nd Ed., London, Oxford Press.

Chun, K.S., Cho, W.J., Lee, J.O., Kim, S.S., Kang, M.J. (1998), "High-level waste disposal technology development". KAERI Report. KAERI/RR-1897/98. (in Korean)

Emsley, S., Slsson, O., Seinberg, L., Alheid, H.J., Falls, S. (1997), ZEDEX - a study of damage and disturbance from tunnel excavation by blasting and tunnel boring. SKB Technical Report 97-30.

Hasselman, D.P.H. (1978), "Effect of cracks on thermal conductivity". Journal of Composite Materials 12(4), 403-407.

Itasca Consulting Group (2008), Particle Flow Code in 2 Dimensions, 4.0th Ed., Minneapolis.

Kwon, S. & Cho, W.J. (2008), "The influence of an excavation damaged zone on the thermal-mechanical and hydro-mechanical behaviors of an underground excavation". Engineering Geology, Vol. 101, 110-123.

Kwon, S., Park, J.H., Choi, J.W., Kang, C.H. (2002), "Thermal-mechanical analysis for determining the optimum design of a deposition hole using FLAC3D". KAERI Report. KAERI/TR-2016/2002. (in Korean)

Kwon, S., Lee, C.S., Cho, S.J., Jeon, S.W., Cho, W.J. (2009), "An investigation of the excavation damaged zone at the KAERI underground research tunnel". Tunnelling and Underground Space Technology, Vol. 24, 1-13.

Martino, J.B. & Chandler, N.A. (2004), "Excavation-induced damage studies at the underground research laboratory". Int. J. Rock. Mech. Min. Sci., Vol. 41(8), 1413-1426.

Min, K.-B., Rutqvist, J., Tsang, C.-F., Jing, L. (2005), "Thermally induced mechanical and permeability changes around a nuclear waste repository - a far-field study based on equivalent properties determined by a discrete approach". Int. J. Rock. Mech. Min. Sci., Vol. 42(5-6), 765-780.

Price, R.H. & Bauser, S.J. (1985), "Analysis of the elastic and strength properties of Yucca Mountain tuff, Nevada". Proceedings of 26th US Symposium on Rock Mechanics, Rapid City.

Sato, T., Kikuchi, T., Sugihara, K. (2000), "In-situ experiments on an excavation disturbed zone induced by mechanical excavation in Neogene sedimentary rock at Tono mine, Central Japan". Engineering Geology, Vol. 56, 97-108.

Wanne, T.S. & Young, R.P. (2008), "Bonded-particle modeling of thermally fractured granite". Int. J. Rock. Mech. Min. Sci., Vol. 45(5), 789-799.

FINITE ELEMENT SIMULATIONS OF MULTIPLE FRACTURE PROPAGATION DURING HYDRAULIC INJECTIONS

Hendrik Sturm
Computational Geomechanics Division at the Norwegian Geotechnical Institute (NGI), Oslo, Norway

Lars Andresen
Computational Geomechanics Division at the Norwegian Geotechnical Institute (NGI), Oslo, Norway

Hans Petter Jostad
Computational Geomechanics Division at the Norwegian Geotechnical Institute (NGI), Oslo, Norway

Fabrice Cuisiat
Petroleum Geomechanics and Geophysics Division at the Norwegian Geotechnical Institute (NGI), Oslo, Norway

ABSTRACT: *In this paper the injection of waste fluids from oil and gas drilling into one or multiple hydraulic driven fracture(s) in rock is analysed numerically. This is accomplished by employing the Finite Element Method (FEM) using coupled cohesive elements implemented in the commercial FE code Abaqus and NGI's in-house FE code Bifurc. Aim of this work is to identify the governing mechanisms of initiation, propagation and interaction of multiple fractures during batch injections. It is found that multiple fractures with planes parallel to the well bore axis are likely to develop. Fracture shape and rate of propagation depend essentially on the initial stress state. Multiple parallel fractures with planes perpendicular to the well bore axis, however, are found to develop in an unstable manner and it is likely that only one single fracture will be active, i.e. will receive the injected fluid, after a relatively short injection period.*

1 INTRODUCTION AND MOTIVATION

Hydraulic driven fracturing is a technique for creating and extending fractures by applying fluid pressure in a well bore drilled into a formations. In the oil and gas industry, fracturing is mainly used for two purposes; stimulating production of a reservoir and disposing waste water and material from drilling. The latter application case is studied in the paper. The fluid is pumped down via a well bore into one or several hydraulic driven fractures in an impermeable rock. If the waste fluid is disposed into multiple fractures which all are well contained in a target zone it is often denoted as a *Disposal Domain* (Peterson et al. 2001).

Prediction of size and orientation of these hydraulic fracture(s) is essential in risk management of waste disposal processes. The hazards are primarily seismic events or uncontrolled growth of fractures leaving the target zone and propagating up to the seabed or down to the reservoir. Monitoring of microseismic activities and tiltmeter arrays at seabed and downhole are methods used to infer the approximate dimensions and orientation of the fractured domain.

Analytical methods for special cases of single fracture propagation have been developed. They can be used to predict geometry, i.e. length and opening width, and fluid pressure. However, no analytical method could be found for describing initiation, propagation and interaction of

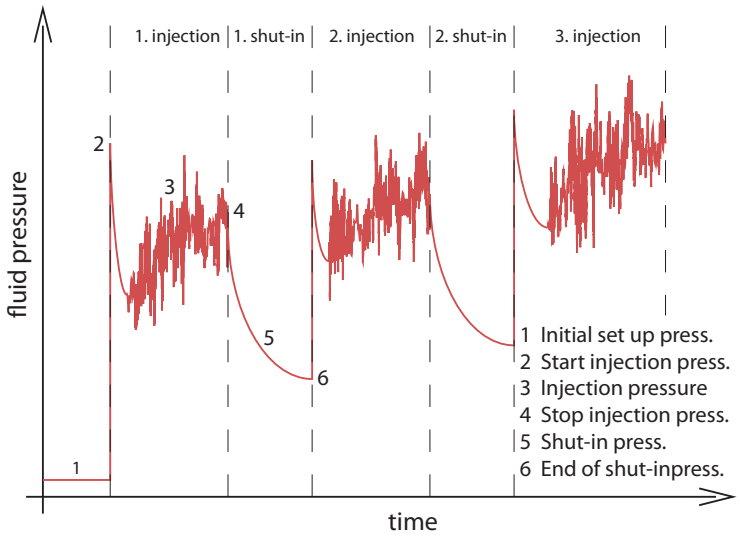

Fig. 1. Representative fluid pressures during batch injections as measured at the pump; e.g. Peterson et al. (2001)

.

multiple fractures. Hence most commercial codes for fracture simulation use single fracture models only.

But theoretical considerations and field measurements support the existence of multiple fractures and the possibility for the development of a Disposal Domain around an injection well bore; e.g. Peterson et al. (2001). In particular, batch injections with intermediate periods where the well bore pressure is shut-in with no flow, as shown in Figure 1, is believed to support the development of a confined Disposal Domain. The existence of a damaged, highly fractured zone around the well bore prior to the actual injection, such as shown in Figure 2, might also promote the development of a system of multiple fractures in the subsequent batch injection.

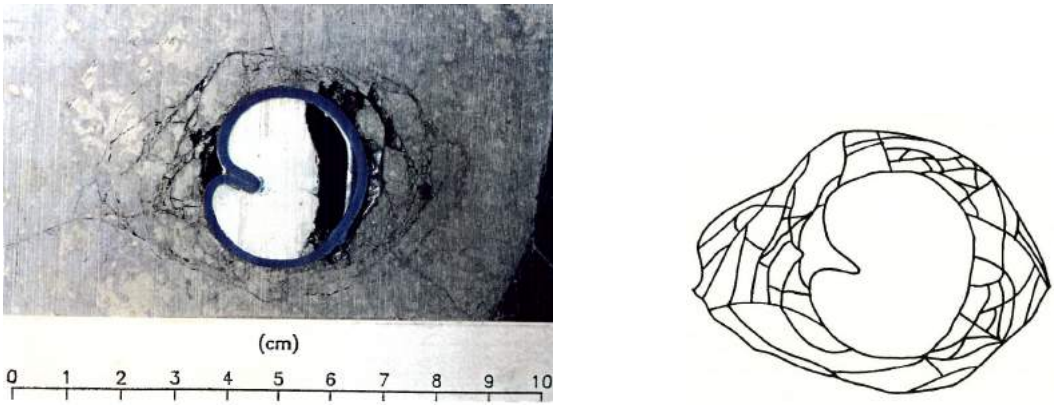

Fig. 2. Photograph and sketch of a fractured zone around a borehole observed in a scaled laboratory failure experiment; NGI (1992). The inner membrane (in blue) is preventing the collapse of fractured material in to the hole.

The Finite Element Method is proved to simulate reliably the coupled hydraulic-mechanical process of single plane fracturing using *cohesive elements* (Jostad & Cuisiat 2007; Papanastasiou 1999). Due to the continuum approach, the FE methods should be suitable to account also for the interaction between several fractures.

In this paper the FE code Abaqus and NGI's in-house FE code Bifurc are used to simulate multiple hydraulic driven fracturing from horizontal and vertical well bores. A validation of the cohesive elements implemented in Abaqus is performed by comparing the results against analytical and published validated numerical solutions. Then, the process of batch injection with intermediate shut-in periods is simulated in the time domain for fracture planes being either parallel or perpendicular to the horizontal well bore axis. The aim of this study is to understand the mechanisms of multiple fracturing and to estimate the existence as well as shape and dimensions of a Disposal Domain.

The problem analysed in this study is based on a documented Cuttings Reinjection project at the Ekofisk Field in the Norwegian sector of the North Sea (Nagel & Strachan 1998).

2 VALIDATION OF THE ABAQUS MODEL

Hydraulic driven fracturing is modelled in frame of this study with so called *cohesive elements* which describe crack initiation and propagation by means of a softening model. Coupled 2d and 3d cohesive elements have one pore pressure and two or three, respectively, displacement degrees of freedoms per node.

The use of these these elements has, however, some limitation with respect to simulation of fracture processes. Fractures can develop in the FE model only along the pre-defined directions discretized with cohesive elements. Also curved, merging or bifurcating fractures is difficult to consider. Thus an iterative procedure is generally required based on an inspection of the stress field in order to identify possible locations and orientations of fractures.

The parameters relevant for the validation of the cohesive elements implemented in Abaqus are fracture opening width w and fluid pressure p which are both computed by means of a damage formulation. The stress-strain response up to a maximum tensile σ_t and, or shear strength τ_t is linear elastic. Continued deformation initiates a progressive damage of the element accompanied with decreasing strength. Complete failure is reached when a critical opening width w_{crit} and / or shear deformation δ_{crit} is exceeded.

Hydraulic fracturing is associated with tensile failure in the injected material, which is denoted in classical fracture mechanics as failure Mode I, (Gross & Seelig 2001; Kuna 2010). In toughness dominated fracture processes, the critical opening width w_{crit} is defined, according to e.g. (Gross & Seelig 2001; Kuna 2010), as

$$w_{\text{crit}} = \frac{2\,K_{IC}^2\,(1-\nu^2)}{E\,\sigma_t} \tag{1}$$

where E and ν are elastic properties of the rock and K_{IC} the *fracture toughness* representing the resistance of a material against crack propagation. The fracture opening width w_{crit} is coupled with the pore pressure by the mass balance, viz.

$$\frac{\partial w(s)}{\partial t} + \frac{\partial q(s)}{\partial s} = 0 \qquad \text{with} \qquad q(s) = -\frac{w(s)^3}{12\,\mu}\,\frac{\partial p}{\partial s} \tag{2}$$

where s denotes the location coordinate along the fracture, t the time and q a unit volume flux which is again a function of the current opening width w, the fluid pressure p and the fluid viscosity μ.

The validation of the Abaqus formulation of the cohesive elements is accomplished by modelling a single plane horizontal fracture in a homogeneous elastic material subjected to a constant injection rate. This problem was first considered by Papanastasiou (1999) and has been

used previously for a validation of the implementation of cohesive elements in NGIs in-house FE code Bifurc (Jostad & Cuisiat 2007). Material parameters and employed boundary conditions are listed in Tables 1 and 2, respectively.

Table 1. Material parameters used in the validation.

	Young's modulus E [GPa]	Poisson's ratio ν	Tensile strength σ_t [MPa]	Fracture toughness K_{IC} [MPa$\sqrt{\text{m}}$]
Rock	25	0.2	-	-
Fracture	6000	-	3	2

Table 2. Boundary conditions used in the validation.

Injection rate q [m^3/(s·m)]	$5 \cdot 10^{-5}$
Isotropic initial stress $\sigma_h = \sigma_v$ [MPa]	25

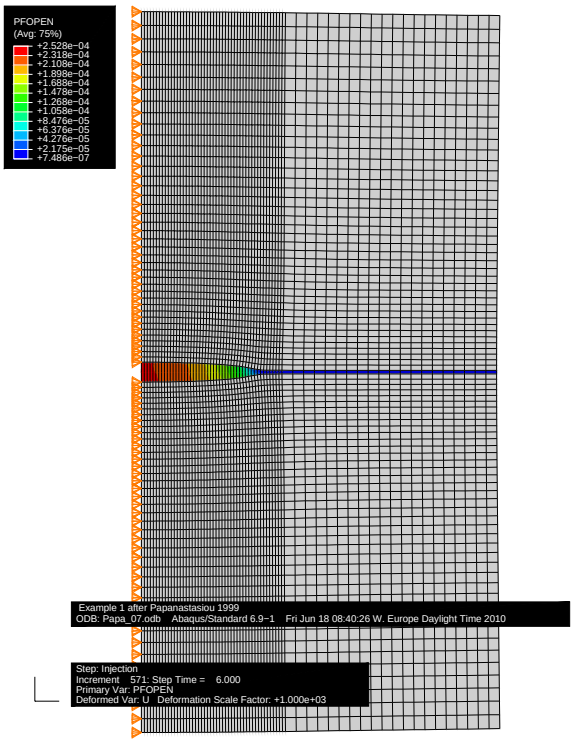

Fig. 3. Contour plot of the deformed FE model used for the validation of cohesive elements provided by Abaqus. The colour shading indicates the fracture opening width. The plane strain model has a width of 5 m and a height of 10 m.

The flow along cohesive elements is modelled as viscous flow having a permeability depending on the total opening width, viz.

$$k = \frac{w^3}{12\,\mu}\left[\frac{\text{m}^3}{\text{kPa}\cdot\text{sec}}\right] \qquad \text{with} \qquad w = w_0 + w_{\text{elastic}} + w_{\text{plast}} \tag{3}$$

where w_{elastic} denotes the elastic deformation of the element up to the corresponding peak strength and w_{plast} the plastic permanent opening width due to damage. Since w_{plast} shall be $\gg w_0 + w_{\text{elastic}}$ an elastic stiffness of $E_f = 240 \cdot E = 6000$ GPa for the fracture is used.

Figure 3 presents the deformed mesh and contours of the fracture opening width after 6 seconds with constant injection rate. The rock is modelled with 5440 4-noded isoparametric elements (CPE4) and the fracture with 68 6-noded cohesive elements (COH2D4P). Average element length along the first 2 m of the fracture is 4.2 cm and along the remaining 3 m approx. 15 cm. Due to numerical reasons, an initial opening width d_0 for coupled cohesive elements has to be defined. In this validation, a width of $d_0 = 1 \cdot 10^{-4}$ cm is chosen, except for the first element at the injection point for which an initial opening width of $d_0 = 1 \cdot 10^{-2}$ cm is used.

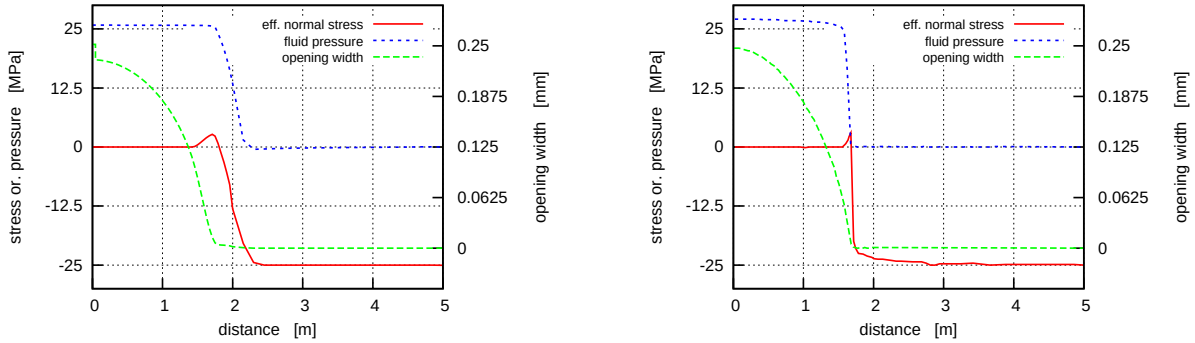

Fig. 4. Predicted state of the fracture after 6 seconds with constant injection rate. Left figure shows the results with Abaqus, right figure the validated results with Bifurc, after Jostad & Cuisiat (2007).

Figure 4 shows the documented and predicted fracture geometry, fluid pressure and effective normal stress in the intact and partially damaged material. Fracture length and opening width agree well. Also the predicted fluid pressure in the fracture is in accordance with analytical solutions and the numerical simulations obtained with Bifurc (Jostad & Cuisiat 2007).

But the fluid pressure and stress degradation at fracture tip is noticeable different. Abaqus predicts a very smooth degradation being actually in front of the fracture tip in the intact rock. A comparison of the actual opening width and the total amount of injected fluid volume reveals, however, that the mass balance is correct and the predicted fluid pressure in front of the tip is probably due to numerical reasons only. Since only fracture geometry, i.e. length and opening width, as well as fluid pressure in the fracture is relevant in this study, the physically incorrect behaviour at fracture tip does not affect the results presented in this paper.

3 PERPENDICULAR RADIAL FRACTURES

3.1 Model description

The first case analysed in this study is a fracture domain containing of radial fractures developed parallel to a horizontal injection well. The modelled plane strain domain is shown in Figure 5. The corresponding geometrical dimensions are listed in Table 3.

The model consists of a large block of intact rock surrounded by a compensating layer. The dimensions are chosen in order to allow varying injection durations and volumes. The purpose of the compensating layer is to incorporate strain compatibility at the outer boundaries, which is, however, relevant only for long fractures and large injected volumes. In addition, the pre-fractured zone around the well, discussed in the previous Section and shown in Figure 2, is

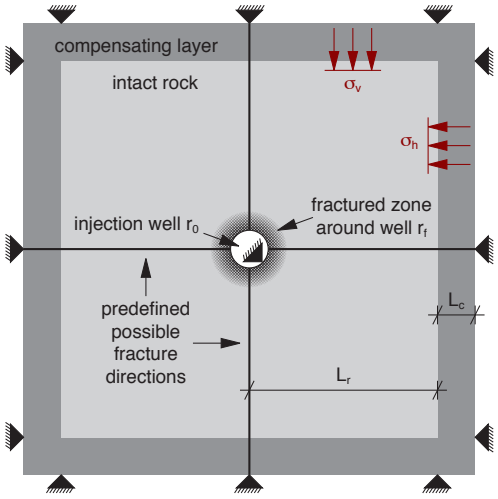

Fig. 5. Sketch of the modelled domain with two radial perpendicular fractures from a horizontal well.

Table 3. Geometrical dimensions of the fracture domain shown in Figure 5.

Dimension	Value
Well diameter	0.14 m
Length and height of the intact rock	200×200 m
Thickness of the compensating layer	10 m
Diameters of the pre-fractured zone	0.28 m, 1.54 m and 14.14 m

considered in the FE model. In this study two radial perpendicular arranged fracture directions being parallel to the principal stress directions are modelled.

Table 4. Material parameters used in the study.

	Young's modulus E [GPa]	Poisson's ratio ν	Tensile strength σ_t [MPa]	Fracture toughness K_{IC} [MPa$\sqrt{\text{m}}$]	Permeability k [$\cdot 10^{-8}$ m/s]
Rock	1	0.45	-	-	-
Compensating layer	0.5	0	-	-	1
Pre-fractured zone	1 and 0.1	0.25	-	-	12.6, 5.57 and 1.9
Fracture	600	-	1	1.1	$k = f(d, ...)$ [m^3/(kPa·s)]

The material parameters used to describe the behaviour of the intact rock, the compensating layer, the pre-fractured zone and the dedicated fractures are listed in Table 4. An anisotropic initial stress field with $\sigma'_v = 7.5\,\text{MPa}$ and $\sigma'_h = 5.2\,\text{MPa}$ is assumed.

The FE plane strain model employs the same type of elements as used in the validation presented in Section 2. The intact rock and the compensating layer are considered to be impermeable, while the pre-fractured zone is modelled with fully coupled elements allowing Darcy flow. The purpose for including pore pressure degree of freedom in the pre-fractured zone is to account for radial stress changes in the intact rock due to high injection pressures and to allow hydraulic communication between the fractures.

Since the opening width of a fracture decreases with increasing number of fractures within a volume, the pre-fractured zone may have a permeability being small enough to cause a pressure drop between the injection well and the actual fractures in the intact rock. The pressure gradient in these (micro-) fractures can be assessed by the analytical solution proposed by McDonald (2008) for two-dimensional flow between parallel plates, viz.

$$\Delta P = \frac{q \cdot 12\,\mu}{n \cdot w^3} \cdot \frac{\Delta r}{H} \tag{4}$$

where Δr denotes the radius of the pre-fractured zone, n the number of fractures and H the fractured height being in this case equal to out-of-plane thickness.

Table 5. Parameter variations performed with the radial fracture model. The injection rates given are in the case of prescribed fluid pressure during injection approximate values.

job ID	prescribed BC during injection		injection rate during inj. q [m^3/s]				properties of pre-fractured zone							
							radius [m]			k [$\cdot 10^{-8}$ m/s]			stiffness	
	fluid press.	*inj. rate*	99	9.9	5.14	3.42	0.14	0.77	7.07	12.6	5.57	1.9	stiff	soft
10	X		X				X			X			X	
10c	X		X				X			X				X
16c		X	X				X			X			X	
16d		X	X				X			X				X

Table 5 presents an excerpt of the performed simulations listing only the results presented in this paper. In total three batches consisting of an injection phase and a shut-in period are considered. The boundary conditions (BC) at the injection point and the elastic stiffness of the pre-fractured zone are varied. Changes of the injection rate, or radius and permeability of the pre-fractured zone are affecting the results qualitatively only.

3.2 Results

Figure 6 presents the computed fluid pressure during the injection phases and the shut-in periods for the first three batches. In the simulations 10 and 10c, a constant fluid pressure in the well during injection is defined.

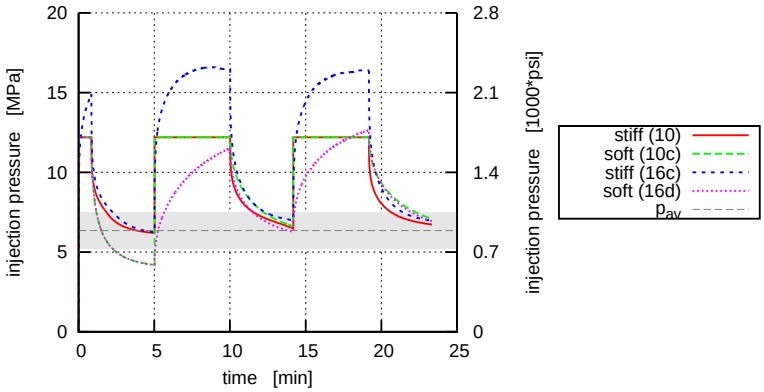

Fig. 6. Fluid pressure at injection well during three batch injections.

The fluid pressure responses are qualitatively similar to the one sketched in Figure 1 which represents typical measurements. In case of prescribed constant injection rate (simulations 16c and 16d), an increase of the required injection pressure during injection is predicted. In the subsequent shut-in periods, the fluid pressure decreases and approaches asymptotically a constant value of $p_{\text{av}} = \frac{1}{2}(\sigma'_v + \sigma'_h)$. In field measurements, the peak pressure values during injection and the residual pressure values during shut-in seem to increase for repeated injections. This is observed in the numerical simulations of the *soft* models only where the pre-fractured zone is much softer than the surrounding intact rock.

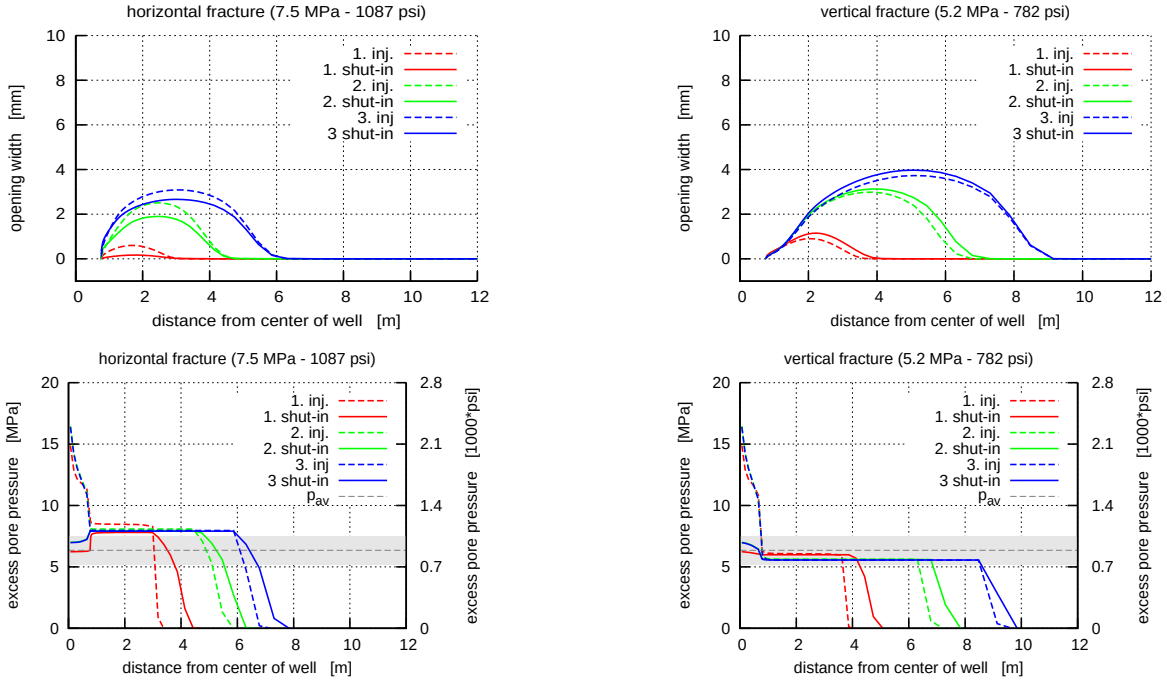

Fig. 7. Fracture geometries and pressures at the ends of injection or shut-in, respectively, for all three batches, predicted with the FE model 16c.

Figure 7 presents opening width and length as well as fluid pressure in the fractures at the end of each injection phase and shut-in period for all three batches, predicted with the stiff model and prescribed injection rate (simulation 16c). It can be seen that cracks are initiated in both (all) modelled fracture directions already during the first injection. The opening width and the length are in all batches smaller in horizontal direction where the normal stress σ_v perpendicular to the fracture is larger.

An interesting behaviour can be observed during shut-in. The integral of the opening width over the length represents the injected volume in a fracture. Since the width decreases for the horizontal and becomes larger for the vertical fracture during shut-in, the fractures *communicate* with fluid flow via the injection well and the pre-fractured zone. For the first and second shut-in period, the vertical fracture even propagates further due to the inflow from the higher pressurized horizontal fracture.

A further relevant observation can be made by comparing the relative volume changes in the fractures for each injection. The vertical fracture grows faster than the horizontal, which becomes even more pronounced for repeated injections. From single fracture theory it is known that the fluid pressure required to keep a fracture open decreases with increasing fracture length. This can be seen also in the numerical simulations shown in the lower two plots of Figure 7. The residual

shut-in pressure in the fractures decreases for repeated injections. Thus, the resistance of a shorter fracture is higher than that of a longer fracture which causes a faster growth of the longer vertical fracture. This behaviour becomes more pronounced for shorter injection phases, because of time effects. The fluid pressure in the injection well at the end of a shut-in period is larger than what is required for fracture propagation in vertical direction. In a subsequent injection phase the fluid pressure has to increase first before a propagation in horizontal direction becomes possible. This, however, requires some time for which reason horizontal fracture growth is somewhat delayed.

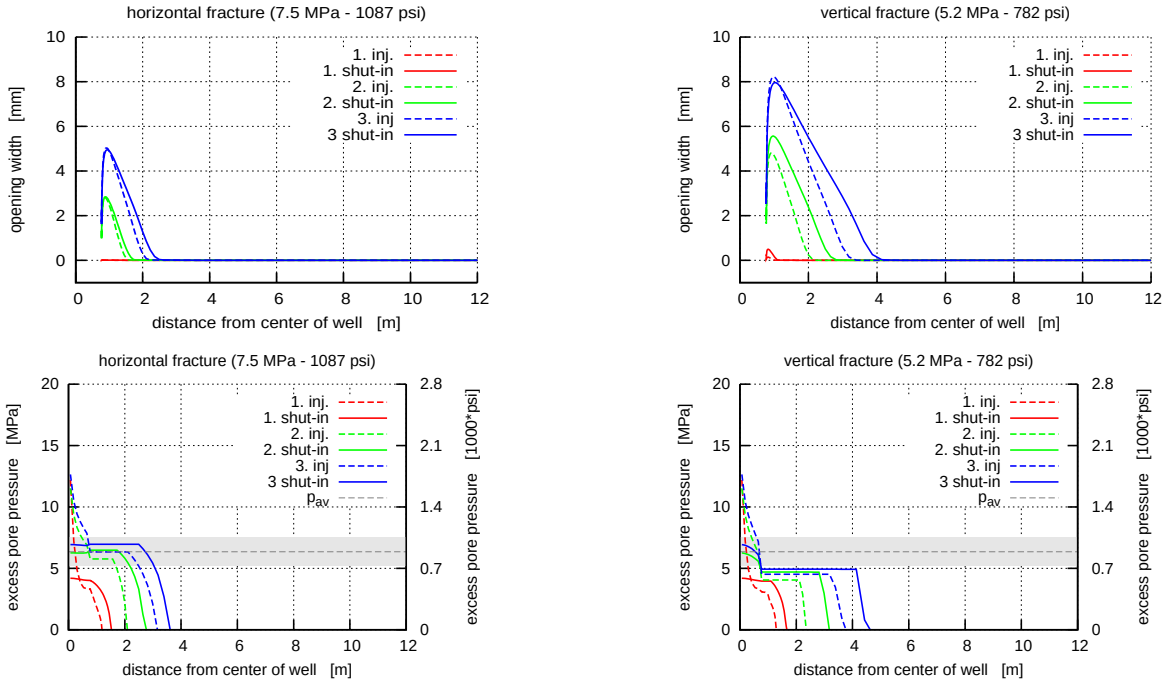

Fig. 8. Fracture geometries and pressures at the ends of injection or shut-in, respectively, for all three batches, predicted with the FE model 16d.

Figure 8 presents the same type of results as shown in Figure 7 but predicted with the soft model which has a lower stiffness of the pre-fractured zone (simulation 16d). The results are qualitatively similar and the observations made for the stiffer model hold also for the softer model.

The predicted fracture shapes and the fluid pressures in the fractures are, however, noticeable different. The ratio between opening widths and lengths is much larger. The fluid pressure predicted is smaller and increases with increasing fracture length. These observations do not agree with single fracture theories as discussed for Figure 7.

The explanation for this behaviour can be found in the radial and tangential stresses in the intact rock at the interface between the pre-fractured zone and the rock. The lower stiffness of the pre-fractured zone allows larger volume changes which yields to larger radial stresses in the surrounding intact rock. But larger radial stresses in an almost incompressible material are accompanied by decreasing tangential stresses. Hence, both the fracture opening resistance and required fluid pressure for keeping a fracture open become smaller. This effect at the near well bore stress filed, however, decreases with increasing fracture length. The predicted fluid pressure for long fractures is govern again by the far-field initial stress state. The fracture shape and the fluid pressure approach for repeated injections the one predicted with the stiffer model shown in Figure 7.

The lower stiffness also affects the consolidation coefficient $c_v \approx \frac{k\,M}{\gamma_w}$ of the pre-fractured zone which yields to lower predicted fluid pressures during the injection phases.

3.3 Discussion

The numerical results presented in this section, are relevant for a prediction of the existence and the shape of a disposal domain. It is found that fractures open initially in both vertical and horizontal direction. Since the considered fracture directions represent two extrema due to their orientation with respect to the principal stress axis, the envelope of all fractures through the fracture tips is described by these two directions. Due to the different length of the vertical and horizontal fracture, the disposal domain is most likely ellipsoid-shaped having its longest extend perpendicular to the lowest principal stress direction, i.e. an upright standing ellipse. The ovality increases further for repeated injections and injected volumes.

The predicted opening width (Figure 7 and 8) is different to the one seen in the numerical validation shown in Figure 4. The largest opening width of a fracture is generally at the fracture initiation point. In the simulations presented in this section, however, the opening width at this point is rather small because of the stiffness of the adjacent element in the pre-fractured zone. Decreasing elastic stiffness yields to an increase of the opening width at the fracture initiation point.

4 PARALLEL FRACTURES

4.1 Model description

Batch injections into parallel fractures with planes perpendicular to the well bore axis are modelled with axi-symmetrical FE models. Simulations of five parallel fractures were performed with Bifurc and simulations with two parallel fractures were performed with Abaqus. Both models incorporate a large block of intact rock surrounded again by a compensating layer. The Abaqus model considers also again the existence of a pre-fractured zone around the injection well bore.

The rock has a radius of 100 m and a height of 200 m. The thickness of the compensating layer is 10 m. The radius of the pre-fractured zone is 14 cm and that of the injection well 7 cm. The modelled injection length, i.e. height, of the pre-fractured zone is 1.5 m.

The material parameters and the boundary conditions are the same as in Section 3. However, different to the plane strain model, an isotropic stress field with

$$\sigma_v = \sigma_h = p_{\text{av}} = \frac{1}{2}(5.2 + 7.5)\,\text{MPa} = 6.85\,\text{MPa}$$

is assumed, representing rather a vertical injection well. A constant injection rate of $q = 2.65 \cdot 10^{-3}$ m^3/s is considered in the simulations.

Like for the horizontal well bore with radial fractures, the effect of a highly fractured low permeable zone around the well on the pressure gradient can be assessed by means of an analytical solution for radial flow between parallel annular plates, proposed by McDonald (2008), viz.

$$\Delta P = \frac{q \cdot 12\,\mu}{2\,\pi \cdot w^3} \cdot \ln\left(\frac{r_o}{r_i}\right) \tag{5}$$

where r_o denotes the outer and r_i the inner radius, being in the case analysed here $r_i = 7$ cm and $r_o = 14$ cm.

Due to numerical reasons, as discussed in the following, only the first injection is evaluated in this study.

4.2 Results

Figure 9 shows the deformed FE mesh with contours of the vertical stress after 90 seconds with a constant injection rate and the development of the fluid pressure with time at the injection point for one and five parallel fractures. In the plot of the deformed mesh can be seen that a symmetrical fracture geometry with respect to the central fracture number 1 is obtained. Both opening width and length is different for the fractures 1 to 3. In addition the width even varies along a fracture.

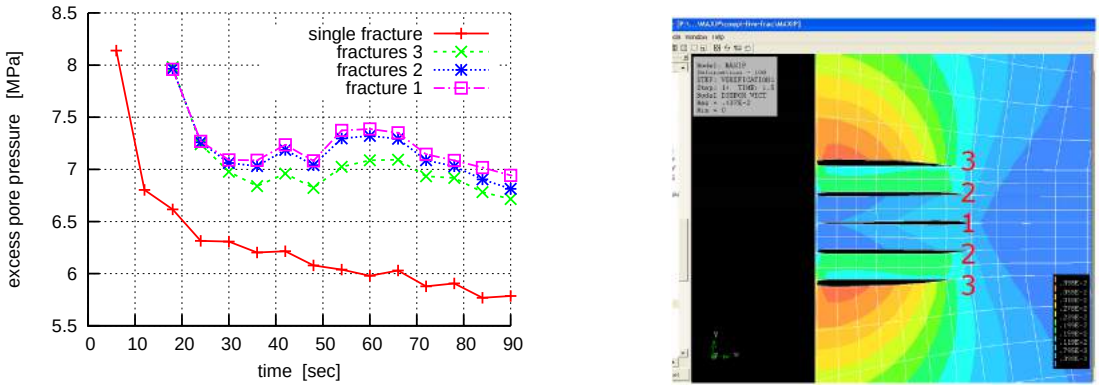

Fig. 9. Fluid pressure development (left) and scaled deformed mesh with contours of the vertical stress (right) for five parallel fractures simulated with Bifurc.

Compared with the single fracture solution, the fluid pressure at the injection point is significantly higher if multiple fractures develop parallel. Also the corresponding stresses in the near-field of the fractures increase. Both indicate a strong interaction between the fractures.

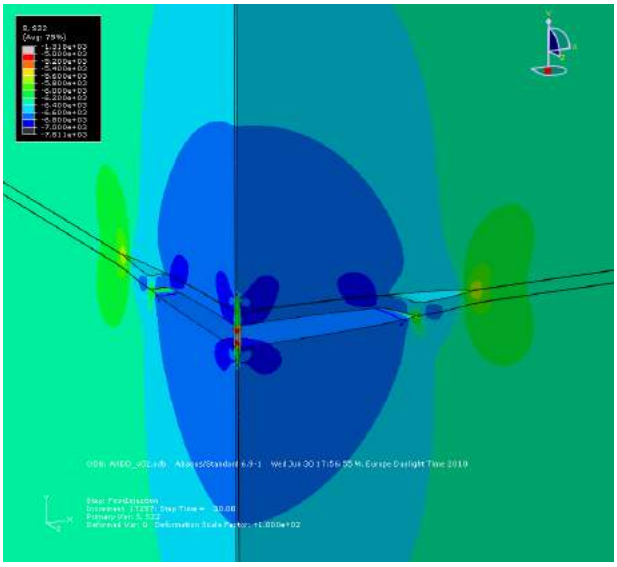

Fig. 10. Scaled deformed mesh with contours of the vertical stress after 30 seconds with a constant injection rate simulated with Abaqus.

A similar result is shown in Figure 10 for two parallel fractures predicted with Abaqus. The corresponding opening widths and injection pressures are shown in Figure 11 together with the development of the injection pressure during the first injection phase. Again, a significant stress increase in the intact rock can be observed. In addition, a noticeable different length of the fractures becomes apparent, which is accompanied with a drop of the fluid stress in that part of the tip of the longer fracture which exceeds the the shorter fracture.

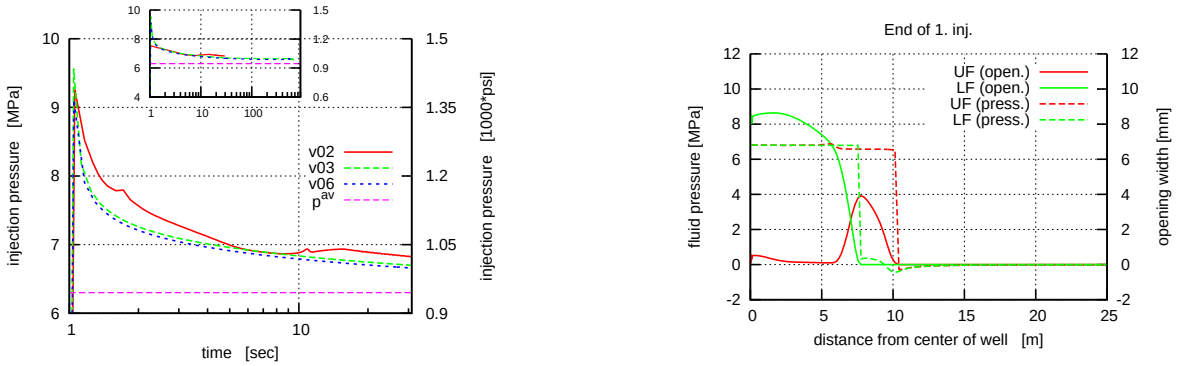

Fig. 11. Development of the fluid pressures (left) and geometries after 30 seconds (right) of the two fractures simulated with Abaqus.

The propagation of two parallel fractures is, however, very unstable. The simulations show that in general only one fracture is active at the time. During the injection, the active fracture changes several times. In Figure 10 and in the right plot of Figure 11, it can be seen that only the lower fracture (LF) is active, while the upper fracture (UF) is almost completely closed.

The instability becomes also apparent in the left plot of Figure 11. An increase of the toughness factor by 10% (v03) and a decrease of the tensile strength by 10% (v06) cause both the development of one fracture only. While in simulation v03 both fractures developed initially from which, however, one stops after some few centimetres, only one fracture develops in simulation v06 (not shown in the figures).

The figure in top of the left plot in Figure 11 shows the development of the well bore pressure during the whole first injection phase and the subsequent shut-in period. Different to the observations made for the model with radial fractures, no pressure drop during shut-in can be seen. This can be explained by means of the isotropic stress field and the different shape (axi-symmetrical) of the pre-fractured zone and its effect on the average permeability.

4.3 Discussion

The simulations with parallel fractures show that the interaction between these fractures cause an increase of the fluid pressure and the stresses in the intact rock. In general, only one fracture seems to be active, i.e. only one fracture receives the injected volume. However, increasing fracture length and batch injections might yield to a switch of the active fracture.

The interaction is complex and *unstable*. Already small changes of the properties triggered the development of only one fracture. Thus, the development of large multiple parallel fractures is very unlikely.

5 CONCLUSIONS

In this paper numerical simulations of the development multiple hydraulic driven fractures are presented. A horizontal well bore with radial fractures parallel to the well and a vertical well bore with parallel fractures perpendicular to the well subjected to batch injections were analysed.

It was shown, that fractures initiate in all directions if the injection pressure exceeds the maximum principal stress. Propagation of an individual fracture, however, depends essentially on the far-field stress state and the relative orientations between the fractures. In case of radial fractures in an anisotropic stress field, fracture growth is asymmetric and faster in the direction perpendicular to the lowest principal stress axis. The envelope of all fractures is in general ellipsoid-shaped.

For the development of parallel fractures becomes unstable when the length is significantly larger than the distance between the fractures. The numerical results indicate that only a very small number of fractures are active, receiving most of the injected fluid.

Cohesive elements have proved suitable to describe the problem analysed in this study despite of their restrictions with respect to number of fractures and fracture geometry and orientation. But the simulations with parallel fractures have pushed the approach with cohesive elements to its limits. The stress increase in the near-field of the fractures would probably cause a merge of some fractures into one, which, however, is not possible to simulate with cohesive elements.

ACKNOWLEDGEMENTS

This work was partially financed by *GEO-INSTALL - Modelling Installation Effects in Geotechnical Engineering* which is supported by the European Community through the program *Marie Curie Industry-Academia Partnership and Pathways* under the contract no. PIAP-GA-2009-230638.

REFERENCES

Gross, D. & Seelig, T. (2001). *Bruchmechanik mit einer Einführung in die Mikromechanik* (4 ed.). Berlin: Springer.

Jostad, H. & Cuisiat, F. (2007). Location of the fluid front in hydraulic fracturing of rocks. In Pande, G. and Pietruszczak, S. (Ed.), *Numerical Models in Geomechanics - NUMOG X*, London, UK, pp. 329–335. Taylor & Francis.

Kuna, M. (2010). *Numerische Beanspruchungsanalyse von Rissen* (2 ed.). VIEWEG+TEUBNER.

McDonald, K. T. (2008). Radial viscous flow between two parallel annular plates 1 problem.

Nagel, N. & Strachan, K. (1998). Implementation of Cuttings Reinjection at the Ekofisk Field. In SPE - Society of Petrolium Engineers (Ed.), *Eurock '98 - SPE/ISRM Rock Mechanics in Petrolium Engineering*, Volume 2, Trondheim, Norway, pp. 95–104.

NGI (1992). Rock mechanical aspects of drilling problems in shales - scaled laboratory borehole failure experiments. Technical Report 542124-5, NGI - Norwegian Geotechnical Institute.

Papanastasiou, P. (1999). The effective fracture toughness in hydraulic fracturing. *International Journal of Fracture 96*, 127–147. 10.1023/A:1018676212444.

Peterson, R., Warpinski, N., Lorenz, J., Garber, M., Wolhart, S., & Steiger, R. (2001). Assessment of the Mounds Drill Cuttings Injection Disposal Domain. In SPE - Society of Petrolium Engineers (Ed.), *SPE Annual Technical Conference and Exhibition*, New Orleans, Louisiana, USA.

ANALYTICAL AND NUMERICAL STUDY OF STEEL BOLT PROFILE TO OPTIMISE SHEAR STRENGTH OF ROCK BOLT

C. Cao, J. Nemcik & N. Aziz
Engineering Faculty, University of Wollongong, NSW 2522, Australia

ABSTRACT: *Fully encapsulated rock bolts have been a key element in the design of ground control system for many years as they offer superior shear resistance to bed separation. The load transfer capacity of fully grouted bolts is a classical topic studied by many researchers, however there are few papers that report on the study of the effectiveness of steel bolt rib configuration. In this paper, the load transfer mechanism of one profile unit of fully grouted bolt is studied with variation of the bolt profile shape and its influence on the resin failure. The resin failure calculations were performed using the derived mathematical equations, while the Fast Lagrangian Analysis Continua (FLAC) program was used to verify the stress tensor accuracy within the resin. The calculation of the stress distribution within the resin/bolt interface has significant bearing on the optimisation of the bolt surface profile design, for effective rock and concrete reinforcement in both civil and mining engineering*.

1 INTRODUCTION

Steel bolts have been widely used for rock reinforcement in civil, tunnelling and mining engineering. Bolts reinforce rock mass through restraining the deformation within the rock. To improve bolt loading capacity through the steel rebar design, it is necessary to have a good understanding of the rock bolt behaviour in deformed medium. This can be acquired through analytical studies, laboratory tests and numerical modelling.

Monitoring of load transfer between the bolt, resin and rock strata indicates that the bolt profile plays an important role in generation of shear strength between the bolt and the surrounding rock. The short encapsulation pull out test of roof bolt indicate significant increase of load transfer at particular bolt rib profile spacing. Other variables such as profile rib angle, its shape and size are also important parameters contributing to the shear strength of rock bolt system. Difficulty in manufacturing the rock bolts with slight variations in rib profile limits the extent of experimental data while the numerical modelling can be used to uncover minute differences between various designs of the bolt profile. The derived mathematical equations presented in this paper describe the stress field at any point within the resin adjacent to the loaded steel bolt making the detailed shear strength analysis possible. The aim of the theoretical stress predictions, supported by numerical modelling is to provide fundamental understanding of

the resin failure and to offer a new tool for research into the best profile geometries to reach optimum shear strength between the bolt and the surrounding rock or composite medium.

Rib profile configuration of steel bolts plays an important role in the load transfer between the resin and the steel bolt surface. A typical definition of the rib profile configuration is shown in Figure 1 below.

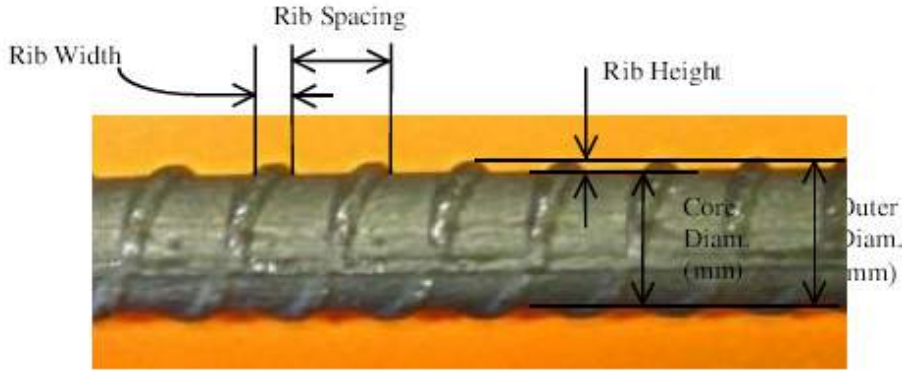

Fig. 1. Steel bolt rib profile configuration

Pullout tests are usually used to examine the anchoring capacity of rock bolts. There are only a few researchers that have carried out laboratory tests on bolt profile configuration performance pioneering work, these include Blumel, *et al,* (1997) and Aziz, et al, (2008). Aziz et al (2008) found that the load capacity and shear stiffness are greatly influenced by bolt profile configurations. Their research work showed that the bolts with rib spacing of 12.5mm exhibit lowest stiffness while larger spacing in the order of 37.5 mm had higher peak and residual strengths as shown in Figure 2. Similar laboratory tests show that the smooth bolt with no ribs has lower peak strength as reported by Aziz and Web (2003). Clearly there is a need for studies on bolt performances other than the laboratory experiments, hence resort to mathematical and numerical modelling would provide a comprehensive understanding of the bolt profile performance, which is the subject of this study.

2 STRESS DISTRIBUTION IN INFINITE ELASTIC MEDIA

Boussinesq (Poulos, 1974) derived fundamental solutions for various loads on infinite or semi-infinite elastic media. While loading an infinite strip on the surface of a semi-infinite mass as shown in Figure 3, the stress tensor anywhere within the media can be calculated as a function of the load, position and material properties. For a uniform normal load, the stress tensor can be calculated using the Boussinesq equations given below:

$$\sigma_z = \frac{P}{\pi}\left[\alpha + sin\alpha\cos(\alpha + 2\delta)\right] \tag{1}$$

$$\sigma_x = \frac{P}{\pi}\left[\alpha - sin\alpha\cos(\alpha + 2\delta)\right] \tag{2}$$

$$\sigma_y = \frac{2P}{\pi}\nu\alpha \tag{3}$$

$$\tau_{xz} = \frac{P}{\pi}sin\alpha\sin(\alpha + 2\delta) \tag{4}$$

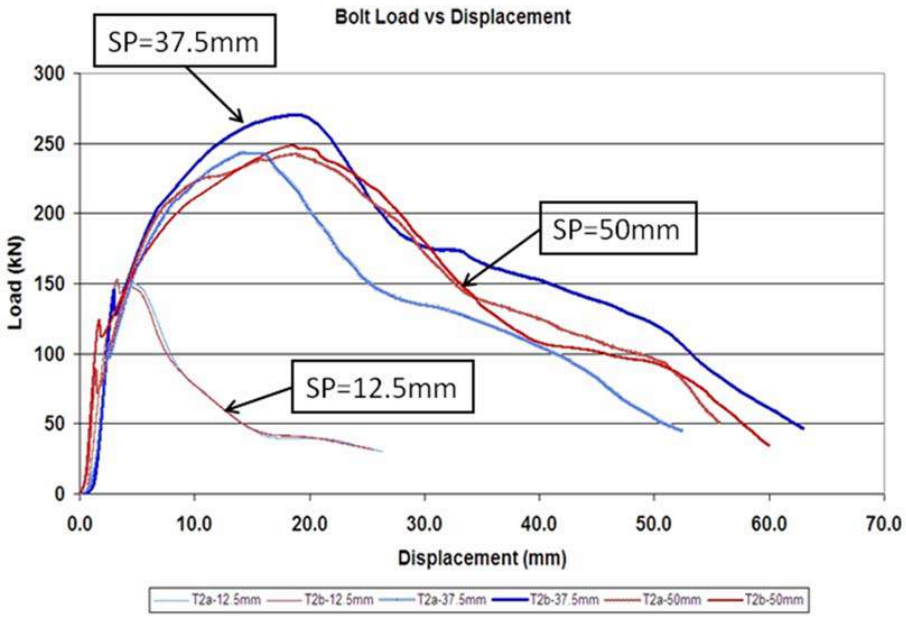

Fig. 2. Previous laboratory studies of steel bolt pull out tests showing the maximum load for various spacing of the bolt profile (after Aziz *at al*, 2008).

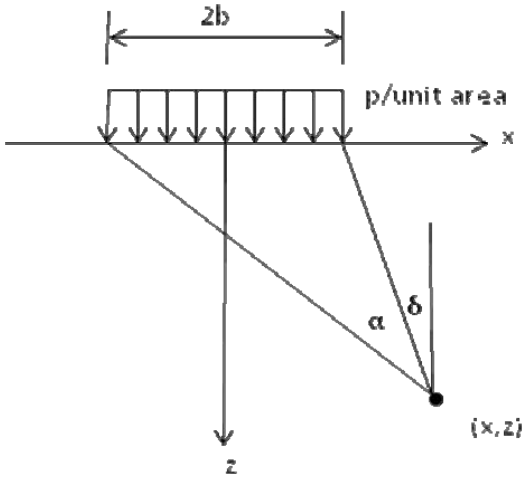

Fig. 3. Calculated stress tensor at any position given by x and z coordinates within the semi-infinite elastic medium loaded by a uniformly distributed load (p)

For the uniform shear load, the stress distribution can also be calculated via Cerutti's equations:

$$\sigma_z = \frac{q}{\sigma}\left[sin\alpha \sin(\alpha + 2\delta)\right] \tag{5}$$

$$\sigma_x = \frac{q}{\pi}\left[ln\frac{R_1^2}{R_2^2} - sin\alpha \sin(\alpha + 2\delta)\right] \tag{6}$$

$$\tau_{xz} = \frac{q}{\pi}\left[\alpha - sin\alpha \cos(\alpha + 2\delta)\right] \tag{7}$$

3 MODELLING OF FULLY GROUTED BOLT PROFILES

To make a connection with the load transfer system and the bolt rib configuration, a single spacing between two bolt profiles as shown in Figure 4 is examined.

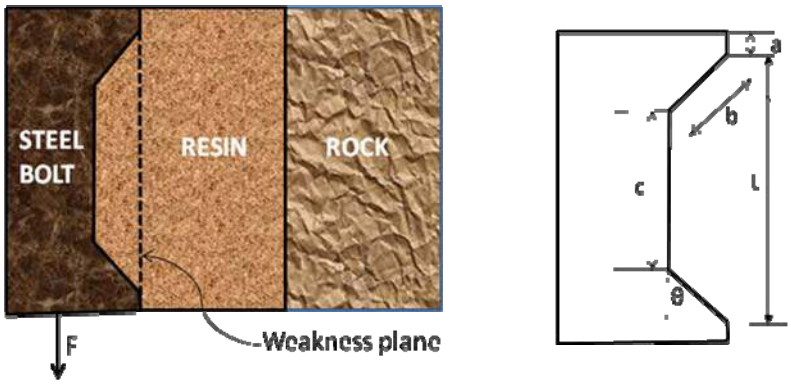

Fig. 4. A schematic drawing of a single spacing between two bolt profiles showing calculation parameters

When the bolt is loaded, the load is transferred to the resin as shown in Figure 5. The direction of these loads only depends on the bolt profile while their magnitudes depend on both the bolt profile and the interface properties. During loading, the loads can be represented as shear forces and normal forces shown in Figure 5 below.

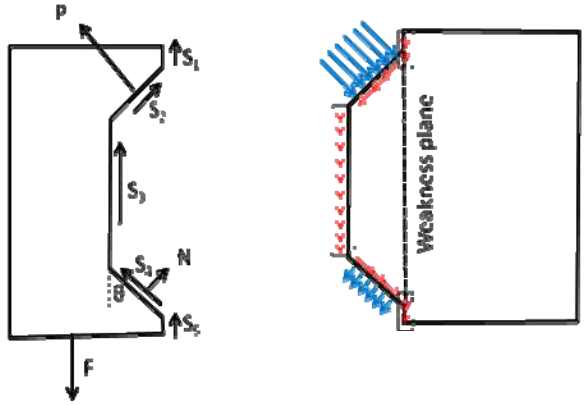

Fig. 5. Load transfer between the steel bolt and the fully encapsulated resin

Assuming that the initial bonding forces S_1, S_3, S_4 and S_5 between the bolt and the resin are very small and when the angle θ is large, then the shear force S_2 is small (shown in Figure 5). Initial assumptions are:

- All shear forces $S_1 = S_2 = S_3 = S_4 = S_5 \approx 0$ N
- N (tension) ≈ 0 N
- p is an evenly distributed load along the bolt profile side.

The free body diagram of the bolt can be thus simplified as shown in Figure 6a where only a normal stress to the inclined bolt profile remains. This stress component plays a major role in stress distribution within the resin. To validate this assumption a FLAC model was used to model a section of the steel bolt as shown in Figure 6b with the angle θ equal to 45˚. The axial force was applied onto the bolt and the generated shear stress contours presented in Figure 6b. These contours were directly compared with the calculated shear stress contours using equation 4. Properties used in the FLAC model are shown in Table 1.

Table 1. Material properties used in FLAC model.

UCS (MPa)	71
Shear strength (MPa)	16.2
E (GPa)	12
Poissons ratio	0.25

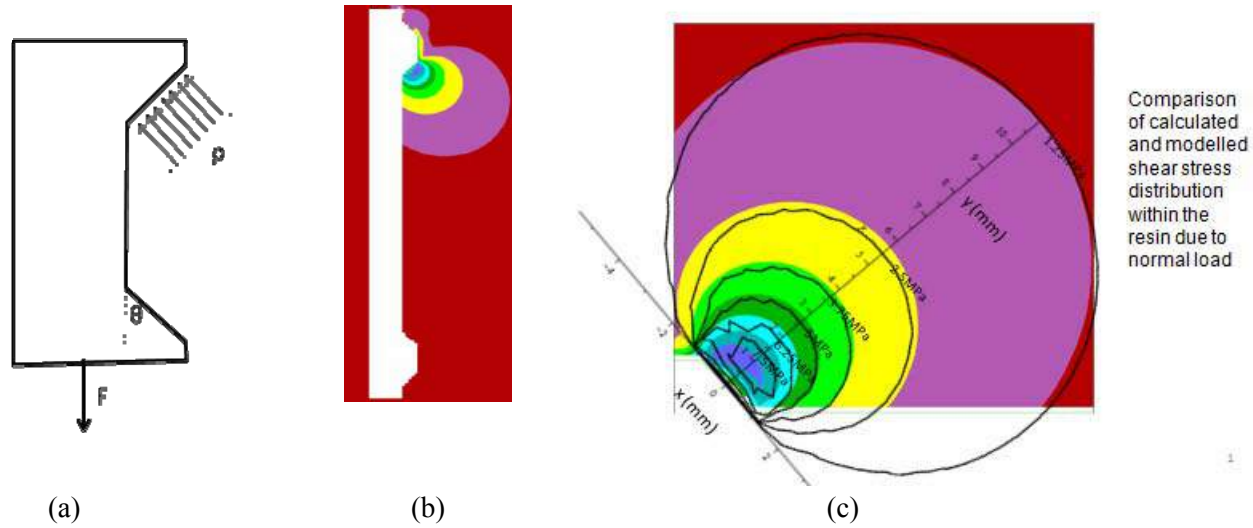

(a) (b) (c)

Fig. 6. (a) Approximation of the active bolt-resin load transfer verified by FLAC model (b) and (c)

4 NORMAL AND SHEAR STRESS ON A FAILURE PLANE

To investigate the type of resin failure that will occur, failure location and stress magnitudes are needed to propagate the failure. Several weakness planes were considered. As a first trial, a plane of weakness spanned between the bolt profile tips is shown in Figure 4. Three failure models can be used in the calculations. These are the shear failure, Mohr-Coulomb and the distortional energy (Von Misses) failure criterion. From the three methods the Mohr-Coulomb criterion of failure was chosen.

The following text details the integrated solutions and stress transformations to calculate the normal and shear stresses to the chosen plane of weakness. The lengthy integrations used to derive the stress tensor solutions are outside the scope of this paper. The Matlab program was also introduced to obtain numerical solutions where the mechanical expressions were too complicated.

For static equilibrium, the sum of forces parallel to the bolt axis is zero, i.e. $\sum F_y = 0$. Assuming that the shear forces are zero:

$$F = pbsin\theta \Rightarrow p = \frac{F}{bsin\theta} \tag{8}$$

where F = axial bolt force, and p = Normal load on bolt boundary b.

5 STRESS DISTRIBUTION IN THE RESIN

The FLAC modelling shows that in comparison to the evenly distributed compressive load (p), other loads have less influence on the stress in the resin and at this stage all shear and tensile forces at the bolt boundary are ignored.

To apply Boussinesq's equations in calculations of the normal and shear stress along the studied failure plane, the coordinate system (x', z') is rotated as shown in Figure 7 so the load (p) becomes vertical with the angle θ between the line of load application and the assumed plane of failure connecting two corners of the bolt shown as a solid line PQ in Figure 7. Point (A) represents any point on the plane of weakness and the variable (h) indicates its distance from point P.

Assuming that the elastic properties of the resin are similar to the surrounding rock and no failure occurs at the rock boundary, the resin boundary can be extended to infinity. Thus, from the geometry shown in Figures 4 and 7 it can be seen that:

$$PQ\,length\,L = c + 2b\,cos\theta \tag{9}$$

$$\alpha + \delta + \theta = \frac{\pi}{2} \tag{10}$$

and

$$sin\alpha = \frac{b\,sin\theta}{\sqrt{b^2 + h^2 - 2b\,h cos\theta}} \tag{11}$$

The stress tensor calculated using the Boussinesq equations (1) to (4) is used to calculate the shear and normal stress along the plane of proposed weakness. Since the final solutions need to calculate stress parallel and perpendicular to the failure plane, the stress tensor needs to be transformed to a coordinate system parallel to the plane of failure. In these equations, α and δ needs to be substituted with rib configuration parameters a, b, c and θ shown in Figure 4. To simplify these calculations, this step can be done after stress transformation.

Stress transformation formulas used:

$$\sigma_x = \frac{1}{2}\left(\sigma_{x'} + \sigma_{z'}\right) + \frac{1}{2}\left(\sigma_{z'} - \sigma_{x'}\right)cos2\theta - \tau_{x'z'}\,sin2\theta \tag{12}$$

$$\sigma_z = \frac{1}{2}\left(\sigma_{x'} + \sigma_{z'}\right) - \frac{1}{2}\left(\sigma_{z'} - \sigma_{x'}\right)cos2\theta + \tau_{x'z'}sin2\theta \tag{13}$$

$$\tau = \frac{1}{2}\left(\sigma_{z'} - \sigma_{x'}\right)sin2\theta + \tau_{x'z'}cos2\theta \tag{14}$$

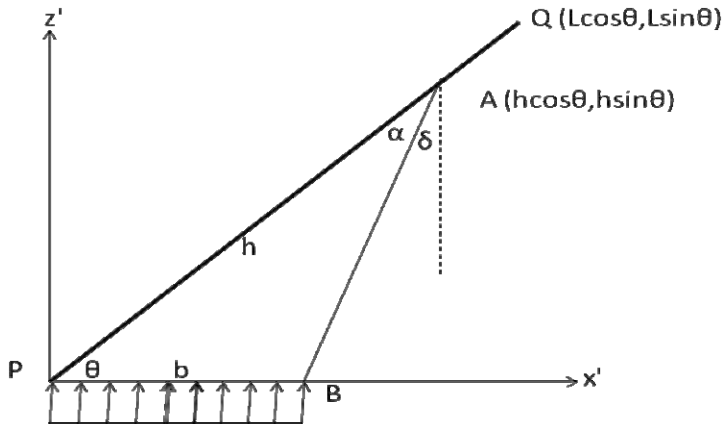

Fig. 7. Rotated axis of the loading diagram with the assumed plane of failure

Thus the normal and shear stress to the failure plane would be:

$$\sigma_n = \frac{1}{2}\left(\sigma_{x'} + \sigma_{z'}\right) + \frac{1}{2}\left(\sigma_{z'} - \sigma_{x'}\right)cos2\theta - \tau_{x'z'}sin2\theta \tag{15}$$

$$\tau = \frac{1}{2}\left(\sigma_{z'} - \sigma_{x'}\right)sin2\theta + \tau_{x'z'}cos2\theta \tag{16}$$

To calculate the normal and shear force $\int\sigma_n dh \, and \int\tau \, dh$

$$\int\sigma_n dh = \int\left(\frac{\sigma_x + \sigma_z}{2} + \frac{\sigma_z - \sigma_x}{2}cos2\theta - \tau_{xz}sin2\theta\right)dh$$

Substituting the three expressions from equations (1), (2) and (4) we get:

$$\frac{\sigma_x + \sigma_z}{2} = \frac{\alpha}{\pi}p; \;\; \frac{\sigma_z - \sigma_x}{2} = \frac{sin\alpha\cos(\alpha + 2\delta)}{\pi}p; \;\; \tau_{xz} = \frac{p}{\pi}sin\alpha\sin\left(\alpha + 2\delta\right) \tag{17}$$

Arranging and substituting $\alpha + \delta + \theta = \frac{\pi}{2}$, $\int\sigma_n dh = \frac{p}{\pi}\int\left(\alpha - sin\alpha\, cos\alpha\right)dh$

In a similar manner $\int\tau \, dh = \int\left(\frac{\sigma_z - \sigma_x}{2}sin2\theta + \tau_{xz}cos2\theta\right)dh = \frac{p}{\pi}\int sin^2\alpha \, dh$ v

After lengthy integrations, rearrangement and substitutions of each term the solution is

$$\int\sigma_n \, dh = \frac{p}{\pi}\int\left(\alpha - sin\alpha\, cos\alpha\right)dh$$

it follows that

$$\int \sigma_n dh = \frac{F}{b\pi \sin\theta}\left[\left(\frac{\pi}{2}-\theta\right)(c+3b\cos\theta)-(c+2b\cos\theta)\tan^{-1}\left(\frac{c\cos\theta+b\cos 2\theta}{c\sin\theta+b\sin 2\theta}\right)+b\cos\theta\tan^{-1}\left(\frac{c+b\cos\theta}{b\sin\theta}\right)\right]$$

and

$$\int \tau\, dh = \frac{P}{\pi}\int \sin^2\alpha\, dh = \frac{F}{\pi}\left[\tan^{-1}\left(\frac{c+b\cos\theta}{b\sin\theta}\right)+\frac{\pi}{2}-\theta\right] \tag{18}$$

6 MOHR-COULOMB FAILURE STUDY ALONG THE PLANE OF WEAKNESS

Two combined stress fields are considered within the resin. The first one is the initial pre-loading stress tensor at the failure surface and the second one is the load induced stress tensor. Due to bolt installation procedure, the initial pre-loading stress within the resin is considered to be small as most of the resin along the bolt cures after pre-tensioning the bolt. Thus, the failure criterion (*f*) is expressed as net resistant force that can be summed together:

$$f = T_0 + T = \left(c_w + \mu\sigma_{n0} - \tau_0\right)L + \left(\int \mu\sigma_n dh - \int \tau\, dh\right)$$

where:

L = c + 2bcosθ = failure length

h = distance from any chosen point along the plane of weakness from 0 to L

$\mu = tan\phi$, where ϕ is an internal angle of friction of the resin

σ_{n0} = initial normal stress

τ_0 = initial shear stress

τ = shear stress introduced by pull out force

b, c and θ are bolt profile parameters

The forces along the plane of weakness are shown in Figure 8 below.
Failure criteria expression can be written as:

$$\begin{aligned} f &= c_w L + L\mu\sigma_{n0} - L\tau_0 + \mu\int \sigma_n dh - \int \tau\, dh \\ &= F_0 + \frac{p\mu}{\pi}\left[\begin{array}{l}\left(\frac{\pi}{2}-\theta\right)\left(c+3b\cos\theta-\frac{b\sin\theta}{\mu}\right)-(c+2b\cos\theta)\tan^{-1}\left(\frac{c\cos\theta+b\cos 2\theta}{c\sin\theta+b\sin 2\theta}\right) \\ +b\left(\cos\theta-\frac{\sin\theta}{\mu}\right)\tan^{-1}\left(\frac{c+b\cos\theta}{b\sin\theta}\right)\end{array}\right] \end{aligned}$$

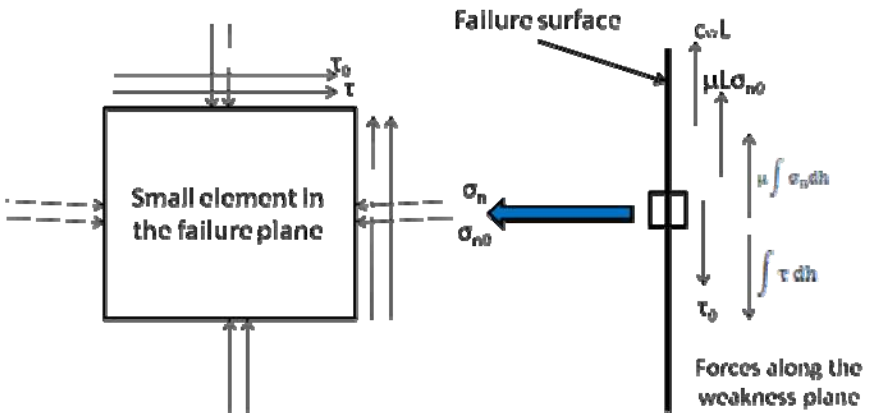

Fig. 8. Forces on a small element and along the plane of weakness

7 APPLICATION EXAMPLE

Assume variable profile shape θ varying from 45˚ to 90˚ as shown in Figure 9. Let the failure length=10mm, a=1 mm, rib height b sin θ =1.5mm, and while c changes from 7 mm to 10 mm, rib slope angle θ will change from 45^0 to 90^0. While θ reaches maximum, the failure may occur on the plane of weakness. While θ is small, the failure is likely to occur elsewhere such as at bolt/resin interface.

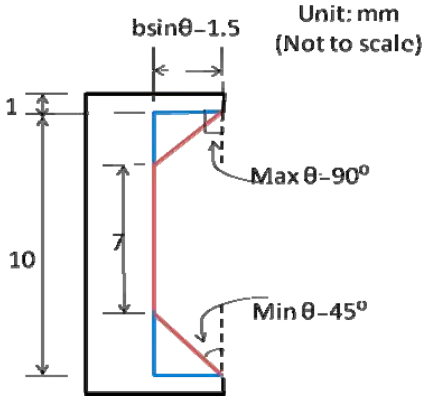

Fig. 9. Colour lines indicate boundaries of the bolt profile

For initial conditions, let

$$\sigma_{n0} = 0 \text{ MPa} \quad \text{and} \quad \tau_0 = 0 \text{ MPa}$$

For material properties, i.e. resin properties, let cohesion c = 16MPa and the angle of internal friction $\phi = 35^0$. Then

$$F_0 = L\left(c_w + \mu\sigma_{n0} - \tau_0\right) = 10\left(16 + tan35^\circ \text{x} 0 - 0\right) = 160\,N$$

Use Failure criteria formula:

$$f = F_0 + \frac{F\mu}{\pi b \sin\theta}\left[\begin{array}{l}\left(\frac{\pi}{2}-\theta\right)\left(c+3b\cos\theta-\frac{b\sin\theta}{\mu}\right)-(c+2b\cos\theta)\tan^{-1}\left(\frac{c\cos\theta+b\cos 2\theta}{c\sin\theta+b\sin 2\theta}\right)+ \\ b\left(\cos\theta-\frac{\sin\theta}{\mu}\right)\tan^{-1}\left(\frac{c+b\cos\theta}{b\sin\theta}\right)\end{array}\right]$$

$$= 160 + F\,G(\theta)$$

where F is pull-out force and G(θ) is the 'influence factor' of the rib slope angle θ. The graph in Figure 10 shows the calculated influence factor versus the rib slope angle θ for this geometry.

If the influence factor is positive, the failure will never occur, no matter how large the applied pull-out force is. If the influence factor is negative, then failure may occur. In addition, for a large negative 'influence factor' the probability of failure is increasing.

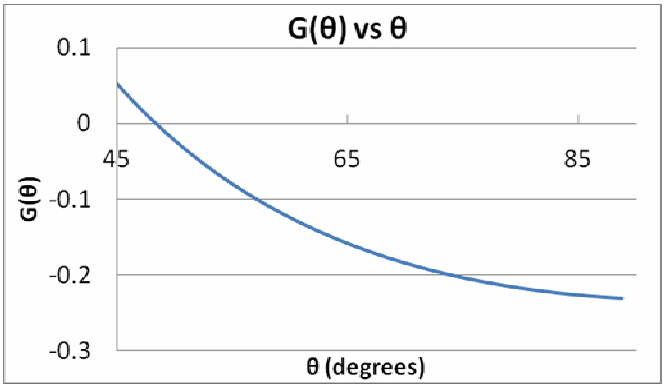

Fig. 10. Influence factor G(θ) versus the rib slope angle θ

- From that diagram it can be concluded that:

  If $\theta < 48^0$, $G(\theta) \geq 0$, then $f = 160 + F\,G(\theta) \geq 0$

  It means that failure will never occur on the plane of weakness. In other words, when $\theta \geq 48^0$ then failure in resin may occur.

- If the influence factor reaches the minimum value G(θ) = -0.23 the forces to resist failure will be at minimum, and Fp = 160/0.23 = 696 N.

- The graph in Figure 10 indicates that the increase in angle θ will increase the probability of the resin failure.

8 DISCUSSION

The initial study of spacing between the adjacent profiles on the bolt surface as presented shows the method of deriving mathematical equations, which calculate both the stress tensor and resin failure adjacent to a changing bolt profile. The method can calculate resin failure in any designated plane or curved surface to represent the plane of weakness at random orientation within the resin along the bolt profile. The important outcome of this study is to show that there is another way to study the stress distribution and resin failure around the bolt of different profile configurations that will compliment the numerical modelling and laboratory tests. This method can stimulate research in designing more efficient bolt profiles for effective rock reinforcement.

Currently, only two dimensional cases of calculations has been suggested, however efforts will be made to extend the calculations to 3-dimensions. Selection of the resin failure criterion can also be made while the post failure model of resin is incorporated into the analysis. The final outcome of this work is to write a computational program to calculate the pull out force for various bolt profile geometries. Selecting a large number of surfaces of potential weakness and calculating the smallest pull out force that occurs at any of the failure surfaces will enable determination of the bolt pull out forces in various stress fields. An optimisation of resin properties can also be studied using this method.

9 CONCLUSIONS

Mathematical simulations have been developed to provide better understanding of the bolt-resin interaction for rock reinforcement. Mohr-Coulomb criteria were found to be the most appropriate solution. The derived mathematical equations have in built bolt geometry parameters of profiles and these can be changed to optimise the bolt shear strength capacity. Various geometries of bolt profile encapsulated within the resin can be trialled using described approach. Future studies will include 3-D simulation of the bolt profile configuration.

REFERENCES

Poulos, H. and Davis, E. 1974. "Elastic solutions for rock mechanics". Textbook by John Willey & Sons, Inc. New York. TA710.P67 624.1513 73-17171, Printed in New York.

Blumel, M., Schweger, H.F. and Golser, H., 1997, "Effect of rib geometry on the mechanical behaviour of grouted rock bolts", World Tunnelling Congress '97, 23rd General Assembly of the International Tunnelling Ass. Wien. 6 p.

Aziz, N.I. and Webb, B., 2003, "Study of load transfer capacity of bolts using short encapsulation push test", Proc. 4th Underground Coal Operators Conference, Coal 2003, February 12-14, Wollongong, pp 72-80.

Aziz, N. I., Jalalifar H. and Concalves, J., 2006. "Bolt surface configurations and load transfer mechanism", Proc.7th Underground Coal Operators Conference, Coal 2006, Wollongong, 5-7 July, pp. 236-244.

Aziz, N, Jalalifar, H, Remennikov, A, Sinclair, S, Green, A, 2008, "Optimisation of the Bolt Profile Configuration for Load Transfer Enhancement", Proc.8th Underground Coal Operators Conference, Coal 2003, February 14-15, Wollongong, pp 125-131. (ed N Aziz and J Nemcik, http://ro.uow.edu.au/coal/11/)

STABILITY ANALYSIS OF SHALLOWLY-EMBEDDED OFFSHORE PIPELINE ON CARBONATE SOIL

T. Takatani
Department of Civil Engineering, Maizuru Nat'l College of Technology, Maizuru, Kyoto, Japan

ABSTRACT: *The cyclic horizontal movement of a shallowly-embedded offshore pipeline under the hydrodynamic environment will lead to a large deformation of pipeline. It is very important to accurately evaluate the cyclic movement of offshore pipeline during cyclic horizontal loading under severe storm condition. The purpose of this paper is to simulate the pipeline behaviour during cyclic horizontal loading under constant vertical loading condition. A two-dimensional non-linear finite element analysis based on an effective stress theory is employed for a pipe-soil interaction problem in order to investigate the stability of the shallowly-embedded offshore pipeline using non-linear joint elements at pipe-seabed soil interface. Pipeline movement behaviour during cyclic horizontal loading is numerically evaluated in terms of the carbonate soil conditions and the constant vertical load.*

1 INTRODUCTION

Shallowly-embedded offshore pipelines are directly exposed to the vertical and horizontal forces induced by the hydrodynamic environment. The cyclic movement of pipeline due to both drag and lift forces caused by waves and currents will lead to a large deformation of pipeline. Recently, Dingle et al. (2008) observed the deformation mechanism during cyclic lateral movement of pipeline through some centrifuge tests. White and Cheuk (2008) proposed a simplified modelling of cyclic lateral pipe-soil interaction, based on the accumulation and deposition of berm materials. Zhou et al.(2008) and Wang et al.(2009) conducted numerical simulations of static and dynamic pipe embedment in softening soil, and also obtained the seabed deformation and the localized remoulding behaviour during pipe embedment to compare with centrifuge modelling study. Chatterjee et al.(2010) studied pipe–soil interaction during vertical penetration and large amplitude lateral pipe motion by a large deformation finite element analysis, and investigated differences in behaviour between light and heavy pipes. Takatani et al.(2008) investigated the stability of a shallowly-embedded offshore pipeline resting on carbonate sandy seabed under severe storm condition using a non-linear spring element to represent a non-linear relationship between pipeline and seabed surface.

The purpose of this paper is to simulate the pipeline movement behaviour during cyclic loading, focusing on the cyclic lift force with the submerged self-weight of pipeline and the pipe-soil interaction effect. In this paper, a two-dimensional non-linear finite element analysis based on an effective stress theory is employed for a pipe-soil interaction problem. To investigate the influences of bonding at pipe-seabed soil interface, non-linear joint elements are used at pipe-seabed soil interface. Pipe is assumed to be 1.0m diameter and 0.25m for its ini-

tial depth, and the seabed is assumed to be a carbonate soil with two relative densities, *Dr*=60% and 80%. Cyclic horizontal loading due to drag force for a 100-year return period storm condition is evaluated using the Fourier decomposition method. In particular, the rotation behaviour of pipeline may be generated by a cyclic twisting moment force induced by the initial depth of pipe and cyclic horizontal loading. The stability of a shallowly-embedded offshore pipeline during cyclic horizontal loading is numerically investigated by taking into consideration the carbonate soil conditions, the amplitude of vertical loading, and the cyclic rotation behaviour of pipeline.

2 STABILITY ANALYSIS OF PIPELINE-SEABED INTERACTION

2.1 Pipeline-seabed interaction analysis

An advanced numerical analysis in this paper is two-dimensional dynamic non-linear finite element method (Takatani et al., 2005a, 2005b, 2008) based on the effective stress theory in order to simulate cyclic movement behaviour of a shallowly-embedded offshore pipeline on carbonate sandy soil under undrained condition. In this finite element analysis, a non-linear relationship between shear stress and shear strain of soil element is accurately expressed by a multi shear spring model (Towhata & Ishihara, 1985) and the Masing rule for loading and unloading curves is employed so as to adjust the amplitude of hysteresis damping for the multi shear spring model. Also the cyclic mobility model (Iai et al., 1990), which is of a generalized plasticity-multiple mechanism type, is adapted to simulate excess pore water pressure. Pore fluid is assumed to be imcompressible, and also the viscous boundary technique (Lysmer et al., 1969) is used to create the infinite of seabed soil in this analysis. There are three governing equations of a kinematic equation between soil and pipeline, pore water input/output balance equation in each pore fluid element, and dynamic water pressure wave propagating equation for pore fluid. Pore water pressure can be expressed by an increment of volumetric strain of soil skeleton because of undrained condition, and also dynamic water pressure wave propagating equation for pore fluid can be represented by a technique that the effect of pore fluid existence can be taken into consideration by applying an additional mass of each pore fluid element to the soil-structure kinematic equation.

Fig.1 shows a finite element mesh for a shallowly-embedded offshore pipeline-seabed

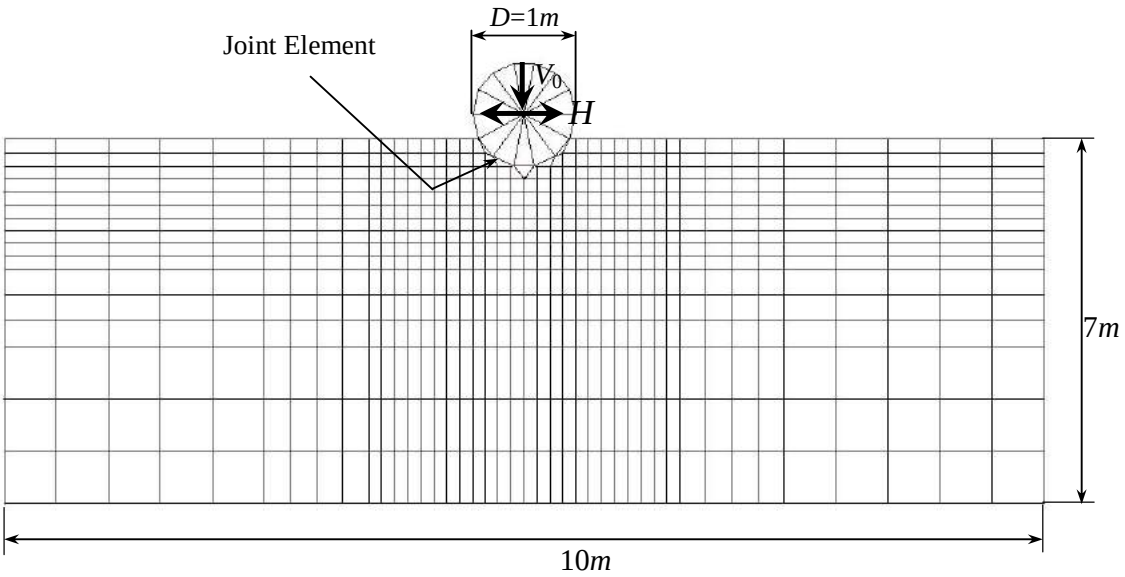

Fig.1. Fem mesh for pipeline-seabed interaction analysis (z_0=0.25*m*) (Takatani et al, 2005a).

interaction analysis considering a liquefaction phenomenon in the seabed around the pipeline. In this paper, the movement behaviour of a shallowly-embedded offshore pipeline resting on carbonate soil is investigated from a view point of carbonate soil characteristics. The joint element is used at contact area between pipeline and sand layer to represent a slip phenomenon at contact area between pipeline and seabed surface (Takatani et al., 2005a). Pipeline movement behaviour during cyclic loading is numerically investigated in terms of the carbonate soil conditions, the amplitude of the constant vertical loading.

2.2 Carbonate sandy soil

In this paper, the analytical domain is $7m \times 10m$ as shown in Fig.1 and is assumed to be a carbonate sand layer. Both 6-node triangle and 8-node square elements are used in this mesh, and also the Selective Reduced Integration method (Hughes, 1980) by which each soil element integration can be separately evaluated for both the volumetric and deviation components is employed in order to make an accurate evaluation for each soil element integration. At every incremental time step, the coordinate of each nodal point is renewed according to the soil deformation, and the stress loading of each element is re-evaluated by a self-weighted analysis result at every time step. This finite element analysis with a coarse mesh in the vicinity of the pipeline shown in Fig.1 can be carried out with sufficient accuracy (Ozutsumi, 2003).

Fig.2 shows the liquefaction resistance curve for carbonate sand (Aramaki, 1997). As a reference, the liquefaction resistance curves for Toyoura sand are indicated in Fig.2, too. The mechanical properties for carbonate soil with two relative densities *Dr*=60% and 80% are evaluated from the liquefaction resistance curves, that is, the effective stress ratio vs. the number of cycles. The carbonate soil with the relative density *Dr*=60% becomes difficult to

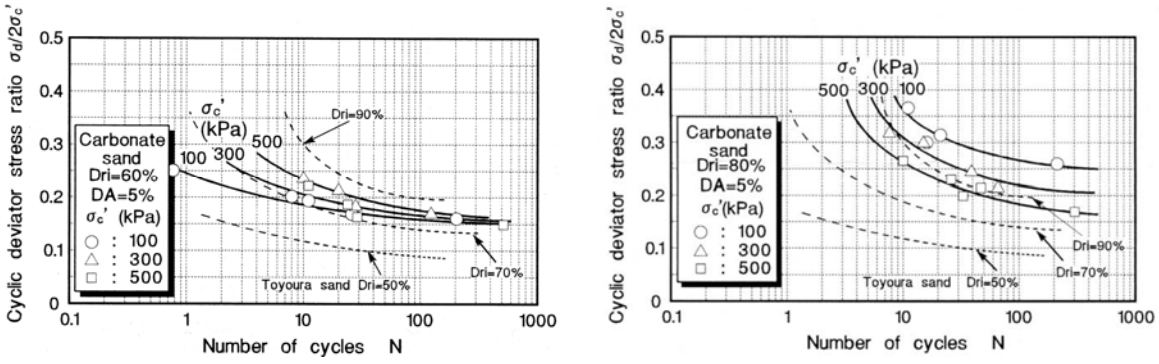

(a) *Dr*=60% (b) *Dr*=80%

Fig.2. Liquefaction resistance curve for carbonate sand (Aramaki, 1997).

Table 1. Material properties of carbonate sand.

Relative density		*Dr*=60%	*Dr*=80%
Initial shear modulus, G_{ma} (kPa)		48,395	75,211
Elastic tangent bulk modulus of soil skeleton, K_{ma} (kPa)		126,207	196,138
Friction angle, ϕ_f (degree)		38.16	39.30
Phase transformation line angle, ϕ_p (degree)		28	28
Material parameters for dilatancy	S_1	0.005	0.005
	w_1	4.634	2.829
	c_1	1.548	1.929
	p_1	0.500	0.500
	p_2	1.037	1.046

liquefy because its liquefaction intensity increases with the confining stress increasing, and also is likely to liquefy when the confining stress is over its yielding point of consolidation. On the other hand, the carbonate soil with the relative density *Dr*=80% becomes easy to liquefy because its liquefaction intensity gradually decreases with the confining stress increasing. The material properties of carbonate soil for two relative densities *Dr*=60% and 80% are shown in Table 1. Five parameters shown in Table 1 which specify the dilatancy are determined by the back-fitting technique to the liquefaction resistance curves of the carbonate sand obtained from the laboratory test. In general, the liquefaction resistance curve is determined by combining the laboratory test data and the bearing capacity test data at the sites for taking the in-situ conditions of soils into account (Morita et al., 1997).

Before the cyclic horizontal movement of pipeline, the self-weighted analysis for pipe-seabed interaction problem is carried out under the completely drained condition to obtain the initial effective stress of each soil element. In this numerical pipe-seabed interaction analysis, a strain space plasticity approach is assumed to be used for cyclic mobility in order to represent the realistic hysteretic damping factor under cyclic loading. In this approach, an actual cyclic shear mechanism is decomposed into a set of one dimensional virtual simple shear mechanism.

Material properties of dilatancy S_1, w_1, c_1, p_1 and p_2 shown in Table 1 are five parameters to define the cumulative volumetric strain of plastic nature for representing cyclic mobility. These parameters define the correlation between the liquefaction front parameter (Iai et al., 1990) and the normalized shear work. The liquefaction front parameter is given by a function of shear work, and Towhata & Ishihara (1985) obtained the correlation between the shear work and the excess pore pressure, and also concluded that the correlation is independent of the shear stress paths with or without the rotation of principal stress axes.

3 NUMERICAL RESULTS

In this numerical analysis based on the effective stress theory for a pipe-seabed interaction problem, drag force shown in Fig.3 is employed for a horizontal force, *H*, acting on a shallowly-embedded offshore pipeline. In general, the drag force acting on the pipeline resting on seabed surface can be estimated by Morison Force model, Peak Force model, Wake model and Fourier Force model and so on (Neil & Hinwood, 1998). In this paper, the drag force acting on a shallowly-embedded offshore pipeline whose diameter is 1m resting on the seabed at 60m water depth is estimated by the Fourier Force model proposed by Sorensen et al.(1986).

Drag force shown in Fig.3 is estimated from the current velocity around the shallowly-embedded offshore pipeline. This force was calculated for regular wave with the wave height

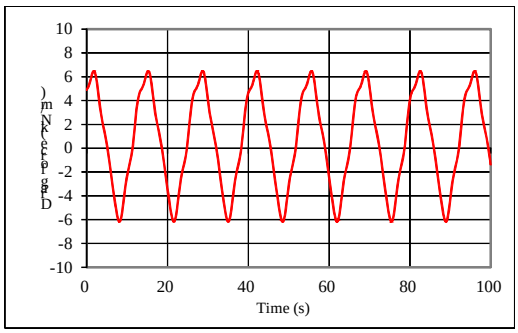

Table 2. Calculation condition of drag and lift forces (regular wave).

Maximum Wave Velocity, U_{wave} (m/s)	2.55
Steady Current Velocity, $U_{current}$ (m/s)	0.58
Wave Frequency (Hz)	0.47
Keulegan-Carpenter Number, K_c	34.34
Current Ratio, α	0.23

Fig.3. Drag force acting on a shallowly-embedded pipeline.

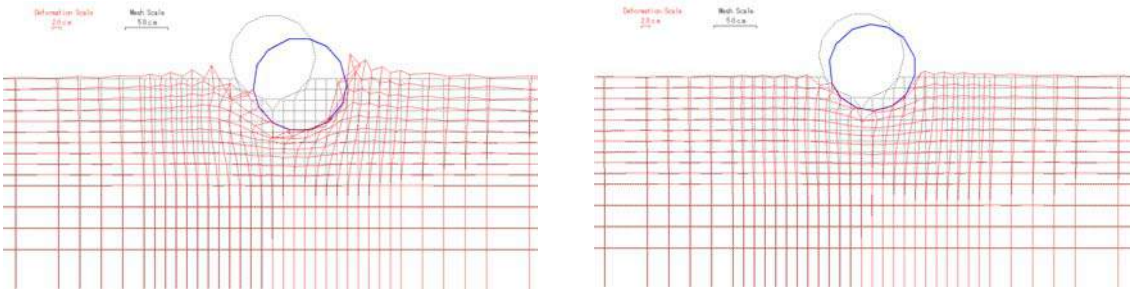

(a) Medium dense carbonate sand, *Dr*=60% (b) Dense carbonate sand, *Dr*=80%

Fig.4. Pipeline and seabed deformation after cyclic loading, 600s (z_0=0.25m, V_0=6kN/m).

13.2m and the wave period 13.5s under severe storm condition with 100-year return period obtained by Lewis et al.(1990) based on JONSWAP spectrum (Hasselmann et al.,1973). The calculation condition of the drag force for regular wave is shown in Table 2. In this paper, a constant vertical load, V_0, is assumed to be operated to the pipeline, and the effect of V_0 on the stability of a shallowly-embedded offshore pipeline is numerically investigated. On the other hand, the joint element is employed in this analysis to simulate a slip phenomenon at contact area between pipe and seabed. The unit tangential stiffness for normal and shear directions, K_n and K_s, for a joint element are used 1.0×10^6 (kN/m) and 1.0×10^5 (kN/m), respectively. The friction angle of joint element is assumed to be 25 degree in this analysis.

Fig.4 indicates the seabed deformation around the shallowly-embedded pipeline after 600s cyclic loading under z_0= 0.25m, V_0=6kN/m and two relative densities *Dr*=60% and 80%. The amplitude of pipeline movement is over 80cm and also the pipeline settlement is over 60cm in the relative density *Dr*=60% shown in Fig.4(a). On the other hand, the amplitude of pipeline movement is over 30cm and also the pipeline settlement is over 25cm in the relative density *Dr*=80% shown in Fig.4(b). This may imply that pipeline movement behaviour greatly depends on the relative density of carbonate sandy seabed.

Fig.5 illustrates the pipeline movement behaviour during 600s cyclic loading for the carbonate seabed with two relative densities *Dr*=60% and 80% under four constant vertical loads, V_0=0, 2, 4 and 6kN/m. It can be observed from these figures that both horizontal and vertical movement behaviour of pipeline in V_0=0kN/m is the largest in four constant vertical loads. The settlement of pipeline becomes larger and the horizontal movement is smaller with the increase of the vertical load, V_0, for two relative densities *Dr*=60% and 80%. This is because the soil resistance is influenced by the increasing settlement of pipeline with cyclic horizontal movement. It should be noted that the constant vertical loading plays an important key role from a view point of the stability of a shallowly-embedded offshore pipeline. Moreover, the settlement and horizontal movement of pipeline for the medium dense carbonate seabed *Dr*=60% are much larger than those for the dense carbonate seabed *Dr*=80% because of the relative density of carbonate seabed soil. This may imply that a shallowly-embedded offshore pipeline resting on the carbonate seabed soil with small relative density will lead to not only a large deformation of pipeline but also a sudden break-out due to cyclic loading under severe storm condition.

Fig.6 shows the cyclic rotation behaviour of pipeline during 600s cyclic loadings. Cyclic rotation of pipeline may be generated by a twisting moment force induced by the initial depth of pipeline and cyclic horizontal loading. It can be found from these figures that the cyclic rotation angle of pipeline becomes smaller with the increase of the vertical load, V_0, for two relative densities *Dr*=60% and 80%. In addition, the cyclic rotation angles of pipeline for the

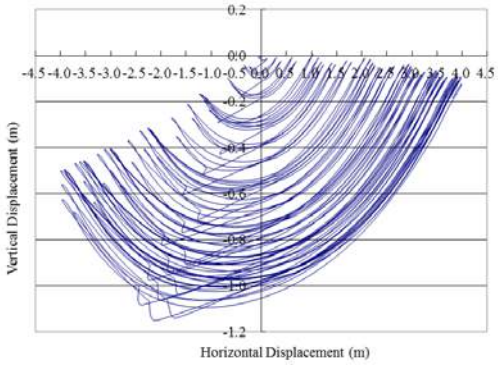

(a) V_0=0kN/m

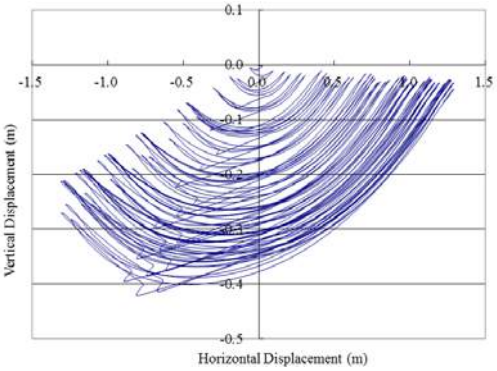

(a) V_0=0kN/m

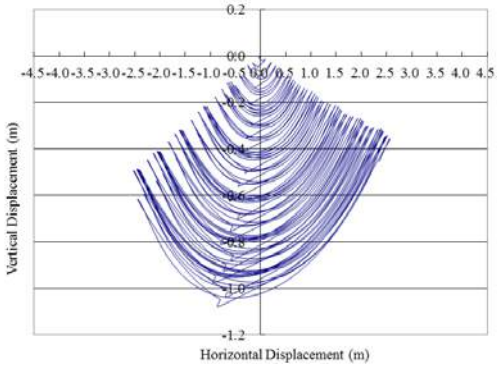

(b) V_0=2kN/m

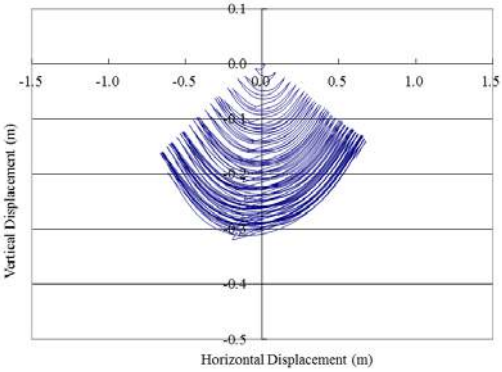

(b) V_0=2kN/m

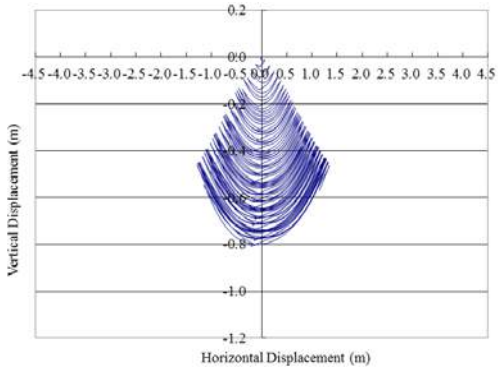

(c) V_0=4kN/m

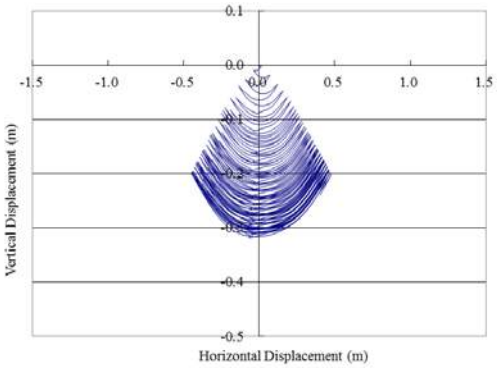

(c) V_0=4kN/m

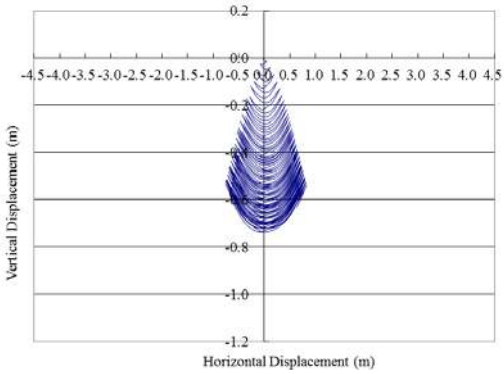

(d) V_0=6kN/m

Medium dense carbonate sand, Dr=60%

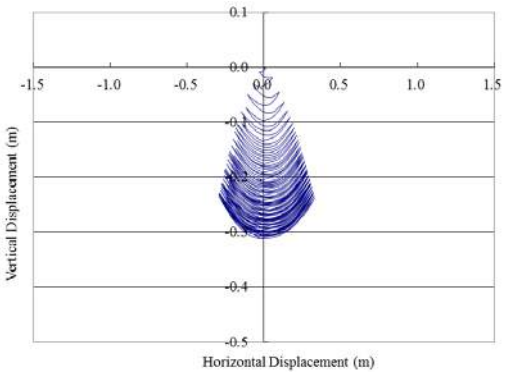

(d) V_0=6kN/m

Dense carbonate sand, Dr=80%

Fig.5. Pipeline cyclic behaviour during cyclic horizontal and vertical loadings (600s).

medium dense carbonate seabed *Dr*=60% are much larger than those for the dense carbonate seabed *Dr*=80%. This may imply that a shallowly-embedded offshore pipeline resting on the carbonate seabed soil with small relative density under the small vertical loading condition will undergo a serious damage caused by a cyclic twisting moment force due to cyclic loading under the severe storm condition. The smaller the relative density of carbonate seabed soil and the constant vertical loading acting on a shallowly-embedded offshore pipeline are,

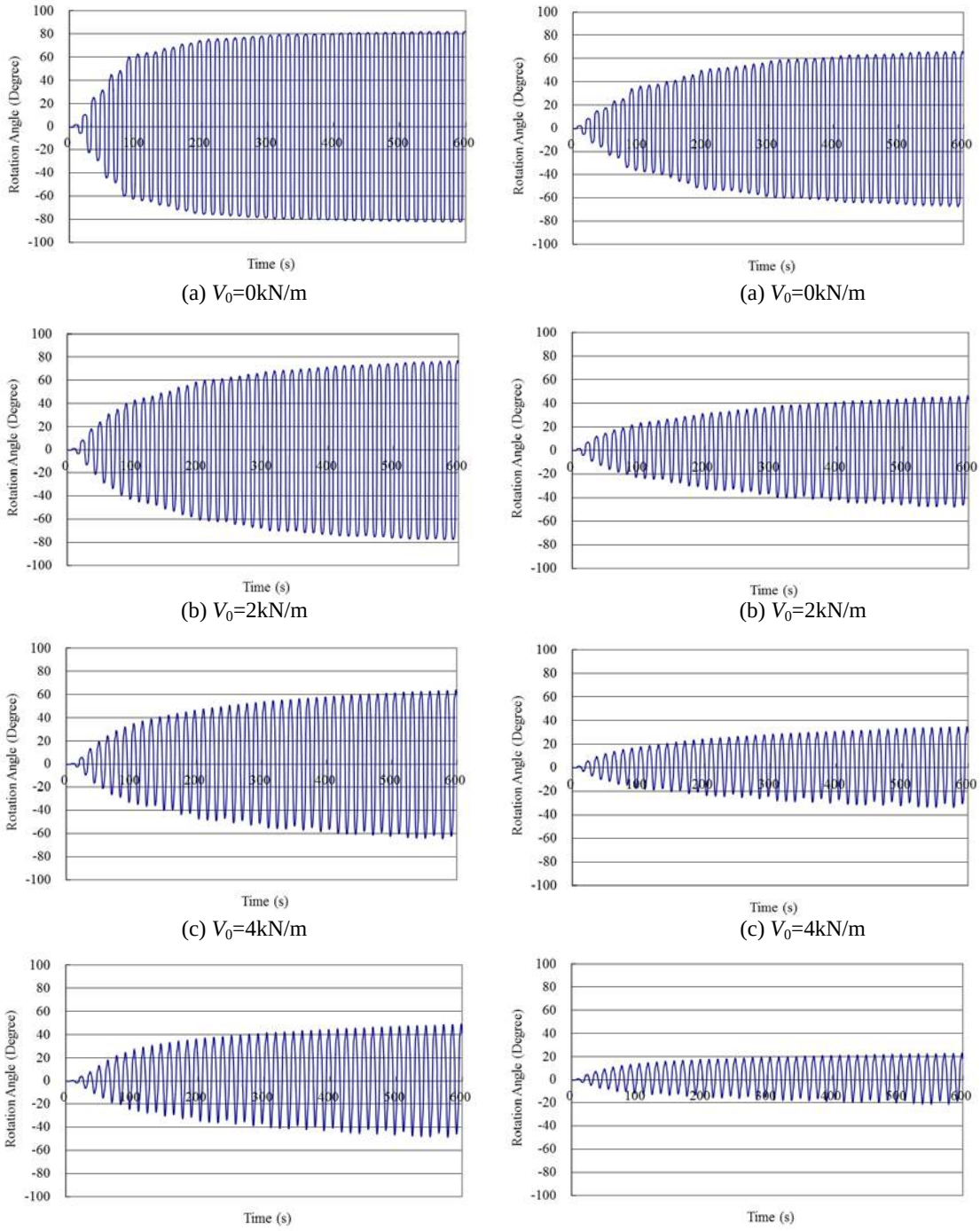

(a) V_0=0kN/m (a) V_0=0kN/m

(b) V_0=2kN/m (b) V_0=2kN/m

(c) V_0=4kN/m (c) V_0=4kN/m

(d) V_0=6kN/m (d) V_0=6kN/m

Medium dense carbonate sand, *Dr*=60% Dense carbonate sand, *Dr*=80%

Fig.6. Pipeline cyclic rotation behaviour during cyclic horizontal and vertical loadings (600s) .

the larger the cyclic rotation angle of pipeline becomes. Consequently, it should be noted that not only the relative density of carbonate seabed soil but also the vertical loading during cyclic horizontal loading plays an important key role on the stability of a shallowly-embedded offshore pipeline during cyclic horizontal loading induced by the drag force under severe storm condition.

4 CONCLUSIONS

In this paper, the pipeline movement behaviour during cyclic loadings was numerically evaluated by a two-dimensional non-linear finite element analysis based on an effective stress theory and also non-linear joint elements were used at pipe-seabed soil interface in order to investigate the influences of bonding at pipe-seabed soil interface. Cyclic horizontal loading due to the drag force for a 100-year return period storm condition was evaluated using the Fourier decomposition method. In particular, the rotation behaviour of pipeline may be generated by a cyclic twisting moment force. The stability of a shallowly-embedded offshore pipeline during cyclic horizontal loading was numerically investigated by taking into consideration the carbonate soil conditions, the amplitude of a constant vertical load, and the cyclic rotation behaviour of pipeline.

In summary, the following conclusions can be made.

1) The constant vertical load during cyclic horizontal loading plays an important key role on the stability of a shallowly-embedded offshore pipeline.
2) Pipeline movement behaviour during cyclic horizontal loading depends on the relative density of carbonate seabed soil, because the soil resistance force acting to the pipeline increases with the relative density.
3) Cyclic rotation behaviour of pipeline is generated by a cyclic twisting moment force induced by the initial depth of pipeline and cyclic horizontal loading, and greatly depends on not only the relative density of carbonate seabed soil but also the amplitude of constant vertical load.

In this paper, the cyclic horizontal movement behaviour of a shallowly-embedded offshore pipeline resting on a carbonate sandy seabed soil was investigated under undrained condition, and also was numerically evaluated under the same cyclic loading condition as the initial depth of pipeline, regardless of the settlement of pipeline during cyclic loadings. In future, there seems to be a need for further consideration on this analytical condition in the pipe-seabed interaction problem. Although the pore pressure accumulation in the seabed around a shallowly-embedded offshore pipeline is not presented in this paper due to the limited space, it is necessary for an intensive study on the effect of pore pressure accumulation on the pipeline movement behaviour because it is the most important key role in the design of the offshore pipeline. In addition, further investigation may be needed to simulate these phenomena mentioned above and make some concrete conclusions.

REFERENCES

Aramaki, N. (1997), “Undrained cyclic and monotonic triaxial behaviour of crushable carbonate soil”, Dr. Eng. Thesis, *Yamaguchi University*.

Chatterjee, S, White, D.J., Wang, D. & Randolph, M.F. (2010), “Large deformation finite element analysis of vertical penetration of pipelines into the seabed”, *Proc 2nd Int Symp Frontiers Offshore Geomech* (ISFOG-2010), Perth, Australia.

Cheuk,C.Y., White, D.J. & Bolton, M.D. (2008), "Uplift mechanism of pipes buried in sand", *J Geotech & Geoenvironmental Eng*, Vol.134(2), 154-163.

Dingle,H.R.C., White, D.J. & Gaudin, C. (2008), "Mechanism of pipe embedment and lateral breakout on soft clay", *Canadian Geotech J*, Vol.45(5), 636-652.

Hasselmann, K., Barneft, T.P., Bouws, E., Carlson, H., Cartwright, D.E., Enke, K., Ewing, J.A., Gienapp, H., Hasselmann, D.E., Kruseman, P., Meerburg, A., Muller, P., Olders, D.J., Richter, K., Sell, W. & Walden, H., (1973), "Measurements of wind-wave growth and swell decay during the Joint North Sea Wave Project (JONSWAP)", *Deutsche Hydr. Zeit*, No.12, 9-95.

Hodder, M.S., White, D.J. & Cassidy, M.J. (2008), "Centrifuge modeling of riser-soil stiffness degradation in the touchdown zone of a steel catenary riser", *Proc 27th Int Conf Offshore Mech Arctic Eng* (OMAE), ASME, Estoril, Portugal, OMAE2008-57302.

Hughes, T.J.R. (1980), "Generalization of selective integration procedures to anisotropic and nonlinear media", *Int J Num Meth Eng*, Vol.15, 1413-1418.

Iai, S., Matsunaga, Y. & Kameoka, T. (1990), "Strain space plasticity model for cyclic mobility", *Report of Port and Harbour Research Institute*, Vol.29(4), 27-56.

Lewis, A. W. and Allos, R. N., (1990), "JONSWAP's Parameters : Sorting out the Inconsistencies", *J Ocean Eng*, Vol.17(4), 409-415.

Lysmer, J. & Kuhlemeyer, R.L. (1969), "Finite dynamic model for infinite media", *J Eng Mech Div*, ASCE, No.EM4, 859-877.

Morita, T, Iai, S, Liu, H, Ichii, K, & Sato, Y. (1997), "Simplified Method to Determine Parameter of FLIP", *Material of Port and Harbour Research Institute*, No 869.

Neill, I.A.R. & Hinwood, J.B., (1998), "Wave and wave-current loading on a bottom-mounted circular cylinder", *J Offshore Polar Eng*, Vol.8(2), 122-129.

Ozutsumi, O. (2003), "Numerical analysis on seismic damage estimation for soil-structure system on liquefied area", Dr. Eng. Thesis, *Kyoto University*.

Sorenson, T., Bryndum, M.B. and Jacobsen, V., (1986), "Hydrodynamic forces on pipelines – Model tests", *Pipeline Research Council International Inc.*

Takatani, T. (2005a), "Pore pressure build up response analysis for horizontal cyclic loading", *Proc 11th Int Conf IACMAG*, Turin, Italy,353-360.

Takatani, T. (2005b), "Pipeline-seabed interaction analysis subjected to horizontal cyclic loading", *Proc Int Symp Frontiers Offshore Geomech*, Perth, 629-635.

Takatani, T. & Kaya, T. (2008), "Unburied offshore pipeline stability analysis based on nonlinear relationship between pipeline and carbonate soil", *Proc 18th Int Offshore Polar Eng Conf*, Vancouver, Canada, Vol.2, 176-185.

Towhata, I. & Ishihara, K. (1985), "Modelling soil behaviour under principal stress axes rotation", *Proc 5th Int Conf Num Method Geomech*., Nagoya, 523-530.

Wang, D., White, D.J. & Randolph, M.F. (2009), "Numerical simulation of pipeline dynamic laying process", *Proc 28th Int Conf Offshore Arctic Eng*, Honolulu, OMAE2009-79199.

White, D.J. & Cheuk, C.Y. (2008), "Modelling the soil resistance on seabed pipelines during large cycles of lateral movement", *Marine Structures*, Vol.21(1), 59-79.

Zhou, H., White, D.J. & Randolph, M.F. (2008), "Physical and numerical simulation of shallow penetration of a cylindrical object into soft clay", *ASCE GeoCongress 2008*, New Orleans, ASCE Special Publication No.179, 108-117.

ON A RATIONAL APPROACH OF GROUND RESPONSE ANALYSES

C. Li, W. Yang, Y.C. Lo, J. Endicott & S.H. Yung
AECOM Asia, Hong Kong

ABSTRACT: *SHAKE has been widely used by engineers to predict ground responses given an earthquake time history at bedrock. However, drastically different results could be obtained by running two deterministic analyses even when range of the soil parameters adopted is similar. Thus, a purely deterministic analysis alone is insufficient and could generate misleading results. To make the analysis more credible and verifiable, sensitivity analyses are critical. In this paper, a series of numerical models are set up to simulate typical geological conditions in real world. Effects of key factors such as initial shear modulus, dynamic shear modulus degradation curves, damping curves, and existence of weak layer on ground response analysis are investigated systematically. Suggestions are then made with regard to procedures to carry out a sound ground response analysis. In addition, finite element models are used to provide comparison to SHAKE analysis and to provide another approach to understand effects of weak soil layers as well as the inadequacy of many current design practices which may underestimate a series of issues associated with presence of weak soil layers. We also identify other application problems where a more rigorous ground response analysis is warranted.*

1 INTRODUCTION

The earthquake design practice has seen great changes over the last decade. For large infrastructure projects, traditional design approaches based on intensity and design spectrum oftentimes cannot adequately reflect effects of local soil conditions. Ground response analyses using computer program (represented by SHAKE) as an alternative, are capable of including much richer information about both the input motion and the local site conditions. This is particularly true for soil-structures such as retaining walls and bridge piers, which we define as structures with significant embedment into surrounding soils; since the dynamic responses of these soil-structures cannot be adequately reflected by a 1-DOF (degree of freedom) spring-mass system which is underlying the design spectrum approaches.

Ground response analyses, powerful and simple enough for being carried out by industrial practitioners, can lead to confusions and errors if not carried out properly and carefully. This paper looks into these issues through sensitivity studies and makes improvement suggestions to current practice by rationally taking into consideration uncertainties associated with dynamic soil parameters, as well as possible weak layers of the ground soils. Statistical analysis could be helpful in these regards, however, deterministic approaches are usually preferred among practicing engineers. In addition, as SHAKE program uses iterations among soil parameters, the statistical dependence of different soil parameters could be rather complex and therefore difficult to quantify. Therefore, in this paper, we choose to use the deterministic approach to explain scattering of data, relative importance and interaction of different dynamic soil parameters based on concrete examples for typical geological settings.

Taking one step forward, for the purpose of linking ground response analysis with soil structure interaction problems, we performed a comparison between the finite element method (FEM) and SHAKE ground response analyses. We will then illustrate difference between two approaches and suggest a rational explanation.

2 MODEL SETTINGS

2.1 Factors affecting ground response analysis

Like any other computer analysis software, inputs to SHAKE software mainly consist of the following categories: geometry, material properties and boundary conditions. This paper is focused on material properties. Two typical geological settings are used for geometric consideration; as to boundary conditions, only the case where a ground motion is applied at the bedrock/soil interface is considered.

Dynamic soil parameters for ground response analyses mainly include the following: initial/maximum shear modulus (G_0/G_{max}), shear modulus degradation curves and damping curves. Depending on nature of each particular site, all these dynamic parameters potentially could possess a large degree of uncertainty. In this paper we illustrate effects of each of these three factors separately and jointly for the typical geological settings considered. Variations of other material properties such as density and Poisson's ratio can be determined relatively in a more straightforward way and are not included in this paper.

2.2 Typical geological Setting 1: sandy soil profile

In geological Setting 1, a typical profile of sandy soils is assumed (see Fig. 1). The bedrock is assumed at 40m depth overlaid with horizontal uniform layers of sandy soils. In SHAKE analysis, this is modeled as 16 uniform soil layers with 2.5m thickness. Since the stiffness of sandy soils usually increases with depth, for this setting, SPT N_{60} values are assumed to vary the linearly from surface to the bottom layer above bedrock. The profile of initial/maximum shear moduli of Setting 1 is shown in Fig. 2.

2.3 Typical geological Setting 2: sandy soil profile with an embedded soft layer

In Setting 2, the soil layers are the same with Setting 1 except for the existence of one soft/weak layer of 5m thickness (see Fig. 3). For the configuration shown in Fig. 3, this weak layer is assumed at depth range 15~20m.

Sensitivity analyses regarding dynamic soil parameters are then carried out for the profile shown in Fig. 3. As normally the depth of the weak layer varies from site to site, a sensitivity analysis with respect to the location of the weak layer is also performed. The profile of initial/maximum shear moduli of this Setting 2 is shown in Fig. 4.

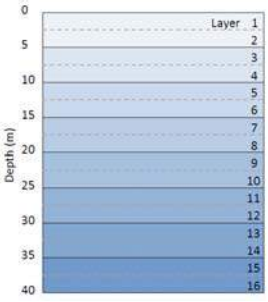

Fig. 1. Geometry of typical geological Setting 1

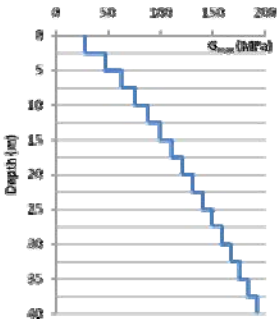

Fig. 2. Profile of initial shear modulus (Setting 1)

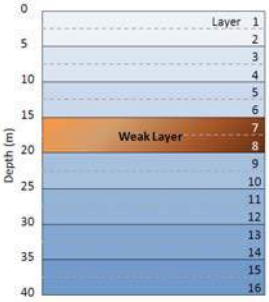

Fig. 3. Geometry of typical geological Setting 2

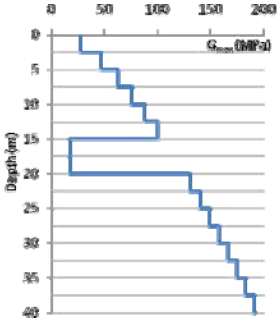

Fig. 4. Profile of initial shear modulus (Setting 2)

Material properties of soils of Settings 1 and 2 are summarized in Table 1. For sandy layers the initial/maximum shear moduli are calculated from SPT-N values using correlations proposed by Seed et al. (1984). For the weak layer, the initial modulus is calculated from an assumed shear wave velocity (V_s = 100m/s).

2.4 Dynamic soil parameters

Initial shear modulus

Initial/maximum shear modulus can be determined either from direct measurement or from correlation of in-situ test, such as SPT and CPT tests. SPT correlations based on Seed et al. (1984) were used in this paper. Fig. 5 shows a typical scatter of data of SPT value for one project the authors worked on (by courtesy of AECOM Asia), from this plot, the deviation from average is approximately 50% (measured by SPT value difference at the depth of 20m).

Dynamic soil curves

For dynamic soil curves, we adopted a set of curves by EPRI (1993) as standard curves, which reflect effects of soil overburden pressure (see Figs. 6 and 7 for details). In many large scale infrastructure works, dynamic soil curves are determined from laboratory tests such as dynamic cyclic triaxial tests. However, data interpretation, limitations of lab test and errors and uncertainties are quite frequently either missing or not fully understood by practicing design engineers. For design engineers to make good use of lab test data, it is important to compare the lab determined curves with these internationally renowned curves (e.g. EPRI (1993) curves) to obtain an overall picture regarding to the validity of these lab test curves. These EPRI (1993) curves are by no means a replacement of lab curves, but it can be quite helpful for interpretation of the lab test, and may, in a certain sense, help to reduce the risk of adopting inappropriate lab curves which could happen due to problematic tests.

Table 1. Dynamic Material Properties of Soil Layers Typical Settings 1 and 2

Soil Layers	Soil Type	Depth Range (m)	Density (kg/m^3)	Initial Shear Modulus (MPa)	Shear Wave Velocity (m/s)	Remarks
1	Sand	0 ~ 2.5	2000	27.4	117.0	
2	Sand	2.5 ~ 5	2000	46.8	153.0	
3	Sand	5 ~ 7.5	2000	62.1	176.2	
4	Sand	7.5 ~ 10	2000	75.6	194.4	
5	Sand	10 ~ 12.5	2000	87.8	209.6	
6	Sand	12.5 ~ 15	2000	99.3	222.8	
7	Sand	15 ~ 17.5	2000	110.1	234.6	
8	Sand	17.5 ~ 20	2000	120.4	245.4	
9	Sand	20 ~ 22.5	2000	130.3	255.2	
10	Sand	22.5 ~ 25	2000	139.8	264.4	
11	Sand	25 ~ 27.5	2000	149.0	272.9	
12	Sand	27.5 ~ 30	2000	157.9	281.0	
13	Sand	30 ~ 32.5	2000	166.6	288.6	
14	Sand	32.5 ~ 35	2000	175.0	295.8	
15	Sand	35 ~ 37.5	2000	183.3	302.7	
16	Sand	37.5 ~ 40	2000	191.3	309.3	
7*	Clay	15 ~ 17.5	1680	16.8	100.0	Weak Layer
8*	Clay	17.5 ~ 20	1680	16.8	100.0	Weak Layer

To help to understand the associated uncertainties related to dynamic soil curves, Figs. 8 and 9 show typical plots of shear modulus degradation and damping curves from EPRI (1993) for sandy soils at 0~6m depth taken from a suite of 50 randomized curves. From this plot it appears that the range of variation is quite large. To calibrate the variation we quite arbitrarily choose to compare the lower and upper bound with the median value of shear modulus and damping ratio at a shear strain level 0.1% (with the consideration that usually for seismic analysis, the strain level of interest is between 0.01% and 1%). Note that the variation of shear modulus degradation curve from the median is about 55%; and the deviation from median damping curve is about 40%).

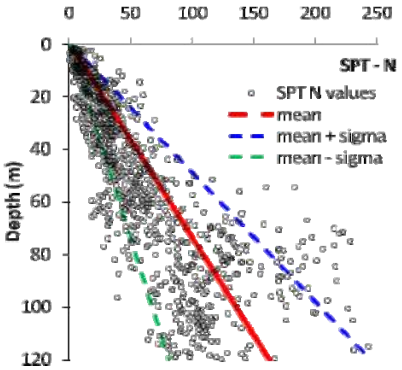

Fig. 5. Typical SPT-N Values vs. Depth

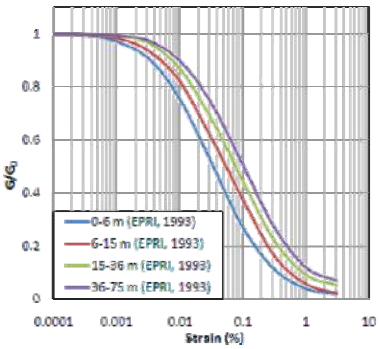

Fig. 6. EPRI (1993) shear modulus degradation curves for sandy soils at depth 0~75m

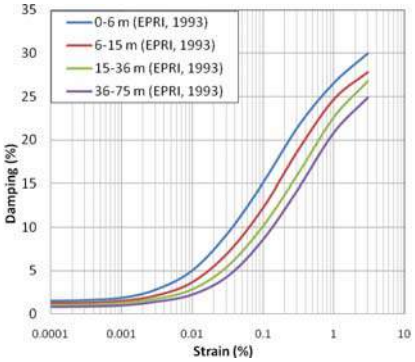

Fig. 7. EPRI (1993) damping curves for sandy soils at depth 0~75m

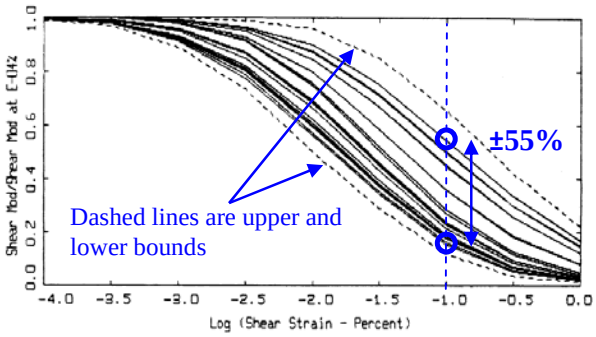

Fig. 8. EPRI (1993) randomized shear modulus degradation curves for sandy soils at depth 0~6m

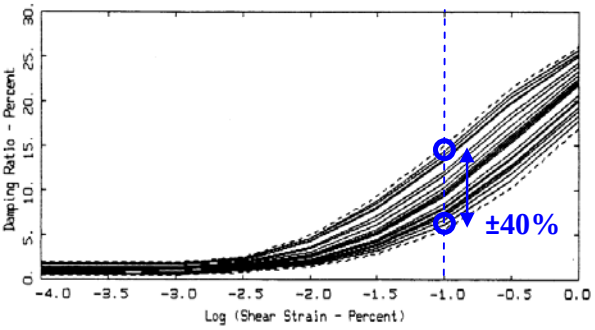

Fig. 9. EPRI (1993) randomized damping curves for sandy soils at depth 0~6m

Also note that comparing with regular engineering design practice; the EPRI (1993) curves were generated from a large amount of data. In practice, depending on the nature of particular project, only a few sets of dynamic curves for each soil category are produced from the lab experiment program. Sometimes these curves show rather good convergence, which may create an impression that these curves are accurately determined. It is therefore important for designers to be cautious and keep in mind that the scatter of data in dynamic curves could be much higher than what appears. As shown later, the effect of scattering of dynamic curves could lead to a significant difference in predicted values of peak ground accelerations (PGA).

3 SENSITIVITY ANALYSIS: TYPICAL SETTINGS 1

3.1 General

As discussed above, geotechnical data for dynamic analysis, e.g. SPT data and dynamic curves, and data from dynamic soil tests usually contain a large degree of uncertainties. When using these data determined from laboratory or field tests, these uncertainties need to be properly considered to give a reasonable estimation with regard to the range of predicted value, typically PGA. As a common industry practice of current days, these uncertainties are typically considered only in the beginning; then the “mean” curves are chosen to predict final quantity of interest, typically PGA. In this way, the uncertainties are essentially not carried forward, leading to the consequence that when the analysis is finished, the degree of uncertainty is not kept track of and a single deterministic value is recommended.

As it is not straightforward for practicing engineers to adopt statistical methods, the challenge becomes how to keep track of all sources of uncertainties while performing deterministic analysis. Our proposed approach is as following: we first isolate each individual factor to illustrate the effect of its uncertainty on the final results (PGA); then we investigate

the joint effects of multiple factors, through which a lower and upper bound can be produced.

In these sensitivity analyses, a typical earthquake time history (referred as Japanese III) from "Highway Bridge Design Specification Part V: Seismic Design", Road Association of Japan, is used as the input motion (scaled to 0.15g). See Fig. 10 for the time-history of this motion.

3.2 Typical Settings 1: uncertainty due to one single factor

The material properties of soil layers required by the ground response program SHAKE include initial/maximum shear modulus and soil dynamic curves. Soil dynamic curves consist of shear modulus degradation curves and damping curves. To carry out the sensitivity analysis, we first perform one analysis based on mean curves of soil dynamic parameters and best estimate of G_0 profile. Variations from the mean curves or best-estimate G_0 profile are then considered. Note that for simplicity, it is assumed that the dynamic curves for all 16 layers vary in a same pattern; i.e. if one factor varies from the mean or best-estimate value by certain percentage, the same degree of variation is assumed for all 16 layers. In this way, the number of analyses for sensitivity study is greatly reduced.

The results of sensitivity analysis regarding to initial shear modulus, damping curves and shear modulus degradation curves are shown in Figs. 11, 12 and 13, respectively. From these figures, a plot of percentage of difference with regard to initial shear modulus, soil damping and shear modulus degradation curves are shown in Figs. 14, 15 and 16. It appears that predicted PGA vs. variations of both initial modulus and shear modulus degradation curves are both highly nonlinear; only the variation of PGA with regard to damping ratio curves is close to linear.

3.3 Typical Settings 1: considering combination of uncertainties

In this Section, we examine the effects of combination of uncertainty types. As suggested from Section 2.4, uncertainty with respect to G_0 is about 50%, with shear modulus degradation curves about 55% and with regard to damping curves 40%. Considering a well-controlled case, where we assume the uncertainty with regard to each single factor is about 25%, the joint effects of uncertainties on PGA are illustrated.

Fig. 17 shows a tree diagram of analysis cases for the combination of uncertainties for three factors. For each possible combination of dynamic curves and initial shear modulus profile, the deviation of PGA from $\overline{PGA}$ (PGA for the standard comparison case, where mean curves of soil dynamic parameters and best estimate of G_0 profile were used) is displayed. It is observed that the deviation from the mean result is -39% on the lower side and 23% on the upper side. Fig. 18 illustrates these two particular combinations which produce the lower and upper bound of PGA. Fig. 19 shows a contour plot of deviation from mean $\overline{PGA}$ given the joint uncertainties in damping and shear modulus degradation curves. For this particular setting, results from Fig. 18 can be viewed as good news since we did not observe a significant amplification of uncertainties. However, since this study is performed on only one typical setting, no general conclusions can be obtained. Nevertheless, this shows that for sound engineering design, recommendations for PGA should more appropriately take the form of a range rather than a single number. This could have significant effects on designs of buildings or retaining walls which are quite sensitive to PGA values.

4 SENSITIVITY ANALYSIS: TYPICAL SETTINGS 2 WITH AN EMBEDDED SOFT LAYER

It is commonplace to have one of more soft/weak layers in the geological profile. In this

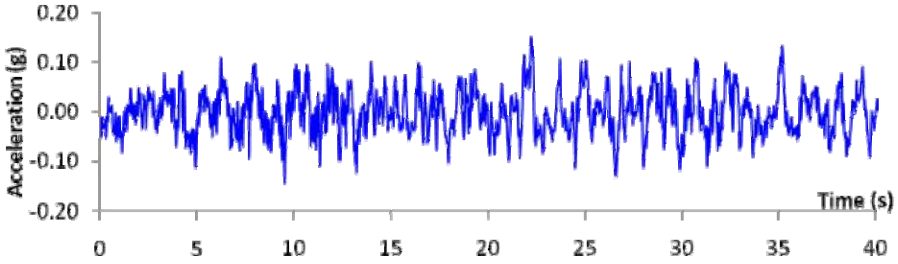

Fig. 10. Time-history of input motion: Japanese III motion

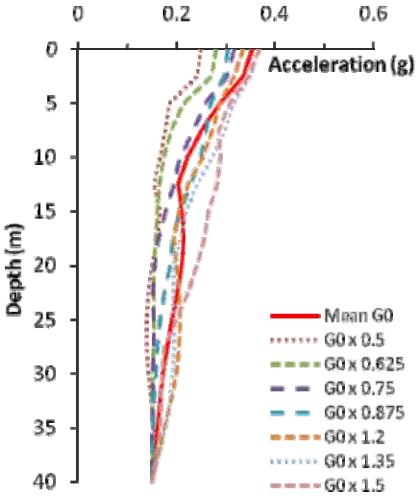

Fig. 11. Profile of maxmimum acceleration for sensitivity study with regard to G_0

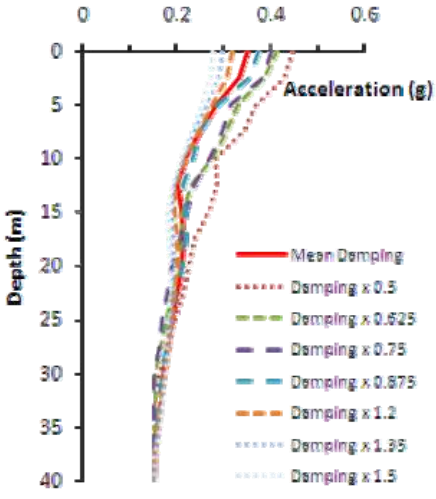

Fig. 12. Profile of maxmimum acceleration for sensitivity study with regard to damping

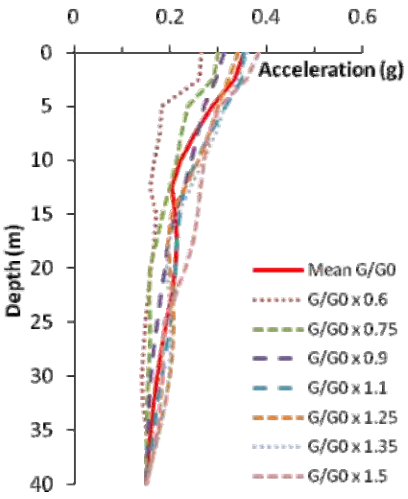

Fig. 13. Profile of maxmimum acceleration for sensitivity study with regard to shear modulus degradation

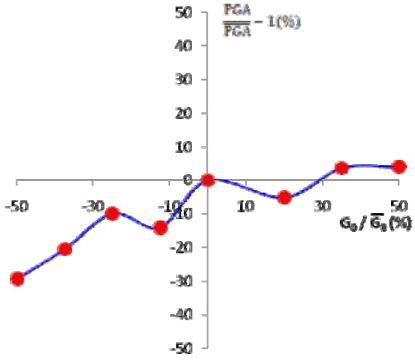

Fig. 14. Sensitivity plot with regard to G_0

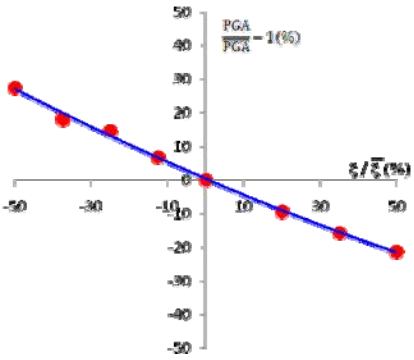

Fig. 15. Sensitivity plot with regard to damping

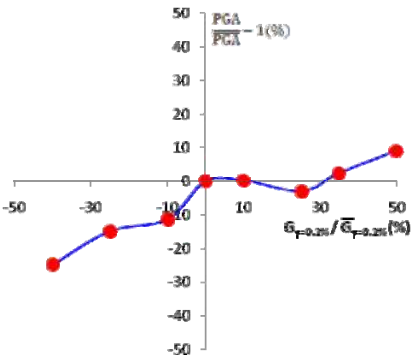

Fig. 16. Sensitivity plot with regard to shear modulus degradation

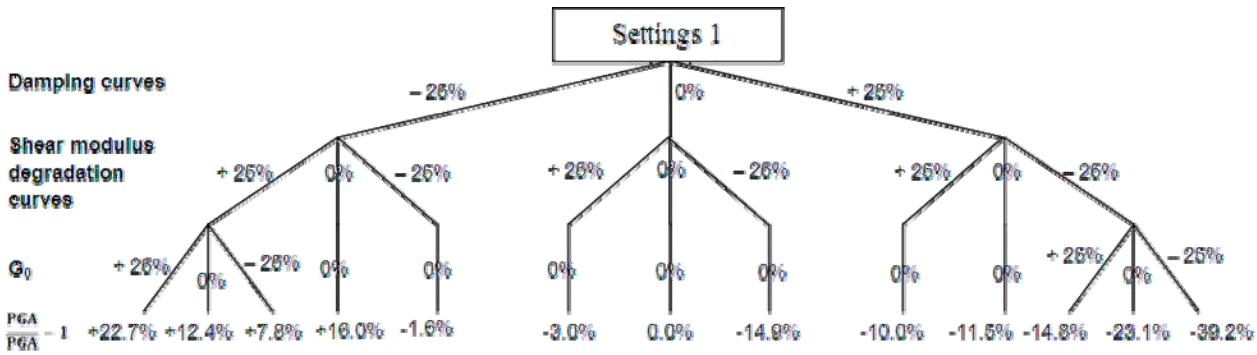

Fig. 17. Combined effect of uncertainty of damping and shear modulus degradation curve

Section we illustrate the complexity of ground responses and interpretation of ground response results in seismic engineering design due to the existence of a soft layer. We will first repeat the sensitivity study exercise of Setting 1 for Setting 2, for the particular case where the soft layer is assumed at 15~20m depth. Then we will consider another uncertainty with respect to the location of this soft/weak layer.

4.1 Variation of initial modulus, damping ratio and shear modulus curves

For the particular setup of Setting 2 with a soft layer between 15~20m (see Fig. 3), we performed a series of sensitivity tests for each individual factors. The sensitivity plots and differences of maximum acceleration profile are presented in Figs. 20 and 23 regarding to G_0; in Figs. 21 and 24 regarding to damping curves; and Figs. 22 and 25 regarding to shear modulus degradation curves. Note that compared to Section 3.2, sensitivities to damping curves are much lower, possibly due to the strong damping effect of the soft layer. Again the uncertainties regarding to damping curves are nearly linear, while uncertainties about initial modulus and shear modulus degradation curves are more nonlinear. However, as we have chosen a particular case for the case with presence of weak layer, we choose not to make general comments regarding to the nonlinearity. For simplicity, the joint effects of individual factors on the prediction of PGA were not examined.

4.2 Variation of location of soft layer

We then investigate the effects of the location of the weak layer. The weak layer is assumed with 5m thickness and its location is assumed randomly between 0~40m with a 5m interval. Fig. 26 shows the profile of maximum acceleration for each location of weak layer. Note that the presence of weak layer causes a shift of maximum acceleration below ground, i.e. the PGA is not equal to $A_{\max\_site}$ (the maximum acceleration of the total site). For the cases where no weak layer exists, PGA = $A_{\max\_site}$.

This could have significant influence on liquefaction evaluation and other design works based on PGA, since regular liquefaction analysis is usually not based on the acceleration profile, but instead is based on only the surface PGA and magnitude of earthquake (Youd et. al. 2001). In Youd et al. (2001) the maximum accelerations for soil layers below surface were assumed to decrease with depth. As seen from Fig. 26, this is clearly not the case when a soft layer exists. As a consequence, the regular liquefaction analysis may significantly underestimate the liquefaction potential for sandy sites with a soft layer. Fig. 27 shows the effects on PGA and $A_{\max\_site}$ due to existence of the soft layer. In Fig. 27, the solid line represents the ratio of PGA to the $\overline{PGA}$, where $\overline{PGA}$ represents the PGA of Setting 1 with no weak layer; the dotted line shows ratio between $A_{\max\_site}$ (the maximum acceleration for the whole site) and $\overline{A_{\max\_site}}$ of the comparison case. We can see that due to the existence of the soft/weak layer, $A_{\max\_site}$ is generally lower than the comparison case, PGA itself would not be able to represent the main characteristics of the site, and the influence on seismic design could be significant.

5 VALIDATION USING THE FINITE ELEMENT METHOD

Frequently in engineering applications, we are concerned with deformation of soil-structure system under seismic loading instead of simply free-field responses. To do that, computer modeling in 2D or 3D using the finite element method (FEM) or the finite difference method, is necessary. For dynamic analysis, some sophisticated FEM programs assume complex

hysteresis soil constitutive models which are much different with the equivalent linear method adopted by SHAKE. The material parameters for these models may not be readily available, and observation or test data are oftentimes lacking; other common geotechnical FEM programs (e.g. PLAXIS) still lack this capacity of modeling cyclic behavior of soils.

To make direct use of commercial software such as PLAXIS, one could obtain the converged soil moduli from SHAKE analysis and use them in PLAXIS for a 2D time history analysis. By doing this a first degree approximation is made to the dynamic soil behaviors under seismic loading; since in this way the shear moduli will remain the same as those of free-field analysis and will not change with additional shear strains due to soil-structure interaction. In other words, the strain-dependent shear modulus is now assumed fixed. This approximation may be rather crude for certain applications, but may still be much superior to the practice of using a regular soil constitutive model, such as Mohr-Coulomb model which will use the static soil parameters. This way of combining SHAKE ground response analysis and FEM analysis can offer a quick solution to regular engineering problems.

This approach also implies a requirement of agreement of predictions for 1D problem between SHAKE and the FEM method (e.g. PLAXIS). A closer examination of these two methods shows that this may or may not be straightforward, as SHAKE is a frequency domain method and PLAXIS is a time domain method, these two methods treat nonlinearity and material damping ratios in somewhat different ways. Therefore it is not always appropriate to juxtapose these two methods and call the equivalent. In the following we will compare the dynamic analyses between SHAKE and one commonly-used geotechnical software PLAXIS and highlight the key differences between the two for time history analysis.

5.1 Comparison of PGA with sine wave input motion

Table 2 shows a series of tests performed to compare PLAXIS and SHAKE solutions assuming sine input motion:

$$a = 0.1g \sin(\frac{2\pi}{T} t) \tag{1}$$

where the period of input motion T varies from 0.5 to 2 seconds. Note that the damping ratios for PLAXIS analysis are typically Rayleigh and therefore will vary with frequency content (see Fig. 28); when calibrating damping ratios, this should be taken into consideration. For Setting 1, in Cases 1, 2 and 3, when matching Rayleigh damping with period of sine wave, the difference is rather small (less than 4%); for Cases 5 and 6, Rayleigh damping is not matched at the period of sine wave, rather noticeable differences are resulted (18% difference for Case 5); for Setting 2, when a soft layer exists, even a direct match of period generates a difference of 15% (Case 8).

5.2 Comparison of PGA with Japanese III input motion

The realistic time history of a seismic excitation is rarely close to simple harmonic. Using the Japanese III motion as shown in Fig. 10, Table 3 shows the analysis cases carried out and the comparison between PLAXIS and SHAKE. Note that the differences between the two approaches are noticeably higher. In addition to the reason explained in Section 5.1, the other reason is that the real-life input motion normally contains different frequency content, therefore no matter at which frequency we set as the minimum damping for Rayleigh damping, differences persist. Note that normally if we match damping ratios of FEM (e.g. PLAXIS) with SHAKE, we expect lower PGA from FEM analysis; since at other frequencies PLAXIS gives a higher damping and therefore, more energy dissipation. However, for Setting 2 with a weak layer, PLAXIS gives a higher PGA. This again shows the strong nonlinearity due to existence of a soft layer.

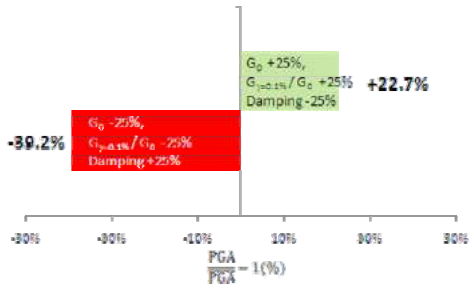

Fig. 18. Comparison on the combination of uncertainties caused maximum deviation from mean PGA

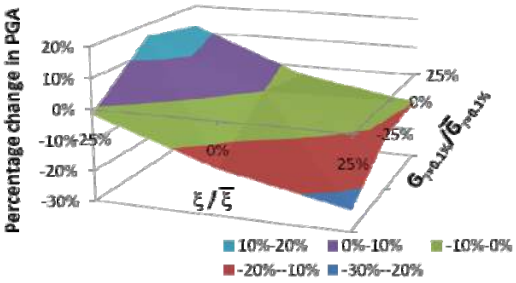

Fig. 19. Effects on PGA due to combination of damping and shear modulus degradation curves (constant G_0)

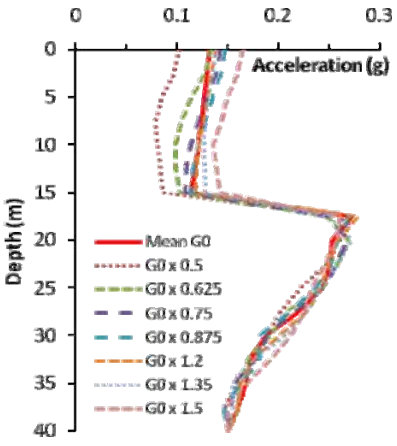

Fig. 20. Profile of maxmimum accelerations with regard to G_0 (Setting 2)

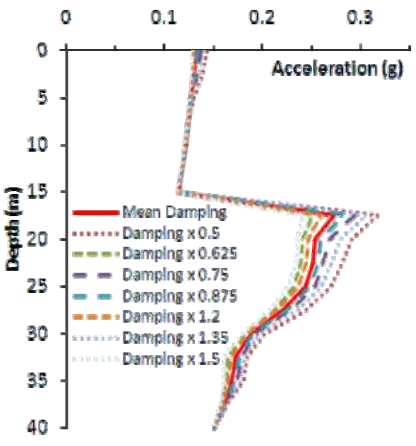

Fig. 21. Profile of maxmimum accelerations with regard to damping (Setting 2)

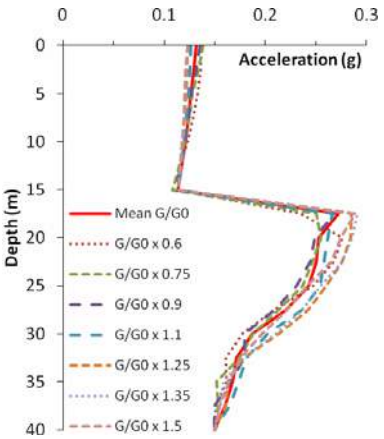

Fig. 22. Profile of maxmimum accelerations with regard to shear modulus degradation (Setting 2)

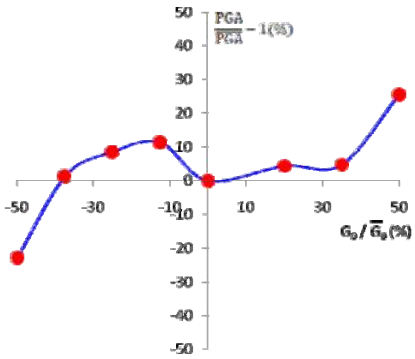

Fig. 23. Sensitivity plot with regard to G_0 (Setting 2)

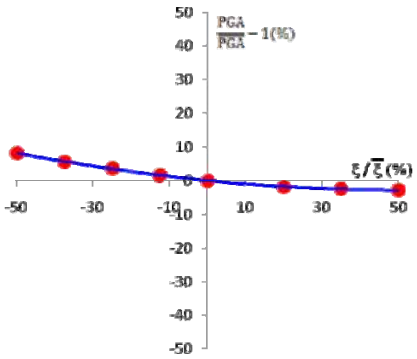

Fig. 24. Sensitivity plot with regard to damping (Setting 2)

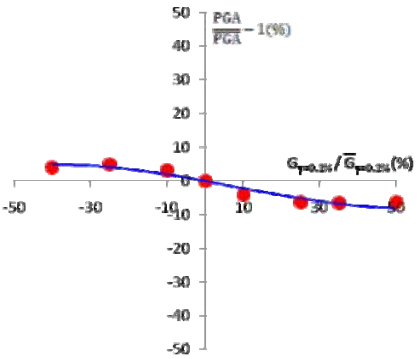

Fig. 25. Sensitivity plot with regard to shear modulus degradation (Setting 2)

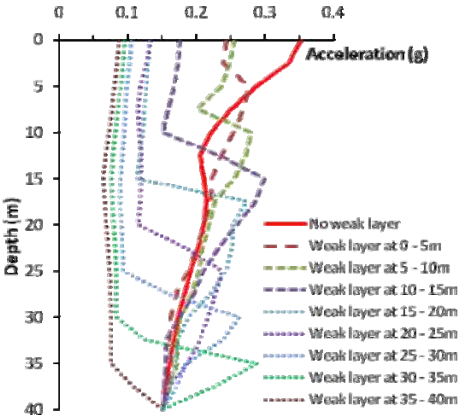

Fig. 26. Profile of maxmimum accelerations for sensitivity study with regard to location of weak layer

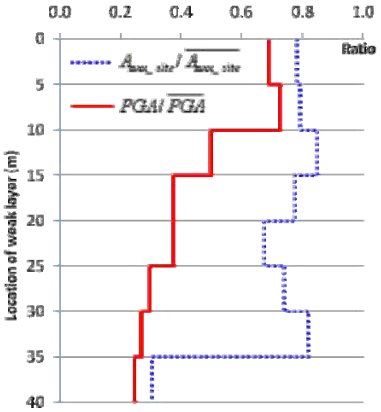

Fig. 27. Effects of weak layer location on PGA and A_{max_site}

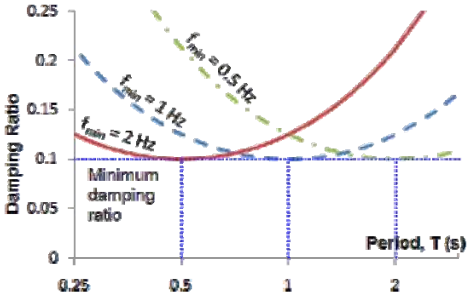

Fig. 28. Rayleigh damping adopted by PLAXIS (assuming minimum damping ratio set as 0.1)

Table 2. Analysis cases for FEM/SHAKE comparison

Case	Soil profile	Period of sine wave	Matching period (minimum damping)	Site period (based on initial modulus)	Site period (based on converged modulus)	PGA (g)		
						SHAKE	PLAXIS	Difference
1	Setting 1	0.5 s	0.5 s	0.72	1.05	0.2041	0.2019	-1%
2	Setting 1	1 s	1 s	0.72	1.55	0.4685	0.4484	-4%
3	Setting 1	2 s	2 s	0.72	0.95	0.1246	0.1243	-0.2%
4	Setting 1	0.5 s	1s	0.72	1.05	0.2041	0.1953	-4%
5	Setting 1	0.5 s	2s	0.72	1.05	0.2041	0.1683	-18%
6	Setting 2	0.5 s	0.5 s	0.83	1.20	0.0494	0.0501	+1%
7	Setting 2	1 s	1 s	0.83	1.38	0.0447	0.0474	+6%
8	Setting 2	2 s	2 s	0.83	1.66	0.1300	0.1490	+15%

If it is desirable to minimize the differences between PLAXIS and SHAKE analyes, one possible remedy could be to adjust the damping ratios such that the PGA of PLAXIS match with those of SHAKE analysis, but this practice is still debatable. Nevertheless, the idea is to generate a close enough 1D response between SHAKE and FEM program such as PLAXIS, and then let the FEM program PLAXIS work out the soil-structure interaction as well as 2D effects.

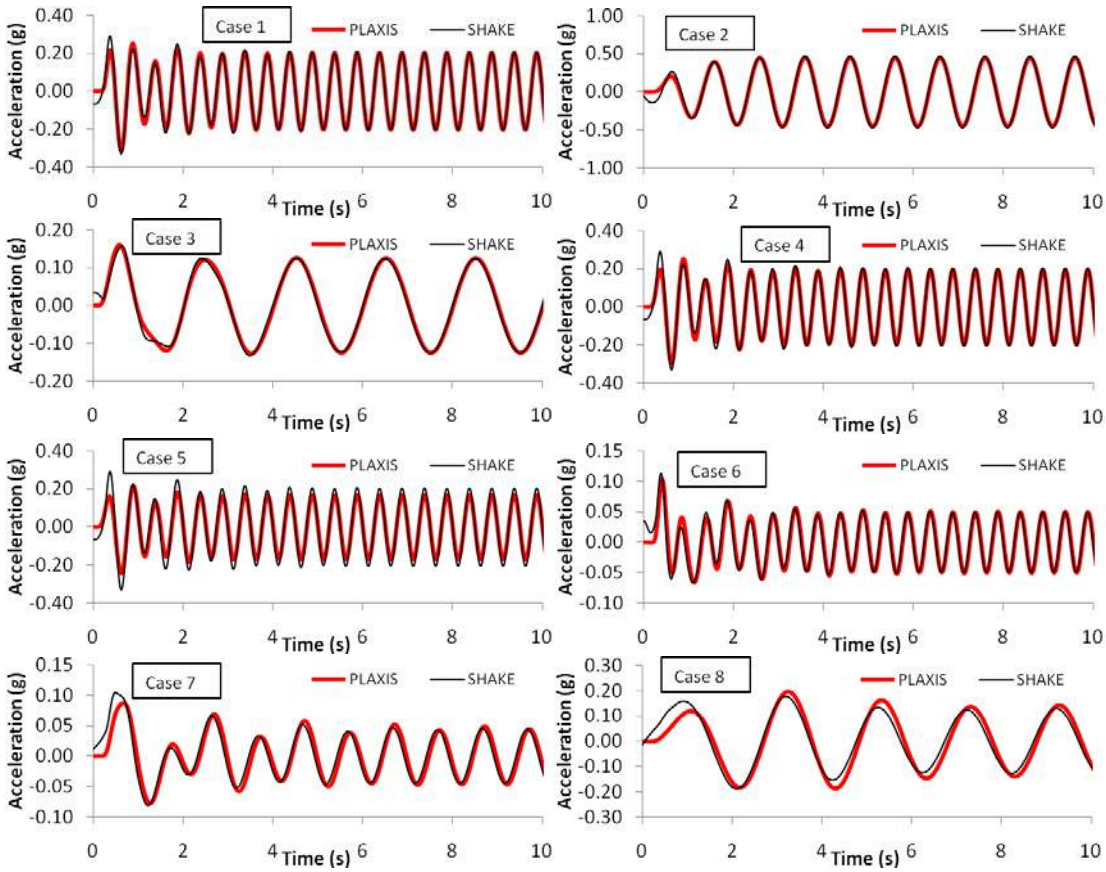

Fig. 29. Time history of acceleration at ground surface, Cases 1~8

5.3 Remarks

In this Section we performed, for these two typical settings, a direct comparison between SHAKE solution and a FEM formulation, PLAXIS DYNAMICS. We noticed the good agreement for certain set of parameters and noticeable difference for the others. Since in PLAXIS analysis, we matched damping ratios at the frequency where damping is at the minimum of Rayleigh damping (see Fig. 28), it is expected that PLAXIS may produce lower PGA than SHAKE in a general sense. However, we found that for Setting 2 where a weak soil layer exists, this is not necessarily the case, possibly due to the strong nonlinearity of the problem and the abrupt change of soil properties at the location of weak soil layer. Due to limitation of space, here we are mostly pointing out the potential problems rather than fully solving them. For a truly nonlinear treatment we refer to Borja (1994) where a bounding surface plasticity model was introduced and Li et al. (2004) where pore water pressure was modeled in a fully coupled way with solid phase displacements. Although it is clearly the direction for ground response analyses and dynamic soil-structure problems, we still acknowledge the dominate usage of simplified engineering software such as SHAKE and its validity within its intended area of applications. The authors here intend to help to improve the state of practice in seismic design and to build a bridge between state-of-practice and state-of-art.

Table 3. Analysis cases for FEM/SHAKE comparison with Japanese III time-history curves

Case	Soil profile	Matching period (minimum damping)	Site period (based on initial modulus)	Site period (based on converged modulus)	PGA (g)		
					SHAKE	PLAXIS	Difference
9	Setting 1	0.5 s	0.72	1.19	0.3520	0.3091	-12%
10	Setting 1	1 s	0.72	1.19	0.3520	0.2976	-15%
11	Setting 1	2 s	0.72	1.19	0.3520	0.2527	-28%
12	Setting 2	1 s	0.83	1.49	0.1316	0.1537	+17%

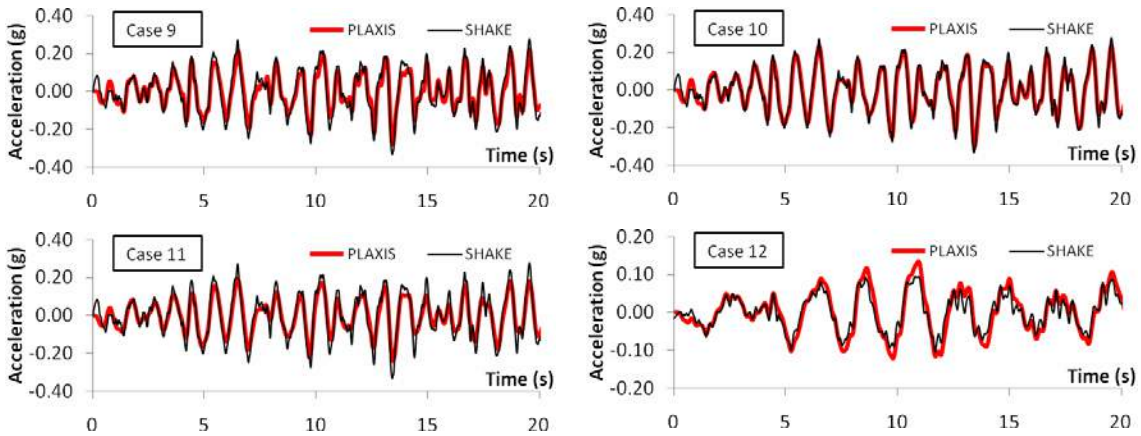

Fig. 30. Time history of acceleration at ground surface, Cases 9~12

6 CONCLUSIONS

In this paper we examined current practices of ground response analyses using SHAKE and proposed a rational way of performing analysis and making recommendations. Using this systematic approach, we considered two typical settings for ground response analyses, and

carried out sensitivity analyses with regard to dynamic soil parameters. From these analyses, we highlighted the importance of sensitivity study and suggested that the PGA from ground response analyses should take the form of a range rather than a single value based on average curves. In this way we can take into account the uncertainties in dynamic soil parameters to give a credible estimate of PGA, which may be used for a number of applications including liquefaction analysis, building design and pseudo-static retaining wall design.

In the second part of the paper we performed a calibration of SHAKE using a FEM program PLAXIS. We highlighted the differences between the two, which are fundamentally due to the differences between the time-domain and frequency domain methods. This should be given particular attention especially when doing soil-structure interaction analysis, to ensure a consistent and rational approach. This paper also motivates truly nonlinear and fully coupled approach for soil-structure interaction problems. Although these methods are still largely used in academia rather than as a regular practice in the industry, it has been more and more a necessity for high profile large scale infrastructure projects with higher demand for seismic design.

ACKNOWLEDGEMENT

We thank AECOM Asia in its support regarding the use of software and other resources. We also thank Professor Ronaldo Borja from Stanford University who provided constructive comments during the preparation of this paper.

REFERENCES

Journal

Borja, R.I. and Amies, A.P. (1994), "Multiaxial cyclic plasticity model for clays", J. Geotech. Eng., ASCE, Vol. 120(6), 1051-1070.

Li, C., Borja, R.I., Regueiro, R.A. (2004), "Dynamics of porous media at finite strain". Comput. Meth. in Appl. Mech. and Eng., Vol. 193(36-38), 3837-3870.

Seed, H. B., Wong, R. T., Idriss, I. M., and Tokimatsu, K. (1984), "Moduli and damping factors for dynamic analyses of cohesionless soils". J. Geotech. Eng., ASCE, Vol. 112(11), 1016-1032.

Youd, T.L., et al. (2001), "Liquefaction resistance of soils: summary report from the 1996 NCEER and 1998 NCEER/NSF workshops on evaluation of liquefaction resistance of soils", J. Geotech. and Geoenvironmental Eng., Vol. 127, 817-833.

Book

EPRI (1993), Guidelines for determining design basis ground motions, Electric Power Research Institute, Palo Alto, CA, Vol. 1, pp. 8-1 through 8-69.

Japan Road Association (2002), Highway Bridge Design Specification Part V: Seismic Design.

LARGE DEFORMATION FINITE ELEMENT ANALYSIS OF OFFSHORE PENETRATION TESTS

Y. Tian
Centre for Offshore Foundation Systems, University of Western Australia, Perth, WA, Australia

D. Wang
Centre for Offshore Foundation Systems, University of Western Australia, Perth, WA, Australia

M. J. Cassidy
Centre for Offshore Foundation Systems, University of Western Australia, Perth, WA, Australia

ABSTRACT: *Large deformations are commonly encountered in offshore geotechnical applications, with typical examples including penetrometer characterization, pipeline laying and buckling, spudcan preloading, anchor installation, and anchor keying and pull out. As the oil and gas industry pushes into deeper water, this large deformation challenges are becoming more severe rather than mitigated. As one example in deep water, full flow penetrometers are widely used in geotechnical site investigations to evaluate the behaviour of soft clay. Offshore engineers therefore require reliable, yet easily accessible, numerical approaches that can consistently simulate these large deformation penetration processes. Although the finite element method is the most popular numerical method in geotechnical engineering, the traditional small strain finite element analysis is challenged in these large deformation events due to the excessive mesh distortion.*

In this paper, the large-amplitude penetration of the full flow penetrometers and pipeline are studied using three approaches based on the general concept of Arbitrary Lagrangian-Eulerian (ALE) method. The three approaches are: the Remeshing and Interpolation Technique with Small Strain, featured with standard Lagrangian increments but with periodic remeshing; the Adaptive Meshing method, using a single mesh typology definition but with adaptive relocation of the element nodes; and the Coupled Eulerian Lagrangian approach. The last methodology employs Eulerian mesh to model the soil and the soil material is allowed to flow through the elements.

After comparing the numerical results from the three ALE approaches, the computing accuracy and robustness are discussed and new insight into the offshore application of the ALE methods is also presented.

1 INTRODUCTION

Large displacement of structural elements relative to seabed sediments is a routine practice in offshore geotechnical engineering. Some examples of this practice are the full-flow penetrometer tests, pipeline laying, lateral buckling and axial walking of the pipeline, spudcan penetration and the pull out of various anchorage systems.

For in-situ geotechnical investigation in deep waters, the full-flow penetrometers, such as the cylindrical T-bar and the spherical ball, are being proven to be more accurate in softer soils than the traditional vane shear test and piezocone penetration test. The latter usually requires corrections of the raw measured cone resistance and involves uncertainties over

appropriate cone factors relating net cone resistance to shear strength. In contrast, as shown in Fig.1, full-flow mechanism is developed around the advancing probe. Since the projected area of the shaft is only ~10 % of that of the probe, the small region where the shaft connects to the cylindrical bar or spherical ball puts negligible influence on the full flow. The advantages of "full-flow" penetrometers over cone penetration tests or vane shear tests have been discussed by Randolph (2004), Einav and Randolph (2005), Chung (2005) and Zhou et al. (2008): (1) The "full-flow" penetrometers have a "flow-around" mechanism and much larger projected area compared with the shaft. Consequently, correction to the measured penetration resistance becomes minimal, which will lead to a more accurate estimation of the soil characteristic; (2) The resistance is less influenced by secondary soil characteristic such as rigidity index or the in situ stress ratio because of the flow around mechanism; (3) The "full-flow" mechanism is well understood by plasticity theory, which gives a robust factor to interpret penetration resistance to soil characteristic; (4) Resistance is also measured during extraction. Cyclic penetration tests can be used to evaluate the remoulded or softening soil characteristic.

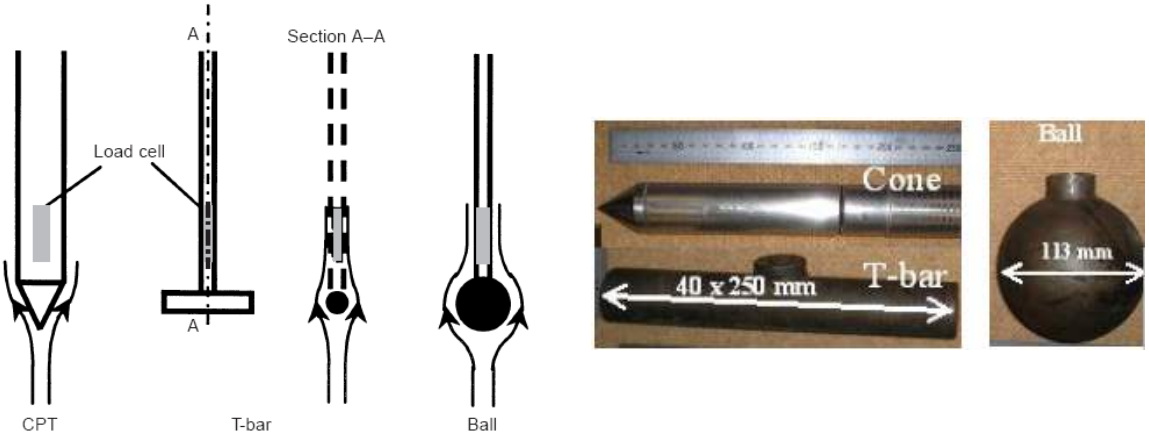

Fig. 1. (a) Schematic of cone, T-bar and ball penetrometers (after Randolph et al. 2000) (b) Model penetrometers (after Zhou and Randolph 2007)

Another typical large-amplitude penetration problem in deep water is the laying of on-bottom pipelines. The embedment of the pipeline is generated due to contact force acting on the touch-down zone, which is much larger than pipe self weight. The movements of the laying vessel and scourring around the pipe can lead to deeper penetration. Offshore engineers require valid, yet easily accessible, numerical approaches to consistently simulate these large deformation penetration problems. However, the traditional small strain finite element programs based on total or updated Lagrangian formula are inadequate in these large deformation applications due to the excess mesh distortion. In this paper, three approaches belonging to the Arbitrary Lagrangian-Eulerian (ALE) are adopted to dealing with the excess mesh distortion. The three approaches are the Remeshing and Interpolation Technique with Small Strain (RITSS) (Hu and Randolph, 1998; Wang et al. 2010a, 2010b), and Adaptive Meshing technique (AM) and Coupled Eulerian-Lagrangian (CEL) approach encoporated in the commercial package ABAQUS/Explicit.

2 LARGE DEFORMATION ANALYSIS METHODS

The ALE method is one of the most effective methods to analyze large deformation problems. The basic concept of the ALE method is to set the material movements independent of the mesh, followed by convection of the material within the fixed elements. The three approaches used in the following studies are essentially different forms of the ALE method:

(1) Remeshing and Interpolation Technique with Small Strain (RITSS) approach: The RITSS approach was proposed by Hu and Randolph (1998) and is based on standard small strain Lagrangian increments but with frequent mesh regeneration. At the beginning of each increment, the deformed soil is remeshed and the stresses and material properties are interpolated from the old mesh to the new mesh. This interpolation is similar to the convection of the materials for Eulerian computation. The advantage of the RITSS strategy is that it can be coupled with any standard FE code. In this paper's study, the commercial package, ABAQUS/Standard, is employed to conduct updated Lagrangian calculation in each increment. The popular stress recovery technique, Superconvergent Patch Recovery, is adopted for interpolation from the old mesh to the new mesh. The detailed procedure of ABAQUS-based RITSS analyses can be found in Wang et al (2010a; 2010b). In this method's analysis cases, the soil is meshed with quadratic triangular elements.

(2) Adaptive meshing (AM) technique incorporated in ABAQUS/Explicit (Dassault Systèmes, 2010): This technique is in principal similar to the RITSS approach except that the mesh topology is unchanged. The nodes in specified adaptive domains are frequently adapted to remain reasonable element shape during large deformation analysis. However, the topology i.e. the number of elements and connectivity of each element is not altered. A second-order advection proposed by Van Leer (1977) is involved in this adaptive technique to map the field variables to the new mesh. The soil is meshed with linear quadrilateral elements in the AM analyses.

(3) Coupled Eulerian-Lagrangian (CEL) approach in ABAQUS/Explicit (Dassault Systèmes, 2010): The soil undergoing large displacements is discretized as Eulerian mesh, whilst the structure elements, such as pipeline, T-bar and Ball penetrometer, are discretized as Lagrangian mesh. The interaction between the structure elements and the soil is modeled with general contact algorithm. The Eulerian elements are fixed in space, with soil material flowing in or out of the elements. Since Eulerian elements may not always be 100% full of material, the material boundaries are tracked automatically to obtain the soil surfaces and structure/soil interfaces. The Eulerian mesh generated before the calculation has to be large enough to accommodate the movements of the soil. Only 3D simulations are available in the current version of ABAQUS CEL, so the plane strain or axial symmetric analyses in this paper are implemented by taking a slice or a quarter. The soil is meshed with 8-node linear hexahedron elements with reduced integration.

3 CALCULATION EXAMPLES OF OFFSHORE PENETRATION

The above mentioned methods are employed to investigate undrained penetrations of T-Bar, pipeline and ball penetrometer in soft clays. The diameters of the penetrometers are taken as representative sizes in the offshore industry (Low, 2009). The soil is modeled as elastic-perfectly plastic material with the Tresca yield criteria. The undrained soil strength is taken as homogeneous or increasing with the soil depth for normally consolidated (NC) clay:

$$s_u = s_{um} + kz \tag{1}$$

where s_u is the undrained shear strength; z is soil depth from the surface and s_{um} is the shear strength at the soil surface; and k is the strength gradient, with $k = 0$ meaning a homogeneous soil. The Young's modulus E of the soil is taken as 500 s_u and the Poisson ratio ν is considered as 0.49 to model the constant volume under undrained conditions.

Since their stiffness is far higher than the soil, the penetrometers or the pipes are modeled as rigid bodys. The interaction between penetrometers and soil is modeled as "hard-contact pairs". The interface is taken as either fully rough or smooth. Due to the suction generated in

the undrained soil behaviour, the soil is assumed to remain attached to the penetrometer or pipe after occurrence of contact in the RITSS and AM. In CEL, however, the above assumption is not allowed due to the "general contact" used (Dassault Systèmes, 2010). The calculation cases are detailed in Table 1. Although the AM and CEL simulations are conducted in explicit dynamic analysis, all these study cases are to investigate the static responses. Therefore, the penetration velocity has to be sufficiently slow to diminish the inertia effect. The velocity of T-bar, pipeline and ball are taken as 0.0024m/s, 0.012m/s and 0.00678m/s respectively. The calculation cases are detailed in Table 1.

Table 1. Calculation cases of cylindrical object penetration

Calculation example	Case name	Penetrometer diameter D (m)	Soil type	Soil shear strength (kPa)	Penetrometer-soil contact condition
T-bar	TSH*	0.04	Homogeneous	5	Smooth
	TRH		Homogeneous	5	Rough
	TSN		Normal consolidated	0.1+1z	Smooth
	TRN		Normal consolidated	0.1+1z	Rough
Pipeline	PSH	1	Homogeneous	9	Smooth
	PRH		Homogeneous	9	Rough
	PSN		Normal consolidated	5+1.5z	Smooth
	PRN		Normal consolidated	5+1.5z	Rough
Ball	BSH	0.113	Homogeneous	5	Smooth
	BRH		Homogeneous	5	Rough
	BSN		Normal consolidated	0.1+1z	Smooth
	BRN		Normal consolidated	0.1+1z	Rough

* The first letter the of Case Name stands for penetrometer: **T**-bar, **P**ipeline or **B**all; the second stands for contact condition: **S**mooth or **R**ough; the third stands for soil type: **H**omogeneous or **N**ormal consolidated.

In the T-bar and pipeline cases, infinite long T-bar or pipeline is considered (plane strain condition). The RITSS and AM can conduct plane strain analysis, whilst a slice of the T-bar or pipeline is utilised in the CEL analyses to mimic the plane strain condition (only 3D is supported in the current ABAQUS version). In the ball cases, axial symmetric conditions are employed in RITSS and AM and a quarter of the three dimensional ball is adopted in the CEL. The mobilized soil resistance is normalized as a bearing capacity factor N_c

$$N_c = \frac{V}{s_u L} \tag{2}$$

where V is the soil resistance; L is the maximum projecting area, $L = D$ under plane strain condition and $L = \pi D^2/4$ under axial symmetric condition; and s_u is adopted as the soil strength at the depth of the structure centre.

For deep T-bar/pipe and ball without shaft, ideal full flow mechanisms are formed and the theoretical solution of N_c from upper and lower bound limit analyses are listed in Table 2 (Randolph & Houlsby, 1984; Einav & Randolph, 2005; Martin & Randolph, 2006). The RITSS approach is first verified by comparison with the analytical solutions. The diameters of penetrometers and soil strength are the same as the corresponding values in Table 1. The penetrometer is "wished in place" with an initial embedment depth of 4.5D. The soil is weightless to remove the effect of overburden pressure on the bearing capacity. The load-

displacement curves from the RITSS are shown in Fig. 2. In general, the RITSS capacity factors agree well with the analytical solution in Table 2.

Table 2. Theoretical solution of deep flow penetration

Penetration condition	Smooth		Rough	
	Lower bound	Upper bound	Lower bound	Upper bound
Plane strain T-bar/Pipeline	9.14	9.2	11.94*	11.94*
Axial symmetric Ball penetrometer	10.97	11.36	15.1	15.31

* The lower bound and upper bound solutions are equal and thus it is the exact solution.

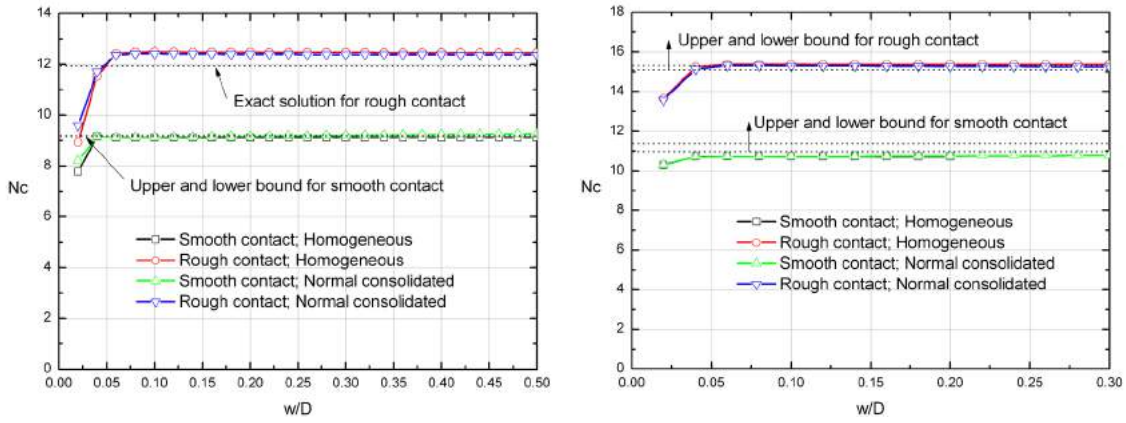

(a) T-bar/pipeline (b) Ball penetrometer

Fig. 2. Wished-In-Place cases

3.1 T-bar penetration

The original mesh used in the three methods is shown in Fig.3 (only half model is used to save computation time). The minimum element size of AM and EL is 0.1D and the size of elements around the T-bar is about 0.05D for RITSS. The dense mesh range is set as an "adaptive" zone in the AM analysis. In the CEL model, the Eulerain domain of soil is initially partly filled with soil material. The elements above the soil surface are set as "void", i.e. no soil initially in these void elements.

The soil bearing capacity factor N_c versus the depth of penetrometer centre below soil surface z is shown in Fig.4.

From the figures, we can see that the RITSS provides the smoothest load-displacement curves. In the AM simulations, the calculation stalls at a penetrate depth z/D < 2. The reason is that the AM is no longer capable to adapt the extremely distorted soil mesh. When the AM tends to keep the original mesh topology, the quality of updated mesh in the adaptive zone becomes poor, as illustrated in Fig.5. The spiky resistance from the CEL is possibly due to the dynamic effect, e.g. inertia produced in the explicit computation. Reducing the penetration velocity will smooth the results but almost linearly increase the calculation time.

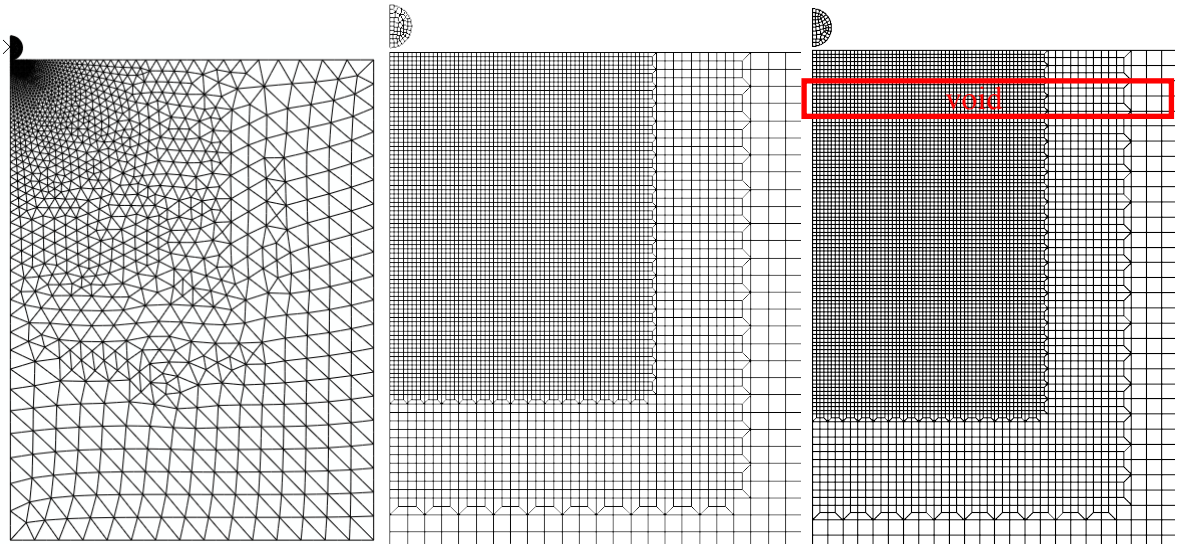

Fig. 3. FE mesh of RITSS, AM and CEL methods

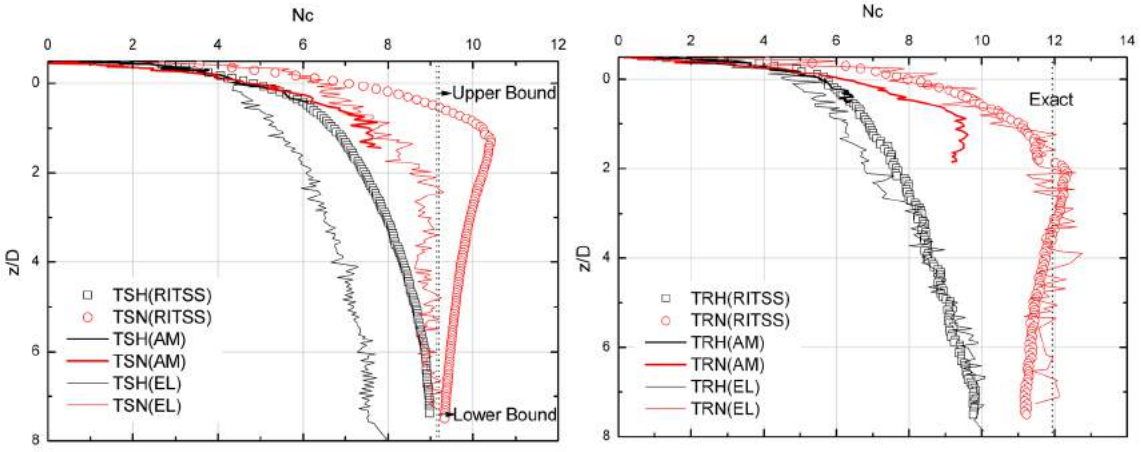

(a) smooth contact (b) rough contact

Fig. 4. Bearing capacity factor N_c versus penetrometer penetration depth z for the T-bar

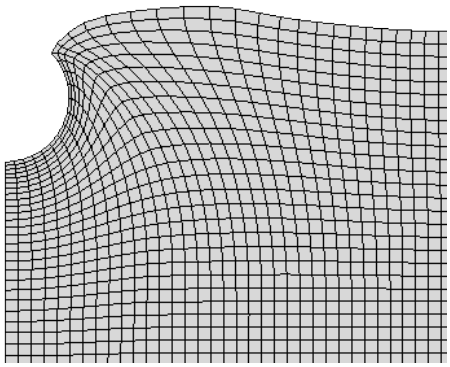

Fig. 5. The distorted mesh in AM method

In Fig. 4(a), an obvious difference between the RITSS and CEL solutions is observed for the smooth T-bar interface. The reason is thought to be the different contact algorithms adopted. In the RITSS, the penetrometer and soil are not allowed to separate once they

contact, which is to simulate the suction developed on the interface. In contrast, this no-separation behaviour is not available in CEL due to software limitations. This can be further proven in homogeneous soil: an inclined wall is formed above the T-bar shoulder in CEL simulation (Fig. 6). The full flow mechanism is not fully mobilized even the T-bar approaches an embedment depth as deep as 7D (CEL at a depth of 6.85*D* and RITSS at 6.7*D* are used because there is not no exact same penetration data due to the difference calculation time increment). Correspondingly, the CEL capacity factor in deep embedment is significantly lower than the analytical solution and the RITSS results. As shown in Fig. 6, the wall also exists in the RITSS simulation, but the gap width above the T-bar is very small, so the deep resistance from RITSS in Fig. 4(a) is marginally lower than the analytical solution.

When the T-bar interface is rough, the CEL and RITSS give close curves for both homogeneous and normally consolidated clay in Fig. 4(b), although bearing capacity factors from both methods are lower than the exact solution. The reason is similar to that presented for the smooth T-bar in homogenous soil: the large gap width above the T-bar prevents a full flow mechanism.

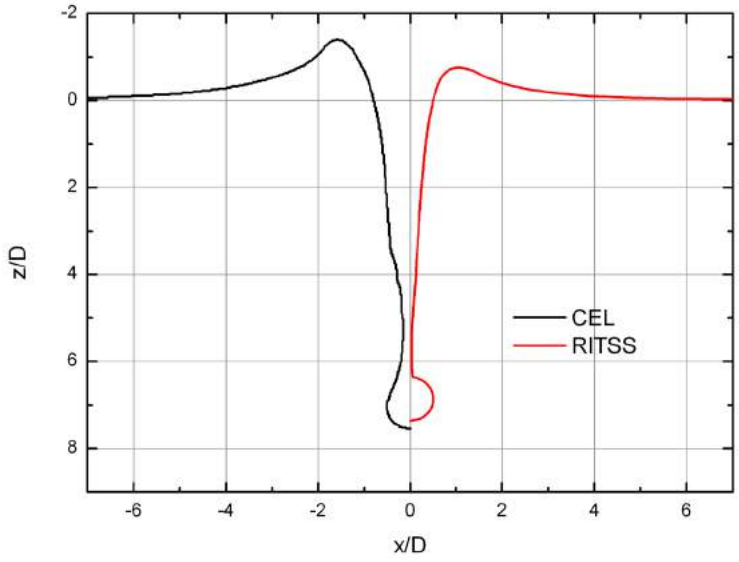

Fig. 6. Comparison of the soil surface profile between RITSS and CEL

3.2 Pipeline penetration

The pipeline penetration is similar as the T-bar analysis except a larger diameter and different soil shear strength (see Table 1). The soil bearing capacity factor N_c versus the depth of penetrometer centre below soil surface z is shown in Fig.7.

For the smooth pipe, the large overburden pressure drives the soil wall collapsing onto the pipeline to form the full flow mechanism. Thus the capacity factors of the smooth pipe reach the ultimate value at a relatively shallower depth. However, for the rough pipe, the gap above the pipe still remains as the pipe embedment depth approaches z/D = 7.5.

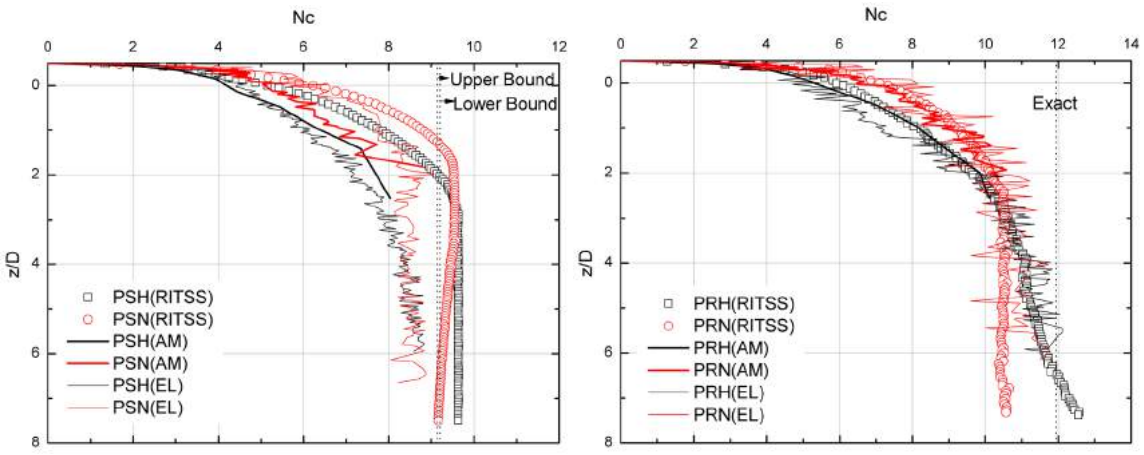

Fig. 7. Bearing capacity factor N_c versus penetrometer penetration depth z for the pipeline

3.2 Ball penetration

The T-bar is modeled as a cylindrical object in plane strain condition while the shaft is neglected. The shaft of ball penetrometer can not be neglected as it has a comparable diameter of 36mm. The density of the mesh is similar to Fig. 3, but with a fine mesh zone generated around the shaft in RITSS.

The variations of capacity factors of the ball penetrometer are shown in Fig. 8. Again, the AM simulations stop as the ball is penetrated to z/D ≈ 2 and the results as z/D < 2 are also suspicious. Comparisons between the RITSS and CEL results are consistent with the interpretation of the T-bar results: (1) for the smooth ball, the lower CEL resistance is due to the gap from the wall to the shaft. The deep capacity factor from the RITSS may be slightly lower than analytical solution due to the shaft considered in large deformation simulations. (2) for the rough ball, the RITSS and CEL give close solutions.

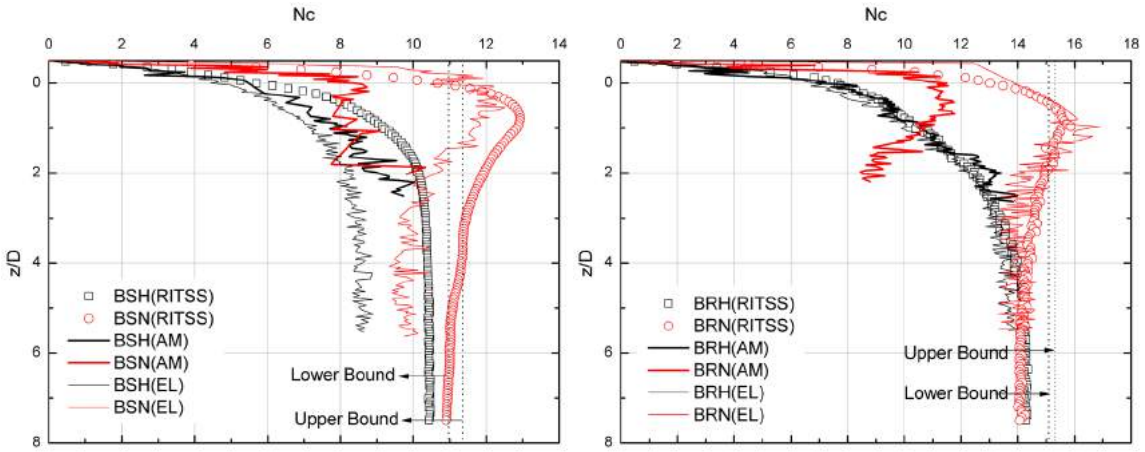

Fig. 8. Bearing capacity factor N_c versus penetrometer penetration depth z for the ball

4 CONCLUSION

Three typical large-amplitude penetration problems encountered in offshore geotechnical applications are simulated using three ALE strategies. In general, the RITSS shows a good performance and smooth results, but the implementation of the RITSS requires experienced user and in-house developed codes. The performance of AM technique in ABAQUS/Explicit is marginal and limited. The simulation stalls or terminates when it can not adapt the mesh effectively. CEL is computationally robust and easy to use even for relative novices.

Although its numerical accuracy is lower than the RITSS (at least in this paper's cases), it is a promising and potential approach.

ACKNOWLEDGEMENT

This research was funded by the Australia-China Natural Gas Technology Partnership Fund and forms part of the activities of the Australian Research Council Centre of Excellence on Geotechnical Science and Engineering. The third author is the recipient of an Australian Research Council Future Fellowship. The IT support from Mr. Kan Yu at The University of Western Australia is appreciated.

REFERENCES

Chung, S.F. (2005). Characterisation of soft soils for deep water developments. PhD Thesis, The University of Western Australia, Perth, WA, Australia

Dassault Systèmes. (2010). Abaqus Analysis User's Manual

Einav, I. and Randolph, M.F. (2005). Combining upper bound and strain path methods for evaluating penetration resistance. Int. J. Numer. Methods Eng. 63(14), 1991-2016

Hu, Y. and Randolph, M. F. (1998). A practical numerical approach for large deformation problem in soil. International Journal for Numerical and Analytical Methods in Geomechanics, Vol. 22, No. 5, 327-350.

Low, H.E. (2009). Performance of Penetrometers in Deepwater Soft Soil Characterisation. PhD Thesis, The University of Western Australia, Perth, WA, Australia

Martin, C. M. and Randolph, M. F. (2006). Upper-bound analysis of lateral pile capacity in cohesive soil. Geotechnique, 56(2), 141-145.

Randolph, M. F. and Houlsby, G. T. (1984). The limiting pressure on a circular pile loaded laterally in cohesive soil. Geotechnique, 34(4), 613-623.

Randolph, M. F., Martin, C.M. and Hu, Y. (2000). Limiting resistance of a spherical penetrometer in cohesive material. Geotechnique, Vo. 50, No.5, 573-582.

Randolph, M. F. (2004). Characterisation of soft sediments for offshore applications, keynote paper, Proc. 2nd Int. Conf. on Site Characterisation, Porto, Portugal, 1, 209-231

Van Leer, B. (1977). Towards the Ultimate Conservative Difference Scheme IV. A New Approach to Numerical Convection. J. Comp. Phy., Vol. 23, 276.

Wang, D., Hu, Y., and Randolph, M. F. (2010a) Three-dimensional large deformation finite element analysis of plate anchor in uniform clay. J. Geotech. Geoenviron. Engrg., 136(2), 355-365.

Wang, D., White, D. J. and Randolph, M. F. (2010b). Large deformation finite element analysis of pipe penetration and large-amplitude lateral displacement. Can. Geotech. J., 47: 842-856.

Zhou, H., White, D.J. and Randolph, M.F. (2008). Physical and numerical simulation of shallow penetration of a cylindrical object into soft clay. Proc. GeoCongress 2008: The Challenges of Sustainability in the Geoenvironment, New Orleans, Louisiana, USA.

Zhou, H. and Randolph, M.F. (2007). Computational techniques and shear band development for cylindrical and spherical penetrometers in strain-softening clay. Int. J. Geomech., ASCE. Vol.7, No. 4, 287-295

PREDICTION OF WELLBORE STABILITY USING AN ELASTOPLASTIC DAMAGE MODEL

A. Mohamad Hussein, D. Press, A. Pearce, G. F. Xi, X. Zhang & N. Koutsabeloulis
Schlumberger Reservoir Geomechanics Center of Excellence, Bracknell, United Kingdom

ABSTRACT: *Over time, oil production causes a change in formation pore pressure, which then leads to a change in effective stress. Localized regions of eroded material may be produced as the increased effective stresses cause shear failure around the wellbore and perforations. In the longer term this will produce 'sanding', as the grains of the sheared material pass from the formation into the oil stream. In this paper, a constitutive model based on elastoplastic damage theory is proposed which reproduces this effect under a wide range of stress changes. The sand volume produced is directly related to the degree of material damage and is dependent on plastic strains. As the damaged zone increases in size, the strength and stiffness of the region reduce. Comparisons of experimental data and numerical simulations show that the model can reproduce the observed pattern. The model has been incorporated into a geomechanical finite-element simulator and applied to a typical reservoir engineering problem under isotropic and anisotropic preproduction initial stress conditions. The results demonstrate the effect of anisotropy on the extent of the damage zone produced. Comparisons illustrate the progressive propagation of the eroded material zone with time.*

1 INTRODUCTION

Sand production usually occurs when fluid (typically oil) is produced under high rates and/or a large pressure drawdown suddenly takes place. Fluid production under such conditions will lead to erosion in certain regions of formation solids. Large amounts of sand production can cause serious problems, such as perforation and borehole instability, particularly for unconsolidated sand reservoirs. On the other hand, sand production can actually help improve oil production in heavy oil reservoirs. Sand production will lead to the formation of cavities around the borehole and thus create an increase in permeability, which will help increase the productivity of oil (Dusseault, 2007; Tremblay, 2009) but has other detrimental consequences.

A number of analytical models exist to predict sand production. These models consider the production of sand that occurs at the point of material failure; however, sands are produced even at pre-failure stages. The onset of sand production is controlled by both plastic yielding and plastic hardening. In this paper, sand production is modelled by using a new elastoplastic damage model. The damage variable is mainly based on the increase in porosity, which is a result of dilatant plastic volumetric strain accompanied by plastic shear strains.

Generally, there is a progressive reduction of elastic properties and mechanical strength with the growth of damage. Numerous authors have developed models for coupled plastic damage; these include Dragon and Mroz (1979), Ju (1989), Hayakawa and Murakami (1997),

and Chiarelli et al. (2003). The first part of this paper is devoted to the mathematical formulation of a new elastoplastic damage model. The emphasis of this study is on the modelling of sand production caused by reservoir depletion. The proposed model includes the basic features of the mechanical behaviour of sands, including plastic deformation, damage evolution, transition from volumetric compressibility to dilatancy, and degradation of mechanical properties due to damage.

The constitutive model was validated with experimental data and then implemented in a finite-element package. Numerical examples were studied to investigate the predicted damage zone and the overall behaviour of sands as a result of production.

2 FORMULATION OF THE CONSTITUTIVE MODEL

This section explains the mathematical formulation of an elastoplastic damage model. The formulated model describes the basic mechanical behavior of the material under prepeak and postpeak loading conditions.

2.1 Characterization of damage

A representation of increase in porosity due to sand production is shown in a volumetric element (Fig. 1). At the initial state (in which no sand is produced), the material has an initial porosity of ϕ_0. The change in reservoir pressure at the perforations may induce yielding, failure of material leading to the production of sand. Owing to the migration of sand grains from the formation, the porosity will tend to increase. This increase of porosity, $\Delta\phi$, is is in addition to that associated with plastic strains (dilatant volumetric and shear components). The dilatant plastic volumetric and plastic shear strains result in an increase in porosity, which is denoted by $\Delta\phi_v$ and $\Delta\phi_\gamma$, respectively.

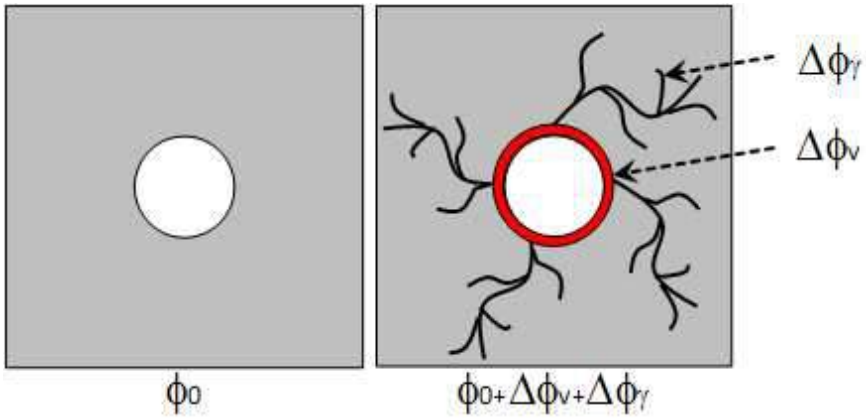

Fig. 1. Illustration of increase in porosity as a result of sand production

The damage variable is taken as the change in total average porosity. The damage is considered isotropic and is described by a scalar variable, *d*. The damage evolution is assumed to be affected by plastic deformation only. The damage scalar variable is thus defined as:

$$d = \phi - \phi_0 = A_d H\left(\varepsilon_v^p\right)\varepsilon_v^p + B_d\gamma_p \tag{1}$$

where ε_v^p is the plastic volumetric strain, γ_p is the generalized plastic shear strain. $H\left(\varepsilon_v^p\right)$ is a Heaviside step function, which describes the increase of porosity due to dilation of sand.

Two parameters, A_d and B_d, determine the evolution of damage as functions of dilatant plastic volumetric and plastic shear strain, respectively. A_d is usually equal to 1. The damage criterion is expressed as follows:

$$f_d = d - A_d H\left(\varepsilon_v^p\right)\varepsilon_v^p - B_d \gamma_p = 0 \tag{2}$$

Based on the general framework of thermodynamics, the constitutive equation is derived as:

$$\overline{\overline{\sigma}} = (1-d)C^0 : \left(\overline{\overline{\varepsilon}} - \overline{\overline{\varepsilon^p}}\right) \tag{3}$$

where $\overline{\overline{\varepsilon}}$ and $\overline{\overline{\varepsilon^p}}$ denote the total strain tensor and the plastic strain tensor, respectively. C^0 is the initial elastic stiffness tensor of undamaged material.

The Young's modulus is affected by damage and is expressed as:

$$E = E^0(1-d) \tag{4}$$

where E^0 is the Young's modulus of undamaged material.

2.2 Characterization of plastic deformation

Laboratory evidence shows that the plastic deformation of sand is dependent on confining pressure. For the determination of plastic deformations in sand, definitions of the plastic yield surface, plastic potential, and plastic hardening law are required. Based on the work of Pietruszczak et al. (1988) and Mohamad-Hussein & Shao (2007), the following nonlinear failure criterion is defined:

$$F = q' - g(\theta) * UCS\left[\frac{1}{c_1}\left(c_2 + \frac{I'}{UCS}\right)\right]^n = 0 \tag{5}$$

$$q' = \sqrt{\frac{3}{2}\overline{\overline{S'}} : \overline{\overline{S'}}}, \quad \overline{\overline{S'}} = \overline{\overline{\sigma'}} - \frac{1}{3}tr\left(\overline{\overline{\sigma'}}\right)\overline{\overline{\delta}}, \quad I' = tr\left(\overline{\overline{\sigma'}}\right) \tag{6}$$

where q' is the deviatoric stress, $\overline{\overline{S'}}$ is the tensor of deviatoric stress, $\overline{\overline{\sigma'}}$ is the effective stress tensor, and I' corresponds to the mean effective stress. c_1, c_2, and n are model parameters that describe the geometric form of the failure surface and are related to the cohesion and internal friction coefficients of the material. The variable θ represents Lode's angle. This function describes the variation of yield stress with loading direction in the deviatoric plane. In this model, emphasis is on the plastic deformation that induces sand production. For sake of simplicity, $g(\theta)$ is taken as equal to 1.

Once plastic strains are developed, the damaged zone tends to increase as a result of an increase in porosity. This increase in damage will affect the material behaviour accordingly. The uniaxial compressive strength UCS will also deteriorate with further damage. The failure surface depends on the uniaxial compressive strength, so it is affected by the damage process. A simple linear relation is proposed:

$$UCS = UCS_0(1-d) \tag{7}$$

where UCS_0 is the uniaxial compressive strength of undamaged sand.

Plastic hardening is an important mechanism in the prediction of sand production. Sands are not only produced at failure, but also at the onset of failure. The onset of sand production is governed by both plastic yielding and plastic hardening. A plastic hardening law is introduced in Eq. (5) and the plastic yield surface can be expressed in the following form:

$$f_p = q' - g(\theta) * \alpha(\gamma_p) * UCS\left[\frac{1}{c_1}\left(c_2 + \frac{I'}{UCS}\right)\right]^n = 0 \tag{8}$$

where $\alpha(\gamma_p)$ is the plastic hardening law that can be identified based on experimental considerations. A positive hardening law is used, which means that softening behaviour is entirely related to damage induced by the amount of sand produced. Inspired by the previous work of Mohamad-Hussein & Shao (2007), a hyperbolic hardening law is used:

$$\alpha(\gamma_p) = \alpha_0 + (1-\alpha_0)\frac{\gamma_p}{B+\gamma_p} \tag{9}$$

with

$$\gamma_p = \int_0^\tau \sqrt{\frac{2}{3}\dot{\overline{\overline{e^p}}} : \dot{\overline{\overline{e^p}}}}\, dt \tag{10}$$

The parameter α_0 defines the initial yield state, and the constant B controls the kinetics of plastic hardening.

Triaxial tests carried out on sand materials show plastic volume dilation caused by the imposed deviatoric stress. In this paper, sand production is related to plastic dilation. It is thus necessary to describe correctly the transition from plastic compressibility to plastic dilation by the use of a nonassociated flow rule. The plastic flow rule is controlled by the plastic potential. Inspired by the plastic models developed by Pietruszczak et al. (1988) and Mohamad-Hussein & Shao (2007), the following plastic potential is used:

$$Q = q' + \mu_c g(\theta)\bar{I}\ln\left(\frac{\bar{I}}{\bar{I}_0}\right) = 0, \quad \bar{I} = c_2 UCS + I' \tag{11}$$

The parameter $\bar{I}_0$ is the intersection point between the plastic potential surface and the axis $\bar{I}$. μ_c represents the slope of the transition line between plastic compressibility and the plastic dilation zone. The plastic strain increment is calculated from

$$d\overline{\overline{\varepsilon^p}} = d\lambda \frac{\partial Q}{\partial \overline{\overline{\sigma'}}} \tag{12}$$

The plastic consistency condition $df_p = 0$ is used to determine the plastic multiplier $d\lambda$. The following expression is thus obtained:

$$d\lambda = \frac{\frac{\partial f_p}{\partial \overline{\overline{\sigma}}'} : C^0 : d\overline{\overline{\varepsilon}}}{\frac{\partial f_p}{\partial \overline{\overline{\sigma}}'} : C^0 : \frac{\partial Q}{\partial \overline{\overline{\sigma}}'} - \frac{\partial f_p}{\partial \gamma_p}\sqrt{\frac{2}{3}\left(\mathrm{K} : \frac{\partial Q}{\partial \overline{\overline{\sigma}}'}\right) : \left(\mathrm{K} : \frac{\partial Q}{\partial \overline{\overline{\sigma}}'}\right)}} \tag{13}$$

where K is the deviatoric fourth-order tensor.

3 NUMERICAL SIMULATION OF TRIAXIAL COMPRESSION TESTS

The numerical model contains nine parameters that can be fully determined from a series of conventional triaxial compression tests. The tests performed on oil-bearing sands, and reported by Kosar (1989), have been used to calibrate the model. The values of the parameters used are listed in Table 1.

The consistency of the mathematical formulations of the model and the procedure for determining the model parameters have been validated by comparison of the numerical response of the model and the triaxial test data from the sand samples. The simulations have been performed for triaxial compression tests at various confining pressures. Fig. 2 shows the comparison of experimental data and numerical simulations for the triaxial compression tests with confining pressures of 50 kPa, 150 kPa, and 250 kPa, respectively. There is a reasonable agreement between the model's prediction and the laboratory test data, particularly at relatively high confining stress levels. The model is able to predict the main features of sand behaviour such as hardening and failure. More importantly, the variation of volumetric strain shows that the transition between plastic compressibility and plastic dilation is reproduced correctly by the model.

Table 1. Model parameters for sand

Plastic Parameters	Damage Parameters
$c_1 = 2.8$	$A_d = 1$
$c_2 = 0.5$	$B_d = 1$
$n = 1$	
$UCS_0 = 20kPa$	
$\eta_c = 0.32$	
$\alpha_0 = 0.20$	
$B = 0.0001$	

4 NUMERICAL EXAMPLE

The constitutive model has been implemented in a finite-element package and the proposed model was applied to a typical reservoir engineering problem. The aim of this application was to study the sand production arising from oil production. The geometries of the borehole and perforations are illustrated in Fig. 3. The diameter of the borehole is 0.30 m. Four perforations were considered, each of 0.5 m length. Both isotropic and anisotropic initial stress (before production) conditions were considered to determine the difference in behaviour on sand production. The initial effective stresses before production were taken as shown in Eqs. (14) and (15). For the case of isotropic preproduction stresses,

$$\sigma'_{xx} = \sigma'_{yy} = -12{,}600kPa \tag{14}$$

For the case of anisotropic preproduction stresses,

$$\sigma'_{xx} = 0.85\sigma'_{yy} = -10{,}710kPa \tag{15}$$

The two cases were solved under plane strain conditions. The oil production process was simulated by applying a drawdown pressure of 1000 kPa at the perforation walls.

Fig. 4 shows the change in pore pressure distribution at different production times. The zone of pressure change is influenced by and is related to the reservoir permeability and production time, respectively.

The changes in pressure around the perforations gave rise to a change in effective stresses and thus plastic yielding of the sand formation. Fig. 5 shows the distribution of plastic shear strain resulting from production for the case of isotropic preproduction stresses. A plastic shear zone developed and propagated between the tips of the perforations. Because of the initial in-situ stresses considered in this example, the distribution of the plastic zone was symmetrical.

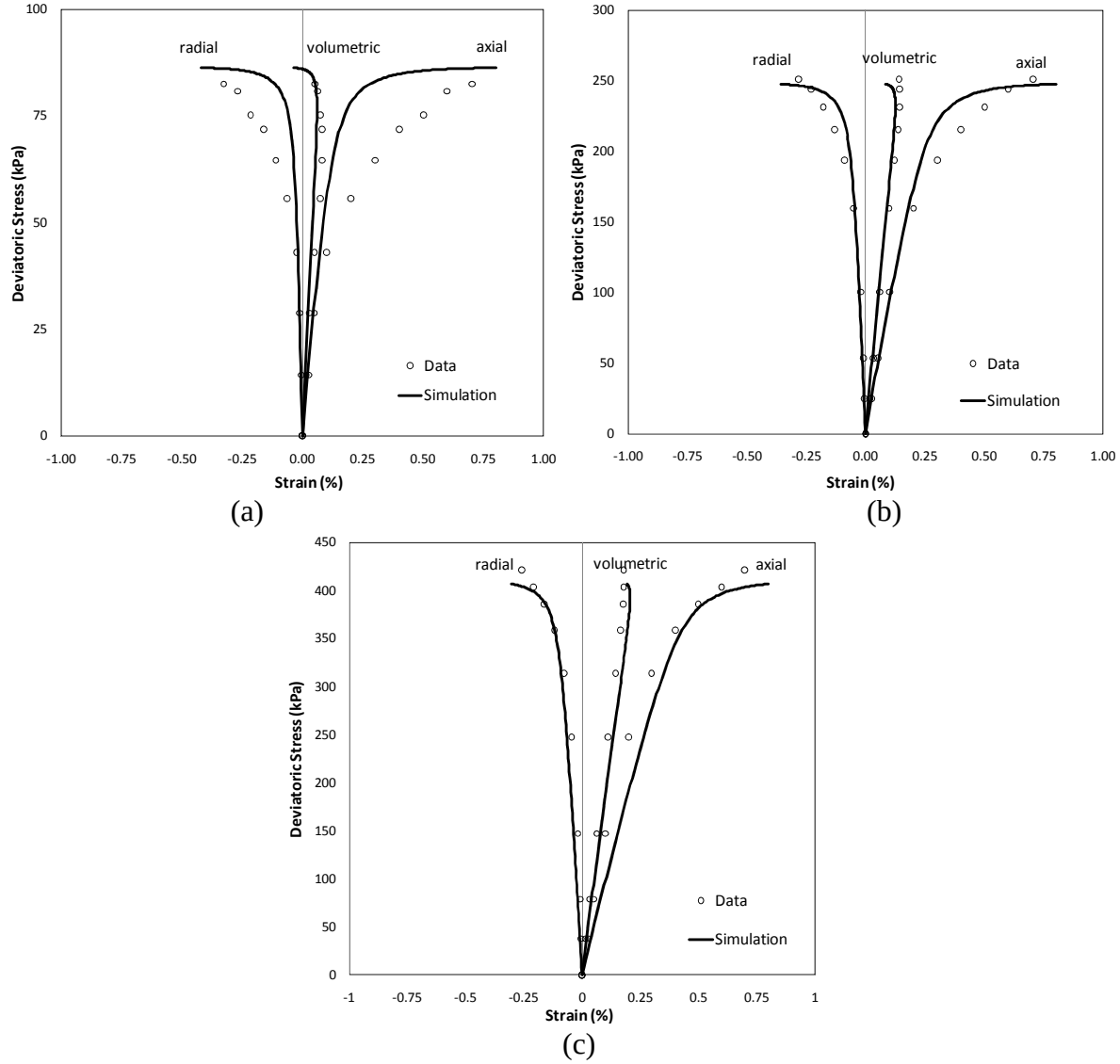

Fig. 2. Comparison of numerical simulations and experimental data in triaxial compression tests with confining pressures of 50 kPa (a), 150 kPa (b), and 250 kPa (c)

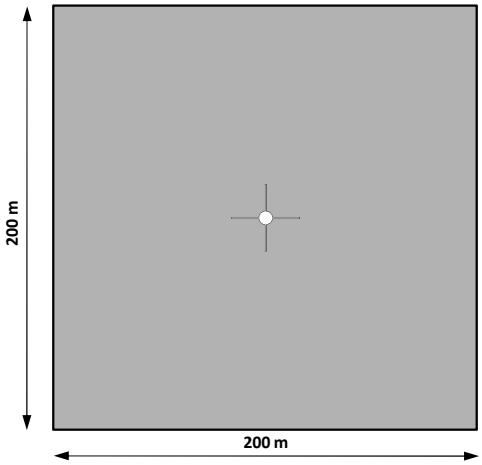

Fig. 3. Geometrical domain of the borehole and perforations

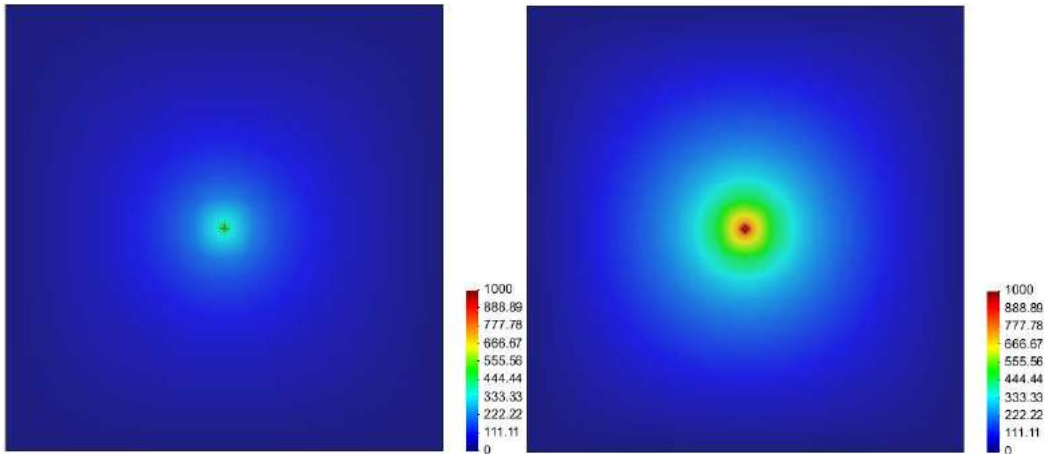

Fig. 4. Pore pressure change (in kPa) distribution at different production times: (left) 5 days; (right) 10 days

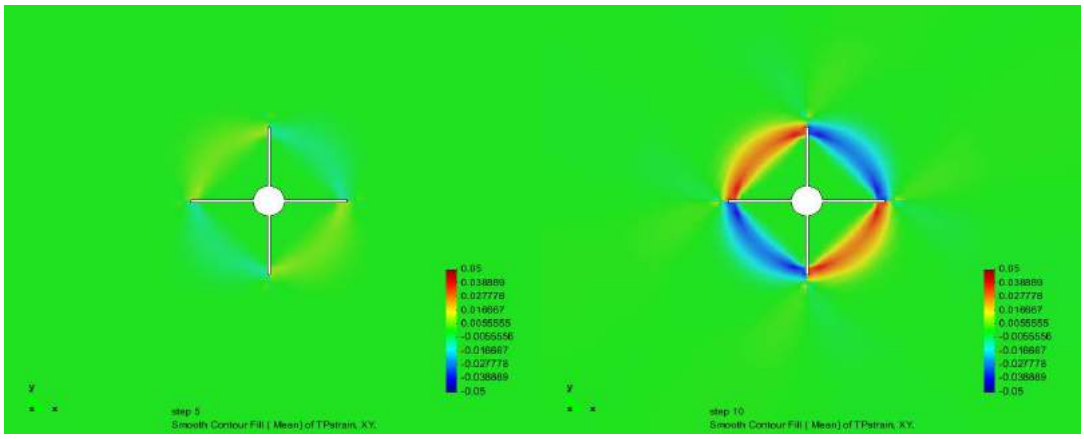

Fig. 5. Plastic shear strain XY distribution at different production times: (left) 5 days; (right) 10 days

As the drawdown pressure increased, the effective stresses tended to increase and the plastic failure criterion was violated. The development of plastic strains (volumetric and shear) was converted to damage. Fig. 6 shows the distribution of damage at different production times. The damage was related to the increase in porosity, which represented the amount of sand produced. The porosity increase reached 0.25 at the tips of the perforations after 10 days of drawdown. This finding indicated the formation of a cavity around the perforation tips. The eroded zones gradually grew in size and the growth and coalescence of the eroded zones gradually formed a ring joining the perforation tips.

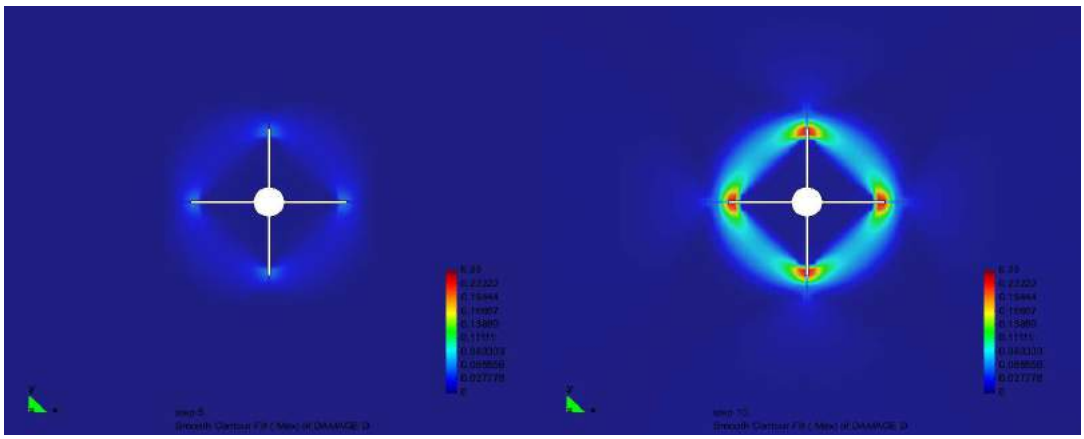

Fig. 6. Damage distribution at different production times: (left) 5 days; (right) 10 days

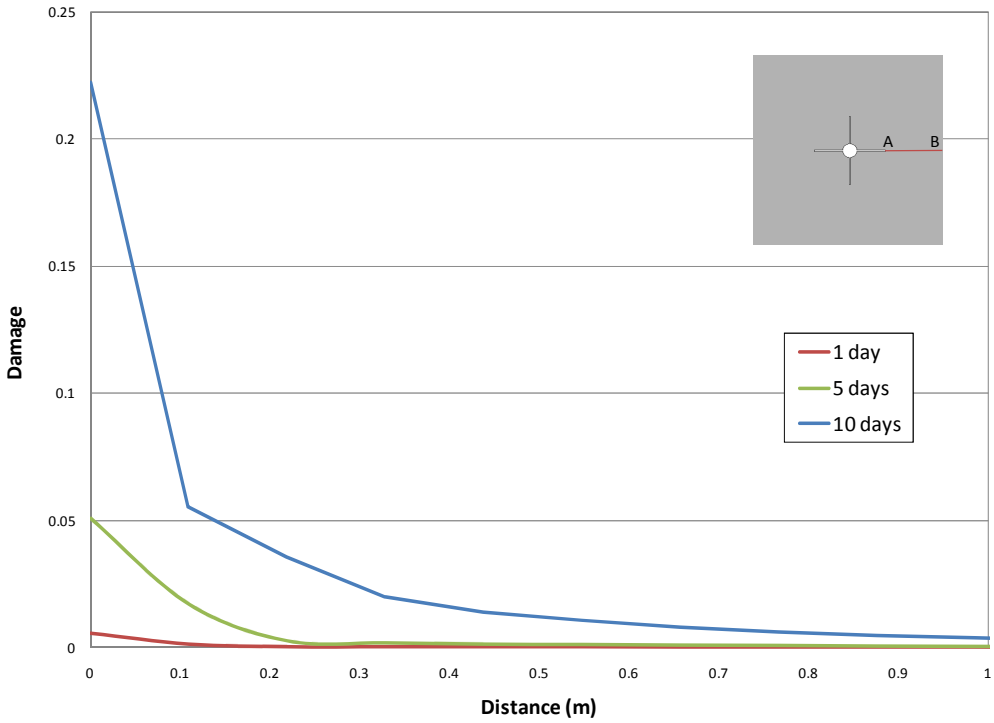

Fig. 7: Evolution of damage with production time around the perforations

The same example was modeled with an anisotropic initial stress state; the numerical results were different from those for the isotropic case. The plastic shear strain and damage distribution are shown in Fig. 8 and Fig. 9, respectively. There is less sand predicted for the perforations aligned with the initial maximum horizontal stress direction than for those aligned with the initial minimum horizontal stress direction.

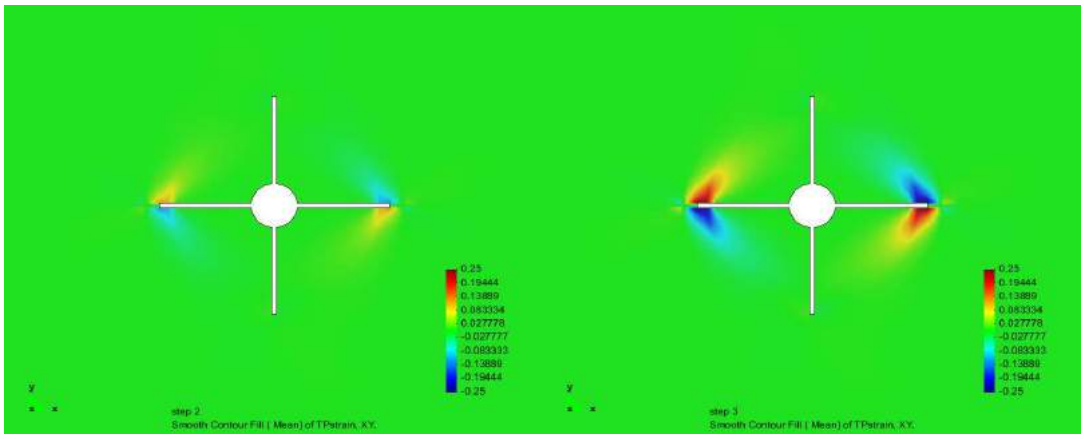

Fig. 8. Plastic shear strain XY distribution at different production times: (left) 5 days; (right) 10 days

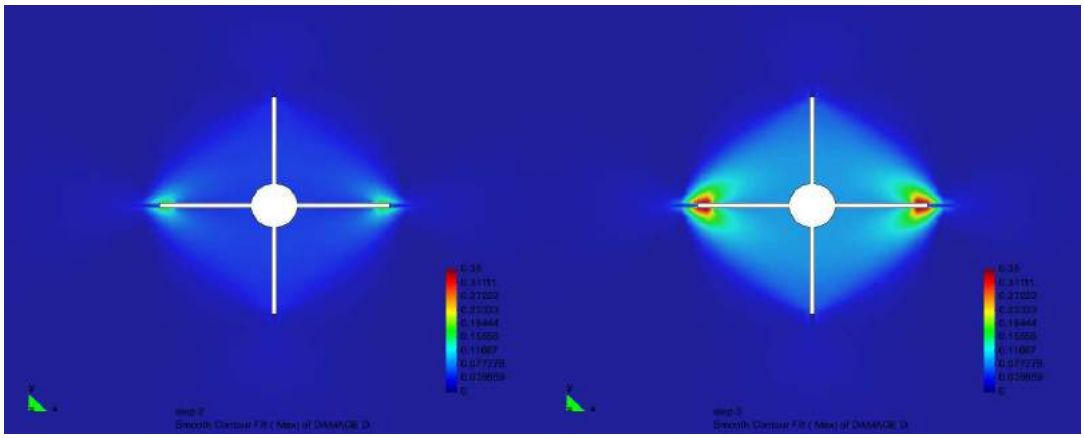

Fig. 9. Damage distribution at different production times: (left) 5 days; (right) 10 days

5 CONCLUSIONS

An elastoplastic damage constitutive model is proposed to predict sand production under a large range of stress changes. The performance of the model has been tested for sand material and has been validated with triaxial compression test data for different confining pressures. The behaviour of the material is correctly described by the model, including plastic deformation, induced material damage, degradation of strength properties, coupling between plasticity and damage, and volumetric compressibility and dilation. The model has been applied to a typical reservoir engineering problem. Two numerical examples have been investigated to show the influence of anisotropy of the initial preproduction stresses on the eroded zones. The production process has been modelled by applying a drawdown pressure at the location of the perforation zone. As a result of the distribution of pore pressure around the perforations, a damage zone developed at the perforation tips. The damage zone represents the zone of erosion and porosity increase.

ACKNOWLEDGEMENT

The authors thank Schlumberger for the permission to publish this paper.

REFERENCES

Chiarelli, A.S., Shao, J.F. & Hoteit, N. (2003), "Modelling of elastoplastic damage behaviour of a claystone". Int. J. of Plasticity, Vol. 19, 23–45.

Dragon, A. & Mroz, Z. (1979), "A continuum model for plastic-brittle behaviour of rock and concrete". Int. J. of Eng. Science, Vol. 17, 121–37.

Dusseault, M. (2007), "Cold Heavy Oil Production with Sand. In Petroleum Engineering Handbook, Volume VI: Emerging and Peripheral Technologies", ed H.R. Warner, Chapter 5. Society of Petroleum Engineers. Dallas.

Hayakawa, K. & Murakami, S. (1997), "Thermodynamical modeling of elastic-plastic damage and experimental validation of damage potential". Int. J. of Damage Mechanics 6, 333–363.

Ju, J.W. (1989), "On energy based coupled elastoplastic damage theories: constitutive modeling and computational aspects". Int. J. of Solids and Structures, Vol. 25(7), 803–33.

Kosar, K.M (1989), "Geotechnical Properties of Oil Sands and Related Strata". Ph.D. thesis, Department of Civil Engineering, University of Alberta, Canada.

Mohamad-Hussein, A. & Shao, J.F. (2007), "Modelling of elastoplastic behavior with non-local damage in concrete under compression". Computers and Structures, Vol. 85, 1757–1768.

Pietruszczak, S., Jiang, J. & Mirza, F.A. (1988), "An elastoplastic constitutive model for concrete". Int. J. of Solids and Structures, Vol. 24(7), 705–22.

Tremblay, B. (2009), "Cold flow: A multi-well cold production (CHOPS) model". J. of Canadian Pet. Tech., Vol. 48(24), 22-28.